

A Novel Electro-magnetic Transient Analysis Method Based on Orthogonal Projection Approach

Heng-Xu Ha¹, Yu-Zhen Tan¹, Bo Chen², and Z. Q. Bo³

¹Shandong University of Technology, Zibo 255049, China

²Dispatching Center, Shaanxi Electric Power Company, 710045, China

³AREVA T&D UK Limited, UK

Abstract— A novel electro-magnetic transient analysis technique by means of the orthogonal projection method for power system is proposed. Due to the approach criterion, the telegraph equation of the transmission line can be approximated to be the linear combination of a certain set of orthogonal basis, for example, the Daubechies basis. After projection onto orthogonal bases, the differential equations related to the voltage and current of transmission line transform to algebraic vector equations can be obtained. Then, the transients of the transmission system can be computed in the projection domain accordingly. EMTP simulation tests are presented which validate the method described.

1. INTRODUCTION

The Electro-magnetic transient analysis for power system, which is the basis of the transient protection, fault analysis, etc, plays an important role in the protection relaying. Modern Electro-magnetic transient analysis techniques are all based on the “characteristic method”, in which the analysis firstly proceeded in frequency domain by Laplace transformation and the time domain solution is obtained by taking the inverse Laplace transform [1, 2]. The Finite Element Method [3, 4] requires the line to be subdivided into a finite number of regions. This allows the telegraph equations to be converted into a one-dimensional differential vector equation related to variable t and the recursive formulas of each element can be obtained. Waveform relaxation techniques can avoid time domain convolution by solving the transmission line equations in frequency domain and employing the faster Fourier transform (FFT) to transform the results back and forth between time and frequency domain at each iteration. However this requires many datum points in order to avoid aliasing effects when fast signals are considered. Recently, growing attention has been devoted to wavelets in applied electromagnetic, mainly for the solution of Galerkin-like problems and as shape functions in the moment method to obtain sparse matrices [5, 6].

This paper presents a novel transient analysis technique for power system utilizing the orthogonal projection method. According to the approximation theory, signals can be approximated by the linear combination of a set of orthogonal basis. Similarly, the differential equations of transmission line can be written as the linear combination of a set of projection values with the orthogonal basis, in the following simulations, the Daubechies wavelet will be regarded as orthogonal basis. After projection onto orthogonal basis, the telegraph equation can transform into algebraic vector equations, based on that the projected equivalent models of each unit can be obtained. Then, the transients of the transmission system can be computed in the projection domain accordingly. EMTP simulation tests are presented which validate the method described.

2. THE BASIC PRINCIPLE

The crucial of transient analysis is the solution of the telegraph equation, shown as formula (1).

$$\begin{cases} -\frac{\partial u(x,t)}{\partial x} = R_0 i(x,t) + L_0 \frac{\partial i(x,t)}{\partial t} \\ -\frac{\partial i(x,t)}{\partial x} = G_0 u(x,t) + C_0 \frac{\partial u(x,t)}{\partial t} \end{cases} \quad (1)$$

R_0 , L_0 , G_0 , C_0 are respectively the series resistance and inductance, shunt conductance and capacitance of the line with the unit of the parameters respectively are ohm/km, H/km, S/km and F/km. $u(x,t)$, $i(x,t)$ are respectively voltage and current at location x of the line.

2.1. The Transmission Line Sampling Equation

Based on the orthogonal projection operator theory and multi-resolution analysis [7–10], one can get the projection equation on the orthogonal base, employing projection of differential operator $h_k = \int_{-\infty}^{\infty} \psi(t)\phi(t-k)dt$. The matrix form of Equation (1) can be expressed as follows:

$$\begin{cases} -\frac{d\mathbf{U}(x)}{dx} = \left(R_0\mathbf{E} + \frac{L_0}{T_s}\mathbf{H} \right) \mathbf{I}(x) = \mathbf{Z}\mathbf{I}(x) \\ -\frac{d\mathbf{I}(x)}{dx} = \left(G_0\mathbf{E} + \frac{C_0}{T_s}\mathbf{H} \right) \mathbf{U}(x) = \mathbf{Y}\mathbf{U}(x) \end{cases} \quad (2)$$

where, $\mathbf{Z} = R_0\mathbf{E} + L_0\mathbf{H}/T_s$; $\mathbf{Y} = G_0\mathbf{E} + C_0\mathbf{H}/T_s$; $\mathbf{U}(x) = [u(x, 1), u(x, 2), \dots, u(x, n)]^T$, $\mathbf{I}(x) = [i(x, 1), i(x, 2), \dots, i(x, n)]^T$ are respectively the sampling vector of voltage and current. The voltage and current are respectively sampled with the sampling interval T_s . \mathbf{E} is an unit matrix. \mathbf{H} is the projection transform matrix of the differential operator, which is consist of differential operator h_k .

Due to the limit of the paper space, the algorithm of computing the matrix \mathbf{H} is not listed in the paper; see the reference [10]. Formula (1) and (2) are called the transmission line sampling equation.

2.2. The Decoupling of Sampling Equation

Obviously, parameter matrix \mathbf{Z} and \mathbf{Y} in sampling Equation (2) is not a normative diagonal matrix, that is to say, the voltage and current at each interval are coupling with each other. To solve the matrix Equation (2), decoupling must be carried on to search a transformation matrix \mathbf{P} , which can convert \mathbf{Z} and \mathbf{Y} into diagonal matrix.

Theorem 1: The transformation matrix \mathbf{P} , which can convert parameter matrix \mathbf{Z} and \mathbf{Y} into diagonal matrix, is also the linear transform matrix of projection matrix \mathbf{H} .

Supposed that, $\mathbf{P}^{-1}\mathbf{H}\mathbf{P} = \Lambda$ is available, Λ is a normative diagonal matrix, then,

$$\mathbf{P}^{-1}\mathbf{Z}\mathbf{P} = \mathbf{P}^{-1} \left(R_0\mathbf{E} + \frac{L_0}{T_s}\mathbf{H} \right) \mathbf{P} = R_0\mathbf{E} + \frac{L_0}{T_s}\Lambda \quad (3a)$$

$$\mathbf{P}^{-1}\mathbf{Y}\mathbf{P} = \mathbf{P}^{-1} \left(G_0\mathbf{E} + \frac{C_0}{T_s}\mathbf{H} \right) \mathbf{P} = G_0\mathbf{E} + \frac{C_0}{T_s}\Lambda \quad (3b)$$

By above provement, it is known that matrix \mathbf{P} can convert \mathbf{Z} and \mathbf{Y} into diagonal matrix.

The decoupling equation can be obtained after sampling Equation (2) left-multiply linear transformation matrix \mathbf{P} .

$$\begin{cases} -\frac{d\mathbf{U}^{(m)}(x)}{dx} = \left(R_0\mathbf{E} + \frac{L_0}{T_s}\Lambda \right) \mathbf{I}^{(m)}(x) = \mathbf{Z}^{(m)}\mathbf{I}^{(m)}(x) \\ -\frac{d\mathbf{I}^{(m)}(x)}{dx} = \left(G_0\mathbf{E} + \frac{C_0}{T_s}\Lambda \right) \mathbf{U}^{(m)}(x) = \mathbf{Y}^{(m)}\mathbf{U}^{(m)}(x) \end{cases} \quad (4)$$

where, $Z^{(m)} = R_0E + \frac{L_0}{T_s}\Lambda$, $Y^{(m)} = G_0E + \frac{C_0}{T_s}\Lambda$, $\mathbf{U}_0^{(m)} = \mathbf{P}^{-1}\mathbf{U}_0$, $\mathbf{I}_0^{(m)} = \mathbf{P}^{-1}\mathbf{I}_0 \cdot \mathbf{U}_0$, \mathbf{I}_0 are respectively vectors consist of voltage and current sampling values at the beginning terminal of line.

3. THE SOLUTION OF SAMPLING EQUATION

After linear transformation, the voltage vector and current vector in Equation (4) is mutually independent.

First, the voltage and current sampling vectors, which are supposed to be known according to transmission line, left-multiply by linear transform matrix \mathbf{P}^{-1} . The solution is shown as formula (5).

$$\begin{cases} \mathbf{U}^{(m)}(x) = \exp(-\Gamma^{(m)}x) \left[\mathbf{U}_0^{(m)} + \mathbf{Z}_c^{(m)}\mathbf{I}_0^{(m)} \right] + \exp(\Gamma^{(m)}x) \left[\mathbf{U}_0^{(m)} - \mathbf{Z}_c^{(m)}\mathbf{I}_0^{(m)} \right] \\ \mathbf{I}^{(m)}(x) = \exp(-\Gamma^{(m)}x) \left[\left(\mathbf{Z}_c^{(m)} \right)^{-1} \mathbf{U}_0^{(m)} + \mathbf{I}_0^{(m)} \right] - \exp(\Gamma^{(m)}x) \left[\left(\mathbf{Z}_c^{(m)} \right)^{-1} \mathbf{U}_0^{(m)} - \mathbf{I}_0^{(m)} \right] \end{cases} \quad (5)$$

Following traditional wave impedance definition, $\mathbf{Z}_c^{(m)} = \sqrt{\mathbf{Z}^{(m)}(\mathbf{Y}^{(m)})^{-1}}$, $\Gamma^{(m)} = \sqrt{\mathbf{Z}^{(m)}\mathbf{Y}^{(m)}}$, which are respectively named as wave impedance matrix and broadcast parameter matrix.

However, the above calculation method is too complicated, not only for the decoupling matrix \mathbf{P} and diagonal matrix Λ are unknown, but for the edge effect is serious. This problem presses for solution. The calculation process will be simplified utilizing the traveling wave definition.

3.1. Forward and Backward Traveling Wave after Projection

Similar to traditional solution of telegraph equation, the new forward traveling wave (FTW) and the backward traveling wave (BTW) after employing the projection method are also defined as follows.

$$\begin{cases} \mathbf{F} = \mathbf{U} + \mathbf{Z}_C \mathbf{I} \\ \mathbf{B} = \mathbf{U} - \mathbf{Z}_C \mathbf{I} \end{cases} \quad (6)$$

Well then, based on Equation (5), the relationship between decoupled traveling wave (FTW and BTW) is:

$$\begin{cases} \mathbf{F}^{(m)}(x) = \exp(-\Gamma^{(m)}x) \mathbf{F}_0^{(m)} \\ \mathbf{B}^{(m)}(x) = \exp(\Gamma^{(m)}x) \mathbf{B}_0^{(m)} \end{cases} \quad (7)$$

While, it is difficult to calculate voltage and current just using decoupling traveling wave. Formula (7) left-multiply by matrix \mathbf{P} to carry on the linear inverse transform.

$$\begin{cases} \mathbf{F}(x) = \mathbf{P}\mathbf{F}^{(m)}(x) = \mathbf{P} \exp(-\Gamma^{(m)}x) \mathbf{P}^{-1} \mathbf{F}_0 = \exp(-\Gamma x) \mathbf{F}_0 \\ \mathbf{B}(x) = \mathbf{P}\mathbf{B}^{(m)}(x) = \mathbf{P} \exp(\Gamma^{(m)}x) \mathbf{P}^{-1} \mathbf{B}_0 = \exp(\Gamma x) \mathbf{B}_0 \end{cases} \quad (8)$$

where, $\mathbf{F}_0 = \mathbf{U}_0 + \mathbf{Z}_C \mathbf{I}_0$, $\mathbf{B}_0 = \mathbf{U}_0 - \mathbf{Z}_C \mathbf{I}_0$ are respectively the forward traveling wave and the backward traveling wave at the beginning terminal. Whilst, $\mathbf{Z}_C = \mathbf{P}\mathbf{Z}_c^{(m)}\mathbf{P}^{-1}$, $\Gamma = \mathbf{P}\Gamma^{(m)}\mathbf{P}^{-1}$ are wave impedance matrix and broadcast parameter matrix of transmission lines.

Above all, if the wave impedance matrix \mathbf{Z}_c and broadcast parameter matrix Γ is calculated firstly, according to the FTW and BTW of beginning terminal, the FTW and BTW at arbitray location on the line can be obtained. And then, the voltage and current at arbitray location on the line can also be calculated.

3.2. The Wave Impedance Matrix and Broadcast Parameter Matrix

Theorem 2: The above wave impedance matrix and broadcast parameter matrix are respectively corresponding to $\mathbf{Z}_C = \sqrt{\mathbf{Z}\mathbf{Y}^{-1}}$, $\Gamma = \sqrt{\mathbf{Z}\mathbf{Y}}$.

Proof: As we know that, $\mathbf{Z}_C = \mathbf{P}\mathbf{Z}_c^{(m)}\mathbf{P}^{-1}$, $\Gamma = \mathbf{P}\Gamma^{(m)}\mathbf{P}^{-1}$,

$$\begin{aligned} \mathbf{Z}_C^2 &= \mathbf{P}\mathbf{Z}_c^{(m)}\mathbf{P}^{-1}\mathbf{P}\mathbf{Z}_c^{(m)}\mathbf{P}^{-1} = \mathbf{P} \left[\mathbf{Z}_c^{(m)} \right]^2 \mathbf{P}^{-1} = \mathbf{P}\mathbf{Z}^{(m)} \left[\mathbf{Y}^{(m)} \right]^{-1} \mathbf{P}^{-1} \\ &= \left[\mathbf{P}\mathbf{Z}^{(m)}\mathbf{P}^{-1} \right] \left[\mathbf{P}\mathbf{Y}^{(m)}\mathbf{P}^{-1} \right]^{-1} = \mathbf{Z}\mathbf{Y}^{-1} \end{aligned} \quad (9)$$

$$\begin{aligned} \Gamma^2 &= \mathbf{P}\Gamma^{(m)}\mathbf{P}^{-1}\mathbf{P}\Gamma^{(m)}\mathbf{P}^{-1} = \mathbf{P} \left[\Gamma^{(m)} \right]^2 \mathbf{P}^{-1} = \mathbf{P}\mathbf{Z}^{(m)}\mathbf{Y}^{(m)}\mathbf{P}^{-1} \\ &= \left[\mathbf{P}\mathbf{Z}^{(m)}\mathbf{P}^{-1} \right] \left[\mathbf{P}\mathbf{Y}^{(m)}\mathbf{P}^{-1} \right] = \mathbf{Z}\mathbf{Y} \end{aligned} \quad (10)$$

The surge impedance and propagation matrix can be calculated off-line, for the fixed point, the two matrices are constants.

4. EMTP SIMULATION TESTS

The simulated transmission network shown in Fig. 1 is simple, only the single source and the single-phase line are considered. The process narrates in detail as follows. First, calculate the voltage and current in node M and N by EMTP. Second, use the new method to calculate the voltage and current of node N according to the value of node M. Finally, compare the result calculating by the new method with that by EMTP in node N.

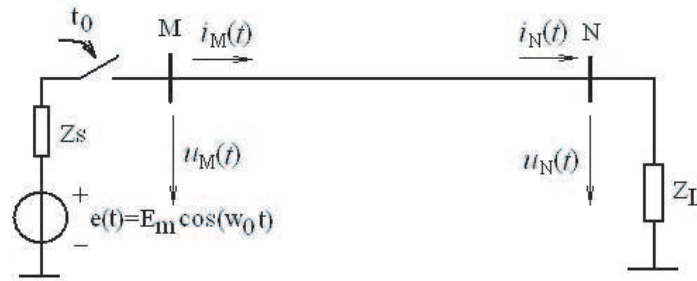


Figure 1: Simulation model.

The parameters of the simulation system are listed as follows: $Z_s = 1 + j32 \text{ Ohm}$; $E_m = 408.2 \text{ kV}$; the length of transmission line $L = 60 \text{ km}$; the sampling period: $T_s = 1.25E - 5 \text{ s}$; the distributed-parameters: $R_0 = 6.614434E - 02 \text{ (Ohm/km)}$; $L_0 = 7.244206E - 01 \text{ (Ohm/km)}$; $C_0 = 2.093913E - 6 \text{ (S/km)}$; $G_0 = 0$.

The simulation result is shown in Fig. 2 as the load is a pure resistance (200 Ohm) in the receiving end.

The curve of the calculation result and error about voltage are shown in Fig. 2(a). The waveform 1 and 2 are calculated by EMTP, which voltage respectively of node M and N. The waveform 3 is the curve of node N which is calculated using the new model according to the value of Node M.

The reason why the surge appears in the end of the waveform 3 originates from the edge effect which arises from the time window of base functions. The duration of the surge is associated with the supported field of orthogonal base functions. The simulation test of current is shown in Fig. 2(b). Similarly, the waveform 1 and 2 are calculated by EMTP, however, waveform 3 is calculated by means of new method.

Form Fig. 2, one can concludes that the new algorithm is accuracy, for the error of voltage and current is respectively less than 1.5 percent and 0.5 percent if the edge-effect is not taken account.

The simulation result shown in Fig. 3 as the load is an inductance ($j200 \text{ Ohm}$) in the end of transmission line. The error of voltage and current is respectively less than 0.6 percent and 0.7 percent. Therefore, the novel algorithm presented in this paper is correct and accuracy.

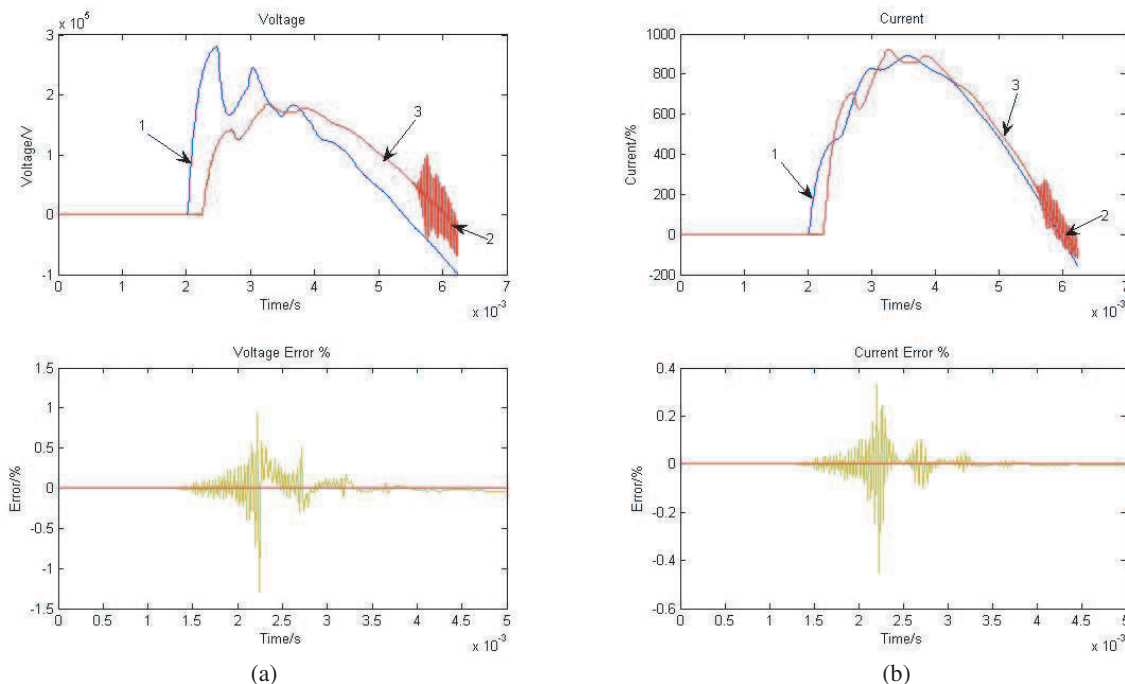


Figure 2: Simulation results in case of pure resistance load.

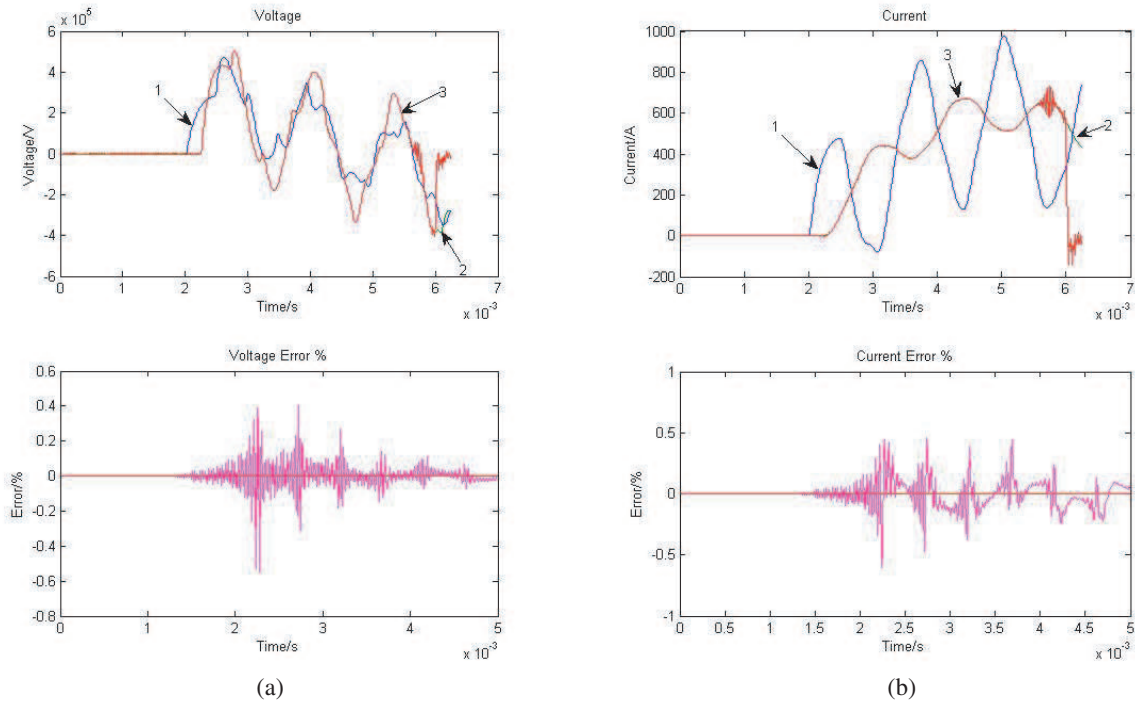


Figure 3: Simulation results in case of pure resistance load.

5. CONCLUSIONS

A novel transient analysis method is proposed, breaking through the traditional techniques, by means of projection operators for the distribution parameter lines. It can be interfaced with the on-line calculation that means the convolution is not necessary any more. Time-domain simulations based on the new model show the good agreement with those calculated by EMTP. This new method is primarily intended for the transient analysis. It can also be used to protective relaying based on the distributed-parameter line model and accurate fault location.

ACKNOWLEDGMENT

The project is supported by National Natural Science Foundation of China (No. 50707002) and Shandong Educational Department Foundation (No. J06B06).

REFERENCES

1. Lin, S. and E. S. Kuh, "Transient simulation of lossy interconnections based on the recursive convolution formulation," *IEEE Trans. on Circuits and Systems-I: Fundamental and Applications*, Vol. 39, No. 11, 879–892, Nov. 1992.
2. Marti, J. R., "Accurate modeling of frequency dependent transmission lines in electromagnetic transient simulation," *IEEE Trans. Power Appar. Syst.*, Vol. 101, 147–155, Jan. 1982.
3. Lee, S. Y., A. Konrad, and R. Saldanha, "Lossy transmission line transient analysis by the finite element method," *IEEE Trans. on Magnetics*, Vol. 29, No. 2, 1730–1732, Mar. 1993.
4. Dao, J. and J. Jin, "A general approach for the stability analysis of the time domain finite element method for electromagnetic simulations," *IEEE Trans. Ant. Prop.*, Vol. 50, No. 11, 1624–1632, 2002.
5. Amaratunga, K. and J. Williams, "Wavelet-Galerkin solution for one-dimensional partial differential equations," *Int. Jour. for Num. Meth. in Eng.*, Vol. 32, 2703–2716, 1994.
6. Pan, G., "Orthogonal wavelets with application in electromagnetism," *IEEE Trans. on Magnetics*, Vol. 32, 975–983, 1996.
7. Chui, C. K., *Wavelets: A Tutorial in Theory and Applications*, Academic Press, New York, 1992.
8. Daubechies, I., "The wavelet transform, time-frequency localization and signal analysis," *IEEE Trans. on Information Theory*, Vol. 36, No. 5, 961–1005, Sept. 1990.

9. Mallat, S. and S. Zhong, “Characterization of signals from multi-scale edge,” *IEEE Trans. on PAMI*, Vol. 14, No. 7, 710–732, Jul. 1992.
10. Saito, N. and G. Beylkin, “Multiresolution representations using the auto-correlation functions of compactly supported wavelets,” *Proceedings of ICASSP-92*, No. 4, 381–384, 1992.

Analytical Expressions of the Magnetic Field Created by Tile Permanent Magnets of Various Magnetization Directions

R. Ravaud and G. Lemarquand

LAUM, UMR CNRS 6613, Université du Maine, Ave Olivier Messiaen, Le Mans 72085, France

Abstract— This paper presents a thorough study of the magnetic field created by tile permanent magnets uniformly magnetized in air. To do so, we use the coulombian model for determining the analytical expressions of the three magnetic field components created by the tile magnets. Moreover, various magnetization directions are considered. Indeed, the direction of the magnetization can be radial, tangential or intermediate between radial and tangential. Thus, this analytical study encompasses most of the magnetization possibilities generally encountered in electrical engineering applications.

1. INTRODUCTION

The modeling of the magnetic field produced by tile permanent magnets was studied by many authors [1–3]. Several analytical methods can be used for calculating the three components of the magnetic field created by permanent magnets [4–9]. According to the coulombian model, the magnets are represented by fictitious magnetic charge densities [10, 11]. This model implies the calculation of surface and volume integrals that represent the surface charge densities and the volume charge densities. We propose in this paper to use the coulombian model for studying the magnetic field created by tile permanent magnets of various magnetization directions. For each configuration studied, all the magnetic charges are taken into account. Consequently, our analytical calculations have been performed without using any simplifying assumption. It has to be noted that such analytical calculations are possible because the tile permanent magnets considered are in air [12, 13] and the structures using these tile magnets are ironless [14].

Then, all the expressions given are expressed in a fully analytical part and a semi-analytical part. For each component, the semi-analytical part cannot be integrated analytically because all the polarizations considered are uniform. Consequently, the expressions cannot be expressed in terms of elliptic integrals of the first, second or third kind.

As a result, the given expressions allow the calculation of the three magnetic field components at any point in the space, may it be outside the magnet as well as inside it. Furthermore, the computational cost is low and so, parametric optimizations can be carried out. Indeed, tile permanent magnets can be assembled in various ways depending on the intended application. For example, radially magnetized tiles can be assembled to form a radially magnetized ring magnet and axially magnetized ring magnets can also be achieved in a similar way with axially magnetized tiles.

Finally, tile permanent magnets of different magnetizations can be associated for the design of Halbach structures and ring permanent magnets can be stacked for the design of magnetic bearings. By using such analytical expressions, the magnetic field created by such assemblies can always be determined accurately and structures using such tile permanent magnets can also be optimized with regard to criteria applying to the magnetic field values and its spatial variations.

2. NOTATION AND GEOMETRY

The geometry considered and the parameters are shown in Fig. 1. We consider one tile permanent magnet whose polarization is given by the angles θ and α . Its angular width is $\theta_2 - \theta_1$, its radial width is $r_2 - r_1$ and its height is $z_2 - z_1$. In the coulombian approach, we must determine the fictitious magnetic charges that are located on the faces of the tile permanent magnet. In our configuration, the polarization is always uniform. Consequently, there are only surface charge densities that are given by the scalar product between the polarization vector \vec{J} and the four normal units. We use two coordinate systems for calculating the magnetic field produced by the tile permanent magnet. The local coordinate system is (O', \vec{i}, \vec{j}) and the global coordinate system is $(O, \vec{u}_x, \vec{u}_y)$. In the cartesian coordinate system (O', \vec{i}, \vec{j}) , the vector \vec{J} is expressed as follows:

$$\vec{J} = J \cos(\alpha) \vec{i} + J \sin(\alpha) \vec{j} \quad (1)$$

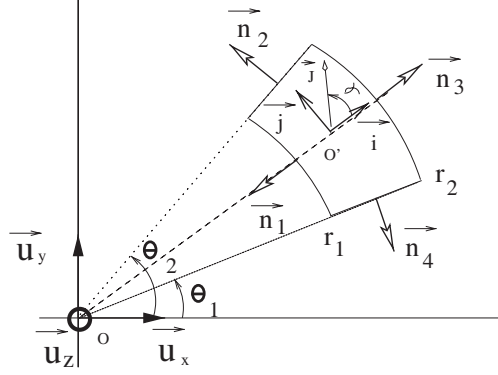


Figure 1: Tile whose polarization is directed in an arbitrary direction.

The relations between the cartesian coordinate systems (O', \vec{i}, \vec{j}) and $(O, \vec{u}_x, \vec{u}_y)$ are the following:

$$\begin{aligned}\vec{i} &= \cos\left(\frac{\theta_1 + \theta_2}{2}\right) \vec{u}_x + \sin\left(\frac{\theta_1 + \theta_2}{2}\right) \vec{u}_y \\ \vec{j} &= -\sin\left(\frac{\theta_1 + \theta_2}{2}\right) \vec{u}_x + \cos\left(\frac{\theta_1 + \theta_2}{2}\right) \vec{u}_y\end{aligned}\quad (2)$$

By using (1) and (2), we obtain:

$$\vec{J} = J \cos(\alpha) \left(\cos\left(\frac{\theta_1 + \theta_2}{2}\right) \vec{u}_x + \sin\left(\frac{\theta_1 + \theta_2}{2}\right) \vec{u}_y \right) + J \sin(\alpha) \left(-\sin\left(\frac{\theta_1 + \theta_2}{2}\right) \vec{u}_x + \cos\left(\frac{\theta_1 + \theta_2}{2}\right) \vec{u}_y \right) \quad (3)$$

We obtain

$$\vec{J} = J \cos\left(\alpha + \frac{\theta_1 + \theta_2}{2}\right) \vec{u}_x + J \sin\left(\alpha + \frac{\theta_1 + \theta_2}{2}\right) \vec{u}_y \quad (4)$$

The four normal units are defined as follows:

$$\begin{aligned}\vec{n}_1 &= -\cos(\theta) \vec{u}_x - \sin(\theta) \vec{u}_y \\ \vec{n}_2 &= -\sin(\theta_2) \vec{u}_x + \cos(\theta_2) \vec{u}_y \\ \vec{n}_3 &= +\cos(\theta) \vec{u}_x + \sin(\theta) \vec{u}_y \\ \vec{n}_4 &= +\sin(\theta_1) \vec{u}_x - \cos(\theta_1) \vec{u}_y\end{aligned}\quad (5)$$

By using the relation $\vec{J} \cdot \vec{n}_i$ for $i = 1 \dots 4$, we obtain the four fictitious magnetic pole surface densities σ_1^* , σ_2^* , σ_3^* and σ_4^*

$$\begin{aligned}\sigma_1^* &= -J \cos\left(\theta - \alpha - \frac{\theta_1 + \theta_2}{2}\right) \\ \sigma_2^* &= -J \sin\left(\frac{\theta_2 - \theta_1}{2} - \alpha\right) \\ \sigma_3^* &= J \cos\left(\theta - \alpha - \frac{\theta_1 + \theta_2}{2}\right) \\ \sigma_4^* &= J \sin\left(\frac{\theta_1 - \theta_2}{2} - \alpha\right)\end{aligned}\quad (6)$$

Therefore, we have determined the four magnetic charge surface densities that are located on the four faces of the tile permanent magnet. The magnetic field can be determined from the scalar potential $\phi(r, \theta, z)$ produced by the four faces of the tile permanent magnet.

$$d\phi(r, \theta, z) = \sum_{z=1}^4 G_z(\vec{r}, \vec{r}') \sigma_z^* dS_z \quad (7)$$

where $G_z(\vec{r}, \vec{r}')$ is the three-dimensional Green's function applied to the four surfaces and dS_z is the elementary surface of each face of the tile permanent magnet. The associated magnetic field is determined as follows:

$$\vec{H}(r, \theta, z) = -\vec{\nabla}\phi(r, \theta, z) = H_r(r, \theta, z)\vec{u}_r + H_\theta(r, \theta, z)\vec{u}_\theta + H_z(r, \theta, z)\vec{u}_z \quad (8)$$

Thus, the three magnetic field component $H_r(r, \theta, z)$, $H_\theta(r, \theta, z)$ and $H_z(r, \theta, z)$ are calculated by projecting $-\vec{\nabla}\phi(r, \theta, z)$ on the four directions \vec{u}_r , \vec{u}_θ and \vec{u}_z .

2.1. Expression of the Radial Field Produced by a Tile Permanent Magnet of Various Magnetization Direction

The radial component $H_r(r, \theta, z)$ of the magnetic field produced by a tile permanent magnet of various magnetization direction can be expressed as follows:

$$\begin{aligned} H_r(r, \theta, z) = & \frac{J}{4\pi\mu_0} \left(\sin\left(\frac{\theta_1 - \theta_2}{2} + \alpha\right) f(\theta_1) + \sin\left(\frac{\theta_1 - \theta_2}{2} - \alpha\right) f(\theta_2) \right) \\ & + \frac{J}{4\pi\mu_0} \sum_{i=1}^2 \sum_{k=1}^2 (-1)^{(i+k)} r_i (-z + z_k) \mathbf{N}[\tilde{\theta}] \end{aligned} \quad (9)$$

where

$$\begin{aligned} f(\theta_k) = & \sum_{i=1}^2 \sum_{k=1}^2 (-1)^{(i+k)} (-\cos(\theta - \theta_j) \log[X_j] + \sin(\theta - \theta_j) \arctan[Y_j]) \\ \mathbf{N}[\tilde{\theta}] = & \int_{\theta_1}^{\theta_2} \frac{(r - r_i \cos(\theta - \tilde{\theta})) \cos\left(\alpha + \frac{\theta_1 - \theta_2}{2} - \tilde{\theta}\right)}{(r^2 + r_i^2 - 2rr_i \cos(\theta - \tilde{\theta})) \epsilon(\tilde{\theta})} d\tilde{\theta} \\ X_j = & z - z_k + \epsilon(\theta_j) \\ Y_j = & \frac{(z - z_k)(r_i - r \cos(\theta - \theta_j))}{r \sin(\theta - \theta_j) \epsilon(\theta_j)} \end{aligned} \quad (10)$$

$$(11)$$

with

$$\epsilon(\beta) = \sqrt{r^2 + r_i^2 + (z - z_k)^2 - 2rr_i \cos(\theta - \beta)} \quad (12)$$

2.2. Expression of the Azimuthal Field Produced by a Tile Permanent Magnet of Various Magnetization Direction

The azimuthal component $H_\theta(r, \theta, z)$ of the magnetic field produced by a tile permanent magnet of various magnetization direction can be expressed as follows:

$$\begin{aligned} H_\theta(r, \theta, z) = & \sin\left(\frac{\theta_1 - \theta_2}{2} - \alpha\right) h(\theta_1) + \sin\left(\frac{\theta_1 - \theta_2}{2} + \alpha\right) h(\theta_2) \\ & + \frac{J}{4\pi\mu_0} \int_{\theta_1}^{\theta_2} \sum_{i=1}^2 \sum_{k=1}^2 \frac{r_i^2 (-z + z_k) \cos\left(\alpha + \frac{\theta_1 - \theta_2}{2} - \tilde{\theta}\right) \sin(\theta - \tilde{\theta})}{(r^2 + r_i^2 - 2rr_i \cos(\theta - \tilde{\theta})) \epsilon(\tilde{\theta})} d\tilde{\theta} \end{aligned} \quad (13)$$

$$h(\theta_j) = \frac{J}{4\pi\mu_0} \sum_{i=1}^2 \sum_{k=1}^2 \sin(\theta - \theta_j) \log[X_j] - \cos(\theta - \theta_j) \arctan[Y_j] \quad (14)$$

2.3. Expression of the Axial Field Produced by a Tile Permanent Magnet of Various Magnetization Direction

The axial component $H_z(r, \theta, z)$ of the magnetic field produced by a tile permanent magnet of various magnetization direction can be expressed as follows:

$$\begin{aligned}
 H_z(r, \theta, z) = & \frac{J}{4\pi\mu_0} \left(\sin \left(\frac{\theta_1 - \theta_2}{2} - \alpha \right) g(\theta_2) + \sin \left(\frac{\theta_1 - \theta_2}{2} + \alpha \right) g(\theta_1) \right) \\
 & + \frac{J}{4\pi\mu_0} \int_{\theta_1}^{\theta_2} \sum_{i=1}^2 \sum_{k=1}^2 \frac{r_i \cos \left(\alpha + \frac{\theta_1 - \theta_2}{2} - \tilde{\theta} \right)}{\epsilon(\theta_j)} d\tilde{\theta} \\
 g(\theta_j) = & \sum_{i=1}^2 \sum_{k=1}^2 \log [r_i - r \cos(\theta - \theta_j) + \epsilon(\theta_j)]
 \end{aligned} \tag{15}$$

3. APPLICATION : STRUCTURE COMPOSED OF TILE PERMANENT MAGNETS WITH ROTATING POLARIZATIONS

We illustrate now the interest of using an exact analytical expression of the magnetic field produced by tile permanent magnets of various magnetization directions in the case of the structure shown in Fig. 2. The structure is composed of 16 tile permanent magnets with rotating polarizations. As each tile is uniformly magnetized, some specific effects appear on account of the curvature of the tile and the uniform polarization. In Fig. 3, the radial field is represented versus the angle θ . Consequently, the radial field produced by such a configuration is not smooth but presents some little discontinuities, as shown in Fig. 3.

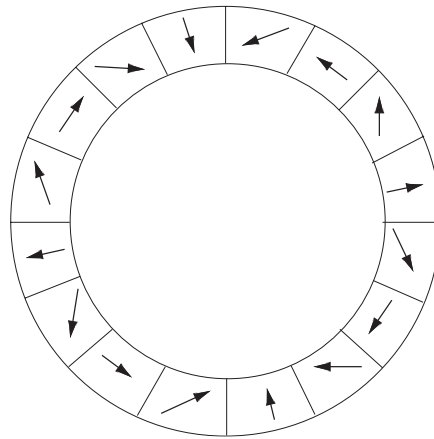


Figure 2: Structure using 16 tile permanent magnets with rotating polarizations.

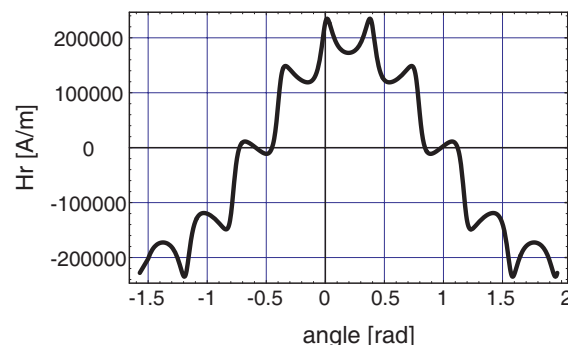


Figure 3: Exact radial field produced by a structure using tile permanent magnets with rotating polarizations, $r_2 = 0.028$ m, $r_1 = 0.025$ m, $r = 0.024$ m, $z_2 - z_1 = 0.003$ m, $z = 0.0015$ m, $J = 1$ T.

4. CONCLUSION

We have presented general analytical expressions of the magnetic field produced by tile permanent magnets of various magnetization directions. The expressions are always given in an analytical part and a semi-analytical part. Such expressions cannot be expressed in terms of elliptic integrals because we consider uniform polarizations, as it is generally the case in practice. Such expressions have a low computational cost and can be used for the study of Halbach structures.

REFERENCES

1. Babic, S. I. and C. Akyel, "Improvement in the analytical calculation of the magnetic field produced by permanent magnet rings," *Progress In Electromagnetics Research C*, Vol. 5, 71–82, 2008.
2. Ravaud, R., G. Lemarquand, V. Lemarquand, and C. Depollier, "Discussion about the analytical calculation of the magnetic field created by permanent magnets," *Progress In Electromagnetics Research B*, Vol. 11, 281–297, 2009.
3. Ravaud, R., G. Lemarquand, V. Lemarquand, and C. Depollier, "Magnetic field produced by a tile permanent magnet whose polarization is both uniform and tangential," *Progress In Electromagnetics Research B*, Vol. 13, 1–20, 2009.
4. Akyel, C., S. I. Babic, and M.-M. Mahmoudi, "Mutual inductance calculation for non-coaxial circular air coils with parallel axes," *Progress In Electromagnetics Research*, PIER 91, 287–301, 2009.
5. Mayergoyz, D. and E. P. Furlani, "The computation of magnetic fields of permanent magnet cylinders in the electrophotographic process," *IEEE Trans. Magn.*, Vol. 33, No. 3, 2317–2321, 1993.
6. Ravaud, R., G. Lemarquand, V. Lemarquand, and C. Depollier, "Analytical calculation of the magnetic field created by permanent-magnet rings," *IEEE Trans. Magn.*, Vol. 44, No. 8, 1982–1989, 2008.
7. Ravaud, R. and G. Lemarquand, "Analytical expression of the magnetic field created by tile permanent magnets tangentially magnetized and radial currents in massive disks," *Progress In Electromagnetics Research B*, Vol. 13, 309–328, 2009.
8. Azzerboni, B. and E. Cardelli, "Magnetic field evaluation for disk conductors," *IEEE Trans. Magn.*, Vol. 29, No. 6, 2419–2421, 1993.
9. Rakotoarison, H. L., et al., "Using coulombian approach for modeling scalar potential and magnetic field of a permanent magnet with radial polarization," *IEEE Trans. Magn.*, Vol. 43, No. 4, 1261–1264, 2007.
10. Ravaud, R., et al., "Permanent magnet couplings: Field and torque three-dimensional expressions based on the coulombian model," *IEEE Trans. Magn.*, Vol. 45, No. 4, 1950–1958, 2009.
11. Charpentier, J. F. and G. Lemarquand, "Calculation of ironless permanent magnet coupling using semi-numerical magnetic pole theory method," *COMPEL*, Vol. 20, No. 1, 72–89, 2001.
12. Selvaggi, J. P., et al., "Calculating the external magnetic field from permanent magnets in permanent-magnet motors-an alternative method," *IEEE Trans. Magn.*, Vol. 40, No. 4, 3278–3285, 2004.
13. Zhilichev, Y., "Calculation of magnetic field of tubular permanent magnet assemblies in cylindrical bipolar coordinates," *IEEE Trans. Magn.*, Vol. 43, No. 7, 3189–3195, 2007.
14. Conway, J., "Inductance calculations for noncoaxial coils using bessel functions," *IEEE Trans. Magn.*, Vol. 43, No. 3, 1023–1034, 2007.

A New Electromagnetic Parameter Model of Giant Magnetostriction Material

Liyi Li, Baiping Yan, and Chengming Zhang

Department of Electrical Engineering, Harbin Institute of Technology, Harbin, China

Abstract— This paper presents a new electromagnetic parameter model that use parameter of permeability and mechanical compliance denotes the conversion between the energy of magnetic and mechanical. Based on the parameter exchange of initial magnetic-mechanical equation, we clearly expressed the micro-model of magnetostriction. Additionally, propose an inter-uniformity assumption between the parameter of permeability, mechanical compliance and the magnetization of material. Through analyze the equations of dynamic micro-energy, educe a result that the stress coefficient of permeability and magnetic field of mechanical compliance is the most important factors of output response. The validity of the electromagnetic parameter model is illustrated by experiment, and the data of parameters exchange can clearly express the relation of magnetization and output response.

1. INTRODUCTION

The linear constitutive piezomagnetic equations of giant magnetostriction material (GMM) describe the conversion between the magnetic and mechanical energy of material through the parameter of magnetoelastic coupling coefficients. But the analyze of magnetoelastic coupling coefficients is just in the phase of concept, and have not carefully study in the space of the energy exchange between the magnetic and mechanical, Additionally, the piezomagnetic equations can't express the micro-model and inner mechanism of material, restrict the used of material in precision mechanical process, micro-orientation system, etc.

The parameter of material is the most intuitionistic expression of the material magnetization, we can analyze coupling of parameters to investigate the magnetization of material and output response. This paper studies the relation between permeability, mechanical compliance and input parameters, analyze the electromagnetic parameter model of material, and explain the veracity of the model and parameter assumption.

2. NEW ELECTROMAGETIC PARAMETER MODEL

The resent model of GMM material is the piezomagnetic equation [1], which is depicted in Equation (1), the equation clearly describe the relation between the input parameter (magnetic field and input stress) and out parameter (stress and strain), and the energy change is illuminated through the parameter of piezomagnetic coefficient, but the equation not clearly describe the inner energy change and the relationship of all parameter, the parameter of the equation, for example, permeability, mechanical compliance, is change with the energy change process, the permeability and mechanical compliance in the equation is just one static parameter of the dynamic process, so we can not truly depict the dynamic change of energy [2].

$$\begin{cases} \varepsilon = \frac{\sigma}{EH} + d_{33}H \\ B = d_{33}\sigma + \mu^\sigma H \end{cases} \quad (1)$$

This article used the dynamic parameter of permeability and mechanical compliance to declare the process of magnetization and mechanical energy output. The Equation (2) is the new description of the material model, σ_i , H_e is the inner stress and magnetic field of material, $S(\sigma, H)$ $\mu(\sigma, H)$ is the mechanical compliance and permeability, because of the deflection of magnetic domain and magnetocrystalline anisotropy of inner stress in material, there will generate a huge inner stress in the action of pre-pressure and field, compare with the inner stress and pre-pressure, the output stress of the material depend on these two stress.

$$\begin{cases} \varepsilon = S(\sigma, H) \cdot \sigma_i \\ B = \mu(\sigma, H) \cdot H_e \end{cases} \quad (2)$$

In the material, the effect field can be described in the Equation (3), H_σ is the magnetic effect of stress. σ_i , H_e is the piezomagnetic behave of the material, and we can describe the piezomagnetic

energy change through the parameter of $S(\sigma, H)$ and $\mu(\sigma, H)$, mechanical compliance is the behave of mechanism stiffness of material, permeability is the behave of the magnetization ability, so we can know the process of mechanical output and magnetization through these parameter, and the micro-energy model of material can clearly be defined by the coupling of parameter [3].

$$H_e = H + \alpha M + H_\sigma \quad (3)$$

The deflection of magnetic domain is the idea of the magnetization in the area of magnetism, but in the area of mechanism, it means the stiffness of material. In the action of magnetic field, as the permeability of material is very small, the magnetization curve of GMM will be linear, and the change of permeability in the process of magnetization will not very large, but the stiffness of material will have a huge change, so it will have a big output stress and strain [4]. In the action of pre-pressure, the permeability will have a huge change, which means the magnetization ability of material will change, and the magnetic domain deflect to the direction of perpendicular field, which will have a bigger stress in the action of huge field, and proper pre-pressure can make material have a optimization mechanical output [5]. So dynamic process of energy change can be described by the new parameter model, which shares the effect of input magnetic field and stress into the inner parameter, and we can use the parameter of permeability and mechanical compliance to describe the effect of piezomagnetic coefficient d_{33} in the process of energy change.

3. INTER-UNIFORMITY ASSUMPTION OF PARAMETER

From the mechanism of deflection of magnetic domain, permeability is behave of the magnetization ability of material and mechanical compliance is behave of the mechanism stiffness of material, the coupling of these two parameter is behave of the micro-energy change, so we can use the change of these two parameter to analyze the dynamic process. This article proposes an inter-uniformity assumption between the parameter of permeability, mechanical compliance and the magnetization of material, and uses the parameters to analyze the magnetization of material.

Through compare the input and output loads, the dynamic process of energy coupling can be divide into micro-small-parts, which will have two static procedure, one is the constant input loads (constant stress and field), the other is the constant output loads (constant strain and magnetic), so we can use the static parameter of micro-small-parts to analyze the process. The state of parameter can be described in the experiment, and in the process of magnetization, the magnetic domain will deflect, the permeability of material will decrease and the stiffness of material will change in the action of inverse piezomagnetic effect, which is accordance with the magnetization curve and the hinder of magnetization.

4. COUPLING OF PARAMETERS

In the dynamic process of material, we can use the static change of parameters to analyze and divide the process into small parts, so the change of static parameter analyze will be the most important thing to describe the dynamic model. For each micro-parts, there are two static state, one is constant stress and field, the other is constant strain and magnetic density, and the micro-model is the change of parameters between these two state, which submit the principle of thermodynamics energy that the free energy in material is change all the times, but it is the lowest when the material in the state of stable. Here use the micro-model to analyze the change of thermodynamics energy.

In the action of field, the magnetization change from moment t_1 to $t_1 + \Delta t$, and here import the function of G to analyze the change of internal energy, which can be express:

$$dG = -\varepsilon d\sigma + \mu_0 H dM - S dT \quad (4)$$

Not consider the effect of temperature, the Equation (4) can be written simply as:

$$dG = \left(H^2 \frac{\partial \mu}{\partial \sigma} - S \sigma \right) d\sigma + \left(H^2 \frac{\partial \mu}{\partial H} + B - \mu_0 H \right) dH \quad (5)$$

$$dG(H, \sigma) = \left(\frac{\partial G}{\partial \sigma} \right)_H d\sigma + \left(\frac{\partial G}{\partial H} \right)_\sigma dH \quad (6)$$

Compare with the Equations (5) and (6),

$$\begin{cases} \left(\frac{\partial G}{\partial \sigma}\right)_H = H^2 \frac{\partial \mu}{\partial \sigma} - S\sigma \\ \left(\frac{\partial G}{\partial H}\right)_\sigma = H^2 \frac{\partial \mu}{\partial H} + B - \mu_0 H \end{cases} \quad (7)$$

Use the continuous of second-order partial differential of function G , we get

$$\frac{1}{\sigma} \frac{\partial \mu}{\partial \sigma} = \frac{1}{H} \frac{\partial S}{\partial H} \quad (8)$$

μ , S is the function of input stress and field, which can be illuminate in the Equation (8), but the coefficient of input loads in permeability and mechanical compliance is different. From the Equation (8), we can know that the pre-pressure coefficient of permeability is larger than mechanical compliance, inverse the magnetic field coefficient of permeability is smaller than mechanical compliance. It can be said that piezomagnetic effect and inverse piezomagnetic effect are the most important factor in the micro-energy change model, the mechanical output mainly depend on the magnetization effect, and the magnetic output mainly depend on the mechanism effect.

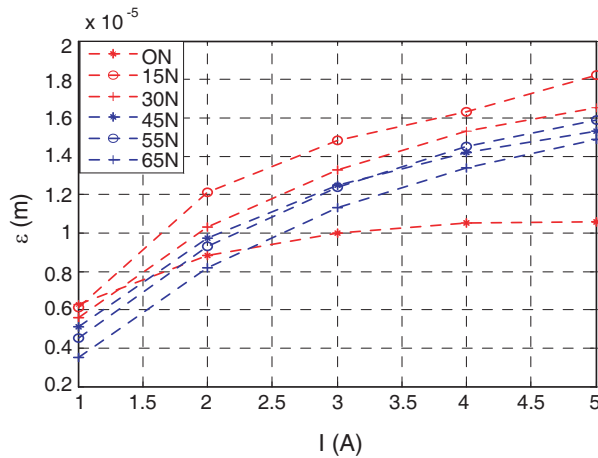


Figure 1: Strain-current characters at different pre-pressure.

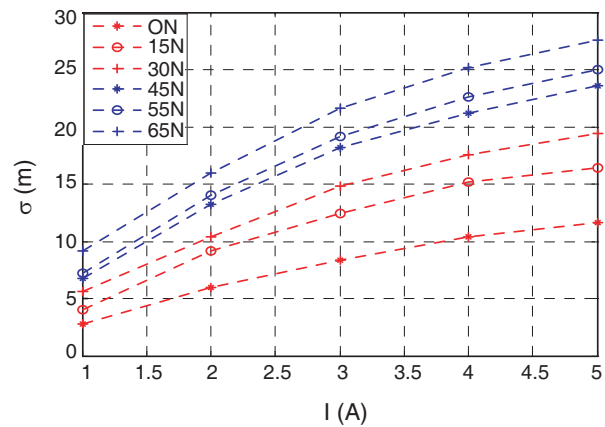


Figure 2: Output stress-current characters at different pre-pressure.

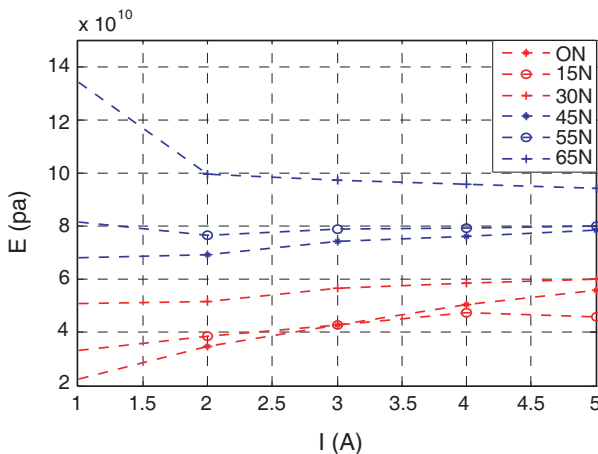


Figure 3: Mechanical compliance-current characters at different pre-pressure.

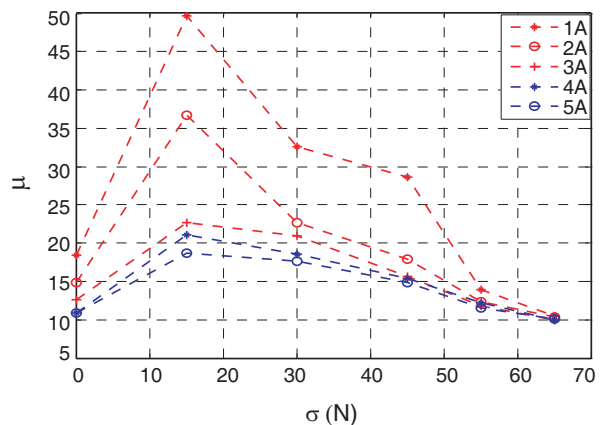


Figure 4: Permeability-pre-pressure characters different current.

5. EXPERIMENTAL

This article definitude the relation between input and output loads, the magnetic field is provided by coils, and pre-pressure is provided by heavy weight. Figs. 1–4 are the experimental result. Fig. 1 is the strain-current characters at different pre-pressure, which explain that suitable pre-pressure can lead the material have more strain, and if the pre-pressure is excess, it will have the inverse effect. Fig. 2 is the output stress-current characters at different pre-pressure, current and pre-pressure are positive effect coefficient of the output stress.

Figure 3 is the mechanical compliance-current characters at different pre-pressure, we can know that with the increase of current, the mechanical compliance will tends to constant, and here, the mechanical compliance is not a simple parameter of mechanical, it also contain the effect of magnetic field. Fig. 4 is the permeability-pre-pressure characters at different current, which like the strain-current characters, it also have a suitable pre-pressure, if the stress is excess, the permeability will decrease, and the permeability have a negative effect of current.

From the top experiment, we clearly the change of all parameter, and we can use the new parameter model to analyze the micro-energy change in material.

6. CONCLUSION

This paper presents a new electromagnetic parameter model, base on this, analyze the relation between the parameters, have the result of the truly intuitionistic output response which is express by parameters.

REFERENCES

1. Lia, S. Y., B. W. Wang, L. Weng, Y. Zhou, Y. Sun, W. M. Huang, “The effect of magnetic field heat treatment on magnetostriction of Terfenol-D 2-2 composites,” *Journal of Magnetism and Magnetic Materials*, Vol. 320, 806–809, 2008.
2. Calkins, F. T., M. J. Dapino, and A. B. Flatau, “Effect of prestress on the dynamic performance of a Terfenol-D transducer,” *SPIE*, Vol. 3041, 1997.
3. Kellogg, R. and A. Flatau., “Stress-strain relationship in Terfenol-D,” *Proceedings of SPIE*, Vol. 4327, 2001.
4. Huang, W., B. Wang, Y. Sun, L. Weng, and W. Zhao, “Investigation on dynamic properties of Terfenol-D actuators,” *Proceedings of SPIE*, Vol. 6423, 64234I, 2007.
5. Sato, Y. and G. Engdahl, “A computational effective material data representation for fast simulation models of giant magnetostrictive materials,” *IEEE Transactions on Magnetics*, Vol. 40, No. 2, 2004.

The Equivalence between Time Reversed Means and Employment of Left Hand Materials to Overcome the Diffraction Limit

J. M. Velázquez-Arcos, J. Granados-Samaniego,
J. L. Fernández-Chapou, and A. L. Rodríguez-Soria

Departamento de Ciencias Básicas, División de Ciencias Básicas e Ingeniería
Universidad Autónoma Metropolitana, Unidad Azcapotzalco
Av. San Pablo 180, Azcapotzalco 02200 D. F., México

Abstract— From microwave spectra time reversed reported experiments we find that it is possible to observe how the necessary conditions to recover the evanescent fields can be provided by a quite different kind of method that at first sight seems to be completely unrelated to the most common one. That is, we make a discussion of the analogies between the general properties of the so called Left Hand Materials (LHM) that allow us to rescue the evanescent waves and the detailed process of time reversed techniques applied to electromagnetic waves. As we know, both ways make possible the overcoming of the diffraction limit. We recall some results from Time Reversed Acoustics that can be easily used in the electromagnetic case in order to perform some kind of mapping from one frame to the other. We hope that our analysis will be useful in designing a wide class of devices which require the breakdown of the aforementioned limit.

1. INTRODUCTION

The classical view of Electrodynamics has imposed a limit on the conventional use of lenses. The so-called diffraction limit has its acoustic counterpart, and it is named the same. In both fields, acoustic and optics, it would be very convenient to be able to overcome it. From an optics perspective this last phenomenon requires the retrieval of lost information, since one does not have available a lens capable of reaching and grabbing a part of the electromagnetic field that an object reemits when it is illuminated. Those wavelengths which are smaller than the dimensions of the body are wasted and the resulting image is incomplete. The technical problem of information recovery begins to find a solution with the use of very peculiar devices, whose existence was suggested not long ago by V. G. Veselago [1]. They consist basically in super-materials with a negative refraction index (also called left hand materials), that is, materials which allow the formation of an image at a point where it is possible to superpose both the lost electromagnetic field and the one usually recovered, and thus get a complete image with details which surpass the traditional diffraction limit. On the other hand, something very similar occurs in acoustics. When an acoustic signal is diffracted by an obstacle the definition precision follows the same rules as in optics. In the acoustic case there exists a peculiar way to recover the lost information. Some authors, like J. de Rosny and M. Fink [2], have observed that if the acoustic system in hand admits time reversibility, then it is possible to get a definition up to a fourteenth of the wavelength of the used signal. The key to this is the perfection in the accomplishment of this process. In this work we will establish an equivalence between the existence of a negative refraction index for electromagnetic waves and the presence of a sink term which appears in the theory of time reversal acoustics when one tries to overcome the diffraction limit. In order to accomplish this, first we review some real devices which have permitted to reach negative refraction indexes as well as an optimal acoustic time reversibility. Then we discuss the results in both fields and suggest a correspondence between the basic principles which allow overcoming of the diffraction limit (ODL).

2. LEFT AND RIGHT HAND MATERIALS

Materials existing in nature have a positive refraction index. These are called Right Hand Materials (RHM) in order to distinguish them from artificially created materials which have a negative refraction index, and which are called Left Hand Materials (LHM). The complex refraction index n is defined as the quotient of the velocities of an electromagnetic wave in the medium and in empty space. This refraction index can be written in terms of the magnetic permeability μ and electric permittivity ε as $n^2 = \mu\varepsilon$. If both μ and ε are negative for a range of frequencies, then $n < 0$. Among other multiple consequences, this means that group and phase velocities are opposite. The extraordinary property of LHM of allowing waves to travel in opposite sense to the transmission of energy translates itself in the fact that the so-called evanescent waves emitted by observed objects

grow inside the material, instead of diminishing. At the end of their journey the electromagnetic waves will have recovered the information which otherwise is normally lost.

3. “LEFT” TRANSMISSION LINES, DOUBLE SPLIT RESONANT RINGS AND METAMATERIALS

In 2002, George V. Eleftheriades [3] and coworkers synthesized a plane and isotropic “left medium” (perpendicular polarization of the electric field), based on a grid of bidimensional transmission lines (TL), loaded with a series of capacitors (C) and deviator inductors (L). A unit cell is shown in Figure 1 and the transmission line lens is shown in Figure 2.

Previously, Pendry [4] suggested the architecture and Shelby et al. [5] proved the existence of LHM. This arrangement has the expected behavior of having a negative refraction index. Besides focusing the electromagnetic field it has the ability to recover the evanescent waves, thus surpassing the diffraction limit. Presently there exist versions of these artificial medium which basically are comprised by unit cells with a lesser power loss or covering different frequency intervals (visible light, ultraviolet, infrared). Tridimensional TL arrangements have also been created which possess a negative refraction index. An alternative way to build the so-called metamaterials (with negative refraction index n) is to create cells which contain concentric and semiclosed rings (rings which produce a negative magnetic permeability μ against alternative magnetic fields perpendicular to the ring planes) known as split resonant rings or SRR). By alternating the SRR with conventional transmission lines (not loaded with capacitors and inductors) perpendicular to the ring planes one obtains the metamaterial cells, since these lines have a negative electric permittivity ϵ . Figure 3(b) shows a cell with SRR and negative magnetic permeability μ , while Figure 3(a) shows a cell built

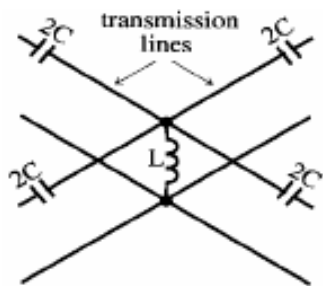


Figure 1: Cell with loaded transmission lines[3].

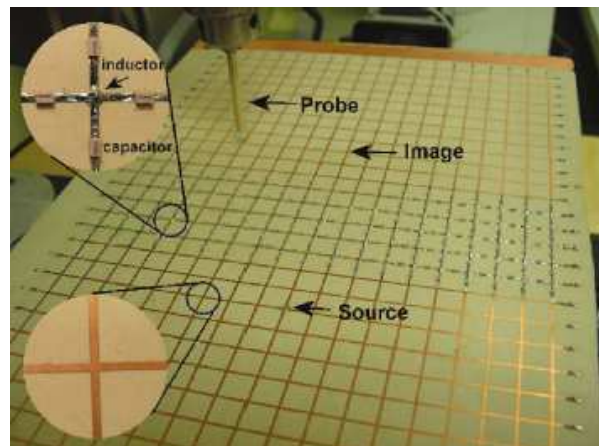


Figure 2: Lens, plane left [3] transmission lines.

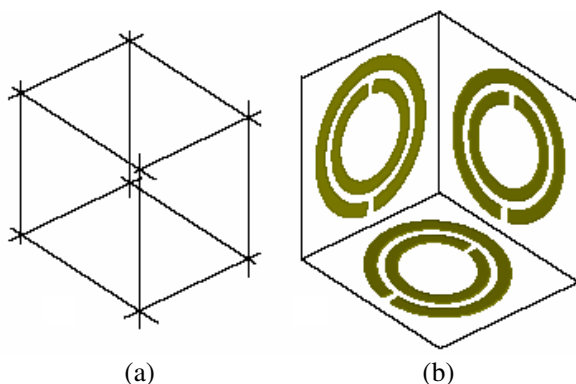


Figure 3: (a) unit cell with negative electric permittivity ϵ . (b) Unit cell with negative magnetic permeability μ .

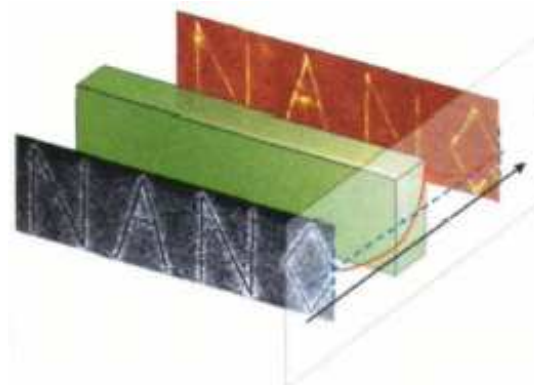


Figure 4: Representation of the experiment described by D. Smith [7].

with thin wires with negative permittivity ε .

4. THIN FILM SUPERLENSES

Among metamaterials we find lenses made up of thin films of some metallic compounds. In particular, an ultrathin film of silver placed between two materials of positive refraction index constitutes a superlens with a negative refraction index n . The reported experimental results are amazing, among other reasons, because they are applied to images in the visible spectrum.

In this case, while evanescent waves are losing amplitude as they go through a “right hand” medium (with a positive refraction index), when they reach the film they grow until, when the image is formed, they superpose with the field that usually forms the image, enhancing it and giving it a higher definition beyond the diffraction limit. The “sandwich” shown in Figure 4 shows the effect of the ultrathin silver film (green medium) in recreating the image of the word NANO with a high resolution of $\lambda/6$ (λ is the wavelength used for illumination).

5. ACOUSTIC TIME REVERSAL AND THE OVERCOMING OF THE DIFFRACTION LIMIT

In optics, overcoming the diffraction limit requires a negative refraction index, while in acoustics this possibility is associated with time reversibility. Due to the fact that the formalism we have developed for the study of time reversibility refers to discrete systems, we will adhere to this type of systems, without losing generality. Firstly, let us recall that the wave equation can be written as

$$k(\bar{r}) \frac{\partial^2 u(\bar{r}, t)}{\partial t^2} = \nabla^2 (u(\bar{r}, t) / \rho(\bar{r})) \quad (1)$$

$\rho(\bar{r})$ being the density and $k(\bar{r})$ the compressibility of the propagation medium, while $u(\bar{r}, t)$ is the acoustic signal that for a discrete system may be written as $u(\bar{r}_j, t) = u_j(t)$, where \bar{r}_j may be the position of a transducer or a dispersion site, a source or a sink. Acoustic time reversibility has its foundations on the fact that the wave equation is second order in time, which allows solutions which travel toward the future or the past, as if a film was ran forwards or backwards. One of the conditions to carry out time reversal successfully is that the system be ergodic, which guarantees that the signal may travel both senses in time. The other condition which permits a full time reversal is the main theme of this work, the overcoming of the diffraction limit. The goal is ensuring the consistency of the description of acoustic signal propagation toward the future or past, that is, that the equation describing both situations is of the same type. Considering a signal travelling towards the future, one may write the wave equation in integral form as

$$u_j(t) = u_j^{(o)}(t) + \sum_{k \neq j} \int_{-\infty}^{\infty} G^{(o)}(\bar{r}_j, t; \bar{r}_k, t') A_k u_k(t') dt' \quad (2)$$

where $G^{(o)}(\bar{r}_j, t; \bar{r}_k, t')$ is the free Green function, A_k are the complex dispersion coefficients and $u_j^{(o)}(t)$ is a source. If now we want to describe a signal travelling toward the past, the corresponding integral equation is

$$u_s(T-t) = u_s^{(o)}(T-t) + \sum_j \int_{-\infty}^{\infty} A_s^* G^{(o)*}(\bar{r}_j, T-t'; \bar{r}_s, t) u_j(T-t') dt' \quad (3)$$

In this equation there is a parameter T , which represents the time during which the outgoing signal (the one travelling toward the future) is being considered (a recording during a time T might have been carried out). In this equation $u_s(T-t)$ is the returning signal that has travelled toward the past. The term $u_s^{(o)}(T-t)$ is a sink term which guarantees that the outgoing and returning equations are both inhomogeneous integral equations.

De Rosny and Fink [2] introduced this term experimentally by making the original acoustic signal source work backwards in time, while Velázquez [8] et al. introduced it theoretically in order to obtain a consistent matrix representation. As a consequence of the introduction of this sink term, De Rosny and Fink [2] have proved that the time reversed signal has a definition of a fourteenth of λ , the wavelength of the used signal (See Figures 5 and 6). The reason for this very high resolution

rests on the fact that the sink term supplies the information as to how the acoustic signal that is made to travel backwards in time is created. This information is fundamental to a successfully time reversal and also permits the inclusion of fine details which show themselves after an appropriate time T has elapsed.

6. COMPARISON OF ACOUSTICS AND OPTICS SUPERRESOLUTION

As we have commented in this work, the mechanism by which an acoustic super-resolution is obtained is the recovery of information concerning the object whose “image” or profile is sought. If for the time being we disregard the specific way of accomplishing this, we may compare it with the mechanism by which one obtains an optical super-resolution: the recovery of the evanescent waves emitted by the object whose “image” is sought. Although the nature of the electromagnetic and acoustic waves origins is quite different, it seems clear that in both cases it is by means of information recovery that one can overcome the diffraction limit. For lack of space we cannot give here a fuller presentation, but we can give a fundamental equation obtained in the matrix formulation of acoustic time reversibility:

$$\bar{g}(\omega) = [\mathbf{1} + \underline{\mathcal{G}}(\omega)] \bar{g}^{(o)}(\omega) \quad (4)$$

in this equation, $\underline{\mathcal{G}}$ is the matrix representation of the Green function, which contains absolutely all information about the acoustic dispersion phenomenon, including sources and sinks, thus guaranteeing an optimal time reversibility and consequently the overcoming of the diffraction limit. As can be noted, this equation contains really the Fourier transforms of the Green function, the acoustic signals, and the sources and sinks.

It is likely that, at least structurally, if is possible to obtain an analogous expression, taking due account of the vector nature of the electromagnetic field, whose usefulness would be the possibility of predicting the phenomenon for each particular medium, once $\underline{\mathcal{G}}$ is determined. On the other hand, another parallelism becomes evident between the mechanisms for diffraction limit overcoming in optics and acoustics, since in a LHM waves travel in opposite direction to the conventional one, as if time elapsed backwards, while in reconstructing an acoustic signal the original signal is made to travel backwards in time. It is as though the LHM time-reversed the effect on the so-called evanescent waves (although not on energy transmission), making them grow in the same way that in acoustics the direct signal from the source is time reversed.

In a recent article [8], Nikolay I. Zheludev refers to a number of procedures that have been proposed to overcome the diffraction limit, some of them having been carried out successfully in practice. For instance, they mention that C.W. Oseen [9] showed in 1922 that an arbitrary proportion of the energy irradiated by a needle-shaped antenna can be emitted in an arbitrarily small solid angle. They also mention that recently Berry and Popescu [10] predict that the diffraction produced

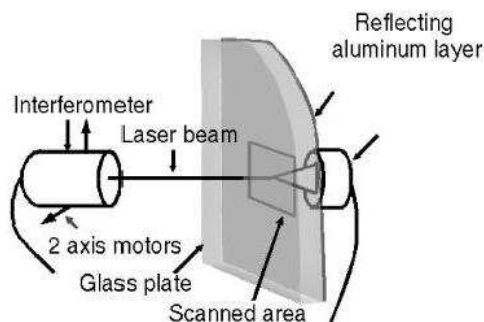


Figure 5: Experimental arrangement of De Rosny and Fink [2].

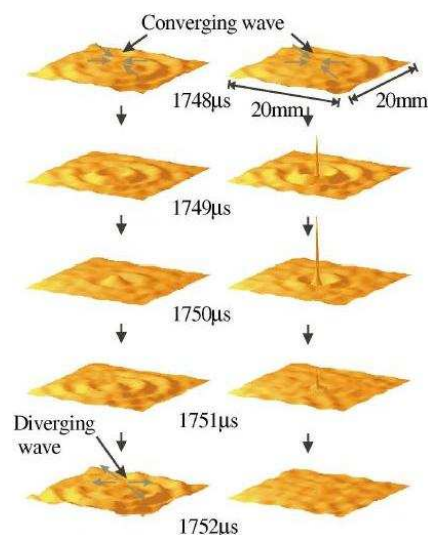


Figure 6: Representation of the ODL phenomenon [2].

by a grating can generate a superlocalization beyond the source wavelength. There exist astounding properties of bidimensional arrangements of nano-holes that can act as superlenses which focus a monochromatic light ray [16, 17] also in regions surpassing the diffraction limit. Besides that we have the phenomenon known as superoscillations which consists in the Fourier development of functions which oscillate more rapidly than any of its components [8].

Going back now to the concept of information recovery, it seems that the inclusion of a theoretical sink term in the matrix equation not only has to do with the recovery of higher frequencies, but also with the more complete description allowed by a propagation medium and the possible existence of a dispersion phenomenon which is more complex than the one originally assumed. This is the reason why we are suggesting that in practice the sink term may be substituted by an artifact or a resource that does not strictly correspond to a time inversion of the initial source. The characteristics of this sink term will depend on the physical system being particularly considered.

In 2008 a work was published in which the methodology of Acoustic Time Reversibility was applied to the focalization of electromagnetic signals in the microwave range using a bundle of fine wires placed irregularly in the field near the microwave source.

Apparently the interaction with the wires excited the evanescent waves and converted them in travelling waves when a time reversed signal was sent obtaining thus a localization that surpassed the diffraction limit.

7. INFORMATION RECOVERY IN OPTICS AND ACOUSTICS

Presently, the problem of information recovery in the fields of acoustics and electromagnetism can be considered nearly solved from a theoretical standpoint, now that the proposal of Victor Veselagol [1] about the properties of the so called Left Handed Materials (LHM) has been rightly recognized.

The technical development of materials with negative refraction index has began in optics, as well as time reversibility devices in acoustics, among which we find the TRM (Time Reversal Mirror) [2]. They have made possible this information recovery and thus the overcoming of the theoretical diffraction limit.

There exist two classes of mechanisms which serve the common goal of completing the spectrum that shapes a well defined image. They are apparently unrelated in theory, except for the final and highly beneficial result. Nevertheless, recently it has been possible to begin to apply the science and technology of acoustic time reversibility to the process of information recovery in the case of electromagnetic waves, generating a much higher resolution, and offering evidence of a greater interdependence. In the next chapter we will compare some of the theoretical results of acoustic time reversibility with the theoretical expressions for the negative permittivity ε and permeability μ , noting also that the imaginary part of the Fourier transform of the acoustic Green function exhibits those properties which allow the information recovery in the experimental process, and how the explicit expressions for ε and μ have an analogy with this description. This last fact suggests a relation between the explicit form of the Fourier transform of the Green function and the permittivity and permeability even in spite that these two last properties always point to an electromagnetic phenomenon. The Green function case is more general, and although the studied matrix equation corresponds to an acoustic discrete particular case, it is possible to describe the electromagnetic phenomenon with an appropriate Green function.

8. EXPRESSIONS FOR ELECTRIC PERMITTIVITY ε AND MAGNETIC PERMEABILITY μ FOR A LHM MATERIAL

In order to make a comparison between acoustic time reversal and negative refraction index we will take a simple example [11] which consists in a periodic arrangement of posts used for creating a range of frequencies for which $\varepsilon_{eff} < 0$, intertwined with a periodic arrangement of split resonant rings (SRR), for which we have $\mu_{eff} < 0$ for the same range of frequencies.

This system can be described by an effective dielectric function

$$\varepsilon_{eff} = 1 - \frac{\omega_p^2}{\omega^2} \quad (5)$$

with the plasma frequency ω_p relative to the geometry of the short arrangement of wire posts. The

medium created by the SRR can be described by an effective magnetic permeability

$$\mu_{eff} = 1 - \frac{F\omega_0^2}{\omega^2 - \omega_0^2 - i\omega\Gamma} \quad (6)$$

The hypothesis of this model is that the arrangements of SRR and posts do not interact directly, and therefore the refraction index of the composite medium will be

$$n(\omega) = \sqrt{\varepsilon_{eff}(\omega)\mu_{eff}(\omega)} \quad (7)$$

With the preceding expressions, ε_{eff} y μ_{eff} are simultaneously negative in region $\omega_0 < \omega < \omega_b$.

Then we may write the refraction index as [11]

$$n(\omega) = \frac{1}{\omega} \sqrt{\frac{(\omega^2 - \omega_b^2)(\omega^2 - \omega_p^2)}{(\omega^2 - \omega_0^2)}} \quad (8)$$

In order to simplify this discussion, let us assume that the material parameters are independent of ω . Let us also assume that the field source is a laminar current in the direction of the z -axis just above the plane yz . We assume that the aforementioned current generates the presence of a wave described by [3]

$$E(x, t) = -2\pi \frac{Z}{c} j_0 e^{i(nk|x-x_0|-\omega t)} \quad (9)$$

where $Z = \sqrt{\frac{\mu}{\varepsilon}} = \frac{\mu}{n}$ is the wave impedance.

In the case that interests us, $n < 0$, it can be noted that while the impedance remains positive in spite of ε and μ being simultaneously negative, the wave is propagated from $\pm\infty$ towards the source at the origin at $x = x_0$, that is, in a contrary sense as if it travelled backwards in time. Nevertheless, a calculation of the propagation direction of energy would indicate that the flux does not alter direction when the refraction index becomes negative. For frequencies such that $\omega_0 < \omega < \omega_b$, Equation (4) gives a negative value for n . In this case the exponentially decaying evanescent waves are converted to propagating waves.

9. THE GREEN FUNCTION OF ACOUSTIC TIME REVERSIBILITY FOR THE DISCRETE CASE

In a previous work we found that the time reversed acoustic signals for the discrete case can be described in terms of a matrix equation which contains the Fourier transform of the complete Green function in Acoustic Time Reversibility (ATR) [6, 12, 15]:

$$\bar{g}(\omega) = [\underline{1} + \underline{\mathcal{G}}(\omega)] \bar{g}^{(o)}(\omega) \quad (10)$$

where

$$\underline{\mathcal{G}}^{\tau*}(-\omega)_{j,k} = \begin{cases} 0 & si \quad j = k \\ A_j^* \underline{\mathcal{G}}_{-\omega}^* (\bar{r}_k, \bar{r}_j) & si \quad j \neq k \end{cases} \quad (11)$$

A_j^* representing the interaction of the emitted signals and the medium.

This equation contains all the information needed to guarantee the overcoming of the diffraction limit (in some experiments one observes a resolution of $\frac{\lambda}{14}$).

In the simple case of only one emitter the matrix Equation (10) is simplified and has the form

$$g_1(\omega) = G_\omega(\bar{r}_1, \bar{r}_0) g_0^{(o)}(\omega) \quad (12)$$

Let us assume now that $g_0^{(o)}(\omega)$ is the Fourier transform of the finite range cosine function (monochromatic pulse of width d)

$$f_0(t) = p_d(t) \cos(\omega_0 t) \quad (13)$$

where $p_d(t)$ represents the unit pulse function of width d

$$g_0^{(o)}(\omega) = \left[\frac{\sin\left(\frac{1}{2}d(\omega - \omega_0)\right)}{\omega - \omega_0} + \frac{\sin\left(\frac{1}{2}d(\omega + \omega_0)\right)}{\omega + \omega_0} \right] \quad (14)$$

Additionally let us assume that $g_1(\omega)$ is the Fourier transform of the function (retarded and with a central peak)

$$f_1(t) = A \frac{\sin[a(t - \Delta t)]}{\pi(t - \Delta t)} \quad (15)$$

In this expression a is the dispersion, A is a normalization constant for the final signal and

$$\Delta t = \frac{|\bar{r}_1 - \bar{r}_0|}{c} \quad (16)$$

We have then

$$g_1(\omega) = \begin{cases} Ae^{-\frac{i\omega|\bar{r}_1 - \bar{r}_0|}{c}} & \text{para } |\omega \leq a| \\ 0 & \text{para } |\omega > a| \end{cases} \quad (17)$$

Substituting (15) and (17) in Equation (12) we see that the Fourier transform of the Green function is then [6, 12]

$$G_\omega(\bar{r}_1, \bar{r}_0) = Ap_{2a}(\omega) e^{-\frac{i\omega|\bar{r}_1 - \bar{r}_0|}{c}} (\omega^2 - \omega_0^2) \times \left\{ (\omega + \omega_0) \sin \left[\frac{1}{2}d(\omega - \omega_0) \right] + (\omega - \omega_0) \sin \left[\frac{1}{2}d(\omega + \omega_0) \right] \right\}^{-1} \quad (18)$$

10. A COMPARISON OF THE EFFECT OF TIME REVERSAL AND THE NEGATIVE REFRACTION INDEX

Equation (10) was obtained with the principle that if took the initially emitted acoustic signal some time T to be registered, and its diverse elements traversed a theoretically fully ergodic space up to their final destination. Since each original signal element takes different paths, it also takes different times to reach its destination. This lack of simultaneity forces the duration of the return emission to be precisely T when the signal is time reversed in its return journey. Any less time in the return emission will generate an information loss. This information loss is analogous of an incomplete phase correction produced by a conventional lens with $n > 0$ for the electromagnetic case. From the example given in the preceding section, what happens is that when $n > 0$, the Maxwell equations impose the condition [6] $\omega^2 c^{-2} < k^2$, since otherwise the exponential in (9) becomes a decreasing term and one has evanescent waves. If we substitute the normal lens for a LHM material, the evanescent waves are converted to travelling waves inside the material, since the exponential in (9) becomes an oscillatory function, that is, a wave propagating inside the LHM material. This means that the information loss due to the restriction on ω can be restituted by the presence of a material with a negative refraction index in the same way that the complete recording time during time T recovers information in acoustic time reversal.

Even though there is still some distance between the contents of the refraction index expression in a LHM material and the expression of the Fourier transform for the ATR Green function, it must be noted that the last one was obtained from very general properties of the acoustic signals, which are shared by any scalar field (although we can generalize it to vector fields) that satisfies the wave equation. From this perspective, theoretically, if the explicit expression of the Green function in Equation (18) should correspond to an electric field component or an electromagnetic potential, then Equation (8) should describe the medium behavior also described by the structure of the Green function. There are still more analogies between (8) and (18), causality [12] among them. The fact that the acoustic signal is initiated from a particular instant makes the imaginary part of the Fourier transform of the Green function different from zero. This same causality determines the structure of $n(\omega)$ (Equation (8)). In concretion, for almost transparent media

$$\frac{d[\varepsilon(\omega)\omega]}{d\omega} > 1 \quad \text{and} \quad \frac{d[\mu(\omega)\omega]}{d\omega} > 1 \quad (19)$$

turn out to be restrictions imposed by causality [11, 13].

11. OVERCOMING OF THE DIFFRACTION LIMIT

The net effect of information recovery, whether by using ATR [2, 14] techniques or employing several devices based on LHM [3, 5, 11], is the overcoming of the traditionally imposed limit on image definition, known as diffraction limit overcoming (ODL). In the preceding section it is stated that

from a theoretical standpoint there does not exist in reality any difference between the information provided by known developments in meta-materials (LHM) characterization, and the techniques and developments in ATR.

In fact, one does not really need the concept of evanescent waves when the final goal is ODL, since according to the analogy mentioned in the preceding section it is possible to apply Equation (10) to an appropriate electromagnetic problem. In practice, G. Lerosey [14] has recently conducted an application of ATR to microwaves, without considering any LHM device, with excellent results for ODL.

12. CONCLUSIONS

An analysis of Equations (8) and (18) has permitted us to recognize the closeness in the description of the information recovery by means of electromagnetic or acoustic waves, which fits perfectly the most recent experimental observations on the use of ATR techniques for the focalization of electromagnetic waves beyond the diffraction limit [14]. Definitely there exists a parallelism between the overcoming of the diffraction limit in optics and acoustics and, although the descriptions are not exactly equal for each particular system, they are nevertheless equivalent.

In fact, as mentioned above, Equation (8) should be able to describe the traversal of electromagnetic waves through an ergodic medium, as long as it is possible to discretize the system with signal emission and reception points.

In a reciprocal manner, Equation (8) should be able to describe some propagation process of acoustic waves through a medium with the equivalent of a negative refraction index, allowing focalization of acoustic waves without making use of time reversibility.

In the acoustics case, a set of micro-transducers would probably play the role of LHM microstructure. Our observations lead us to conclude that it is a good idea to explore the parallelism between diffraction limit overcoming in optics and acoustics. These descriptions are not exactly equal, since on the one side we have a scalar field and on the other a vector field, but they support the usefulness we have been trying to show for the matrix equation in the acoustics discrete case.

As mentioned before, there exists an analogy between a time reversal effect and growing evanescent waves, since the individual electromagnetic waves travel in fact in opposite sense to the energy propagation direction and of course in opposite sense to the propagation of waves before penetrating and exiting the LHM, particularly in response to the various frequencies, as if time was being reversed. This does not mean that we should disregard consideration of those systems and mechanisms employed nowadays to overcome the diffraction limit in electromagnetic waves, as for instance, among others, the use of nano-holes, that we mentioned before. We propose that in some of these, in which it is possible to make a discrete description it is feasible to use the matrix Equation (4) or (10), since it includes a term which allows overcoming of the diffraction limit. This leads to an equivalence between the mechanisms of diffraction limit overcoming in optics and acoustics, as related to the information recovery concept.

REFERENCES

1. Veselago, V. G., *Sov. Phys. Usp.*, Vol. 10, 509, 1968.
2. De Rosny, J. and M. Fink, "Overcoming the diffraction limit in wave physics using a time reversal mirror and a novel acoustic sink," *Phys. Rev. Lett.*, Vol. 89, 2, 2002.
3. Grbic, A. and G. V. Eleftheriades, "Overcoming the diffraction limit with a planar left-handed transmission-line lens," *Phys. Rev. Lett.*, Vol. 92, 11, 2004.
4. Pendry, J. B., *Phys. Rev. Lett.*, Vol. 85, 3966, 2000.
5. Shelby, R. A., D. R. Smith, and S. Shultz, *Science*, Vol. 292, 77, 2001.
6. Velázquez-Arcos, J. M., C. A. Vargas, J. L. Fernández-Chapou, and J. Granados-Samaniego, "Overcoming of the diffraction limit for the discrete case in time reversed acoustics," *AIP Proceedings, RIAO/OPTILAS 2007, 6th Ibero-American Conference on Optics(RIAO); 9th Latin — American Meeting on Optics, Lasers and Applications (OPTILAS)*, 21–26, October 2007, Campinas, Sao Paulo, Brazil; Vol. 991, Ed., Niklaus Ursus Wetter, Jaime Frejlich, Springer, 2008.
7. Smith, D., "Superlens breaks optical barrier," *Physics World*, Institute of Physics Publishing, 2006.
8. Zheludev, N. I., "What diffraction limit," *Nature Materials*, Vol. 7, 420–422, 2008.
9. Oseen, C. W., *Annln Phys*, Vol. 374, 202–204, Leipz, 1922.
10. Berry, M. V. and S. J. Popescu, *J. Phys. A*, Vol. 39, 6965–6977, 2006.

11. Smith, D. R. and N. Kroll, “Negative refractive index in left-handed materials,” *Phys. Rev. Lett.*, Vol. 85, No. 14, 2933, 2000.
12. Velázquez-Arcos, J. M., A. Ramírez-Rojas, and C. A. Vargas, “Time reversibility in acoustic signals,” *Journal of Applied Research and Technology*, Vol. 2, No. 2, 107–115, August 2004.
13. Ziolkowski, R. W. and A. D. Kipple, “Causality and double-negative metamaterials,” *Phys. Rev. E*, Vol. 68, 026615, 2003.
14. Lerosey, G., J. de Rosny, A. Tourin, and M. Fink. “Focusing beyond the diffraction limit with far-field time reversal,” *Science*, Vol. 315, 1120, 2007.
15. Velázquez-Arcos, J. M., J. L. Fernández-Chapou, J. Granados-Samaniego, and C. A. Vargas, “Time reversed acoustics, Green’s function and the overcoming of the diffraction limit,” *Proceedings of the 13 Reunión Anual de Física y Matemáticas, Escuela Superior de Física y Matemáticas*, Instituto Politécnico Nacional, Mexico City, September 2008.
16. Huang, F. M., N. Zheludev, Y. Chen, and F. J. G. de Abajo, *Appl. Phys. Lett.*, Vol. 90, 091119, 2007.
17. Huang, F. M., Y. Chen, F. J. G. de Abajo, and N. I. Zheludev, *J. Opt. A*, Vol. 9, S285–S288, 2007.

Hertz Tensor, Current Potentials and Their Norm Transformations

J. L. Fernández Chapou, J. Granados Samaniego,
C. A. Vargas, and J. M. Velázquez Arcos

Departamento de Ciencias Básicas, División de Ciencias Básicas e Ingeniería
Universidad Autónoma Metropolitana, Unidad Azcapotzalco
Av. San Pablo 180, Azcapotzalco, 02200 D.F., México

Abstract— In unified tensorial form, we develop the Hertz and Current super potentials. We are doing, also, a detailed study of associated Norm Transformations demonstrating that if an electromagnetic field (EM) can be represented in a Hertz Tensor, for a given choice of current potentials, then exist another current potentials for which the representation of the same field EM is expressed like the new Hertz super potential transformed by means of a Norm Transformation.

1. INTRODUCTION

In physics literature, by inexplicable way, the applications of the Hertz potentials vectors in favor of working directly with ϕ , and \vec{A} , scalar and vector potentials respectively, have been discarded. We consider that this has been an omission in many problems where it is possible to solve them, in a few rows, using the Hertz potentials, but it has been preferred to use directly ϕ and \vec{A} even though it results in making complicated mathematical manipulations, before to obtain the corresponding solution. The use of the Hertz potential vectors to solve problems, allows defining an electromagnetic field in terms of a single vectorial field. Perhaps one of examples more mentioned, where the vector of Hertz is introduced, is that of distant radiation of the field produced by an oscillator. These ideas are, also, usually applied to problems with waveguides and antennas. In resolution of this type of problems, are introduced an electric type vector of Hertz and another one of magnetic type. These vectors are so also called super potentials because they allow us to obtain the potentials \vec{A} and ϕ which generate the electric and magnetic field. In the present work one becomes study the Hertz vector potentials and the covariant formulation, which allows us to unify both, an electric type and a magnetic type, Hertz vectors into a skew tensor of rank two.

2. HERTZ'S VECTORS

The equations of electrodynamics in the presence of materials and without free electric charges and electrical currents are:

$$\nabla \cdot \vec{D} = 0 = \nabla \cdot \vec{B}, \quad \nabla \times \vec{E} + \frac{1}{c} \frac{\partial \vec{B}}{\partial t} = 0 = \nabla \times \vec{H} - \frac{1}{c} \frac{\partial \vec{D}}{\partial t}. \quad (1)$$

with

$$\vec{D} = \vec{E} + 4\pi\vec{P}, \quad \vec{H} = \vec{B} - 4\pi\vec{M}, \quad (2)$$

where \vec{P} and \vec{M} are representing the electric polarization and magnetic density vectors of the materials, respectively. Substituting (2) in (1) we have

$$\nabla \cdot \vec{E} = 4\pi\nabla \cdot \vec{P}, \quad (3a)$$

$$\nabla \cdot \vec{B} = 0, \quad (3b)$$

$$\nabla \times \vec{E} + \frac{1}{c} \frac{\partial \vec{B}}{\partial t} = 0, \quad (3c)$$

$$\nabla \times \vec{B} + \frac{1}{c} \frac{\partial \vec{E}}{\partial t} = \frac{4\pi}{c} \left(\frac{\partial \vec{P}}{\partial t} + c\nabla \times \vec{M} \right). \quad (3d)$$

Formally, these are the Maxwell's equations without free charges. Now, if the charge and current densities are identified like

$$\rho_P = -\nabla \cdot \vec{P}, \quad \vec{J}_P = \frac{\partial \vec{P}}{\partial t} + c(\nabla \times \vec{M}) \quad (4)$$

The index P point out that are quantities associated to the polarization of matter.

From these equations it is easy to obtain the continuity equation

$$\nabla \cdot \vec{J}_P + \frac{\partial \rho_P}{\partial t} = 0, \quad (5)$$

Equations (3b) and (3c) implies the existence of a scalar ϕ and vector \vec{A} fields, such that

$$\vec{E} = -\nabla\phi - \frac{1}{c} \frac{\partial \vec{A}}{\partial t}, \quad \vec{B} = \nabla \times \vec{A}. \quad (6)$$

Substituting Equations (6) in (3a) and (3d) we obtain

$$\phi = -4\pi\rho_P, \quad \vec{A} = -\frac{4\pi}{c} \vec{J}_P, \quad (7)$$

With $\equiv \nabla^2 - \frac{1}{c^2} \frac{\partial^2}{\partial t^2}$, and working with Lorentz's gauge for \vec{A} and $\vec{\phi}$:

$$\nabla \cdot \vec{A} = -\frac{1}{c} \frac{\partial \phi}{\partial t}. \quad (8)$$

Integrating Equation (7) it is possible to obtain ϕ and \vec{A} directly in terms of the polarization vectors \vec{P} and \vec{M} but the resultant relations are very complicated. Heinrich Hertz introduced a method that solve this situation, proposing two vectors \vec{S}_e and \vec{S}_m such that

$$\phi = -\nabla \cdot \vec{S}_e, \quad \vec{A} = \frac{1}{c} \frac{\partial \vec{S}_e}{\partial t} + \nabla \times \vec{S}_m. \quad (9)$$

The index e and m in Hertz vectors indicate that \vec{S}_e and \vec{S}_m are associated with **electric** and **magnetic** effects respectively. Substituting (9) in (7) we can probe that

$$\vec{S}_e = -4\pi\vec{P}, \quad \vec{S}_m = -4\pi\vec{M}, \quad (10)$$

that is, we can see \vec{S}_e and \vec{S}_m like solutions of inhomogeneous wave equation with source \vec{P} for \vec{S}_e and source \vec{M} for \vec{S}_m . Now, we define the current four-vector

$$J_p^\mu : J_p^0 = \rho_P, \quad J_p^i = \frac{1}{c} (J_P)_i,$$

with $\mu, \nu, \dots = 0, 1, 2$ or 3 and $i, j, k, \dots = 1, 2$, or 3 . By observing Equations (4) and (5) we can see that it is possible introduce the polarization skew tensor $M^{\mu\nu} = -M^{\nu\mu}$ such that

$$M^{0i} = \left(\vec{P} \right)_i \quad \text{and} \quad M^{ij} = \varepsilon^{ijk} \left(\vec{M} \right)_k,$$

where ε^{ijk} is the Levi-Civita permutation symbol, and we had taking into account the Einstein convention for sum when equal indexes appear. So that, Equations (4) and (5) can be written in Lorentz's covariant way like:

$$M_{,\nu}^{\mu\nu} = -J_P^\mu, \quad (11)$$

$$J_{P,\mu}^\mu = 0, \quad (12)$$

here, $0 \equiv \frac{\partial}{\partial x^0}$, and $i \equiv (\nabla)_i$ represents partials derivatives. Equation (12) follows directly from Equation (11) due to anti symmetry properties of $M^{\mu\nu}$ and the commutative properties of partial derivatives.

3. ELECTROMAGNETIC FIELD TENSOR

The electromagnetic field four-potential A^μ is defined like $A^0 = \phi$, and $A^i = (\vec{A})_i$. The electromagnetic field skew tensor $F^{\mu\nu} = -F^{\nu\mu}$ is defined in such a way that

$$F^{0i} = (\vec{E})_i, \quad F^{ij} = \varepsilon^{ijk} (\vec{B})_k.$$

Then the Maxwell's equations are:

$$F_{,\nu}^{\mu\nu} = 4\pi J^\mu, \quad (13a)$$

$$*F_{,\nu}^{\mu\nu} = 0, \quad (13b)$$

with $*F^{\mu\nu} \equiv \frac{1}{2}\varepsilon^{\mu\nu\alpha\beta}F_{\alpha\beta}$, and $J^0 \equiv \rho$, $J^i \equiv (\vec{J})_i$. Here J^μ is the current four-vector that represents the sources of electromagnetic field. Equation (13b) implies the existence of a four-vector A^μ such that

$$F_{\mu\nu} = A_{\nu,\mu} - A_{\mu,\nu}, \quad (13c)$$

This is, precisely, the covariant expression that establishes the relationship between potentials and electromagnetic field tensor. From Equation (13a) we can obtain $J_{,\mu}^\mu = 0$, the continuity equation in Lorentz's covariant way.

4. HERTZ'S TENSOR

Using Lorentz's gauge, we have

$$A_{,\mu}^\mu = 0, \quad (14)$$

which implies that there exist an skew tensor $\Pi^{\nu\mu} = -\Pi^{\mu\nu}$, such that

$$A^\mu = \Pi_{,\nu}^{\mu\nu} \quad (15)$$

With Equation (15) for A^μ it follows that Equation (14) is fulfilled automatically. In covariant form the Equations (13a) and (13b) are

$$A^\mu = -4\pi J^\mu, \quad (16)$$

and substituting (15) in (16) we can obtain

$$\Pi_{,\nu}^{\mu\nu} = -4\pi J^\mu, \quad (17)$$

since mathematical operators Δ and $_{,\mu}$ commute, then:

$$(\Pi^{\mu\nu})_{,\nu} = -4\pi J^\mu. \quad (18)$$

In general $J^\mu = J_l^\mu + J_p^\mu$ where J_l^μ represents the free current produced by the macroscopic movement of electric charges. In materials media without free currents $J_l^\mu = 0$ and $J_p^\mu \neq 0$. In this case and substituting (3) in (18) we have that

$$(\Pi^{\mu\nu})_{,\nu} = -4\pi M_{,\nu}^{\mu\nu}$$

this implies that

$$\Pi^{\mu\nu} = -4\pi M^{\mu\nu} \quad (19)$$

without materials media $M^{\mu\nu} = 0$, then $\Pi^{\mu\nu} = 0$, that is, $\Pi^{\mu\nu}$ must be harmonic. Comparing Equation (19) with Equation (10) it is possible to establish a relationship between the components of this tensor with those of Hertz's vectors in such a way that

$$\Pi^{0i} = (\vec{S}_e)_i, \quad \Pi^{ij} = \varepsilon^{ijk} (\vec{S}_m)_k$$

for this reason, the tensor $\Pi^{\mu\nu}$ is called Hertz potential tensor or simply Hertz tensor. The previous equations indicate that space-time components of Hertz tensor correspond to the electric type Hertz vector components and that purely spatial components are corresponding with magnetic type Hertz vector.

5. CURRENT POTENTIALS

Suppose that $J_l^\mu \equiv J^\mu \neq 0$, then Equation (19) do not satisfy. However, from $J_{,\mu}^\mu = 0$ it follows that exist $Q^{\mu\nu} = -Q^{\nu\mu}$ such that

$$J^\mu = Q^{\mu\nu}, \quad (20)$$

substituting in Equation (18), $J_T^\mu = Q^{\mu\nu}_{,\nu} + M^{\mu\nu}_{,\mu}$ we can get

$$\Pi^{\mu\nu} = -4\pi (M^{\mu\nu} + Q^{\mu\nu}). \quad (21)$$

We define

$$H^{\mu\nu} = F^{\mu\nu} - 4\pi M^{\mu\nu}, \quad (22)$$

then Maxwell's equations in materials media are

$$H^{\mu\nu}_{,\nu} = 4\pi J^\mu, \quad *F^{\mu\nu}_{,\nu} = 0. \quad (23)$$

Substituting Equation (15) in Equation (13c) we can get

$$F^{\mu\nu} = \partial_\alpha^{\mu\nu} \Pi_{,\beta}^{\alpha\beta} \quad \text{or} \quad *F^{\mu\nu} = * \partial_\alpha^{\mu\nu} \Pi_{,\beta}^{\alpha\beta} \quad (24)$$

here $\partial_\alpha^{\mu\nu} = -\partial_\alpha^{\nu\mu} \equiv \delta_\alpha^\nu \partial^\mu - \delta_\alpha^\mu \partial^\nu$ is the Stokian and $*\partial_\alpha^{\mu\nu} \equiv \frac{1}{2} \varepsilon^{\mu\nu\lambda\tau} \partial_{\lambda\tau\alpha}$. With (21) and (24) in (22) we obtain

$$H^{\mu\nu} = \partial_\alpha^{\mu\nu} \Pi_{,\beta}^{\alpha\beta} + \Pi^{\mu\nu} + 4\pi Q_{\mu\nu}. \quad (25)$$

It is suitable to define another "current potential". The tensor $*F^{\mu\nu} + 4\pi *R^{\mu\nu}$ with $*R^{\mu\nu}_{,\nu} = 0$ is solution of Maxwell's homogeneous equation. In the case that somebody may discover magnetic charges the Maxwell's homogeneous equation is substituted for

$$*F^{\mu\nu}_{,\nu} = 4\pi J_m^\mu. \quad (26)$$

Clearly $J_{m,\mu}^\mu = 0$, implies that exist $*R^{\mu\nu} = -*R^{\nu\mu}$ such that $J_m^\mu = *R^{\mu\nu}_{,\nu}$, so that $*R^{\mu\nu}$ is a magnetic current potential. If $J_m^\mu = 0$, $*R^{\mu\nu}$ may be non-zero. Then for $F^{\mu\nu}$ we can write

$$F^{\mu\nu} = \partial_\alpha^{\mu\nu} \Pi_{,\beta}^{\alpha\beta} - 4\pi R^{\mu\nu} \quad (27)$$

Substituting (26) and (27) into (22) we obtain

$$\Pi^{\mu\nu} = -4\pi (M^{\mu\nu} + Q^{\mu\nu} + R^{\mu\nu}). \quad (28)$$

In order to satisfy this equation is sufficient to take like $Q^{\mu\nu}$ and $*R^{\mu\nu}$ some particular integral for $H^{\mu\nu}$ and $*F^{\mu\nu}$, respectively.

To conclude this section we will mention the case that $J_m^\mu \neq 0$. The field equations will be those written in (13a) and (26). Even more, we will have two four-potentials A_e^μ and A_m^μ such that $F^{\mu\nu} = \partial_\alpha^{\mu\nu} A_e^\alpha + * \partial_\alpha^{\mu\nu} A_m^\alpha$. If we define $f^{\mu\nu} \equiv \partial_\alpha^{\mu\nu} A_e^\alpha$ and $b^{\mu\nu} \equiv * \partial_\alpha^{\mu\nu} A_m^\alpha$, substituting in field Equations (13a) and (26) we obtain $f^{\mu\nu}_{,\nu} = 4\pi (J_e^\mu + M^{\mu\nu}_{,\nu})$, $*f^{\mu\nu}_{,\nu} = 0$, $*b^{\mu\nu}_{,\nu} = 4\pi J_m^\mu$ and $b^{\mu\nu}_{,\nu} = 0$. The second and fourth of these equations are identities that follows from the definition of $f^{\mu\nu}$ and $b^{\mu\nu}$. From the equations for $b^{\mu\nu}$ it can be deduced that $A_m^\mu = -4\pi J_m^\mu$, $A_{m,\mu}^\mu = 0$.

Then exist a magnetic type Hertz tensor $\Pi_m^{\mu\nu} = -\Pi_m^{\nu\mu}$ such that $A_m^\mu = \Pi_m^{\mu\nu}_{,\nu}$ fulfilling the wave equation $\Pi_m^{\mu\nu} = -4\pi *R^{\mu\nu}$. The expressions for the variables of the fields are obtained simply adding a term of the form $* \partial_\alpha^{\mu\nu} \Pi_{m,\beta}^{\alpha\beta}$ (and substituting $\Pi^{\mu\nu} \rightarrow \Pi_e^{\mu\nu}$) to Equations (25) and (27). The structure of matter is not made with atoms containing magnetic charges so that it has no sense a magnetic polarization tensor and then the tensors $\Pi_e^{\mu\nu}$ and $\Pi_m^{\mu\nu}$ cannot play a symmetric role in the electromagnetic field (E&M field) variables.

The theory exposed in this section is valid for **whatever** type of material. When the media is nonconductor and non-polarized (J^μ and $M^{\mu\nu}$ prewritten), the right hand side of wave Equation (25) is a function of the coordinates x^μ , and the solution of this equation is obtained for well known methods. In the other case, right hand side of (25) is a function of the variables of the E&M field and, of course, of $\Pi^{\mu\nu}$; Equation (25) then goes on to integrodifferential equations for the Hertz tensor or the variables of the E&M field.

6. GAUGE TRANSFORMATIONS

The Maxwell inhomogeneous equation written in terms of A^μ is

$$(A^\nu_{,\nu})^{;\mu} - A^\mu = -4\pi J^\mu.$$

The mathematical expression for $F^{\mu\nu}$ in terms of A^μ is invariant to gauge transformations

$$A'^\mu = A^\mu + \xi^{;\mu}, \quad (29)$$

where A'^μ is another possible vector potential and ξ is an arbitrary function. Making use of this fact, we can select the potential A^μ such that

$$A^\mu_{,\mu} = 0, \quad (30)$$

$$A^\mu = -4\pi J^\mu. \quad (31)$$

If we impose to ξ the condition that $\xi = 0$, then (30) and (31) are invariants under (29). The potential tensors introduced in previous section, are not unique for some charge distributions and electromagnetic fields given.

Equations (20) and (28) remain invariants if $Q^{\mu\nu}$ and $R^{\mu\nu}$ are replaced for

$$Q'^{\mu\nu} = Q^{\mu\nu} + {}^* \partial_\alpha^{\mu\nu} G^\alpha, \quad R'^{\mu\nu} = R^{\mu\nu} + \partial_\alpha^{\mu\nu} G L^\alpha, \quad (32)$$

G^α and L^α are the components of arbitrary vector fields. Since we can use whatever set of current potentials, given by (32), the solutions to the Maxwell's equations given by (25), (27) and (28) can be written in the general form

$$\begin{aligned} H^{\mu\nu} &= 4\pi Q^{\mu\nu} + \partial_\alpha^{\mu\nu} \Pi_{,\beta}^{\alpha\beta} + \Pi^{\mu\nu} + 4\pi {}^* \partial_\alpha^{\mu\nu} G^\alpha, & F^{\mu\nu} &= 4\pi R^{\mu\nu} + \partial_\alpha^{\mu\nu} \Pi_{,\beta}^{\alpha\beta} + 4\pi {}^* \partial_\alpha^{\mu\nu} L^\alpha, \\ \Pi^{\mu\nu} &= -4\pi (M^{\mu\nu} + Q^{\mu\nu} + R^{\mu\nu} + {}^* \partial_\alpha^{\mu\nu} G^\alpha + \partial_\alpha^{\mu\nu} L^\alpha). \end{aligned} \quad (33)$$

It is interesting to compare the role that plays the vector field (L^μ) and the vector potential (A^μ). Formally, the second of Equation (33) is simply the sum of the expression (27) in terms of $\Pi^{\mu\nu}$ and the expression (13c) in terms of $A^\mu (= 4\pi L^\mu)$, satisfying the three forms of $F^{\mu\nu}$ the Maxwell's Equation (13b).

Substituting in the other Maxwell's Equation (13a) we can obtain, when use A^μ only, the wave Equation (31) (with $J^\mu \equiv J_l^\mu + J_p^\mu$) for A^μ ; however, the presence of L^μ in the expression of $\Pi^{\mu\nu}$ means that L^μ do not satisfy the wave equation since stay arbitrary and appears in the third of Equation (33) as source of Hertz tensor. Similar observations apply to G^α which must correspond to the four-potential for $H^{\mu\nu} + 4\pi Q^{\mu\nu}$.

Let us consider now the Hertz potential. We can see from Equation (13) that A^μ is invariant under the gauge transformation of type employed in Equation (32). However, due that A^μ is not unique, we have even a great grade of arbitrarily for $\Pi^{\mu\nu}$. Let $\Pi'^{\mu\nu}$ be such that

$$\Pi'^{\mu\nu} = \Pi^{\mu\nu} + \partial_\alpha^{\mu\nu} \Gamma^\alpha + {}^* \partial_\alpha^{\mu\nu} \Delta^\alpha, \quad (34)$$

with Γ^α and Δ^α arbitrary. Calculating A^μ in terms of $\Pi'^{\mu\nu}$:

$$A'^{\mu\gamma} = A^\mu + (\Gamma^\nu_{,\nu})^{;\mu} - \Gamma^\mu.$$

This expression shows that if Δ^α is arbitrary but Γ^α satisfy

$$\Gamma^\mu = \zeta^{;\mu}, \quad (35)$$

where ζ is arbitrary (may be zero), then over A^μ we induce a gauge transformation (29) with norm $\xi = \zeta + \Gamma^\nu_{,\nu}$ which in turn satisfy $\xi = 0$. To see the effect of gauge transformations in terms of $\Pi^{\mu\nu}$, we can apply them to the Equations (25) and (27), obtaining

$$H'^{\mu\nu} = H^{\mu\nu} + {}^* \partial_\alpha^{\mu\nu} (\Delta^\alpha + 4\pi G^\alpha), \quad F'^{\mu\nu} = F^{\mu\nu} + {}^* \partial_\alpha^{\mu\nu} (\Gamma^\alpha + 4\pi L^\alpha),$$

The Equations (25), (27) and (28) are invariants under gauge transformations (34) with **arbitrary** norms Γ^μ and Δ^μ under the condition that the current potential tensors are, at the same time,

under the transformations (32) with four-vectors of norm related with those of Equation (34) by mean of the formulas

$$4\pi G^\alpha = -\Delta^\alpha + \eta'^\alpha, \quad 4\pi L^\alpha = -\Gamma^\alpha + \gamma'^\alpha, \quad (36)$$

where η and γ are arbitrary functions (they may be zero). We can remark that the previous transformations over Hertz tensor also apply to **whichever** of the representations in the Equation (33), then the values of G^α and L^α given by Equation (36) are additives to the arbitrary values of the same quantities that take place in the Equation (33). Also, if Δ^α is not arbitrary but satisfy Equation (35), then the second of Equation (36) probes that L^α is zero, and therefore $F^{\mu\nu}$ is invariant under the gauge transformation (34) without any change in the current potential $R^{\mu\nu}$. This result was previously obtained when we considered to the four-vector A^μ . Similarly, if Γ^α is such that the right hand side of the first of Equation (36) goes zero, $H^{\mu\nu}$ is invariant under (34) without any change in the current potential $Q^{\mu\nu}$.

7. CONCLUSIONS

We obtained from unified way the Hertz super-potentials within the covariant formulation of electrodynamics, introducing a tensor that it generates the four-potential A^μ in the Lorentz's gauge. We did a detailed study of the associated gauge transformations, demonstrating that:

“If a given electromagnetic field can be represented by the Hertz tensor $\Pi^{\mu\nu}$ for a given election of current potentials, then other current potentials exists for which the representation of the same field is given by the Hertz potential $\Pi'^{\mu\nu}$ transformed under the gauge transformation expressed by the Equation (34)”.

REFERENCES

1. Marion, J. B. and M. A. Heald, *Classical Electromagnetic Radiation*, Academic Press, New York, 1980.
2. Panofsky, W. K. and M. Phillips, *Classical Electricity*, Addison Wesley, Reading Mass., 1972.
3. Essex, E. A., *Am. J. Phys.*, Vol. 45, 1099–1101, 1977.
4. Nisbet, A., *Proc. Roy. Soc. A*, Vol. 231, 250–263, 1955.

Near Field Coupling with Small RFID Objects

Arnaud Vena and Pascal Roux

R&D Department, ACS Solutions France SAS, France

Abstract— This paper presents a study on the coupling between a reader and a contactless object in order to define some good working rules to deal with objects with small antennas (NFC mobile phones, key fobs. . .). We will define a model representing the magnetically coupled system composed of the reader and the RFID object in order to introduce the coupling factor which is the key parameter. The coupling factor variation according to reading distance and antennas shapes is a must to predict the overall system performance.

1. INTRODUCTION

Today, the working group in charge of ISO/IEC 14443 standard [1] is defining new contactless objects antenna classes smaller than the very popular “Class 1” card format. We will study such classes and analyze their compatibility with existing readers. In transportation sector, contactless validators use antennas with a typical size of 10 cm by 10 cm to assure a good communication range. But with smaller classes of contactless objects, the magnetic coupling factor (and therefore the reading range) tends to reduce. To calculate the coupling factor, we have to define each antenna loop self inductance and the mutual inductance between them. The calculation of coaxial loops self inductances and mutual inductance can be done with analytical formulas for usual shapes. In all other cases, we can use numerical methods like Finite elements or PEEC method [2]. In near field RFID, antennas are usually closed loops which can be approximated by filaments loops. In this case the numerical Neumann method is an alternative simple way to obtain accurate values of mutual inductance and even self inductance with minimal computation efforts. With this method we will calculate the coupling factor in free space in several cases, for common readers and various RFID object antennas in order to determine the operating volume in each situation. The theoretical values will be compared to experimental coupling factor measurements.

2. MODEL OF THE SYSTEM

In near field RFID [3], we can assimilate the system composed of a reader and an RFID object with an RF transformer. The corresponding electrical model is shown in Figure 1.

The main difference is about the magnetic coupling factor k value which is much lower. In proximity card systems operating at 13.56 MHz, k is usually comprised between 0.03 and 0.3. To transmit power with such low values, the transformer primary and secondary circuits must be tuned close to operating frequency. The transformer primary circuit represents the reader source with matching circuit and antenna. The transformer secondary circuit represents the RFID object with its antenna associated with C_2 capacitor to make a resonant circuit with a frequency generally comprised between 13.56 and 19 MHz. The RFID object antenna inductance is chosen to get the maximum power which means several turns. For “Class 1” reference card [1], the number of turns is 4 and the inductance is about 2300 nH. The resistance R_{load} represents the IC current consumption and also allows the load modulation of the operating field. The expression of the transfer function

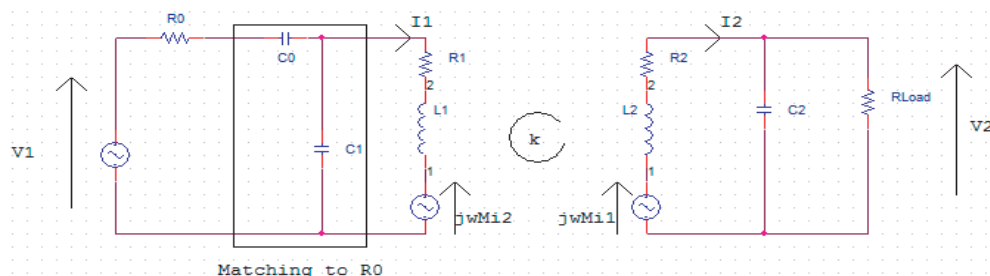


Figure 1: Electrical model of a coupled system composed of a reader and an RFID object.

to obtain the voltage gain at load is the following (1):

$$H_1 = \frac{V_2}{V_1} = \frac{Z_{out}j\omega M}{(Z_0j\omega C_1+1)(j\omega M)^2 - (Z_0 + (Z_0j\omega C_1+1)ZL_1)(Z_{out}+ZL_2)} \quad (1)$$

with $Z_0 = R_0 + \frac{1}{j\omega C_0}$, $ZL_1 = R_1 + j\omega L_1$, $ZL_2 = R_2 + j\omega L_2$ and $Z_{out} = \frac{1}{j\omega C_2 + \frac{1}{R_{load}}}$

The power transmitted to the load is simply V_2^2 / R_{load} . In this system, the resistive load R_{load} is variable to modulate the current I_2 and by the way the voltage at the transformer primary with a value in function of both the mutual inductance and the carrier frequency (2).

$$V_{BackEMF} = j\omega M I_2 \quad (2)$$

The power transmitted to the RFID object and the level of its response mainly depend on the mutual inductance, therefore on the coupling factor. The frequency tuning of the secondary coil between 13.56 and 19 MHz doesn't influence a lot the results. The expression of the transfer function is independent from the object antenna shape thanks to the coupling factor value. So we can say that if we keep the same self inductance value for the new smaller classes then the operating limit will be identically determined by the same minimum coupling factor. The formula (3) gives the coupling factor value in function of both the mutual and the two self inductances:

$$k = \frac{M}{\sqrt{L_1 L_2}} \quad (3)$$

In this equation, we can see that the coupling factor value is not influenced by the number of turns if the radius of each loop is identical. Only the geometrical antenna shape influences this value. The smaller the object antenna size, the closer the distance to the reader for the same coupling factor. We will evaluate the reading range in function of the object antenna size keeping usual reader antenna shapes.

3. DEFINITION OF THE MINIMUM COUPLING FACTOR

The minimum coupling factor is determined by minimal power transfer from reader to RFID object and by minimum signal response from RFID object to reader. A proximity card as defined in ISO/IEC 14443 operates with minimum field strength of 1.5 A/m. While this field produces sufficient power in Class 1 cards it produces a lower power in smaller objects because the received flux is lower and the IC embedded on such objects must work with less power. Another important point is the signal sent by the object and received by the reader. The mutual inductance depends on the object area and when this area is smaller, the signal received by the reader is smaller. By experimental measurements we determined that the minimum coupling factor with usual cards is about $k = 0.03$ and corresponds to field strength of 1.5 A/m. Such a coupling factor value with a smaller RFID object is found at closer distance and therefore with higher field strength. This fact pushes us to say that the coupling factor parameter is more representative than the field strength value. The only way to enhance reading range or at least to keep the one that we get with Class 1 format is to have a more sensitive reader and an object which need less power. In this way, the usual coupling factor limit of $k = 0.03$ will decrease.

4. MAGNETIC COUPLING FACTOR CALCULATION METHOD

The method used to calculate the coupling factor is based on Neumann Formula (4). The analytical equation is computed with a numerical algorithm to get value of the mutual and the self inductances of approximated filaments closed loops.

$$M = \frac{\mu_0}{4\pi} \oint_{C_1} \oint_{C_2} \frac{dr_1 \vec{1} \cdot dr_2 \vec{2}}{|r_1 \vec{1} - r_2 \vec{2}|} \quad (4)$$

This method presents an interest for the simplicity of its implementation in any kind of programming language or dedicated numerical calculation software [4] and for its performances in terms of computation efforts. To validate the numerical Neumann method we will compare its results with the analytical formulas ones. We will use several value of discretization step to build loop antenna

paths in order to define a rule for choosing this parameter. A very small discretization step will increase the result accuracy but the computation time will also increase a lot. So we have to find a compromise between accuracy and computation time. The analytic expression of the Neumann equation can be transposed into the following numerical expression (5):

$$M_{num} = \frac{\mu_0}{4\pi} \sum_{k=1}^{N_1-1} \sum_{l=1}^{N_2-1} \frac{\Delta r_{1_x}(k)\Delta r_{2_x}(l) + \Delta r_{1_y}(k)\Delta r_{2_y}(l) + \Delta r_{1_z}(k)\Delta r_{2_z}(l)}{\sqrt{(r_{1_x}(k) - r_{2_x}(l))^2 + (r_{1_y}(k) - r_{2_y}(l))^2 + (r_{1_z}(k) - r_{2_z}(l))^2}} \quad (5)$$

In this expression, r_1 and r_2 represent the two loops, defined in Cartesian coordinates as a discretized parametric equation. We have N_1 elements to compose C_1 path and N_2 elements to compose C_2 path. The Δ value represents the discretization step and is determined in order to obtain a good approximation of the mutual or self inductance value. To get a self inductance value with this method we have to take $C_2 = C_1 + \Delta Z$ [5]; this means that C_2 path is located on the wire boundary to avoid any singularities. If the wire is round, ΔZ will be equal to the wire radius a . If the wire is rectangular, we have firstly to approximate it by a round wire with the same perimeter as defined by the expression (6):

$$a = \frac{(e + w)}{\pi} \quad (6)$$

with e , the wire thickness and w , its width.

In this way, the external surface of this equivalent round conductor will be equal to the initial rectangular conductor one. Therefore the current density will be nearly equivalent if we consider that the current mainly flows in the conductor surface because of the skin effect. To be more accurate, the intrinsic inductance value must be taken into account. It only depends on the loop length, i.e., the perimeter in case of closed loop. Finally the analytical equation becomes (7):

$$L = \frac{\mu_0}{4\pi} \left[\frac{d}{2} + \iint_{C_1 C_2} \frac{dr\vec{1} \cdot dr\vec{2}}{|r\vec{1} - r\vec{2}|} \right] \quad (7)$$

with d , the path length

And using the expression of mutual inductance (5), the equivalent numerical expression becomes (8):

$$L_{num} = \frac{\mu_0}{4\pi} \frac{1}{2} \sum_{k=1}^{N_1-1} \sqrt{(\Delta r_{1_x}(k))^2 + (\Delta r_{1_y}(k))^2 + (\Delta r_{1_z}(k))^2} + M_{num} \quad (8)$$

In order to evaluate this method we use the analytical expression described by *T. Thompson* [6] as a reference. We find that to get an accurate value of the round wire self inductance for any shape, we have to define a discretization step equal to the wire radius. In the same way, to get an accurate value of the mutual inductance between two loops, the discretization step must be less than or equal to minimum distance between the two loops. Obviously the step has to be small enough to describe the geometrical shape with precision. In case of a circular shape, the discretization step has to be much smaller than the loop radius.

5. EXPERIMENTAL RESULTS

In this section, we evaluate the communication capability with usual readers in function of the object antenna size and shape. We measure the coupling factor in free space taking the following coupling factor expression (9):

$$k = \frac{VL_2}{VL_1} \sqrt{\frac{L_1}{L_2}} \quad (9)$$

Knowing values of L_1 and L_2 , we have just to measure the voltage at any coil. For our study we have defined two new smaller classes, the Class S_1 (e.g., for key fobs) and the Class S_2 (e.g., for mobile phones) with new dimensions as shown in Figure 2. The usual Class 1 dimensions of 72 mm by 42 mm are given for reference.

We have realized measurements with two different reader antennas and for each one with Class 1, Class S_1 and Class S_2 RFID objects. For each reader antenna we have made several measures,

varying Z distance to get k values while keeping loops coaxial and therefore parallel to each other. In Figure 3, we can see the coupling factor evolution in function of Z distance respectively with a circular loop reader antenna and with a rectangular loop reader antenna for each defined RFID object class. With the circular loop, we can see that the maximum range which correspond to a coupling factor $k = 0.03$ is respectively 37 mm for Class S_1 and 5 mm for Class S_2 . With the rectangular reader antenna, results are similar and the maximum range for Class S_1 is 43 mm and 5 mm for class S_2 . In comparison, the Class 1 antenna range is greater than 50 mm with the two reader antennas.

The theoretical values are close to the experimental results. We notice an error of approximately 10%, probably due to imperfection in voltage VL_1 measurement and position of RFID object. The

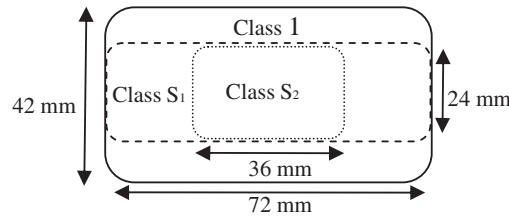


Figure 2: Dimensions of usual Class 1 and smaller classes S_1 and S_2 used for experiments.

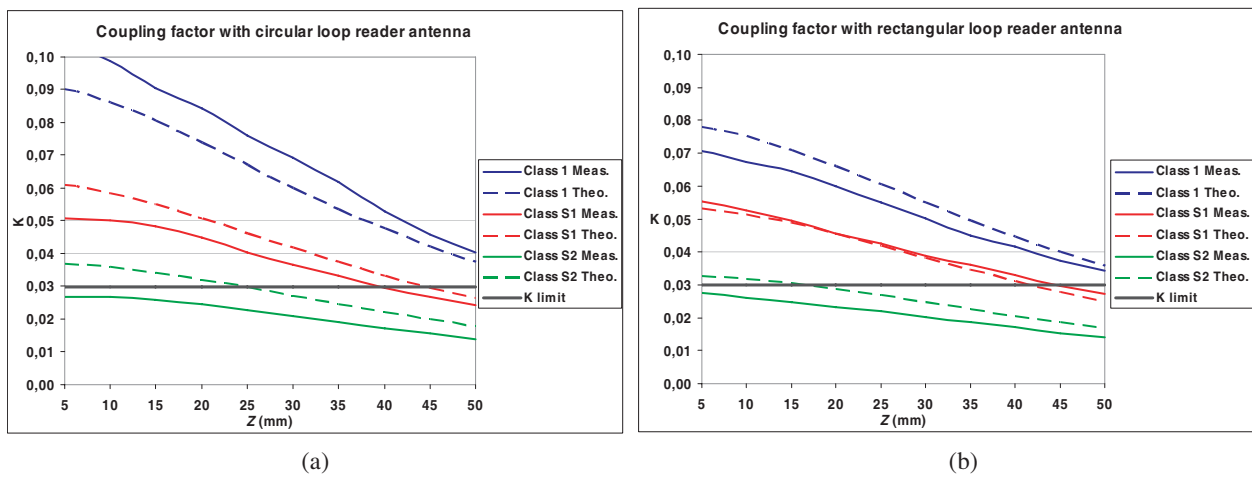


Figure 3: Coupling factor as a function of Z distance when loops are coaxial. (a) With a 6.5 cm radius circular reader loop, (b) with a 12 cm by 13 cm rectangular loop. Dashed lines are the theoretical values and plain lines are measured values.

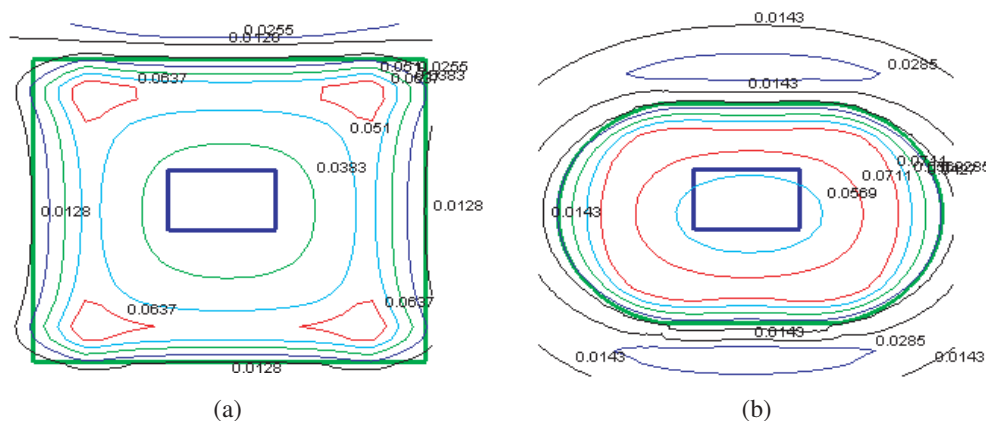


Figure 4: coupling factor 2D map at a distance Z of 5 mm, between RFID object Class S_2 (bold blue loop) and reader antenna (bold green loop). (a) 12 cm by 13 cm rectangular reader antenna, (b) 13 cm by 9 cm oval reader antenna. Note: The coupling factor is maximal in the red zone.

theoretical and measured curves shapes are very similar. The major difficulty in the measurement method is to get the real value of VL_1 voltage because with a high Q antenna the voltage can reach 100 V and the matching is very sensitive to the probe capacity. This is why we set a high impedance resistive voltage divisor in parallel of the antenna and we use a differential active probe to realize the measurement. Another way consists in measuring the reader antenna current loop to deduce voltage VL_1 . The main interest of this calculation method is to gain time in determining if any shape of new RFID object is able to work with a usual reader antenna. The must is to determine the communication volume by representing the coupling map in 2D at any Z distance. With experimental measurements this task is very long and difficult. In Figure 4(a), we can see the calculated coupling factor 2D map between the rectangular loop reader antenna and the RFID object Class S_2 .

We notice that the maximum coupling is obtained when the RFID object is in a corner of the reader antenna. And this was experimentally verified. In Figure 4(b), the calculation method is applied for an unusual shape like a 13 cm by 9 cm oval loop reader antenna. This last antenna is better for smaller Class S_2 thanks to its smaller size. Further simulations with various reader antennas confirm that smaller class RFID objects benefit from a smaller reader antenna size.

6. CONCLUSION

The numerical Neumann method is very efficient to calculate the coupling factor in every position and for every shape. The experimental measurements have validated theoretical values with an error of 10%. The results show that new smaller classes of card have a loss in range at center of antennas of 40% for Class S_1 and 90% for Class S_2 with usual reader antennas. Globally, such new classes of RFID object need smaller reader antennas and interoperability with usual readers is not guaranteed. A way to increase interoperability with these small objects is to develop reader antennas which combine both a good reading range with present cards, e.g., by keeping their usual size, and a zone of high coupling for smaller RFID objects, e.g., in a corner of a rectangular loop.

REFERENCES

1. ISO/IEC 14443-1, 2008.
2. Reinhold, C., P. Scholz, W. John, and U. Hilleringmann, "Efficient antenna design of inductive coupled rfid-systems with high power demand," *Journal of Communications*, Vol. 2, No. 6, November 2007.
3. Finkenzeller, K., *RFID Handbook: Fundamentals and Applications in Contactless Smart Cards and Identification*, Wiley, April 2003.
4. Kiusalaas, J., *Numerical Method in Engineering with Matlab*, Cambridge University Press, 2005.
5. Gardiol, F., *Traité d'électricité, Electromagnétisme*, T3, Presses Polytechniques et Universitaires Romandes, 2001.
6. Thompson, T. and M. Phd, "Inductance calculation technique, Part II: Approximations and handbook methods," *Power Control and Intelligent Motion*, December 1999.

Mutual Inductance Calculation between Circular Coils with Lateral and Angular Misalignment

Slobodan I. Babic, Cevdet Akyel, and Mohamed-Mehdi Mahmoudi
École Polytechnique de Montréal, Montréal, Québec, Canada

Abstract— The purpose of this paper is to present a relatively easy approach for the 3D calculation of the mutual inductance between circular coils with lateral and angular misalignment. The filament method and Grover formulas for the mutual inductance between filamentary circular coils with parallel and inclined axes are used in this approach. The semi-analytical formulas of the mutual induction given in the integral form cover all possible coil configurations and lead to very accurate and fast results. This easy and lucid approach is suitable either for micro-coils or large coils so that one does not need to use modern numerical methods such as FEM and BEM frequently employed in such calculations. Computed mutual-inductance values obtained by the proposed approach, by the software *FastHenry* (based on FEM) and by already published data are in a very good agreement.

1. INTRODUCTION

The magnetically coupled coils are important in magnetically controllable devices and sensors, in modern medicine and telemetric systems applied in biomedical engineering (long-term implantable devices such as pacemakers, cochlear implants, defibrillators, instrumented orthopaedic implants), in conventional medical MRI systems, tokamaks, superconducting coils. In all these applications it is necessary to calculate or measure the mutual inductance of magnetically coupled coils [1–3]. The problem of the accurate and fast calculation of the mutual inductance of circular coils in air has a long history in the electrical engineering [4–17]. The mutual inductance of circular coils can be obtained by analytical, semi-analytical and numerical methods. In this paper, we use Grover formulas expressed over the complete elliptical integrals of the first and second kind [4] for calculating the mutual inductance between two filamentary circular coils with parallel and inclined axes. The filament method [8] is used to replace circular coils of the rectangular cross section (either with lateral or with angular misalignment) by the set of filamentary circular coils. The simple numerical integration is required to integrate the kernel functions. In this paper, we use Romberg numerical integration and Gaussian numerical integration in singular cases.

2. THEORY

2.1. Circular Coils of the Rectangular Cross Section with Lateral Misalignment

Let us take into consideration the system of two non-coaxial circular coils of rectangular cross section with parallel axes (lateral misalignment), (Fig. 1), with N_1 and N_2 , the total number of turns of the windings. It is assumed that the coils are compactly wound and the insulation on the wires is thin, so that the electrical current can be considered uniformly distributed over the whole cross-sections of the winding. The corresponding dimensions of these coils are shown in Fig. 1. The cross-sectional area of the first coil I is divided into $(2K+1)$ by $(2N+1)$ cells and the second coil II into $(2m+1)$ by $(2n+1)$ cells. Each cell in the first coil I contains one filament, and the current density in the coil cross-section is assumed to be uniform, so that the filament currents are equal. The same assumption applies to the second coil II [8]. Using the filament method and Grover's Formula (2) [4] for the mutual inductance between two circular filamentary coils with parallel axes, the mutual inductance between two circular coils of rectangular cross section with parallel axes is given by,

$$M = \frac{N_1 N_2 \sum_{g=-K}^{g=K} \sum_{h=-N}^{h=N} \sum_{p=-m}^{p=m} \sum_{l=-n}^{l=n} M(h, l, g, p)}{(2K+1)(2N+1)(2m+1)(2n+1)} \quad (1)$$

$$M(h, l, g, p) = \frac{\mu_0}{\pi} \sqrt{R_P(h)R_S(l)} \int_0^\pi \frac{\left(1 - \frac{d}{R_S(l)} \cos \phi\right) \Phi(k)}{\sqrt{V^3}} d\phi \quad (2)$$

$$\alpha(h, l) = \frac{R_S(l)}{R_P(h)}, \quad \beta(h, g, p) = \frac{z(g, p)}{R_P(h)}, \quad k^2(h, l, g, p) = \frac{4\alpha(h, l)V(l)}{(1 + \alpha(h, l)V(l))^2 + \beta^2(h, g, p)}$$

$$V(l) = \sqrt{1 + \frac{d^2}{R_S^2(l)} - 2\frac{d}{R_S(l)} \cos \varphi}, \quad \Phi(k) = \left(\frac{2}{k} - k\right) K(k) - \frac{2}{k} E(k)$$

$$R_P(h) = R_P + \frac{h_P}{(2N+1)}h; \quad h = -N, \dots, 0, \dots, N, \quad R_S(l) = R_S + \frac{h_S}{(2n+1)}l; \quad l = -n, \dots, 0, \dots, n$$

$$R_P = \frac{R_1 + R_2}{2}, \quad R_S = \frac{R_3 + R_4}{2}, \quad h_P = R_2 - R_1, \quad h_S = R_4 - R_3$$

$$R_P = \frac{R_1 + R_2}{2}, \quad R_S = \frac{R_3 + R_4}{2}, \quad h_P = R_2 - R_1, \quad h_S = R_4 - R_3$$

$$z(g, p) = c + \frac{a}{(2K+1)}g + \frac{b}{(2m+1)}p, \quad g = -K, \dots, 0, \dots, K; \quad p = -m, \dots, 0, \dots, m$$

2.2. Circular Coils of the Rectangular Cross Section with Angular Misalignment

Let us take into consideration the system of two inclined circular coils of rectangular cross section (angular misalignment), (Figs. 1 and 2), with N_1 and N_2 , the total number of turns of the windings. It is assumed that the coils are compactly wound and the insulation on the wires is thin, so that

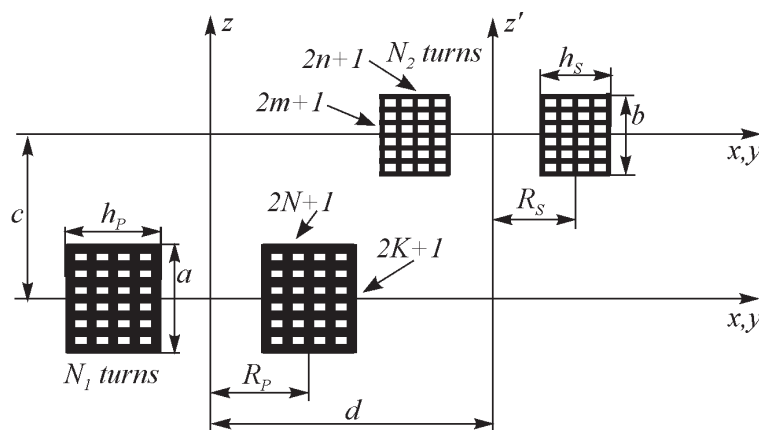


Figure 1: Configuration of mesh coils: Two circular coils of rectangular cross section with lateral misalignment (parallel axes).

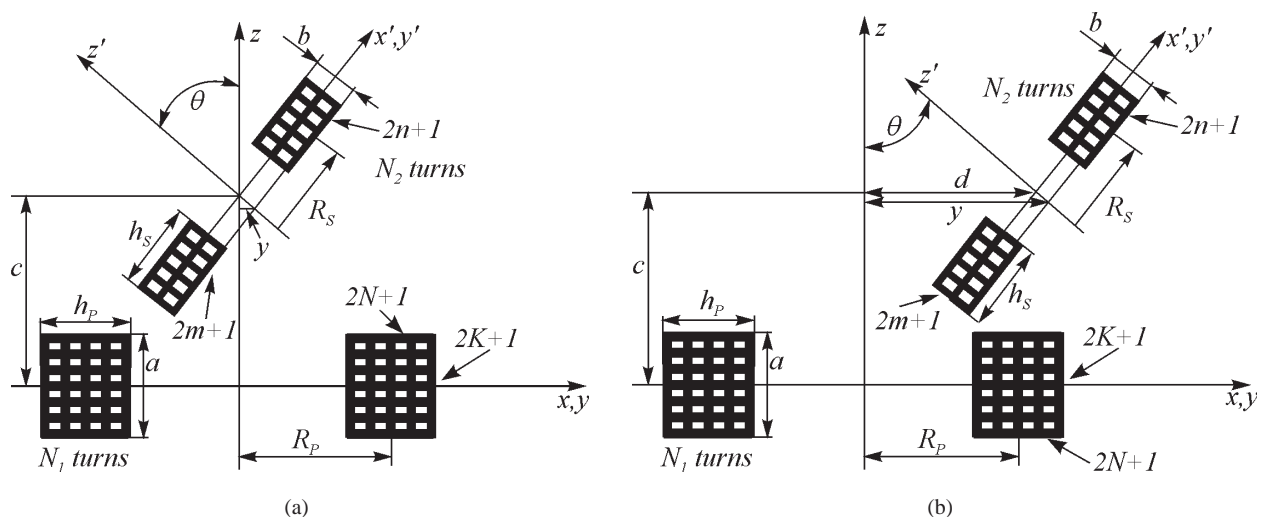


Figure 2: Configuration of mesh matrix: (a) Two circular coils of rectangular cross section (axes intersect at the center of one of the coils). (b) Two circular coils of rectangular cross section (axes intersect but not at the center of either).

the electrical current can be considered uniformly distributed over the whole cross-sections of the winding. The corresponding dimensions of these coils are shown in Figs. 1 and 2. The cross-sectional area of the first coil I is divided into $(2K + 1)$ by $(2N + 1)$ cells and the second coil II into $(2m + 1)$ by $(2n + 1)$ cells. Each cell in the first coil I contains one filament, and the current density in the coil cross-section is assumed to be uniform, so that the filament currents are equal. The same assumption applies to the second coil II [9]. Using the filament method and Grover's Formula (4) [4] for the mutual inductance between two circular filamentary coils with inclined axes, the mutual inductance between two circular coils of rectangular cross section with inclined axes is given by

$$M = \frac{N_1 N_2 \sum_{g=-K}^{g=K} \sum_{h=-N}^{h=N} \sum_{l=-n}^{l=n} \sum_{p=-m}^{p=m} M(g, h, l, p)}{(2K + 1)(2N + 1)(2m + 1)(2n + 1)} \quad (3)$$

$$M(g, h, l, p) = \frac{\mu_0}{\pi} \sqrt{R_P(h)R_S(l)} \int_0^\pi \frac{\left[\cos \theta - \frac{d(p)}{R_S(l)} \cos \phi \right] \Phi(k)}{\sqrt{V^3}} d\phi \quad (4)$$

$$V = \sqrt{1 - \cos^2 \phi \sin^2 \theta - 2 \frac{d(p)}{R_S} \cos \phi \cos \theta + \frac{d(p)^2}{R_S^2}}, \quad k^2 = \frac{4\alpha V}{(1 + \alpha V)^2 + \xi^2}, \quad \xi = \beta - \alpha \cos \phi \sin \theta$$

$$\alpha = \frac{R_S}{R_P(h)}, \quad \beta = \frac{z(g, p)}{R_P(h)}, \quad y(p) = \frac{b \sin \theta}{(2m + 1)} p; \quad p = -m, \dots, 0, \dots, m$$

$$d(p) = d + y(p) = d + \frac{b \sin \theta}{(2m + 1)} p; \quad p = -m, \dots, 0, \dots, m$$

$$R_P(h) = R_P + \frac{h_P}{(2N + 1)} h; \quad h = -N, \dots, 0, \dots, N, \quad R_P = \frac{R_1 + R_2}{2}, \quad h_P = R_2 - R_1$$

$$R_S(l) = R_S + \frac{h_S}{(2n + 1)} l; \quad l = -n, \dots, 0, \dots, n, \quad R_S = \frac{R_3 + R_4}{2}, \quad h_S = R_4 - R_3$$

$$z(g, p) = c + \frac{a}{(2K + 1)} g - \frac{b \cos \theta}{(2m + 1)} p, \quad g = -K, \dots, 0, \dots, K; \quad p = -m, \dots, 0, \dots, m$$

$K(k)$ and $E(k)$ are complete elliptic integrals of the first and the second kind [19, 20].

3. NUMERICAL RESULTS AND DISCUSSION

In many electromagnetic applications the optimal magnetic coupling between thin circular coils is required regarding to lateral and angular misalignment. From two general cases given in this paper it is possible to obtain all coil combinations for which the mutual inductance is calculated. In this section, we present numerical results obtained by proposed approach compared by already published data and by the software *FastHenry*.

Ex.1: Calculate the mutual inductance between two equal non-coaxial disks with dimensions: $R_P = R_S = 20$ cm, $h_P = h_S = 2.5$ cm, $c = d = 20$ cm. The number of turns is $N_1 = N_2 = 100$.

This coil configuration can be obtained by (1) putting $a = b = 0$ and omitting two sums regarding to variables g and p . The presented approach (1) gives the mutual inductance (the number of subdivisions was $N = n = 100$),

$$M = 516.463 \mu\text{H}$$

By the software *FastHenry* [18], the mutual inductance is,

$$M_{\text{FastHenry}} = 516.554 \mu\text{H}$$

The discrepancy between compared results is about 0.02%.

Ex.2: Find the mutual inductance between two loosely coupled coils (two wall solenoids) for which the given constants are: $R_P = R_S = 2.5$ cm and lengths $a = b = 5$ cm, $d = 25$ cm, $c = 0$ cm, $N_1 = N_2 = 125$, (Grover) [4].

This coil configuration can be obtained by (1) putting $h_P = h_S = 0$ and omitting two sums regarding to variables h and l .

By Grover [4], the mutual inductance is

$$M = -0.3826 \mu\text{H}$$

By the presented work (the number of subdivision was $N = n = 50$) the mutual inductance is,

$$M = -0.3825 \mu\text{H}$$

Applying the software *FastHenry* [18], the mutual inductance is,

$$M_{FastHenry} = -0.3977 \mu\text{H}$$

Obviously the presented work and [4] give the mutual inductance values which are in a very good agreement (about 0.02%) but they differ from those obtained by the software *FastHenry* about 3.95%.

Ex.3: In this example, we treat two disk coils (pancakes) where the centers of filamentary coils that replace the second inclined disc are on the axis of the primary coil. Given: $R_P = 50$ mm, $R_S = 20$ mm, $h_P = 20$ mm, $h_S = 10$ mm, $d = 0$ mm, $N_1 = 200$, $N_2 = 100$. Calculate the mutual inductance between disks when their axes are inclined at an angle whose cosine is 0.4. This coil configuration can be obtained by (3) putting $a = b = 0$ and omitting two sums regarding to variables g and p . The presented approach (3) gives the mutual inductance (number of subdivisions was $N = n = 50$),

$$M = 47.5414 \mu\text{H}$$

Applying the software *FastHenry* [18], the mutual inductance is,

$$M_{FastHenry} = 47.0538 \mu\text{H}$$

The discrepancy between compared results is about 1.03%.

Ex.4: Calculate the mutual inductance between two inclined solenoids [3] for which $R_P = 6$ cm, $R_S = 5$ cm, $a = 12$ cm, $b = 4$ cm, $c = 6$ cm, $d = 0$ cm, $N_1 = 120$, $N_2 = 60$ and $\cos(\theta) = 0.8$.

By Grover [4], the mutual inductance is

$$M = 56.3431 \mu\text{H}$$

By the presented work (the number of subdivision was $N = n = 50$) the mutual inductance is,

$$M = 56.3426 \mu\text{H}$$

Applying the software *FastHenry* [18], the mutual inductance is,

$$M_{FastHenry} = 56.5121 \mu\text{H}$$

All results are in a very good agreement. The discrepancy between compared results is about 0.03%.

From previous results (Ex.1–Ex.4), we can conclude that all obtained results are in a very good agreement even though there are some anticipated discrepancies because our approach uses thin circular filamentary coils that replace real coils and the software *FastHenry* uses coils turns that are not round, but approximated with square conductors. Also, the software *FastHenry*, based on the finite-element method, whose tools are developed for micro coils and not very well suited for larger coils [1]. To achieve high accuracy for these and other cases, it is necessary to create a new mesh in the model using more elements and nodes that can increase the computational time. Thus, we find our approach easy, lucid and accurate for calculating the mutual inductance between circular coils with lateral and angular misalignment either applicable for macro or micro-coils.

ACKNOWLEDGMENT

We would like to thank the Natural Science and Engineering Research Council of Canada (NSERC) that supported this work under Grant RGPIN 4476-05 NSERC NIP 11963.

REFERENCES

1. Puers, R., K. Van Schuylenbergh, M. Catrysse, and B. Hermans, “Wireless inductive transfer of power and data,” *Analog Circuit Design*, 395–414, Springer, 978-1-4020-3884-6, 2006.
2. Matsukawa, M., S. Ishida, A. Sakasai, K. Urata, I. Senda, G. Kurita, H. Tamai, S. Sakurai, Y. M. Miura, K. Masaki, K. Shimada, and T. Terakado, “Design and analysis of plasma position and shape control in superconducting tokamak JT-60SC,” *Fusion Engineering and Design*, Vol. 66–68, 703–708, ELSEVIER, 2003.
3. Pichorim, S. F. and P. J. Abbati, “Design of coils for millimeter- and submillimeter-sized biotelemetry,” *IEEE Trans. on Biom. Eng.*, Vol. 51, No. 8, 1487–1489, Aug. 2004.
4. Grover, F. W., *Inductance Calculations*, Dover, New York, 1964.
5. Kalantarov, P. L., *Inductance Calculations*, National Power Press, Moscow, 1955.
6. Snow, C., *Formulas for Computing Capacitance and Inductance*, National Bureau of Standards Circular 544, Washington D.C., Dec. 1954.
7. Dwight, H. B., *Electrical Coils and Conductors*, McGraw-Hill Book Company, INC., New York, 1945.
8. Kim, K.-B., E. Levi, Z. Zabar, and L. Birenbaum, “Mutual inductance of noncoaxial circular coils with constant current density,” *IEEE Trans. on Magn.*, Vol. 33, No. 5, 3916–3921, Sep. 1997.
9. Babic, S. and C. Akyel, “Calculating mutual inductance between circular coils with inclined axes in air,” *IEEE Trans. on Magn.*, Vol. 44, No. 7, 1743–1750, Jul. 2008.
10. Babic, S. I. and C. Akyel, “New mutual inductance calculation of the magnetically coupled coils: Thin disk coil — Thin wall solenoid,” *Journal of Electromagnetic Waves and Applications*, Vol. 20, No. 10, 1281–1290, 2006.
11. Babic, S. I. and C. Akyel, “New analytic-numerical solutions for the mutual inductance of two coaxial circular coils with rectangular cross section in air,” *IEEE Trans. on Magn.*, Vol. 42, No. 6, 1661–1669, Jun. 2006.
12. Babic, S. and C. Akyel, “An improvement in calculation of the self- and mutual inductance of thin-wall solenoids and disk coils,” *IEEE Trans. on Magn.*, Vol. 36, No. 4, 678–684, Jul. 2000.
13. Akyel, C., S. Babic, and S. Kincic, “New and fast procedures for calculating the mutual inductance of coaxial circular coils (disk coil — Circular coil),” *IEEE Trans. on Magn.*, Vol. 38, No. 5, 1367–1369, Part 1, Sep. 2002.
14. Babic, S., C. Akyel, and S. J. Salon, *IEEE Trans. on Magn.*, Vol. 38, No. 5, 1234–1237, Mar. 2003.
15. Babic, S., S. Salon, and C. Akyel, “Inductance calculations for noncoaxial coils using Bessel functions,” *IEEE Trans. on Magn.*, Vol. 40, No. 2, 822–825, Mar. 2004.
16. Conway, J. T., “Inductance calculations for noncoaxial coils using Bessel functions,” *IEEE Trans. on Magn.*, Vol. 43, No. 3, 1023–1034, Mar. 2007.
17. Conway, J. T., “Noncoaxial inductance calculations without the vector potential for axisymmetric coils and planar coils,” *IEEE Trans. on Magn.*, Vol. 44, No. 4, 453–462, Apr. 2008.
18. Kamon, M., M. J. Tsuk, and J. White, “FASTHENRY: A multipole-accelerated 3-D inductance extraction program,” *IEEE Trans. Micro. Th. Tech.*, Vol. 42, 1750–1758, Sep. 1994.
19. Gradshteyn, I. S. and I. M. Ryzhik, Dover, New York, 1972.
20. Abramowitz, M. and I. A. Stegun, *Handbook of Mathematical Functions*, 595, Series 55, Washington D.C., Dec. 1972.

Optimization Research on Electric Field of 500 kV Standard Capacitor

Shizuo Li¹ and Shiyu Kang²

¹Institute of Electrical Engineering, Guangxi University, Nanning 530004, China

²Guangxi Vocational & Technical Institute of Industry, Nanning 530001, China

Abstract— Surface charge density method is presented to calculation the electric field of standard capacitor which is an infinite field with conductor and dielectric material. This method supposes that free charges distribute continuously on the surface of conductor and bound charges exist on the interface of two dielectrics, then expresses surface charges density by linear interpolation and forms the simultaneous linear equations by boundary or interface condition. Optimization shows that the maximum of electric intensity in the air can be reduced to a certain limit by adjusting the height of voltage balance ring.

1. INTRODUCTION

Capacitance stability of high voltage standard capacitor is very important to testing result, and the main factor to stability of capacitance is air ionization. Usually, in the interior of capacitor, the electric field is even and SF₆ gas which has good insulated characteristic is filled, no gas ionization will occur. But on the out of capacitor, medium is air and the electric field is asymmetry, air ionization may occur in the zone which electric field intension is very high to a certain limit. Electric field distribution of standard capacitor is needed to calculate accurately and the structure of it is needed to optimize to reduce the maximum of electric field intension.

Now finite element method is used to calculate the electric field of standard capacitor, but this method have some shortcoming, it is not suit for infinite field firstly, then it use potential as solving variable, the quantities such as charges density and electric intensity need to differentiate with respect to the potential, and will lead to more error. Lastly, more triangle elements and calculation time must be needed to get an accurate result.

Surface charge density method is presented in this paper. Height of the voltage balance rings is selected as maximizing variable to reduce the maximum of electric intension in the air.

2. SURFACE CHARGE DENSITY METHOD

500 kV standard capacitor which structure is rotational symmetry is shown in Fig. 1, it is composed of high voltage pole, low voltage pole, fiber reinforced plastics (FRP) supporter, two voltage balance ring with same radius.

Because power frequency is very low, the electric field of 500 kV standard capacitor can be treated as electrostatic field. According to electromagnetic field theory, the potential φ in the field satisfies:

$$\nabla^2 \varphi = 0 \quad (1)$$

And the boundary condition: (1) $\varphi = U$, on the surface of high voltage poles and voltage balance rings; (2) $\varphi = 0$, on the surface of low voltage pole and ground; (3) $\varphi_1 = \varphi_2$ and $\varepsilon_1 \frac{\partial \varphi_1}{\partial n} = \varepsilon_2 \frac{\partial \varphi_2}{\partial n}$, on the surface of FRP supporter, here the dielectric constant of air $\varepsilon_1 = \varepsilon_0 = 8.85 \times 10^{-12}$ F/m, and the dielectric constant of FRP supporter $\varepsilon_2 = 3.4\varepsilon_0$.

It is supposed that the free charges of capacitor distribute continuously on the surface of electric poles and voltage balance rings. On the surface of FRP supporter, the dielectrics of two sides are different, and the vertical components of electric intensity are not equal, this means that there are net bound charges on the surface. If these bound charges have been treated as equivalent charge source, the calculating field can be regarded as even dielectric with same constant ε_0 , the potential produced by there bound charges is similar as those by the free charges on electric pole.

Due to axis of symmetry on the structure of standard capacitor, only the charge distribution on the meridional plane is needed to simulate and calculate. Divide the cross curves of the meridional plane with the surface of electric poles or FRP supporter into many line segments, and set the

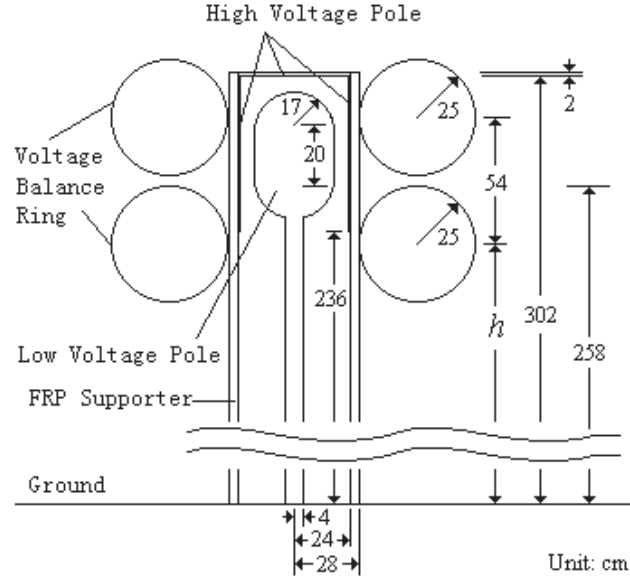


Figure 1: 500 kV standard capacitor.

surface charges density of every node be σ_i , $i = 0, 1, 2, \dots, n$, then the surface charges density of any point on any line segment is:

$$\sigma(r) = \frac{r - r_{i+1}}{r_i - r_{i+1}} \sigma_i + \frac{r - r_i}{r_{i+1} - r_i} \sigma_{i+1} \quad (2)$$

Cingulum surface charges as shown in Fig. 2 have been studied for convenience. The potential of any point $P(R, Z)$ produced by any cingulum surface charges and its mirror to the ground is:

$$\begin{aligned} \varphi(R, Z) &= \frac{1}{4\pi\epsilon_0} \int_0^{2\pi} \int_{r_i}^{r_{i+1}} \left(\frac{r \sqrt{1 + \left(\frac{z_{i+1} - z_i}{r_{i+1} - r_i} \right)^2} \left(\frac{r - r_{i+1}}{r_i - r_{i+1}} \sigma_i + \frac{r - r_i}{r_{i+1} - r_i} \sigma_{i+1} \right)}{\sqrt{\left[Z - z_i - \frac{z_{i+1} - z_i}{r_{i+1} - r_i} (r - r_i) \right]^2 + [r \cos(\theta)]^2 + [R - r \sin(\theta)]^2}} \right) dr d\theta \\ &\quad - \frac{1}{4\pi\epsilon_0} \int_0^{2\pi} \int_{r_i}^{r_{i+1}} \left(\frac{r \sqrt{1 + \left(\frac{z_{i+1} - z_i}{r_{i+1} - r_i} \right)^2} \left(\frac{r - r_{i+1}}{r_i - r_{i+1}} \sigma_i + \frac{r - r_i}{r_{i+1} - r_i} \sigma_{i+1} \right)}{\sqrt{\left[Z + z_i + \frac{z_{i+1} - z_i}{r_{i+1} - r_i} (r - r_i) \right]^2 + [r \cos(\theta)]^2 + [R - r \sin(\theta)]^2}} \right) dr d\theta \\ &= c_i \sigma_i + c_{i+1} \sigma_{i+1} \end{aligned} \quad (3)$$

For the nodes on the surface of electric poles and voltage balance rings which potential is given, potential of these nodes produced by all charges (include free charges and bound charges) can be calculated by (3), and some linear equations can be set up.

For the nodes on the surface of FRP supporter, those potential is unknown, and dielectric interface condition is used to form the other linear equations. As shown in Fig. 3, when point M approach point Q on the direction of n which is vertical to dielectric interface, then:

$$\frac{\partial \varphi_1}{\partial n} = \lim_{M \rightarrow Q} \frac{\partial \varphi_M}{\partial n} = -\frac{\sigma_Q}{2\epsilon_0} + \int_{S-Q} \frac{\sigma}{4\pi\epsilon_0} \frac{n \cdot t^0}{t^2} dS \quad (4)$$

Here $S - Q$ means all charges on the point Q , and t is the vector from the point of the charge source to the point Q .

When point N approach point Q on the inverse direction of n which is vertical to dielectric interface, then:

$$\frac{\partial \varphi_2}{\partial n} = \lim_{N \rightarrow Q} \frac{\partial \varphi_N}{\partial n} = \frac{\sigma_Q}{2\epsilon_0} + \int_{S-Q} \frac{\sigma}{4\pi\epsilon_0} \frac{n \cdot t^0}{t^2} dS \quad (5)$$

Substitute (4) and (5) into dielectric interface condition, then:

$$\frac{\varepsilon_1 + \varepsilon_2}{\varepsilon_1 - \varepsilon_2} \frac{\sigma_Q}{2\varepsilon_0} - \int_{S-Q} \frac{\sigma}{4\pi\varepsilon_0} \frac{n \cdot t^0}{t^2} dS = \frac{\varepsilon_1 + \varepsilon_2}{\varepsilon_1 - \varepsilon_2} \frac{\sigma_Q}{2\varepsilon_0} - E_n = 0 \quad (6)$$

E_n is the vertical component of electric intensity on point Q , and the contribution of cingulum surface charges shown Fig. 2 and its mirror to E_n can be calculated:

$$\begin{aligned} dE_n(R, Z) &= \frac{1}{4\pi\varepsilon_0} \int_0^{2\pi} \int_{r_i}^{r_{i+1}} \left(\frac{r \sqrt{1 + \left(\frac{z_{i+1}-z_i}{r_{i+1}-r_i}\right)^2} \left(\frac{r-r_{i+1}}{r_i-r_{i+1}}\sigma_i + \frac{r-r_i}{r_{i+1}-r_i}\sigma_{i+1}\right) n \cdot t^0}{\left[Z - z_i - \frac{z_{i+1}-z_i}{r_{i+1}-r_i}(r-r_i)\right]^2 + [r \cos(\theta)]^2 + [R - r \sin(\theta)]^2} \right) dr d\theta \\ &\quad - \frac{1}{4\pi\varepsilon_0} \int_0^{2\pi} \int_{r_i}^{r_{i+1}} \left(\frac{r \sqrt{1 + \left(\frac{z_{i+1}-z_i}{r_{i+1}-r_i}\right)^2} \left(\frac{r-r_{i+1}}{r_i-r_{i+1}}\sigma_i + \frac{r-r_i}{r_{i+1}-r_i}\sigma_{i+1}\right) n \cdot tt^0}{\left[Z + z_i + \frac{z_{i+1}-z_i}{r_{i+1}-r_i}(r-r_i)\right]^2 + [r \cos(\theta)]^2 + [R - r \sin(\theta)]^2} \right) dr d\theta \\ &= d_i\sigma_i + d_{i+1}\sigma_{i+1} \end{aligned} \quad (7)$$

Here

$$t = -r \cos(\theta)i + [R - r \sin(\theta)]j + \left[Z - z_i - \frac{z_{i+1} - z_i}{r_{i+1} - r_i}(r - r_i) \right] k$$

and

$$tt = -r \cos(\theta)i + [R - r \sin(\theta)]j + \left[Z + z_i + \frac{z_{i+1} - z_i}{r_{i+1} - r_i}(r - r_i) \right] k$$

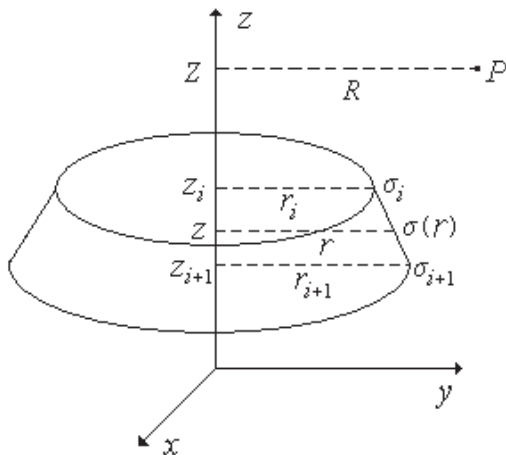


Figure 2: Cingulum surface charges.

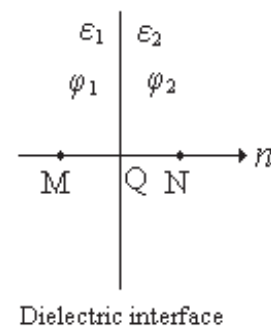


Figure 3: Dielectric interface condition.

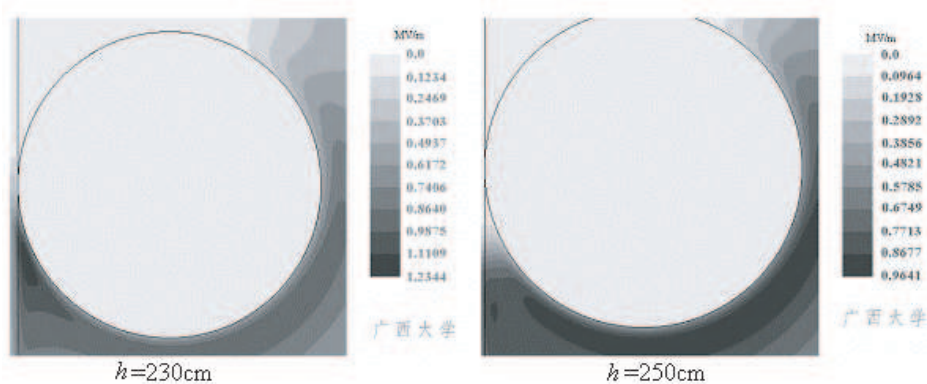


Figure 4: Distribution of electric intensity.

Linear equations of the nodes on the surface of FRP supporter can be set up by (6) and (7), along with the equations of the nodes on the surface of electric poles, charges density can be determined by solving simultaneous linear equation.

3. OPTIMIZATION OF ELECTRIC FIELD

In order to avoid air ionization, electric intensity of the air around the standard capacitor must reduce to a certain limit $E_{\max} = 1.06 \text{ mV/m}$. Here, height of the voltage balance rings is selected as maximizing variable to optimize the electric field. Fig. 4 shows the distribution of electric intensity near the nether voltage balance ring when $h = 230 \text{ cm}$ and $h = 250 \text{ cm}$. Fig. 5 shows the equipotential distribution.

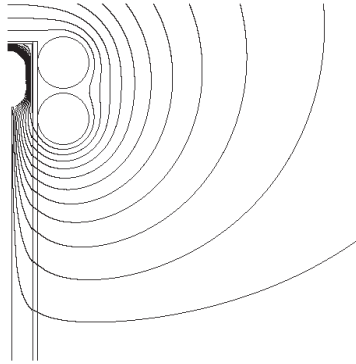


Figure 5: Equipotential distribution.

4. CONCLUSIONS

Surface charge density method supposes that free charges distribute continuously on the surface of conductor and bound charges exist on the interface of two dielectrics, then expresses surface charges density by linear interpolation and forms the simultaneous linear equations by boundary or interface condition. It is very efficient to infinite field with conductor and dielectric material.

Height of voltage balance ring may affect the electric intensity distribution of the standard capacitor, the maximum of electric intensity in the air can be reduced to a certain limit by optimization.

REFERENCES

1. Sheng, J. N., ???, 1991.
2. Zhou, K. D., ???, 1986.
3. Daffe, J. and R. G. Olsen, "An integral equation technique for solving rotationally symmetric electrostatic problems in conducting and dielectric material," *IEEE Trans. on PAS*, 1979.

On Analog Approach for Current Lissajous Undulator

S. Micloş¹, D. Savastru¹, and V. I. R. Niculescu²

¹National Institute of R&D for Optoelectronics INOE-2000
09 Atomistilor Str., POB MG-5, Magurele, Ilfov, Romania

²National Institute of R&D for Lasers, Plasma and Radiation Physics INFPLR
409 Atomistilor Str., POB MG-36, Magurele, Ilfov, Romania

Abstract— In free-electron laser (FEL) research and development one of the main trends is the elaboration of the compact devices. The undulator is the principal component where the phenomenon of coherent radiation take place. A new theoretical model of an undulator for free electron lasers in a modified Lissajous magnetic field is presented. The undulator is a stack of wires which are described in xy plane by modified Lissajous equations. Analogic simulation is more intuitive and also enables a validation of the numerical simulation. The modified Lissajous, comprizing a Lissajous portion and a linear, is implemented using analog gates controlled by gate signals.

1. INTRODUCTION

In free-electron laser (FEL) research and development one of the main trends is the elaboration of the compact devices [1–3]. The undulator is the principal component where the phenomenon of coherent radiation take place.

A new theoretical model of an undulator for free electron lasers in a modified Lissajous magnetic field is presented. The undulator is a stack of wires which are described in xy plane by modified Lissajous equations.

The undulator is a stack of wires which are described in xy plane by a modified Lissajous equations (in polar coordinates), which is basically a Lissajous:

$$x = a \cdot \cos(\theta) \quad y = -\sin(2 \cdot \theta)$$

for Lissajous portion: for $\theta = 0 \dots \frac{\pi}{2} - \theta_0$, for $\theta = \frac{\pi}{2} + \theta_0 \dots \frac{3\pi}{2} - \theta_0$ and, finally, for $\theta = \frac{3\pi}{2} + \theta_0 \dots 2 \cdot \pi$, where $\theta_0 = \arcsin(y_0)$ is the limit angle that separates the Lissajous and linear portions of the curve. The linear portion of the modified Lissajous has the next equations:

$$x = -x_0 \dots x_0 \quad y = y_0$$

for the upper region and

$$x = -x_0 \dots x_0 \quad y = -y_0$$

for the lower region of the linear portion.

Here x_0 and y_0 are the coordinates of the frontier point:

$$x_0 = a \cdot \cos(\theta_0) \quad y_0 = -\sin(2 \cdot \theta_0)$$

Figure 1 shows the modified Lissajous graph in cartesian coordinates. Modified Lissajous in polar coordinates is presented in Figure 2. The modified Lissajous profile is used then to get the vector potential components B_x , B_y and B_z by integrating over the wire profile. Modified Lissajous wire stack is presented in Figure 3.

2. METHODS

The equations describing the model of the magnetic field generated by the undulator are the next.

In the next equations x_p , y_p , z_p denotes the coordinates of the reference point, while z_c denotes the current position of the wire.

— for the linear portion of the domain:

$$c_1 = (y_p - y_0)^2 + (z_p - z_c)^2 \quad c_2 = \frac{x_p - x_0}{c_1 \sqrt{(x_p - x_0)^2 + c_1}} \quad c_3 = \frac{x_p + x_0}{c_1 \sqrt{(x_p + x_0)^2 + c_1}}$$

$$B_x = 0 \quad B_y = (c_2 - c_3) \cdot (z_p - z_c) \quad B_z = -(c_2 - c_3) \cdot (y_p - y_0)$$

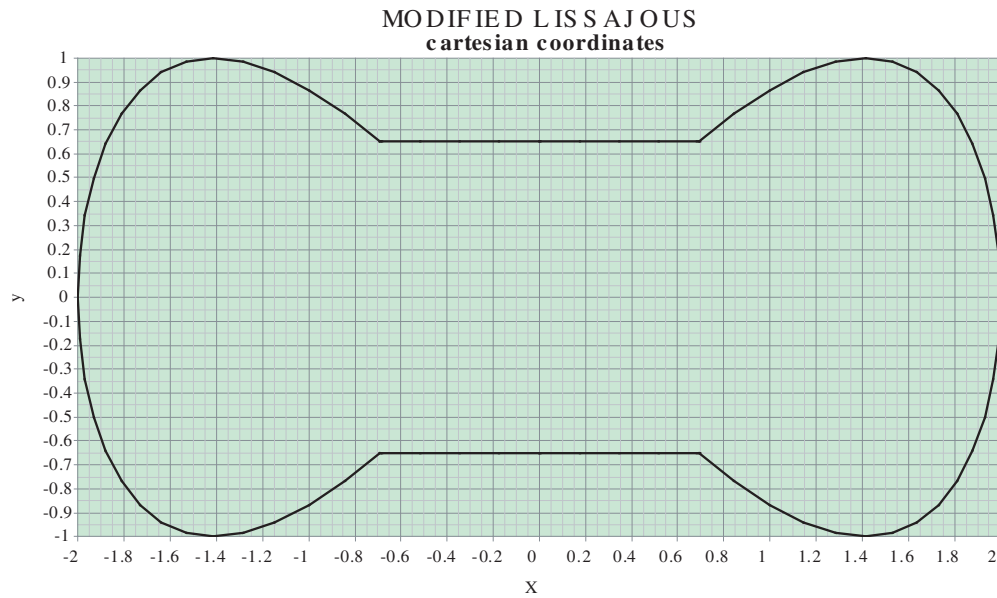


Figure 1: Modified Lissajous in cartesian coordinates.

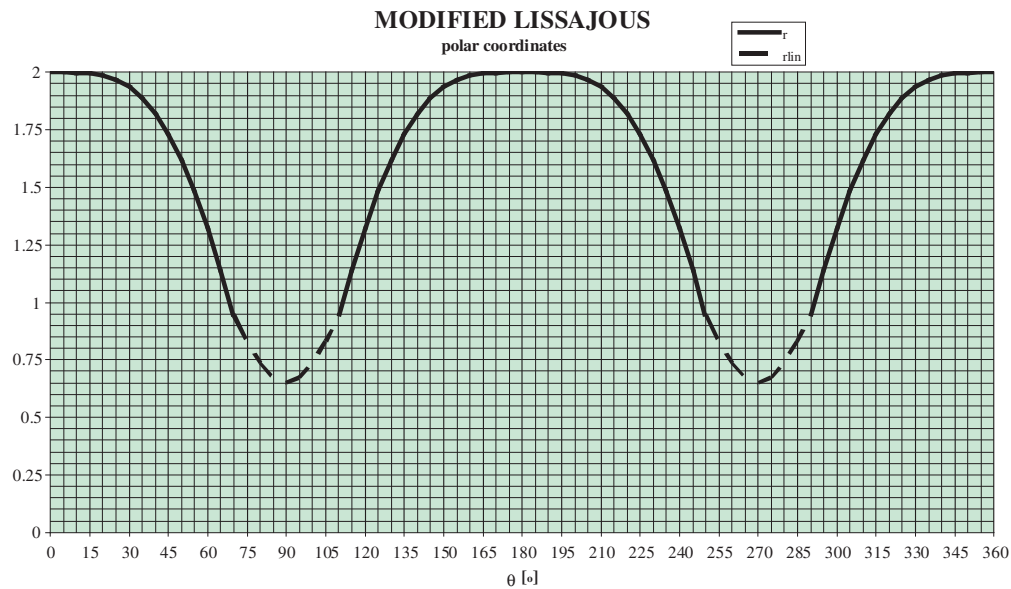


Figure 2: Modified Lissajous in polar coordinates.

— for the lemniscate portion of the domain:

$$\begin{aligned}
 x_1 &= \sqrt{2 \cdot \cos(2 \cdot \theta)} \cdot \sin(\theta) & y_1 &= \sqrt{2 \cdot \cos(2 \cdot \theta)} \cdot \cos(\theta) \\
 c_4 &= \frac{-\sqrt{2} \cdot \sin(3 \cdot \theta)}{\sqrt{\cos(2 \cdot \theta)}} & c_5 &= \frac{\sqrt{2} \cdot \sin(\theta)}{\sqrt{\cos(2 \cdot \theta)}} \\
 B_x &= \int_{\theta_i}^{\theta_f} \frac{c_4 \cdot (z_p - z_c) \cdot d\theta}{\left[(x_p - x_1)^2 + (y_p - y_1)^2 + (z_p - z_c)^2 \right]^{3/2}} \\
 B_y &= \int_{\theta_i}^{\theta_f} \frac{c_5 \cdot (z_p - z_c) \cdot d\theta}{\left[(x_p - x_1)^2 + (y_p - y_1)^2 + (z_p - z_c)^2 \right]^{3/2}} \\
 B_z &= \int_{\theta_i}^{\theta_f} \frac{(-c_5 \cdot (x_p - x_1) - c_4 \cdot (y_p - y_1)) \cdot d\theta}{\left[(x_p - x_1)^2 + (y_p - y_1)^2 + (z_p - z_c)^2 \right]^{3/2}}
 \end{aligned}$$

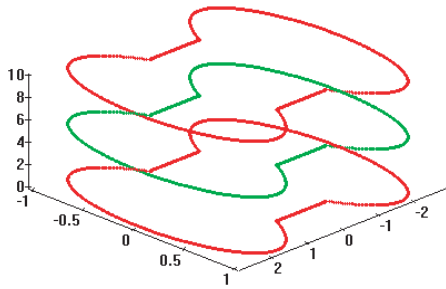


Figure 3: Modified Lissajous wire stack.

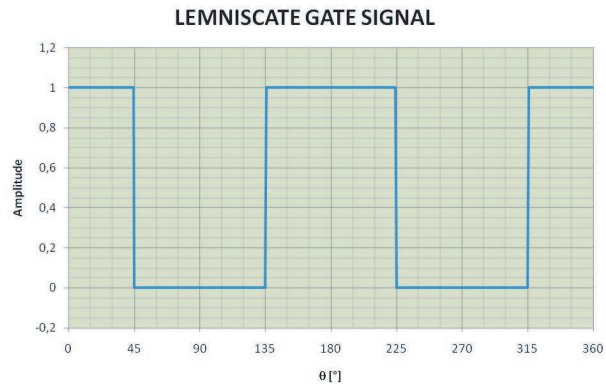


Figure 4: Lemniscate gate signal.

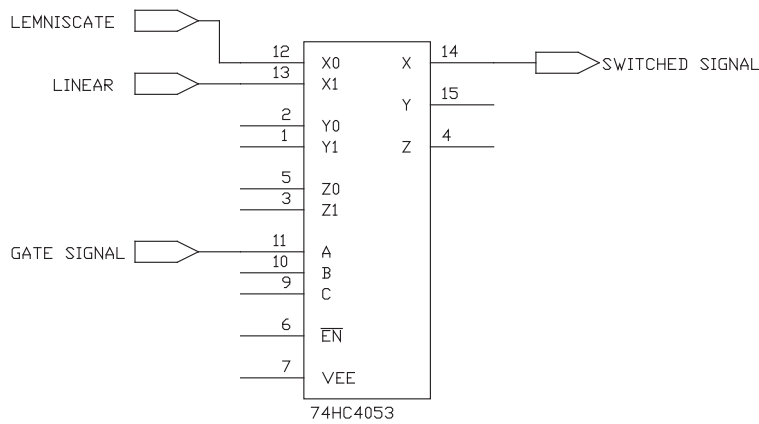


Figure 5: Analog gate switching between lemniscate and linear portion.

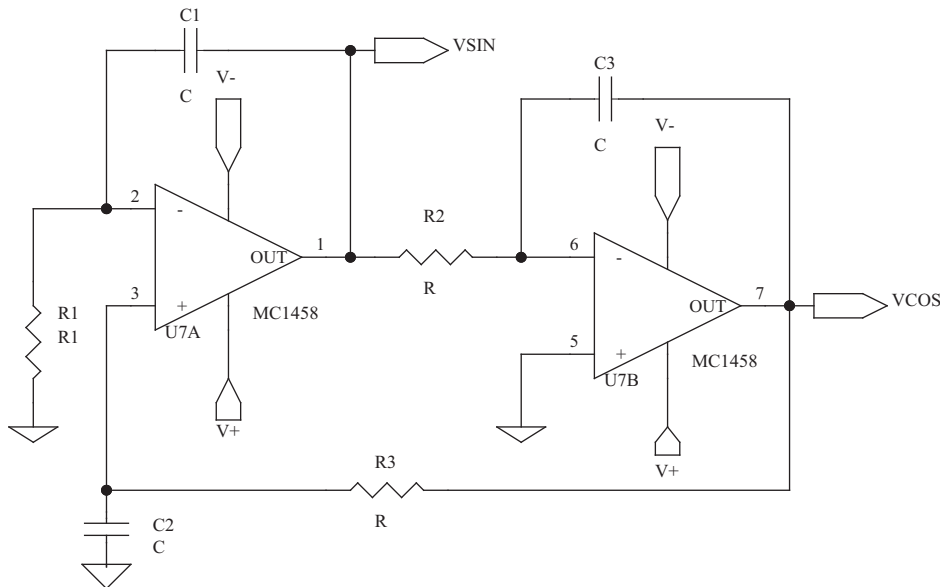


Figure 6: Sine/cosine generator.

The limits of the integration are the frontier points between lemniscate and linear portions.

The two portions are implemented separately and then are mixed using an analog gate (74HC5053) controlled by a gate signal, shown in Figure 4. The analog gate implementation is shown in Figure 5.

Besides the numerical computation approach of the magnetic field generated by the undulator current, the other possibility is the analogic simulation. Such an approach is more intuitive and versatile and also enables a validation of the numerical simulation.

For this reason the equations describing the model of the magnetic field generated by the un-dulator were, besides the numerical evaluation, simulated using an electrical analogical model.

Analog computation was accomplished dividing the equations into small pieces that may be easily implemented using elementary functional analogic blocks. In fact the equation comprises mathematical operations like integration, multiplication, division, addition, subtraction, square root, sine and cosine functions. All these may be simulated by an analogical circuitry, using appropriate functional modules. These functional modules are detailed in the next chapter.

3. RESULTS

The model was built using some functional blocks, as: sine/cos generator, analog multipliers, analog dividers, square root device, operational amplifiers and integrators.

The sine/cos generator is a classical harmonic oscillator with both outputs (sine and cos), built using two MC 1458 operational amplifiers, as can be seen in Figure 6.

Sine and cos of 2θ and 3θ were generated using some AD 633 analog multipliers and MC 1458 operational amplifiers. In Figure 7 is shown the generation of $\sin(2\theta)$ and $\cos(2\theta)$.

In Figure 8 is shown the generation of $\sin(3\theta)$. We used in schematic the symbol “X” for the analog multiplier and “+” for the analog adder (with inverter).

The square root was generated using a MC 1458 operational amplifier and an AD 633 analog multiplier. An inverter stage, using another MC 1458 operational amplifier, was needed because the input voltage in the square root generator must be negative. The schematic of this device is shown in Figure 9.

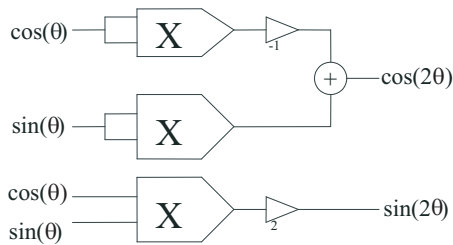


Figure 7: $\sin(2\theta)/\cos(2\theta)$ generator.

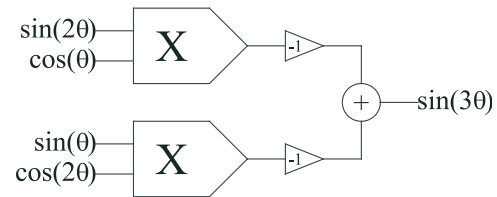


Figure 8: $\sin(3\theta)$ generator.

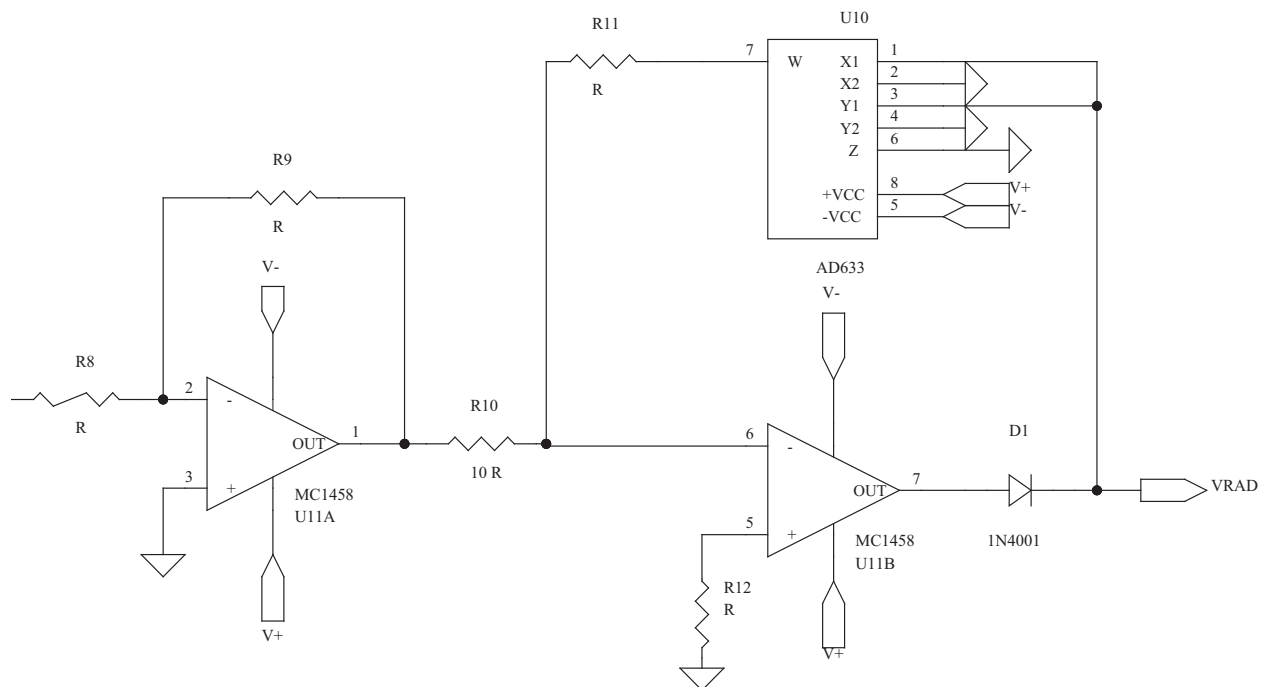


Figure 9: Square root.

The division is achieved using a solution quite similar of the square root: the same MC 1458 operational amplifier and an AD 633 analog multiplier, but no diode at amplifier's output. The inverter stage may be needed, as the circuit generates $-x/y$. The schematic of this device is shown in Figure 10. The integrator is also a classical one, using the same MC 1458 operational amplifier and can be seen in Figure 11. Because of the symmetry, B_x and B_y equal to 0, so it remains only B_z . The dependence of B_z of z is shown in Figure 12.

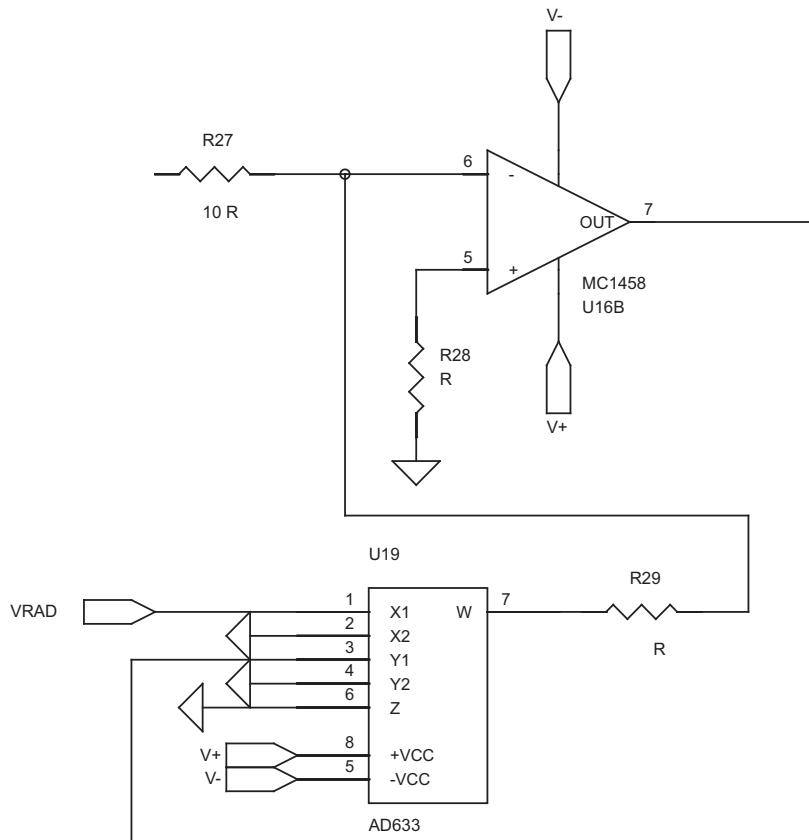


Figure 10: Divisor.

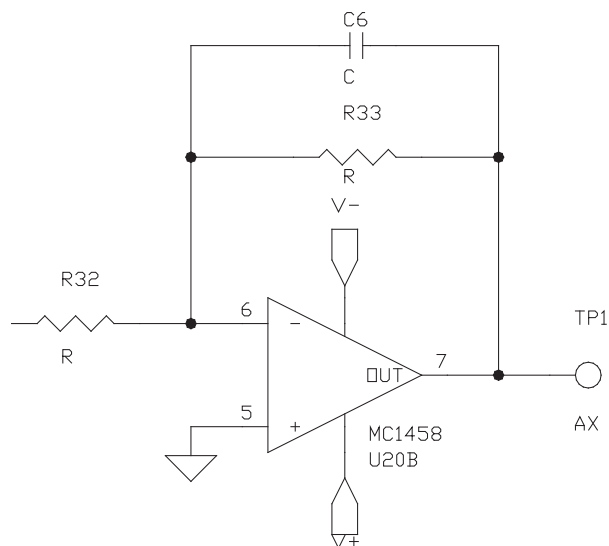


Figure 11: Integrator.

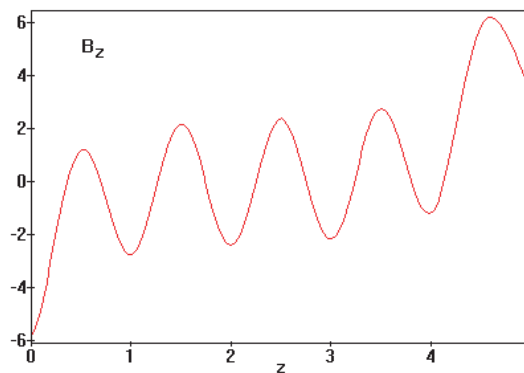


Figure 12: The undulator B_z magnetic field component vs. z direction.

4. CONCLUSIONS

In this paper a new model of an undulator for free electron lasers is presented. The current undulator structure is given by a series of modified lemniscate wires. Each wire presents 90 degree symmetry. The magnetic field integrals components are analytical computed. The middle magnetic field aspect is mainly longitudinal. The transversal aspect was created by electrons with transversal components. This new treatment of the problem reduces the time and complexity for magnetic components evaluation for this structure. The model is sought for structures with two beams simultaneously.

The analogic simulation for field magnetic components is easier and more quickly than the numerical one.

REFERENCES

1. Möser, H. O. and C. Z. Diago, "Finite-length field error and its compensation in superconducting miniundulators," *Nucl. Instr. and Meth. in Phys. Res.*, Vol. A535, 606, 2004.
2. Niculescu, V. I. R., V. Babin, A. Mihalache, M. R. Leonovici, F. Scarlat, and C. Stancu, "On a skeleton cassini ovals current undulator," *European Particle Accelerators Conference EPAC'06*, Edinburgh, Scotland, UK, June 26–30, 2006.
3. Miclos, S., M. I. Rusu, C. Radu, V. Savu, L. Giurgiu, and V. I. R. Niculescu, "A schematic layout of the magnetic field for a two beams huygens undulator," *ROMOPTO 2006 International Conference*, Sibiu, Romania, August 28–31, 2006.

Analysis for Squarely V-shaped Groove Guide

Yinqin Cheng¹, Guojian Li¹, Shuwen Wang¹, Binzhao Cao², and Fuyong Xu²

¹Northwest University for Nationalities, China

²Lanzhou University, China

Abstract— The squarely V-shaped groove guide has been studied by using the method of moment. The cut-off and dispersion characteristics of the dominant mode have been gotten and discussed. It is of important values in theoretical studies and practical engineering applications of V-shaped groove guide for millimeter waves.

1. INTRODUCTION

As one of millimeter wave transmission line, groove guide [1, 2] has many advantages such as low loss, little dispersion, wide bandwidth, easy manufacture and so on, so that it is widely applied to the millimeter wave fields. Squarely V-shaped groove [3, 4] guide is a kind of special groove guide. So, study of its transmission characteristics is of important meanings. In this paper, the cut-off and dispersion characteristics of squarely V-shaped groove guide are obtained and discussed by using the method of moment(MOM) [5]. It is of important values in engineering design and applications of V-shaped groove guide. And our results make basis for further study of arbitrarily V-shaped groove guide.

2. THEORY ANALYSIS

The cross section of open squarely V-shaped groove guide and its geometrical dimensions are shown in Fig. 1. Whole groove guide can be divided into central groove region I and parallel plane region II. The Cartesian coordinate system is adopted. When electromagnetic wave propagates along the z direction, the transverse wave function $\psi(x, y)$ satisfies two-dimensional Helmholtz's equation in the cross section of groove guide as follows:

$$\nabla_T^2 \psi(x, y) + k_c^2 \psi(x, y) = 0. \quad (1)$$

where ∇_T^2 is transverse Laplacian operator. wave function $\psi(x, y)$ is E_Z for TM modes or H_Z for TE modes. $k_c^2 = k^2 - \beta^2$, here k_c is called longitudinal cut-off wavenumber of waveguide, k is wavenumber in the free space and β is phase-shift constant.

On the boundary of the cross-section of the groove guide, Equation (1) satisfies Dirichlet boundary condition $\psi = 0$ for the TM modes or the Neumann boundary condition $\partial\psi/\partial n$ for the TE modes.

On the plane $x = a$, the matching condition of two regions can be written as

$$\begin{cases} \psi_1 = \psi_2 & \text{for } |y| \leq c \\ \frac{\partial\psi_1}{\partial x} = \frac{\partial\psi_2}{\partial x} & \text{for } |y| \leq c \end{cases} \quad (2)$$

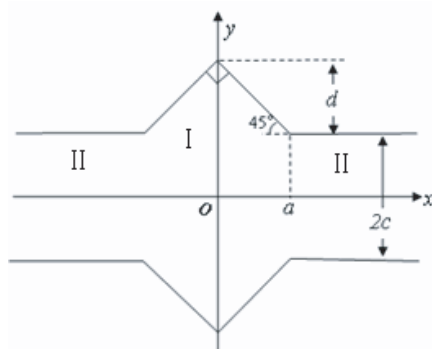


Figure 1: The cross-section of squarely V-shaped groove guide.

Let $L = -\nabla_T^2 = -\frac{\partial^2}{\partial x^2} - \frac{\partial^2}{\partial y^2}$, $\xi = k_c^2$, Equation (1) can be written as

$$L\psi = \xi\psi \quad (3)$$

The Equation (3) is just the eigenvalue problem of the MOM. Based on the Galerkin's Method of MOM, considering boundary condition and matching condition of two regions, the following equation can be obtained

$$|\mathbf{A} - \xi\mathbf{B}| = 0 \quad (4)$$

Equation (4) is the characteristic equation of the squarely V-shaped groove guide and can be solved as general eigenvalue problem.

3. NUMERICAL RESULTS AND DISCUSSIONS

Power function is used as the base function in central groove region and exponential function, which attenuates along x direction, is used as the base function in parallel plane region II. They satisfy the electromagnetic boundary condition. According to the above theory analysis, the cut-off and dispersion characteristic curves for main mode TE_{11} of **squarely** V-shaped groove guide can be gotten and shown in Fig. 2–Fig. 7.

As are shown in Fig. 2–Fig. 4 that, in general, the cut-off wavelength of squarely V-shaped groove guide increases with increasing parameter a , d and c . Moreover, the varying tendency of cut-off wavelength of squarely V-shaped groove guide with a , d and c is nonlinear.

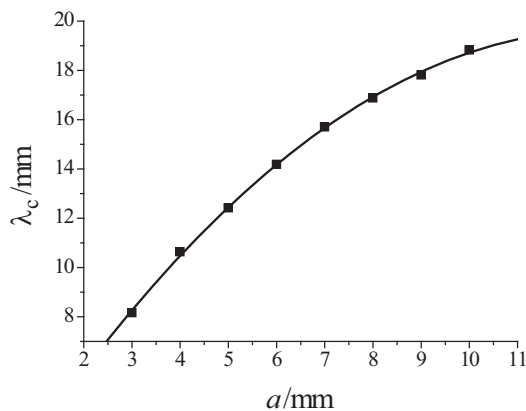


Figure 2: Cut-off curve of squarely V-shaped groove guide with a .

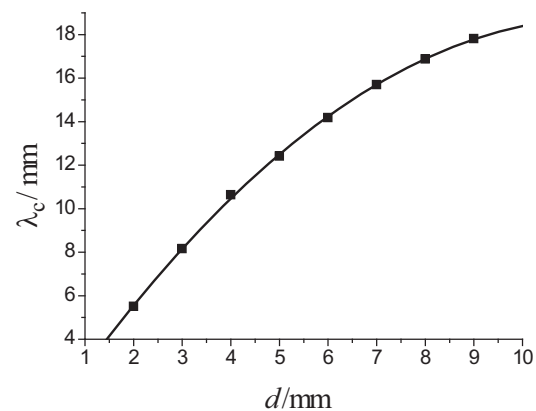


Figure 3: Cut-off curve of squarely V-shaped groove guide with d .

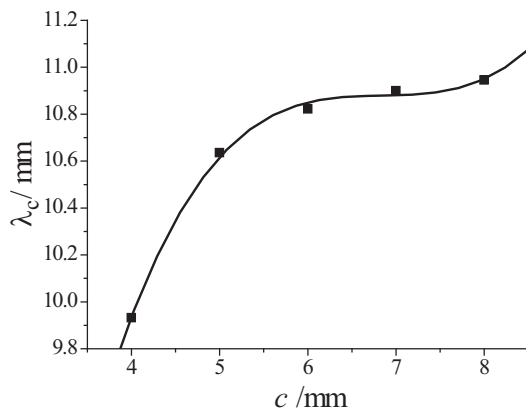


Figure 4: Cut-off curve of squarely V-shaped groove guide with c .

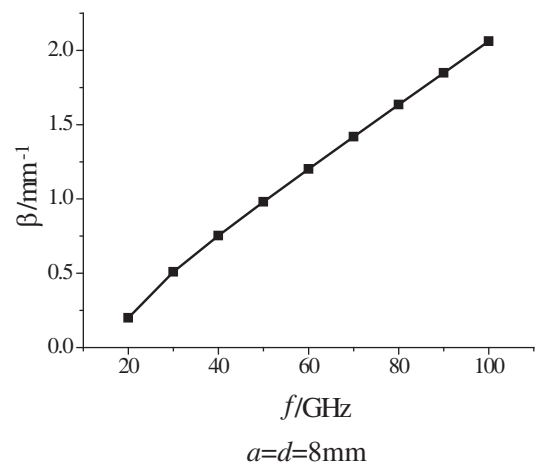


Figure 5: Dispersion curve of squarely V-shaped.

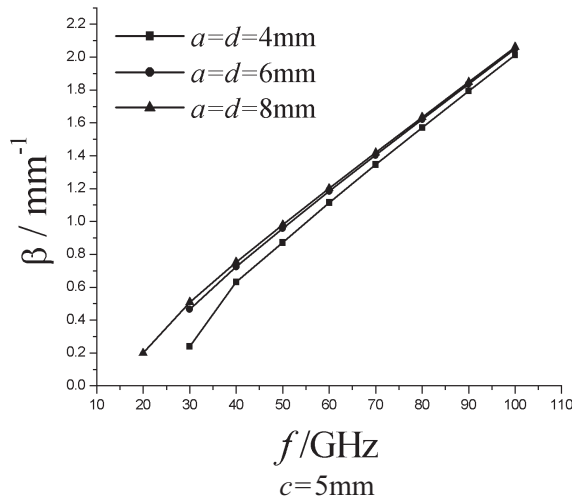


Figure 6: Dispersion curve of squarely V-shaped groove guide with a and d .

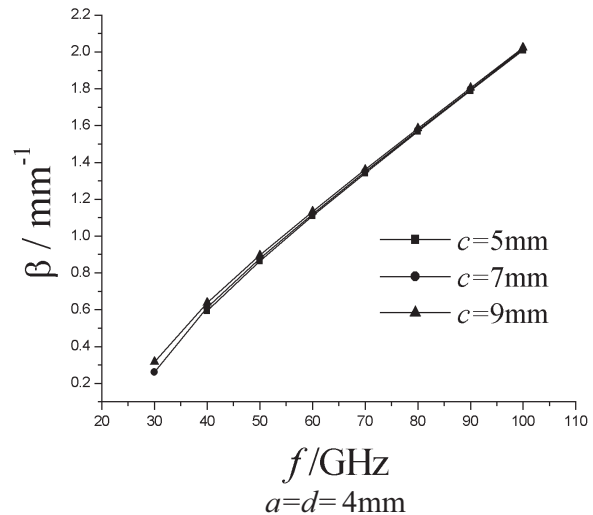


Figure 7: Dispersion curve of squarely V-shaped groove guide with c .

It can be seen from Fig. 5 that the dispersion property of squarely V-shaped groove guide is almost a straight line. From Fig. 6 and Fig. 7, it can be gotten that the dispersion property of squarely V-shaped groove guide is rarely influenced by the dimensions of squarely V-shaped groove guide. That is, it is of good dispersion performances.

4. CONCLUSIONS

Using the method of moment, the eigenvalue equation of squarely V-shaped groove guide is obtained. And the cut-off and dispersion characteristics of dominant mode is gotten and discussed. The numerical results show that squarely V-shaped groove guide is of good dispersion characteristics. The obtained results are of important application values in analyzing and computing the V-shaped groove guide performances in practical engineering problems.

REFERENCES

1. Tischer, F. J., "The groove guide, a low loss waveguide for millimeter waves [J]," *IEEE Trans. MTT*, Vol. 11, No. 9, 291–296, 1963.
2. Choi, Y. M. and D. J. Harris, "Groove guide for short millimetric waveguide systems [J]," *Infrared and Millimeter Waves*, Vol. 11, No. 12, 99–140, 1984.
3. Ho, T. K. and D. J. Harris, "Millimetric wave groove guide with V-shaped grooves [J]," *Electron. Lett.*, Vol. 20, No. 19, 777–778, 1984.
4. Choi, Y. M., D. J. Harris, and K.-F. Tsang, "Theoretical and experimental characteristics of single V-groove guide for X-band and 100 GHz operation [J]," *IEEE Trans. MTT*, Vol. 36, No. 4, 715–723, 1988.
5. Harrington, R. F., translated by Wang Erjie, *Field Computation by Moment Methods*, 144–191, National Defence Industry Press, Beijing, 1981.

Study on Trapezoidal Groove Guide with Arbitrary Inclination Angle

Yinqin Cheng¹, Guojian Li¹, Shuwen Wang¹, Binzhao Cao², and Fuyong Xu²

¹Northwest University for Nationalities, China

²Lanzhou University, China

Abstract— The trapezoidal groove guide with arbitrary inclination angle has been studied with method of moment. The transmission properties of the dominant mode have been obtained and discussed. It is of important values in theoretical studies and practical engineering applications of arbitrarily trapezoidal groove guide for millimeter waves.

1. INTRODUCTION

As one of millimeter wave transmission line, groove guide [1, 2] has many advantages such as low loss, little dispersion, wide bandwidth, easy manufacture and so forth, so that it is widely applied to the millimetre wave fields. Trapezoidal groove guide [3, 4] is a kind of typical groove guide. So, research of its transmission characteristics is of important meanings. In this paper, the cut-off and dispersion properties of trapezoidal groove guide with arbitrary inclination angle are gotten and discussed by using the method of moment(MOM) [5]. It is of important values in engineering design and applications of trapezoidal groove guide.

2. THEORY ANALYSIS

The cross section of open trapezoidal groove guide with arbitrary inclination angle α and its geometrical dimensions are shown in Fig. 1. Whole groove guide can be divided into central groove region I and parallel plane region II. The Cartesian coordinate system is used. When electromagnetic wave transmits along the longitudinal direction of groove guide, which is z direction, the transverse wave function $\psi(x, y)$ in groove guide satisfies two-dimensional Helmholtz's equation as follows

$$\nabla_T^2 \psi(x, y) + k_c^2 \psi(x, y) = 0. \quad (1)$$

where ∇_T^2 is transverse Laplacian factor. wave function $\psi(x, y)$ is E_Z for TM modes or H_Z for TE modes. $k_c^2 = k^2 - \beta^2$, here k_c is called longitudinal cut-off wavenumber of waveguide, k is wavenumber in the free space and β is phase-shift constant.

On the boundary of the cross-section of the groove guide, Equation (1) satisfies Dirichlet boundary condition for the TM modes or the Neumann boundary condition for the TE modes, i.e.,

$$\begin{cases} \psi = 0 \\ \frac{\partial \psi}{\partial n} = 0 \end{cases} \quad (2)$$

On the interface $x = a$, the matching condition between groove region and parallel plane region II can be described as

$$\begin{cases} \psi_1 = \psi_2 & \text{for } |y| \leq c \\ \frac{\partial \psi_1}{\partial x} = \frac{\partial \psi_2}{\partial x} & \text{for } |y| \leq c \end{cases} \quad (3)$$

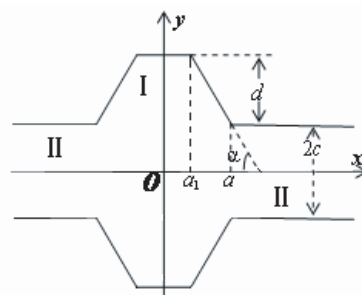


Figure 1: The cross-section of trapezoidal groove guide with arbitrary inclination angle.

Let $L = -\nabla_T^2 = -\frac{\partial^2}{\partial x^2} - \frac{\partial^2}{\partial y^2}$, $\xi = k_c^2$, Equation (1) can be written as

$$L\psi = \xi\psi \quad (4)$$

The Equation (3) is exactly the eigenvalue problem of the MOM. Based on the Galerkin's Method of MOM, considering boundary condition (2) and matching condition (3), the following equation can be obtained

$$|\mathbf{A} - \xi\mathbf{B}| = 0 \quad (5)$$

Equation (5) is the characteristic equation of trapezoidal groove guide with arbitrary inclination angle and can be solved as general eigenvalue problem.

3. NUMERICAL RESULTS AND DISCUSSIONS

In central groove region I, power function is used as the base function. In parallel plane region II, exponential function, which attenuates along x direction, is used as the base function. According to the above theory analysis, the cut-off and dispersion characteristic curves for dominant mode TE_{11} of trapezoidal groove guide with arbitrary inclination angle can be gotten and shown in Fig. 2–Fig. 9.

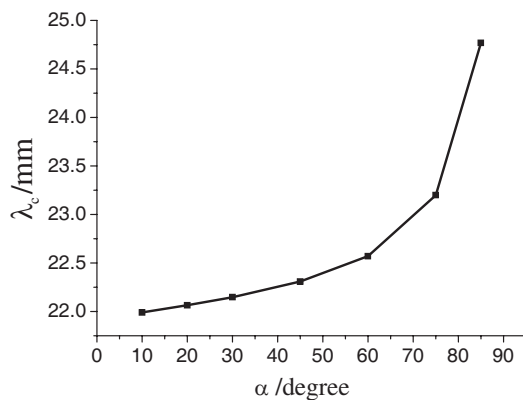


Figure 2: Cut-off curve of arbitrary trapezoidal groove guide with α .

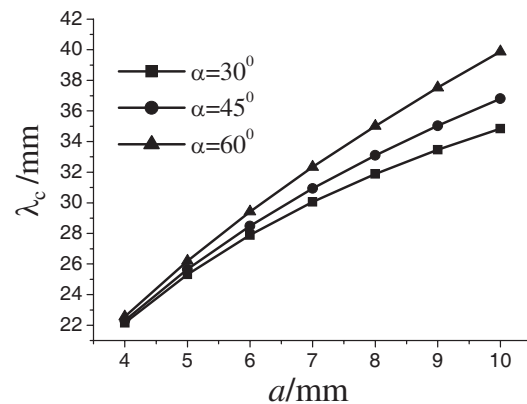


Figure 3: Cut-off curve of arbitrary trapezoidal groove guide with a and α .

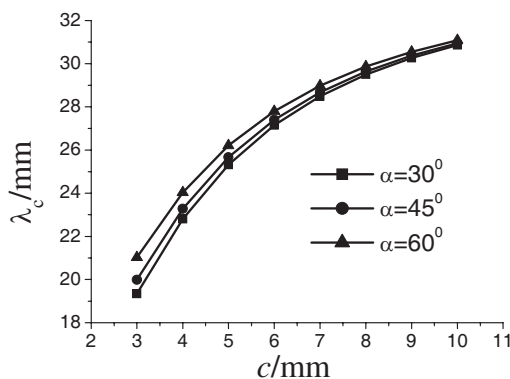


Figure 4: Cut-off curve of arbitrary trapezoidal groove guide with c and α .

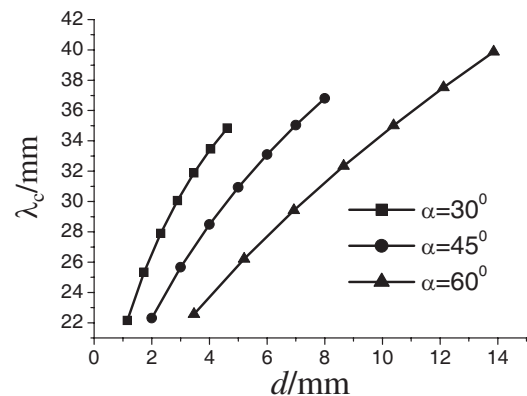


Figure 5: Cut-off curve of arbitrary trapezoidal groove guide with d and α .

Cut-off properties for dominant mode of the arbitrarily trapezoidal groove guide are shown in Fig. 2–Fig. 5. It is shown in Fig. 2 that the cut-off wavelength increases with increasing inclination angle. As are shown in Fig. 3–Fig. 5 that the cut-off wavelength increases with increasing parameter a , c and d . Moreover, for the same a and c , the larger the angle is, the larger the cut-off wavelength is. Meanwhile, for the same d , the less the angle is, the larger the cut-off wavelength is.

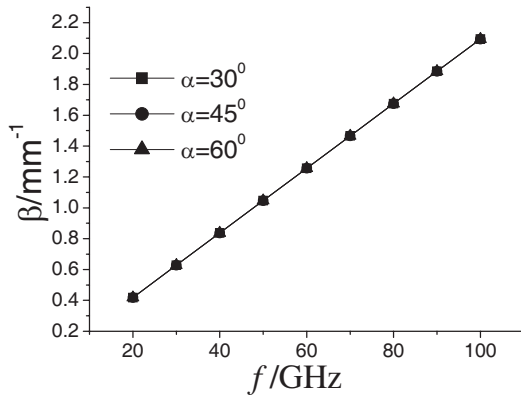


Figure 6: Dispersion curve of arbitrary trapezoidal groove guide with α .

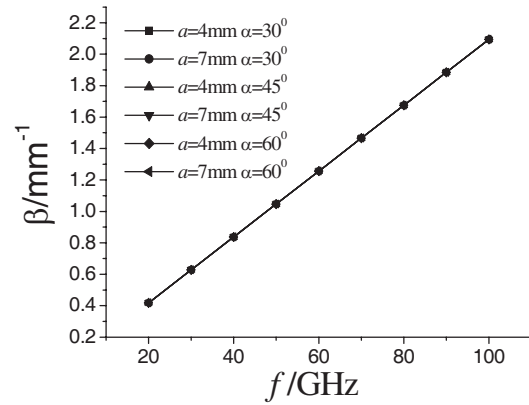


Figure 7: Dispersion curve of arbitrary trapezoidal groove guide with a and α .

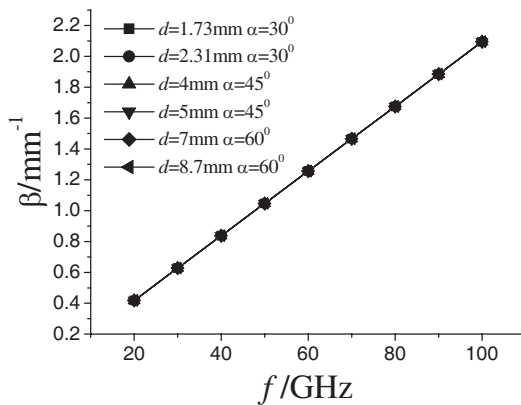


Figure 8: Dispersion curve of arbitrary trapezoidal groove guide with d and α .

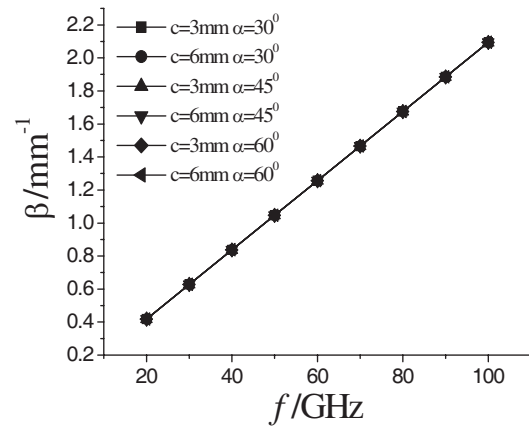


Figure 9: Dispersion curve of arbitrary trapezoidal groove guide with c and α .

Dispersion properties for dominant mode of the arbitrarily trapezoidal groove guide are shown in Fig. 6–Fig. 9. It can be seen that the dispersion curves with parameter a , d , c and α is almost a straight line. And the influence on dispersion when varying geometrical dimensions of groove guide is very slight. In a word, the arbitrarily trapezoidal groove guide is of good dispersion performances.

4. CONCLUSIONS

Using the method of moment, the trapezoidal groove guide with arbitrary inclination is studied. And the cut-off and dispersion characteristics of dominant mode is gotten and discussed. The numerical results show that this kind of groove guide is of good dispersion properties. The obtained results are of important application values in analyzing and designing the groove guides performances in practical engineering problems.

REFERENCES

1. Tischer, F. J., "The groove guide, a low loss waveguide for millimeter waves [J]," *IEEE Trans. MTT*, Vol. 11, No. 9, 291–296, 1963.
2. Choi, Y. M. and D. J. Harris, "Groove guide for short millimetric waveguide systems [J]," *Infrared and Millimeter Waves*, Vol. 11, No. 12, 99–140, 1984.
3. Xu, F. Y., K. Y. Zhao, B. You, and X. H. Lin, "Analysis for transmission properties of arbitrarily trapezoidal groove waveguide for millimeter waves [J]," *International Journal of Infrared and Millimeter Waves*, Vol. 21, No. 1, 45–56, 2000.
4. Xu, F., Y. Lin, and B. You, "Analysis for transmission characteristics of closed trapezoidal-groove waveguide with boundary element method [J]," *International Journal of Infrared and Millimeter Waves*, Vol. 20, No. 9, 1691–1699, 1999.
5. Harrington, R. F., translated by Wang Erjie, *Field Computation by Moment Methods*, 144–191, National Defence Industry Press, Beijing, 1981.

An Efficient Algorithm for Combining Linear Lumped Networks with the FDTD Method

Hsin Hsiang Su¹, Chih Wen Kuo¹, and Toshihide Kitazawa²

¹Department of Electrical Engineering, National Sun Yat-Sen University, Kaohsiung 804, Taiwan

²Department of Electrical and Electronic Engineering, Ritsumeikan University
Kusatsu 525-8777, Japan

Abstract— In this study, an efficient approach is presented for processing two terminal networks consisting of arbitrary linear lumped elements into a single grid of FDTD (finite difference time domain) method. The relation of the node voltage to current of the networks can be expressed as a rational function (transfer function) in frequency domain. Field-updating equations and the rational function can be combined together into a new rational function since a single FDTD grid can be regarded as a Norton (or Thevenine) equivalent circuit. The proposed method is based on control theory and leads to an explicit efficient updating algorithm. A six-order circuit terminated with a transmission line is simulated to demonstrate the accuracy and efficiency of the proposed method. The simulation time of the proposed methods is about 30% less than a similar configuration using the equivalent current source (ECSM) method. Simulation results agree well with data from the ECSM and Agilent’s commercial software ADS.

1. INTRODUCTION

In order to analyze the electromagnetic (EM) effect of high speed circuits upon the print circuit board (PCB), the full-wave methods can be easily applied to predict the wave phenomena of the PCB. One of the popular methods is the finite difference time domain (FDTD) method [1]. To analyze the microwave circuits in FDTD, several works [2–7] were proposed to incorporate the circuits into a single FDTD cell. Usually, the voltage/current relations (admittance or impedance) of the circuits are pre-analyzed and incorporated into FDTD. The proposed method is based on control theory using a rational function representation of the circuit response that leads to an efficient explicit updating algorithm.

2. FORMULATION

The lumped network can be incorporated into a single FDTD grid using Maxwell’s curl \mathbf{H} equation. Furthermore, this grid can be regarded as a Norton equivalent circuit (Fig. 1), and the Maxwell’s equation on this grid can be modified as follows (assuming the lumped networks is connected along the z -direction)

$$I_N = C_N \frac{dV_L}{dt} + I_L \quad (1)$$

where

$C_N = \varepsilon \Delta z / \Delta x \Delta y$ is the value of the equivalent capacitance of the FDTD grid

I_N is the total current from the FDTD grid

$V_L = E z \Delta z$ is the device voltage

I_L is the device current.

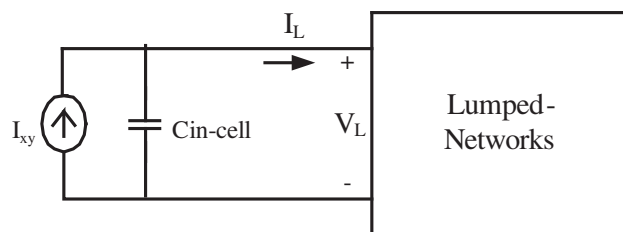


Figure 1: The equivalent circuit of lumped networks on the single FDTD grid.

For arbitrary linear lumped networks, the impedance (or admittance) of the network can be expressed as a transfer function in Laplace domain as

$$Z(s) = \frac{V_L(s)}{I_N(s)} = \frac{V(s)}{I(s)} = \frac{b_1s^{q-1} + b_2s^{q-2} + \dots + b_{q-1}s + b_q}{s^q + a_1s^{q-1} + \dots + a_{q-1}s + a_q} \tag{2}$$

The transfer function with coefficients $(b_1 \dots b_q$ and $a_1 \dots a_q)$ is obtained by standard circuit theory. It is noted that q is the order of the transfer function which is the total number of the inductors and capacitors of the network. Multiplying the denominator and numerator of (2) by a dummy variable $R(s)$, the transfer function can be written as

$$V(s) = (b_1s^{q-1} + b_2s^{q-2} + \dots + b_{q-1}s + b_q) R(s) \tag{3}$$

$$V(s) = (b_1s^{q-1} + b_2s^{q-2} + \dots + b_{q-1}s + b_q) R(s) \tag{4}$$

By taking the inverse Laplace transform of Equations (3) and (4), we will have

$$v(t) = b_1r^{(q-1)}(t) + b_2r^{(q-2)}(t) + \dots + b_qr(t) \tag{5}$$

$$i(t) = r^{(q)}(t) + a_1r^{(q-1)}(t) + a_2r^{(q-2)}(t) + \dots + a_qr(t) \tag{6}$$

where $r^{(q)}(t)$ is denoted $d^q r(t)/dt^q$. Thus, we can defined the state variables $x_1 = r, x_2 = r'(t) = \dot{x}_1, x_3 = r''(t) = \dot{x}_2, \dots, x_q = d^{q-1}r(t)/dt^{q-1} = \dot{x}_{q-1}$. Substituting the state variables into (5) and (6), we can obtain

$$\begin{aligned} \dot{x}_1 &= x_2 \\ \dot{x}_2 &= x_3 \\ &\vdots \\ \dot{x}_q &= -a_qx_1 - a_{q-1}x_2 - \dots - a_1x_q + i \\ v &= b_qx_1 + b_{q-1}x_2 + \dots + b_1x_q \end{aligned}$$

The above equations can be written as a dynamic equation

$$C\dot{x}(t) = Gx(t) + Bi(t) \tag{7}$$

$$v(t) = Lx(t) \tag{8}$$

where $x(t) = [x_1 \ x_2 \ \dots \ x_q]^T_{q \times 1}, B = [0 \ 0 \ 0 \ 1]^T_{q \times 1}, L = [b_q \ b_{q-1} \ \dots \ b_1]_{1 \times q}$,

$$C = \begin{bmatrix} 1 & 0 & 0 & \dots & 0 \\ 0 & 1 & 0 & \dots & 0 \\ \vdots & 0 & 1 & 0 & \vdots \\ \vdots & \vdots & 0 & \ddots & 0 \\ 0 & 0 & \dots & 0 & 1 \end{bmatrix}_{q \times q}, \text{ and } G = \begin{bmatrix} 0 & 1 & 0 & \dots & \dots & 0 \\ 0 & 0 & 1 & 0 & \vdots & 0 \\ \vdots & \vdots & \vdots & \ddots & \dots & 0 \\ 0 & 0 & 0 & 0 & 1 & 0 \\ -a_q & -a_{q-1} & -a_{q-2} & \dots & -a_2 & -a_1 \end{bmatrix}_{q \times q}.$$

An implicit finite difference method is invoked to solved (7). Therefore, (7) and (8) can be expressed as

$$C(x^{n+1} - x^n)/\Delta t = Gx^{n+1} + Bi^{n+1/2} \quad v = Lx^{n+1} \tag{9}$$

After some manipulations, the above equation becomes

$$C_1x^{n+1} = G_1x^{n+1} + B_1i^{n+1/2} \tag{10}$$

where $C_1 = C - \Delta tG = \begin{bmatrix} 1 & -\Delta t & 0 & 0 & \dots & 0 \\ 0 & 1 & 0 & 0 & \dots & 0 \\ 0 & 0 & 1 & 0 & \dots & 0 \\ \vdots & \vdots & 0 & \ddots & 0 & 0 \\ 0 & 0 & \dots & 0 & 1 & -\Delta t \\ \Delta ta_q & \Delta ta_{q-1} & \Delta ta_{q-2} & \dots & \Delta ta_2 & 1 + \Delta ta_1 \end{bmatrix}_{q \times q}, G_1 = C_{q \times q}$, and $B_1 =$

$\Delta tB = [0 \ 0 \ 0 \ \Delta t]^T_{q \times 1}$. Taking the elementary row operation of (10), we can obtain

$$C_2x^{n+1} = G_2x^{n+1} + B_2i^{n+1/2} \tag{11}$$

where

$$C_2 = \begin{bmatrix} 1 & -\Delta t & 0 & \cdots & 0 \\ 0 & 1 & -\Delta t & & \vdots \\ \vdots & 0 & \ddots & \ddots & \vdots \\ \vdots & & \ddots & 1 & -\Delta t \\ 0 & \cdots & \cdots & 0 & 1 \end{bmatrix}_{q \times q}, \quad G_2 = \begin{bmatrix} 1 & 0 & \cdots & 0 \\ 0 & 1 & 0 & \vdots \\ \vdots & 0 & \ddots & 0 \\ 0 & \cdots & \cdots & 1 & 0 \\ \frac{c_{r0}}{c_{l(q-1)}} & \frac{c_{r1}}{c_{l(q-1)}} & \cdots & \cdots & \frac{c_{r(q-1)}}{c_{l(q-1)}} \end{bmatrix}_{q \times q},$$

$$B_2 = \begin{bmatrix} 0 \\ \vdots \\ 0 \\ \frac{u_{r0}}{c_{l(q-1)}} \end{bmatrix}_{q \times 1}, \quad c_{l(q-1)} = 1 + \sum_{m=1}^q a_m (\Delta t)^m, \quad c_{r0} = -\Delta t a_q,$$

$$c_{ri} = -\Delta t (a_{q-i} + c_{r(i-1)}), \quad i = 1, 2, \dots, k-1, \quad c_{r(q-1)} = 1, \quad u_{r0} = \Delta t,$$

and $v = b_q x_1 + b_{q-1} x_2 + \dots + b_1 x_q$.

Finally, we have

$$\begin{aligned} x_q^{n+1} &= \frac{c_{r0}}{c_{l(q-1)}} x_1^n + \frac{c_{r1}}{c_{l(q-1)}} x_2^n + \dots + \frac{c_{r(q-1)}}{c_{l(q-1)}} x_q^n + \frac{u_{r0}}{c_{l(q-1)}} i^{n+1/2} \\ x_{q-1}^{n+1} &= x_{q-1}^n + \Delta t x_q^{n+1} \\ x_{q-2}^{n+1} &= x_{q-2}^n + \Delta t x_{q-1}^{n+1} \\ &\vdots \\ x_1^{n+1} &= x_1^n + \Delta t x_2^{n+1} \\ E^{n+1} &= (b_q x_1^{n+1} + b_{q-1} x_2^{n+1} + \dots + b_1 x_q^{n+1}) / \Delta z \end{aligned} \quad (12)$$

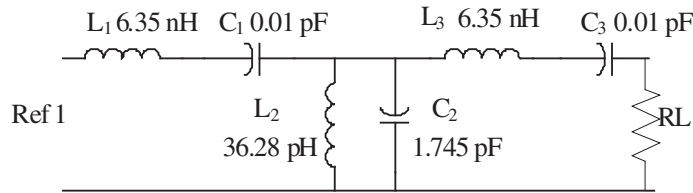


Figure 2: A high order circuit.

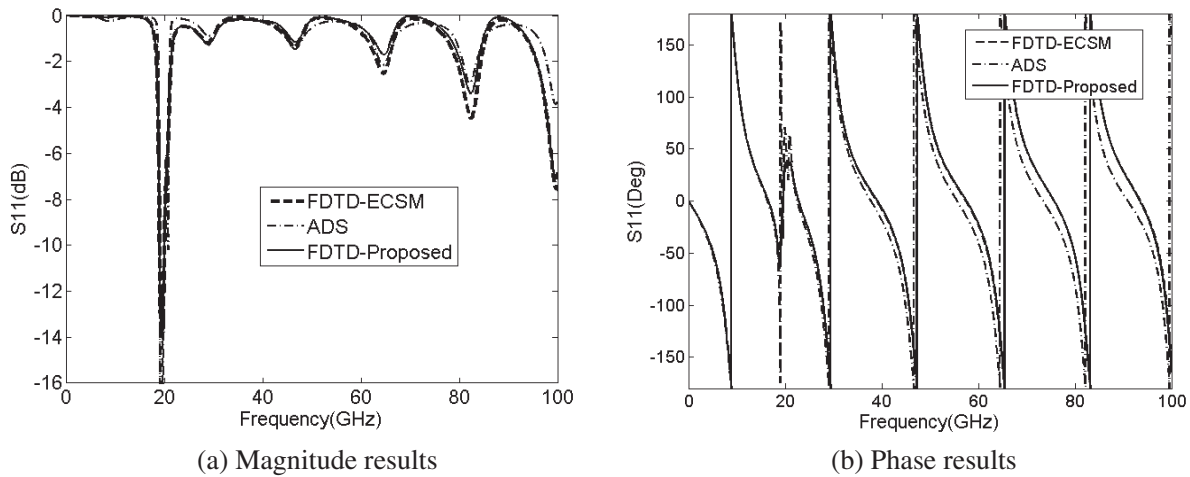


Figure 3: Comparison the results of the proposed method with ECSM and ADS. (a) Magnitude results. (b) Phase results.

the E field can be calculated from (12) ($E^{n+1} = \Delta z v^{n+1}$), without solving any inversion of matrix. For a q -order lumped elements circuit, this improved formulation needs $q + 1$ explicit equations and $3q + 1$ variables.

3. NUMERICAL VALIDATION

A parallel transmission line connected to a high order circuit at the terminal is simulated to demonstrate the validity of the proposed method. The thickness of the print circuit board is 16 mil. The length and width of this transmission are 8 mil and 240 mil, respectively. The parameters of this circuit are shown in Figure 2. The cell size of the FDTD grid is set to $\Delta x = \Delta y = 4$ mil, and $\Delta z = 8$ mil, respectively. The time step is $\Delta t = 0.25$ ps, and the excitation is a Gaussian pulse with a source resistance 50Ω . The simulation results are compared with equivalent current source method. Figure 3 demonstrates the results of the magnitude and phase of S_{11} .

4. CONCLUSIONS

This paper presents an efficient and stable scheme to incorporate arbitrary linear two terminal lumped networks into FDTD method. It is observed that the simulation results agree well with equivalent current source method (ECSM) and Agilent's commercial software ADS. The simulation time of the proposed methods are about 30% less than a similar configuration using ECSM.

ACKNOWLEDGMENT

This work is supported by the Aim for the Top University Plan of Ministry of Education, Taiwan.

REFERENCES

1. Yee, K. S., "Numerical solution of initial boundary value problems involving Maxwell's equations in isotropic media," *IEEE Trans. Antennas Propagat.*, Vol. 14, No. 3, 300–307, May 1966.
2. Kuo, C. N., B. Houshmand, and T. Itoh, "FDTD analysis of active circuits with equivalent current source approach," *IEEE AP-S International Symposium Digest*, Vol. 3, 1510–1513, Jun. 1995.
3. Pereda, J. A., F. Alimenti, P. Mezzanotte, L. Roselli, and R. Sorrention, "A new algorithm for the incorporation of arbitrary linear lumped networks into FDTD simulators," *IEEE Trans. Microw. Theory Tech.*, Vol. 47, No. 6, 943–949, Jun. 1999.
4. Shao, Z. H. and G. W. Wei, "DSC time-domain solution of Maxwell's equations," *J. Comput. Phys.*, Vol. 189, No. 2, 427–453, Aug. 2003.
5. Shao, Z. and M. Fujise, "An improved FDTD formulation for general linear lumped microwave circuits based on matrix theory," *IEEE Trans. Microwave Theory Tech.*, Vol. 53, No. 7, 2261–2266, Jul. 2005.
6. El-Raouf, H. E. A., W. Yu, and R. Mittra, "Application of the Z-transform technique to modelling linear lumped loads in the FDTD," *Microwaves, Antennas and Propagation, IEE Proceedings*, Vol. 151, No. 1, 67–70, Feb. 2004.
7. Lee, J.-Y., J.-H. Lee, and H.-K. Jung, "Linear lumped loads in the FDTD method using piecewise linear recursive convolution method," *IEEE Microwave and Wireless Components Lett.*, Vol. 16, No. 4, 158–160, Apr. 2006.

Dispersion Characteristics of Dielectric Loaded V Ridge-Trough Waveguide

Guojian Li¹, Shuwen Wang¹, Yinqin Cheng¹, and Fuyong Xu²

¹Northwest University for Nationalities, China

²Lanzhou University, China

Abstract— A new kind of V ridge-Trough waveguide is presented in this paper. The transmission problem is solved by edge element for the first time. The field patterns of the waveguide for different values of dielectric constant have been presented. Variations of the cutoff wavelength with the ridge dimensions for different values of dielectric constant are investigated in detail. The results will be of practical significance in designing waveguide components in microwave and millimeter wave engineering.

1. INTRODUCTION

Ridge-trough waveguide (RTW) was first introduced as a transition between the coplanar waveguide and rectangular waveguide in the design of V-band wafer probe. Mai Lu and Paul J. Leonard studied the field patterns of the TE modes in ridge-trough waveguide by finite element method. Sun and Balianis studied quadruple-ridged square waveguides (QRSW) by MFIE [1].

Ridge waveguide plays an essential role in microwave and millimetre component. A variety of ridge waveguide have been proposed and developed, because of their unique characteristics such as low cutoff frequency, wide bandwidth, and low impedance characteristics [2, 3]. Ridge waveguide partially filled with dielectric have an important feature, i.e., ridge waveguide can be miniaturized by loading dielectric in it, which is very useful in practical applications.

A number of different methods are available for solving waveguide problems. Mai Lu studied dielectric loaded double trapezoidal-ridge waveguide by finite element method [3]. Helszajn systematically investigated the dielectric loaded square waveguide by numerical calculations [4]. G. Li and F. Xu studied multiple symmetric elliptical ridge waveguide [5]. Ng and Chan studied dielectric-loaded ridge waveguide by mixed spectral-domain method [6].

Finite element method offers the most powerful and efficient numerical solution to the various problems in electrical and electronic engineering, especially to waveguide problems [7]. By ensuring only tangential continuity of the field components across element boundary completely the edge-based FEM wipe out the spurious modes. This article will discuss the dispersion characteristics, such as the cutoff wavelength and single-mode bandwidth in dielectric loaded V ridge-trough waveguide (DLVRTW) by employing the edge-based FEM.

2. THEORY ANALYSIS

To analyze electromagnetic field in an inhomogeneous waveguide, the edge-based finite element method is employed in the framework of the Galerkin formulation of the weighted residual method to solve the vector Helmholtz equations.

The DLVRTW is shown in Fig. 1. a and b are used to described the outer dimensions of the rectangular waveguide. c_1 and d_1 are used to describe the width and the height of the ridge. c_2 and d_2 are used to describe the width and the height of the trough. ε_r is the relative permittivity.

Subdividing the electric field and the magnetic field into transverse \mathbf{E}_T , longitudinal \mathbf{E}_z parts and transverse \mathbf{H}_T , longitudinal \mathbf{H}_z parts respectively, Maxwell's equations in DLVRTW can be written as

$$\nabla_T \times \mathbf{H} = j\omega\varepsilon_r\varepsilon_0\mathbf{E} \quad (1)$$

$$\nabla_T \times \mathbf{E} = -j\omega\mu_r\mu_0\mathbf{H} \quad (2)$$

where, ε_0 and μ_0 are the permittivity and permeability of free space, respectively. ε_r and μ_r are the relative permittivity and relative permeability, respectively. By substituting Eq. (1) into Eq. (2), it yield the vector Helmholtz equations

$$\nabla_T \times \left(\frac{1}{\varepsilon_r} \nabla_T \times \mathbf{H} \right) - K_c^2 \mu_r \mathbf{H} = 0 \quad (3)$$

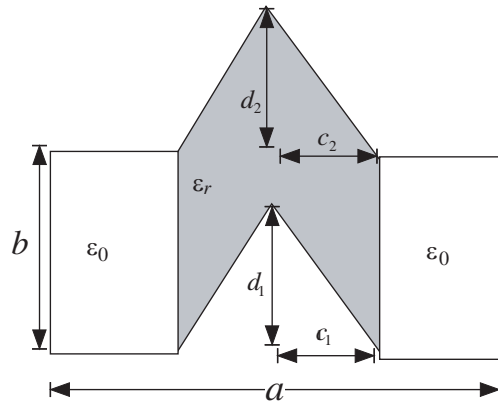


Figure 1: Dielectric loaded V ridge-trough waveguide.

where, ∇_T represents the two-dimensional Laplacian operate, and K_c represents the cutoff wavenumber. Since the Galerkin formulation is adopted, each set of weighting functions is equal to the corresponding set of basis functions. Assume $\mathbf{W}_i = \mathbf{W}_{ti} + W_{zi}\vec{z}$,

$$h_t = \sum_{i=1}^{N_i} h_{ti} \mathbf{W}_{ti} \quad (4)$$

$$h_z = \sum_{i=1}^{N_i} h_{zi} W_{zi} \quad (5)$$

where \mathbf{W}_{ti} and W_{zi} represents the shape function of the element associated with interpolation edge i and node i . The summation index runs over the interpolation edges and nodes. In this paper, the DLERTW is meshed into triangular elements. By applying Galerkin's method into Eq. (3), an eigenvalue equation can be obtained [8].

$$[\mathbf{A}] [\phi] = K_c^2 [\mathbf{B}] [\phi] \quad (6)$$

where, \mathbf{A} and \mathbf{B} are known matrixes, while \mathbf{h}_t and \mathbf{h}_z are unknown vectors of the magnetic field. The full and necessary condition of having non-vanishing solution of Eq. (6) is it's coefficient determinant equal to zero, that is

$$|\mathbf{A} - K_c^2 \mathbf{B}| = 0 \quad (7)$$

Equation (7) is the characteristic equation and can be solved as generalized eigenvalue problems.

Table 1: Comparisons of the cut-off frequencies in the dielectric loaded rectangular waveguide.

Modes	Cut-off Frequency f_c /GHz		
	This Article	Ref. [3]	Relative errors /%
Dominant	1.8198	1.7975	1.24
2nd-Higher	3.4964	3.5212	0.70
3rd-Higher	3.6322	3.6385	0.17
4th-Higher	3.9802	3.9972	0.42
5th-Higher	4.0268	4.0222	0.11
6th-Higher	4.8715	4.7789	1.93
7th-Higher	4.9685	4.9983	0.59

3. NUMERICAL RESULTS AND DISCUSSIONS

To demonstrate the performances, the edge-based finite element method is first used to solve the dielectric loaded rectangular waveguide. It is clear that the results of the proposed method correspond to reference [3] very well, as shown in Table 1.

Figure 2 shows the variations of the normalized cutoff wavelength λ_{c1}/a of the dominant mode of DLVRTW with fixed aspect ratio $2c_1/a = 0.5$, $d_1 = d_2$ and $c_1 = c_2$ for different values of ϵ_r respectively. It is noted that λ_{c1}/a increase with d/b . It is shown that λ_{c1}/a is considerably increased as ϵ_r increase from 1.0 to 20.0.

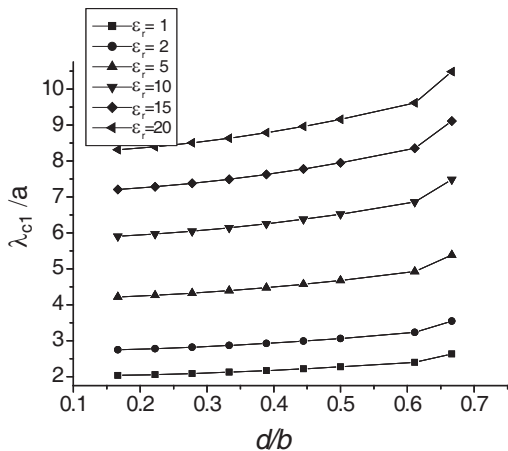


Figure 2: Normalized cut-off wavelength λ_{c1}/a of dominant mode versus d/b for double V ridge-trough waveguide with varied ϵ_r .

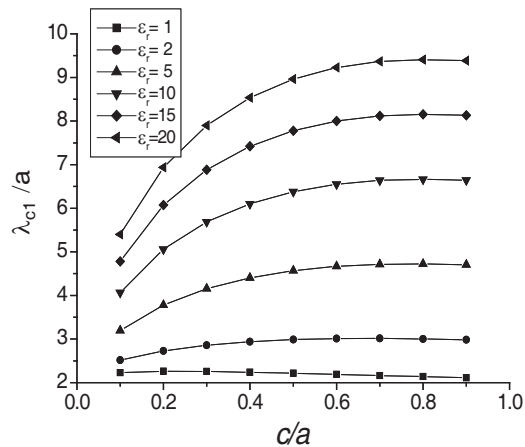


Figure 3: Normalized cut-off wavelength λ_{c1}/a of dominant mode versus c/a for double V ridge-trough waveguide with varied ϵ_r .

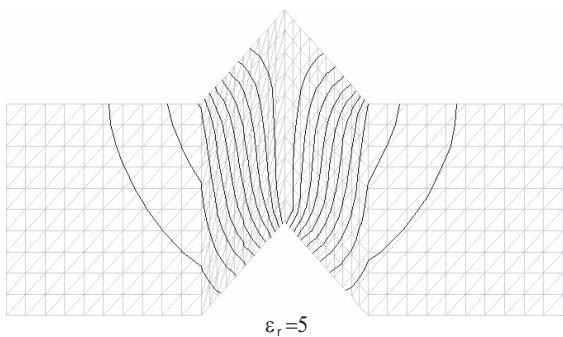


Figure 4: Electrical field patterns of the dominant mode in V ridge-trough waveguide.

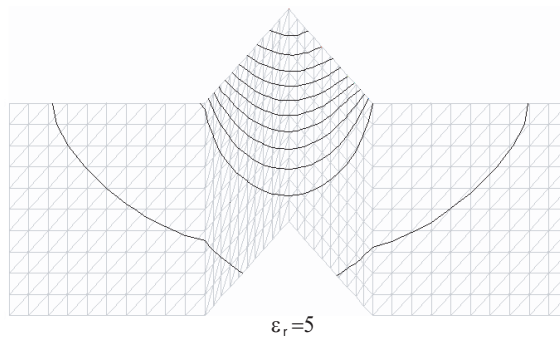


Figure 5: Electrical field patterns of the first higher mode in V ridge-trough waveguide.

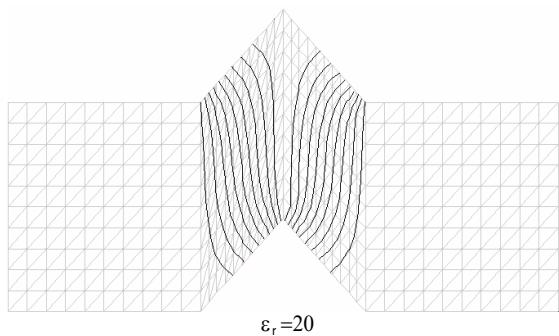


Figure 6: Electrical field patterns of the dominant mode in V ridge-trough waveguide.

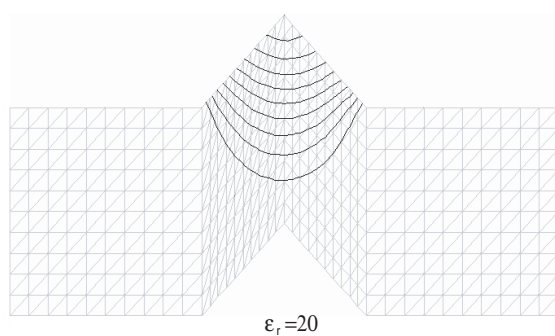


Figure 7: Electrical field patterns of the first higher mode in V ridge-trough waveguide.

Figure 3 shows the variations of the normalized cutoff wavelength λ_{c1}/a of the dominant mode of DLERTW with fixed aspect ratio $d_1/b = 0.2$, and $c_1 = c_2$ for different values of ε_r respectively. It is shown that λ_{c1}/a increase cautiously with c/a . It is shown that λ_{c1}/a is considerably increased as ε_r increase from 1.0 to 20.0.

The calculated field patterns in DLERTW are shown in Figs. 4–7. The thinner lines in each figure represent finite element mesh, while the thicker ones are the electrical field lines of the corresponding mode. The density of the lines indicates the relative strength of the field. The results can be summarized as follows:

1. The electrical field is distributed with a concentration in ridge-trough regions.
2. For the dominant mode, the electrical field will split into two symmetrical parts.
3. The electrical field is concentrated in area very well as ε_r increase.

4. CONCLUSION

Using the edge-based finite element, the dispersion characteristics of a new ridge-trough waveguide are calculated accurately in this paper. It is demonstrated that an increase of the dielectric constant in ridge-trough area boosts the cutoff wavelength of the dominant mode. It is shown that an increase of the dielectric constant will lead the electromagnetic field to be concentrated in the dielectric area. It could be used as an alternative to conventional rectangular ridge-trough waveguide.

REFERENCES

1. Lu, M. and P. J. Leonard, "Design of trapezoidal-ridge waveguide by finite element method," *IEE Proc. — Microwave Antennas Propag.*, Vol. 151, No. 3, 205–211, 2004.
2. Sun, W. and C. A. Balanis, "Analysis and design of quadruple-ridged waveguides," *IEEE Transactions on Microwave Theory and Techniques*, Vol. 42, No. 12, 2201–2207, 1994.
3. Lu, M. and M. Persson, "Transmission characteristics of dielectric loaded double trapezoidal-ridge waveguide," *Microwave and Optical Technology Letters*, Vol. 49, No. 1, 1–4, 2007.
4. Heszajni, J. and L. Shrimpton, "Propagation constant of dielectric loaded square waveguide," *Electronics Letters*, Vol. 32, No 24, 2250–2251, 1996.
5. Li, G., F. Xu, and A. Ma, "Transmission characteristics of multiple elliptical ridge waveguide," *Microwave and Optical Technology Letters*, Vol. 49, No. 12, 3082–3085, Dec. 2007.
6. Ng, K. T. and H. C. Chan, "Unified solution of various dielectric-loaded ridge waveguides with a mixed spectral-domain method," *IEEE Transactions Microwave Theory and Techniques*, Vol. 37, 2080–2085, 1989.
7. Khalaj-Amirhosseini, M., "Microwave filters using waveguides filled by multi-layer dielectric," *Progress In Electromagnetics Research*, PIER 66, 105–110, 2006.
8. Jin, M., *The Finite Element Method in Electromagnetics*, 2nd edition, Wiley, New York, 2002.

Analysis of the Pulse-Modulated Microwave Propagation into 3D Anisotropic Heart Model by SIE Method

L. Nickelson¹, S. Asmontas¹, R. Martavicius², and V. Engelson³

¹Semiconductor Physics Institute, A. Gostauto 11, Vilnius, Lithuania

²Electronic System Department, Gediminas Technical University, Vilnius, Lithuania

³Linköping University, SE-58183, Linköping, Sweden

Abstract— Here we present the electro-dynamical analyses of microwave pulses propagation in a 3D anisotropic heart model for the first time. The electro-dynamical rigorous solution of Maxwell's equations related to the microwave pulse propagation in the 3D heart model with anisotropic and isotropic media is presented here. The myocardium tissue media is an anisotropic lossy media and blood is an isotropic lossy media. The boundary problem was solved by using the singular integral equations' (SIE) method. Our solution, obtained by the SIE method, is electro-dynamically rigorous. The false roots do not appear and the boundary conditions have to be satisfied only on the surfaces dividing different materials. The frequency of the carrier microwave is 2.45 GHz. The modulating signals are triangular video pulses with the on-off time ratio equal to 5 and 100. The pulse durations were always equal to 20 μ s. Microwave electric field distributions were analysed at three longitudinal cross-sections of the heart model. The distributions of electric field for the anisotropic and isotropic heart models are compared here.

1. INTRODUCTION

A human heart may be under influence of the microwave radiation for the medical examination of patients [1] or because of hazardous environment [2]. The tissue of a heart, in the normal state possesses anisotropic properties; however, the anisotropy of heart tissue grows with some illnesses [3, 4]. Desiring to diagnose diseases of heart with the help of the microwave equipment it is necessary to investigate the process of microwave interaction with the anisotropic heart tissue. Research data of the anisotropic properties of heart tissue along and across of myocardium muscle fibers are given in [3].

An electro-dynamical analysis of the diffraction problem relating to scattering of the pulse-modulated microwave on the anisotropic heart model is given in this article. We solve this problem, using the SIE method [5]. In our case the model of heart contains both isotropic and anisotropic area. The model that contains simultaneously anisotropic and isotropic media we will call an anisotropic model. The model that contains only isotropic media we will call an isotropic model.

2. THE FORMULATION OF THE ELECTRODYNAMICAL PROBLEM

The 3D heart model, which has the anisotropic layer of myocardium, is located in the homogeneous dielectric medium, with permittivity and permeability ϵ_3 , μ_3 (Fig. 1). These magnitudes are $\epsilon_3 = \mu_3 = 1$. The point source, which radiates pulse-modulated microwaves, is placed in the point with coordinates $y = 0$, $x = 0$, $z = 9$ (cm). Anisotropic layer of the myocardium muscle is located between the surfaces $S_3 - S_1$, $S_3 - S_2$ and $S_2 - S_1$ (Fig. 1).

We assume that the volumes limited by surfaces S_1 and S_2 , are filled with the isotropic substance, which according to the electrophysical properties corresponds to the blood, which is located in two atriums and ventricles with the complex permittivity ϵ_2 . The heart model has an intricate shape and it limited by a non-coordinate shape surfaces. The surfaces of the 3D heart model were created in the 3D Studio MAX. This tool exports the surfaces as a set of triangles with a normal vector on certain surface points. The solution of electro-dynamical problem let us to analyze the distribution of the microwave electric field inside of the anisotropic heart model.

3. EXPRESSION OF THE MICROWAVE ELECTRIC FIELD IN THE ISOTROPIC MEDIA

The components of electromagnetic field are determined from the solution of differential equation $(\nabla^2 + k^2) G(r, r_0) = -\delta/|r - r_0|$. The Fourier transformation makes it possible to express the unknown Green's function for the isotropic media of heart model through the spherical Bessel functions. The fundamental solutions of the differential equation are used as the kernel of integrals in the SIE method. The solution of the problem for isotropic heart model, are given in [6, 7].

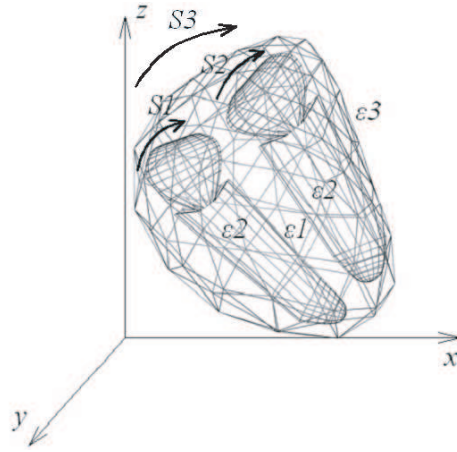


Figure 1: Anisotropic Heart Model, which consists of two atriums and ventricles, which are limited by the surfaces of S_1 , S_2 .

4. THE EXPRESSION OF THE MICROWAVE ELECTRIC FIELD IN THE ANISOTROPIC MEDIA

In order to establish scattering microwave on the anisotropic medium we are also utilized the concept of the point electrical and magnetic sources [5]. Anisotropic medium is described by the components of the tensor $\hat{\epsilon}_1 = \text{diag}[\epsilon_{xx}, \epsilon_{yy}, \epsilon_{zz}]$. The expression of the electric field, obtained from the Maxwell equations for the case of weak anisotropy is:

$$\vec{E}(\vec{r}) = \int_{S_i} \mu_m(\vec{r}_0) \frac{1}{\epsilon_0 \epsilon_{zz} r} \frac{\partial \psi_h^{tr}}{\partial \theta} ds - \int_{S_i} \mu_e(\vec{r}_0) \frac{\omega}{ik_y^2 r \sin \theta} \frac{\partial^2 \psi_e^{tr}}{\partial r \partial \varphi} ds$$

Here the functions ψ_h^{tr} or ψ_e^{tr} characterizing field in the anisotropic substance:

$$\psi_h^{tr} = \frac{\sin \varphi}{\omega \eta_0} \sum_{n=1}^{\infty} a_n j_\beta(k_y r) P_n^1(\cos \theta), \quad \psi_e^{tr} = \frac{\cos \varphi}{\omega} \sum_{n=1}^{\infty} b_n j_\alpha(k_y r) P_n^1(\cos \theta), \quad \eta_0 = \sqrt{\mu_0 / \epsilon_0},$$

$$a_n = \frac{iF_n}{\sqrt{\epsilon_{yy}^{-1}} (h_n(k_0 r) j'_\alpha(k_y r)) - h'_n(k_0 r) j_\alpha(k_y r)}, \quad b_n = \frac{iF_n}{h_n(k_0 r) j'_\beta(k_y r) - \sqrt{\epsilon_{yy}^{-1}} (h'_n(k_0 r) j_\beta(k_y r))},$$

$$\alpha = \left| \sqrt{\frac{n(n+1)}{|\epsilon_{yy}/\epsilon_{xx}|} + \frac{1}{4} - \frac{1}{2}} \right|, \quad \beta = \left| \sqrt{n(n+1) + \frac{1}{4} - \frac{1}{2}} \right|, \quad F_n = \frac{i^{-n} (2n+1)}{n(n+1)},$$

here $j_\alpha(k_y r)$, $j_\beta(k_y r)$, $h_n(k_3 r)$ are the spherical Bessel functions of the first and second order, $P_n^1(\cos \theta)$ is the Legendre Polynomials, $k_y = \sqrt{k^2 \epsilon_{yy} \mu_r - h^2}$, $k_3 = \omega \sqrt{\epsilon_3 \mu_3 / c}$.

5. ANALYSIS OF ELECTRIC FIELD DISTRIBUTIONS IN THE ANISOTROPIC HEART MODEL

Calculations are carried out for the case when the carrier microwave frequency f_0 is equal to 2.45 GHz. The permittivity of the blood medium is $\epsilon_2 = 58 - i19$. The cardiac muscle tensor components are $\epsilon_{xx} = 53 - i3$, $\epsilon_{yy} = 53 - i2.5$, and $\epsilon_{zz} = 55 - i17$. The width of our heart model was 9 cm, the length was 13 cm and the depth was 8 cm. In Figs. 2 and 3 are shown distributions of the normalized electric field modulus $|\vec{E}|/|\vec{E}_{\max}|$ of pulse-modulated microwave along the z -axis in the plane xOz . The plane xOz intersects the heart model at the coordinate $y = 0$. Here the magnitude \vec{E}_{\max} is the amplitude of the microwave electric field in the point of microwave source and the electric field modulus is $|\vec{E}| = \sqrt{E_x^2 + E_y^2 + E_z^2}$.

The microwave pulse is obtained when the monochromatic carrier microwave with frequency f_0 is modulated by the triangular video pulses. In our calculations a video pulse is formed of harmonics (spectrum components) [7]. In Figs. 2 and 3 are shown the electric field distributions when the

microwave was modulated by the triangular video pulse with two different on-off time ratio T/τ and the pulse durations were always equal to $\tau = 20 \mu\text{s}$. Since the pulse period T is not very large in the comparison with the value τ , then we take an amount of the spectrum components equal to $K = 2T/\tau$. The amount of the spectrum components is equal to $K = 10$ and $K = 200$ in our calculations in Fig. 2 and Fig. 3 correspondingly.

Figures 2 and 3 show the distributions in three heart model cross-sections which are removed from the microwave source by the distance 0.3 cm, 3 cm and 7 cm. Curve with black dots shows the electric field distribution at the nearest cross section to the microwave source. We see that the electric field amplitude is the largest in this nearest cross-section of the heart to the microwave source location, when $x = 0.3 \text{ cm}$. So the closer a cross-section to the microwave source the larger is the amplitude of the electric field in that cross section. We see that the microwave electric field amplitude changes asymmetrically to the microwave source location. It happened because the chambers of the heart model from which surfaces reflected the microwave pulse are located slightly asymmetrically with respect to the microwave source location. Analysing Figs. 2 and 3 we see that the distributions of the microwave electric field inside of the heart model are stipulated by the phenomena of the microwave pulse propagation inside of an inhomogeneous media which has a complicated shape.

Since the video pulse we describe as a sum of harmonics and a number of harmonics which approximate the video pulse is chosen proportional to the pulse on-off time ratio then distributions

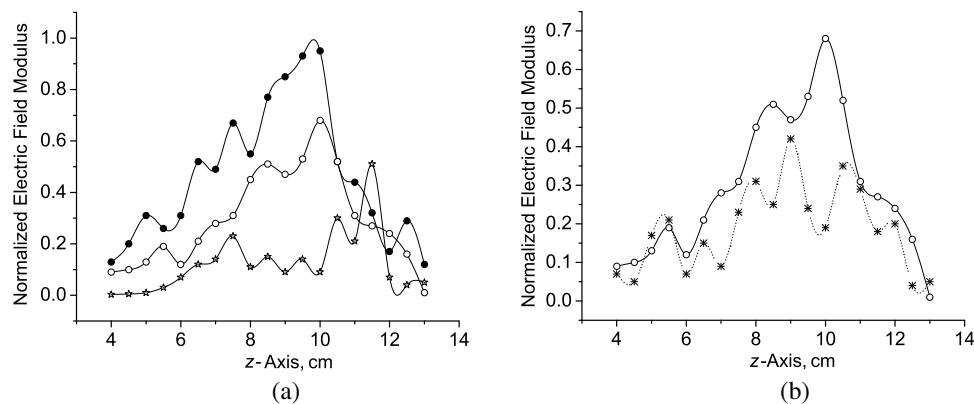


Figure 2: Distribution of magnitude $|\vec{E}|/|\vec{E}_{\max}|$ along the z -axis in three transversal cross sections with the coordinates $x = 0.3 \text{ cm}$ (curve with black dots), 3 cm (curve with circles), 7 cm (curve with stars) when a modulating signal is a triangular video pulse with the on-off time ratio $T/\tau = 5$ (a) and a comparison of the distributions for anisotropic (curve with circles) and isotropic (curve with crosses) heart models in the section with $x = 3 \text{ cm}$ (b).

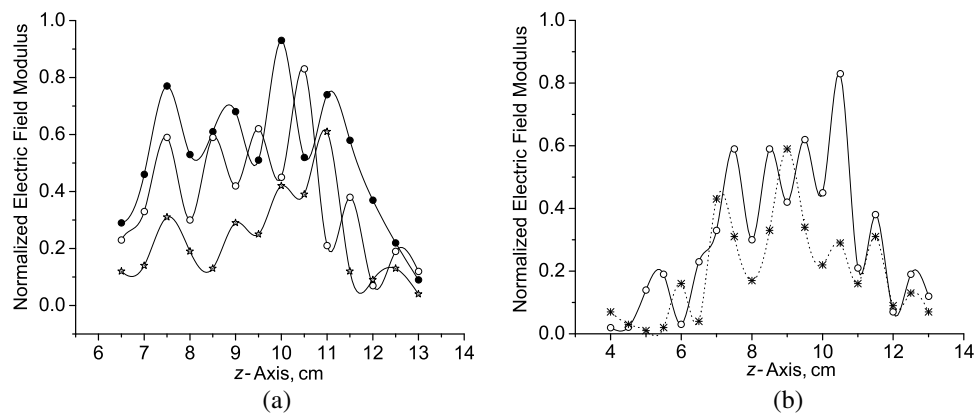


Figure 3: Distribution of magnitude $|\vec{E}|/|\vec{E}_{\max}|$ along the z -axis in three transversal cross sections with the coordinates $x = 0.3 \text{ cm}$ (curve with black dots), 3 cm (curve with circles), 7 cm (curve with stars) when a modulating signal is a triangular video pulse with the on-off time ratio $T/\tau = 100$ (a) and a comparison of the distributions for anisotropic (curve with circles) and isotropic (curve with crosses) heart models in the section with $x = 3 \text{ cm}$ (b).

in Fig. 3 have more interference extrema in the comparison with Fig. 2. Harmonics of the microwave pulse can reflect repeatedly from the interior and external heart model surfaces and the harmonics interference occurs inside of the heart model. The media of the heart model is the cardiac muscle and blood which are the lossy materials with complex dielectric permittivities which have large imaginary parts and therefore a microwave signal can be attenuated.

It is important to note several features of the microwave pulse propagation into anisotropic heart model. We see that in the majority of the cases the electric field has the great significance in the anisotropic model, than in the isotropic model. This can be explained by the fact that some components of the permittivity tensor of anisotropic tissue have the smaller values of imaginary parts of the complex permittivity in the comparison with the isotropic case.

6. CONCLUSIONS

1. We investigated microwave electric field distributions at several cross-sections of 3D anisotropic heart model. We found that the microwave electric field distribution depends on the on-off time ratio of modulating video pulses when their magnitudes differ in twenty times.

2. We found that in the majority of the cases the electric field has great significances in the anisotropic model, than in the isotropic model. This can be explained by the fact that some components of the tensor of anisotropic layer have the smaller values of the imaginary parts of the permittivity in the comparison with the isotropic case.

3. Maxima of electric field distributions of the anisotropic heart model displaces to the side of the great significances of the z -coordinate in the comparison with the isotropic case.

4. We found that the amplitude of the electric field decreased in different way dependent on the direction while the microwave pulses were moving away from the point pulse-modulated microwave source. This happened because the 3D heart model consists of different lossy materials which were described by complex permittivities and the heart boundary surfaces have intricate shapes.

REFERENCES

1. Rosen, A., A. J. Greenspon, and P. Walinsky, "Microwaves treat heart disease," *IEEE Microwave Magazine*, Vol. 8, No. 1, 70–75, 2007.
2. Kubacki, R., "Biological interaction of pulse-modulated electromagnetic fields and protection of humans from exposure to fields emitted from radars," *Conf. Proc. of 17th Intern. Conf. on Microwaves, Radar and Wireless Communications, MIKON-2008, May 19–21, 2008*, Vol. 2, 360–366, Wrocław, Poland, 2008.
3. Ramon, C., P. Schimpf, Y. Wang, A. Ishimaru, and J. Haueisen, "The effect of volume currents due to myocardial anisotropy on body surface potentials," *Phys. Med. Biol.*, Vol. 47, No. 7, 1167–1184, 2002.
4. Paulinas, M., D. Miniotas, M. Meilūnas, and A. Ušinskas, "An algorithm for segmentation of blood vessels in images," *Electronics and Electrical Engineering*, Vol. 83, No. 3, 25–28, 2008.
5. Nickelson, L. and V. Shugurov, *Singular Integral Equations' Methods for the Analysis of Microwave Structures*, 348, VSP Brill Academic Publishers, Leiden-Boston, 2005.
6. Nickelson, L., S. Asmontas, V. Shugurov, R. Martavicius, and V. Malisauskas, "SIE method of analysing microwave fields of a 3D heart model," *Journal of Electromagnetic Waves and Applications*, Vol. 20, No 2, 193–206, 2006.
7. Nickelson, L., S. Asmontas, R. Martavicius, and V. Engelson, "Singular integral method for the pulse-modulated microwave electric field computations in a 3d heart model," *Progress In Electromagnetics Research*, PIER 86, 217–228, 2008.

Analysis of Slow and Fast Modes of Lossy Ceramic SiC Waveguides

L. Nickelson¹, S. Asmontas¹, T. Gric², and R. Martavicius²

¹Semiconductor Physics Institute, A. Gostauto 11, Vilnius, Lithuania

²Electronic System Department, Gediminas Technical University, Vilnius, Lithuania

Abstract— Here we are going to present an electrodynamic analysis of the rectangular and circular SiC rod waveguides. Two computational algorithms in this work were used. The first algorithm, intended for calculating the square waveguides, is based on the method of singular integral equations (SIE). Another algorithm, intended for calculating the circular waveguides is based on the partial area method. We present dispersion characteristics of the SiC waveguide concerning the fact that the longitudinal propagation constant $\underline{h} = h' - ih''$ is the complex number. For searching of complex roots of the dispersion equation we use the modified Muller method. We carried out a test of the algorithm stability and made the algorithms regularization when the material losses were quite large. We analysed here dependencies of values h' and losses h'' on frequencies as well as the electric components of slow and fast modes of SiC waveguides. Here we present the pictures of the electric field strength lines and electric field intensities of modes propagating in the circular SiC rod.

1. INTRODUCTION

The circular and rectangular waveguides and different devices based on them have been accurately investigating during the last few years [1, 2]. The SiC material attracts much attention today because of its perspective use in a large number of power electronic devices [3, 4].

Here we are going to present the electrodynamic analysis of the SiC rectangular and circular waveguides. We present the dispersion characteristics taking into account also the dependences of losses upon frequency as well as the electric field distributions.

2. ANALYSIS OF THE RECTANGULAR SIC WAVEGUIDE

The Maxwell's equations for this electrodynamic problem have been solved by the SIE method. All the boundary conditions are satisfied.

The longitudinal and transversal components of the electric field at the contour points have the form [5]:

$$E_z(\vec{r}) = \int_L \mu_e(\vec{r}_s) H_0^{(2)}(k_\perp r') ds, \quad (1)$$

$$(E_x)^\pm = \mp \frac{2\mu_0\mu_r\omega \cos\theta}{k_\perp^{\pm 2}} \mu_h^\pm(s_j) - V \times \left[k_\perp^\pm \sum_{j=1}^n (\mu_h(s_j))^\pm \int_{\Delta L} H_1^{(2)}(k_\perp^\pm r') \frac{y_s - y_0}{r'} ds \right] \\ + Q \times \left[k_\perp^\pm \sum_{j=1}^n (\mu_e(s_j))^\pm \int_{\Delta L} H_1^{(2)}(k_\perp^\pm r') \frac{x_s - x_0}{r'} ds \right] \quad (2)$$

$$(E_y)^\pm = \mp \frac{2\mu_0\mu_r\omega \sin\theta}{k_\perp^{\pm 2}} \mu_h^\pm(s_j) - Q \times \left[k_\perp^\pm \sum_{j=1}^n (\mu_e(s_j))^\pm \int_{\Delta L} H_1^{(2)}(k_\perp^\pm r') \frac{y_s - y_0}{r'} ds \right] \\ - V \times \left[k_\perp^\pm \sum_{j=1}^n (\mu_h(s_j))^\pm \int_{\Delta L} H_1^{(2)}(k_\perp^\pm r') \frac{x_s - x_0}{r'} ds \right] \quad (3)$$

where $V = i\mu_0\mu_r\omega/k_\perp^{\pm 2}$, $Q = ih/k_\perp^{\pm 2}$, s is the arc abscissa. The field components and the values of the functions $\mu_h(s_j)$ and $\mu_e(s_j)$ are noted in the upper-right corner with the sign corresponding to different waveguide regions, for instance, the functions $\mu_h^+(s_j)$, $\mu_e^+(s_j)$ or $\mu_h^-(s_j)$, $\mu_e^-(s_j)$. These functions at the same contour point are different for the field components in the regions S^+ and S^-

and $\mu_h^+(s_j) \neq \mu_h^-(s_j)$ [5]. The contour L is divided into n parts, $j = 1, \dots, n$. $H_0^{(2)}$ is the Hankel function of the zeroth order and of the second kind; $H_1^{(2)}$ is the Hankel function of the first order and of the second kind; k_{\perp}^{\pm} is the transverse wave number in two different regions.

The SiC waveguide has been analyzed at the temperature $T = 1000$ °C. The geometrical dimensions of the rectangular SiC waveguide are the following. The vertical dimension of the cross-section is 3 mm and the horizontal one is 3 mm.

The dispersion characteristics of the rectangular SiC waveguide are presented in Fig. 1.

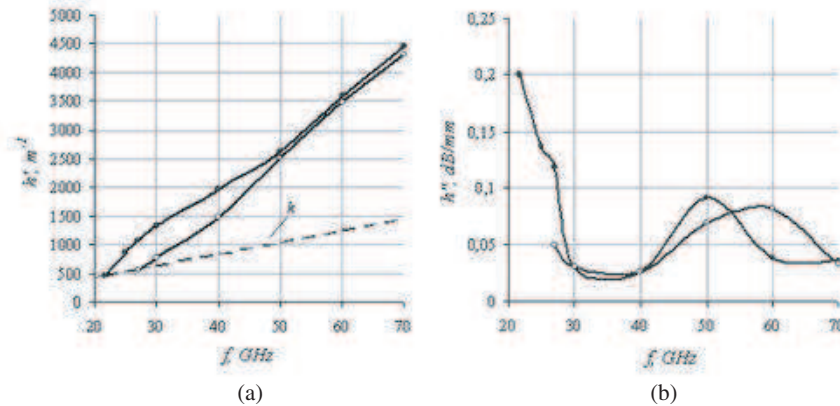


Figure 1: Dispersion characteristics of the rectangular SiC waveguide (a) dependence of the $\text{Re}(\underline{h})$ upon frequency, (b) dependence of the $\text{Im}(\underline{h})$ upon frequency. The main mode is denoted with points, and the higher mode is denoted with circles. The magnitude k is the wave number ($k = \omega/c$).

In Fig. 1(a), we have depicted modes which are analogue to the main and the first higher modes propagating in the circular waveguide [6]. In Fig. 1(b), we see that the dependences of losses of the main and the first higher modes on frequency have the waving character. When the frequency is lower than 30 GHz, the losses of the main mode are larger than losses of the first higher mode at the same frequency interval. When the frequency is higher than 30 GHz, the losses of these modes have approximately the same values. The losses of the same mode oscillate at the different frequency ranges. Comparing the modes depicted in Fig. 1 with the analogue modes propagating in the circular waveguide, we should notice that the main mode is the hybrid HE_{11} mode and the first higher mode is the hybrid EH_{11} mode. We should notice that there are several higher modes between the main HE_{11} and the first higher EH_{11} ones propagating in the circular waveguide. The mentioned higher modes are the analogs of the higher modes with the first index equal to the even number 0, 2 and 4 propagating in the circular waveguide. However these higher modes are not shown.

3. ANALYSIS OF THE CIRCULAR SiC WAVEGUIDE

The method we have used here to solve the electrodynamic problem is based on the partial area method. The electrodynamic model of solution for the circular waveguides has already been presented in our articles [7, 8]. Here we investigate the SiC rod waveguide.

The radius of the SiC rod waveguide is 3 mm. The SiC waveguide has been analyzed at the temperature $T = 1000$ °C. The permittivity of the SiC material at this temperature is $\underline{\epsilon} = 7 - i$ [9].

The dependences of the real part $h' = \text{Re}(\underline{h})$ and imaginary part (propagation losses) $h'' = \text{Im}(\underline{h})$ of the complex propagation constant $\underline{h} = h' - ih''$ of the SiC waveguide with the radius $R = 3$ mm when $T = 1000$ °C on the operating frequency f are presented in Figs. 2(a) and (b).

The electric field distributions of all the propagated modes were calculated at the frequency $f = 55$ GHz. The got results are presented in Figs. 3–5. Here we present the electric field strength lines and the electric field intensities.

In Fig. 3, we see that the electric field distribution of the main mode has one variation by radius. The strongest electric field of this mode concentrates in the centre of the waveguide in the small enough area.

In Fig. 4, we see that the strongest electric field of this mode concentrates in the large part of the waveguide in the form of two twisted lobes.

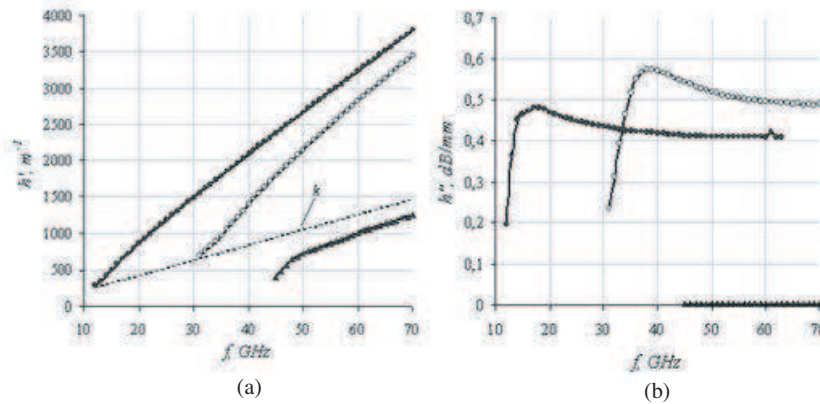


Figure 2: Dispersion characteristics of the SiC waveguide (a) dependence of the $\text{Re}(\underline{h})$ upon frequency, (b) dependence of the $\text{Jm}(\underline{h})$ upon frequency. The main mode is denoted with points, the higher mode is denoted with circles, the fast mode is denoted with triangles. The magnitude k is the wave number ($k = \omega/c$).

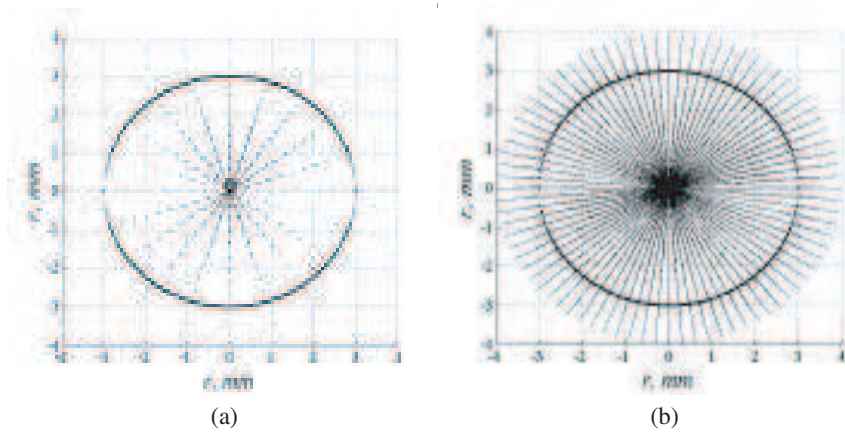


Figure 3: The electric field distribution of the main mode propagating in the SiC waveguide at $f = 55$ GHz; (a) the electric fields strength lines, (b) the electric field intensities.

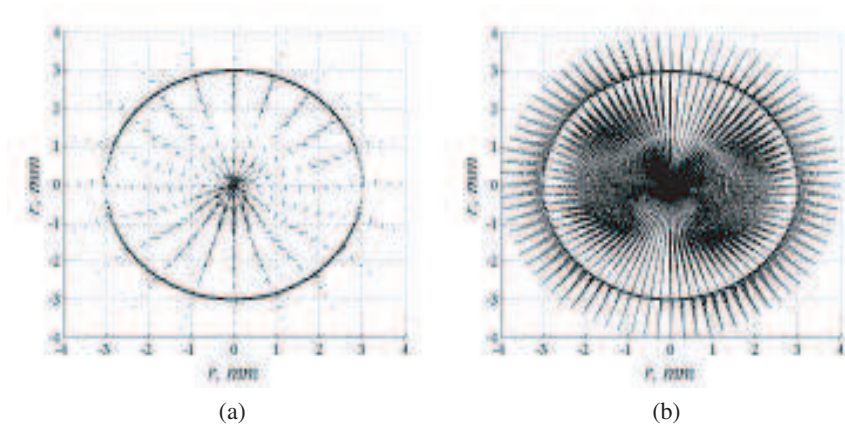


Figure 4: The electric field distribution of the first higher slow mode propagating in the SiC waveguide at $f = 55$ GHz; (a) the electric fields strength lines, (b) the electric field intensities.

In Fig. 5, we see that the electric field distribution of the fast mode has three variations by radius. The strongest electric field of this mode concentrates in the centre of the waveguide in the form of two lobes and outside it.

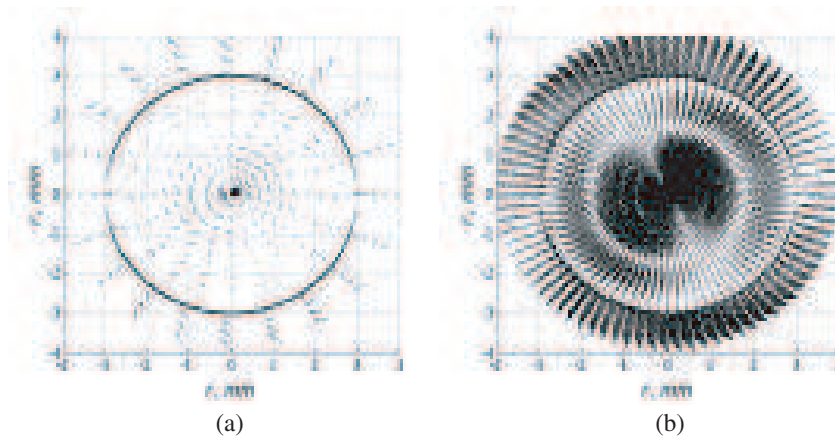


Figure 5: The electric field distribution of the second higher fast mode propagating in the SiC waveguide at $f = 55$ GHz; (a) the electric fields strength lines, (b) the electric field intensities.

4. CONCLUSIONS

- The losses of modes propagating in the rectangular SiC waveguide are smaller than the ones of modes propagating in the circular SiC waveguides.
- The cutoff frequency of the main mode propagating in the rectangular waveguide moves to the region of the higher frequencies in comparison with the circular waveguide. Therefore the bandwidth of the rectangular waveguide is narrower than of the circular waveguide.
- The strongest electric field of the main mode propagating in the circular waveguide concentrates in the centre of this waveguide in the small area. Therefore the breakdown energy of this mode is higher in comparison with other modes.
- The electric field of the fast mode propagating in the circular SiC waveguide concentrates outside the waveguide. The losses of the fast mode are smaller in 60 times in comparison with the losses of the slow modes propagating in the circular waveguide.

REFERENCES

1. Dussreaux, R. and C. Faure, "Telegraphist's equations for rectangular waveguides and analysis in nonorthogonal coordinates," *Progress In Electromagnetics Research*, PIER 88, 53–71, 2008.
2. Nickelson, L. and T. Gric, "Electric field distributions in the cross-sections of the metamaterial hollow-core and rod waveguides," *Proceedings of MIKON-2008*, 497–500, Wroclaw, Poland, May 2008.
3. Pandraud, G., P. J. French, and P. M. Sarro, "PECVD silicon carbide waveguides for multi-channel sensors," *Proceedings of IEEE Sensors 2007 Conference*, 395–398, Atlanta, Georgia, USA, October 2007.
4. Liu, Y. M. and P. R. Prucnal, "Low-loss silicon carbide optical waveguides for silicon-based optoelectronic devices," *IEEE Photonics Technology Letters*, Vol. 5, No. 6, 704–707, 1993.
5. Nickelson, L. and V. Shugurov, *Singular Integral Equations' Methods for the Analysis of Microwave Structures*, VSP Publ. Int. Sci. Publ., Leiden-Boston, 2005.
6. Nickelson, L. and T. Gric, "Dispersion characteristics and electric field distributions of modes propagating in the open electrically gyrotropic semiconductor rod waveguide," *Proceedings of MIKON-2008*, 501–504, Wroclaw, Poland, May 2008.
7. Nickelson, L., T. Gric, S. Asmontas, and R. Martavicius, "Electrodynamical analyses of dielectric and metamaterial hollow-core cylindrical waveguides," *Electronics and Electrical Engineering*, Vol. 82, No. 2, 3–8, 2008.
8. Nickelson, L., T. Gric, and S. Asmontas, "Dispersion characteristics of metamaterial hollow-core cylindrical waveguide," *Lithuanian Journal of Physics*, Vol. 47, No 3, 273–279, 2007.
9. Baeraky, T. A., "Microwave measurements of the dielectric properties of silicon carbide at high temperature," *Egypt. J. Sol.*, Vol. 25, No. 5, 263–273, 2002.

On the Preconditioning of the Algebraic Linear Systems Arising from the Discretization of the EFIE

G. Angiulli, P. Quattrone, and S. Tringali

DIMET, Univ. Mediterranea, via Graziella 1, Loc. Feo di Vito, Reggio Calabria 89122, Italy

Abstract— The rate of convergence of the Generalized Minimum Residual Method (GMRES) applied to the dense linear systems arising from discretization of EFIE integral equation by Method of Moment (MoM) depends heavily by preconditioning. In this work, we evaluate the performances of a simple preconditioner based on the skew hermitian component \mathbf{S} of MoM impedance matrix \mathbf{Z} for the case of plane wave scattering by CEP bodies.

1. INTRODUCTION

The integral equations involved in electromagnetics are discretized by subdomain or entire domain-type MoM. These eventually result into complex linear systems of equations, whose size depends on both the meshing fineness and the electrical dimensions of the structures at hand. So MoM is ultimately dependent in a critical way on the availability of efficient solvers for algebraic dense linear systems of equations, and this is a topic of active research at present in the computational electromagnetics community [1]. Though at times we can still think of employing direct factorization, as far as the structures are small or the mesh is coarse, this approach is useless in practice, as the size of the discretized problem grows. Then the only concrete alternative is the use of nonstationary iterative methods, i.e., Krylov Subspace methods. In these last years a great interest has been deserved to the Generalized Minimum Residual Method (GMRES), as it has been variously tested to offer higher performances (see [2] and references within) than the standard Coniugate Gradient Method (CGM), especially for indefinite systems. However, in the case of algebraic linear systems produced by discretization of EFIE by MoM, GMRES converges very slowly or not at all. This behavior is caused by unfavorably spectral properties of the impedance matrix \mathbf{Z} . Therefore, it is crucial to use GMRES in conjunction with an efficient preconditioner. In technical literature, researches relevant preconditioning have been mainly directed toward the design of preconditioners as AINV, SPAI and ILUT (see [1] and references within) based on purely algebraic techniques. In this work, we evaluate the performances of a preconditioner derived by simple considerations on the nature of EFIE. It is based on the skew hermitian component \mathbf{S} of the \mathbf{Z} impedance matrix. This choice ensures that the spectrum of the preconditioned system will be located around the point $(1, 0)$ of the complex plane [4] causing an enhancement of GMRES convergence rate as confirmed by numerical experiments.

2. GMRES BASIC THEORY

In this section we review briefly GMRES method for solving an algebraic linear system of the form

$$\mathbf{Z}\mathbf{x} = \mathbf{b}, \quad (1)$$

where $\mathbf{Z} \in \mathbb{C}^{n,n}$ denotes MoM impedance matrix, $\mathbf{b} \in \mathbb{C}^n$ the righthand side (the excitation vector) and $\mathbf{x} \in \mathbb{C}^n$ the solution vector. Without loss of generality, let us consider the equivalent system

$$\mathbf{Z}\mathbf{y} = \mathbf{r}_0, \quad \text{where } \mathbf{r}_0 = -\mathbf{Z}\mathbf{x}_0 + \mathbf{b} \text{ and } \mathbf{y} = \mathbf{x} - \mathbf{x}_0. \quad (2)$$

The GMRES method is based upon the Arnoldi recursion, which can be simplified as it follows:

1. Given a vector \mathbf{v}_1 with $\|\mathbf{v}_1\| = 1$, compute $\mathbf{v}_{k+1} = \mathbf{Z}\mathbf{v}_k$, for $k = 2, 3, \dots$
2. For each k and for $i = 1, 2, \dots, k$, compute

$$h_{i,k} = \mathbf{v}_i^H \mathbf{v}_{k+1} \text{ and } \mathbf{v}_{k+1} = \mathbf{v}_{k+1} - h_{i,k} \mathbf{v}_i. \quad (3)$$

3. For each k , compute $h_{k+1,k} = \|\mathbf{v}_{k+1}\|$ and $\mathbf{v}_{k+1} = \mathbf{v}_{k+1}/h_{k+1,k}$.

Theoretically, $V_k = \{\mathbf{v}_1, \mathbf{v}_2, \dots, \mathbf{v}_k\}$ is an orthonormal basis of the Krylov subspace $\mathcal{K}_k(\mathbf{Z}, \mathbf{v}_1)$ and the Hessemberg matrix $H_k = (h_{ij})$ is a matrix representation of the Krylov subspace $\mathcal{K}_k(\mathbf{Z}, \mathbf{v}_1)$ with respect to the V_k . In fact, the preceding implementation is a modified Gram-Schmidt orthogonalization. In GMRES, $\mathbf{v}_1 = \mathbf{r}_0/\|\mathbf{r}_0\|$ in the first step of Arnoldi recursion. Theoretically, GMRES select its iterates (say \mathbf{y}_k^G and \mathbf{y}_k^F) from the same Krylov subspaces but subject to different constraints on the corresponding residual vectors, \mathbf{r}_k^G and \mathbf{r}_k^F . At the k -th iteration in GMRES, the iterate is selected so that the norm of the corresponding residual vector \mathbf{r}_k^G is minimized over the k -th Krylov subspace corresponding to \mathbf{Z} and \mathbf{r}_0 . For each k ,

$$\|\mathbf{r}_k^G\| = \min_{y \in \mathcal{K}_k(\mathbf{Z}, \mathbf{r}_0)} \|\mathbf{r}_0 - \mathbf{Z}y\| = \|\mathbf{r}_0 - \mathbf{Z}\mathbf{y}_k^G\|, \quad (4)$$

which Saad proved equivalent to the Petrov-Galerkin condition $\mathbf{r}_k^G \perp \mathcal{K}_k(\mathbf{Z}, \mathbf{r}_0)$ [2].

3. PRECONDITIONING

From a theoretical point of view, \mathbf{Z} obeys to the Half Plane Condition [2], i.e., its eigenvalues must have real part greater than zero. This is a direct consequence of the Poynting theorem applied on EFIE [3]. The Half Plane Condition is a desirable property because it ensures the convergence of GMRES without preconditioning [2]. However, due to discretization errors, \mathbf{Z} always lacks of it and preconditioning becomes mandatory. As well-known, this operation transforms the original algebraic linear system (1) into another one

$$\mathbf{P}^{-1}\mathbf{Z}\mathbf{x} = \mathbf{P}^{-1}\mathbf{b} \quad (5)$$

named *preconditioned system*, which has spectral properties able to enhance the convergence rate. In the case of the linear systems arising from EFIE discretization, \mathbf{P} can be selected as follows. Let

$$\mathbf{Z} = \mathbf{S} + \mathbf{H} = \mathbf{S}(\mathbf{U} + \mathbf{S}^{-1}\mathbf{H}) \quad (6)$$

where $\mathbf{H} = \frac{1}{2}(\mathbf{Z} + \mathbf{Z}^*)$ and $\mathbf{S} = \frac{1}{2}(\mathbf{Z} - \mathbf{Z}^*)$ are the hermitian part and the skew hermitian part of \mathbf{Z} and $\mathbf{U} = \text{diag}(1, 1, \dots, 1)$ is the identity matrix of the same size as Z , respectively. Since in the near-field zone we have a predominance of the reactive energy on the active one, we can expect that $\|\mathbf{S}\| \gg \|\mathbf{H}\|$, i.e., the skew-Hermitian component \mathbf{S} dominates (in the sense of the matrix norm $\|\cdot\|$) the Hermitian component \mathbf{H} . If this condition is fulfilled, it follows that the spectrum $\sigma(\mathbf{S}^{-1}\mathbf{H})$ of $\mathbf{S}^{-1}\mathbf{H}$ will be clustered around the origin of the complex plane [4]. Consequently, selecting $\mathbf{P} = \mathbf{S}$ in (5), we have that the spectrum of the preconditioned coefficient matrix

$$\mathbf{P}^{-1}\mathbf{Z} = \mathbf{S}^{-1}\mathbf{S}(\mathbf{U} + \mathbf{S}^{-1}\mathbf{H}) = \mathbf{U} + \mathbf{S}^{-1}\mathbf{H} \quad (7)$$

$\sigma(\mathbf{P}^{-1}\mathbf{Z}) = \sigma(\mathbf{U} + \mathbf{S}^{-1}\mathbf{H})$ will be located around the point (1,0) of the complex plane [4] obtaining in this way the desired preconditioning effect [4].

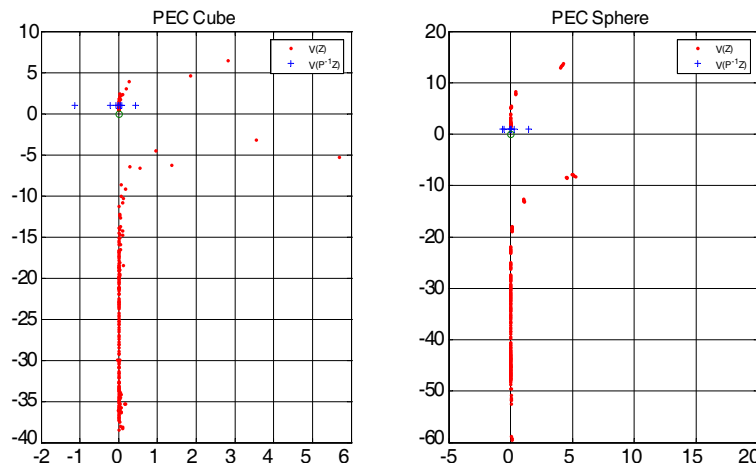


Figure 1: Spectrum of the system before (in red dots) and after (in blue crosses) the preconditioning (on the left: PEC cube; on the right: PEC sphere).

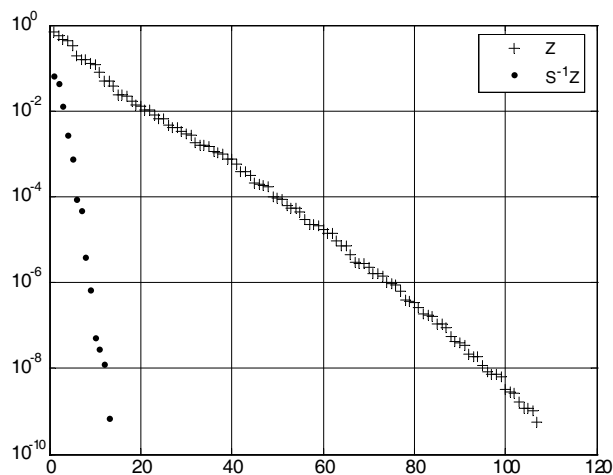


Figure 2: History of the residual norm before (in blue crosses) and after (in red dots) the preconditioning, in the case of a 1-meter PEC cube.

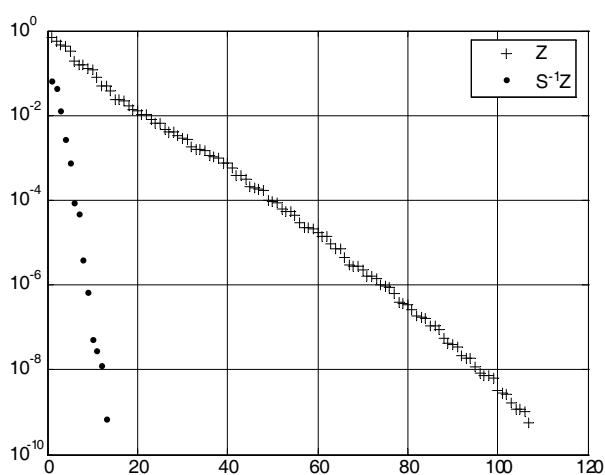


Figure 3: History of the residual norm before (in blue crosses) and after (in red dots) the preconditioning, in the case of a 1-meter PEC sphere.

4. NUMERICAL RESULTS AND CONCLUSIONS

The GMRES without restart has been tested on the linear systems (1) coming out from MoM analysis of EFIE for the scattering from *i*) a PEC cube of 1-meter edges and *ii*) a PEC sphere of 1-meter radius by an incident θ -polarized plane wave ($f=200$ MHz). In Figure 1 is reported the distribution of the spectrum for unpreconditioned case and preconditioned one, respectively. It can be noticed as the preconditioning causes a clustering of the spectrum. In Figures 2 and 3 the histories of the residual norm are reported.

The preconditioning results in a significant reduction of the overall number of iterations that are necessary to attain convergence within a fixed tolerance $\epsilon = 10^{-12}$ (starting from an initial guess $\mathbf{x}_0 = \mathbf{0}$). All algorithms have been implemented in a MATLAB code on a personal computer equipped with a 2 GHz AMD Athlon processor and 2 GB of DDR2 RAM, with a particular attention devoted to coding time-critical routines using FORTRAN.

REFERENCES

1. Chew, W. C., et al., *Fast and Efficient Algorithms in Computational Electromagnetics*, Artech House Inc., 2001.
2. Saad, Y. and M. H. Schultz, "GMRES: A generalize minimal residual algorithm for solving nonsymmetric linear systems," *SIAM J. Sci. Stat. Comput.*, Vol. 7, 856–869, 1986.
3. Canning, F. X., "Physical and mathematical structure determine convergence rate of iterative techniques," *IEEE Trans. on Magnetics*, Vol. 25, No. 4, 2825–2827, 1997.
4. Bai, Z. Z., G. Golub, and M. K. Ng, "Hermitian and skew-Hermitian splitting methods for non hermitian positive definite linear systems," *SIAM J. Matrix. Anal. Appl.*, Vol. 24, 603–626, 2003.

The Effective 3D Modeling of Electromagnetic Waves' Evolution in Photonic Crystals and Metamaterials

A. V. Zakirov¹ and V. D. Levchenko²

¹Moscow Institute of Physics and Technology, Russia

²Keldysh Institute of Applied Mathematics, Russia

Abstract— For a large class of problems based on simulations of Maxwell's equations, numerical modeling is often necessary. But this modeling may require a large computational resources. So naturally arises the problem of creation the programs that can satisfy the requirements of these tasks and the possible problems in the future.

In the work, the realization of algorithm of high effectiveness is offered. This algorithm based on numerical modelling of Maxwell's equations with FDTD method with different arbitrary boundary conditions including the PML. High-speed calculations, not the limited amount of data handled, as well as good parallelization is achieved by using Local-recursive nonlocal-asynchronous algorithm (LRnLA). It is possible to simulate the following types of materials: Nondispersive medium with real permittivity $\varepsilon(\vec{r})$ and magnetic permeability $\mu(\vec{r})$ depending on the coordinates in space, materials with dispersion $\varepsilon(\omega, \vec{r})$ and $\mu(\omega, \vec{r})$, based on the Drude model, as well as conductors and metamaterials (materials with negative refractive index), presented as consequence of this model.

1. INTRODUCTION

Up-to-date artificial optical devices and materials such as photonic crystals, metamaterials (Left-Handed Materials), streamlined surfaces are usually very complicated structures. Analytical calculations for propagation of electromagnetic waves in this media are possible only in simplest cases. On application of computational algorithms the difficulties appear due to large dimensions of calculation area. It results in necessity of effective algorithm development and realization for this calculations, because the the existing systems [1, 2], usually unable to perform an effective three-dimensional calculation, even if sufficient computing resources are given. "Effective" algorithm means such one, that has real rate coming up to theoretical. In the work, the implementation of such algorithm is offered for Maxwell's equations' modeling.

In the capacity of difference scheme, the Finite-difference time-domain method (FDTD) [4] is used. For method of cell rounding (sequence of calculations), the Local-recursive nonlocal-asynchronous algorithm (LRnLA) [3] is used, which makes possible to reach the high rate of program's effectiveness. The computational area contains of many Yee cells, that form the rectangular parallelepiped. This area is rounded from 5 faces by Perfectly Matched Layer (PML) [7]. So we can set absorption boundary conditions. In many cases, it is the necessary requirement for limited areas studying. At the 6th face there are the source and reflecting boundary conditions. In addition, the reflecting or periodic boundary conditions are available to set at the any face. It is developed the methods for modeling of the following media:

- The simple undispersion materials with real permittivity ε and magnetic permeability μ , which are depended only on the position in space.
- The media with dispersion described by Drude model, where $\varepsilon = 1 + \frac{e^2}{m} \sum \frac{N_k}{\omega_k^2 - \omega^2 + i\gamma_k \omega}$. Conductors and the Negative Index Media (NIM, same as LHM) are under this model too.
- Anisotropic media.
- Nonlinear media.

The optimization the software package makes possible to use the advantages of modern processors for acceleration of calculations and allows to use many cores or processors in single calculations without descending of rate. The rate of calculations in all cases is nevertheless than 40% beside the theoretical estimation on the assumption of CPU clock and doesn't depend on capacity of analyzed data that is the computational area. Due to the such results, we can use the existent program for modeling of many electrodynamics problems of today.

2. GENERAL FORMULATION

A full three-dimensional numerical simulation of the evolution in time of electromagnetic field described by Maxwell's equations in a bounded domain with a different boundary conditions. The certain model of media is set with the help of the material equations.

2.1. Difference Scheme

Electromagnetic field in the problem is described by the values of the electric vector (\vec{E}, \vec{D}) and magnetic (\vec{B}, \vec{H}) fields that are known at certain time moments. The changes of this values are described by explicit difference scheme, that approximates Maxwell's equations together with certain material equations.

FDTD (Finite-Difference Time-Domain) method is used in the capacity of explicit difference scheme. It makes possible to find the values of components of electromagnetic field at the next time layer through the values at the current layer. Below it is present its brief description for handy using in numerical computations.

Initially, We describe the variant for elemental model of undispersion dielectric. It will be described by means of material equations, that represent linear scalar dependence between electric field and electric displacement field, and also between magnetic field and magnetizing field, and on this dependence affect only space coordinates at that.

We will use Maxwell's equations in the differential form:

$$\operatorname{rot}(\mathbf{H}) = \frac{\partial \mathbf{D}}{\partial t}, \quad \operatorname{rot}(\mathbf{E}) = -\frac{\partial \mathbf{B}}{\partial t}. \quad (1)$$

The speed of light in vacuum is set as 1. Dimensions of other variables are chosen in the following way:

$$[x, t, E, H] = d, 1/d, E_0, H_0$$

Here d — Typical length in the problem, $E_0 H_0$ — Initial amplitudes of, correspondingly, electrical and magnetic components of wave in vacuum.

2.2. Boundary conditions

The features of Maxwell's equations, and, therefore, the difference scheme, are such that tangential values of components of electromagnetic field at the border of the computational area are cannot be found definitely and they should be redefined by the use of boundary conditions. At present, there are realized the following types of boundary conditions at the border of computational area:

Periodic Boundary Conditions. The components of electromagnetic field at the opposite boundaries are set as equal ones.

Reflecting Boundary Conditions. There are possible 2 models of full ideal reflection: Reflection with zero tangential components of electric field (classical ideal reflection from conductive surface), or magnetic one.

Predefined Values. Unknown variables era redefined by specified functions of coordinates and time, it is also possible the trivial case (redefinition as zero).

Mixed Conditions. The combination of two preceding conditions. Now these conditions are used for waves' source modelling at the one border.

Absorption Boundary Conditions PML (Perfectly Matched Layer) [7]. They are set by means of additional cells of computational area on the side of corresponding boundary, in which there are modeled an exponential attenuation of electromagnetic wave. The factor of attenuation depends on remoteness from the main boundary and is increased as distance in the depth of PML. This absorption boundary conditions make it possible to model the spreading of electromagnetic field in the bounded area with opened boundaries. So long as limited resources, and also peculiarities of problem lead to necessity of analysis only the bounded area, than such boundary conditions become urgent in the most cases.

3. ATGORITHM OF CELL ROUNDING OF DEPENDENCE GRAPH IN DIFFERENCE SCHEME

The certain explicit difference scheme with specified initial and boundary conditions may be presented as cellular automaton. The values in all cells are changed simultaneously during one iteration. It means that sequence of calculations of lattice's cells during the iteration, doesn't affect on result. In addition, in case of locality of cellular automaton, it is possible to perform the next iteration

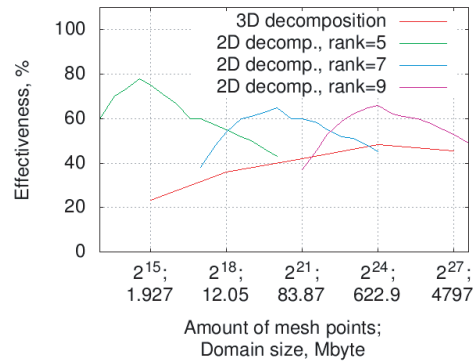


Figure 1: Effectiveness.

without finishing the previous one at the all cells, that also doesn't affect on result. Nevertheless, the certain algorithm of cell rounding affects on the rate of code performance, and it becomes appreciably already for data size, that exceeds the size of processor cache, and for the large sizes of processed datas becomes determinative. Deceleration comes from that the delays of memory controller considerably exceeds one processor stroke. Thereby, the best algorithm will be such one, that will make possible to reduce time of using of memory controller. In some way, such algorithm may be considered LRnLA (Local-recursive nonlocal-asynchronous) algorithm [3]. Its main idea may be said to use the recursive rounding of cellular automaton both on space and on time. There is no any losses with program paralleling, that is one else advantage of this algorithm.

At the Fig. 1, there are given the graphs of calculating effectiveness's dependence (the ratio of theoretical time of computing on the assumption of processor strokes and its speed rate and the real practice time of calculation) for different parameters of algorithm.

4. EXAMPLES

4.1. The Distribution of Electromagnetic Field after Plane Wave's Incidence on the 3D Photonic Crystal

The computational area is a cube with dimensions $256 \times 256 \times 256$ computational cells (the dimensions of one cell, that is the array pitch for space, are $1 \times 1 \times 1$). PML conditions are set on the borders on the 5 sides, and on the 6th side, that is placed perpendicularly to axe Z , are set the mixed boundary conditions (reflection plus generation of plane wave). Inside the computational area there is dispose the photonic crystal, whose cells are the cubes with refractive indexes $n_1 = \sqrt{2}$ $n_2 = \sqrt{3}$ arranged in 3D chequer-wise as shown in the figure. The period of photonic crystal is 20. With respect to the computational area in this case the photonic crystal is asymmetrically, so the distribution of the field in results (Fig. 3) is asymmetrically too.

In the Fig. 2, there are presented the projections of computational area on three mutually perpendicular cube sides (axes X , Y , Z turn along the edges), and also the resultant 3D picture for obviousness.

The incident wave is the wave packet, that limited with function $(1 + \cos \Omega t)$ by time and the same function by coordinates X and Y with linear polarization. The carrier frequency is 0.05, thereby, we have 20 mesh points for the one wave length in vacuum.

In the Fig. 3(a) are shown two projections of the electromagnetic field's component E_x (the intensity expressed by color) along the axes Z and X at time moments $256\Delta t$, $768\Delta t$ and $1280\Delta t$ ($\Delta t = 0.25$) for case when the carrier frequency of incident wave is 0.05, in Fig. 3(b), the carrier frequency is 0.033, and in Fig. 3(c), the frequency of source wave is for area without photonic crystal. Fig. 3(d) corresponds to calculation, in which photonic crystal is fully displaced by dielectric with refractive index $n = 0.5(n_1 + n_2) = (\sqrt{2} + \sqrt{3})/2$.

The Fig. 4 represents the full energy inside the computational area for three experiments described above (Figs. 3(a), 3(b), 3(d)). This energy calculated as difference of energy that has come in and has come out through the sides of computational cube. The Fig. 5 represents the ratio of energy, that has come out through the sides X and Y , and the energy, that has been generated by source by current time moment. Axe Z is a normal to the natural direction of wave's distribution as shown in Fig. 3.

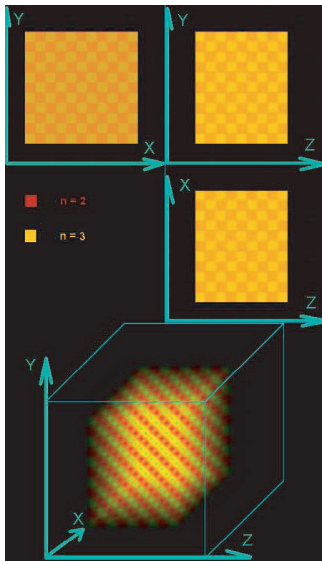


Figure 2: Photonic crystal.

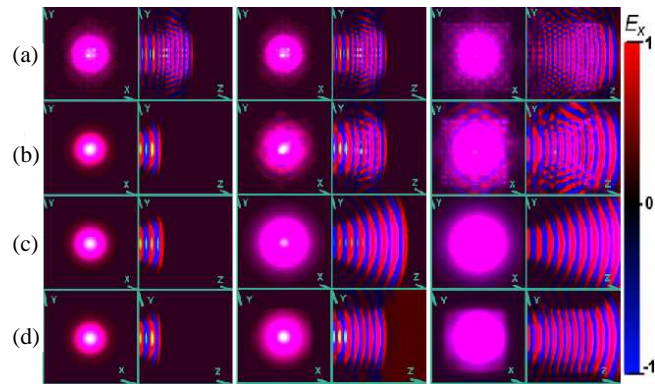
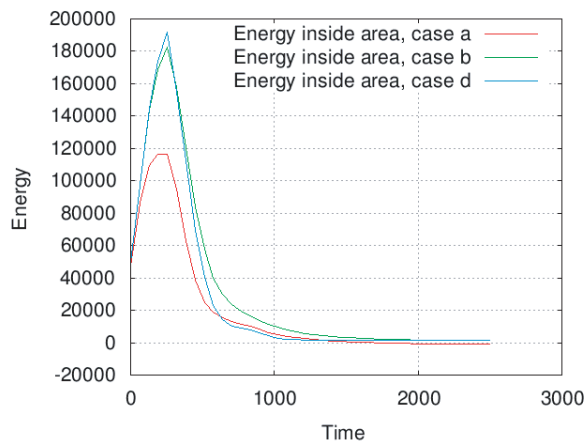
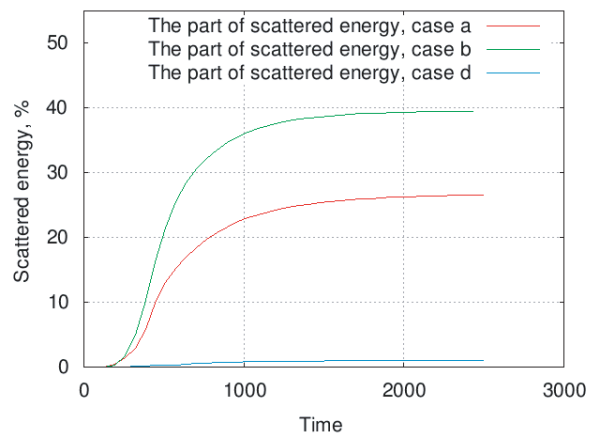

 Figure 3: Distribution of field's component E_x at the different time moments: (a) For carrier frequency 0.05, (b) for carrier frequency 0.033, (c) for frequency 0.033 in vacuum, (d) for frequency 0.033 for displacement photonic crystal by dielectric.


Figure 4: Amount of energy inside the computational cube for cases from Fig. 3(a), 3(b), 3(d), calculated as difference of energy that has come in and out through the sides of computational cube.


 Figure 5: The part of energy, that has come out through the sides $X Y$ with respect to the energy, that has come in the computational area in cases from Fig. 3(a), 3(b), 3(d).

4.2. Wave's Propagation through the Prism with Negative Refractive Index

The prism in the Fig. 6(top) is the model of metamaterial with the following equations for ε and μ :

$$\begin{aligned} \varepsilon &= 1 - \frac{\omega_e^2}{\omega^2}, \\ \mu &= 1 - \frac{\omega_m^2}{\omega^2}. \end{aligned} \quad (2)$$

For the carrier frequency of incident wave packet, the prism's refractive index equals -1 . The incident wave isn't monochrome, nevertheless in the Fig. 6(bottom) the effect of negative refractive index is observed very well.

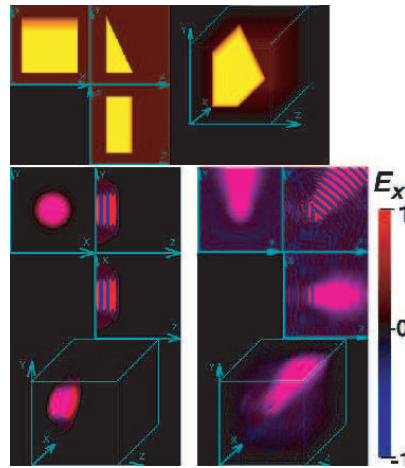


Figure 6: Top: The prism with negative refractive index. Bottom: The distribution of the field's component E_x at different time moments.

5. CONCLUSION

It is realized the code, that can model the evolution of electromagnetic field in medium during time. So long as the main aim is the application for problems, that requires large computational resources, than the main idea of code, that distinguishes it from the existent analogs, is effective algorithm using (in particular LRnLA algorithm). At the moment, the program develops in the direction of gradually complex models of medium with a view to its possible application to a large class of topical problems of electrodynamics, such as the implementation of models of anisotropic media and media with nonlinear material equations.

Thus the main result is now a feasible possibility of solution is quite a large class of complex computational point of view problems in the above-described models.

ACKNOWLEDGMENT

This work was supported by RFBR grant 06-01-00569.

REFERENCES

1. <http://www.cst.com/Content/Products/MWS/Overview.aspx>.
2. <http://ab-initio.mit.edu/wiki/index.php/Meep>.
3. Levchenko, V. D., "Information technology and computing systems," Vol. 1, No. 68, 2005.
4. Taflove, A., *Computational Electrodynamics: The Finite-difference Time-domain Method*, Artech House, Norwood, MA, 1998.
5. Yee, K., "Numerical solution of initial boundary value problems involving Maxwell's equations in isotropic media," *IEEE Transactions on Antennas and Propagation*, Vol. 14, 302–307, 1966.
6. Tikhonov, A. N. and A. A. Samarskiy, *The Equations of Mathematical Physics*, Nauka, 1972.
7. Berenger, J.-P., "Three-dimensional perfectly matched layer for the absorption of electromagnetic waves," *Journal of Computational Physics*, Vol. 127, 363–379, 1996.
8. Intel Corporation, Intel Architecture Optimization Reference Manual, 1999.
9. Sletter, J., *Dielectrics, Semiconductors, Metals*, 1969.
10. Veselago, V. G., "Electrodynamics of substances with simultaneously negative values of ϵ and μ ," *Physical Sciences*, Vol. 92, 517–526, 1967.

Transient Response Analysis of Conducting Bodies by Combination of MoM/AWE and Vector Fitting Techniques

D. Wójcik and M. Surma
Silesian University of Technology, Gliwice, Poland

Abstract— Efficient method for determining transient response of conducting bodies is outlined in this paper. The method is based on robust pole-residue representation of frequency domain response by using of vector fitting technique and then applying inverse Laplace transform to convert into the time domain. The frequency behavior of current is approximated from relatively small number of discrete frequency samples and derivatives of samples obtained from MoM/AWE method.

1. INTRODUCTION

To perform transient analysis of high resonant structure by using of direct time-domain methods long lasting computations are usually required. The analysis can be carried out applying frequency domain integral equation method, such as method of moments (MoM) [1], combined with inverse fast Fourier transform (IFFT). However, the approach is very ineffective, especially when electrically large structures over wide frequency range are analyzed, because of a huge number of samples required by IFFT. To speed-up frequency domain calculations, MoM combined with asymptotic waveform evaluation (AWE) technique [2] and complex frequency hopping (CHF) algorithm [3] can be successively employed. AWE is based on rational approximation of current over wide frequency range from relatively small number of discrete frequency and frequency derivatives samples, while CHF algorithm is very helpful to locate frequency points which derivatives are calculated for. As a result, one obtains frequency response as a form of a set of rational functions: Each function describes the frequency behavior of observable on certain frequency subrange. If the frequency response is described by one rational function covering the whole frequency range, time (transient) response will be obtained analytically by using of inverse Laplace transform. In this paper, to obtain one rational representation from the set of rational functions vector fitting (VF) technique is employed. The VF is a robust macromodelling tool that circumvents ill-conditioning problems which usually occur in high order rational approximations [9]. The VF method ensures also stability and passivity of the response, which is not guaranteed by AWE algorithm.

2. MOM/AWE TECHNIQUE

The AWE technique derives from frequency-domain method of moments. The MoM is based on Pocklington's integral equation describing unknown current distribution on the surface of the objects under investigation [1]. Method of moments reduces Pocklington's equation to a system of linear equations with respect to N coefficients of unknown current vector $\mathbf{I}(f)$. In matrix notation, it can be expressed as

$$\mathbf{Z}(f)\mathbf{I}(f) = \mathbf{U}(f), \quad (1)$$

where f is operating frequency, $\mathbf{Z}(f)$ denotes impedance matrix describing properties of the object, and $\mathbf{U}(f)$ — known excitation vector. It should be emphasized that matrix Equation (1) must be solved repeatedly for each individual frequency of interest. Therefore, MoM computations over wide frequency range can be very time consuming process.

Wide band analysis by MoM can be significantly speeded-up by employing the AWE technique [4, 5]. The essence of AWE consists in description of frequency behavior of the current by means of rational function

$$I(f) = \frac{A(f)}{B(f)} = \frac{a_0 + a_1f + a_2f^2 + a_3f^3 + \dots + a_Nf^N}{1 + b_1f + b_2f^2 + b_3f^3 + \dots + b_Df^D} \quad (2)$$

where N and D denotes the order of the numerator and denominator, respectively. In case of usage of standard interpolation we need $N + D + 1$ "selected" frequency samples of $I(f)$ computed by MoM to obtain unknown a_i and b_i coefficients. However, it is well-known that the interpolation does not guarantee proper behavior of (2) for frequencies between the interpolation nodes. More

The vector fitting technique bases on partial fraction expansion of $I(s)$

$$I(s) \approx \sum_{i=1}^N \frac{r_i}{s + p_i} \quad (7)$$

where $s = j\omega$ is the complex frequency, r_i and p_i are residues and poles, respectively. Lets introduce an unknown function

$$\sigma(s) = \sum_{i=1}^N \frac{\tilde{r}_i}{s + \tilde{p}_i} + 1 \quad (8)$$

and assume the rational approximation for $\sigma(s)I(s)$ as [9, 10]

$$\sigma(s)I(s) \approx \sum_{i=1}^N \frac{\tilde{r}_i}{s + \tilde{p}_i} \quad (9)$$

Note, that both (8) and (9) have the same poles. In VF, it is also assumed that initial localizations of poles are known. Multiplying the both sides of (8) by (7) and comparing the result to (9), one can obtain

$$\sum_{i=1}^N \frac{\tilde{r}_i}{s + \tilde{p}_i} \approx \left(\sum_{i=1}^N \frac{\tilde{r}_i}{s + \tilde{p}_i} + 1 \right) I(s) \quad (10)$$

Since the poles \tilde{p}_i are specified, Equation (9) can be solved with respect to \tilde{r}_i and \tilde{r}_i as least square problem if proper number of frequency samples of $I(s)$ are known. Next, zeros of $\sigma(s)$ can be determined. It can be shown that the zeros are simultaneously the poles of $I(s)$ approximation [9]. Thus, residues r_i of (7) can be now determined by solving a system of linear equations, and accuracy of approximation (7) can be verified by comparison to original samples of $I(s)$. If needed, next iteration is further performed with new poles \tilde{p}_i . In practice, convergence is often reached within a few iterations only. In each iteration, it is controlled that the poles are stable and come in perfectly accurate complex pairs [9]. When the VF process is finished, inverse Laplace transform can be employed to obtain time domain response

$$I(t) = \sum_{i=1}^N r_i e^{-p_i t} \quad (11)$$

4. NUMERICAL RESULTS

To examine efficiency and accuracy of proposed approach, a numerical example is considered. The structure under investigation consists of three parallel wires located above infinite perfect conducting plane, as it is depicted in Figure 1. The diameter of each wire is equal to 1 mm. For numerical purposes, the wires are modelled by 159 linear segments. The structure was excited by voltage generator locates at a third of the length of middle wire. The derivative of Gaussian pulse is used as excitation signal. The highest frequency in the spectrum of the pulse was equal to 2400 MHz.

In the first stage, MoM/AWE technique was employed to analyse the response of the structure in frequency range from 1 to 2400 MHz at the feeding point. The orders of the numerator and denominator of rational functions was assumed to be 4 and 5, respectively. 20 expansion points were needed for CFH algorithm to achieve assumed accuracy ($\varepsilon = 5\%$). Next, the VF technique is employed for 50 poles of (7) and 2400 uniformly spaced frequency samples obtained from MoM/AWE

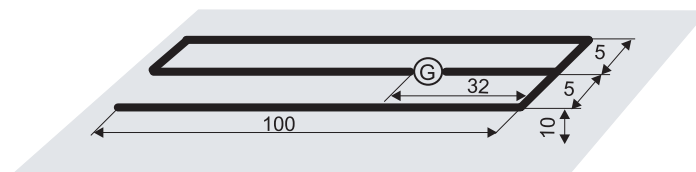


Figure 1: The structure under investigation.

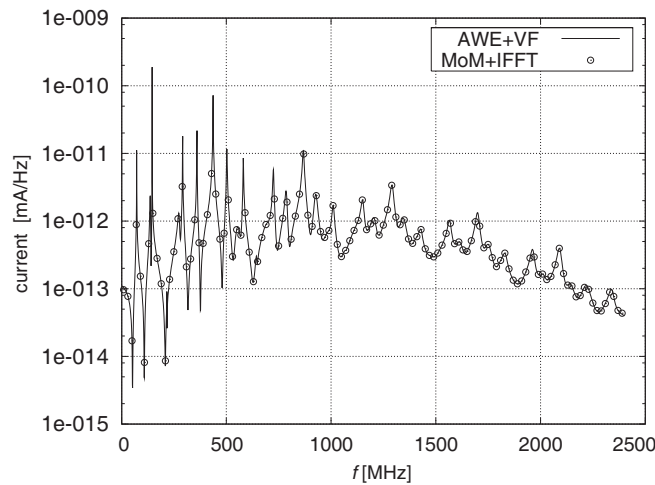


Figure 2: Frequency response of current at feeding point of the structure.

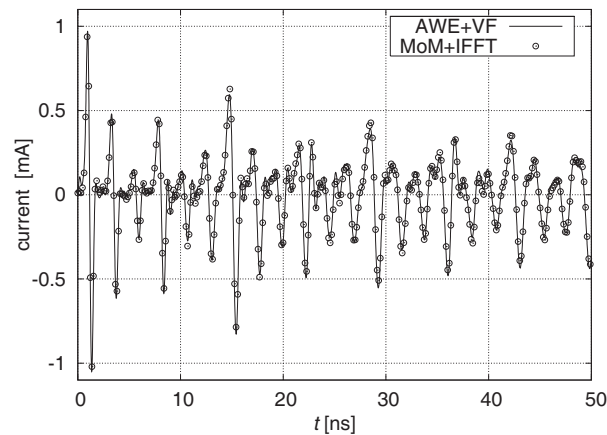


Figure 3: Transient response of current at feeding point of the structure.

approximation. Finally, transient response is calculated by using of (11). To compare accuracy of proposed approach, conventional analysis was performed by MoM combined with IFFT technique for 9600 uniformly spaced frequency domain samples. Comparison of frequency spectrum of the signals and transient response are depicted in Figure 2 and Figure 3, respectively. As it can be easily observed, the accuracy of the results obtained by AWE+VF are very good compared to conventional MoM+IFFT approach. Time of analysis using AWE+VF is 1604s, which is almost 4 times shorter than MM+IFFT technique. All analyses were carried out with CPU Pentium 4, 1.7GHz and 1GB RAM.

5. CONCLUSION

The method presented in this paper is devoted to efficient transient response analysis of high resonant conducting bodies. The method combines the MoM/AWE and the VF techniques to obtain robust pole-residue representation of frequency domain response from relatively small number of discrete frequency samples and derivatives of samples. Then, transient response are obtained by using of inverse Laplace transform. The numerical results clearly demonstrate the usefulness and efficiency of the the proposed approach. For the analyzed structure the results are obtained about four times faster in comparison to classical MoM-IFFT approach. It should be emphasized that the bigger structure under investigation is the bigger the speed-up ratio will be achieved. Indeed, for electrically large structures the time of analysis using AWE is much shorter compared to time of analysis using method of moments [8].

ACKNOWLEDGMENT

This work is partially supported by the Polish Ministry of Science and Higher Education under Grant N N517 467934.

REFERENCES

1. Harrington, R. F., *Filed Computation by Moment Methods*, MacMillan, 1968.
2. Cockrell, C. R. and F. B. Beck, "Asymptotic Waveform Evaluation (AWE) technique for frequency domain electromagnetic analysis," *NASA Technical Memor. 110292*, November 1996.
3. Kolbedhari, M. A., M. Srinirasan, M. S. Nakhla, Q. J. Zhang, and R. Achor, "Simultaneous time and frequency domain solutions of EM problems using finite element and CFH technique," *IEEE Trans. Microwave Theory Tech.*, Vol. 49, No. 8, 1419–1430, 2001.
4. Reddy, C. J., M. D. Desphande, C. R. Cockrell, and F. B. Beck, "Fast RCS computation over a frequency band using method of moments in conjunction with asymptotic waveform evaluation technique," *IEEE Trans. Microwave Theory Tech.*, Vol. 46, No. 8, 1229–1233, 1998.
5. Erdemli, Y. E., J. Gong, C. J. Reddy, and J. L. Volakis, "Fast RCS pattern using AWE technique," *IEEE Trans. Microwave Theory Tech.*, Vol. 46, No. 11, 1752–1753, 1998.
6. Chew, W. C., J. M. Jin, E. Michielssen, and J. Song, *Fast and Efficient Algorithms in Computational Electromagnetics*, Artech House Publisher, Boston, 2002.
7. Surma, M., "Efficient method for obtaining derivatives of current vector for AWE techniques," *Proceedings of XVI International Conference on Mirowaves, Radar and Wireless Communications*, 398–401, Krakow, Poland, May 2006.
8. Karwowski, A., M. Surma, and D. Wójcik, "Efficient wideband analysis of electromagnetic scattering and radiation problems using the AWE/MBPE adaptive method wit the method of moments," *Proceedings of 15th International Zurich Symposium and Technical Exhibition on Electromagnetic Compatibility*, 263–266, Zurich, Switzerland, February 2003.
9. Gustavsen, B. and A. Semley, "Rational approximation of frequency domain responses by vector fitting," *IEEE Trans. Power Deliv.*, Vol. 14, No. 3, 1052–1061, 1999.
10. Kocar, I., J. Mahseredjian, and G. Olivier, "Weighting method for transient analysis of underground cables," *IEEE Trans. Power Deliv.*, Vol. 23, No. 3, 1629–1635, 2008.
11. Wang, W., L. Zhang, Q. Li, and W. H. Siew, "Parameter identification of transfer functions using an improved vector fitting method," *Proceedings of 2008 Asia-Pacific Symposium on Electromagnetic Compatibility & 19th International Zurich Symposium on Electromagnetic Compatibility*, 375–378, Singapore, May 2008.

The Numerical Solution of the Three-dimensional Helmholtz Equation with Sommerfeld Boundary Conditions

Géza Hegedűs

Department of Georgikon Faculty, Pannon University, Deák F. u. 16, H-8360, Keszthely, Hungary

Abstract— Many physical phenomena in acoustics, optics and electromagnetic wave theory are governed by the scalar wave equation. In the frequency-domain, the wave equation is called Helmholtz equation. In this study, we start with the 3D Helmholtz equation.

In this contribution, we look for the solution of the Helmholtz equation using finite difference discretizations in a rectangular domain. We approximate the Laplacian with the second order accurate 7-point finite difference stencil. The discretization results in a system of linear equations. The system matrix is a large but sparse matrix with complex values. In order to obtain an accurate numerical solution, the number of gridpoints per wavelength should be sufficiently large. As a result, the linear system becomes extremely large.

In this work, method is presented to generate a solution to the problem. Through informatics solution I was trying to minimise runtime. Efforts were made to place the most valuable data possible into the memory to be made processable with the fastest operations.

The linear equation system describing the studied wave-range is composed of seven diagonal matrices, which can be transformed into seven matrices containing seven valuable lines. This is, however, still too big to be kept in the memory simultaneously. To reduce the necessary memory capacity, a work-window of optimum size should be defined to go into the main memory — and regarding its organization — it should demand the minimum possible data-pouring over the whole matrix. Within the work-window a direct procedure was used based on the Gaussian elimination. Considering all that, depending on the capacity of the main memory, we can achieve a good calculation capacity if the wave-range is determined with the optimum selection of the valuable data segment in the memory, and ideal rate and organization of the applied variables.

The effectiveness of the presented method is investigated by means of the numerical example of the beam propagation in a homogeneous medium.

1. INTRODUCTION

Let $u = u(x, y, z) \in \mathbb{C}$ be the wave function on the range Ω . The Helmholtz equation on the range Ω is

$$\Delta u + k^2 u = 0 \quad (1)$$

where $\Delta u = \frac{\partial^2 u}{\partial x^2} + \frac{\partial^2 u}{\partial y^2} + \frac{\partial^2 u}{\partial z^2}$ and k is the wave number. We apply Sommerfeld boundary condition $\frac{\partial u}{\partial n} - iku = 0$ on a set $\Gamma = \partial\Omega \setminus \Gamma_1$, where $\partial\Omega$ is the boundary of domain Ω , and $\Gamma_1 \subset \partial\Omega$. Let n denote the normal of $\partial\Omega$, and i the imaginary unit. The preliminary values $u(x, y, z)$ are known in the points of domain Ω . The examined domain Ω should be covered by an equidistant grid of spacing d , centered in a certain (x, y, z) coordinate grid-point. Thus, $u(x, y, z) = u(pd, qd, rd) = u_{pqr}$ with $0 \leq p \leq a$ $0 \leq q \leq b$ $0 \leq r \leq c$ $p, q, r \in \mathbb{N}$, as it is shown in Fig. 1. The aim of the work is to determine the value of u according to the boundary conditions.

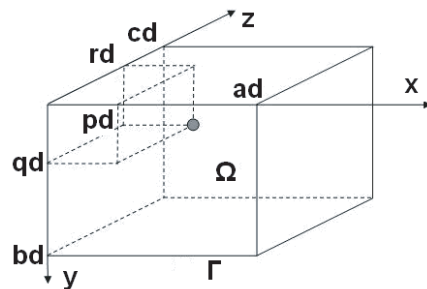


Figure 1. The studied domain Ω with boundary $\Gamma = \partial\Omega \setminus \Gamma_1$, and the applied grid centered in the gray point.

2. THE DIFFERENCE AND BOUNDARY EQUATIONS

Inside the domain the studied point are elements of an equidistant grid which can be seen in Fig. 2. The Equation (1) is approached by the 7-point difference scheme:

$$u_{p-1qr} + u_{p+1qr} + u_{pq-1r} + u_{pq+1r} + u_{pqr-1} + u_{pqr+1} + (k^2 d^2 - 6) u_{pqr} = 0 \quad (2)$$

Three types of boundary points can be found. Fig. 3(a) shows the $x = a$ wall points, except for the edges. Calculating with grid points beyond the plane:

$$2u_{p-1qr} + (d^2 k^2 - 2ikd - 6) u_{pqr} + u_{pq-1r} + u_{pq+1r} + u_{pqr-1} + u_{pqr+1} = 0 \quad (3)$$

We can follow the same procedure on the other side-walls.

On the $x = a, y = b$ edges of the domain, applying the boundary condition, considering that the walls are perpendicular

$$iku_{pqr} = \frac{\partial u_{pqr}}{\partial n} = -\frac{\sqrt{2}}{2} \frac{\partial u_{pqr}}{\partial x} - \frac{\sqrt{2}}{2} \frac{\partial u_{pqr}}{\partial y} \quad (4)$$

Based on (4) we can obtain:

$$2u_{p-1qr} + 2u_{pq-1r} + u_{pqr-1} + u_{pqr+1} + (d^2 k^2 - 2\sqrt{2}dki - 6) u_{pqr} = 0 \quad (5)$$

which can be applied for the other edges as well.

At the corner points $(a, b, 0)$, applying the boundary condition, considering that the walls are perpendicular:

$$iku_{pqr} = \frac{\partial u_{pqr}}{\partial n} = -\frac{\sqrt{3}}{3} \frac{\partial u_{pqr}}{\partial x} - \frac{\sqrt{3}}{3} \frac{\partial u_{pqr}}{\partial y} + \frac{\sqrt{3}}{3} \frac{\partial u_{pqr}}{\partial y} \quad (6)$$

Based on the above (6) relation we get:

$$2u_{p-1qr} + 2u_{pq-1r} + 2u_{pqr+1} + (k^2 d^2 - 2\sqrt{3}ikd - 6) u_{pqr} = 0 \quad (7)$$

Similar procedure is true for the other corners.

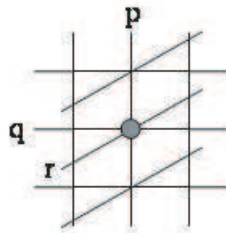


Figure 2. The equidistant grid for finite differences method.

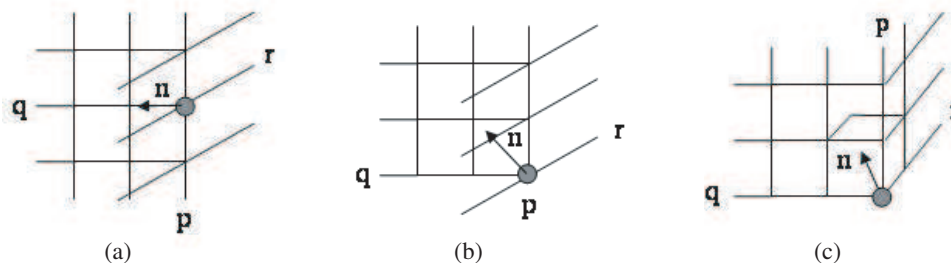


Figure 3. The boundary points of type (a) wall, (b) edge, (c) corner.

3. NUMERICAL SOLUTION

Applying the conditions (2), (3), (5) and (7), we receive a 7 diagonal homogenous linear set of equations containing the equation of $(a+1)(b+1)(c+1)$. Fig. 4(a) represents the extended matrix of simultaneous equations in the case of $a = b = c = 3$. The black spaces indicate 0 value, while the white ones some complex values different from 0.

In certain points, by giving the value u , we receive the extended matrix of the equation system as indicated in Fig. 4(b). A large sparse equation system matrix resulting from the Helmholtz equation with special preliminary conditions. White dots represent the non-zero complex values, black dots are zeros.

The size of the matrix is too big compared to the stored information. The necessary storing capacity can be reduced the following way. The last column can be detached, and stored in a separate vector. The valuable diagonal dots' (x, y, z) coordinates can be transformed into a row formation according to

$$(x, y) \mapsto (x - ((y - (a+1)(b+1)) \bmod (a+1)(b+1)(c+1)), y) \quad (8)$$

Fig. 4(c) demonstrates the state after the row transformation.

Only the first $2(a+1)(b+1) + 1$ rows of the matrix are kept, it is unnecessary to occupy space for the others. After this reduction extra care needs to be taken in order not to step out of the reduced $(2(a+1)(b+1) + 1) \times (a+1)(b+1)(c+1)$ matrix during the elimination of the coefficients.

The elimination can first be achieved under the row $((a+1)(b+1) + 1)$, according to the increasing column index (Procedure I), to be followed from row $((a+1)(b+1) + 1)$ according to decreasing column index (Procedure II).

A further decrease in storing capacity can be obtained if the reduced matrix falls into the following rows: $((a+1)(b+1) + 1)$, $((a+1)(b+1) + a + 2)$ and the last row is stored in 3 different vectors, while the rest in a $((a+1)(b+1) + 1) \times (a+1)(b+1)(c+1)$ matrix, which can be seen in Fig. 4(d).

For Procedure I, a $(a+1)(b+1) \times ((a+1)(b+1) + 1)$ sliding matrix is used, which is filled by values from separate vectors for an iteration step, and this sliding matrix also stores the transitional values of the elimination process under the "transformed main diagonal", as it can be seen in Fig. 4(e).

When moving the sliding matrix one step to the right, the new incoming column can be written to the place of the outgoing column, thus there is no need to rewrite the whole matrix. The columns can be referred to with the modulo-index $(2(a+1)(b+1) + 1)$.

With the first procedure, the range above the row $((a+1)(b+1) + 1)$ gets saturated with transitional values, which is to be eliminated with Procedure II.

With the changes made so far, with the condition $a = b$ given, our space-saving factor is

$$\mu_1(a) = \frac{(a+2)((a+1)^2 + 1) + 3(a+1)}{(a+1)^4}$$

It becomes obvious that, basically it is the distance of the two side-diagonals that determines the size of the storage demand according to the above method. On the other hand, this distance depends on the values of the border dimensions "a" and "b" in the studied range.

We can further decrease the simultaneous memory demand if the space is divided with planes diagonal to axis z . Let it now be plane $x = a/2$ and $y = b/2$.

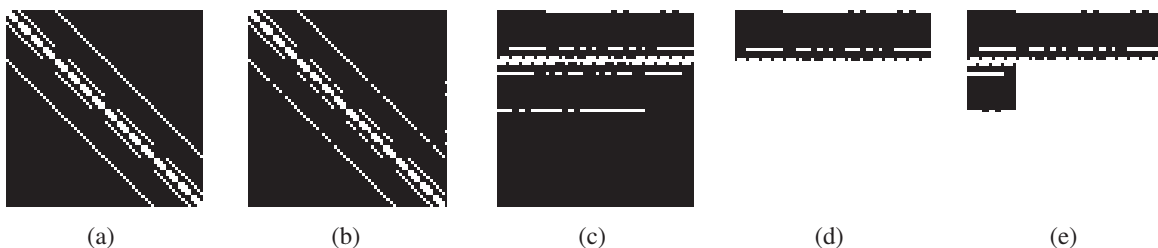


Figure 4.

With the condition $a = b$ given, the space saving factors belonging to the four one quarter wave ranges are:

$$\mu_2(a) = \frac{4(a/2 + 2) ((a/2 + 1)^2 + 1) + 12(a/2 + 1)}{(a + 1)^4}$$

The ratio of the two space saving factors can be approximated by

$$\frac{\mu_2}{\mu_1} = \frac{4d^3 + 16d^2 + 36d + 28}{8d^3 + 16d^2 + 18d + 7} \approx \frac{1}{2}.$$

By overlapping 3 grid-planes of the adjacent partial spaces in the wave space dividing method we can provide a good-quality transfer among the partial spaces. Another advantage of dividing is that the calculations for the partial spaces can be carried out parallel. During parallel computation at least two steps are needed, first the internal then the external wave sources need to be considered.

The results of the space dividing method with two separate regions can be seen in Fig. 5. The continuous transmission of wave fronts between the blocks can be clearly traced. The parameters were $d = 10^{-5}$ m, $\lambda = 10^{-4}$ m, $a = b = c = 31$, The sources were in Cell (X, Y, Z) : $(7, 6, 7)$ and in Cell $(X + ad, Y, Z)$: $(20, 10, 18)$.

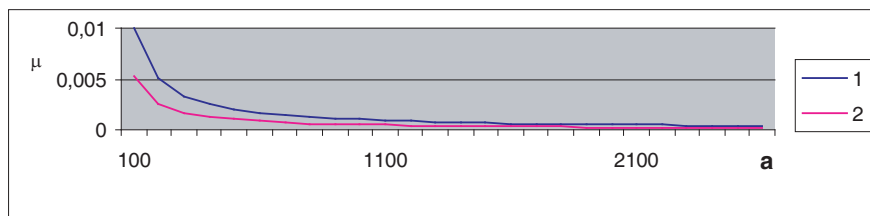


Figure 5. The values of μ_1 (indicated as 1) and μ_2 (indicated as 2) as a function of the size of the system a .

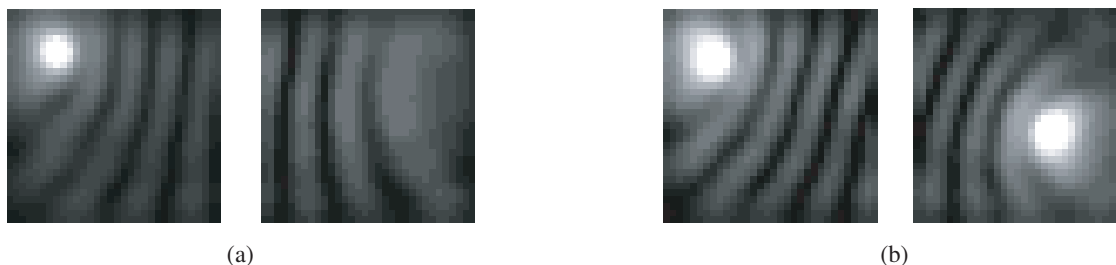


Figure 6. Wave fronts generated by the space dividing method with two cells, with two sources in both cells. Subplot (a) shows the $z = 8$ section, while (b) shows the section $y = 8$.

4. CONCLUSION

With the development of hardware and software technology, together with increasing calculation capacities and memory-optimization, the direct method can also be used successfully in the case of small-sized electromagnetic wave-ranges of relatively long wavelength. For reducing the required storing capacity, a special matrix reduction method was introduced, using sliding matrices. For aiding parallel computing, a wave space dividing method was also introduced and tested with small overlaps ensuring the wavefront transmission between the space parts with very good results.

REFERENCES

1. Buzbee, B. L., F. W. Dorr, J. A. George, and G. H. Golub, "The direct solution of the discrete Poisson equation on irregular regions," *SIAM J. Numer. Anal.*, Vol. 8, 722, 1971.
2. Duff, I. S., A. M. Erisman, and J. K. Reid, *Direct Methods for Sparse Matrices*, Clarendon, Oxford, 1986.

Analysis of Complex Radiating Structures by Hybrid FDTD/MoM-PO Method

A. Noga, T. Topa, and D. Wójcik
Silesian University of Technology, Gliwice, Poland

Abstract— In this paper, the FDTD/MoM-PO hybrid technique is presented. The method combines the ability of the FDTD method to deal with arbitrary material properties, and the versatility of the MoM-PO method for conducting structures. The proposed approach is applied to complex electromagnetic problems such as those involving antennas radiating in the presence of dielectric bodies. Numerical results show that the FDTD/MoM-PO hybrid technique offers a noticeable memory and CPU time savings.

1. INTRODUCTION

This paper is devoted to numerical modelling of antennas radiating in the presence of both electrically large conducting objects and inhomogeneous lossy dielectric bodies. That structures could be analyzed by using of conventional full-wave approach, such as method of moments (MoM) [1], finite element method (FEM) [2] or finite-difference time-domain method (FDTD) [3, 4]. However, the well-known limitation of all these full-wave techniques are the computer CPU time and storage needed to perform computations. Since that computer resources increase dramatically with electrical size of structure under investigation, the full-wave techniques appear to be computationally efficient for analysis of electrically small and medium sized structures.

For the considered class of radiators the hybrid FDTD/MoM-PO method is proposed in this paper. The hybrid approach employs the frequency domain MoM for metallic bodies and the FDTD method for analysis of dielectric scatterer [5–8]. Thereby the method brings together the ability of the FDTD scheme to deal with arbitrary material properties, and the versatility of the MoM to accurately model conducting structures. Additionally, to improve an efficiency of the method in analysis of large reflector antennas, MoM is combined with physical optics (PO) approach [14].

2. METHOD

The main idea of the hybrid technique is presented in Figure 1. The algorithm starts with subdivision of the structure into three regions: FDTD region contains all dielectric objects, while the antenna and electrically large platforms constitute the MoM and PO regions, respectively. In the first step, frequency-domain calculations in MoM and PO regions are carried out omitting the influence of dielectric scatterer. In the second step, computations are performed in FDTD region illuminated by the fields from MoM and PO regions. Then, MoM-PO algorithm is again employed for evaluating the current on the antenna due to new excitation, taking into account back-scattered steady-state FDTD fields. The procedure is repeated until a specified convergence criterion is met [5].

The MoM-PO method applied in this paper is based upon well-known triangular patch-wire model. The current on the metallic body is approximated by RWG basis functions and their equivalents for wires and junctions of patches and wires [12]. The unknown current on the conductors is expanded in terms of N^{MoM} and N^{PO} basis functions in the MoM and the PO regions, respectively. The problem is formulated analytically in terms of the electric field integral equation (EFIE) for current in the MoM-region, whereas current in the PO-region is obtained through the physical optics approximation [10]

$$\mathbf{J}^{\text{PO}} = \begin{cases} 2\hat{\mathbf{n}} \times \mathbf{H} & \text{in the lit area,} \\ \mathbf{0} & \text{in the shadow area,} \end{cases} \quad (1)$$

where \mathbf{H} denotes the impressed magnetic field and $\hat{\mathbf{n}}$ is a unit vector normal to the surface. The current \mathbf{J}^{PO} is considered as the result of “illumination” of the PO-region by the field originated from the current \mathbf{J}^{MoM} in the MoM-region

$$\mathbf{J}^{\text{PO}} = \mathbf{A}_{21}^h \mathbf{J}^{\text{MoM}}, \quad (2)$$

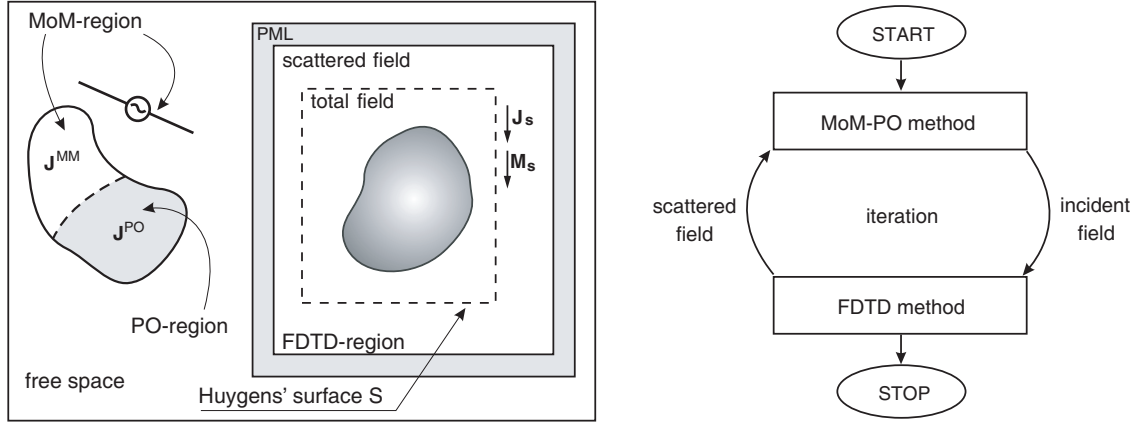


Figure 1: Subdivision of the structure in the FDTD/MoM-PO technique (on the left), and flow chart of the hybrid FDTD/MoM-PO method (on the right).

where the matrix \mathbf{A}_{21}^h represents the electromagnetic coupling between the MoM and PO regions through the magnetic field. The boundary condition ($\mathbf{E}_{\text{tan}} = 0$) for the total electric field in the MoM-region may be written as [11]

$$\left[\mathbf{Z}_{11}^e + \mathbf{Z}_{12}^e \mathbf{A}_{21}^h \right] \mathbf{I}_1 = \mathbf{V}_1 \quad (3)$$

where \mathbf{Z}_{11}^e represents the mutual interactions between the current elements within the MoM-region, and the product $\mathbf{Z}_{12}^e \mathbf{A}_{21}^h$ — Interactions between the MoM and PO regions. \mathbf{I}_1 is the MoM current vector and \mathbf{V}_1 denotes the known excitation vector. Solution of (3) yields the current \mathbf{J}^{MoM} , then the current \mathbf{J}^{PO} can be derived from (2).

Once the first-order current approximation in the MoM and PO regions are obtained, the near-field components $\mathbf{E}^{\text{MoM-PO}}$ and $\mathbf{H}^{\text{MoM-PO}}$ on the Huygens surface surrounding the FDTD-region are computed, as it is presented in Figure 1. Next, the electric surface current \mathbf{J}_S and magnetic surface current \mathbf{M}_S are derived according to the equivalence principle [9]:

$$\mathbf{J}_S = -\hat{\mathbf{n}} \times \mathbf{H}^{\text{MoM-PO}}, \quad (4)$$

$$\mathbf{M}_S = \hat{\mathbf{n}} \times \mathbf{E}^{\text{MoM-PO}}, \quad (5)$$

where $\hat{\mathbf{n}}$ is a Huygens' surface unit outward normal vector. These currents are employed to obtain incident field in FDTD total field region using the simple Fourier transforms, taking into account, the magnitude and the phase of EM fields for one frequency only. For instance, electric currents in time domain is expressed as

$$\mathbf{J}_S = \mathbf{J}_{S0} \sin(\omega t + \phi) b(t), \quad (6)$$

where $b(t)$ is an envelope function. In practice, direct calculation of $\mathbf{E}^{\text{MoM-PO}}$ and $\mathbf{H}^{\text{MoM-PO}}$ may become an excessive burden on CPU time because of huge number of discrete point at which the fields are to be determined. A considerable saving in CPU time is possible by spatial interpolation over the Huygens' surface, i.e., computing the incident fields $\mathbf{E}^{\text{MoM-PO}}$ and $\mathbf{H}^{\text{MoM-PO}}$ directly from MoM-PO currents on relatively coarse spatial grid and then interpolating it to approximate their values on the required ne grid. For this purpose, the two-dimensional Newton interpolation technique is employed in this paper, as it is proposed in [13].

The FDTD computations for total/scattered field are carried out until steady-state is achieved, and then, back-scattered fields on Huygens surface is obtained. The field is now employed to compute back-scattered excitation of MoM-PO body using near-field to near-field transformation:

$$\Delta \mathbf{J}^{\text{PO}} = 2\hat{\mathbf{n}} \times \mathbf{H}^{\text{FDTD}}, \quad (7)$$

$$\Delta \mathbf{V}_1 = \hat{\mathbf{n}} \times \mathbf{E}^{\text{FDTD}}. \quad (8)$$

Then, new current \mathbf{I}_1 in MoM region is obtained by solving the modied (3) equation:

$$\left[\mathbf{Z}_{11}^e + \mathbf{Z}_{12}^e \mathbf{A}_{21}^h \right] \mathbf{I}_1 = \mathbf{V}_1 - \mathbf{Z}_{12}^e \Delta \mathbf{J}^{\text{PO}} + \Delta \mathbf{V}_1 \quad (9)$$

In the next step, PO currents are calculated, then new incident field for FDTD region is determined and computations by FDTD method are performed. The procedure (see Figure 1) is repeated until a steady-state solution is obtained [13,15], that means: 1) No significant changes can be observed both on \mathbf{E} and \mathbf{H} incident field components in the FDTD region or 2) current distribution on source bodies barely changes during iteration process.

3. NUMERICAL RESULTS

To exam efficiency and accuracy of proposed approach two numerical example is considered. The numerical results obtained by FDTD/MoM-PO method are compared to those calculated by the commercial software CST MWS [16] as well as the classical FDTD (in-house).

The testing structures are presented in Figure 2. The first structure contains a monopole antenna (length $d = 0.5\lambda$, radius 0.001λ) attached to the centre of a square conducting ground plane with an edge length of $a = 2\lambda$. The antenna and the shaded part of the plate constitute the MoM region, whereas the remaining part of the platform is assigned to PO region. For numerical purposes, the antenna is modelled by 800 triangular patches and 20 linear segments. The number of unknowns associated with the MoM and PO are 116 and 1064, accordingly. The antenna is coupled to a rectangular box (height \times width \times thickness = $2\lambda \times 2\lambda \times 0.2\lambda$) of lossy dielectric ($\epsilon_r = 41$, $\sigma = 13\text{ S/m}$). Figure 3 shows the horizontal gain pattern for the operating frequency 300 MHz. As it can be see, the gain functions obtained by the FDTD/MoM-PO method compare well with the reference waveforms. As it is depicted in Table 1, proposed approach reduces about three times memory requirements (in comparison to both FDTD and CST) and time of computations (four and two times in comparison to FDTD and CST, respectively).

The second structure consist of one meter long dipole located at a distance $d = 0.25\text{ m}$ in front of square reflector with an edge length $L = 2\text{ m}$. For numerical purposes, the reflector and the dipole are subdivided into 1800 triangular patches and 42 linear segments, respectively. The total number of unknowns associated with the structure is 2681. Since the whole reflector constitutes PO-region, 2640 unknowns are assigned to this region. The remaining 41 basis functions are associated with the dipole which constitutes the MoM-region. The dipole radiates above rectangular dielectric sheet (height \times width \times thickness = $2\text{ m} \times 2\text{ m} \times 0.1\text{ m}$, $\epsilon_r = 46$, $\sigma = 1.3\text{ S/m}$). The whole

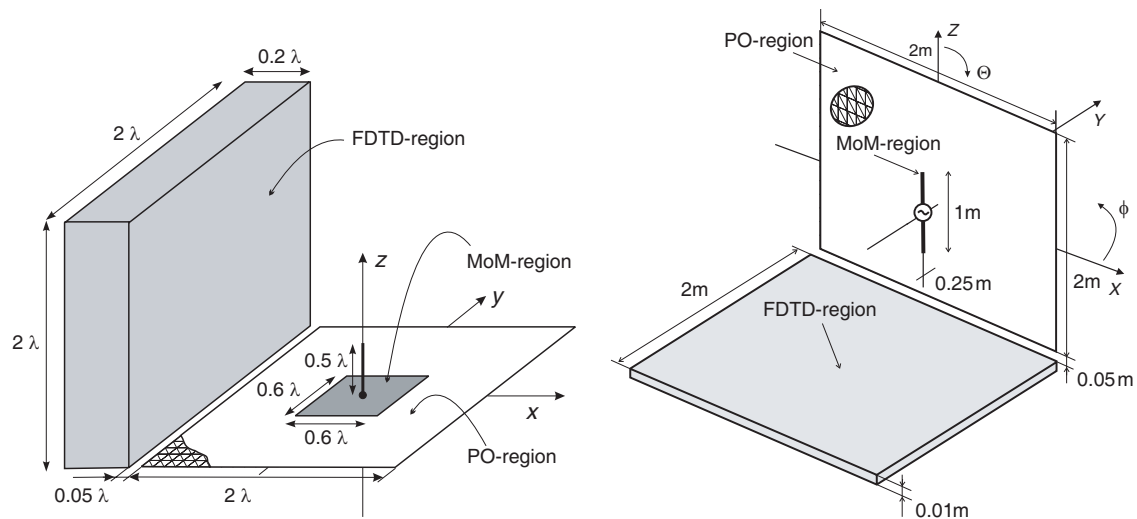


Figure 2: The structures under investigation: Monopole antenna (on the left), and dipole antenna (on the right).

Table 1: CPU time and computer storage for CST, FDTD, and FDTD/MoM-PO methods.

	storage [MB]			CPU time [s]		
	CST	FDTD	FDTD/MoM-PO	CST	FDTD	FDTD/MoM-PO
monopole	730	815	245	2200	5100	1320
dipole	676	746	185	3820	4400	472

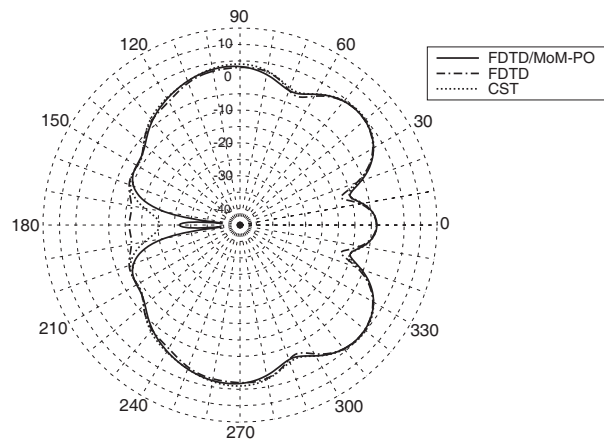


Figure 3: The gain pattern of monopole antenna for $\theta = 90^\circ$.

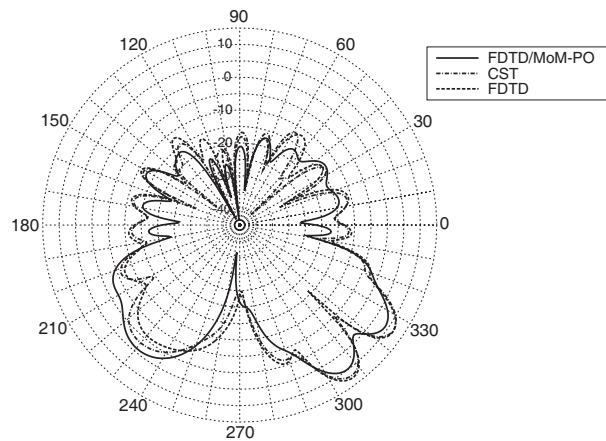


Figure 4: The gain pattern of dipole antenna for $\phi = 90^\circ$.

sheet belongs to FDTD region. The vertical gain pattern of the antenna for frequency 500 MHz is shown in Figure 4. Again, results obtained by the FDTD/MoM-PO method compares acceptable with the reference waveforms. In this case, proposed approach reduces about four times memory requirements (in comparison to both FDTD and CST) and time of computations (almost nine and eight times in comparison to FDTD and CST, respectively).

4. CONCLUSION

A method for analysis of antennas radiating near complex objects based upon combination of the hybrid frequency-domain MoM-PO technique and the FDTD method has been presented. The hybrid FDTD/MoM-PO method enables good estimation of the mutual coupling effects between the antenna and its complex environment. The numerical results clearly demonstrate the usefulness and efficiency of the the proposed approach, which offers reasonable accuracy that seems to be fully acceptable for practical purposes. The FDTD/MoM-PO method offers noticeable computational savings in terms of both CPU time and memory storage relative to the traditional full-wave FDTD method.

ACKNOWLEDGMENT

This work is partially supported by the Polish Ministry of Science and Higher Education under Grant No. N517 467934.

REFERENCES

1. Harrington, R. F., *Field Computation by Moment Methods*, MacMillan, 1968.
2. Jin, J., *The Finite Element Method in Electromagnetics*, CRC Press, 2002.
3. Taove, A. and S. C. Hagness, *Computational Electrodynamics: The Finite-difference Time-domain Method*, 3rd Edition, Artech House, 2005.
4. Kunz, K. S. and R. J. Luebbers, *The Finite Time Domain Method for Electromagnetics*, John Wiley & Sons, 2002.
5. Abd-Alhameed, R. A., P. S. Excell, and A. M. Mangoud, "A hybrid computational electromagnetics formulation for simulation of antennas coupled to lossy dielectric volumes," *IEEE Trans. Broadcast.*, Vol. 50, No. 3, 253–259, 2004.
6. Mangoud, M. A., R. A. Abd-Alhameed, and P. S. Excell, "Simulation of human interaction with mobile telephones using hybrid techniques over coupled domains," *IEEE Transactions on Microwave Theory and Techniques*, Vol. 48, No. 11, 2014–2021, 2000.
7. Cerri, G., P. Russo, and A. Schiavoni, "Electromagnetic coupling between arbitrarily bent wires and scatterers by a hybrid MoMTD/FDTD approach," *IEEE Proc. — Microw. Antennas Propag.*, Vol. 147, No. 4, 261–266, 2000.
8. Thiel, W., K. Sabet, and L. P. Katehi, "A hybrid MoM/FDTD approach for an efficient modeling of complex antennas on mobile platforms," *2003 EuMC Conf. Proc.*, Vol. 2, 719–722, Ann Arbor, MI, USA, Oct. 2003.
9. Balanis, C. A., *Advanced Engineering Electromagnetics*, John Wiley & Sons, 1989.

10. Jakobus, U. and F. M. Landstorfer, “Improved PO-MoM hybrid formulation for scattering from three-dimensional perfectly conducting bodies of arbitrary shape,” *IEEE Trans. Antennas Propagat.*, Vol. 49, No. 2, 162–169, 1995.
11. Hodges, R. E. and Y. Rahmat-Samii, “An iterative current-based hybrid method for complex structures,” *IEEE Trans. Antennas Propagat.*, Vol. 45, No. 2, 265–276, Oct. 1997.
12. Hwu, S.-U. and D. R. Wilton, “Electromagnetic scattering and radiation by arbitrary configurations of conducting bodies and wires,” Final Report, Contract No. N66001-85-0-2-3, San Diego State University, May 23, 1988.
13. Wei, D., S. Mochizuki, S. Watanabe, M. Taki, and Y. Yamanaka, “A new hybrid MoM/FDTD method for antennas located off the Yee’s Lattice,” *2004 URSI EMTS Conf. Proc.*, Vol. 2, 436–438, 2004.
14. Karwowski, A. and A. Noga, “Fast MM-PO-based numerical modelling technique for wide-band analysis of antennas near conducting objects,” *Electronics Letters*, Vol. 43, No. 4, 486–487, 2007.
15. Topa, T. and A. Karwowski, “Efficient 2D interpolation technique for evaluation of equivalence principle-sources in MoM-FDTD method,” *2nd European Conference on Antennas and Propagation, EuCAP 2007*, Nov. 2007.
16. <http://www.cst.com>.

On the Relationship between Nonuniqueness of Electromagnetic Scattering Integral Equations and Krylov Subspace Methods

G. Angiulli, P. Quattrone, and S. Tringali

Dimet, Univ. Mediterranea, via Graziella 1, Loc. Feo di Vito, 89122 Reggio Calabria, Italy

Abstract— Some relevant operator equations used to describe natural phenomena can *degenerate*. This is actually the case of the electric (EFIE) and magnetic (MFIE) field integral equations in scattering theory, both failing to provide a unique solution (at least in a standard sense) in correspondence of some set of frequencies (known as *resonances*), for which they lack injectivity.

One of the most common expedient to the problem deals with the concept of a generalized solution (say a *pseudo-solution*), whose computation is numerically related to the Moore-Penrose pseudo-inverse of some large and generally dense square matrix $A \in \mathbb{C}^{n,n}$ resulting by the discretization of the integral model via the Method of Moments (MoM) or different projective schemes and its consequent approximation (in the sense of the uniform operator limit) by means of a linear system of algebraic equations such as $Ax = b$. Ultimately this involves the very time-consuming task of computing the singular value decomposition (SVD) of A , in order to filter the noisy effects introduced on the unknown current by the almost-singularity of A when EFIE or MFIE are applied in the neighborhood of a resonance.

In this paper, we try to give an answer and provide theoretical motivations and numerical evidence to prove it should be the right one, relying on the inherent capability of some Krylov subspace methods to extract the minimum norm solution to the linear system $Ax = b$ to the extent that b lies in the range of A .

1. INTRODUCTION

It is a well-known fact in the literature on operator theory and its applications that some familiar equations describing real-world phenomena suffer from some pathologies, that make them ill-posed (in the Hadamard sense [1]) in terms of the actual values attained by one or more parameters which they are dependent on.

Two important cases are represented by the electrical (EFIE) and magnetic (MFIE) integral equations, that are currently employed to study the direct scattering of a time-harmonic electromagnetic field from perfect conducting bodies [2, 3]. Both equations, in fact, suffer from the so-called *problem of resonances*. Ultimately this consists in the existence of some (discrete or continuous) set of frequencies such that the null space of the underlying linear operators $\mathcal{L}_E : X \rightarrow Y$ and $\mathcal{L}_M : X \rightarrow Y$ are no longer trivial, i.e., contains some other vectors apart from the zero of X , provided that X and Y are proper topological vector spaces of (even generalized) functions (e.g., separable Hilbert spaces), respectively standing for the domain and codomain of \mathcal{L}_E and \mathcal{L}_M .

From a theoretical point of view, the degenerate behaviors of any linear operator $\mathcal{L} : X \rightarrow Y$ is usually countered weakening the standard notion of an inverse to the extent of the so-called Moore-Penrose pseudo-inverse [4], which can be defined even if the operator in question is not bijective (i.e., one-to-one and onto), at least as far as \mathcal{L} is Fredholmian and X and Y are locally convex spaces. Then solving the original problem is equivalent to optimize some nonnegative auxiliary functional $F : X \rightarrow \mathbb{R}$, on condition that it has exactly one optimum point. Indeed this holds in many interesting cases in which the model doesn't yield an ordinary solution.

In fact, since generally an operator equation like $\mathcal{L}f = g$, where $g \in Y$ is given, cannot be solved in a *closed form*, providing an analytical representation of its (pseudo-)solution $f \in X$ in terms of some set of elementary functions and operations, we are often left with no other chance than solving it by numerical methods. But X and the range $\mathcal{L}(X)$ of \mathcal{L} are most often topological spaces of infinite dimensions (in the sense of Hamel algebraic bases), so the operator equation must be discretized.

This is performed by projecting the original problem onto finite n -dimensional subspaces of X and Y through suitable schemes of discretization, with the provision that one can prove the resulting discrete model is a faithful approximation of the analytical model (in the sense of the uniform operator limit) as $n \rightarrow \infty$. Now, there exist many of these projection procedures, but certainly the most used in the survey of computational electromagnetics is the Method of Moment (MoM) [5],

especially when treating integral operator equations. Anyway, no matter which technique you are making use of, the final result is always a linear system of equations such as

$$Ax = b, \quad A \in \mathbb{C}^{n,n} \text{ and } b \in \mathbb{C}^n \quad (1)$$

where the coefficient matrix A is generally dense, unstructured and indefinite. But the system is not as innocent as it looks like. In fact, in the limit case that \mathcal{L} is degenerate, so in particular in a neighborhood of a resonance for the E -field or M -field integral equations, the ill-posed nature of the analytical model is reflected in the nearly-singular character of the linear system (1). This means that, even if A is (mathematically) invertible, as a consequence of the natural regularizing effect induced by the approximation process, A is expected to have a very large condition number. This is quite undesirable, and usually makes (1) far from easy to solve, since ill-conditioning causes noise on data and rounding errors to be more and more amplified by computer procedures, making the numerical solution even completely useless.

This is all the more true in the relevant cases of the EFIE and the MFIE, since it is known that any integral operator has a *smoothing effect* on the data, in the sense that high-frequency components in the input will be mapped over to vectors containing high-frequency components with very low amplitude in the output. This is mimicked by the discrete model of the problem, in such a way that x contains high-frequency components with very high amplitude, whenever b contains high-frequency components and the coefficient matrix A is numerically singular (e.g., because the working frequency is near to the resonance). So it may be necessary to polish numerical solutions from their unstable components.

In principle many numerical methods are suitable for the goal. The mostly used ones, at least to the best of our knowledge, are some special instances of the truncated singular value decomposition (TSVD) [6], combined with fast factorization methods like the QR-algorithm [7]. Anyway all of these take up a large amount of memory and are very time-consuming, since the complexity of any factorization technique tends to blow up, while n grows larger and larger.

Thus it would be quite useful if we could have the use of some general technique succeeding to solve the linear system (1) without any need of distinguishing between the case when A is regular and the case when A is singular or near to singularity. Actually we think this is possible and provide some clues to prove it is *really* possible inquiring some properties of Krylov subspace methods, focusing our attention, in particular, on the generalized minimal residual method (GMRES) [8].

2. ITERATIVE METHODS AND REGULARIZATION

As anticipated in the foregoing section, when discrete ill-posed problems need to be solved, special care has to be taken with the solution of the linear system (1). This leads to the concept of *regularization*, which is a way to obtain a *useful* solution, but not necessarily the *true* one, and it can be done imposing some suitable constraints (e.g., that it consists only of low-frequency components or that it is piecewise constant). Not all the general methods in the literature can be used directly on discrete ill-posed problems. Some can, however, if the problem is adjusted in a certain way, and others again can be made to have a regularizing effect in themselves. For instance this is the case of some iterative solvers (by using the iteration step as regularization parameter).

Now, the direct methods work fine but need a lot of computing power and memory for large problems. On the contrary iterative methods are very well suited for large-scale problems, thus it is interesting to investigate their capability *to regularize while solving*. To the best of our knowledge, this is somewhat different from any other approach to the problem of stabilization. Whenever successful, it would supply a useful solution without any concrete need of treating the degenerate models by means of some ad-hoc techniques.

Really such a point is discussed in the upcoming subsection, where it is shown how the inherent ability of Krylov subspace methods to recover the minimum norm solution of the linear system (1), as far as b lies in the range of A (so even if A is mathematically singular), provides us with a *natural* way to filter unstable components without any further processing.

2.1. Krylov Subspace Methods and Ill-posed Problems

The regular case is well-established, so we concentrate on the circumstance that the system (1) is not fully-ranked. Then assume the Jordan decomposition of A is given as $A = XJX^{-1}$, where $X \in \mathbb{C}^{n,n}$ is regular. Then $Ax = b$ if and only if $XJX^{-1}x = b$, i.e., if and only if $J\xi = \beta$, provided

that $\xi = X^{-1}x$ and $\beta = X^{-1}b$. On the other hand, since A is singular, J splits in a block form like

$$J = \begin{bmatrix} B & \\ & N \end{bmatrix} \quad (2)$$

where B and N are square and all the non-null eigenvalues of A belong to the spectrum of B . From this it follows that B is regular and N is nilpotent, so there exists an integer $k \geq 1$ such that $N^k = O$ and $N^{k-1} \neq O$. Here O is the matrix of zeros having the same size as N . Luckily, the nilpotent index coincides with the index of the zero eigenvalue. Suppose that a Krylov solution exists, that is we have $x = \sum_{j=0}^p \alpha_j A^j b$ for some $p \in \mathbb{N}$, i.e.,

$$\xi = \sum_{j=0}^p \alpha_j J^j \beta = \sum_{j=0}^p \alpha_j \begin{bmatrix} B^j & \\ & N^j \end{bmatrix} \beta \quad (3)$$

If we now let $\xi = [\xi_B \ \xi_N]^t$ and $\beta = [\beta_B \ \beta_N]^t$, where the splitting mimicks that of J and t denotes a matrix transposition, then

$$\xi_B = \sum_{j=0}^p \alpha_j B^j \beta_B \quad \text{and} \quad \xi_N = \sum_{j=0}^p \alpha_j N^j \beta_N \quad (4)$$

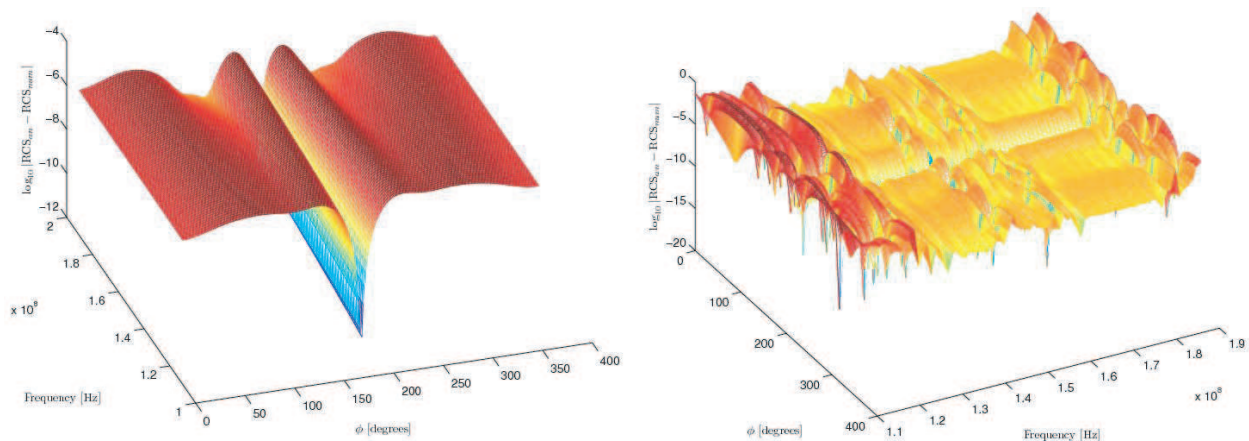


Figure 1: Absolute value (in a logarithmic scale) of the difference between the analytical and numerical radar cross sections (RCS) for a PEC circular cylinder of 1-meter radius, with respect to the E -field (on the left) and M -field (on the right) integral models.

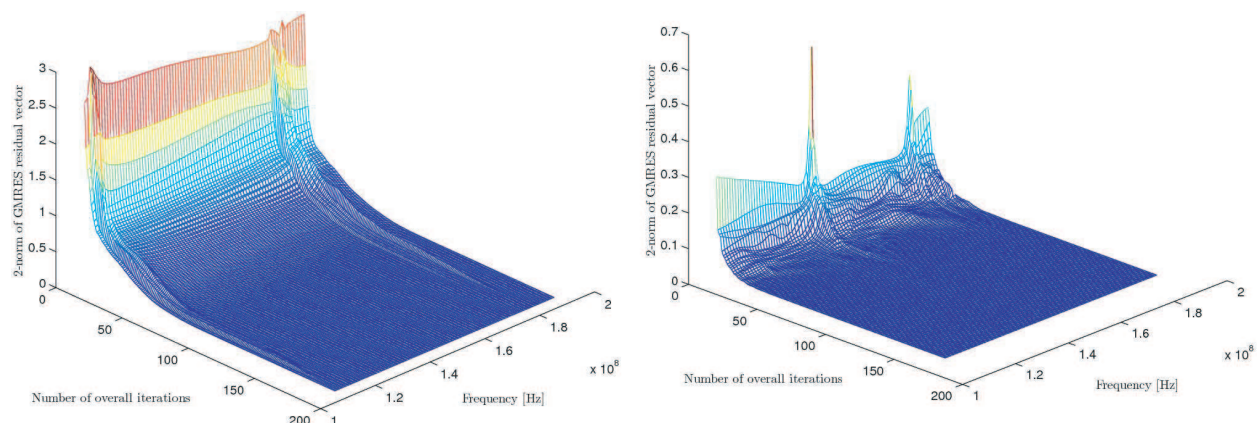


Figure 2: The 2-norm of the residual vector observed when the GMRES is applied to the iterative solution in the same cases of the previous figure. when applied to solve the MoM system with respect to the E -field (on the left) and M -field (on the right) integral models.

From here, since $J\xi = \beta$, we also have $N\xi_N = \beta_N$, so

$$N \cdot \sum_{j=0}^p \alpha_j N^j \beta_N = \beta_N \quad \Longrightarrow \quad \left(I - \sum_{j=0}^p \alpha_j N^{j+1} \right) \beta_N = O \quad (5)$$

where I is the identity matrix of the same size as N . Now observe that the matrices N^j , for $j = 2, 3, \dots, p$, are upper triangular and have only zeros along the main diagonal. This implies that the matrix in the right-most parenthesis above will be regular. So if a Krylov solution exists, necessarily $\beta_N = 0$. Another way of saying this is that we must have

$$\beta \in \text{range} \left(\begin{bmatrix} B & \\ & N^j \end{bmatrix} \right) = \text{range} \left(\begin{bmatrix} B^k & \\ & N^k \end{bmatrix} \right) = \text{range}(J^k) \quad (6)$$

where $\text{range}(B) = \text{range}(B^k)$ holds, as B is regular. Conversely let us assume $\beta \in \text{range}(J^k)$, so that $\xi = [\beta_B \ 0]^t$, and $\xi = [B^{-1}\beta_B \ 0]^t$. Now, since B is regular and its minimal polynomial has degree $m - k$, there exists $q \in \mathbb{C}[x]$ of degree $m - k - 1$ such that $q(B) = B^{-1}$. Then

$$\xi = \begin{bmatrix} B^{-1}\beta_B \\ 0 \end{bmatrix} = \begin{bmatrix} q(B) & 0 \\ 0 & 0 \end{bmatrix} \cdot \begin{bmatrix} \beta_B \\ 0 \end{bmatrix} = \begin{bmatrix} q(B) & 0 \\ 0 & q(N) \end{bmatrix} \beta = q(J)\beta \in \mathcal{K}_{m-k}(J, \beta) \quad (7)$$

where $\mathcal{K}_{m-k}(J, \beta)$ is the order- $(m - k)$ Krylov subspace [9] generated by J and β . So we have proved that a Krylov solution to the linear system (1) exists if and only if b lies in the range of A^k , where k is the algebraic multiplicity of the zero eigenvalue of A (by the way, notice that this statement is equally valid when A is nonsingular, since then $k = 0$). Moreover we have shown that, when a Krylov solution to $Ax = b$ exists, then $x \in \mathcal{K}_{m-k}(A, b)$. This means Krylov methods return an useful solution, even if the model is degenerate. But how useful? To answer this last question we provide the results of some numerical experiments in the subsequent section.

3. NUMERICAL RESULTS AND CONCLUSIONS

We have tested the ideas outlined in the foregoing sections evaluating the performances provided by GMRES in order to solve the algebraic linear system arising by Mom discretization of EFIE and MFIE integral equations in the simple case of TMz scattering by a plane wave from a perfect conducting circular cylinder (the radii is 1 meter). It can be observed as resonance phenomenon is positively handled by GMRES for the EFIE case, where good agreement is shown between the numerical results and analytical ones (see Figure 1, left side where RCS results are reported). On the contrary, for the MFIE case, numerical solution is heavily corrupted from it (see Figure 1, right side where RCS results are reported). The different performances provided by GMRES are confirmed by the behaviour of the residual surface, plotted over the considered frequency band of interest (see Figure 2, left: E -field case, right: H -field case).

ACKNOWLEDGMENT

Many grateful thanks to Paolo Leonetti from Bocconi University for proofreading this paper and offering valuable advice.

REFERENCES

1. Tikhonov, A. N. and V. Y. Arsenin, *Solutions of Ill-Posed Problems*, Winston, NY, 1977.
2. Cakoni, F. and D. Colton, *Qualitative Methods in Inverse Scattering Theory*, Springer-Verlag, Berlin, 2006.
3. Colton, D. and R. Kress, *Integral Equation Methods in Scattering Theory*, John Wiley & Sons Inc., New York, 1983.
4. Groetsch, C. W., *Generalized Inverses of Linear Operators*, Pure and Applied Mathematic 37, Marcel Dekker, Inc., New York, Basel, 1977.
5. Harrington, R. F., *Field Computation by Moment Methods*, IEEE Press, 1993.
6. Canning, X. F., "Protecting EFIE-based scattering computations from effects of interior resonances," *IEEE Trans. Ant. Propagat.*, Vol. 39, No. 11, 1545–1552, 1991.
7. Angiulli, G. and S. Tringali, "EFIE stabilization at internal resonances computing its numerical null space," *The XIII Biennial IEEE Conference on Electromagnetic Field Computation (CEFC)*, Athens (GR), 2008.

8. Saad, Y. and M. H. Schultz, “GMRES: A generalized minimal residual algorithm for solving nonsymmetric linear systems,” *SIAM J. Sci. Stat. Comput.*, Vol. 7, 856–869, 1986.
9. Saad, Y., *Iterative Methods for Sparse Linear Systems*, 2nd Edition, 2003.

Field Dependence of Complex Permittivity of LDPE Filled with PZT

S. N. Tkachenko, O. S. Gefle, and S. M. Lebedev

High-Voltage Research Institute, Tomsk Polytechnic University, Tomsk, Russia

Abstract— Study results of the field dependence of the complex permittivity of LDPE filled with a ferroelectric ceramic powder are presented in this paper. A novel method of the breakdown strength prediction based on the estimation of the dielectric relaxation spectra parameters is offered for filled polymeric materials.

1. INTRODUCTION

It has been shown [1] that the dielectric spectroscopy method gives completed information concerning behaviour of composite polymeric materials (CPMs) in a low electric field over the temperature-frequency range and this method allows the change of their properties depending on structure of a polymeric matrix and filler content to be predicted. However the study of the complex permittivity not only in low electric field but also in high electric field is necessary for control of structure and properties of CPMs. It is caused by that the introduction of modifying agents into a polymeric matrix can result in different behavior of CPMs in a high electric field due to a high local field at the interface polymeric matrix/filler [2].

The estimation of the local Lorentz field for low density polyethylene (LDPE) filled with $C = 40$ vol. % of a ferroelectric ceramic powder lead zirconate titanate (PZT) has been reported in [3]. In this case the local field in a non-polar matrix is increased by a factor of 3 compared with the external electric field E_0 . It can result in the local breakdown of a dielectric in the high field.

It is obvious that increase of local electric field in the polymeric bulk should result in decrease of breakdown strength over the frequency range of an external electric field. That is change in the specific volume resistivity ρ_v and permittivity ε of a dielectric due to introduction of modifying agents and additives at the external electric field $E_0 \leq 10^4$ V/m can give incorrect information concerning a possible behaviour of CPMs in the high electric field.

Thus, the study of influence of an external electric field on the real ε' and imaginary ε'' parts of the complex permittivity of LDPE filled with PZT and an establishment of interrelation between parameters of a dielectric relaxation spectrum and breakdown strength of CPMs was the aim of this work.

2. SAMPLES AND EXPERIMENTAL TECHNIQUE

LDPE and ferroelectric ceramic powder PZT with the average size of spherical particles ~ 800 nm were used as a polymeric matrix and filler respectively. Filled composite materials on the basis of LDPE were prepared by the extrusion method. Samples were prepared by hot pressing in a hydraulic press at temperature 180°C and a slow cooling under pressure in air. The filler content in a polymeric matrix was changed from 10 to 40 vol. %.

Samples for measurements of the complex permittivity were prepared as parallel-plane disks 75 mm in diameter. Thickness of samples Δ was changed from 0.25 to 1.2 mm. The silver electrodes were evaporated in vacuum on both surfaces of sample.

Measurements of ε' and ε'' were carried out in standard electrode system by means of measuring instrument Haefely Trench Tettex AG at the power frequency 50 Hz in the voltage range from 2 up to 11 kV.

Measurements of the breakdown voltage V_b were carried out in the uniform electric field in the test cell filled with silicon oil by the ramp test method at a voltage rising rate 2 kV/s. It was tested not less than 10 samples at corresponding conditions.

3. EXPERIMENTAL RESULTS AND DISCUSSION

It is well known that the filling of a polymer by nano- or micro-particles modifies its structure and properties due to inter-phase interaction and formation of a boundary layer at the interface matrix/filler particles [4, 5]. It has been shown [1] that the effective value of the permittivity ε_{eff} at 50 Hz for LDPE filled with PZT at $C = 40$ vol. % is increased approximately by a factor of

5 compared to that for LDPE. It is necessary to note that the permittivity of PZT depends on the electric stress due to presence of the domain polarization resulting in a non-linear dependence $\varepsilon = f(E)$ in contrast to LDPE.

It was found that values of ε' and ε'' are increased by 1% and 350% respectively for CPMs on the basis of LDPE at the filler content $C = 10$ vol. % with increasing the test voltage by a factor of 3.75. At $C = 30$ and 40 vol. % the value of ε' is increased by 20 and 30% respectively, while the value of ε'' — by a factor of 5 ... 6 (see Fig. 1).

The increase in the real ε' and imaginary ε'' parts of the complex permittivity of CPMs at $C \geq 30$ vol. % testifies the dispersion of the complex permittivity at the fixed frequency of an external electric field is caused by non-linear dependence of polarization inside a ceramic phase on the electric field stress.

It is necessary to note here that the relation between ε'' and ε' on the complex plane below and above the critical voltage V_{0c} (at which non-linear change of the relation $\varepsilon'' = f(\varepsilon')$ begins) may be approximated by two functions, namely: a linear function at $V \leq V_{0c}$, and the Debye function at $V > V_{0c}$ (Fig. 1).

Formally, at $V \leq V_{0c}$, relations $\varepsilon'' = f(\varepsilon')$ in Fig. 1 may be approximated by the equations of direct lines at the correlation coefficient $R^2 \geq 0.98$:

$$\varepsilon'' = 0.5056 \cdot \varepsilon' - 1.6709, \quad \text{at } C = 10 \text{ vol. \%} \quad (1)$$

$$\varepsilon'' = 0.6027 \cdot \varepsilon' - 4.6063, \quad \text{at } C = 30 \text{ vol. \%} \quad (2)$$

$$\varepsilon'' = 0.6621 \cdot \varepsilon' - 7.5998, \quad \text{at } C = 40 \text{ vol. \%} \quad (3)$$

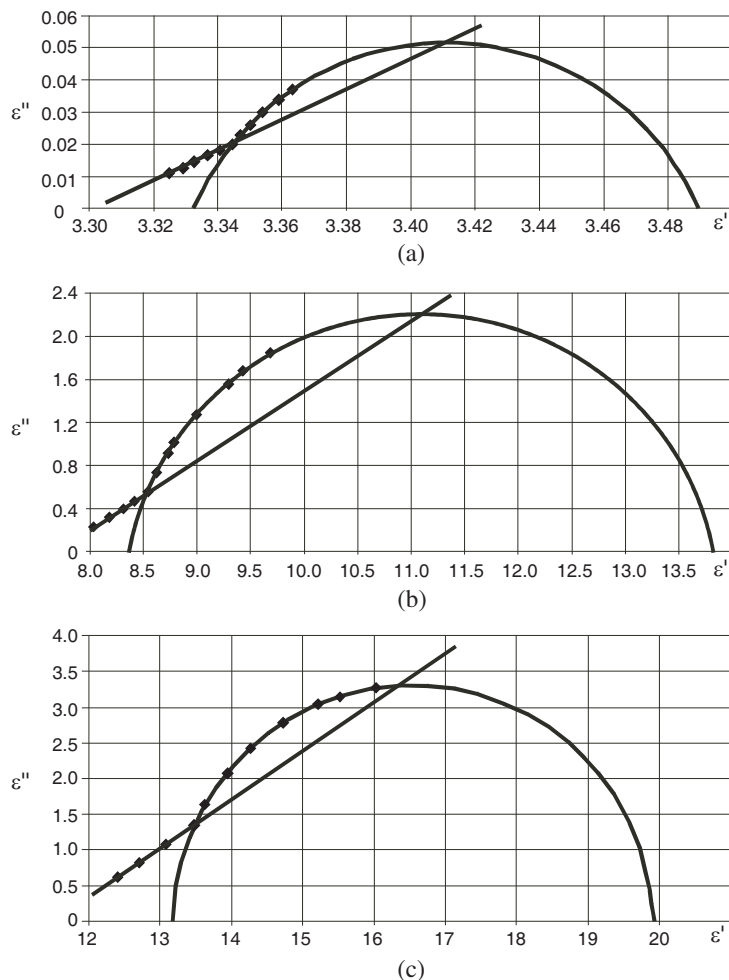


Figure 1: Relations $\varepsilon'' = f(\varepsilon')$ with voltage increase from 2.0 up to 7.5 kV for CPMs with different filler content: (a) 10 vol. %; (b) 30 vol. %; and (c) 40 vol. %.

and at $V > V_{0c}$ these relations may be fitted by the equations of circles:

$$(\varepsilon' - 3.411)^2 + (\varepsilon'' + 0.034)^2 = 0.00734, \quad \text{at } C = 10 \text{ vol. \%} \quad (4)$$

$$(\varepsilon' - 11.08)^2 + (\varepsilon'' + 0.587)^2 = 7.784, \quad \text{at } C = 30 \text{ vol. \%} \quad (5)$$

$$(\varepsilon' - 16.54)^2 + (\varepsilon'' + 0.0517)^2 = 11.325, \quad \text{at } C = 30 \text{ vol. \%} \quad (6)$$

The direct line crosses a semi-circle in two points. The first crossing point corresponds to the critical voltage V_{0c} , and the second point corresponds to the voltage V_c at which maximal values of ε''_{\max} or $\tan \delta_{\max} = \varepsilon''_{\max}/\varepsilon'_{cs}$ are observed, where ε'_{cs} is the value of the real part of the complex permittivity corresponding to the center of the semi-circle. On the other hand, the linear part of relations $\varepsilon'' = f(\varepsilon')$ at $V \leq V_{0c}$ can be written as

$$\varepsilon''_i = \bar{\alpha} \cdot \varepsilon'_i \cdot V_i/V_{0c}, \quad (7)$$

where ε''_i and ε'_i are values of the imaginary and real parts of the complex permittivity at i -th voltage V_i , and $\bar{\alpha}$ is the proportionality coefficient.

Non-linear part of the relation $\varepsilon'' = f(\varepsilon')$ at $V > V_{0c}$ can be approximated by the Debye function

$$\varepsilon''_i = \frac{\Delta\varepsilon}{1 + (V_c/V_i)^2}, \quad (8)$$

where $\Delta\varepsilon$ is the overall width of the complex permittivity dispersion.

At $V_i = V_{0c}$, $\varepsilon'_i = \varepsilon'_{cs}$, and $\varepsilon''_i = \varepsilon''_{\max}$ therefore the crossing point of (7) and (8) should correspond to a condition

$$\bar{\alpha} \cdot \varepsilon'_i \cdot V_i/V_{0c} = \frac{\Delta\varepsilon}{1 + (V_c/V_i)^2} = \frac{\Delta\varepsilon}{2} \quad (9)$$

Because $\Delta\varepsilon = 2 \cdot \varepsilon''_{\max}$, then from (9), we can write

$$V_c = V_{0c} \cdot \varepsilon''_{\max}/(\varepsilon'_{cs} \cdot \bar{\alpha}) = V_{0c} \cdot \tan \delta_{\max}/\bar{\alpha}, \quad (10)$$

where $\bar{\alpha} = \frac{\sum_{i=1}^N \tan \delta_i \cdot V_i/V_{0c}}{N}$, $\tan \delta_i$ is the loss factor at V_i , and N is number of measurements.

Parameters $\bar{\alpha}$, ε''_{\max} , and ε'_{cs} calculated by using Eqs. (1)–(8) are as $\bar{\alpha} = 0.0073$, $\varepsilon''_{\max} = 0.05$, $\varepsilon'_{cs} = 3.41$ for $C = 10$ vol. %; $\bar{\alpha} = 0.00796$, $\varepsilon''_{\max} = 2.2$, $\varepsilon'_{cs} = 11.2$ for $C = 30$ vol. %; and $\bar{\alpha} = 0.1182$, $\varepsilon''_{\max} = 3.5$, $\varepsilon'_{cs} = 16.3$ for $C = 40$ vol. %. Calculated results for V_{0c} , V_c , $E_{0c} = V_{0c}/\Delta$, $E_c = V_c/\Delta$, ε_{0c} , and $\varepsilon_c = \varepsilon'_{cc}$ for CPMs with different thickness are listed in table, where $V = S \cdot \Delta = \pi \cdot R^2 \cdot \Delta$ is the dielectric volume at the radius of the measuring electrode $R = 20$ mm.

Experimental dependences of the average breakdown voltage V_b for CPMs of different thickness are presented in Fig. 2. It can be seen that the breakdown voltage at same dielectric thickness $\Delta = 1$ mm is decreased by a factor of 1.7 with increase in the filler content from 10 to 40 vol. %.

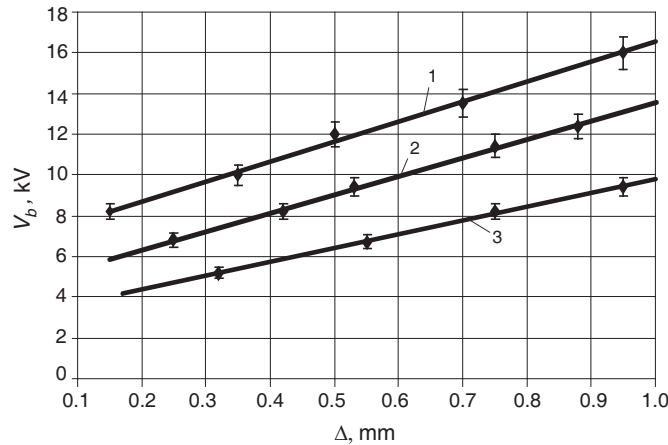


Figure 2: Relations $V_b = f(\Delta)$ for CPMs with different filler content: 1, 10 vol. %; 2, 30 vol. %; and 3, 40 vol. %.

By comparing the experimental data (Fig. 2) and calculated results (table) we can note that values of V_b correspond to V_c calculated by using (10).

It means that V_{0c} corresponds to the beginning voltage of ionization processes in CPMs which caused by the local field increase at the interface polymer/filler. The value V_c is the critical voltage at which the dielectric breakdown occurs. Average values of ε_{0c} and ε_c corresponding to V_{0c} and V_c for CPMs of different thickness are constant values depending only on the filler content in a polymeric matrix. It is necessary to note that relations $\varepsilon', \varepsilon'' = f(E)$ for the fixed power frequency $F = 50$ Hz at the confidence level 95% allow the breakdown voltage or breakdown strength for CPMs to be predicted without HV tests.

Table 1: Calculated results for CPMs with different filler content.

C , vol. %	V_{0c} , 10^3 V	V_c , 10^3 V	E_{0c} , 10^6 V/m	E_c , 10^6 V/m	ε_{0c}	ε_c	Note
10	4.182	8.365	16.73	33.46	3.35	3.41	$\Delta = 2.5 \cdot 10^{-4}$ m; $V = 3.14 \cdot 10^{-7}$ m ³ ;
	5.0	10.0	14.0	28.0			$\Delta = 3.57 \cdot 10^{-4}$ m; $V = 4.486 \cdot 10^{-7}$ m ³ ;
	5.9	11.83	11.80	23.66			$\Delta = 5.10^{-4}$ m; $V = 6.283 \cdot 10^{-7}$ m ³ ;
	8.365	16.73	8.37	16.73			$\Delta = 1.10^{-3}$ m; $V = 1.257 \cdot 10^{-6}$ m ³ ;
30	2.925	7.344	9.75	24.45	8.55	11.2	$\Delta = 3.10^{-4}$ m; $V = 3.767 \cdot 10^{-7}$ m ³ ;
	4.0	9.873	7.38	18.20			$\Delta = 5.42 \cdot 10^{-4}$ m; $V = 6.81 \cdot 10^{-7}$ m ³ ;
	4.705	11.611	6.274	15.48			$\Delta = 7.5 \cdot 10^{-4}$ m; $V = 9.42 \cdot 10^{-7}$ m ³ ;
	5.434	13.41	5.434	13.41			$\Delta = 1.10^{-3}$ m; $V = 1.257 \cdot 10^{-6}$ m ³ ;
40	2.77	4.923	9.814	17.58	13.55	16.3	$\Delta = 2.8 \cdot 10^{-4}$ m; $V = 3.518 \cdot 10^{-7}$ m ³ ;
	4.0	7.267	6.85	12.44			$\Delta = 5.84 \cdot 10^{-4}$ m; $V = 7.338 \cdot 10^{-7}$ m ³ ;
	4.768	8.664	5.745	10.44			$\Delta = 8.3 \cdot 10^{-4}$ m; $V = 1.043 \cdot 10^{-6}$ m ³ ;
	5.234	9.51	5.234	9.51			$\Delta = 1.10^{-3}$ m; $V = 1.257 \cdot 10^{-6}$ m ³ ;

4. CONCLUSION

- It was found that for CPMs on the basis of LDPE filled with PZT there are two regions of the complex permittivity dispersion:
 - the first, at $E \leq E_{0c}$, where a linear relation between the imaginary and real parts of the complex permittivity is observed; and
 - the second, at $E > E_{0c}$, where the relation between the imaginary and real parts of the complex permittivity can be approximated by the Debye function.
- The breakdown of dielectrics occurs when the imaginary part of the complex permittivity within the non-linear region will be maximum $\varepsilon''_{\max} = \Delta\varepsilon/2$.

3. The estimation of parameters both in linear and non-linear regions of the dielectric relaxation spectrum allows the dielectric strength for CPMs to be predicted at the confidence level not less than 95% without HV tests.

REFERENCES

1. Gefle, O. S., S. M. Lebedev, Y. P. Pokholkov, et al., “Study of dielectric relaxation spectra of composite materials by the dielectric spectroscopy method,” *Proc. Intern. Symp. Elect. Ins. Matter.*, A2–4, Kitakyushu, Japan, June 2005.
2. Tareev, B. M., *Physics of Dielectrics*, Energoizdat, Moscow, 1982.
3. Gefle, O. S., S. M. Lebedev, and Y. P. Pokholkov, *The Barrier Effect in Dielectrics*, TML-press, Tomsk, 2007.
4. Lewis, T. J., “Interfaces and nanodielectrics are synonymous,” *Proc. Intern. Conf. Solid Diel.*, Vol. 2, 792–795, Vinchester, England, July 2004.
5. Tanaka, T., “Aging of polymeric and composite insulating materials,” *IEEE Trans. Diel. Elect. Ins.*, Vol. 9, No. 5, 704–716, 2002.

Polymeric Blends and Compositions with High Permittivity

S. N. Tkachenko, O. S. Gefle, and S. M. Lebedev

High-Voltage Research Institute, Tomsk Polytechnic University, Tomsk, Russia

Abstract— Electric and thermophysical properties of composite materials with high permittivity on the basis of low density polyethylene and polyvinylidene fluoride were studied in this work. Methods of dielectric spectroscopy in frequency domain and differential scanning calorimetry allow both electrical properties and fields of application of filled polymeric dielectrics with high permittivity to be established. The higher permittivity can be achieved for polymeric compositions on the basis of a polar matrix and polar filler due to the high interphase interaction between a polymeric matrix and filler.

1. INTRODUCTION

Novel composite polymeric materials (CPM's) with a high permittivity have received considerable attention because of their wide use as materials for electrical engineering, high energy storage device, electronics and other industries [1–6]. These materials should possess high permittivity, electric strength, specific resistivity and low dielectric losses ($\tan\delta$) over operating frequency range. CPM's with high permittivity on the basis of polymeric materials consist of a polymeric matrix and large amount of additives and modifying agents which should change matrix's properties. Adding fillers (inorganic or organic origin) into polymeric matrixes allows the modification of both electrical and thermophysical properties of CPM's to be performed [1–6]. Much works in this field has been devoted to the study of properties of polymeric materials filled with micro-scale ferroelectric ceramic powders, for example, lead zirconate titanate (PZT) [2–6, 7, 8].

Appearance of a novel class of sub-micro- and nano-scale fillers results in the development of nano-structured composite dielectrics [9, 10]. Nano-fillers possess a very high surface activity (or surface energy) and their interaction with polymeric matrix is much more compared with micro-scale fillers. Filling a polymeric matrix with ultra-dispersed inorganic fillers results in the modification of both the polymer structure and characteristics of CPM's due to interphase interaction and formation of nano-layer at the interface matrix/filler particles [9, 10].

Study of electrical and thermophysical characteristics of polymeric blends and compositions with high permittivity on the basis of both non-polar and polar matrixes was the aim of this work.

2. SAMPLES AND EXPERIMENTAL TECHNIQUE

Low density polyethylene (LDPE 10803-020, “Angarsk Polymer Plant”, Angarsk, Russia) and polyvinylidene fluoride (PVDF, type A, JSC “Plastpolymer”, St-Petersburg, Russia) were used as polymeric matrixes for CPM's with high permittivity. Chlorococane ($C_{23}H_nCl_m$) was used as a modifying agent in LDPE. Ferroelectric ceramic powder lead zirconate titanate PZT and titanium dioxide TiO_2 with average dimension of spherical particles 800 nm and 400 nm respectively were used as fillers. All blends and compositions were produced by means of the Banbury mixer. Additives and fillers were gradually introduced into the polymer up to the required fraction, while mixing until they were evenly distributed in the polymeric matrix. Then blends and CPM's were granulated by means of a pelletizer. Blends and compositions used in this study are listed in table.

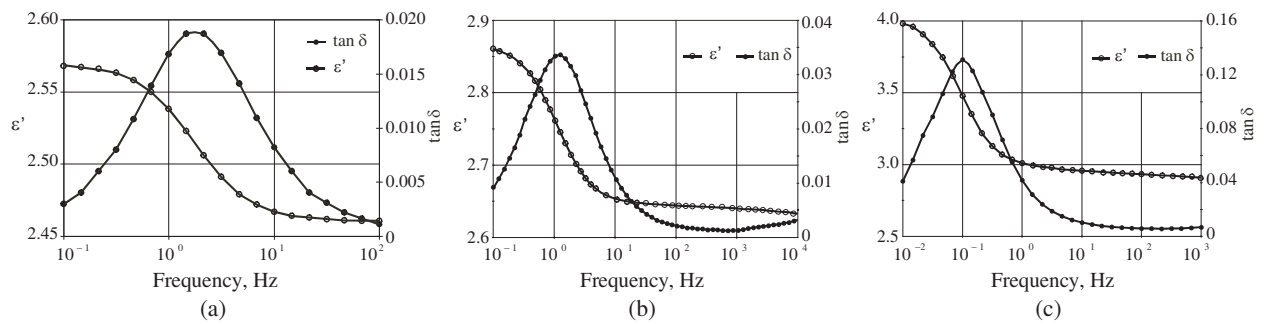
Samples were prepared from pellets by hot pressing in a hydraulic press with heated plates with a subsequent slow cooling under pressure in air. Samples for the study were prepared as discs 75 mm in diameter and thickness from 50 to 100 μm .

Measurements of the real part ϵ' of the complex permittivity and $\tan\delta$ were carried out by the dielectric spectroscopy method under the voltage 3 V in the frequency range from 10^{-2} Hz to 1 MHz by means of the Solartron Instrument (Impedance/Gain-Phase Analyzer Solartron 1260 + Dielectric Interface Solartron 1296) [11]. From five to ten measurements per decade over the frequency range were performed for all samples.

Temperatures and temperature intervals of melting and decomposition of blends and CPM's were measured by the differential scanning calorimetry method (DSC) using a combined DSC-DTA-TGA analyzer Q600 “TA Instruments”. The weight of samples was 12.5...35 mg. The heat flow and a weight loss of samples put into Al_2O_3 -crucible were recorded in the temperature range from 25 to 500°C at a heating rate of 3°C/min in an argon atmosphere.

Table 1: Blends and compositions on the basis of LDPE and PVDF.

Composition Number	Composition
C1	LDPE + 5 wt% ChC
C2	LDPE + 10 wt% ChC
C3	LDPE + 25 wt% ChC
C4	LDPE + 10 vol% PZT
C5	LDPE + 30 vol% PZT
C6	LDPE + 40 vol% PZT
C7	PVDF + 45 vol% TiO ₂
C8	PVDF + 30 vol% PZT

Figure 1: Frequency dependencies of ε' and $\tan\delta$ for blends: (a) C1, (b) C2, and (c) C3.

3. EXPERIMENTAL RESULTS AND DISCUSSION

The first group of materials on the basis of non-polar LDPE-matrix includes blends with various content of chlorococane (ChC) — C1 ... C3 (Table 1). This group is characterized by the dispersion of the complex permittivity in the ultra-low frequency range. Typical frequency dependencies of ε' and $\tan\delta$ for blends C1 ... C3 are presented in Fig. 1. It is a well-known fact that the dielectric relaxation spectrum of LDPE at room temperature does not possess any relaxation maxima in the frequency range from 10^{-2} up to 10^6 Hz [12]. Adding a ChC into a LDPE-matrix results in the appearance of the relaxation peak of dielectric losses at the infra-low frequency range. The relaxation frequency which corresponds to the $\tan\delta$ peak is shifted towards to the lower frequency from 1.8 to 0.1 Hz with increase in ChC content from 5 to 25 wt%. The value of ε' is increased from 2.52 to 2.9 (e.g., at frequency 10^1 Hz) and the maximum value of $\tan\delta$ is increased by a factor of 7.5. It testifies that both the interaction between the LDPE-matrix and additive and the relaxation time of the dipole-group polarization of ChC molecules are increased. Insofar as the relaxation maximum of $\tan\delta$ for all blends of this group is observed at the infra-low frequency range, these materials can be used as insulating materials in the frequency range from 10^1 to 10^6 Hz.

Filling a LDPE-matrix with PZT results in the appearance of a relaxation maximum of dielectric losses in the high frequency range for the second group of materials C4 ... C6 (Fig. 2). It can be seen that values of ε' and $\tan\delta$ are increased and the $\tan\delta$ peak is shifted towards to the lower frequency with increase in PZT content from 10 to 40 vol% (compositions C4 ... C6). It is obvious that increase in ε' for compositions on the basis of LDPE in the frequency range from 10^{-2} to 10^3 Hz is not more than 12 ... 13.5 even at the filler content 40 vol% in spite of the fact that the permittivity of PZT is approximately 1700. It testifies that the interaction between non-polar LDPE-matrix and polar PZT-filler is not so good. Compositions C4 ... C6 can be applied in the frequency range from 10^{-2} to 10^3 Hz in contrast to LDPE modified by ChC.

The third group of materials on the basis of polar PVDF-matrix includes compositions C7 and C8. This group of materials is characterized by the dispersion of the complex permittivity both in the low frequency range and in the high frequency one. Typical frequency dependencies of ε' and $\tan\delta$ for PVDF-matrix and compositions C7 and C8 are shown in Fig. 3. It can be seen that the filling of a PVDF-matrix with high permittivity fillers results in increase of the value of ε' by a

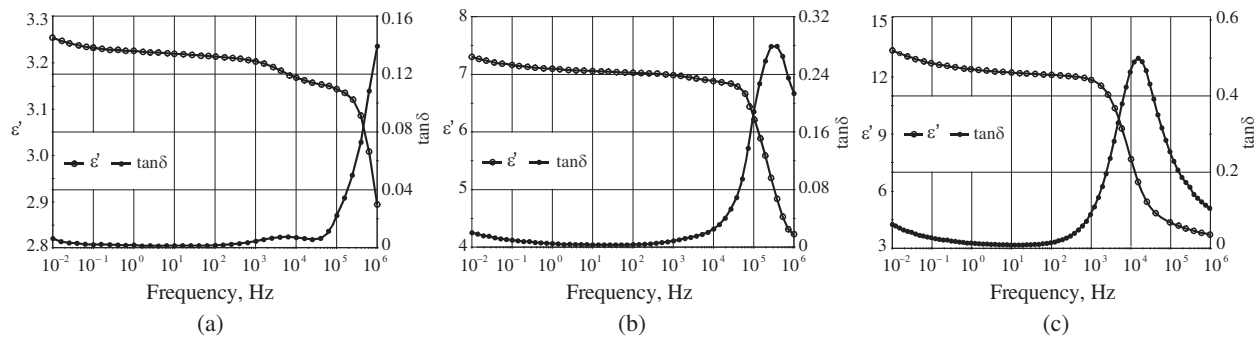
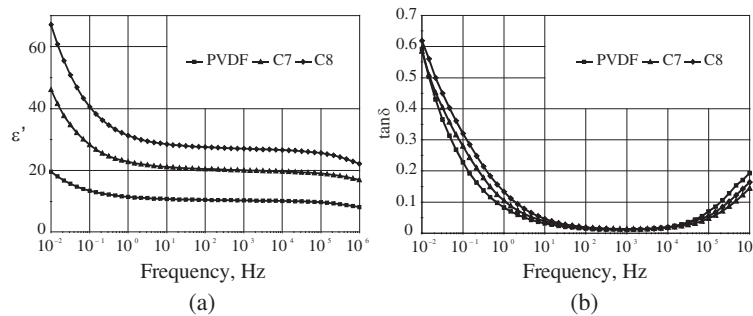
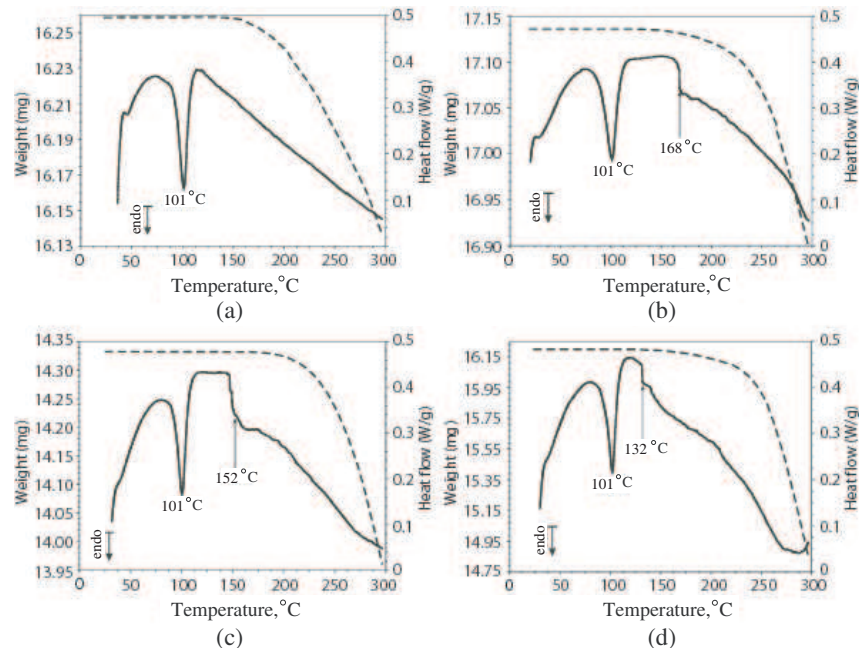

 Figure 2: Frequency dependencies of ε' and $\tan\delta$ for compositions: (a) C4, (b) C5, and (c) C6.

 Figure 3: Frequency dependencies of (a) ε' and (b) $\tan\delta$ for PVDF and compositions C7 and C8.


Figure 4: Temperature dependencies of a heat flow (solid line) and a sample weight loss (dotted line): (a) LDPE, (b) C1, (c) C2, and (d) C3.

factor of 2 and 3 for C7 and C8 respectively compared to that for PVDF in the frequency range from 10^0 to 10^5 Hz. In doing so, dielectric losses in this frequency range for PVDF, C7 and C8 does not practically differ. Compositions C7 and C8 are suitable for the frequency range from 10^0 to 10^5 Hz because at other frequencies their dielectric losses will be considerably increased.

When studying polymeric dielectrics by DSC method, phase transitions and chemical transformations accompanied by exothermic or endothermic effects can be registered at the curve of the heat flow. Fig. 4 shows typical temperature dependencies of the heat flow and sample weight loss for LDPE and compositions C1 ... C3.

It is obvious that the temperature of the first phase transition corresponding to the melting

process of materials is practically constant and it equals 101°C . It testifies that the modification of LDPE by small amount of ChC does not practically change the melting temperature of blends compared to that for LDPE. Modifying LDPE by ChC results in visible change of the heat flow and beginning decomposition temperature of blends. Change of the heat flow at temperatures 168, 152 and 132°C is caused by the breaking of weak bonds between ChC and LDPE-matrix. The beginning temperature of this phase transition is decreased approximately by 36°C with changing the ChC content in LDPE from 5 to 25 wt%.

Similar results of DSC-analysis for compositions C4 ... C6 are shown in Fig. 5. It can be seen that two endothermic minimums corresponding to the melting and decomposition processes at temperatures 101°C and $405\text{--}446^{\circ}\text{C}$ respectively are observed for all compositions. Moreover, the decomposition temperature is decreased from 446°C to 405°C with changing PZT content in LDPE from 10 vol% up to 40 vol%.

Other peculiarity for these CPM's is the appearance of a characteristic area in the temperature range $335\text{--}370^{\circ}\text{C}$. This phase transition is caused by presence of a coating layer on the surface of filler particles. PZT powder particles were coated by a stearic acid before the mixing with a polymeric matrix to increase polymer interaction between PZT-particles and LDPE-matrix and to exclude the formation of agglomerates of filler particles. Temperature range of the phase transition at $335\text{--}370^{\circ}\text{C}$ well correlates with the boiling temperature of a stearic acid [13].

Figure 6 shows the experimental results of DSC measurements for PVDF. It is obvious that two phase transitions are observed for this material. The first area is corresponded to the PVDF melting temperature at 152°C and the second one to the decomposition temperature at 375°C .

Figure 7 shows similar results for compositions C7 and C8. The melting temperature for C7 and C8 is decreased by $4\text{--}5^{\circ}\text{C}$ compared with PVDF-matrix. Exothermic peaks connected with the oxidation reaction are observed at 312 and 458°C for compositions C7 and C8 respectively in contrast to the endothermic peak at 375°C for PVDF. It is caused by that both TiO_2 and PZT contain oxygen. Titanium dioxide is chemically inert filler therefore its interaction with a PVDF-matrix is very weak. Absence of interaction between a polymeric matrix and filler at high filler content usually leads to deterioration of mechanical properties of CPM's. Decrease in temperature at which the weight loss begins for C7 ($\sim 307^{\circ}\text{C}$) compared to that for PVDF ($\sim 356^{\circ}\text{C}$) means that TiO_2 is a substance accelerating thermo-oxidative destruction of a polymeric matrix. Ferroelectric ceramics PZT is active filler in contrast to TiO_2 . Therefore interaction between polar filler and polar PVDF-matrix is much more than for compositions C7 and LDPE/PZT. It results in both

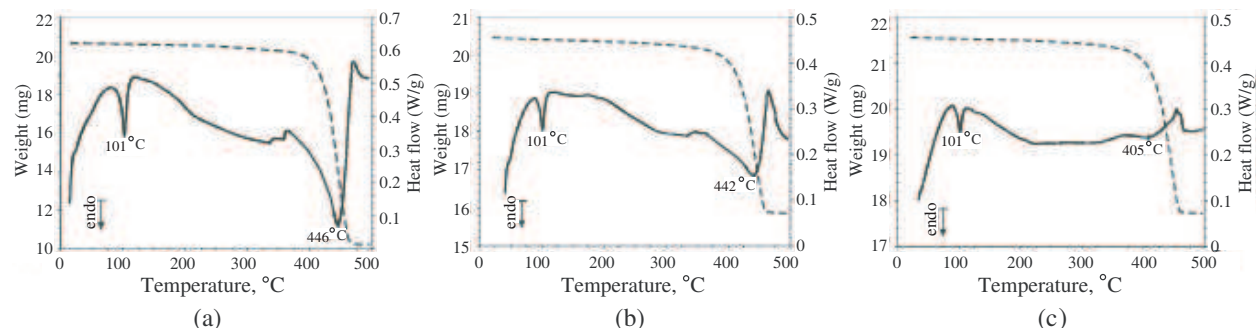


Figure 5: Temperature dependencies of a heat flow (solid line) and a sample weight loss (dotted line): (a) C4, (b) C5, and (c) C6.

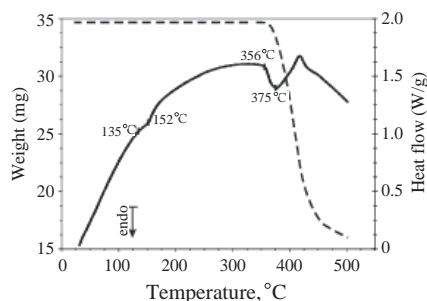


Figure 6: Temperature dependencies of a heat flow (solid line) and a sample weight loss (dotted line) for PVDF.

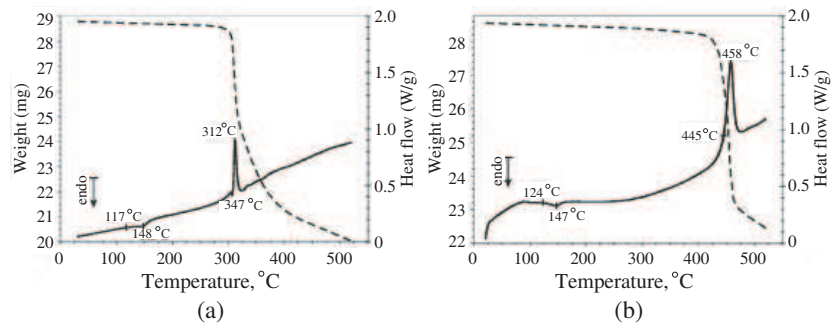


Figure 7: Temperature dependencies of a heat flow (solid line) and a sample weight loss (dotted line): (a) C7, and (b) C8.

slowing down thermo-oxidative destruction and increase of temperature at which decomposition of C8 begins ($\sim 445^\circ\text{C}$) compared with PVDF and C7.

4. CONCLUSIONS

1. Adding chlorococane into the LDPE-matrix results in the appearance of the complex permittivity dispersion at the infra-low frequency range. Blends on the basis of LDPE modified by chlorococane can be applied as insulating materials in the frequency range from 10^1 to 10^6 Hz.
2. Compositions on the basis of LDPE filled with ferroelectric ceramics PZT can be applied as insulating materials in the frequency range from 10^{-2} to 10^3 Hz because the relaxation maximum of dielectric losses for these compositions is observed in the high frequency range from 10^4 to 10^7 Hz.
3. Compositions on the basis of PVDF filled with ferroelectric ceramics PZT are suitable for usage in the frequency range from 10^0 to 10^5 Hz because they do not possess dispersion of the complex permittivity in this frequency range.

REFERENCES

1. Das-Gupta, D. K. and K. Doughty, "Polymer-ceramic composite materials with high permittivities," *Thin Solid Films*, Vol. 158, 93–105, 1988.
2. Gefle, O. S., S. M. Lebedev, A. I. Zatulii, et al., "Influence of high-permittivity barriers on the treeing process characteristics for PMMA," *Russian J. Electricity*, No. 10, 65–67, 1988.
3. Gefle, O. S., S. M. Lebedev, and Y. P. Pokholkov, *Barrier Effect in Dielectrics*, TML-Press, Tomsk, 2007.
4. Chan, H. L. W., Y. Chen, and C. L. Choy, "Thermal hysteresis in the permittivity and polarization of lead zirconate titanate/vinylidene fluoride-trifluoroethylene 0-3 composites," *IEEE Trans. Diel. Electr. Insul.*, Vol. 3, 800–805, 1996.
5. Gefle, O. S., S. M. Lebedev, and Y. P. Pokholkov, "The barrier effect in dielectrics. The role of interfaces in the breakdown of inhomogeneous dielectrics," *IEEE Trans. Diel. Electr. Insul.*, Vol. 12, 537–555, 2005.
6. Chan, H. L. W., W. K. Chan, Y. Zhang, et al., "Pyroelectric and piezoelectric properties of lead titanate/polyvinylidene fluoride-trifluoroethylene 0-3 composites," *IEEE Trans. Diel. Electr. Insul.*, Vol. 5, 505–512, 1998.
7. Chan, H. L. W., Q. Q. Zhang, W. Y. Ng, et al., "Dielectric permittivity of PCLT/PVDF-TRFE nanocomposites," *IEEE Trans. Diel. Electr. Insul.*, Vol. 7, 204–206, 2000.
8. Gefle, O. S., S. M. Lebedev, V. A. Volokhin, et al., "Dielectric spectra of elastomeric materials filled with ferroelectric ceramic powder," *Proc. IEEE Conf. Power Tech.*, 176, St-Petersburg, June 27–30, 2005.
9. Lewis, T. J., "Nanometric dielectrics," *IEEE Trans. Diel. Electr. Insul.*, Vol. 1, 812–825, 1994.
10. Tanaka, T., "Dielectric nanocomposites with insulating properties," *IEEE Trans. Diel. Electr. Insul.*, Vol. 12, 914–928, 2005.
11. Operating manual, Impedance/Gain-Phase Analyzer 1260 and Dielectric Interface 1296, 2001.
12. Lewis, T. J., "Polyethylene under electrical stress," *IEEE Trans. Diel. Electr. Insul.*, Vol. 9, 717–729, 2002.
13. Zefirov, N. S., "Chemical encyclopedia," *The Greater Russian Encyclopedia*, Vol. 4, Moscow, 1995.

Magnetic Field Created by Thin Wall Solenoids and Axially Magnetized Cylindrical Permanent Magnets

G. Lemarquand¹, V. Lemarquand¹, S. Babic², and C. Akyl³

¹Laboratoire d'Acoustique de l'Universite du Maine, UMR CNRS 6613, Le Mans, France

²Departement de Genie Physique, Ecole Polytechnique Montreal, Canada

³Departement de Genie Electrique, Ecole Polytechnique Montreal, Canada

Abstract— This paper presents the calculation of the magnetic field created by axially magnetized cylindrical permanent magnets and thin wall solenoids in air. It emphasizes the equivalence of the source models: charged planes and current sheet. It shows that although the starting formulations, magnetic scalar potential, Coulomb's law, vector potential, Biot-Savart's law often depend in the literature on the source nature, they shouldn't. Indeed, it presents the magnetic field calculation for each point of view and explains which lead to analytical solutions. Then it presents the calculation of forces between permanent magnets and shows that it is equivalent to the calculation of the mutual inductance between two coils.

1. INTRODUCTION

It is well-known that coils and permanent magnets are equivalent sources of magnetic field even though, depending on the application, the latter or the former may be more interesting or advantageous. However, the physical nature of the magnetic field source influences the scientist who intends to calculate the created magnetic field. Indeed, scientists dealing with permanent magnets generally either calculate the magnetic scalar potential and derive it to obtain the magnetic field or use Coulomb's law to calculate the magnetic field directly, whereas scientists dealing with coils rather calculate the vector potential and use Biot-Savart's law.

This paper intends to emphasize the equivalence of the source models but also to highlight the fact that some formulations will lead more easily to analytical formulations than others. So, a very simple example is considered: an axially magnetized cylindrical permanent magnet in air. Indeed, it can be modelled either by a thin wall solenoid, a current sheet or two charged planes. Inversely, a thin wall solenoid could be considered, which would then be modeled by a current sheet or a cylindrical magnet axially magnetized or by two charged planes. The point is that the charge model corresponds to a coulombian approach and the coil model to an amperian approach. This paper gives the initial expressions for the magnetic field calculation for each possible point of view. Then it presents the calculation of forces between permanent magnets and thus show that it is fully equivalent to the calculation of the mutual inductance between two coils.

2. BASIC EQUIVALENCES

A cylindrical permanent magnet with an uniform axial polarization, J , creates the same magnetic field as the thin wall solenoid of same diameter and height as the magnet, when currents flow in it with a linear density (Fig. 1). This solenoid creates also the same field as the cylindrical current sheet, \vec{K} , which is linked to \vec{J} as follows:

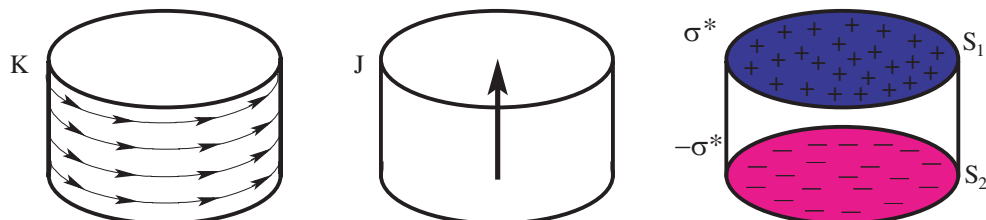


Figure 1: Equivalent source models for a cylinder of radius R and height h . Left: current sheet, K . Center: permanent magnet with axial polarization, J . Right: charged planes, charge surface density σ^* .

$$\vec{K} = \frac{\vec{J}}{\mu_0} \quad (1)$$

Furthermore, it also creates the same magnetic field as the two charged planes, corresponding to the top and bottom caps of the cylinder and separated by a distance equal to the cylinder height. These planes are charged with opposite charge surface densities $+\sigma^*$ and $-\sigma^*$ related to the polarization and defined by:

$$\sigma^* = \vec{J} \cdot \vec{n} \quad (2)$$

where \vec{n} is the vector normal to the face.

For neodymium iron boron magnets, $J = 1.4 \text{ T}$, $\sigma^* = 1.4 \text{ T}$, $K = 1.11 \cdot 10^6 \text{ A/m}$. Moreover, the magnetic sources considered in this paper are in ironless structures. This allows to obtain analytical formulations for the magnetic field.

3. MAGNETIC FIELD CALCULATIONS

3.1. Magnetic Scalar Potential

As said in the introduction, it is striking how the method used to calculate the magnetic field depends on the source nature. When it comes to magnets, the prevalent method in literature is the calculation of the scalar potential and its subsequent derivation (gradient). Indeed, one can write the magnetic scalar potential function as

$$\varphi(\vec{r}) = \frac{J}{4\pi\mu_0} \iint_{S_1} \frac{1}{|\vec{r} - \vec{r}'|} ds_1 - \frac{J}{4\pi\mu_0} \iint_{S_2} \frac{1}{|\vec{r} - \vec{r}'|} ds_2 \quad (3)$$

where the radius \vec{r} defines the observation point M position, \vec{r}' the position of the elementary source on the charged surface, S_1 the positive charged surface, S_2 the negative one. The scalar potential is expressed in amperes. This calculation uses the representation of the magnetic source by charge surface densities. Of course, it supposes a linear behavior so as to calculate the total scalar potential by the application of the superposition principle.

The magnetic field is then calculated by :

$$\vec{H} = -\overrightarrow{\text{grad}}\varphi \quad (4)$$

However, the difficulty in this method lies in the fact that one has to integrate a function first and then to derive the integration result. Various methods, using Green's functions or toroidal functions have been proposed to solve this problem but few of them lead to a complete analytical formulation of the magnetic field. Indeed, a numerical calculation is often required as last step in most of them.

3.2. Coulomb's Law

When the charge surface density model is chosen another way to calculate the magnetic field is to use Coulomb's law directly as in Eq. (5)

$$\vec{H}(\vec{r}) = \frac{J}{4\pi\mu_0} \iint_{S_1} \frac{1}{|\vec{r} - \vec{r}'|^2} ds_1 - \frac{J}{4\pi\mu_0} \iint_{S_2} \frac{1}{|\vec{r} - \vec{r}'|^2} ds_2 \quad (5)$$

On account of the cylindrical symmetry the magnetic field is a function on r and z only and its azimuthal component, $H_\theta(r, z)$, is equal to zero. Thus, the magnetic field can be expressed as follows:

$$\begin{aligned} \vec{H}(r, z) = & \frac{J}{4\pi\mu_0} \int_0^{2\pi} \int_0^R \frac{(r - r_1 \cos(\theta)) \vec{u}_r - r_1 \sin(\theta) \vec{u}_\theta + (z - z_1) \vec{u}_z}{(r^2 + r_1^2 - 2rr_1 \cos(\theta) + (z - z_1)^2)^{\frac{3}{2}}} r_1 dr_1 d\theta \\ & - \frac{J}{4\pi\mu_0} \int_0^{2\pi} \int_0^R \frac{(r - r_2 \cos(\theta)) \vec{u}_r - r_2 \sin(\theta) \vec{u}_\theta + (z - z_2) \vec{u}_z}{(r^2 + r_2^2 - 2rr_2 \cos(\theta) + (z - z_2)^2)^{\frac{3}{2}}} r_2 dr_2 d\theta \end{aligned} \quad (6)$$

where the indexes 1 (resp. 2) are related to the positive (resp. negative) charged face. Once again, the linearity is supposed, but it is consistent with the behavior of modern permanent magnets. The solution of these integrals can be fully analytically formulated with elliptic integrals of the first, second and third kind. Moreover, the three components of the magnetic field are obtained and the result is valid in all the space, inside as well as outside the magnet [1–5].

One should remark here that these methods, though mainly developed for permanent magnet sources, can also apply to coils. Indeed, the modelling of a magnetic source results from a choice and not from the nature of the source itself. Furthermore, the attention is drawn on the fact that with the charged plane model the magnetic field, \vec{H} , is calculated first. Indeed, the values obtained are valid in all the space. Then, the magnetic flux density, \vec{B} , is deduced. One shouldn't forget either that the magnetic field presents a discontinuity on the charged planes. This sometimes generates punctual numerical difficulties for the calculation of numerical values with the analytical formulations.

3.3. Magnetic Vector Potential

Generally, scientists dealing with coils use models naturally related to currents and calculate either the vector potential or use Biot-Savart's law. This section discusses methods related to the former [6–8]. The vector potential, \vec{A} , is defined as

$$\vec{A}(\vec{r}) = \frac{\mu_0}{4\pi} \iint_S \frac{\vec{K}}{|\vec{r} - \vec{r}'|} ds \quad (7)$$

The magnetic flux density is then deduced by derivation (curl):

$$\vec{B} = \text{rot} \vec{A} \quad (8)$$

Here again, the difficulty may lie in the fact that integrations have to be calculated to obtain formulations of the potential vector which have then to be derived. The results can be written analytically with elliptic integrals of the first, second and third kind.

3.4. Biot-Savart's Law

In fact, boths previous steps, expression of the vector potential and its derivation to obtain the magnetic flux density can be summarized by Biot-Savart's law. Indeed, the latter gives a way to calculate the magnetic flux density directly:

$$\vec{B}(\vec{r}) = \frac{\mu_0}{4\pi} \iint_S \frac{\vec{K} \times (\vec{r} - \vec{r}')}{|\vec{r} - \vec{r}'|^3} ds \quad (9)$$

At this point, some remarks have to be done. First, although these methods were traditionnaly proposed by scientists who wanted to calculate the magnetic flux density created by coils and windings in air, they present nevertheless a great interest for the calculation of the magnetic field created by permanent magnets. Indeed, as the integrals to be calculated depend on the model they don't have the same boundaries and one model may lead to an analytical solution where the other fails. This was experienced by the authors. Moreover, both methods calculate the magnetic flux density and the magnetic field, when needed, is deduced from the former. As the magnetic flux density is continuous in the space, this may be a reason why solutions are found with this modelling which the coulombian approach don't give. But it has to be noted, that the reverse situation is to be found too! The point is then, that the choice of the model is free and shouldn't depend on the source nature. The model which has to be chosen is the one that gives fully analytical formulations of the magnetic field for the geometry considered. Indeed, the final formulation is the same.

4. FORCE CALCULATIONS

Magnetic sources, coils or magnet, have two great kinds of applications. Of course, they are primarily used to create magnetic fields (as in MRI devices, wigglers, sensors...) but two sources are also widely used to interact and thus create forces and torques (as in electrical machines, magnetic couplings...). This section deals with the force calculation. Then, three interactions can physically exist: between two magnets, between two coils and between a coil and a magnet. But as the sources are modelled for the calculation the methods that have to be considered are rather related to the models. Therefore, Coulomb's law can be used for the charge model and Lorentz's force for the current model. Moreover, in the last case, the force calculation is also closely related to the calculation of the mutual inductance of the coils.

4.1. Force and Mutual Inductance

The calculation of the magnetic attraction between two current-carrying coils is closely related to the calculation of their mutual inductance. Since their mutual energy is equal to the product of their mutual inductance and the currents in the coils, the component of the magnetic force of attraction or repulsion in any direction is equal to the product of the currents multiplied by the differential coefficient of the mutual inductance taken with the respect to that coordinate. Thus, the magnetic force may be calculated by simple differentiation in cases where a general formula for the mutual inductance is available,

$$F = I_a I_b \frac{M}{g} \quad (10)$$

where I_a and I_b are the currents in the two coils, M their mutual inductance and g the generalized coordinate [9–13].

4.2. Magnetic Vector Potential and Lorentz's Force

This section considers the case when the sources are modelled by current sheets and the magnetic flux density is expressed by the vector potential. Then, the interaction between the two coils can be described by Lorentz's force. Indeed, the magnetic flux density, \vec{B}_a , created by one of the coil interacts with the current sheet of the second one, \vec{K}_b :

$$\vec{F} = \iint_S (\vec{K}_b \times \vec{B}_a) ds \quad (11)$$

For coaxial sources, only the axial force occurs because of the symmetry of the problem. As a result, the axial force exerted between two axially polarized cylinder permanent magnet which are coaxial can be expressed analytically with elliptic integral of the first, second and third kind [14, 15].

4.3. Coulomb's Law

In the case of sources modelled by two charged planes, the force between the sources is described by Coulomb's law. This force is the sum of the four interactions between the four charged planes:

$$\begin{aligned} \vec{F}(\vec{r}) = & \frac{J^2}{4\pi\mu_0} \iint_{S_{1a}} \iint_{S_{1b}} \frac{ds_{1a} ds_{1b}}{|\vec{r}_{1a}' - \vec{r}_{1b}'|^2} - \frac{J^2}{4\pi\mu_0} \iint_{S_{1a}} \iint_{S_{2b}} \frac{ds_{1a} ds_{2b}}{|\vec{r}_{1a}' - \vec{r}_{2b}'|^2} \\ & - \frac{J^2}{4\pi\mu_0} \iint_{S_{2a}} \iint_{S_{1b}} \frac{ds_{2a} ds_{1b}}{|\vec{r}_{2a}' - \vec{r}_{1b}'|^2} + \frac{J^2}{4\pi\mu_0} \iint_{S_{2a}} \iint_{S_{2b}} \frac{ds_{2a} ds_{2b}}{|\vec{r}_{2a}' - \vec{r}_{2b}'|^2} \end{aligned} \quad (12)$$

where the indexes a are related to the first source, the indexes b to the second one, the radii \vec{r}_{1a}' and \vec{r}_{1b}' are the position of the elementary source on the positive charged surfaces, the radii \vec{r}_{2a}' and \vec{r}_{2b}' the position of the elementary source on the negative charged surfaces. Furthermore, the sources are supposed to be coaxial and the considered force is the axial one. In this expression, three of the four integrations in each term can be solved analytically. So, only one remains that has to be numerically calculated and the calculation is globally very fast.

5. STIFFNESS CALCULATIONS

Depending on the application, the knowledge of the force may not be sufficient. For example, the dimensioning of magnetic couplings require the value of the stiffness. Then, a general remark is that as long as the considered model leads to the calculation of a force, the notion of stiffness makes sense. But when the model leads to the calculation of a mutual inductance in place of the force, the notion of stiffness can't be derived. At this stage, this may be a guideline to help choosing the model.

For coaxial sources, the axial stiffness, K_z is defined by:

$$K_z = -\frac{\partial}{\partial z} F_z \quad (13)$$

where F_z is the axial force.

6. GENERALIZATION

This paper presents methods for calculations in a very simple case: a cylindrical source. It must be emphasized here that it thus gives the basis for more complicated geometries. Indeed, numerous geometries can be considered as the superposition of this basic geometry, but with different dimensions or orientations. For example, an axially polarized ring permanent magnet can be seen as the superposition of two cylinder permanent magnets of same heights, opposite polarizations and different radii (the radii difference giving the ring radial thickness).

7. CONCLUSION

In conclusion, this paper emphasizes the equivalence of the source models for the calculation of the magnetic field created by axially magnetized cylindrical permanent magnets and thin wall solenoids in air. It shows that the starting formulations should not depend on the source nature as some lead more easily to analytical solutions. Eventually, it shows that the calculation of forces between permanent magnets is equivalent to the calculation of the mutual inductance between two coils.

REFERENCES

1. Ravaud, R., G. Lemarquand, V. Lemarquand, and C. Depollier, "Analytical calculation of the magnetic field created by permanent-magnet rings," *IEEE Trans. Magn.*, Vol. 44, No. 8, 1982–1989, 2008.
2. Ravaud, R., G. Lemarquand, V. Lemarquand, and C. Depollier, "Discussion about the analytical calculation of the magnetic field created by permanent magnets," *Progress In Electromagnetics Research B*, Vol. 11, 281–297, 2009.
3. Durand, E., *Magnetostatique*, Masson Editeur, Paris, France, 1968.
4. Ravaud, R., G. Lemarquand, V. Lemarquand, and C. Depollier, "The three exact components of the magnetic field created by a radially magnetized tile permanent magnet," *Progress In Electromagnetics Research*, PIER 88, 307–319, 2008.
5. Babic, S. and C. Akyel, "Improvement in the analytical calculation of the magnetic field produced by permanent magnet rings," *Progress In Electromagnetics Research C*, Vol. 5, 71–82, 2008.
6. Urankar, L. K., "Vector potentiel and magnetic field of current carrying finite arc segment in analytical form, part 2: Thin sheet approximation," *IEEE Trans. Magn.*, Vol. 18, No. 3, 911–917, 1982.
7. Furlani, E. P. and M. Knewston, "A three-dimensional field solution for permanent-magnet axial-field motors," *IEEE Trans. Magn.*, Vol. 33, No. 3, 2322–2325, 1997.
8. Azzerboni, B., E. Cardelli, M. Raugi, A. Tellini, and G. Tina, "Magnetic field evaluation for thick annular conductors," *IEEE Trans. Magn.*, Vol. 29, No. 3, 2090–2094, 1993.
9. Babic, S. and C. Akyel, "Magnetic force calculation between thin coaxial circular coils in air," *IEEE Trans. Magn.*, Vol. 44, No. 4, 445–452, 2008.
10. Babic, S. and C. Akyel, "Improvement in calculation of the self and mutual inductance of thin wall solenoids and disk coils," *IEEE Trans. Magn.*, Vol. 36, No. 4, 1970–1975, 2000.
11. Babic, S., C. Akyel, and S. Salon, "New procedures for calculating the mutual inductance of the system: Filamentary circular coil-massive circular solenoid," *IEEE Trans. Magn.*, Vol. 39, No. 3, 1131–1134, 2003.
12. Babic, S., S. Salon, and C. Akyel, "The mutual inductance of two thin coaxial disk coils in air," *IEEE Trans. Magn.*, Vol. 40, No. 2, 822–825, 2004.
13. Ravaud, R. and G. Lemarquand, "Analytical expression of the magnetic field created by tile permanent magnets tangentially magnetized and radial currents in massive disks," *Progress In Electromagnetics Research B*, Vol. 13, 309–328, 2009.
14. Lang, M., "Fast calculation method for the forces and stiffnesses of permanent-magnet bearings," *8th International Symposium on Magnetic Bearing*, 533–537, 2002.
15. Charpentier, J. F., V. Lemarquand, and G. Lemarquand, "A study of permanent-magnet couplings with progressive magnetization using analytical exact formulation," *IEEE Trans. Magn.*, Vol. 35, No. 5, 4206–4217, 1999.

Method for Calculating Interference Protection Ratio of ATSC System from Mobile WiMAX System

Sung Woong Choi¹, Wang Rok Oh², and Heon Jin Hong¹

¹Broadcasting & Telecommunications Convergence Research Lab., ETRI, Korea

²Division of Electrical & Computer Engineering, Chungnam National University, Korea

Abstract— In this paper, we proposed the method for calculating the Protection Ratio (PR) of the Advanced Television Systems Committee (ATSC) broadcasting system from the Mobile WiMAX system (Wireless Broadband: WiBro in Korea) through the computational experiment. For this, the transmitter/receiver of the ATSC system and transmitter of the WiBro system were modelled. By integrating those, the computational simulator for setting up the PR of the ATSC system from the WiBro system was implemented. The ATSC TV signal was regarded as the desired one and the WiBro signal was regarded as the interfering one. In order to simplify the simulation complexity it modelled sending/receiving signals of the IF band instead of those of the RF band. It was assumed that one received signal was considered in the channel modelling.

1. INTRODUCTION

According to the rapid development of the digital technology, the broadcasting environments are changing into the digital television transmission including the ATSC, ISDB-T, DVB-T, etc of the high quality and high-efficiency from the existing analog television transmission. Due to the high efficiency characteristics of digital television, the unprecedented amount of spectrum that will be freed up in the switchover from analog to digital terrestrial TV is known as the Digital Dividend. Most of countries in the world collect the digital frequency generated by the analog television broadcasting switch off and plan to use that frequency in the different service like the next generation mobile communication, and etc. At that time, it must be considered that interference effect between Digital TV and new service in order to introduce the new services in the digital dividend.

Until now, it is general that the field test data are used for setting up the PR between the broadcasting systems [1, 2]. But it needs much time and cost in order to collect and analyze the field test data. Therefore, by drawing method for setting up the PR based on the computational simulation, it is easy to calculate the PR about the corresponding system.

In this paper, we proposed the method for calculating the PR of the ATSC broadcasting system from the WiBro system, one of the Mobile WiMAX systems through the computational experiment. For this, the transmitter/receiver of the ATSC system and transmitter of the WiBro system were modeled. By integrating those, the computational simulator for setting up the PR of the ATSC system from the WiBro system was implemented. The ATSC TV signal was regarded as the desired one and the WiBro signal was regarded as the interfering one. In order to simplify the simulation complexity, it modeled sending/receiving signals of the IF band instead of those of the RF band. It was assumed that one received signal was considered in the channel modelling In ATSC receiver, the symbol error rate (SER) 0.2 of the trellis decoder input signal was used as the Threshold of Visibility (TOV) performance [3].

2. ATSC AND WIBRO SYSTEM MODELLING

2.1. ATSC 8VSB System Modeling

The ATSC system was specifically designed to permit an additional digital transmitter to be added to each existing NTSC transmitter. The ATSC Digital Television Standard was developed by the Advanced Television Systems Committee in the United States [4, 5]. The ATSC system was designed to transmit high-quality video and audio (HDTV) and ancillary data over a single 6 MHz channel. The ATSC Vestigial Sideband modulation with 8 discrete amplitude levels (8-VSB) system transmits data in a method that uses trellis-coding with 8 discrete levels of signal amplitude. A pilot tone provided to facilitate rapid acquisition of the signal by receivers. Complex coding techniques and adaptive equalization are used to make reception more robust to propagation impairments such as multipath, noise and interference. It can reliably deliver about 19.39 Mbps of data throughput in a 6 MHz bandwidth.

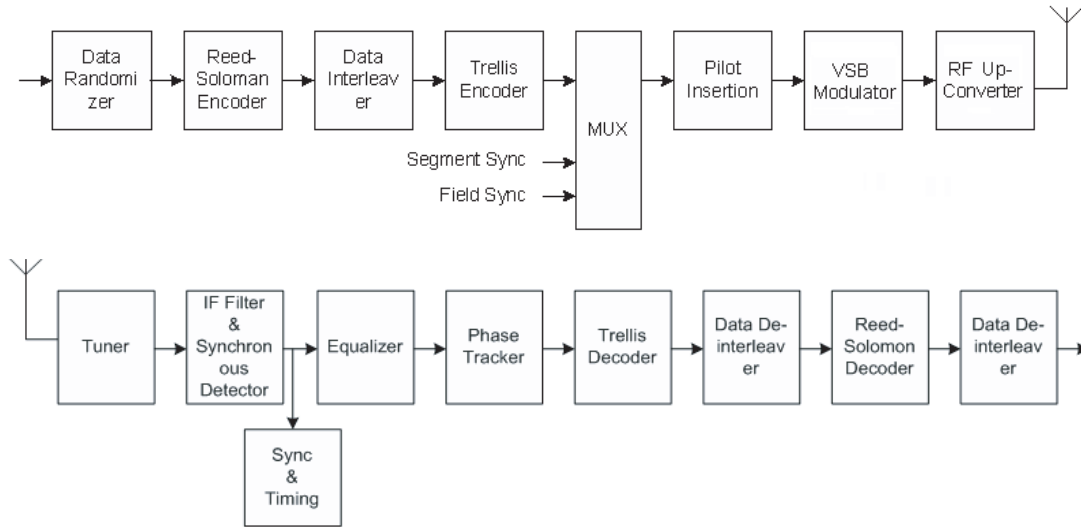


Figure 1: Functional block diagram ATSC transmitter/receiver.

Table 1: Parameters for ATSC 8VSB transmission modes.

Parameter	ATSC 8VSB
Bandwidth	6 MHz
Excess bandwidth	11.5%
Symbol rate	10.76 MSPS
Bits/Symbol	3
Trellis FEC	2/3 rate
Payload data rate	19.39 Mb/s
C/N threshold	14.9 dB

Figure 1 presents a functional block diagram of 8 VSB transmitter and receiver. The 8-VSB transmitter can represent to three parts, the Forward Error Correction (FEC), the Insertion of the sync signals, and 8-VSB modulation.

2.2. WiBro System Modelling

In this chapter, we review the WiBro system that is the name of the Mobile WiMAX system in Korea [6]. WiBro is the one of the Wireless internet access standard. WiBro system uses the TDD (Time Division Duplex) for transmit and receive simultaneously, OFDMA (Orthogonal Frequency Division Multiple access) for multiple access, and have the 8.75 MHz bandwidth. It is designed to overcome the limited data rate of mobile telephone system such as the CDMA 1x, and added the mobile characteristic to broadband internet access such as ADSL or wireless LAN.

Figure 2 shows a functional block diagram of the WiBro transmitter. As shown in the figure, the transmitter is mainly comprised of two parts: Baseband modulator and RF transmitter. Baseband modulator consists of FEC Encoder, interleaving, symbol mapping, pilot adding, OFDM Framing, the IFFT block and Guard Interval Insertion, etc.

3. SIMULATION FOR PROTECTION RATIO

3.1. Simulation Method

Here, we describe the method for calculating the PR of the ATSC system from the WiBro system through the computational experiment. For this, the transmitter/receiver of the ATSC system and transmitter of the WiBro system were modeled. The wanted transmitter and receiver use the ATSC 8-VSB system and the interfering transmitter uses the WiBro system. In order to simplify the simulation complexity it modeled sending/receiving signals in the IF band instead of those in the RF band. It was assumed that channel modeling considered one received signal and there's no AWGN. In ATSC receiver, the SER 0.2 of the trellis decoder input signal was used as the TOV

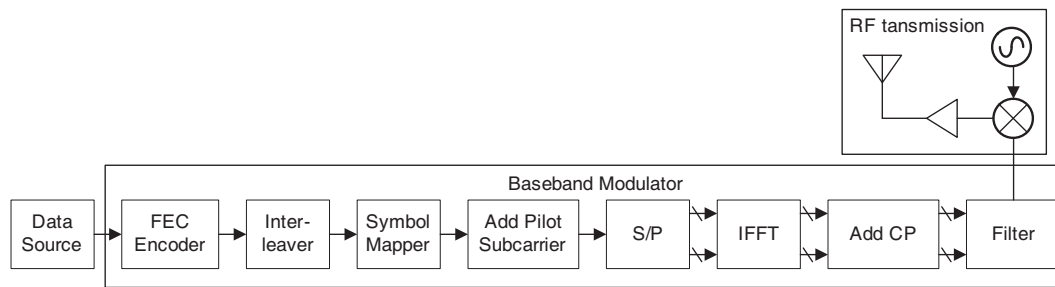


Figure 2: Functional block diagram of WiBro transmitter.

Table 2: Parameters for WiBro system.

Standard	IEEE 802.16e
Duplexing	TDD
Multiple access	OFDMA
Bandwidth	8.75 MHz with 1K-FFT
sampling frequency	8.45 MHz
FFT size	128, 512, 1024, 2048
Data modulation	QAM, 16QAM, 64QAM
Pilot boosting	2.5 dB

performance.

Figure 3 shows the simulation block diagram for the protection ratio calculation for ATSC system from WiBro system. The implemented simulation system comprises 8-VSB transmitter/receiver and WiBro interfering signal transmitter. The transmitting signal moves to 5.38 MHz of the IF band after the Random Data Generator and Up-sampling, Pulse Shaping, and the Modulation of the ATSC 8-VSB system. Next, 8-VSB wanted signal in IF band is added with the WiBro interfering signal, and arrives the receiver end. Fig. 4 shows the wanted/interfering signal modelling. The Δf is the difference between the center frequencies of interfering and desired signal and α is the relative power between the desired and interfering signal. The PR for the ATSC system from the WiBro system is measured by calculating the SER value. Fig. 5 shows the flowchart for calculating the PR.

- 1) Set up the $\Delta f = 0$ and $\alpha = 1$.
- 2) By controlling the α , find the α when the SER value becomes 0.2, that is the protection ratio

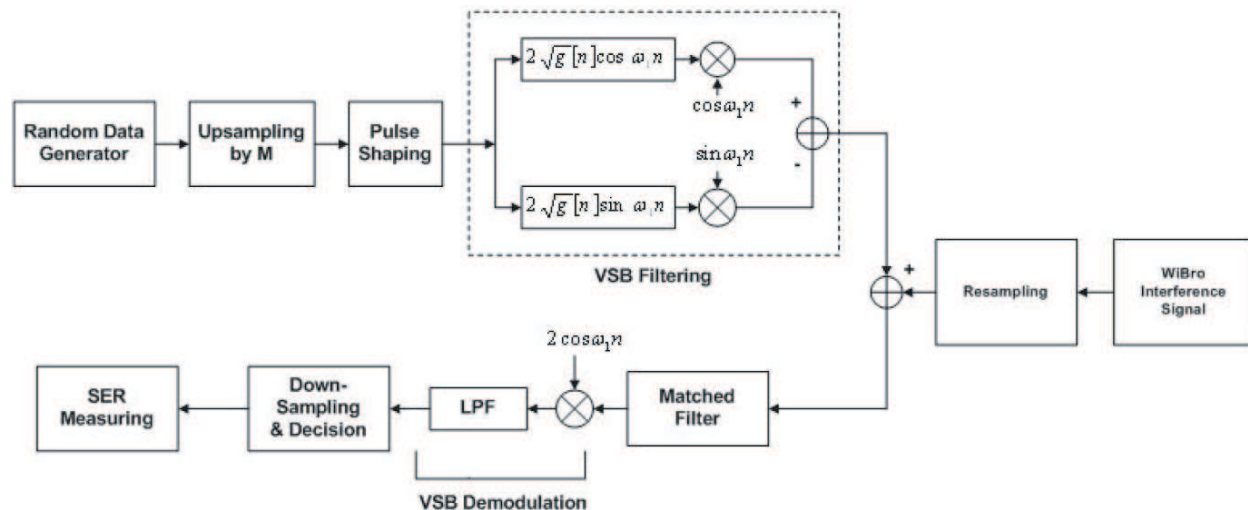


Figure 3: Simulation block diagram.

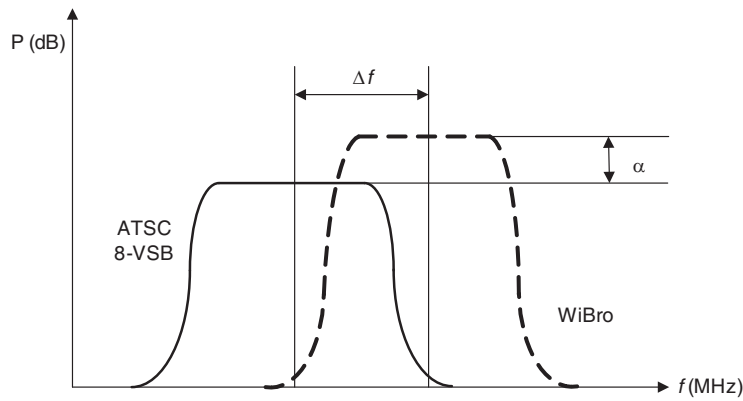


Figure 4: Wanted/interfering signal modelling.

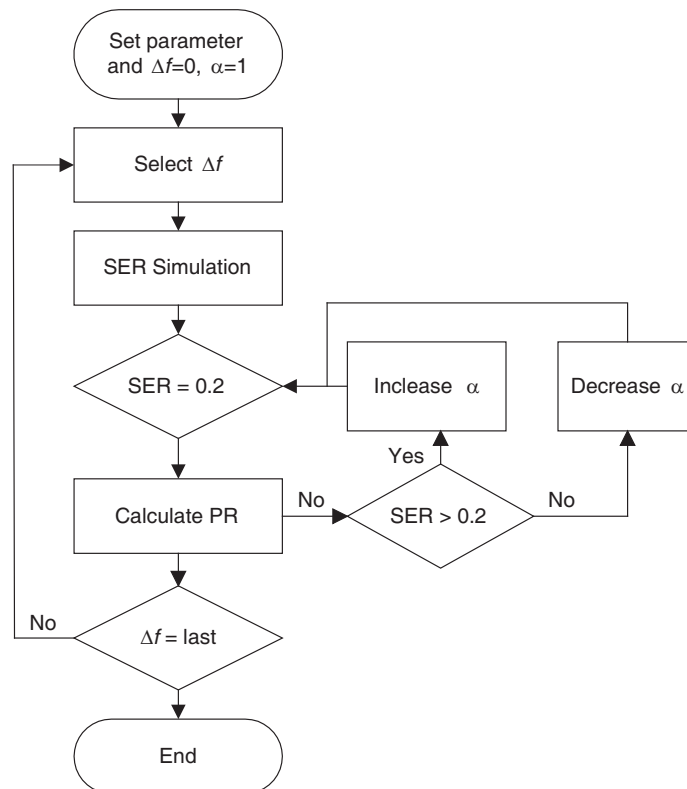


Figure 5: Flowchart for calculating protection ratio.

in co-channel.

- 3) Change the Δf .
- 4) By controlling the α , find the α when the SER value becomes 0.2.
- 5) Repeat 3), 4) until the Δf is final value.

3.2. Simulation Result

Figure 6 shows PR values according to Δf . The maximum bandwidth of WiBro system, 8.75 MHz is larger than 6 MHz of ATSC, and PR value does not change in -1 to $+1$ of Δf . Except for such case, we can confirm that the PR value decreases as the Δf increases. Because the affect of the interference signal is decreased as the Δf increases, although it transmits relatively low power of the signal, SER = 0.2 can be obtained. It is assumed that the cell loading is the 100%.

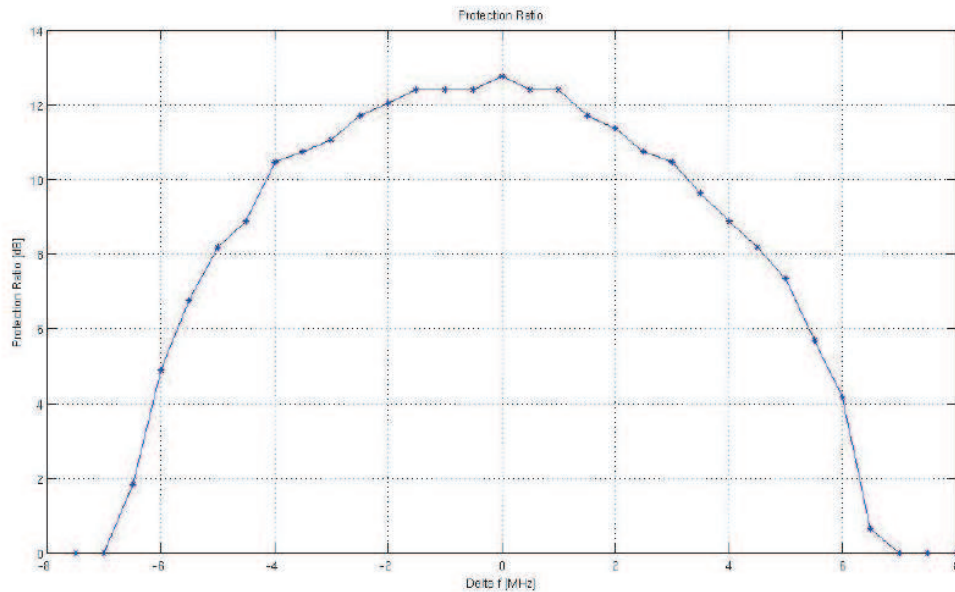


Figure 6: Protection ratios according to Δf [dB].

4. CONCLUSION

In this paper, we proposed the method for calculating the PR among broadcasting systems through the computational experiment, and calculate the PR value of the ATSC broadcasting system from the Mobile WiMAX system such as WiBro in Korea. As the technology develops, the new broadcasting and communication system show up. But whenever the new broadcasting and communication system show up, it is hard to find the PR through a measurement. Therefore, by using this kind of method, it will be able to easily calculate the PR between the new digital broadcasting system and new communication system.

REFERENCES

1. Doc. 11A/6, Digital Terrestrial Television Transmission — User's Needs and System Selection, Feb. 1998.
2. Protection Ratio Experiments and Results for ISDB-T.
3. Ghosh, M. "Blind decision feedback equalization for terrestrial television receivers," *Proceedings of the IEEE*, Vol. 86, No. 10, 2070–2081, Oct. 1998.
4. Doc. A/53, ATSC Digital Television Standard, Sep. 1995.
5. Mathematical Modelling of VSB-Based Digital Television Systems.
6. Doc. Specification for 2.3 GHz Band Portable Internet Service — Physical & Medium Access Control Layer, Dec. 2005.
7. Wu, Y., "Comparison of terrestrial DTV transmission systems: The ATSC 8-VSB, the DVB-T COFDM, and the ISDB-T BST-OFDM," *IEEE Transactions on Broadcasting*, Vol. 46, No. 2, Jun. 2000.

Electric Field Calculation of High Voltage Transmission Line

Yong Lu

Guangxi Electric Power Institute of Vocational Training, Nanning 530007, China

Abstract— Electric field around the overhead transmission line is researched in this paper. Surface charges method is introduced to calculate the surface charges density of every splitting conductor, the surface of every splitting conductor is divided into many arc segments, and linear interpolation is used to express the charges density of every arc segment. In the meantime, partial capacitors between two phases have been studied. An example is presented to illustrate the advantage and the precision of the new given method.

1. INTRODUCTION

Electric field around the overhead transmission line is needed to calculate accurately for design and environment evaluation. Now, there are two calculation methods as following. (1) Equivalent charges method. This method assumes that the charge of transmission line is concentrating on the centre line of the splitting conductors, and can not give the maximums of surface charges density and electric field intensity. (2) Finite element method. This method is not suit for infinite field firstly, then it use potential as solving variable, the quantities such as charges density and electric field intensity need to differentiate with respect to the potential, and will lead to more error. Lastly, surface of the splitting conductors is very difficult to dissect into small triangle element, more triangle elements and calculation time must be need.

Surface charges method for calculating electrostatic field around the double circuit compact overhead transmission line on same tower is given in this paper. This method supposes that the charges of transmission line distribute continuously on the surface of the splitting conductors, and the surface of every splitting conductor is divided into many arc segments, linear interpolation is used to express the charges density of every arc segment. The surface charges density of the splitting conductors is calculated, and maximums of surface charges density and electric field intensity can be determined. Example shows the advantage and the precision of this method.

In the present time, the concept of phase operating capacitor is used to evaluate the imbalance of three phases in power transmission design widely. This concept may have some mistake theoretically, and partial capacitors between two phases are introduced to substitute this concept.

2. SURFACE CHARGES METHOD

Every phase conductor of 500 kV compact overhead transmission line has six splitting conductors which position on a circle with same interval, as shown in Fig. 1.

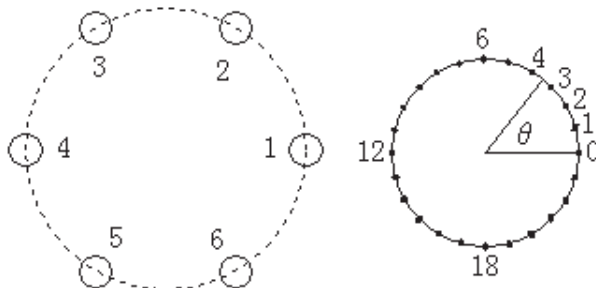


Figure 1: Splitting conductor arrangement and dissection of splitting conductor surface.

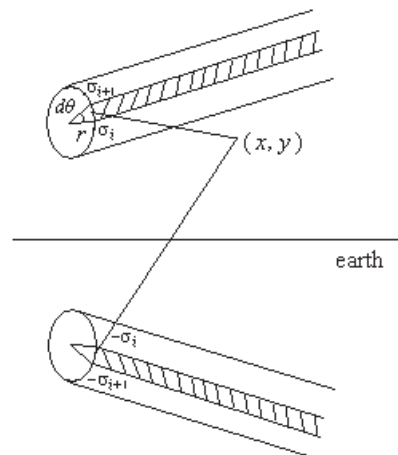


Figure 2: Infinite length line charges and its mirror.

Because power frequency is very low, the electric field around the transmission line can be treated as electrostatic field, and the transmission line is supposed as infinite length linearly, the field can be simplified as a parallel plane field.

Separate the surface of every splitting conductor into 24 arc segments with same length, and number all nodes from 0 to 23, as shown in Fig. 1. Set the surface charges density of every node be σ_i , $i = 0, 1, 2, \dots$, then the surface charges density of any point on the splitting conductor surface which have a angle θ is:

$$\sigma(\theta) = \frac{2\pi(i+1) - \theta}{24} \sigma_i + \frac{\theta - 2\pi i}{24} \sigma_{i+1} \text{ if } \frac{2\pi}{24}i < \theta < \frac{2\pi}{24}(i+1) \quad (1)$$

Thus, the surface charges on splitting conductor can be regarded as many infinite length line charges with a line density $r\sigma(\theta)d\theta$, as shown in Fig. 2.

According to electrostatic field theory, the potential of any point (x, y) produced by infinite length surface charges with an arc segment width and its mirror to the ground is:

$$d\varphi(x, y) = \frac{1}{2\pi\epsilon_0} \int_{\frac{2\pi}{24}i}^{\frac{2\pi}{24}(i+1)} r\sigma(\theta) \ln \frac{R_2}{R_1} d\theta = c_i\sigma_i + c_{i+1}\sigma_{i+1} \quad (2)$$

$$R_1 = \sqrt{(x_0 + r \cos(\theta) - x)^2 + (y_0 + \sin(\theta) - y)^2} \quad (3)$$

$$R_2 = \sqrt{(x_0 + r \cos(\theta) - x)^2 + (y_0 + \sin(\theta) + y)^2} \quad (4)$$

Here: (x_0, y_0) is the coordinates of splitting conductor circle centre, r is radius of splitting conductor, c_i and c_{i+1} are coefficient that can be calculated by actual coordinates.

Double circuits have 36 splitting conductors and two ground lines, there are $N = 38 \times 24 = 912$ nodes and arc segments. The potential of nodes on the ground lines are zero, that is $u_E = 0$, and the potential of nodes on the conductors may be as following according its phase sequence.

$$\begin{cases} u_A = 500 \cos(\beta)/\sqrt{3} \\ u_B = 500 \cos(\beta - 2\pi/3)/\sqrt{3} \\ u_C = 500 \cos(\beta + 2\pi/3)/\sqrt{3} \end{cases} \quad (5)$$

Here β is original phase angle.

Calculate the coefficient of every arc segment to every node using (2), then add up, then we get a linear equations:

$$u = \mathbf{A}\sigma \quad (6)$$

Here: u is the vector of nodes potential, σ is the vector of nodes surface charges density, \mathbf{A} is an $N \times N$ matrix.

The surface charges density of every node can be obtained by solving (6), then the unit length charges of every splitting conductor is:

$$q_S = \sum_{i=0}^{23} \int_{\frac{2\pi}{24}i}^{\frac{2\pi}{24}(i+1)} r\sigma(\theta) d\theta \quad (7)$$

The total charges of each phase per unit length is the sum of charges of six splitting conductor. The potential and electric field intensity of any point can be calculated also.

3. PARTIAL CAPACITORS

In the engineering, operating capacitor per unit length of each phase is used to evaluate the imbalance of the charges on each phase. At the present time, the operating capacitor per unit length of each phase is defined as the ratio of its charges of unit length and potential. Because three phases is not symmetrical geometrically, the partial capacitors between two phases are not equivalent, and this definition of the operating capacitor is not correct theoretically.

Partial capacitors of the overhead transmission line are illustrated in Fig. 3.

Take A phase for example. The Charges of A phase is:

$$q_A = C_{A0}u_A + C_{AB}(u_A - u_B) + C_{CA}(u_A - u_C) \quad (8)$$

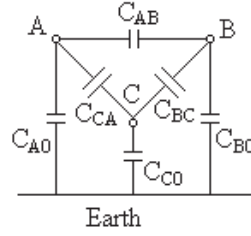


Figure 3: Partial capacitor.

If $C_{AB} = C_{BC} = C_{CA}$, then we get:

$$q_A = (C_{A0} + 3C_{AB})u_A \quad (9)$$

Thus, phase charge is proportionate to phase potential, so we can define the operating capacitor as the ratio of phase charges and phase potential.

But if C_{AB} , C_{BC} and C_{CA} are not equivalent, the charges of any phase is not proportionate to its phase potential, the ratio of phase charges and phase potential will vary along with the original phase angle β , so this definition of the operating capacitor has no meaning.

Partial capacitors are more useful than the operating capacitor. The imbalance of the charges on three phases can be evaluated by the imbalance of partial capacitors.

Partial capacitor can be calculated repeatedly as following by numerical method proposed above:

(1) Set $u_A = u$ and $u_B = u_C = 0$, calculate $C_1 = q_A/u$. (2) Set $u_B = u$ and $u_A = u_C = 0$, calculate $C_2 = q_B/u$. (3) Set $u_C = u$ and $u_A = u_B = 0$, calculate $C_3 = q_C/u$. (4) Set $u_A = u_B = u$ and $u_C = 0$, calculate $C_4 = (q_A + q_B)/u$. (5) Set $u_B = u_C = u$ and $u_A = 0$, calculate $C_5 = (q_B + q_C)/u$. (6) Set $u_A = u_C = u$ and $u_B = 0$, calculate $C_6 = (q_A + q_C)/u$. Here u is an arbitrary number.

These capacitors have a relationship with partial capacitors as:

$$\begin{cases} C_{A0} + C_{AB} + C_{CA} = C_1 \\ C_{B0} + C_{AB} + C_{BC} = C_2 \\ C_{C0} + C_{BC} + C_{CA} = C_3 \\ C_{A0} + C_{BC} + C_{CA} + C_{B0} = C_4 \\ C_{B0} + C_{AB} + C_{CA} + C_{C0} = C_5 \\ C_{A0} + C_{BC} + C_{AB} + C_{C0} = C_6 \end{cases} \Rightarrow \begin{cases} C_{A0} = (C_4 + C_6 - C_2 - C_3)/2 \\ C_{B0} = (C_4 + C_5 - C_1 - C_3)/2 \\ C_{C0} = (C_5 + C_6 - C_1 - C_2)/2 \\ C_{AB} = (C_1 + C_2 - C_4)/2 \\ C_{BC} = (C_2 + C_3 - C_5)/2 \\ C_{CA} = (C_1 + C_3 - C_6)/2 \end{cases} \quad (10)$$

Partial capacitors are six unaltered constants, they are determined only by medium and geometrical parameters of the transmission line, and have no relationship with phase potential.

4. CALCULATING RESULT

Surface charges density on every splitting conductor of A phase is shown in Fig. 4 when the original phase angle β is zero. Surface charges density of the No. 1 and No. 6 splitting conductor of A phase are biggest, then the No. 2 and No. 5 secondly, that of the No. 3 and No. 4 splitting conductor are smallest.

Figure 5 shows the Equipotential line distribution.

Table 1: Partial capacitors (pF/m).

C_1	C_2	C_3	C_4	C_5	C_6
14.0997	14.969	13.9402	21.1835	20.7510	20.7556
C_{A0}	C_{B0}	C_{C0}	C_{AB}	C_{BC}	C_{CA}
6.9512	6.9473	6.6551	7.0131	7.3861	7.3843

Table 1 shows the values of partial capacitors. Due to the shield effect of A phase and C phase, it can be seen that the partial capacitor of C phase to earth is smaller than the other two.

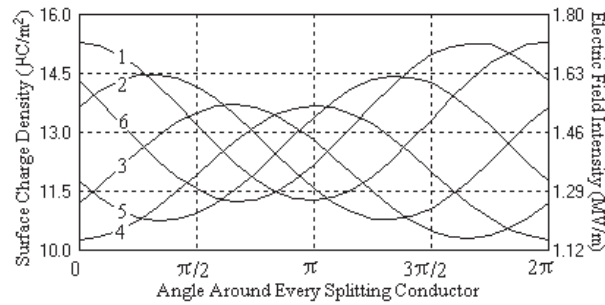


Figure 4: Surface charges density of the splitting conductors.

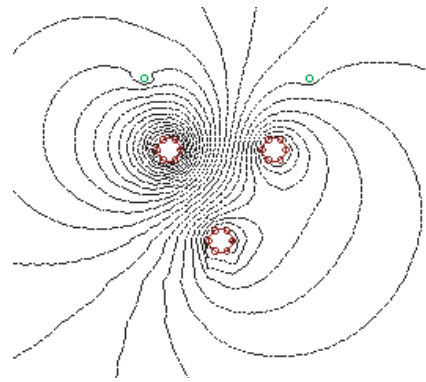


Figure 5: Equipotential line distribution.

5. CONCLUSION

Surface charges method base on strictly that the charges distribute continuously on the surface of every splitting conductor, and use linear interpolation to express the surface charges density of every arc segment. This new method is more adaptive to calculate the charges distribution on the surface of conductors.

The current concept of operating capacitors has some mistake theoretically, and partial capacitors are introduced to instead of them. Partial capacitors are more useful than operating capacitor in engineering application.

REFERENCES

1. Lee, B. Y. and J. K. Park, "An effective modelling method to analyze electric field around transmission Lines and substations using a generalized finite lines charge," *IEEE on PD*, Vol. 12, No. 3, 1143, 1997.
2. Florkowska, B., A. Jaekowicz-Korczynski, and M. Timler, "Analysis of electric field distribution around the high-voltage overhead transmission lines with an ADSS fiber-optic cable," *IEEE Tran. on PD*, Vol. 19, No. 3, 1183–1189, 2004.
3. Zhang, Q. C., J. J. Ruan, and J. H. Yu, "Mathematical models for electric field under high voltage overhead line," *High Voltage Engineering*, Vol. 26, No. 1, 19–21, 2000.

Coupling onto the Two-wire Transmission Line Enclosed in Cavities with Apertures

Ying Li, Gu-Yan Ni, Jian-Shu Luo, Ji-Yuan Shi, and Xu-Feng Zhang

College of Science, National University of Defense Technology
Changsha 410073, China

Abstract— In this paper, we consider the field penetration through apertures and their coupling with a two-wire transmission line. By the Modal Green's Function with the method of moment (MoM) and Baum-Liu-Tesche (BLT) equation, a semi-analytical solution is obtained for the load response of the two-wire transmission line in the cavity.

1. INTRODUCTION

Conducting wires located close to an aperture are specifically vulnerable to the external electromagnetic pulse (EMP) excitations. The coupled cable energy is transmitted further into other internal circuitry which could damage critical components. To protect a system against such EMP threats, vulnerability studies must be carried out to understand the interaction processes. Such a study will also provide the necessary information needed to harden electrical network systems for counter measures [1–10].

Electromagnetic interaction problems on very large and complex system, such as an aircraft, can be simulated through codes based on electromagnetic topology. An important element of topological analysis is the determination of a mechanism to represent external-internal coupling through a small aperture and the subsequent propagation process. By combining methodologies suggested earlier [1], an equivalent source relating the electromagnetic coupling at the exterior surface and the transfer function through free space generated by it can be created by assuming an imaginary transmission line as a source of aperture radiation [2, 3].

In this paper, on the aperture, basing on the equivalence principle, we obtain the equivalence source, which similarly shown in Ref. [4], by a semi-analytical approach using the Modal Green's Function with the method of moment (MoM). Then the BLT equation is used to compute the load response of two-wire transmission line in the cavity.

2. FORMULATIONS OF THE INTERIOR ELECTROMAGNETIC FIELD

Consider a rectangular cavity with a slot aperture shown in Figure 1 illuminated by a harmonic plane wave. This field is described by angles of incidence ψ and ϕ , as well as a polarization angles α , which defines the E-field vector direction relative to the vertical plane of incidence.

We introduce the equivalent magnetic current

$$\vec{M} = \vec{E} \times \hat{z} = \hat{x}E_y - yE_x \quad (1)$$

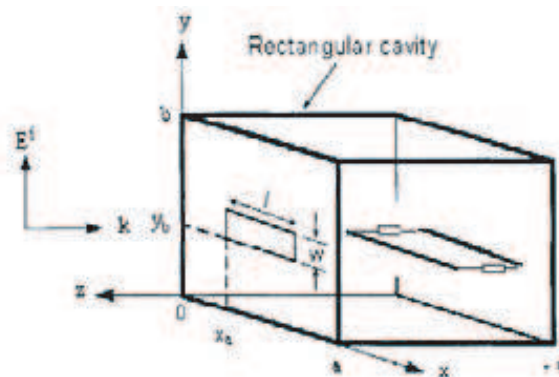


Figure 1: Cavity geometry enclosing two-wire transmission line.

just to exterior at $z = 0^+$. To ensure continuity of the tangential electric field, the currents on the interior of the aperture (at $z = 0^-$) must equal to the negative of those at $z = 0^+$, namely,

$$\bar{M}' = \bar{E}^b \times (-\hat{z}) = -\bar{M}, \quad (2)$$

where \bar{E}^b is the electric field interior to the cavity.

To solve for the unknown current \bar{M} , we shall enforce continuity of the tangential magnetic field across the aperture. Then, we have

$$\hat{z} \times [\bar{H}^a(\bar{M}) + \bar{H}^i] = \hat{z} \times \bar{H}^b(\bar{M}'), \quad z = 0, \quad (3)$$

where \bar{H}^a refer to the exterior scattered magnetic field, and \bar{H}^b to a corresponding magnetic field interior to the cavity.

The exterior scattered field can be expressed as the radiation caused by the equivalent magnetic current \bar{M} , say,

$$\bar{H}^a(\bar{r}) = -jk_0 Y_0 \int_S 2\bar{M}(\bar{r}') \cdot \bar{\Gamma}_0(\bar{r}; \bar{r}') ds', \quad (4)$$

where S denotes the surface of the aperture and $\bar{\Gamma}_0(\bar{r}; \bar{r}')$ is the free space dyadic Green's function given by

$$\begin{aligned} \bar{\Gamma}_0(\bar{r}; \bar{r}') &= \left(\bar{I} + \frac{1}{k_0^2} \nabla \nabla \right) \frac{e^{-jk_0 |\bar{r} - \bar{r}'|}}{4\pi |\bar{r} - \bar{r}'|}, \\ |\bar{r} - \bar{r}'| &= \sqrt{(x - x')^2 + (y - y')^2}. \end{aligned} \quad (5)$$

The interior field can be formulated as the radiation due to \bar{M} on S . Using the available dyadic Green's functions for the cavity, we express the interior field as

$$\bar{E}^b(\bar{M}') = - \int_S \nabla \times \bar{G}_{HM} \cdot \bar{M}' ds', \quad (6a)$$

$$\bar{H}^b(\bar{M}') = -j\omega\epsilon \int_S \bar{G}_{HM} \cdot \bar{M}' ds', \quad (6b)$$

where the dyadic Green's function is defined as

$$\begin{aligned} \bar{G}_{HM} &= -\frac{1}{k_0^2} \hat{z} \hat{z} \delta(\bar{R} - \bar{R}') - \sum_{m,n} \frac{2(2 - \delta_{mn})}{ab(k_{xm}^2 + k_{yn}^2) k_{mn} \sin(k_{mn}c)} \\ &[\bar{M}_{oe}(z+c)\bar{M}'_{oe}(0) + \bar{N}_{eo}(z+c)\bar{N}'_{eo}(0)], \end{aligned} \quad (7)$$

where the vector wave functions are given in Ref. [4], δ_{mn} ($= 1$ for $m = 0$ or $n = 0$, and 0 otherwise) denotes the Kronecker delta. As usual, $k_{xm} = \frac{m\pi}{a}$, $k_{yn} = \frac{n\pi}{b}$, and $k_{mn} =$

$$\begin{cases} -j\sqrt{k_{xm}^2 + k_{yn}^2 - k_b^2}, & k_b < \sqrt{k_{xm}^2 + k_{yn}^2}, \\ \sqrt{k_b^2 - k_{xm}^2 - k_{yn}^2}, & k_b > \sqrt{k_{xm}^2 + k_{yn}^2}. \end{cases}$$

The equivalent magnetic current components now are expanded as

$$\begin{aligned} M_x(x, y) &= \sum_{p=1}^{P-1} \sum_{q=1}^Q M_{xpq} T_p(x - x_a) P_q(y - y_b), \\ M_y(x, y) &= \sum_{p=1}^P \sum_{q=1}^{Q-1} M_{ypq} P_p(x - x_a) T_q(y - y_b), \end{aligned} \quad (8)$$

where x_a and y_b denote the lower left hand corner of the slot, and $T_s(t)$ and $P_s(t)$ denote the triangular and pulse functions (see Ref. [10]).

Substituting (7) and (8) into (6), by the aperture discretization, we obtain

$$H_y^b = \sum_{m,n} \left[-k_{xm} A_{mn} + \frac{k_{yn} k_{mn}}{k_b^2} B_{mn} \right] \cos(k_{xm} x) \sin(k_{yn} y) \cos(k_{mn} (z + c)), \quad (9a)$$

$$E_z^b = - \sum_{m,n} \frac{j Z_b}{k_b} (k_{xm}^2 + k_{yn}^2) A_{mn} \sin(k_{xm} x) \sin(k_{yn} y) \cos(k_{mn} (z + c)), \quad (9b)$$

in which

$$A_{mn} = - \frac{2j k_b Y_b}{k_{mn} a b \sin(k_{mn} c) (k_{xm}^2 + k_{yn}^2)} [\varepsilon_n k_{yn} I_x^{mn} - \varepsilon_m k_{xm} I_y^{mn}], \quad (10a)$$

$$B_{mn} = - \frac{2j k_b Y_b}{a b \sin(k_{mn} c) (k_{xm}^2 + k_{yn}^2)} [\varepsilon_n k_{xm} I_x^{mn} + \varepsilon_m k_{yn} I_y^{mn}], \quad (10b)$$

where

$$\varepsilon_s = \begin{cases} 1, & s = 0, \\ 2, & s > 0 \end{cases} \quad (11)$$

and

$$I_x^{mn} = \sum_{p=1}^{P-1} \sum_{q=1}^Q M_{xpq} \frac{1}{k_{xm}^2 k_{yn} \Delta x} \{ \sin [k_{xm} (x_a + (p-1) \Delta x)] - 2 \sin [k_{xm} (x_a + p \Delta x)] \\ + \sin [k_{xm} (x_a + (p+1) \Delta x)] \} \cdot \{ \sin [k_{yn} (y_b + (q-1) \Delta y)] - \sin [k_{yn} (y_b + q \Delta y)] \}, \quad (12a)$$

$$I_y^{mn} = \sum_{p=1}^P \sum_{q=1}^{Q-1} M_{ypq} \frac{1}{k_{yn}^2 k_{xm} \Delta y} \{ \sin [k_{yn} (y_b + (q-1) \Delta y)] - 2 \sin [k_{yn} (y_b + q \Delta y)] \\ + \sin [k_{yn} (y_b + (q+1) \Delta y)] \} \cdot \{ \sin [k_{xm} (x_a + (p-1) \Delta x)] - \sin [k_{xm} (x_a + p \Delta x)] \}, \quad (12b)$$

We obtain the formulations of the interior z-component E-field and y-component H-field in which M_{xpq} , M_{ypq} are constants to be determined.

In accordance with the method of weighted residuals [9], the integral equation to be solved for M_{xpq} , M_{ypq} is

$$\int_S \hat{z} \times [\bar{H}^a(\bar{M}) - \bar{H}^b(\bar{M}')] \cdot \bar{W} ds' = - \int_S \hat{z} \times \bar{H}^i \cdot \bar{W} ds', \quad z = 0, \quad (13)$$

where \bar{W} is a weighting function, $\bar{H}^a(\bar{M})$ and $\bar{H}^b(\bar{M}')$ are given by (4) and (6), respectively. To discretize (13), the corresponding weighing function components are given by

$$W_{xp'q'}(x, y) = P_{p'}(x - x_a) T_{q'}(y - y_b), \\ W_{yp'q'}(x, y) = T_{p'}(x - x_a) P_{q'}(y - y_b). \quad (14)$$

Substitution of (8) and (14) into (13) yields a system:

$$[Y^{a+b}] [M] = [C^{inc}]. \quad (15)$$

The solution of this system (15) yields the coefficients M_{xpq} , M_{ypq} in the magnetic current. There are some novel works for the system (15) (see Ref. [4] and Ref. [10]).

3. THE BLT EQUATION FOR THE TWO-WIRE TRANSMISSION LINE

The BLT equations provide a compact expression for the load current and voltage, and can be used for studying the behavior of the terminal responses for many different types of excitation fields [11, 13].

We assume the case of a lossless two-wire line which is illuminated by a coupling EM field and the direction of the two-wire transmission line along the y direction as illustrated in Figure 2. So we can let $y = y_0$.

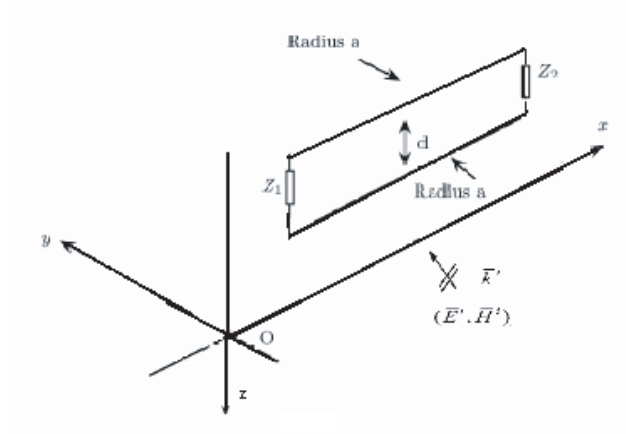


Figure 2: Isolated two-wire line excited by the interior field.

Denote L the length of the line, Z_1 and Z_2 the load impedances at $x = x_0$ and $x = x_0 + L$ ends, respectively, and Z_c the characteristic impedance of the line. Let $\rho_i = \frac{Z_i - Z_c}{Z_i + Z_c}$ for $i = 1, 2$. The separation of the wires d is large compared with radius r_a ($d \gg r_a$). Considering the total voltage (Taylor) formulation, at the end of the line, the induced voltages and currents can be expressed in matrix form as

$$\begin{bmatrix} I(x_0) \\ I(x_0 + L) \end{bmatrix} = \frac{1}{Z_c} \begin{bmatrix} 1 - \rho_1 & 0 \\ 0 & 1 - \rho_2 \end{bmatrix} \begin{bmatrix} -\rho_1 & e^{\gamma L} \\ e^{\gamma L} & -\rho_2 \end{bmatrix}^{-1} \begin{bmatrix} S_1 \\ S_2 \end{bmatrix}, \quad (16)$$

$$\begin{bmatrix} V(x_0) \\ V(x_0 + L) \end{bmatrix} = \begin{bmatrix} 1 + \rho_1 & 0 \\ 0 & 1 + \rho_2 \end{bmatrix} \begin{bmatrix} -\rho_1 & e^{\gamma L} \\ e^{\gamma L} & -\rho_2 \end{bmatrix}^{-1} \begin{bmatrix} S_1 \\ S_2 \end{bmatrix}. \quad (17)$$

The source vector is given by

$$\begin{bmatrix} S_1 \\ S_2 \end{bmatrix} = \begin{bmatrix} \frac{1}{2} \int_{x_0}^{x_0+L} e^{\gamma x} [V'_{S_1}(x) + Z_c I'_{S_1}(x)] dx \\ -\frac{1}{2} \int_{x_0}^{x_0+L} e^{\gamma(L-x)} [V'_{S_1}(x) - Z_c I'_{S_1}(x)] dx \end{bmatrix}, \quad (18)$$

in which the distributed voltage and current sources V'_{S_1} and I'_{S_1} are given by

$$V'_{S_1}(x) = -j\omega\mu_0 \int_{z_0}^{z_0+d} H_y^b(x, y_0, z) dz, \quad (19a)$$

$$I'_{S_1}(x) = -j\omega C' \int_{z_0}^{z_0+d} E_z^b(x, y_0, z) dz, \quad (19b)$$

where

$$C' = \frac{\pi\epsilon}{\ln(d/r_a)} (d \gg r_a). \quad (20)$$

4. THE LOAD RESPONSE OF TWO-WIRE TRANSMISSION LINE

Substituting (9) into (19), we get the following voltage and current sources formulations:

$$V'_{S_1}(x) = -j\omega\mu_0 \sum_{m,n} \left[-\frac{k_{xm}}{k_{mn}} A_{mn} + jY_b \frac{k_{yn}}{k_b} B_{mn} \right] C_{mn} \cos(k_{xm}x), \quad (21a)$$

$$I'_{S_1}(x) = \omega C' \sum_{m,n} Z_b \left(\frac{1}{k_{mn}} - \frac{1}{k_b} \right) A_{mn} C_{mn} \sin(k_{xm}x), \quad (21b)$$

with

$$C_{mn} = \sin(k_{yn}y_0) [\sin(k_{mn}(z_0 + d + c)) - \sin(k_{mn}(z_0 + c))] \quad (22)$$

Substituting (21) into (18), we have

$$\begin{aligned}
 S_1 = & \frac{1}{2}\omega \sum_{m,n} C_{mn} \{ -D_{mn}e^{\gamma x_0} [-\gamma \cos(k_{xm}x_0) - k_{xm} \sin(k_{xm}x_0)] \\
 & + e^{\gamma L} [\gamma \cos(k_{xm}(x_0 + L)) + k_{xm} \sin(k_{xm}(x_0 + L))] \\
 & + E_{mn}e^{\gamma x_0} [k_{xm} \cos(k_{xm}x_0) - \gamma \sin(k_{xm}x_0)] \\
 & + e^{\gamma L} [-k_{xm} \cos(k_{xm}(x_0 + L)) + \gamma \sin(k_{xm}(x_0 + L))] \}, \quad (23a)
 \end{aligned}$$

$$\begin{aligned}
 S_2 = & \frac{1}{2}\omega \sum_{m,n} C_{mn} \{ D_{mn}e^{-\gamma x_0} [e^{\gamma L} [\gamma \cos(k_{xm}x_0) - k_{xm} \sin(k_{xm}x_0)] \\
 & - \gamma \cos(k_{xm}(x_0 + L)) + k_{xm} \sin(k_{xm}(x_0 + L))] \\
 & + E_{mn}e^{-\gamma x_0} [e^{\gamma L} [k_{xm} \cos(k_{xm}x_0) + \gamma \sin(k_{xm}x_0)] \\
 & - k_{xm} \cos(k_{xm}(x_0 + L)) - \gamma \sin(k_{xm}(x_0 + L))] \}, \quad (23b)
 \end{aligned}$$

with

$$D_{mn} = \frac{j\mu_0}{\gamma^2 + k_{xm}^2} \left[-\frac{k_{xm}}{k_{mn}} A_{mn} + jY_b \frac{k_{yn}}{k_b} B_{mn} \right] \quad (24)$$

and

$$E_{mn} = \frac{C' Z_c Z_b}{\gamma^2 + k_{xm}^2} \left(\frac{1}{k_{mn}} - \frac{1}{k_b} \right) A_{mn}, \quad (25)$$

where A_{mn} , B_{mn} and C_{mn} are given in (10) and (22), respectively.

Combining the Formulations (16), (17) and (23), we can obtain the expressions of the load currents and voltages.

5. CONCLUSION

For the issue of the field penetration through apertures and their coupling with a two-wire transmission line, we use the Modal Green's Function with the method of moment (MoM) and Baum-Liu-Tesche (BLT) equation to solve the load response of the two-wire transmission line in the cavity with a plane-wave excitation. This method can also be used for electromagnetic interaction problems on more complex system.

ACKNOWLEDGMENT

This work was supported by China Postdoctoral Science Foundation (No. 20080431399) and the National Natural Science Foundation of China (No. 10871231).

REFERENCES

1. Yang, F. C. and C. E. Baum, "Use of Matrix norms of interaction supermatrix blocks for specifying electromagnetic performance of subshields," *Interaction Notes*, Vol. 427, 1983.
2. Kirawanich, P., R. Gunda, N. Kranthi, J. C. Kroenung, and N. E. Islam, "Methodology for interference analysis using electromagnetic topology techniques," *Appl. Phys. Lett.*, Vol. 84, No. 15, Apr. 2004.
3. Nanevich, J. E., E. F. Vance, W. Radasky, M. A. Uman, G. K. Soper, and J. M. Pierre, "EMP susceptibility insights from aircraft exposure to lightning," *IEEE Transactions on Electromagnetic Compatibility*, Vol. 30, 463–472, Nov. 1988.
4. Yang, T., "Coupling onto radio frequency components enclosed within canonical structures," A dissertation for the Ph.D. in the university of Michigan, 2006.
5. Li, M., J. L. Drewniak, S. Radu, J. Nuebal, T. H. Hubing, R. E. DuBroff, and T. P. VanDoren, "An EMI estimate for shielding-enclosure evaluation," *IEEE Transactions on Electromagnetic Compatibility*, Vol. 43, 295–304, 2001.
6. Lail, B. A. and S. P. Castillo, "Coupling through narrow slot apertures to thin-wire structures," *IEEE Transactions on Electromagnetic Compatibility*, Vol. 42, 276–283, 2000.

7. Thomas, D. W. P., A. C. Denton, T. Benson, C. Christopoulos, J. E. Dawson, A. Marvin, S. J. Potter, and P. Sewell, "Model of the electromagnetic fields inside a cuboidal enclosure populated with conducting planes or printed circuit boards," *IEEE Transactions on Electromagnetic Compatibility*, Vol. 43, 161–169, 2001.
8. Azaro, R., S. Caorsi, M. Donelli, and G. L. Gragnani, "A circuital approach to evaluating the electromagnetic field on rectangular apertures backed by rectangular cavities," *IEEE Transactions on Microwave Theory and Techniques*, Vol. 50, 2259–2266, 2002.
9. Barkeshli, K. and J. L. Volakis, "Electromagnetic scattering from an aperture formed by a rectangular cavity recessed in a ground plane," *Journal of Electromagnetic Waves and Applications*, Vol. 5, 715–734, 1991.
10. Jin, J.-M. and J. L. Volakis, "TM Scattering by an inhomogeneously filled aperture in a thick conducting plane," *IEE proceedings*, Vol. 137, No. 3, Jun. 1990.
11. Tesche, F. M., M. V. Ianoz, and T. Karlsson, *EMC Analysis Methods and Computational Models*, John Wiley and Sons, New York, 1997.
12. Butler, C., Y. Rahmat-Samii, and R. Mittra, "Electromagnetic penetration through apertures in conducting surfaces," *IEEE Transactions on Electromagnetic Compatibility*, Vol. 20, No. 1, Feb. 1978.
13. Ni, G.-Y., L. Yan, and N.-C. Yuan, "Time-domain analytic solutions of two-wire transmission line excited by a plane-wave field," *Chinese Physics B*, Vol. 17, No. 10, Oct. 2008.

Surface Mounting Packaging of SAW Low-loss High Stop-band Rejection Filter

Peng Fu and Xiaoqin Hao

Nanjing Research Institute of Electronic Technology, China

Abstract— The assembly technology which is used in SAW filter with surface mounting package in this paper. The problem of the stop-band response's decay is simulated in HFSS and solved. A harmless test fixture for the SMD mass-production was also designed and manufactured. This experiment is important for the enhancement of SAW filter's post-packaging stop band rejection feature, and valuable for miniaturization for receiver on antenna.

1. INTRODUCTION

A special type low loss SAW filter chip (about $4 \times 5 \times 0.5 \text{ mm}^3$) was used to be packaged in a cylinder cap ($\Phi 15.8 \text{ mm} \times 5 \text{ mm}$, pins were not measured). For a new application in compact chassis assemblies, it would be packaged into SMT packaging ($6.5 \times 13.3 \times 1.8 \text{ mm}^3$). This chip worked below 500 MHz and had a bandwidth about 2%, insert loss about 4 dB, stop-band rejection above 50 dB. It was a low-loss high stop-band rejection SAW filter.

In the compact packaging process, the stop-band response was severely degraded. There was about 30 dB's difference between the close in selective before packaging and after packaging. In the same time, needed a new test fixture to test it promptly and harmlessly.

2. SMD PACKAGING PROBLEM'S SIMULATION AND SOLUTION

The electrodes of this chip were designed for the cylinder cap ($\Phi 15.8 \text{ mm}$), its location and the size could not fit for the small SMD. So the electrical performance (especially stop-band performance) was degraded. The outline and internal bonding diagram is shown. (Fig. 1)

It was important that rebuilding the model in software simulation environment for solving this problem properly. There were a lot of advantages to solve this problem in FEM. So HFSS software (Ansoft company) was chosen to be the simulation environment to simulate this bonding and packaging. According to the actual mounting/measuring condition of the SMD, a coaxial-to-microstrip adaptor model was setup just like in the real test fixture to support those structure would not influence the result of simulation and consideration (see Fig. 2). The frequency bandwidth was much wider than the filter worked, so that the far off electrical performance was in sight and a action which ignoring the degrading of the far-off selective would not be chosen. After simulation, the pads' wrong position caused too long bonding wires orthogonal to the signal transmission route was defined to the major reason (see Fig. 3, the left one is the result of the long orthogonal bonding wires and the right one is the result of the short parallel bonding wires).

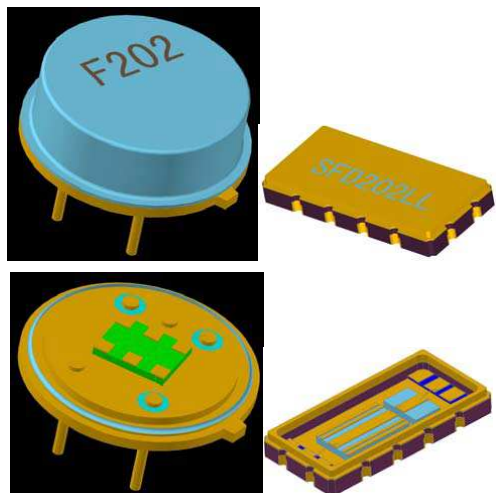


Figure 1: Diagram of two types of packaging.

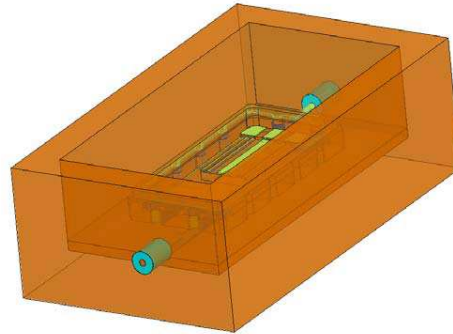


Figure 2: Simulation model in HFSS.

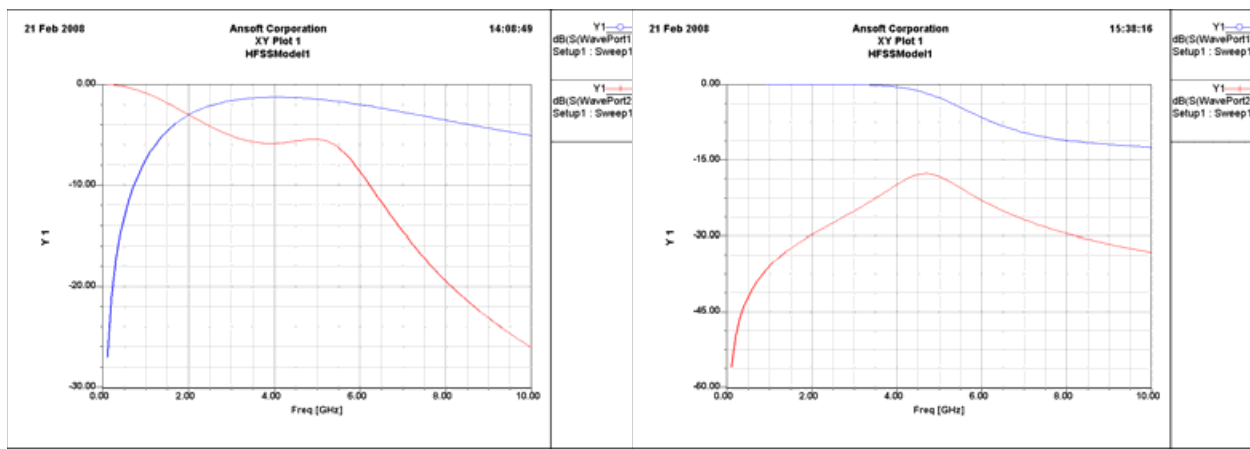


Figure 3: The results between the different chip and bonding wires.

According to this result, the chip’s layout was changed to ensure the signal transmission in chip parallel to the packaging. At the same time, the grounding area was extended along the extended pads. After this action, stop-band rejection (measurement results) was upgraded just like in the simulations. The two layouts were shown in Fig. 4, and the measurement results were shown in Fig. 5.

3. MULTI-ACCESS HARMLESS TEST FIXTURE

The process of testing and measuring in a large mass should be prompt and harmless. At the same time, because there are too many devices had similar packaging, the test fixture should be general in some special area. A multi-access harmless test fixture was designed and manufactured (Fig. 5).

There were those several parts of this test fixture: The first was a metal frame 4 millimeter thick, which had two mounting base of SMA-KFD19 type coaxial-microstrip RF adaptor. There were two moveable metal frames inside the large one. And they were settled on the large frame (moveable in a special range) with 2 screws per side, also were adapted to another products. There were holes in the four corners of the small metal frames to fix the printed circuit boards which hold

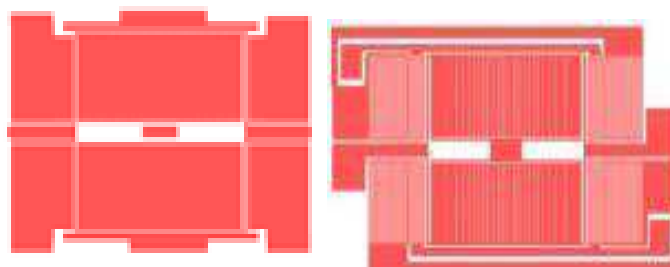


Figure 4: Original chip layout (left) and upgraded chip layout (right).

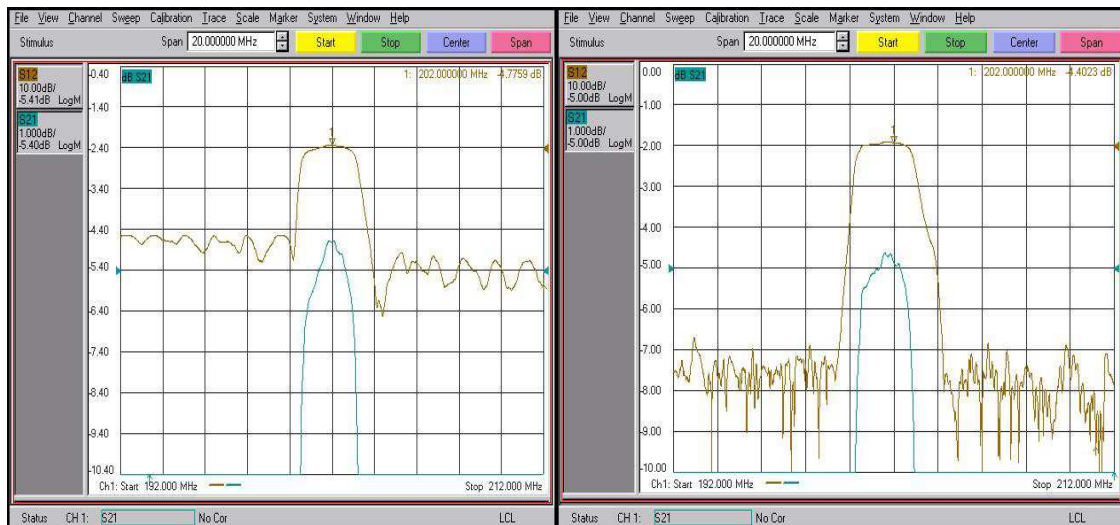


Figure 5: Original measurement results (left) and upgraded measurement results (right).

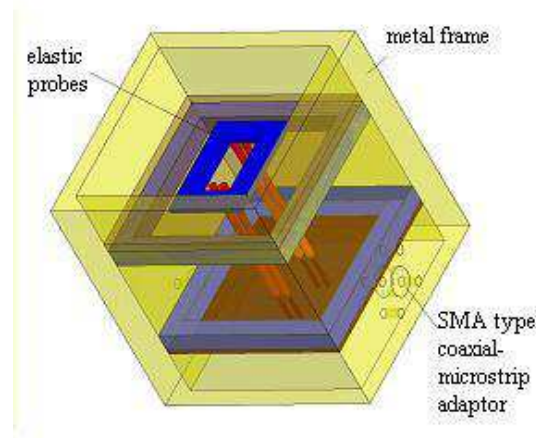


Figure 6: Multi-access harmless test fixture (left) and the head of the probe (right).

on the elastic metal probes and transmit the RF signal. Four metal probes were 2 signals and two grounds. Standing grounded sheets were setup between two signal probes for shielding. The top of the probe was a moveable. The length of the and the shape of the top were optional. To ensure a expected touching, springs were long enough and the tips were cylinders with cave (See Fig. 5). It operated well in actual testing.

4. CONCLUSIONS

During the modifying of Low-Loss High Stop-Band Rejection SAW filter's packaging, stop-band rejection's decay was simulated in HFSS software and solved according to the results. The filter turned smaller and lighter for miniaturization. And a prompt harmless test fixture for mass-production was designed and manufactured.

REFERENCES

1. Harper, C. A., *Electronic Packaging & Interconnection Handbook*, Ed. 2, McGraw-Hill, 1997.
2. *Electro-Magnetics and Calculation of Fields*, Ed. 2, Springer-Verlag, 1999.

Design of a Compact Narrow Band Pass Filter Using the Rectangular CSRRs

Dong-Muk Choi, Dang-Oh Kim, and Che-Young Kim

School of Electrical Engineering and Computer Science, Kyungpook National University
Sankyuk-dong, Puk-gu, Daegu 702-701, Korea

Abstract— In this paper, a design method of the compact narrow band pass filter on the microstrip board is proposed using the complementary split-ring resonators (CSRRs). The design technique of this filter is based on cascading filter stages consisting of the combination of rectangular CSRRs, capacitive gaps between patches, and inductive grounded stubs with the meander configuration. The first design key is the introduction of the shunt connected wire in the structure, which allows us to improve frequency selectivity and the out-of-band rejection of the filter. The second feature makes an addition of gap capacitance resulting in the desired phase shift. By these means, it was possible to get the nearly symmetric frequency responses, adjustable bandwidths, and compact sizes. And also excellent characteristic of the out-of-band rejection is achieved in contrast to the conventional filter design technique. The frequency selectivity at both band edges is high enough with approximately symmetric transition bands. Cell lengths are smaller than the signal wavelength realizing a compact filter size. The results of the frequency response measured on the fabricated band pass filter substrate show satisfactory agreement with the simulated frequency responses by the HFSS in the region of interest. The newly proposed filter by this article can be found its application on the design of compact filters with planar circuit technology.

1. INTRODUCTION

Recent proliferation of mobile communication technology has created a demand to accommodate a lot of communication channels. However, this requirement leads to interference problem between channels and results in severe performance degradation so that it is essential to design the band pass filters having a high frequency selectivity and sharp cutoff at the band edge. In order to realize the filter with these features, the generalized approach is to design the filter with the multiple poles. However, introducing the multiple poles inevitably cause the insertion loss and signal distortion as well as rise of cost and circuit pattern size. For this reason, a key challenge of filter design is to maintain good frequency selectivity even in lower order filter size. Efforts to accomplish this requirement have been investigated using the resonator structures implemented with the microstrip lines to meet the miniaturization needs [1–4]. However, the resonators with the microstrip lines have a low quality factor and a spurious response due to harmonic components which cause poor stop band characteristic spreading over the broad band. To reduce these unwanted harmonic components, many design techniques are presented and studied [5, 6].

To cope with the mentioned problems, recently the filter with CSRRs has been introduced and its usefulness is tested [7–10]. CSRRs allow the filter to have not only the high quality factor at its resonant frequency but also to have a reduced dimension. The main goal of this paper is to design the narrow band pass filter having excellent frequency selectivity together with compact size with the help of CSRRs. This goal may be completed by using the rectangular CSRRs etched on the ground plane, combined with two series gaps and two shunt stubs connected with the metallic meander wires grounded by means of vias. By adjusting inductive grounded stubs and capacitive gaps between patches, we can obtain the filter with excellent frequency selectivity and the out-of-band rejection characteristics.

2. FILTER TOPOLOGY AND DESIGN METHOD

Generalized band pass filter shown Figure 1 is constructed with the cascaded inverters alternating with shunt-connected resonators tuned at the center frequency f_0 [11].

The basic cell of the proposed filter is described in Figure 2(a). This cell consists of a rectangular CSRRs etched on the ground plane, combined with two series gaps and two shunt stubs connected metallic wires, which are grounded by means of vias. Figure 2(b) shows the equivalent-circuit model on this basic cell. CSRRs are modeled in terms of an LC resonant tank (L_r and C_r), while their coupling to the line is understood by the capacitance C_c , which depends on the portion of the

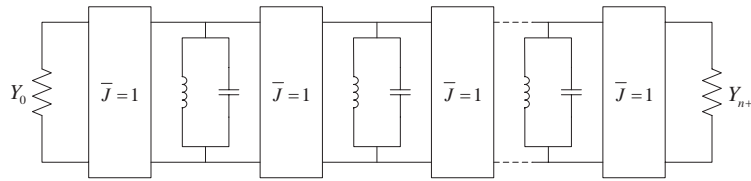


Figure 1: Generalized band pass filter network with admittance and shunt resonators.

inter-metallic region between the series gaps that lies face-to-face to the metal inside the inner slot of CSRRs. The grounded stubs with meander structure are represented by a shunt inductance L_p , while C_s accounts for the series gaps. The introduction of the shunt connected wires in the structure is a consequence of the need to improve the upper transition band and the out-of-band rejection of the filter. Another key advantage of the structure of Figure 2 is related to the admittance inverter. Since ninety degree phase shift is required to realize the admittance inverter, a small gap is etched between patches. This intended small gap provides the desired phase shift what the admittance inverter would need in its realization, otherwise the lengthy transmission line might be used. Due to the intentionally etched gaps, the additional device reduction could be furthermore achieved because these gaps played the role of transmission line.

With the aid of equivalent circuit shown in Figure 2, we can design band pass filter having the center frequency $f_0 = 1$ GHz and fractional bandwidth (FBW) being 5%, respectively.

At the center frequency, the phase difference between the input and output ports of the basic cell is $\theta = 90^\circ$ and Bloch impedance (Z_B) is given by the reference impedance at the ports as Z_0 [8, 10]. The phase θ and impedance Z_B for the periodic structure formed by cascading the basic cell seen in Figure 2(b) are given by

$$\cos \theta = 1 + \frac{Z_s(j\omega)}{Z_p(j\omega)} \quad (1)$$

$$Z_B = \sqrt{Z_s(j\omega) [Z_s(j\omega) + 2Z_p(j\omega)]} \quad (2)$$

The port conditions of the basic cell at f_0 lead us to get $Z_s = -jZ_0$ and $Z_p = jZ_0$. From these

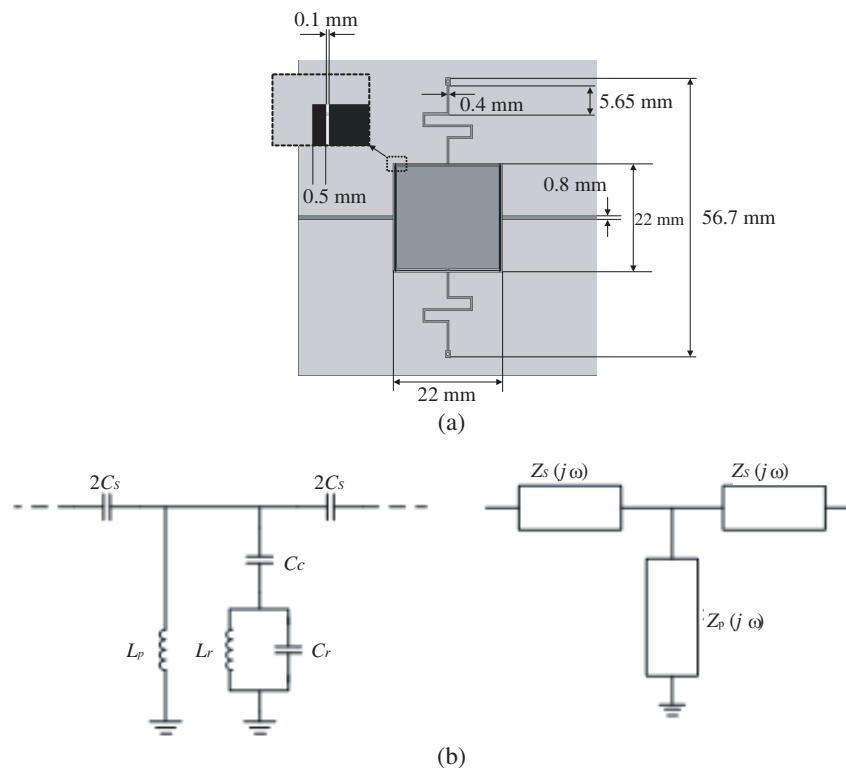


Figure 2: Basic cell of the proposed filters and its equivalent circuit. (a) Basic cell, (b) equivalent circuit.

impedance values, the gap capacitance is found to be

$$C_s = \frac{1}{2\omega Z_0} \quad (3)$$

The shunt reactance Z_p is implicitly represented by

$$\frac{L_p L_r \omega_0^3 (C_c + C_r) - L_p \omega_0}{L_r \omega_0^2 (C_c + C_r) - C_c L_p \omega_0^2 (L_r C_r \omega_0^2 - 1) - 1} = Z_0 \quad (4)$$

Since the value of Z_p depends on four circuit elements, we need three additional conditions to determine these unknown elements. Among these conditions, one is to force the transmission being zero. This is given by the frequency that nulls the shunt impedance in the following

$$f_Z = \frac{1}{2\pi \sqrt{L_r (C_c + C_r)}} \quad (5)$$

The two remaining conditions are on the 3 dB bandwidth of the resonators such that

$$\Delta = \frac{\omega_2 - \omega_1}{\omega_0} \quad (6)$$

In here, ω_0 is the resonant angular frequency, and ω_1 and ω_2 are the lower and upper 3 dB frequencies, respectively. These quantities are related to the filter's fractional bandwidth [10], FBW, according to

$$\Delta = \frac{2 \text{FBW}}{g_i} \quad (7)$$

where g_i denotes the element values of the low pass filter prototype. At the 3 dB frequencies, the shunt impedance becomes $Z_p = jZ_0/2$ and infinity, respectively. These conditions can be expressed as

$$\frac{L_p L_r \omega_1^3 (C_c + C_r) - L_p \omega_1}{L_r \omega_1^2 (C_c + C_r) - C_c L_p \omega_1^2 (L_r C_r \omega_1^2 - 1) - 1} = \frac{Z_0}{2} \quad (8)$$

$$L_r \omega_2^2 (C_c + C_r) - C_c L_p \omega_2^2 (L_r C_r \omega_2^2 - 1) - 1 = 0 \quad (9)$$

Since the designed filter in this paper is the periodic structure formed by cascading the basic cell shown in Figure 2(b), all resonators must have the same Δ and accordingly the same g_i . To obtain the value of g_i , we have considered an order-3 low pass filter prototype with identical element values, and we have forced it to exhibit the 3 dB cutoff at the normalized $\omega = 1$ [rad/s]. From these conditions, we obtained $g_i = 1.521$ by circuit simulation using Agilent ADS.

The criteria to set the transmission zero frequency f_Z obeys the compromise between the need to obtain a sharp transition in the upper band edge and the facility optimize the out-of-band performance of the filter. In this paper, we have set transmission zero frequency $f_Z = 2f_0$. The

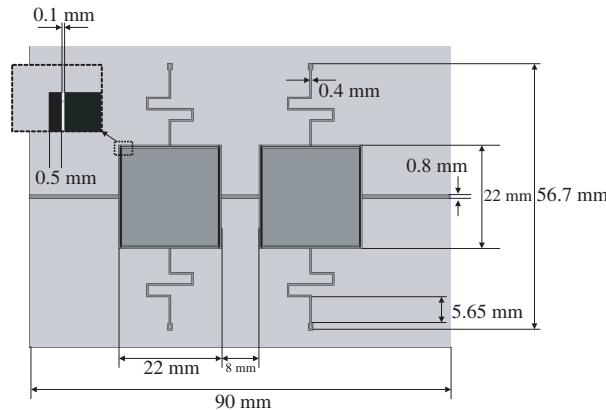


Figure 3: Configuration for the proposed filter.

model cited in [12] has been used to obtain an initial guess for CSRR dimensions. The coupling capacitance C_c has been adjusted by partially removing the metal delimited by the CSRR contour. The stubs width, length, line-to-line distances and gap size consisted in the inductance L_p and series capacitance C_s are obtained by Ansoft HFSS simulation. Figure 3 is a layout of the designed filter.

3. EXPERIMENTAL RESULTS AND DISCUSSION

The proposed filter is fabricated on Duroid 5880 substrate with thickness $h = 0.254$ [mm], size 64×90 [mm²] and dielectric constant $\epsilon_r = 2.2$. The layout for fabricated filter is shown in Figure 4.

The frequency characteristics are measured using the Anritsu 37397C network analyzer. The simulated and measured results are shown in Figure 5.

Figure 5(a) shows return loss S_{11} and insertion loss S_{21} in narrow band. The measured insertion loss is about -4.1 dB at the center frequency and the passband return loss is less than -9.4 dB. The 3 dB FBW is approximately 6.4%. These values are adequate enough to be used in communication channel filtering. Figure 5(b) shows S_{11} and S_{21} in extended frequency range. It is noticed that the excellent characteristic of the out-of-band rejection can be achieved due to the introduced grounded stubs.

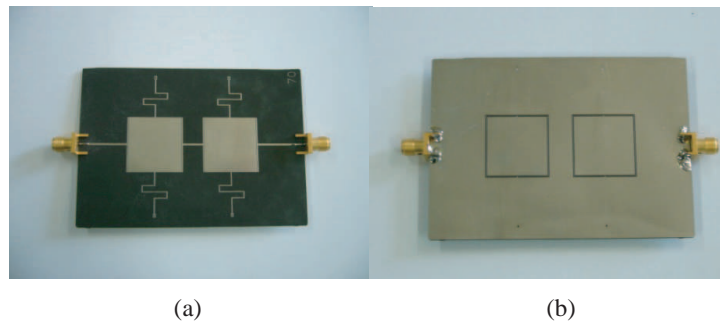


Figure 4: The photograph of the fabricated filter. (a) Top view, (b) bottom view.

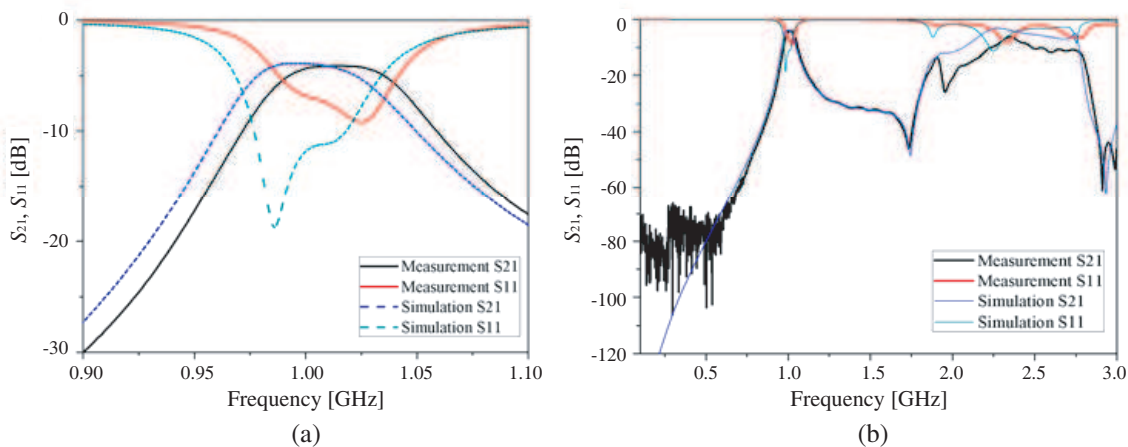


Figure 5: Measured and simulated frequency response on the designed filter. (a) 0.9–1.10 GHz range, (b) 0.5–3.0 GHz range.

4. CONCLUSION

In this paper, the design and fabrication of the compact narrow band pass filter based on the complementary split-ring resonators (CSRRs) have been presented. Our findings are that the measured insertion loss is about -4.1 dB at the center frequency and passband return loss is less than -9.4 dB. The 3 dB FBW is approximately 6.4%. With the help of CSRRs, the excellent characteristic of the out-of-band rejection can be achieved in contrast to the conventional filter

design technique. The results of the frequency response measured on the fabricated band pass filter substrate show satisfactory agreement with the simulated frequency responses by the HFSS in the region of interest. The newly proposed filter by this article can be found its application on the design of compact filters with planar circuit technology.

REFERENCES

1. Atia, A. E. and A. E. Williams, "A Solution for narrow-band coupled cavities," *COMSAT Laboratories Tech. Memo. CL-39-70*, Sep. 22, 1970.
2. Atia, A. E. and A. E. Williams, "Narrow band-pass waveguide filters," *IEEE Trans. Microwave Theory Tech.*, Vol. 20, 258–265, Apr. 1972.
3. Atia, A. E., A. E. Williams, and R. W. Newcomb, "Narrow-band multiple-coupled cavities synthesis," *IEEE Trans. Circuits Systems*, Vol. 21, 649–655, Sep. 1974.
4. Cameron, R. J. and J. D. Rhodes, "Asymmetric realizations for dual-mode bandpass filters," *IEEE Trans. Microwave Theory Tech.*, Vol. 29, 51–58, Jan. 1981.
5. Chen, C. F., T. Y. Huang, and R. B. Wu, "Novel compact net-type resonators and their applications to microstrip bandpass filters," *IEEE Trans. Microwave Theory Tech.*, Vol. 54, No. 2, 755–762, Feb. 2006.
6. Lin, S. C., P. H. Deng, Y. S. Lin, C. H. Wang, and C. H. Chen, "Wide-stopband microstrip bandpass filters using dissimilar quarter-wavelength stepped-impedance resonators," *IEEE Trans. Microwave Theory Tech.*, Vol. 54, No. 3, 1011–1018, Mar. 2006.
7. Falcone, F., T. Lopetegi, J. D. Baena, R. Marques, F. Martin, and M. Sorolla, "Effective negative- ϵ stopband microstrip lines based on complementary split ring resonators," *IEEE Microwave and Wireless Components Letters*, Vol. 14, No. 6, 280–282, Jun. 2004.
8. Bonache, J., I. Gil, F. Martin, I. Gil, J. Garcia-Garcia, R. Marques, and M. Sorolla, "Microstrip bandpass filters with wide bandwidth and compact dimensions," *Microwave and Optical Technology Letters*, Vol. 46, No. 4, 343–346, Aug. 2005.
9. Gil, M., J. Bonache, I. Gil, J. Garcia-Garcia, and F. Martin, "On the transmission properties of left-handed microstrip lines implemented by complementary split rings resonators," *Int. J. Numerical Modelling*, Vol. 19, 87–103, Mar. 2006.
10. Bonache, J., I. Gil, I. Gil, J. Garcia-Garcia, and F. Martin, "Novel microstrip bandpass filters based on complementary split rings resonators," *IEEE Trans. Microwave Theory Tech.*, Vol. 54, No. 1, 265–271, Jan. 2006.
11. Hong, J. S. and M. J. Lancaster, *Microwave Filter for RF/Microwave Applications*, John Wiley & Sons, New York, 2001.
12. Baena, J. D., J. Bonache, F. Martin, R. M. Sillerol, F. Falcone, T. Lopetegi, M. A. G. Laso, J. Garcia-Garcia, I. Gil, M. F. Portillo, and M. Sorolla, "Equivalent-circuit models for split-ring resonators and complementary split-ring resonators coupled to planar transmission lines," *IEEE Trans. Microwave Theory Tech.*, Vol. 53, No. 4, 1451–1461, Apr. 2005.

Quad Flat Non-lead Package Characterization and Circuit Modeling

M. Sigalov^{1,2,3}, D. Regev², E. Kabatsky³, and R. Shavit¹

¹Department of Electrical and Computer Engineering, Ben-Gurion University of the Negev
Beer-Sheva 84105, Israel

²Elipse-RFIC Array Devices, Kfar Neter 40593, Israel

³Department Electrical and Electronics Engineering, Sami Shamoon College of Engineering
Beer-Sheva 84100, Israel

Abstract— The increasing demand for faster data transmission rate and higher capacity channels is pushing the communication systems toward higher microwave frequencies with more complex radio frequency integrated circuits (RFIC). At such high frequencies the electrical parasitic effects of the packages become significant and degrade the RFIC's performance. One way to improve the functionality and performance of the RFIC devices is to develop accurate broadband electrical circuit models of the packages for optimization purpose. The objective of this work is to investigate the characteristics of a chip scale (CS) quad flat no-lead (QFN) package electrical circuit model. This objective is obtained by utilizing three-dimensional electromagnetic (EM) numerical simulation results and extraction of the equivalent circuit parasitic elements from a model based on the physical structure of the package.

1. INTRODUCTION

The QFN is a CS leadless package where electrical contact to the printed circuit board (PCB) is made by soldering (by conductive solder) the leads on the bottom surface of the package to the PCB, instead of using the conventional leads. The bottom-lead package structure is able to provide good electrical interconnections to the PCB. The exposed die paddle on the bottom of the chip efficiently conducts the heat to the PCB and provides a stable ground for the bonds. The small size and weight with excellent thermal and electrical performance [1, 2] make the QFN package an ideal choice for handheld portable applications such as cell phones or any other application where size, weight and package performance are required.

In this work, our attention was concentrated on the characterization and circuit modeling of a fully encapsulated plasticmolded QFN package. The equivalent wideband (up to 25 GHz) electrical circuit model of the package that accounts for the high-frequency parasitic effects, such as resonance, coupling, and frequency-dependent losses was developed. The parasitic elements of the equivalent circuit models have been extracted from the 3D electromagnetic (EM) simulation.

2. QFN CHARACTERIZATION AND CIRCUIT MODELING

An interconnect path of the package can be electrically modeled by different equivalent circuits models like: A single lumped element connected to a transmission line with fixed impedance and time delay, a lumped element section, or by a distributed element circuit with per unit length parameters. The choice of a model depends on the electrical length of interconnects. A package interconnects path, is considered to be “electrically short” if, at the highest operating frequency of interest, the interconnect length is physically shorter than approximately one-tenth of the wavelength [3]. Otherwise, it is “electrically long”. Therefore, an interconnect can be modeled using a lumped element circuit if it is shown to be “electrically short”, while distributed models are required to model “electrically long” interconnects. To investigate individual components of the package, e.g., wirebond, lead, pad, a distributed model that models each impedance discontinuity along the propagation path is required. Depending on the complexity of the model used, the electrical modeling requires the calculation of self-capacitances, inductances, resistances, and mutual couplings for use in the equivalent circuit.

In Fig. 1, one can observe the cross-section view of the QFN package (one bondwire) and its two ports equivalent Π circuit model [2, 4].

To calculate the C_L , C_{pg} , R_w and L_w values of the model one can use the following expressions:

$$C_L = \frac{\text{Im}(Y_{11} + Y_{12})}{\omega} \quad \text{and} \quad C_{pg} = \frac{\text{Im}(Y_{22} + Y_{21})}{\omega} \quad (1)$$

$$L_w = \frac{\text{Im}(Y_{12})}{\omega(\text{Re}(Y_{12})^2 + \text{Im}(Y_{12})^2)} \quad \text{and} \quad R_w = \frac{\text{Re}(Y_{12})}{(\text{Re}(Y_{12})^2 + \text{Im}(Y_{12})^2)} \quad (2)$$

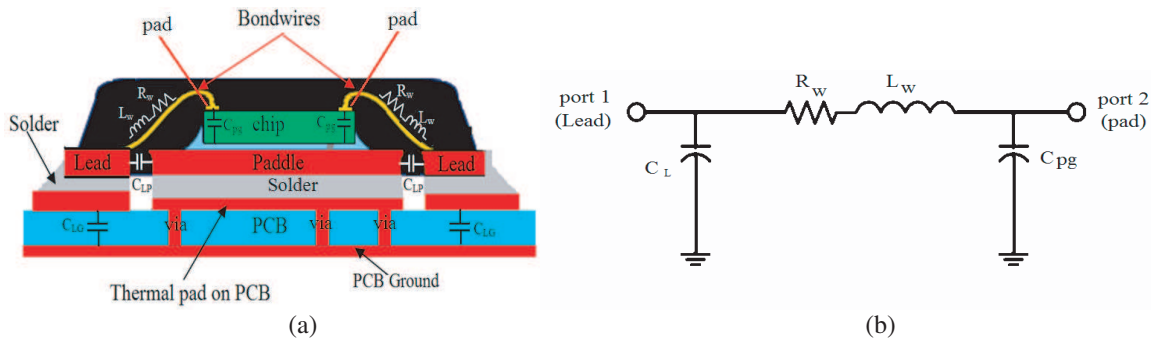


Figure 1: (a) Cross-section view of the QFN package, (b) equivalent Π circuit model of the two ports QFN package ($C_L = C_{LP} + C_{LG}$ capacitance of the lead to the ground, C_{pg} capacitance of the pad to ground, R_w and L_w resistance and inductance of the bond wire).

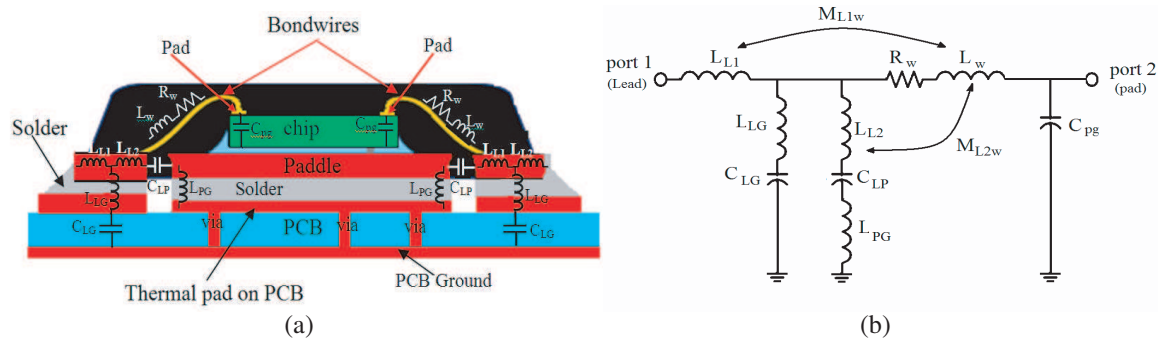


Figure 2: (a) Cross-section view of the QFN package, (b) equivalent high frequency model of the two ports QFN package.

These expressions are derived from the two port network analysis of the equivalent circuit shown in Fig. 1(b). The Y parameters can be obtained from an EM simulator or measurements [5].

The model shown in Fig. 1(b) is a simple model that gives good correlation to the measurements or EM simulation results up to 6 GHz [2]. For higher frequencies the sizes of leads are comparable to one-tenth of the EM field wavelength. So, there is a need to consider the distributed currents on the lead surfaces. These distributed currents lead to additional inductance effects. Consequently, a more complex (high frequency) model is necessary for the two port QFN characterization.

In Fig. 2, it is shown the cross-section view of the QFN package and the proposed upgraded (high frequency) equivalent Π circuit model.

From Fig. 2, one can see that the lead high frequency inductance effects can be modeled as a serial inductance L_{L1} at the input of port 1, a serial inductance L_{LG} to the capacitance C_{LG} , a serial inductance L_{L2} to the capacitance C_{LP} , a mutual inductance M_{L1w} and a mutual inductance M_{L2w} . The inductance L_{PG} is due to the distributed currents on the paddle surface.

The simplified two port model shown in Fig. 2 is not sufficient to model the package frequency performance when coupling effects to the neighboring bondwires need to be considered. In Fig. 3, it is shown such an improved four port circuit model taking in consideration, the coupling between the bondwires.

C_{L1L2} — is the mutual capacitance between two adjacent leads and bondwires. C_{P1P2} — is the mutual capacitance between two adjacent die pads. M_{w1w2} — is the mutual inductance between two adjacent bond wires. M_{1L1L2} , M_{2L1L2} , and M_{3L1L2} represent the mutual inductances between two adjacent leads.

3. SIMULATION AND OPTIMIZATION RESULTS

In this work, we used Ansoft HFSS EM simulator for modeling and characterization of a QFN-48 structure with 48 bottom leads. The package size is $7 \times 7 \times 0.2$ mm. The size of the paddle is 5.6×5.6 mm. The lead pitch is 0.5 mm and the lead dimensions are $0.23 \times 0.6 \times 0.2$ mm. The size of the die pads is 50×5 μ m. The diameter of the gold bond wires is 1.2 mil and the length of the

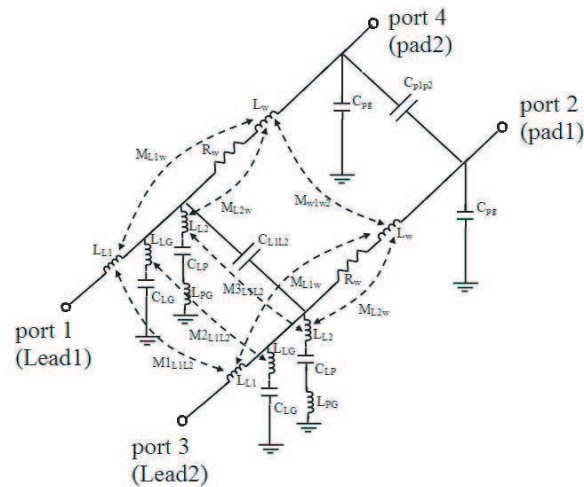


Figure 3: Equivalent high frequency model of the four ports QFN package.

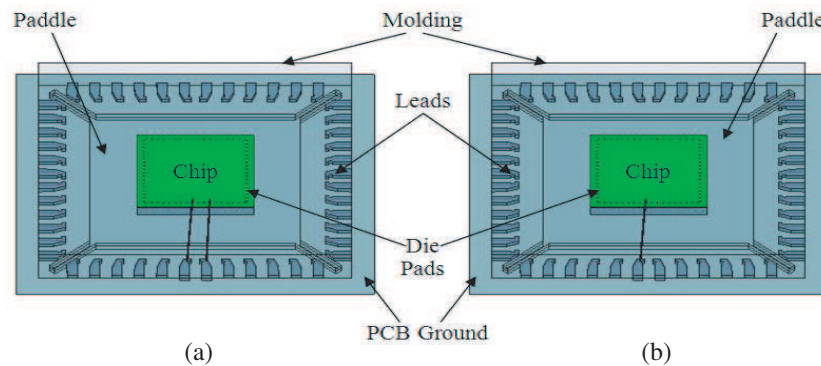


Figure 4: QFN-48 structures: (a) One bondwire simulation (two ports), (b) two bondwires simulation (four ports).

bond wires is 1.8 mm. The dielectric constant of the molding compound is 3.7.

Geometric models of the simulated one and two bondwires QFN48 structures are shown in Figs. 4(a) and 4(b), respectively.

From Fig. 4, one can notice that the geometry simulated by HFSS includes board, package, die and bond wires. The package is surrounded by an air volume which has, on its external surface, a radiation boundary condition. This condition allows the EM field to radiate freely in the space. On the lower surface of the board a perfectly electric conductor (PCB ground) is chosen. This plane is a common reference both for the ports of the leads, directly connected to it, and for the ports on the pads connected to it through the die paddle.

In the next two figures, it is shown the comparison between the S parameters obtained from the full EM HFSS simulation of the two (Fig. 5) and four (Fig. 6) ports QFN-48 structures and the S parameters obtained from the equivalent circuit model presented in Fig. 2(b) and Fig. 3, correspondingly.

One can observe that the S parameters of the improved high frequency equivalent models presented in Fig. 2(b) and Fig. 3 yield very good correlation with the HFSS results up to 25 GHz.

The final equivalent circuit (Fig. 3) parameters values are based on the parameters extracted from the EM simulation and after circuit optimization. The optimization was performed with RF Designer of the ADS circuit simulation program from Agilent Company. The extracted parasitic parameters of the equivalent circuit models of the QFN-48 package are listed in Table 1.

Due to the small values the mutual inductances $M1_{Lw}$, $M2_{Lw}$, and $M3_{Lw}$ they don't affect the performance of the equivalent circuit and can be neglected.

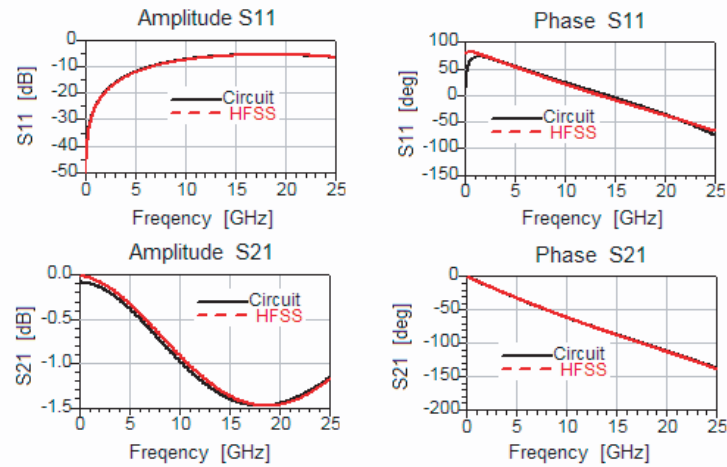


Figure 5: Comparison between the S parameters obtained from the full EM HFSS simulation of the two ports QFN-48 structure and the S parameters obtained from the high frequency equivalent circuit model presented in Fig. 2(b).

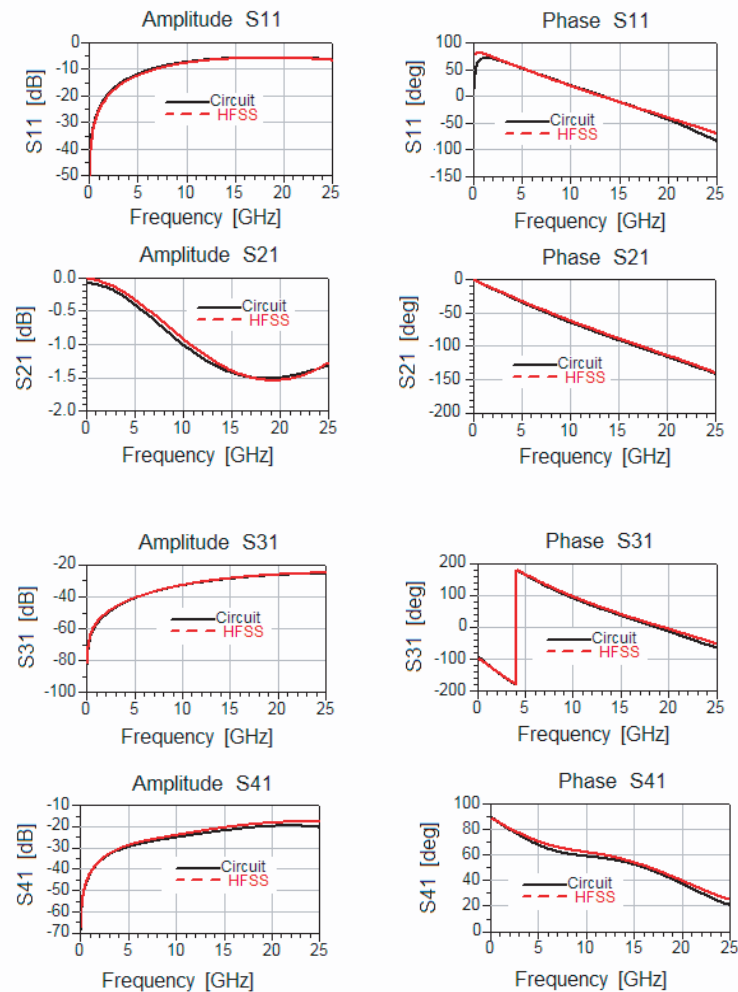


Figure 6: Comparison between the S parameters obtained from the full EM HFSS simulation of the full four ports QFN-48 structure and the S parameters obtained from the high frequency equivalent circuit model presented in Fig. 3.

Table 1: Extracted parasitic elements of the equivalent circuit model of the QFN package.

C_{LG}	C_{LP}	C_{pg}	C_{L1L2}	L_{L1}
38.3 fF	106.5 fF	41.4 fF	20.2 fF	0.15 nH
L_{L2}	L_{LG}	L_{PG}	L_w	M_{w1w2}
0.24 nH	0.01 nH	0.1 nH	1.26 nH	0.066 nH
$M1_{Lw}$	$M2_{Lw}$	$M1_{L1L2}$	$M2_{L1L2}$	$M3_{L1L2}$
0.008 nH	0.496 nH	0.008 nH	0.008 nH	0.008 nH

4. CONCLUSION

In this study, the equivalent wideband electrical circuit model of a fully encapsulated plastic-molded QFN package that accounts for the high-frequency parasitic effects was developed. The parasitic elements of the equivalent circuit models were extracted from the 3D EM simulations. It was shown that the developed model gives a very good correlation to the results obtained from the EM simulation up to 25 GHz. The equivalent circuit model developed in this work can be used in RFIC circuit level simulators for high level system simulations up to 25 GHz.

ACKNOWLEDGMENT

This work was supported by the ELTA Systems Ltd. a group and subsidiary of Israel Aerospace Industries.

REFERENCES

1. Kühnlein, G., "A design a manufacturing solution for high-reliable, non-leaded CSPs like QFN," *Proc. 51st Electron. Comp. Technol. Conf.*, 47–53, Jun. 2001.
2. Chen, N., K. Chiang, T. D. Her, Y. L. Lai, and C. Chen, "Electrical characterization and structure investigation of quad flat non-lead package for RFIC applications," *Solid-State Electron.*, Vol. 47, 315–322, Feb. 2003.
3. Burghartz, J. N., M. Soyuer, and K. A. Jenkins, "Microwave inductors and capacitors in standard multilevel interconnect silicon technology," *IEEE Trans. Microw. Theory Tech.*, Vol. 44, No. 1, 100–104, Jan. 1996.
4. Lai, Y. L. and C. Y. Ho, "Electrical modeling of quad flat no-lead packages for highfrequency IC applications," *IEEE Tencon Conf.*, Vol. 4, 344–347, Nov. 2004.
5. McGibney, E. and J. Barrett, "An overview of electrical characterization techniques and theory for IC packages and interconnects," *IEEE Trans. Adv. Packag.*, Vol. 29, No. 4, 131–139, Feb. 2006.

A New Bandstop Cascaded Defected Microstrip Structure (CDMS) Filter with 10 GHz Symmetrical Bandwidth

M. Kazerooni¹, A. Cheldavi¹, and M. Kamarei²

¹College of Electrical Engineering, Iran University of Science and Technology, Tehran, Iran

²Faculty of Electrical and Computer, University of Tehran, Tehran, Iran

Abstract— This paper presents a new bandstop filter to obtaining the broad-bandwidth rejection in microstrip transmission line. This structure is a cascaded defected microstrip structure (CDMS). To this property, two defects with similar directions and connecting line between them is designed and simulated. Then, its performance is investigated and discussed.

1. INTRODUCTION

In recent years, several structures have been proposed and developed to decrease the size of transmission lines in microwave circuits such as MICs and MMICs [1–3].

The two procedures that are employed to decrease the length of the length of microstrips are called defected ground structure (DGS) and electromagnetic bandgap (EBG). DGSs are structures which are realized by defecting ground planes [4]. If DGSs are repeated periodically, it is called as electromagnetic bandgap (EBG). The effect of DGSs is to place parallel inductance and capacitance in the lumped model that can be expressed as making a distortion in the fields of ground plane, increasing permittivity, increasing effective inductance and capacitance properties in transmission lines and making a low pass filter [5].

In this paper a novel cascaded defected microstrip structures (CDMS) are proposed in order to improve the bandwidth rejection.

2. CDMS STRUCTURE

CDMS structure increases the electric length and the associated inductance of the microstrip. So, improvement in filter characteristics of the circuits can be achieved and size of the filter circuits can be reduced. The important application of CDMS is to reject some frequency band at the output ports. By employing the CDMS structure the unwanted harmonics can be suppressed with appropriate selected slit length tuned to the specific harmonic band and great rejection can be obtained. This effect can be used in amplifier linearization.

The geometries of rejection filter with CDMS section being investigated in this letter and its details is illustrated in Fig. 1. This structure are made by etching two numbers of slit over a conventional microstrip and etching the very small slits perpendicular to the main slits. Also this configuration is very useful in millimeter wave circuit design. In this frequency band the radiation from the circuit area is a source of a very catastrophic error in the measurement procedure and reduction of the area is a properly desired function.

The filter is designed on the substrate which has a relative permittivity $\epsilon_r = 2.33$ and thickness $h = 0.787$ mm.

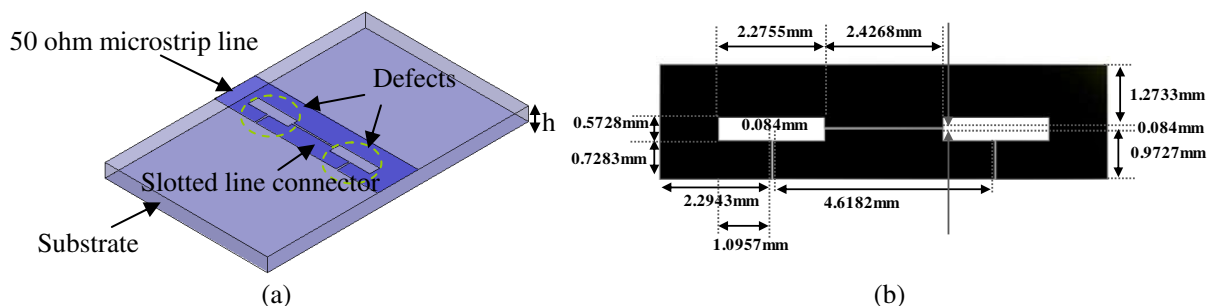


Figure 1: (a) Proposed CDMS with similar directions of defects and a slotted line connector between them. (b) Parameters values.

The S -parameters of proposed CDMS filter has been shown in Fig. 2. The filter has very sharp and wide stop band response. In this case, using two numbers of etched cells makes the wide and sharp symmetric stop band. It's clearly that the edge effect, which is proportional to the etched CDMS cells and fringing fields, will not be appeared even in very high frequency. In this circuit BW/f_0 value is about 40%. This ratio in is more than three times of DMS having one etched cell. Also, by changing the slots dimensions we can move the bandgap region. So, the CDMS circuit is much attractive in applications which need wide stop band frequency such as, in the phased array antenna for rejection the wide band spurious harmonics, feeding of array antenna, broad band antennas, broad band microstrip filters, fractal patch antennas, power amplifiers and branch line couplers.

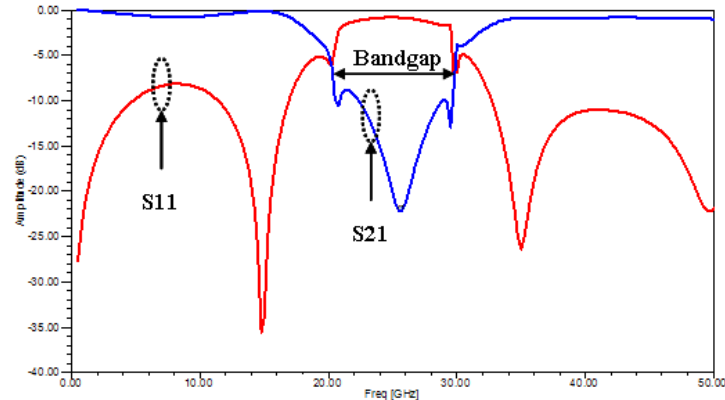


Figure 2: Proposed CDMS amplitude simulation.

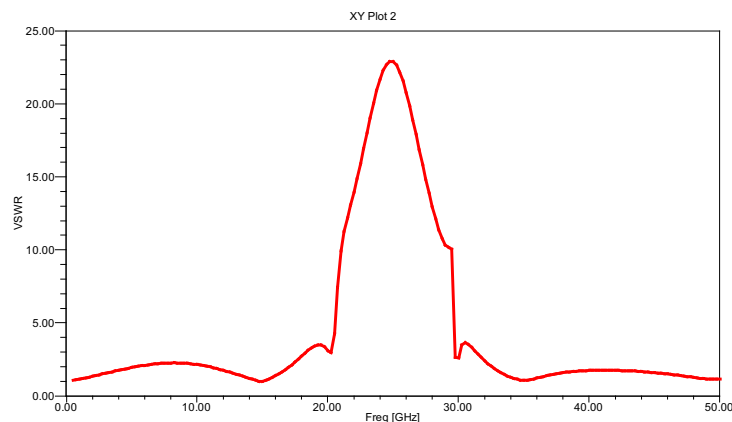


Figure 3: VSWR parameter of proposed CDMS.

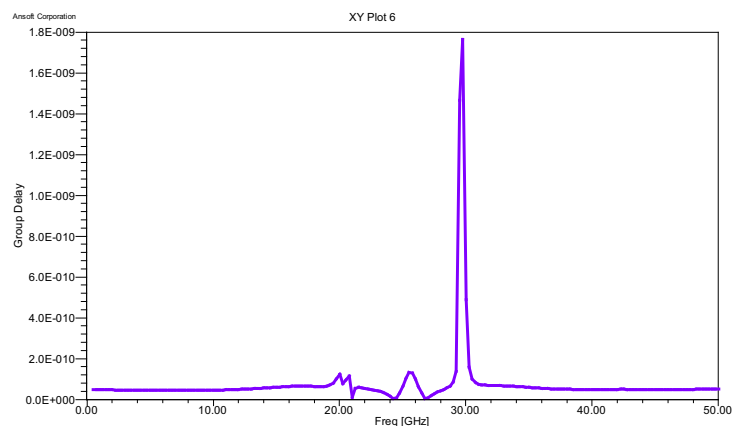


Figure 4: Group delay parameter of proposed CDMS.

3. INVESTIGATION OF FREQUENCY RESPONSE AND PERFORMANCE

For illustration the level of suppression in bandgap region, the VSWR parameter is shown in Fig. 3. As can be seen, the VSWR value in the center bandgap frequency is 23. This value is shown that even high power harmonics can be completely rejected. For investigation of the linear distortion of the filter, we plot the group delay in Fig. 4. It is revealed that the delay is almost constant up to the 50 GHz except as in 30 GHz. this problem is not important. Because that this frequency falls in band gap region and not affects the signal passing in operating frequency.

4. EXTRACTION OF CIRCUIT MODELING

The current path of CDMS is shown in Fig. 5. Using this current path, the model of the CDMS circuit is illustrated in Fig. 6.

In this case the rectangular etched area represents the inductance and the perpendicular dis-

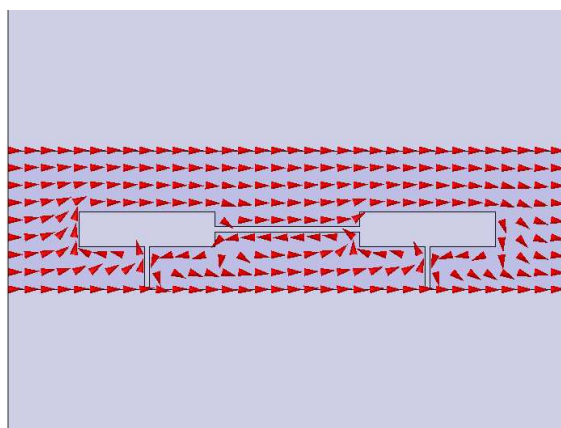


Figure 5: Current distribution of proposed CDMS.

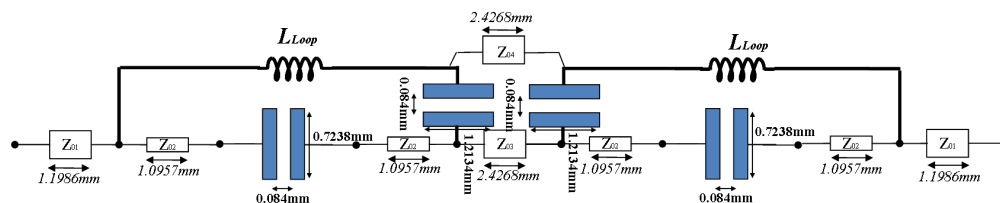


Figure 6: Circuit model of proposed CDMS. The Z_{01} is proportional to 50Ω , Z_{02} is proportional to width of 0.7283 mm, Z_{03} is proportional to width of 0.9727 mm and Z_{03} is proportional to width of 1.2733 mm.

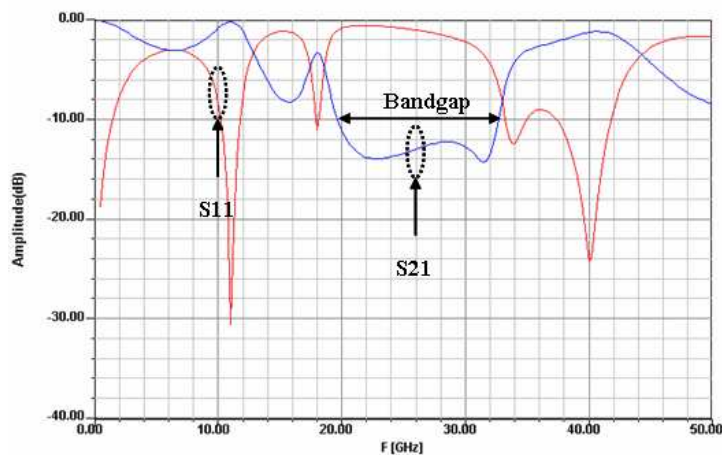


Figure 7: The proposed circuit simulation.

continuity gap (T-cell foot's) of the microstrip line can be represented as a microstrip gap. Using the very simple circuit approach the value of L_{Loop} become 1.8772 nH. As can be seen in Fig. 7, the amplitude circuit simulation is relatively good agree with full wave analysis that take about several hours for precious analysis using ordinary computer. Due to we have not consider the dispersion in our proposed model, the result fewness move away from full wave analysis result at the very high frequencies. So, this technique is very near to full wave analysis in a wide range of frequency without incorporating dispersive effect in the analysis.

5. SURVIVING OF BANDGAP PROPERTY AND RADIATION DUE TO DEFECTS

To visualize the bandgap feature of current suppression, the magnitude of surface current in CDMS circuit is graphically presented. Figs. 8–9 show the magnitudes at a transmission frequency such as 1 GHz and bandgap frequency such as 25.5 GHz for comparison. The difference of current level due to the bandgap characteristics is obvious. So, determination of the current distribution along the CDMS structure is a good gauge for prediction of EMC properties. Because of the slots in this filter the radiation is a very important parameter. For comparison the radiation level in a typical transmission frequency and a bandgap frequency, their E-field gain patterns has been illustrated in Fig. 10. From Fig. 10 the radiation in bandgap region with respect to the transmission region is more than 30 dB. This means that the EMI radiation noise in the bandgap region is greater than the EMI radiation noise in transmission band.

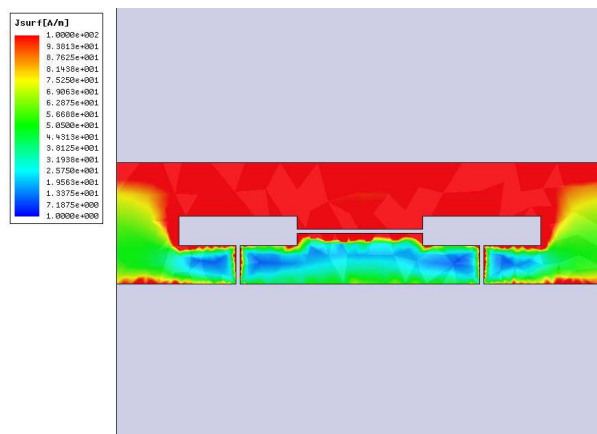


Figure 8: Surface current representation at the transmission frequency (1 GHz).

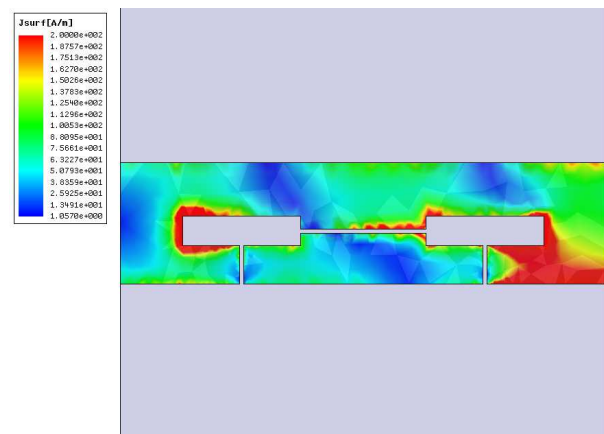


Figure 9: Surface current representation at the bandgap frequency (25.5 GHz).

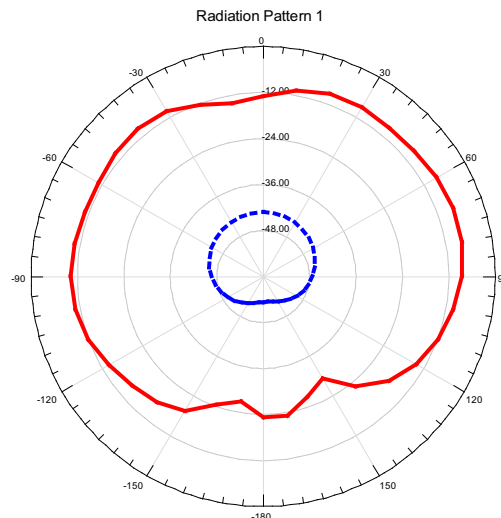


Figure 10: Radiation levels in transmission frequency (dash line) and bandgap frequency (solid line).

6. CONCLUSIONS

This paper introduces a novel structure of CDMS, which is suitable for design of symmetrical bandstop MMIC microwave and millimeter wave filters with very wide stop band frequency response for several applications. This circuit is very useful, because the area of the circuits is small. This CDMS structure was modeled using lumped elements based on current distribution. The good agreement with full wave analysis is obtained. Also some transmission and bandgap parameters and EMI radiation noise are investigated and analyzed.

REFERENCES

1. Scardelletti, M. C., G. E. Ponchak, and T. M. Weller, "Miniaturized wilkinson power divider utilizing capacitive loading," *IEEE Microwave and Wireless Components Letters*, Vol. 12, No. 1, 6–8, Jan. 2002.
2. Shamsinejad, S., M. Soleimani, and N. Komjani, "Novel miniaturized wilkinson power divider for 3G mobile receivers," *Progress In Electromagnetics Research Letters*, Vol. 3, 9–16, 2008.
3. Papapolymeroul, J., G. E. Ponchak, and E. M. Tentzeris, "A wilkinson power divider on a low resistivity Si substrate with a polyimide interface layer for wireless circuits," *IEEE MTT-S International Microwave Symposium Digest*, Vol. 1, 593–596, Jun. 2002.
4. Weng, L. H., Y. C. Gue, X. W. Shi, and X. Q. Chen, "An overview on defected ground structure," *Progress In Electromagnetics Research B*, Vol. 7, 173–189, 2008.
5. Chen, J., Z. B. Weng, Y. C. Jiao, and F. S. Zhang, "Lowpass filter design of Hilbert curve ring defected ground structures," *Progress In Electromagnetics Research*, PIER 70, 269–280, 2007.

Design and Simulation of a Wideband Dualpolarized Conical Doubleridged Horn Antenna

M. Moshiri, H. Abiri, and A. A. Dastranj
ECE Department, Shiraz University, Shiraz, Iran

Abstract— Dual-polarized antennas are widely used in many fields including measurements, equipments, electromagnetic compatibility tests, electronic warfare, etc. These antennas in pyramidal horn shape have been investigated before. In this paper, the design and analysis of a dual polarized doubleridged conical horn antenna with dual polarization, high gain and low cross polarization for wide band applications is presented. These antennas have higher gain and lower side lobe level than pyramidal antennas. The designed antenna has a voltage standing wave ratio (VSWR) less than 2.5 for the frequency range of 8–18 GHz. Moreover, the proposed antenna exhibits a very good dual polarization, low cross polarization, low side lobe level, high gain, and relatively stable far-field radiation characteristics in the entire operating bandwidth. Quad-ridged horn antennas also can produce dual polarization but these antennas have two input ports and have hard manufacturing processes. In this paper, a five layers slant linear polarizer is used. Five layer polarizer has lower VSWR than other multilayer polarizer. In order to achieve dual polarizations, the strips width, spacing between two adjacent strips and dielectric layers thickness are optimized. Dielectric material between layers is Styrofoam ($\epsilon = 1.03$). The proposed antenna is simulated with commercially available packages, such as CST Microwave Studio (Sax Software Corp.) and Ansoft HFSS (Ansoft Corp.), in the operating frequency range. Excellent agreement is observed between two simulation results. The best result is achieved for $\lambda/4$ strips spacing where λ is the wave length at the mid frequency. Simulation results agree with the theoretical results. Simulation results for the VSWR, radiation patterns, and gain of the designed antenna over the frequency band 8–18 GHz are presented and discussed.

1. INTRODUCTION

The applications of Double-Ridged Horn (DRH) antennas in ultra wide band communication technologies continue to increase. They can be used in different systems such as reflector feeds, electronic warfare, electromagnetic compatibility test (EMC), radar and detection systems, etc. These various applications result from the special characteristics of these antennas such as wide bandwidth, simple construction and high gain [1, 2]. Ref. [3], introduces a novel dual-polarized double-ridged pyramidal horn antenna for 8–18 GHz bandwidth. A quad-ridged horn antenna on the 2–26.5 GHz bandwidth with $VSWR < 3.1$ has been used for dual polarization over the wide band frequency range [4]. In this paper, based on the doubleridged circular waveguide, a dual polarized double-ridged conical horn antenna with a 50Ω coaxial feed input is proposed. The proposed antenna is simulated with commercially available packages such as Ansoft HFSS which is based on the finite element and CST Microwave Studio which is based on the finite integral technique. Simulation results for the VSWR, gain, and radiation patterns of the designed antenna at various frequencies are presented.

2. DUAL-POLARIZED DOUBLE-RIDGED HORN ANTENNA STRUCTURE

In Fig. 1, the proposed antenna is shown. The dual-polarized double-ridged horn antenna is composed of three parts: the feeding part, tapered (flared section) part and multilayered polarizer. The design process of each part is explained in the next sections. The overall length of the designed antenna (including the length of back cavity) and the radius of the horn aperture are 63 mm and 33 mm, respectively.

2.1. Coaxial to Double-ridged Circular Waveguide Transition

The transition between coaxial probe and the double-ridged waveguide is important for return loss performance. The main goal is obtaining low levels of VSWR throughout transformation of TEM-mode in coaxial to TE-mode in circular waveguide. For achieving low VSWR, a cavity back is introduced at the back of circular waveguide for which the dimensions and probe spacing from the ridged edge are optimized using a software package. The length of the cavity back is 3 mm.

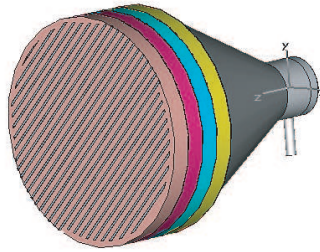


Figure 1: Dual-polarized conical double-ridged horn antenna.

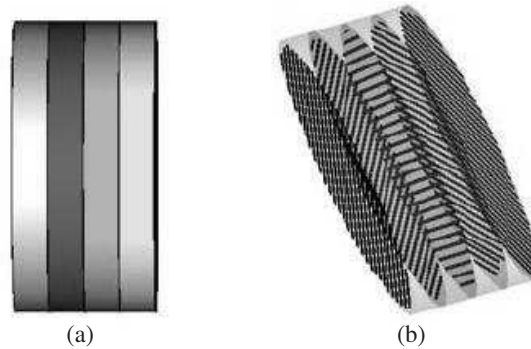


Figure 2: Configuration of the five layer strips of the polarizer. (a) Side view, (b) overall view.

2.2. Design of Tapered Part

As described before, double-ridged waveguides are used for single mode propagation in a wide frequency range. In tapered part, ridges vary the impedance of the guide from $0Z_0 = 50\ \Omega$ at the feeding point (double-ridged waveguide) to $Z_l = 120\pi\ \Omega$ at the aperture of the horn antenna [5]. The impedance variations in the tapered part is according to:

$$Z(z) = Z_0 e^{kz} \quad \text{for } 0 \leq z \leq l \quad (1)$$

where z is the distance from the waveguide aperture and $k \stackrel{\text{def}}{=} \frac{\ln(Z_l/Z_0)}{l}$.

If the tapered length is divided into subsections, the geometrical dimensions of each sub sections are represented in Table 1.

3. DESIGN OF MULTILAYERED POLARIZER

In this part, we consider the multilayered polarizer placed in front of the double-ridged conical horn antenna for providing dual polarization in the frequency range of 8–18 GHz. The multilayered polarizer is named slant 45 degree polarizer. This device converts linear polarization to slant 45 degree, so that the antenna becomes versatile to all incoming practical signal polarizations without affecting the antenna characteristics. Wire grid polarizers have been studied extensively in literature and applied to antennas [6–8]. In multilayered polarizer, incoming and outgoing wave polarization should be perpendicular to the direction of the first and the last strips of the polarizer respectively [9]. Increasing the number of layers of the polarizer will reduce the antenna gain significantly and increases the weight. Also more number of polarizers with different orientations of metal strips make fabrication and optimization difficult and complicated [10]. For obtaining lower VSWR we have used five layer polarizer. The angle between each layer of strips is 11.25 degrees (Fig. 2). In order to achieve good dual polarization, the strip width, spacing between two adjacent strips and dielectric layer thickness should be optimized. Dielectric material that we used is Styrofoam ($\epsilon = 1.03$). According to [9, 11, 12], electric field component in circular waveguide which is perpendicular to the strip direction (in the first layer) is transmitted. Clearly minimum absolute value of reflection of this component is desired. According to Eq. (11) in [9], this minimum (which is equal to 0.02) is obtained if: $\varphi = (2\pi ss/\lambda)$ or $ss = \lambda/4$ where φ is the electrical length of the spacing between strip layers, ss is its physical length and λ is the wavelength at the mid

frequency. Also, according to Eq. (8) in [12], to consider a limitation for the spacing of adjacent strips; $s \ll \lambda$ we have taken $s \cong 0.1\lambda$. Eq. (10) in [11] and Eq. (11) in [12], are used to obtain the strips width. By simulations with CST, the best results are achieved. On the other hand, the proper spacing between antenna and the first layer of the polarizer is obtained by simulation as 0.1 mm. The designed wide band polarizer specifications are listed in Table 2.

Table 1: Dimensions of the tapered section.

Subsection Number	Waveguide aperture Radius (in mm)	Tapered ridge Height (in mm)	Tapered ridge Width (in mm)
1	7	6.5	3
2	9.53	8.8	3
3	12.4	10.5	3
4	13.4	10.8	3
5	14.7	11.2	3
6	16	11.5	3
7	17.6	12	3
8	19	12.2	3
9	20	11.8	3
10	21.8	12.2	3
11	23	11	4
12	24.4	9.5	4
13	26	7.5	4
14	27.7	5	4
15	32.7	4.2	4

Table 2: Specification of wideband polarizer.

First layer dielectric thickness (mm)	0.1
Other dielectric thickness (mm)	5.77
Strip thickness (mm)	0.1
Spacing between strips (mm)	1.65
Strip width (mm)	0.65
Dielectric material (mm)	styrofoam

4. SIMULATION RESULTS

In this part, simulation results of the designed antenna is presented. Input VSWR versus frequency is plotted in Fig. 3. A good agreement is observed for the simulation by CST and HFSS simulators. The maximum value of the VSWR is less than 2.4 over the entire bandwidth except at $f = 12.6$ GHz where it reaches 2.6. The E_θ and E_ϕ patterns of the antenna for the x - z and the y - z planes for various frequencies (8, 13, 18 GHz) are shown in Figs. 4–6. The E_θ and E_ϕ patterns represent vertical and horizontal polarization patterns in the x - z and y - z planes. The close values of vertical and horizontal maximum fields represent the good dual polarization of the proposed antenna. In conventional double-ridged horn antenna with rectangular aperture for the 8–18 GHz band [3], at the mid frequency side lobe level is less than -9 dB, half power beam width is about 42.5 degree and the absolute value of the maximum fields is 12.2 dBi where in conical form, side lobe level is less than -13 dB, half power beam width is about 32 degree and the absolute value of the maximum fields is 13.7 dBi. Also, quad-ridged horn antennas can produce dual polarization. In Ref. [4], a quad-ridged horn antenna on the 2–26.5 GHz bandwidth with $VSWR < 3.1$ has been used for dual polarization. With the advantage of wider frequency band, but VSWR is larger and has two input ports so that it has hard manufacturing processes.

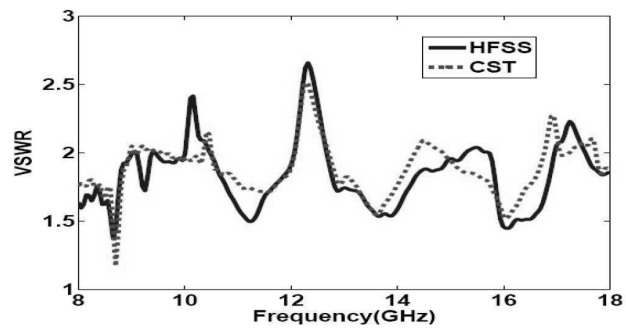


Figure 3: VSWR of dual-polarized conical DRH antenna.

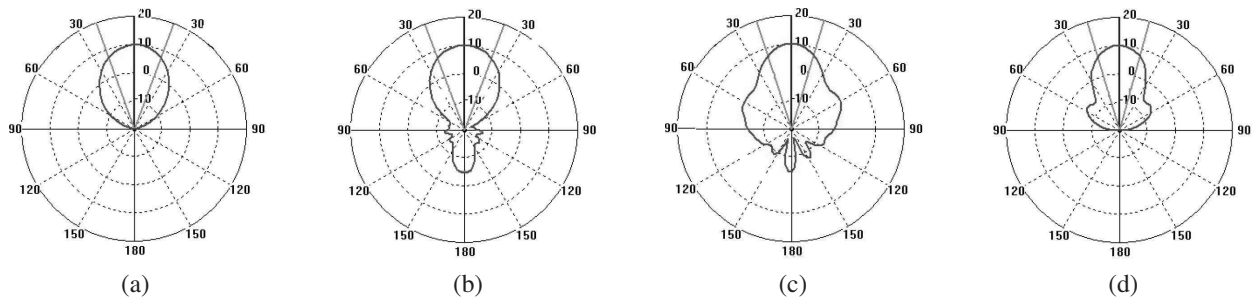


Figure 4: Radiation pattern of dual-polarized conical DRH antenna at 8 GHz. (a) E_{θ} (x - z plane), (b) E_{ϕ} (x - z plane), (c) E_{θ} (y - z plane), (d) E (y - z plane).

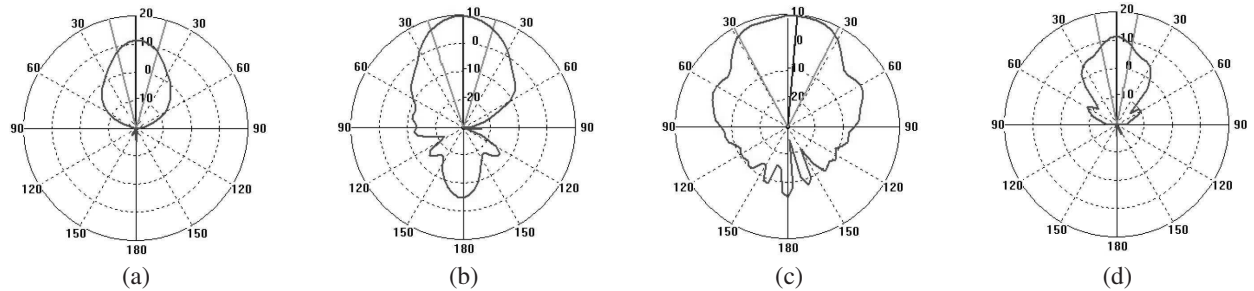


Figure 5: Radiation pattern of dual-polarized conical DRH antenna at 13 GHz. (a) E_{θ} (x - z plane), (b) E_{ϕ} (x - z plane), (c) E_{θ} (y - z plane), (d) E (y - z plane).

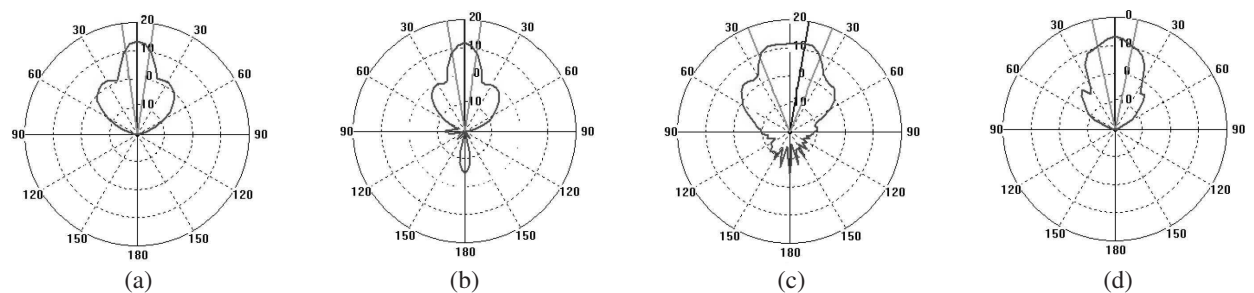


Figure 6: Radiation pattern of dual-polarized conical DRH antenna at 18 GHz. (a) E_{θ} (x - z plane), (b) E_{ϕ} (x - z plane), (c) E_{θ} (y - z plane), (d) E (y - z plane).

5. CONCLUSION

In this paper, a dual-polarized double-ridged conical horn antenna with high gain and low side lobe level has been proposed for the 8–18 GHz band. The dimensions of the conical horn and the tapered part have been optimized by simulation and the dimensions of the polarizer have been obtained by theoretical results. Compared to the dual polarized double-ridged pyramidal horn

antennas, the designed conical horn antenna has lower Side Lobe Level (*SLL*) and higher gain. Besides, dual polarized double-ridged pyramidal horn antennas have notch in radiation patterns. Quad-ridged horn antennas have two input ports and have hard manufacturing processes but this double-ridged horn antenna has one input port and easy manufacturing processes. As result, the proposed antenna is a good choice for dual polarization applications.

REFERENCES

1. Barrow, W. L. and L. J. Chu, "Theory of the electromagnetic horn," *Proc. IRE*, Vol. 27, 51–64, 1939.
2. Kerr, J. L., "Short axial length broad-band horns," *IEEE Tran. Ant. Prop.*, Vol. 21, 710–714, Sep. 1973.
3. Mallahzadeh, A. R., A. A. Dastranj, and H. R. Hassani, "A novel dual-polarized double-ridged horn antenna for wideband applications," *Progress In Electromagnetics Research B*, Vol. 1, 67–80, 2008.
4. Shen, Z. and C. Feng, "A new dual-polarized broadband horn antenna," *IEEE Antennas and Wireless Propagation Letters*, Vol. 4, 270–273, 2005.
5. Walton, K. L. and V. C. Sundberg, "Broadband ridged horn design," *Microwave J.*, 96–101, Mar. 1964.
6. Josefsson, G. L., "Wire polarizers for microwave antenna," Tech. Report, No. 81, Chalmers University of Technology, 1978.
7. Larson, J., "A survey of the theory of wire grids," *Microwave Theory and Techniques, IRE Transactions on*, Vol. 10, 191–201, May 1962.
8. Wait, J. R., "Reflection at arbitrary incidence from a parallel wire grid," *Appl. Sci. Res.*, Vol. B4, 393–400, Mar. 1954.
9. Adel, N. A. and A. M. Saleh, "Broad-band wide-angle quasi-optical polarization rotators," *IEEE Tran. Ant. and Prop.*, Vol. 31, No. 1, 73–76, Jan. 1983.
10. Kumar, A., R. Pal, and V. C. Misra, "Ultra broad band slant polarized omni azimuthal antenna," Defence Electronics Research Lab, India, 1993.
11. Adel, A. M. S., "An adjustable quasi-optical band pass filter — Part I: Theory and design formula," *IEEE Trans. Microwave and Tech.*, Vol. 22, No. 7, 728–734, Jul. 1974.
12. Adel, A. M. S., "An adjustable quasi-optical band pass filter — Part II: Practical considerations," *IEEE Trans. Microwave and Tech.*, Vol. 22, No. 7, 734–739, Jul. 1974.

Beam Steering Capability Based on Microstrip CRLH Transmission Line

Mostafa Barati, Manouchehr Kaamyab, and Ali Azimi Fashi

Electrical Engineering Department, K. N. Toosi University of Technology (KNTU)
Tehran, Iran

Abstract— In this paper, an improved version of Leaky Wave (LW) antenna with capability to scan the pattern continuously versus frequency is presented. The LW transmission line is consisting of 10 cells, each cell is made in the form of 8 finger interdigital capacitor and a shorted stub to the ground through a via. The antenna is printed on Taconic TLY5 substrate. The radiation pattern scans from left to right depending on the excitation frequency at input port. Property of leaky wave antenna using transmission line with left hand materials has been studied recently and results are represented in literature [1, 2]. In this paper, we focus on Composite Right Left Hand (CRLH) effects to study the leaky wave antenna. We are able to obtain a pattern that moves from backward to forward as we increase operating frequency. A wide scanning angle from -80 to 50 Degree has been achieved experimentally. The frequency range for the implemented structure is from 1.5 GHz to 3.6 GHz; scanning for backwards occurs from 1.5 GHz to 2.3 GHz, the forward scanning is performed from 2.4 GHz to 3.5 GHz and for 2.3 to 2.4 GHz the pattern oriented almost broadside.

1. INTRODUCTION

Leaky wave transmission line using metamaterial structures have received lots of attention in recent years, this kind of antennas have capability of pattern steering which have extensive applications in communication and radar systems. This kind of antenna for beam scanning against frequency was first presented in [1] where it was indicated that for CRLH, propagation constant, β , is negative for lower frequencies which implies backward radiation (LH), $\beta = 0$ for broadside radiation and $\beta > 0$ for higher frequencies resulting in forward radiation (RH). The theory of CRLH structures is extensively discussed in [2, 4–6], there are some equivalent circuit for a unit cell of the antenna which accomplished earlier in [3]. Beam scanning array can be performed by using active feed network containing varactor diodes which add to complexity in the structure of designed array [7, 8].

The proposed antenna in this paper shows reduction in return loss (based on simulation and experimental results) in comparison to the structure presented in [1, 2]. The antenna shows reasonable gain in LH and RH areas. So the antenna can have similar performance in different point of space and frequencies. The simulation and measurement results in [1–3] show that the pattern in LH, Broadside and RH has some undesired side lobes, but as it is indicated in this paper, side lobes in most of the frequencies are much smaller than the main lobe and can be neglected; It is confirmed in this paper by comparing simulation (with Ansoft HFSS and CST Microwave Studio) and experimental results which are in good accordance with each other.

2. DESIGN OF PROPOSED STEERABLE CRLH LW ANTENNA

To design composite Right-Left hand structure antenna, especially when we wish to use microstrip technology, there is not a closed formula. But in reference [2] a general method has been presented in which by choosing central frequency and applying a series of conditions like matching impedances and band width limits, 4 equations can be obtained that must be solved to obtain 4 unknowns LC network parameters: L_L , C_R , C_L , L_R . However, to implement achieved capacitors and inductors on microstrip lines, there is not any closed formula available so in this paper easier steps have been used to extract required design parameters. In this technology, capacitors can be achieved in the form of Ineterdigital tracks and inductors can be in stub inductor forms.

The structure shown in Figure 1 is constituted of series (interdigital) capacitors C_L and shunt (stub) inductors L_L . As currents flow along C_L , magnetic fluxes are induced and therefore a series inductance L_R is also present; in addition, voltage gradients exist between the upper conductors and the ground plane, which corresponds to a shunt capacitance C_R .

The LW transmission line is consisting of 10 cells, each cell is made in the form of 8 finger interdigital capacitor, width of digits 0.4 mm, and all spacings 0.25 mm, and a shorted stub to the ground through a via. The antenna is printed on Taconic TLY5 substrate with dielectric

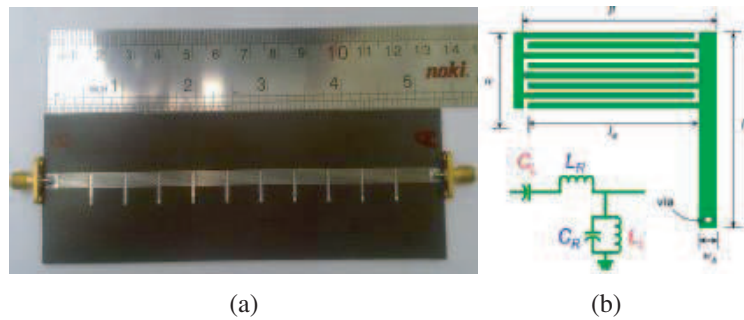


Figure 1: (a) Plan view of proposed structure, (b) equivalent circuit of a cell ($p = 11.4$, $l_s = 10.9$, $l_c = 10.5$, $w_s = 1$, $w = 4.95$ mm).

constant $\epsilon_r = 2.2$ and thickness $h = 62$ mil (loss tangent = 0.0009). It should be noted to achieve the aforementioned dimensions following steps should take into account to extract preliminary parameters for the initial design and following that the optimization has been done in the simulation:

Step 1 ($w = 4.95$ mm): Width of the track is sized with respect to properties of substrate to be matched with 50 Ohm impedance in input and output ports. Hence to ease the matching and to avoid complexity in input and output this width has been selected.

Step 2: Equivalent impedance for stub can be approximately calculated by $L_L \approx \frac{Z_c}{\omega} \text{tg}(\beta l)$ so; the electrical length of stub shall be less than $\lambda/4$ so that inductor value is positive. Since variation of Tangent is more even in 0 to $\pi/4$ intervals, to have a wider band width it is better that stub length is lower than $\lambda/8$ or to be on the safe side the stub length is better to be close to this value. With central frequency of 2.3 GHz:

$$l_s \approx \frac{\lambda_g}{8} \approx \frac{C_0}{8f_0\sqrt{\epsilon_r}} \approx 11 \text{ mm}$$

Step 3: As it is explained in [2], An effectively homogeneous structure is a structure whose structural average cell size p is much smaller than the guided wavelength λ_g , so in order to have a homogeneous structure, electrical length of each cell need to be much smaller than wavelength which in this case it is supposed to be smaller than $\lambda_g/8$, so $l_c < 11$ mm is chosen for the initial design.

Step 4: In the initial design, 10 fingers for each interdigital capacitor port is supposed (0.3 mm width for each finger with 0.2 mm spacing between fingers). After simulation and reduction of fingers better results achieved and number of fingers reduced to 8 with 0.4 mm width and 0.25 mm spacing between them.

3. EXPERIMENTAL AND SIMULATION RESULTS

3.1. Scattering Parameters

S_{11} and S_{21} curves for this structure have been shown in Figure 3. Return loss in such structure is high and the reason is the discontinuity caused by interdigital lines.

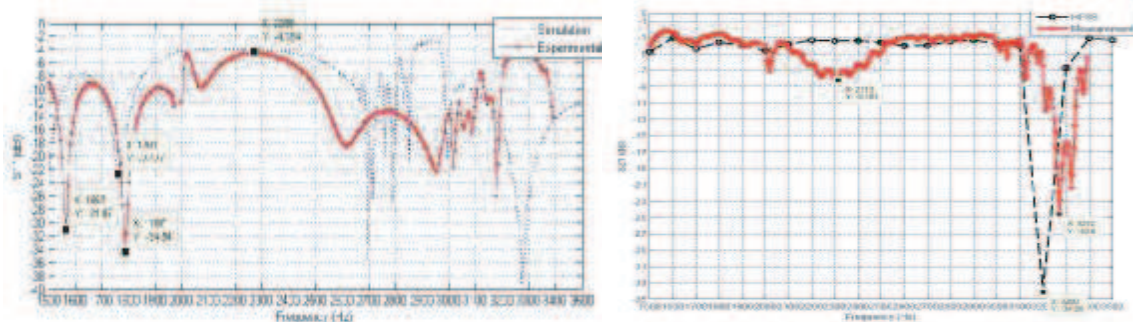


Figure 2: S_{11} and S_{21} curves vs frequency for structure shown in Figure 1 and comparison of measurement result with full wave simulation.

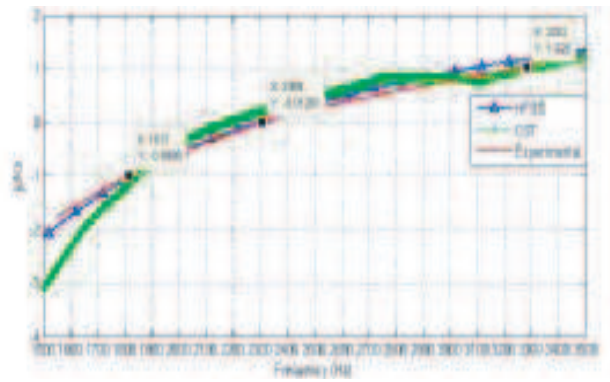


Figure 3: Dispersion diagram for structure shown in Figure 1 (balanced CRLH, $L_L C_R = L_R C_L$) and comparison of the results from experimental measurements and 2 full wave simulations.

In Figure 2, it is shown that in the desired frequency band, S_{21} does not exceed -3 dB and this shows that the structure can radiate. Figure 2 shows that the experimental results and full wave simulation are compatible to an acceptable extent.

3.2. Dispersion (β) Diagram

Dispersion (β) diagram for this structure is shown in Figure 3. As is obvious in this figure, at 2.3 GHz frequency, β reaches zero and Right-Left behavior is seen. According to full wave simulations left and right bands are from 1.8 to 2.3 GHz ($-K_0 < \beta < 0$) and 2.3 to 3.3 GHz ($0 < \beta < K_0$) respectively. We should mention, in order to get β diagram, it is sufficient to work out S_{21} phase as:

$$S_{21} = |S_{21}|e^{j\varphi} = e^{-\alpha d}e^{-j\beta l} \tag{1}$$

3.3. Radiation Characteristics

To investigate radiation field properties of the Antenna, one port is matched to 50 Ohm load and the other port is excited. Figure 4 shows normalized electrical field pattern in $\varphi = 90^\circ$ plane for frequencies 2.1 GHz to 2.3 GHz with 100 MHz increments.

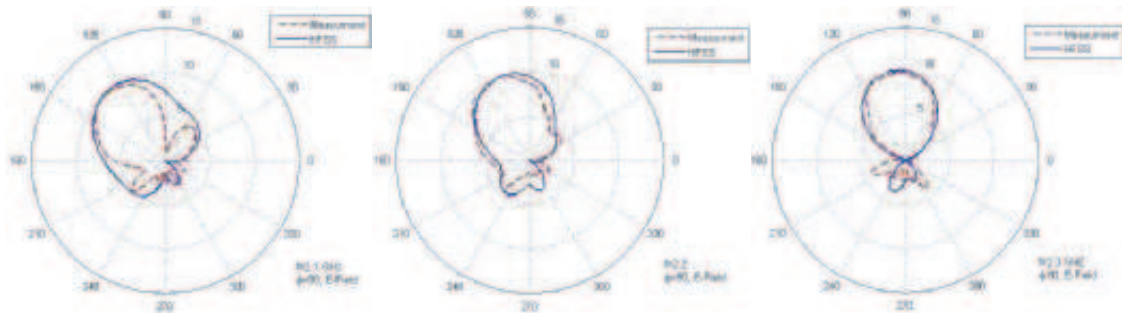


Figure 4: Normalized electrical field pattern in plane $\varphi = 90^\circ$ for frequencies 2.1, 2.2 and 2.3 GHz, fullwave simulation and experimental results are in good accordance.

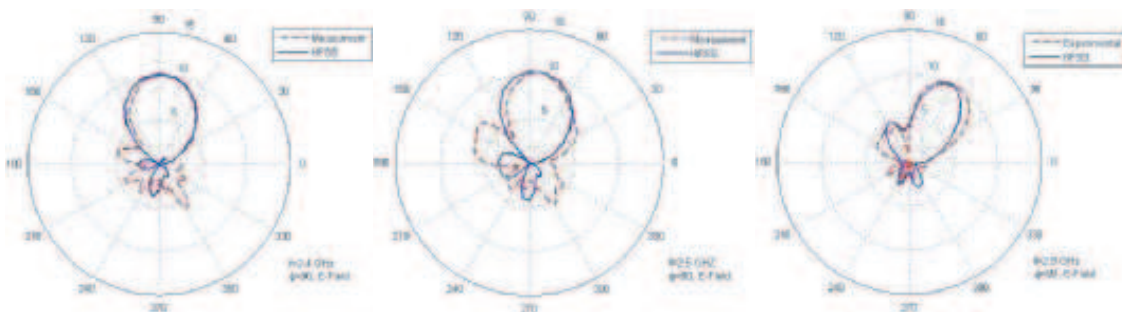


Figure 5: Normalized electrical field pattern in plane $\varphi = 90^\circ$ for frequencies 2.4, 2.5 and 2.9 GHz.

3. Caloz, C. and T. Itoh, "Novel microwave devices and structures based on the transmission line approach of meta-materials," *IEEE-MTT Int'l Symp.*, Vol. 1, 195–198, Philadelphia, PA, Jun. 2003.
4. Sanada, A., C. Caloz, and T. Itoh, "Characteristics of the composite right/left-handed transmission lines," *IEEE Microwave Wireless Compon. Lett.*, Vol. 14, No. 2, 68–70, Feb. 2004.
5. Caloz, C. and T. Itoh, "Application of the transmission line theory of left-handed (LH) materials to the realization of a microstrip LH transmission line," *Proc. IEEE-AP-S USNC/URSI National Radio Science Meeting*, Vol. 2, 412–415, San Antonio, TX, Jun. 2002.
6. Lai, A., C. Caloz, and T. Itoh, "Composite right/left handed transmission line metamaterials," *IEEE Microwave Mag.*, Vol. 5, No. 3, 34–50, Sep. 2004.
7. Lim, S., C. Caloz, and T. Itoh, "Metamaterial-based electronically-controlled transmission line structure as a novel leaky-wave antenna with tunable radiation angle and beamwidth," *IEEE Trans. Microwave Theory Tech.*, Vol. 53, No. 1, 161–173, Nov. 2004.
8. Lim, S., C. Caloz, and T. Itoh, "Electronically scanned composite right/left handed microstrip leaky-wave antenna," *IEEE Microwave Wireless Compon. Lett.*, Vol. 14, No. 6, Jun. 2004.

A Novel Dual-frequency Planar Inverted-F Antenna

Jian-Wu Zhang and Yi Liu

Department of Telecommunication, Hangzhou Dianzi University, China

Abstract— A new dual-frequency planar inverted-F antenna (PIFA) is developed for GSM 900 and DCS 1800. A U-shaped slot and a rectangle shaped slot are cut in the antenna radiation patch, which can obtain 2 operating frequencies. It has been demonstrated by simulation and measured that the presented antenna can cover the operating frequencies of GSM 900 and DCS 1800.

1. INTRODUCTION

The planar inverted-F antenna (PIFA) is one of the most popular antennas for various wireless communication systems due to its high efficiency, compact size and simple structure. This structure can be easily incorporated into personal communication equipment as reported in [1, 2]. In addition, mobile communication has developed rapidly, the number of mobile users is increasing quickly and the spectrum resources become more and more tense in the recent years. In order to meet the rapid growth of users, it requires to achieve dual-band or multi-frequency work in the communication system [3], therefore, the studies of dual-band and multi-frequency antenna becomes a hot spot [4–6]. The slot-loaded technology on single layer patch, which is usually called as slotting in the surface of patch, is caught a general concern for its advantages of simple, easy processing, and reduce the antenna size [7–9].

In [9], the authors presented a U-slot microstrip antenna, which mainly discussed the impact of U-slot parameters and the size of the floor to the frequency bands of antenna. Based on the above analysis, we present a novel U-slot planar inverted-F dual-frequency microstrip antenna. The main features of the antenna is to cut a U-slot in the radiation patch and a small slot in the end of U-slot, as well as cut a rectangular slot in the middle patch surrounded by the U-slot to achieve the dual-band work. Its biggest advantage is not only realizing the work of a dual-band microstrip but also meeting the requirements of small antenna. The configuration of the compact planar antenna is described in Section 2, while simulation and measured results are presented in Section 3, the conclusion is given in Section 4.

2. THE ANTENNA DESIGN

Figure 1(a) shows the configuration of the proposed antenna. The antenna structure includes a radiation patch, a floor, a coaxial and a short-circuited line. The antenna and the floor are made by the 0.25 mm copper, which has a certain degree of strength to ensure the stability of the antenna structure. The medium between the radiation patch and the floor is air. The antenna floor simulates a handheld device floor, which size is 40 mm × 40 mm. The radiation patch installed on the upper floors, the size of the radiation patch is 33 mm × 15 mm, the distance between the radiation patch and the floor is 7 mm. The radiation patch connects to the floor through a w width short-circuited line. The antenna taken coax-fed the central feeding pin and the grounding point are respectively connected to the radiation patch and the back of the floor. The location of the feeding point is regulated to achieve the impedance matching with the 50 Ω coax, reduce the return loss, increase the gain and satisfy the mobile communication frequency. As shown in Fig. 1(b), the distance from the antenna's hemline to the feeding point is d .

The size of a planar inverted-F antenna can be determined approximately from [10]:

$$f = \frac{c}{4(w+l)} \quad (1)$$

Where c is the velocity of light, w and l are the width and length of the antenna radiation patch, respectively, and f is the operating frequency. It is observed that the several major dimensions of antenna structure can be got when the antenna resonant frequency is known. As shown in Fig. 1(b), due to the U-slot in the radiation patch, the antenna is divided into two patches, which can achieves multi-frequency function and the U-slot can greatly reduce the size of the antenna. The outside U-shaped patch (patch 1) is mainly working in the GSM 900; the inside small U-shaped patch (patch 2) is working in the DCS 1800. By changing the size of these patches, it can acquire the

required resonant frequency. At last, the detailed dimension of the patch is summarized in Table 1. In addition, in order to obtain the two-band matching and greater bandwidth, the values of t , w and G can be optimized in the simulation to achieve the best results.

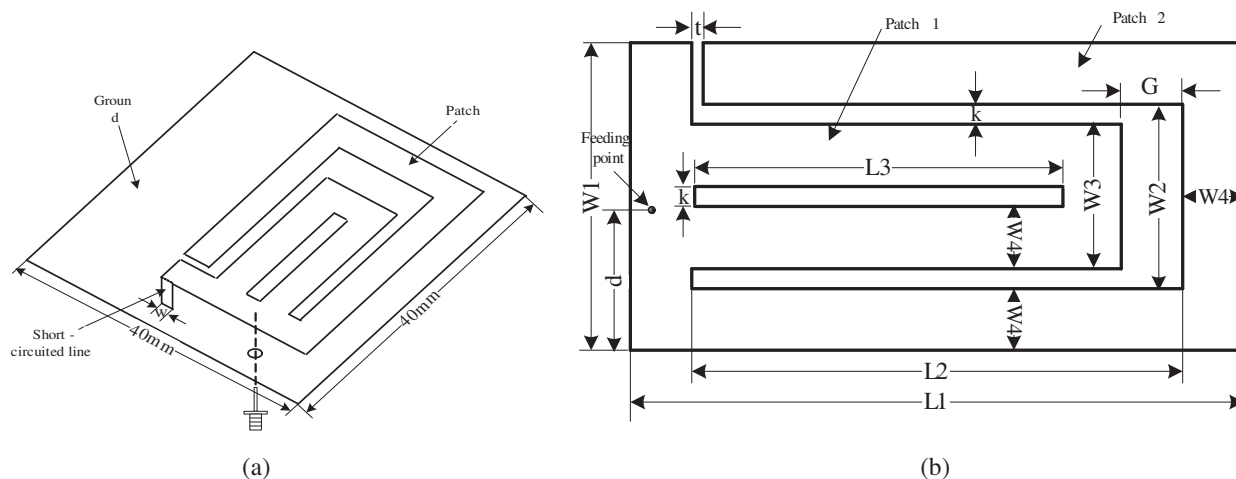


Figure 1: The configuration of the proposed antenna.

Table 1: Antenna dimension (mm).

$L1$	$W1$	$L2$	$W2$	$L3$	$W3$	$W4$	k	d
33	15	27	9	20.5	7	3	1	7

3. ANTENNA ANALYSIS

3.1. Simulation Results

In order to compare the effects of the main parameters on the antenna’s operating frequencies and bandwidth, and clarify the radiation mechanism of the slotted antenna, a lot of simulation was done by HFSS v10.0 (the software based on the FEM (finite element method)).

First, the cases of different values of G and w are simulated, the matching conditions of the antenna are shown in Fig. 2. It is observed that the matching condition of the two frequency bands

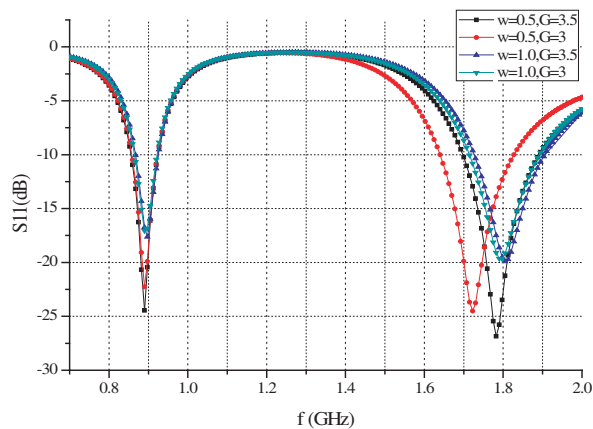


Figure 2: Simulated results for return loss of the antenna with different values of w and G ($t = 0.5$, other parameters are the same as in Table 1).

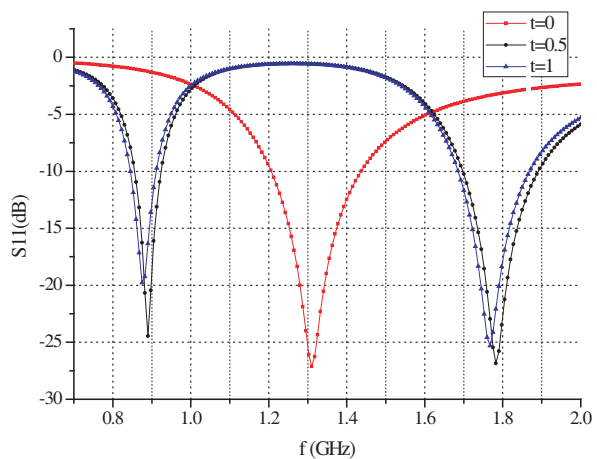


Figure 3: Simulated results for return loss of the antenna with different values of t ($w = 0.5$ mm, $G = 3.5$ mm, other parameters are the same as in Table 1).

is quite good while $G = 3.5$ mm and $w = 0.5$ mm. It is found that the antenna's simulation bands are 850–935 MHz in the lower band and 1700–1900 MHz in the upper band.

Next, Fig. 3 shows the simulation results in the cases of the different values of t . It is observed that the antenna becoming a single band antenna while without the small slot ($t = 0$), the operating frequency is 1210–1440 MHz. While with the small slot and the values of t is 0.5 mm, the matching condition of the two frequency bands is quite good.

3.2. Measured Result

To verify the performance of the presented antenna, a prototype was fabricated and measured. From the description of the antenna's configuration in Section 2, the antenna can be easily fabricated. The metal radiation patch can be cut from a metal plate (a 0.25-mm-thick copper plate is used in this study). Photograph of the fabricated antenna is shown in Fig. 4.

The return loss of the antenna was measured by S-parameter network analyzer (Agilent 8753ES), the central frequency is 1.35 GHz and span is 1300 MHz. The measured result is given in Fig. 5. We can see that two operating frequency bands of the antenna are 855–935 MHz and 1720–1900 MHz while the return loss is below -10 dB, and cover the frequency bands of GSM 900/DCS 1800. In general, the simulation and measured results are in good agreement.

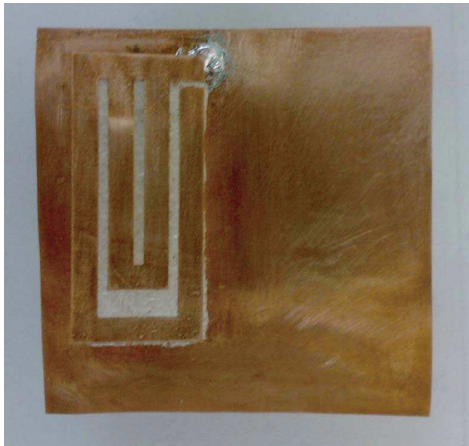


Figure 4: Photograph of the fabricated antenna.

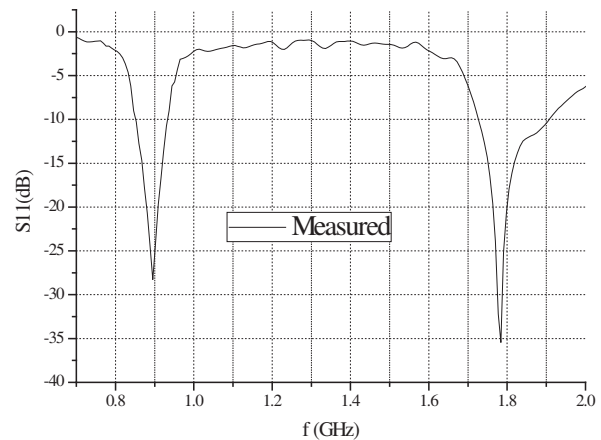


Figure 5: The measured result of return loss ($t = 0.5$ mm, $w = 0.5$ mm, $G = 3.5$ mm, other parameters are in Table 1).

4. CONCLUSION

A novel planar inverted-F antenna operating at the dual-frequency bands of GSM 900/DCS 1800 is presented in this paper. With the adoption of cutting a U-slot in the antenna radiation patch, the dual frequency operation is realized which cover the frequency bands of 855–935 MHz of GSM 900 and 1720–1900 MHz of DCS 1800. With the size of 33 mm \times 15 mm \times 7 mm, the antenna meets the demands of miniature, simple structure and dual-band operation of terminal antennas.

ACKNOWLEDGMENT

The work is supported by Zhejiang provincial Natural Science Foundation of China under grant number R105473.

REFERENCES

1. Boyle, K. R. and P. G. Steeneken, "A five-band reconfigurable PIFA for mobile phones," *IEEE Transactions on Antennas and Propagation*, Vol. 55, No. 11, 3300–3309, 2007.
2. Nguyen, V.-A., R. A. Bhatti, and S.-O. Park, "A simple PIFA-based tunable internal antenna for personal communication handsets," *Antennas and Wireless Propagation Letters*, Vol. 7, 130–133, 2008.
3. Morishita, H., Y. Kim, and K. Fujimoto, "Design concept of antennas for small mobile terminals and the future perspective," *IEEE Antennas and Propagation Magazine*, Vol. 44, No. 5, 30–43, 2002.

4. Li, R. L., B. Pan, and J. Laskar, "A compact broadband planar antenna for GPS, DCS-1800, IMT-2000, and WLAN applications," *IEEE Antennas and Wireless Propagation Letters*, Vol. 6, 25–27, 2007.
5. Song, C. T. P., P. S. Hall, H. Ghafouri-Shiraz, and D. Wake, "Triple band planar inverted F antennas for handheld devices," *Electron. Lett.*, Vol. 36, No. 2, 112–114, 2000.
6. Moon, J. I. and S. O. Park, "Small chip antenna for 2.4/5.8-GHz dual ISM-band applications," *IEEE Antenna and Wireless Propagation Letters*, Vol. 21, 313–315, 2003.
7. Yang, F., X.-X. Zhang, and X.-N. Ye, "Wide-band E-shaped patch antennas for wireless communications," *IEEE Transactions on Antennas and Propagation*, Vol. 49, No. 7, 1094–1100, 2001.
8. Nashaat, D. M., H. A. Elsadek, and H. Ghali, "Single feed compact quad-band PIFA antenna for wireless communication applications," *IEEE Transactions on Antennas and Propagation*, Vol. 53, No. 8, 2631–2635, 2005.
9. Row, J. S., "Studies of the planar inverted-F antenna with a U-shaped slot," *2003 IEEE Antennas and Propagation Society International Symposium*, 561–564, Columbus, Ohio, USA, June 2003.
10. Ogawa, K. and T. Uwano, "A diversity antenna for very small 800-MHz band portable telephones," *IEEE Transactions on Antennas and Propagation*, Vol. 42, No. 9, 1342–1345, 1994.

Influence of the Human Head in the Radiation of a Mobile Antenna

P. Pinho^{1,2} and J. Casaleiro¹

¹Instituto Superior de Engenharia de Lisboa (ISEL), Portugal

²Instituto de Telecomunicações, Portugal

Abstract— The big proliferation of mobile communication systems has caused an increased concern about the interaction between the human body and the antennas of mobile handsets. In order to study the problem, a multiband antenna was designed, fabricated and measured to operate over two frequency sub bands 900 and 1800 MHz. After that, we simulated the same antenna, but now, in the presence of a human head model to analyze the head's influence. First, the influence of the human head on the radiation efficiency of the antenna has been investigated as a function of the distance between the head and the antenna and with the inclination of the antenna. Furthermore, the relative amount of the electromagnetic power absorbed in the head has been obtained. In this study the electromagnetic analysis has been performed via FDTD (*Finite Difference Time Domain*).

1. INTRODUCTION

The cellular phone market has increased substantially during the last decade. The global commercial success of GSM has driven a great variety of cellular mobile radio systems. Along with market growth the possible risks related to the use of cellular phones have become an issue. A lot of research studies have been carried out based on this interaction [1–3], dealing generally with two aspects.

The first aspect is the mobile phone antenna influence on the human body in particular on the head. In fact, when a cellular phone works, the transmitting antenna is placed much closed to the user's head where a substantial part of radiated power is absorbed. It's important to characterize and quantify the distribution of the electromagnetic fields and the energy levels absorbed by the human tissues. In order to characterize the absorbed radiation by the human body, we use the Specific Absorption Rate (SAR) that represents the levels which is absorbed by a mass unit of tissue.

The second aspect is the influence of the user's body on radiation properties of the mobile phone, which is significant from the antenna design point of view. Antenna characteristics that are mostly affected by the presence of the human body are radiation pattern, input impedance and radiation efficiency [4]. The presence of the human body (and more specifically of the head) close to the handset causes generally degradation of its performance in comparison with the operation of the handset alone. The measure of this performance is the radiation efficiency of its antenna.

2. ANTENNA FOR GSM 900/1800

In this work, numerical simulations and measurements of a multi band antenna is presented for GSM 900/1800 MHz. The antenna was designed and simulated with the FDTD [6, 7], and a prototype of the final version was fabricated and measured. To obtain an antenna with two resonances we used a single U slot patch antenna [5] with two short pins, as shown in Figure 1. In the same figure, the radiation pattern of the antenna for 1800 MHz is presented.

3. INFLUENCE OF THE HUMAN HEAD IN THE RADIATION PROPRIETIES OF THE ANTENNA

In this section, we simulated the antenna in the presence of a human head model and analyze the head's influence. To studying this interaction, it is most important to understand the electromagnetic properties of body tissues. The dielectric properties of body tissues at radio frequencies and microwave frequencies have been examined by several authors. A recent comprehensive study is described in [8]. As a starting point of our research an anatomically-realistic model of the human head has been used. This model is known as SAM (Specific Anthropomorphic Mannequin), and uses a grid of $5 \times 5 \times 5$ mm. It is as most approximate to real heterogeneous human head as recommended in safety standards. The EM simulation is performed using FDTD method, which allows processing of the complicated heterogeneous geometries. It's important to refer that 3D simulation is time and computational resource consuming.

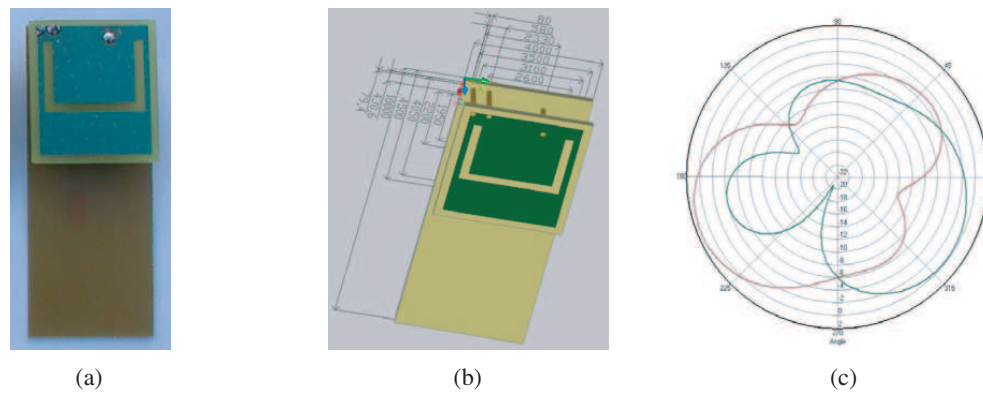


Figure 1: Antenna for GSM 900/1800. (a) Antenna prototype. (b) Antenna dimensions. (c) Radiation pattern for $\phi = 90^\circ$ (green) and $\theta = 90^\circ$ (red).

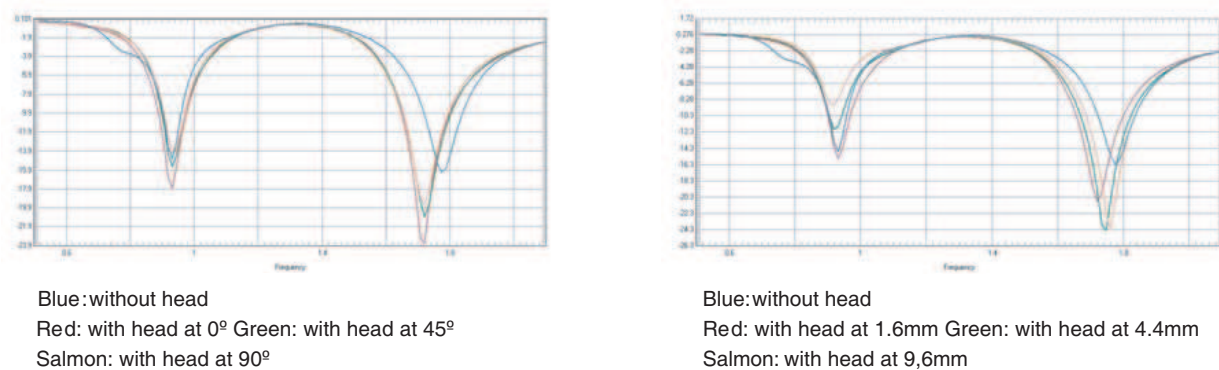


Figure 2: Return loss of the multiband antenna with and without head.

Based on theoretical and experimental results, the influence of the human head on the radiation efficiency of the antenna has been investigated as a function of the distance between the head and the antenna and with the inclination of the antenna. The considered distances were 1.6 mm, 4.4 mm and 9.6 mm. The antenna's inclinations were 0° , 45° , and 90° . In Figure 2, in the left we present the simulated results of the return loss for an antenna distance of 1.6 mm from the head to the handset, and for handset's inclinations of 0° , 45° , and 90° . In right, we present the simulated results for an inclination's antenna of 45° and distances of 1.6 mm, 4.4 mm and 9.6 mm.

Analyzing the Figure 2, it's possible to see that for the 900 MHz there are no significant differences in the level of return loss as well as the resonance frequency. For the 1800 there is a shift of resonance frequency to the left about 100 MHz but the level of return loss is improved.

In Figure 3, we present the radiation patterns of the antenna at 1800 MHz for $\theta = 90$. In the left the distance from the antenna to head is 1.6 mm and the inclination is 0° , 45° , and 90° . In the right, the antenna inclination is 45° and the distances are 1.6 mm, 4.4 mm and 9.6 mm. In Figure 4 we present the same results but for the plane $\phi = 90$. From the Figure 3 and Figure 4, we conclude that radiation patterns are much modified with the antenna inclination, moreover, with the distance there are no significant alterations, but the head presence change the radiation pattern.

4. SAR AS FREQUENCY FUNCTION

Furthermore, the relative amount of the electromagnetic power absorbed in the head has been obtained. The measurement of this type on the inside of the human body is extremely complicated and due to this fact, it is imperative the use of numerical methods. In this work, also presents the value of SAR as a function of handset's inclinations and the distance between the head and the handset, at the two frequencies, as we can see in the Figure 5. Investigations have shown that the SAR value depends on excitation frequency. The SAR for 900 MHz is more than double that obtained for 1800 MHz. There are no significant differences in SAR values between different inclinations of the handset, however when the distance from the head to antenna increase the SAR

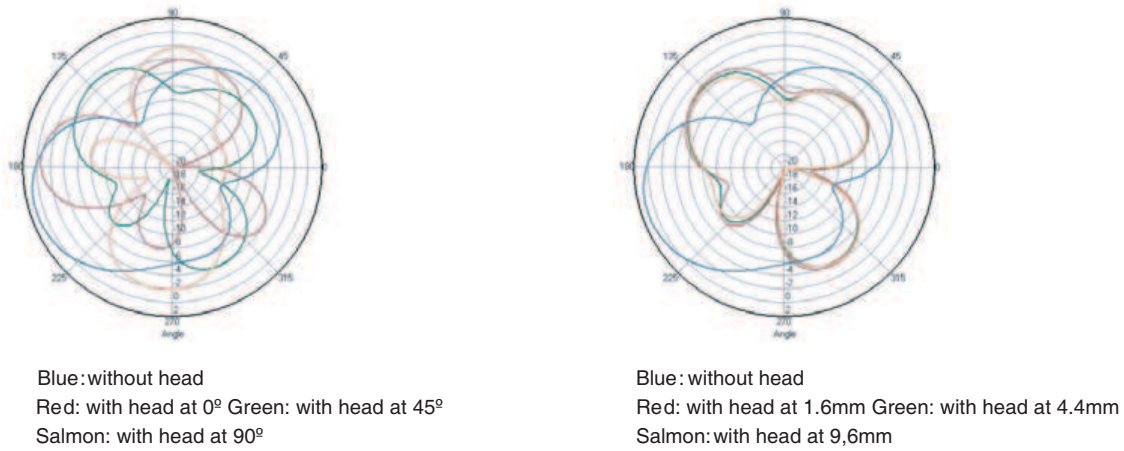


Figure 3: Radiation pattern of the antenna with and without head — xoy plane.

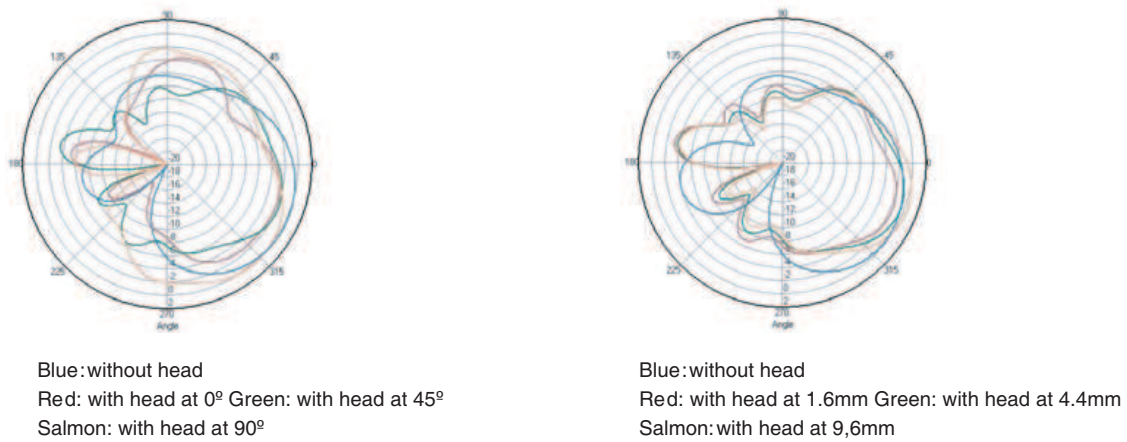


Figure 4: Radiation pattern of the antenna with and without head — yOz plane.

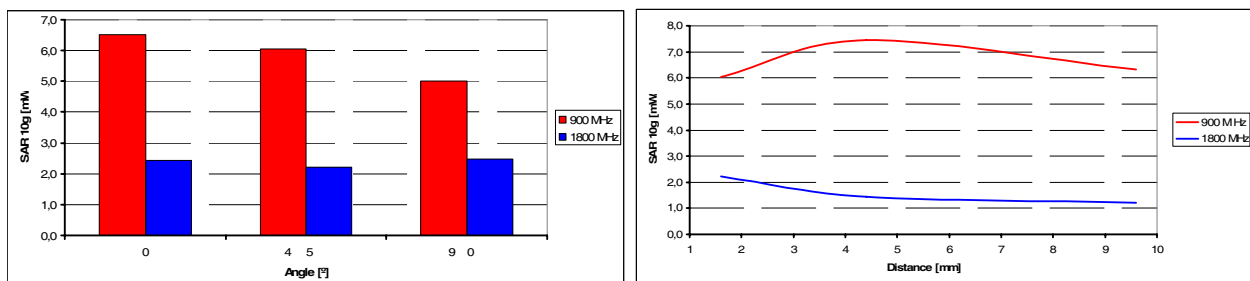


Figure 5: SAR as frequency function.

level tends to decrease but that decrease is not significant.

5. CONCLUSIONS

In this paper we present the influence of human head in the radiation patterns and in the return loss of a multiband antenna. It's possible to conclude that the radiation patterns have a strong change with the handset inclination, but the omnidirectional behavior remains. Moreover, with the distance there are no significant alterations, but the head presence changes the radiation pattern. In relation to the return loss the human head presence lead a shift in the resonance frequency especially for the 1800 MHz. Investigations have shown also that the SAR level depends on excitation frequency, and for 1800 MHz this value is lower than for 900 MHz.

REFERENCES

1. Zervos, T., A. Alexandridis, V. Petrović, K. Dangakis, B. Kolundžija, D. Olcan, A. Dordević, and C. Soras, “Accurate measurements and modelling of interaction between the human head and the mobile handset,” *Proc. 7th WSEAS Int. Multiconf. CSCC*, 2003.
2. Alexandridis, A., V. Petrović, K. Dangakis, B. Kolundžija, P. Kostarakis, M. Nikolić, T. Zervos, and A. Dordević, “Accurate modelling and measurements of a mobile handset EM radiation,” *Proc. 2nd Intern. Workshop on Biol. Effects of Electromagnetic Fields*, 251–259, 2002.
3. Jensen, M. A. and Y. Rahmat-Samii, “EM interaction of handset antennas and a human in personal communications,” *Proc. IEEE*, Vol. 83, 7–17, 1995.
4. Pedersen, G., M. Tartiere, and M. Knudsen, “Radiation efficiency of handheld phones,” *Proc. IEEE Vehicular Technology Conf.*, 1381–1385, Tokyo, Japan, May 2000.
5. Bhalla, R. and L. Shafai, “Resonance behavior of single U-slot and dual slot antenna,” *Antennas and Propagation Society International Symposium*, 700–703, 2001.
6. Yee, K. S., “Numerical solution of initial boundary value problems involving Maxwell’s equations in isotropic media,” *IEEE Trans. Antennas and Propagation*, Vol. 14, 302–307, April 1966.
7. Taflove, A. and S. Hagness, *Computational Electrodynamics — The Finite-Difference Time-Domain Method*, Artech House, 2005.
8. Gabriel, C., “Compilation of the dielectric properties of body tissues at RF and microwave frequencies,” Brooks Air Force Technical Report, AL/OE-TR-1996-0037, 1996.

A Novel Small Resonant Antenna Using the Meta-materials Array

Ali Azimi Fashi, Manoochehr Kamyab, and Mostafa Barati

Electrical Engineering Department, K. N. Toosi University of Technology (KNTU)
Seyedkhandan, Dr. Shariati Ave, Tehran, Iran

Abstract— A novel resonant antenna array based on the meta-materials zeroth-order resonator (ZOR) is presented in this paper. Since the resonant frequency of the zeroth-order resonator is independent of physical length of the resonator, therefore, antenna size can be reduced with no changes in operation frequency and due to the array structure antenna gain can be enhanced. A small-sized two-elements ZOR antenna array with 57% effective area reduction compared with a conventional array with a acceptable gain and broad radiation pattern is implemented at 3.94 GHz.

1. INTRODUCTION

Meta-materials or Left-handed materials (LHM) are characterized by simultaneously negative permittivity (ϵ) and permeability (μ) in a certain frequency band. Though LHM has not been found in the nature so far, recently, researches demonstrated the practical realization of LHM with left-handed transmission lines (TLs) [1]. The left-handed TL support backward waves in which phase velocity and group velocity have opposite signs. It can be shown that the dual of the simple transmission line shown in Fig. 1(a) propagates backward waves. The phase propagation constant (assuming to be lossless case) can be expressed as following:

$$\beta(\omega) = -1/\omega\sqrt{L_L C_L} \quad (1)$$

Therefore, the propagation phase velocity and group velocity are as follows:

$$v_p = -\omega^2\sqrt{L_L C_L}, \quad v_g = +\omega^2\sqrt{L_L C_L} \quad (2)$$

It can be drew from formula (2) that the phase velocity and group velocity are anti-parallel. LH-TL average cell size should be at least smaller than a quarter of wavelength to ensure that TL is an effectively homogeneous structure [2–6]. Since a real LH structure necessarily includes parasitic series inductances (L'_R) and shunt capacitances (C'_R) as shown in Fig. 1(b), therefore, a purely LH (PLH) structure does not exist, even in a restricted frequency range. This was the motivation for the definition of the term “Composite Right/Left-Handed” (CRLH) TL, allowing to account for the exact natural of practical LH media [2]. The essential characteristics of a CRLH TL is similar to a PLH TL at low frequencies and a PRH TL at high frequencies. Microwave applications with unusual properties have been proposed and implemented based on the CRLH TL theory [2, 7–10].

One of the applications of the CRLH structures is zeroth-order resonator (ZOR) [2] in which the CRLH TL supports an infinite wavelength at a finite microwave frequency, i.e., the voltage or currents distribution are uniform in the entire structure. When a CRLH TL is open-ended as shown in Fig. 2(a), it produces standing waves due to the open boundary condition and resonates when $l = m\lambda/2$ or $\theta_m = \beta_m l = m\pi$, where l is the physical length of the resonator and m is the mode number (see Fig. 2(b)) [11]. The real CRLH TL, which consists of unit cells, can resonate at the zeroth-order mode ($m = 0$) with an infinite wavelength as well as $m = \pm 1, \pm 2, \dots, \pm(N - 1)$ modes in which N is the number of unit cells. The zeroth-order resonant frequency depends only on the circuit elements of the unit cell and not on the physical length l of the resonator, thus a zeroth-order resonator could be made arbitrary small. When the zeroth-order resonator is used as a resonant antenna, due to the frequency independence of physical length, there is one degree of freedom in antenna design in terms of radiation pattern or gain choice, which will be an advantage of the zeroth-order resonating antenna. In this paper, a novel ZOR antenna array based on the CRLH TL is proposed and demonstrated. A small-sized antenna array with two five-unit-cell ZOR elements in the microstrip configuration is designed at 3.94 GHz and tested with simulation and experiment.

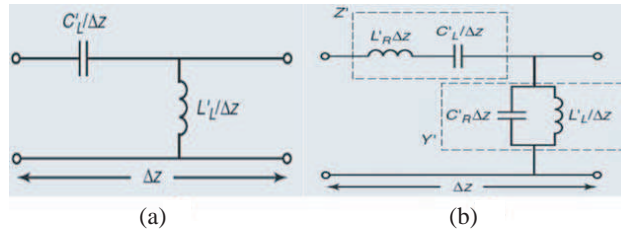


Figure 1: Equivalent circuits for Meta-materials TLs. (a) Pure left-handed TL, (b) the CRLH TL with a parasitic series inductance and a shunt capacitance.

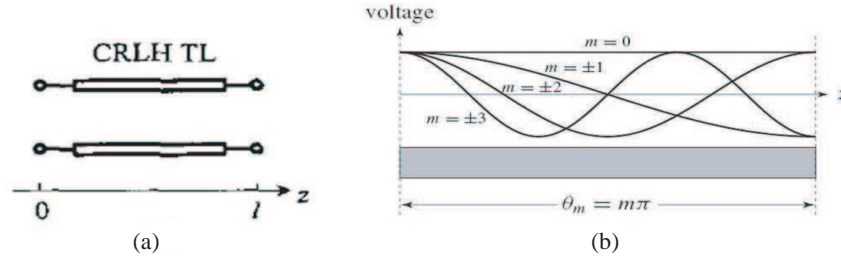


Figure 2: Resonant modes in an open-ended CRLH TL. (a) Open-ended ideal homogeneous CRLH TL, (b) resonant modes of the open-ended CRLH TL resonator.

2. ZERO-ORDER RESONATOR ANTENNA ARRAY

Figure 3(a) shows the proposed two-elements ZOR antenna array implemented with microstrip technology. Each of the ZOR elements consists of sequential connected unit cells each of which has a series interdigital capacitor and a shunt meander line inductor connected to a patch. When the virtual ground patch capacitor is large, the reactance of the total shunt branch in the unit cell becomes inductive [2] and the characteristics of CRLH TLs as in the circuit of Fig. 1(b) are achieved. The loss-less equivalent circuit of the unit cell shown in Fig. 3(b). The dispersion relation of the equivalent circuit of unit cell shown in Fig. 3(b) can be expressed as following [2]:

$$\beta = \frac{1}{p} \cos^{-1} \left\{ 1 - \frac{1}{2} \left[\frac{\omega_L^2}{\omega^2} \zeta + \frac{\omega^2}{\omega_R^2} - \left(\frac{\omega_{sh}^2}{\omega_R^2} \zeta + \frac{\omega_{se}^2}{\omega_R^2} \right) \right] \right\} \quad \text{where} \quad \zeta = \frac{\omega^2}{\omega^2 - \omega_g^2} \quad (3)$$

and $\omega_L = 1/\sqrt{L_L C_L}$, $\omega_R = 1/\sqrt{L_R C_R}$, $\omega_{se} = 1/\sqrt{L_R C_L}$, $\omega_{sh} = 1/\sqrt{L_L C_R}$ and $\omega_g = 1/\sqrt{L_L C_g}$. In addition, β is the phase constant and p is the period of the unit cell. Fig. 4 shows the dispersion relation of (3) [11]. The CRLH TL resonates when:

$$\beta_m = \frac{m\pi}{l} \quad (m = 0, \pm 1, \pm 2, \dots, \pm(N-1)) \quad (4)$$

Here, N is the number of unit cells in the resonator and is obtained as:

$$N = l/p \quad (5)$$

The resonant frequencies (ω_m) are sampled with a sampling rate of π/l in the β variable on the dispersion curves as shown by the dots in Fig. 4. By applying the condition $\beta = 0$ to the input impedance of the open-ended CRLH TL shown in Fig. 3, one can obtain the zeroth-order resonant frequency of the structure as:

$$\omega_{res}^{open} = \sqrt{\omega_{sh}^2 + \omega_g^2} \quad (6)$$

For the short-ended CRLH resonator, the zeroth-order resonant frequency becomes:

$$\omega_{res}^{short} = \omega_{se} \quad (7)$$

In the zeroth-order resonator, for both configuration (open- and short-ended), the resonance frequency depends only on the circuit elements of the unit cell, and not the physical length of the resonator as in (6) and (7). In the balanced case in which $\omega_o = \omega_{se} = \omega_{sh}$, the zeroth-order resonance occurs for both open-ended and short-ended resonators.

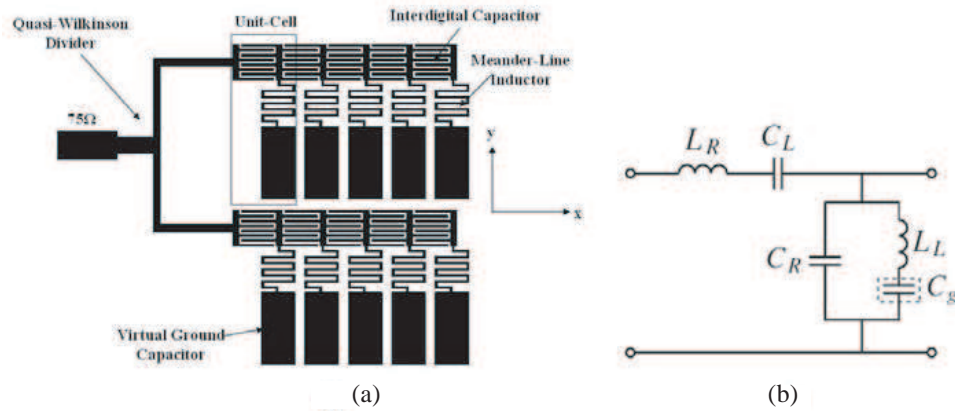


Figure 3: Microstrip ZOR antenna array implementation. (a) Circuit pattern, (b) loss-less equivalent circuit of the unit cell.

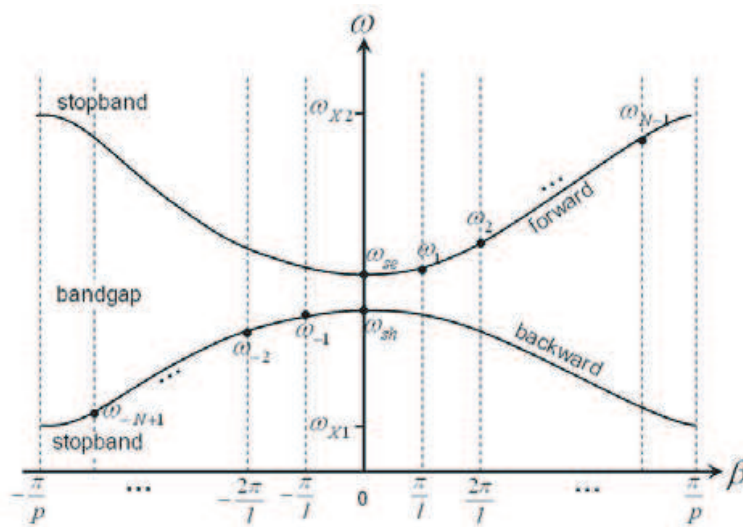


Figure 4: Typical dispersion diagram of the CRLH TL. The resonant frequencies of an open-ended or short-ended CRLH TL resonator are specified with dots on the $v_g > 0$ branch. ($\omega_{se} > \omega_{sh}$).

3. ZOR ARRAY DESIGN AND EXPERIMENTS

A ZOR antenna array with two 5-cell elements of Fig. 3(a) is designed on the Taconic TLY-5 substrate with a thickness of 1.57 mm and relative permittivity $\epsilon_r = 2.2$. The period of the unit cell p is 3.68 mm and a quarter of guided wavelength at operation frequency is about 12.6 mm, therefore, effective homogeneous condition is satisfied. The width of the interdigital electrodes is 0.182 mm and the space between them is 0.218 mm. The number of electrodes is 8 and the width of meander lines is 0.182 mm. The virtual ground plane size is $6 \times 2.8 \text{ mm}^2$ and the space between two elements is 1 mm. The ZOR elements are fed uniformly by a quasi-wilkinson power divider in which the input line size is $3 \times 1.4 \text{ mm}^2$ connected to the 75Ω line with length of 4 mm and the output lines size is about $13 \times 0.6 \text{ mm}^2$.

The length of the output lines is about one quarter of guided wavelength and the characteristics impedance of the each output line is almost $\sqrt{2}$ times more than of the input line. Fig. 5(a) shows the fabricated ZOR antenna array. The footprint area is reduced about 57% compared with a $\lambda/2$ conventional antenna array on the same substrate as shown in Fig. 5(b). Fig. 6 shows the simulation and experiments result for $|S_{11}|$ at the input port of the array. The measured zeroth-order resonant frequency is at 3.94 GHz and negative mode resonant frequencies are below the zeroth-order resonant frequency in the left-handed frequency band. In this structure $\omega_{sh} < \omega_{se}$, therefore, in the $|S_{11}|$ diagram, the first resonant frequency in the left of the bandgap is the ZOR frequency. The positive mode resonant frequencies are above the bandgap in the right-handed region. The simulated antenna gain is about 6.6 dB at resonant frequency as shown in Fig. 7. Fig. 8 shows

measured and simulated radiation patterns of the ZOR array antenna at its operation frequency of 3.94 GHz. As shown in Figs. 6 and 8, the measured results agree well with simulated results and broad directivity with no undesired side lobes is obtained. Measured return loss is about -12.5 dB and cross-polar level is within the acceptable range.

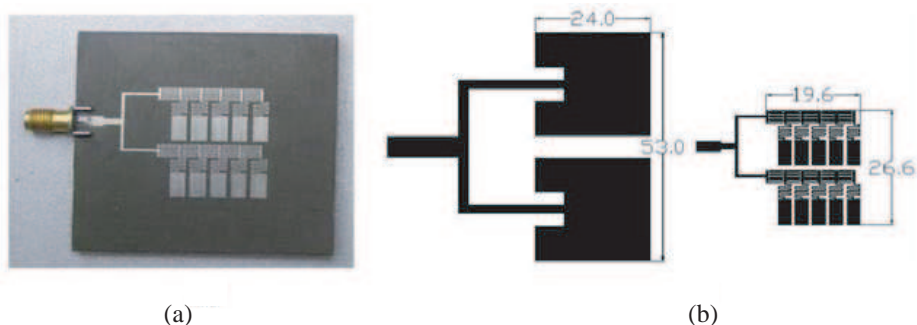


Figure 5: (a) Two-elements ZOR antenna array ($f = 3.94$ GHz), (b) footprint area of the ZOR array compared with a conventional array at the same frequency (the dimensions are based on the millimeter scale).

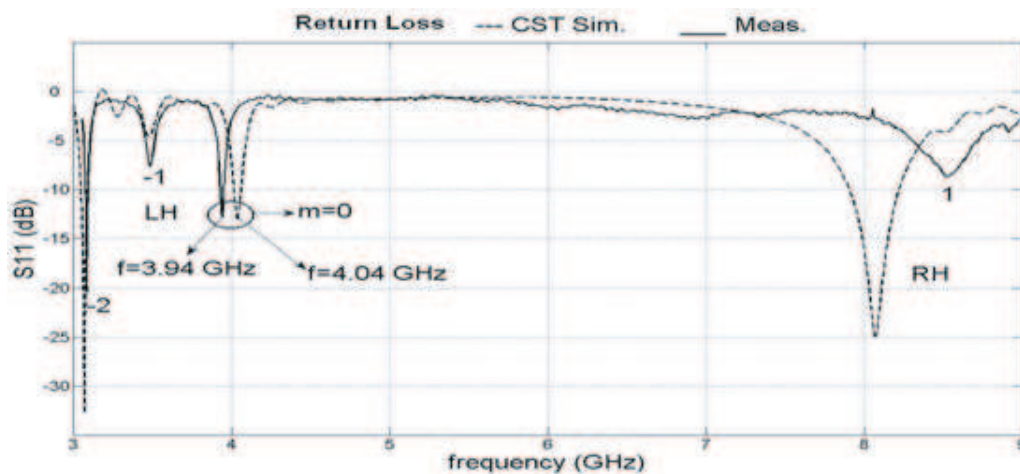


Figure 6: Measured and simulated $|S_{11}|$ of the prototype ZOR array antenna.

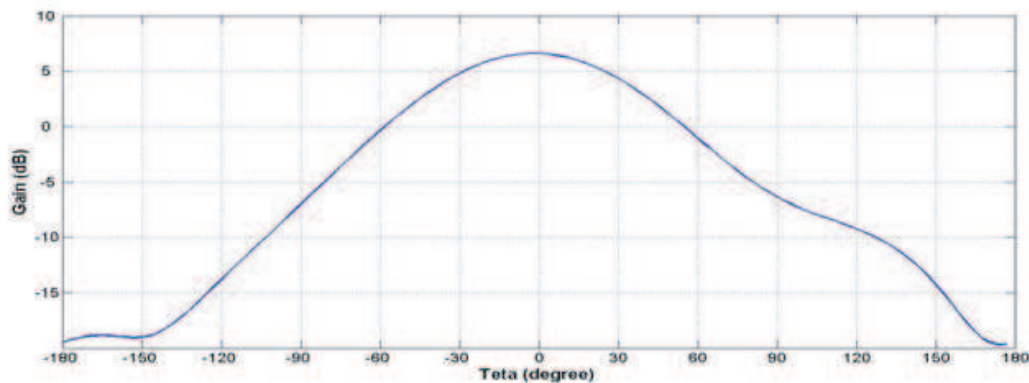


Figure 7: The variation of the simulated (CST) gain of the antenna with θ in plane $\varphi = 0$ at resonant frequency.

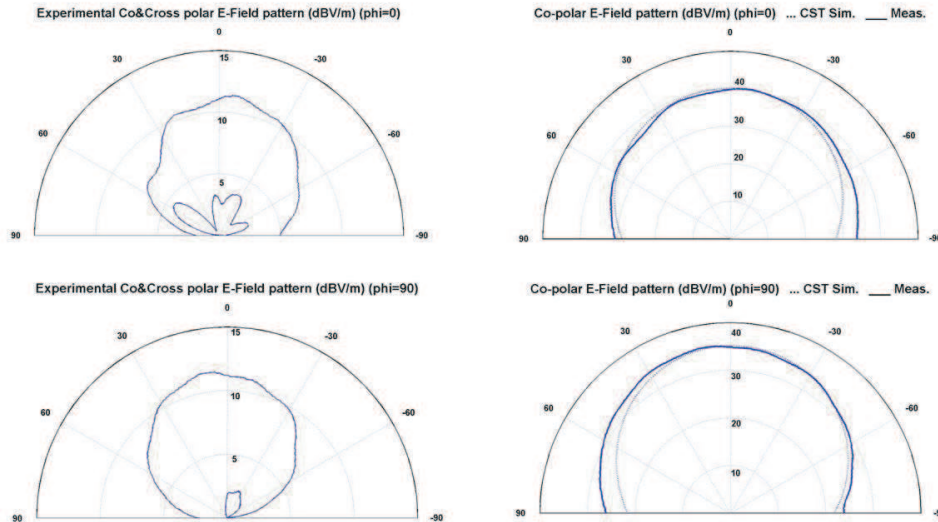


Figure 8: Measured and simulated radiation pattern.

4. CONCLUSION

A novel microstrip ZOR antenna array has been presented. The antenna size is determined only by reactances loaded in the unit cell and the space between elements and not by the physical length of the resonators. A small-sized and enhanced gain ZOR antenna with 57% effective area reduction compared with a conventional array with a broad directivity is demonstrated at 3.94 GHz.

ACKNOWLEDGMENT

This work is supported by Iran Telecommunication Research Center.

REFERENCES

1. Li, Y. and S. Xu, "A novel microstrip antenna array fed with CRLH-TL structure," *IEEE Antenna and Propagation Society International Symposium*, 4153–4156, July 2006.
2. Caloz, C. and T. Itoh, *Electromagnetic Metamaterials: Transmission Line Theory and Microwave Applications*, John Wiley & Sons, Inc., 2006.
3. Qi, Z. and L. Huan, "Design of printed antenna with left-handed array," *Asia-Pacific Microwave Conference Proceedings*, Vol. 4, 3, Dec. 2005.
4. Caloz, C. and T. Itoh, "Application of the transmission line theory of the left-handed (LH) materials to the realization of a microstrip LH transmission line," *IEEE-APS Int'l Symp. Digest*, Vol. 2, 412–415, Jun. 2002.
5. Oliner, A. A., "A periodic-structure negative-refractive-index medium without resonant elements," *IEEE-APS/URSI Int'l Symp. Digest*, 41, Jun. 2002.
6. Eleftheriades, G. V., A. K. Lyster, and P. C. Kremer, "Planar negative refractive index media using periodically L-C loaded transmission lines," *IEEE Trans. on Microwave Theory Tech.*, Vol. 50, No. 12, 2702–2712, Dec. 2002.
7. Sanada, A., C. Caloz, and T. Itoh, "Characteristics of the composite right/left-handed transmission lines," *IEEE Microwave and Wireless Component Letters*, Vol. 14, No. 2, 68–70, Feb. 2004.
8. Caloz, C., A. Sanada, and T. Itoh, "A novel composite right/left-handed coupled-line directional coupler with arbitrary coupling level and broad bandwidth," *IEEE Trans. on Microwave Theory Tech.*, Vol. 52, No. 3, 980–992, Mar. 2004.
9. Sanada, A., C. Caloz, and T. Itoh, "Planar distributed structures with negative refractive index," *IEEE Trans. on Microwave Theory Tech.*, Vol. 52, No. 4, 1252–1263, Apr. 2004.
10. Sanada, A., C. Caloz, and T. Itoh, "Novel zeroth-order resonance in composite right/left-handed transmission line resonator," *Asia-Pacific Microwave Conference Proceedings*, 1588–1591, Nov. 2003.
11. Sanada, A., M. Kimura, I. Awai, C. Caloz, and T. Itoh, "A planar zeroth-order resonator antenna using a left-handed transmission line," *European Microwave Conference*, Vol. 3, 1341–1344, Oct. 2004.

Radar Cross Section Measurements and Simulations of a Model Airplane in the X-band

I. M. Martin^{1,2}, M. A. Alves¹, G. G. Peixoto^{1,3}, and M. C. Rezende^{1,3}

¹Instituto Tecnológico de Aeronáutica, ITA-CTA, Brazil

²Universidade de Taubaté, UNITAU, Brazil

³Instituto de Aeronáutica e Espaço, Divisão de Materiais, IAE-CTA, Brazil

Abstract— The objective of this study was to illustrate how different methods of obtaining the Radar Cross Section (RCS) of an object may produce different results. RCS diagrams of a metallic airplane model (length, 0.64 m) were obtained in an anechoic chamber, with a Lab-Volt RCS system, and simulated with a simulation software. The measurements and simulations were carried out at the radar frequency of 9.4 GHz. The resulting RCS diagrams show that although there was a good correspondence between the main features in the RCS diagrams, some differences can still be observed, highlighting the need for different techniques to fully represent the RCS of an object.

1. INTRODUCTION

Radar cross section (RCS) diagrams are usually difficult to interpret due to the fact that they are two-dimensional representations of three-dimensional objects. Moreover, the difficulty in interpreting RCS diagrams is dependent upon the geometry of the object and, sometimes, on the techniques used to measure or calculate the RCS. Measurements are also affected by many external factors, such as instrumental errors, spurious reflections and interferences, which can degrade the quality of the experimental data. In this study, we measured the RCS of an airplane model with a conducting surface using two different experimental set-ups, and also simulated its RCS using commercial electromagnetic simulation software. The comparison of the data obtained shows that differences will arise regardless of the care taken while performing an experiment or carrying out simulations and that these differences should be taken into consideration when interpreting the data.

2. EXPERIMENTAL MEASUREMENTS

The experimental data were collected using two different experimental setups: One inside an anechoic chamber and another in a laboratory room using the Lab-Volt Radar Training System.

The anechoic chamber, is located in the Instituto de Fomento Industrial (IFI/CTA, Brazil). Figure 1 shows the radar antennas used in the measurements. These X-band horn antennas were manufactured by M2SAT (Brazil); each antenna has a gain of 10 dBi, and symmetric radiation patterns with low level of secondary lobes. The radar operated at 9.4 GHz, in a quasi-monostatic configuration and vertical polarization. A HP8360B (HP, USA) synthesized CW generator was used to generate the microwave radiation and the reflected signal was analyzed by a HP8593E (HP, USA) spectrum analyzer. It is estimated that the deviation of the RCS measurements was within 0.7 dB. The model used in the measurements is also shown in Figure 1; it is a scale model of a Boeing 777 with total length of 0.64 m ($\sim 20\lambda$). The body of the model is composed of an epoxy resin and its surface is coated with aluminum (the thickness of the coating is about 10 times larger than the skin depth of the aluminum at this frequency). The distance between the radar antennas and the model was about 6 m.

Electronic Warfare Laboratory (LGE/CTA, Brazil), consisting of interconnected subsystems that allow detailed studies of RCS in a laboratory environment. Measurements were carried out with inverse synthetic aperture radar, operating also at 9.4 GHz at short range, in the presence of noise and clutter. The effects of noise and clutter were removed using time-gating and subtraction techniques during the measurements. For the measurements, the distance between antenna and model was the same one used for the measurements in the anechoic chamber. Figure 2 shows the arrangement of the radar antenna and the model in the laboratory. The model was placed on a Styrofoam pedestal, invisible to radar waves.



Figure 1: Horn radar antennas (transmitting and receiving) (left), and model mounted on a rotating pedestal (right), inside the anechoic chamber.



Figure 2: Target mounted on a rotating pedestal and antenna (A) used in the lab-Volt radar training system.

3. RCS SIMULATION

The simulation software CADRCS [3] was used for the simulations. CADRCS uses physical optics combined with ray-tracing and shadowing of objects for the accurate calculation of the RCS of objects greater than radar wavelength [4]. A commercially available CAD model of the Boeing 777 was used in the simulations. The surface of the CAD model was discretized into triangular elements using Rhinoceros modeling tool [6] and imported to the simulation software. A Pentium 4 3.2 GHz PC computer with 4 GB of RAM was used. Figure 3 shows the CAD model used in the simulations, the surface of this model was discretized into 28555 triangular elements. The dimensions of the CAD model (length, wing span) were identical to the model used for the anechoic chamber and Lab-Volt measurements.

4. RESULTS

Both simulations and measurements were performed under the same conditions such as wave polarization and frequency, and distance between radar and object surface. The models were rotated in azimuth with respect to an axis perpendicular to their main symmetry axis. The measurements were obtained in a near-field situation since the distance, r , between the model and the radar antenna did not satisfy the far-field condition, $r > 2d^2/\lambda$, where d is the largest dimension of the model, and λ is the wavelength of the radar [5]. In the simulation, RCS values were calculated at 0.25° intervals; the measurements in the anechoic chamber and with the Lab-Volt system were ob-



Figure 3: CAD model of the Boeing 777 airplane used in the simulations, length 0.64 m.

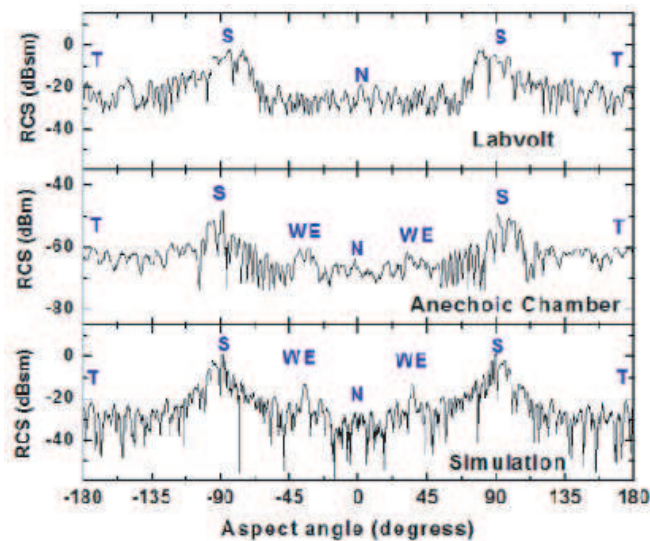


Figure 4: Comparison of RCS diagrams obtained from measurements (Lab-Volt, Anechoic Chamber), and simulations. In the figure, T, S WE, and N indicate that the tail, side, wing edge and nose of the airplane, respectively, were oriented toward the radar antennas. RCS values obtained from simulations and Lab-Volt measurements are displayed in dBsm, and results obtained in the anechoic chamber are displayed in dBm.

tained at approximately at 0.4° and 0.35° intervals, respectively. Figure 4 shows the RCS diagrams obtained from measurements and simulations.

The Lab-Volt Radar Training System, which has been described in detail elsewhere [1, 2], is located in the Of the three diagrams, the one obtained from simulations shows the highest level of detail and symmetry. This was expected, since simulations are not hindered by experimental or instrumental problems. The RCS diagram in this case clearly shows major features of the model, such as the sides of the airplane, corresponding to high reflectivity values, and the wing edge of the airplane. The anechoic chamber RCS diagram also shows these features, with the relative amplitude of the main features being similar to those in the simulation RCS diagram, but one observes that the diagram is not as symmetrical and that lobes corresponding to the same aspect angle have different widths. The RCS diagram obtained with the Lab-Volt system shows the least level of detail, failing the register, for instance, the wind edge, which is a prominent feature of the model; but the diagram in this case shows a good level of symmetry.

Differences between diagrams and the reduced symmetry in a diagram can be the result of many factors such as differences between the CAD model and the actual model, minor misalignments between the antennas and the model and of the model, incorrect positioning of the model on the pedestal, spurious reflections, and instrumental error. Since the diagrams are two-dimensional representations of three dimensional objects it is very difficult to identify sources of problems in the experimental procedures, especially when the experiments were set-up carefully.

5. CONCLUSION

The correct determination of the RCS of an object is a rather difficult task due to the many factors involved in the measurements such as the experimental sources of errors and that can alter significantly the RCS diagram of an object; and once the results are collected the RCS diagram itself is not easily interpreted due to its two-dimensional nature. On the other hand, simulations produce results free from experimental errors and can be carried out taking into account a larger of configurations number, but they depend on high computing power and can be time consuming. The results obtained above suggest that, whenever possible, simultaneous techniques should be used to determine the RCS more precisely.

ACKNOWLEDGMENT

The authors are thankful to the Ministry of Defense, Brazilian Air Force and Comando-Geral de Tecnologia Aeroespacial (CTA) for the technical support, to the personell of the anechoic chamber (IFI/CTA) for assisting with the measurements, the Laboratório de Guerra Eletrônica (LGE/CTA)

for the Lab-Volt measurements. The authors also acknowledge the financial support and the fellowships received from the Brazilian funding agency CNPq.

REFERENCES

1. Lab-Volt Radar Training System, <http://www.labvolt.com/products/telecommunications/dsp/radar-training-system-8096>, April 20, 2009.
2. Alves, M. A., I. M. Martin, A. C. Coelho, L. C. Folguera, and M. C. Rezende, “Measurement and interpretation of radar cross section data in an educational setting: A comparison between simulations and experiments,” *PIERS Proceedings*, 297–300, Beijing, China, March 23–27, 2009.
3. CADRCS-PC based software for radar simulation, <http://www.cadrcs.com>, April 20, 2008.
4. Essen, H., S. Boehmsdorff, G. Briegel, and A. Wahlen. “On the scattering mechanism of power lines at millimeter-waves,” *IEEE Trans. on Geoscience and Remote Sensing*, Vol. 40, No. 9, 1895–1903, 2002.
5. Knott, E. F., J. F. Schaeffer, and M. T. Tuley, *Radar Cross Section*, Artech House, Norwood, MA, 1993.
6. Rhinoceros — NURBS Modelling for Windows, <http://www.rhino3d.com>, April 20, 2008.

A Medium Open Range Radar Cross Section Facility in Brazil

G. G. Peixoto^{1,2}, M. A. Alves¹, I. M. Martin^{1,3}, and M. C. Rezende^{1,2}

¹Instituto Tecnológico de Aeronáutica, ITA-CTA, Brazil

²Instituto de Aeronáutica e Espaço, Divisão de Materiais, IAE-CTA, Brazil

³Universidade de Taubaté, UNITAU, Brazil

Abstract— In this paper, we report the establishment of a new radar measuring facility in Brazil. This facility has a radar operating in the X-, C- and S-bands. To the best of our knowledge, this facility is the first of its kind in Brazil and Latin America. Some of the first RCS measurements carried out in this facility are presented.

1. INTRODUCTION

The modernization of the Brazilian aeronautical industry requires that a better knowledge of the reflecting properties of aircraft and other flying objects be acquired. In order to understand and predict the response to radar waves of several types of objects, and fill a void in this area of the Brazilian technology, a medium range facility for the measurement of the radar cross section (RCS) has begun operating in Brazil. The main task of this facility is to measure the RCS of small- and medium-sized objects and to characterize radar absorbing materials. This facility is located in the Aeronautics and Space Institute (IAE/CTA) in the city of São José dos Campos, Brazil. Figure 1 shows a satellite image of the facility.



Figure 1: Aerial view of the RCS facility. The positions of the receiving and transmitting radar antennas and the support pylon are indicated by “A” and “P”, respectively. The antennas are located at the corner of the building facing the pylon P. The ground between the antennas and the pylon is composed of compacted soil covered with low vegetation. (Image Google Earth).

2. THE EXPERIMENTAL SET-UP

This is an open-air range, where the distance between antennas and target is 230 m. Objects whose RCS will be measured are placed on a rotating table (in azimuth) on the top of a pylon. The pylon used is a four-column square-based structure made of reinforced concrete, Figure 2(a). The height of the pylon is 7.95 m, the inner distance between columns is 1.0 m and its total width is 1.4 m. Atop the pylon there is a structure built from welded steel I-beams which houses a turntable assembly; the pylon and the turntable were designed to hold targets up to 2000 kg. In order to minimize its RCS, the surface of pylon will be covered by radar absorbing materials during measurements. This design, albeit not ideal, is a compromise between costs and design. A study of the RCS of the pylon was performed so that it could be oriented in order to minimize its radar reflection [1].

The radar antennas are placed on a metal structure and their height and orientation are fully adjustable. In Figure 2(b) are shown a pair of parabolic antennas with a diameter of 1.5 m. The height of the antennas is at the same level as the top of the pylon. The radar can operate in the S-, C- and X-bands (2–12 GHz). In the far-field condition, $r \geq 2D^2/\lambda$, where r is the distance between target and antenna, D is the largest dimension of the target and λ is the wavelength of

the radar [2], this setup can measure the RCS of objects with dimensions from 1.8 m, at 18 GHz, to 4.2 m at 2 GHz.

Figure 3 shows a block diagram of the instrument set-up used for RCS measurements. The transmitting branch of the circuit is composed of synthesized microwave generator (Agilent, model E8257D) operating from 250 kHz to 40 GHz and power of 15.85 mW (12 dBm) coupled to a 20 W power amplifier operating from 0.8 GHz to 20 GHz (Amplifier Research, model 20ST1G18). An isolator protects the microwave generator against return signals. The microwave generator allows the modulation of the width of the pulse from 10 ns to 42 s. The amplified signal from the generator is then coupled to the transmitting antenna.

The energy scattered back from the target is collected by the receiving antenna; this signal is transmitted to a low-noise amplifier. The output of the amplifier is sent to a spectrum analyzer (Anritsu, model MS6226C), operating from 9 kHz to 40 GHz, that displays or stores the RCS signature of the target. A DC blocker protects the spectrum analyzer against spurious signals. Low-loss flexible coax cables (Huber-Suhner, model SF10426.5) are used in the set-up.

The facility has now become fully operational. In the next section are shown some of the first RCS measurements carried out in this facility.

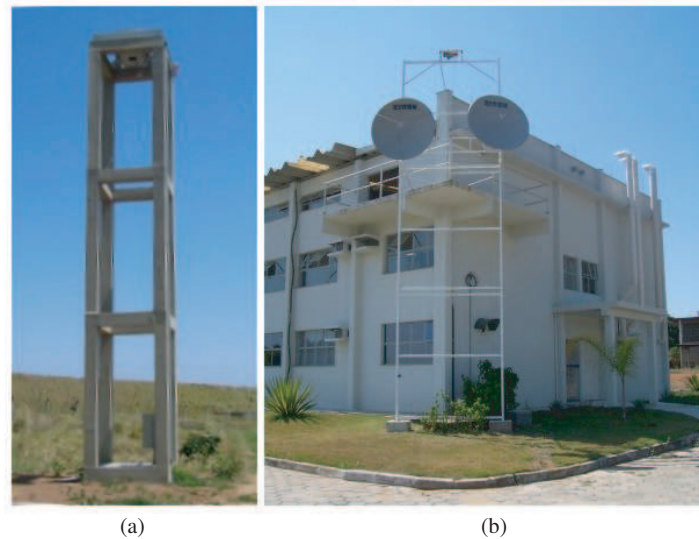


Figure 2: Support pylon, height of 7.95 m (right); and receiving and transmitting radar antennas, diameters of 1.5 m (left). Photos not to scale.

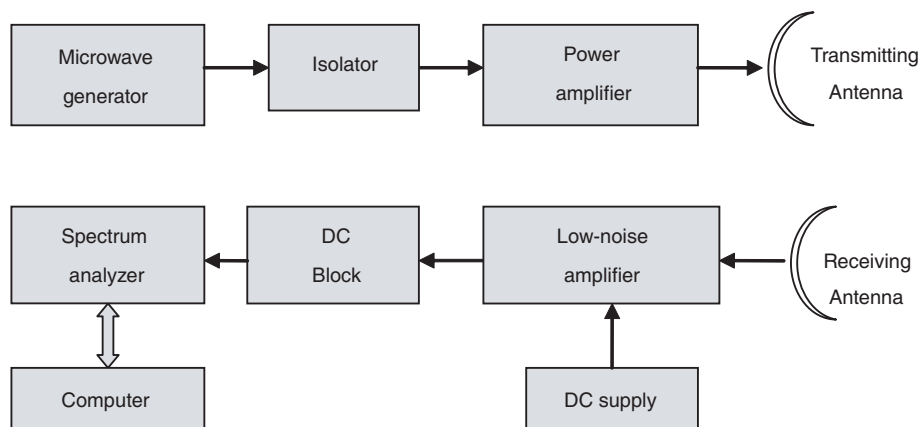


Figure 3: Block diagram of the transmitting-receiving circuit.

3. RCS MEASUREMENTS

As examples of the type of measurements that will be carried in this facility we present the RCS measurements of objects with simple and complex geometries.

First, the RCS of conducting objects with simple geometries such as a flat square panel ($1\text{ m} \times 1\text{ m}$) and a right dihedral ($0.5\text{ m} \times 0.5\text{ m}$). In Figure 4 are shown screenshots of the spectrum analyzer display of the RCS signature obtained for these two targets at 10 GHz and using different powers.

Comparison of the results shown in Figure 4 with those found in the literature [2, 3] show the overall good agreement in the recorded RCS pattern, which attests the quality of measurements obtained with the set-up. One can observe that the patterns are symmetric, and the RCS lobes are very well defined.

As an example of an actual target, the RCS of a decommissioned air-to-air missile is shown next. In Figure 5, one can see the missile being mounted on the pylon.

This missile has a conducting surface (aeronautical aluminum); a drawing of it is shown in Figure 6. The RCS diagram of this missile obtained as a function of the aspect angle is shown in Figure 7. For the measurements, the angle between by the fins and the horizontal plane was 45° .

The RCS plot shows, as expected, that the lateral view (90° and 270°) of the missile is the most reflective as a result of its larger reflecting area. Overall, the RCS plot has good symmetry; small deviation can be attributed to irregularities on the surface of the missile or minor misalignment of the missile with respect to the radar antennas. These results are in good agreement with the literature [4].

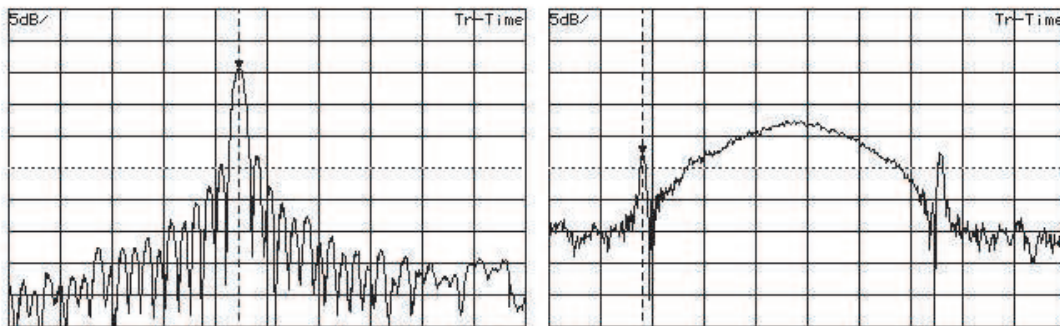


Figure 4: Screenshots of the spectrum analyzer. RCS patterns of a conducting flat plate (left), and a conducting right dihedral (right) at 10 GHz. Measurements were made with the targets on the rotating table on top the pylon.



Figure 5: Mounting of a decommissioned air-to-air missile on the pylon with a boom crane.

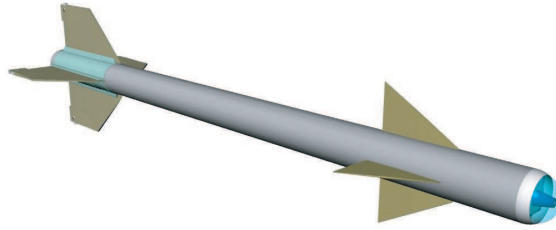


Figure 6: Decommissioned air-to-air missile used in RCS measurements. The overall length of the missile is 2.9 m.

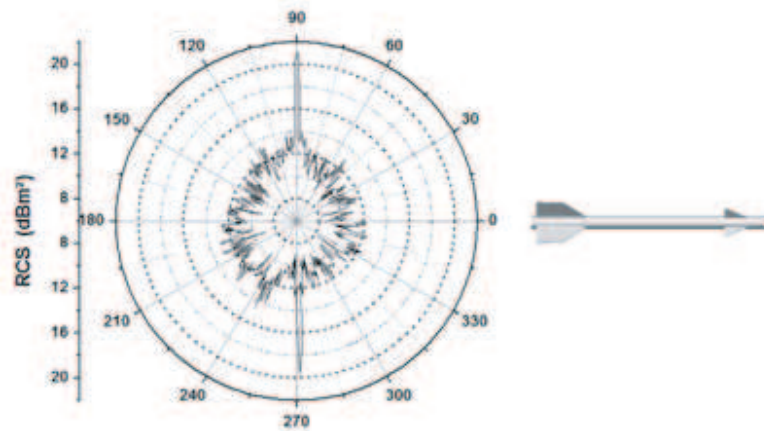


Figure 7: Polar plot of the RCS of a missile. RCS units in dBm^2 . The figure of the missile to the left shows the orientation of the missile.

4. CONCLUSION

The radar range facility will be used in the study of the RCS of small- and medium-sized objects as well as in the characterization of radar absorbing materials. It is fully operational and it is expected that it will contribute in the development of new materials and methods. This is the first facility of its kind in Brazil and it will help fill a void in the research related to scattering of radar waves and new materials for aeronautical and electronic industries.

ACKNOWLEDGMENT

The authors are thankful to the Ministry of Defense, Brazilian Air Force and Comando-Geral de Tecnologia Aeroespacial (CTA) for the technical support, and the Brazilian funding agencies CNPq and FINEP for the financial support and fellowships.

REFERENCES

1. Alves, M. A., G. G. Peixoto, and M. C. Rezende, "Orientation of a support pylon used in radar cross section measurements," *Proceeding of the Microwave and Optoelectronics Conference, IMOC 2007. SBMO/IEEE MTT-S Internacional*, 406–408, Salvador, Brazil, November 2007.
2. Knott, E. F., J. F. Schaeffer, and M. T. Tuley, *Radar Cross Section*, Artech House Inc., Norwood, MA, 1993.
3. Curri, N., *Radar Reflectivity Measurement: Techniques & Application*, Artech House, Norwood, MA, 1989.
4. Alves, M. A., G. G. Peixoto, and M. C. Rezende, "Simulations of the radar cross section of a generic air-to-air missile covered with radar absorbent materials," in *Proceeding of the Microwave and Optoelectronics Conference, IMOC 2007. SBMO/IEEE MTT-S Internacional*, 409–412, Salvador, Brazil, November 2007.

Suppression of Antenna's Radiation Sidelobes Using Particle Swarm Optimisation

Nik Noordini Nik Abd Malik, Mazlina Esa,
Sharifah Kamilah Syed Yusof, and Jayaseelan Marimuthu
Faculty of Electrical Engineering, Universiti Teknologi Malaysia
81310 UTM Skudai, Johor, Malaysia

Abstract— The presence of large sidelobe radiation beam levels of an antenna is undesirable as the antenna performance and efficiency will be greatly degraded. Antenna structures especially in array arrangements have the capability to provide interference reduction, improvement of the channel capacity and expanding the range of a signal's coverage. In this paper, Particle Swarm Optimization (PSO) is utilized to optimize the inter-element position of even-element linear antenna arrays (LAA). The objective is to produce as close to desired radiation pattern as possible that exhibits sidelobe level (SLL) suppression. The PSO algorithm can be successfully used to locate the optimum element positions based on symmetric and even-element LAAs of isotropic radiators. The results obtained showed that the PSO algorithm is capable of finding the optimal solution in most cases with superior performance over conventional method.

1. INTRODUCTION

Numerous studies on antenna arrays have been widely applied in phase array radar, satellite communications and other fields. The array pattern of an antenna array should possess high power gain, lower sidelobe levels, controllable beamwidth [1] and good azimuthal symmetry. The desired radiation pattern of the antenna array can be realized by determining the physical layout of the antenna array and by choosing suitable complex excitation of the amplitude and phase of the currents that are applied on the array elements. Thus, evolutionary optimization algorithm such as genetic algorithm (GA), simulated annealing (SA), and particle swarm optimization (PSO) have been introduced in antenna designs. Each algorithm has shown better performance due to its versatility, flexibility and capability to optimize complex multidimensional problem [2].

Currently, PSO algorithm is applied in many practical problems especially in electromagnetics. It has been used to obtain excitation coefficients of reconfigurable antenna arrays [3]; optimize the amplitude, phase, spacing and position of the elements in 37-element hexagon array [4] and suppress the SLL of linear array [5, 6].

In this paper, the PSO is exploited to produce the array radiation pattern that is nearest to the desired objective which exhibits sidelobe level (SLL) suppression and/or null placement. The inter-element position of even element linear arrays is optimized and re-located whilst maintaining uniform excitation over the array aperture. The work compliments [7] on node coordination.

2. LINEAR ANTENNA ARRAY SYNTHESIS

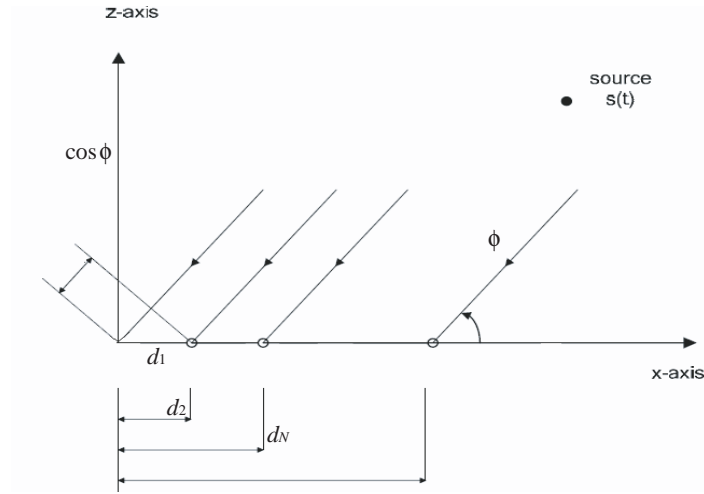
A one-dimensional symmetric LAA is assumed which is placed along the x -axis as depicted in Fig. 1. It has even number of elements up to N . Assuming uniform excitation of amplitude, $I_n = 1$ and phase $\beta_n = 0$, the array factor can be written as:

$$AF(\phi) = 2 \sum_{n=1}^N \cos[kd_n \cos(\phi)]. \quad (1)$$

where k , I_n , β_n , ϕ , and d_n are the wavenumber $\beta = 2\pi/\lambda$, excitation amplitude, phase, observation angle, and location of the n th element from the reference node at the origin, respectively. PSO will explore for the optimum element positions, d_n by aiming at the target objective which reduces the problem of SLL suppression and/or null placement.

3. PARTICLE SWARM OPTIMIZATION METHOD

Consider a set of population or swarm of matrix X , with elements that are referred as particles or agents. Each particle represents possible solution in defined population size, S . For an N -

Figure 1: $2N$ linear array geometry.

dimensional problem, the position of the i -th particle ($i = 1, \dots, S$) is represented as:

$$X = \begin{bmatrix} x_{11} & x_{12} & \cdots & x_{1N} \\ x_{21} & & & x_{2N} \\ \vdots & & \ddots & \vdots \\ x_{i1} & x_{i2} & \cdots & x_{iN} \end{bmatrix} \quad (2)$$

i.e., the position coordinates of the elements. x_{i1} is limited between two boundaries, U_1 and L_1 , i.e., ($L_1 \leq x_{i1} \leq U_1$) and x_{iN-1} is limited between two other boundaries, U_N and L_N i.e., ($L_N \leq x_{iN-1} \leq U_N$). The i -th particle in the solution space is determined by fitness function value which depends on the position coordinates. Every time the value of the fitness function i.e., F is minimized, the particle position is improved. The best previous position, pbest of the i -th particle can be defined as position matrix for an individual particle's best fitness function, pbest:

$$P = \begin{bmatrix} p_1 \\ p_2 \\ \vdots \\ p_i \end{bmatrix} \quad (3)$$

The global best position, gbest, is the position in the search space at which the best fitness function was achieved among all particles. It is defined as:

$$G = [g_1 \quad g_2 \quad \cdots \quad g_N] \quad (4)$$

Each particle should know its pbest and gbest. The positions and velocities of particles are then updated in each iteration according to the following equation:

$$v_{iN}(t+1) = wv_{iN}(t) + c_1 \text{rand}(t)[p_i(t+1) - x_{iN}(t)] + c_2 \text{Rand}(t)[g_N(t+1) - x_{iN}(t)] \quad (5)$$

where

$$V = \begin{bmatrix} v_{11} & v_{12} & \cdots & v_{1N} \\ v_{21} & & & v_{2N} \\ \vdots & & \ddots & \vdots \\ v_{i1} & v_{i2} & \cdots & v_{iN} \end{bmatrix} \quad (6)$$

is the velocity matrix of the particles. The velocity of each particle depends on the distance of the current position to the position with the best fitness function. In Eq. (5), $(t+1)$ and t refer to the time index of the current and previous iterations, $\text{rand}(t)$ and $\text{Rand}(t)$ are functions that generate random numbers between 0.0 and 1.0. The parameters c_1 and c_2 are the relative weight of the

pbest and gbest. It is selected as a value of 2.0 [5]. The parameter w is termed the inertial weight with value of 0.4. After time step, the new position of the particle is given by:

$$X(t+1) = X(t) + V(t+1) \quad (7)$$

The PSO is employed to optimize the optimum element position in order to improve the radiation pattern of the LAA, with $S = 30$. The objective of the algorithm is to find the gbest coordinates, G , that corresponds to the minimum value of the fitness function, F_{\min} or $F(g_1, g_2, \dots, g_N)$. The fitness function identifies how good the position vector of each particle satisfies the requirements of the optimization problem. The fitness function is computed using:

$$F = \sum_{s=i}^{s=j} |AF(\phi_s)|^2 + \sum_n |AF(\phi_n)|^2 \quad (8)$$

where s is the region where the SLL is suppressed and n is the angle where the nulls are placed. As the fitness function decreases, the radiation pattern improves with related particle's position x_{iN} . Therefore, when the fitness function discovers its optimized minimum value, the PSO algorithm will terminate successfully.

4. RESULTS AND DISCUSSION

A $2N$ -element LAA with different numbers of elements and desired radiation pattern have been considered to assess the effectiveness of the PSO in the optimization. The LAA is assumed to be symmetric about the x -axis with uniform interelement spacing of $\lambda_0 = \lambda/2$. Initially, the particle position, X is randomly generated in the range of 0 to 1.5 to produce more diverse possible solutions. Some boundary conditions are also defined to d_n which is allowed to vary from $0.8\lambda_0$ to $1.5\lambda_0$ except for d_1 which is allowed to vary from $0.3\lambda_0$ to $1.0\lambda_0$. The applied parameters are: Swarm size, $S = 30$, particle size depends on the problem dimension, c_1 and c_2 equal to 2.0, internal weight $w = 0.4$. The particles are represented by the spacing between the neighbor elements.

Case 1. A 14-element LAA is simulated for SLL suppression. The element positions for both conventional and PSO methods are given in Fig. 2 which is symmetrical by the y -axis. The radiation pattern is presented in Fig. 4. It is clearly seen that the PSO algorithm provides improvement to the SLL suppression. Almost all sidelobes have been minimized particularly the first SLL and far sidelobes.

Case 2. A 10-element LAA is designed for null placement at 76° and 104° . Fig. 5 shows that deep nulls of -58 dB have shown in Fig. 4. From Fig. 5, it can be inferred that larger beamwidth is obtained by using PSO because of the null placement at the desired angle. In addition, there are also decrements of all SLLs. The total length of the element by using PSO has increased to merely 4.2 which is less than that of the conventional method as in Fig. 4.

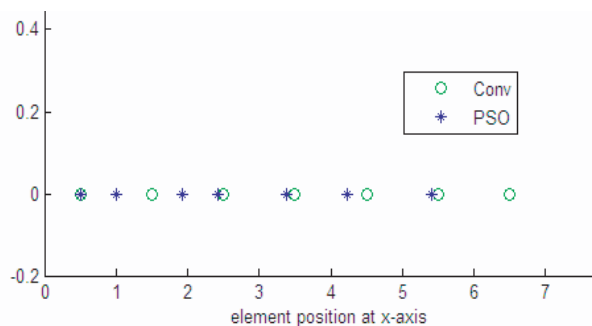


Figure 2: Element position of the 14-element LAA using PSO and conventional methods. Numbers are normalized wrt $\lambda_0 = \lambda/2$.

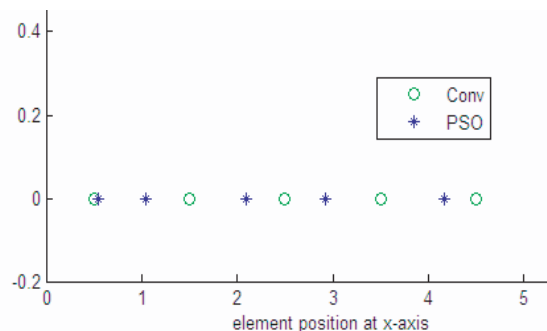


Figure 3: Element position of the 10-element LAA using PSO and conventional methods. Numbers are normalized wrt $\lambda_0 = \lambda/2$.

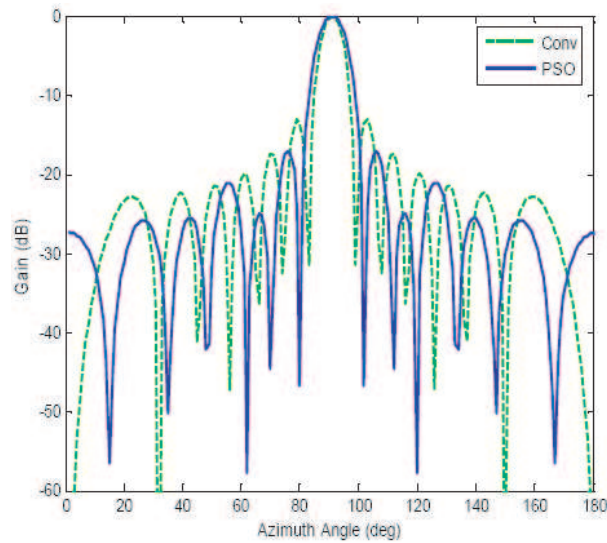


Figure 4: Radiation patterns of 14-element LAA by using PSO and conventional methods. SLL suppression at $(0^\circ, 80^\circ)$ and $(99^\circ, 180^\circ)$.

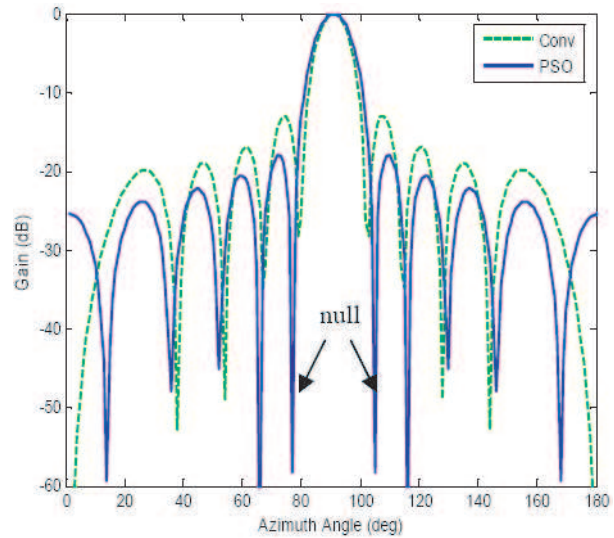


Figure 5: Radiation patterns of 10-element LAA by using PSO and conventional methods. The null placement are at 76° and 104° .

5. CONCLUSION

The PSO algorithm has been shown to successfully improve the radiation pattern of the LAA as desired. All the design requirements of the radiation pattern simulation for the LAA is presented and highly satisfied. The developed PSO algorithm has successfully optimized the position of the array elements to demonstrate a radiation pattern with either suppressed SLL, null placement, or both.

ACKNOWLEDGMENT

The work is supported by Universiti Teknologi Malaysia and Ministry of Higher Education, Malaysia.

REFERENCES

1. Zaharis, Z., D. Kampitaki, A. Papastergiou, A. Hatzigaidas, P. Lazaridis, and M. Spasos, "Optimal design of a linear antenna array using particle swarm optimization," *Proc. of the 5th WSEAS Int. Conf. on Data Networks, Communications and Computers*, 69–74, Bucharest, Romania, October 16–17, 2006.
2. Rattan, M., M. S. Patterh, and B. S. Sohi, "Design of a linear array of half wave parallel dipoles using particle swarm optimization," *Progress In Electromagnetics Research M*, Vol. 2, 131–139, 2008.
3. RahmatSamii, Y., D. Gies, and J. Robinson, "Particle swarm optimization (PSO): A novel paradigm for antenna designs," *The Radio Science Bulletin*, Vol. 305, 14, 2003.
4. Chen, T. B., Y. B. Chen, Y. C. Jiao, and E. S. Zhang, "Synthesis of antenna array using particle swarm optimization," *Asia-Pacific Microwave Conference Proceedings 2005 (APMC 2005)*, Vol. 3, 4, December 4–7, 2005.
5. Khodier, M. M. and C. G. Christodoulou, "Linear array geometry synthesis with minimum sidelobe level and null control using particle swarm optimization," *IEEE Transactions on Antennas and Propagation*, Vol. 53, No. 8, August 2005.
6. Bevelacqua, P. J. and C. A. Balanis, "Minimum sidelobe levels for linear arrays, antennas and propagation," *IEEE Transactions on Antennas and Propagation*, Vol. 55, No. 12, 3442–3449, December 2007.
7. Malik, N. N. N. A., M. Esa, and S. K. S. Yusof, "Intelligent optimization of node coordination in wireless sensor network," *Conference on Innovative Technologies in Intelligent Systems & Industrial Applications (CITISIA 2009)*, 25–26, July 2009.

Small Size and Multiband Monopole F-shaped Antenna Configuration for Wireless Communications Applications

Fawwaz J. Jibrael and Majd F. Yuhanna

Electrical and Electronic Engineering Department, University of Technology, Baghdad, Iraq

Abstract— The performance and analysis of a small size and multiband monopole F-antenna (MFA) are introduced. The proposed antenna design, analysis and characterization are performed using the Method of Moments (MoM) technique. The radiation characteristics, VSWR, reflection coefficient, input impedance, gain, and polarization of the proposed antenna are described and simulated using 4NEC2 software package. The proposed antenna operates at higher than frequency band (3 or 4 bands) depending on dimensions of the antenna.

1. INTRODUCTION

In today's world of expanding wireless communications, there is increasing need for more compact, multiband, and moderate gain antennas for portable communication systems to respond to the great demand for both military and commercial communication systems. Multi-band and wideband antennas are desirable in personal communication systems, small satellite communication terminals, and other wireless applications. Wideband antennas also find applications in Unmanned Aerial Vehicles (UAVs), Counter Camouflage, Concealment and Deception (CC&D), Synthetic Aperture Radar (SAR), and Ground Moving Target Indicators (GMTI). Some of these applications also require an antenna be embedded into the airframe structure. Monopole F-Antenna (MFA) designs can assist in meeting these design requirements.

The designed antenna operates at more than one frequency, characterized by its small size, whose design depends on variable dimensions, and is not printed antenna [1–3]. It offers high gain ranging between 4-to-10 dB.

2. PROPOSED ANTENNA GEOMETRY AND DESIGN

Figure 1 depicts the proposed antenna, known as monopole F-antenna (MFA), placed in YZ -plane. This antenna is divided into three parts: L_1 , L_2 , and L_3 , as shown in Figure 1 with relevant dimensions. This antenna is simulated using commercial numerical modeling software 4NEC2, a Method of Moment-based software. The Method of Moment (MoM) is used to calculate the current distribution along the monopole F-antenna, and hence the radiation characteristics of the antenna [4]. The 4NEC2 program is used in all simulations. This is very effective in analyzing antennas that can be modeled with wire segments, such as the one under consideration here. To suit the requirements, the antenna is modeled with no dielectric present, although some of the practical implementations do require dielectric support [5]. The modeling process is simply done by dividing all straight wires into short segments where the current in one segment is considered constant along the length of the short segment. It is important to make each wire segment as short as possible without violating computational restrictions maximum segment length to radius ratio. In NEC, to model wire structures, the segments should follow the paths of conductor as closely as possible [6].

Feed source of this antenna is set at 1 volt and the design frequency is chosen as 750 MHz, which gives design wavelength λ of 0.4 m (40 cm), giving length (L_1) of the corresponding $\lambda/4$ monopole antenna length of 10 cm and the wire conductor radius of 1 mm, as shown in Figure 1.

Figure 1 consists of two ((a) and (b)) different shapes of the proposed antenna, differing only in dimension (L_3). The effect of dimensions' variation can be seen on input impedance, gain, VSWR, and frequency bands in the results subsection later.

3. ANTENNAS SIMULATIONS AND RESULTS

From the results of Method of Moment simulation code (NEC), used to perform detailed study of VSWR, reflection coefficient, gain, input impedance, polarization and radiation pattern characteristics of the monopole F-antenna.

The real and imaginary parts of the input impedance of these proposed antennas (Figure 1(a) and 1(b)) are shown in Table 1. It shows the multiple resonance characteristics of the antenna together

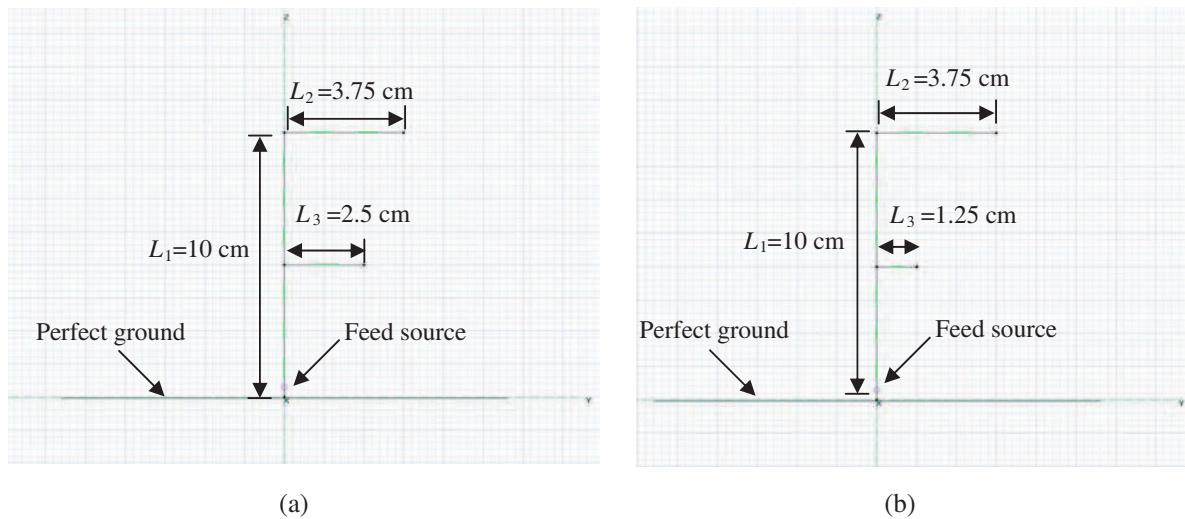


Figure 1: Proposed antenna geometry.

with VSWR of the antenna. It is found that the proposed antenna 1 (Figure 1(a)) has triple-band behavior at the resonance frequencies 519 MHz, 3110 MHz, and 5966 MHz with acceptable bandwidth for reflection coefficients < -10 dB, at these frequencies (VSWR < 2). However, the proposed antenna 2 (Figure 1(b)) has four-band behavior at the resonance frequencies 527 MHz, 1574 MHz, 3697, and 6097 MHz with acceptable bandwidth for reflection coefficients < -10 dB, at these frequencies (VSWR < 2). Table 2 shows the gain at each frequency in the XZ -plane and YZ -plane for the two proposed antennas.

The radiation patterns at these resonant frequencies in the planes YZ -plane and XZ -plane are depicted in Figure 2 for the two proposed antennas.

Table 1: Resonant frequencies and input impedances for proposed antenna.

	Frequency (MHz)	Input impedance (Ω)		VSWR	Reflection coefficient (dB)	Bandwidth (MHz)
		R	X			
Proposed antenna 1 $L_1 = 0.1$ m, $L_2 = 0.0375$ m, $L_3 = 0.025$ m	519	27.42	0.321	1.823	-10.7	36
	3110	43.3	-0.11	1.155	-22.9	250
	5966	87.47	0.075	1.749	-11.3	211
Proposed antenna 2 $L_1 = 0.1$ m, $L_2 = 0.0375$ m, $L_3 = 0.0125$ m	527	29.48	-0.3	1.696	-11.8	48
	1574	26.92	-0.34	1.857	-10.5	30
	3697	62.8	-0.02	1.256	-18.9	260
	6097	56.15	-0.005	1.123	-24.7	382

Table 2: The gain of the proposed antenna at the resonant frequencies in the two planes.

	F (MHz)	Gain (dB)	
		XZ -plane ($\phi=0$)	YZ -plane ($\phi=90$)
Proposed antenna 1 $L_1 = 0.1$ m, $L_2 = 0.0375$ m, $L_3 = 0.025$ m	519	5	5
	3110	7.64	4.19
	5966	7.64	9.84
Proposed antenna 2 $L_1 = 0.1$ m, $L_2 = 0.0375$ m, $L_3 = 0.0125$ m	527	5.01	5.01
	1574	6.61	5.26
	3697	7.57	6.1
	6097	7.4	9.37

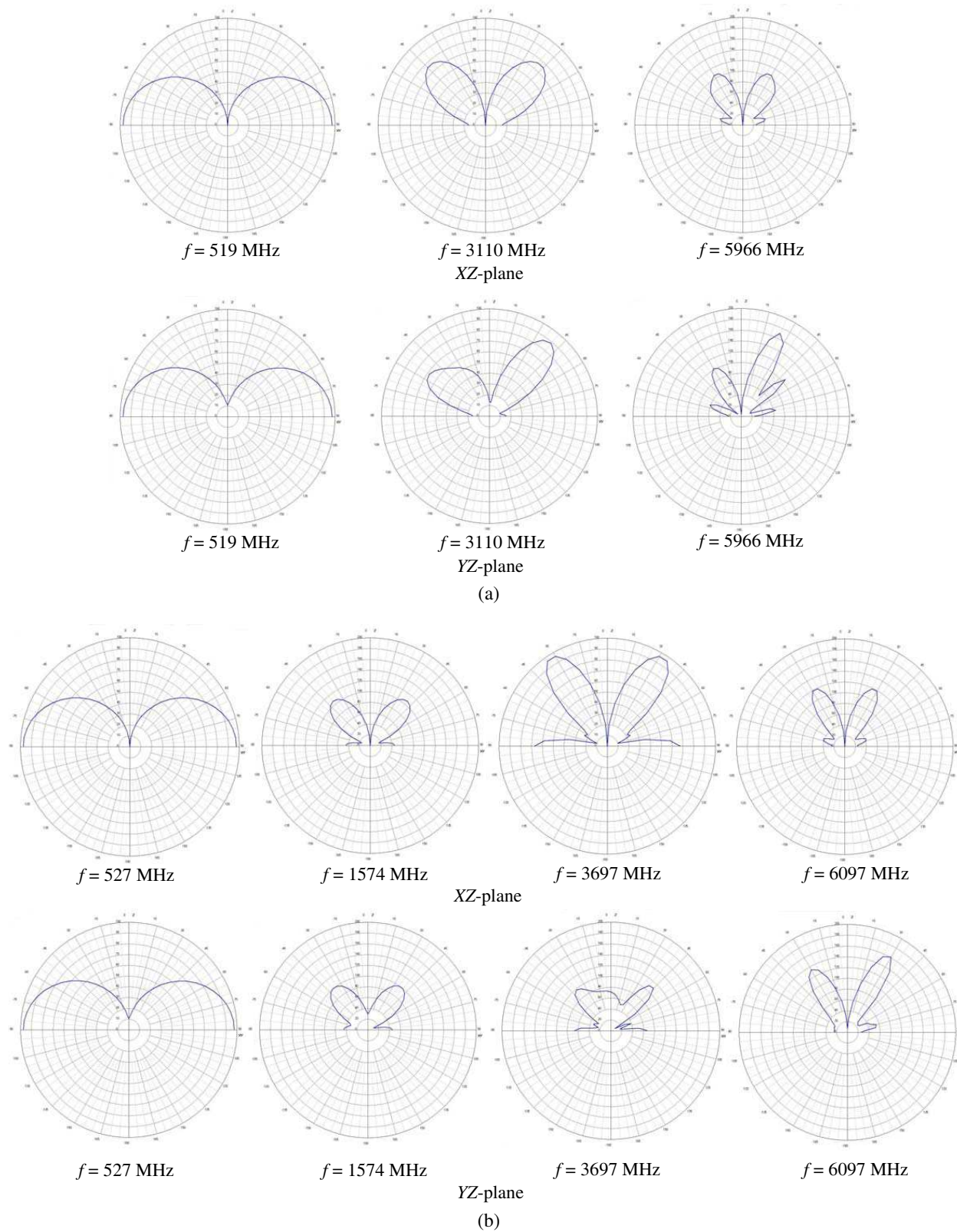


Figure 2: Radiation patterns of the modeled antenna. (a) Radiation patterns of the proposed antenna 1 ($L_1 = 0.1$ m, $L_2 = 0.0375$ m, $L_3 = 0.025$ m), (b) radiation Patterns of the proposed antenna 2 ($L_1 = 0.1$ m, $L_2 = 0.0375$ m, $L_3 = 0.0125$ m).

4. CONCLUSION

A monopole F-antenna for multiband wireless communications systems has been designed. The simulation results obtained by 4NEC2 show good agreement with measured results. It is shown that the proposed antenna 1 with dimensions ($L_1 = 0.1$ m, $L_2 = 0.0375$ m, $L_3 = 0.025$ m) operates at triple-band frequencies, while the proposed antenna 2 with dimensions ($L_1 = 0.1$ m, $L_2 = 0.0375$ m, $L_3 = 0.0125$ m) operates at four-band frequencies. The VSWR of the proposed antennas is found less than 2, which gives reflection coefficients less than -10 dB. In addition, these antennas have high gain greater than 3 dB with axial ratio equal to zero in YZ -plane which gives linear polarization, while in XZ -plane, the axial ratio is been variable with theta angles, giving elliptical polarization with senses in right, left, and linear directions.

REFERENCES

1. Yang, H. Y. D., "Printed straight F antennas for WLAN and bluetooth," *IEEE Antennas and Propagation Society International Symposium*, Vol. 2, 918–921, 2003.
2. Song, P., P. S. Hall, H. Ghafouri-Shiraz, and D. Wake, "Triple-band planar inverted F antenna," *IEEE Antennas and Propagation Society International Symposium*, Vol. 2, 908–911, 1999.
3. Lee, C.-J., K. M. K. Leong, and T. Itoh, "Broadband small antenna for portable wireless application," *Antenna Technology: Small Antennas and Novel Metamaterials, iWAT 2008*, 10–13, 2008.
4. Balanis, C. A., *Antenna Theory: Analysis and Design*, 2nd Edition, Wiley, 1997.
5. Vinoy, K. J., K. A. Jose, et al., "Hilbert curve fractal antenna: A small resonant antenna for VHF/UHF applications," *Microwave Optical Technol. Lett.*, Vol. 29, 215–219, 2001.
6. Burke, G. J. and A. J. Poggio, *Numerical Electromagnetic Code (NEC) Program Description*, Lawrence Livermore Laboratory, 1981.

Design and Manufacturing the Balance Amplifier Using the Lange Coupler in X-Band

Mohammad Nikfal Azar, Manochehr Kamyab, and Mehrdad Djavid
K. N. Toosi University of Technology, Iran

Abstract— In this paper we demonstrate and manufacturing the balance amplifier with 10 GHz central frequency using the microelectronic technology. we designed this structure in the range of 8 to 12 GHz frequency and utilize a lange coupler as an input and output port which has 17 dBm returned power. The coupler has been designed in HFSS as well as IE3D software and a substrate which is for this coupler is TMM6.

1. INTRODUCTION

For designing a wideband amplifier with constant gain there is a need to design a special matching network or using a feedback network. Using a balance amplifier (Fig. 1) is a common method for manufacturing a wideband amplifier with constant gain and an acceptable returned power in input and output ports. The advantages of a balance amplifier are:

- (1) The input and output VSWR are depended on the coupler.
- (2) There is a wide stability range.
- (3) If one of the amplifiers is disconnected balance amplifier will work with decreasing a 6 dB power.
- (4) We can connect a balance amplifier structure to another structure easily.

The input and output VSWR are small, so tow units have been isolated by coupler. We used a 3 dB power divider in input port and a 3 dB power mixer in output port of our final structure. One of the 3 dB structures that can have a 3 dB wideband coupling is Lange coupler (Fig. 2) that has four ports as 2 inputs and 2 outputs.

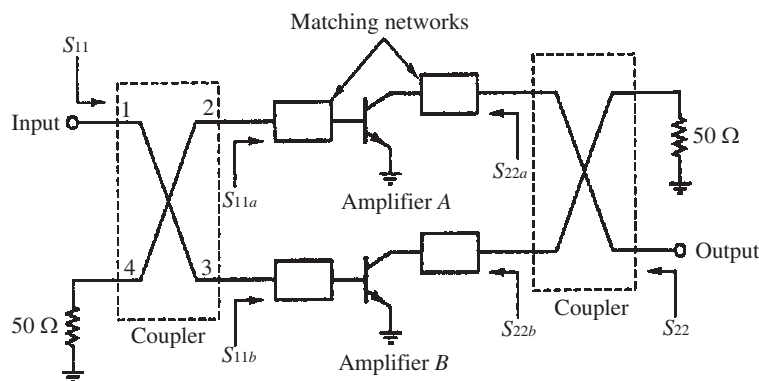


Figure 1: Lange coupler structure.

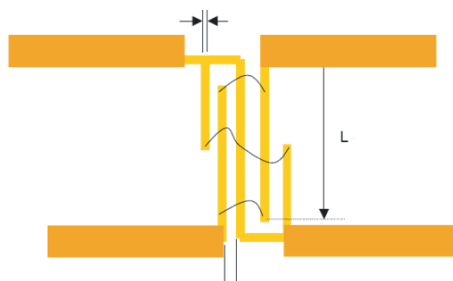


Figure 2: 3 dB Lange coupler structure.

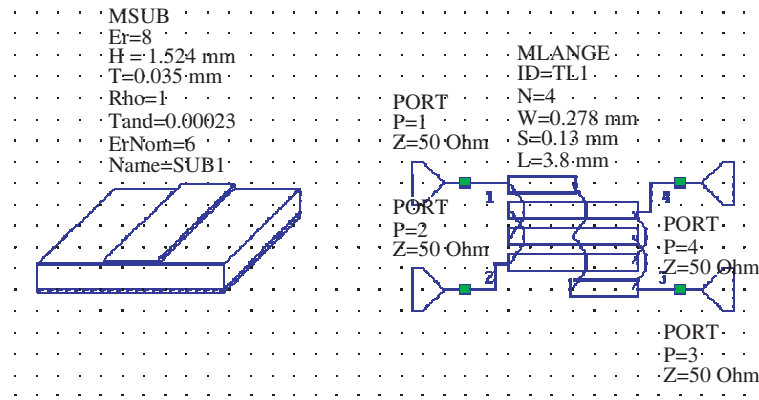


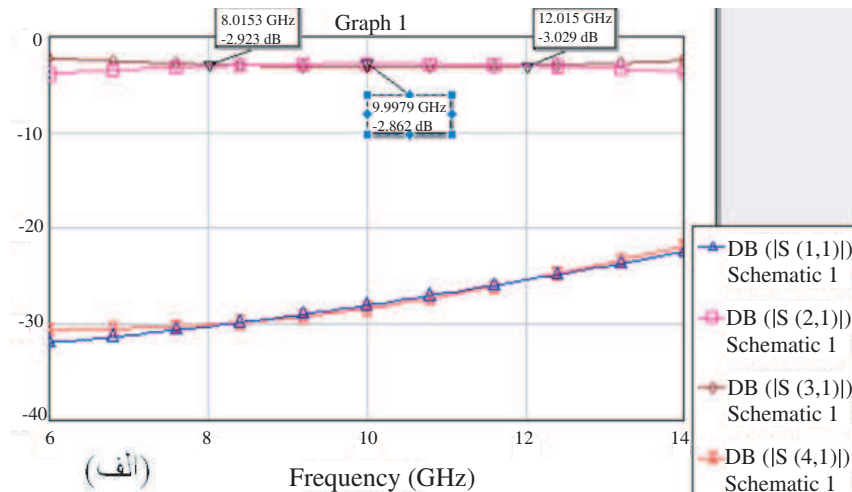
Figure 3: Lange coupler schematic using TMM6 substrate.

2. LANGE COUPLER DESIGN

2.1. Lange Coupler

Directional couplers do not have large amount of coupling because of their short length and long width. This produces Interdigital couplers that are improved by Lange. Lange coupler has been designed for 3 dB coupling in 4 to 8 GHz. Designing a 3 dB Lange coupler needs a special substrate. This substrate is TMM6 with 1.524 mm height and er of 6. The requirements for designing of our lang coupler are:

- (1) Distance between lines (s)
- (2) Lines width (w)
- (3) Lines length that is $\lambda/4$ in using frequency.

Figure 4: S_{11} , S_{21} , S_{31} , S_{41} plot.

We can calculate the s , w using below formulas:

$$C = 10^{-3/20} = 0.7079$$

$$Z_{oo}/Z_{oe} = R = \frac{C}{(C+1)(N-1)} \left(\sqrt{1 + (1/C^2 - 1)(N-1)^2} - 1 \right)$$

$$R = 0.29786 \quad Z_{on} = 50 \Omega$$

$$\sqrt{Z_{oo} \cdot Z_{oe}} = \frac{Z_{on} \sqrt{(N-1+R)(N-1)(R+1)}}{(1+R)} = 96.272 \Omega$$

$$Z_{oe} = \sqrt{\frac{(\sqrt{Z_{oo} \cdot Z_{oe}})^2}{R}} = 176.4 \Omega \quad Z_{oo} = \sqrt{(\sqrt{Z_{oo} \cdot Z_{oe}})^2 \cdot R} = 52.5 \Omega$$

2.2. Amplifier

There is a need to design a matching network for A and B amplifiers design. Designing has been done in ADS and AWR. Our matching network has been simulated with fullwave ADS software. Transistor used in our Amp is NE325S01 and the substrate is RD4003 with 508 mm height and dielectric constant 3.38. It should be noted that 1 dB changes in working range.

3. MANUFACTURING RESULTS

3.1. Lange Coupler

Thin film or MMIC technologies are useful structures for making Lange couplers because of coupled lines sharpness and accuracy. We want to make microelectronic structure with below limitations:

- (1) 100 μm minimum distances between lines.
- (2) Measuring accuracy to Copper thickness, between 50–80 μm .
- (3) Substrate resistance for fixing bonding.
- (4) Accurate design in PCB plots.

Directional couplers cannot have high coupling because of short length and long width. This produces interdigital couplers that are improved by Lange. Lange coupler has been designed in 8 to 12 GHz with 4 lines and 50 Ohm coupling.

Designing 3 dB, Lange coupler for microelectronic technology needs a high quality substrate to reduce shining. This substrate should have high dielectric constant and suitable height according to manufacturing technology. we can see the results of this simulation achieved AWR in Fig. 3. Also the results of output ports between 6 to 14 GHz has been shown in Fig. 4.

Second and third terminals have 90 degree phase difference. According to HFSS simulation with 0.025 mm gold bonding wire diameters and copper thickness is 50 μm . The results are written as follows:

$$\begin{cases} S = 0.13 \text{ mm} \\ w = 0.278 \text{ mm} \\ L = 3.8 \text{ mm} \end{cases} \longrightarrow \begin{cases} S = 0.1 \text{ mm} \\ w = 0.266 \text{ mm} \\ L = 3.56 \text{ mm} \end{cases}$$

The reason for width changes and line distances is for accuracy in AWR software with special substrates. In addition, the reason for line width changes is output taper frequency shift. Because output tapers have coupled on each other that causes line length and frequency shift. Reflection coefficient is lower than -15 dB. Also giving signal from port is -15 dB in isolated port.

Manufacturing results of two serial couplers balance structure are obtained with respect to Fig. 4. We have used connectors with core radius of 0.6 mm in input and output ports and there is a 50 Ohm load in 4th port.

We used gold bonding instead of bridge because of short distance between lines (Fig. 6). To reduce inductive effect we have used 2 bonds for each unit. The results of second port output power to first port input power and reflection coefficients are shown in Fig. 7 that as we can see reflection coefficients are lower than -15 dB in working bandwidth.

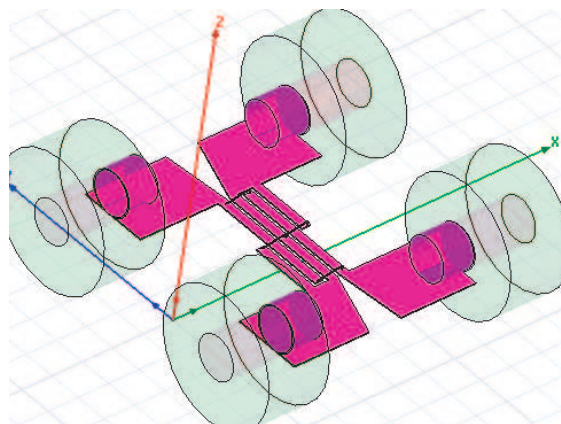


Figure 5: Lange coupler simulated structure with HFSS.

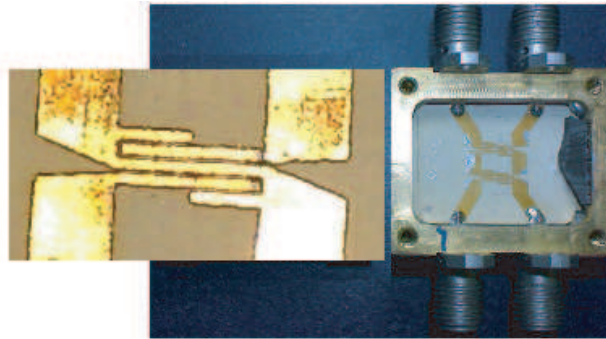


Figure 6: Lange coupler structure.

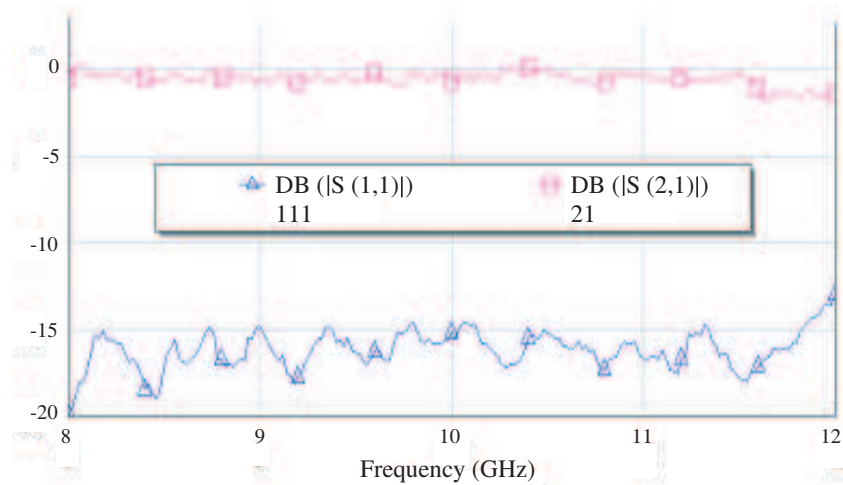
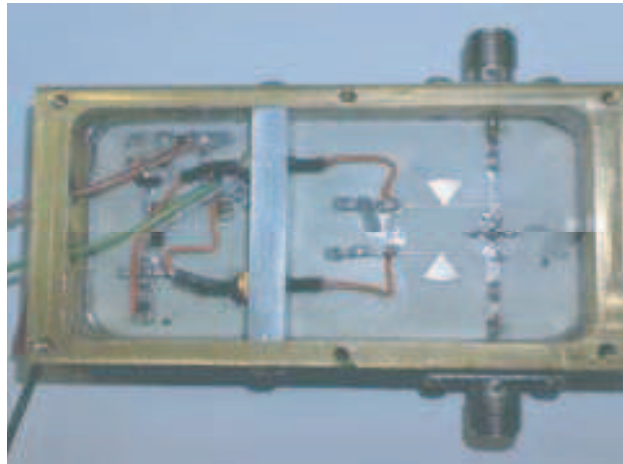


Figure 7: Results of manufacturing Lange coupler.

Figure 8: *x*-band amplifier structure.

3.2. Amplifier

The results of manufacturing amplifier with NE325S01 by 10 ma current in drain are shown in Fig. 8 that S_{21} has a variation about 1 dB in the working range. Also the measured S_{11} by network analyzer has been shown in Fig. 9. The amount of S_{11} is less than -70 dBm.

3.3. Balance Amplifier

Finally we mix two Lange couplers and two parallel amplifiers shown in Fig. 10. We can see the results of this in Fig. 11. Because of box resonance and radiation coupler lines due to substrate height we have used grounded walls between amplifiers and the couplers input and output. The measured results have an acceptable accuracy comparing with simulations and we face just about 2 dB variation that is acceptable for microelectronic technology.

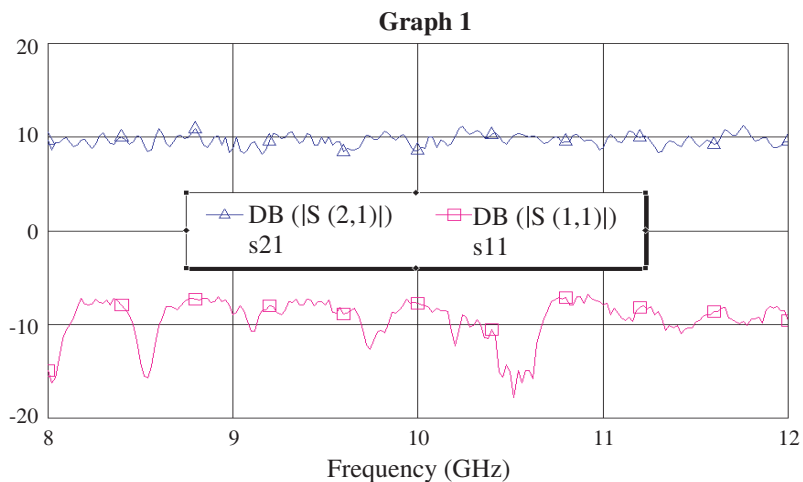


Figure 9: Results of manufacturing *x*-band amplifier using NE325S01.

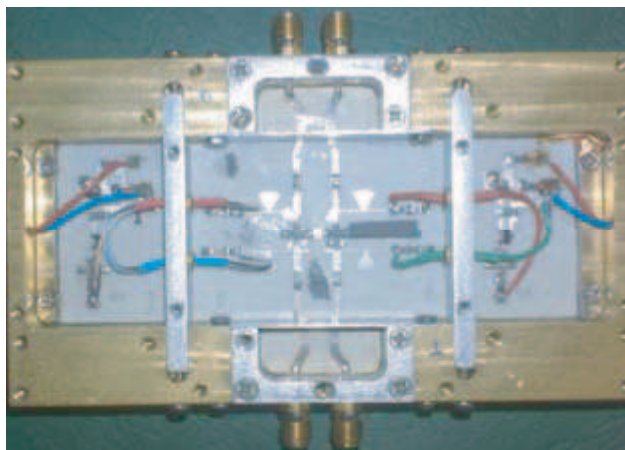


Figure 10: Structure of *x*-band balance amplifier.

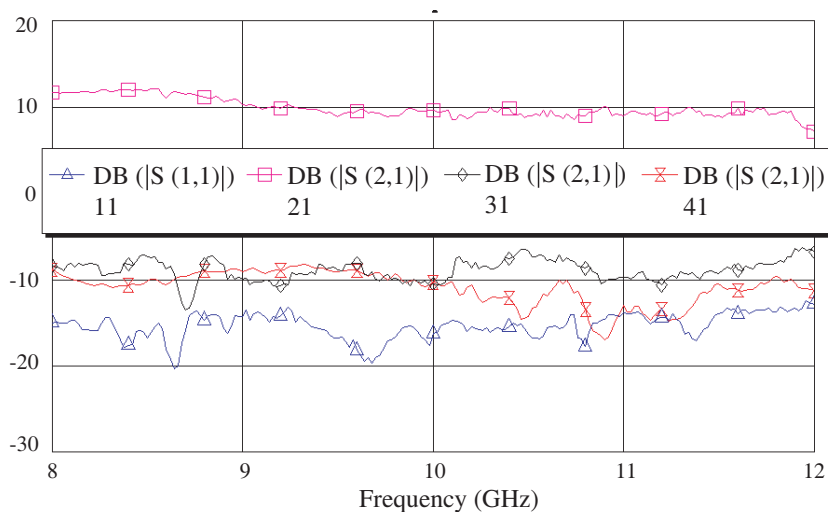


Figure 11: Results of manufacturing *x*-band balance amplifier using NE325S01 transistor.

P1 dB variations by changing transistors are another important matter (Fig. 12). With 3 dBm input it enters to a saturated range that is 3 dB more than previous condition. This is one of the advantages of balance amplifier.

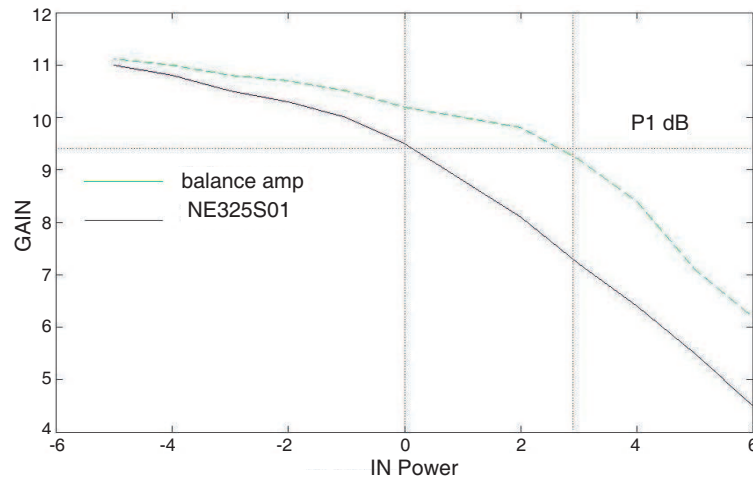


Figure 12: Comparison NE325S01 and balance amplifier for P1 dB.

4. CONCLUSION

The results of manufacturing balance amplifier in x -band with using the microelectronic technology is near to simulated results in AWR software except S_{11} which is near to HFSS results. S_{21} has 200 MHz frequency shift because of box effect shift. Also P1 dB has been increased about 3 dB using a balance structure.

Using microelectronic technology S limitations for lange coupler in this frequency is less than 30% of gained amounts in AWR and by increasing the height of substrate should be fixed output bends angles in HFSS and copper height effect according to plating should be one of the steps that has to be around 50–80 microm.

REFERENCES

1. Lange, J., "Interdigital strip line quadrature hybrid," *IEEE Trans. Microwave Theory Tech.*, Vol. 17, 1150–1151, Dec. 1969.
2. Presser, A., "Interdigitated microstrip coupler design," *IEEE Trans. Microwave Theory Tech.*, Vol. 26, 801–805, Oct. 1978.
3. Kajfez, D., Z. Paunovic, and S. Pavlin, "Simplified design of lange coupler," *IEEE Trans. Microwave Theory Tech.*, Vol. 26, 806–808, Oct. 1978.
4. Pieters, P., S. Brebels, E. Beyne and R. Mertens, "Generalized analysis of coupled lines in multilayer microwave MCM-D technology-application: Integrated coplanar lange couplers," *IEEE Trans. Microwave Theory Tech.*, Vol. 47, 1863–1872, Sep. 1999.
5. Subramanyam, G., "A ferroelectric tunable microstrip lange coupler for k -band applications," *IEEE 0-7803-5687-X/00/\$10.00*, 2000.
6. www.cel.com/pdf/datasheets/ne325s01.pdf
7. Ayasli, Y., L. T. Reynolds, R. Mozzi, and L. K. Hanes, "2–20 GHz GaAs traveling-wave power amplifier," *IEEE Trans. Microwave Theory Tech.*, Vol. 32, 290–295, 1984.
8. www.odysseus.nildram.co.uk/RFMicrowave_Circuits_Files/Balanced%20Amplifiers.pdf
9. Cole, J. B. and A. Platzker, "Design technique for high power, high efficiency, broadband distributed amplifiers," *Proc. IEEE MTT-S Inr. Microwave Symp. Dig.*, Vol. 94, 1–944, 1989.
10. Mongia, R., I. Bahl, and P. Bhartia, *RF and Microwave Coupled-line Circuit*, Artech house, 1999.

A New Microwave Bandstop Filter Using Defected Microstrip Structure (DMS)

M. Kazerooni¹, N. P. Gandji¹, A. Cheldavi¹, and M. Kamarei²

¹College of Electrical Engineering, Iran University of Science and Technology, Tehran, Iran

²Faculty of Electrical and Computer, University of Tehran, Tehran, Iran

Abstract— This paper presents a new bandstop filter by creation of some slots on the strip. These slots perform a serious LC resonance property in certain frequency and suppress the spurious signals. In the high frequencies applications, the board area is seriously limited, so using this filter; the circuit area is minimized. The proposed filter is very suitable for high density MMIC circuits.

1. INTRODUCTION

In many applications reduction of size and weight of filters is very important. Thus, planar filters utilizing printed circuit technology seems very suitable [1]. Slot on the strip that is called defected strip structure (DMS) [2] makes a defect on the circuit which can be used in designing filters, dividers, amplifiers, etc.. This defect creates resonance characteristics in the frequency response. This kind of structures is constructed by removing T-shaped pattern etched from the top conductor of microstrip and can be used as a band reject filter [3]. The DMS is advantageous in high frequency designs and millimeter wave applications. DMS circuits are more immune than defected ground structure (DGS) from crosstalk and ground plane interference.

In this paper, a new approach for making a bandstop filter using DMS is presented. We report two filter structures and extract their equivalent circuits. These new circuits have the same central frequencies but one has the wider bandwidth than the other.

2. BANDSTOP FILTER STRUCTURE AND EXTRACTION OF CIRCUIT MODEL

Several examples of DMS filter is shown in Fig. 1(a). Also the dimensional parameters of rectangular DMS filter which result in a resonance characteristic is sketched in Fig. 1(b). The resonance effect is due to the abrupt change of the current path. The dashed line presents this path.

In Fig. 1(b); a , b and c are 0.2 mm, 0.4 mm and 10 mm, respectively and w is the strip width. The mentioned structure is a bandstop filter whose frequency specification is shown in Fig. 3. For this microstrip filter the substrate is Rogers RT/duroid 5870 with the dielectric constant of $\epsilon_r = 2.33$ and thickness of 0.787 mm. The width of substrate is 2.33 mm to obtain 50 ohm characteristic impedance.

In full wave method the analysis of this filter will take very long time. So, for solving this problem, using the circuit model is very suitable. We obtain the circuit model by tracking the path of the current. As the path is discontinued by foot of T-shaped slot, a capacitive characteristic will be appeared. Also we can deduce an inductive property due to the current loop at the edge of the T-shaped slot. The proposed circuit model is shown in Fig. 2.

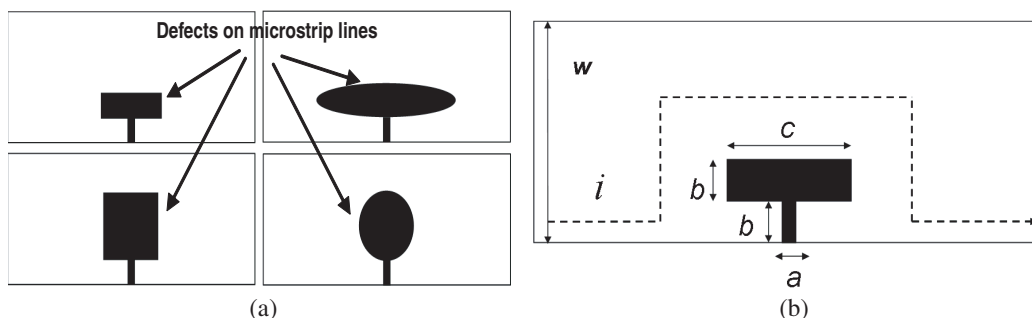


Figure 1: (a) Several examples of DMS filter. (b) Parameters of DMS with one slot pattern.

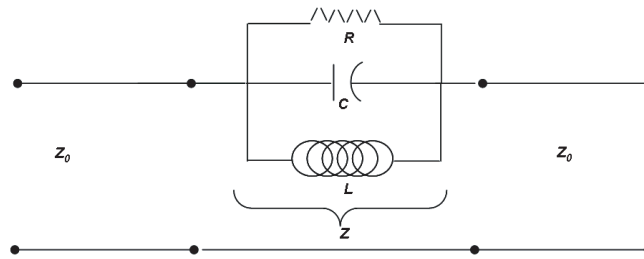


Figure 2: The related circuit model of DMS introduced in Fig. 1(b).

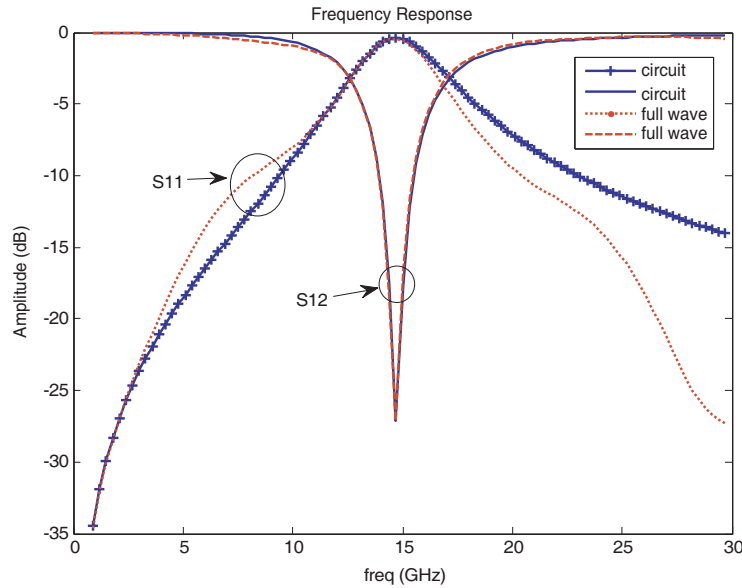


Figure 3: Comparison between full wave and circuit model analysis.

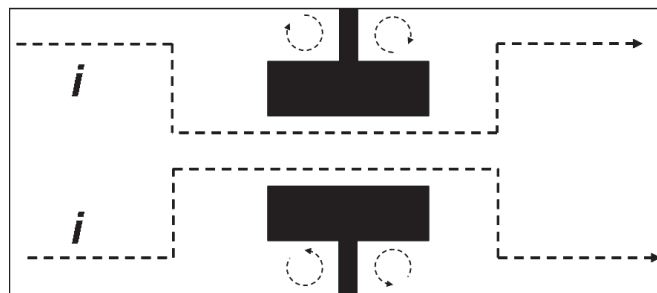


Figure 4: The proposed bandstop filter with two slots.

In Fig. 2, $R = 2172.5 \Omega$, $C = 0.34979 \text{ pF}$ and $L = 0.33512 \text{ nH}$. These values are obtained from curve fitting of the frequency response with the first order Butterworth filter. The magnitude of the S_{11} and S_{12} obtained from full wave and circuit model analysis are depicted in Fig. 3.

3. BANDSTOP FILTER WITH TWO T-SHAPED SLOTS ON THE STRIP

The bandstop filter structure with two T-shaped slots is shown in Fig. 4. The path of current is sketched with dashed lines. The dimension of slots is the same as the filter mentioned above with one slot. As can be seen in the Fig. 4, the width of the current path has become narrower and then the equivalent capacitor is decreased. Actually this circuit acts as a step microstrip circuit [4].

The proposed circuit model is like the one shown in Fig. 2, but the R , L and C values have changed to 2255 ohm , 1.1055 nH and 0.10603 pF respectively. Since the width of the current path is decreased the equivalent resistance will be larger than bandstop filter with one slot.

The magnitude of the S_{11} and S_{12} parameters of circuit model and full wave analysis is shown in Fig. 5. By comparing these parameters can be conclude that there is a good agreement in full wave frequency response and the equivalent circuit model. As can be seen, increase in equivalent resistance lead to more bandwidth.

For determining the level of interference signal rejection in frequency response, it is suitable to compare the VSWR parameters of these two circuits. This comparison is depicted in Fig. 6. It is seen that the VSWR in the centre frequency is more than 40, which is wonderful.

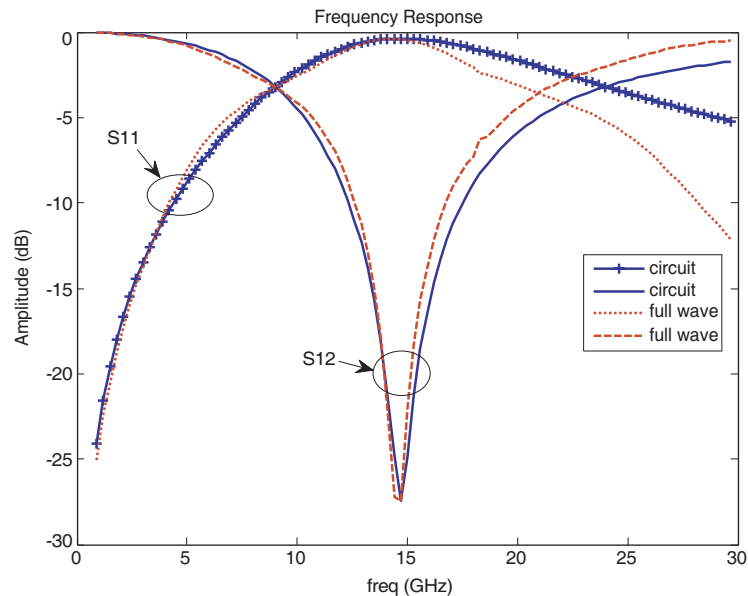


Figure 5: S_{11} and S_{12} parameters of circuit model and full wave analysis.

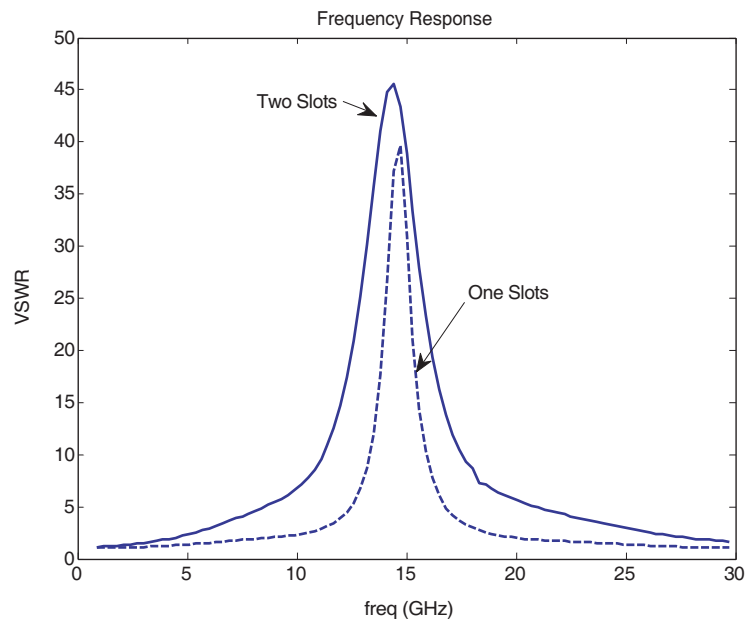


Figure 6: The comparison of VSWR.

4. CONCLUSION

In this paper, a new two T-shaped slots microstrip bandstop filter with great rejection of interference signals capability is presented. Also the equivalent circuit model is extracted. The most important advantageous of this kind of filter is improved bandwidth. These two slots are constructed on the strip of the circuit. For this circuit there is an ability of easy cascading with other component.

REFERENCES

1. Hong, J. S. and M. J. Lancaster, “Theory and experiment of novel microstrip slow-wave open-loop resonator filters,” *IEEE Transactions on Microwave Theory and Techniques*, Vol. 45, No. 12, December 1997.
2. Kazerooni, M., G. R. Rad, and A. Cheldavi, “Behavior study of simultaneously defected microstrip and ground structure (DMGS) in planar circuits,” *PIERS Proceedings*, 895–900, Beijing, China, March 23–27, 2009.
3. Park, J. S. and J. S. Yun, “A design of the novel coupled-line bandpass filter using defected ground structure with wide stopband performance,” *IEEE Transactions on Microwave Theory and Techniques*, Vol. 50, No. 9, September 2002.
4. Gupta, K. C. and I. Bahl, *Microstrip Lines and Slots*, 189–195, Artech House, Boston, London, 1996.

Retrodirective Array Composed of Two-port Dual Polarized Elements

The Nan Chang and Jui-Shuan Wu
E. E. Department, Tatung University, Taipei, Taiwan

Abstract— Microstrip retrodirective array having two-dimensional self-tracking ability is investigated. Each element has one vertical and one horizontal port. By proper connection of these elements, we can reduce ground reflection not only for linearly but also for circularly polarized waves.

1. INTRODUCTION

In a retrodirective array, fields scattered from antenna elements, connecting transmission lines, and ground plane are unavoidably coupled together to yield a ripple-like total field. Most of the works are based on linear polarized arrays. In [1], one unique technique is proposed to reduce ground reflection by connecting vertical port to the horizontal port and vice versa for each diagonal pair of elements. While retro-directing a linearly polarized wave, polarization states between transmitting and receiving antennas are orthogonal to each other (one vertical and one horizontal). Therefore, it is not very convenient.

In this paper, we found that when the structure is used to retro-direct a circular polarized wave, both transmitting and receiving antenna can be of the same polarization state. The ground reflection can also automatically be rejected from reception as its polarization state is orthogonal to that of the transmitting antenna.

2. RETRODIRECTIVE ARRAY

The proposed retrodirective array is shown in Fig. 1. It is a bi-layer structure with $\epsilon_{r1} = \epsilon_{r2} = 2.33$ and $h_1 = h_2 = 0.65$ mm. Each annular ring antenna element has an inner diameter $Di = 1.9$ mm and an outer diameter $Do = 10$ mm. The ring elements are fed by coupled strip lines. The inter element spacing in both dimensions are both chosen as $0.75\lambda_0$ ($\lambda_0 = 22.5$ mm). The stripline connecting the upper left 1 and lower right 1' rings are 28.32 mm long while the upper right 2 and lower left 2' are 80.16 mm. It should be noted that their difference is around $2.5\lambda_g$, which is due to the fact that the paired ring elements are not fed from the same side and a $0.5\lambda_g$ difference is needed to compensate for change in the feeding direction. In Fig. 1, each vertical port is connected to the horizontal port and vice versa for each diagonal pair of elements. For easy discussion, we concentrate on two elements as shown in Fig. 2.

In simulation, a right-hand circularly polarized (RHCP) wave is assumed to be incident from far field. The incident angle increase gradually from 0° to 40° in 10° step and the scattered field in each case is observed. The scattered field can be divided into right-hand and left-hand (E-right & E-left) components. Figs. 3(a) and 3(b) shows E-left and E-right pattern respectively. We found that E-right component in Fig. 3 can successfully retro-direct the incident RHCP wave. The retro-direct direction follows direction of the incident wave from 0° to 40° in 10° step. At 10° , 20° , 30° , and 40° , E-left component is relatively smaller than E-right component.

At 0° incident angle, it is shown that the scattered E-left component is comparable with the E-right component (due to retro-directive connection). However, the E-left component is mainly due to ground reflection. The two components can still easily be separated as they are orthogonally polarized. One important advantage using connecting scheme shown in Fig. 2 is that the polarization direction of scattered field caused by ground reflection is orthogonal to that of scattered field caused by retro-direction. This is vital especially for incident a CP wave at normal direction. To say in another word, we can easily separate ground reflection from the desired retro-direct field using a receiving antenna having the same polarization state as the incident transmitting antenna.

The above operational principle can be extended to a two-dimension array. Fig. 4 shows measured and simulated scattered patterns of the array. The measured results are quite agreeable with simulated predictions. The measured relative 10-dB beam width is about 130° which is a little wider than simulated beam width.

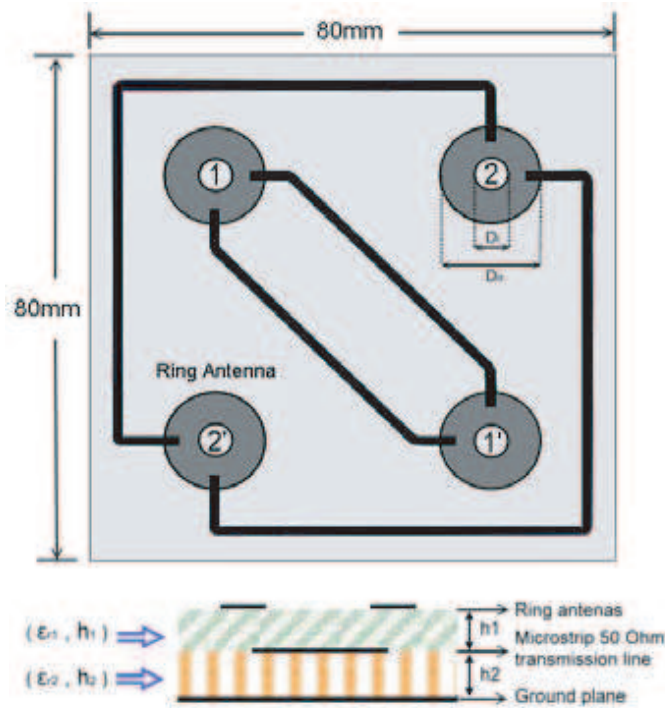


Figure 1: A retrodirective array consisted of annular ring elements.

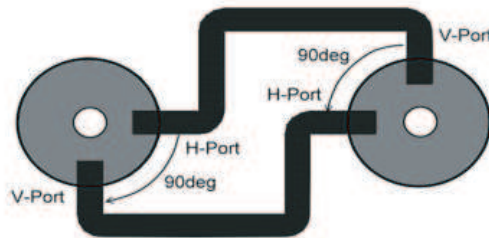


Figure 2: Two connection scheme for each diagonal pair.

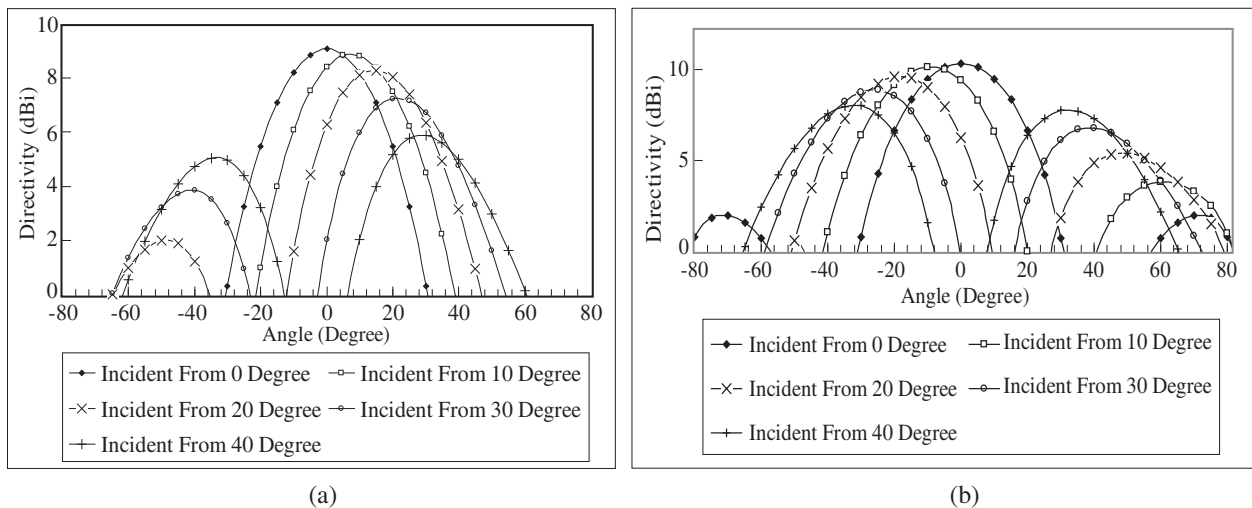


Figure 3: Scattered fields of the array from a RHCP incident wave. (a) E-right component, (b) E-left component.

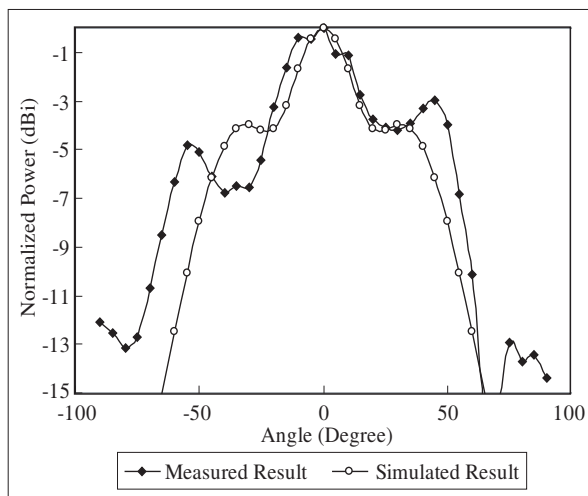


Figure 4: Measured and simulated scattered E-right fields for an array incident by a RHCP wave.

3. CONCLUSION

In this paper, we design a retro directive array with 2-D retro directivity. We validate that circular polarization retro-directivity can be achieved by choosing both transmitting and receiving antenna having the same polarization state (either both of RHCP or both of LHCP). The ground reflection can automatically be rejected from reception as its polarization state is orthogonal to that of the transmitting antenna.

REFERENCES

1. Christodoulou, M. G. and D. P. Chrissoulidis, "2D Van Atta retrodirective array using dual polarized two-port square microstrip patches," *International Conference on Antennas and Propagation*, No. 480, April 17–20, 2001.

Comparing Effects of Electromagnetic Fields (60 Hz) on Seed Germination and Seedling Development in Monocotyledons and Dicotyledons

Azita Shabrangi¹ and Ahmad Majd²

¹Department of Biological Sciences, Faculty of Science
Tehran Tarbiat Moallem University, Tehran, Iran

²Islamic Azad University, North Branch, Tehran, Iran

Abstract— Various biological effects of exposure to extremely low frequency electromagnetic fields (ELF-EMFs) have been documented so far, but very little work has been carried out on plants. In this research, two states of seeds (wet, dry) of *Brassica napus* L. (dicot) and *Zea mays* L. (monocot) were exposed to pulsed EMFs (15 min on, 15 min off) by magnitude of 1 to 7 mT in steps of 2 mT and the highest intensity was 10 mT for 1 to 4 hours in steps of 1 h. Exposure to EMFs was performed by a locally designed EMF generator. Three replicates, with 30 seeds in each one were placed in germinator with 23°C temperature after treatment. The number of germinated seeds was registered on the 2nd day after moisturizing in *Brassica napus* and 6th day after moisturizing in *Zea mays*. Developmental growth characteristics including: root and shoot length, fresh and dried biomass weight of 7 days seedlings were measured.

Seedlings grown from dry pretreated seeds of *Brassica napus* showed the most significant increase in developmental growth at 10 mT and seedlings grown from wet treated seeds showed the most significant decrease in developmental growth at 10 mT comparing to control ($p < 0.05$) we observed an overall stimulating effects of EMFs in *Zea mays* with respect to developmental growth characteristics and the most significant increase observed at 10 mT ($p < 0.05$). All experimental data suggested Monocotyledons are more resistant than Dicotyledons against EMFs as abiotic stress.

1. INTRODUCTION

The biological effects of extremely low frequency magnetic fields on living organisms have been explored in many studies. Most of them demonstrate the biological effects caused by 50/60 Hz magnetic fields or pulsed magnetic fields. Low frequency fields appears to be more bioactive (3). The basic mechanism is the forced-vibration of all the free ions on the surface of a cell plasma membrane, caused by an external oscillating field. Therefore vibration of electric charge is able to irregularly gate electro sensitive channels on the plasma membrane and thus cause disruption of the cells bioelectrical balance and function (14). The optimal external electromagnetic field could accelerate the activation of seed germination [5, 11]. But the mechanism of these actions is still poorly understood [8, 19]. It has been reported that external electromagnetic fields induce both the activation of ions and the polarization of dipoles in living cells [4, 16]. Electric and magnetic treatments are assumed to enhance seed vigor by inducing the biochemical processes that involve free radicals and by stimulating the activity of proteins and enzymes [10, 15, 20]. Field tests reported greater than 10% increase in the field of maize and wheat, after submitting the seeds to carefully controlled electric fields [13]. These effects were mainly attributed to the field — induced intensity cation of the biological processes in Seeds. The crop increase could also be related to the sterilizing effect of high-voltage application. Previous studies indicated that suitable magnetic treatment increased the absorption and assimilation of nutrients (6), and ameliorated photosynthetic activities (7). It has been also reported that MF increased seed germination, seedlings growth and biomass in lentil. Stress enzymes increased as well (16).

In this paper, the effects of AC electromagnetic fields on canola and maize seed germination have been carried out experimentally to investigate the potential of augmentation of seed germination and seedling developmental growth by the field intensity and exposure time. Authors aimed to compare effects of EMFs on monocotyledons and dicotyledons. Different growth characteristics of seeds treated of canola as a representative of dicotyledons and maize, a representative of monocotyledons were analyzed and compared with those of the untreated seeds.

2. MATERIAL AND METHODS

Exposure to EMFs was performed by a locally designed EMF generator. The electrical power was provided by a 220 V, AC power supply with variable voltages and currents. This system consisted of one coil, cylindrical in form, made of polyethelen with 12 cm in diameter and 50 cm in length. The number of turns is 1000 of 0.5 mm copper wire, which were in two layers. A fan was employed to avoid the increase of temperature ($22 + 1^{\circ}\text{C}$). Calibration of the system as well as tests for the accuracy and uniformity of EMFs (60 Hz) were performed by a tesla meter with a probe type of hall sound. Three replicates, with 30 seeds in each one were used. They were spread in moist filter paper (for wet seeds) on Petri dishes. They were placed in the coil. Analogous groups were used as control. The wet and dry seeds of two species were exposed to pulsed EMFs (15 min on, 15 min off) by magnitude of 1 to 7 mT in steps of 2 mT and the highest intensity was 10 mT for 1 to 4 hours in steps of 1 h. Then dry seeds in Petri dishes were moistened and all Petri dishes were placed in germinator with 23°C temperature. The number of germinated seeds was registered on the 2nd and 6th days after moisturizing in canola and maize. Five 7 days seedlings from each replicate were randomly taken for measuring shoot and root length in cm. Then fresh weights of them were measured. Subsequently, they were dried in an oven at 60°C for 24 hours and dried weight of them was measured too. The data was analyzed using the software SPSS12. The variance analyses ANOVA and DUNCAN's tests were used to calculate the level of differences of all measured traits among EMFs, duration of exposure and their interaction ($P < 0.05$).

3. STATISTICAL ANALYSIS

Statistical analysis of the data was performed by using ANOVA. We applied Duncan's multiple range test to compare the experimental results of groups exposed to an electromagnetic field for seed germination rate, seedling shoot and root length, fresh and dried biomass with control. For statistical evaluation of results, significance was defined by a probability level of $p < 0.05$.

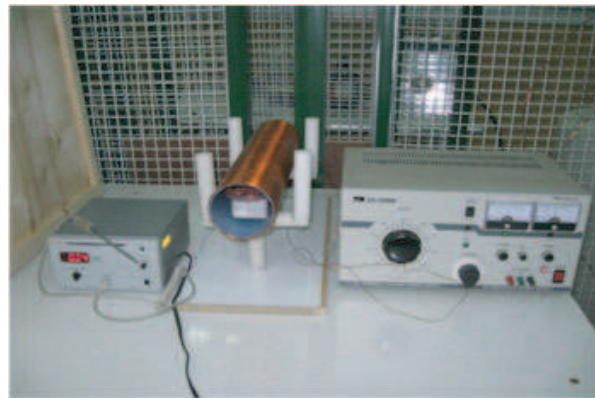


Figure 1: Set up of system.

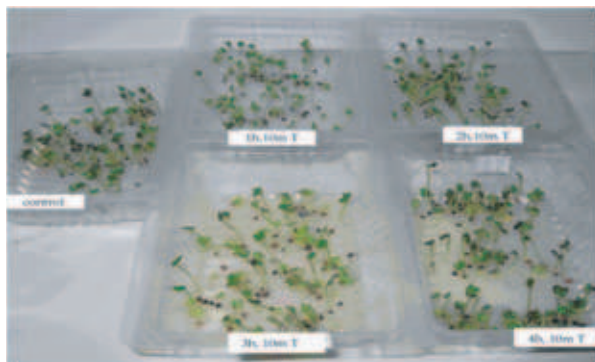


Figure 2: Dry pretreated seeds of canola by 10 mT. Intensity for different periods of time.

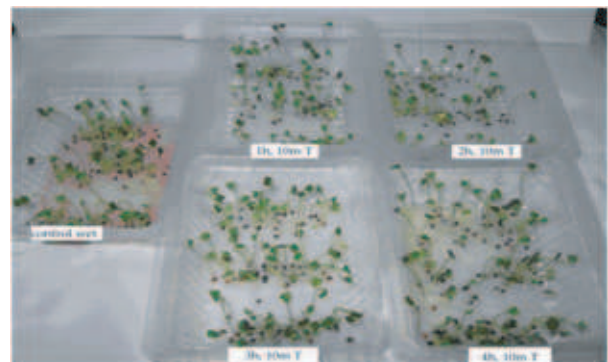


Figure 3: Wet treated seeds of canola by 10 mT. Intensity for different periods of time.

4. RESULTS

All experimental data and statistic calculations have attracted attention to interaction of EMFs and exposure time. Seed germination rate of wet treated seeds in maize and dry pretreated seeds in canola showed significant differences between all intensities of EMFs, duration of exposure and their interaction (Tables 1 and 2). Other developmental growth parameters including: root and shoot length of 7 days seedlings, fresh and dried biomass weights in canola showed just significant differences between intensities of EMFs. On the other hand in maize most of developmental growth parameters in seedlings grown from both wet and dry pretreated seeds showed significant differences between intensities of EMFs, duration of exposure and their interaction (Tables 1 and 2).

Table 1: Significant differences between intensities of EMF, duration of exposure and their interaction ($p < 0.05$)*.

time	seed germination	root & shoot length	fresh & dried biomass (\pm SD)		
Dry pretreated seeds in canola (10 mT)					
0	*95.4 \pm 5	3.2 \pm 0.9	1.7 \pm 0.35	0.057 \pm 0.003	0.0037 \pm 0.0005
1 h	*88.7 \pm 8.1	4.2 \pm 0.9	2.2 \pm 0.1	0.071 \pm 0.002	0.0037 \pm 0.0003
2 h	*89.7 \pm 8.5	3.7 \pm 0.4	2.1 \pm 0.5	0.062 \pm 0.016	0.004 \pm 0.0002
3 h	88.4 \pm 4	5.1 \pm 0.6	1.9 \pm 0.35	0.056 \pm 0.008	0.0037 \pm 0.0004
4 h	*92 \pm 3.54	1 \pm 0.3	2.4 \pm 0.35	0.057 \pm 0.006	0.0038 \pm 0.0002
Dry treated seeds in maize (10 mT)					
0	70.7 \pm 0	*2.2 \pm 0.38	*1.4 \pm 0.67	*0.54 \pm 0.14	0.231 \pm 0
1 h	79.7 \pm 0	*1.6 \pm 0.31	*0.9 \pm 0.12	0.7 \pm 0.1	0.249 \pm 0
2 h	79.7 \pm 0	*4.2 \pm 0.76	*1.9 \pm 0.46	*0.67 \pm 0.1	0.273 \pm 0
3 h	77.4 \pm 0	*0.8 \pm 1.13	*1.8 \pm 0.25	*0.69 \pm 0.11	0.261 \pm 0
4 h	79.7 \pm 0	*2.9 \pm 0.78	*1. \pm 0.28	*0.54 \pm 0.14	0.266 \pm 0

Table 2: Significant differences between intensities of EMF, duration of exposure and their interaction ($p < 0.05$)*.

time	seed germination	root & shoot length	fresh & dried biomass (\pm SD)		
Wet treated seeds in canola (10 mT)					
0	96.7 \pm 3.6	5.6 \pm 0.6	3.2 \pm 0.355	0.075 \pm 0.002	0.0043 \pm 0.0004
1 h	92 \pm 3.6	5.4 \pm 0.1	2.5 \pm 0.215	0.036 \pm 0.015	0.0029 \pm 0.0008
2 h	88.7 \pm 5.1	4.9 \pm 1.6	2 \pm 0.89	0.067 \pm 0.015	0.0036 \pm 0.0004
3 h	92 \pm 5.1	5.6 \pm 0.5	2.7 \pm 0.365	0.064 \pm 0.009	0.0035 \pm 0.0001
4 h	94.4 \pm 12	5 \pm 0.8	2.8 \pm 0.2	0.057 \pm 0.013	0.0032 \pm 0.0006
Wet treated seeds in maize (10 mT)					
0	*48.7 \pm 5.7	2.08 \pm 0.38	*2.08 \pm 0.14	*0.528 \pm 0.09	0.257 \pm 0.02
1 h	*45.4 \pm 7.2	1.9 \pm 0.173	*1.43 \pm 0.23	*0.54 \pm 0.08	0.282 \pm 0.03
2 h	*44.4 \pm 1.7	2.43 \pm 0.55	*1.46 \pm 0.4	*0.585 \pm 0.13	0.272 \pm 0.03
3 h	*56.4 \pm 6.8	3.3 \pm 0.776	*2.66 \pm 0.14	*0.692 \pm 0.06	0.269 \pm 0.02
4 h	*69.7 \pm 11.9	3.27 \pm 0.901	*3.3 \pm 1.35	*0.717 \pm 0.1	0.279 \pm 0.06

It indicates that certain combination of EMF and duration like 10 mT for 4 h (Figs. 4 and 5) in maize seedlings grown from wet treated seeds has highly effects on enhancing most of developmental growth. Furthermore, in canola EMFs intensities were highly effective in enhancing or avoiding growth parameters. There is a window at 10m T intensity for 2 hours time treatment in wet states seeds of canola, which negatively interacts and reduce the seedlings growth traits compared to

control (Fig. 3). Beside, at the same intensity of EMF, seedlings grown from dry pretreated seeds were highly effective in enhancing growth parameters (Fig. 2). Therefore in canola two states of seeds treatment showed different results. However, we observed overall stimulating effects of EMFs in maize with respect to developmental growth characteristics.

Seed germination rate and developmental growth characteristics including: root and shoot length, fresh and dried biomass weight of 7 days seedlings, which were treated by 10 mT intensity of EMF for different periods of time, are shown in Figs. 6 to 10. Each figure shows comparing one of growth parameter in different states of seeds and species.



Figure 4: Wet treated seeds of maize by 10 mT. Intensity for 4 hours treatment.



Figure 5: Wet treated seeds of maize by 10 mT. Intensity for different periods of time.

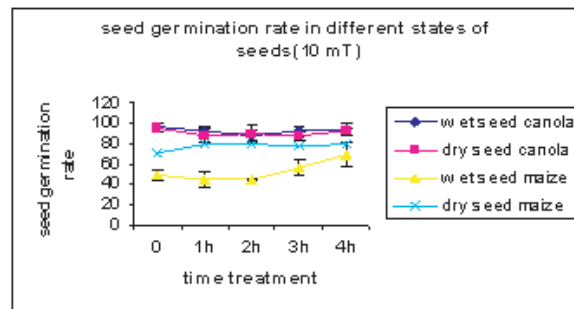


Figure 6: Comparing seed germination rate in different species and states of seeds treated by 10 mT for different time treatment.

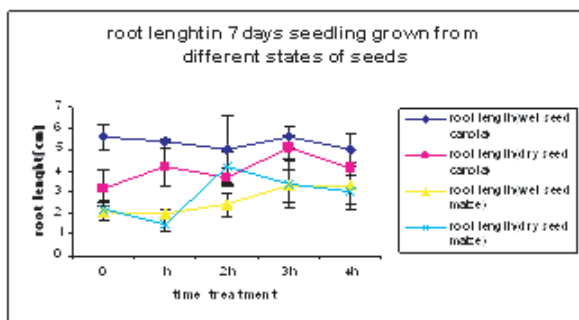


Figure 7: Comparing root length in different species and states of seeds treated by 10 mT for different time treatment.

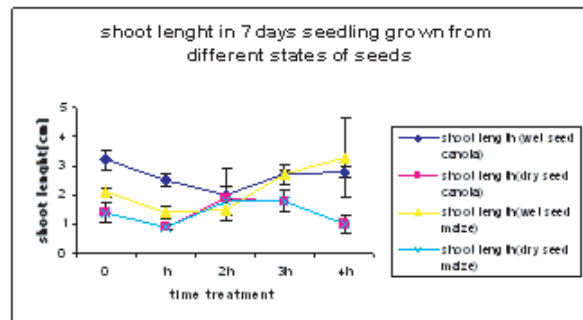


Figure 8: Comparing shoot length in different species and states of seeds treated by 10 mT for different time treatment.

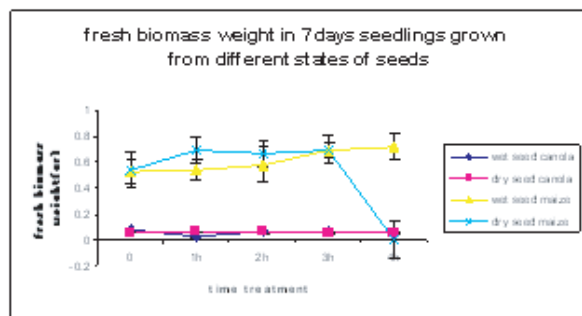


Figure 9: Comparing fresh biomass weight in different species and states of seeds treated by 10 mT for different time treatment.

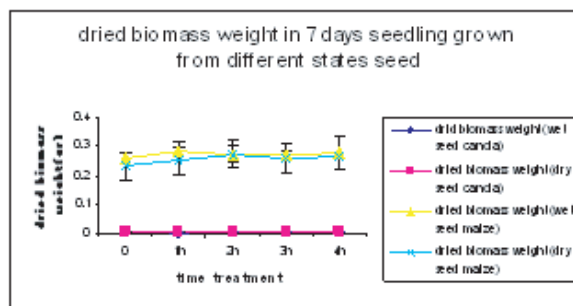


Figure 10: Comparing dry biomass weight in different species and states of seeds treated By 10 mT for different time treatment.

5. CONCLUSION

Monocotyledons are assumed to be more evolved than dicotyledons in phylogenetic trends. As one of physical pre-sowing seed treatments that increased growth of cultivated plants, effects of electromagnetic flux density field treatment on biological systems, had been discussed for more than a century. Our results showed that electromagnetic fields treatment can affect seed germination rate and developmental growth characteristics, which was consistent with some previous studies (10) and (11). The authors found that suitable EMFs treatment (10 mT) could speed up seedling development and increase biomass. Similar results were also reported in cauliflower, tomato and cucumber (21). The effects of different intensities and exposure time of AC electric fields and AC magnetic fields on tomato seed germination have been investigated as a potential means to accelerate the germination of the seeds.

In this research, the rate of germination of different states treated seeds was higher than untreated seed in maize and we observed overall stimulating effects of EMFs in Maize with respect to developmental growth characteristics. In contrast, seedlings grown from two states of seeds under EMFs effects showed different results. We observed decreasing in seedlings growth and biomass of canola, which were grown from wet treated seeds, exposing to 10 mT intensity. Therefore, it would be deduced that Monocotyledon plants (maize) are more resistant than dicotyledons (canola). Authors believe these differences between two kinds of species depend on not only the genotype of species, but also hardness of seeds and stored polysaccharides in seeds which cover embryo.

The present study, in accordance with other studies demonstrates that pulsed fields can have increased biological action in relation to continuous (uninterrupted) fields. Considering that these plants have ferritin cells containing 4500 Fe atoms, it is obvious that they have an outstanding role in the plants growth. As the last spin magnetic moment of the Fe atom posed to an external magnetic field, the composition of them creates an oscillator in the system. Then we have a moment of force on ferritin cells. This oscillator exerts its energy and locates in the field direction. The relaxed energy increased the internal temperature. This phenomenon occurs in the initial minutes of applying the magnetic field. So it depends on the number of times of locating the plant in magnetic field (19). On the other hand, a cell is considered to be an electrical system and electrical loading body. In fact, EMFs forced ions, molecules, macromolecules. Their interactions with biological constructions may cause changing in their energy level and also alteration in their construction. Therefore effects of potential energy of EMFs on cellular physiological functions need more research.

In conclusion, maize as a representative of monocotyledons is more resistant than canola (dicotyledons) against EMFS as a biotic stress.

REFERENCES

- Bertholon, A., UG berElektrizitaK t in Berziehung auf die P#anzen, Leipzig, 1785.
- Nelson, S. O. and E. R. Walker, *J. Agric. Eng.*, Vol. 42, 688, 1961.
- Huang, H. H. and S. R. Wang, "The effects of inverter magnetic fields on early seed germination of mung beans," *Bioelectromagnetics*, Vol. 29, 649–657, 2008.
- Johnson, C. C. and A. W. Guy, "Non ionizing electrostatic wave effects in biological materials and system," *Proc. IEEE*, Vol. 60, No. 6, 692–718, 1972.

5. Kavi, P. S., “The effect of non-homogeneous gradient magnetic field susceptibility values in situ ragi seed material,” *Mysore J. Agric. Sci.*, Vol. 17, 121–123, 1983.
6. Lebedev, I. S. and L. T. Litvinenko, “After effect of a permanent magnetic field on photochemical activity of chloroplast,” *Sovient Plant Physiol.*, Vol. 24, 394–395, 1977.
7. Maeda, H., “Do the living things feel the magnetics,” *Kodansha*, Tokyo, 1993.
8. Morar, R., A. Iuga, and L. Dascalescu, “Separation and bio stimulation of Soybeans using high-intensity electric fields,” *Proceedings of the International Conference on Modern Electrostatics*, 158–160, Beijing, China, 1988.
9. Murphy, J. D., “The influence of magnetic field on seed germination,” *Am. J. Bot.*, Vol. 29, 15, 1942.
10. Murr, L. E., “Plant growth response in electrostaticfield,” *Nature*, Vol. 207, 1177–1178, 1965.
11. Oomor, U. I., *Bioelectromagnetics and Its Applications*, Chap. 2.1.2, 340–346, Fuji Technosystem Ltd., 1992.
12. Panagopoulos, D. J., et al., “Mechanism for action of electromagnetic fields on cells,” *Biochemical and Biophysical Research Communications*, Vol. 298, 2002.
13. Shabrangi, A. and A. Majd, “Effects of magnetic fields on growth and antioxidant system in plants,” *Progress In Electromagnetics Research*, PIER 29, 1089–1094, 2009.
14. Sidaway, G. H. and G. F. Asprey, “Influence of electrostatic fields on seeds germination,” *Nature*, Vol. 211, 303, 1966.
15. Takahashi, H., *Electricity and Life*, Institute Publication Center, Tokyo, 1986.
16. Townsend, J. S., “The diffusion and mobility of ions in a magnetic field,” *Proc. Roy. Soc. A&B*, 571–577, 1912.
17. Vaezzadeh, M., et al., “Excitation of growth in dormant temperature by steady magnetic field,” *Magnetism and Magnetic Material*, Vol. 302, 105–108, 2005.
18. Xiyao, B., M. Ancheng, M. Jingrun, and L. Xiaoling, “Physiological and biochemical experiments in electrostatic treated seeds,” *Proceedings of the International Conference on Modern Electrostatics*, 161–165, Beijing, China, 1988.
19. Yinan, Y., et al., “Effect of seed pretreatment by magnetic field on the sensitivity of cucumber (*Cucumis sativus*) seedlings to ultraviolet-B radiation,” 2004.
20. Ming, Y. J., “Effects of high-voltage electrostatic field on growth in plants,” *Proceedings of the International Conference on Modern Electrostatics*, 161–165, Beijing, China, 1988.

Effect of AC and DC Magnetic Fields on Seed Germination and Early Vegetative Growth in *Brassica Napus L*

Ahmad Majd¹, Azita Shabrangi², Mahmood Bahar³, and Soheilla Abdi³

¹Islamic Azad University, Tehran North Branch, Tehran, Iran

²Department of Biological Sciences, Faculty of Science
Tehran Tarbiat Moallem University, Tehran, Iran

³Physic Department, Islamic Azad University, Tehran North Branch, Tehran, Iran

Abstract— Because of the important role of plants on the earth, studying about the environmental factors which affect on plant growth is essential. Nowadays effects of electric and magnetic fields have attracted considerable attention. In this research we studied the effects of different intensities (3.7 mT and 4.5 mT) of DC magnetic fields ,different intensities (2.7 mT and 3.5 mT) of AC magnetic fields and duration of exposure (30, 60 and 90 min) on seed germination and seedlings primary growth of *Brassica napus L*. Seeds were divided into four sets and each set to three replicates. The treated and untreated seeds were then germinated under an identical condition of the water-bedded Petri-dish in a temperature and relative humidity. The growth factors were measured every day in the same time for a week.

Results indicated that the magnetic fields have no significant effect on seed germination rate of *Brassica napus* ($P < 0.05$) The roots length increased about 1.1 times in low intensity of AC magnetic field (without diode) and 1.1–1.2 times in high intensity of DC magnetic field (with diode) comparing with the untreated seeds. The growth of hypocotyls increased about 1.1 times in the intensity of 2.7 mT (AC) in all exposure times compared with control ($P < 0.05$). However an inhibitory effect about 10% to 40% on hypocotyls growth were observed in the case of AC and DC magnetic fields and the maximum inhibitory effect were observed in the intensity of 3.7 mT. The number of axillaries roots increased about 25% in the intensity of 4.5 mT compared with untreated seeds.

All the results suggested that AC and DC magnetic fields have no significant effect on seed germination rate of *Brassica napus*. However magnetic fields can affect the primary growth of seedlings and these effects are altered in different intensities and duration of exposure.

1. INTRODUCTION

During the evolution process, all living organisms experienced the action of the Earths magnetic field (geo-magnetic, GMF), which is a natural component of the air environment. Previously many scientists believed that permanent magnetic fields are not biologically active. However, the results obtained have revealed the high sensitivity of plants to permanent magnetic fields, in Particular, in the intensity range from GMF level to very low ones. Interplanetary navigation will introduce man animals and plants in magnetic environment where the magnetic field is near 0 mT. This brought a new wave of interest in WMFs role in regulating plant growth and development. It has been also reported that AC and DC magnetic fields provide different effects on alive tissue [10]. In this study, we used *Brassica napus L* which is a kind of strategic plant. we object to determine the optimal range of magnetic field intensities for increasing germination rate and growth and health of *Brassica napus* and generally finding the effect of magnetic field on plant in different aspects.

2. MATERIAL AND METHODS

The electrical power was provided by a 220 V, AC and DC power supply with variable voltages and currents he circuit consisted of a decreasing transformator (enter 220 V, exit 12 V) Diode, electrical pill (1000 F μ) and resistance (10 k Ω). This system consisted of one coil, cylindrical in form, made of p.v.c with 10 cm in diameter and 30 cm in length. The number of turns is 1200 of 1 mm copper wire in 4 layers. Design was in a form, that AC fields without Diode and DC fields with Diode were provided. Therefore in the coil different intensities of magnetic fieldswere provided (3.7, 4.5 mT for DC current and 3.5, 2.7 for AC current) Calibration of the system as well as tests for the accuracy and uniformity of MFs were performed by a digital tesla meter HOLIDAY three-D sensor.

In this experimental design three replicates ($n = 3$), with 20 seeds in each one were used. Thus groups of 50 seeds, which were selected in uniform size and shape, were subjected to each magnetic treatment, and analogous groups were used as control. Magnetic treatment was Provided, varying

the exposure time (30, 60 and 90 minutes) and magnetic fields induction. Seeds were disinfected with detergent. Then they were spread in moist filter paper on Petri dishes (8 cm in diameter) and were placed in the coil. Germination test was performed at the end of spring under laboratory conditions. The natural light cycle was 14-h Light/10 h darkness and temperature $21 \pm 2^\circ\text{C}$. Growth and developmental characteristics, including seed germination rate, root and shoot length of 5 days seedlings and the numbers of lateral roots were measured. These parameters have been calculated using the seed calculator software for seed germination data analysis specifically developed by plant research international. Having calculated the best fit, the software then calculates the germination parameters of the three replicates and mean germination data, including standard errors.

3. STATISTICAL ANALYSES

Seed calculator software analyzed the cumulative germination data, percentage of germinated seeds and time required for germination. A student t-test was done to find the significant differences between each magnetic treatment and control. Statistical analyses of the data of growth was performed with SPSS for windows software. The results were subjected to an analysis of variance (ANOVA) to detect differences between mean parameters of pretreated seeds with control.

4. RESULTS

Cumulative germination data and seedling data including standard error were calculated and the seed calculator software plotted the best fit of the curves. The canola seed germination rate did not show significant differences by MF-treatment ($P < 0.05$). Fig. 2 illustrated the germination characteristics of the seed for various applied magnetic flux densities and exposure times at each fixed pretreatment time period of 30, 60 and 90 minutes (Fig. 2). Root length of seedlings are shown to have increased values of 1.1 times in all treatment times when the magnetic field intensity of 2.7 mT (AC) was applied. But in 60 minutes treatment showed significant differences ($P < 0.01$). The same augmentation was observed in 30 and 60 minutes treatment when magnetic field

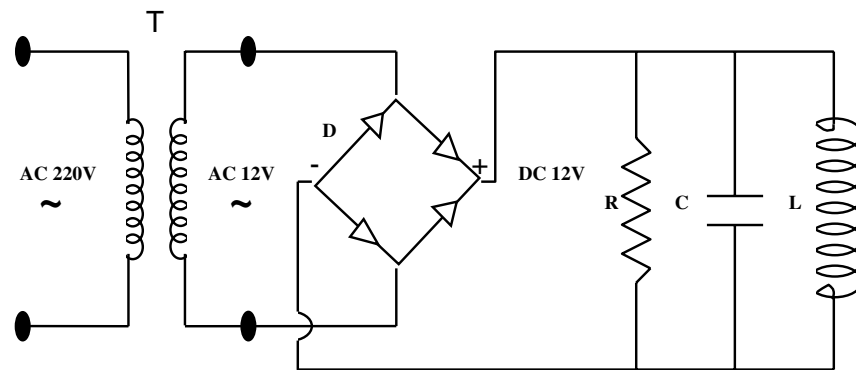


Figure 1: Schematic diagram of experimental set up.

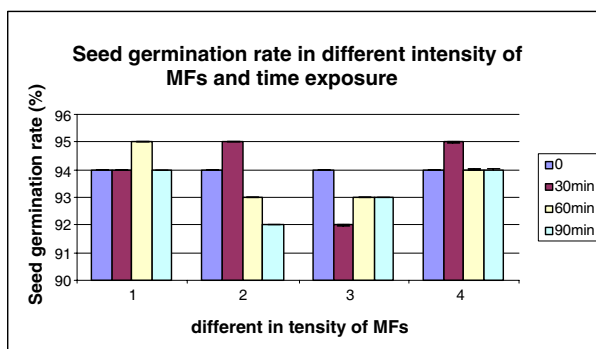


Figure 2: In this figure MF intensities were shown by numbers (1 = 2.7, 2 = 3.5 AC and 3 = 3.7, 4 = 4.5 DC).

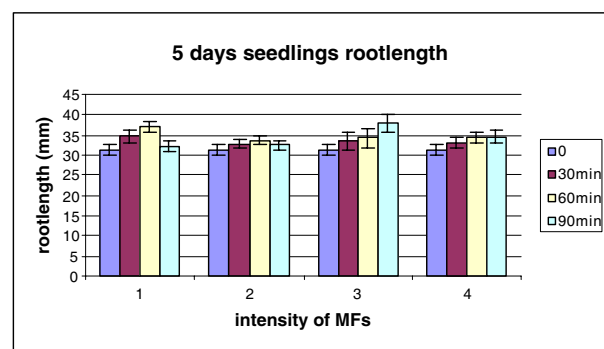


Figure 3: In this figure MF intensities were shown by numbers (1 = 2.7, 2 = 3.5 AC and 3 = 3.7, 4 = 4.5 DC).

intensity of 3.7 mT (DC) was applied, which did not show significant differences. In this intensity with 90 minutes treatment, root length of seedlings are shown to have increased values of 1.2 times comparing to control (Fig. 3).

Shoot length of 5 days seedlings increased 1.1 times in comparison with control in 30 and 60 minutes treatment when magnetic field intensity of 2.7 mT (AC) was applied (Fig. 4). Number of lateral roots did not show significant difference, except in 4.5 mT intensity of MF for 60 minutes treatment ($p < 0.05$) (Fig. 5).

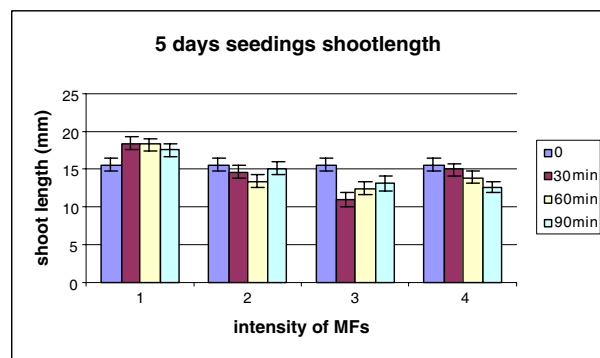


Figure 4: In this figure MF intensities were shown by numbers (1 = 2.7, 2 = 3.5 AC and 3 = 3.7, 4 = 4.5 DC).

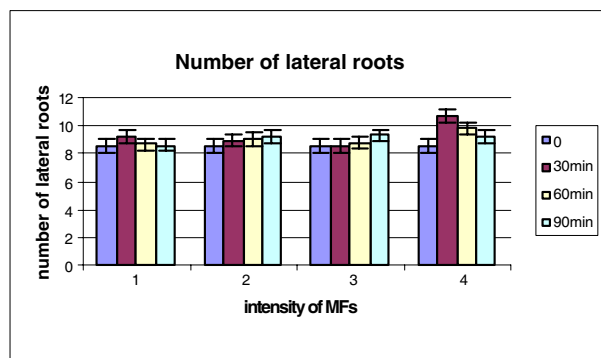


Figure 5: In this figure MF intensities were shown by numbers (1 = 2.7, 2 = 3.5 AC and 3 = 3.7, 4 = 4.5 DC).

time MFs	root length (mm)				shoot length (mm)			
	control	30 min	60 min	90 min	control	30 min	60 min	90 min
AC								
2.7 mT	31 ± 1.4	35 ± 1.4	37 ± 1.4**	32 ± 1.4	15.6 ± 0.86	18.4 ± 0.86*	18.3 ± 0.86*	17.5 ± 0.86
3.5	31 ± 1.4	32 ± 1.1	33 ± 1.1	32 ± 1.1	15.6 ± 0.86	14.6 ± 0.85	13.4 ± 0.85	15 ± 0.85
DC								
3.7 mT	31 ± 1.4	34 ± 2.2	34 ± 2.2	33 ± 2.2***	15.6 ± 0.86	10.9 ± 0.96**	12.5 ± 0.94*	13.1 ± 0.95
4.5	31 ± 1.4	33 ± 1.4	35 ± 1.3	35 ± 1.4	15.6 ± 0.86	14.9 ± 0.8	13.9 ± 0.8	12.6 ± 0.8

time MFs	seed germination rate				number of lateral roots (mean ± SD)			
	control	30 min	60 min	90 min	control	30 min	60 min	90 min
AC								
2.7 mT	94 ± 0.01	94 ± 0.01	90 ± 0.01	94 ± 0.01	8.5 ± 0.45	9.2 ± 0.45	8.6 ± 0.44	8.6 ± 0.45
3.5	94 ± 0.01	90 ± 0.01	93 ± 0.01	94 ± 0.01	8.5 ± 0.45	8.9 ± 0.45	9 ± 0.45	9.2 ± 0.45
DC								
3.7 mT	94 ± 0.01	92 ± 0.02	93 ± 0.02	93 ± 0.02	8.5 ± 0.45	8.6 ± 0.49	8.8 ± 0.47	9.3 ± 0.47
4.5	94 ± 0.01	90 ± 0.03	94 ± 0.03	94 ± 0.03	8.5 ± 0.45	10.6 ± 0.48	9.8 ± 0.48**	9.3 ± 0.48

5. DISCUSSION

A magnetic field is an inescapable environmental factor for plants on the earth. However, its impact on plant growth is not well understood.

Several theories have been proposed, including biochemical changes [9] Researchers carried out an experiment study on water absorption by lettuce seeds previously treated in a stationary magnetic field of 1 to 10 mT. They reported an increase in water uptake rate due to the applied magnetic field, which may be the explanation for the increase in the germination seed of treated lettuce seeds [3]. Lentil seedlings from magnetically pretreated seeds grew more than the untreated, and also biomass and root growth were significantly increased. Biomass increasing needs

metabolic changes particularly increasing protein synthesis [12]. The mechanism of stimulating effect of MF-treatment on seed germination and seedling growth was unknown. Although most seemed to involve changes in intracellular levels of Ca^{2+} and in other ionic current density across cellular membrane [2, 6] which caused alteration in osmotic pressure and changes in capacity of cellular tissues to absorb water [3, 4]. Magnetic fields can remove bound of Ca^{2+} from cell membrane which is essential for the stability of membranes. Consequently their loss will increase temporary pore formation under the mechanical stresses from pressure differences within cell and abrasion by its moving content. This would be account for virtually some biological effect of magnetic fields, including changes in metabolism [1].

In this research seedlings root length grown from pre-treated seeds increased in all intensities and duration of exposure. But significant difference ($p < 0.01$) were observed in 2.7 mT, 60 minutes treatment and 3.7 mT, 90 minutes treatment. Other researchers had similar results [8]. Seedling shoot length grown from pre-treated seeds by 2.7 mT increased significantly ($p < 0.05$). But increasing intensity of MF caused decrease in seedlings shoot length.

It is assumed that MFs may cause augmentation in ability of life and this effects would change by altering duration of exposure [11]. Decreasing in seedlings shoot length would be the results of MF as abiotic stress, which decrease biosynthesis of essential substances for shoot growth. Authors postulated that interaction between some intensities of MF and frequencies can cause biological effects. Transferring energy of MF inside alive tissues might happen, when frequency of fields are similar to frequency of mobile ion cyclotron resonance. As a result, macromolecules constructions would change [4] and consequently alteration in activity of channel gate might occur. These phenomenon affect on cellular functions like gene expression, mitosis pace and cellular metabolism.

In conclusion, the magnetic field pre-treatment enhanced seed germination rate and seedling emergence percentage. Also it has positive effect on canola seedlings, such as stimulating seedling growth and development.

REFERENCES

1. Akoyunoglou, G., "Effect of magnetic field on carboxy dismutase," *Nature*, Vol. 4931, 452–454, 1964.
2. Belyavskaya, N. A., "Ultrastructure, and calcium balance in meristem cells of pea roots exposed to extremely low magnetic fields," *Advances Space Research*, Vol. 28, No. 4, 645–650, 2001.
3. Calatayud, A., et al., "Effect of 2-month ozone exposure in spinach leaves on photosynthesis, antioxidant systems and lipid peroxidation," *Plant Physiology and Biochemistry*, Vol. 41, 839–845, 2003.
4. Chang, F. H., "Enhancement of plant form at ion from embryo culture of *Taxus mairei* using suitable culture medium and pvp," *Botanical Bulletin of Academia Sinica*, Vol. 37, 35–40, 1996.
5. Constance, N., "Gibberellin and seed development in Maize," *Plant Physiol*, Vol. 122, 1081–1088, 2001.
6. Florez, M., et al., "Exposure of maize seeds to stationary magnetic fields: Effects on germination and early growth," *Environmental and Experimental Botany*, 2005.
7. Isobe, S., et al., "Effect of electric field on physical states of cell associated water in germinating morning glory seeds observed by H-NMR," *Biochemica et Biophysica Acta*, Vol. 1426, 17–31, 1998.
8. Garcia, F., and L. I. Arzea, "Influence of a stationary magnetic field on water relations in lettuce seeds. Part I: Theoretical considerations," *Bioelectromagnetics*, Vol. 22, No. 8, 589–595, 2001.
9. Gubbels, G. H., "Seedling growth and yield response of flax, buck wheat, sunflower and field pea after presowing magnetic treatment," *Can. J. Plant Sci.*, Vol. 62, 61–64, 1982.
10. Erdem, G. and S. Oldacay, "Employment of RAPD technique to assess the genetic stability of *Helianthus annuus* treated with different mutagenic agents," *Journal of Applied Sciences*, Vol. 4, No. 2, 277–281, 2004.
11. Kavi, P. S., "The effect of non-homogeneous gradient magnetic field susceptibility values in situ ragi seed material," *Mysore J. Agric. Sci.*, Vol. 17, 121–123, 1983.
12. Lebedev, I. S. and L. T. Litvinenko, "After effect of a permanent magnetic field on photochemical activity of chloroplast," *Sovient Plant Physiol.*, Vol. 24, 394–395, 1977.
13. Lednev, V. V., "Bioeffects of weak combined, static and alternating magnetic fields," *Biofizika*, 224–232, 1996 (in Russian).

14. Pashley, D. H., C. K. Claycomb, and G. W. Summers, "Liberation of hydroxyproline from gelatin by acid hydrolysis," *Analytical Biochemistry*, Vol. 15, 154–156, 1966.
15. Martines, E., M. V. Carbonell, and M. Florez, "Magnetic biostimulation of initial growth stages of wheat," *Electromagn. Biol. Med.*, Vol. 21, No. 1, 43–53, 2002.
16. Mcleod, B. R., A. R. Liboff, and S. D. Smith, "Biological systems in transition sensitivity to extremely low-frequency fields," *Electro. Magnetobiol.*, Vol. 11, 29–42, 1992.
17. Murr, L. E., "Plant growth response in electrostatic field," *Nature*, Vol. 207, No. 1965, 1177–1178.
18. Murphy, J. D., "The influence of magnetic field on seed germination," *Am. J. Bot. (Suppl.)*, Vol. 29, 15, 1942.
19. Negishi, Y., et al., 1999, "Growth of pea epicotyl in low magnetic field implication for space research," *Advances in Space Research*, Vol. 23, No. 12, 2029–2032, 1999.
20. O'Hara, K., "Electric and magnetic field in the environment," 1999.
21. Pittman, U. J., "Effects of magnetic seed treatment on yields of barley, wheat and oats on Southern Alberta," *Can. J. Plant Sci.*, Vol. 57, 37–45, 1977.
22. Potencz, I., et al., "Magnetic fluids improving effect in in vitro regenerates in hypogravity conditions," *Journal of Magnetism and Magnetic Materials*, 1998.
23. Proussakova, G., "Effects of low frequencies magnetic field on the moss *Physcomitrella patens*," 2000.
24. Qadan, A., et al., "PFG NMR and internal magnetic field gradients in plant-based materials," *Magnetic Resonance Imaging*, Vol. 20, No. 7, 567–573, 2002.

Radio Studies of Ionospheric Sporadic E (1950–1960)

Ernest K. Smith

ECE Department, University of Colorado at Boulder, USA

Abstract— In the spring of 1950 as a young graduate student I entered the office of Prof. Henry G. Booker, recently from Cambridge. I was his first thesis student at Cornell University. I asked for a masters thesis topic. “Sporadic E or spread F” he replied “Take your pick”. I chose sporadic E whereupon he picked up a large manila envelope from his desk. “These are over 400 reports of reception of television stations at distances of 500 to 1600 miles sent to me by Hugo Gernsback of Radio Electronics magazine. They are due to sporadic-E propagation. See if you can prove it”. I did so successfully in my masters thesis with the result that Booker took me on as a Ph.D. student. My Ph.D. thesis was published in 1957 by the National Bureau of Standards as “Worldwide Occurrence of Sporadic E”, Circular 582, perhaps the first macroscopic study of the subject. The title soon showed up in the New Yorker magazine under the category “Irrelevant and Wasteful Government Publications”.

Sporadic E (not yet known by that name) was identified by Sir Edward Appleton in 1930 based on the observation that the otherwise Chapman-like E layer showed occasional irregularities. These irregularities came to be known as sporadic E, abbreviated Es. During the International Geophysical year (IGY, 1957–1959) more definitions came into vogue including a listing of 8 types of sporadic E. The number of ionosonde stations (vertical-incidence sweep-frequency radars) reached a peak during the IGY and a more detailed set of world Es maps became possible (see page 166–177 by H. I. Leighton, A. H. Shapley and E. K. Smith for maps and Es types in *Ionospheric Sporadic E*, E. K. Smith and S. Matsushita, Eds., Pergamon Press, 1962). By then there was a plethora of radio techniques and rocket observations. But explanations for the cause, structure and temporal behavior of sporadic E were still unsatisfactory at the end of the IGY. (e.g., see J. A. Thomas and E. K. Smith, “A survey of present knowledge of sporadic-E ionization”, JATP, Vol. 13, 295–314, 1959). However, at the 1960 URSI General Assembly, it was reported that Prof. J. D. Whitehead had just developed a windshear theory for sporadic E. This started a new era of sporadic-E studies. Post-1960 research is described in J. D. Whitehead, “Recent work on midlatitude and equatorial sporadic E”, JATP, Vol. 51, 401, 1989.

1. INTRODUCTION

This will be pretty much of a personal odyssey. While I entered graduate school with prior knowledge of the tools of the ionospheric trade, it is to Prof. Henry G. Booker, to Kenneth Norton, and to federal funding which I feel I owe my success in sporadic-E research.

I entered ionospheric research, particularly for sporadic E, at an opportune time. I had come to the US from China in 1940, an enthusiast in amateur radio as a teenager, and, thinking radio was taught in physics departments I majored in physics at Swarthmore college, graduating in 1944 with the recognition that my talents lay elsewhere. Promptly drafted into the Army I was fortunate to land in Dana Bailey’s Ionosphere Utilisation Unit (9463rd TSU, Holabird Signal Depot, Baltimore). There we learned ionospheric radiowave propagation from Dana and from lectures by speakers from the National Bureau of Standard, the Pentagon and the Carnegie Institution of Washington. I worked with the published products from IRPL/NBS, particularly the monthly measurements of ionosonde stations maintained by Walter Chadwick, and with the beautiful maps of E-and F2-layer predictions, six months in advance, based on the McNish-Lincoln Sunspot prediction, for the world divided into three geomagnetic zones E, I, and W, assuming an earth-centered magnetic dipole field.

In January 1946 upon discharge from the Army I joined the Plans and Allocations Division, headed by A. M. “Pete” Johnson, of the Mutual Broadcasting System in New York City. Pete had been Deputy Chief of the FCC Broadcast Bureau, a factor which provided me an entrance into the FCC engineering department, and, more importantly, to the vhf measurements made at its field stations. During my three and a half years at MBS the number of affiliates in the network increased from from 200 to 550 to which our department played a significant role. When Pete Johnson became Vice President for Engineering for Mutual I inherited his title of Chief Plans and Allocations Engineer for the network.

In the fall of 1949, I entered Cornell University, which I chose because of the prominence of Prof. Charles Burrows in radio propagation in World War II. But once in the EE Department I

discovered Prof. Henry G. Booker a just-arrived don from Cambridge University. I won't repeat the first paragraph of the abstract, but Henry Booker was the finest teacher I have ever encountered and I was fortunate to have him as my advisor for both my masters degree and Ph.D.

After completing my masters degree in 1951 I went to work for the Central Radio Propagation Laboratory (CRPL) of NBS in Boulder, CO. CRPL was getting too big for the limited campus NBS had in Washington DC, so it was transferred out, beginning in 1951, as had two other war-related-efforts earlier: the Manhattan Project and the Diamond Ordinance Fuse Laboratory. A difference was that CRPL in Boulder remained part of NBS. In Boulder I worked for Kenneth A. Norton and his deputy Jack Herbstreit. I had learned of both in WW II. Ken Norton was a genius in his self-made way. Previously at the FCC he had been largely responsible the shift in frequency allocations for the FM band and low-band TV. His motto seems to have been "don't believe the naysayers, collect all the data you can find or measure on a phenomenon and see where it leads you".

After a year in Boulder I returned to Cornell to start on my thesis and complete the course requirements for my Ph.D.. I returned to Boulder in 1954, finished my thesis under Signal Corps support and received my Ph.D. in 1956. I was then in the Radio Propagation Physics Division. Our Division Chief, Dr. Ralph M. Slutz, was sufficiently impressed with my thesis to have it published in book form by NBS as Circular 582.

In it I had:

- * Defined the latitudinal zones for equatorial, mid-latitude and auroral sporadic E quantitatively. Mid-latitude sporadic E was bounded near the equator by plus and minus 10 degrees from the equatorial electrojet and to the north and south by the 15% auroral isochasm (as defined by Vestine) in the Arctic and antarctic respectively.
- * In drawing world maps of sporadic E occurrence ($fEs > 7$ MHz) from the worldwide-network of ionosonde data I had uncovered, among other features, the longitude peak of mid-latitude sporadic E near Taiwan and Japan.
- * In comparing 50 MHz measurements of TV stations made at FCC monitoring stations with comparable measurements in Japan there was an apparent 30 dB enhancement in field strength during sporadic E events in Japan as compared to the US at a probability of 0.01% of the time at oblique distances of 600 miles.
- * I could find no particular correlation of mid-latitude sporadic E with sunspot number in the 7-years of data I had to work with, nor with thunderstorms.
- * I defined "magnetic latitude" as derived from the true magnetic dip (in contrast to "geomagnetic latitude" derived from an earth-centered magnetic dipole), in order to make the data make sense. I believe I was the first ionosphericist to do so.

At first Booker was not much impressed. There was no elegant mathematics, no powerful application of magneto-ionic theory, in fact little indication that the work was done under his supervision. It was only when J. A. Radcliffe, Booker's mentor at Cambridge, congratulated Booker on it and invited me to be one of two sporadic-E "experts" at the upcoming Cambridge symposium on sporadic E, that Booker took notice. Further recognition occurred in 1960 when I was invited to make the presentation on sporadic E at the URSI General Assembly in London in 1960. There I can remember infuriating Prof. Karl Rawer, who rose during the question period to say "You have only described your own work"! It was true. I had asked Prof. Robert Helliwell of Stanford what I should say and he had replied "It's a great chance to describe your own work". I confess, like most young researchers, I did think my work on sporadic E to be the most interesting that had been done in recent years. This changed during that 1960 conference when we heard of Prof. J. David Whitehead's windshear theory of sporadic E from the chairman of the Australian delegation. David Whitehead later told to me that he had used my work to come to his conclusions.

I submitted a proposal to the NSF in 1956 for the US International Geophysical year program to test the longitude effect of VHF sporadic E over comparable 50 MHz circuits in the Americas and in the Far East. Some insisted I had already proved the point but the project was approved and was great fun. Fellow Cornelians Kenneth L. Bowles and Robert S. Cohen had a similar program for which they had developed 50 MHz crystal-controlled transmitters and narrow-band (100 Hz) receivers for use on circuits down the coast of South America, particularly across the equatorial electrojet. These transmitters and receivers had been built at NBS. I copied their equipment down to the five-element yagi antennas. The sporadic E program included the following circuits:

1. Margarita, Panama, CZ transmitting to Guantanamo Bay, Cuba (1364 km).
2. Poro Point, Luzon transmitting to Onna, Okinawa (1270 km).

In addition we provided a transmission from Okuma, Okinawa beamed towards Japan as part of a cooperative program. This transmission was received at Yonago and Hiraiso Japan by the Radio Research Laboratory, Kokubunji. Another transmission was directed southward from, Margarita, C. Z. and received by Drs. Bowles and Cohen at Guayaquil Ecuador. The results, published in JGR by Smith and Finney in 1960 were as predicted for sporadic E in both occurrence and intensity.

The most pleasant outcome of the project was the chance to become acquainted with such outstanding Japanese researchers as Dr. Kenichi Miya and Dr. Kasuhiko Tao.

REFERENCES

1. Smith, E. K., *World Wide Occurrence of Sporadic E*, Circular 582, NBS, March 15, 1957.
2. Smith, E. K. and J. W. Finney, "Peculiarities of the ionosphere in the far east: A report of IGY observation of sporadic E and F-region scatter," *Journal of Geophysical Research*, Vol. 65, No. 3, 885–892, March 1960.
3. Vestine, E. H., I. Lange, L. Laporte, and W. E. Scott, *The Geomagnetic Field, Its Description and Analysis*, Publication 580, Carnegie Institution of Washington, 1947.

Analysis of Beam Efficiency in Multiple Beam Reflector Antennas

José Alberto Bava^{1,2}, Alberto Maltz³, and Mario Garavaglia^{2,4}

¹Departamento de Electrotecnia, Facultad de Ingeniería
Universidad Nacional de La Plata, Calle 1 y 47, 1900 La Plata, Argentina

²Centro de Investigaciones Ópticas (CIOP),
Camino Centenario y 506, 1897 Gonnet, La Plata, Argentina

³Departamento de Matemática, Facultad de Ciencias Exactas
Universidad Nacional de La Plata, Calle 50 y 115, 1900 La Plata, Argentina

⁴Departamento de Física, Facultad de Ciencias Exactas
Universidad Nacional de La Plata, Calle 49 y 115, 1900 La Plata, Argentina

Abstract— Over the last few years there has been a significant growth in the use of multiple beam reflectors for radiometric satellite applications. Beam efficiency has proven to be an important characterizing variable in the performance of these reflector antennas. High beam efficiency is required to achieve the detection of brightness variation in a specific field of view on earth. This paper presents an analysis of beam efficiency using feeder illumination tapers on the reflector's edge as a variable. Analytical results of the central beam from a prototype reflector antenna are shown, including their comparison with computed values. A particular case of multiple beams is also examined.

1. INTRODUCTION

Beam efficiency has proven to be an important measure for characterizing the performance of reflector antennas in satellite use. For radiometer applications, in particular, high beam efficiency is required to achieve the necessary contrast for the brightness variation.

The determination with good approximation of the beam efficiency characteristic is very important in order to know the effect on radiometer calibration. The purpose of this paper is to analyze the behavior of beam efficiency for different configurations of the main beam. Computer values will allow us to determine the model which best represents the phenomenon to characterize. Because the effect of the illumination tapers on the reflector's edge affects the main beam, these will be studied in the determination of beam efficiency together with the study of the footprint and the beam efficiency on a multiple beam offset parabolic torus reflector antenna (MBTA) of a remotely sensed radiometer.

2. BEAM EFFICIENCY DEFINITION

Given the radiation intensity or radiation pattern [1] ($F_n(\theta, \phi)$), respectively, normalized respect the copular maximum, and θ, ϕ the elevation and azimuth angles relative to the beam axis where they are both zero, the antenna pattern solid angle (Ω_p) is defined by:

$$\Omega_p = \iint_{4\pi} F_n(\theta, \phi) \cdot d\Omega, \quad (1)$$

and the main beam solid angle (Ω_{MB}) is defined as:

$$\Omega_{MB} = \iint_{MB} F_n(\theta, \phi) \cdot d\Omega. \quad (2)$$

Thus, the main beam efficiency η_{MB} can be defined as:

$$\eta_{MB} = \frac{\iint_{4\pi} F_n(\theta, \phi) \cdot d\Omega}{\iint_{MB} F_n(\theta, \phi) \cdot d\Omega} = \frac{\Omega_M}{\Omega_p}. \quad (3)$$

Then the main beam efficiency evaluates the capacity to receive the thermal emission through the main beam with those received from other contributions through the remains of the antenna pattern's main beam, characterizing the fraction of power received by the main lobe.

The main lobe angular range is typically defined within the spacing between the first nulls on both sides of the peak of the antenna pattern [1],

$$\Omega_{MB} = \Omega_{null}, \quad (4)$$

where Ω_{null} is the angle at which the first minimum of $F(\theta, \phi)$ occurs. However, in practice it has been found advantageous to use the following approximation:

$$\Omega_{MB} \cong nx\Omega_{3\text{dB}}, \quad (5)$$

where $\Omega_{3\text{dB}}$ is the half power beamwidth and n is a factor that allows approximating the main beam to many practical situations.

This definition overcomes the ambiguity of defining the null location for beam patterns without sharp nulls. For numerical calculation, Equation (4) may not be the most convenient representation of the beam efficiency. For a good estimate of the field of view on earth, there are References [2–4] which have defined the main beam as the angle of 2.5 times the half power angle ($2.5\Omega_{1/2}$). Using this latter equation, the implications of the taper edge of the feeders in the beam efficiency will be studied.

An analysis of the beam efficiency of a prototype of a multiple beam receptor antenna for satellite use in a microwave radiometer of remote sensing was also made. This led the authors to make an analysis of this characteristic at a frequency of 36.5 GHz.

3. ANALYSIS OF THE BEAM EFFICIENCY

As defined by the main beam efficiency (Equation (3)), the main lobe is taken as the area between the first valleys, (angular region α_{null} [1]). In many cases the valleys between the main lobe and the first secondary lobe are not clearly formed and the definition is not representative of what is needed to be quantified. On this issue there are several decisions that need to be made to define the area of the main beam. That is why values such as 2.5 times the 3 dB beamwidth [2–4] are adopted, a coefficient that defines a more realistic main beam in order to determine its efficiency.

The simulation of a parabolic offset antenna system was made, with similar characteristics to a MBTA prototype, built and tested with the aim of determining the beam efficiency and analyzing the implications of the edge taper in the determination of this parameter. Figure 1 shows the graphic of an offset reflector antenna system with similar characteristics to the MBTA, which simulated a frequency of 36.5 GHz, using main feeders with different values of edge taper (–10 dB, –15 dB and –20 dB). The graph shows a widening of the main beam as the illumination at the edges increases, producing a fusion between the main beam and the first lateral lobe. It also shows an increase of the α_{null} for feeders with higher edge tapers.

Table 1 shows the beam efficiency for the antenna simulated in Figure 1. Beam efficiency was determined considering the main beamwidth as 2.5 times the 3 dB beamwidth ($2.5\Omega_{3\text{dB}}$) for feeders with edge tapers of –10 dB, –15 dB & –20 dB.

Table 1: Beam efficiency for simulated model.

EDGE TAPER [dB]	BEAM EFFICIENCY [%]
–10	98.0
–15	99
–20	98.8

For the analyzed antenna system, that is, for a parabolic offset reflector, the best beam efficiency values were obtained with edge taper –15 dB.

The results shown in Table 1 were made on simulations with feeders positioned in the focal point. The beam efficiency values were determined by applying the linear function interpolation method $F_n(\theta, \phi)$, estimating integral values with Riemann Summations.

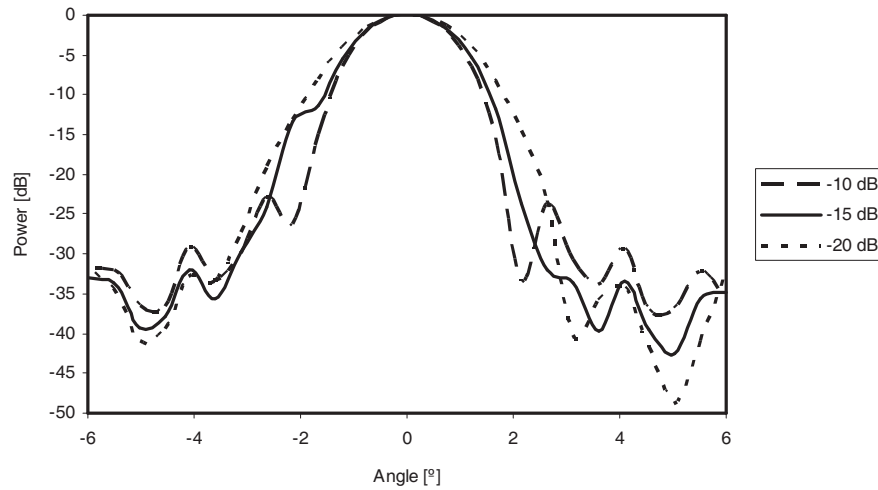


Figure 1: Simulated antenna pattern for a parabolic offset reflector having feeders with edge tapers of -10 dB, -15 dB & -20 dB.

4. RESULTS OF A MBTA

A particular case of a MBTA was analyzed: with eight asymmetrical light beams, mainly using the conical corrugated horn type with an edge taper of -15 dB, installed in a multiple beam offset parabolic torus reflector antenna with disc dimensions of $360 \text{ mm} \times 530 \text{ mm}$. Figure 2 shows the layout of the feeders which are located above and below the focal arc of the toroidal offset reflector with rotation axis perpendicular to its central axis [5, 6].

A MBTA illumination graphic is shown in Figure 3(a); in which each of the eight beams has 2° of half power beamwidth, with a total swath of 350 km . In this situation the illumination of the beams and their link with the main beam efficiency were analyzed.

Note that Figure 3(b) is a mere approximation with the sole purpose of representing the footprints. The axes are a flat representation of the distances on the meridians and parallels, while the dotted lines are trying to show the movement of the satellite on its orbit and its projection on the ground.

The MBTA was measured in far field. The response of each feeder was measured in two orthogonal positions and the diagrams of irradiation were obtained in the central working frequency (36.5 GHz).

Using the same mathematical process as in Table 1, the beam efficiency values of the eight beams were measured. Results are shown in Table 2.

Table 2: MBTA beam efficiency.

FEEDER	BEAM EFFICIENCY [%]
1	91.7
2	97.4
3	97.9
4	98.6
5	98.0
6	98.5
7	97.5
8	97.2

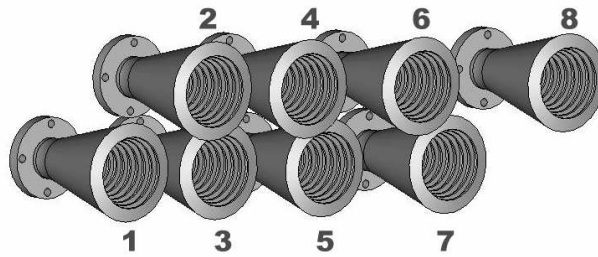


Figure 2: Feeder arrangement of the MBTA.

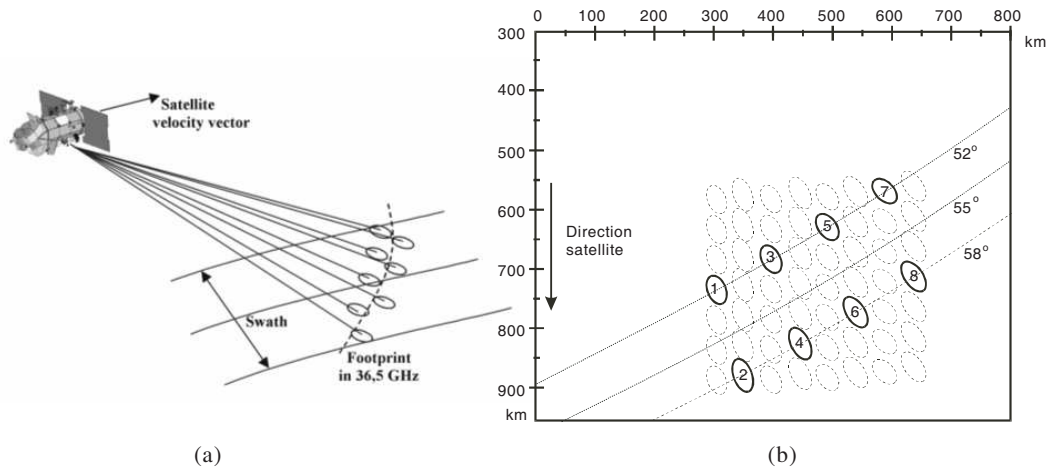


Figure 3: (a) Satellite field of view; (b) MBTA Footprint under study.

5. CONCLUSION

The best beam efficiency in simulations for a parabolic offset reflector system with feeders of different edge tapers was obtained with a -15 dB edge taper, as shown in Table 1.

Good beam efficiency results have been obtained in the MBTA model built with conic corrugated horn type feeders with an edge taper of -15 dB. The results of an eight beam offset parabolic torus reflector antenna (Table 2), show that the central feeders (4, 5 & 6) give the highest efficiency values, ranging from 98.0 to 98.6, while the farthest from the central axis of the reflector (feeders 1, 2, 7 & 8) give smaller values of beam efficiency.

REFERENCES

1. Ulaby, F. T., R. K. Moore, and A. K. Fung, *Microwave Remote Sensing, Active and Passive*, Addison-Wesley Publishing Company, 1981.
2. Hewison, T. J. and R. Saunders, "Measurements of the AMSU-B antenna pattern," *IEEE Transactions on Geosciences and Remote Sensing*, Vol. 34, No. 2, March 1996.
3. Rahmat-Samili, Y., R. A. Hoferer, and H. Mosallaei, "Beam efficiency of reflector antennas: The simple formula," *IEEE Antennas and Propagation Magazine*, Vol. 40, No. 5, October 1998.
4. Mo, T., "AMSU — A antenna pattern corrections," *IEEE Transactions on Geosciences and Remote Sensing*, Vol. 37, No. 1, January 1999.
5. Bava, J. A., V. S. Sacchetto, A. Maltz, G. Rodriguez, and A. Szymanowski, "Obtención y medidas de superficies reflectora para antena de uso satelital, empleando CNC," *IV Congreso Panamericano de END — 2007*, ISBN 978-987-23957-0-4, <http://www.ndt.net/article/panndt2007/papers/9.pdf>, 2007.
6. Bava, J. A., V. S. Sacchetto, A. Maltz, G. Rodriguez, A. Szymanowski, and y J. P. Ciafardini, "Antenas offset toroidal con haces multiples asimétricos," *IV Congreso Argentino de Tecnología Espacial*, Bs As-Mayo, 2007.

Use of TDR to Determine the Dielectric Constant of Vermiculite

G. Fontgalland¹, S. E. Barbin^{2,3}, and I. F. Dos Anjos¹

¹Electrical Engineering Department
Federal University of Campina Grande — UFCG
Campina Grande, PB, Brazil

²Department of Telecommunication and Control Engineering
Polytechnic School of Engineering University of São Paulo, SP, Brazil
³Center for Information Technology Renato Archer, Campinas, SP, Brazil

Abstract— The measurement of water content and bulk soil electrical conductivity (EC) using Time Domain Reflectometry (TDR) has had substantial advances in the last two decades. TDR has the advantage of permitting an accurate measurement of the permittivity of a material and the fact that there is a close relationship between the permittivity of a material and its water content. Topp et al. (1980) showed an equation that makes possible to evaluate the water content of soil using its dielectric constant. The objective of this study is to use TDR to determine the dielectric constant of mineral ores specially the dielectric constant of raw vermiculite in order to make possible the modelling and developing of a microwave industrial furnace to produce expanded vermiculite. With this study we wait to increase the amount of expanded vermiculite and prove that the usage of microwave energy can make a difference in industrial mineral processes, through a better control of the process and improving an increase in the final product value and reducing waste materials. A low cost reflectometer developed at UFCG will be used in this study and the data obtained will be used in the modelling of the microwave furnace. The measurement of the humidity of vermiculite will also be important permitting a better selection and classification of the raw material.

1. WHAT IS TIME DOMAIN REFLECTOMETRY

1.1. History

As early as 1939, geologists and others recognized a relationship between the dielectric properties of soil, rock and other materials, and their moisture content. However, they lacked the instrumentation necessary to make full use of it. Time Domain Reflectometry, commonly known as TDR, largely developed as the result of World War II radar research, offered a method to define these dielectric relationships. With the advent of commercial TDR research oscilloscopes in the early 1960's, it became feasible to test this new technology. Today, TDR technology is the “cutting edge” methodology for many diverse applications including the determination of basic soil water, material/water relationships.

2. PRINCIPLES AND METHODS FOR TIME DOMAIN REFLECTOMETRY

Time domain reflectometry (TDR) has become increasingly popular for the determination of soil water content. The technique depends on the measurement of the travel time of an electronic pulse through a wave guide (also called a probe) inserted in the soil. Topp et al. (1980) and other early researchers determined travel times in TDR probes by fitting tangent lines to wave form features by hand, either reading directly off the instrument screener working with photographs of the screen. Since then, automatic wave form acquisition systems have been created that allow the collection of thousands of wave forms thus necessitating the creation of computer programs for automatic interpretation of the wave form to find travel times. Several impediments have been encountered. Wave forms acquired in the field are often not as reproducible as those found in the laboratory. Wave form shape can change depending on probe construction or installation. Wave form shape varies quite dramatically with soil water content, bulk density, and salinity changes in the soil over time; with clay content changes between horizons and across the field; and with noise caused by various external factors or the data acquisition system itself. Since 1991 a set of algorithms was developed, field tested, and improved, leading to a reliable computer program for real time, unattended determination of travel times from TDR wave forms.

2.1. The TDR method for Water Content Determination

The TDR method depends on the change in apparent permittivity of the soil which occurs when soil water content changes. The permittivity of the mineral matter in soil varies between 3 and 5. The permittivity of air, which may take up as much as 45% of the soil volume, is negligible. By contrast, the permittivity of water is about 80 (depending on temperature). As soil wets and dries its apparent permittivity, ε_a , changes accordingly, though not in a linear fashion. For four fine textured mineral soils, Topp et al. (1980) found that a single polynomial function described the relationship between ε_a and volumetric water content, θ :

$$\theta = (-530 + 292\varepsilon - 5.5\varepsilon^2 + 0.043\varepsilon^3) \times 10^{-4} \quad (1)$$

Commonly, implementation of the method employs a TDR cable tester which was designed to find the location of faults in a cable. The cable tester consists of an electronic function generator which outputs a square wave signal with a very fast rise time (120 ps) and an oscilloscope timed to the square wave. The vertical axis of the oscilloscope screen has units of voltage while the horizontal axis has units of distance along the cable (or other waveguide). The units of the horizontal axis are set using the distance per division (DIST/DIV) setting. The horizontal axis is divided into ten divisions so that if DIST/DIV is set, for example to 0.2m then the entire screenwidth represents 2m. The cable tester also has a setting for the relative propagation velocity, V_{pr} . This is the ratio of the velocity at which the signal propagates in a cable or other waveguide, v , to the velocity of light in a vacuum, c . The propagation velocity depends on the permittivity ε , and the magnetic permeability μ ,

$$V_p = v/c(\varepsilon\mu)^{-0.5} \quad (2)$$

The permittivity of different insulations is different and the velocity of the signal changes accordingly. For example, for polyethylene insulation the velocity of the signal is about 0.66 times c so the relative propagation velocity is 0.66. The magnetic permeability is usually assumed to be unity. It is important to understand that the oscilloscope measures time not distance. Therefore, in order to display distance on the horizontal axis of the screen the cable tester internally converts measured times to distances. The propagation velocity, v , is used to make the conversion. If the relative propagation velocity, V_{pr} is set to 0.99 then the assumed propagation velocity is correspondingly,

$$v = 0.99c = 0.99 \times 0.299792 \times 10^9 \text{ m/s} \quad (3)$$

To convert from time to distance, the cable tester uses this assumed value of v and the measured time in the following equation which relates the one-way distance, d , to the one-way travel time,

$$t_d = vt \quad (4)$$

in a cable tester usually there is a knob named ‘Distance’ which allows the user to change the delay between signal propagation and oscilloscope scan. This delay amounts to the time that it takes the signal to travel a given distance down the cable and back to the oscilloscope pickup. Thus, the user can adjust the screen to show portions of the signal being reflected from different distances down the cable. Again, the cable tester uses the propagation velocity that we have chosen to convert the delay time to distance units so that the ‘Distance’ dial shows the correct distance. The distance will only be correct if we have chosen the correct relative propagation velocity. The signal trace on the oscilloscope screen will be flat except where discontinuities in the cable cause impedance changes and a partial reflection, or loss, of the signal. Reflections are caused by increases in impedance such as an open or broken conductor while signal loss is caused by decreases in impedance such as a short to ground.

For a cable the propagation velocity is known because the permittivity of the insulation is known. Therefore the time, required for the signal to travel to an impedance change and back again, can be used to calculate the distance to the impedance change. In the soil the apparent permittivity is unknown. However, we can construct probes (waveguides) which cause two impedance changes at a known distance from each other in the soil. Then we can use the cable tester to measure the time for the signal to travel from one impedance change to the next and use Eq. (2) to calculate the apparent permittivity which is the basic datum needed to calculate water content from Topp’s equation. If t_t is the two-way travel time measured by the oscilloscope for the signal to travel from one impedance change to the other and back again, and L is the distance between the impedance changes then $v = 2L/t_t$

Substituting this into Eq. (2), assuming $\mu = 1$, and rearranging we can calculate the apparent permittivity, $\varepsilon_a = [ct_t/(2L)]^2$ [5].

Our problem is now reduced to finding the travel time, t_t , give the trace from the cable tester screen for a probe of known length, L . Note that we do not have to know the actual propagation velocity to get the correct value of t_t from the cable tester. We only have to know the propagation velocity factor that was set on the cable tester, when the wave form was measured, in order to convert the distance units reported by the cable tester back to time units by inverting Eq. (4).

In typical TDR signal from a 2 wire TDR probe constructed for water content measurements, when the square wave signal reaches the point where the coaxial cable is connected to the rods a partial open circuit occurs because the outer braid is pulled away from the inner conductor. This partial open represents an increase in impedance which causes a reflection (increase in voltage) of the signal just before point v_0 . Immediately after passing through this partial open the signal leaves the insulating handle of the TDR probe and enters the rods buried in the soil (in our experiment we will use row vermiculite). The moist soil causes a partial closed circuit (partial short circuit) compared to the handle and the signal voltage decreases (wave form height descends). The sudden increase and then decrease in reflected wave form height as the signal passes through the probe handle and into the soil causes the peak in wave form height at point v_t . As the signal passes through the rods buried in the soil it typically encounters only small changes in permittivity and conductor configuration so no reflections are seen. This is shown in the low and flat part of the signal between points v_0 and v_t . When the signal reaches the ends of the rods in the soil it encounters an open circuit and is strongly reflected causing the increase in wave form height at point v_t .

3. DETERMINATION OF THE DIELECTRIC CONSTANT OF VERMICULITE

Using the principles explained above, we decide to use the TDR technique to determine the dielectric constant of the Vermiculite in order to use this information to develop the modelling of an industrial furnace using microwave power to produce exfoliated Vermiculite. As observed in the minerals literatures, there is no information about the dielectric constant of Vermiculite. Since the commercial TDR equipments are very expensive, we developed a prototype of a low cost reflectometer to determine the vermiculite's permittivity. The basic characteristics of the equipment are: a pulse generator, a two wire probe, and an oscilloscope. With this equipment we aim to determine the dielectric constant, and the tangent of loss, and use the data obtained during the tests, accurately determine the dimensions of our experimental microwave cavity. As we can observe in the Topp's equation, it is also possible to determine the humidity of the Vermiculite, which is a very important information to predict the amount of expanded Vermiculite that can be obtained through the microwave power processing of row Vermiculite. In a second stage, we will implement a microprocessing reflectometer, which could process the signal of the probe directly from the samples of Vermiculite and automatically determine, the dielectric constant and humidity. This would not only simplify the measurements but also help the analysis of quality of row Vermiculite in a mining process.

REFERENCES

1. Topp, G. C., J. L. Davis, and A. P. Annan, "Electromagnetic determination of soil water content: Measurements in coaxial transmission lines," *Water Resour. Res.*, Vol. 16, No. 3, 574–582, 1980.
2. Dalton, F. N., W. N. Herkelrath, D. S. Rawlins, and J. D. Rhoades, "Time-domain reflectometry: Simultaneous measurement of soil water content and electrical conductivity with a single probe," *Science*, Vol. 224, 989–990, 1984.
3. Dalton, F. N. and M. Th. van Genuchten, "The time-domain reflectometry method for measuring soil water content and salinity," *Geoderma*, Vol. 38, 237–250, 1986.
4. Dasberg, S. and F. N. Dalton, "Time domain reflectometry field measurements of soil water content and electrical conductivity," *Soil Sci. Soc. Am. J.*, Vol. 49, 293–297, 1985.
5. Topp, G. C., M. Yanuka, W. D. Zebchuk, and S. Zegelin, "Determination of electrical conductivity using time domain reflectometry: Soil and water experiments in coaxial lines," *Water Resour. Res.*, Vol. 24, 945–952, 1988.
6. Baker, J. M. and R. R. Allmaras, "System for automating and multiplexing soil moisture measurement by time-domain reflectometry," *Soil. Sci. Soc. Am. J.*, Vol. 54, No. 1, 1–6, 1990.

7. Herkelrath, W. N., S. P. Hamburg, and F. Murphy, "Automatic, real-time monitoring of soil moisture in a remote field area with time domain reflectometry," *Water Resour. Res.*, Vol. 27, No. 5, 857–864, 1991.
8. White, I., J. H. Knight, S. J. Zegelin, and G. C. Topp, "Comments on 'Considerations on the use of time-domain reflectometry (TDR) for measuring soil water content' by W. R. Whalley," *European J. Soil Sci.*, Vol. 45, 503–508, December 1994.
9. Lapid, I., "Time domain reflectometry measurements of water content and electrical conductivity of layered soil columns," *Soil Sci. Soc. Am. J.*, Vol. 55, 938–943, 1991.
10. Dalton, F. N., "Development of time domain reflectometry for measuring soil-water content and bulk soil electrical conductivity," *Advances in Measurement of Soil Physical Properties: Bringing Theory into Practice*, G. C. Topp, W. D. Reynolds, and R. E. Green (eds.), Soil Sci. Soc. Am., Madison, WI, 1992.

Experimental Characterization of Electromagnetic Properties of ASPHALT Material

O. Louhichi¹, D. Bechevet¹, and S. Tedjini²

¹MIND, Archamps, Haute Savoie, France

²LCIS, Grenoble-INP, Valenc, France

Abstract— This communication describes an applicable experimental method for the dielectric permittivity and losses factor measurement. It is used to determine the “asphalt” electromagnetic properties in order to use it for wireless applications.

1. INTRODUCTION

Study of electromagnetic propagation environment are increasing with the dramatic expansion of wireless communications applications and devices. Electromagnetic waves propagation model in different materials is possible only if their permittivity, permeability and conductive properties are known. Thus, permittivity and permeability measurements are required in numerous applications for a large variety of materials, at a given frequency bands. Most widely used techniques for characterization are: cavity resonators, free space and open-ended coaxial probe and transmission line. Each method has advantages and drawbacks. The cavity method is the most attractive since it is suitable for different material state (liquid, solid, thin sheets...). On the other hand, the accuracy of the method is generally because it is based on quite closed cavity, which minimizes the spurious coupling and avoids the radiation losses. Another significant advantage of the cavity method is the use of a calibration procedure based on a “standard” material. This method has been already considered in several previous works [2, 5].

2. METHOD OF CHARACTERIZATION

To study asphalt electromagnetic characteristics, we chose resonant cavity method. It is one of the most efficient and suitable techniques for measuring the permittivity. We choose it because of its flexibility and accuracy.

Complexity of electromagnetic analysis depends on cavity shape and the filling factor. The easiest form is the rectangular one and the most efficient deem bedding technique is obtained for a full filled cavity. This can be obtained with the asphalt after some practical precautions dealing with the filling method.

The operating principle of a resonant cavity is based on resonance of electromagnetic waves phenomenon.

Network analyzer generates an electromagnetic wave into the empty cavity volume, the metal enclosure and the shape of the cavity will result in specific electromagnetic field distributions corresponding to a set of discrete and given frequencies known as resonance frequencies. The resonance modes of the cavity are noted TE_{mnp} and TM_{mnp} . The differences observed between the resonances frequencies of empty cavity and the resonances frequencies with the cavity filled with a material (as Asphalt), allows the dielectric characterization of the material. The use of different excitation antenna into the cavity allows the measurement of several resonant frequencies corresponding to different modes.

Formulas below summarize how to recover the value of the dielectric constant [1, 4]:

$$fr_{TE_{mnp}} = \frac{1}{2\sqrt{\mu\varepsilon}} \cdot \sqrt{\left(\frac{m}{a}\right)^2 + \left(\frac{n}{b}\right)^2 + \left(\frac{p}{d}\right)^2}, \quad \text{with } \left. \begin{array}{l} m = 0, 1, 2 \dots \\ n = 0, 1, 2 \dots \\ p = 1, 2, 3 \dots \end{array} \right\} m = n \neq 0 \quad (1)$$

where a , b and d are respectively width, height and length of the cavity and $fr_{TE_{mnp}}$ represents the resonant frequency of cavity Electrical Transverse Mode and m , n and p are numbers related to the different Modes.

$$\varepsilon = \varepsilon_0 \cdot \varepsilon_r \quad (\text{Permittivity inside the cavity}) \quad \varepsilon_0 = 8,854 \times 10^{-12} \quad (2)$$

$$\mu = \mu_0 \cdot \mu_r \quad (\text{Permeability inside the cavity}) \quad \mu_0 = 4 \cdot \pi \times 10^{-7} \quad (3)$$

In practice we developed this approach with a cavity full filled with asphalt, and mixed Equations (1)–(3) to obtain Equation (4):

$$\varepsilon_r = \frac{c^2}{4 \cdot f^2} \cdot \left(\frac{m^2}{a^2} + \frac{n^2}{b^2} + \frac{p^2}{d^2} \right) \quad (4)$$

3. RESULTS

Several simulations with CST Microwave Studio software were made to validate characterization by electromagnetic resonant cavity principle. In this case, we simulated an existing cavity with imposed size: $a = 100$ mm (width), $b = 26$ mm (height) and $d = 200$ mm (length). We validated the use of the Formula (5) by simulating the same empty cavity filled with a material with known characteristics [4].

The next figure (Figure 1) shows the simulated cavity design with 2 ports and 2 loops. These 2 ports allow, for instance, measurement of transmission coefficient S_{21} (dB) (Figure 3).

Next graph (Figure 3) shows two results of transmission coefficient versus frequency. The first one (green line) is related to empty cavity and the second one (red line) to cavity filled with bitumen (similar to asphalt). We simulated with some bitumen because its dielectric characteristics are known [3] ($\varepsilon_r = 2.41$ and $\tan \delta = 0.0043$ at $f = 1000$ MHz).

The aim is to deduce permittivity and losses parameters of a material with this method. With results on Figure 2, we obtain a fixed resonance frequency at 1082 MHz on the first mode TE_{101} through the bitumen. Using Equation (4) and known parameters leads to bitumen's permittivity.

$$\begin{aligned} \varepsilon_r &= \frac{c^2}{4 \cdot f^2} \cdot \left(\frac{m^2}{a^2} + \frac{n^2}{b^2} + \frac{p^2}{d^2} \right) \\ &= \frac{(3 \times 10^8)^2}{4 \times (1.082 \times 10^9)^2} \cdot \left(\frac{1^2}{(100 \times 10^{-3})^2} + \frac{0^2}{(26 \times 10^{-3})^2} + \frac{1^2}{(200 \times 10^{-3})^2} \right) = 2.41 \quad (5) \end{aligned}$$

This result validates the method. We would use it on practical test to characterize asphalt with the cavity and a Vector Network Analyzer (VNA). The next step is to use this knowledge [4] to characterize our specific material which is Asphalt.

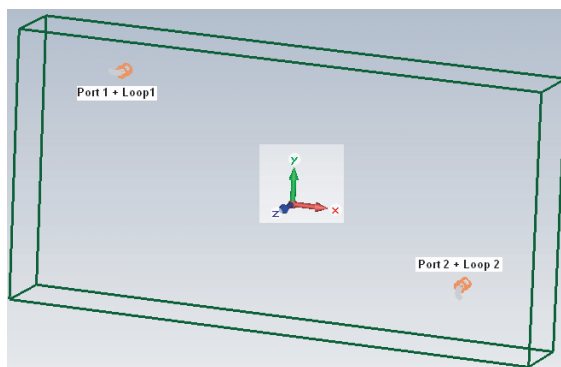


Figure 1: Cavity simulated with CST Microwave Studio.

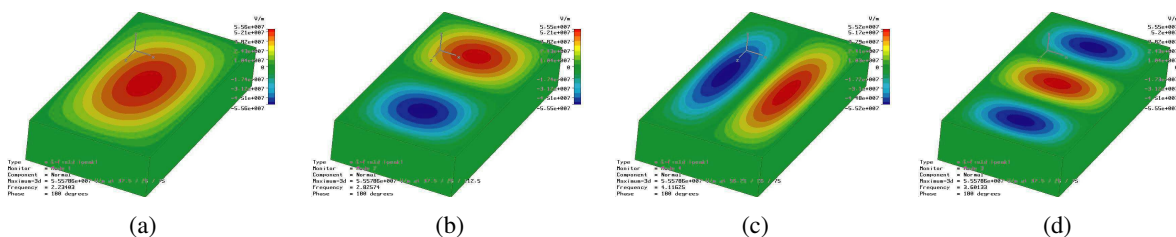


Figure 2: Modes (a) TE_{101} , (b) TE_{102} , (c) TE_{103} , (d) TE_{201} .

There are some important parameters which characterize the cavity (tools which allow the material characterization):

- The resonance frequency of the different mode (TE_{101} , TE_{102} , $TE_{103} \dots$) can be found theoretically as (6):

$$f_{r_{TE_{mnp}}} = c \cdot \sqrt{\left(\frac{m}{2a}\right)^2 + \left(\frac{n}{2b}\right)^2 + \left(\frac{p}{2d}\right)^2} \quad \text{and we need them to identify.} \quad (6)$$

- Quality Factor (Q). This is an important parameter which characterizes the measurement efficiency of our cavity.

The next figure (Figure 4) shows the transmission S -parameter (S_{21} (dB)) versus the frequency measured with a Vectorial Network Analyzer (VNA). It represents the first Electric Mode TE_{101} inside empty cavity. We used it to calculate the Quality factor of the cavity.

The quality factor of a cavity is defined as the ratio of the resonance frequency to the width of the resonance curve.

First mode (TE_{101}) appears at 1.67 GHz and 2 others values at 3 dB below (f_1 and f_2). We obtain Q factor as [6]:

$$Q = \frac{f_r}{\Delta f} = \frac{f_{r_{TE_{101}}}}{f_{2(-3\text{dB})} - f_{1(-3\text{dB})}} = \frac{1.6763828 \times 10^9}{(1.6765832 - 1.6761935) \times 10^9} = 4301 \quad (7)$$

Then we proceeded to measurements with cavity filled by Asphalt.

We show in the next figure (Figure 5) the S_{21} (dB) in 2 cases, empty (air) and filled with Asphalt. These measurements lead to dielectric parameters characterization.

Here are two results of transmission coefficient versus frequency. The first one (blue curve) represent the empty case (reference) and the second one (red curve) is related to cavity filled with Asphalt case.

Using Equation (5) leads to:

$$\begin{aligned} \epsilon_r &= \frac{c^2}{4 \cdot f^2} \cdot \left(\frac{m^2}{a^2} + \frac{n^2}{b^2} + \frac{p^2}{d^2} \right) \\ &= \frac{(3 \times 10^8)^2}{4 \times (1.108 \times 10^9)^2} \cdot \left(\frac{1^2}{(100 \times 10^{-3})^2} + \frac{0^2}{(26 \times 10^{-3})^2} + \frac{1^2}{(200 \times 10^{-3})^2} \right) = 2.291 \quad (8) \end{aligned}$$

We approximate the permittivity of the medium inside the cavity at 2.3. We can assimilate it to an effective permittivity (mix of asphalt and airvacuum) because the cavity is not totally full, due to granulates composing asphalt: there is air between each others.

The next step is to quantify the volume of the asphalt and the volume of the air vacuum inside the cavity to characterize exactly the value of asphalt permittivity.

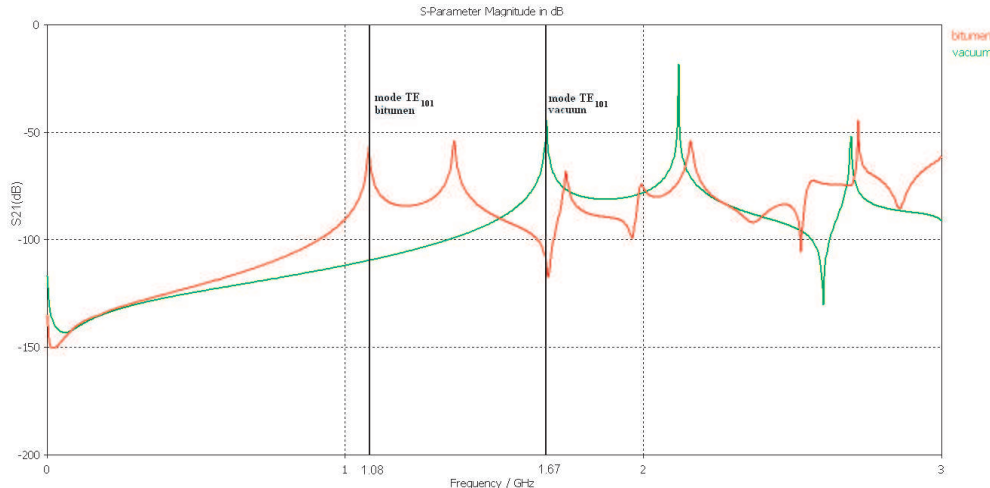
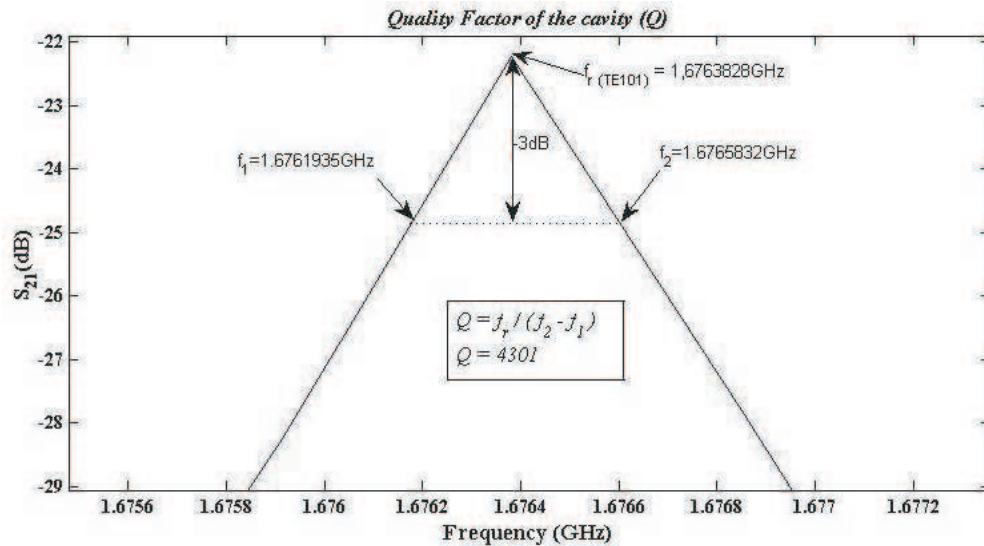
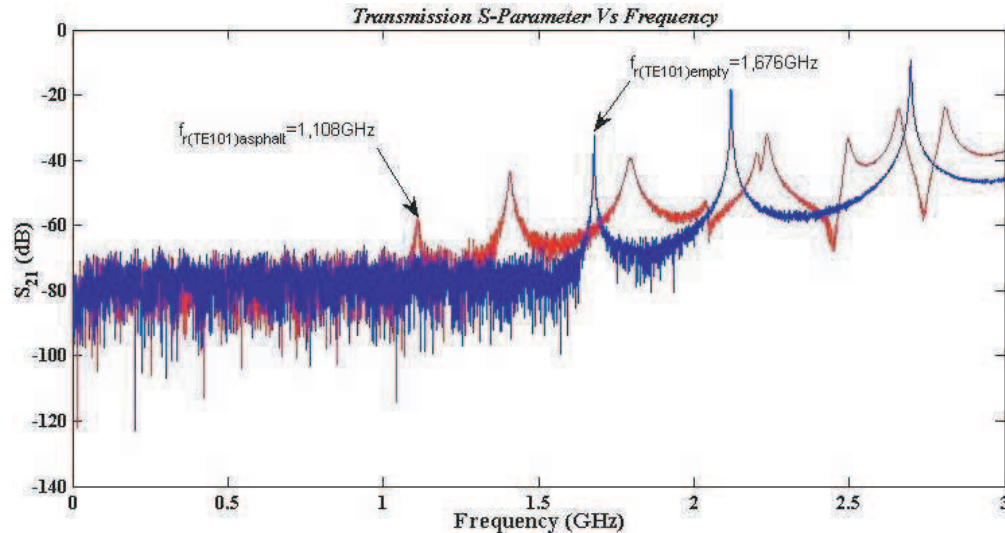


Figure 3: Two simulation results, S_{21} (dB) vs f (GHz) with empty and filled with bitumen cavity.


 Figure 4: Calcul of the quality factor of the cavity (Q).

 Figure 5: Transmission S -Parameter S_{21} (dB) vs f (GHz).

4. CONCLUSION

This work uses the electromagnetic method in order to measure the dielectric permittivity and dielectric losses. This allows characterization of dielectric properties of civil engineering materials, especially asphalt material in the ISM frequencies band and specially UHF. The Electrical Transverse mode of the cavity appears at 1670 MHz, thus, if we want to characterize our material at a lower frequency as 868 MHz, either we have to change the cavity's dimensions or we extrapolate our results to recover permittivity at the desired frequency. The method would be used to characterize different compositions of asphalt.

REFERENCES

1. Bechevet, D., T.-P. Vuong, and S. Tedjini, "Design and measurements of antennas for RFID, made by conductive ink on plastics," *Oral Presentation, 2005 IEEE AP-S International Symposium and USNC/URSI National Radio Science Meeting*, Washington DC, USA, July 3–8, 2005.
2. Meng, B., J. Booske, and R. Cooper, "Extended cavity perturbation technique to determine the complex permittivity of dielectric materials," *IEEE MTT*, Vol. 43, No. 11, November 1995.
3. Adous, M., P. Quéffélec, and L. Laguerre, "Coaxial/cylindrical transition line for broadband

- permittivity measurement of civil engineering materials,” *Measurement Science and Technology*, Vol. 17, 2241–2246, 2006.
4. Collin, R. E., *Foundations for Microwave Engineering*, 2nd Edition, 2004.
 5. Sucher, M., “Dielectric constants,” *Handbook of Microwave Measurements*, Vol. 2, M. Sucher and J. Fox Eds., Chap. 9, Polytechnic Press, Brooklyn, N.Y., 1963.
 6. Cheng, D. K., *Field and Wave Electromagnetics*, 2nd Edition, Addison-Wesley, 1989.

Achievements and Perspectives of the COSMO-SkyMed Mission

Giovanni Valentini, Fabrizio Battazza, Alessandro Coletta, Fabio Covello, and Gemma Manoni
ASI — Italian Space Agency, Viale Liegi 26, Rome I-00198, Italy

Abstract— In 2007 and 2008 ASI (Agenzia Spaziale Italiana/Italian Space Agency) launched three out of four X-band SAR satellites of the COSMO-SkyMed (Constellation of small Satellites for Mediterranean basin Observation) constellation, making available to the users a unique SAR constellation dedicated to the Earth Observation.

The constellation will be completed with the launch of the fourth satellite in 2010.

COSMO-SkyMed is the largest Italian investment in Space Systems for Earth Observation, commissioned and funded by Italian Space Agency (ASI) and Italian Ministry of Defense (MoD). COSMO-SkyMed is a Dual-Use (Civilian and Defence) end-to-end Earth Observation System aimed to establish a global service supplying provision of data, products and services relevant to a wide range of applications, such as Risk Management, Scientific and Commercial Applications and Defence/Intelligence Applications.

The system consists of a constellation of four Low Earth Orbit mid-sized satellites, each equipped with a multi-mode high-resolution Synthetic Aperture Radar (SAR) operating at X-band. The system is completed by dedicated full featured Ground infrastructures for managing the constellation and granting ad-hoc services for collection, archiving and distribution of acquired remote sensing data.

The first and second COSMO-SkyMed satellites are in the operational phase while the third one is completing its commissioning phase.

The results coming from the utilisation of the two first satellites, after the first year of life, revealing an excellent performance of the X-band SAR and the importance of a fast response time in several application as risk and emergency management (i.e., China's earthquake, Myanmar and Haiti flood), ice monitoring (reduction of the glaciers, Wilkins Ice Shelf disintegration), multi-temporal acquisition for agriculture monitoring, ship detection, interferometry, landslides monitoring, maritime surveillance and security, rapid mapping.

A further step forward will be realized when COSMO-SkyMed 3 will be operative, since the third satellite is positioned in the so-called "one-day interferometry configuration", it will allow the constellation to detect interferometric acquisitions with a de-correlation time equal to one day.

The first COSMO-SkyMed Announcement of Opportunity for scientific data exploitation will give the chance to achieve innovative and valuable results using the COSMO-SkyMed data, products and services.

1. INTRODUCTION

COSMO-SkyMed (Constellation of small Satellites for Mediterranean basin Observation) is the first Italian dual Space System dedicated to the Earth Observation. It is the largest Italian investment in Space Systems for Earth Observation, commissioned and funded by ASI (Agenzia Spaziale Italiana) and Ministero della Difesa (Italian Ministry of Defence).

The system consists of a constellation of four LEO mid-sized satellites, each equipped with a multi-mode high-resolution SAR operating at X-band.

ASI in cooperation with Ministero della Difesa manages the contract assigned to an Italian industrial team, where Thales Alenia Space Italia (TAS-I), in charge to develop the project, is the Prime Contractor.

2. CONSTELLATION DEVELOPMENT

COSMO-SkyMed-1 and COSMO-SkyMed-2 are already operative, while COSMO-SkyMed-3 is ultimately the commissioning phase.

The entire constellation will be completed during 2010 and the system will be fully operative by the end of 2010.

All satellites have been placed in the expected stable orbital configuration and the orbit and system parameters were all nominal.

During the Commissioning Phase the verification of the functionalities, the performance and the operations of both satellites and of the overall System have been completed.

All the calibration activities have been completed testing and verifying the SAR antenna of each satellite. The verification and validation of the whole System (satellites, sites and support System) have been completed.

3. ACHIEVEMENTS IN 2008

COSMO-SkyMed 1 and 2 are in operational phase and they are currently used by both civilian and defence users for their specific applications exploiting the COSMO-SkyMed data. Following, a set of significant applications conducted by ASI and e-GEOS during 2008 is shown.

These applications reveal the innovative contribution of the Italian SAR constellation to the studies and analyses of phenomena related to risk management (as floods and earthquake events), ice monitoring, agriculture etc, thanks to the high geometric and radiometric resolution and the short revisit time.

3.1. Ocean and Ice Applications (March 2008–September 2008)

Several oil spills have been detected and monitored using the SAR sensors of the constellation. An example is here reported in Figure 1: the 9th of September 2008, a large oil spill near the Chinese port of Qingdao due to a big shipwreck.

After the alert based on the data collected by ENVISAT satellite of the European Space Agency (ESA), COSMO-SkyMed-1 and COSMO-SkyMed-2 detect data of the Wilkins Ice Shelf disintegration event, acquiring several images in the Antarctic region (see Figure 2).

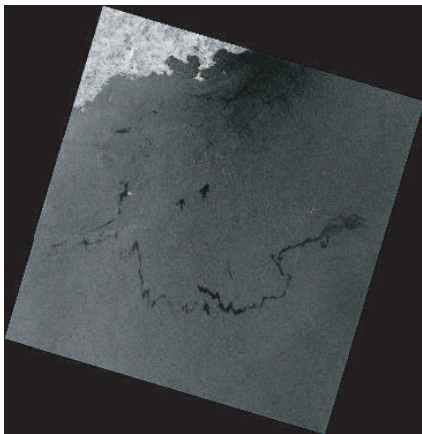


Figure 1: Stripmap-HIMAGE collected on the 9th of Sep. 2008. Large oil spill occurred after a shipwreck, China.



Figure 2: Stripmap HIMAGE collected on the 31st of March: disintegration of the Wilkins Ice Shelf, Antarctica.

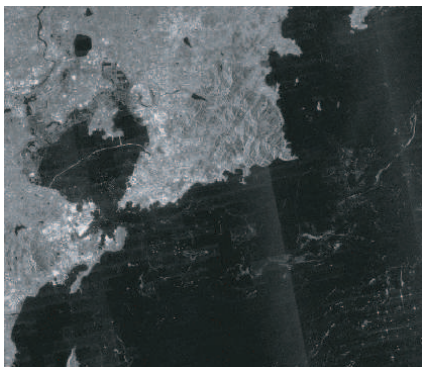


Figure 3: ScanSAR WR image collected on the 6th of July 2008 showing algae filaments and ships close to Qingdao.

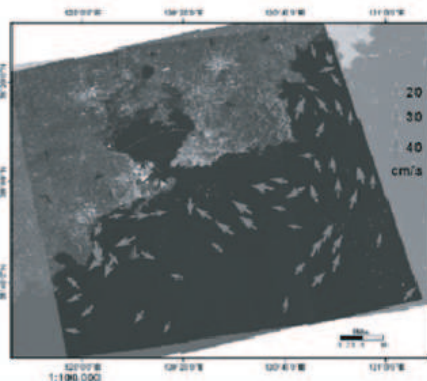


Figure 4: Current fields in the bay of Qingdao, derived by a COSMO-SkyMed 48 minutes image pair.

ScanSAR Wide Region (100×100 km swath) and Stripmap HIMAGE (40×40 km) acquisition modes have been used to monitor the overall phenomenon through the detection of the ice

movements over large and medium areas and the current fields.

During summer 2008 a macro-algae bloom occurred in the bay of Qingdao (China). Using the two satellites available at that time, positioned 180° apart on the same orbit plane and of the left/right looking capabilities of the satellites, two images were collected with time separation of 48 minutes (half orbit cycle); current fields were derived by the analysis of the image pairs (see Figures 3 and 4).

3.2. China Earthquake (May 2008)

COSMO-SkyMed processed the first image over the China's south-western Sichuan province, subject to a strong earthquake (magnitude 7.8) the 12th may 2008. The Response Time has been 16 hours from the alarm.

Figure 5 reports an image of the Guan-Xian area (in Sichuan province), acquired one day after the quake and used for monitoring the damage and the overall situation over the Guan-Xian area. Potential damages of the dike (highlighted by the circle at the top left of the image) were monitored so as to monitor it and prevent the collapse of the dike with consequent devastations in the area.

The monitoring and observation of natural disasters of this relevance in every atmospheric conditions and during the day and night, conducted in Near Real Time with fast products delivery, are crucial to guarantee fast rescue actions.

The images acquired by the two COSMO-SkyMed satellites, in the days immediately after the earthquake, demonstrating the relevant contribution of a SAR space constellation as COSMO-SkyMed in emergency situations like this.

Many cases of partial/total collapses were detected after the quake and change detection application was always used to detect the changes happened in the area.

3.3. Agriculture Multi-temporal Acquisition (May–July 2008)

A multi-temporal acquisition over agricultural fields have been performed on the 25th of May, 26th of June and 28th of July 2008 over Kumagaya (Japan) area, near Tokyo city (Figure 6). The area of acquisition is essentially composed of agricultural fields. Three COSMO-SkyMed images have been acquired (Spotlight mode) in the same acquisition conditions with a repeat cycle of 32 days so as to allow the production of a co-registered product. This highlights a strong signal on the 28th of July that should be due to the presence of the rice fields (confirmed by observations in situ).

On May the rice fields are just at the beginning of the cultivation status and on May–June the presence of the water becomes quite relevant (in such cases the radar signal is weak), on July the first rice plants begin to grow up and their presence strengthens the SAR backscattering signal as represented in the following image.

3.4. Flood (Myanmar, May 2008)

In 2008 a seasonal cyclone in the northern Indian Ocean devastated Burma (Myanmar). Cyclone Nargis brought winds of 130 mph and gusts of 150–160 mph, which is the equivalent of a strong Category 3 or minimal Category 4 hurricane. At least 10,000 people were killed, and thousands more were missing. The 6th of May over COSMO-SkyMed-1 acquired an image Rangoon area



Figure 5: Spotlight collected on the 13th of May 2008 over Guan-Xian city, China.



Figure 6: Spotlight collected on the 25th of May, 26th of June and 28th of July 2008 over Kumagaya area, Japan.

(SCANSAR — Huge Region) with a fast Response Time, allowing the identification of the areas affected by the flood and then of the main zones to be rescued with high priority.

The wide flood areas are identified with the dark areas (highlighted by the circles).

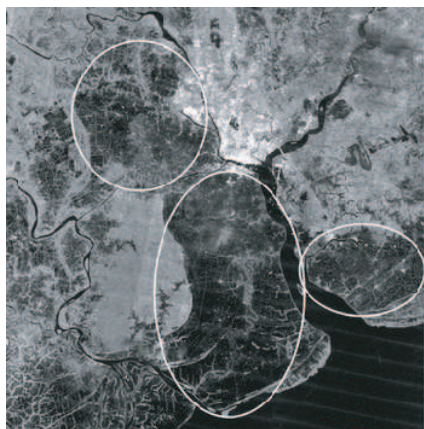


Figure 7: ScanSAR Huge Region collected on the 6th of May over Rangoon Area, Burma (Myanmar).

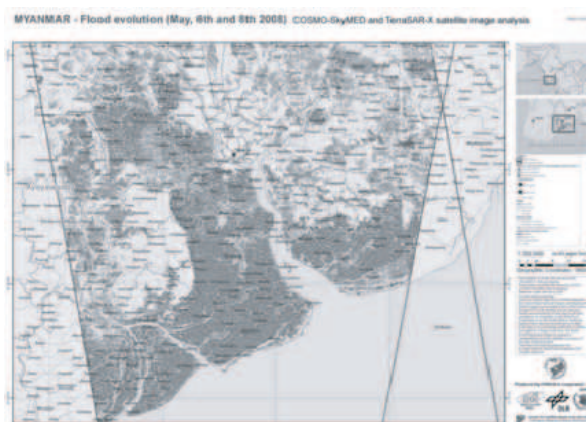


Figure 8: Flood evolution map [Credits to WFP].

4. CONCLUSION

All the described applications made during 2008, reveal the strong contribution of the X-band SAR sensors to study and analyse risk management (as floods and earthquake events), ice monitoring, agriculture matters. Thanks to the high geometric and radiometric resolution of the sensors and the short revisit time of the constellation, the COSMO-SkyMed products use for these objectives is innovative and unique, making the Italian SAR constellation an advance space Earth Observation asset for civilian and defence users.

REFERENCES

1. Agenzia Spaziale Italiana, “COSMO-SkyMed system description & user guide,” ASI — Agenzia Spaziale Italiana, Roma, Italy, <http://eopi.asi.it>, 2007.
2. Agenzia Spaziale Italiana, “COSMO-SkyMed SAR products handbook,” ASI — Agenzia Spaziale Italiana, Roma, Italy, <http://eopi.asi.it>, 2007.
3. Battazza, F., A. Capuzi, A. Coletta, F. Caltagirone, G. Valentini, S. Fagioli, G. Angino, F. Impagnatiello, and R. Leonardi, “COSMO-SkyMed program: Mission and system description of an advanced space EO dual-use asset,” *Proceedings of 27th EARSeL Symposium*, Bolzano, Italy, June 4–7, 2007.
4. BBC News, “China’s earthquake report,” www.bbc.co.uk, 2008.
5. Caltagirone, F., A. Capuzi, R. Leonardi, S. Fagioli, G. Angino, and F. Impagnatiello, “COSMO-SkyMed: An advanced dual use system for earth observation,” *Proceedings of IGARSS 2007*, Barcelona, Spain, July 23–27, 2007.
6. Coletta, A., G. Valentini, A. Capuzi, F. Caltagirone, M. De Carlo, G. De Luca, F. Battazza, and F. Covello, “Il programma COSMO-SkyMed: Descrizione della missione e del sistema e primi risultati,” *Rivista italiana di telerilevamento 2008*, Vol. 40, No. 2, 5–13, 2008.
7. Covello, F., F. Battazza, A. Coletta, E. Lopinto, C. Fiorentino, L. Pietranera, G. Valentini, and S. Zoffoli, “COSMO-SkyMed an existing opportunity for observing the earth,” *Journal of Geodynamics — Special Issue WEGENER*, 2008.

The Overview of the L-band SAR Onboard ALOS-2

Yukihiro Kankaku, Yuji Osawa, Shinichi Suzuki, and Tomohiro Watanabe
JAXA, Japan

Abstract— Advanced Land Observing Satellite-2 (ALOS-2) is the post-ALOS mission. The L-band SAR onboard ALOS-2 has higher resolution, lower noise equivalent sigma zero (NESZ), and higher signal to ambiguity ratio (S/A) than PALSAR in order to meet the requirements for land and disaster monitoring. To realize these requirements, the new technologies have been adopted: the maximum bandwidth allocation for L-band SAR and the spotlight mode with active phased array antenna (APAA) for high resolution, the development of high power and efficient device for high NESZ, and chirp modulation technique for high S/A. In addition, very accurate orbit control (orbital tube < 500 m) and short repeat-pass orbit (14 days) achieve the higher coherence of INSAR both between stripmap modes and between ScanSAR modes.

This paper introduces the overview of the L-band SAR onboard ALOS-2 as the post-ALOS mission.

1. INTRODUCTION

Advanced Land Observing Satellite-2 (ALOS-2) is a post-ALOS mission. JAXA has been operating the Advanced Land Observing Satellite (ALOS) “Daichi” since January 2006. The PALSAR onboard ALOS is the L-band Synthetic Aperture Radar (SAR) to observe large area by electronic beam steering with active phased array antenna (APAA) technology, and has the full-polarimetric measurement capability first in the world. The L-band microwave can penetrate leaves and grasses to measure the ground directly. By this unique characteristic, PALSAR has been used for monitoring the world forest, the polar ice and the crustal movements and so on. Especially PALSAR has contributed to domestic and international disaster management activities by its interferometry capability (INSAR) with high coherence. ALOS has completed nominal three years mission life and continues to work. “ALOS-2” is the satellite carrying an L-band SAR succeeding to PALSAR.

2. LOS-2 DESCRIPTION

ALOS-2 is a satellite with L-band SAR based on APAA technology. The APAA of ALOS-2 allows not only conventional stripmap and ScanSAR but also Spotlight mode with electric beam steering to direction of azimuth. To cover wide areas, ALOS-2 has the capability to wide incidence angle 8 to 70 deg with electric beam steering and the left or right looking by satellite maneuver in about 2 minutes from nominal look direction of nadir looking to Right- or Left-looking. And ALOS-2 shall be continuously controlled to an orbit tube of ± 500 m to a reference orbit for high coherence repeat pass SAR interferometry both between stripmap modes and between ScanSAR modes.

Table 1 summarizes the characteristics values of the orbit parameters, while Table 2 shows the system parameters. Figure 1 shows the ALOS-2 overview on orbit.

Table 1: ALOS-2 orbit parameters.

Nominal orbit height at the equator	628 km
Orbit type	Sub-synchronous
Orbits/day	15–3/14
Revisit time	14 days
LST	12 : 00 \pm 15 min
Inclination	Approx. 98 deg
Orbit control for reference orbit	± 500 m
Mission life	5 years (goal to 7 years)
Duty per orbit	50%

Table 2: ALOS-2 system parameters.

Radar carrier frequency	1257.5 MHz and more
Band	L
Wave length	0.229 m
PRF	1500 to 3000 Hz
Range bandwidth	14/28/42/84 MHz
polarization	SP/DP/FP/CP
Look direction	Right and Left
Antenna width	2.9 m
Antenna length	9.9 m
Incidence angle	8 to 70 deg
Range resolution	3 m/6 m/10 m/100 m
Azimuth resolution	1 m/3 m/6 m/10 m/100 m

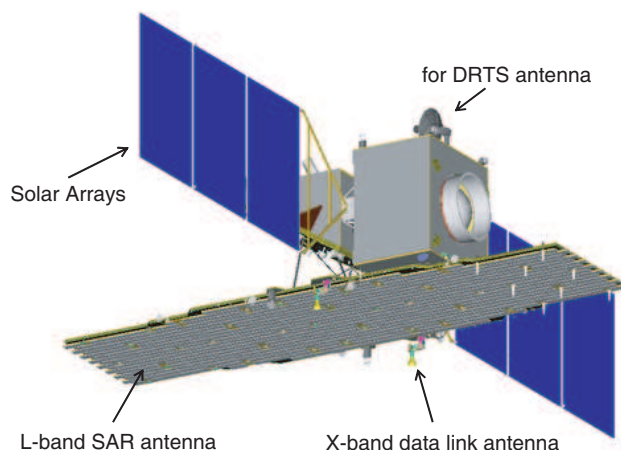


Figure 1: ALOS-2 overview on orbit.

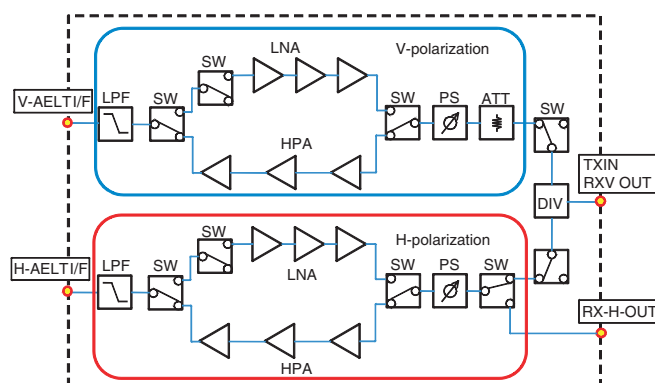


Figure 2: ALOS-2 TRM architecture.

3. L-BAND SAR PAYLOAD

3.1. SAR Antenna

The L-band SAR of ALOS-2 instrument comprises an active phased array antenna which allows electronic beam steering direction to range and azimuth. The antenna has a horizontal dimension of 9.9 m and vertical dimension of 2.9 m, and is composed of 5 identical electrical panels. The antenna consists 1080 radiation elements as a whole which are driven by 180 Transmit-Receive-Modules (TRMs). It enables to steer and form the beam in elevation and azimuth direction for several imaging modes Stripmap, Spotlight and ScanSAR. The antenna nominal pointing is nadir direction and it is pointing 30 deg away from nadir when it observes.

The antenna is dual receive antenna system that the full aperture or 3/5 aperture antenna is used for transmission but in receive the antenna is divided into two separate partitions in along track. The signals of both receiving antenna are detected and recorded separately which allows the acquisition wide swath.

3.2. Transmit-Receive-Modules(TRM)

TRMs enable to select polarization of Single (HH/VV/HV), Dual (HH + HV/VV + VH), Quad (HH + HV + VV + VH), and Compact polarimetry (Tx: Oriented 45 deg or Circular, Rx: H or V) by transmitting H and V polarization simultaneously. In L-band propagation disturbances and especially ionospheric effects like Faraday rotation and phase delay have to be considered and if possible corrected. And quad polarimetry mode uses alternative pulse of H and V which increase PRF and makes narrow swath. So, ALOS-2 has compact polarimetry mode as an experimental mode with transmission of a linear polarization oriented at 45 deg or Circular (LHCP or RHCP) selectable by command. An output power of 34 W is provided at the TRM output port with low loss and high power SSPA using gallium nitride (GaN) HEMT, and the overall output power of 5100W at the antenna output port with full aperture. Figure 2 shows the TRM architecture.

Table 3: L-band SAR onboard ALOS-2 target characteristics.

mode		Spotlight	Stripmap			ScanSAR
		Spotlight	Ultra-Fine	High-sensitive	Fine	ScanSAR
Frequency		1257.5 MHz		1257.5 MHz or 1236.5/1278.5 MHz (T.B.D.) selectable		
Incidence angle range		8~70 deg				
Band width		84 MHz	84 MHz	42 MHz	28 MHz	14 MHz
Ground Res.		Rg × Az: 3 m × 1 m	3 m	6 m	10 m	100 m
Swath		Rg × Az: 25 × 25 km	50 km	50 km (FP:30 km)	70 km (FP:30 km)	350 km 5scans
Selectable Pol		SP	SP/DP	SP/DP/FP/CP	SP/DP/FP/CP	SP/DP
NESZ		≤ -24 dB	≤ -24 dB	≤ -28 dB	≤ -26 dB	≤ -26 dB
S/A	Rg	25 dB	25 dB	23 dB FP:Co-pol: 23 dB FP:X-pok: 15 dB	25 dB FP:Co-pol: 20 dB FP:X-pok: 10 dB	25 dB
	Az	20 dB	25 dB	20 dB	23dB	20 dB

4. L-BAND SAR CHARACTERISTICS

L-band SAR onboard ALOS-2 is enhanced performance from ALOS (PALSAR). L-band SRA has 3 imaging modes, Spotlight as new mode, Stripmap, and ScanSAR mode which are conventional modes, and 5 observation modes. Table 3 summarizes L-band SAR target characteristics.

The center frequency of Spotlight and Ultra-Fine mode is 1257.5 MHz to achieve the range resolution 3 m using 84 MHz bandwidth within the 85 MHz allocation to Space-to-Earth Earth Exploration Satellite Service (EESS) (active) in L-band from 1215 MHz to 1300 MHz. However, the frequency of L-band from 1215 MHz to 1300 MHz is allocated Radio Navigation Satellite Service (RNSS), too. So, to make the influence on RNSS a minimum, other modes operate at selectable center frequencies 1236.5 MHz/1257.5 MHz/1278.5 MHz (T.B.D.).

The feature of each observation mode is as follows, all modes use dual receive antenna system without Fine mode.

► Spotlight mode

The azimuth resolution is 1 m for a detailed observation of the disaster area with APAA technique which is electronic beam steering $+/- 3.5$ deg in the direction of the azimuth away from nadir to increase the illumination time, i.e., the size of the synthetic aperture.

► Ultra-Fine mode

In nominal, Ultra-Fine mode collects base-map for interferometry (InSAR) in Japan with high resolution and wide swath. Within all the range of incidence angle, the swath is satisfied 50 km. Ultra-Fine mode is the basically mode to observe the disaster in Japan.

► High-sensitive mode

High-sensitive mode is designed for only flood disaster. This mode has better NESZ for observation water area where the back scattering coefficient is small, so the resolution is lower than Ultra-Fine mode though higher than PALSAR.

► Fine mode

Fine mode is conventional mode that succeed to PALSAR. The resolution and swath are almost equal to PALSAR.

► ScanSAR mode

ScanSAR mode is conventional mode, too. The resolution and swath are almost equal to PALSAR with 5 scans.

The one of the new technique of ALOS-2 is the chirp modulation in order to decreased the influenced of range ambiguity than PALSAR at high incidence angle. ALOS-2 uses Up/Down chirp alternately transmitted with phase modulation (zero or pi using maximal length sequences), while PALSAR uses only down linear chirp. As a result, it is confirmed that the range ambiguity improved about 10 dB than without chirp modulation. Figure 3 shows the simulation result. The simulation area is TOMAKOMAI where is selected as distribution target, and the data is Pi-SAR data which is the airborne L-band SAR. The (c) is figure where (a) and (b) were matched, when the main signal level is equal to the ambiguity. Using chirp modulation, the ambiguity that exists in Figure 3(c) has disappeared in Figure 3(d).

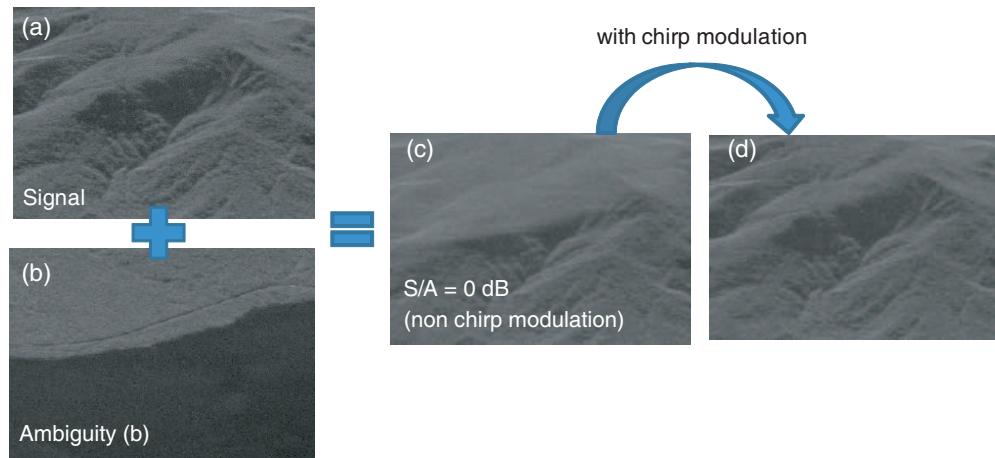


Figure 3: The simulation result of chirp modulation.

5. PROJECT STATUS

Launch of the ALOS-2 is planned for 2013. After commissioning phase of 6 months duration the operational phase will start. The mission life is designed at least 5 years and goal to 7 years operation. The Preliminary Design Review (PDR) for L-band SAR subsystem and satellite segment will be held in 2009 Summer to Autumn.

6. CONCLUSION

ALOS-2 mission will provide a new class of high quality L-band SAR products by using new techniques. High resolution is due to Spotlight mode and wide bandwidth, the wide swath is due to dual receiving antenna system and compact polarimetry, lower NESZ is due to high power and low loss SSPA (GaN), better S/A is due to chirp modulation. ALOS-2 will contribute to the domestic and international Land management, Earth resource management, Earth resource exploration, disaster management activities and any mission using these techniques.

However, in order to achieve the mission, ALOS-2 needs cooperation from each space agency especially RNSS in L-band. ALOS-2 ask for RNSS in each community support and cooperation.

Application of PSInSAR for Monitoring Urban Subsidence in Beijing

Hong-Li Zhao^{1,2}, Jian-Ping Chen^{1,2}, Xiao-Fang Guo³, and Jing-Hui Fan³

¹School of the Geosciences and Resources, China University of Geosciences (Beijing)
Beijing 100083, China

²Beijing Land Resources Information Development Research Laboratory
Beijing 100083, China

³China Aero Geophysical Survey & Remote Sensing Centre for Land & Resources
Beijing 100083, China

Abstract— Subsidence has seriously affected Beijing’s city planning and construction, and brought harm to citizens’ lives and properties. Although Beijing’s in-situ subsidence monitoring system is necessary and reliable, its sparse data grid in the area is a limitation which makes it difficult for us to understand the whole deformation field.

PSInSAR (Persistent Scatterers for SAR Interferometry) technique can analyze a set of SAR data suitable for InSAR processing, identify the pixels that corresponding to temporarily stable natural reflectors or persistent scatterers (PS), and get high accuracy deformation measurements even the SAR data with long temporal and space baselines. While selecting PS candidates, in addition to using the amplitude dispersion index as a threshold, we also make use of the coherence value. The 2 thresholds together can identify the pixels with stable amplitude statistics characteristic and exclude the ones corresponding to weak and incoherent scatterers, for example, water.

18 ENVISAT ASAR images covering the period from June 2003 to March 2007 have been selected to retrieve the subsidence phenomena in eastern Beijing area. The result shows the distribution and the relative deformation value of the displacement field and reveals 4 subsidence cones in the study area.

1. INTRODUCTION

In many cities all over the world, overexploitation of groundwater, especially the concentrated well fields’ pumping, has caused the constant drawdown of the regional groundwater level accompanied with the lacunaris media compact and the land subsidence. To satisfy the water needs of tens of millions of citizens, Beijing, an ever-enlarging, urbanizing city, has had to exploit underground water, which contributes to almost two thirds of the city’s life-use water. As a result, subsidence has seriously affected Beijing’s city planning and construction, and caused certain damage to city infrastructures, thus brought harm to citizens’ lives and properties [1–6]. The in-situ subsidence monitoring system of Beijing is mainly made up of the monitoring stations, the bedrock bench marks, the layered bench marks, the groundwater level observation wells, the pore-water pressure observation wells, the exterior groundwater observation wells, the GPS monitoring sites and the special monitoring sites [7].

By the end of 2003, according to the ground monitoring results, five subsidence areas in the Beijing area had been determined [6], with the biggest one reaching 722 mm, affecting an area of nearly 5,000 km². Subsidence at the eastern suburb, such as Changping, Shunyi, Fengtai, Tongzhou and Daxing etc, appeared more serious than other parts in Beijing and was over 1800 km².

Although Beijing’s in-situ subsidence monitoring system is necessary and reliable, its sparse data grid in the area is a limitation which makes it difficult for us to understand the whole deformation field. Spaceborne differential radar interferometry (DInSAR) has proven a remarkable potential for mapping ground deformation phenomena over tens-of-kilometers-wide areas with centimeter-scale accuracy on a more dense space grid and time series.

2. METHOD

Geometrical and temporal decorrelation factors are important hindrances that prevent DInSAR from being an operational tool for displacement monitoring. Moreover, atmospheric inhomogeneities produce an atmospheric phase screen (APS) on every SAR image, which can contaminate the results of the deformation monitoring [8, 9].

By identifying temporarily stable natural reflectors or persistent scatterers (PS), Persistent Scatterers InSAR (PSInSAR) technique can overcomes the drawbacks and analyzes this subset of

pixels in SAR images, even with long temporal and space baselines, and then detects displacements in urban areas with millimeter accuracy per year [8, 9].

The procedure of PSInSAR applied in this paper is similar to the one discussed by [10] and illustrated in Fig. 1. Compared with traditional DInSAR process, PSInSAR's special steps mainly include: (1) Calibration of the SLC images; (2) Persistent Scatterers Candidates (PSC) selection; (3) Triangulation of PSC and calculation of the phase difference of each PSC couple; (4) Estimation of the differential linear deformation velocity and DEM error between each PSC couple; (5) Integration the linear deformation velocity based on one reference PSC; (6) Dealing with the atmospheric phase screen (APS); (7) detection of all PS and re-estimation of the linear deformation velocity. Unlike the method in [10], we use both the amplitude dispersion index and the averaged coherence map of all InSAR image pairs as threshold while selecting PS candidates. The 2 thresholds together can identify the pixels with stable amplitude statistics characteristic and exclude the ones corresponding to weak and incoherent scatterers, for example, water.

3. DATA PROCESSING

Using ENVISAT ASAR images, we apply PSInSAR method in the eastern Beijing area to detect the deformation phenomena. 18 ENVISAT ASAR images covering the period from June 2003 to March 2007 have been selected to retrieve the subsidence phenomena in the research area. In the data stack, each SAR image is named as the observation date and the image 20050309 is selected as the master image, which optimizing the distribution of the baselines. For the 18 interferometric pairs, the absolute values of perpendicular baselines are less than 1000 m, and the time baselines vary from -630 to 735 d (see Fig. 2).

In the master image 20040827, the study area, having 20000-line and 3400-column pixels, is cropped. The red rectangle in Fig. 3(a) shows the preliminary position of the study area in Google Earth. Some remarkable targets are sketched and labeled on the averaged amplitude image of 18 SAR data (see Fig. 3(b)).

During the course of computing the reference phase, i.e., "flat earth phase", the precise DELFT orbits are used. In the process of removing topographic component from the interferometric images, SRTM DEM data are used. While the orbit data of ENVISAT have been referenced to the WGS84 ellipsoid, the EGM96 geoid has been chosen as the reference for the SRTM DEM height values. So the geoid height in the area has been compensated. The procedure of traditional DInSAR is completed in Doris [11].

For the selection of PSC, the 2 threshold, the amplitude dispersion index and the averaged coherence value, are respectively set to 0.18 and 0.35. Because a PS's backscattered signal is

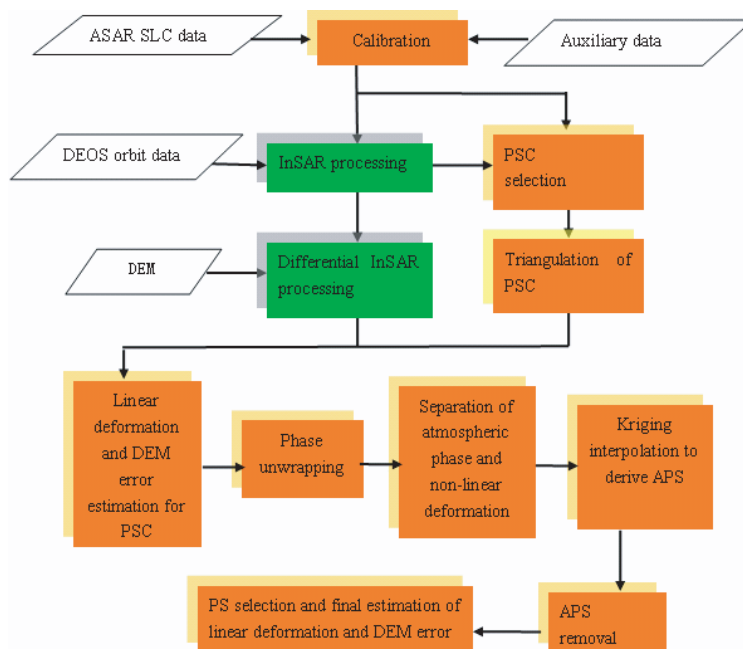


Figure 1: Flowchart of PSInSAR technique.

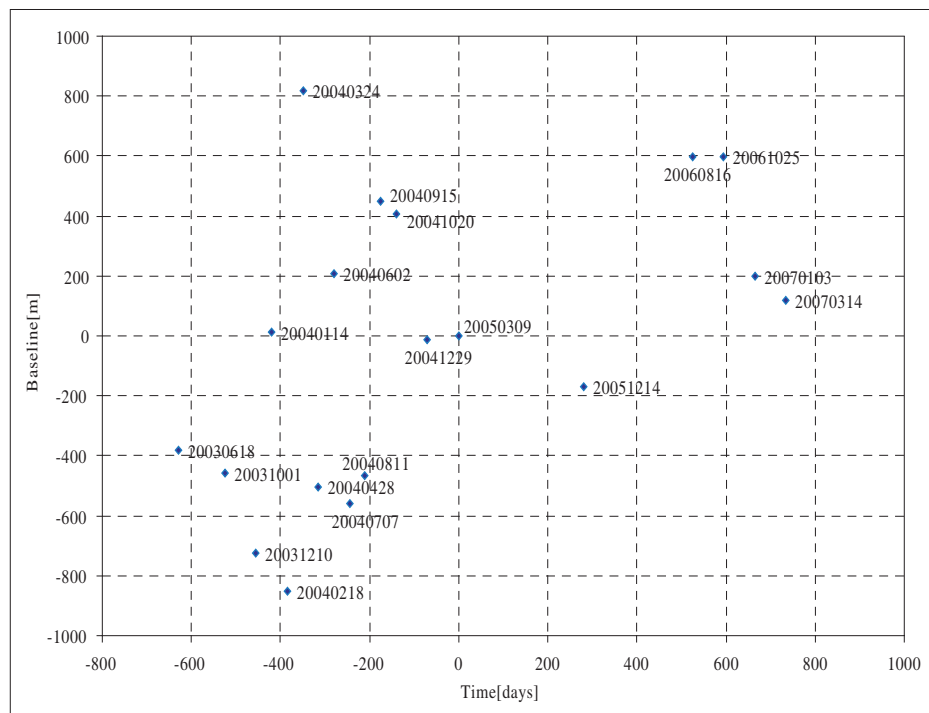


Figure 2: Time baselines in days and perpendicular baseline in meters with image 20050309 as the master.

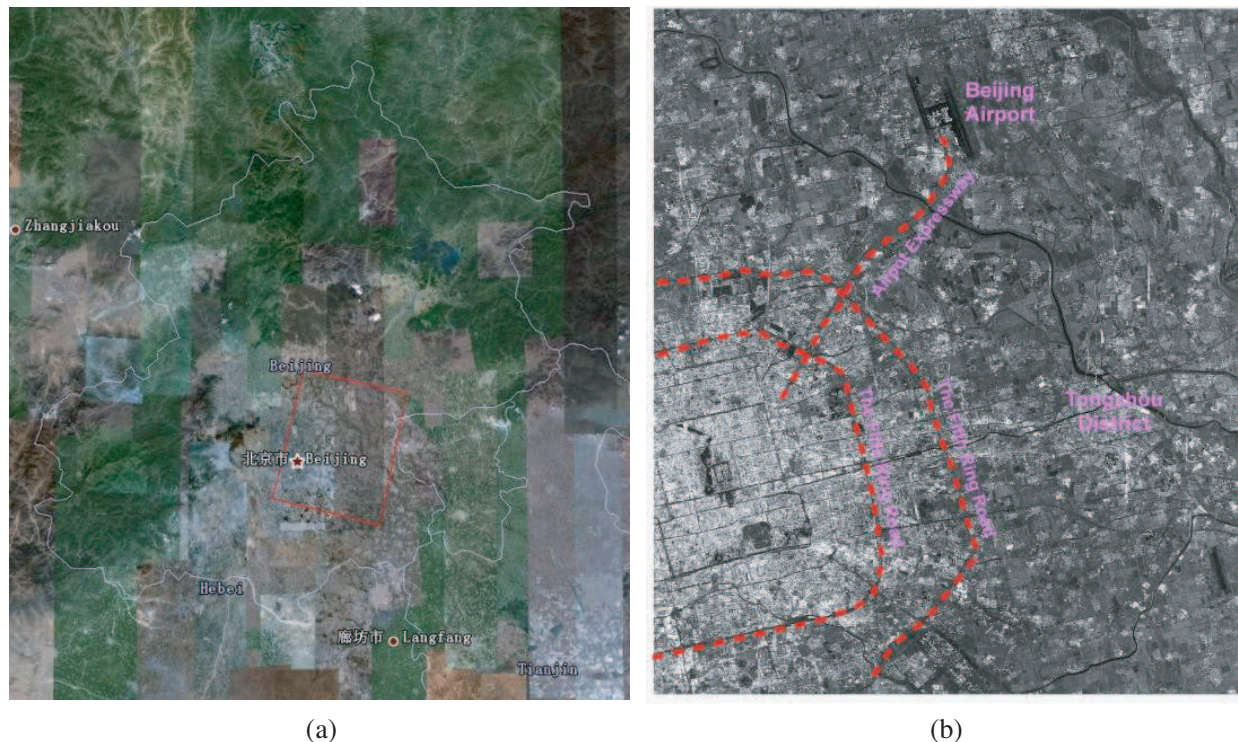


Figure 3: Preliminary position of the study area (a) and some targets on the averaged amplitude image (b) (The underlying in (b) is averaged amplitude image which has been mirrored and multilooked by factor 5 in the azimuth direction).

relatively strong and may contaminate the phase of its surrounding pixels, in a square space whose side length is 600 meters, we further select PSC with lowest amplitude dispersion index in a cluster of pixels and discard other pixels. Then we triangulate the selected 2201 PSC to a grid and the distance of each couple of PSC is less than 1.5 km for retaining the atmosphere correlation. While

the steps (4) to (7) are carried out, the procedure is same to [10] .

4. RESULTS AND ANALYSIS

The results of PSInSAR in the eastern Beijing area are shown in Fig. 4. From this figure, 4 main subsidence cones are revealed, and they can be described as below:

- (1) East Beijing: In the study area, not only the subsidence velocity but also the area of this cone is the largest. include Tongzhou district and the area between Tongzhou and the eastern 5th ring road are the mainly extent of this cone.
- (2) North-east Beijing: The area of this cone is just smaller than East Beijing subsidence cone. The extent of this cone is outside the north-east 5th ring road and along the airport expressway. Actually there are 2 sub-cones respectively at the two sides of the airport expressway and the northern is larger than the eastern one.
- (3) North airport: The cone lies in the north of Beijing airport. Although this subsidence area is not be entirely included in the deformation map, we still can infer from the overall trend that a serious, large subsidence bowl exists.
- (4) South airport: This deformation bowl is in the south of Beijing airport and it has the smallest area and the lowest deformation velocity.

Because the reference point selected for phase unwrapping may be unstable, the deformation value given by this paper should be validated by ground measurements.

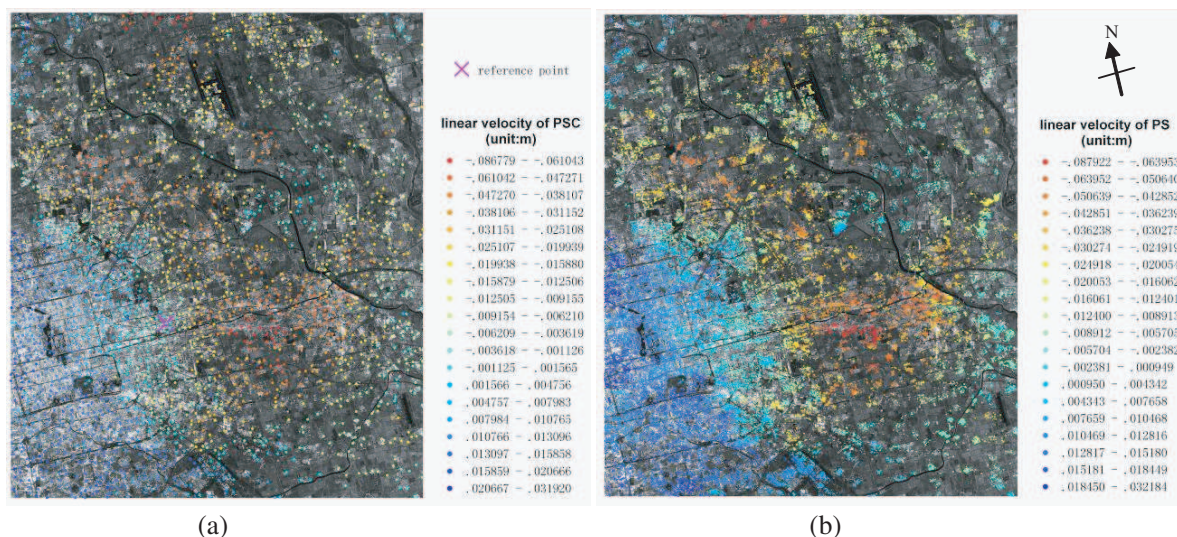


Figure 4: The relative linear LOS deformation velocities of the PSC (a) and the ones of the PS (b).

5. CONCLUSIONS

Using PSInSAR technique and ENVISAT ASAR data, we reveal the linear deformation field of the eastern Beijing area from June 2003 to March 2007. From the result, 4 main subsidence areas are recognized. But the deformation value given by this paper should be validated by ground measurements as the reference point selected for phase unwrapping may be unstable.

ACKNOWLEDGMENT

This work was supported by the Ministry of Land and Resources (Project No.: 200811053). And the authors wish to thank Dr. Liu Guang in CEODE, CAS, China for his kind helps.

REFERENCES

1. Du, T., "General situation of geological disasters in Beijing city," *Beijing Geology*, No. 4, 21–23, 2000 (in Chinese).
2. Jia, S.-M., H.-G. Wang, S.-S. Zhao, and Y. Luo, "A tentative study of the mechanism of land subsidence in Beijing," *City Geology*, Vol. 2, No. 1, 20–26, 2007 (in Chinese).

3. Liu, Y., C. Ye, and S.-M. Jia, "Division of water-bearing zones and compressible layers in Beijing's land subsidence areas," *City Geology*, Vol. 2, No. 1, 10–15, 2007 (in Chinese).
4. Ma, B., "Ground subsidence and water level for prevention of up-floating of Beijing Sha He area," *Geotechnical Engineering Technique*, Vol. 21, No. 4, 202–204, August 2007 (in Chinese).
5. Sun, C.-Z., Y.-A. Gao, X.-T. Hu, G.-Y. Zhang, and J.-K. Zhang, "Analyses of ground setting in the eastern suburbs of Beijing," *Geotechnical Engineering World*, Vol. 5, No. 11, 27–29, 2002 (in Chinese).
6. Li, Z., J. Sun, S. Zhang, S. Wang, and X. Guo, "Distribution characteristics and counter-measures of the environmental geology problems in the Huang-Huai-Hai plain," available in January 2009, http://old.cgs.gov.cn/zt_more/34/zhaiyao/html/04/408.htm.
7. People's Daily, "Beijing launches pre-warning, forecast system for ground subsidence," available in January 2009, http://english.peopledaily.com.cn/200407/23/eng20040723_150623.html.
8. Ferretti, A., C. Prati, and F. Rocca, "Nonlinear subsidence rate estimation using permanent scatterers in differential SAR interferometry," *IEEE Trans. Geosci. Remote Sens.*, Vol. 38, 2202–2212, 2000.
9. Ferretti, A., C. Prati, and F. Rocca, "Permanent scatterers in SAR interferometry," *IEEE Trans. Geosci. Remote Sens.*, Vol. 39, 8–20, 2001.
10. Fan, J., X. Guo, H. Guo, Z. He, D. Ge, and S. Liu, "Mapping subsidence in Tianjin area using ASAR images based on PS technique," *Proceeding of International Geoscience and Remote Sensing Symposium 2007*, CD ROM.
11. Kampes, B., R. Hanssen, and Z. Perski, "Radar interferometry with public domain tools," *Proceedings of FRINGE 2003*, Frascati, Italy, December 1–5, 2003.

Electromagnetic Phenomena in Resistance Spot Welding and Its Effects on Weld Nugget Formation

Yong Bing Li, Zhong Qin Lin, Xin Min Lai, and Guan Long Chen

Shanghai Key Lab of Digital Auto-body Engineering, Shanghai Jiao Tong University
Shanghai 200240, China

Abstract— Resistance Spot Welding is a major sheet-metal joining process in automotive industry. During the RSW, a very large welding current flows through workpieces and induces a very large magnetic field in weld nugget. According to electromagnetics, the current density field and the magnetic field will interact with each other to produce a strong electromagnetic force. Once molten metals appear in the nugget, the force will act on and drive the metals to move. In this research, a multi-physics finite element model, which consists of a two-dimensional electric model, a three-dimensional magnetic model, and a two-dimensional fluid dynamics model, is utilized to investigate the features of electric, magnetic, magnetic force, thermal and flow fields in the weld nugget and their interactions. Research showed that the electromagnetic force in the nugget results in a symmetric flow and substantially changes the heat transfer in the weld nugget.

1. INTRODUCTION

Resistance Spot Welding (RSW) has been known as a process involving electromagnetic, thermal, fluid flow, mechanical and metallurgical variables [1, 2]. During RSW, a large current flows through copper electrodes and workpieces, and induces a large magnetic field in weld nugget. Based on electromagnetic theory, the current and magnetic field interact with each other to produce a huge electromagnetic stirring (EMS) force, which will affect the fluid flow and heat transfer in the nugget. As such, in order to reveal the nugget formation, a model, which comprehensively considers the coupling of electric, magnetic, thermal and flow fields, should be developed. However, because of the complexity of the RSW process, the current published models rarely consider the effect of the induced EMS force. In 1990, Alcini [3] performed experiments to measure the temperature change in the weld nugget. His research showed that strong fluid convection appears in the nugget and the thermal field in the nugget is relatively uniform in the radial and thickness directions, which is obviously different from the large temperature gradient of traditional electric-thermal model [4].

In this research, a magneto-hydro-dynamic (MHD) finite element (FE) model, which couples the electric field, thermal field, flow field, magnetic field, is used to investigate the electromagnetic phenomena in RSW and its effects on the nugget formation.

2. NUMERICAL MODEL

In order to reduce the complexity of the multi-physics process, the molten metal in the nugget is assumed as incompressible, viscous, laminar, and Newtonian fluid [5]. The electromagnetic field is viewed as quasi-stable, in view that working frequency of welding power supply is too low to cause obvious lag between the magnetic field and its source. The metallic fluid in the weld nugget is assumed to keep electric neutrality, in view that the electromagnetic field in the nugget varies slowly with the low frequency current [6]. Based on the above assumptions, MHD equations describing the multi-physics process can be given as follows:

$$\nabla \cdot \vec{V} = 0; \quad (1)$$

$$\rho \left(\frac{\partial V_i}{\partial t} + \vec{V} \cdot \nabla V_i \right) = \left(\vec{J} \times \vec{B} \right)_i + \frac{\partial}{\partial x_j} \left[-\delta_{ij} P + \mu_e \left(\frac{\partial V_i}{\partial x_j} + \frac{\partial V_j}{\partial x_i} \right) \right], \quad (i, j = x, y); \quad (2)$$

$$\rho C_M \left(\frac{\partial T}{\partial t} + \vec{V} \cdot \nabla T \right) = \nabla \cdot (k \nabla T) + S_h; \quad (3)$$

$$\left. \begin{aligned} \nabla \times \vec{E} &= 0 \\ \nabla \times \vec{H} &= \vec{J} \\ \nabla \cdot \vec{B} &= 0 \\ \nabla \cdot \vec{J} &= 0 \\ \vec{J} &= \sigma \vec{E} \\ \vec{B} &= \mu_r \mu_0 \vec{H} \end{aligned} \right\} \quad (4)$$

where, \vec{E} is the electric field intensity, \vec{B} the magnetic flux density, \vec{H} the magnetic field intensity, \vec{J} the current density, \vec{V} the flow velocity, δ_{ij} the Kronecker sign, P the hydrostatic pressure, μ_e the effective viscosity coefficient, and $C_M = C_P - L_h \partial f_s / \partial T$ the modified heat capacity with L_h and f_s being the latent heat and ratio of solid phase, respectively. A linearly varying f_s is used in this research [5]. Source term S_h in Eq. (3) describes the resistance heat generation density in workpieces, electrodes and contact surfaces.

Because of the axisymmetric feature of the fields involved in RSW, a 1/2 axisymmetric model is used to model the electric field and electrical contact behaviors, and a 1/4 axisymmetric model is used to model the fluid dynamics behaviors. For the magnetic analysis, based on right-hand law, the magnetic field induced by the welding current, which flows within the axisymmetric plane, is normal to the axisymmetric plane, thus a 3D wedge-shaped model is used to reduce meshes. Moreover, a layer of infinite elements [7] adjacent to outer surface of finite air layer is created to model the infinite open space. Fig. 1 shows the multi-physics FE meshes of RSW process. Successive element refinements have been conducted to reduce the mesh sensitivity.

For the electric model shown in Fig. 1(a), a uniform welding current and a zero electric potential are applied at the upper and lower ends, respectively. Because an AC welding machine is used in this research, a sinusoidal current input is used to improve the simulation accuracy. Contact pairs [7] are used to model the electric contact along the workpiece/electrode (W/E) and workpiece/workpiece (W/W) interfaces. For the 3D magnetic model in Fig. 1(b), a B-flux normal condition is applied to the symmetrical plane, and B-flux parallel conditions are applied to the cutting planes. For the far field surfaces, the magnetic vector potential in all directions is restrained to zero. For the fluid dynamics model in Fig. 1(c), the electrode is defined as solid region, so the momentum equation is not solved for this region, and the internal wall of the water cooling cavity is restrained to water temperature; the whole workpiece is defined as flow region and the moving solid-liquid interface is handled with imaginary viscosity method, e.g., the unmelted metal is assigned a very high viscosity so that it does not move under the EMS force. Because the molten nugget is always a very small part of the workpiece, the velocity of the outer surfaces of the workpiece is set to 0 m/s.

3. RESULTS AND DISCUSSION

In this research, the materials are 1.5 mm thick mild steel sheet. The welding time and holding time are 20 cycles and 5 cycles, respectively. Working frequency of power current is 60 Hz, and ambient temperature is 21°C. Unless specifically stated, a RMS welding current of $I_w = 8700$ A is used.

A commercial FE code ANSYS/Multiphysics and its parametric design language is used in this work to realize the complicated coupling of the electric, magnetic, thermal and flow fields involved

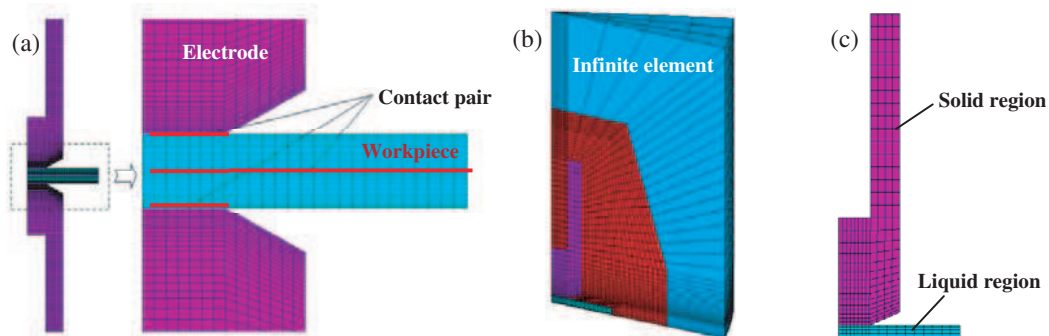


Figure 1: Multiphysics FE model. (a) Electric field sub-model; (b) Magnetic field sub-model; (c) Fluid dynamics sub-model.

in RSW. For each time step, the electric analysis is first performed to output current density and time-integrated joule heat, and then the magnetic analysis is done to get time-averaged magnetic force. Lastly, the fluid dynamics analysis is done with the calculated joule heat and magnetic force field as inputs.

In each time step, temperature-dependent physical properties, such as electric resistivity, thermal conductivity, specific heat and electric contact conductance [8, 9] are updated based on the calculated temperature field. The copper electrode is paramagnetic throughout the RSW process. However, the steel's magnetic permeability is a function of temperature. In this research, the EMS occurs in the molten region, thus, only the computation accuracy of the magnetic field in the molten region is needed to be assured. As shown in Fig. 2, the red molten region is surrounded by the thick yellow unmelted region. Moreover, both the red and yellow regions are beyond the Curie point (about 770°C for steel), and thus physically paramagnetic. Based on Ampere circuital theorem, during RSW process, the magnetic field within the red and yellow regions is not affected by the regions where the temperature field is below Curie point. As a result, during the magnetic field analysis, the whole workpieces are treated as paramagnetic to reduce the material nonlinearity.

It is difficult to measure the flow velocity, magnetic flux density and temperature in a closed nugget with present technological means. In view that the EMS behaviors in the nugget comprehensively affect the nugget formation, therefore, the final nugget's profile is used to validate the proposed multi-physics FE model. As shown in Fig. 3, there is a good agreement in size and shape between the numerical and experimental nuggets.

3.1. Electromagnetic Field in the RSW

Figure 4 shows the current density vector field in the upper workpiece. Obviously, in the middle of the workpiece, the welding current evenly flows through the upper and lower surfaces of the workpiece. However, at the edge, because of the geometry discontinuity of the upper electrode and the upper workpiece, the welding current flows outward and is away from the nugget center. At the faying surface, because the electric contact resistance away from the nugget center is much

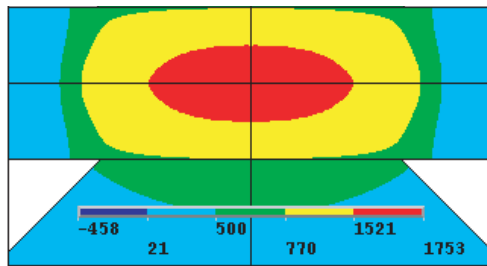


Figure 2: Para- and ferro-magnetic regions in the nugget.

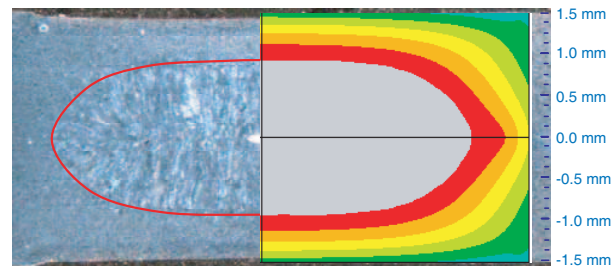


Figure 3: Experimental validation of the multi-physics numerical model.

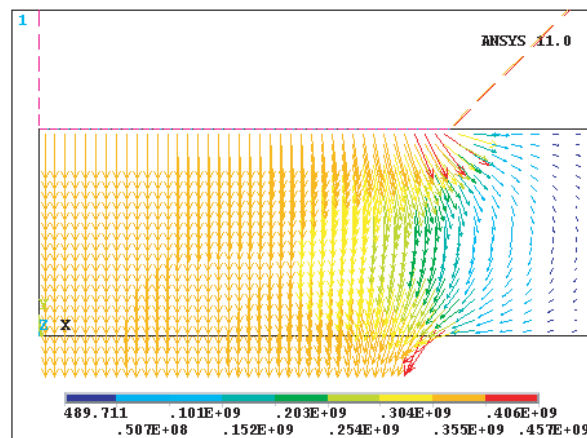


Figure 4: Calculated current density field. The unit is A/m^2 .

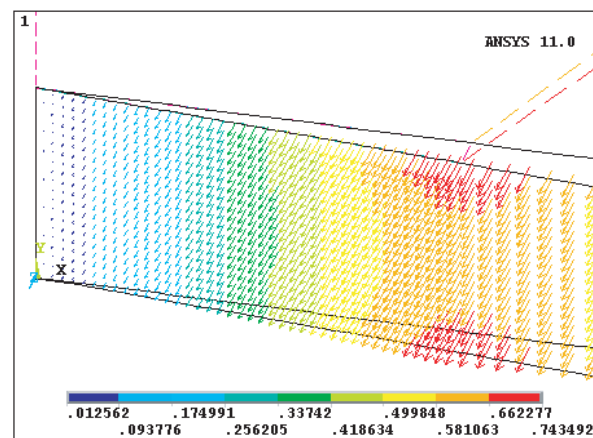


Figure 5: Calculated magnetic flux density distribution. The unit is Tesla.

larger than that in the nugget center, the welding current flows back into the nugget center again. This kind of current flow pattern directly determines the distribution of the induced magnetic flux density. As shown in Fig. 5, the induced magnetic field is normal to the axisymmetric plane, and gradually increases from the center of the nugget to the edge. Moreover, the maximum magnetic flux density appears at the same locations as the current density field does.

3.2. Magnetic Force Field and the Induced Flow Field in the Nugget

According to left-hand law, the magnetic force field, which is the product of the current density vector and magnetic flux density vector, is located in the axisymmetric plane. Fig. 6 shows the calculated magnetic force field in the upper sheet. Obviously, in the middle of the sheet, the magnetic force field is normal to the axisymmetric axis and gradually diminishes from the brim of the nugget to symmetry axis in the width direction, however, in the other region, the magnetic force field deviates toward the thickness direction, and diminishes from the upper and bottom surfaces of the workpiece to the middle. The maximum magnetic force also appears at the same locations as the current density field and magnetic flux density field do. This kind of magnetic force distribution finally determines the flow field in the nugget. As shown in Fig. 7, in each quarter of the nugget, the molten metal flows out of the nugget along the faying surface and flows back into the nugget along the edge of the nugget, which is because the maximum magnetic force around the edge of the nugget pushes the molten metal away from the faying surface and flows into the nugget along the boundary of the nugget.

3.3. Effect of MHD Behaviors on Nugget Formation

The flow of the molten metal will definitely affect the heat transfer behaviors in the nugget. For traditional models, which can not consider the mass transfer in the nugget, the temperature gradient in any direction is large because of the consistent cooling, as shown in Fig. 8. However, for the MHD model, the strong flow substantially disturbs the regular thermal conduction and mixes the hot and cold metal through mechanical stirring, and greatly reduces the temperature gradient in the nugget, as shown in Fig. 9.

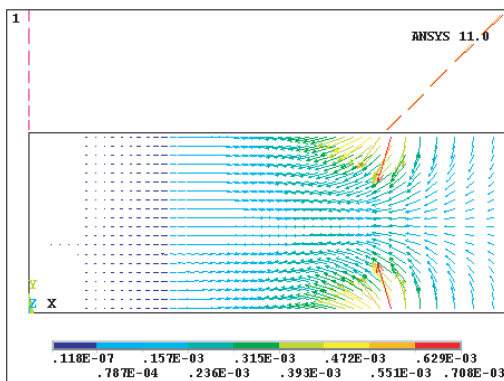


Figure 6: Calculated magnetic force field. The unit is N/mm^3 .

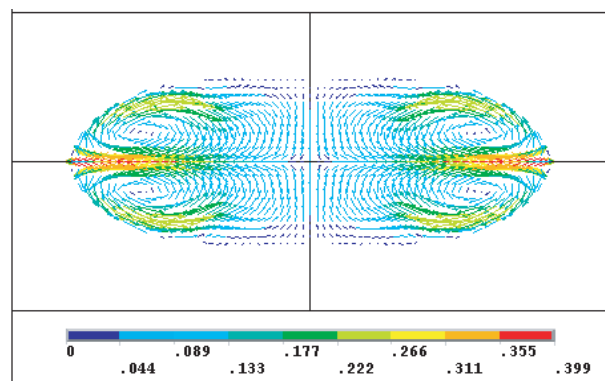


Figure 7: Calculated flow field in the nugget. The unit is m/s .

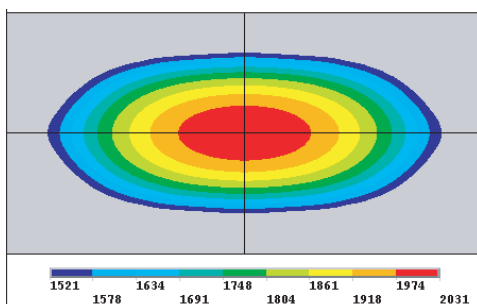


Figure 8: Calculated nugget with traditional electro-thermal model.

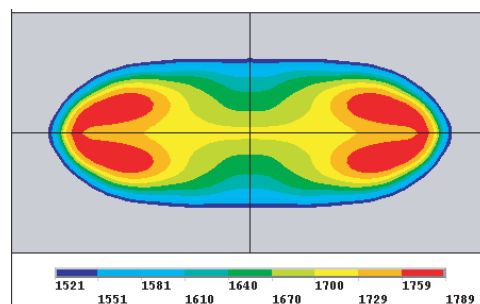


Figure 9: Calculated nugget with the MHD model. The unit is $^{\circ}\text{C}$.

4. CONCLUSION

A multi-physics FE model is used to model the electromagnetic phenomena in RSW. Researches showed that the magnetic force field, which is produced by the welding current and the induced magnetic field, is very regular, and causes the molten metal in the nugget to make regular flow in four cores. The flow dramatically changes the heat transfer in the weld. Different kinds of thermal gradient will results in different crystallization process, therefore, it is very necessary to consider the effect of the electromagnetic phenomena in modelling the RSW process.

ACKNOWLEDGMENT

The authors would like to acknowledge the supports of NSFC (Grant No. 50705059) and National Key Technology R & D Program (Grant No. 2007BAF10B00).

REFERENCES

1. Cunningham, A. and M. L. Begeman, "A fundamental study of project welding using high speed photography computer," *Welding Journal*, Vol. 44, 381s–384s, 1965.
2. Wei, P. S., S. C. Wang, and M. S. Lin, "Transport phenomena during resistance spot welding," *Transactions of the ASME Journal of Heat Transfer*, Vol. 118, No. 3, 762–773, 1996.
3. Alcini, W. V., "Experimental measurement of liquid nugget heat convection in Spot Welding," *Welding Research Supplement*, Vol. 69, No. 4, 177s–180s, 1990.
4. Long, X. and S. K. Khanna, "Numerical simulation of residual stresses in a spot welded joint," *Transactions of the ASME Journal of Engineering Materials and Technology*, Vol. 125, 222–226, 2003.
5. Li, Y. B., Z. Q. Lin, S. J. Hu, and G. L. Chen, "Numerical analysis of magnetic fluid dynamics behaviors during resistance spot welding," *Journal of Applied Physics*, Vol. 101, No. 5, 053506, 2007.
6. Wang, Q. and G. D. Li, *Basic Theory of Electromagnetic*, Science Publishing House, Beijing, 1998.
7. *ANSYS Documentation*, ANSYS, Inc., 2001.
8. Tsai, C. L., W. L. Dai, D. W. Dicknson, and J. C. Papritan, "Analysis and development of a real-time control methodology in resistance spot welding," *Welding Research Supplement*, Vol. 70, No. 12, 339s–351s, 1991.
9. Li, W., C. Daniel, and A. G. Gerald, "A comparative study of single-phase AC and multiphase DC resistance Spot Welding," *Transactions of the ASME Journal of Manufacturing Science and Engineering*, Vol. 127, No. 8, 583–589, 2005.

New Solutions of Nonlinear Force-free Magnetic Field

Xu-Feng Zhang, Jian-Shu Luo, and Ying Li

Science College, National University of Defense Technology, Changsha 410073, China

Abstract— The force-free magnetic field equation looks very simple, but very few solutions have been obtained so far. For a special class of nonlinear force-free magnetic field equation in cylindrical coordinates, we found new analytic solutions. And a general approach to get some new solutions from known ones for this type of field is presented.

1. INTRODUCTION

Force-free magnetic fields are vector fields that the Lorentz force density vanishes. This condition can be written as

$$(\nabla \times \mathbf{H}) \times \mathbf{H} = 0 \quad (1)$$

which implies that

$$\nabla \times \mathbf{H} = \alpha \mathbf{H} \quad (2)$$

where α may be a function of position, called force-free factor. And we can classify the force-free fields as

potential fields	$\alpha = 0$
linear force-free fields	$\alpha = C$
non-linear force-free fields	$\alpha = \alpha(\mathbf{r})$

Taking the rotation of Equation (1), we obtained that $\nabla \alpha \cdot \mathbf{H} = 0$. This means that α must be a constant on any given field line. Force-free magnetic fields play an important role in the fields such as astrophysics and laboratory plasmas. For ideal plasmas in a closed domain, the minimum energy states for a given helicity are linear force-free magnetic fields [1, 2].

2. THE SOLUTIONS OF FORCE-FREE MAGNETIC FIELDS

The force-free magnetic field Equation (2) looks very simple, but very few solutions and properties have been obtained so far.

We consider a special case in cylindrical coordinates, where $\mathbf{H} = (0, H_\theta(r), H_z(r))$. When α is a constant, the result is well known as the Lundquist field $\mathbf{H} = A(0, J_1(\alpha r), J_0(\alpha r))$ [3]. When α is not a constant, we denote $\mathbf{H} = (0, f(r), g(r))$. Then Equation (1) is simplified as

$$f f' + \frac{f^2}{r} = -g g', \quad (3)$$

this is the same as

$$\frac{1}{2} \frac{df^2}{dr} + \frac{f^2}{r} = -\frac{1}{2} \frac{dg^2}{dr} = \varphi(r), \quad (4)$$

where $\varphi(r)$ is an arbitrary function of r . The solution of this equation is [4]

$$\begin{cases} g^2 = -2 \int \varphi(r) dr + C \\ f^2 = A r^{-2} + 2 r^{-2} \int r^2 \varphi(r) dr \end{cases},$$

where A and C are arbitrary constant of integration. Let $s = r^2$, $F = f^2(s)$, $G = g^2(s)$, Then Equation (4) can be rewritten as

$$-\frac{dG}{ds} = \frac{1}{s} \frac{d(sF)}{ds} = \psi(s). \quad (5)$$

where $F(s) > 0$, $G(s) > 0$, and have no singular points, also $F(s)$, $G(s)$ should be convergent to zero as $s \rightarrow \infty$.

The problem of resolving the force-free magnetic field equation has thus been converted into finding the physically reasonable function $\psi(s)$.

3. RESULTS

If we choose $\psi(s)$ as

$$\psi(s) = \frac{\alpha}{\sqrt{s}} J_0(\alpha\sqrt{s}) J_1(\alpha\sqrt{s})$$

or

$$\psi(s) = \frac{2a^2}{(a^2 + s)^3}$$

The solutions

$$\mathbf{H} = A(0, J_1(\alpha r), J_0(\alpha r)),$$

and

$$\mathbf{H} = \left(0, \frac{r}{a^2 + r^2}, \frac{a}{a^2 + r^2} \right),$$

are the constant α solution of Lundquist and Gold-Hoyle solution [5].

If we choose $\psi(s)$ as

$$\psi(s) = \frac{1}{1 + s^2}$$

Then, we obtain the force-free magnetic field

$$\mathbf{H} = \begin{cases} \left(0, \sqrt{\frac{\ln(1 + r^4)}{2r^2}}, \sqrt{\text{arc cot } r^2} \right), & r > 0 \\ \left(0, 0, \sqrt{\pi/2} \right), & r = 0 \end{cases}$$

This field is physically reasonable because it has no singular points, and be convergent to zero even at infinity. For this field, the force-free factor is

$$\alpha(r) = -\frac{\sqrt{2}r^2}{(1 + r^4)\sqrt{\ln(1 + r^4)}\sqrt{\text{arc cot } r^2}}.$$

Figure 1 displays the general behavior of $H_\theta(r)$, $H_z(r)$ and $\alpha(r)$, Fig. 2 displays the angle $\arctan(H_\theta(r)/H_z(r))$ between \mathbf{H} and the z -axis.

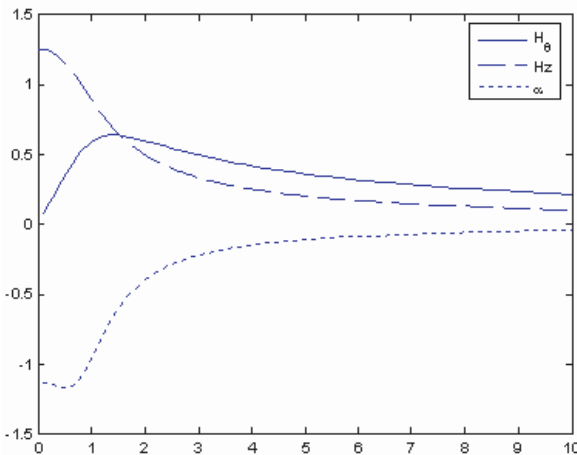


Figure 1: Magnetic field components $H_\theta(r)$, $H_z(r)$ and the force-free factor $\alpha(r)$.

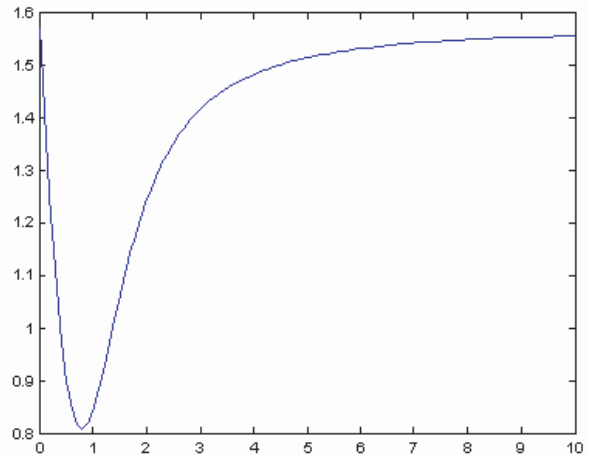


Figure 2: The angle $\arctan(H_\theta(r)/H_z(r))$ between \mathbf{H} and the z -axis.

Noting that the Equation (5) is linear, we can obtain that if \mathbf{H}_1 , \mathbf{H}_2 are force-free magnetic fields as $\mathbf{H} = (0, H_\theta(r), H_z(r))$, then $\mathbf{H}_3 = \sqrt{\mathbf{H}_1^2 + \mathbf{H}_2^2}$ will be a force-free magnetic field. So we can get some new solutions from known ones. Then

$$\mathbf{H} = A \left(0, \sqrt{J_1^2(\alpha_1 r) + J_1^2(\alpha_2 r)}, \sqrt{J_0^2(\alpha_1 r) + J_0^2(\alpha_2 r)} \right)$$

is a force-free field, and

$$\alpha(r) = \frac{\alpha_1 J_0(\alpha_1 r) J_1(\alpha_1 r) + \alpha_2 J_0(\alpha_2 r) J_1(\alpha_2 r)}{\sqrt{J_1^2(\alpha_1 r) + J_1^2(\alpha_2 r)} \sqrt{J_0^2(\alpha_1 r) + J_0^2(\alpha_2 r)}}.$$

4. CONCLUSION

In summary, for a special class of nonlinear force-free magnetic field equation in cylindrical coordinates, a approach to get solution is presented, and a method to get new solutions from known ones for this type of field is obtained.

REFERENCES

1. Taylor, J. B., "Relaxation of toroidal plasma and generation of reverse magnetic fields," *Phys. Rev. Lett.*, Vol. 33, No. 19, 1139–1141, 1974.
2. Taylor, J. B., "Relaxation and magnetic reconnection in plasmas," *Rev. Mod. Phys.*, Vol. 58, No. 3, 741–763, 1986.
3. Lundquist, S., "Magneto-hydrostatic fields," *Ark. Fys.*, Vol. 2, No. 35, 361–365, 1951.
4. Marsh, G. E., *Force-free Magnetic Fields: Solutions, Topology and Applications*, World Scientific, Singapore, 1996.
5. Gold, T. and F. Hoyle, "On the origin of solar flares," *Mon. Not. R. Astro. Soc.*, Vol. 120, No. 2, 89–105, 1960.

Frequency Dependence of Permittivity of Free and Bound Water in Soils for Different Textures

P. P. Bobrov^{1,2}, V. L. Mironov², O. V. Kondratieva¹, and A. V. Repin^{1,2}

¹Omsk State Pedagogical University, Russia

²Kirensky Institute of Physics SB RAS, Krasnoyarsk, Russia

Abstract— In microwave methods of the soil moisture remote sensing it is necessary to have models for determining the complex dielectric permeability (CDP) dependence on moisture, frequency, mineralogy and particle-size distribution. The soil permeability measurement shows that the basic contribution to the CDP is introduced by free and bound water, and permeability of soil water depends on a soil type. To establish the influence of particle-size distribution of soil particles on CDP of the bound and free soil water we carried out the measurements of the frequency and moisture dependencies of refraction index of artificial sandy-clay mixes having different mineral structure and particle-size distribution. The carried out research at the frequencies from 30 MHz up to 4 GHz has shown that the refraction index of free soil water depends on the quartz granules sizes, as well as on the clay fraction relative content. The characteristic feature of the free soil water is the increase of refraction index at frequency reduction. This dependence is the stronger the more clay the sample has. The similar properties are also observed in the bound water.

1. INTRODUCTION

For algorithms creation of data processing of microwave radiometric and radar remote sensing of the Earth surface it is necessary to have the model of the complex dielectric permeability (CDP) of soil which determines the dependence of CDP at a given temperature on moisture, electromagnetic frequency, particle-size distribution and mineral structure of a soil cover. The basic contribution to the soil CDP is introduced by a soil moisture being in free and bound water conditions [1]. The experimental researches have shown, that CDP of various soils depends on particle-size distribution and mineral structure [1–4]. The frequency dependences analysis of moist soils CDP in the frequency range from 1 MHz up to 4 GHz has shown that the increase of real and imaginary parts of CDP occurs at the frequencies below 50 MHz [3, 5] and in some investigations below 500 MHz [6]. This growth is most noticeable for the soils with the large content of clay and organic matter. However, the dielectric characteristics of the bound and free soil water and the influence on these values of particle-size distribution and soil mineral structure at frequencies lower than 500 MHz are investigated insufficiently. In the present work the results of the research of a soil water refraction index in artificial mixes simulating grounds with different particle-size distribution are given.

2. EXPERIMENT DESCRIPTION

According to the refractive model [1] a complex refractive index of soil ($\hat{n} = n + j\kappa = \sqrt{\hat{\epsilon}}$ is the square root of CDP) is found from the formula

$$\hat{n} = n_d + (n_b - 1)W_t + (n_u - 1)(W - W_t) \quad (1)$$

where n_d is a complex refractive index of dry soil, n_b and n_u — complex refractive indices of bound and free water, respectively, W_t is maximum volume fraction of bound water, W is volumetric moisture. The results of experimental studies show that the parameter of the model n_u , fitted for the best correspondence with the experiment, has a value that differs from the refractive index of free water. Therefore, in the future, this component of the mixture we will call free soil water.

Dielectric measurements of artificial mixes were made by using a vector network analyzer, which measures the scattering matrix components at the frequency range from 30 MHz to 4 GHz. To measure CDP at these frequencies the sample under investigation was placed in a segment of coaxial line with the section of 7/3 mm. The bentonite clay (sample No. 13 in Table 1) and three types of quartz particles in the form of nearly spherical granules (samples NoNo 1–3) were used to create mixtures. The mixtures containing quartz granules and bentonite clay in the following proportions by mass: 95 : 5, 70 : 30, 50 : 50 for each type of granules (samples NoNo 4–12) were investigated. As you can see from the data given in Table 1, the clay content increases with increasing the number

of a sample. Samples NoNo 1, 4, 7 and 10 contain the largest quartz granules, and samples NoNo 3, 6, 9, 12 contain the quartz granules of the smallest sizes.

The mineralogical composition of bentonite is 70% of montmorillonite, 15% of quartz, 3–5% of feldspar, 3–5% of calcite + dolomite and the mass share of each of other minerals does not exceed 1%.

The samples were wetted with distilled water, then were kept in hermetically sealed containers at a constant temperature (22–25°C) during the day and night to distribute the moisture in the mixture evenly. The samples with zero moisture were obtained by drying them at a temperature of 105°C for 12 hours. After conducting the dielectric measurements the sample was weighed and dried for several hours, then it was weighed again. According to measured data the moisture and dry bulk density of the sample was calculated.

3. EXPERIMENT RESULTS AND DISCUSSION

In Fig. 1, we show the measured values of the real part of the refractive index depending on the volumetric moisture W of two samples — pure quartz sand grains with the size of 40–70 microns (sample No. 2) and the same sand mixed with bentonite clay in the ratio of 70:30 in weight (sample No. 8). The same piecewise linear dependences as shown in Fig. 1 were observed for all survey results, given this work.

One can see that the regression lines slope angles for the pure sand and sand with bentonite in the values of the free soil water (for the sand it is the entire range of moisture, but for a mixture of

Table 1: The distribution of particles due to their sizes in the studied samples.

No sample	The distribution of particle sizes in mm (in mass fractions)			
	1–0.25 mm	0.25–0.05 mm	0.05–0.01 mm	< 0.01 mm
1	0.133	0.867	0	0
2	0	0.90	0.10	0
3	0	0.042	0.958	0
4	0.128	0.824	0.012	0.036
5	0.002	0.855	0.107	0.036
6	0.002	0.04	0.921	0.037
7	0.105	0.607	0.073	0.215
8	0.012	0.63	0.143	0.215
9	0.012	0.03	0.743	0.216
10	0.086	0.433	0.121	0.359
11	0.02	0.5	0.171	0.359
12	0.02	0.021	0.6	0.359
13	0.04	0	0.242	0.718

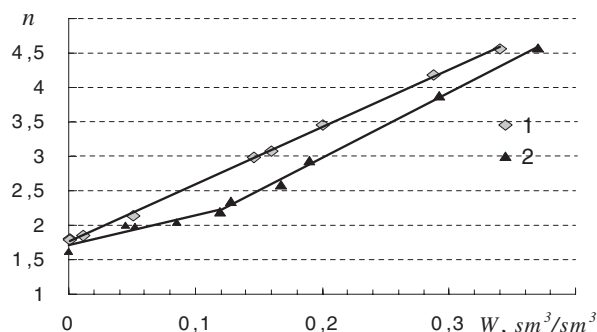


Figure 1: The dependence of the refractive index due to moisture sample No. 2 (1) and sample No. 8 (2) at a frequency of 1 GHz.

sand with bentonite it is the value of moisture in excess of $0.12 \text{ sm}^3/\text{sm}^3$) differ significantly. As it is seen from (1) the tangent of the inclination angle of regression line is $(n_u - 1)$, hence, the refractive index n_u of free soil water in the mixture of sand with bentonite is considerably higher than in pure sand (9.4 and 8.1, respectively). This difference is larger than the error of measurement. A relative root mean square error for determining n_u evaluated by the Monte Carlo method, is equal to 2.3%.

The measurement n_u in different samples in the frequency range 0.1–4 GHz are shown in Fig. 2. You can see that the values of n_u in sand mixtures without clay are highly dependent on the size

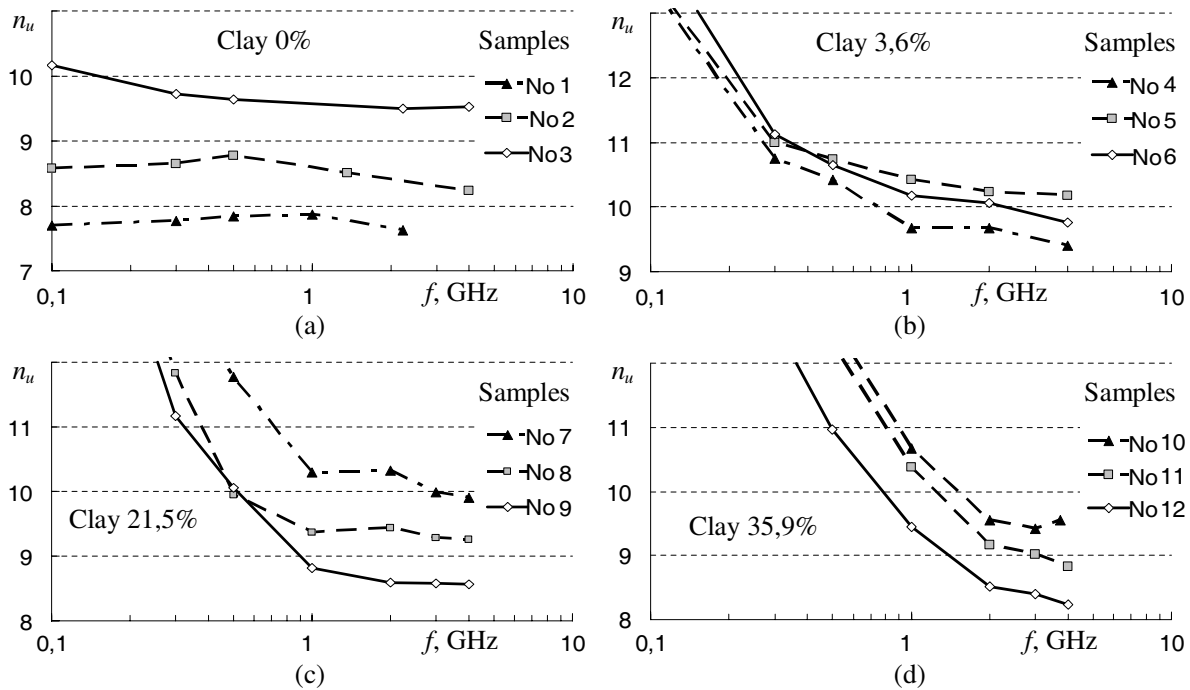


Figure 2: The values of refractive index of free water, due to the content of clay in the mixtures containing a variety of quartz granules.

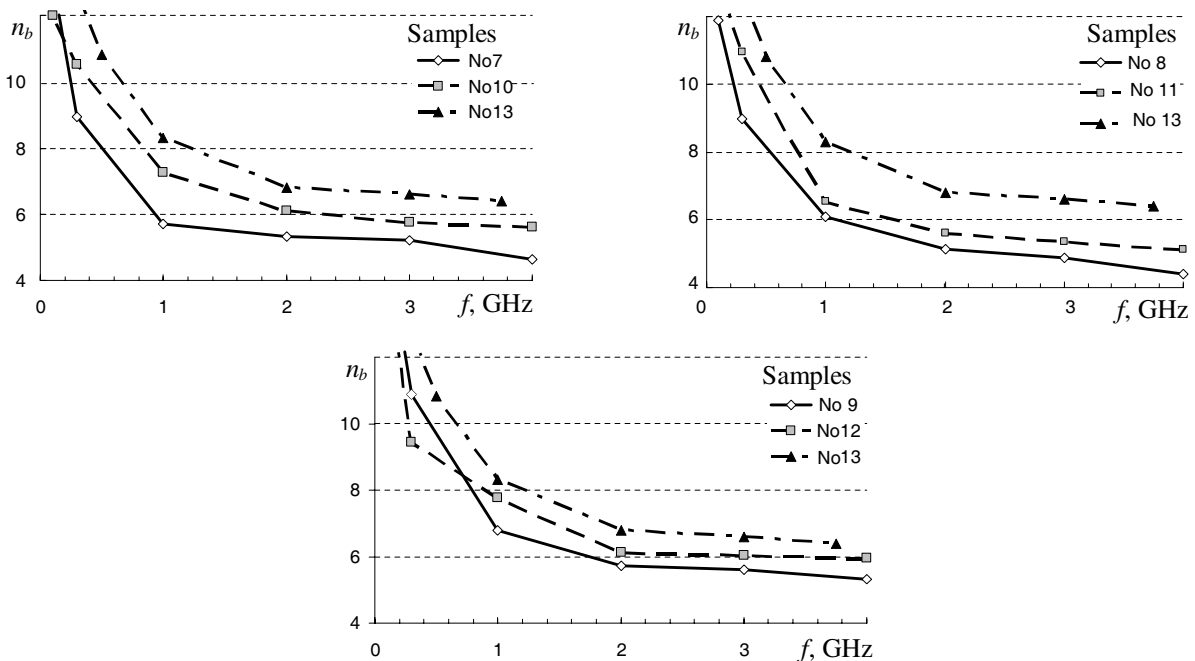


Figure 3: The values of indices of refraction of bound water, depending on the clay content in the mixtures containing a variety of quartz granules.

of quartz particles — they decrease with increasing particle sizes (Fig. 2(a)).

When you add clay (a clay fraction is the fraction consisting of particles smaller than 10 microns) to the samples of quartz sand which differ in size of granules, even in small amounts (3.6% by mass) first we can observe, the reduction of disparities n_u , in mixtures with different sizes of quartz grains, secondly, we can see a considerable increase of the refractive index at the frequencies below 1 GHz for all samples containing clay. The difference in the refractive indexes of free soils water for the samples containing the same amount of clay but having different sizes of quartz granules is comparable to the accuracy of measurements (Fig. 2(b)).

In mixtures containing 21.5% clay, the influence of quartz particles on n_u increases and the differences in n_u exceed the measurement error. The data given in Fig. 2(c) show that in mixtures containing the largest quartz granules, n_u is of the largest value, i.e., the influence of the size of grains mixed with clay is opposite to their influence in the sand samples.

In samples with high clay content (Fig. 2(d)) the influence of the size of quartz grains remains the same. In sample No. 13 has that has the largest clay content the refractive index of free soil water has a value of about 9 at frequencies 2–4 GHz and considerably increases with decreasing frequency (up to 20.8 units at a frequency of 100 MHz). The higher the clay content is in the sample, the larger n_u increases with decreasing frequency (Fig. 2).

Figure 3 shows the frequency dependence of the refractive index of bound n_b water in the samples NoNo 7–13. You can see that the values of n_b increase with increasing clay content at all frequencies. We can also see, an increase in n_b with a decrease of frequency. Sample No. 13 with the largest clay content takes the highest value n_b . Having the same clay content, the values of indices of refraction of bound water weakly depends on the size of quartz grains. There is a decrease n_b in the size of granules, but the differences are comparable to the accuracy of determining the n_b (relatively root mean square error is equal to 7%).

A regression analysis, which shows the dependence of n_u and n_b on proportion of different fractions was made. This dependence is presented by the following equation:

$$n_t = k_1x_1 + k_2x_2 + k_3x_3 + k_4x_4 \quad (2)$$

where x_1 is a fraction part with a particle size of 1–0.25 mm, x_2 is the proportion of fractions with particle sizes of 0.25–0.05 mm, x_3 is share fractions with particle size of 0.05–0.01 mm and x_4 is a share fraction with particle size of less than 0.01 mm, k is coefficients of regression. Similar calculations were used for bound water. Table 2 presents regression coefficients for multiple frequencies.

Table 2: The frequency dependence of the coefficients of the regression equation.

f , GHz	Free soil water					Bound soil water				
	k_1	k_2	k_3	k_4	R^2	k_1	k_2	k_3	k_4	R^2
0.5	24.01	10.01	9.07	13.10	0.69	9.89	5.519	8.08	11.85	0.87
1	16.66	9.60	8.26	10.63	0.8	7.01	4.74	6.47	9.26	0.88
2	17.02	9.72	8.29	8.65	0.94	8.93	4.27	5.32	7.27	0.96
3	15.55	9.54	8.28	8.57	0.95	9.31	3.977	5.32	6.95	0.99
4	16.65	9.30	8.08	8.77	0.89	8.93	3.39	5.07	6.91	0.93

4. CONCLUSION

Dielectric measurements of samples with different structure in the frequency range from 30 MHz to 4 GHz were made. It was found out that the refractive index of free soil water in the sand soil increases with decreasing the size of the mixture. It was found out that with decreasing frequency the increase of the refractive index of free soil water is observed in samples containing clay content. Moreover, the intensity of increasing depends on the amount of clay. This is also particularly true for the bound water. Regressive dependences for finding the refractive mixture indices at different frequencies due to the particle-size distribution mixture were found out.

REFERENCES

1. Mironov, V. L., M. C. Dobson, V. H. Kaupp, S. A. Komarov, and V. N. Kleshchenko, "Generalized refractive mixing dielectric model for moist soils," *IEEE Trans. Geosci. Remote Sensing*, Vol. 42, No. 4, 773–785, 2004.
2. Curtis, J. O., "Moisture effects on the dielectric properties of soils," *IEEE Trans. Geosci. Remote Sensing*, Vol. 39, No. 1, 125–128, January 2001.
3. Campbell, J. E., "Dielectric properties and influence of conductivity in soils at one to fifty megahertz," *Soil Sci. Soc. Am. J.*, Vol. 54, 332–341, 1990.
4. Peplinski, N. R., F. T. Ulaby, and M. C. Dobson, "Dielectric properties of soils in the 0.3–1.3-GHz range," *IEEE Trans. Geosci. Remote Sensing*, Vol. 33, No. 3, 803–807, May 1995.
5. Flaschke, T. and H.-R. Trankler, "Dielectric soil water content measurements independent of soil properties," *Instrumentation and Measurement Technology Conference, 1999, IMTC/99, Proceedings of the 16th IEEE*, Vol. 1, 37–41, 1999.
6. Hipp, J. E., "Soil electromagnetic parameters as function of frequency, soil density, and soil moisture," *Proceedings of the IEEE*, Vol. 62. No. 1. 98–103, January 1974.

Depth Information from Holographic Radar Scans

C. G. Windsor¹, A. Bulletti², L. Capineri², P. Falorni², S. Valenini², M. Inagaki³,
T. Bechtel⁴, E. Bechtel⁴, A. Zhuravlev⁵, and S. Ivashov⁵

¹116, New Road, East Hagbourne, OX11 9LD, UK

²Dipartimento Elettronica e Telecomunicazioni, Università di Firenze, Firenze, Italy

³Walnut Ltd, 4-2-54 Sakaecho Tachikawa 190, Japan

⁴Enviroscan Inc, 1051 Columbia Avenue, Lancaster, PA 17603, USA

⁵Remote Sensing Laboratory, Bauman Moscow State Technical University, Russia

Abstract— Holographic radar has several potentially important advantages over conventional pulsed radar for buried object location and identification. In particular the sensor can be lightweight, of low cost and provide images of the object with good resolution. This work reports that it can give some depth information also. Two simple experiments using the Rascan system operating at 5 discrete frequencies between 1.5 and 2.0 GHz are described. The first “calibration” experiment used an aluminium plate buried in sand and inclined at a known angle to give a range of depths between 0 and 85 ± 5 mm over a length of 300 mm. The sensor was manually moved on a thin plate of glass placed over the sand above the plate. The scan down the plate showed characteristic bands in the background-corrected reflected intensity — the “zebra effect”. The five reflected amplitudes at each frequency are seen to vary differently with depth. These are interpreted qualitatively in terms of the simple theory involving interference between the reflected wave and the incident wave at the sensor position. This theory does demonstrate the zebra effect and suggests that the amplitude variation with frequency is characteristic of the depth. The cyclic nature of the zebra stripes means that the more frequencies available, the better the depth discrimination. Quantitatively the true theory is complex, especially in the presence of the glass. However we suggest that the measurements can at least be used as calibration signals for a metal reflector at a given depth. The second “test” experiment involved nine US pennies buried in sand at known depths between 0 and 56 mm with a lateral separation of about 50 mm. A background-corrected total reflected intensity (the summed modulus of the reflected amplitude over all frequencies) revealed the outline of each penny quite distinctly. For each penny the set of reflected signal amplitudes at each frequency was determined at the position over the penny where the signal was maximized. This “best” response for each penny gave a response over the five frequencies which was distinctive and is indeed characteristic of the depth. A precise simulation theory is not available but the best frequency response of each penny could be compared with the frequency response curves from the aluminium plate as a function of the known depth. A least squares fit was made between the best amplitudes of as a function of frequency for each penny, compared to the amplitude variation of each frequency as a function of known depth in the inclined aluminium plate experiment. With arbitrary amplitude scaling a least squares residual minimum as a function of depth was always obtained for any one penny. There were some problems. The amplitude scaling varied for each penny, presumably as its surface quality and orientation altered the intensity reflected into the sensor. Also the signal quality deteriorated with depth, and the frequency variation became less distinct at depths greater than 4 cm. However for the six pennies covering the depth range up to 3.4 cm the fitted depth agreed with the actual measured depth to within a standard deviation of 3 mm.

1. INTRODUCTION

Ground penetrating radar has many advantages for the detection of buried objects [1]. However the cost of conventional pulsed systems of order \$200,000 has limited its use particularly in the important area of mine detection. The invention of holographic radar [2] offers similar or better performance for around \$5000 [3]. Holographic radar’s simplicity arises from its use of continuous signals at several different frequencies. The signal is extracted through interference between the wave reflected from the object with the emitted wave. The image of the buried object is built up by moving a scanning head and observing both amplitude and phase changes in the signal. In the Rascan system there are five discrete frequencies between 1.5 and 2.0 GHz and both parallel and perpendicular polarisations [4]. The antenna is moved by hand across the surface to be scanned as shown in Figure 1. The small attached wheel measures the distance along the scan and the operator uses a ruler to determine the scan positions in the perpendicular direction.

The working of the holographic radar system can be expressed most simply by assuming a planar antenna and receiver and a planar reflector at a depth d into the ground. The equation for



Figure 1: The Rascan system in use on the sand bed at Enviroscan, USA.

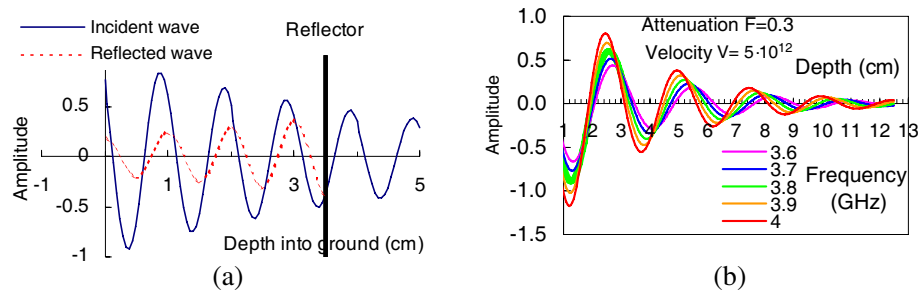


Figure 2: (a) The incident and reflected wave amplitude as a function of depth into the ground with a reflector present at 3.5 cm depth. The phase and amplitude of the two signals are identical at the reflector. (b) The interference signal at the antenna position as a function of the reflector depth as a function of frequency. A velocity of 20 cm, and some frequency dependent exponential attenuation has been assumed.

an incident plane wave travelling along a one-dimensional depth variable x , at time t is $y_{inc}(x) = \cos(2\pi\nu t + 2\pi x/V + \phi_0)$ where ν is the frequency, V is the velocity in the material, and ϕ_0 is a phase factor. The dark continuous line in Figure 2 shows an incident wave of this sort travelling into the ground with some small attenuation factor $\exp(-F(\nu)x)$. The reflected wave from the object at unknown depth d , shown by the dashed line, will travel back in the opposite direction and will have the same phase (or the opposite phase depending on the material) at that spatial position at all times, a different amplitude A , but the same frequency and velocity. Its equation is $y_{ref}(x) = A \cos(2\pi\nu t + 2\pi(d-x)/V + \phi_0)$. When the reflected wave arrives back at the antenna interference holography is performed by effective multiplication of the incident and reflected signals at the position of the antenna. The resulting holographic signal $y_{hol}(0)$ is given by the integration over all phase angles

$$\begin{aligned} y_{hol}(0) &= \int_{0,2\pi} \cos(2\pi\nu t + \phi_0) A \cos(2\pi\nu t + 4\pi d/V + \phi_0) \exp(-F(\nu)2d) d\phi \\ &= 1/2A \cos(4\pi\nu d/V) \exp(-F(\nu)2d) \end{aligned} \quad (1)$$

and so is sinusoidal with a period depending on frequency, depth and velocity, with an amplitude depending on the position of the reflector as shown in Figure 2(b).

The amplitude is immediately seen to be periodic in depth, with a period $2\nu d/V$ dependent on the frequency. This is the origin of the intensity bands or “zebra effect” seen from sloping objects. It is seen that, at any one depth, the order of the signal as a function of frequency, varies and is to some extent characteristic of the depth. This is particularly true at depths within the first oscillation period. At greater depths, the dependences of amplitude on frequency with depth become similar although remain distinct. It is this distinct variation that offers the opportunity to determine an object’s depth from its variation of reflected amplitude with frequency.

However the simple Equation (1) is not valid in practical situations. In fact the incident wave is created by an antenna of finite shape and distinct geometry. The reflecting object is unlikely to be an infinite plane. There are likely to be other reflecting surfaces, particularly the ground reflections, which cannot be neglected. The ground itself, soil or sand, will introduce its own background scattering. All these effects can in principle be included and a mathematical model of the synthesized microwave hologram for point objects has been presented [4]. At present we have

no such comprehensive model. The method of this paper is to use experimental observations as the model for understanding the reflections from unknown objects.

2. THE INCLINED ALUMINIUM PLATE EXPERIMENT — THE CALIBRATION

A simple sheet of aluminium was used in this experiment to calibrate the holographic signals from an extended metallic reflector as a function of depth. The sheet was about 2 mm thick and 350 mm long and was buried in the sand pit so that it had an inclination of 85 ± 5 mm in 300 mm horizontal distance (15.8°). The top edge of the plate just touched the surface as shown in Figure 3. The Rascan head was scanned along the inclined direction at intervals of 10 mm with the scans separated in the direction perpendicular to the inclination of 10 mm. There were 60 measurements along the direction of inclination and 30 measurements in the perpendicular direction. Measurements were taken in both parallel and perpendicular directions but the results were very similar and only the parallel direction is considered here.

The scan is seen to contain a considerable area of “background”, an “edge” area of complex behaviour which we shall neglect, and an area of “uniform” response from which we can extract as essentially one-dimensional response from the extended plate as a function of depth. A background analysis was first made. This is essential if quantitative amplitudes are to be extracted. A histogram of amplitudes was made over 6 of the scans within the background area and the mean taken for each frequency, and subtracted from the raw amplitude data. 4 scans within the uniform area were averaged and a mean amplitude level evaluated for each frequency as a function of the calculated depth.

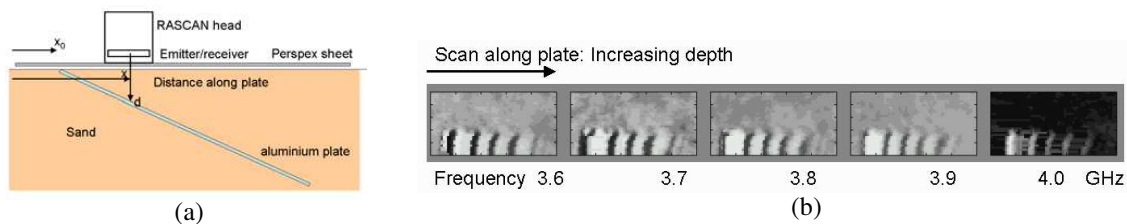


Figure 3: (a) The layout of the inclined aluminium sheet experiment. The Rascan head was manually scanned parallel to the direction of inclination. (b) The grey scale presentation of the holographic data at each frequency presented in the plane of the sheet.

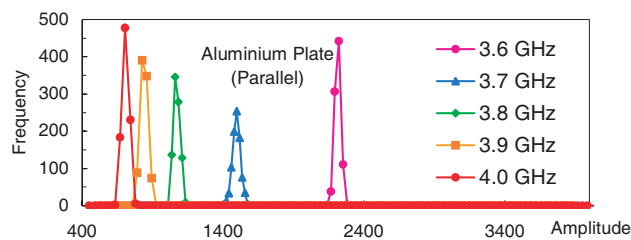


Figure 4: Background determination From six scans in the upper half of the image. The amplitude of each pixel in the image is plotted as a histogram. The centres of the amplitude histogram peak for each frequency is quite distinct.

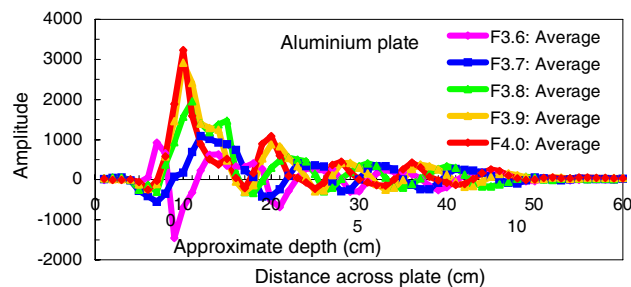


Figure 5: The background-corrected averaged signal from the inclined aluminium plate as a function of distance along the plate for the five distinct frequencies (F) shown.

Having subtracted the mean background level at each frequency, four scans in the lower region of the image showing a strong signal were averaged together for each frequency. The results shown

in Figure 5 show a generally decaying set of amplitudes with the characteristic “zebra” bands of positive and negative amplitude with respect to the background at that frequency. The centres of the bands move characteristically with frequency and this is the key to the depth information.

Figure 5 shows generally a strong similarity to the theoretical description in Figure 2(b). The main difference is around the zero nominal depth position where the experimental curves extend around a centimetre below the nominal zero position. This is not because of the plastic sheet overlaying the sand. In holographic radar the signal from this would be expected to be independent of position and change only the background signal. The most likely causes were mentioned above. The antenna has finite extent and the wavelength of the radar is of order x cm in sand. Both of these cause resolution effects making the measured signal extend beyond the edge of the plate. Of course a similar effect occurs at the deep edge of the plate and the reflected signal is seen to disappear to background levels at around 40 cm lateral displacement.

3. THE BURIED PENNIES EXPERIMENT — THE TEST SITUATION

Nine US pennies were buried in sand at increasing depths from on the surface to 56 mm deep in the same area of sand used in the aluminium plate experiment. Figure 6 shows them as buried, before covering with more sand. The same 60 cm RASCAN was made over the pennies in the direction of increasing depth. Figure 7 shows the resulting images at each frequency.

The scans across the pennies were analysed to find that scan which gave the largest amplitude over each penny. Most of these lay on a single scan, but a few pennies lay off this line and gave a maximum response on other scans. These maximum amplitudes are shown as a function of penny number and frequency in Figure 8. It is a curious graph. The most shallow penny #1 gives only a modest signal with relatively little change of amplitude with frequency. The nominally 10 mm deep penny #2 shows the largest amplitude with a large frequency variation. Pennies #3 to #7 show similar amplitudes but a distinctive frequency variation. Pennies #8 and #9 are distinctly weaker.

These data were analyzed for each penny by least squares fitting the 5 amplitudes from each frequency with the set of amplitudes as a function of depth derived from the aluminium sheet experiment. It was necessary to introduce a arbitrary scaling factor for each penny. Possibly the thickness, reflectivity and specular reflection of the angle of each penny were different leading to a different amplitude factor. However the factor is assumed independent of frequency. Figure 9 shows the actual and fitted amplitudes for the most shallow five pennies. Finally we show in Figure 10 by closed circles the best fitted depths for each penny plotted against the actual measured depths with crosses and error bars. The fit is always within the error bars for the pennies where a good fit was obtained and the standard deviation of the fitted and actual depths is only about 3 mm.

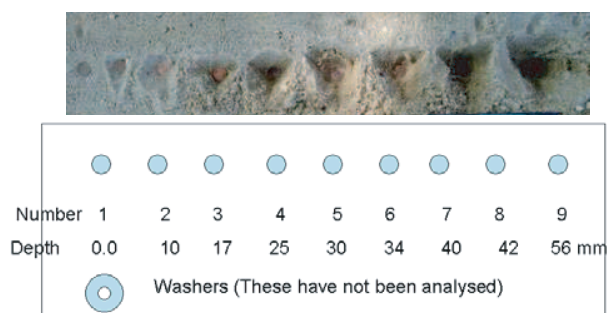


Figure 6: The buried pennies experiment. shows a photograph of the pennies in the sand before being buried. After covering the pennies with more sand their depths were measured by poking with a wooden stick. The radar scans also show a line of metal washers which proved too close together. For accurate analysis, and some foreign Coins of random depths.

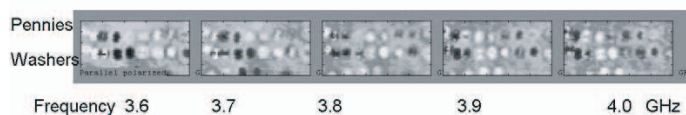


Figure 7: The manual scan of the pennies experiment as a function of increasing penny depth. The variable nature of the phase of the signal is clear. Even the amplitude of the signal appears almost random. While the penny signals appear reasonably separated, this cannot be said of the washers, which have not therefore been analysed.

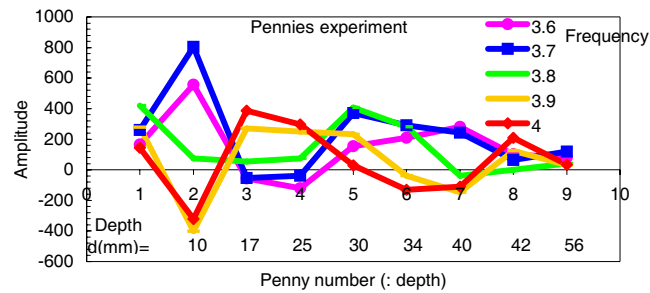


Figure 8: The maximum set of amplitudes seen in any one scan from each penny as a function of frequency.

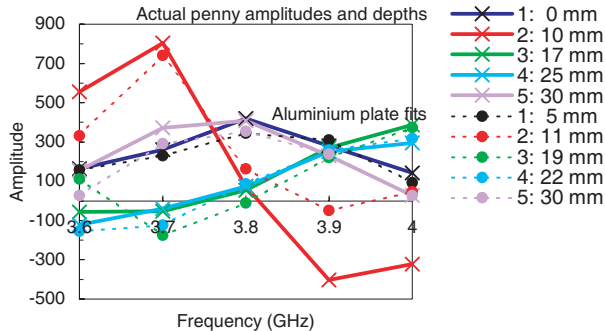


Figure 9: The measured set of amplitudes for each penny (crosses and full lines) fitted to those measured from the aluminium plate experiment as a function of depth (closed circles and dashed lines). The measured depths and the fitted depths are shown. Pennies at greater depths failed to give a good signal.

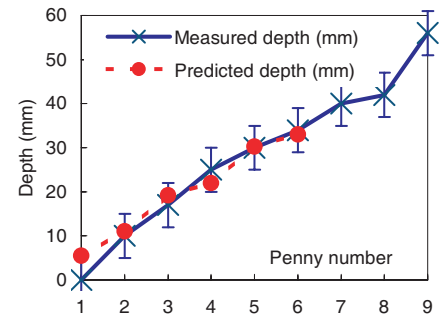


Figure 10: The fitted depths of each penny (closed circles) compared to the a measured depths (crosses with likely errors).

4. CONCLUSIONS

The sloping aluminium plate experiment and the simple theory of beating the incident wave with a reflected wave with phase shift $4\pi\nu/d$ ($d = \text{depth}$) clearly showed the origins and explanation of the stiped “zebra” effect from inclined reflectors.

A good fit to theory is not possible because of the complications of the full probe emitter and object geometry.

The US pennies experiment was analyzed to determine the depths of isolated buried objects. The distinctive frequency response of each penny enabled the depth to be estimated by looking for the same amplitude pattern within the aluminium plate experiment.

The fit to experiment for the first 6 pennies was good to ± 3 mm. More frequencies would lead to a more robust depth algorithm.

REFERENCES

1. GPR Equipment and Service Providers, US Department of Transport pamphlet: <http://www.fhwa.dot.gov/infrastructure/asstmgmt/gprbroc.pdf>.
2. Daniels, D. J., “Surface penetrating radar for industrial and security applications,” *Microwave Journal*, 68–82, December 1994.
3. Chapursky, V. V., S. I. Ivashov, V. V. Razevig, A. P. Sheyko, and I. A. Vasilye, “Microwave hologram reconstruction for the RASCAN type subsurface radar,” *Proceedings of the Ninth International Conference on Ground Penetrating Radar, GPR 2002*, 520–526, Santa Barbara, California, USA, April 29, 2002.
4. Capineri, L., S. Ivashov, T. Bechtel, A. Zhuravlev, P. Falorni, C. Windsor, G. Borgioli, I. Vasiliev, and A. Sheyko, *12th International Conference on Ground Penetrating Radar, GPR 2008*, Birmingham, UK, 2008.
5. Ivashov, S. I., et al., “Holographic subsurface radar technique and it applications,” *12th International Conference on Ground Penetrating Radar, GPR 2008*, Birmingham, UK, 2008.

Noise Performances of Two Recently Reported Electromagnetic Target Classification Techniques in Resonance Region: A Comparative Study for the WD-PCA Based Classifier and the MUSIC Algorithm Based Classifier

E. Ergin^{1,2} and G. Turhan-Sayan¹

¹Department of Electrical and Electronics Engineering
Middle East Technical University (METU), Ankara, Turkey

²STM-Savunma Teknolojileri Muh. A.S., Ankara, Turkey

Abstract— Recognition of targets from their electromagnetic scattered signals is a complicated problem as such data are highly aspect and polarization dependent. Most of the suggested target recognition techniques in resonance region make use of target's system poles either directly or indirectly because the complete set of system poles constitutes an aspect and polarization independent descriptor of a given scattering object. The WD-PCA based classifier and the MUSIC algorithm based classifier are recently suggested electromagnetic target classifiers demonstrated to be very successful in classifying both conducting and dielectric objects of arbitrary shapes using their late-time (natural resonance based) scattered data recorded in resonance region. In this paper, noise performances of these two target classification techniques are investigated in a comparative manner using a set of five perfectly conducting spheres with radii of 8, 9, 10, 11 and 12 cm. This target library is chosen as a worst case testing library under noisy data because the natural resonances of a conducting sphere decay very fast in time, and hence, even a small amount of random noise can badly contaminate its late-time scattered response. It is demonstrated in this work that a slightly noisy set of reference data (instead of noise-free reference data) must be used in the classifier design phase of both techniques to obtain acceptable noise performance in classifying low- Q targets (i.e., targets having natural resonances with low quality factors) such as perfectly conducting spheres.

1. INTRODUCTION

Providing sufficiently high correct classification rates under practically low SNR (signal-to-noise ratio) conditions is the most important performance criterion in electromagnetic target classifier design. Classification accuracy at the ideal noise-free case or at very high SNR values can be maximized by using proper target feature extraction techniques. Unprocessed electromagnetic scattered signals are highly sensitive to aspect angle and polarization conditions. Therefore, decision comparisons based on such data can not lead to acceptable accuracy rates. Instead, such raw data should be processed by sophisticated signal processing techniques to extract aspect and polarization invariant descriptors of candidate targets, which are called target features. Target features utilized in resonance region electromagnetic classification techniques are almost always related to the natural resonance mechanism which was described by the SEM (Singularity Expansion Method) formalism [1]. The complete set of CNR (complex natural resonance) frequencies, i.e., the set of target's system poles, is determined uniquely by the size, shape and material properties of a given object and these pole values are totally independent of aspect angle and polarization conditions. In other words, target poles are perfect target features; however, their extraction from measured scattered data is highly susceptible to noise. Therefore, extraction of target features describing the variation of natural response over a properly chosen late-time interval (to avoid the highly aspect/polarization variant early time scattered signal components) turns out to be a more feasible approach in classifier design. The Wigner Distribution/Principal Component Analysis (WD-PCA) based classifier design technique [2–4] and the Multiple Signal Classification (MUSIC) algorithm based classifier design technique [5, 6] are recently proposed resonance region techniques using this latter target feature extraction approach. They were both demonstrated to be successful in classifying both conducting and dielectric objects of arbitrary shapes under noise-free design/test conditions. Furthermore, noise performances provided by both classifier design techniques were found satisfactory when tested against targets whose scattered natural response waveforms decay slowly in time. In such cases, the effective SNR values over the chosen optimal late-time design/testing intervals becomes sufficiently high. Some targets such as perfectly conducting spheres, on the other hand,

have quickly decaying natural resonances leading to extremely low signal levels over the late-time interval to be chosen for target classifier design and testing. This situation may seriously reduce the accuracy rate of a classifier when tested against noisy signals. In fact, a very poor noise performance was reported in [4] in classifying conducting spheres where a WD-PCA based classifier was designed by using noise-free scattered signals at several reference aspects. In this paper, motivated by the need for a more effective technique to classify such “low quality factor” targets, we designed four different WD-PCA based and MUSIC algorithm based classifiers for a set of five conducting spheres with similar sizes by using both noise-free and slightly noisy (with 20 dB SNR) reference data, and compared their noise performances.

2. THEORY

Basic theory and fundamental design steps of the WD-PCA based and the MUSIC algorithm based classification techniques are briefly described below:

- (a) In the WD-PCA Based Classification Technique, the design database contains a total of $K \times M$ different time-domain scattered signals (measured or numerically computed over the same frequency band in resonance region) at M reference combinations of aspect angle/polarization for each of K library targets. Next, the Wigner-Ville distribution (WD) is computed for each design signal $x(t)$ using

$$W_x(t, f) = \int_{-\infty}^{\infty} e^{-j2\pi f\tau} x(t + \tau/2)x^*(t - \tau/2)d\tau \quad (1)$$

where the output represents an energy density function over the joint time-frequency plane, in the approximate sense. To characterize the natural response behavior of the target, it is enough to partition the total time span T_0 of the signals into Q equally-wide intervals and use the WD output over a selected late time interval [3] to construct a late-time feature vector (LTFV) defined as $\bar{e} = [\bar{E}_{q^*} \ \bar{E}_{q^*+1}]$ where \bar{E}_q is the q th partition vector of length $(N/2)$ defined on the q th time interval with its entries computed as

$$E_q(f_m) = \int_{(q-1)\frac{T_0}{Q}}^{q\frac{T_0}{Q}} W_x(t, f_m)dt \text{ for } q = 1, 2, \dots, Q, \ m = 1, 2, \dots, \frac{N}{2} \text{ and } f_m = (m-1)\frac{1}{T_0} \quad (2)$$

where N is the number of samples of the discrete time domain scattered signal. The methods for choosing parameters Q and q^* are given in [3]. Then, the well known PCA technique is used to reduce the aspect dependency of the extracted features. In fact, the PCA technique is used to extract main patterns common to M different aspect/polarization dependent LTFV features of a given library target. The result is a fused feature vector (FFV) which characterizes that target all by itself. The same procedure is repeated for each library target to completely design the classifier’s feature database. Then, during the real-time classification phase, the LTFV of the measured test signal is computed as described above and its correlation coefficient with respect to each FFV in the classifier library is computed to determine the library target with the highest matching score.

- (b) The MUSIC algorithm based classification technique uses the same type of design database as described above ($K \times M$ time-domain reference scattered signals for K targets at M aspect/polarization combinations) where the natural response component of each noisy signal over a properly chosen late-time interval is modeled as

$$y(n) = x(n) + w(n) = \sum_{i=1}^L d_i e^{s_i n} + w(n), \quad n = 1, 2, \dots, N, \quad i = 1, 2, \dots, L \quad (3)$$

where $s_i = \alpha_i + j\omega_i$ is the i th target pole, L is the total number of poles over the measurement bandwidth and $w(n)$ is the Gaussian noise signal. As the first step of the classifier design, the sampled correlation matrix

$$IR = \frac{1}{N} \sum_{n=m}^N \overline{y(n)} \overline{y(n)}^H \quad (4)$$

is computed for a given noisy scattered signal. Then, by using the singular value decomposition (SVD) method, the \mathbf{G} matrix is constructed as $\mathbf{G} = [e_{L+1} \dots e_m]$ in terms of a subset of eigenvectors e_i of the correlation matrix for $i = L + 1, \dots, m$ for which the corresponding eigenvalues are found to be $\lambda_i = \sigma^2$ with σ^2 being the variance of Gaussian noise. Then, the MUSIC Spectrum Matrix (MSM) is computed in the complex frequency domain as the discrete form of the function $P(s)$ which is given as

$$P(s) = \frac{1}{a^H(s)GG^H a(s)} \quad \text{where } a(s) = [1 \quad e^{-s} \quad \dots \quad e^{-s(m-1)}]^T \quad \text{and } s = \alpha + j\omega \quad (5)$$

Details of the theory behind the MUSIC algorithm, the method for choosing a proper late-time interval and the criteria for choosing proper values for the parameters L and m (such that $L < m < N$) for a given frequency bandwidth can be found in [5, 6]. Finally, the normalized MSM features obtained for a given library target at M different aspect/polarization combinations are all added to get the Fused Music Spectrum Matrix (FMSM) as the main feature of that target. This procedure is repeated for each library target to form the classifier's feature database to be compared to the test signal's MSM feature during the real-time classification phase. The highest correlation coefficient computed between the test target's MSM and the FMSMs of the classifier determines the identity of the test target.

3. APPLICATIONS AND RESULTS

In these applications, the classifier library contains $K = 5$ perfectly conducting spheres S_1, S_2, S_3, S_4 and S_s of similar sizes with radii of 8, 9, 10, 11 and 12 cm, respectively. A conducting sphere is known to be one of the few canonical targets for which analytical field solutions are available. Accordingly, far field scattered responses of our library targets were computed in frequency domain (in response to an x -polarized uniform plane wave that propagates in $+z$ -direction) using the Mie series over the frequency range from zero to 19.1 GHz at 90 degrees azimuth angle and for bistatic aspect angles (θ_b) of 1, 15, 30, 45, 60, 75, 90, 105, 120, 135, 150, 165 and 175 degrees. Out of these 13 bistatic aspects, $M = 5$ reference aspects are chosen to be used in classifier designs which are $\theta_b = 1^\circ, 45^\circ, 90^\circ, 135^\circ$ and 175° . Then, a total of $K \times M = 25$ scattered time-domain signals are obtained by using IFFT to be used in the classifier design database. The rest of the data are used only for performance testing. Also, noisy signal databases were prepared by Gaussian noise with imposed standard deviations to produce scattered signals with SNR = 40, 30, 20, 15, 10 and 5 dB levels at all 13 aspects for noise performance testing.

First, the WD-PCA based classifier is designed using noise-free reference signals for conducting spheres with $N = 1024$, $T_0 = 26.81$ ns, $Q = 32$ and $q^* = 9$ leading to an optimal late-time design interval [6.70 ns–8.38 ns]. The fused feature vectors (FFVs) of each sphere was computed on this interval and stored to be used for testing.

Next, the MUSIC algorithm based classifier was designed using exactly the same noise-free scattered signal database. With design parameters $N = 128$, $L = 32$, $m = 64$, the optimal

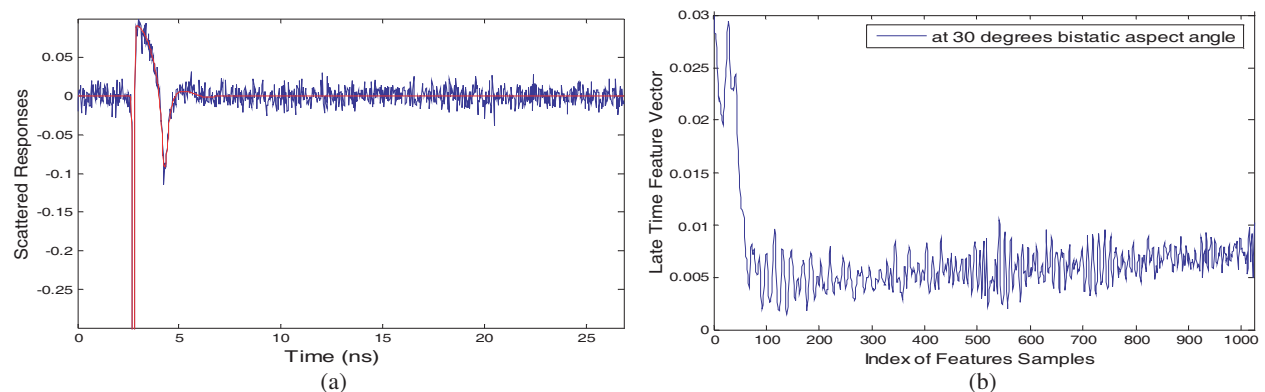


Figure 1: (a) Scattered response of the target S_2 at 30 degrees bistatic aspect angle at SNR = 10 dB (Blue line) and at noise free (Red line) case. (b) The Late-Time Feature Vector (LTFV) of the noisy signal shown in part (a).

late-time design interval was estimated to be [5.5 ns–8.8 ns]. The fused MUSIC spectrum matrix (FMSM) of each target was computed over this design interval and stored to be used later for testing.

After the WD-PCA and MUSIC based classifiers were designed at noise-free conditions, they were tested by both noise-free and noisy scattered data at the SNR levels stated earlier. As an example, the noisy scattered response of the target S_2 (the sphere with 9 cm radius) at 30 degrees bistatic aspect angle with SNR = 10 dB is plotted in Figure 1(a) while the associated late-time feature vector (LTFV) is shown in Figure 1(b). The contour plot of the MUSIC Spectrum Matrix (MSM) computed for this test signal is also given in Figure 2. Both classifiers provided about 100 percent accuracy at noise-free tests but their correct classification rates dropped catastrophically below 50 percent even at 40 dB SNR level as shown in Figure 3. Then, classifier designs based on both techniques were repeated using a set of slightly noisy reference data with 20 dB SNR. This time, the WD-PCA based classifier designed over [4.2 ns–5.9 ns] and the MUSIC based classifier designed over [3.0 ns–6.3 ns] intervals produced much better overall noise performances as shown in Figure 3.

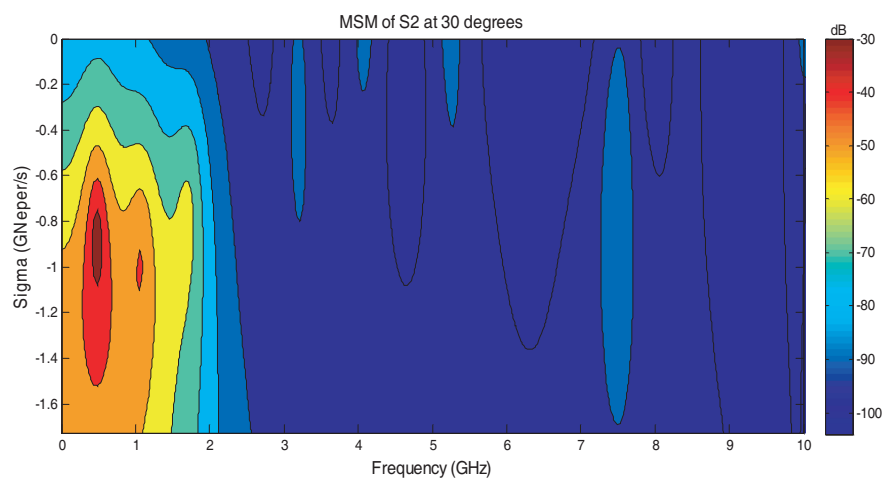


Figure 2: The MUSIC Spectrum Matrix (MSM) of S_2 at 30 degrees bistatic aspect angle with SNR = 10 dB.

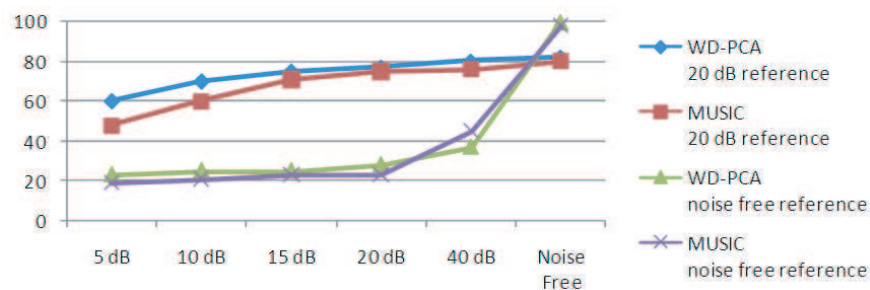


Figure 3: Correct Decision Rates versus SNR Levels for both classifiers.

4. CONCLUSION

In this paper, noise performances of two recently proposed resonance region target classification techniques (the WD-PCA based and MUSIC algorithm based techniques) were compared when they were applied to classify five perfectly conducting spheres of similar sizes. In classifying such low- Q targets with very small late-time signal energy, both techniques produced very poor results when the classifiers were designed by noise-free reference signals. However, substantial improvement was demonstrated in the noise performance of the classifiers when they were designed by a slightly noisy set of reference data. The WD-PCA based classifier designed at 20 dB SNR level displayed slightly better accuracy (up to 10 percent) especially at lower SNR levels as compared to the MUSIC based classifier which is also designed at 20 dB SNR level.

REFERENCES

1. Baum, C. E., E. J. Rothwell, K. M. Chen, et al., “The singularity expansion method and its application to target identification,” *Proc. IEEE*, Vol. 79, No. 10, 1481–1492, Sep. 1991.
2. Turhan-Sayan, G., “Natural resonance-based feature extraction with reduced aspect sensitivity for electromagnetic target classification,” *Pattern Recognition*, Vol. 36, No. 7, 1449–1466, Jul. 2003.
3. Turhan-Sayan, G., “Real time electromagnetic target classification using a novel feature extraction technique with PCA-based fusion,” *IEEE Transactions on Antennas and Propagation*, Vol. 53, No. 2, Feb. 2005.
4. Ayar, M., *Design of an Electromagnetic Classifier for Spherical Targets*, M.S. Thesis, METU, Ankara, Turkey, Apr. 2005.
5. Secmen, M., *A Novel Music Algorithm Based Electromagnetic Target Recognition Method in Resonance Region for the Classification of Single And Multiple Targets*, Ph.D. Dissertation, METU, Ankara, Turkey, Feb. 2008.
6. Secmen, M. and G. Turhan-Sayan, “A radar target classification method with reduced aspect dependency and improved noise performance using music algorithm,” *IET Radar, Sonar & Navigation*.

Eddy-current NDE Using an AMR Magnetometer

D. F. He

Superconducting Materials Center, National Institute for Materials Science
1-2-1 Sengen Tsukuba, Ibaraki 305-0047, Japan

Abstract— Using a commercially available AMR (anisotropic magneto-resistance) sensor of HMC1001 as the magnetic field sensor, an eddy-current nondestructive evaluation (NDE) system was developed. A 50 turn 2 cm double-D coil wound by 0.1 mm copper wire was used to produce the excitation field. Instead of moving the sample, we fixed the AMR sensor with an X-Y stage and moved the sensor with the X-Y stage for the 2D scanning. The artificial hole defects under 6 mm aluminum plate could be successfully detected. The experiments were done in unshielded environment.

1. INTRODUCTION

Due to their low price, high sensitivity and easy operation, AMR (anisotropic magneto-resistance) sensors or GMR (giant magneto-resistance) sensors have been used as the magnetic field sensors in the eddy-current NDE equipments [1, 2]. Compared with GMR sensor, AMR sensor has lower noise at low frequency (below 1 kHz) [3], therefore, AMR sensor has advantage for deep defect detection, where low excitation frequency is necessary.

Using a commercially available AMR sensor of HMC1001, we developed a high sensitive AMR magnetometer [4]. By increasing the bias voltage and using low noise preamplifier, the magnetic field resolutions of the AMR magnetometer are improved to about $12 \text{ pT}/\sqrt{\text{Hz}}$ at 1 kHz and about $20 \text{ pT}/\sqrt{\text{Hz}}$ at 100 Hz. The readout circuit of the AMR sensor can operate in feedback mode or amplifier mode. The linearity can be improved when it operates in feedback mode, and the AMR magnetometer is suitable for the applications in unshielded environment. In this paper, we will report our NDE experiments in unshielded environment using the AMR magnetometer developed by us

2. SETUP OF THE EDDY-CURRENT NDE SYSTEM

Figure 1 shows the setup of the eddy-current NDE system using the AMR magnetometer. In this system, the AMR sensor was fixed with an X-Y stage to do the 2D scanning instead of moving the specimen. The movement resolution of the X-Y stage was about $50 \mu\text{m}$, but the step of our measurement was set to 1 mm. The movement of the X-Y stage could be controlled by a computer. The moving speed of the X-Y stage was about 1 cm/s. Fig. 2 shows the scanning method of the X-Y stage.

A 50 turn 2 cm double-D coil wound by 0.1 mm copper wire was attached to the bottom of the AMR sensor to produce the excitation field. It was used to cancel the influence of the excitation field. The position of the coil was adjusted to make sure that the AMR sensor had smallest response to the excitation field.

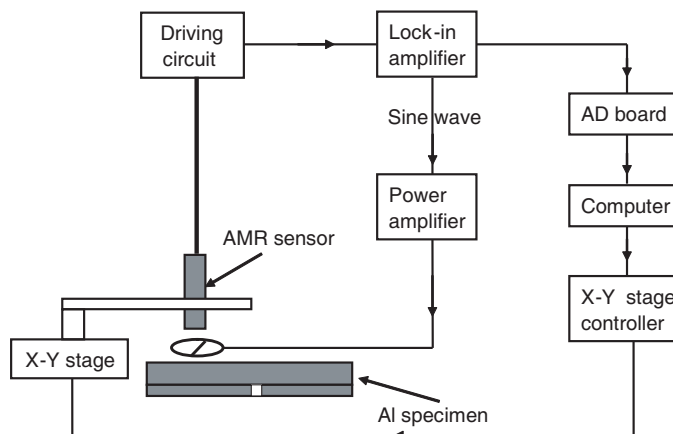


Figure 1: The setup of eddy-current NDE system using AMR sensor.

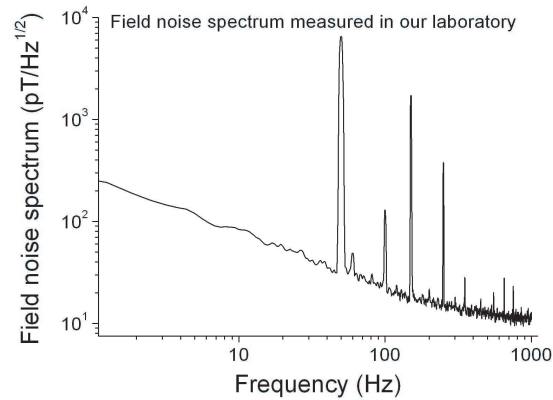


Figure 2: The magnetic field noise spectrum measured in our laboratory.

To detect deep defect, a lower excitation frequency of 175 Hz was used. The corresponding penetration depth in Aluminum was about 6.4 mm. A lock-in amplifier was used to get the amplitude signal and the phase signal. The sine wave was also produced by the lock-in amplifier and was sent to a power amplifier, then sent to the excitation coil. The current flow in the excitation coil was about 100 mA. A USB controlled AD board was used to the data acquisition.

3. EXPERIMENTS AND RESULTS

We used aluminum plates as the specimen. A 3 mm hole was made in a 2 mm thick aluminum plate, and it was covered by another 6 mm thick aluminum plate. The lift off distance between the AMR sensor and the surface of the specimen was about 1 mm.

The AMR magnetometer operated in feedback mode. A compensating current was feedback to the offset strip of the AMR sensor to compensate the applied field, thus the working point of the AMR sensor was fixed and the linearity of the AMR magnetometer could be improved.

Our experiments were done in unshielded environment. Fig. 2 shows the magnetic field noise spectrum measured in our laboratory. The peaks in the spectrum were the 50 Hz line interference and its harmonics. We should choose the excitation frequency to be not at the peaks to reduce the influence of environmental noises. In our experiments, the excitation frequency of 175 Hz was used.

The experiment result was shown in Fig. 3. Fig. 3(a) shows the one scanning signal produced by the hole defect. Due to double-D excitation coil was used, there were 2 peaks (one is positive and another is negative) for one hole defect. Fig. 3(b) shows the 2D contour map of the defect.

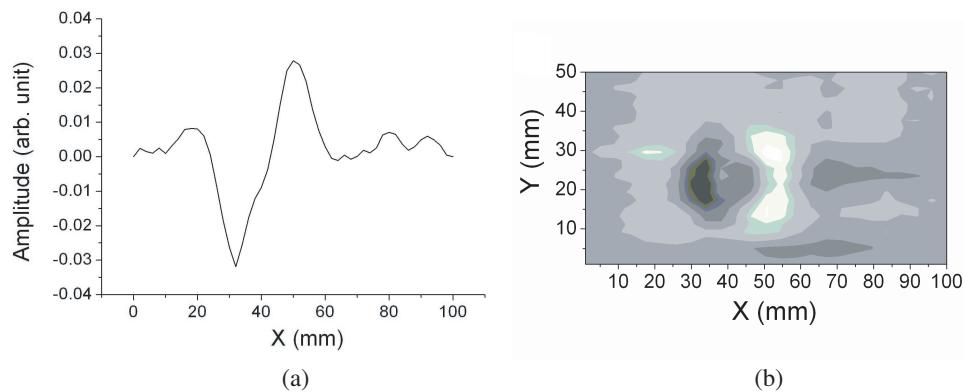


Figure 3: (a) The one scan signal of hole defect, (b) the 2D contour map of the hole defect.

4. CONCLUSION

An eddy-current NDE system using AMR magnetometer was developed, and 3 mm hole defect under 6 mm aluminum plate could be successfully detected in unshielded environment.

ACKNOWLEDGMENT

We give our thanks to Prof. H. Itozaki, Dr. M. Tachiki, and Mr. K. Komori for their helpful discussion.

REFERENCES

1. Allweins, K., M. Von Kreutzbruck, and G. Gierelt, "Defect detection in aluminum laser welds using an anisotropic magnetoresistive sensor array," *J. Appl. Phys.*, Vol. 97, No. 10, 10Q102, 2005.
2. Vacher, F., F. Alves, and C. Gilles-Pascaud, "Eddy current nondestructive testing with giant magneto-impedance sensor," *NDT & E International*, Vol. 40, No. 6, 439–442, 2007.
3. Stutke, N. A., S. E. Russek, D. P. Pappas, and M. Tondra, "Low-frequency noise measurements on commercial magnetoresistive magnetic field sensors," *J. Appl. Phys.*, Vol. 97, No. 10, 10Q107, 2005.
4. He, D. F., M. Tachiki, and H. Itozaki, "Highly sensitive anisotropic magnetoresistance magnetometer for eddy-current nondestructive evaluation," *Rev. Sci. Instrum.*, Vol. 80, 036102, 2009.

Equations for Electromagnetic Radiation Transfer in Dielectric Random Media with Effects of Near Fields and Opposite Wave Streams' Interference

Yu. N. Barabanenkov¹ and M. Yu. Barabanenkov²

¹Institute of Radioengineering and Electronics, Russian Academy of Sciences
Mohovaya 11, 103907 Moscow, GSPC3, Russia

²Institute of Microelectronics Technology and High Purity Materials, Russian Academy of Sciences
142432 Chernogolovka, Moscow Region, Russia

Abstract— A radiative transfer theory for electromagnetic wave multiple scattering in dielectric random media with effects of near fields is presented. The theory is based on Sommerfeld-Weyl angular spectrum decomposition of wave amplitudes and technique of Dyson and Bethe-Salpeter equations for the ensemble averaged angular spectrum amplitudes and the coherence matrix of angular spectrum amplitudes, respectively. We derive the four integral equations' system, for two autocorrelations of waves propagating forward and backward with respect to embedding parameter into the medium slab and two cross-coherences of evanescent waves decaying in opposite directions. In so doing the equations for autocorrelations describe basically the usual radiative transfer with wave intensity multiple scattering by random inhomogeneities (scatterers) and free path between them. In the contrary the equations for cross-coherences demonstrate a new effect of elementary evanescent waves' virtually exciting inside an inhomogeneity in pairs of opposite decaying directions and contribution of these evanescent pairs to wave energy flux.

1. INTRODUCTION

Propagation of waves through disordered systems is one of the most challenging topics in theoretical physics. A traditional approach does use the phenomenological radiative transfer theory [1]. But this phenomenological approach is derived from the theory of wave multiple scattering in random media at neglecting the repeated scattering of a monochromatic wave by just the same random inhomogeneity (scatterer) — so-called single-group approximation, together with the far-field approximation for fields scattered by inhomogeneities [2] when the effects of near fields are neglected. During the last several years a substantial progress has been reached in theoretical study the near field effects in electromagnetic wave multiple scattering by inhomogeneous dielectric media. This progress was based on Sommerfeld-Weyl angular spectrum decomposition of wave amplitudes and included in itself the effect of energy emission from evanescent wave at scattering by a dielectric structure, with proving the extended unitarity for 2×2 block S -scattering matrix [3] and interpreting the above energy emission as consequence of interference between two opposite decaying evanescent waves [4]. To study the near field effects in the case of random dielectric media, the Dyson equation in the Bourret approach for the ensemble averaged angular spectrum amplitudes and the Bethe-Salpeter equation in the ladder approximation for the coherence matrix of angular spectrum amplitudes can be applied (see, for example [5]).

In this paper, we split the matrix Bethe-Salpeter equation into system of four equations, two of which are written for autocorrelations of waves propagating forward and backward with respect to embedding parameter and close in form and physical sense to phenomenological radiative transfer, corrected on near field effects at multiple scattering by random inhomogeneities. A subject of principal interest are two another equations for cross-coherences of evanescent waves decaying in opposite directions. These two complex conjugate equations reveal a new mechanism of radiative transfer named as tunneling one, with exciting inside of a random inhomogeneity a pair of elementary opposite decaying evanescent waves and contributing of them because interference into the energy flux.

2. LINEAR SYSTEM FOR ANGULAR SPECTRUM AMPLITUDES AND TOTAL ENERGY FLUX

Following [3], we consider a dielectric medium with scalar dielectric permittivity $\epsilon(\vec{r})$ occupying a region between the planes $z = 0$ and $z = L$ of the Cartesian coordinate system x, y, z . The electric field $E_\alpha^0(\vec{r})$ of a monochromatic electromagnetic wave with frequency ω to be incident onto the left

boundary plane $z = 0$ is written as $(2\pi)^{-2} \int d\vec{k}_\perp \exp(i\vec{k}_\perp \vec{r}_\perp) E_\alpha^0(\vec{k}_\perp) \exp(i\gamma_k z)$, where \vec{k}_\perp is the transverse to the z axis component of a wave vector \vec{k} and the Greek subscripts take the values x, y, z with agreement about the summation over repeated Greek subscripts in what follows. The angular spectrum amplitude $E_\alpha^0(\vec{k}_\perp)$ of the incident electric field describes either a propagating or an evanescent wave, depending on whether $k_\perp < k_0$ and $\gamma_k = \sqrt{k_0^2 - k_\perp^2}$ is real or $k_\perp > k_0$ and $\gamma_k = i\sqrt{k_\perp^2 - k_0^2}$ is a purely imaginary quantities, respectively. The quantity k_0 is the wave number in the background with dielectric permittivity ϵ_0 . An electromagnetic wave can be incident onto the right boundary plane $z = L$ with an angular spectrum amplitude $\tilde{E}_\alpha^0(\vec{k}_\perp)$ of the electric field.

Split virtually the dielectric medium under consideration into a stack of slices with splits between them, as in [4]. The local electric wave field $\mathbf{E}_\alpha(\vec{r})$ inside a split between slices is found to be

$$\mathbf{E}_\alpha(\vec{r}) = (2\pi)^{-2} \int d\vec{k}_\perp \exp(i\vec{k}_\perp \vec{r}_\perp) \gamma_k^{-1/2} \left[\exp(i\gamma_k z) F_{1\alpha}(\vec{k}_\perp, z) + \exp(-i\gamma_k z) F_{2\alpha}(\vec{k}_\perp, z) \right] \quad (1)$$

Here $F_{1\alpha}(\vec{k}_\perp, z)$ and $F_{2\alpha}(\vec{k}_\perp, z)$ are angular spectrum amplitudes of local waves inside splits, going forward and backward, respectively, and renormalized by multiplying on the factor $\gamma_k^{1/2}$. Vector-column $F = (F_1, F_2)'$ with matrix elements F_1 and F_2 satisfies the following linear differential matrix equation of the first order

$$\frac{dF}{dz} = \Sigma_z \delta \mathbf{S} F \quad (2)$$

with radiative conditions on the slab boundaries

$$F_1(z = 0) = f; \quad F_2(z = L) = \tilde{f} \quad (3)$$

where $f_\alpha(\vec{k}_\perp) = \gamma_k^{1/2} E_\alpha^0(\vec{k}_\perp)$ and $\tilde{f}_\alpha(\vec{k}_\perp) = \gamma_k^{1/2} \tilde{E}_\alpha^0(\vec{k}_\perp)$ are renormalized angular spectrum amplitudes of incident waves going forward and backward, respectively. In Equation (2) $\Sigma_z = \begin{pmatrix} 1 & 0 \\ 0 & -1 \end{pmatrix}$

is the 2×2 block matrix generalization of the usual Pauli matrix σ_z . Symbol $\delta \mathbf{S}$ denotes a quantity in the equation $\mathbf{S} = \mathbf{I} + \delta \mathbf{S} \Delta z$ for scattering matrix [3] of infinitesimally thin slice of the medium, with slice thickness Δz tending to zero and \mathbf{I} being the identity block matrix. Elements of an infinitesimal scattering matrix $\delta \mathbf{S}$ are given in [6] and written in terms of the spatial Fourier transforms $V(\vec{k}_\perp, z)$ and $v(\vec{k}_\perp, z)$ of the effective scattering potential $V(\vec{r}) = -k_0^2[\epsilon(\vec{r}) - \epsilon_0]/\epsilon_0$ and a function $v(\vec{r}) = -k_0^2[\epsilon(\vec{r}) - \epsilon_0]/\epsilon(\vec{r})$, respectively, with respect to the transverse to the z axis component of the position vector.

Consider a representation for the total energy flux $\bar{P}_z(z)$ along the z axis inside an inhomogeneous dielectric medium in terms of angular spectrum amplitudes of forward and backward going waves. Such representation has a form

$$\begin{aligned} \frac{8\pi\omega}{c^2} \bar{P}_z(z) &= (2\pi)^{-2} \int d\vec{k}_\perp H^{pr}(k_\perp) \left[\rho_{11\alpha\alpha}(\vec{k}_\perp, \vec{k}_\perp; z) - \rho_{22\alpha\alpha}(\vec{k}_\perp, \vec{k}_\perp; z) \right] \\ &+ (2\pi)^{-2} \int d\vec{k}_\perp i H^{ev}(k_\perp) \left[\rho_{12\alpha\alpha}(\vec{k}_\perp, \vec{k}_\perp; z) - \rho_{21\alpha\alpha}(\vec{k}_\perp, \vec{k}_\perp; z) \right] \end{aligned} \quad (4)$$

Here the density matrix $\rho(z)$ of angular spectrum amplitudes is defined by $\rho_{mm'\alpha\alpha'}(\vec{k}_\perp, \vec{k}'_\perp; z) = F_{m\alpha}(\vec{k}_\perp, z) F_{m'\alpha'}^*(\vec{k}'_\perp, z)$, with the “star” superscript meaning a complex conjugate quantity and Latin subscripts $m, m' = 1, 2$ denoting forward and backward propagation directions. The symbols $H^{pr}(k_\perp)$ and $H^{ev}(k_\perp)$ denote projectors on a propagating $k_\perp < k_0$ and an evanescent $k_\perp > k_0$ waves, respectively. As can be seen, the contribution of propagating waves into the total energy flux along the z axis is related to angular spectrum intensities of forward and backward going waves, whereas the contribution from evanescent waves is explicitly related to a cross-product of angular spectrum amplitudes of opposite decaying waves.

3. DYSON EQUATION FOR AVERAGED ANGULAR SPECTRUM AMPLITUDES

The linear differential Equation (2) with boundary conditions (3) is reduced to an integral equation in a matrix form

$$F(z) = F^{(0)} + \int_0^L dz' h^{(0)}(z, z') \nu(z') F(z') \quad (5)$$

Here the first term in the right hand side means a vector-column including the boundary conditions, $F^{(0)} = (f, \tilde{f})'$; in the integrand the first factor is a specific matrix Green function of the empty slab, $h^{(0)}(z, z') = \text{diag}(H(z - z'), -H(z' - z))$, with the Heaviside step function $H(x) = 1$ as $x \geq 0$ and $H(x) = 0$ as $x < 0$, the second factor is a matrix $\nu(z) = \Sigma_z \delta \mathbf{S}(z)$.

We think of the matrix $\nu(z)$ further as a random one. Applying to integral Equation (5) the Bourret approach leads to a Dyson equation for the ensemble averaged angular spectrum amplitudes $\langle F(z) \rangle$ in a form

$$\langle F(z) \rangle = F^{(0)} + \int_0^L dz' \int_0^L dz'' h^{(0)}(z, z') \mu(z', z'') \langle F(z'') \rangle \quad (6)$$

with a mass operator $\mu(z, z') = \langle \nu(z) h^{(0)}(z, z') \nu(z') \rangle$.

Our next task consists in simplifying expression for the mass operator. With this aim we restrict ourselves by scalar wave case replacing the above complicated matrix $\nu(z)$ to a more simple form

$$\nu_{mm'}(\vec{k}_\perp, \vec{k}'_\perp; z) = \Sigma_{zm} \frac{1}{2i} \exp[-i(\xi_m \gamma_k - i\xi_{m'} \gamma_{k'})z] \frac{1}{\sqrt{\gamma_k}} V(\vec{k}_\perp - \vec{k}'_\perp; z) \frac{1}{\sqrt{\gamma_{k'}}} \quad (7)$$

with $\xi_1 = 1$ and $\xi_2 = -1$. The matrix mass operator is written as, $\mu_{mm'}(\vec{k}_\perp; z, z')(2\pi)^2 \delta(\vec{k}_\perp - \vec{k}'_\perp)$. Substitute this one into the Dyson Equation (6) and use supposition about a slow varying (weak space dispersion) of averaged spectrum amplitudes with respect to z replacing approximately $\langle F(z'') \rangle$ to $\langle F(z') \rangle$. Such replacement opens possibility to integrate the mass operator $\mu(z', z'')$ with respect to z'' that we perform approximately also supposing a point with z' coordinate to be far enough from the slab boundaries in spatial scale of scattering potential correlation function $B(\vec{r} - \vec{r}') = \langle V(\vec{r}) V(\vec{r}') \rangle$. Our last simplification supposes the correlation function $B(\vec{r})$ to be even with respect to the transverse to the z axis component of the position vector.

The described simplifications transform the Dyson integral Equation (6) to the purely differential equation with original boundary conditions (3). This differential equation becomes more physically transparent by transition to the fast varying averaged angular spectrum amplitudes $\langle \hat{F}_m(\vec{k}_\perp, z) \rangle = \exp(i\xi_m \gamma_k z) \langle F_m(\vec{k}_\perp, z) \rangle$. The seeking solution is presented as, $\langle \hat{F}_m(\vec{k}_\perp, z) \rangle = \Phi_{mm'}(k_\perp, z) \hat{f}_{m'}(\vec{k}_\perp)$. Here $\Phi_{mm'}(k_\perp, z)$ is a boundary matrix Green function for averaged angular spectrum amplitudes satisfying a homogeneous equation

$$\frac{d}{dz} \Phi_{mm'}(k_\perp, z) = i\xi_m \gamma_k \Phi_{mm'}(k_\perp, z) + \mu_{mm''}(k_\perp) \Phi_{m''m'}(k_\perp, z) \quad (8)$$

and unit boundary conditions, $\Phi_{1m'}(k_\perp, 0) = \delta_{1m'}$ and $\Phi_{2m'}(k_\perp, L) = \delta_{2m'}$. Functions, $\hat{f}_1(\vec{k}_\perp) = f(\vec{k}_\perp)$ and $\hat{f}_2(\vec{k}_\perp) = \exp(-i\gamma_k L) \tilde{f}(\vec{k}_\perp)$ are the boundary conditions for fast varying averaged angular spectrum amplitudes. An agreement about the summation over repeated Latin subscripts is kept. The matrix $\mu_{mm'}(k_\perp)$ has only independent element according to representation, $\mu_{11} = \mu_{12}$ and $\mu_{21} = \mu_{22} = -\mu_{11}$ where

$$\mu_{11}(k_\perp) = -\frac{1}{4\gamma_k} (2\pi)^{-2} \int d\vec{k}'_\perp \frac{1}{\gamma'_k} \left[B^+(\vec{k}_\perp - \vec{k}'_\perp, \gamma_k - \gamma'_k) + B^-(\vec{k}_\perp - \vec{k}'_\perp, \gamma_k + \gamma'_k) \right] \quad (9)$$

We denote $B^{(\pm)}(\vec{k}_\perp, k_z)$ some sort of one-side Fourier transformations of the scattering potential correlation function according to

$$B^{(\pm)}(\vec{k}_\perp, k_z) = \int d\vec{r} H(\pm z) \exp(-i\vec{k}_\perp \vec{r}_\perp - ik_z z) B(\vec{r}) \quad (10)$$

Equation (8) shows that ensemble averaged angular spectrum amplitudes of local electromagnetic waves inside the random medium slab can be evaluated as angular spectrum amplitudes of waves in a deterministic medium slab with effective complex dielectric permittivity $\epsilon_1(k_\perp)$ defined by, $(\epsilon_1 - \epsilon_0)/\epsilon_0 = \frac{2}{ik_0^2} \gamma_k \mu_{11}(k_\perp)$. Explicit expressions for elements of boundary matrix Green function introduced are written in terms of forward and backward going waves in the deterministic medium slab with a longitudinal wave number $\gamma_{1k} = \sqrt{k_1^2 - k_\perp^2}$, where the effective wave number $k_1 = (\omega/c)\epsilon_1^{1/2}$.

In the next section we shall meet a specific matrix Green function $\langle h_{mm'}(k_{\perp}; z, z') \rangle$ for averaged angular spectrum amplitudes that for the averaged fast angular spectrum amplitudes is expressed in terms of the boundary matrix Green function by, $\langle \hat{h}_{mm'}(k_{\perp}; z, z') \rangle = \Phi_{mm'}^{(0)}(k_{\perp}, z) h_{m''m''}^{(0)}(z, z') \Phi_{m''m''}^{-1}(k_{\perp}, z')$, where $\Phi_{mm'}^{-1}(k_{\perp}, z)$ denotes the matrix elements of the inverse boundary Green function matrix.

4. BETHE-SALPETER EQUATION FOR COHERENCE MATRIX

Coherence matrix of angular spectrum amplitudes, $\bar{\rho}_{mn}(\vec{p}, \vec{q}; z, \zeta) = \langle F_m(\vec{p}, z) F_n^*(\vec{q}, \zeta) \rangle$, is defined as ensemble averaged density matrix of angular spectrum amplitudes with two embedding parameters. We rename here and henceforth the transverse to the z axis components $\vec{k}_{\perp}, \vec{k}'_{\perp}, \dots$, and so on of wave vectors to \vec{p}, \vec{p}', \dots and so on, for simplicity. Matrix Bethe-Salpeter equation in the ladder approximation for the coherence matrix of angular spectrum amplitudes is written as

$$\begin{aligned} \bar{\rho}_{mn}(\vec{p}, \vec{q}; z, \zeta) &= \langle F_m(\vec{p}, z) \rangle \langle F_n^*(\vec{q}, \zeta) \rangle + \int_0^L dz_1 \int_0^L d\zeta_1 \int_{\vec{p}_1} \int_{\vec{q}_1} \langle h_{mm_1}(p; z, z_1) \rangle \langle h_{nn_1}^*(q; \zeta, \zeta_1) \rangle \\ &K_{m_1n_1, m_2n_2}(\vec{p}, \vec{q}; \vec{p}_1, \vec{q}_1; z_1, \zeta_1) \bar{\rho}_{m_2, n_2}(\vec{p}_1, \vec{q}_1; z_1, \zeta_1) \end{aligned} \quad (11)$$

with an matrix intensity operator giving by $K_{mn, m'n'}(\vec{p}, \vec{q}; \vec{p}', \vec{q}'; z, \zeta) = \langle v_{mm'}(\vec{p}, \vec{p}'; z) v_{nn'}^*(\vec{q}, \vec{q}'; \zeta) \rangle$ and using a denotation $\int_{\vec{p}} = (2\pi)^{-2} \int d^2\vec{p}$.

To simplify this matrix equation we first use again the supposition about slow varying the angular spectrum amplitudes $F_m(\vec{p}, z)$ with respect to z in spatial scale of the scattering potential correlation function. Second, we neglect purely coherent reflection of waves on the slab boundaries putting for specific matrix Green function of ensemble averaged fast angular spectrum amplitudes approximately $\langle \hat{h}_{mm'}(p; z, z') \rangle \approx \exp[i\xi_m \gamma_{1p}(z - z')] h_{mm'}^{(0)}(z, z')$. In particular this approximation gives $\langle \hat{F}_m(\vec{p}, z) \rangle = \exp(i\xi_m \gamma_{1p} z) f(\vec{p})$ if a wave be incident on the left boundary of the slab. The adopted simplifications enables one to split the matrix Bethe-Salpeter Equation (11) into four physically transparent ones.

5. EQUATIONS FOR AUTO-COHERENCES AND CROSS-COHERENCES OF ANGULAR SPECTRUM AMPLITUDES

Let us introduce a fast varying coherence matrix of angular spectrum amplitudes $\hat{\rho}_{mn}(\vec{p}, \vec{q}; z, \zeta) = \exp(i\xi_m \gamma_p z - i\xi_n \gamma_q^* \zeta) \bar{\rho}_{mn}(\vec{p}, \vec{q}; z, \zeta)$. An auto-coherence (intensity) of waves propagating forward is defined as $\hat{\rho}_{11}(\vec{p}, \vec{p}; z, z)$ for $p < k_0$ and satisfies the equation

$$\begin{aligned} \hat{\rho}_{11}(\vec{p}, \vec{p}; z, z) &= \exp(-2\Im \gamma_{1p} z) |f(\vec{p})|^2 + \int_0^z dz_1 \exp[-2\Im \gamma_{1p}(z - z_1)] \int_{\vec{p}'} \frac{1}{4|\gamma_p| |\gamma_{p'}|} \\ &[B(\vec{p} - \vec{p}', \gamma_p - \gamma_{p'}) \hat{\rho}_{11}(\vec{p}', \vec{p}'; z_1, z_1) + B(\vec{p} - \vec{p}', \gamma_p + \gamma_{p'}) \hat{\rho}_{22}(\vec{p}', \vec{p}'; z_1, z_1) \\ &+ B(\vec{p} - \vec{p}', \gamma_p - \gamma_{p'}) \hat{\rho}_{12}(\vec{p}', \vec{p}'; z_1, z_1) + B(\vec{p} - \vec{p}', \gamma_p + \gamma_{p'}) \hat{\rho}_{21}(\vec{p}', \vec{p}'; z_1, z_1)] \end{aligned} \quad (12)$$

In the right hand side of this equation a quantity $\hat{\rho}_{22}(\vec{p}, \vec{p}; z, z)$ defined for $p < k_0$ is the auto-coherence of waves propagating backward and a quantity $\hat{\rho}_{12}(\vec{p}, \vec{p}; z, z)$ and its complex conjugate with transposed subscripts defined for $p > k_0$ are the cross-coherences of forward and backward decaying evanescent waves. A function $B(\vec{k}_{\perp}, k_z)$ denotes the 3D Fourier transform of the scattering potential correlation function. A quantity $\Im \gamma_{1k}$ is the imaginary part of the longitudinal wave number in the deterministic medium slab. Equation (12) presents one of the phenomenological radiative transfer equation corrected by two last terms in the integrand on accounting the evanescent waves contribution. The obtained equation has a transparent physical structure that gives possibility write out an analogical equation for the auto-coherence of waves propagating backward automatically.

Turn to equation for the cross-coherence of opposite decaying evanescent waves that has a form

$$\begin{aligned} \hat{\rho}_{12}(\vec{p}, \vec{p}; z, z) &= \int_0^z dz_1 \int_z^L d\zeta_1 \exp[i\gamma_{1p}(z - z_1)] \exp[i\gamma_{1p}^*(z - \zeta_1)] \int_{\vec{p}'} \frac{1}{4|\gamma_p| |\gamma_{p'}|} \\ &B(\vec{p} - \vec{p}', z_1 - \zeta_1) \sum_{m, n} \exp[-i\xi_m \gamma_{p'}(z - z_1)] \exp[i\xi_n \gamma_{p'}^*(z - \zeta_1)] \hat{\rho}_{mn}(\vec{p}', \vec{p}'; z, z) \end{aligned} \quad (13)$$

where a function $B(\vec{k}_\perp, z)$ is the 2D Fourier transform of the scattering potential correlation function with respect to the transverse to the z axis component of the position vector.

A structure of Equation (13) is different from the case of Equation (12) in principle. One can see that in the double integral of the right hand side (13) an inequality is fulfilled, $z_1 < z < \zeta_1$, with difference $\zeta_1 - z_1 \approx r_0$ being the order of the spatial scale r_0 of the scattering potential correlation function. It means that an observation point z and two scattering points z_1 and ζ_1 are placed simultaneously inside the same inhomogeneity (scatterer), and two appeared in the scattering points elementary evanescent waves are decaying forward and backward, respectively, to interfere in the observation point. This interference results in the following tunneling energy flux

$$-2 \int_{\vec{p}(k_0 < p < p_0)} \Im \hat{\rho}_{12}(\vec{p}, \vec{p}; z, z) = \frac{g}{1-g} \int_{\vec{p}(p < k_0)} [\hat{\rho}_{11}(\vec{p}, \vec{p}; z, z) - \hat{\rho}_{22}(\vec{p}, \vec{p}; z, z)] \quad (14)$$

This result is obtained under supposition about small scale random inhomogeneities when in Equation (13) both evanescent waves, incident and scattered by an inhomogeneity, are small decaying in the inhomogeneity scale, $|\gamma_p| r_0 \ll 1$ and $|\gamma_{p'}| r_0 \ll 1$, with $k_0 < p < p_0$ and $k_0 < p' < p_0$ where $p_0 \approx 1/r_0$ is some cut off parameter. A parameter g of tunneling energy flux is order $g \approx r_0/\ell$ of inhomogeneity scale r_0 divided by propagating wave mean free path ℓ , defined as $1/\ell = \langle V^2 \rangle r_0^3$. The observation point z is supposed to be far enough from the slab boundaries in inhomogeneity scale.

The formula (14) demonstrates a homogeneous tunneling energy flux existence inside random medium slab proportional to usual for the phenomenological radiative transfer energy flux of propagating waves. Coefficient of proportionality is small compared with one for the weakly fluctuating random media. But in the case of a strongly fluctuating medium, for example with resonances of dielectric permittivity, the above coefficient can become of more value in its magnitude.

6. CONCLUSION

A radiative transfer theory for electromagnetic wave multiple scattering in dielectric random media with effects of near fields has been presented. It was shown that this theory reveals a tunneling mechanism of radiative transfer, with exciting inside of a random inhomogeneity a pair of elementary opposite decaying evanescent waves and contributing of them because interference into the energy flux.

ACKNOWLEDGMENT

This work is supported by the grant from Russian Foundations for Basic Research number 09-02-00920; by the Russian Academy of Sciences projects “Passive multichannel radio — and acousto-thermotomography of a human body in the near zone”, Novel physical solutions for infocommunication nets.

REFERENCES

1. Chandrasekhar, S., *Radiative Transfer*, Dover, New York, 1960.
2. Barabanenkov, Y. N. and V. M. Finklberg, *Sov. Phys. JETP*, Vol. 20, 587, 1968.
3. Gulyaev, Y. V. and Y. N. Barabanenkov, M. Y. Barabanenkov, and S. A. Nikitov, *Phys. Rev. E*, Vol. 72, 026602, 2005.
4. Barabanenkov, M. Y., Y. N. Barabanenkov, Y. V. Gulyaev, and S. A. Nikitov, *Phys. Lett. A*, Vol. 364, 421, 2007.
5. Rytov, S. M., Y. A. Kravtsov, and V. I. Tatarskii, *Principles of Statistical Radiophysics*, Vol. 3, Springer, Berlin, 1989.
6. Barabanenkov, Y. N. and M. Y. Barabanenkov, *Progress In Electromagnetics Research Symposium Proceedings*, 10, Cambridge, USA, March 26–29, 2006.

Matrix Form of VRTE Solution for Vertically Stratified Slab

A. I. Brill¹, V. P. Budak², Ya. A. Ilyushin³, S. V. Korkin², and S. L. Oshchepkov¹

¹National Institute for Environmental Studies, Tsukuba, Japan

²Moscow Power Engineering Institute (TU), Moscow, Russia

³Moscow State University, Moscow, Russia

Abstract— The physical basis of the radiative transfer theory is the ray approximation that causes spatial singularities in the solution of the vectorial radiative transfer equation (VRTE). It is possible to formulate an equation upon the analysis of the angular spectrum of the Stokes vector — the modification of the spherical harmonics method (MSH). The MSH is an approximate solution of the VRTE that includes the solution singularities together with the anisotropic part. The source function built upon the MSH does not change the form of the VRTE boundary problem for the regular smooth part. The regular part of the boundary problem is solved using the discrete ordinates method. The same method allows to obtain exact analytical solutions for the discretized VRTE in the matrix form and to describe the vertical heterogeneity of the slab through the division of the complete radiation stream upon the descending and ascending ones and thus to include the symmetry of the VRTE boundary problem in case of the plane unidirectional source.

1. INTRODUCTION

For the interpretation of results the increased measurement precision of the optical remote sensing systems demands the development of the solution methods of the radiative transfer equation (RTE) without any prior limitations on the medium properties taking into account the polarization of radiation [1]. Since the measurements are carried out for the huge number of spectral ranges (hyperspectral systems) one of the major requests to the RTE solution algorithms is the computational speed.

All the numerical methods of RTE solution are based on the substitution of the scattering integral by the final sum [2]. The ray approximation underlying RTE generates inevitably the singularities in the spatially — angular radiance distribution: any break in the boundary conditions spreads deeply into the medium. The presence of singularities in the radiance angular distribution doesn't allow conducting the scattering integral replacement by the final sum [3]. For the angular δ -singularity elimination Chandrasekhar offered [4] to subtract the direct non-scattered radiation and to state the boundary value problem for the diffused radiation. However all the scattering media (let it be the atmosphere or the ocean) have the suspended particles with the size much larger than light wavelength that according to G. Mie theory gives strong anisotropic light scattering on them. In these conditions the scattered radiation is indistinguishable from the direct radiation and Chandrasekhar method loses its effectiveness. In the series of articles the procedure of the phase scattering function smoothing is offered [2], however it is equal to the neglect of the coarse aerosol fraction from analysis. This problem becomes especially nagging at transferring to RTE solution for the media with 3D geometry, where the radiance angular distribution has the hyperbolic and logarithmic singularities in the first two orders of scattering along with the δ -singularity in the direct radiation [5].

In the paper [6] the different solution approach of the singularities elimination problem in the radiance spatially — angular distribution or in the more general case of the polarized radiation of Stokes vector is offered. The approach [6] is based on the derivation of the approximated equation describing the solution anisotropic part, including all the singularities, and on the statement of the boundary value problem for the rest smooth regular part. The simplest way to formulate the separation of the solution anisotropic part is analyzing the radiance angular spectrum, which should be monotonically slowly descending for the anisotropic component.

2. SOLUTION ANISOTROPIC PART

Let's consider the boundary value problem of the vectorial radiative transfer equation (VRTE) for the turbid medium slab irradiated from above by a plane unidirectional (PU) source of light with

arbitrary polarization

$$\left\{ \begin{array}{l} \mu \frac{\partial}{\partial \tau} \vec{L}(\tau, \hat{\mathbf{i}}) + \vec{L}(\tau, \hat{\mathbf{i}}) = \frac{\Lambda}{4\pi} \oint \vec{R}(\hat{\mathbf{i}} \times \hat{\mathbf{i}}' \rightarrow \hat{\mathbf{z}} \times \hat{\mathbf{i}}) \vec{x}(\hat{\mathbf{i}}, \hat{\mathbf{i}}') \vec{R}(\hat{\mathbf{z}} \times \hat{\mathbf{i}} \rightarrow \hat{\mathbf{i}} \times \hat{\mathbf{i}}') \vec{L}(\tau, \hat{\mathbf{i}}') d\hat{\mathbf{i}}'; \\ \vec{L}(\tau, \mu, \varphi) \Big|_{\tau=0, \mu>0} = \vec{L}_0 \delta(\hat{\mathbf{i}} - \hat{\mathbf{i}}_0); \quad \vec{L}(\tau, \mu, \varphi) \Big|_{\tau=\tau_0, \mu<0} = \vec{0}; \end{array} \right. \quad (1)$$

where $\vec{L}(\tau, \hat{\mathbf{i}})$ is the Stokes vector at the optical depth τ in the sighting direction $\hat{\mathbf{i}}$; $\vec{x}(\hat{\mathbf{i}}, \hat{\mathbf{i}}')$ is the scattering phase matrix, Λ is the single scattering albedo. The unit vector is marked by the symbol $\hat{}$. The equation is written in Cartesian coordinates system $OXYZ$, the origin O of which is located on the upper slab boundary, and the axe OZ is directed downwards perpendicularly to the boundary; $\mathbf{r} = x\hat{\mathbf{x}} + y\hat{\mathbf{y}} + z\hat{\mathbf{z}}$ is the radius-vector of the medium point; $\tau = \varepsilon z$ is the optical depth, ε is the attenuation coefficient, τ_0 is the slab optical thickness. $\hat{\mathbf{i}} = \{\sqrt{1 - \mu^2} \cos \varphi, \sqrt{1 - \mu^2} \sin \varphi, \mu\}$, $\hat{\mathbf{i}}_0 = \{\sqrt{1 - \mu_0^2}, 0, \mu_0\}$ is the direction of the slab irradiation. $\vec{R}(\hat{\mathbf{i}} \times \hat{\mathbf{i}}' \rightarrow \hat{\mathbf{z}} \times \hat{\mathbf{i}})$ is the matrix of Stokes parameter transformation by the rotation of the reference plane from $\hat{\mathbf{i}} \times \hat{\mathbf{i}}'$ to $\hat{\mathbf{z}} \times \hat{\mathbf{i}}$ -rotator. $\vec{L}_0 = L_0 [1, p \cos \alpha, -p \sin \alpha, q]^T$ is the vector of polarization, L_0 is the radiance, p is the degree of polarization, α is the azimuth of polarization, q is the ellipticity of the incident radiation, the upper index T means the transposition. Hereafter we will designate the column-vector by the symbol $\ll \rightarrow \gg$, the row-vector by the symbol $\ll \leftarrow \gg$, and the matrix by the symbol $\ll \leftrightarrow \gg$.

For the statement of the equation for the anisotropic part we will transfer to the radiance angular spectrum. Let's represent the angular distribution of Stokes parameters and the phase matrix in the form of the series on the generalized surface harmonics in the circular polarization presentation (CP-presentation) [6, 7]:

$$\vec{L}(\tau, \hat{\mathbf{i}}) = \sum_{m=-\infty}^{\infty} \sum_{k=0}^{\infty} \frac{2k+1}{4\pi} \vec{Y}_m^k(\nu) \vec{f}_m^k(\tau) \exp(-im\varphi), \quad [\vec{x}(\hat{\mathbf{i}}, \hat{\mathbf{i}}')]_{r,s} = \sum_{k=0}^{\infty} (2k+1) x_{r,s}^k(\tau) P_{r,s}^k(\hat{\mathbf{i}} \cdot \hat{\mathbf{i}}'), \quad (2)$$

that reduces VRTE to the infinite ordinary differential equation set [6]:

$$\begin{aligned} & \frac{1}{2k+1} \frac{\partial}{\partial \tau} \left\{ \mu_0 \left[\vec{A}_m^{k+1} \vec{f}_m^{k+1}(\tau) + \vec{B}_m^k \vec{f}_m^k(\tau) + \vec{A}_m^k \vec{f}_m^{k-1}(\tau) \right] + \frac{i}{2} \sqrt{1 - \mu_0^2} \right. \\ & \times \left[\vec{h}_1 \vec{f}_{m-1}^{k-1}(\tau) + \vec{h}_2 \vec{f}_{m-1}^k(\tau) + \vec{h}_3 \vec{f}_{m-1}^{k+1}(\tau) + \vec{h}_4 \vec{f}_{m+1}^{k-1}(\tau) + \vec{h}_5 \vec{f}_{m+1}^k(\tau) + \vec{h}_6 \vec{f}_{m+1}^{k+1}(\tau) \right] \left. \right\} \\ & + \left(\vec{1} - \Lambda \vec{x}^k \right) \vec{f}_m^k(\tau) = \vec{0}, \end{aligned} \quad (3)$$

where $\vec{Y}_m^k(\nu) = \text{diag}[P_{m,+2}^k(\nu), P_{m,+0}^k(\nu), P_{m,-0}^k(\nu), P_{m,-2}^k(\nu)]$ are the generalized surface harmonics in the matrix form, $\nu = (\hat{\mathbf{i}}, \hat{\mathbf{i}}_0)$, $\vec{A}_m^k, \vec{B}_m^k, \vec{h}_j$ are the matrices depending only on the indices k and m .

For the equation determination of the anisotropic part let's make the following assumptions:

1. introducing the continuous dependence $\vec{f}^m(k, \tau)$ on the index k , which in integer points coincides with values of the expansion coefficients $\vec{f}_m^k(\tau)$;
2. at a strong anisotropy of the angular distribution of Stokes parameters its spectrum $\vec{f}^m(k, \tau)$ is a slowly monotonically decreasing function of the index k , that allows to expand it in a Taylor series preserving the first two terms

$$\vec{f}^m(\tau, k \pm 1) \approx \vec{f}^m(\tau, k) \pm \frac{\partial \vec{f}^m(\tau, k)}{\partial k}; \quad (4)$$

3. owing to the anisotropy of the radiance angular distribution the basic contribution to the solution is given by the terms with $k \gg 1$ and its anisotropy is much greater than its asymmetry $k \gg m$.

These assumptions allow reducing the infinite ordinary differential equation set (3) to one partial equation

$$\mu_0 \frac{\partial \vec{f}^m}{\partial \tau} + \frac{\sqrt{1-\mu_0^2}}{2} \frac{\partial}{\partial \tau} \left[- \left(\frac{\partial \vec{f}^{m-1}}{\partial \kappa} + \frac{\partial \vec{f}^{m+1}}{\partial \kappa} \right) + \frac{m}{\kappa} \left(\vec{f}^{m-1} - \vec{f}^{m+1} \right) \right] = - \left(\vec{1} - \Lambda \vec{x}^k \right) \vec{f}^m(\tau, \kappa), \quad (5)$$

where $\kappa = \sqrt{k(k+1)}$. The items of the order κ^{-1} were eliminated by the derivation of the Equation (5).

Let's introduce the function $\vec{\omega} = \vec{\omega}(\tau, \psi, k)$, the azimuthal spectrum of which is the unknown expansion coefficient of the Stokes parameters angular distribution

$$\vec{\omega}(\tau, \psi, \kappa) = \sum_{m=-\infty}^{\infty} \vec{f}^m(\tau, \kappa) \exp(im\psi); \quad \vec{f}^m(\tau, \kappa) = \frac{1}{2\pi} \int_0^{2\pi} \vec{\omega}(\tau, \psi, \kappa) \exp(-im\psi) d\psi, \quad (6)$$

that reduce to the equation

$$\frac{\partial}{\partial \tau} \left[\mu_0 - i \left(\hat{\mathbf{1}}_{0\perp}, \nabla_{\kappa} \right) \right] \vec{\omega}(\tau, \psi, \kappa) = - \left(\vec{1} - \Lambda(\tau) \vec{x}^k(\tau) \right) \vec{\omega}(\tau, \psi, \kappa). \quad (7)$$

The received equation describes the angular spectrum taking into account the mesh of azimuthal harmonics that allows describing the rotation of the radiance angular distribution maximum from the incident direction near the boundary to the vertical direction in the medium depth. Since our concern is only the anisotropic part near the slab boundary, we can neglect the second item in the approximation of the small incident angle $\sqrt{1-\mu_0^2} \rightarrow 0$ that permits to get the analytically simple solution of the Equation (7)

$$\vec{f}^m(\tau, k) = \exp \left\{ -\tau \left(\vec{1} - \Lambda \vec{x}^k \right) / \mu_0 \right\} \vec{f}^m(0, k) = \vec{Z}_k(\tau) \vec{f}^m(0, k). \quad (8)$$

Substituting the boundary conditions and returning the Stokes polarization presentation (SP-presentation) we will get the expression for the solution regular part:

$$\vec{L}_a(\tau, \hat{\mathbf{1}}) = L_0 \sum_{k=0}^{\infty} \frac{2k+1}{2\pi} \left\{ \vec{P}_R^{k,0}(\nu) \vec{Z}_k(\tau) \begin{bmatrix} 1 \\ 0 \\ 0 \\ q \end{bmatrix} - \vec{P}_R^{k,2}(\nu) \vec{Z}_k(\tau) \begin{bmatrix} 0 \\ p \cos 2\varphi \\ p \sin 2\varphi \\ 0 \end{bmatrix} - \vec{P}_I^{k,2}(\nu) \vec{Z}_k(\tau) \begin{bmatrix} 0 \\ p \sin 2\varphi \\ p \cos 2\varphi \\ 0 \end{bmatrix} \right\}, \quad (9)$$

$$\vec{P}_R^{k,m}(\mu) = \begin{bmatrix} Q_k^m & 0 & 0 & 0 \\ 0 & R_k^m & 0 & 0 \\ 0 & 0 & R_k^m & 0 \\ 0 & 0 & 0 & Q_k^m \end{bmatrix}, \quad \vec{P}_I^{k,m}(\mu) = \begin{bmatrix} 0 & 0 & 0 & 0 \\ 0 & 0 & T_k^m & 0 \\ 0 & -T_k^m & 0 & 0 \\ 0 & 0 & 0 & 0 \end{bmatrix}, \quad \begin{aligned} Q_k^m(\mu) &= P_{m,0}^k(\mu), \\ R_k^m(\mu) &= 0.5i^m (P_{m,+2}^k(\mu) + P_{m,-2}^k(\mu)), \\ T_k^m(\mu) &= 0.5i^m (P_{m,+2}^k(\mu) - P_{m,-2}^k(\mu)). \end{aligned}$$

3. SOLUTION REGULAR PART

Now let's consider the smooth part of Stokes parameters field in the slab irradiated from above by a PU-source (1). In this case we have VRTE

$$\mu \frac{\partial}{\partial \tau} \vec{L}(\tau, \hat{\mathbf{1}}) + \vec{L}(\tau, \hat{\mathbf{1}}) = \frac{\Lambda}{4\pi} \oint \vec{R}(\hat{\mathbf{1}} \times \hat{\mathbf{1}}' \rightarrow \hat{\mathbf{1}} \times \hat{\mathbf{1}}_0) \vec{x}(\hat{\mathbf{1}}, \hat{\mathbf{1}}') \vec{R}(\hat{\mathbf{1}}_0 \times \hat{\mathbf{1}}' \rightarrow \hat{\mathbf{1}} \times \hat{\mathbf{1}}') \vec{L}(\tau, \hat{\mathbf{1}}') d\hat{\mathbf{1}}' + \vec{\Delta}(\tau, \hat{\mathbf{1}}), \quad (10)$$

where the complete solution is presented by the expression [6]

$$\vec{L}(\tau, \mu, \varphi) = \vec{\tilde{L}}(\tau, \mu, \varphi) + \vec{L}_a(\tau, \mu, \varphi), \quad (11)$$

and the source function is

$$\vec{\Delta}(\tau, \hat{\mathbf{1}}) = \frac{\Lambda}{4\pi} \oint \vec{R}(\hat{\mathbf{1}} \times \hat{\mathbf{1}}' \rightarrow \hat{\mathbf{1}} \times \hat{\mathbf{1}}_0) \vec{x}(\hat{\mathbf{1}}, \hat{\mathbf{1}}') \vec{R}(\hat{\mathbf{1}}_0 \times \hat{\mathbf{1}}' \rightarrow \hat{\mathbf{1}} \times \hat{\mathbf{1}}') \vec{L}_a(\tau, \hat{\mathbf{1}}') d\hat{\mathbf{1}}' - \mu \frac{\partial}{\partial \tau} \vec{L}_a(\tau, \hat{\mathbf{1}}) - \vec{L}_a(\tau, \hat{\mathbf{1}}). \quad (12)$$

Then we deal with the scattering integral. In CP-presentation all the coefficients in VRTE become complex that makes it difficult to use the effective numerical methods of the VRTE solution that is based on the sorting algorithm. We convert all the functions under the integral to CP-presentation, expand the scattering matrix in series on a generalized spherical harmonics, use the addition theorem and return to SP-presentation. It can be written down as follows:

$$\begin{aligned} \vec{T}_S &= \vec{T}_{SC} \frac{\Lambda}{4\pi} \oint \vec{T}_{CS} \vec{R}(\chi) \vec{T}_{SC} \vec{T}_{CS} \vec{x}(\hat{\mathbf{i}}, \hat{\mathbf{i}}') \vec{T}_{SC} \vec{T}_{CS} \vec{R}(\chi') \vec{T}_{SC} \vec{T}_{CS} \vec{L}(z, \hat{\mathbf{i}}') d\hat{\mathbf{i}}' \\ &= \frac{\Lambda}{4\pi} \oint \left(\sum_{k=0}^{\infty} (2k+1) \sum_{m=-k}^k e^{im(\varphi-\varphi')} \vec{P}_m^k(\mu) \vec{\chi}_k \vec{P}_m^k(\mu') \right) \vec{L}(\tau, \hat{\mathbf{i}}') d\hat{\mathbf{i}}', \end{aligned} \quad (13)$$

where $\vec{\chi}_k = \vec{T}_{SC} \vec{x}_k \vec{T}_{CS}$, \vec{T}_{SC} , \vec{T}_{CS} are the transfer matrices from SP-presentation to CP and vice-versa accordingly [6].

It is easy to get convinced by the direct verification that $\vec{P}_m^k(\mu) = \overline{\vec{P}_{-m}^k(\mu')}$, where the line above indicates the complex-conjugate number. It means that the local transformation matrix is a real function. Therefore there is no need to keep all the terms in the azimuth series (13) and to combine the terms of the series with m and $-m$. Then we determine the matrices

$$\begin{aligned} \vec{\phi}_1(\varphi) &= \text{diag}\{\cos \varphi, \cos \varphi, \sin \varphi, \sin \varphi\}, \quad \vec{\phi}_2(\varphi) = \text{diag}\{-\sin \varphi, -\sin \varphi, \cos \varphi, \cos \varphi\}; \\ \vec{D}_1 &= \text{diag}\{1, 1, 0, 0\}, \quad \vec{D}_2 = \text{diag}\{0, 0, -1, -1\}; \quad \vec{\Pi}_k^m(\mu) = \begin{bmatrix} Q_k^m(\mu) & 0 & 0 & 0 \\ 0 & R_k^m(\mu) & -T_k^m(\mu) & 0 \\ 0 & -T_k^m(\mu) & R_k^m(\mu) & 0 \\ 0 & 0 & 0 & Q_k^m(\mu) \end{bmatrix}, \end{aligned} \quad (14)$$

that allows transforming (13) into the following form

$$\vec{I}_S = \frac{\Lambda}{4\pi} \oint \left(\sum_{k=0}^{\infty} (2k+1) \sum_{m=0}^k (2-\delta_{0,m}) \left(\vec{\phi}_1(m(\varphi-\varphi')) \vec{A} \vec{D}_1 + \vec{\phi}_2(m(\varphi-\varphi')) \vec{A} \vec{D}_2 \right) \right) \vec{L}(\tau, \hat{\mathbf{i}}') d\hat{\mathbf{i}}', \quad (15)$$

where $\vec{A}_k^m(\mu, \mu') = \vec{\Pi}_k^m(\mu) \vec{\chi}_k \vec{\Pi}_k^m(\mu')$.

Let's consider the source function (12) from the Equation (10). It is possible to show that using (12), (15) and (14) after some tedious transformations we can get the expression for the source function

$$\vec{\Delta}(\tau, \mu, \varphi) = \sum_{m=0}^{\infty} \sum_{k=m}^{\infty} \frac{2k+1}{2} \left(\vec{\phi}_1(m\varphi) \vec{\Pi}_m^k(\mu) \vec{\Phi}_k(\tau) \vec{\Pi}_m^k(\mu_0) \vec{D}_1 + \vec{\phi}_2(m\varphi) \vec{\Pi}_m^k(\mu) \vec{\Phi}_k(\tau) \vec{\Pi}_m^k(\mu_0) \vec{D}_2 \right) \vec{f}_k(0), \quad (16)$$

where $\vec{\Phi}_k(\tau) = \frac{1}{2k+1} \left[\vec{A}_{k+1} \vec{b}_{k+1} \vec{\Xi}_{k+1}(\tau) \vec{a}_k + 4 \frac{(2k+1)}{k(k+1)} \vec{b}_k \vec{\Xi}_k(\tau) \vec{B} + \vec{A}_k \vec{b}_{k-1} \vec{\Xi}_{k-1}(\tau) \vec{a}_k \right] - \vec{b}_k \vec{\Xi}_k(\tau)$, $\vec{b}_k = \vec{1} - \Lambda \vec{\chi}_k$, $\vec{\Xi}_k(\tau) = \vec{T}_{SC} \vec{Z}_k(\tau) \vec{T}_{CS}$, $\vec{a}_k = \text{diag}\{k, \kappa, \kappa, k\}$, $\vec{A}_k = \frac{\vec{a}_k}{k}$, $\vec{B} = \text{diag}\{0, 1, 1, 0\}$, $\kappa = \sqrt{k^2 - 4}$.

Let's present the smooth part of the solution similar to the source function (16)

$$\vec{L}(\tau, \mu, \varphi) = \sum_{m=0}^{\infty} \left[\vec{\phi}_1(m\varphi) \vec{L}_1^m(\tau, \mu) + \vec{\phi}_2(m\varphi) \vec{L}_2^m(\tau, \mu) \right], \quad (17)$$

that gives us two integral equations ($i = 1, 2$)

$$\mu \frac{\partial}{\partial \tau} \vec{L}_i^m(\tau, \mu) + \vec{L}_i^m(\tau, \mu) = \frac{\Lambda}{2} \sum_{k=0}^{\infty} (2k+1) \int_{-1}^1 \vec{A}_k^m(\mu, \mu') \vec{L}_i^m(\tau, \mu') d\mu' + \vec{\Delta}_i(\tau, \mu). \quad (18)$$

with the boundary conditions

$$\vec{L}_i^m(0, \mu) \Big|_{\mu \geq 0} = 0, \quad \vec{L}_i^m(\tau_0, \mu) \Big|_{\mu \geq 0} = - \left[\vec{L}_a^m(\tau_0, \mu) \right]_i, \quad (19)$$

where $\vec{\Delta}_i(\tau, \mu) = \sum_{k=0}^{\infty} \frac{2k+1}{2} \vec{\Pi}_m^k(\mu) \vec{\Phi}_k(\tau) \vec{\Pi}_m^k(\mu_0) \vec{D}_i \vec{f}_k(0)$.

4. MATRIX-OPERATOR METHOD

Since $\vec{L}_i^m(\tau, \mu)$ is a smooth function, the Equation (18) can be directly solved by the discrete ordinate method (DOM), but it is better to take into account the plane symmetry of the boundary value problem and to use the double Gaussian quadrature [2] for the scattering integral representation in (18)

$$\int_{-1}^1 \vec{f}(\mu') d\mu' = \int_{-1}^0 \vec{f}(\mu') d\mu' + \int_0^1 \vec{f}(\mu') d\mu' \approx \frac{1}{2} \sum_{j=1}^{N/2} w_j \vec{f}(\mu_j^-) + \frac{1}{2} \sum_{j=1}^{N/2} w_j \vec{f}(\mu_j^+), \quad (20)$$

where $\vec{f}(\mu') = \vec{A}_k^m(\mu, \mu') \vec{L}_i^m(\tau, \mu')$, $\mu_j^+ = 0.5(\mu_j + 1)$, $\mu_j^- = 0.5(\mu_j - 1)$, μ_j is the zeros of Legendre polynomial $P_{N/2}(\mu_j) = 0$, N is the complete number of ordinates. The upper index $\ll + \gg$ or $\ll - \gg$ by the ordinates corresponds to the cosine sign and determinates the direction, in which this stream propagates: upward or downward.

The equation set of DOM according to (20) takes the following form

$$\begin{aligned} \mu_i^\pm \frac{\partial}{\partial \tau} \vec{L}(\tau, \mu_i^\pm) = & -\vec{L}(\tau, \mu_i^\pm) + \frac{\Lambda}{4} \sum_{k=0}^K \sum_{j=1}^{N/2} (2k+1) w_j \left(\vec{A}(\mu_i^\pm, \mu_j^-) \vec{L}(\tau, \mu_j^-) + \vec{A}(\mu_i^\pm, \mu_j^+) \vec{L}(\tau, \mu_j^+) \right) \\ & + \vec{\Delta}(\tau, \mu_i^\pm), \end{aligned} \quad (21)$$

where we omitted the obvious indices c , m and k .

Now let's introduce the following designation for $4N \times 4N$ matrices and $2N \times 1$ vectors:

$$\begin{aligned} \vec{F} = & \left\{ \sum_{k=0}^K (2k+1) \vec{A}(\mu_i^\pm, \mu_j^+) \quad \sum_{k=0}^K (2k+1) \vec{A}(\mu_i^\pm, \mu_j^-) \right\}; \\ \vec{M} = & \begin{bmatrix} \vec{\mu}^+ & \vec{0} \\ \vec{0} & \vec{\mu}^- \end{bmatrix}; \quad \vec{L}_\pm = \begin{bmatrix} \vec{L}(\mu_1^\pm) \\ \vdots \\ \vec{L}(\mu_{N/2}^\pm) \end{bmatrix}; \quad \vec{\Delta}_\pm = \begin{bmatrix} \vec{\Delta}(\mu_1^\pm) \\ \vdots \\ \vec{\Delta}(\mu_{N/2}^\pm) \end{bmatrix}, \end{aligned}$$

that allows to rewrite the equation set (21) in the matrix form

$$\frac{d}{d\tau} \begin{bmatrix} \vec{L}_+ \\ \vec{L}_- \end{bmatrix} + \vec{B} \begin{bmatrix} \vec{L}_+ \\ \vec{L}_- \end{bmatrix} = \vec{M}^{-1} \begin{bmatrix} \vec{\Delta}_+ \\ \vec{\Delta}_- \end{bmatrix},$$

where $\vec{B} \equiv \vec{M}^{-1}(\vec{1} - 0.25\Lambda\vec{F}\vec{W})$, $\vec{W} = \text{diag}(w_j)$.

Taking into account the boundary conditions (19) and using the scalar transformation [8] the solution of this set can be presented as follows

$$\begin{aligned} \begin{bmatrix} -\vec{u}_{12} & e^{+\vec{\Gamma}-\tau_0} \vec{u}_{11} \\ -e^{-\vec{\Gamma}+\tau_0} \vec{u}_{22} & \vec{u}_{21} \end{bmatrix} \begin{bmatrix} \vec{L}_-(0) \\ \vec{L}_+(\tau_0) \end{bmatrix} = \\ \begin{bmatrix} \vec{S}_- + e^{-\vec{\Gamma}+\tau_0} \vec{u}_{21} \vec{L}_S \\ \vec{S}_+ + \vec{u}_{22} \vec{L}_S \end{bmatrix} + \begin{bmatrix} \vec{u}_{11} & -e^{+\vec{\Gamma}-\tau_0} \vec{u}_{12} \\ e^{-\vec{\Gamma}+\tau_0} \vec{u}_{21} & -\vec{u}_{22} \end{bmatrix} \begin{bmatrix} \vec{L}_+(0) \\ \vec{L}_-(\tau_0) \end{bmatrix}, \end{aligned} \quad (22)$$

where $\begin{bmatrix} \vec{S}_+ \\ \vec{S}_- \end{bmatrix} \equiv \begin{bmatrix} e^{\vec{\Gamma}-\tau} & \vec{0} \\ \vec{0} & \vec{1} \end{bmatrix} \int_0^{\tau_0} \exp(\vec{\Gamma}t) \vec{U}^{-1} \vec{M}^{-1} \begin{bmatrix} \vec{\Delta}_+ \\ \vec{\Delta}_- \end{bmatrix} dt$; $\exp(\vec{B}t) = \vec{U} \exp(\vec{\Gamma}t) \vec{U}^{-1}$, $\vec{\Gamma} = \begin{bmatrix} \vec{\Gamma}_- & \vec{0} \\ \vec{0} & \vec{\Gamma}_+ \end{bmatrix}$,

$\vec{\Gamma}_\pm = \text{diag}\{\gamma_i\}$, $\gamma_{i-1} < \gamma_i$; $\vec{U}^{-1} = \begin{bmatrix} \vec{u}_{11} & \vec{u}_{12} \\ \vec{u}_{21} & \vec{u}_{22} \end{bmatrix}$. $\vec{L}_+(0)$, $\vec{L}_-(\tau_0)$ are the external radiation incidents on the slab from above and below correspondingly.

The solution of Equation (22) can be presented in the following form

$$\begin{bmatrix} \vec{L}_-(0) \\ \vec{L}_+(\tau_0) \end{bmatrix} = \begin{bmatrix} \vec{J}_- \\ \vec{J}_+ \end{bmatrix} + \begin{bmatrix} \vec{R}_- & \vec{T}_- \\ \vec{T}_+ & \vec{R}_+ \end{bmatrix} \begin{bmatrix} \vec{L}_+(0) \\ \vec{L}_-(\tau_0) \end{bmatrix}, \quad (23)$$

$$\text{where } \begin{bmatrix} \vec{J}_- \\ \vec{J}_+ \end{bmatrix} = \vec{H} \begin{bmatrix} \vec{S}_- + e^{-\vec{\Gamma}_+\tau_0} \vec{u}_{21} \vec{L}_S \\ \vec{S}_+ + \vec{u}_{22} \vec{L}_S \end{bmatrix}, \quad \begin{bmatrix} \vec{R}_- & \vec{T}_- \\ \vec{T}_+ & \vec{R}_+ \end{bmatrix} = \vec{H} \begin{bmatrix} \vec{u}_{11} & -e^{+\vec{\Gamma}_-\tau_0} \vec{u}_{12} \\ e^{-\vec{\Gamma}_+\tau_0} \vec{u}_{21} & -\vec{u}_{22} \end{bmatrix},$$

$$\vec{H} = \begin{bmatrix} -\vec{u}_{12} & e^{+\vec{\Gamma}_-\tau_0} \vec{u}_{11} \\ -e^{-\vec{\Gamma}_+\tau_0} \vec{u}_{22} & \vec{u}_{21} \end{bmatrix}^{-1}.$$

In the case of the semi-infinite slab $\tau_0 \rightarrow \infty$: $\vec{J}_+ = 0$, $\vec{T}_- = \vec{T}_+ = 0$, $\vec{L}_-(\tau_0) = \vec{L}_+(\tau_0) = 0$, and it is possible to write down the solution of (23) at once

$$\vec{L}_-(0) = -\vec{u}_{12}^{-1} \vec{S}_-. \quad (24)$$

The expression (24) is the solution of Milne-Ambartsumian problem for the arbitrary scattering phase function taking into account the polarization effect.

Using the matrix-operator method and the Equation (23) one can transfer to VRTE solution for the vertically stratified turbid medium slab. In this case it is possible to replace two adjacent slabs by one with some effective parameters, where the radiation transfer will be described by the expression like (23) — the principle of invariance. This approach allows easily including into the consideration the radiation transfer through the interface between two slabs with refraction [2, 9].

REFERENCES

1. Yokota, T., et al., "A nadir-looking 'SWIR' sensor to monitor CO₂ column density for Japanese 'GOSAT' project," *Proceedings of the Twenty-Fourth International Symposium on Space Technology and Science*, 887, Japan Society for Aeronautical and Space Sciences and ISTS, Miyazaki, 2004.
2. Thomas, G. E. and K. Stamnes, *Radiative Transfer in the Atmosphere and Ocean*, Cambridge, University Press, 2002.
3. Krylov, V. I., *Approximate Calculation of Integrals*, Dover Publications, New York, 2006.
4. Chandrasekhar, S., *Radiative Transfer*, Dover Publications, New York, 1960.
5. Germogenova, T. A., *Local Properties of the Transport Equation Solutions*, Nauka, Moscow, 1986 (in Russian).
6. Budak, V. P. and S. V. Korokin, "On the solution of vectorial radiative transfer equation in arbitrary three-dimensional turbid medium with anisotropic scattering," *JQSRT*, Vol. 109, 220, 2008.
7. Kušcer, I. and M. Ribarič, "Matrix formalism in the theory of diffusion of light," *Optica Acta*, Vol. 6, No. 1, 42–51, 1959.
8. Karp, A. H., J. Greenstadt, and J. A. Fillmore, "Radiative transfer through an arbitrary thick scattering atmosphere," *JQSRT*, Vol. 24, No. 5, 391–406, 1980.
9. Tanaka, M. and T. Nakajima, "Effects of oceanic turbidity and index refraction of hydrosols on the flux of solar radiation in the atmosphere-ocean system," *JQSRT*, Vol. 18, No. 1, 93–111, 1977.

Matrix Green's Functions Method in Statistical Optics

V. P. Budak¹ and B. A. Veklenko²

¹Moscow Power-Engineering Institute (Technical University), Moscow, Russia

²Joint Institute for High Temperature, Russian Academy of Science, Moscow, Russia

Abstract— It is shown that the method of matrix Green's functions elaborated for the solution of quantum mechanic kinetic problems can be used successfully in classical optics. It occurs to be useful in the investigation of the light propagation in randomly perturbed media. The coupled evolution of the determinate and fluctuating components of the classic electromagnetic field can be adequately described in the terms of two-point matrix Green's functions. This method allows avoiding the unwieldy formalism of the Bethe-Salpeter equation, and advancing for this reason the theory much further. In the case of random media there is an independent equation for the determined (coherent) component of radiation describing the interference phenomena. The second member of the integral equation for the fluctuating (non-coherent) component of radiation contains an interference figure formed by the coherent channel of scattering, which serves as a source forming the non-coherent channel. Thus the non-coherent channel of scattering depends on the coherent channel that is on the phase properties of radiation, the memory about which is erased in time. The method covers such phenomena as the boson peak, flickering noise, backscattering processes, van Cittert-Zernicke theorem, radiative transfer equation, Fresnel formulas etc.

The evolution of the radiation described by the vector potential $\mathcal{A}^\nu(\mathbf{r}, t)$ is described as

$$\nabla^2 \mathcal{A}^\nu - \frac{1}{c^2} \frac{\partial^2 \mathcal{A}^\nu}{\partial t^2} - \nabla^\nu \nabla^{\nu_1} \mathcal{A}^{\nu_1} = -\frac{1}{c} j^\nu$$

in the random media, the susceptibility $X_r^{\nu\nu'}(x, x')$ of which

$$\frac{1}{c} j^\nu(x) = - \int X_r^{\nu\nu'}(x, x') \mathcal{A}^{\nu'}(x') dx', \quad x = \{\mathbf{r}, t\},$$

is subjected to fluctuations with a given correlator $\langle \delta X_r^{\nu_1\nu_2}(x_1, x_2) \delta X_r^{\nu_3\nu_4}(x_3, x_4) \rangle$. The angular brackets mean the average on the ensemble of identical systems. The formalism of two-particle matrix Green's functions $\mathcal{D}_{ll'}^{\nu\nu'}(x, x')$, $l, l' = 1, 2$ is offered in the form of the following equation

$$\mathcal{D}_{ll'}^{\nu\nu'}(x, x') = \overset{\circ}{\mathcal{D}}_{ll'}^{\nu\nu'}(x, x') + \int \overset{\circ}{D}_{ll_1}^{\nu\nu_1}(x, x_1) X_{l_1 l_2}^{\nu_1\nu_2}(x_1, x_2) \overset{\circ}{D}_{l_2 l'}^{\nu_2\nu'}(x_2, x') dx_1 dx_2, \quad (1)$$

where

$$\overset{\circ}{\mathcal{D}}_{ll'}^{\nu\nu'}(x, x') = \overset{\circ}{\mathcal{D}}_{ll'}^{\nu\nu' vac} - \frac{i}{\hbar c^2} (-1)^{l'} \overset{\circ}{\mathcal{A}}^\nu(x) \overset{\circ}{\mathcal{A}}^{\nu'}(x'), \quad l, l' = 1, 2,$$

$$\overset{\circ}{\mathcal{D}}_{12}^{\nu\nu' vac}(x, x') = i \sum_{\mathbf{k}\lambda} \frac{e_{\mathbf{k}\lambda}^\nu e_{\mathbf{k}\lambda}^{\nu'}}{2\omega(\lambda)V} \exp\{-i\mathbf{k}(\mathbf{r} - \mathbf{r}') + i\omega(\lambda)(t - t')\}, \quad \overset{\circ}{\mathcal{D}}_{21}^{\nu\nu' vac}(x, x') = -\overset{\circ}{\mathcal{D}}_{12}^{\nu\nu' vac}(x', x),$$

$$\overset{\circ}{\mathcal{D}}_{11}^{\nu\nu'} = \overset{\circ}{\mathcal{D}}_{21}^{\nu\nu'} \vartheta^> + \overset{\circ}{\mathcal{D}}_{12}^{\nu\nu'} \vartheta^<, \quad \overset{\circ}{\mathcal{D}}_{22}^{\nu\nu'} = \overset{\circ}{\mathcal{D}}_{12}^{\nu\nu'} \vartheta^> + \overset{\circ}{\mathcal{D}}_{21}^{\nu\nu'} \vartheta^<, \quad \omega(\lambda) = \begin{cases} c\sqrt{\mu^2 + k^2}, & \lambda = 1, 2; \\ c\mu, & \lambda = 3. \end{cases}$$

Here $e_{\mathbf{k}\lambda}^\nu$ are the projections of the unit vectors of linear polarization on coordinate axes, \mathbf{k} and λ are a wave vector and an index of the linear polarization accordingly. Thus $\lambda=3$ corresponds to the longitudinal polarization of a monochromatic wave, $\lambda=1,2$ correspond to the transverse polarization. The normalization volume is marked by V , which is set $V \rightarrow \infty$ at the end of calculations. $\vartheta^> = \vartheta(t - t')$, $\vartheta^< = \vartheta(t' - t)$, where $\vartheta(t)$ is the unit step function. The constant

\hbar , having the dimension of the action function, is included in $\overset{\circ}{\mathcal{D}}_{12}^{\nu\nu'}$ thus the items defining this quantity have the identical dimension. The constant \hbar falls out of the final results. The auxiliary

value μ is set equal to zero at the end of calculations. The external field is denoted by $\overset{o}{\mathcal{A}}^\nu$. The matrix $X_{ll'}^{\nu\nu'}$ is uniquely determined by the matrix $X_r^{\nu\nu'}$. It is shown that

$$\mathcal{D}_{12}^{\nu\nu'} - \mathcal{D}_{12}^{\nu\nu'vac} = \frac{i}{\hbar c^2} \mathcal{A}^\nu(x) \mathcal{A}^{\nu'}(x'), \quad (2)$$

where $\mathcal{D}_{12}^{\nu\nu'vac}$ is the solution of the Equation (1) at $\overset{o}{\mathcal{A}}^\nu = 0$. The combined equations set for the determined field component $\langle \mathcal{A}^\nu \rangle$ (coherent channel of scattering) and its fluctuation component $\langle \mathcal{A}^\nu \mathcal{A}^{\nu'} \rangle - \langle \mathcal{A}^\nu \rangle \langle \mathcal{A}^{\nu'} \rangle$ (non-coherent channel of scattering) are followed from (1) and (2). It turns out that the determined field component is described by the wave equation with the effective longitudinal and transverse permittivities

$$\varepsilon^l(\mathbf{k}, \omega) = 1 - \frac{c^2}{\omega^2} \langle X_r^l(k, \omega) \rangle - \frac{c^2}{\omega^2} \pi_r^l(k, \omega), \quad (3)$$

$$\varepsilon^{tr}(\mathbf{k}, \omega) = 1 - \frac{c^2}{\omega^2} \langle X_r^{tr}(k, \omega) \rangle - \frac{c^2}{\omega^2} \pi_r^{tr}(k, \omega), \quad (4)$$

and

$$\pi_r^{\nu\nu'}(\mathbf{k}, \omega) = \left(\delta_{\nu\nu'} - \frac{k_\nu k_{\nu'}}{k^2} \right) \pi_r^{tr}(k, \omega) + \frac{k_\nu k_{\nu'}}{k^2} \pi_r^l(k, \omega), \quad \pi_r^{\nu\nu'} = \pi_{11}^{\nu\nu'} + \pi_{12}^{\nu\nu'} = \pi_{22}^{\nu\nu'} + \pi_{21}^{\nu\nu'}.$$

In the small fluctuations approximation we have the following expression

$$\pi_{ll'}^{\nu\nu'}(x, x') = \int \langle \delta X_{ll_1}^{\nu\nu_1}(x, x_1) \delta X_{l_2 l'}^{\nu_2 \nu'}(x_2, x') \rangle \langle \mathcal{D}_{l_1 l_2}^{\nu_1 \nu_2}(x_1, x_2) \rangle dx_1 dx_2. \quad (5)$$

The offered formalism allows to write down in an explicit form the polarization operator $\pi_{ll'}^{\nu\nu'}$ in any order on the powers of correlator $\langle \delta X_r^{\nu_1 \nu_2}(x_1, x_2) \delta X_r^{\nu_3 \nu_4}(x_3, x_4) \rangle$.

As to the fluctuating component of an electro-magnetic field described by the function $\langle \mathcal{D}_{12}^{\nu\nu'} \rangle$, it is in its turn broken up to the sum of the coherent and non-coherent parts

$$\langle \mathcal{D}_{12}^{\nu\nu'} \rangle = \langle \mathcal{D}_{12}^{\nu\nu'} \rangle^{(c)} + \langle \mathcal{D}_{12}^{\nu\nu'} \rangle^{(n)},$$

and

$$\langle \mathcal{D}_{12}^{\nu\nu'} \rangle^{(c)} - \langle \mathcal{D}_{12}^{\nu\nu'} \rangle^{(c)vac} = \frac{i}{\hbar c^2} \langle \mathcal{A}^\nu \rangle \langle \mathcal{A}^{\nu'} \rangle.$$

Evidently the component $\langle \mathcal{D}_{12}^{\nu\nu'} \rangle^{(c)}$ gives nothing new in the comparison with the determined channel. For the component $\langle \mathcal{D}_{12}^{\nu\nu'} \rangle^{(n)}$ in approach (5) there is the following integral equation

$$\langle \mathcal{A}^\nu \mathcal{A}^{\nu'} \rangle = \langle \mathcal{A}^\nu \rangle \langle \mathcal{A}^{\nu'} \rangle + \langle \mathcal{D}_r^{\nu\nu_1} \rangle \langle \delta X_r^{\nu_1 \nu_2} \rangle \langle \langle \mathcal{A}^{\nu_2} \mathcal{A}^{\nu_3} \rangle \rangle \langle \delta X_a^{\nu_3 \nu_4} \rangle \langle \mathcal{D}_a^{\nu_4 \nu'} \rangle, \quad (6)$$

and

$$\begin{aligned} \langle \mathcal{D}_r^{\nu\nu'} \rangle &= \overset{0}{\mathcal{D}_r^{\nu\nu'}} + \overset{0}{\mathcal{D}_r^{\nu\nu_1}} (\langle X_r^{\nu_1 \nu_2} \rangle + \pi_r^{\nu_1 \nu_2}) \langle \mathcal{D}_r^{\nu_2 \nu'} \rangle, \\ \overset{0}{\mathcal{D}_r^{\nu\nu'}} &= \overset{0}{\mathcal{D}_{11}^{\nu\nu'}} - \overset{0}{\mathcal{D}_{12}^{\nu\nu'}} = -\overset{0}{\mathcal{D}_{22}^{\nu\nu'}} + \overset{0}{\mathcal{D}_{21}^{\nu\nu'}}, \quad \langle \mathcal{D}_a^{\nu\nu'} \rangle = \langle \mathcal{D}_r^{\nu\nu'} \rangle. \end{aligned} \quad (7)$$

From (6), it follows that by means of the product $\langle \mathcal{A}^\nu \rangle \langle \mathcal{A}^{\nu'} \rangle$ the source for the non-coherent component of the radiation is the interference figure formed by the determined component, which is calculated independently. Thus the phase relations of the electromagnetic field show themselves through the initial and the boundary conditions in the non-coherent channel. The superposition principle is absent in the non-coherent channel because of quadratic dependence (6) on $\langle \mathcal{A}^\nu \rangle$. In the extreme case of the small concentrations in a right hand member of (6) it is possible to use

the approximation $\langle \mathcal{A}^\nu \rangle \langle \mathcal{A}^{\nu'} \rangle \approx \overset{o}{\mathcal{A}}^\nu \overset{o}{\mathcal{A}}^{\nu'}$. Now the “memory effect” detected in [1] follows from (6) and demonstrates the manifestation of the electromagnetic field phase relations in the non-coherent channel of radiation. Another example demonstrating the traces of the phase relations in

the non-coherent channel is a backscattering process. It follows from the Equation (6) in the next (quadratic) approach $\pi_r^{\nu\nu'}$ of the power of the correlator $\langle \delta X \delta X \rangle$. Van Cittert-Zernicke theorem follows also from the Equation (6).

The non-coherent channel, in its turn, exerts influence upon the behavior of the determined average field $\langle \mathcal{A}^\nu \rangle$ in the fluctuating media via the dependence of permittivity $\varepsilon^{tr}(k, \omega)$ and $\varepsilon^l(k, \omega)$ from the polarization operators $\pi_r^{tr}(k, \omega)$ and $\pi_r^l(k, \omega)$. The corollary of such effect appears in the increase of the permittivity imaginary part and the determined signal attenuation in accordance with its propagation in medium owing to the mechanism of scattering on fluctuations. Less obviously, that according to (3)–(4) the medium fluctuations exert influence on a real part of permittivities $\varepsilon^{tr}(k, \omega)$ and $\varepsilon^l(k, \omega)$ through the value $\text{Re}\pi_r^{\nu\nu'}$. Thus the intensity of the medium parameters fluctuations affects the refraction angle of a beam incident on the boundary of two media, on Fresnel formulas, Brewster angle, Faraday effect etc. The solution of the Equation (6) is as following

$$-i \langle \mathcal{A}^\nu \mathcal{A}^{\nu'} \rangle + i \langle \mathcal{A}^\nu \rangle \langle \mathcal{A}^{\nu'} \rangle = \langle \mathcal{D}_r^{\nu\nu_1} \rangle N^{\nu_1\nu'} - N^{\nu\nu_1} \langle \mathcal{D}_a^{\nu_1\nu'} \rangle,$$

where $N^{\nu\nu'}$ is a new unknown function, that allows to receive the conventional radiation transfer equation.

The offered formalism throws daylight upon the problems connected with the nature of the flicker noise and the boson peak. The specialization of correlator $\langle \delta X \delta X \rangle$ using the approximation

$$\langle X_r^{\nu\nu'}(x, x') \rangle = \langle X_r^{\nu\nu'}(t - t') \rangle \delta(\mathbf{r} - \mathbf{r}') \frac{\delta \rho^0(\mathbf{r})}{\rho^0} \quad (8)$$

where ρ^0 is a medium mass density, and the relation

$$\frac{\langle \delta \rho^0(\mathbf{r}) \delta \rho^0(\mathbf{r}') \rangle}{(\rho^0)^2} = \frac{\delta(\mathbf{r} - \mathbf{r}')}{n},$$

where n is the concentration of scattering particles in the medium, allow to show that in the lack of spatial dispersion for transverse waves and positive frequencies the next expression appears

$$\pi_r(\omega) \approx \frac{1}{6\pi^2 n} \langle X_r(\omega) \rangle^2 \int_0^{k_c} \frac{k dk}{\frac{\omega}{c} - k + i0}. \quad (9)$$

If the radiation propagation occurs in the solid-state medium the integration over the variable k is restricted to Debye wavelength $k_c = 2\pi/\lambda_D$. Designating a polarization coefficient of the separate scatterer through $\alpha(\omega)$ we get $\langle X_r(\omega) \rangle = n\alpha(\omega)\omega^2/c^2$ and in the frequency domain, where $\langle X_r(\omega) \rangle$ is a real quantity for the extinction coefficient $h(\omega) = \text{Im}\varepsilon(\omega)\omega/c$, we find that

$$h(\omega) = \frac{n}{6\pi} \frac{\omega^4}{c^4} \alpha^2(\omega) \vartheta \left(k_c - \frac{\omega}{c} \right). \quad (10)$$

The Rayleigh formula follows from here on condition $\omega < ck_c$ [2]. At the weak dependence $\alpha(\omega)$ on the frequency the value $h(\omega) \sim \omega^4 \vartheta(ck_c - \omega)$, that is identified with the boson peak in the paper [3]. In other words, the boson peak is treated as the effect of wave scattering on the random spatial medium inhomogeneities. In such a case the appearance of the boson peak is typical of any wave processes spreading in the random media. It is exhibited the most clearly at the acoustic wave propagation in amorphous bodies, where its connection with Debye wavelength is well-established [4]. The formula (10) allows estimating a typical frequency of the boson peak in amorphous bodies. The velocity of acoustic waves $c \sim 10^5$ cm/s, λ_D is determined by the sizes of atoms or molecules $k_c \sim 2\pi/\lambda_D \sim 10^8$ cm Thus $\omega_c = ck_c \sim 10^{13}$ s⁻¹ that completely corresponds to the experimental values.

The restriction in (9) the limits of integration by quantity k_c and the solution of the combined equations set (5), (7)–(8) concerning $\pi_r^{\nu\nu'}$ allows to construct the theory of the flicker noise [5].

So the usage of the relatively complete developed theory of the optical phenomena allows explaining such problematic effects as the flicker noise and the boson peak.

REFERENCES

1. Feng, S., C. Kane, P. A. Lee, and A. D. Stone, “Correlations and fluctuations of coherent wave transmission through disordered media,” *Phys. Rev. Lett.*, Vol. 61, No. 7, 834–837, 1988.
2. Rayleigh, L., “On the light from the sky, its polarization and colour,” *Philos. Mag.*, Vol. 41, 107–120, 274–279, 1871.
3. Veklenko, B. A., “Flicker nose and boson peak as one and the same phenomenon,” *Applied Physics*, No. 1, 5–13, 2008 (in Russian).
4. Ovsyuk, N. N. and V. N. Novikov, “Influence of structural disorder on Raman scattering in amorphous porous silicon,” *Phys. Rev. B*, Vol. 57, No. 23, 14615–14618, 1998.
5. Veklenko, B. A., “Thermal $1/\omega$ fluctuations of a quantum oscillator under a parametric effect of a random field,” *JETP*, Vol. 101, No. 3, 568–574, 2005.

Broadband Terahertz Metamaterial for Negative Refraction

C. Sabah and H. G. Roskos

Physikalisches Institute, Johann Wolfgang Goethe-University
D-60438, Frankfurt am Main, Germany

Abstract— Negative refraction metamaterials can be realized with structures containing elements with negative material parameters, electric permittivity ε and magnetic permeability μ . A well-known resonating structure that can be used to obtain negative permeability is a circular split-ring resonator (CSRR), which creates nonlinear magnetic behavior due to the resonant interaction between the inductance of the rings and the capacitance across the gaps. The effective magnetic permeability of CSRRs for a unit cell of N can be modeled by the summation expression for frequency dependence to obtain wide negative refraction band at terahertz (THz) frequency band. Numerical results illustrate that the wider frequency range of magnetic response can be achieved by combining the CSRRs. Then, a material with negative index of refraction can be constructed by combining proposed structure with an array of wires, incorporating one thin copper wire into each CSRR layer. This produces a negative permittivity effect in a frequency region that overlaps with the negative permeability region of the CSRRs. It is shown that the proposed model can be used to realize the broadband metamaterials for negative refraction for desired frequency range.

1. INTRODUCTION

In recent times, several metamaterial studies have been presented in the literature and the science community continues to contribute to literature with such kind of studies since metamaterials have wide potential application areas. These metamaterials are commonly used in the technology these days and theoretically started to discuss first by Veselago in 1968 [1]. In his study, the possibility of negative refractive index and electromagnetic wave propagation in such metamaterials are discussed in detail. Nearly all these Veselago's predictions came true approximately thirty years later. At first, Pendry and his colleagues were theorized a practical way to obtain negative permittivity over a certain frequency range using periodic array of wires [2]. Second, Pendry et al. presented their study on the effective negative permeability and how the negative permeability can be realized physically [3]. Next, Smith and his collaborators created a composite metamaterial using split-ring resonators (CSRRs) with wire arrays and they did several microwave experiments to test the unusual features of the created metamaterial in 2000 [4]. Then, numerical study of left-handed metamaterials (LHMs) using an improved version of the transfer-matrix method is studied by Markos and Soukoulis in 2001 [5]. The transmission, reflection, phase of reflection, and absorption were calculated and compared with experiments for both single split ring resonators and left-handed metamaterials in their work. In 2002, Engheta et al. presented the role of the geometry of the metallic inclusion in metamaterial structures and explored the electromagnetic wave interaction with these inclusions with various shapes [6]. In addition, how some of the geometries can lead to media with double negative parameters is also illustrated. Once more in 2002, Bayindir et al. proposed and demonstrated a composite metamaterial which is constructed by combining thin copper wires and square SRRs on the same and separate boards [7]. The transmission measurements were performed in free space and the experimental study were presented for the manufactured metamaterial samples. After that, free space transmission and the first reflection measurements of a double negative (DNG) metamaterial composed of the CSRRs and discontinuous thin wires were reported by Ozbay and his coworkers in 2003 [8]. They observed very high transmission values of the metamaterial within a frequency range for which both effective permeability and permittivity are expected to be negative. At the same time, the design, fabrication, and testing of several metamaterials that exhibit DNG medium properties at X-band frequencies are reported by Ziolkowski [9]. In his study, simulation and experimental results were given that demonstrate the realization of DNG metamaterials matched to free-space and it was shown that the metamaterials studied exhibit DNG properties in the frequency range of interest. In 2008, Sabah et al. presented a new metamaterial whose unit cell has triangular split ring resonator and wire strip is studied [10]. Simulation results were given to show the properties of the new metamaterial which exhibits double negative properties in the frequency region of interest. In addition to mentioned studies, several additional studies can be given as an example to the different type of metamaterial studies because

creating new and different metamaterials is still popular in the science community. Beside that, design and realization of novel metamaterials with negative refractive index for high frequency (i.e., terahertz — THz) band are especially important since many materials are not active at THz region and therefore technology strongly needs some new tools to create devices operating within this range. For that reason, many researchers have been started to intensely study the THz metamaterials which can play a key role in high frequency devices. In 2004, Yen et al. presented that negative magnetic response at terahertz frequencies can be achieved in a planar structure formed from an array of nonmagnetic and conductive square SRRs [11]. They also proposed that the negative refraction metamaterials at high frequencies can be created by combining the negative magnetic response structures with plasmonic wires. Again in 2004, Linden et al. illustrated that an array of square SRRs can be used to implement a negative magnetic resonance at 100 THz [12]. They also suggested that these square SRRs can be used together with the negative electric response structures to produce the negative refraction metamaterials. Furthermore, the researchers continue to study the THz metamaterials to be able to generate more efficient structures working in high frequency range [13–21].

In this work, it is shown that the frequency range of negative refraction index can be increased by introducing a periodic structure combining two different SRRs and wires in a unit cell. In our model, the magnetic effects of SRR are greatly improved by using two different SRRs and combining their effects to achieve a greater range of working frequencies for negative refraction at terahertz (THz) frequencies. Our unit cell is made of two SRRs that exhibit negative effective permeability functions around 3 THz. The negative root must be chosen for the index of refraction when the permittivity and permeability are simultaneously negative, thus the refractive index for this structure is negative at frequencies between 2.7 and 4.0 THz. It is shown that our structure offers more favorable frequency dispersion for material parameters than single SRRs. This model can be taken further to incorporate additional SRRs for an even more dispersive index of refraction.

2. ANALYSIS AND NUMERICAL RESULTS

The magnetic effects of CSRR are greatly improved by introducing two different CSRRs and combining their effects to achieve a greater range of working frequencies for negative refraction at THz frequencies. The effective magnetic permeability, μ_{eff} , for a unit cell of N can be modeled by the following summation expression for frequency dependence [22, 23]:

$$\mu_{eff} = 1 - \sum_{k=1}^N \frac{\frac{\pi r_k^2}{a_k^2}}{1 + i \frac{2l_k \sigma_k}{\omega r_k \mu_o} - \frac{sl_k c_o^2}{\pi \omega^2 \ln \frac{2c_k}{d_k} r_k^3}} \quad (1)$$

The unit cell of the designed structure is shown in Figure 1. Our unit cell is made of two CSRRs that exhibit negative effective permeability functions around 3 THz. The two CSRRs are designed with lattice parameter $a = 55 \mu\text{m}$, stacked at a layer spacing of $l = 20 \mu\text{m}$. Each layer contains two split ring resonators: CSRR1 with r , d , and c at $14.5 \mu\text{m}$, $0.88 \mu\text{m}$, and $5 \mu\text{m}$, and CSRR2 with r , d , and c at $22 \mu\text{m}$, $1 \mu\text{m}$, and $1 \mu\text{m}$, respectively.

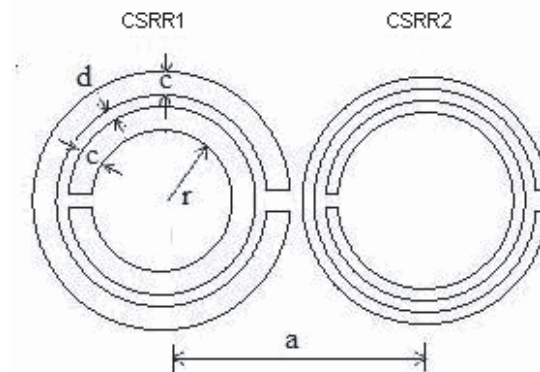


Figure 1: Unit cell with two different split-ring resonators.

The numerical results are performed using a home developed simulation program code. The Lorentz and Drude models are used in the computation. Figure 2 shows the frequency dispersion of the effective permeability for the individual CSRRs and for our structure, illustrating the wider frequency range of magnetic response achieved by combining the CSRRs. The response for the CSRR2 is obtained by changing the size and dimensions of CSRR1. By doing this, it can be possible to control the negative band for the permeability of the structure. This means, it is possible to shift the negative band region to the desired frequency range and also to design new structures having wide frequency bandwidth in which the refractive index is negative.

In addition, a negative refraction metamaterial structure can be constructed by combining these CSRRs with an array of wires with $r = 2.5 \mu\text{m}$ and spaced at $l = 20 \mu\text{m}$, incorporating one thin copper wire into each unit cell of CSRR layers. This produces a negative permittivity effect in a frequency region that overlaps with the negative permeability region of CSRRs. The negative root must be chosen for the index of refraction when the permittivity and permeability are simultaneously negatives thus the refractive index for our design is negative at frequencies between 2.7 and 4.0 THz. It is presented in Figure 3. Therefore, it is shown that our structure offers more favorable frequency dispersion for material parameters than single CSRRs. This model can be taken further to incorporate additional CSRRs for an even more dispersive index of refraction. In addition, polarization effect will also be studied during the project to investigate the possible realization of the electromagnetic polarization filters.

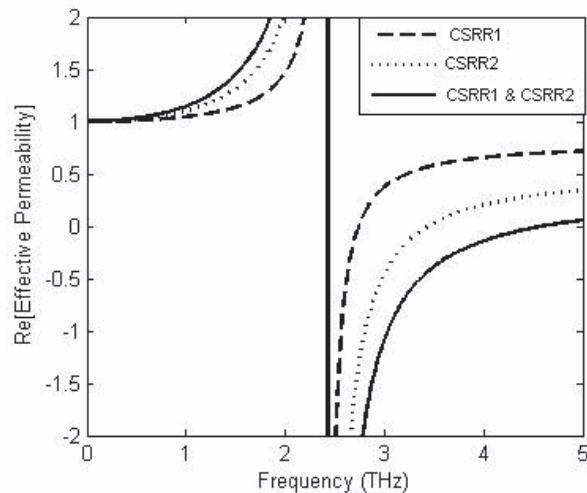


Figure 2: Real part of effective permeability frequency dispersion of individual CSRRs (dashed and dotted curves) and combined structure (solid curve).

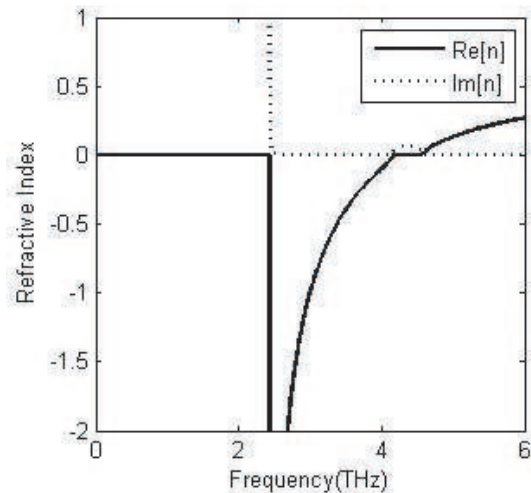


Figure 3: Frequency dispersion of refractive index for broadband negative refraction metamaterial structure combining copper wires with two different CSRRs.

3. CONCLUSION

It is shown that proposed negative refraction metamaterial structure offers more favorable frequency dispersion for material parameters than single CSRRs. This model can be taken further to incorporate additional CSRRs for an even more dispersive index of refraction to design new structures with negative wide-bandwidth for the desired higher and/or lower frequency range. Simulation and experimental study for the proposed structure is now under investigation.

REFERENCES

1. Veselago, V. G., "The electrodynamics of substances with simultaneously negative values of ϵ and μ ," *Physics Uspekhi*, Vol. 10, 509–514, 1968.
2. Pendry, J. B., A. J. Holden, W. J. Stewart, and I. Youngs, "Extremely low frequency plasmons in metallic mesostructures," *Physical Review Letters*, Vol. 76, 4773–4776, 1996.
3. Pendry, J. B., A. J. Holden, D. J. Robbins, and W. J. Stewart, "Magnetism from conductors and enhanced nonlinear phenomena," *IEEE Trans. on Microwave Theory and Techniques*, Vol. 47, 2075–2084, 1999.

4. Smith, D. R., W. J. Padilla, D. C. Vier, S. C. Nemat-Nasser, and S. Schultz, “Composite medium with simultaneously negative permeability and permittivity,” *Physical Review Letters*, Vol. 84, 4184–4187, 2000.
5. Markos, P. and C. M. Soukoulis, “Numerical studies of left-handed materials and arrays of split ring resonators,” *Physical Review E*, Vol. 65, 036622.1–036622.8, 2002.
6. Engheta, N., S. R. Nelatury, and A. Hoorfar, “The role of geometry of inclusions in forming metamaterials with negative permittivity and permeability,” *Proc. XXVII URSI Gen. As.*, Netherlands, August 2002.
7. Bayindir, M., K. Aydin, E. Ozbay, P. Markos, and C. M. Soukoulis, “Transmission properties of composite metamaterials in free space,” *Applied Physics Letters*, Vol. 81, 120–122, 2002.
8. Ozbay, E., K. Aydin, E. Cubukcu, and M. Bayindir, “Transmission and reflection properties of composite double negative metamaterials in free space,” *IEEE Transaction on Antennas and Propagation*, Vol. 51, 2592–2595, 2003.
9. Ziolkowski, R. W., “Design, fabrication, and testing of double negative metamaterials,” *IEEE Transaction on Antennas and Propagation*, Vol. 51, 1516–1529, 2003.
10. Sabah, C. and S. Uckun, “Triangular split ring resonator and wire strip to form new metamaterial,” *Proc. XXIX General Assembly of the International Union of Radio Science*, Chicago, Illinois, USA, August 2008.
11. Yen, T. J., W. J. Padilla, N. Fang, D. C. Vier, D. R. Smith, J. B. Pendry, D. N. Basov, and X. Zhang, “Terahertz magnetic response from artificial materials,” *Science*, Vol. 303, 1494–1496, 2004.
12. Linden, S., C. Enkrich, M. Wegener, J. Zhou, T. Koschny, and C. M. Soukoulis, “Magnetic response of metamaterials at 100 Terahertz,” *Science*, Vol. 306, 1351–1353, 2004.
13. Moser, H. O., B. D. F. Casse, O. Wilhelmi, and B. T. Saw, “Terahertz response of a microfabricated rod-split-ring-resonator electromagnetic metamaterial,” *Physical Review Letters*, Vol. 94, 063901.1–063901.4, 2005.
14. Gokkavas, M., et al., “Experimental demonstration of a left-handed metamaterial operating at 100 GHz,” *Physical Review B*, Vol. 73, 193103.1–193103.4, 2006.
15. Chen, H.-T., W. J. Padilla, J. M. O. Zide, A. C. Gossard, A. J. Taylor, and R. D. Averitt, “Active terahertz metamaterial devices,” *Nature*, Vol. 444, 597–600, 2006.
16. Casse, B. D. F., et al., “Fabrication of 2D and 3D electromagnetic metamaterials for the terahertz range,” *Journal of Physics: Conference Series (International MEMS Conference 2006)*, Vol. 34, 885–890, 2006.
17. Chen, H.-T., et al., “Complementary planar terahertz metamaterials,” *Optics Express*, Vol. 15, 1084–1095, 2007.
18. Gundogdu, T. F., et al., “Simulation and micro-fabrication of optically switchable split ring resonators,” *Photonics and Nanostructures — Fundamental and Applications*, Vol. 5, 106–112, 2007.
19. Chen, H.-T., et al., “Electromagnetic metamaterials for terahertz applications,” *Terahertz Science and Technology*, Vol. 1, 42–50, 2008.
20. Alici, K. B. and E. Ozbay, “Characterization and tilted response of a fishnet metamaterial operating at 100 GHz,” *Journal of Physics D*, Vol. 41, 135011.1–135011.5, 2008.
21. Han, J., A. Lakhtakia, and C.-W. Qiu, “Terahertz metamaterials with semiconductor split-ring resonators for magnetostatic tunability,” *Optics Express*, Vol. 16, 14390–14396, 2008.
22. Pendry, J. B., “Negative refraction makes a perfect lens,” *Physical Review Letters*, Vol. 85, 3966–3969, 2000.
23. Ahmed, A. and M. A. Alsunaidi, “Design of wide-band metamaterials based on the split ring resonator model,” *Proceeding of META’08 & the NATO ARW*, 523–528, Marrakesh, Morocco, May 2008.

Electromagnetic Fields of Medical Devices as Risk Factor for Medical Personnel

N. B. Rubtsova, D. V. Markov, and S. Yu. Perov
RAMS Institute of Occupational Health, Moscow, Russian Federation

Abstract— Medical personnel is one of staff, that is professionally exposed by electromagnetic field (EMF). New medical appliances — Magnetic Resonance Imaging (MRI) systems generate complex of electromagnetic factors. Static magnetic fields levels on work places of medical staff can be up to 500 mT and pulsed radiofrequency EMF.

New kinds of surgery appliances can also be a source of potential electromagnetic hazard for medical staff during surgical procedures. New kinds of physiotherapy devices, including cosmological appliances, are also the sources of combined exposure of EMF of different frequency ranges, including pulsed. A number of appliances are the emitters of EMF modes without hygienic standards that prevents from evaluation those type exposure actual health risks. Thus, methods and technologies improvement of EMF of different frequency ranges and modes of medical application with their advantages for diagnostics and treatment of various health disorders can be additional risk factor for medical personnel. There were suggested new hygienic norms for EMF frequency ranges and exposure mode that had no before hygienic rules in the Russian Federation.

1. INTRODUCTION

Electromagnetic field (EMF) as occupational factor is potential health risk factor for different professional groups. One of these professional groups occupationally exposed by EMF is medical personnel. EMF of different frequency ranges, intensity, modulation high biological efficiency is used broad in medicine for diagnostics, preventive maintenance and treatment of different diseases, but can be the source of different group medical staff possible unfavorable health effects. If patients are exposed by EMF several times only (under diagnostics or treatment) medical personnel are exposed by EMF regularly. EMF for this personnel group is professional factor.

2. MODERN MEDICAL EQUIPMENT AS EMF RISK FACTOR

Last year's medical equipment use different type of EMF not only electrical, but magnetic component (static, variable, pulsed) for diagnostics, surgery, physiotherapy and cosmetology. Some kinds of equipment are the sources of not only basic irradiation; the collateral radiations connected either with equipment operation mode or with use in the medical purposes combined exposure of magnetic field and another type of irradiation (optical, infra-red, etc.) (See Table 1).

Table 1.

Main sources of medical personnel EMF occupational exposure	
LAST YEARS	TODAY
– Short-Wave diathermy	– Magnetic resonance imaging
– Ultra-short wave physiotherapy	– Electrical surgery
– Microwave physiotherapy	– Physiotherapy by means of static electric field, static magnetic field, variable and pulsed EMF in broad frequency range: short waves, ultra-short waves, microwaves(from 0 Hz to 300 GHz)
	– Creation of combined EMF different frequency ranges and exposure regimes

There are hygienic standards of discrete frequency ranges occupational exposure in Russian Federation: static electrical and magnetic fields, 50 Hz electrical and magnetic field (pulsed MF

including), from 10 kHz to 300 MHz electrical and magnetic fields, from 300 MHz to 300 GHz electromagnetic field.

Selective research of new medical equipment samples test show that at work place of surgeon radiofrequency EMF levels can be several times more occupational exposure hygienic norm — permissible limit values (PLV). So system bipolar electrosurgical “Versapoint”: (340–450 kHz frequency range) at surgeon’ work place create EMF levels from 10.3 to 138.4 V/m (EMF hygienic norm for frequency range ≥ 0.03 –3.0 MHz are from 50 V/m for all work day to 500 V/m for 4.8 min per work day).

Electrosurgical device “UES-40” is the source of EMF in frequency range from 350 kHz to 1 MHz and create at surgeon work place near his hand EMF levels up to 470 V/m, and near device itself — up to 320 V/m (permissible time duration of occupational exposure not more than 5.4 min per work day).

Electrosurgical device “Wavetronic 5000 Digital” (4 MHz work frequency) create near surgeon hand EMF level up to 1080 V/m, and near cable of electrode holder — up to 1300 V/m.

The most interesting there are Magnetic Resonance Imaging (MRI) systems, wide spread used now for clinical diagnostics. MRI systems have distant system of control but after put in operation are the constant source of static magnetic field (MF) inside of screening chamber, and under diagnostics are the sources of pulsed radiofrequency EMF (from 240 Hz to 100 MHz) too. Static magnetic field values measurement show levels up to 450 mT at work place inside of diagnostics chamber (that is more than 10 times higher than short time PLV occupational whole body exposure — 30 mT). In medical personnel hand location area magnetic field induction can be up to 1500 mT (30 times more than short time extremity’ occupational exposure hygienic norms), at that in a room of management it makes 0.05–0.16 mT only. Radiofrequency EMF measurements show that, for example, under maintenance of 1.5 T MRI system inside of camber electric field levels achieve levels not over all work day hygienic norms, but magnetic field levels near table of patient end only were not over than hygienic norm 3.0 A/m for time duration not more than 0.08 h per work day (Sanitary Rules and Norms 2.2.4.1191-03) [2].

As an example of physiotherapeutic equipment samples exposure to personnel it is possible to give the results of testing follows:

- Magneto-therapy device “TESLAMED”: creation of bipolar single pulses of magnetic field 2, 4, 8 and 16 Hz frequency or double pulses up to 25 ± 5 per minute with maximal intensity 220–1300 mT (near medical personnel hand measured MF level were from 5 to 29 mT);
- Electric stimulator portable for exposure to biological active points and areas “DENAS” and “DIADENS” series: stimulus generation with frequency 10, 20, 60, 77, 140 and 200 Hz (near hand measured MF level were from 0.10–0.17 mT);
- Device for running pulsed MF and electrical current combined exposure “BIOMAG” (near hand measured MF level were from 0.30–0.49 mT);
- Medical lamps for light therapy “BIOPTRON” series: treatment principle base in exposure of source created visible and infra-red light, and also crates EMF in frequency range from 150 kHz up to > 800 MHz. Measured levels were up to $771 \mu\text{W}/\text{cm}^2$ that limits the duration of medical personnel work up to 0.25 h per work day or increase in distance from work place — not less than 1 m.

As a whole health risks of new physiotherapeutic equipment is different for 4 types of devices: electrical therapy, magnetic therapy, radiofrequency physiotherapy, cosmetological devices. All cases EMF exposure MF therapeutic exposure excluding apparently, it is not necessary to regard as health risk factor. Magnetic therapy devices create at medical personnel work places static MF with levels up to 11.4 mT, 50 Hz and 100 Hz variable MF — up to 0.29 mT, from 0.1 to 100 Hz pulsed MF — up to 26 mT. This MF levels can be evaluated as potential health risk factor.

3. EMF AT WORK PLACES IN PHYSIOTHERAPY CABINETS AS HEALTH RISK FACTOR

The data of hygienic evaluation of EMF at medical staff of physiotherapeutic cabinet work places show that pulsed MF levels in frequency range from 10 to 50 Hz even by comparison with nearest hygienic standard of 50 Hz MF occupational exposure (for contact welding case) demand restriction of work time till 4 h per work day under case of local exposure (to extremities).

100 Hz magnetic field level near magnetic therapy devices is up to 4.1 ± 0.9 mT, and 100 Hz pulsed MF levels was about 2.7 ± 0.5 mT. 0.7 kHz and 1.0 kHz magnetic field levels at work places

were from 0.08 ± 0.02 up to 1.1 ± 0.3 mT (880 A/m). Hygienic standards of these frequency ranges and generation modes are not developed in RF.

For modern physiotherapeutic equipment maintenance created EMF in frequency ranges without hygienic norms medical personnel health risk evaluation and risk management it is the most expedient to extrapolate operating hygienic standards with the partial account of principles accepted in Directive 2004/40/EC [1].

So for variable EMF in frequency range from > 1 Hz up to < 50 Hz are offered to use frequency dependence that allows to regulate electric and magnetic field levels under following formulas:

- Electric field (EF) MPV — $250/f$ (kV/m);
- Magnetic field MPV — $5000/f$ (μ T);

For pulsed MF with pulse frequency from > 1 up to < 50 Hz, and > 50 Hz up to 100 Hz suggest as temporary hygienic norm use value adopted for 50 Hz pulsed MF — 1.75 mT, expanding thus frequency range of its activity.

For variable EMF from > 50 Hz to < 10 kHz frequency range it is obviously possible to use as temporary hygienic norms for 10–30 kHz frequency range: EF MPV — 500 V/m; MF MPV — 50 A/m, i.e., use more “strict” hygienic standards (that is caused by increased of EMF biological efficiency with frequency increase).

EMF hygienic evaluation in frequency ranges from 3 MHz to 300 GHz show essential health risk of physiotherapy devices exposure at medical personnel work places. Measured electric field levels in frequency range from 3 to 30 MHz were up to 1111.36 ± 13.15 V/m (almost in 4 times above maximal PLV, according RF hygienic norms); in frequency range from 30 to 50 MHz — up to 1105.8 ± 244.8 V/m (almost in 14 times above maximal PLV); in frequency range from 300 MHz to 300 GHz — up to 18197 ± 449 μ W/cm² (in 18 times above maximal PLV).

Radiofrequency EMF hygienic standards in Russian Federation are based in “dose” approach in view of intensity-time exposure standardization (not only maximal permissible value of electric, magnetic field, or power density of EMF). Calculation of power exposition (PE) MPV is based in next formulas:

- For frequency range from ≥ 30 kHz to 300 MHz: $PE_E = E^2 \cdot T$, $(V/m)^2 \cdot h$, and $PE_H = H^2 \cdot T$, $(A/m)^2 \cdot h$;
- For frequency range from ≥ 300 MHz to 300 GHz: $PE_{PD} = PD \cdot T$ (W/m^2) h; ($\mu W/cm^2$) h,

where: E — electric field strength, V/m; H — magnetic field strength, A/m; PD — power density, W/m², μ W/cm²; T — time per work day, h.

According to this, comparison with hygienic norms shows, that PLV by PE value excess on workplaces of physiotherapeutic cabinets personnel for these frequency ranges makes from 1.8 up to 25 times. Evaluated with Hygienic classification of working condition Manual (R 2.2.2006-05) [2] class of working conditions of this staff were from the second class — “permissible” (at use of low-power devices) up to third class — “hazard” from first (3.1) to third degree (3.3). Thus the degree of risk validity was 1B for the frequencies having the hygienic standards and 2 (in connection with absence of hygienic rules) for pulse modulated modes of generation.

At simultaneous work in physiotherapy cabinet of devices created EMF in frequency range from 3 MHz up to 300 GHz, EF intensity on distance from devices were from 0.8 ± 0.1 V/m up to 61.3 ± 0.4 V/m. It depends on amount, power and an arrangement of devices. At arrangement of personnel stationary workplace in such cabinet the excess of permissible PE value is probable. Health risk of such exposure can be qualified only as suspected (2 category) because of EF intensity vector under summation of several frequency ranges moves on specific trajectory, and for such EMF kind hygienic rules does not exist.

4. CONCLUSION

The data of hygienic evaluation of frequency, value, and time EMF parameter as generated by new equipment, as on work places of physiotherapy cabinets medical personnel show very complex picture of electromagnetic environment, especially in cases of exploration of radiofrequency devices, and possibility of significant excess even maximal permissible levels. Personnel exposed to EMF different frequency ranges and regimes, including the modes which are not having hygienic standards, despite of much given about its high physiotherapeutic (medical) efficiency.

Presented above data presented show that medical personnel electromagnetic safety maintenance questions represent an independent problem now.

Thus for the majority of cases of work with physiotherapeutic devices, generating radiofrequency EMF medical personnel health preservation can be proved by means of devices operation time reduction or removal of medical staff workplace at carrying out of procedures (protection by time and/or distance).

Medical health preservation maintenance requires several measures of electromagnetic safety:

- Development of hygienic rules of EMF occupational exposure for frequency ranges and modes of generation, characteristic for the modern medical equipment;
- Development of adequate methods of hygienic evaluation of electromagnetic factors complex occupational exposure (in physiotherapeutic cabinets especially) in view of simultaneous and/or consecutive different sources exposure opportunity;
- Development of preventive measures directed on medical personnel electromagnetic safety maintenance.

REFERENCES

1. “Directive 2004/40/EC of the European Parliament and the Council of 29 April 2004 on the minimum health and safety requirements regarding the exposure of workers to the risks arising from physical agents (electromagnetic fields),” EN Official Journal of the European Union, Vol. L159, Apr. 30, 2004.
2. “Electromagnetic fields under occupational environments,” *Sanitary Rules and Norms (San-RaN)*, 2.2.4.1191-03, Moscow, 2003 (in Russian).

Temperature Reconstruction in Depth of Biological Object by Acoustical Radiometer

Yu. N. Barabanenkov¹, A. A. Anosov^{1,2}, A. S. Kazanskij¹,
A. D. Mansfel'd³, and A. S. Sharakshane⁴

¹Institute of Radioengineering and Electronics of RAS, Russia

²Sechenov Moscow Medical Academy, Russia

³Institute of Applied Physics of RAS, Russia

⁴Institute of Biochemical Physics of RAS, Russia

Abstract— Acoustothermometrical measurements were carried out for the model biological objects. As model objects we used the plasticine bodies placed in the water. In the experiment the model objects were being heated up and cooled down. The temporal dependences of their acoustobrightness temperatures were obtained and the reconstruction of the 2-D temperature distribution was made. The position, size and temperature of the thermal source were detected. The reconstruction error was about 1–2 mm for the position and size and about 1 K for the temperature. These results were obtained when the measurement time was about 50 s. As well we carried out the acoustothermometrical control during the laser hyperthermia of the mammary gland. The medicine procedure was continued 10 min and the maximum gland acoustobrightness temperature was increased at about 7 degrees.

1. INTRODUCTION

It is well known that the temperature in depth of a human body can be measured using the thermal electromagnetic radiation of the body. Bowen [1] suggested to use for this purpose the thermal acoustic radiation in megahertz frequency range. This radiation emitted from an object results from the thermal movement of atoms and molecules in it. The intensity of the thermal acoustic radiation is determined by the absolute temperature and absorption coefficient in the object. Both methods have the advantages and imperfections. The advantage of the acoustothermography over the radiothermography is the better spatial resolution for the temperature reconstruction because of the small wave length (about 1 mm). The advantage of the radiothermography is the smaller measurement error because of the bigger frequency bandpass. We suggest to use the acoustothermography for the temperature distribution reconstruction in depth of a human body.

The physical basis of acoustothermography was considered theoretically and checked experimentally by Passechnik [2]. The theoretical estimations [3] show that the acoustothermography method permits to detect the internal temperature at the depth of up to 5–10 cm with accuracy approximately up to 0.5–1 K in the volume of about 1 cm³. The objective of our work is to carry out the acoustothermometrical measurements during modeling hyperthermia, to reconstruct the temperature distribution for model object and to conduct the acoustothermometrical control during laser hyperthermia of human tissues.

2. APPARATUS AND METHOD

The scheme of the model hyperthermia experiments is shown in Fig. 1. These experiments were carried out in a thermostat tank (43 × 43 × 15 cm³) filled with water. The plasticine cylinder (base diameter 22 mm) was placed vertically in a cavity (base square 13 × 18 cm²) with glycerin water solution. The side walls of the cavity were made from acoustically transparent film (from thin polyethylene). A metallic rod (4 mm diameter) of a soldering iron (25 W power) was used as thermal source in the plasticine. Mercury and electronic thermometers controlled the temperature of the tank and the model objects with precision of 0.2 K. The thermal acoustic radiation measurements were carried out with acoustothermometers constructed by Mansfeld's group from the Institute of Applied Physics of RAS, Nizhny Novgorod, Russia [4]. The frequency region of the receivers was 1.8 ± 0.4 MHz and the diameter was 10 mm. The acoustothermometers registered the pressure of acoustic waves, transformed it to voltage and amplified it. Then electrical signal passed through square detector and was received by a computer where was averaged over several seconds. The acoustothermometers were placed in a horizontal plane on different sides of the plasticine cylinder.

The thermal acoustic radiation pressure has the nature of a noise signal with zero mean value. The mean value of the pressure square was used to obtain meaningful information. This value is

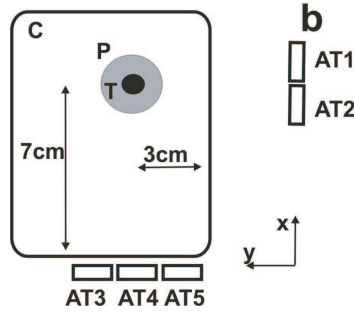


Figure 1: The scheme of the experiment: T is the source of heat, AT1-5 are the acoustothermometers, C is the cavity, P is the plasticine cylinder.

proportional to the acoustobrightness temperature T_A of the object [2]. It is convenient to operate with the increment of the acoustobrightness temperature $\Delta T_A = T_A - T_0$, where T_0 is the tank temperature. The acoustobrightness temperature increment is given by

$$\Delta T_A = \int_{\Omega(y)} \int dx dz \int_0^{+\infty} \alpha(x, y, z) A(x, y, z) \Delta T(x, y, z) \exp\left(-\int_0^y \alpha(x, y, z) dy\right) dy, \quad (1)$$

where $\Delta T(x, y, z) = T(x, y, z) - T_0$ is the increment of the internal temperature distribution $T(x, y, z)$, axis y is directed along the acoustothermometer acoustical axis and the integration along y axis is calculated in the region where $\Delta T > 0$, $A(x, y, z)$ is the directive pattern of the acoustothermometer and $\Omega(y)$ is the transversal region of the directive pattern, $\alpha(x, y, z)$ is the absorption coefficient distribution. In the experiment conditions the absorption coefficients were measured and equal to 0.11 cm^{-1} for the glycerin water solution and 5.0 cm^{-1} for the plasticine. For the thermal acoustic radiation measurements the wideband receiver was used. The relation of the frequency region to the mean frequency was equal to 44%. Therefore the acoustothermometer directive pattern was approximated by Gaussian function

$$A(x, y, z) = \frac{1}{2\pi d_A(y)^2} \exp\left(-\frac{x^2 + z^2}{2d_A(y)^2}\right), \quad (2)$$

where $d_A(y)$ is the transversal size of the directive pattern at the distance y from the receiver. In the experiment conditions the measured value $d_A(y)$ can be considered as a constant value equal about 3 mm.

The reconstructed 2-D temperature distribution was given by Gaussian function

$$\Delta T = \Delta T_0 \exp\left(-\frac{(x - x_0)^2 + (y - y_0)^2}{2d^2}\right) \quad (3)$$

with four parameters: coordinates x_0 and y_0 of the heated region center, its maximum temperature ΔT_0 and its size d . The actual size of the thermal source (the plasticine cylinder) was equal to 22 mm (see above) and was greater than the transversal size of the receiver directive pattern. Therefore the directive patterns of the acoustothermometers can be considered as the rays. In these conditions the acoustobrightness temperatures of five acoustothermometers can be calculated as follows:

$$\begin{aligned} \Delta T_{Ai} &= \Delta T_0 \exp\left(-\alpha y_0 - \frac{(x_{ATi} - x_0)^2}{2d^2}\right), \quad \text{if } i = 1, 2; \\ \Delta T_{Ai} &= \Delta T_0 \exp\left(-\alpha x_0 - \frac{(y_{ATi} - y_0)^2}{2d^2}\right), \quad \text{if } i = 3, 4, 5 \end{aligned} \quad (4)$$

where i are the acoustothermometer numbers, x_{ATi} and y_{ATi} are the coordinates of the acoustothermometers centers, ΔT_{Ai} are the acoustobrightness temperature increments, $\alpha = 0.11 \text{ cm}^{-1}$.

The coordinates of the heated region center were calculated as follows:

$$\begin{aligned} x_0 &= \frac{x_{i+1} + x_i}{2} + \frac{(\Delta T_{Ai+1} - \Delta T_{Ai})(x_{i+1} - x_i)}{2\Delta T_{Ai+1}}, \\ y_0 &= \frac{y_{i+1} + y_i}{2} + \frac{(\Delta T_{Ai+1} - \Delta T_{Ai})(y_{i+1} - y_i)}{2\Delta T_{Ai+1}}, \end{aligned} \quad (5)$$

where x_{i+1} (y_{i+1}) and x_i (y_i) are the coordinates of the neighbouring acoustothermometer centers. The minimization of function $F(\Delta T_0, d)$ allowed to detect the temperature ΔT_0 and size d of the source:

$$F(\Delta T_0, d) = \sum_{i=1}^5 (\Delta T_{AiEXP} - \Delta T_{Ai}(\Delta T_0, d))^2 \rightarrow \min, \quad (6)$$

where ΔT_{AiEXP} are the experimental acoustobrightness temperatures, ΔT_{Ai} are the acoustobrightness temperatures determined by Eq. (4).

3. RESULTS AND DISCUSSION

Temporal variations of the acoustobrightness temperature increment of the plasticine cylinder were connected with the experiment script too. The signals have increased when the heating was switched on (after some time delay), and the signals have decreased when the heating was switched off (again after some time delay). These delays were connected with the heat transfer inside the plasticine cylinder. For the reconstruction the experimental data were averaged over 50 s. The position, size and temperature of the thermal source were detected. Both the reconstructed position and the size of the heat source were close to the actual values and changed insignificantly (in limits of about 1 mm). The temporal dependences of the reconstructed effective temperatures were connected with the experimental script very close. All these results shown that the reconstruction of the temperature distribution inside the model object was quite good. These results allowed us to pass to the next experiment where the acoustothermometrical control of the laser hyperthermia of human tissies was carried out.

The acoustothermometrical measurements during the laser hyperthermia of the mammary gland were carried out in Central Hospital of RAS. The infrared laser radiation (wave length 1060 nm) was introduced through the optical fiber in the mammary gland. The power of the laser was 3 W. The time of the procedure was about 10 minutes. The laser impulse and pause time were equal to half of second. The laser radiation was absorpted in the soft tissues, and they were heated up. Acoustothermometrical measurements were conducted with two acoustothermometers. The acoustical axis of the first acoustothermometer was directed into the center of the heated region

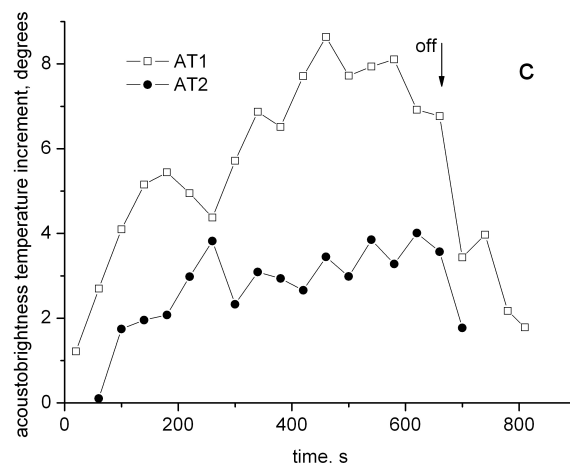


Figure 2: The temporal dependences of the acoustobrightness temperature increments during the laser hyperthermia of the mammary gland. Zero corresponds to the temperature of the body before the heating. The moment of the heat switching off is shown with arrow.

and the acoustical axis of the second acoustothermometer was directed about 1 cm sideways. The experimental data averaged over 40 s were presented in Fig. 2. We can see that the acoustobrightness temperature increments rised after switching on the laser and reduced after switching off the laser. According to the experimental scheme the data obtained with the first acoustothermometer were greater than ones obtained with the second acoustothermometer. Before switching the heating off the acoustobrightness temperature measured by first acoustothermometer was equal to about 7.5 degrees and measured by the second acoustothermometer was equal to about 3 degrees. In these conditons a question remains unanswered: what temperature was in the depth of the human tissues?

The measurements of infrared thermal electromagnetic radiation were used to answer this question. These measuments give information about the surface temperature of an object. The portable computer thermograph IRTIS-2000 developed by “IRTIS” Ltd. was used to control the model hyperthermia of the tumour which was cut out from the mammary gland [5]. For the laser hyperthermia simulation the optical fiber was entered into the tumour at the depth about 2 mm from the investigated surface. The hyperthermia duration was 10 min. The experimental data allowed us to estimate the temperature maximum $\Delta T_0 \approx 14$ K and the transversal size of the heated region $d \approx 1$ cm. We suggested that these results can be used for the estimate the temperature distribution in the actual laser hyperthermia. The temperature distribution was given by 3-D Gaussian function. We suggested also that the heated region center was at the depth 1 cm and the absorption coefficient was equal to 0.4 cm^{-1} . The calculations with help of Eq. (1) gave the values 6.2 degrees for the first acoustothermometer and 3.3 degrees for the second acoustothermometer. These results were close to the experimental data.

Thus, the results of both the model experiments and the acoustothermometrical mesurements of the actual laser hyperthermia show that the acoustothermography can be used during the laser hyperthermia for the temperature control.

ACKNOWLEDGMENT

This work has been supported by Russian Foundation for Basic Research (# 08-02-00240).

REFERENCES

1. Bowen, T., “Acoustic radiation temperature for noninvasive thermometry,” *Automedica*, (UK) Vol. 8, No. 4, 247–267, 1987.
2. Passechnick, V. I., “Verification of the physical basis of acoustothermography,” *Ultrasonics*, Vol. 32, No. 4, 293–299, 1994.
3. Passechnick, V. I., A. A. Anosov, and M. G. Isrefilov, “Potentialities of passive thermoacoustic tomography of hyperthermia,” *Int. J. Hyperthermia*, Vol. 15, No. 2, 123–144, 1999.
4. Anosov, A. A., R. V. Bel’aeV, V. A. Vilkov, A. S. Kazanskij, A. D. Mansfel’d, and A.S. Sharakshane, “Detection of temperature change dynamics in model object with acoustothermography method,” *Acoustical Physics*, Vol. 54, No. 4, 464–468, 2008.
5. Anosov, A. A., Y. N. Barabanenkov, K. M. Bograchev, R. V. Garskov, A. S. Kazanskij, and A. S. Sharakshane “A combined application of acoustothermography and IR imaging for the temperature control in the model biological object heating procedure,” *Acoustical Physics*, Vol. 54, No. 3, 432–436, 2008.

Inversion Algorithm for Microwave Breast Cancer Detection Using Level Sets

N. Irishina, D. Álvarez, O. Dorn, P. Medina, and M. Moscoso
University Carlos III de Madrid, Spain

Abstract— This work focuses on the application of breast cancer detection from microwave data. We present a novel shape-based reconstruction algorithm that makes use of level set techniques. Our reconstruction algorithm consists of several stages of increasing complexity in which more details of the anatomical structure of the breast interior are incorporated successively. In particular, the algorithm approximates first the fibroglandular and fatty regions, and then determines the presence and characteristics of the tumor, such as its size and dielectric properties. The shape-based approach implies an implicit regularization of the inverse problem that creates the images, in the form of prior knowledge regarding the types of tissues present in the breast. This reduces the dimensionality of the inverse problem helping to stabilize the reconstruction process. In addition, it provides well defined interfaces between the tissues. Our results demonstrate the potential and feasibility of this approach to detect, locate, and characterize tumors in their early stages of development.

1. INTRODUCTION

Lately, there has been increased interest in the use of microwaves for the early detection of breast cancer. The high contrast of electromagnetic parameters of malignant tissue with respect to healthy tissue makes this technique a very promising alternative to the more traditional technique of X-ray imaging which suffers from low contrast images and a potential health risk due to the ionizing nature of the probing radiation.

Despite of the relative simplicity of the microwave imaging technique, there is still many difficulties to overcome. This is at least due in part to the high level of heterogeneity of breast tissue which is composed, among others, of fibroglandular and fatty tissues giving rise to complicated internal structures. These two type of tissue have very different dielectric properties [1, 2] that lead to significant clutter. Imaging in clutter with broadband array imaging techniques that synthetically focus the recorded signals at each point of the domain (see [3], and references therein) may lead to unstable images that cannot be used for practical purposes. We mention, though, that new broadband imaging techniques specially designed for imaging in noisy environments are currently under investigation [4, 5].

On the other hand, tomographic reconstruction techniques that use a ‘classical’ shape-based approach suffer from similar drawbacks when the data is acquired in very noisy environments, and the commonly used homogeneous interior assumption is adopted during the reconstruction. In ‘classical’ shape-based approaches, one assumes during the reconstruction that the dielectric properties are piecewise constant over the domain with only two possible values: one for the healthy tissue and other for the tumor [6]. In other words, the very complicated interior structure is not taken into account when inverting the data.

Figure 1(a) shows that the homogeneous interior assumption breaks down and that a more complicated algorithm is needed to detect the tumor. The top left and top right images represent the reference and reconstructed permittivity profiles, respectively. The level set function, which define the tumor shape, and a cross section through the tumor location, are shown in the bottom images.

Therefore, there are still several fundamental problems to be resolved before microwave data can be used for the early diagnosis of breast cancer in clinical situations. We believe that the current work is an attempt to provide one significant step toward this direction. Indeed, we consider MRI-derived breast models that capture the real heterogeneity, and show that a good estimate of the internal breast structure is essential prior to the detection of small tumors.

For this purpose, we present a four stage algorithm where we also invert for the internal structure of the breast [7]. In our algorithm, the complexity of the permittivity map increases at each new stage of the algorithm, until arriving at the complete breast model. In this way, we incorporate our findings to the subsequent stages in the form of prior knowledge about the internal structure. In other words, we use submodels of increasing complexity at each new stage of the reconstruction

process, so that the result of each preceding stage is used as the starting guess for the next one. Therefore, at each new stage, the reconstructed breast model is more refined and contains more details than the previous one.

Figure 1(b) shows the result of our reconstruction algorithm applied to the same data as in Fig. 1(a). It is apparent that with our new strategy the tumor has been detected reliably, its location has been estimated correctly, and its size and permittivity value have been approximated well. The arrangement of this figure is similar to the one in Fig. 1(a).

It is important to note that in this work the shape of the fibroglandular and fatty tissues, together with their average dielectric properties are reconstructed directly from the microwave boundary data. The properties and the width of skin are assumed to be known. In references [7, 8] we assumed that, a priori, the average dielectric properties of the healthy tissue and the shape of the skin were known.

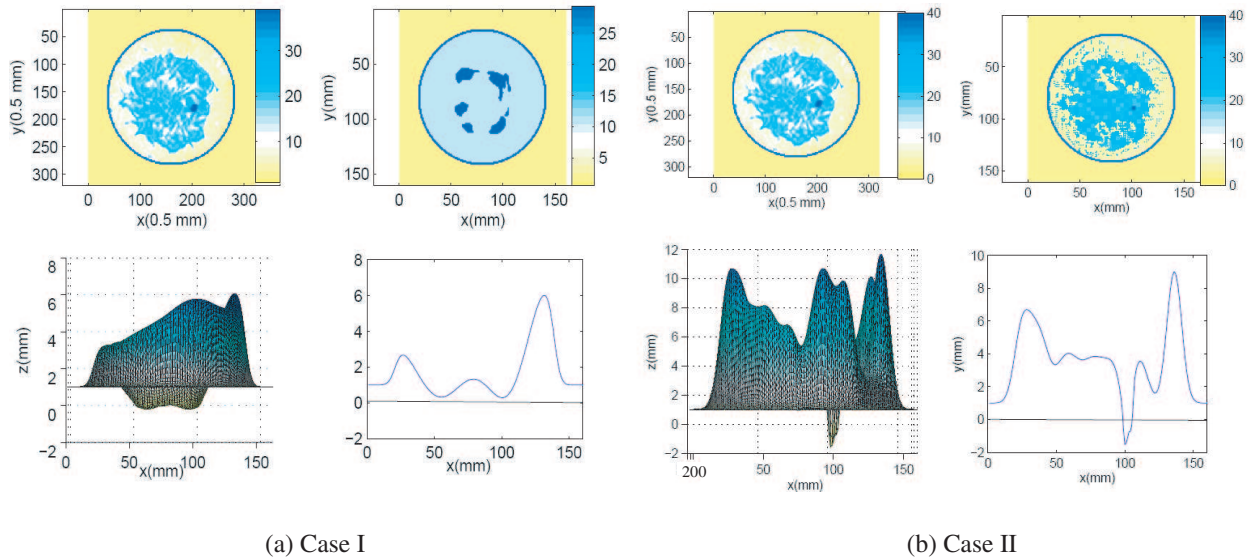


Figure 1: Simulation results for multi frequency small tumor detection in realistic breast model, using the algorithm for simplified breast model in Case I, and the new proposed inversion algorithm in Case II. In both cases, top row: left-the static permittivity map of reference, right- the reconstruction result; bottom row: left-final level set function side view, right-cross section of the final level set function through the tumor location.

2. FORWARD MODEL

We consider a heterogeneous 2D medium Ω (see the top left images of Figs. 1(a) and (b)), illuminated by TM waves. To describe the non zero component of the electric field, we use the scalar Helmholtz equation

$$\Delta u + \kappa(\mathbf{x})u = -q(\mathbf{x}) \quad \text{in } \Omega \quad (1)$$

with $\kappa(\mathbf{x}) = \omega^2 \mu_0 \epsilon_0 \epsilon_r^*(\mathbf{x})$, where $\epsilon_r^*(\mathbf{x})$ is the complex relative permittivity. The field u is required to satisfy the Sommerfeld radiation and is assumed to be continuous together with its normal derivatives across interfaces.

We solve Eq. (1) numerically with a second order centered finite differences scheme and a perfectly matching layer (PML) for numerically terminating the computational domain. To avoid the inverse crime we use different meshes for the ‘true’ data (320×320 pixels of size $0.5 \times 0.5 \text{ mm}^2$) and for the reconstruction (160×160 pixels of size $1 \times 1 \text{ mm}^2$). We use 40 antennas, situated equidistantly around the breast. The microwaves of frequencies 1–5 GHz with sampling rate of 1.0 GHz are used to define the shapes of the fibroglandular region and the tumor and their dielectrical properties.

To model the dispersion in biological tissue, we use the single pole Debye relaxation model [2], in which the complex relative permittivity is introduced as follows:

$$\epsilon_r^* = \epsilon_\infty + \frac{\epsilon_{st} - \epsilon_\infty}{1 - i\omega\tau} + i \frac{\sigma_{st}}{\omega\epsilon_0}, \quad (2)$$

where ϵ_∞ is the high frequency infinite permittivity, ϵ_{st} is the low frequency static permittivity, and σ_{st} is the static conductivity, τ is the relaxation time.

With this model there are three independent parameters to be reconstructed. Motivated by the results of Table 1 in [9], we simplify our model assuming that there exists a linear relation between them. We will assume that they approximately follow the relations $\epsilon_\infty = 7.700 - 0.0677\epsilon_{st}$ and $\sigma_{st} = 0.03 + 0.01\epsilon_{st}$. Hence, in our model the only parameter to be reconstructed is ϵ_{st} . The other two parameters are given automatically by the previous relations.

For our numerical experiments we use a MRI-derived numerical breast model. The MRI pixel intensities are mapped to the Debye parameters. The average Debye parameters are arbitrary, so they are chosen from representative values published in the literature [1]. The fibroglandular and fat average static permittivity value are $\epsilon_{st}^{fiber} = 23, 19$ and $\epsilon_{st}^{fat} = 8.20$. The skin layer is 1.5-mm thick with Debye parameters $\epsilon_{st}^{skin} = 37$, $\epsilon_\infty^{skin} = 4$, and $\sigma_{st}^{skin} = 1.1$ S/m. The surrounding medium has parameters $\epsilon_{liquid} = 2.6$, $\sigma_{liquid} = 0.04$ S/m. Since relaxation time is similar for different biological tissues, we set $\tau = 7.0$ ps in all tissues.

For simplicity, all the tumors have $\epsilon_\infty^{tumor} = 3.9$ and $\sigma_{st}^{tumor} = 0.7$ S/m, and their dielectric parameters are spatially independent.

3. LEVEL SET FORMULATION OF THE INVERSE PROBLEM

In the level set approach of shape reconstruction, the unknown shapes of the fibroglandular region and the tumor will be implicitly represented by two different ‘level set functions’ $\psi(\mathbf{x})$ and $\phi(\mathbf{x})$. We introduce two sufficiently smooth level set functions ψ and ϕ such that

$$\kappa(\mathbf{x}) = \begin{cases} \kappa_{tumor}(\mathbf{x}) & \text{where } \phi(\mathbf{x}) \leq 0, \\ \kappa_{fib}(\mathbf{x}) & \text{where } \phi(\mathbf{x}) > 0 \text{ and } \psi(\mathbf{x}) \leq 0, \\ \kappa_{fat}(\mathbf{x}) & \text{where } \phi(\mathbf{x}) > 0 \text{ and } \psi(\mathbf{x}) > 0. \end{cases} \quad (3)$$

Here, the functions κ_{fib} and κ_{fat} denote the (squared) wavenumber inside the fibroglandular and fatty tissue regions, respectively, and κ_{tumor} denotes the wavenumber inside the tumor. In order to derive evolution laws for the individual unknowns, we write (3) in the alternative form

$$\kappa(\mathbf{x}) = \kappa_{tumor}(1 - H(\phi)) + H(\phi) \left[\kappa_{fib}(1 - H(\psi)) + \kappa_{fat}H(\psi) \right], \quad (4)$$

where H denotes the Heaviside step function whose value is zero for negative arguments and one for positive arguments. Here, $\kappa = \kappa(\phi, \psi, \kappa_{fib}, \kappa_{fat})$, and our goal is to reduce and eventually minimize the least squares cost functional

$$J(\kappa(\phi, \psi, \kappa_{fib}, \kappa_{fat})) = \frac{1}{2} \|R(\kappa(\phi, \psi, \kappa_{fib}, \kappa_{fat}))\|^2.$$

Here, $R(\kappa)$ denotes the difference between the measured data and the calculated by the forward solver using the parameter distribution κ given by (3). Notice that we have formally not included κ_{tumor} in the list of unknowns since we will treat this important parameter with a special technique in our approach as explained further below.

Let us introduce an artificial evolution time t for the above specified unknowns of the inverse problem. Then, the goal is to find evolution laws

$$\frac{d\phi}{dt} = f(t), \quad \frac{d\psi}{dt} = g(t), \quad \frac{d\kappa_{fib}}{dt} = h_{fib}(t), \quad \frac{d\kappa_{fat}}{dt} = h_{fat}(t), \quad (5)$$

such that the cost functional J decreases with time. It can be shown by straightforward formal calculation [8], that the following choices for the forcing functions point into descent directions of J :

$$\begin{aligned} f(t) &= -C_\phi(t) \text{Re} \left[R'[\kappa]^* R[\kappa] \left(\kappa_{fib}(1 - H(\psi)) + \kappa_{fat}H(\psi) - \kappa_{tumor} \right) \right], \\ g(t) &= -C_\psi(t) \text{Re} \left[R'[\kappa]^* R[\kappa] H(\phi) (\kappa_{fat} - \kappa_{fib}) \right], \\ h_{fib}(t) &= -C_{fib}(t) \text{Re} \left[R'[\kappa]^* R[\kappa] H(\phi) (1 - H(\psi)) \right], \\ h_{fat}(t) &= -C_{fat}(t) \text{Re} \left[R'[\kappa]^* R[\kappa] H(\phi) H(\psi) \right]. \end{aligned} \quad (6)$$

In these expressions, $R'[\kappa]^*$ is the adjoint of the linearized residual operator $R[\kappa]$, and the expression $R'[\kappa]^*R[\kappa]$ represents the Fréchet derivative of $R[\kappa]$ with respect to κ . Positive-valued constants C_ϕ , C_ψ , C_{fib} and C_{fat} steer the speed of the evolution of each component individually. These constants can also be chosen zero, in which case the corresponding quantity does not evolve.

Numerically discretizing the evolution laws by a straightforward finite difference time-discretization with time-step $\delta t^{(n)} > 0$ in step n yields the iteration rules

$$\begin{aligned} \phi^{(n+1)} &= \phi^{(n)} + \delta t^{(n)} f^{(n)}, \quad \psi^{(n+1)} = \psi^{(n)} + \delta t^{(n)} g^{(n)}, \\ \kappa_{fib}^{(n+1)} &= \kappa_{fib}^{(n)} + \delta t^{(n)} h_{fib}^{(n)}, \quad \kappa_{fat}^{(n+1)} = \kappa_{fat}^{(n)} + \delta t^{(n)} h_{fat}^{(n)}, \end{aligned} \quad (7)$$

with suitable initializations for the four quantities at the (discretized) evolution time $t^{(0)}$.

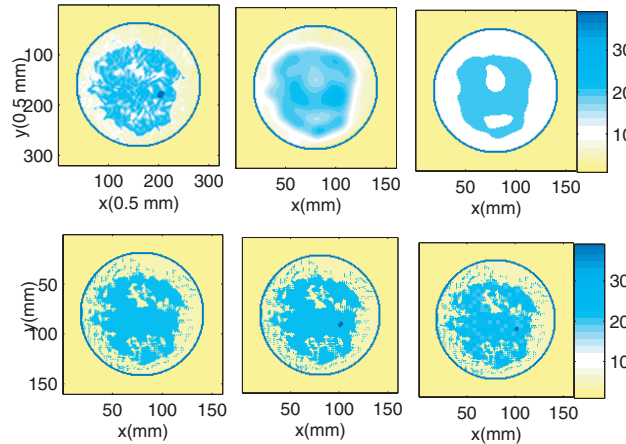


Figure 2: Top row from left to right: reference static permittivity profile, the reconstructed static permittivity map at the end of stage I, and the initial guess at the beginning of stage II. Bottom row from left to right: the reconstruction at the end of stage II, reconstruction at the end of stage III, and the final reconstruction corresponding to the minimum value of the cost functional during the IV stage.

4. INVERSION ALGORITHM FOR REALISTIC BREAST MODEL

The four stages of our algorithm are illustrated in Fig. 2. The reference permittivity profile is shown in the top left image. Hence, we start the reconstruction from an arbitrary homogeneous profile composed only of healthy tissue. We set $\phi = 1$ and $\psi = 1$ everywhere within the domain, $C_\phi = C_\psi = C_{fib} = 0$, and $C_{fat} > 0$.

The *first stage* is a pixel based reconstruction. The result at the end of this first stage is displayed in the top middle image of the figure. Note that it is very hard or even impossible to determine whether or not there is a tumor present within the breast. This is so, because pixel-based reconstruction strategies typically oversmooth estimates of the breast profile.

The *second stage* carries out a shape-based reconstruction of the fibroglandular region. To this end, we first replace the reconstructed pixel by pixel profile by a bimodal distribution, as it is shown in the top right image of Fig. 2. Again, we only consider healthy tissue (fat and fibroglandular) in this stage, ignoring the possible presence of the tumor. Hence, we set $\phi = 1$, and $C_\phi = 0$, $C_\psi > 0$, $C_{fib} > 0$, and $C_{fat} > 0$. Starting from our initial guess (top right image), we apply our algorithm and arrive to the reconstruction shown in the bottom left image when the cost functional J does not decrease any more.

During the *third stage*, we search for the location and the shape of the tumor. We assume no initial tumor shape in this stage so, initially, $\phi = 1$. If a tumor is detected, we fix its static permittivity value to $\epsilon_{tum}^{(0)} = 35$. During this stage, $C_\phi > 0$, $C_\psi > 0$, and $C_{fib} = C_{fat} = 0$. Starting from the reconstructed profile achieved at the end of the previous stage, we apply the algorithm and we obtain the profile shown in the bottom middle image. The result shows that the tumor has been located properly and its shape has been estimated well.

The *fourth stage* probably deals with the most difficult task: to specify the correct dielectric properties and shape of the small tumor. We now assume that the shapes and internal properties of the fatty and fibroglandular regions have already been estimated well, so we keep $(\psi, \epsilon_{fib}, \epsilon_{fat})$

fixed. Therefore, $C_\psi = C_{fib} = C_{fat} = 0$ and $C_\phi > 0$. To find the optimal values $(\phi^{opt}, \epsilon_{tum}^{opt})$ that fit the data, corresponding to the global minimum of the cost functional, we use a hybrid strategy combining a gradient technique for the shape of the tumor and a sampling strategy for its dielectric properties. At the end, we pick the reconstruction corresponding to the global minimum of J . See the resulting map in Fig. 2 bottom right image. Our algorithm is able to identify a very small tumor taking into account the high heterogeneity of the breast, and provides useful information on its size and dielectric properties.

5. CONCLUSION

Our reconstruction strategy is able to detect millimeter size tumors and simultaneously determine their locations, sizes, and permittivity values, applied to realistic MRI derived breast models. Being able to recover the dielectric properties of a detected object in the breast could help to discriminate between benign and malignant tumors, and may lead to determine whether a normal tissue is in the process of becoming malignant. Our algorithm can be used to determine the type of the internal breast structure, as well. The use of the level set technique may be important for the design of new microwave imaging systems.

REFERENCES

1. Meaney, P. M., M. W. Fanning, T. Raynolds, C. J. Fox, Q. Fang, C. A. Kogel, S. P. Poplack, and K. D. Paulsen, "Initial clinical experience with microwave breast imaging in women with normal mammography," *Acad. Radiol.*, Vol. 14, 207–218, 2007.
2. Lazebnik, M., M. Okoniewski, J. Booske, and S. Hagness, "Highly accurate debye models for normal and malignant breast tissue dielectric properties at microwave frequencies," *IEEE Microwave and Wireless Components Letters*, Vol. 17, 822–824, 2007.
3. Fear, C. E., S. C. Hagness, P. M. Meaney, M. Okoniewski, and M. A. Stuchly, "Enhancing breast tumor detection with near-field imaging," *IEEE Microwave Mag.*, 48–56, March 2002.
4. Kosmas, P. and C. Rappaport, "A matched filter FDTD-based time reversal approach for microwave breast cancer detection," *IEEE Trans. Antennas Propagat.*, Vol. 54, 1257–1264, 2006.
5. Borcea, L., G. Papanicolaou, and C. Tsogka, "Adaptive interferometric imaging in clutter and optimal illumination," *Inverse Problems*, Vol. 22, 1405–1436, 2006.
6. Irishina, N., M. Moscoso, and O. Dorn, "Detection of small tumors in microwave medical imaging using level sets and MUSIC," *PIERS Proceedings*, 43–47, USA, March 26–29, 2006.
7. Irishina, N., M. Moscoso, and O. Dorn, "Microwave imaging for early breast cancer detection using a shape-based strategy," *IEEE Trans. Biomed. Eng.*, in press, 2009.
8. Irishina, N., O. Dorn, and M. Moscoso, "A level set evolution strategy in microwave imaging for early breast cancer detection," *Computers and Mathematics with Applications*, Vol. 56, 607–618, 2008.
9. Winters, D. W., E. J. Bond, B. D. Van Veen, and S. C. Hagness, "Estimation of the frequency-dependent average dielectric properties of breast tissue using a time-domain inverse scattering technique," *IEEE Transactions on Antennas and Propagation*, Vol. 54, 3517–3528, 2006.

SQUIDS for Magnetic Resonance Imaging at Ultra-low Magnetic Field

A. N. Matlashov, V. S. Zotev, R. H. Kraus, Jr., H. Sandin,
A. V. Urbaitis, P. L. Volegov, and M. A. Espy
Los Alamos National Laboratory, Applied Modern Physics Group,
MS D454, Los Alamos, NM 87545, USA

Abstract— Nuclear magnetic resonance methods are widely used in medicine, chemistry and industry. One application area is magnetic resonance imaging or MRI. It is among the most effective diagnostic tools in medicine. Modern medical MRI scanners use strong magnetic fields. Recently it has become possible to perform NMR and MRI in ultra-low field regime that requires measurement field strengths only of the order of 1 gauss. These ultra-low field techniques exploit the advantages offered by superconducting quantum interference devices or SQUIDS. We describe the world's first multichannel SQUID-based instruments that are capable of performing ULF MRI for different applications.

1. INTRODUCTION

Superconducting quantum interference device or a SQUID is the most sensitive detector of magnetic flux known [1, 2]. SQUIDS can be used for precision measurements of any kind of physical values or signals that can be transformed into magnetic flux [3]. For instance, extremely sensitive devices for measuring magnetic field and field gradients can be built using SQUIDS. The first practical SQUID magnetometer was invented in mid 60s and used in 1969 for a magnetocardiogram [4]. This invention created new research field called 'Biomagnetism' — investigations of magnetic fields generated by living organisms [5]. Magnetoencephalography (MEG) or investigation of magnetic fields generated by the brain became one of the most important areas of Biomagnetism [6]. Its clinical application, however, has been impeded by the need to superpose the MEG-localized neuronal activity with anatomical information obtained using a separate MRI scanner. Acquiring functional (MEG) and anatomical (MRI) data with two separate instruments leads to significant co-registration errors [7]. ULF MRI became a promising new method for structural brain imaging that can be done simultaneously with MEG using the same instrument [8].

Conventional MRI instruments use strong magnetic fields for nuclear spin polarization and Faraday coil variants for signal detection. NMR signal strength and frequency is proportional to the strength of the polarizing field. In addition, the sensitivity of Faraday coil based receivers increases with frequency. The common trend in NMR and MRI instrumentation is the pursuit of the highest possible field strength. Although high field enhances signal strength, it also places significant restrictions on many applications.

Recently it has become possible and practical to perform MRI at microtesla-range magnetic fields, the so-called ultra-low field (ULF) regime; see for example [9]. The drawback of this method, the low signal intensity, can be mitigated by sample pre-polarization and the use of ultra-sensitive detectors such as SQUIDS. The simplified field generation allows flexibility in pulse sequences such as measurement field reversal and the ability to trivially change field strength. In contrast to conventional MRI, relative homogeneity of the measurement field is not crucial, because microtesla-range magnetic fields of even modest relative homogeneity are highly homogeneous on the absolute scale. SQUID sensing technology is a key component for Biomagnetism instrumentation. Modern MEG systems have a few hundred SQUID detectors and operate inside large magnetically shielded rooms. Such SQUID arrays can be used to record MEG signals and acquire anatomical images by means of ULF MRI.

Another promising ULF MRI application is detection of liquid explosives at airport security checkpoints [10]. We present recent results from a ULF MRI system that was designed for the non-invasive inspection of liquids at airports. The system utilizes many of the advantages of ULF MR, in particular exploiting the power of MR relaxometry to fingerprint materials, the relatively simple MRI instrumentation suitable for the airport setting, and the ability to perform imaging through metal foils and cans. While relaxometry is used to classify materials as "threat" or "benign", ULF MR imaging allows examination of multiple bottles simultaneously and without opening. Such ULF MRI system was built and tested in Albuquerque airport in 2008.

2. METHOD

A typical ULF MRI instrument consist of the following basic components: one or more pre-polarization field coils, one coil set to produce uniform measurement field, three magnetic gradient coil sets, and SQUID-based gradiometers (inside a liquid helium cryostat) for signal reception. The pre-polarization field B_P should be as strong as possible for each particular application. It can be relatively non-uniform, for instance, 10–30% non-uniformity is good enough. It makes such coils inexpensive. The relative non-uniformity of the measurement field B_M should be about 0.1% or lower. B_M is oriented perpendicular to the pre-polarizing coil axis. Three coil sets generate encoding gradients G_X , G_Y and G_Z similar to conventional MRI systems. One or more SQUID gradiometers are placed inside a liquid helium cryostat in close proximity to a sample. The gradiometer design is very similar to that used for biomagnetic research with only one important difference — a protection circuit should be used to suppress transient from pulsing pre-polarizing field that can damage SQUID sensor. To decrease the Earth's magnetic field and ambient magnetic noise, a ULF MRI system is placed inside a large magnetic shield. Alternatively, 3D compensation coils can be used.

3. INSTRUMENTS

3.1. Medical Ultra-low Field MRI System

The system we have developed for simultaneous ULF MRI and MEG measurements, described in detail elsewhere [11, 12], includes seven second-order axial gradiometers connected to SQUID sensors. The gradiometers have 37 mm diameter and 60 mm baseline. They are placed parallel to one another with one gradiometer in the middle and six others surrounding it in a hexagonal pattern shown in Figure 1(a). The seven channels are installed at a flat bottom of a fiberglass cylindrical cryostat. The cryostat is filled with 14 liters of liquid helium and can keep SQUIDS at temperature 4K for one week. The distance between the gradiometers and the outside cryostat surface is about 20 mm. This is how close the gradiometers can be located to room temperature objects. The cryostat is positioned along the Y -axis about 30 mm above the center of the coil system. A human subject is placed on a bed along the Z -axis with the head between the B_P coils and touching the bottom of the cryostat.

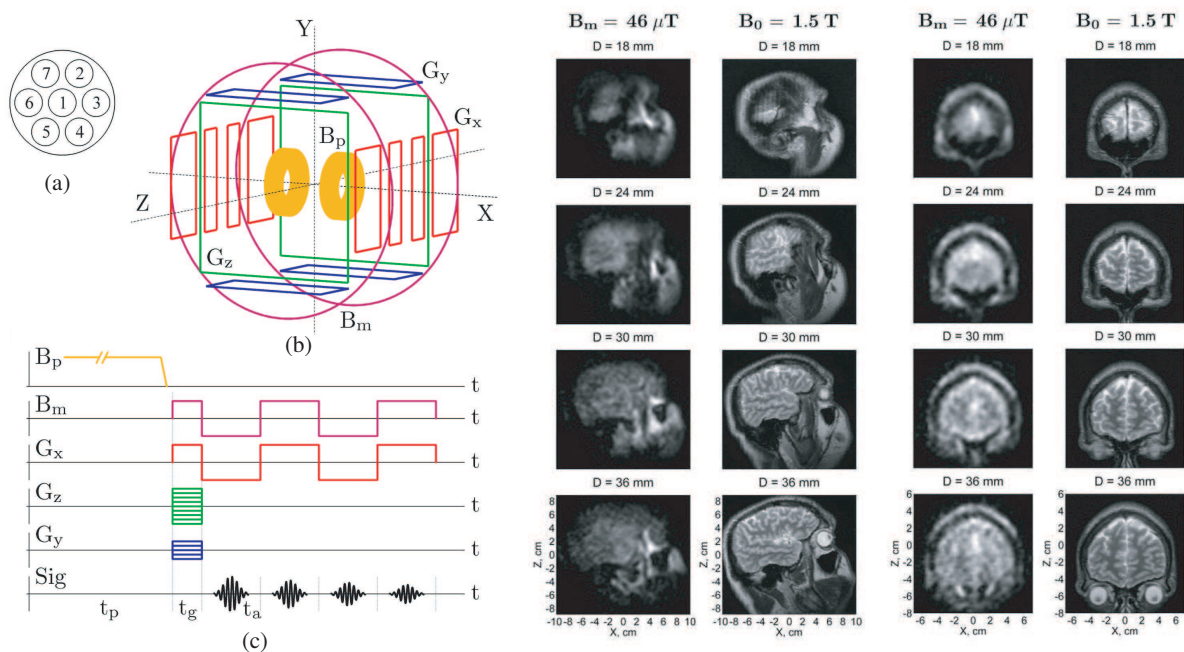


Figure 1: Design and performance of the 7-channel ULF MRI system for medical imaging [8]. Left: Seven gradiometers position (a), Coils shapes and positions (b), Fields and gradients sequences (c). Right: MR images of the human brain recorded at 46 μ T using ULF MRI technique and at 1.5 T using conventional medical MRI scanner. Parameter D is the depth of each image layer.

Schematic layout of the coil system for 3D ULF MRI is exhibited in Figure 1(b). The system includes five sets of coils. A pair of round Helmholtz coils, 120 cm in diameter, provides 46 μT measurement field B_M along the Z -axis at 750 mA. Three sets of coils generate three gradients for 3D Fourier imaging. The longitudinal gradient $G_z = dB_z/dz$ is produced by two 80 cm square Maxwell coils. The magnitude of this gradient at 1 A current is 120 $\mu\text{T}/\text{m}$. A set of eight rectangular coils on two 48 cm \times 96 cm frames orthogonal to the X -axis creates the transverse gradient $G_x = dB_z/dx$. The G_x strength is 80 $\mu\text{T}/\text{m}$ at 1 A. The second transverse gradient, $G_y = dB_z/dy$, is generated by a set of four rectangular coils on two 62 cm \times 96 cm frames orthogonal to the Y -axis. The magnitude of G_y is 140 $\mu\text{T}/\text{m}$ at 1 A. Each of these coil sets is symmetric with respect to the center of the system. The system as a whole is carefully centered inside a two-layer magnetically shielded room designed for conventional biomagnetic applications.

The imaging procedure is described in detail elsewhere [11, 12]. The prepolarization time t_p was 1 s, and the pre-polarizing field B_P about 30 mT along the X -axis. The measurement field B_M along the Z -axis corresponded to Larmor frequency about 2 kHz. The encoding t_g and acquisition t_a times were 28 ms and 56 ms, respectively. The frequency encoding gradient G_x had $\pm 140 \mu\text{T}/\text{m}$ values. The phase encoding gradient G_z had maximal values $\pm 140 \mu\text{T}/\text{m}$ with 61 phase encoding steps. A total of 11 phase encoding steps were taken for the Y -direction, with the maximal gradient values $G_y = \pm 70 \mu\text{T}/\text{m}$. The described sequence provided 3 mm \times 3 mm \times 6 mm imaging resolution. Results of a human brain imaging experiment [8] with the described system are exhibited in Figure 1 (right).

3.2. Liquid Explosives Detection ULF MRI — MagViz System

The design of the MagViz instrumentation is shown schematically in Figure 2 [10]. The MagViz system uses seven second-order wire-wound gradiometer pick-up coils, which are 90 mm diameter and 90 mm baseline. The arrangement of the gradiometers is the same as in Figure 1(a). The intrinsic noise of the gradiometers and the commercial cryostat is about 0.5 fT/ $\sqrt{\text{Hz}}$, although external noise sources increase the total system noise at 3.2 kHz measurement frequency to about 1.5 fT/ $\sqrt{\text{Hz}}$. Such noise sources include the gold-plated radio frequency shield around the cryostat, the measurement field and gradient electronics, feedback electronics, etc. We currently work on reducing the system noise, and expect to achieve sub-femtotesla magnetic field resolution.

Figure 2 shows the arrangement of magnetic fields and gradient generation coils. The pre-polarization coil, generating the field B_P as high as 50 mT in a sample volume, is cooled with a fluorine-based industrial coolant, FluorinertTM, allowing continuous system operation without substantial heating. Fluorinert was chosen instead of water for cooling to avoid hydrogen NMR signal background. After some pre-polarization time (ranging between 1 and 3 seconds), the B_P field is turned off with a ramp-down time of 10 ms and the 75 μT measurement field B_M is applied perpendicular to B_P to induce nuclear spin precession. A measurement field echo technique, which would be impossible with a conventional MRI system, is used to reduce the effects of magnetic field inhomogeneity.

The encoding scheme is based on the 3D Fourier protocol with a frequency encoding gradient $G_x = dB_z/dx$ and two phase encoding gradients, $G_z = dB_z/dz$ and $G_y = dB_z/dy$. The following imaging parameters were used in the present work: $G_x = \pm 60 \mu\text{T}/\text{m}$, $|G_z| \leq 24 \mu\text{T}/\text{m}$, 9 encoding

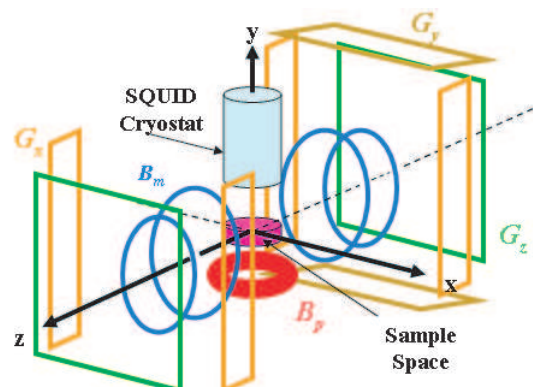


Figure 2: Schematic of the MagViz system. One pair of G_y gradient coils is not shown for clarity. Seven SQUID gradiometers are installed inside a fiberglass cryostat.

steps, $|G_y| \leq 7 \mu\text{T/m}$, 3 steps, $t_p = 1\text{ s}$ and 3 s , $t_g = 50\text{ ms}$, and $t_a = 85\text{ ms}$. The measurement field and gradient sequence is the same as in Figure 1(c). The system is placed inside a two-layer magnetic shield. A conveyor system through the shield is used for sample handling. The actual MagViz hardware is shown in Figure 3. Sample photographs and corresponding MR images are shown in Figure 4. Red and yellow ovals indicate detected threats (highly concentrated hydrogen peroxide) inside bottles and in one of the two aluminized milk packages.



Figure 3: Photograph of the inside of the MagViz system.

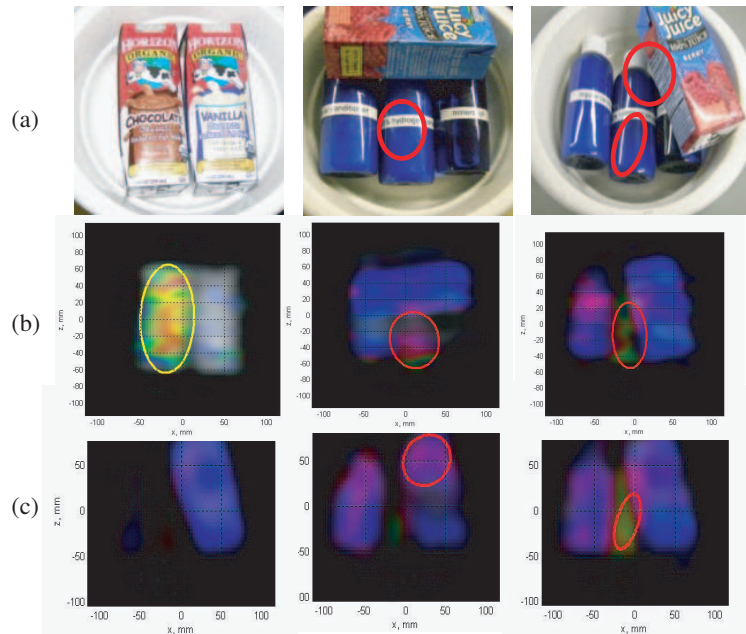


Figure 4: Row (a): photographs of items. (b): 2-D images with threat detection. (c): 3-D slices through the items shown in row (a), far right.

4. CONCLUSION

While we are enthusiastic about the potential of MagViz-like systems for airport security, we believe the real potential of ULF MRI may extend greatly beyond this application. A simple, mobile, inexpensive MRI system could open up many new markets for MRI. For example, because of the large cost of conventional MRI magnets, many people in resource-poor locations do not have access to MRI. Moreover, the ULF MR approach may provide open MRI systems for emergency rooms and field hospitals. Without any hardware modification at all, the MagViz system has already shown itself to be a capable imaging device. While the spatial resolution remains below that of conventional MRI scanners, we expect this to improve as we increase the pre-polarization field and reduce system noise. The real potential of ULF MRI as a medical research tool is yet to be determined.

ACKNOWLEDGMENT

The authors gratefully acknowledge the support of the U.S. Department of Energy, the U.S. National Institutes of Health and the U.S. Department of Homeland Security for this work. We also thank the members of the SQUID Team as well as the Engineering Team at LANL who contributed to the design and manufacturing of the ULF MRI instruments.

REFERENCES

1. Clarke, J. and A. Braginski, *The SQUID Handbook*, WILEY-VCH Verlag GmbH & Co. KGaA, Vol. 1, Weinheim, 2004.
2. Weinstock, H., *SQUID Sensors: Fundamentals, Fabrication and Applications*, Kluwer Academic Publishers, 1996.
3. Clarke, J. and A. Braginski, *The SQUID Handbook*, WILEY-VCH Verlag GmbH & Co. KGaA, Vol. 2, Weinheim, 2006.
4. Cohen, D., E. A. Edelsack, and J. E. Zimmerman, "Magnetocardiograms taken inside a shielded room with a superconducting point contact magnetometer," *Appl. Phys. Lett.*, Vol. 16, 278–280, 1970.
5. Williamson, S. J., M. Hoke, G. Stroink, and M. Kotani, *Advances in Biomagnetism*, Plenum Press, New York, 1989.
6. Hamalainen, M., R. Hari, R. J. Imoniemi, J. Knuutila, and O. V. Lounasmaa, "Magnetoencephalography — Theory, instrumentation and applications to noninvasive studies of the working human brain," *Rev. Mod. Phys.*, Vol. 65, 413–497, 1993.
7. Adjamian, P., et al., "Co-registration of magnetoencephalography with magnetic resonance imaging using bite-bar fiducials and surface-matching," *Clin. Neurophysiol.*, Vol. 115, 691–698, 2004.
8. Zotev, V. S., et al., "Microtesla MRI of the human brain combined with MEG," *Journal of Magn. Res.*, Vol. 194, No. 1, 115–120, 2008.
9. Clarke, J., et al., "SQUID-detected magnetic resonance imaging in microtesla fields," *Annu. Rev. Biomed. Eng.*, Vol. 9, 2.1–2.25, 2007.
10. Espy, M., et al., "Applications of ultra-low field magnetic resonance for imaging and materials studies," *IEEE Trans. on Appl. Supercond.*, accepted for publication, 2009.
11. Zotev, V. S., A. N. Matlashov, P. L. Volegov, A. V. Urbaitis, M. A. Espy, and R. H. Jr. Kraus, "SQUID-based instrumentation for ultra-low-field MRI," *Superconducting Science and Technology*, Vol. 20, No. 11, S367–S373, 2007.
12. Zotev, V. S., et al., "Multi-channel SQUID system for MEG and ultra-low-field MRI," *IEEE Trans. on Applied Superconductivity*, Vol. 17, No. 2, 839–842, 2007.

X-rays Source Using Thermal Excitation of Pyroelectric Crystal for Medical Application

S. Fukao¹, Y. Nakanishi¹, Y. Guan¹, Y. Sato¹, Y. Ito², and S. Yoshikado¹

¹Department of Electronics, Doshisha University, Kyoto, Japan

²Institute for Chemical Research, Kyoto University, Kyoto, Japan

Abstract— In order to develop miniaturized X-ray devices that provide localized X-ray irradiation for medical applications, the dependences of the X-ray intensity on the ambient gas pressure and the type of case material were investigated for LiNbO₃ single crystals polarized parallel to the *c*-axis for N₂ gas pressures in the range of approximately 7×10^{-3} to 5 Pa. X-ray irradiation was performed with no case and with cases constructed from oxygen-free copper, aluminum, nickel, stainless steel, and polytetrafluoroethylene. For cases of the same size, the pressure dependence of the X-ray intensity was independent of the type of case material and it had a local maximum at a pressure of approximately 4.2 Pa. In high vacuums, the X-ray intensity increased as the pressure was reduced. Based on these results, stainless steel, which is chemically stable, nonmagnetic and prevents X-ray leakage, is considered to be the most suitable material for constructing cases for medical devices.

1. INTRODUCTION

A high intensity electric field can be generated by varying the temperature of a polarized pyroelectric single crystal, such as LiNbO₃ or LiTaO₃, in low vacuums [1–7]. The gas molecules around the crystal are ionized by this electric field, producing electrons and positive ions. It has been reported that both white X-rays (i.e., continuous spectrum X-rays) and characteristic X-rays specific to the elements of the crystal or target metal for X-ray radiation are radiated by bremsstrahlung generated by the electrons colliding with a target. Electrons are accelerated by the electric field generated by the electric dipole moments in the crystal and the surface charges on the crystal [1–12]. Such devices can be miniaturized because they do not require an electron gun (which is an electron source) or an external high voltage source. For example, it will be possible to develop a fiberscope that uses a compact X-ray radiation source. Such a fiberscope produces soft X-rays, which interact strongly with biological tissue, so that it can be used to treat skin cancer and cancers of internal organs such as the stomach and the large intestine by directly destroying cancer cells. It can also destroy cavity-causing bacteria.

The X-ray radiation mechanism can be explained as follows. An effective surface charge is generated by intrinsic polarization on the intrinsic surface of a pyroelectric crystal due to poling. However, this effective surface charge is electrically neutralized by the adsorption of ions from the ambient gas, which is in equilibrium with the crystal surface. Hence, the net surface charge becomes zero and no electric field is formed. If the crystal temperature is altered, the intrinsic polarization changes due to a small displacement of the ions in the crystal. However, the adsorption and desorption times of the ions are much longer than the time for the intrinsic polarization to change so that the crystal surface acquires a net charge. For example, when a negatively charged surface ($-z$ -surface) of the crystal is placed opposite a target and its temperature is increased, the $-z$ -surface acquires a net positive charge. This is because the negative electric charge of the $-z$ -surface decreases, causing positive ions to be desorbed, which delays the temperature change on the $-z$ -surface of the crystal. On the other hand, the $-z$ -surface acquires a net negative charge when the temperature is reduced. An electric field is generated by the net surface charge on the $-z$ -surface of the crystal. The gas molecules are ionized by this electric field, producing electrons and positive ions. Electrons are then accelerated by the electric field towards the target and the case, and X-rays are generated when the electrons collide with them. When the $-z$ -surface of the crystal is placed opposite a target, X-rays are radiated from the $-z$ -surface when the temperature is increased and they are radiated from the target and the case when the temperature is reduced.

In order for such an X-ray source that uses a pyroelectric crystal to be downsized so that it can be used in medical devices that provide local irradiation of X-rays, the distance between the crystal and the case needs to be reduced. In addition, the case material must prevent leakage of X-rays so that it is harmless to humans. Thus, it is necessary to consider the case material and the target separately. The electric field distribution generated by the crystal is thought to vary with the

distance between the case and crystal. When the target and the case are constructed from different materials, characteristic X-rays of both materials may be generated by bremsstrahlung produced by electrons colliding with the target and the case. Thus, in this study, to clarify the contribution of the case to the emitted X-rays, the X-ray intensities were measured without a case and with cases constructed from different materials, including both metals and insulator. Aluminum (Al) is a suitable target for producing soft X-rays. However, oxygen-free copper (Cu) was selected as the target in this study, because silicon (Si) semiconductor detectors have low detection sensitivities to the characteristic X-rays of aluminum.

2. EXPERIMENTAL METHOD

A z -cut single crystal of LiNbO_3 (Yamaju Ceramics, $10 \times 10 \text{ mm}^2$ area, 5 mm thick, nonstoichiometric composition) polarized along the c -axis (z -axis) was used. The positively charged surface ($+z$ -surface) of the crystal was pasted on a Peltier device with silver (Ag) paste through a $10\text{-}\mu\text{m}$ -thick Cu or platinum (Pt) foil. The crystal temperature was changed from 5 to 70°C by supplying a triangular-wave bias voltage to the Peltier device. A vacuum chamber made of stainless steel (SUS 304, hereafter SUS) with an inner diameter of 146 mm and an inner height of 164 mm was used. A Cu foil with a thickness of $10\text{ }\mu\text{m}$ and a diameter of 37 mm was used as the target. The crystal with a Peltier device was placed at the center of a hollow cylindrical case with an inner diameter of 26 mm and a height of 21 mm (see Fig. 1). The case materials used were Cu, Al, nickel (Ni), SUS with various work functions and chemical properties and polytetrafluoroethylene (PTFE) (which is chemically inert, has a low permittivity and is an electrical insulator) The $-z$ -surface of the crystal was set parallel to the target at a distance of 27 mm. The ambient gas used was nitrogen (N_2) and the pressure P in the vacuum chamber was set in the range 7×10^{-3} to 5 Pa. The gas pressure was measured using an absolute pressure gauge (MKS Baratron 127), which functions independently of the ambient gas species at low vacuums, or a hot-cathode ionization gauge (ULVAC, GI-TL3) for high vacuums. When the hotcathode ionization gauge was used, a constant pressure was maintained prior to measuring the X-ray intensity, and the gauge was turned off during measurements to eliminate the effect of thermal electrons. The target, cylinder, and the Cu or Pt foil under the $+z$ -surface of the crystal were all electrically grounded. The spectrum of the X-rays that penetrated the Cu target was measured using a Si semiconductor detector (Amptek, XR-100CR, detector dimensions: area of 7 mm^2 , $300\text{ }\mu\text{m}$ thick) and a multichannel analyzer (Laboratory Equipment Corporation, 2100 C/MCA). An iron radioisotope (^{55}Fe) was used to calibrate the X-ray energy. When the number of photons incident on the detector exceeds approximately 10^4 counts per second (cps), the input-output characteristics become nonlinear. Thus, a 0.5-mm-thick lead (Pb) plate with an approximately 0.3 mm diameter hole in the center was inserted between the beryllium (Be) window of the detector and the target. The X-ray intensity corresponding to a detection area of 7 mm^2 was then obtained by multiplying the measured intensity by a factor of approximately 100. Furthermore, at low and high energies, where the detection sensitivity was low, the X-ray intensity was calibrated using an energy calibration curve. The temperature of the lower part of the crystal was measured using a thermosensitive register sensor ($10 \text{ k}\Omega$ at 20°C) attached to

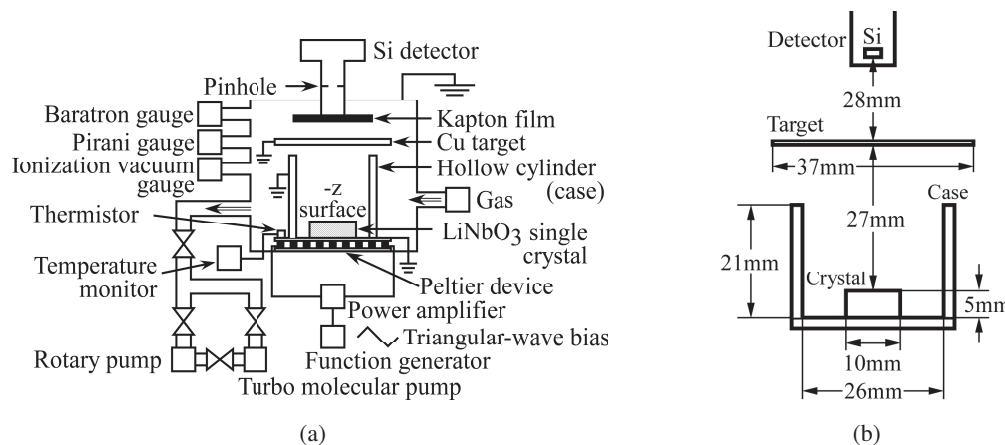


Figure 1: Schematic drawing of experimental apparatus.

the Cu or Pt foil. The crystal temperature was increased to 70°C at a rate of 0.13°C/s and reduced to 5°C at a rate of 0.13°C/s. This temperature cycle was repeated, with the duration of each cycle being 1000 s (the heating and cooling processes were both approximately 500 s in duration).

3. ELECTRIC FIELD STRENGTH GENERATED BY THE CRYSTAL

Both electric field intensity and electron density are considered necessary for generating X-rays. In this section, the maximum electric field produced by changing the crystal temperature is estimated. The electric dipoles inside a uniaxially polarized pyroelectric crystal are all aligned in one direction. Consequently, the strength of the electric field formed outside the crystal can be calculated by summing the electric field strengths generated by each electric dipole. As shown in Fig. 2, the electric field generated by the pyroelectric crystal at an arbitrary point $A(x, y, z)$ outside the crystal is considered. The area of the electric surface is $a \times b$, the thickness of the crystal (the center of which is at O) is d and the top surface is the $-z$ -surface. The center point of each electric dipole inside the crystal is defined as $B(x', y', z')$. The strength vector of the electric field $\vec{E}(A)$ at $A(x, y, z)$ is given by

$$\vec{E}(A) = -\frac{1}{4\pi\epsilon_0} \int_{x'=-\frac{a}{2}}^{\frac{a}{2}} \int_{y'=-\frac{b}{2}}^{\frac{b}{2}} \int_{z'=-\frac{d}{2}}^{\frac{d}{2}} \frac{-3(\vec{r} \cdot \vec{P})\vec{r} + r^2\vec{P}}{r^5} dx' dy' dz', \quad (1)$$

where ϵ_0 is the permittivity in a vacuum, \vec{r} is the position vector of A relative to B , r is the distance between A and B and \vec{P} is the polarization vector inside the crystal. When the crystal is polarized along the z -axis, \vec{P} is given by

$$\vec{P} = (0, 0, -P). \quad (2)$$

For a LiNbO₃ single crystal, the pyroelectric coefficient P is 7.6 nC/cm²/K [6].

The maximum strength of the electric field formed by changing the crystal temperature can be estimated using Equations (1) and (2). The surface charge of the crystal is electrically neutralized at the first state in the low vacuum range. The rate of change of the maximum strength of the electric field generated by changing the temperature can be calculated using Equations (1) and (2). The rates of change of the maximum strength of electric field at the center of the $-z$ -surface, at the inner wall of the case (which is the same height as the $-z$ -surface) and the center of the target are approximately 28 kV/cm/K, 1.8 kV/cm/K and 0.25 kV/cm/K, respectively. For example, the maximum electric field generated at the center of the $-z$ -surface is approximately 1 MV/cm if the temperature is changed by 70 K. However, the actual electric field generated by the crystal is lower than the maximum value calculated above because positive ions are adsorbed on the $-z$ -surface of the crystal due to ionization of the ambient gas that occurs when the temperature is changed. On the other hand, the number of electrons adsorbed on the $-z$ -surface in a high vacuum decreases with decreasing pressure. It is estimated that a high-intensity electric field will be generated in a high vacuum because the number of positive ions adsorbed on the $-z$ -surface due to the intrinsic polarization change caused by the change in the temperature is much fewer in a high vacuum than in a low vacuum. For a LiNbO₃ single crystal, the intrinsic polarization P is approximately 75 $\mu\text{C}/\text{cm}^2$ at 20°C [6]. When the intrinsic surface charge is not electrically neutralized by positive ions adsorbed on the crystal surface, the maximum strengths of the electric field generated by the

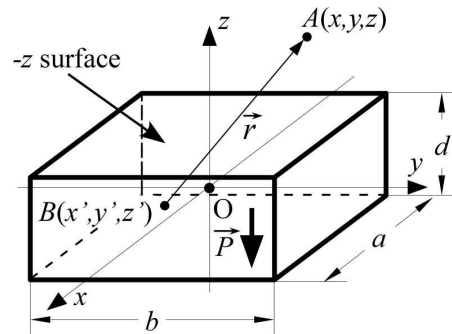


Figure 2: Diagram for calculating the electric field strength generated by a uniaxially polarized LiNbO₃ single crystal.

crystal at the center of the $-z$ -surface, at the inner wall of the case (which is the same height as the $-z$ -surface) and at the center of the target are calculated using Equations (1) and (2) to be approximately 280 MV/cm, 17 MV/cm and 2.5 MV/cm, respectively.

4. RESULTS AND DISCUSSION

Figures 3(a) and (b) show the energy characteristics of the X-ray intensity (i.e., the X-ray spectra) per cycle and the time dependences of the integrated X-ray intensity in the energy range 1 to 20 keV for a SUS case in N_2 gas at pressures of approximately 4.2 and 7×10^{-3} Pa, respectively. The energies of the X-ray emission lines for each material are given in Table 1 [13]. The X-ray spectra for a pressure of 7×10^{-3} Pa shows the same tendencies as those for a pressure of 4.2 Pa, although the integrated X-ray intensity for a pressure of 7×10^{-3} Pa is approximately one order of magnitude smaller than that for a pressure of 4.2 Pa. The characteristic X-rays of K_α and K_β for the Cu target were detected at 8.041 keV and 8.905 keV respectively, and characteristic X-ray of K_α for Fe in the SUS case was detected at 6.399 keV for both pressures.

Table 1: Energies (in keV) of X-ray emission lines for principal K- and L-shell emission lines.

Element	K_α	K_β	L_α	L_β
H	0.054	–	–	–
C	0.109	–	–	–
O	0.525	–	–	–
F	0.677	–	–	–
Al	1.487	1.557	–	–
Cr	5.412	5.947	0.573	0.583
Mn	5.895	6.490	0.637	0.649
Fe	6.399	7.058	0.705	0.719
Co	6.925	7.649	0.776	0.791
Ni	7.472	8.265	0.852	0.869
Cu	8.041	8.905	0.930	0.950
Pt	66.201	75.748	9.434	11.117

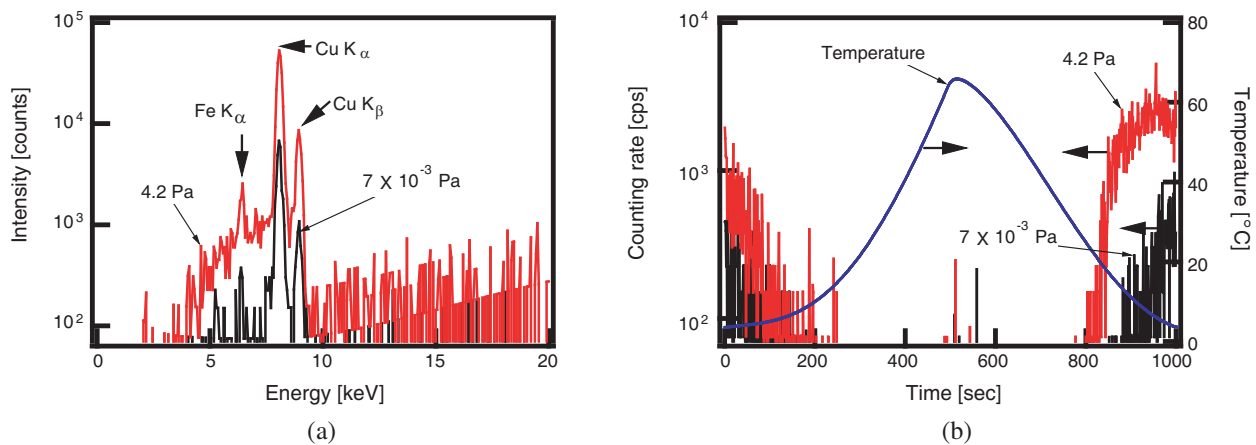


Figure 3: (a) Spectra of X-rays per cycle and (b) time dependences of the integrated X-ray intensity in the energy range 1 to 20 keV and the crystal temperature using a SUS case in N_2 gas at pressures of approximately 4.2 and 7×10^{-3} Pa.

4.1. X-rays Radiation for a Low Vacuum

Figures 4(a) and (b) show the pressure dependences of the integrated X-ray intensity in the energy range 1 to 20 keV for each case material in N_2 gas for low vacuums (between 1 and 5 Pa) when the

temperature was increased and during one temperature cycle, respectively. As shown in Fig. 4(a), when the case material is a metal, the logarithm of the integrated X-ray intensity when the temperature was increased was proportional to the pressure. The logarithm of the integrated X-ray intensity with no case was also proportional to the pressure, but the pressure dependence curve was shifted to a lower pressure. When the case material was PTFE, X-rays were not detected when the temperature was increased. As shown in Fig. 4(b), the integrated X-ray intensity during one temperature cycle showed a local maximum at a pressure (P_{\max}) of approximately 4.2 Pa and this pressure was independent of the case material. The integrated intensity of the characteristic X-ray for the case material was proportional to the pressure for pressures $P > P_{\max}$, but not for pressures $P < P_{\max}$. Although P_{\max} for the PTFE case, which is an insulator and has a low permittivity, was the same as that for the metal cases, the integrated X-ray intensity I_{\max} at a pressure of P_{\max} for the PTFE case was approximately 1.5 times higher than that for the metal cases. P_{\max} when no case was used was half that for the PTFE case, and I_{\max} with no case was 1.5 times higher than that with the PTFE case.

Both electric field intensity and electron density are considered to be necessary for generating X-rays. Therefore, the integrated X-ray intensity I is assumed to be proportional to the product of the electric field intensity and the number of electrons in the space between the crystal and target. If the contribution of multiple electrons emitted from the pyroelectric crystal is not taken into account [10], I is given by [7]

$$I = -C_1 \left(P - \frac{1}{2C_2} N_S \right)^2 + \frac{1}{4} \frac{C_1}{C_2^2} N_S^2, \quad (3)$$

where C_1 is a proportionality constant and N_S is the number of surface charges on the $-z$ -surface without adsorption ions. $C_2 = N^+ / P \cdot N^+$ is the number of positive ions adsorbed on the $-z$ -surface and it is given by

$$N^+ = C_3 P \exp(-\alpha E_i), \quad (4)$$

where C_3 is a proportionality constant, α is a constant and E_i is the first ionization energy of the ambient gas molecules. N^+ is proportional to the pressure. The electric field generated by the crystal was formed over the entire volume enclosed by the target and the case. However, the mean free path of an electron lies between 6.4 and 1.3 mm for pressures between 1 and 5 Pa in low vacuums [14]. This result indicates that the mean free path of an electron is much shorter than the distance between the target and the crystal (see Fig. 1(b)). Therefore, it is speculated that the electrons that contribute to the X-ray radiation are near the target or the case. Similarly, the positive ions adsorbed on the $-z$ -surface are near the crystal. From Equation (1), I is found to have a maximum value at P_{\max} .

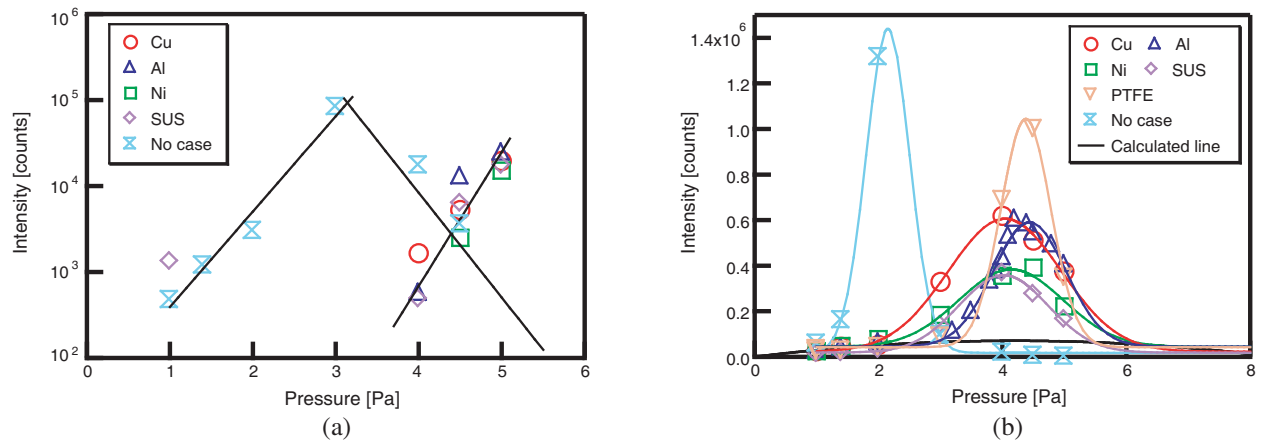


Figure 4: Pressure dependence of the integrated X-ray intensity with Cu, Al, Ni, SUS and PTFE cases and without a case in N_2 gas at low pressures. (a) For increasing temperature, (b) for one temperature cycle.

$$P_{\max} = \frac{N_S}{2C_2}. \quad (5)$$

P_{\max} is independent of the area of the $-z$ -surface of the crystal, S , because both N_S and C_2 are proportional to S . As discussed later, the reason for the shift in P_{\max} to a low pressure when

the case is removed is speculated to be (based on Equation (5)) that the number of positive ions adsorbed on the $-z$ -surface increases.

Equation (3) indicates that the integrated X-ray intensity I is a quadratic function of P , which is upwardly convex. Thus, the integrated X-ray intensity is predicted to have a local maximum at P_{\max} and become zero at $2P_{\max}$ [7]. The solid line shown in Fig. 4(b) represents the values calculated from Equation (3), and the measured values are almost equal to the calculated lines for low pressures. However, the measured values were larger than the calculated values at pressures near P_{\max} . I was fitted by a Gaussian function given by Equation (6) at pressures near P_{\max} .

$$I = C_4 + C_5 \exp \left[-\frac{(P - C_6)^2}{C_7^2} \right], \quad (6)$$

where C_4 , C_5 , C_6 and C_7 are constants. When C_5 is $\exp(C_8)$ and C_4 is assumed to be $C_4 \ll \exp[-(P - C_6)^2/C_7^2 + C_8]$, Equation (6) can be written as

$$\log_e I = -\frac{(P - C_6)^2}{C_7^2} + C_8. \quad (7)$$

Equation (7) indicates that the logarithm of the integrated X-ray intensity I is a quadratic function of P , which is upwardly convex. The reason why I is described by Equation (7) can be explained as follows. An X-ray that irradiates the target and inner wall of the case undergoes multiple reflections and causes an Auger electron to be emitted from the target or the inner wall of the case. This electron is accelerated by the high electric field and collides with the target and the case. Consequently, an X-ray is generated by this Auger electron and undergoes multiple reflections. The amount of fluorescent X-ray radiation depends on the atomic weights of the target and the case materials, whereas the amount of Auger electrons produced is independent of them. Therefore, it is speculated that the number of Auger electrons increases markedly as the integrated X-ray intensity increases and that the X-ray intensity increases markedly as the pressure approaches P_{\max} . At pressures $P > P_{\max}$, the X-ray intensity decreases because the number of positive ions increases, the positive ions are rapidly adsorbed on the crystal, and the electric field generated by the crystal becomes weaker [7].

Figure 5 shows the direction of the electric field vector generated by the pyroelectric crystal with no case or target when the temperature is reduced; it is calculated using Equation (1) for low vacuums. Fig. 5 also shows the positions of the positive ions and electrons generated by ionization of gas molecules caused by the electric field produced by the crystal. Fig. 6 shows the distribution of the maximum electric field strength on the upper surface ($-z$ -surface) of the crystal along the x -axis. The electric field outside the case was zero for a conductive case material that was grounded. This is because the electric field is shielded by the case. On the other hand, when the case material is PTFE, which is an insulator and has a low permittivity, the electric field outside the case was

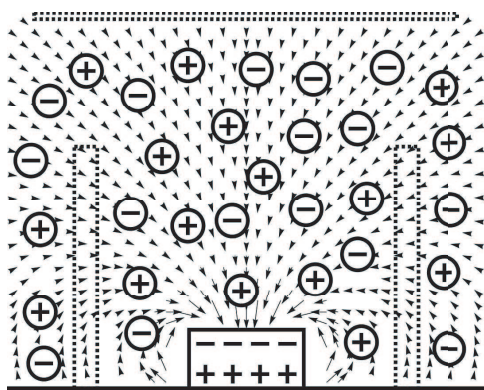


Figure 5: The electric field generated by a pyroelectric crystal without a case and a target. \oplus : positive ion, \ominus : electron.

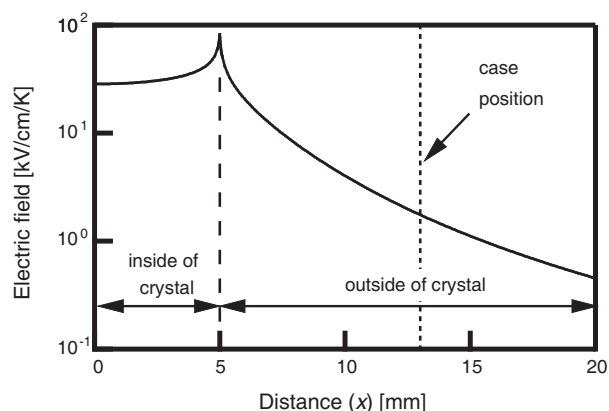


Figure 6: Dependence of the electric field strength on the distance from the crystal center when no case is used.

non-zero. However, the number of positive ions and electrons for the PTFE case is speculated to be the same as that for a conductive case material. This is because the positive ions and electrons, which are generated by ionization of gas molecules outside the PTFE case, do not move inside the PTFE case. When the case is removed, the positive ions are adsorbed on the $-z$ -surface of the crystal due to the electric field when the temperature is increased. These results suggest that C_2 in Equation (5) increases because C_2 is proportional to N^+ . Consequently, it is speculated that P_{\max} decreases. It is also speculated that the X-ray intensity increases when there is no case because the number of electrons that collide with the crystal and the target increases. These results are verified from Fig. 4(b).

4.2. X-ray Radiation for Pressures between Medium and High Vacuums

As shown in Fig. 3(a), the characteristic X-rays of K_α and K_β for the Cu target and those of K_α for Fe in the SUS case were detected at pressures below 1 Pa, which is intermediate between a medium vacuum and a high vacuum. Fig. 7 shows the pressure dependence of the integrated X-ray intensity up to high pressures. For pressures of less than 1 Pa (i.e., intermediate between medium and high vacuums), X-rays were not detected with a case when the temperature was increased, although X-rays were detected when the temperature was reduced. The integrated X-ray intensity was a minimum in the pressure range between 7×10^{-3} and 1 Pa. The integrated X-ray intensity is almost independent of the type of metal case at a pressure of 7×10^{-3} Pa. The integrated characteristic X-ray intensity of Fe, which is an element in SUS, showed the same pressure dependence as the integrated X-ray intensity in the energy range 1 to 20 keV. As shown in Fig. 3(b), when the pressure was 4.2 Pa, the time at which X-rays began to be radiated became earlier, and the maximum integrated X-ray intensity over 1 s was larger than that at a pressure of 7×10^{-3} Pa. The integrated characteristic X-ray intensity for K_α of Fe was approximately 2% of that for K_α and K_β of Cu at a pressure of 4.2 Pa. The sample stage was surrounded by an alumina plate and a Pt foil, the work functions of which are large; these were used to ground the $+z$ -surface. However, the X-ray intensities were the same.

In a high vacuum, it has been reported that the X-ray intensity increases when thermal electrons were supplied from outside [11, 12]. The integrated X-ray intensity increased by a factor of approximately 100 when the hotcathode ionization gauge was moved to at approximately 250 mm from the crystal so that thermal electrons were emitted. Thus, X-ray radiation emission in high vacuums is the rate-determining process for electron supply (electron density). It was also confirmed that the crystal generates an electric field in a high vacuum. Based on the above results, the mechanism of X-ray generation in a high vacuum is discussed as follows. The $-z$ -surface does not have a net charge because positive ions are adsorbed on the $-z$ -surface under the initial equilibrium condition at a constant temperature. However, if the crystal temperature is increased, the negative charge on the $-z$ -surface decreases and fewer intrinsic surface negative charges than positive ions. Thus, the $-z$ -surface acquires a net positive charge and an electric field is generated. The number Z of gas molecules with thermal motion that collide with a target of unit area per second is given by [14]

$$Z = \frac{1}{4}nv = \frac{1}{4} \cdot \frac{P}{k_B T} \cdot \sqrt{\frac{8k_B T}{\pi m}} = \sqrt{\frac{P^2}{2k_B T \pi m}}, \quad (8)$$

where n is the density of gas molecules, v is the average molecular speed, k_B is the Boltzmann constant, T is the gas temperature and m is the mass of a gas molecule. From Equation (8), the number of collisions Z at pressures of 7×10^{-2} Pa and 4.2 Pa are calculated to be approximately 2.0×10^{20} and 1.2×10^{23} , respectively. Because the diameter of a N_2 molecule is approximately 0.38 nm, the number of layers at pressures of 7×10^{-2} Pa and 4.2 Pa that the gas molecules collide with per second are 23 and 1.4×10^4 , respectively. The negative charge of the crystal can be neutralized by collisions of positive ions with 0.5 layer, because the charge density of the $-z$ -surface without positive ions absorbed on it is $75 \mu\text{C}/\text{cm}^2$. Therefore, the high vacuum used in this study makes it possible to completely neutralize the negative charge of the crystal due to the ionization of the gas molecules that collide with the crystal. The electrons and positive ions are generated by ionization of gas molecules adsorbed on the crystal surface due to the high electric field generated by the crystal and they are accelerated by the electric field. Consequently, electrons collide with the $-z$ -surface and positive ions collide with the target or the case. Because a positive ion has a greater mass and size than an electron, the energy of a positive ion is lost in almost instantaneously when it collides with the target, so that the positive ion does not penetrate inside

the target. Thus, the characteristic X-rays of Cu and high intensity X-rays are generated have a pulse-like temporal profile. However, the reason why these pulsed X-rays were not detected in this experiment is conjectured to be because the Si detector used in this study can only detect X-rays with energies up to 20 keV and it has a poor temporal resolution. On the other hand, the mean free paths of an electron at pressures of 0.2 Pa and 7×10^{-3} Pa are approximately 32 mm and 910 mm, respectively [14]; these paths are longer than the distance between the crystal and the target.

Balancing of the charges does not occur even if the crystal temperature is a maximum. This is because there are more positive ions than negative charges on the crystal surface. Therefore, balancing of the charge occurs when the temperature is reduced. After balancing of the charges, the number of negative charges on the crystal surface exceeds the number of positive ions adsorbed on the crystal, so that the crystal surface acquires a net negative charge and the electric field is formed in the opposite direction that generated when the temperature is increased. This electric field ionizes some of the gas molecules, which collide with the crystal and are adsorbed on the crystal surface. The generated positive ions are accumulated on the $-z$ -surface. Meanwhile, the generated electrons are accelerated toward the target and the case they collide with them generating continuous X-rays and the characteristic X-rays of the elements in the target and the case. At low pressures, the number of collisions of electrons with residual gas molecules decreases and the number of electrons that collide with the target increases. For this reason, the X-ray intensity is speculated to increase with a reduction in the pressure. If the pressure is further reduced, the number of gas molecules that collide with the $-z$ -surface of the crystal decreases. Thus, the X-ray intensity is considered to decrease due to a reduction in the number of gas molecules ionized by the electric field generated by the crystal. Fig. 7 shows that the integrated X-ray intensity increases when the PTFE case or no case is used. This result is conjectured to be due to the contribution of electrons emitted from the inner wall of the chamber by field emission. Fig. 8 shows the integrated X-ray intensity measured over 50 temperature cycles for Cu case in N_2 gas at pressures of approximately 4.0 and 7×10^{-3} Pa. The integrated X-ray intensity was almost stable. The same stability was obtained for the different pressures. When the X-ray was radiated over 50 temperature cycles, the pressure dependence of the integrated X-ray intensity was almost the same as obtained in Fig. 7.

For a miniaturized X-ray radiation source to be used in a medical device, it must emit soft X-rays. Thus, Al is suitable a material for both the target and the case. However, if the case material is Al, white X-rays with a high energies will pass through the case and leak outside. PTFE also has a risk of X-ray leakage for the same reason as Al. Moreover, Ni and Cu are unsuitable, because Ni is a magnetic material and Cu is a readily oxidizable metal. For the above reasons, the SUS is considered to be the most suitable case material, since it is chemically inert, nonmagnetic and will not leak X-rays.

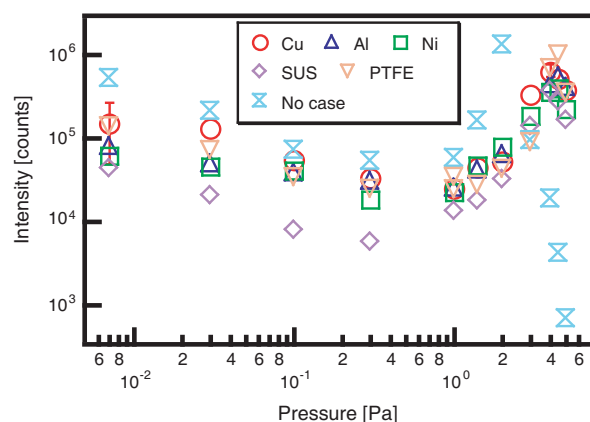


Figure 7: Pressure dependences of the integrated X-ray intensity per cycle in the energy range 1 to 20 keV for Cu, Al, Ni, SUS and PTFE cylindrical cases and with no case in N_2 gas.

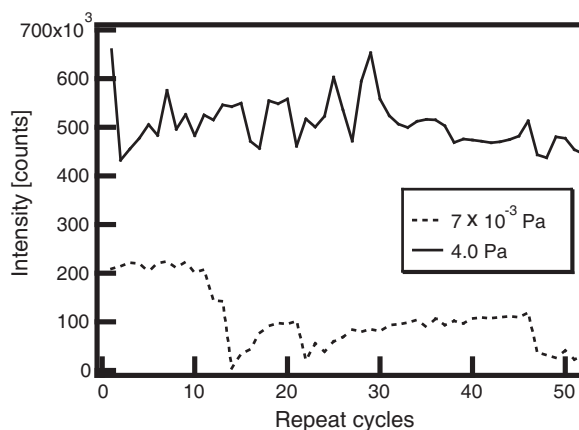


Figure 8: Integrated intensities of X-rays over 50 temperature cycles for Cu case in N_2 gas at pressures of approximately 4.0 and 7×10^{-3} Pa.

5. CONCLUSION

In a low vacuum, a high-intensity electric field is generated by changing the crystal temperature and the surrounding gas molecules are ionized by this field. Consequently, electrons and positive ions are generated. However, only the gas molecules near the target and the case were found to contribute to X-ray emission, because the mean free path of an electron is shorter than the distance between the crystal and the target. The X-ray intensity was found to be independent of the type of case material. The strength of the electric field was confirmed to decrease with increasing pressure since positive ions generated by the ionization of gas molecules are adsorbed on the $-z$ -surface.

In a high vacuum, the X-ray intensity was found to be independent of the work function of the case material because the X-ray intensity is the rate-determining factor for the number of electrons accumulated on the $-z$ -surface. The X-ray intensity was found to increase with decreasing temperature because the mean free path of an electron becomes increases and the number of electrons that collide with the target increases. However, the X-ray intensity is estimated to decrease below a certain pressure because the number of gas molecules adsorbed on the $-z$ -surface of the crystal decrease.

For applications of miniaturized X-ray radiation sources for medical applications, it was found that the optimum pressure for X-ray emission is in the low vacuum region and it is found by adjusting the pressure so that the X-ray intensity is maximized. The optimum case material is stainless steel, since it is chemically stable, nonmagnetic and prevents X-ray leakage.

ACKNOWLEDGMENT

This work was supported by the Japan Society for the Promotion of Science (JSPS).

REFERENCES

1. Brownridge, J. D., "Pyroelectric X-ray generator," *Nature*, Vol. 358, 287–288, 1992.
2. Brownridge, J. D. and S. M. Shafroth, "X-ray fluoresced high-Z (up to $Z = 82$) K x rays produced by LiNbO_3 and LiTaO_3 pyroelectric crystal electron accelerators," *Appl. Phys. Lett.*, Vol. 85, 1298–1300, 2004.
3. Brownridge, J. D. and S. Raboy, "Investigations of pyroelectric generation of x rays," *J. Appl. Phys.*, Vol. 86, 640–647, 1999.
4. Brownridge, J. D. and S. M. Shafroth, *Trends in Lasers and Electro-optics Research*, 1st Edition, Nova Science Publishers, New York, 2006.
5. Fukao, S., J. Kondo, Y. Nakanishi, Y. Ito, and S. Yoshikado, "Excitation of X-rays using polarized LiNbO_3 single crystal," *Key Eng. Mater.*, Vol. 301, 205–208, 2005.
6. Nakanishi, Y., H. Mizota, Y. Ito, M. Takano, S. Fukao, S. Yoshikado, K. Ohyama, K. Yamada, and S. Fukushima, "Relation between x-ray emission mechanism and crystal structure in LiNbO_3 ," *Phys. Scr.*, Vol. 73, 471–477, 2006.
7. Fukao, S., Y. Nakanishi, T. Mizoguchi, Y. Ito, and S. Yoshikado, "Radiation of X-rays using polarized LiNbO_3 single crystal in low-pressure ambient gas," *IEEE TUFFC Piezoelectric Ceramics*, in press.
8. Geuther, J., Y. Danon, and F. Saglime, "Nuclear reactions induced by a pyroelectric accelerator," *Phys. Rev. Lett.*, Vol. 96, 054803, 2006.
9. Brownridge, J. D. and S. M. Shafroth, "Self-focused electron beams produced by pyroelectric crystals on heating or cooling in dilute gases," *Appl. Phys. Lett.*, Vol. 79, 3364–3366, 2001.
10. Brownridge, J. D., S. M. Shafroth, D. W. Trott, B. R. Stoner, and W. M. Hooke, "Observation of multiple nearly monoenergetic electron production by heated pyroelectric crystals in ambient gas," *Appl. Phys. Lett.*, Vol. 78, 1158–1159, 2001.
11. Fukao, S., Y. Nakanishi, T. Mizoguchi, Y. Ito, T. Nakamura, and S. Yoshikado, "Radiation of X-rays using uniaxially polarized LiNbO_3 single crystal," *Mater. Res. Soc. Symp. Proc.*, Vol. 1034, 1034-K11-11, 2008.
12. Fukao, S., Y. Nakanishi, T. Mizoguchi, Y. Ito, T. Nakamura, and S. Yoshikado, "Radiation of X-Rays using uniaxially polarized LiNbO_3 single crystal," *AIP Conference Proceedings*, Vol. 1099, 88–91, 2009.
13. Kortright, J. B. and A. C. Thompson, "X-ray data booklet," Lawrence Berkeley National Laboratory, California, 2001.
14. Dushman, S. and J. M. Lafferty, *Scientific Foundations of Vacuum Technique*, 2nd Edition, John Wiley & Sons, New York, 1962.

Reflection and Scattering of Electromagnetic Waves in Spatial Grids Consisting of Multiple Lossy Waveguides

Yasumitsu Miyazaki

Department of Media Informatics, Aichi University of Technology
50-2 Manori, Nishihasama-cho, Gamagori 443-0047, Japan

Abstract— Medical diagnosis technologies using X-ray and optical wave transmitted tomography have been rapidly developed with computer processing. X-ray and optical transmitted field characteristics in CT, that depend on biomedical absorption due to bio-molecules and atoms, yield biomedical information of human body tissues and cells. However, X-ray and optical transmitted field signals at receiving output of diagnosis CT sensors are disturbed by scattering waves in random bio-medical inhomogeneities around objects of body tissues and cells. Before signal processing by computer, hardware tools of spatial filtering of disturbing scattering fields for absorption characteristics in bio-medical tissues and cells are very useful system functions.

Spatial filtering of scattered fields by grid arrays consisting of transversely multiple lossy waveguides is one of excellent device function for spatial filtering in X-ray and optical diagnosis. Spatial filter of grid arrays consisting of multiple lossy waveguides is waveguide array consisting of waveguides with transparent cores and lossy clads. Each waveguide has core size, clad size and waveguide length. Scattered fields in random bio-medical media are incident on input plane of spatial filter array, and coupled to lower modes of low losses for small scattering angles and higher modes of large losses for large scattering angles, in lossy waveguide array. Low angle scattered fields couple to lower modes and large angle scattered fields couple to lossy higher modes.

Scattered fields coupled to lossy higher modes are filtered in lossy grid arrays. Mode characteristics in lossy grid arrays excited by scattered field in random bio-medical media are discussed by mode expansion methods using boundary condition at input plane of lossy grid array, and filtered fields at output plane of lossy grid array are shown by integral equations using Green's dyadics. Mode characteristics and filtered fields are also investigated by the Wiener-Hopf method with spectral functions.

1. INTRODUCTION

Medical image diagnosis and computer aided diagnosis are very important medical techniques using laser and X-ray. Optical wave and X-ray are important physical tools for medical diagnosis and recently automatic image diagnosis using optical wave and X-ray with computers is rapidly developed [1–3]. However, in image processing for medical diagnosis, based on photo-electric absorption, interactions between electrons and photons of optical waves and X-rays, physiological and physical phenomena of optical waves and X-rays in biomedical media have been studied. The spatial characteristic in the received optical image is determined by the intensity of transmitted and attenuated optical waves and X-rays superposed with scattered waves. The characteristics of transmitted waves depend on both the absorption and scattering characteristics [4–7]. Therefore, for the identification characteristics of biomedical media by optical and X-ray transmission, signal to noise ratio of primitive optical and X-ray diagnosis without scattering filtering is not so high. Although the use of the X-ray grid and optical grid are efficient to remove the scattering wave from the transmitting wave, the grid has not been studied sufficiently. Also, by using spatial grid filter and the characteristic investigation of scattering, absorption, dispersion and spectroscopy, it may be possible to find more accurate new method of image diagnosis. In order to find excellent computer aided diagnosis system based on the electromagnetic wave characteristics, primarily, the scattering filter characteristics of beam using the grid consisting of lossy waveguide arrays have been studied [8–10]. Based on this analysis, the optimum scattering wave filter may be found.

Statistical theory of optical propagation in random media consisting of biological tissues is shown by integral equations with Green's function, using correlation functions of random media. Scattering characteristics of incident Gaussian beam in random physiological media consisting of biological materials such as biological cells are discussed. Electromagnetic filtering properties by electromagnetic waveguides with lossy clad for scattered fields are discussed using mode characteristics of electromagnetic waveguides consisting of lossy clad.

Spatial filtering characteristics are discussed by spectral functions of input waves, transmitted waves and scattered waves, and waveguide transfer functions for spatial frequencies. Electromagnetic characteristics of spatial grids consisting of waveguide arrays are studied, and eigen modes in waveguide arrays with homogeneous cores and inhomogeneous cores, and lossy clads are discussed. Coupling and transmitted electromagnetic waves with scattered waves in random media are shown in spatial grids consisting of multiple lossy waveguides.

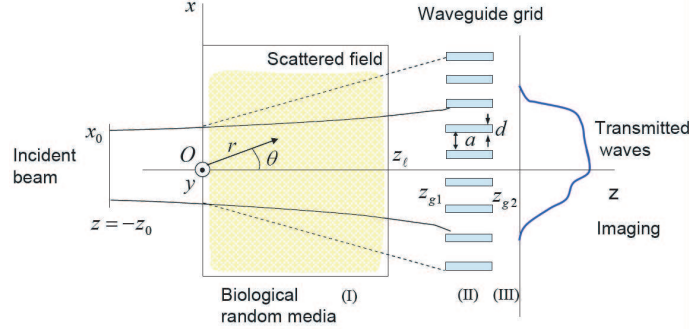


Figure 1: Scattering and waveguide grid.

2. SCATTERED FIELD IN MEDICAL RANDOM MEDIA

In the biological body region, transmitted and scattered waves through random biomedical media are studied. Electromagnetic waves are incident on random media (I) ($0 \leq z \leq \ell$) from left side in Fig. 1 [2, 3]. Incident wave has y -direction linearly polarization $\mathbf{E} = \phi(x, z) \mathbf{i}_y$. Biological random media in the region (I) have dielectric constants as

$$\varepsilon_t = \varepsilon + \varepsilon \Delta\eta(\mathbf{r}_t) \quad (1)$$

where $\Delta\eta$ is random function and $\varepsilon = \varepsilon' - j\varepsilon''$. Here, $\mathbf{r}_t = x\mathbf{i}_x + z\mathbf{i}_z$, and we consider two dimensional scattering fields. The field function $E(x, z)$ concerned with electric field of y polarization satisfies the following wave equations, using $k^2 = \omega^2\varepsilon\mu = (k_r - jk_i)^2$

$$\nabla_{xy}^2 E(\mathbf{r}_t) + k^2 E(\mathbf{r}_t) = -\omega^2 \varepsilon \Delta\eta E(\mathbf{r}_t) \quad (2)$$

Incident Gaussian beam of $\mathbf{E}^{inc} = E_{inc}(\mathbf{r}_t) \mathbf{i}_y$

$$\mathbf{E}_{inc}(\mathbf{r}_t) = \mathbf{i}_y \frac{A}{\sqrt{1-j\zeta}} e^{-jk(z+z_0)} e^{-\frac{x^2}{x_0^2(1-j\zeta)}} \quad (3)$$

where beam parameters are $\zeta = \frac{2(z+z_0)}{kx_0^2}$, beam waist is $z = -z_0$, and beam spot size is x_0 .

For length of random media ℓ with correlation length ρ_0 , we have scattered field intensities for the cylindrical coordinate (r, θ) assuming attenuation factor $g(k_i | \mathbf{r}_t - \mathbf{r}'_t |) = e^{-2k_i |z_\ell - z'|}$ in random media of $0 \leq z \leq z_\ell$,

$$\langle \mathbf{I}_s \rangle = \mathbf{i}_r \frac{k}{\omega\mu} \frac{\sqrt{2\pi}}{16} \Delta\eta^2 A^2 k^3 x_0 \rho_0^2 \frac{1}{|\mathbf{r}|} e^{-k^2 \rho_0^2 \sin^2 \frac{\theta}{2}} e^{-2k_i(z_\ell + z_0)} z_\ell \quad (4)$$

Figure 2 shows angular distribution of Thomson scattering with $k = 2\pi/\lambda$. For large $k\rho_0$, forward scattering is large and small $k\rho_0$, scattering is homogeneous.

3. FILTERING CHARACTERISTICS OF LOSSY WAVEGUIDE GRID

Lossy waveguides with absorption clad layers have large propagation losses for higher modes and may have filtering characteristics of incident waves of large incident angles. Lossy waveguide grids with period of $a + d$ for the x direction of core width a and clad width $d/2$ are shown in Figs. 1 and 3. These waveguides have mode characteristics for the E_y component as

$$\Phi_m(x, z) = \Psi_m(x) e^{-j\beta_m z} \quad (5)$$

$$\int_{-\frac{a+d}{2}}^{\frac{a+d}{2}} \Psi_m(x) \Psi_n^*(x) dx = \delta_{mn} \quad (6)$$

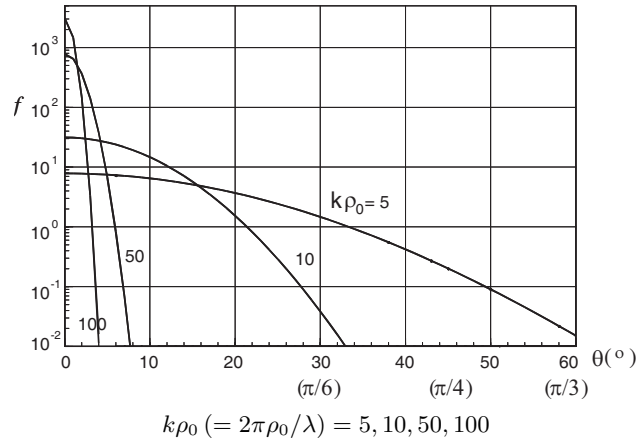


Figure 2: Angular distribution of Thomson scattering. $\frac{|\mathbf{I}_s|}{|\mathbf{I}_0|} = \overline{\Delta\eta^2}(kx_0) \left(\frac{z_\ell}{|\mathbf{r}|} \right) f$, $f = \frac{\sqrt{2\pi}}{8} (k\rho_0)^2 e^{-(k\rho_0)^2 \sin^2 \frac{\theta}{2}}$.

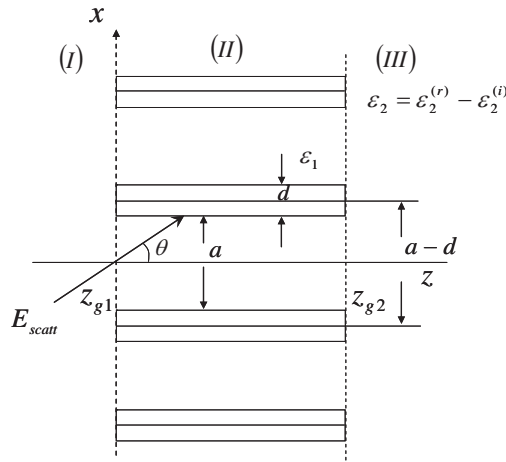


Figure 3: Lossy waveguide grid for scattering filter.

where propagation constants $\beta_m = \beta_m^{(r)} - j\beta_m^{(i)}$ have large attenuation characteristics of $\beta_m^{(i)}$. When scattered waves with scattered angles θ are incident to lossy waveguide (II) at the input $z = z_{g1}$ from region (I), fields in the waveguide region (II) can be expressed as, for one grid section, assuming $E^{(s)}(x, z) = E(x + (a+d)s, z)$ for each s section of total $2W$ sections

$$E_y^{(II)}(x, z) = \sum_{s=-W}^W E^{(s)}(x, z) = \sum_{s=-W}^W \sum_m a_m^{(s)} \Psi_m(x) e^{-j\beta_m(z-z_{g1})} \quad (7)$$

$$a_m^{(s)} = \int_{-\frac{a+d}{2}}^{\frac{a+d}{2}} E_{scatt}^{(s)}(x, z_{g1}) \Psi_m^*(x) dx$$

Scattered field $E^{(I)}(x, z)$ is written for each s section

$$E^{(I)}(x, z) = \sum_{s=-W}^W b^{(s)}(x) e^{-jk_x x - jk_z z} \quad (8)$$

The mode amplitude $a_m^{(s)}$ is for at $z = 0$, $k_x = k_0 \sin \theta$,

$$a_m^{(s)} = \int_{\frac{(2s-1)(a+d)}{2}}^{\frac{(2s+1)(a+d)}{2}} b^{(s)}(x) e^{-jk_x x} \phi_n^{(s)}(x) dx \quad (9)$$

Mode coefficients $a_m^{(s)}$ show filtering characteristics. At the output of waveguide grids, $z = z_{g2}$, only lower modes that couple with incident fields of small scattering angles propagate through lossy

waveguides and higher modes that couple with high angle scattered fields can not pass through the waveguides.

Filtered fields in the region (III) are derived by, using Green's function, for one grid section,

$$\begin{aligned}
 E_{fil}^{(III)}(x, z) &= \int_{-\frac{a+d}{2}}^{\frac{a+d}{2}} \left\{ -G \frac{\partial E_y^{(II)}}{\partial z} + E_y^{(II)} \frac{\partial G}{\partial z} \right\} dx \\
 &= \left(-\frac{j}{4} \right) \sum_{s,m} (jk + j\beta_m) \sqrt{\frac{2}{\pi k z'}} e^{-jkz' + j\frac{\pi}{4} a_m^{(s)}} e^{-j\beta_m z'} \int_{-\frac{a+d}{2}}^{\frac{a+d}{2}} e^{-j\frac{k}{2z}(x-x')^2} \Psi_m(x') dx' \quad (10)
 \end{aligned}$$

where $z' = z - z_{g2}$ and a_m for large m is very small.

If we describe filtering characteristics using spatial frequencies $k_x = \sqrt{k^2 - k_z^2}$, in these three regions, for $t = I, II, III$, Fourier components are

$$E^{(t)}(k_x) = \int_{-\infty}^{\infty} E^{(t)}(x) e^{+jk_x x} dx \quad (11)$$

Filtering characteristics of lossy waveguide grids $\hat{F}(k_x^{(II)})$ are defined as

$$\hat{E}^{(I)}(k_x^{(I)}) \hat{F}(k_x^{(II)}) = \hat{E}^{(III)}(k_x^{(III)}) \quad (12)$$

Spatial frequency $k_x^{(II)}$ of lossy waveguide grid filter in Fig. 4 is proportional to mode number m .

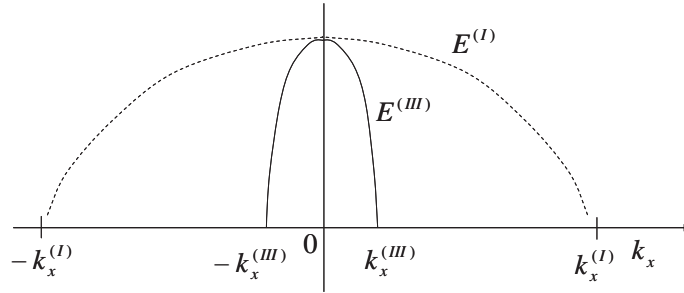


Figure 4: Spatial frequency and filtering characteristics.

4. ELECTROMAGNETIC CHARACTERISTICS IN LOSSY X-RAY GRID WAVEGUIDES

Electromagnetic characteristics of electromagnetic waves in lossy waveguide arrays with lossy clads consisting of grid structures are expressed by mode expansions of lossy modes. In the region (II) of grid arrays in Fig. 3, propagation core spaces (II)-(1) of permittivity ϵ_1 are $z_{g1} \leq z \leq z_{g2}$, $a/2 + s(a+d) \leq x \leq a/2 + s(a+d)$, $s = -W, -(W-1), \dots, -1, 0, 1, \dots, W-1, W$ and lossy metal material clad spaces (II)-(2) of ϵ_2 for X-rays are $z_{g1} \leq z \leq z_{g2}$, $a/2 + s(a+d) \leq x \leq a/2 + d + (a+d)$. Widths of a, d are very wider than wavelengths.

For the TE mode case of y polarization, and $i = 1, 2$

$$\begin{aligned}
 H_z^{(i)} &= \sum_{n=0}^{\infty} F_n^{(i)} h_n^{(i)2} \psi_n^{(i)}(x) e^{-j\beta_n z}, \\
 E_y^{(i)} &= \sum_{n=0}^{\infty} (j\omega\mu) F_n^{(i)} \frac{\partial \psi_n^{(i)}(x)}{\partial x} e^{-j\beta_n z}, \\
 H_x^{(i)} &= \sum_{n=0}^{\infty} (j\beta_n) F_n^{(i)} \frac{\partial \psi_n^{(i)}(x)}{\partial x} e^{-j\beta_n z}
 \end{aligned} \quad (13)$$

where $\varepsilon_2 = \varepsilon_{2r} - j\varepsilon_{2i}$, $\sqrt{\varepsilon_2} = 1 - \delta - j\eta$, $k_i^2 = \omega^2\varepsilon_i\mu$ and $u_n = \sqrt{k_1^2 - \beta_n^2} = h^{(1)}$, $h^{(2)} = jv_n = j\sqrt{\beta_n^2 - k_2^2}$, electric fields are given as, for $x^{(s)} = x + (a+d)s$

$$\begin{aligned} E_{yn}^{(1)} &= A_n \cos u_n 2x^{(s)} + B_n \sin u_n 2x^{(s)} & \left(-\frac{a}{2} \leq x^{(s)} \leq \frac{a}{2}\right) \\ E_{yn}^{(2-)} &= (A_n \cos u_n - B_n \sin u_n) \left(C_n \cosh v_n 2x^{(s)} - D_n \sinh v_n 2x^{(s)}\right) & \left(-\frac{a}{2} - d \leq x^{(s)} \leq -\frac{a}{2}\right) \\ E_{yn}^{(2+)} &= (A_n \cos u_n + B_n \sin u_n) \left(C_n \cosh v_n 2x^{(s)} + D_n \sinh v_n 2x^{(s)}\right) & \left(\frac{a}{2} \leq x^{(s)} \leq \frac{a}{2} + d\right) \end{aligned} \quad (14)$$

Complex eigen modes for isolated waveguides with large absorption clad are derived by

$$\tan u_n = \frac{2u_n v_n}{u_n^2 - v_n^2}$$

When propagation constants are $|k_2| < |\beta_n| < |k_1|$, lossy guided modes have small loss characteristics for small n , and higher modes of large n have large loss characteristics. Radiation modes of $|\beta_n| \leq |k_2|$ have large losses.

In case of lossy waveguide walls of conductivity σ , impedance boundary condition is $\mathbf{n} \times \mathbf{E} = \frac{1}{2}\delta\mu\omega(1+j)\mathbf{H}$, $\delta = \sqrt{2/\omega\mu\sigma}$, propagation constant $\beta_n = \beta_n^{(r)} - j\beta_n^{(i)}$ are derived as perturbations from waveguide modes for perfect conductivity, when $R_s = \sqrt{\frac{\omega\mu}{2\sigma}}$, $\varsigma = \sqrt{\frac{\mu}{\varepsilon}}$,

$$\beta_n^{(r)} = \sqrt{k^2 - \left(\frac{n\pi}{a}\right)^2}, \quad \beta_n^{(i)} = \frac{R_s 2k (h_n/k)^2}{\varsigma a \sqrt{k^2 - h_n^2}}$$

Hence, we have

$$\gamma_n = j\beta_n^{(r)} + \beta_n^{(i)}, \quad P = \frac{1}{2}\omega\mu \sum_{n=1}^{\infty} |B_n|^2 \beta_n^{(r)} e^{-\beta_n^{(i)}z} \quad (15)$$

Using large attenuation constants of higher modes, spatial filtering of incident off-axis scattered fields can be estimated.

Mode power characteristics are shown as statistical coefficients as, $G_n = j\omega\mu\sqrt{\frac{a}{2}}$

$$\left\langle |F_n^{(s)}|^2 \right\rangle = |F_n^{(s),(inc)}|^2 + \left\langle |F_n^{(s),(scatt)}|^2 \right\rangle \quad (16)$$

where

$$|F_n^{(s),(inc)}|^2 = \frac{1}{|G_n|^2} \frac{A^2}{\sqrt{1+\zeta^2}} e^{-2k_i(z_\ell+z_0)} e^{-\frac{2x_s^2}{x_0^2(1+\zeta^2)}} \left[\frac{a}{n\pi} (1 - (-1)^n) \right]^2$$

and

$$\left\langle |F_n^{(s),(scatt)}|^2 \right\rangle = \frac{1}{|G_n|^2} 2\sqrt{\frac{\mu}{\varepsilon}} \frac{k}{\omega\mu} \frac{\sqrt{2\pi}}{16} \Delta\eta^2 A^2 k^3 x_0 \rho_0^2 \frac{1}{|\mathbf{r}|} e^{-k^2 \rho_0^2 \sin^2 \frac{\theta_s}{2}} e^{-2k_i(z_\ell+z_0)} z_\ell |g(n, \theta)|^2$$

Here,

$$\tan \theta_s = \frac{x_s}{|\mathbf{r}|}, \quad g(n, \theta_s) = \begin{cases} \frac{n\pi/a}{(n\pi/a)^2 - k^2 \sin^2 \theta_s} & \text{when } \frac{n\pi}{a} \neq k \sin \theta_s \\ a/2 & \frac{n\pi}{a} = k \sin \theta_s \end{cases}$$

From Eq. (16), it is found that off-axis scattered fields of scattering angle θ_s excite higher n modes as $k \sin \theta_s \cong n\pi/a$ with large attenuations as $\beta_n^{(i)} \propto h_n^2 = (n\pi/a)^2$. Lossy grid waveguide array may keep only transmitted waves with absorption effects due to energy structures of biological tissues, by filtering of scattered waves. Hence, lossy grid waveguides are very useful elements to improve image resolution for medical image processings.

5. CONCLUSION

For optical and X-ray CT in medical diagnosis using laser and X-ray, spatial filtering of scattered waves by waveguide arrays with lossy cladding is very useful to obtain precise image processing. Scattering characteristics in random bio-medical media consisting of bio-molecules, are shown by statistical theory of electromagnetic field. Attenuation of scattered waves in spatial grids consisting of multiple lossy waveguides are discussed. Electromagnetic characteristics of eigen modes in grid arrays consisting of lossy waveguides are studied. Attenuation properties of higher modes that are excited by scattered fields of large scattering angles are investigated and based on higher mode characteristics, spatial filtering characteristics of scattered fields are discussed for improvement of precise diagnosis.

REFERENCES

1. Aichinger, H., et al., *Radiation Exposure and Image Quality in X-ray Diagnostic Radiology*, Springer-Verlag, 2004.
2. Miyazaki, Y., “Electromagnetic characteristics of grid structures for scattering fields of nanometer electromagnetic waves and X-rays,” *PIERS Proceedings*, 643–647, Tokyo, Japan, August 2–5, 2006.
3. Miyazaki, Y., “Spatial filtering of optical scattered waves in bio-medical media by inhomogeneous waveguide grids for optical CT,” *Proc. APMC 2007*, TH-A1-D4, 527–530, Bangkok, Thailand, 2007.
4. Miyazaki, Y., “Electromagnetic characteristics of waveguide-type grid filters for scattered nanometer waves in transmitted X-ray diagnostic images,” *Proc. of EMTS 2007*, EMTS128, Ottawa, ON, Canada, July 2007.
5. Miyazaki, Y., “Synchrotron radiation and application technology of X-ray electronics,” *J. IE-ICE*, Vol. 83, No. 2, 132–136, 2000.
6. Miyazaki, Y., “Light scattering of laser beams by random micro-inhomogeneities in glasses and polymers,” *Jpn. Jour. Appl. Phys.*, Vol. 13, No. 8, 1238–1248, 1974.
7. Ishimaru, A., *Wave Propagation and Scattering of Laser Beams by Random Media*, Vol. 1, 2, Academic Press, N.Y., 1978.
8. Miyazaki, Y., “Partially coherent optical waves in random gradient fibers,” *Optical and Quantum Electronics*, Vol. 9, 153–165, 1977.
9. Miyazaki, Y., “Beam propagation and radiation fields in a uniformly curved X ray dielectric gradient waveguides,” *Trans. IEE of Japan*, Vol. 120-C, No. 1, 68–73, January 2000.
10. Miyazaki, Y., “Spatial filtering characteristics of scattered fields by inhomogeneous waveguide grids for x-ray image diagnosis,” *PIERS Proceedings*, 539–545, Cambridge, USA, July 2–6, 2008.

Electromagnetic Analysis of Propagation and Scattering Fields in Dielectric Elliptic Cylinder on Planar Ground

Yasumitsu Miyazaki¹, Tadahiro Hashimoto², and Koichi Takahashi¹

¹Department of Media Informatics, Aichi University of Technology
50-2 Manori, Nishihasama-cho, Gamagori, Aichi 443-0047, Japan

²Broadband Technology Department, Synclayer, Inc.
1-20 Himegaoka, Kani, Gifu 509-0249, Japan

Abstract— Radio wave technologies using electromagnetic waves of microwaves and ultra-high frequencies have been rapidly developed for high bit rate wireless communications and RFID application in out-door and in-door spaces. Signal detection evaluation is very important factor in these systems including several objects along propagation paths of urban streets and country suburb, and, in houses and building.

In order to estimate scattering and interference fields in many environments, typical useful models for scattering objects are dielectric elliptic cylinders on the planar ground. Field intensity distributions of electromagnetic waves in these circumstances are studied by Mathieu function expansion with addition theorems. Incident and scattering fields are expanded by Mathieu function series and coefficients of series are derived by electromagnetic field continuity equations of boundary conditions on the elliptic cylinder and planar surface.

Reflection and scattered fields by elliptic cylinders on planar ground are shown by these series coefficients, and also fields in shadow regions between dielectric elliptic cylinders and planar ground. Field intensities in the elliptic cylinder including resonance cases for particular frequencies are evaluated. Reflection and scattered fields are compared with computer simulation results derived by numerical calculation of the FDTD method. Based on these field calculations optimum system design of WiMAX wireless communications and RFID systems in out-door and in-door space regions are investigated. Positions and locations of radiating and receiving antenna for RF stations and RF readers may be decided from field results of this theory.

1. INTRODUCTION

Recently mobile communication is used in many applications such as WiMAX wireless communications and RFID systems. WiMAX wireless communication has been rapidly developed for broadband mobile communication of image and TV transmission. Mobile WiMAX communication system uses microwave carrier of 2.5 GHz frequency band and modulation system is mainly OFDM for transmission of signals. To improve coverage and provide high-data-rate services in a cost-effective manner, Femto cell is proposed for ubiquitous indoor and outdoor communication, using a single access technology such as WiMAX. Particularly, femto access point can improve indoor coverage, where the signal from macro base station may be weak. When the same carrier frequency is used by macro/micro base station and femto access point, the effect of the co-channel interference becomes an important factor for design of excellent wireless communication system.

To evaluate pass loss and received level of the electric field in microcell and femto cell environment, wave reflection, scattering and diffraction due to the presence of obstacles on the ground are studied [1]. Here the scattering model consists of an infinite cylindrical conductor near an infinite planar ground. This scattering problem involving the conducting plane can be exchanged with that of two elliptic cylinders, using the theory of images. Expansion of fields in terms of Mathieu functions is used to analytically describe the scattered field. To apply the boundary conditions, we have used the addition theorem of Mathieu functions. We have reported the plane wave scattering from a girder bridge on the plane analytically by replacing the problem with scattering by two elliptic cylinders using the image theory [2]. Particularly, numerical results showed the variation of field distribution in shadow region when the height of the elliptic cylinder was different.

Also, we have studied the received level of the electric field by presence of forest in WiMAX wireless communications and street walls in RFID systems [3–6]. In this paper, we consider an elliptic cylinder on the planar ground as a simple object and study the electromagnetic scattering analytically using field expansion in terms of Mathieu function. Reflection and scattering fields are compared with the numerical results by FDTD method.

2. ANALYSIS METHOD USING FIELD EXPANSION BY MATHIEU FUNCTION

The elliptic cylinder located at an arbitrary height h from the perfectly conducting plane is considered. The parameters of the elliptic cylinder are its focal c_0 , the length of major axis a and the length of minor axis b . The coordinate system is represented by an elliptic cylindrical coordinate system (ξ_1, η_1, z) and (ξ_2, η_2, z) .

For the incident wave and scattered wave, we have, for $i = 1, 2$

$$E_y = A \sum_{n=0}^{\infty} \{C_n Ue_n(\xi_i) ce_n(\eta_i) ce_n(\alpha) + S_n We_n(\xi_i) se_n(\eta_i) se_n(\alpha)\} \quad (1)$$

where ce_n and se_n are Mathieu functions of order n and, $Ue_n = Ce_n, Me_n^{(2)}$ and $We_n = Se_n, Ne_n^{(2)}$ are the modified Mathieu functions of order n . α is the angle of incidence. For the scattered wave, C_n and S_n are the unknown coefficients and are determined by boundary condition on the elliptic cylinder and the plane.

3. FDTD ANALYSIS OF ELECTROMAGNETIC SCATTERING

Microwave scattering and diffraction by shielding objects are very important phenomena for wireless broadband communication such as mobile WiMAX. Computer simulation using FDTD method is useful to evaluate these characteristics numerically. Two-dimensional analysis model for microwave scattering by elliptic cylinder on the ground is shown in Fig. 1. Analysis region is defined as $\ell_x \times \ell_z$. In FDTD simulations, the incident wave is assumed to be a traveling wave from base station antenna at a far distance. The incident wave is y-polarized Gaussian beam wave with angular frequency $\omega = 2\pi f$, beam waist $z = z_0$ and beam spot size S . In the simulation model, the electromagnetic fields at point (i, j) and time $n\Delta t$ are calculated by difference equations. The elliptic cylinder is located at an arbitrary height h on the planar ground. The parameters of the elliptic cylinder are the length of major axis a and the length of minor axis b .

Table 1: Numerical parameters for FDTD analysis.

Parameters	Values
ℓ_x : Length of analysis space (x)	13 m (108.3 λ)
ℓ_z : Length of analysis space (z)	20 m (166.7 λ)
ℓ_g : Width of planar ground	1 m (8.3 λ)
ΔS : Length of a cell	10^{-2} m ($\lambda/12$)
Δt : Time increment	0.02 ns ($T_0/20$), $T_0 = 1/f$
f : Frequency of incident wave	2.5 GHz
λ : Wavelength of incident wave	0.12 m (c/f)
t_0 : Peak time of incident pulse	5 ns
T : Pulse width of incident wave	2 ns
x_0 : Center point of the beam (x)	6.0 m
S : Beam spot size at $z = 0$	3.0 m (25 λ)
a : Major axis length/Half rectangle length	4.8 m Case 1 Case 2 Case 3
b : Minor axis length/Half rectangle height	2.1 m 4.8 m 2.4 m
h : Height of elliptic cylinder	2.7 m 0 m
ε_1 : Dielectric constant of objects	Case 1-1, 2 Case 2-1, 2 Case 3-1, 2
ε_2 /Plane	$4\varepsilon_0$ $4\varepsilon_0$ $4\varepsilon_0$
σ_1 : Conductivity of objects	∞ 10^{-4} S/m ∞ 10^{-4} S/m ∞ 10^{-4} S/m
σ_2 /Plane	

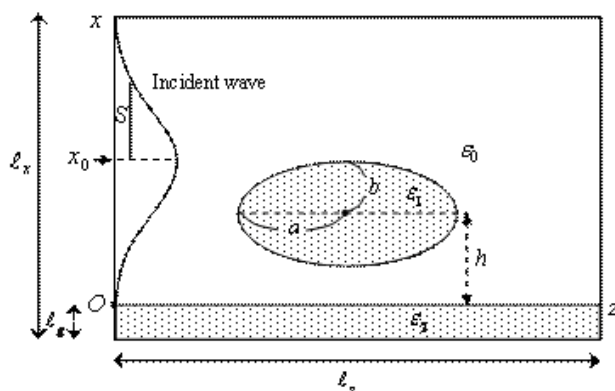


Figure 1: Dielectric elliptic cylinder on planar ground.

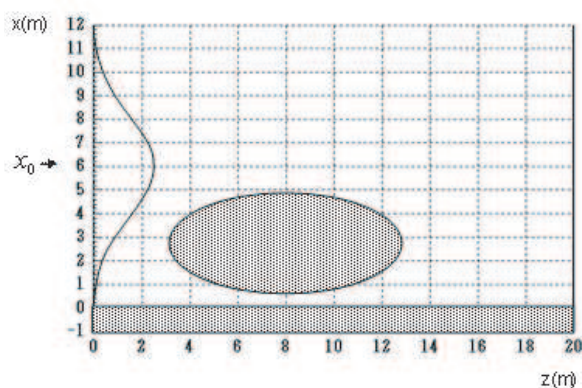
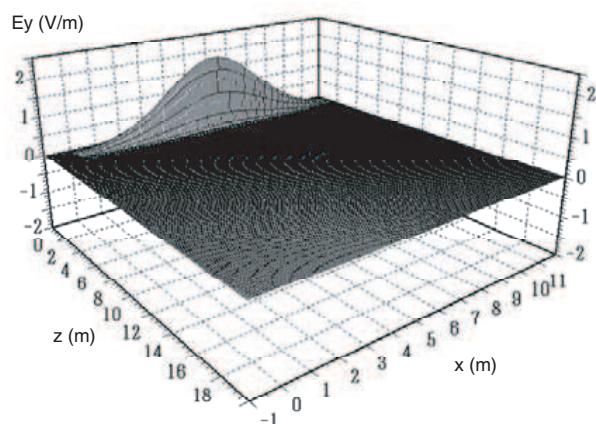


Figure 2: Cylinder over ground (Case 1).

Figure 3: Electric field at $t = 400 \Delta t = 8 \text{ ns}$ (Case 1-1).

The incident wave is generated by current density in FDTD equations,

$$J_y^n(i, 1) = J_0 \exp \left\{ - \left(\frac{i \Delta s - x_0}{S} \right)^2 \right\} \exp \left\{ - \left(\frac{n \Delta t - t_0}{T} \right)^2 \right\} \sin(2\pi f n \Delta t) \quad (2)$$

where f is the frequency of incident wave, x_0 is the center point of incident beam, S is the beam spot size at $z = z_0(j = 1)$, T is the parameter for transmission pulse width.

4. NUMERICAL RESULTS

The results of numerical calculations of the electric fields near the elliptic cylinder on planar ground are shown in this section. We carried out calculations using parameters $f = 2.5 \text{ GHz}$, $\lambda = 0.12 \text{ m}$, $E_0 = 1 \text{ V/m}$, $\Delta s = 0.01 \text{ m}$, $\Delta t = 0.02 \text{ ns}$. In the analysis region of Fig. 1, $l_x = N_x \Delta s = 1300 \Delta s = 13 \text{ m}$ and $l_z = N_z \Delta s = 2000 \Delta s = 20 \text{ m}$, where N_x and N_z are the number of the cell in x and z direction, respectively. $l_g = 100 \Delta s = 1 \text{ m}$ is the width of the planar ground. In FDTD analysis, three structure models are considered. In conductor case, the elliptic cylinder and the plane are perfectly electric conductor and in dielectrics case, those objects have dielectric constant $\epsilon_1 = \epsilon_2 = 4\epsilon_0$ and conductivity $\sigma_1 = \sigma_2 = 10^{-4} \text{ (S/m)}$. The electric field amplitude in shadow region due to the presence of an obstacle is studied using simple models.

Figure 2 shows the analysis model in Case 1. The electric field of the incident wave is shown in Fig. 3. Fig. 4 shows that the amplitude in shadow region of $x < b + h$ is very weak in both Case 1-1 and 1-2. However, in conductor case of Case 1-1, many reflected waves are observed at $x = 4 \text{ m}$ and 2 m , compared with the dielectric case of Case 1-2 as shown in Fig. 5. Fig. 6 shows the envelope of the electric field at propagation distance $z = 10, 18$ and 20 m . In Case 1-2, strong amplitude is observed in the dielectric cylinder at $t = 73 \text{ ns}$. Around $x = 2 \text{ m}$ in shadow region, the amplitude is highly attenuated due to the elliptic cylinder.

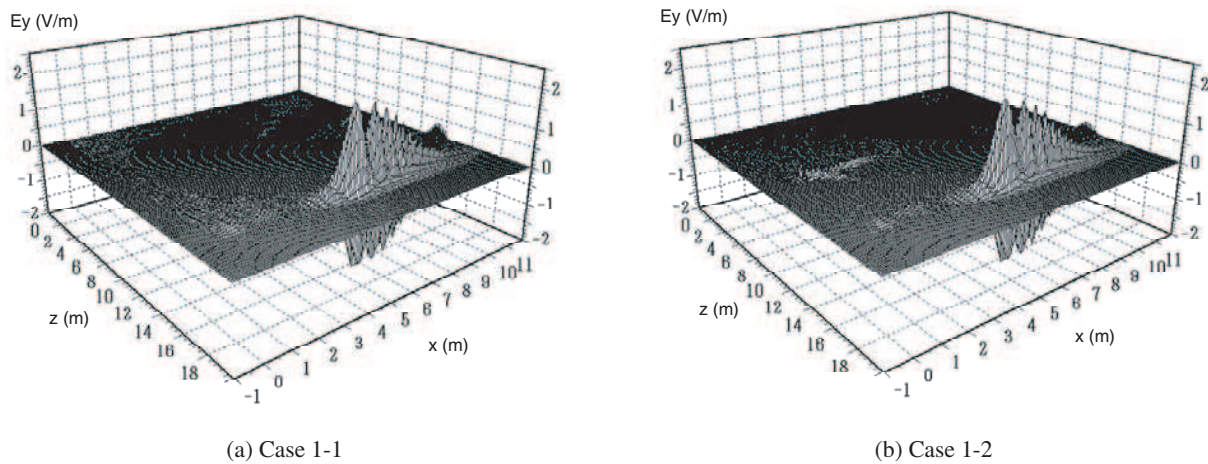


Figure 4: Electric field at $t = 3000 \Delta t = 60 \text{ ns}$ (Case 1-1 and 1-2).

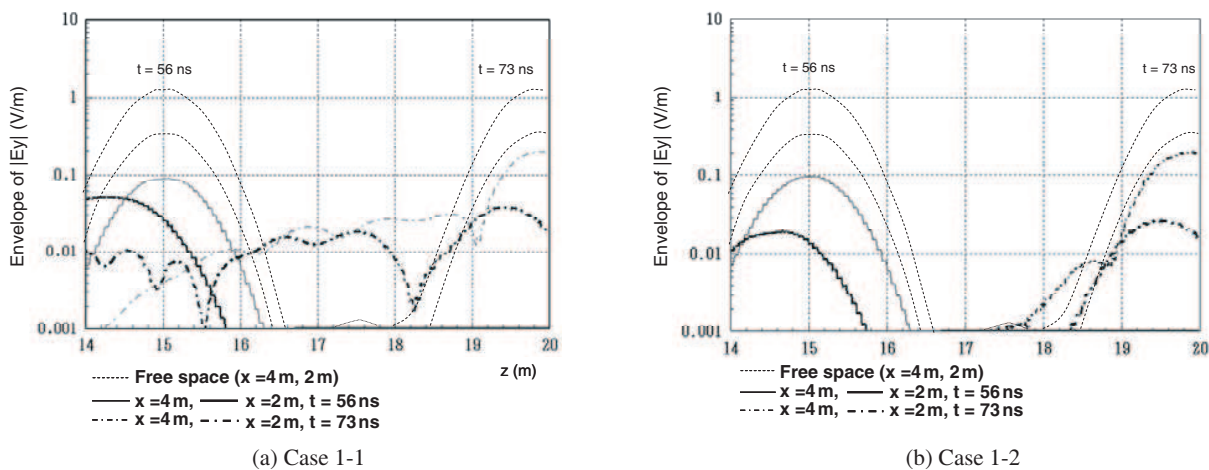


Figure 5: Envelope of electric field at $t = 56 \text{ ns}$ and 73 ns (Case 1-1 and 1-2).

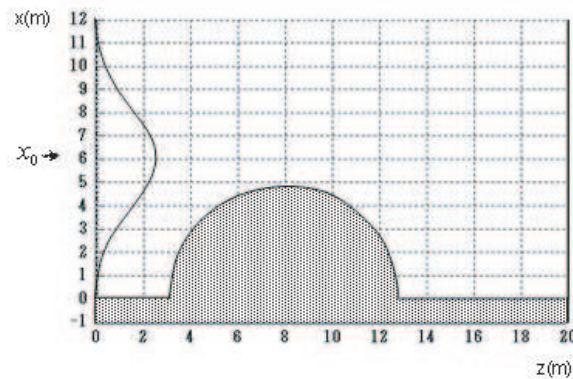
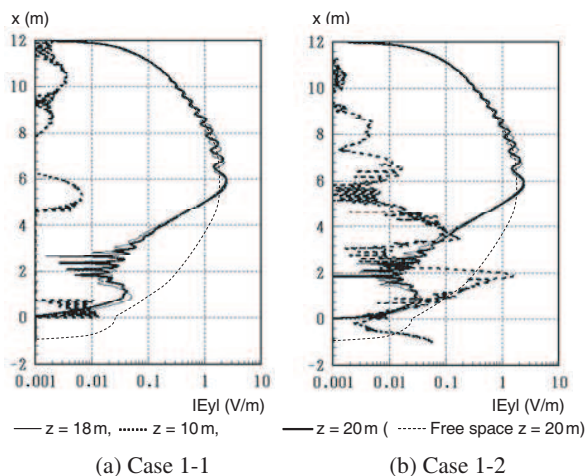


Figure 6: Envelope of electric field at $(t, z) = (66 \text{ ns}, 18 \text{ m}), (73 \text{ ns}, 10 \text{ m})$ and $(73 \text{ ns}, 20 \text{ m})$ in Case 1-1 and 1-2.

Figure 7: Cylinder on ground (Case 2).

Analysis model in Case 2 is shown in Fig. 7. There is no space between the elliptic cylinder and the plane. Fig. 8 and Fig. 9 show the electric field amplitude in Case 2-1 and 2-2. Figs. 11 and 12 shows the wave scattering and diffraction by a rectangular object in Case 3. Stronger amplitude of transmitted wave is observed in rectangular object at $z = 10 \text{ m}, t = 73 \text{ ns}$ as shown in Fig. 13. However, diffracted wave is very weak in these cases compared with the results in Cases 1 and 2.

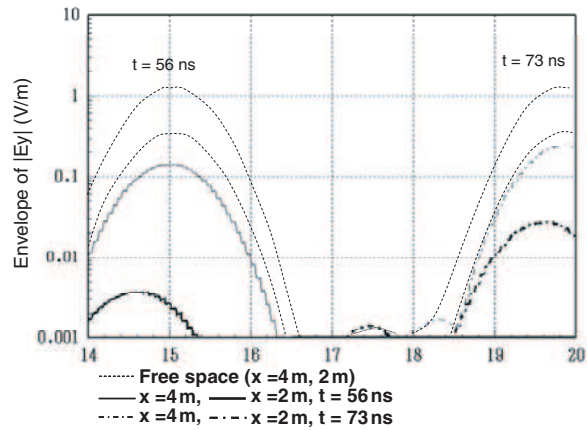


Figure 8: Envelope of electric field at $t = 56$ ns and 73 ns (Case 2-2).

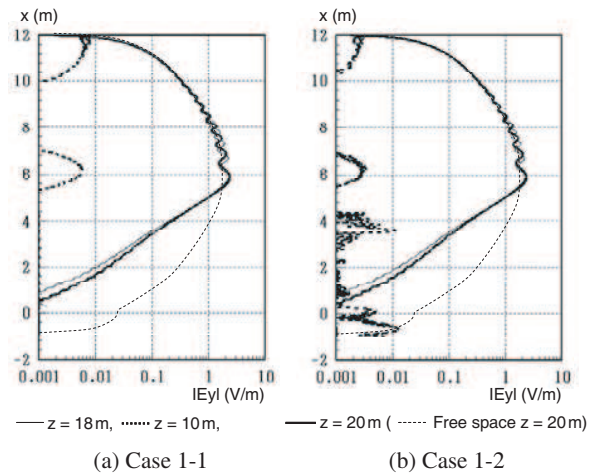


Figure 9: Envelope of electric field at $(t, z) = (66$ ns, 18 m), (73 ns, 10 m) and (73 ns, 20 m) in Case 2-1 and 2-2.

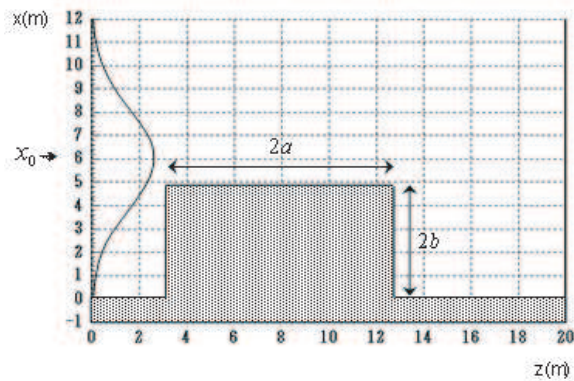


Figure 10: Rectangle on ground (Case 3).

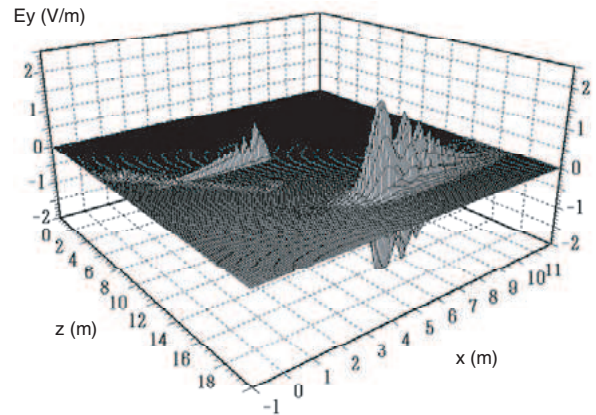


Figure 11: Electric field at $t = 3000 \Delta t = 60$ ns (Case 3-2).

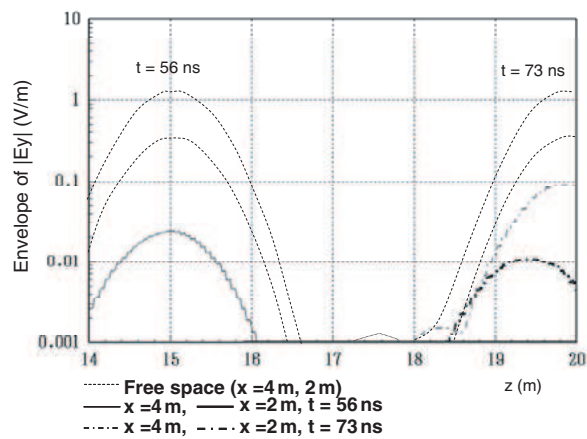


Figure 12: Envelope of electric field at $t = 56$ ns and 73 ns (Case 3-2).

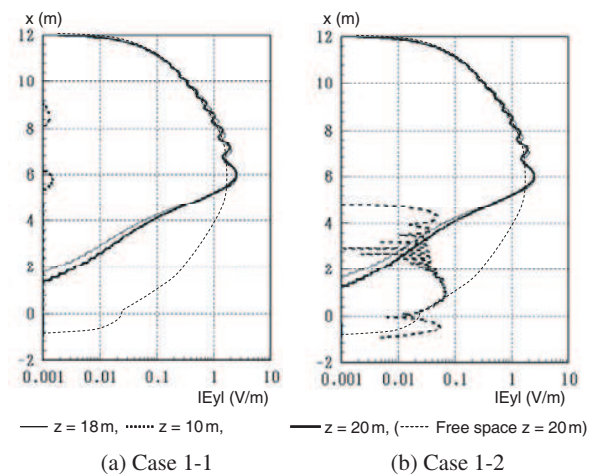


Figure 13: Envelope of electric field at $(t, z) = (66$ ns, 18 m), (73 ns, 10 m) and (73 ns, 20 m) in Case 3-1 and 3-2.

5. CONCLUSION

The phenomenon of scattering from an infinitely long elliptic cylinder on the planar ground is considered. We obtained numerical solution for conductor case and dielectrics case, using FDTD method. Numerical results were shown for near fields of elliptic cylinder and rectangular object near the plane. In future, we calculate the exact solution by field expansion using Mathieu function and investigate the characteristics of shadow effect of the elliptic conductor on the ground precisely.

REFERENCES

1. Masuda, T. and Y. Miyazaki, "Scattering characteristics of electromagnetic environment by construction on the ground," *Trans. IEE Japan*, Vol. 118-C, No. 1, 112–117, 1998.
2. Masuda, T. and Y. Miyazaki, "Analysis of plane wave scattering by a conducting elliptic cylinder near a ground plane," *Proc. of EMC'99*, 19A307, 292–295, Tokyo, 1999.
3. Selormey, P. and Y. Miyazaki, "Electromagnetic compatibility characteristics of buildings in mobile radio waves propagation channel," *Trans. IEE Japan*, Vol. 119-C, No. 1, 97–104, 1999.
4. Rodriguez, G., Y. Miyazaki, and N. Goto, "Matrix-based FDTD parallel algorithm for big areas and its applications to high-speed wireless communications," *IEEE Trans. Antennas & Propag.*, Vol. 54, No. 3, 785–796, 2006.
5. Miyazaki, Y., T. Takada, and K. Takahashi, "Propagation and scattering characteristics of microwaves over forests in WiMAX wireless communications using FDTD method," *PIERS Proceedings*, 546–550, Cambridge, USA, July 2–6, 2008
6. Masuda, T., Y. Miyazaki, and Y. Kashiwagi, "Analysis of electromagnetic wave propagation in out-door active RFID system using FD-TD method," *PIERS Online*, Vol. 3, No. 6, 937–939, 2007.

Eigenvalue Analysis of Waveguides and Planar Transmission Lines Loaded with Full Tensor Anisotropic Materials

C. S. Lavranos, D. G. Drogoudis, and G. A. Kyriacou

Department of Electrical and Computer Engineering, Microwaves Lab.

Democritus University of Thrace, Xanthi, Greece

Abstract— An eigenvalue analysis of curved waveguides and planar transmission lines loaded with full tensor anisotropic materials is presented. This analysis is based on our previously established two-dimensional Finite Difference Frequency Domain eigenvalue method formulated in orthogonal curvilinear coordinates. This is properly extended herein in order to accurately handle arbitrarily shaped curved geometries filled or partially loaded with full tensor anisotropic materials. Numerous investigations are carried out involving all type of forward or backward propagating modes.

1. INTRODUCTION

The eigenvalue analysis, providing the propagation constants and the corresponding fields distributions, of waveguiding structures comprise a significant key tool in the design of several microwave devices, e.g., filters, dividers and couplers. Due to the interest of the subject, a variety of such techniques have been proposed in the literature [1–3]. But, to the authors knowledge, none of them can handle curved geometries or planar bend waveguides. These can be found in a plethora of microwave circuits and systems, such as airborne platforms, modern phased arrays and Radar systems. Moreover, the recent adoption of “smart skin” ideas demands the whole RF front end to be conformal to the host objects surface. Thus, the accurate design of conformal systems demands the knowledge of curved waveguides and printed transmission lines characteristics.

In parallel, the dispersion characteristics of microwave structures involving anisotropic materials (e.g., printed phase shifters in magnetized ferrite’s substrate) have sparked a growing interest in the field of applications for nonreciprocal devices. Such devices could also follow a curved surface since they can be parts of a conformal system. Also these could be used for specific applications, e.g., magnetic surface wave ring interferometers, curved dielectric cylinders with ferrite sleeves, printed phase shifters on curved anisotropic substrates [4]. Hence, the eigenanalysis of wave propagation along curved anisotropic surfaces becomes essential. Moreover, curved or bend transmission lines may offer additional degrees of freedom in the design of non-reciprocal devices.

Our research effort is based on a two-dimensional Finite Difference Frequency Domain (2-D FDFD) eigenvalue method formulated in orthogonal curvilinear coordinates. The theoretical basics and a variety of applications have been presented in our previous works, e.g., [5, 6]. An inherent feature of the elaborated FDFD method is the well-known Finite Difference ability of handling anisotropic materials. In particular, its implementation in matrix-form in conjunction with its formulation with complex mathematics enables the introduction of anisotropic materials, including their losses, through a simple modification of the corresponding permittivity or permeability matrices. However, until now, our work was mainly focused on isotropic or diagonally anisotropic materials. Thus, in this paper our method is extended in order to accurately handle arbitrarily shaped curved geometries full or partially loaded with full tensor anisotropic materials, like ferroelectrics or magnetized ferrites, or even artificial metamaterials. Besides, the operating modes characterization, the present effort aims at revealing any new design features offered by the curved or bend geometry.

2. FDFD METHOD FOR CURVILINEAR COORDINATES

As mentioned above, our research effort is based on a two-dimensional Finite Difference Frequency Domain (2-D FDFD) eigenvalue method formulated in orthogonal curvilinear coordinates [5, 6]. The finite difference discretization is applied by means of an orthogonal curvilinear grid (u_1, u_2, u_3), which leads to an eigenvalue problem formulated for the complex propagation constants and the corresponding fields distributions of curved structures. Following a 2-D scheme this analysis is restricted to structures uniform along the propagation direction, while the cross section of the waveguide structure can be of arbitrary shape loaded with inhomogeneous and in general anisotropic materials. Its direct implementation in orthogonal curvilinear coordinates leads to an accurate

description of curved or bend geometries with a coarse enough grid but free of the well known stair case effect. The waveguiding structure can be curved in all directions (obeying some limitations with respect to the curvature along the propagation axis) and this constitutes its main advantage.

The main contribution of this work refers to the analysis of general anisotropic media, where complex tensors constitutive parameters (dielectric permittivity $\bar{\epsilon}$ and magnetic permeability $\bar{\mu}$) are used. The dielectric permittivity tensor $\bar{\epsilon}$ constitutes the relation between the electric flux density $\bar{\mathbf{D}}$ and the electric field intensity $\bar{\mathbf{E}}$ as:

$$\begin{bmatrix} \mathbf{D}_1 \\ \mathbf{D}_2 \\ \mathbf{D}_3 \end{bmatrix} = \begin{bmatrix} \epsilon_{11} & \epsilon_{12} & \epsilon_{13} \\ \epsilon_{21} & \epsilon_{22} & \epsilon_{23} \\ \epsilon_{31} & \epsilon_{32} & \epsilon_{33} \end{bmatrix} \begin{bmatrix} \mathbf{E}_1 \\ \mathbf{E}_2 \\ \mathbf{E}_3 \end{bmatrix} \quad (1)$$

Similarly, magnetic permeability tensor $\bar{\mu}$ constitutes the relation between the magnetic flux density $\bar{\mathbf{B}}$ and the magnetic field intensity $\bar{\mathbf{H}}$ as:

$$\begin{bmatrix} \mathbf{B}_1 \\ \mathbf{B}_2 \\ \mathbf{B}_3 \end{bmatrix} = \begin{bmatrix} \mu_{11} & \mu_{12} & \mu_{13} \\ \mu_{21} & \mu_{22} & \mu_{23} \\ \mu_{31} & \mu_{32} & \mu_{33} \end{bmatrix} \begin{bmatrix} \mathbf{H}_1 \\ \mathbf{H}_2 \\ \mathbf{H}_3 \end{bmatrix} \quad (2)$$

For each unit cell, the dielectric or magnetic material is assigned at its four transverse and four longitudinal components, as shown in Fig. 1. Particularly, the dielectric permittivities $(\epsilon_{11}, \epsilon_{21}, \epsilon_{31}) \rightarrow e_1$ are defined on the same points as the E_1 transverse electric components, the dielectric permittivities $(\epsilon_{12}, \epsilon_{22}, \epsilon_{32}) \rightarrow e_2$ are defined on the same points as the E_2 transverse electric components and the dielectric permittivities $(\epsilon_{13}, \epsilon_{23}, \epsilon_{33}) \rightarrow e_3$ are defined on the same points as the E_3 longitudinal electric components. Analogously happens for the magnetic permeability tensors. Thus, half cell homogeneity is imposed. This is accurate in the case of dielectric (or magnetic) materials, where the electric (or magnetic) grid can be properly designed in order to precisely follow the material boundaries. However, in the case of a lossy inhomogeneous or anisotropic material with both $\bar{\epsilon} \neq 1$ and $\bar{\mu} \neq 1$, the half-cell misalignment is inevitable. This is due to the electric and magnetic grid half cell shifting and can be reduced by using a denser grid near the material boundaries, or some advanced techniques such as the condensed nodes technique [7].

3. NUMERICAL RESULTS

The first geometry analyzed is a vertically curved rectangular waveguide, filled with a full permittivity tensor $\bar{\epsilon}_r$ but scalar permeability (μ_r) material, as shown in Fig. 2. Retaining their tensor (or matrix) representation they read:

$$\bar{\epsilon} = \epsilon_0 \begin{pmatrix} 18.5875 - j2.57 & -3.8841 + j1.029 & 0 \\ -3.8841 + j1.029 & 14.1025 - j1.39 & 0 \\ 0 & 0 & 11.86 - j0.80 \end{pmatrix}, \quad \bar{\mu} = \mu_0 \begin{pmatrix} 1 & 0 & 0 \\ 0 & 1 & 0 \\ 0 & 0 & 1 \end{pmatrix} \quad (3)$$

This waveguide is curved downward, but, due to its symmetry, the same behavior occurs when it is curved upward. The orthogonal curvilinear coordinates system and the corresponding metric

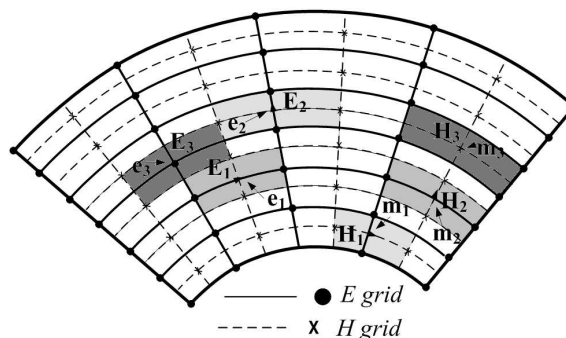


Figure 1: Discretization of dielectric and/or magnetic material tensors according to the electric or magnetic curvilinear grid.

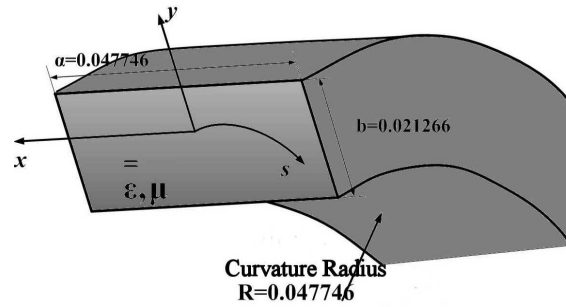


Figure 2: A downward curved rectangular waveguide filled with full tensor dielectrically anisotropic material, ($a = 47.746$ mm, $b = 21.26$ mm, Curvature Ratio: $R/b = 2.25$).

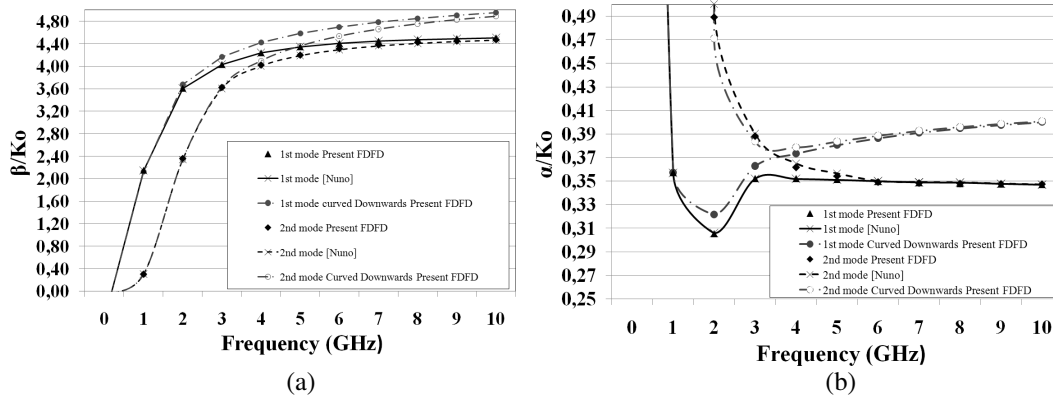


Figure 3: Normalized propagation constants for the curved waveguide of Fig. 2, compared against those of the straight waveguide, Nuno [3]: (a) phase constants, (b) attenuation constants.

coefficients for this case are given by [8] as:

$$u_1 = x, \quad u_2 = y, \quad u_3 = s \quad \text{and} \quad h_1 = 1, \quad h_2 = 1, \quad h_3 = 1 + \frac{y}{R} \quad (4)$$

The phase constants for the first two modes are presented in Fig. 3(a), along with those for the corresponding straight waveguide (of the same cross section). Moreover, in Fig. 3(b) the attenuation constants for the same complex modes are also compared against those of the corresponding straight waveguide.

The results for the straight waveguide are obtained by the proposed FDFD method and compared with those given by Nuno [3], while those for the curved waveguide are obtained exclusively by the proposed FDFD method. As shown in Fig. 3, the phase and attenuation constants for the straight case are very close to those given by Nuno [3], since a maximum deviation about to 0.1% is observed.

Figure 3(a) shows a continuous increase in the normalized phase constants versus frequency for both modes, as compared to the straight case. This increase leads to +11% for the first and +10.7% for the second mode at 10 GHz, for a curvature ratio equal to $R/b = 2.25$. In parallel, the attenuation constants for both modes are also shifted upwards comparing to the straight case, but this increase starts well beyond the cutoff frequency. Both shiftings rise to +15% at 10 GHz.

The second examined case is a vertically (downward) and sideways (bend right) curved rectangular waveguide partially loaded with a ferrite slab. The coordinate system and the corresponding metric coefficients are given by (4) for the downward curvature, while for the sideways (bend right) curvature, only the h_3 metric coefficient is changed as:

$$h_3 = 1 + \frac{x}{R} \quad (5)$$

The ferrite bias DC magnetic field H_0 is vertical, parallel to the waveguide's short dimension. Thus, the direction of the DC bias for the curved structures must be always transverse to the

waveguide's cross section, perpendicular to the propagation direction curved arc. The ferrite slab has an isotropic (scalar) dielectric permittivity and an anisotropic-gyrotropic magnetic permeability equal to:

$$\bar{\epsilon} = \epsilon_0 \begin{pmatrix} 10 & 0 & 0 \\ 0 & 10 & 0 \\ 0 & 0 & 10 \end{pmatrix}, \bar{\mu} = \mu_0 \begin{pmatrix} 0.875 & 0 & -j0.375 \\ 0 & 1 & 0 \\ j0.375 & 0 & 0.875 \end{pmatrix} \quad (6)$$

Due to the ferrite transverse bias, the wave propagation is non-reciprocal, theoretically expected to yield different positive β_+ and negative β_- phase constants. Specifically, the forward wave propagation (toward positive \hat{s}) should have different phase constants as compared to the backward wave propagation (toward negative \hat{s}). This is indeed observed in the numerical results of Fig. 5, where the normalized dispersion curves for the forward and backward propagating dominant mode of the curved waveguides are presented. These are also compared against those for the corresponding straight waveguide (of the same cross section). Note, that even not shown in Fig. 5, the forward ($\beta_+ > 0$) and backward ($\beta_- < 0$) phase constants have different signs, with their fields proportional to $e^{-j\beta_+s}$ and $e^{+j\beta_-s}$ (with $\beta_- < 0$) respectively. For better presentation and direct comparison reasons, all phase constants are depicted as absolute values, $|\beta_{\pm}/K_0|$.

Again, the results for the straight waveguide are obtained by the proposed FDFD method and compared with those given by Nuno [3], while those for the curved waveguide are obtained exclusively by the proposed FDFD method. As shown in Figs. 5(a) and 5(b), the phase constants for the straight case are very close to those given by Nuno [3], since a maximum deviation about to 0.5% is observed.

When the waveguide is curved downward, a continuous increase in the normalized phase constants for both propagating modes, as compared to the straight case, is observed, which leads to +12% for both modes at 3 GHz. On the other hand, the sideways curvature leads to a continuous decrease in the normalized phase constants for both propagating modes comparing to straight

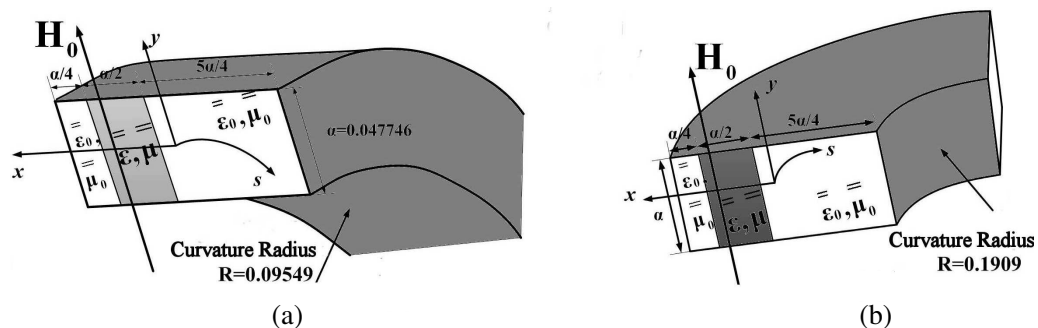


Figure 4: Curved rectangular waveguide ($a = 47.746$ mm) partially loaded with a transversely magnetized ferrite slab: (a) Vertical (downwards) curvature ($R/a = 2$), (b) sideways (bend right) curvature ($R/2a = 2$).

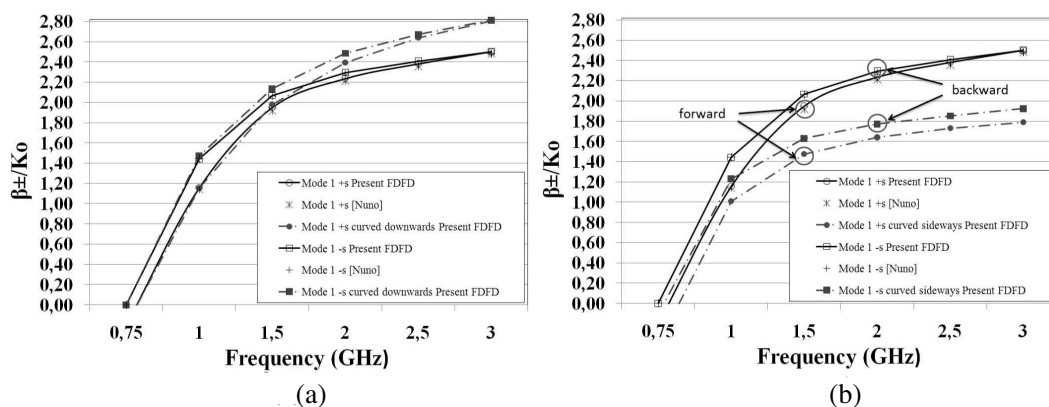


Figure 5: Normalized phase constants for the forward and backward propagating dominant mode of the curved waveguides shown in Fig. 4, compared against those of the straight waveguide, Nuno [3]: (a) Downward curvature, (b) sideways curvature.

waveguide, which leads to -24% for backward and -28% for forward propagating mode at 3 GHz. The different behavior can be explained by the cross section's asymmetry due to the asymmetric location of the ferrite slab, as clearly explained in [5].

4. CONCLUSION

An eigenvalue analysis of curved waveguides loaded with full tensor anisotropic materials was validated herein. A variety of simulations for different curved anisotropic structures (practical microwave ferrite or ferroelectric devices) will be presented at the conference. Our next task refers to eigenanalysis of open curved waveguiding structures.

ACKNOWLEDGMENT

This work is implemented in the framework of Measure 8.3 through the O.P. Competitiveness 3rd Community Support Programme and is co-funded by: 75% of the Public Expenditure from the European Union — European Social Fund, 25% of the Public Expenditure from the Hellenic State — Ministry of Development — General Secretariat for Research and Technology, and Private Sector (INTRACOM SA).

REFERENCES

1. Hwang, J.-N., "A compact 2-D FDFD method for modeling microstrip structures with nonuniform grids and perfectly matched layer," *IEEE Transactions on Microwave Theory and Techniques*, Vol. 53, No. 2, 653–659, 2005.
2. Valor, L. and J. Zapata, "Efficient finite element analysis of waveguides with lossy inhomogeneous anisotropic materials characterized by arbitrary permittivity and permeability tensors," *IEEE Transactions on Microwave Theory and Techniques*, Vol. 43, No. 10, 2452–2459, 1995.
3. Nuno, L., J. V. Balbastre, and H. Castane, "Analysis of general lossy inhomogeneous and anisotropic waveguides by the finite-element method (FEM) using edge elements," *IEEE Transactions on Microwave Theory and Technique*, Vol. 45, No. 3, 446–449, 1997.
4. Srivastava, N. "Propagation of magnetostatic waves along curved ferrite surfaces," *IEEE Transactions on Microwave Theory and Techniques*, Vol. 26, No. 4, 252–256, 1978.
5. Lavranos, C. S. and G. A. Kyriacou, "Eigenvalue analysis of curved waveguides employing an orthogonal curvilinear frequency domain finite difference method," *IEEE Transactions on Microwave Theory and Techniques*, Vol. 57, No. 3, 594–611, 2009.
6. Lavranos, C. S. and G. A. Kyriacou, "Eigenvalue analysis of curved waveguides employing FDFD method in orthogonal curvilinear coordinates," *Electronics Letters*, Vol. 42, No. 12, 702–704, 2006.
7. Afande, M. M., K. Wu, M. Giroux, and R. G. Bosisio, "A finite-difference frequency domain method that introduces condensed nodes and image principle," *IEEE Transactions on Microwave Theory and Techniques*, Vol. 43, No. 4, 838–846, 1995.
8. Lewin, L., D. C. Chang, and E. F. Kuester, *Electromagnetic Waves and Curved Structures*, Peregrinus, London, UK, 1977.

Numerical Investigation of Sensitivity Matrix in Three-dimensional Microwave Tomography

D. G. Drogoudis¹, G. A. Kyriacou¹, and J. N. Sahalos²

¹Department of Electrical & Computer Engineering, Democritus University of Thrace, Xanthi, Greece

²Department of Physics, Aristotle University of Thessaloniki, Thessaloniki, Greece

Abstract— Jacobian matrix is a critical component in many reconstruction algorithms used in Microwave tomography. Its important to have a way of constructing this matrix in closed form expression as well as to investigate the critical components that contribute to its ill-posedness and affect image quality. In this work a closed formula is used for the calculation of the Jacobian matrix based on adjoint network theorem and reciprocity theorem of electromagnetics. Further a numerical singular value decomposition is used and according the singular spectrum the degree of ill-posedness is calculated. Comparing this degree for different reconstruction configurations a better reconstruction scheme can be proposed.

1. INTRODUCTION

Sensitivity analysis is widely used during optimization for the design of various microwave devices as well as in microwave tomography to evaluate their performance or to locate any critical parameters. Exploiting the field distributions over the structure, obtained through a number of electromagnetic simulations with appropriate sources, the sensitivities can be evaluated through closed form expressions. The latter can be extracted by combining the adjoint network theorem and the reciprocity theorem of electromagnetics [1–3]. The present effort is focused on microwave tomography application. So the desired sensitivities are the derivatives of the electric field with respect to the object's complex permittivity.

$$\varepsilon^* = \varepsilon_0 \varepsilon_r (1 - j \tan \delta) = \varepsilon \left(1 - j \frac{\sigma}{\omega \varepsilon} \right) \quad (1)$$

First two sets of Maxwell equations are considered, one for the normal problem-normal fields and one for the adjoint problem — adjoint fields. Combining these two sets in a procedure similar to that used in the derivation of the reciprocity theorem and defining the adjoint sources we conclude to the final sensitivity equation. Now considering that the Finite Element method (FEM) is used for the solution of the forward problem the unknown sensitivity integrals can be calculated since their integrands are comprised of the FEM basis functions. So following this procedure the sensitivity matrix for a microwave tomography application can be efficiently evaluated. A numerical investigation of this matrix will be given in terms of the antennas number, position, and frequency and in terms of the number of the problem unknowns. The numerical investigation will be based on a Singular Value Decomposition (SVD) of the Sensitivity Matrix [4] and the degree of ill-posedness will be calculated for each case. The resulting singular vectors constitute the numerical basis functions on which the reconstruction scheme is developed. The aim of the present analysis is to investigate how these singular vectors cover the whole domain to be imaged, as well as how each one of them can be realized through appropriate excitation. In turn, this knowledge will be exploited in the establishment of an appropriate data collection strategy. Namely define the appropriate antenna position, orientation and polarization for both transmit (illumination) and receive (sensing) functions.

2. FORWARD PROBLEM SOLUTION

The geometry of the forward problem is shown in Fig. 1. The object to be imaged is embedded in a lossy homogeneous surrounding medium. This in turn is enclosed within a fictitious cylindrical boundary along which absorbing boundary conditions are applied.

An array of (N) infinitesimal thin electric dipoles equidistantly located around a circular periphery of radius 15 cm is considered. All dipoles are vertically oriented along the z -axis and for each projection angle only one of them is driven (excited) while all the others are sensors measuring the electric field. The present effort is restricted to unknown dielectrical objects with uniform permeability $\mu = \mu_r \mu_0 = \text{const}$, and transversely inhomogeneous conductivity $\sigma(\vec{r}) = \sigma(x, y)$ and

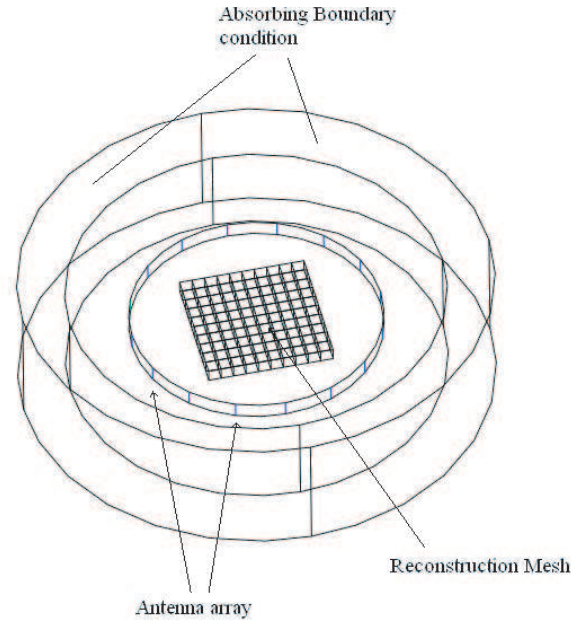


Figure 1: Geometric configuration of the 3D scattering problem.

permittivity $\varepsilon(\vec{r}) = \varepsilon(x, y)$ distributions which are also uniform along the z -axis. Since the dipoles are assumed electrically thin and z -oriented they support only a z -component current density as $\vec{J} = J_z(\vec{r})\hat{z}$ for both transmit and receive functions. Hence, the transmitting dipole generates only a z -oriented (polarized) electric field (E_z) and the receiving dipoles can sense only an E_z field. The above described structure is sometimes called as a “2.5-D, two and a half dimensional” to discriminate it from the infinitely extended two-dimensional and the fully three-dimensional one. In turn the E_z electric field generated by the driven infinitesimal dipole is governed by a scalar Helmholtz wave equation of the form

$$\vec{\nabla}^2 E_z(\vec{r}) - j\omega\mu[\sigma(\vec{r}) + j\omega\varepsilon(\vec{r})]E_z(\vec{r}) = j\omega\mu J_z(\vec{r}) \quad (2)$$

or

$$\vec{\nabla}^2 E_z(\vec{r}) + k_0^2 \mu_r \varepsilon_{rc}(\vec{r}) E_z(\vec{r}) = j\omega\mu J_z(\vec{r}) \quad (3)$$

where the complex dielectric constant is $\varepsilon_{rc} = \varepsilon_r - j\sigma/(\omega\varepsilon_0)$ and $k_0 = \omega\sqrt{\mu_0\varepsilon_0} = \omega/c$ the free space wavenumber.

For the solution of Helmholtz equation the Finite Element Method (FEM) employing nodal tetrahedral elements is used, in conjunction with a Dual-mesh scheme. The field values are defined on the forward (fine) mesh, while the material properties σ and ε_r are defined on the reconstruction (coarse) rectangular mesh. In this manner field values on the reconstruction mesh are interpolated from the forward mesh and properties values on the forward mesh are interpolated from the reconstruction mesh. For this to be achieved a mapping between the two different meshes needs to be established. Using this scheme a more realistic model and an accurate forward solution is obtained, while the number of unknowns in the inverse problem is kept low. Note that the reconstruction mesh is conformal to the forward mesh and each node of the coarse mesh belongs to the fine mesh as well.

3. CALCULATION OF THE JACOBIAN MATRIX

The reconstruction algorithm is based on the modified perturbation method that was developed for the conductivity imaging in Electrical Impedance Tomography [5, 6]. The aim now is its application in imaging at microwave frequencies. The new algorithm is based again on the Jacobian matrix (J). The components of the Jacobian are the partial derivatives (or the sensitivities) of the electric field \vec{E}_r measured at the r th antenna with respect to the complex permittivity ε_{rc}^k of the k th element-pixel, when the s th antenna is activated. This is in turn evaluated through closed form expressions resulting from the reciprocity theorem and the employment of an adjoint problem. For this purpose an approach similar to that given by Oldenburg [7] and the original research referenced

therein is adopted. Namely, the two Maxwell curl equations are written for the source (\vec{J}_s) at s th antenna producing a field distribution (\vec{E}, \vec{H}), which is then differentiated with respect to the k th element complex permittivity. For the adjoint fields (E^a, H^a) these two curl equations are written considering a source (\vec{J}_r) at the r th antenna. The four curl equations are in turn combined following the reciprocity theorem procedure to end up to the so called sensitivity formula:

$$J_{((s,r),k)} = \frac{\partial \vec{E}(\vec{r})}{\partial \varepsilon_{rc}^k} = \iint_S i\omega \vec{\psi}_k(\vec{r}) \vec{E}^a \cdot \vec{E} \quad (4)$$

Since the integration is restricted over the k th element, then the field \vec{E} and \vec{E}^a are replaced by the finite elements interpolation (shape) functions of the k th element to yield:

$$J_{((s,r),k)} = \frac{\partial \vec{E}(\vec{r})}{\partial \varepsilon_{rc}^k} = \iint_{S^k} i\omega \sum_i E_i \cdot N_i^k \sum_j E_j^a \cdot N_j^k dV \quad (5)$$

or in matrix form

$$J_{((s,r),k)} = i\omega [E^k] \cdot [F^k] \cdot [E^{ak}]^T \quad (6)$$

where the subscripts i, j denote the nodes of the triangles in Fig. 2(b) and

$$[F_{ij}^k] = \iint_{S^k} \{N_i^k\} \cdot \{N_j^k\} dS \quad (7)$$

Recall at this point that FEM is applied on a three dimensional fine mesh of tetrahedral node elements, while the image reconstruction is carried out on a coarse cartesian grid. Since the material properties are assumed uniform in the z -direction this coarse grid is two-dimensional comprised of rectangular elements as shown in Fig. 1. Its cross section is assumed at the mid-height of the structure and for convenience this coarse grid is made conformal to the fine one. As shown in Fig. 2(b), each rectangular element coincides with the bases of four tetrahedral elements of the fine mesh. Hence, each rectangular reconstruction element is comprised of 5 degrees of freedom assigned to its 5 nodes and the field values E^k, E^{ak} are readily available from the FEM solution through a simple mapping of nodes. Likewise, the interpolation functions N_i, N_j are those of the tetrahedral elements. Correspondingly, these functions are integrated in Eq. (7) to yield a 3×3 matrix F^k which through Eq. (6) results to a partial Jacobian matrix for each triangular element of Fig. 2(b). However, the desired Jacobian is that of the rectangular element. For its evaluation, the F^k matrices are assembled together according to the classical FEM procedure to yield a 5×5

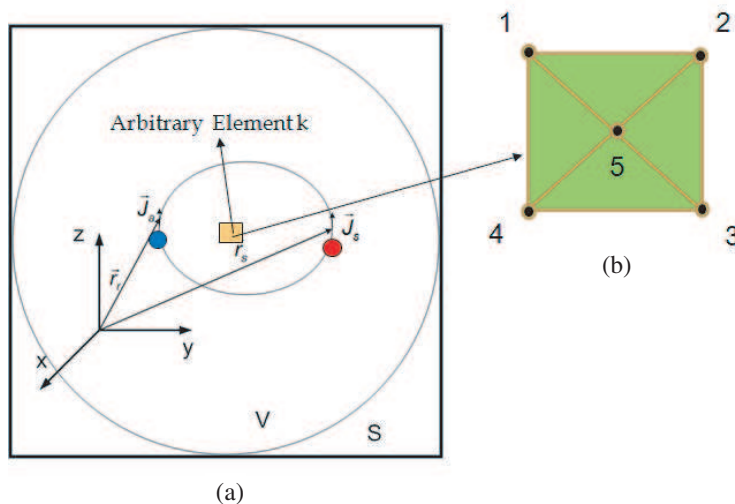


Figure 2: (a) Geometry for the reciprocity theorem definition. (b) A rectangular element of the coarse mesh.

matrix K^e , where e the global number of the rectangular element. Note that this matrix depends only on the geometry (independent of ε_{rc} distribution) and its calculated only once. Consequently, the Jacobian matrix for the e th element reads.

$$J_{((s,r),e)} = i\omega [E^e] \cdot [K^e] \cdot [E^{ae}]^T \quad (8)$$

where $[E^e] = [E_1^e, E_2^e, E_3^e, E_4^e, E_5^e]^T$ and $[E^{ae}] = [E_1^{ae}, E_2^{ae}, E_3^{ae}, E_4^{ae}, E_5^{ae}]^T$.

4. SVD OF THE JACOBIAN MATRIX

The Singular Value Decomposition (SVD) of the total Jacobian matrix representing the whole structure is carried out using Matlab. As usual J is decomposed in three matrices as:

$$J = U\Sigma V^T \quad (9)$$

where $U = \{u_1, u_2, \dots, u_p\}$ and $V = \{v_1, v_2, \dots, v_p\}$ are both column orthogonal matrices. Σ is a diagonal matrix with non-negative real values arranged in decreasing order, i.e., $\Sigma = \text{diag}(\{\sigma_i\}_{i=1}^p)$ with $\sigma_1 \geq \sigma_2 \geq \dots \geq \sigma_p \geq 0$. Vectors u_i and v_i are referred to as the i th left and right singular vectors respectively, while σ_i is the i th singular value. The sequence $\{\sigma_1, \sigma_2, \dots, \sigma_n\}$ is referred to as the singular spectrum of J .

In Fig. 3, the magnitude of some right singular vectors is plotted over the reconstruction area. These vectors comprise the energy components-patterns that are used during the reconstruction process. As can be observed from Fig. 3 each singular vector focuses on a different subdomain. Thus, a number of singular vectors can be selected to form an appropriate “basis function” aiming at an optimum reconstruction. The row of the Jacobian corresponding each singular vector is identified, in turn this corresponds to a specific locations of transmitting and receiving dipoles. Hence, a mapping between the singular vectors and the illumination position (projection angle) can be established which serves to devise the data collection strategy.

5. RESULTS

In this section the impact of various imaging parameters on the singular spectrum of the Jacobian matrix, and consequently the potential quality of the reconstructed image, is studied. The problem configuration used here is defined in Fig. 1. The numerical singular spectrum of the Jacobian matrices were computed using different system parameters. In order to compare different spectra the definition for the degree of ill-posedness according to Fang [3] was used. This definition is a modification of that discussed in [8], as:

“If there exists a positive real number α , for a singular spectrum $\{\sigma_i\}_i^N$, and if $\sigma_i/\sigma_1 = O(\exp(-\alpha i))$, then, α is called the degree of ill-posedness of the spectrum.”

Hence, according to [8] a linear regression was performed on the series of singular values $\{\log(\sigma_i) - \log(\sigma_1)\}_i^N$ (N is the numerical rank of the Jacobian), where the slope was used to estimate α .

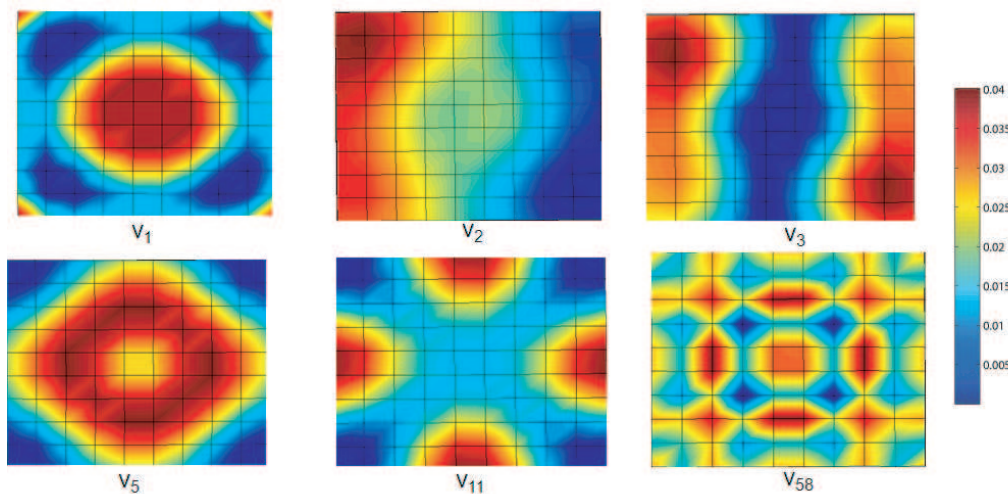


Figure 3: Magnitude of some right singular vectors.

First the singular values spectrum of the Jacobian for various signal frequencies was calculated. The background and the object permittivity and conductivity were first assumed identical $\epsilon_r = 30$ and $\sigma = 0.3 \text{ S/m}$ (absence of inhomogeneity). The number of the unknown elements-pixels for the coarse-reconstruction mesh was $K = 100$. Two sets of elementary dipoles arrays were used, one with $N = 16$ dipoles and one with $N = 32$ dipoles. The number of linearly independent measurements for $N = 16$ is $M = N(N - 1)/2 = 120$, while for $N = 32$ is $M = 496$. In the first case M is close to K so marginal resolution is expected while for $N = 32$ the sensitivity and the ill-posedness should be much better.

In Fig. 4(a) the singular values spectrum for $f = 2.5 \text{ GHz}$ is shown. From Fig. 4(b) it is observed that for higher frequencies the degree of ill-posedness is lower indicating that in these frequencies the reconstructed image quality might be better. Moreover, for $N = 32$ dipoles α is lower than $N = 16$ for all frequencies as expected. One may arrive at the same conclusion by plotting one row of the Jacobian (one pair of transmitting — receiving antennas) over the reconstruction area for different frequencies, e.g., $f = 1 \text{ GHz}$ and $f = 2.5 \text{ GHz}$. As it is shown in Fig. 5 the sensitivity is higher along the fictitious axes connecting a pair of transmitting and receiving antennas, however its distribution is more uniform for the higher frequency (2.5 GHz).

In a second investigation the background electrical permittivity was varied from $\epsilon_r = 10$ to $\epsilon_r = 90$. The operating frequency was $f = 1 \text{ GHz}$. The permittivity and conductivity of the object was $\epsilon_r = 30$ and $\sigma = 0.3 \text{ S/m}$. The number of the unknown elements-pixels was again $K = 100$ and two sets of dipole arrays with $N = 16$ and $N = 32$ dipoles were considered. The results of Fig. 6(a) shows that higher number of dipoles reduce the singularity degree. Likewise the singularity is decreased when the background permittivity is increased beyond that of the object. In this case

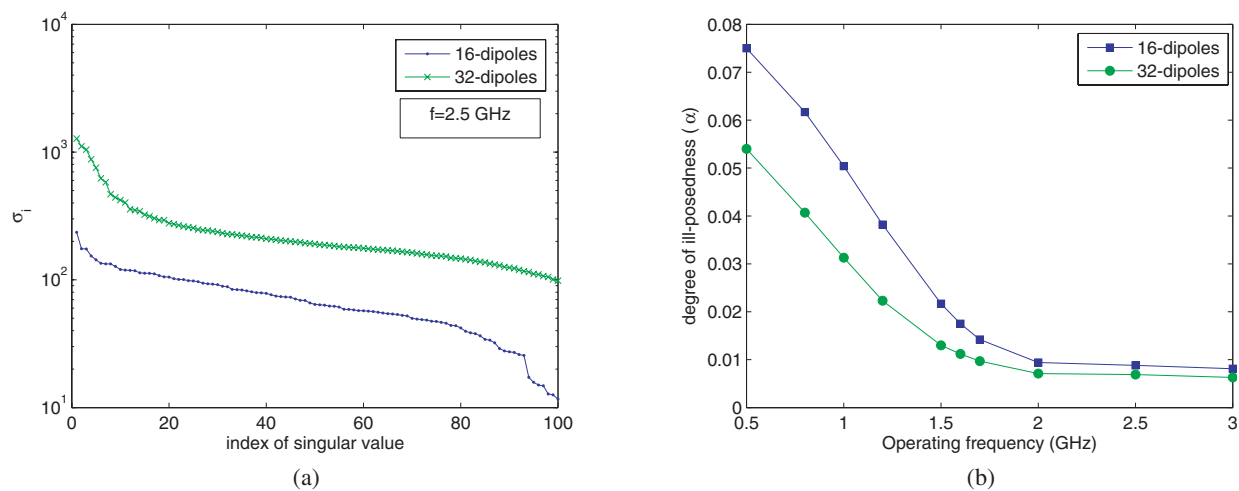


Figure 4: (a) Spectrum of singular values for $f = 2.5 \text{ GHz}$. (b) Degree of ill-posedness as a function of frequency.

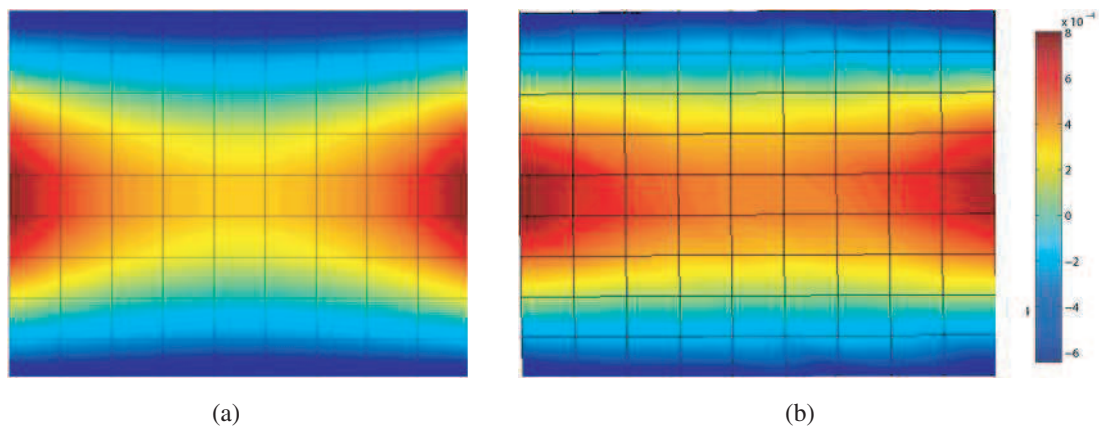


Figure 5: Plot of a single Jacobian row over the parameter mesh (a) for $f = 1 \text{ GHz}$, (b) for $f = 2.5 \text{ GHz}$.

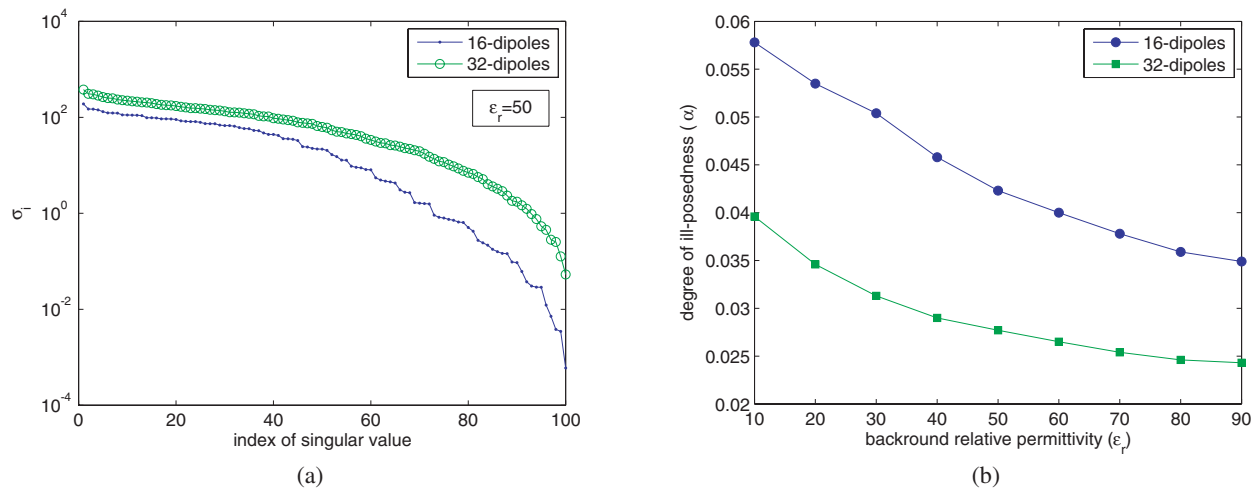


Figure 6: (a) Spectrum of singular values for a rectangular object with $\epsilon_r = 30$, $\sigma = 0.3$ S/m embedded in a homogeneous background with $\epsilon_r = 50$ and at $f = 1$ GHz. (b) Degree of ill-posedness as a function of background permittivity.

the energy is concentrated in the background medium (higher ϵ_r) creating a more homogeneous field distribution over the object area.

The results are presented in Fig. 6(a) and as the background permittivity is increasing the energy of the electromagnetic wave is concentrated on the inner imaging area so the degree of ill-posedness is decreased. Again using more dipoles we have lower α as expected.

6. CONCLUSIONS

A calculation for the Jacobian matrix based on adjoint network theorem and reciprocity theorem of electromagnetics was proposed. A numerical investigation of the Jacobian was made based on singular value decomposition and the degree of ill-posedness of the matrix was made. Three parameters were investigated, the operating frequency, the background permittivity value, and the number of dipoles. Further work can be done investigating more parameters of the reconstruction scheme such as dipole spacing and position or mesh density in order to define the best data collection strategy.

ACKNOWLEDGMENT

This work is implemented in the framework of Measure 8.3 through the O.P. Competitiveness 3rd Community Support Program and is co-funded by: (75%) of the Public Expenditure from the European Union — European Social Fund, (25%) of the Public Expenditure from the Hellenic State — Ministry of Development — General Secretariat for Research and Technology, and Private Sector (INTRACOM SA).

REFERENCES

1. Nikolova, N. K., Z. Jiang, L. Dongying, M. H. Bakr, and J. W. Bandler, "Sensitivity analysis of network parameters with electromagnetic frequency-domain simulators," *IEEE Trans. on Microwave Theory and Techniques*, Vol. 54, No. 2, 2006.
2. Dyck, D. N., D. A. Lowther, and E. M. Freeman, "A method of computing the sensitivity of electromagnetic quantities to changes in materials and Sources," *IEEE Trans. on Magnetics*, Vol. 30, No. 5, 1064–1076, 1994.
3. Song, Y. and N. K. Nikolova, "Memory-efficient method for wideband self-adjoint sensitivity analysis," *IEEE Trans. on Microwave Theory and Techniques*, Vol. 56, No. 8, 1917–1927, 2008.
4. Fang, Q., P. M. Meany, and K. D. Paulsen, "Singular value decomposition of the jacobian matrix in microwave image reconstruction," *IEEE Trans. on Antennas and Propagation*, Vol. 54, No. 88, 2006.
5. Kyriacou, G. A., C. S. Koukourlis, and J. N. Sahalos, "A reconstruction algorithm for of electrical impedance tomography with optimal configuration of the driven electrodes," *IEEE Trans. on Medical Imaging*, Vol. 12, 430–438, 1993.

6. Drogoudis, D. G., G. Trichopoulos, G. A. Kyriacou, and J. N. Sahalos, “A modified perturbation method for three-dimensional time harmonic impedance tomography,” *PIERS Online*, Vol. 1, No. 1, 151–155, 2005.
7. Oldenburg, D. W., “Practical strategies for the solution of large-scale electromagnetic inverse problems,” *Radio Science*, Vol. 29, 1081–1099, 1994.
8. Hansen, P. C., *Rank-deficient and Discrete Ill-posed Problems: Numerical Aspects of Linear Inversion*, Philadelphia, PA, SIAM, 1997.

Modeling of Infinite Periodic Arrays with Dielectric Volumes and Quasi-3D Oriented Conductors

V. Volski and G. A. E. Vandenbosch

ESAT-TELEMIC, Katholieke Universiteit Leuven, Belgium

Abstract— A new asymptotic extraction technique is used within the Method of Moments to model periodic quasi-3D arrays consisting of complex elements including vertical/horizontal conductors and dielectric volumes. The extraction uses special asymptotes closely connected to the actual Green's functions. These asymptotes can be used both for single elements and periodic arrays of elements. This step facilitates the simultaneous development of new features for both topologies.

1. INTRODUCTION

The modeling of periodic arrays composed of complex elements including horizontal/vertical conductors and dielectric volumes is of interest in different applications including antenna design, frequency selective surfaces and so on. The design of such arrays in many cases is facilitated if the modeling of a single element is also available. These two topologies can be very useful to estimate the mutual coupling in arrays. Nowadays there are several software tools available based on different techniques that can be used to treat these two topologies. Some of the software tools are better suited to model single elements, while others are better suited to model antennas enclosed in an environment with periodic or waveguide boundary conditions. The switch between different software tools is not always straightforward because the input/output formats are very often incompatible. Thus, it is of great interest to have a single code that is able to treat efficiently these topologies using the same approach in both cases.

The MoM method in combination with Mixed Potential Integral Equations (MPIE) has proven to be very efficient in the modeling of conductors in layered structures [1]. This approach is based on the construction of spatial Green's functions (GFs). This method can be used for a single element and a periodic array of elements. The GFs construction for a single element and for a periodic array encounters different types of problems despite that in both cases it is based on the Inverse Fourier Transform (IFT) of the same spectral GFs, which are known in a closed form. The IFT is expressed in terms of double integrals for a single element or in terms of double series for a periodic array. The convergence of the spectral GFs is normally insufficient for a direct numerical evaluation. In the case of a single element, moreover, a special precaution should be taken to deal correctly with branch cuts and poles. In the case of a periodic array, these problems are avoided because the needed spectrum is discrete. This last difference contributes enormously to the fact that the construction of the GFs is typically treated separately for a single element and a periodic array resulting in different algorithms and software codes. As a consequence available software tools are normally better suited for a single element or a periodic array.

The aim of this paper is to report an efficient algorithm and its implementation within a single code, with only minor differences between a single element and a periodic array. This technique was consecutively applied to model periodic arrays only with horizontal conductors, and then with a combination of vertical and horizontal conductors. The application of this technique was shown at EUCAP 06 for horizontal conductors and at EUCAP07 for horizontal and vertical conductors. In this paper, dielectric volumes are included. The combination of vertical and horizontal conductors with dielectric volumes widens considerably the variety of topologies that can be modeled.

2. THEORY

The MPIE in the MoM formulation requires the calculation of the GFs in the spatial domain for different source types (electric horizontal and vertical conductors and volumes). The algorithm to calculate them is quite cumbersome and its implementation needs a lot of effort. The approach chosen in this paper relies on a strong resemblance between the two algorithms to calculate GFs for a single source and a periodic array of sources. The original algorithm for a single source is slightly adjusted in such a way that the periodicity of the elements can be implemented very easily. In practice, this means that major steps like the calculation of GFs in the spectral domain can remain almost the same and only a few additional procedures are required. The main advantage

of this approach is that it is a modular analysis technique, which allows to develop and to test new features in the global modeling scheme simultaneously for a single element and a periodic array of elements.

It is important to mention that the MPIE formulation is widely used to model periodic arrays consisting of elements composed of horizontal conductors only. The reason for this is that the number of required GFs is small in this case and there are several efficient approaches for their calculation available [2]. In the case of 3D conductors in the layered medium, the number of GFs starts to depend on the chosen approach. In our approach, the number of GFs remains relatively small due to a partial implementation of the current dependency in the GFs. All current components on the vertical conductors are expressed in terms of rooftop basis functions and these vertical rooftop basis functions are considered as elementary sources for the GFs components. However, these more complex sources do not alter our general procedure. The GFs in the spatial domain for periodic arrays can be expressed in the following form [2]

$$G_{ij}(x, y) = \sum_{k_{mx}} \sum_{k_{my}} \tilde{G}_{ij}(\beta_{mn}) e^{-j(k_{mx}x + k_{my}y)}, \quad \beta = \sqrt{k_{mx}^2 + k_{my}^2} \quad (1)$$

where $\tilde{G}_{ij}(\beta_{mn})$ is the spectral GF. In general, this series has a poor convergence. Using a so-called Kummer's transformation, the poor convergence of the GF in (1) is improved by subtracting specially selected asymptotes.

$$\begin{aligned} G_{ij}(x, y) &= G_{ij}^{\text{spectral}}(x, y) + G_{ij}^{\text{spatial}}(x, y) \\ G_{ij}^{\text{spectral}}(x, y) &= \sum_m \sum_n \left[\tilde{G}_{ij}(\beta_{mn}) - \tilde{G}_{ij}^{as}(\beta_{mn}) \right] e^{-j(k_{mx}x + k_{my}y)} \\ G_{ij}^{\text{spatial}}(x, y) &= \sum_m \sum_n g_{ij}^{as}(r_{mn}) = \sum_m \sum_n \tilde{G}_{ij}^{as}(\beta_{mn}) e^{-j(k_{mx}x + k_{my}y)} \end{aligned} \quad (2)$$

In order to construct an efficient algorithm, this double series in the spatial domain should also have a good convergence. These conditions can be satisfied by selecting the following asymptotes:

$$\tilde{G}_{ij}^{as}(\beta, t) = \frac{(1 - e^{-\beta t})^m e^{-\beta \Delta}}{\beta^m} \quad (3)$$

The asymptote in (3) has the necessary leading term for large values of β , that annihilates the leading term of $\tilde{G}_{ij}(\beta)$, and it has no singularity at $\beta = 0$. The Fourier transform of (3) is known in a closed form.

$$g^{as}(r) \frac{1}{\sqrt{\rho + \Delta^2}} - \frac{1}{\sqrt{\rho^2 + (\Delta + t)^2}}, \quad \text{for } m = 1 \text{ and} \quad (4a)$$

$$g^{as}(x, y, z) = \ln \left[\frac{\left(\sqrt{\rho^2 + (\Delta + t)^2} + \Delta + t \right)^2}{\left(\sqrt{\rho^2 + \Delta^2} + \Delta \right) \left(\sqrt{\rho^2 + (\Delta + 2t)^2} + \Delta + 2t \right)} \right], \quad \text{for } m = 2. \quad (4b)$$

Asymptotes for different sources (horizontal and vertical conductors and volume) can be constructed using these basic asymptotes. Each asymptote can be considered as a static combined source of 2 anti-phased sources separated in the z -direction by a small distance t . These asymptotes are relatively simple and it is possible to perform the integration over the source and observation domains if it is necessary.

Although the convergence of the series is improved with the Kummer's transformation, the efficiency can be increased further using special acceleration routines. Acceleration algorithms can reduce the required number of terms in series. Series with oscillating terms in the spectral domain are accelerated using Shank's transform [3]. Series in the spatial domain are accelerated using the rho-algorithm [4], a technique more suited for monotone behavior. The general idea works very well. However there are some practical problems that maybe require particular attention. The convergence of series in the spectral and in the spatial domains depends on many factors

like the periodicity of the cells, the chosen parameter t . Only for GFs associated with horizontal conductors, this problem is well investigated [2]. Although the main guidelines remain valid for vertical conductors, the situation is more complex because these GFs are expressed in terms of more complex functions making the definition of the spectral threshold above which the leading asymptotic term becomes dominant more complex. The convergence of the series and the choice of the parameters are of interest in ongoing research. For instance, the minimal number of terms that has to be actually calculated in a series is about 10 by 10 in the spectral and spatial domains for accuracy normally required in practical applications. For structures containing only horizontal conductors this gives normally a good approximation. If the period of an array is decreasing, then the convergence in the spectral domain is improving and the convergence in the spatial domain is decreasing. This can be partially corrected by adjusting the parameter t in (3) and (4).

3. NUMERICAL RESULTS

As examples, we consider 2 structures consisting of horizontal, vertical conductors and volumes. The addition of volumes widens the range of structures that can be analyzed enormously. The resonant frequency of an antenna depends not only on the antenna shape but also on the antenna environment. The presence of dielectric layers close to the antenna can change very noticeably its properties. The thickness and permittivity of layers used in the structure have to be chosen from a list of available materials. This rather limited choice can be widened using partial dielectric filling, when part of the dielectric is removed or added. The properties of the obtained structures can be described using some effective permittivities whose values depend on the permittivity and the volume ratio between different inclusions. The effective permittivity can be estimated using effective medium theory [5]. However this theory provides a very good approximation when the size of the inclusions is small in terms of wavelengths. In the other case a full wave modeling is preferable.

The examples considered further in the paper demonstrate the efficiency of tuning using partial dielectric volume filling.

The first example is an approximation of a magnetic conductor. This structure is inspired by the mushroom cell considered in [6]. A periodic set of patches is mounted on a ground plane. Each patch is fixed on a square stem that is connected also to the ground plane. The period of the array is 2.4 mm, the patch size is 2.25 mm and the thickness is 1.6 mm. Then a square dielectric gasket (dielectric permittivity 2.2 and thickness 1.6 mm) is placed under the patch. Changing the gasket size varies the dielectric filling from 0 mm (no dielectric) to 2.4 mm (full filling). The topology is shown in Fig. 1.

The structure is excited by a plane wave. The calculated reflection coefficient is plotted in Fig. 1 for different volume fillings. In contrast to a typical ground plane where the reflection coefficient phase is about 180 degrees, the reflection coefficient phase of the mushroom structure is about zero in a certain frequency band. That corresponds to the behavior of a magnetic conductor. As expected the filling variation allows to tune the frequency very efficiently.

The next example is an array of crosses. The period of the array is 10 mm. The cross length L is 6.875 mm and its width is 0.625 mm. This topology is inspired by [7]. As in the previous case, a square dielectric gasket is placed under the cross. The gasket dielectric permittivity is 4 and its

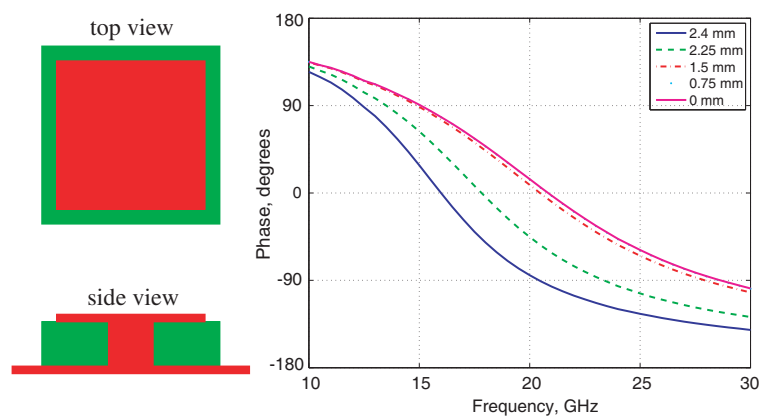


Figure 1: Modeling of a magnetic conductor.

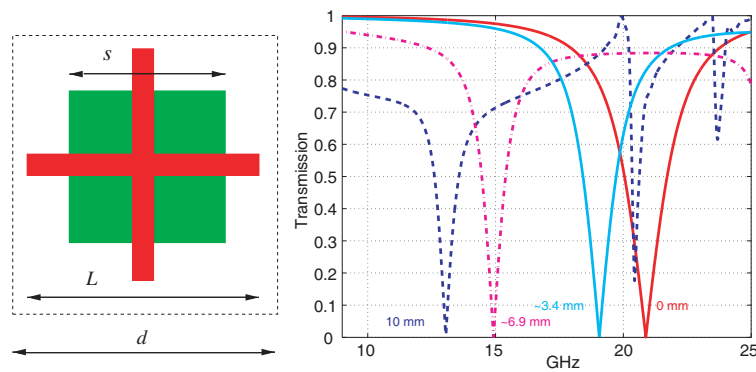


Figure 2: Modeling of the array of crosses.

thickness is 0.3 mm. The structure is excited again by a plane wave from the top. The calculated transmission is plotted for different dielectric fillings in Fig. 2. This structure behaves like a very good reflector in some frequency band. This band can be tuned using partial dielectric filling.

4. CONCLUSION

In this paper, it is demonstrated that an asymptote extraction technique using the same asymptotes can be used to model a single element and a periodic array of elements in planar layered media. Each element can be composed from horizontal/vertical conductors and dielectric volumes. Our progress in the implementation of dielectric volumes is reported. The combination of different components (horizontal and vertical conductors with dielectric volumes) allows to consider very complex antenna topologies. Several examples illustrate the possibility of our approach.

REFERENCES

- Peterson, A. F., S. L. Ray, and R. Mittra, *Computational Methods for Electromagnetics*, IEEE Press, 1998.
- Valerio, G., P. Baccarelli, P. Burghignoli, and A. Galli, "Comparative analysis of acceleration techniques for 2D and 3D Green's functions in periodic structures along one and two directions," *IEEE Trans. Antennas Propagation*, Vol. 55, No. 6, 1630–1643, 2007.
- Shanks, D., "Non-linear transformations of divergent and slowly convergent sequences," *J. Math. Phys.*, Vol. 34, 1–42, 1955.
- Singh, S. and R. Singh, "On the use of rho-algorithm in series acceleration," *IEEE Antennas Propagation*, Vol. 39, No. 10, 1514–1516, 1991.
- Collin, R., *Field Theory of Guided Waves*, IEEE Press, 1990.
- Sievenpiper, D., L. J. Zhang, R. F. J. Broas, N. G. Alexopolous, and E. Yablonovitch, "High-impedance electromagnetic surfaces with a forbidden frequency band," *IEEE Trans. Microwave Theory Techniques*, Vol. 47, No. 11, 2059–2074, 1999.
- Cwik, T. and R. Mittra, "The cascade connection of planar periodic surfaces and lossy dielectric layers to form an arbitrary periodic screen," *IEEE Trans. Antennas Propagation*, Vol. 35, No. 12, 1397–1405, 1987.

Microwave Penetrating and Heating of Metallic Powders

A. P. Anzulevich¹, V. D. Buchelnikov¹,
I. V. Bychkov¹, and D. V. Louzguine-Luzgin²

¹Chelyabinsk State University, Russia

²WPI Advanced Institute for Materials Research, Tohoku University, Japan

Abstract— Owing to so-called skin-effect bulk metals reflect microwaves (MWs) and can hardly be heated. They can undergo only surface heating due to limited penetration of the MW radiation. Whereas metallic powders can be penetrated into itself and absorb such radiation and efficiently heat. So, in the present work, we theoretically studied the MW penetrating mechanisms, the possible MW heating mechanisms of metallic powders and provide some theoretical explanation of the MW penetrating and MW heating behavior.

1. INTRODUCTION

Recently MW heating has been successfully applied to powdered metals and fully sintered samples were obtained in 1999 in a multimode cavity [1, 2]. Later, MW heating in separated electric (E-) field and magnetic (H-) field of a standing wave was performed [3, 4]. The MW sintering of various metals powders, steels and non-ferrous alloys helped to produce sintered samples within tens of minutes at sintering temperature ranges from 1370 K to 1570 K [5]. Moreover, nanomaterials and some composite materials can also be produced by such a technique [6, 7].

2. THEORETICAL MODEL

The reason of heating of metallic powders has not been clarified fully yet. Here for explanation of MW heating of metallic powders we propose the following model (Fig. 1). We consider the metallic powder as some composite medium. This composite medium consists from the mixture of spherical metallic particles covered by thin oxide dielectric shell and gas (or vacuum) [8, 9].

The scheme for the model is divided onto three parts. First region lies on the left side of the plate. Second region corresponds to the plate and third region is a distance between right side of the plate and fully reflecting massive medium (designated as a reflector). For the calculation of the electromagnetic fields in all regions, we used the transition matrix method [10].

In our case, the plate of metallic powder will be mean a randomly distributed in gas (vacuum) mixture of metallic cores (R_1 , ε_1) with dielectric shells (R_2 , ε_2). For calculations of the effective dielectric permittivity and magnetic permeability of such structure we will use the effective medium approximation (EMA) model [11, 12]:

$$p\zeta \frac{\varepsilon_2 [3\varepsilon_1 + (\zeta - 1)(\varepsilon_1 + 2\varepsilon_2)] - \varepsilon_{eff} [3\varepsilon_2 + (\zeta - 1)(\varepsilon_1 + 2\varepsilon_2)]}{2\alpha\varepsilon_{eff} + \beta\varepsilon_2} + (1 - p\zeta) \frac{\varepsilon_g - \varepsilon_{eff}}{\varepsilon_g + 2\varepsilon_{eff}} = 0, \quad (1)$$

where p is the volume fraction of a metal in the effective medium, $\zeta = (R_2/R_1)^3 = (1 + l)^3$, l is the relative thickness of the dielectric shell on the surface of the metallic core: $l = (R_2 - R_1)/R_1$, $\alpha = (\zeta - 1)\varepsilon_1 + (2\zeta + 1)\varepsilon_2$, $\beta = (2 + \zeta)\varepsilon_1 + 2(\zeta - 1)\varepsilon_2$, dielectric permittivity of gas is $\varepsilon_g = 1$.

For calculation of the heating curves of the composite plate of metallic powder we used the heat conduction equation subject to heat source is penetrating into metallic powders plate electromagnetic field. This equation can be written as:

$$Q_{eh} = Q_e + Q_h = \frac{\omega}{8\pi} \left(\varepsilon'' |\bar{e}|^2 + \mu'' |\bar{h}|^2 \right), \quad (2)$$

where Q_e is electrical part of heat, and Q_h is ones magnetic part.

3. INDUCING FIELD BY ONE CONDUCTIVE PARTICLE

Let's consider one spherical conductive particle of radius a ($\sim 25 \mu\text{m}$) on which one electromagnetic wave falls and calculate scattered by this particle field [13] for obviously comprehension of penetrating and heating mechanisms of such plate from metallic powder. Let's consider quasi-stationary approximation, because the dimension of the particle much less a wavelength of falling

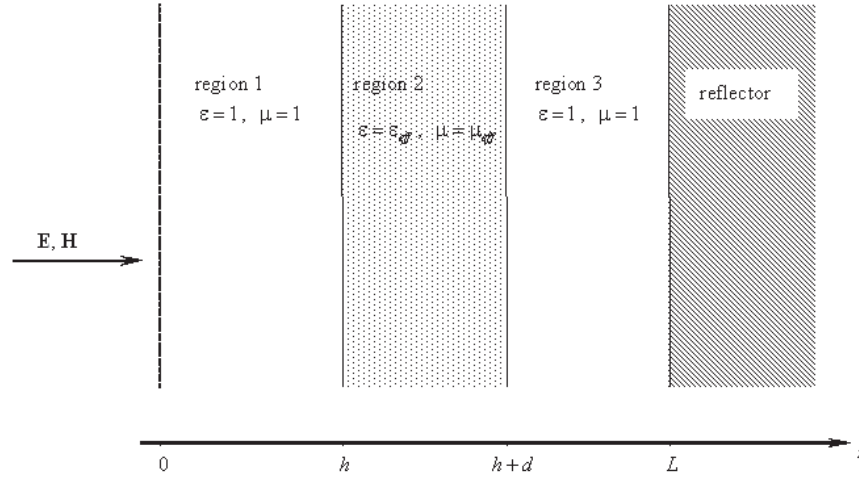


Figure 1: The scheme for the theoretical model. The regions 1 and 3 correspond to the gas (vacuum). Region 2 is the plate from composite conductive material and the region 4 is the ideal massive conductive medium (reflector). The electromagnetic wave falls on these regions from the left side.

electromagnetic radiation. This approximation allows to obtaining distribution of electromagnetic fields inside and closely of conductive particle.

Faraday induction law assigns that changing of magnetic induction \bar{B} gives in conductor electric field \bar{E} which magnitude and direction are determined by relation:

$$\nabla \times \bar{E} = -\frac{1}{c} \frac{\partial \bar{B}}{\partial t} \quad \text{or} \quad \bar{E} = -\frac{1}{c} \frac{\partial \bar{A}}{\partial t}, \quad (3)$$

c is velocity of light in free space.

As soon as electric field appears in conductor then electrical current arise into conductor by Ohm's law. Let as σ is conductivity, and \bar{j} is current density then Equation (3) can rearrange in the form

$$\bar{j} = -\frac{\sigma}{c} \frac{\partial \bar{A}}{\partial t}. \quad (4)$$

These currents generate into medium with permeability μ magnetic field determined by:

$$\nabla^2 \bar{A} = -\frac{4\pi\mu\bar{j}}{c}. \quad (5)$$

From Equations (4) and (5), we can easily get equation for \bar{A} , \bar{B} , and \bar{j} :

$$\frac{4\pi\sigma\mu}{c^2} \frac{\partial \bar{A}}{\partial t} = \nabla^2 \bar{A}, \quad \frac{4\pi\sigma\mu}{c^2} \frac{\partial \bar{B}}{\partial t} = \nabla^2 \bar{B}, \quad \frac{4\pi\sigma\mu}{c^2} \frac{\partial \bar{j}}{\partial t} = \nabla^2 \bar{j}. \quad (6)$$

Solving these equations and assumed that vector-potential of eddy currents must be zero at infinity and finite at $r = 0$ can obtain:

$$a < r < \infty, \quad \bar{A}_e = \bar{\varphi} \frac{1}{2} B (r + Dr^{-2}) \sin \theta, \quad (7)$$

$$0 < r < a, \quad \bar{A}_i = \bar{\varphi} \frac{1}{2} BCr^{-1/2} I_{3/2} \left[(ip)^{1/2} r \right] \sin \theta, \quad (8)$$

where C , D is some complex constants which can find from boundary conditions:

$$C = \frac{3\mu v a^{3/2}}{(\mu - \mu_0) v I_{-1/2} + [\mu_0 (1 + v^2) - \mu] I_{1/2}}, \quad D = \frac{(2\mu + \mu_0) v I_{-1/2} - [\mu_0 (1 + v^2) + 2\mu] I_{1/2}}{(\mu - \mu_0) v I_{-1/2} + [\mu_0 (1 + v^2) - \mu] I_{1/2}} a^3,$$

$I_{3/2} \left[(ip)^{1/2} r \right]$ is modified Bessel function of the first kind and with real order, $p = \frac{4\pi\sigma\mu}{c^2} \omega$, ω is frequency of electromagnetic wave, B is external magnetic field, $\bar{\varphi}$ is a unit vector in the line of φ .

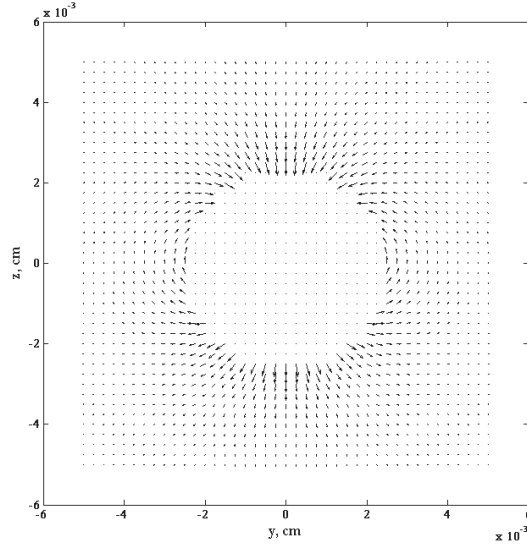


Figure 2: Distribution of vector of magnetic induction B_e^c in plane $x = 0$. The maximum value of amplitude of induction vector is 1 for $y = 0$, $z = 0.0025$, $z = -0.0025$.

We can obtain magnetic field inducing by eddy currents taking rotor from received vector-potential of eddy currents (7), (8) outside of particle:

$$B_{e\theta}^c = -\frac{1}{r} \frac{\partial (r A_{e\varphi}^c)}{\partial r} = \frac{1}{2} \frac{BD}{r^3} \sin \theta, \quad B_{er}^c = \frac{1}{r \sin \theta} \frac{\partial (\sin \theta A_{e\varphi}^c)}{\partial \theta} = \frac{BD}{r^3} \cos \theta, \quad (9)$$

inside of particle:

$$B_{i\theta} = -\frac{1}{r} \frac{\partial (r A_{i\theta})}{\partial r} = -\frac{1}{2} \frac{BC}{r^{1/2}} \left[\frac{1}{2} r^{-1} I_{3/2} + I'_{3/2} \right] \sin \theta, \quad B_{ir} = \frac{1}{r \sin \theta} \frac{\partial (\sin \theta A_{ir})}{\partial \theta} = \frac{BC}{r^{3/2}} I_{3/2} \cos \theta \quad (10)$$

Here $I_{3/2}$ and $I'_{3/2}$ is functions of $x = (ip)^{1/2} r$.

According to these expressions distribution of vector of magnetic induction around the particle shown in Fig. 2. The radius of the particle is $a = 0,0025$ cm, conductivity is $\sigma = 8 \times 10^{16} \text{ s}^{-1}$, permeability is $\mu = 10^3$, frequency of electromagnetic wave is $\omega = 2.45 \times 10^9 \text{ s}^{-1}$, permeability of environment is $\mu_0 = 1$, amplitude of external magnetic field is $B = 1$.

So, electromagnetic field of eddy currents in spherical conductive particle likes magnetic dipole field.

4. CONCLUSION

Thus eddy currents can penetrate into metallic powders at a depth of the size of metallic particles due to sphericity of the skin-depth of these particles [13]. Whereas in bulk metals eddy currents can penetrate into a planar skin-depth only. But eddy currents in metallic powders can be generated on all surface of conductive particle if allowed a condition of quasistationarity. Condition of quasistationarity is requirement that a size of conductive domains less than wavelength of incident MWs.

In turn, these currents induce electromagnetic field behind first “layer” of particles that is able to generate eddy currents into particles of subsequent “layer”. Dielectric shells on the surface of the conductive particles act the part of isolator that blocks generation of more difficulty configurations of eddy currents at less depth of the sample.

At interaction microwaves with ensemble of conductive particles not forming large conductive clusters eddy currents are generated on all surface of each particle independently of the particle disposition depth in layer. Due to this volumetric character of microwave absorption and internal heating are provided.

So, in the present work, we theoretically studied using a model of conductive composite the MW penetrating and scattering mechanisms, the possible MW heating mechanisms of metallic powders and provide some theoretical explanation of the MW penetrating and MW heating behavior for iron powder (Fig. 3).

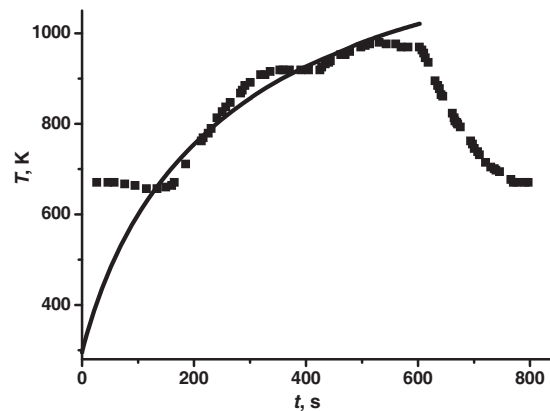


Figure 3: The time dependence of temperature for iron powder. The solid line is the modeling results; the dark square is the experimental ones.

ACKNOWLEDGMENT

This work was supported by the grant RFFI_URAL 07-02-96030.

REFERENCES

- Roy, R., D. Agrawal, J. Cheng, and S. Gedevisanishvili, "Unexpected sintering of powdered metals parts in microwaves," *Nature*, Vol. 399, 664, 1999.
- Anklekar, R. M., K. Bauer, D. K. Agrawal, and R. Roy, "Improved ductility and microstructure related properties of microwave sintered P/M copper and nickel steels," *Powder Metall.*, Vol. 48, 39, 2005.
- Roy, R., R. Peelamedu, L. Hurtt, J. Cheng, and D. Agrawal, "Definitive experimental evidence for microwave effects: Radically new effects of separated E and H fields, such as decrystallization of oxides in seconds," *Mat. Res. Innovat.*, Vol. 6, 128, 2002.
- Yoshikawa, N., E. Ishizuka, and S. Taniguchi, "Heating of metal articles in a single-mode microwave applicator," *Mater. Trans.*, Vol. 47, 898, 2006.
- Anklekar, R. M., D. K. Agrawal, and R. Roy, "Microwave sintering and mechanical properties of P/M steel," *Powder Metall.*, Vol. 44, 355, 2001.
- Inoue, A., "Nanoquasicrystalline and nanocrystalline alloys in Al-based systems," *Progress in Materials Science*, Vol. 43, 365, 1998.
- He, Y., G. J. Shiflet, and S. J. Poon, "A XANES study of the structure of passive films on amorphous AlFeCe alloys," *Acta Metall. Mater.*, Vol. 43, 83, 1995.
- Buchelnikov, V. D., D. V. Louzguine-Luzgin, G. Xie, S. Li, N. Yoshikawa, A. P. Anzulevich, I. V. Bychkov, and A. Inoue, "Heating of metallic powders by microwaves: Experiment and theory," *J. Appl. Phys.*, Vol. 104, No. 9, 2008.
- Anzulevich, A. P., V. D. Buchelnikov, I. V. Bychkov, D. V. Louzguine-Luzgin, N. Yoshikawa, M. Sato, and A. Inoue, "Penetration of microwave radiation into and through metallic powders," *Solid State Phenomena*, Vol. 152–153, 361–364, 2009.
- Born, M. and E. Wolf, "Elements of the theory of diffraction," *Principles of Optics*, Pergamon, New York, 1986.
- Bruggeman, D. A. G., "Berechnung verschiedener physikalischer konstanten von heterogenen substanzen," *Ann. Phys.*, Vol. 416, 636, Leipzig, 1935.
- Landauer, R., "The electrical resistance of binary metallic mixtures," *J. Appl. Phys.*, Vol. 23, 779, 1952.
- Smythe, W. R., *Static and Dynamic Electricity*, 2nd Edition, New York, Toronto, London, 1950.

Effective Medium Approximation for Composite from Three-layered Spherical Particles

D. M. Dolgushin¹, A. P. Anzulevich¹, V. D. Buchelnikov¹,
I. V. Bychkov¹, and D. V. Louzguine-Luzgin²

¹Condensed Matter Physics Department, Chelyabinsk State University, Chelyabinsk 454021, Russia

²WPI Advanced Institute for Materials Research, Tohoku University, Sendai 980-8577, Japan

Abstract— It is known that bulk metallic samples reflect microwaves while powdered samples can absorb such radiation and be heated efficiently. In the present work we studied mechanisms of microwaves absorption of the metallic powders from three-layered particles. The present paper shows dependence of the effective permittivity from the volume fraction of particles and from the thickness of shell for different volume fraction of particles. Also we show the distribution of heat absorbed inside the plate from the composite plate.

1. INTRODUCTION

Microwave (MW) radiation frequencies range from 0.3 GHz to 300 GHz corresponding to wavelengths of 1 m to 1 mm. They cover the electromagnetic spectrum from radio wave frequencies to far-infrared frequencies. In the field of materials processing microwave radiation has been successfully and substantially applied to ceramics and non-metallic glasses. The absorbed microwave energy converts into heat within the material and increases its temperature. All states of matter: solids, liquids, gases and plasma can interact with microwaves.

In materials science microwave radiation has been traditionally applied to ceramics. It has been shown that microwave energy could be used for processing full-scale ceramic products. As microwave radiation causes internal heating of the material then lower temperatures and shorter times can be used compared to those applied at conventional heating. Microwave processing can reduce sintering time by a factor of 10 in some cases and minimize grain growth.

In the present work we studied heating mechanisms of metallic powders from three-layered particles by microwaves with frequency is 2.45 GHz.

2. THEORETICAL MODEL

Equations, figures, tables and references should follow a sequential numerical scheme in order to ensure a logical development of subject matter.

Let us consider the three-layered spherical particles, which randomly distributed in gas (for example, in air) or vacuum. According to effective medium approximation (EMA) an average value of electric displacement of effective medium connects with an average value of electric field strength as

$$\langle \bar{D} \rangle = \varepsilon_{eff} \langle \bar{E} \rangle = \varepsilon_{eff} \bar{E}_0 \quad (1)$$

where ε_{eff} is the effective permittivity of composite, \bar{E}_0 is the external electric field, $\langle \bar{D} \rangle = (1/V) \int_V \bar{D} dV$, V is the volume of the whole composite. It is follow from (1), that for calculation of effective permittivity of composite we need to know the expressions for electric field strength in spherical particle and gas (vacuum).

Firstly we consider one spherical particle. Let the radius of core is R_1 , the external radius of intermediate layer is R_2 and the external radius of shell is R_3 . According to the electrostatic theory [1] expressions for electric potential inside and outside the particle can be presented as

$$\begin{aligned} \varphi_1 &= C_0 r \cos \theta, & r < R_1, \\ \varphi_2 &= (C_1 r + C_2 / r^2) \cos \theta, & R_1 < r < R_2, \\ \varphi_3 &= (C_3 r + C_4 / r^2) \cos \theta, & R_2 < r < R_3, \\ \varphi_4 &= (-E_0 r + C_5 / r^2) \cos \theta, & r > R_3, \end{aligned} \quad (2)$$

where C_i is constants which are calculated from standard boundary conditions

$$\begin{aligned} \varphi_1|_{r=R_1} = \varphi_2|_{r=R_1}, \quad \varphi_2|_{r=R_2} = \varphi_3|_{r=R_2}, \quad \varphi_3|_{r=R_3} = \varphi_4|_{r=R_3}, \\ \varepsilon_1 \frac{\partial \varphi_1}{\partial r} \Big|_{r=R_1} = \varepsilon_2 \frac{\partial \varphi_2}{\partial r} \Big|_{r=R_1}, \quad \varepsilon_2 \frac{\partial \varphi_2}{\partial r} \Big|_{r=R_2} = \varepsilon_3 \frac{\partial \varphi_3}{\partial r} \Big|_{r=R_2}, \quad \varepsilon_3 \frac{\partial \varphi_3}{\partial r} \Big|_{r=R_3} = \varepsilon_4 \frac{\partial \varphi_4}{\partial r} \Big|_{r=R_3}. \end{aligned} \quad (3)$$

Here ε_1 is the effective dielectric permittivity of core, ε_2 is the dielectric permittivity of intermediate layer, ε_3 is the dielectric permittivity of shell, ε_4 is the dielectric permittivity of gas (vacuum). After substitution Equations (3) in the boundary conditions (2) we find the constants C_i . Final expressions for electric potentials are:

$$\begin{aligned} \varphi_1 &= -\frac{9\varepsilon_3\varepsilon_4x_2\beta_2}{2\varepsilon_4A - \varepsilon_3B} \left(1 + \frac{\alpha_1}{\beta_1}\right) \bar{E}_0\bar{r}, \quad r < R_1, \\ \varphi_2 &= -\frac{9\varepsilon_3\varepsilon_4x_2\beta_2}{2\varepsilon_4A - \varepsilon_3B} \left(\frac{\alpha_1}{\beta_1}\bar{E}_0\bar{r} + \frac{x_1R_2^3}{r^3}\bar{E}_0\bar{r}\right), \quad R_1 < r < R_2, \\ \varphi_3 &= \frac{3\varepsilon_4}{2\varepsilon_4A - \varepsilon_3B} \left[x_2(2x_1\beta_1\beta_2 - \alpha_1\alpha_2)\bar{E}_0\bar{r} + (\alpha_1\beta_2 - x_1\alpha_3\beta_1)\frac{R_3^3}{r^3}\bar{E}_0\bar{r}\right], \quad R_2 < r < R_3, \\ \varphi_4 &= -\bar{E}_0\bar{r} - \frac{(\varepsilon_4A + \varepsilon_3B)}{(2\varepsilon_4A - \varepsilon_3B)}\frac{R_3^3}{r^3}\bar{E}_0\bar{r}, \quad r > R_3, \end{aligned} \quad (4)$$

where

$$\begin{aligned} A &= x_1\beta_1(2\varepsilon_2(1 - x_2) + \varepsilon_3(1 + 2x_2)) - \alpha_1(\varepsilon_2(1 - x_2) - \varepsilon_3(1 + 2x_2)), \\ B &= x_2(2x_1\beta_1\beta_2 - \alpha_1\alpha_2) - 2(\alpha_1\beta_2 - x_1\beta_1\alpha_3), \quad x_1 = (R_1/R_2)^3, \quad x_2 = (R_3/R_2)^3, \\ \alpha_1 &= \varepsilon_1 + 2\varepsilon_2, \quad \alpha_2 = \varepsilon_2 + 2\varepsilon_3, \quad \alpha_3 = \varepsilon_3 + 2\varepsilon_2, \quad \beta_1 = \varepsilon_2 - \varepsilon_1, \quad \beta_2 = \varepsilon_2 - \varepsilon_3. \end{aligned}$$

The electric field strength and the electric potential are connected by help of equation $\bar{E} = -\nabla\varphi$. Substitution expressions (4) in this equation give us the following results:

$$\begin{aligned} \bar{E}_1 &= \frac{9\varepsilon_3\varepsilon_4x_2\beta_2}{2\varepsilon_4A - \varepsilon_3B} \left(1 + \frac{\alpha_1}{\beta_1}\right) \bar{E}_0, \quad r < R_1, \\ \bar{E}_2 &= \frac{9\varepsilon_3\varepsilon_4x_2\beta_2}{2\varepsilon_4A - \varepsilon_3B} \left(\frac{\alpha_1}{\beta_1}\bar{E}_0 + \frac{x_1R_2^3}{r^3}\bar{E}_0 - \frac{3x_1R_2^3}{r^5}\bar{r}(\bar{E}_0\bar{r})\right), \quad R_1 < r < R_2, \\ \bar{E}_3 &= -\frac{3\varepsilon_4}{2\varepsilon_4A - \varepsilon_3B} \left[x_2(2x_1\beta_1\beta_2 - \alpha_1\alpha_2)\bar{E}_0 + (\alpha_1\beta_2 - x_1\alpha_3\beta_1)\frac{R_3^3}{r^3}\bar{E}_0 \right. \\ &\quad \left. - 3(\alpha_1\beta_2 - x_1\alpha_3\beta_1)\frac{R_3^3}{r^5}\bar{r}(\bar{E}_0\bar{r})\right], \quad R_2 < r < R_3, \\ \bar{E}_4 &= \bar{E}_0 + \frac{(\varepsilon_4A + \varepsilon_3B)}{(2\varepsilon_4A - \varepsilon_3B)}\frac{R_3^3}{r^3}\bar{E}_0 - \frac{3(\varepsilon_4A + \varepsilon_3B)}{(2\varepsilon_4A - \varepsilon_3B)}\frac{R_3^3}{r^5}\bar{r}(\bar{E}_0\bar{r}), \quad r > R_3. \end{aligned} \quad (5)$$

In EMA we deal with a mixture of two types of spherical particles, which are randomly distributed in the effective medium. The first type of particles is three-layered particles. As second type of particles we will consider spherical inclusions of gas (vacuum). It is considered that the permittivity of such a composite is equal to the permittivity of the effective medium.

The electric field inside the second type of particles is determined as [1]

$$\bar{E}_g = \frac{3\varepsilon_{eff}}{\varepsilon_g + 2\varepsilon_{eff}} \bar{E}_0. \quad (6)$$

Here ε_g is the dielectric permittivity of gas or vacuum. The electric fields inside the first type of particles are expressed by the Formula (5) in which $\varepsilon_4 = \varepsilon_{eff}$ (because both kinds of particles are distributed in the effective medium).

After substitution of electrical fields (5) and (6) in Equation (1) and their integration we find the final equation for calculation of the effective permittivity of composite from three-layered spherical

particles

$$\begin{aligned}
 & (\varepsilon_1 - \varepsilon_{eff})K_1p\frac{x_1}{x_2} + (\varepsilon_2 - \varepsilon_{eff})K_2p\frac{1-x_1}{x_2} + (\varepsilon_3 - \varepsilon_{eff})K_3p\left(1 - \frac{1}{x_2}\right) \\
 & + 3(1-p)\frac{(\varepsilon_g - \varepsilon_{eff})(2\varepsilon_{eff}A - \varepsilon_3B)}{\varepsilon_g + 2\varepsilon_{eff}} = 0,
 \end{aligned} \tag{7}$$

where

$$K_1 = 9\varepsilon_3x_2\beta_2\left(1 + \frac{\alpha_1}{\beta_1}\right), \quad K_2 = 9\varepsilon_3x_2\frac{\alpha_1\beta_2}{\beta_1}, \quad K_3 = 3x_2(\alpha_1\alpha_2 - 2x_1\beta_1\beta_2),$$

p is the volume fraction of solid spherical particles in effective medium.

Let us consider the dependencies of effective permittivity of the powder and electric and magnetic fields inside the powder sample from different parameters which are contained in Equation (7).

Figure 1 presents the dependence of the effective permittivity from the volume fraction of the solid spherical particles p . It is seen from Fig. 1 that the effective permittivity at small volume fraction of the particles is close to the effective permittivity of gas (vacuum).

Figure 2 presents the dependence of the effective permittivity from the thickness of the shell of particle at different volume fraction of solid spherical particles. The real part of the effective permittivity first increases at increasing of the shell thickness then reaches a maximum and after that decreases asymptotically to an almost constant value. The imaginary part of effective permittivity at small thickness of shell has the maximum value and with increasing of shell thickness fast decrease to constant value. The effective permittivity also increases with increasing volume fraction of the solid spherical particles.

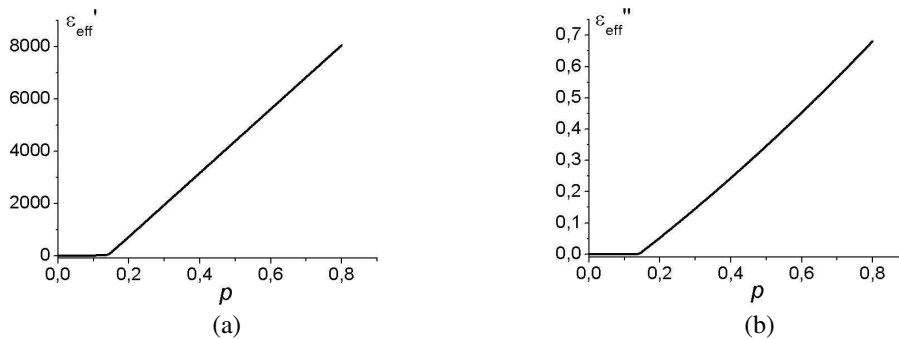


Figure 1: The dependences of (a) real and (b) imaginary parts of effective permittivity of composite from the volume fraction of solid spherical particles for one set of parameters.

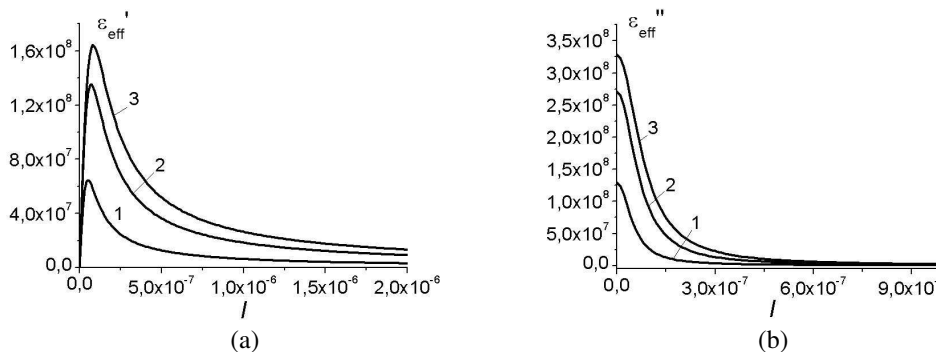


Figure 2: The dependence of (a) real and (b) imaginary parts of effective permittivity of powder from the thickness of shell for different volume fraction of solid spherical particles p : 1) -0.3 , 2) -0.6 , 3) -0.8 . ($R_1 = 0.69$ cm, $R_2 = 0.87$ cm, $R_3 = 0.1$ cm)

In all cases we suppose that permittivity of gas (vacuum) is $\varepsilon_g = 1$, the permittivity of the each layer of particle is $\varepsilon = \varepsilon_\infty + i4\pi\sigma/\omega$ (ε_∞ is the permittivity of the layer of particle at high frequencies $\omega \rightarrow \infty$; σ is the conductivity of the layer of particle), the conductivity of core is $\sigma_1 = 36.9 \cdot 10^{16} \text{c}^{-1}$, the conductivity of intermediate layer is $\sigma_2 = 4.9 \cdot 10^{16} \text{c}^{-1}$, the permittivity of core is $\varepsilon_1 = 10 + i4\pi\sigma_1/\omega$, the permittivity of intermediate layer is $\varepsilon_2 = 10 + i4\pi\sigma_2/\omega$, the permittivity of shell is $\varepsilon_3 = 3.8 + i0.000228$, the amplitude of external alternative electromagnetic field is $h_0 = 1 \text{ Oe}$, and the frequency of external alternative electromagnetic field is $\omega/2\pi = 2.45 \text{ GHz}$.

It is known [1], that a heat density absorbed in the plate per second is a sum of electric Q_e and magnetic Q_h parts of heat and it is expressed as

$$Q = Q_e + Q_h = \frac{\omega}{8\pi} \left(\varepsilon'' |\bar{e}|^2 + \mu'' |\bar{h}|^2 \right). \quad (8)$$

Here the square of modulus of electric and magnetic strengths can be written as [2]

$$|\bar{e}|^2 = \left[\frac{\mu\omega}{ck} h_1 \exp(ikz) - \frac{\mu\omega}{ck} h_2 \exp(-ik(z-d)) \right] \times \left[\frac{\mu\omega}{ck} h_1 \exp(ikz) - \frac{\mu\omega}{ck} h_2 \exp(-ik(z-d)) \right]^*, \quad (9)$$

$$|\bar{h}|^2 = [h_1 \exp(ikz) + h_2 \exp(-ik(z-d))] \times [h_1 \exp(ikz) + h_2 \exp(-ik(z-d))]^*,$$

where an asterisk means a complex conjugation. Here k is the wave number in the plate

$$k = \frac{\omega}{c} \sqrt{\mu\varepsilon} = \frac{\omega}{c} \sqrt{\mu(\varepsilon_\infty + 4\pi\sigma/\omega)}, \quad (10)$$

μ is the magnetic permeability. We suppose that magnetic permeability is $\mu = \mu' + i\mu'' = 1 + i0.1$.

Figure 3 shows the distribution of electric Q_e and magnetic Q_h contributions to a whole heat absorbed inside the plate from the composite.

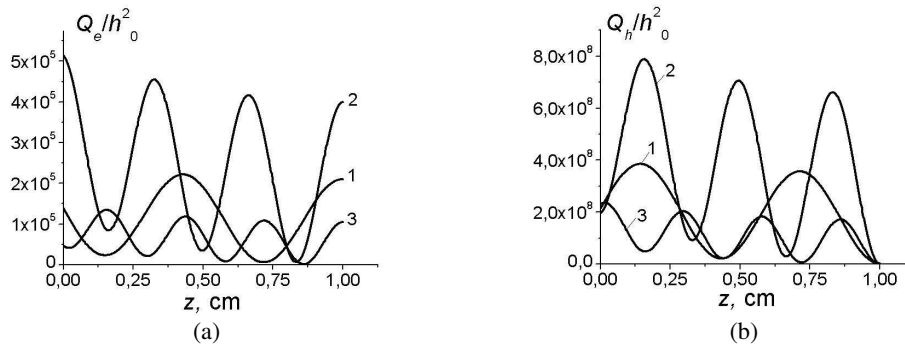


Figure 3: The distribution of (a) electric and (b) magnetic parts of heat absorbed inside the plate from powder for different volume fraction of solid spherical particles p : 1) -0.3 , 2) -0.6 , 3) -0.8 . The thickness of plate is 1 cm. ($R_1 = 0.008 \text{ cm}$, $R_2 = 0.0108 \text{ cm}$, $R_3 = 0.011 \text{ cm}$).

REFERENCES

1. Landau, L. D., E. M. Lifshits, and L. P. Pitaevskii, *Electrodynamics of Continuous Media*, 2nd Edition, Pergamon, New York, 1984.
2. Buchelnikov, V. D., D. V. Louzguine-Luzgin, G. Xie, S. Li, N. Yoshikawa, M. Sato, A. P. Anzulevich, I. V. Bychkov, and A. Inoue, "Heating of metallic powders by microwaves: Experiment and theory," *Journal of Applied Physics*, Vol. 104, No. 1, 2008.

Measurement of Dielectric Properties and Finite Element Simulation of Microwave Pretreatment for Convective Drying of Grapes

S. R. S. Dev, Y. Gariépy, and G. S. V. Raghavan

Department of Bioresource Engineering, McGill University, QC, Canada

Abstract— In this study, the dielectric properties (dielectric constant — ϵ' and dielectric loss factor — ϵ'') of grapes were measured on a matrix of frequencies (from 200 MHz to 10 GHz) and temperatures (5°C to 80°C). Empirical relationships relating the dielectric properties to both temperature and frequency were developed. A Finite Element Model (FEM) of the microwave pretreatment of the grapes was made. Simulation studies were conducted for grapes subjected to 5 minutes of pretreatment under 915 MHz and 2450 MHz. Different power densities of 0.5 W/g, 5 W/g and 50 W/g were used in order to visualize and investigate the energy distribution within the berries.

1. INTRODUCTION

Raisins are well known for its medicinal and nutraceutical properties. It is a good source of potassium, magnesium and fibre. Fresh grapes contain about 80–85 per cent moisture content on wet basis. In the process of raisin making it is reduced to 18 per cent (wet basis). This is done traditionally by sun drying or convective drying. The natural waxy coating on the grapes delays moisture removal. Dipping in hot water and the use of chemicals such as sulphur, NaOH, and ethyl or methyl oleate emulsions are some of pretreatments widely used for grape drying to remove the waxy coating and increase drying rate in raisin making.

According to Tulasidas et al. [7] microwave processing is an energy efficient drying technique for raisin production. Due to its high moisture content heat absorption is very effective. With a view to find alternate methods that could reduce drying time without using chemicals, pre-treatment with microwaves (MW) and pulsed electric field (PEF) were studied by Dev et al. [3] and found that microwave pretreatment significantly enhances the drying rate and quality of raisins.

Measurements and modelling of dielectric helps understanding, explaining, and simulating the microwave heating of the materials [4]. There are studies on the measurement and modelling of dielectric properties of grapes at 2.45 GHz for different temperatures [7]. But there is no data available on the dielectric properties of grapes at different frequency. Such data will give a better understanding of the behaviour of the grapes on a broader electromagnetic spectrum and helps further simulation studies at other permitted frequencies like 915 MHz.

Yen and Clary [10] state that during microwave heating once moisture in the berry is heated to a saturation temperature, the temperature rises with pressure resulting in volume expansion causing the berry to rupture. If the rate of vaporization is controlled by the level of microwave energy applied, a puffed nature can be achieved by the rupture of different layers. In grapes, this rupturing is reported to start near the surface and propagate into the interior giving the raisins a puffy texture, thus providing the necessary pathways for moisture migration from different layers of the berry. This might enhance the drying rate in further drying process.

There is poor understanding of the mechanisms involved in creating new channels for moisture migration and actual energy distribution inside the grapes when subjecting them to electromagnetic field. The electromagnetic field distribution inside the microwave oven can be traced out by solving the Maxwell's equations [5]. Finite Element Method (FEM) is commonly used for solving Maxwell's equations to get the energy distribution in a complex object or within a multimode cavity and it is capable of simulating power density distribution in 3-D space [8, 9].

FEM technique competes very favourably with the other numerical methods, as it is based on reducing the Maxwell's equations to a system of simultaneous algebraic linear equations [2]. FEM can readily model heterogeneous and anisotropic materials as well as arbitrarily shaped geometries. It can also provide both time and frequency domain analyses which are important to microwave heating problems like field distribution, scattering parameters and dissipated power distribution for various materials and geometries [1].

Taking into account all the above mentioned facts, in this study, measurement and modeling of the dielectric properties of grapes was conducted on a matrix of frequencies (from 50 MHz to 10 GHz) and temperatures (5°C to 80°C). Using the results obtained, a Finite Element Model (FEM) of

the microwave pretreatment of the grapes was made and simulation studies were conducted for grapes subjected to 5 minutes of pretreatment under 915 MHz and 2450 MHz and power densities of 0.5 W/g, 5 W/g and 50 W/g in order to visualize and investigate the energy distribution within the berries.

2. MATERIALS AND METHODS

In this study, the mechanisms involved in enhancement of drying rate by microwave pretreatment were investigated by FEM simulations. At first, dielectric properties of the grapes were measured at temperatures ranging from 5°C to 80°C, and at frequencies ranging from 200 MHz to 10 GHz. Empirical relationships were then obtained to express dielectric properties as a function of temperature and frequency. In the second part, a Finite Element Model was made in order to simulate the microwave heating of grapes.

2.1. Measurement of Dielectric Properties

2.1.1. Grape Samples

Grapes (Thomson seedless variety) were purchased from the local market. They were washed, separated, destemmed, and surface dried. Each grape berry was taken into custom made 25 mm diameter tube for heating in a temperature controlled dry heating bath.

2.1.2. Equipment

Measurements of the dielectric properties were made with the open ended coaxial probe technique (Agilent 8722 ES *s*-parameter Network Analyzer equipped with a slim type probe model 85070B, Santa Clara, USA) and controlled by a computer software (Agilent 85070D Dielectric Probe Kit Software Version E01.02, Santa Clara, USA). According to the manufacturer, the equipment has an accuracy of $\pm 5\%$ for the dielectric constant (ϵ') and ± 0.005 for the loss factor (ϵ'') (HP, 1992). A diagram of the experimental setup used for the measurement of dielectric properties is shown in Figure 1.

2.1.3. Experimental Procedure

The grapes taken in the 25 mm diameter tubes were placed one at a time in a temperature controlled dry heating bath (Isotemp[®] Model: 2001FS from Fisher Scientific, USA). The temperature at the centre point of the grape berry, which was set to be the measuring point for the dielectric properties, was measured using a K type thermocouple (Thermo Fisher Scientific, USA). The temperature of the dry bath was set to 2°C higher than the measurement temperature in order to allow the gradient for steady state heat flow. Once the centre point of the grape reached the required temperature, the temperature across berry was assumed to have stabilized and measurements were taken after removing the thermocouple and inserting the dielectric probe into the berry. The dielectric properties were measured at 100 different frequencies ranging from 200 MHz to 10 GHz.

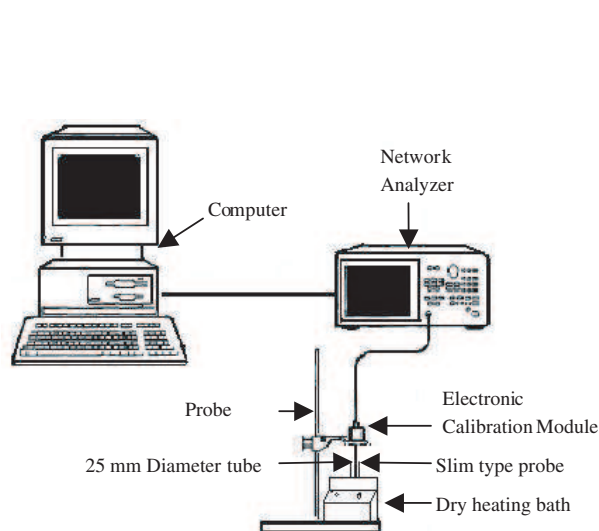


Figure 1: Dielectric properties measurement setup.

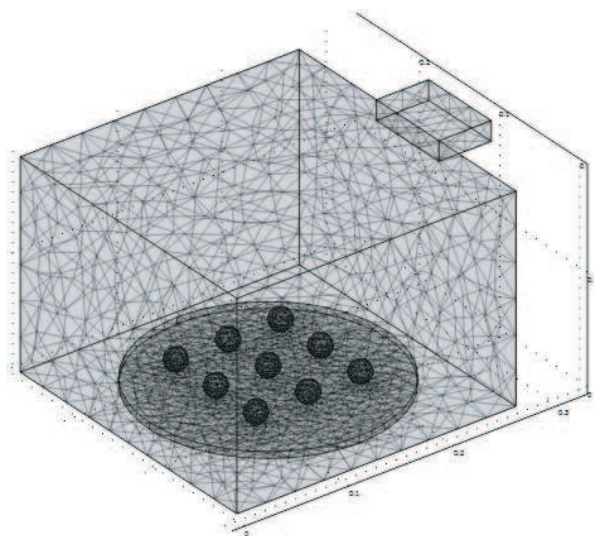


Figure 2: FEM mesh structure with grapes.

2.1.4. Data Analysis

MATLAB version R2009a was used to analyze the collected data and to establish the mathematical relationships for the dielectric constant and loss factor as a function of frequency and temperature.

2.2. Finite Element Modeling and Simulation

A 3D Finite Element Model was developed using COMSOL Multiphysics version 3.5 (COMSOL Inc., USA) software package to simulate the MW pretreatment process for grapes for three different power densities (0.5, 50 and 50 W/g) for regular domestic microwave oven configuration. The meshed structure for 2.45 GHz along with the grapes is shown in Figure 2. The cavity The 915 MHz cavity had a similar structure with bigger cavity dimensions. The cavity dimensions were taken as 0.267 m × 0.270 m × 0.188 m and 1.07 m × 1.22 m × 1.47 m for 2.45 GHz and 915 MHz respectively.

The simulations performed were a virtual replication of the actual pretreatments performed by Dev et al. [3–5] except for the power densities used, wherein the drying temperature of 65°C was used as a microwave cut off temperature. Also they had a microwave on/off cycle time of 60/5 seconds. So the similar conditions were applied for the simulation. The grapes were heated from 25°C to 65°C in the simulation. The temperature dependent properties of grapes like density, thermal conductivity, electrical conductivity and specific heat capacity were taken from Tulasidas et al. [7].

A custom built computer with two AMD Opteron quadcore 2.4 GHz processors and 32 GB primary memory was used to run the simulations.

2.2.1. Mathematics of the Model

Electromagnetics

The Maxwell's equations that govern the electromagnetic phenomena evolving in a given configuration resolved in 3D space were solved for the Electric field intensity (E) ($V \cdot m^{-1}$) and H Magnetic Field Intensity ($A \cdot m^{-1}$) [1]. The dynamically changing dielectric constant ϵ' and loss factor ϵ'' were calculated using equations derived from the measurement of dielectric properties.

The time average power dissipated (P_{av}) in each element in a dielectric material was obtained by integrating the poynting vector (P_c) over the closed surface S for each tetrahedral element (Eq. (1)) (Jia and Jolly, 1992).

$$P_{av} = -\frac{1}{2} \int_S P_c \cdot dS \quad (1)$$

where $P_c = E \times H$. Volumetric heat generation Q can be expressed in terms of power intensity in three orthogonal directions as shown in Eq. (2) (Lin et al., 1989).

$$Q = \frac{\partial P_{av(x)}}{\partial V} + \frac{\partial P_{av(y)}}{\partial V} + \frac{\partial P_{av(z)}}{\partial V} \quad (2)$$

where the suffixes x , y and z indicate time average power dissipated in the corresponding directions and V is the volume in which the heat is generated.

Boundary Conditions [8]

Perfect Electrical Conductor (PEC) boundary condition ($n \times E = 0$) was used for the walls of the cavity and Perfect Magnetic Conductor (PMC) boundary condition ($n \times H = 0$) was used for the symmetry boundaries.

Boundary conditions at the port were taken as follows

$$H_y = A \cos(\Pi x/\alpha) \cos(\omega t + \beta y) \quad (3)$$

$$E_z = (\omega \mu_0 \alpha / \Pi) A \sin(\Pi x/\alpha) \sin(\omega t + \beta y) \quad (4)$$

$$H_x = (\beta \alpha / \Pi) A \sin(\Pi x/\alpha) \sin(\omega t + \beta y) \quad (5)$$

where the x , y and z indicate the corresponding axes and A is the cross sectional area of the waveguide, ω is the phase angle and α & β are arbitrary constants.

Heat Transfer

For an incompressible food material heated under constant pressure, the thermal energy equation is given by Eq. (14) [9]

$$\rho C_p \frac{\partial T}{\partial t} = \nabla \cdot (K \nabla T) + Q \quad (6)$$

where ρ is the density ($\text{kg} \cdot \text{m}^{-3}$), C_p is the specific heat ($\text{kJ} \cdot \text{kg}^{-1} \cdot \text{K}^{-1}$) and K is the thermal conductivity of the material and T is the absolute temperature in Kelvin.

Different mesh element sizes were used for different sub-domains based on the dielectric properties of the sub-domain and the precision required in the sub-domain of interest.

3. RESULTS AND DISCUSSION

3.1. Measurement and Modelling of Dielectric Properties of Grapes

The moisture content of the grapes tested was found to be 81%_{w.b.}, based on the oven drying method. The ϵ' and ϵ'' values obtained were much closer to that of water. At any given temperature and frequency, repeatability of the measurements was excellent and the variances calculated among replicates were smaller than 0.15.

A linear additive model was used to relate ϵ' or ϵ'' to temperature and frequency. Its general form of the relationship is given by Eq. (7). The ϵ' for grapes were decreasing with increasing temperature and frequency (Eq. (8)) whereas the ϵ'' decreased with increase in temperature and increases with increase in frequency (Eq. (9)).

$$(\epsilon' \text{ or } \epsilon'') = a \pm b \cdot T \pm c \cdot F \quad (7)$$

where,

T is the temperature in $^{\circ}\text{C}$,

F is the frequency in GHz, and

a, b, c are the model coefficients

Regression analysis performed on the collected data yielded the following relationships for egg white

$$\epsilon' = 79.92 - 0.18 \cdot T - 1.75 \cdot F \quad (R^2 = 0.965) \quad (P < 0.01) \quad (8)$$

$$\epsilon'' = 17.22 - 0.11 \cdot T + 2.21 \cdot F \quad (R^2 = 0.978) \quad (P < 0.01) \quad (9)$$

Figure 3 shows the change in dielectric properties with temperature at 2450 MHz and 915 MHz.

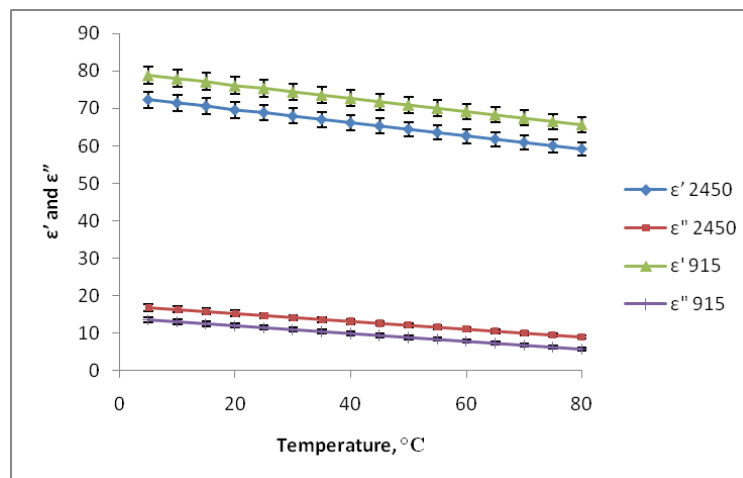


Figure 3: Change in dielectric properties with temperature at 2450 MHz and 915 MHz.

3.2. Finite Element Modelling and Simulation of Microwave Pretreatment for Grapes

Figures 4 and 5 show the temperature profiles and thereby the heat distribution inside the grape berries during microwave pretreatment for 0.5 W/g, 5 W/g and 50 W/g power densities at 2450 MHz and 915 MHz respectively.

As 65 $^{\circ}\text{C}$ was set as the microwave cutoff temperature, several cycles of microwave heating happened in the pretreatment duration of 5 mins and the number of such cycles depended on the power density applied. Due to these repeated on/off cycles, the heat got dissipated with time and the temperature distribution was pretty uniform all over the berry in about 2–3 mins, depending on the power density applied. The figures show the temperature gradient during the first cycle of

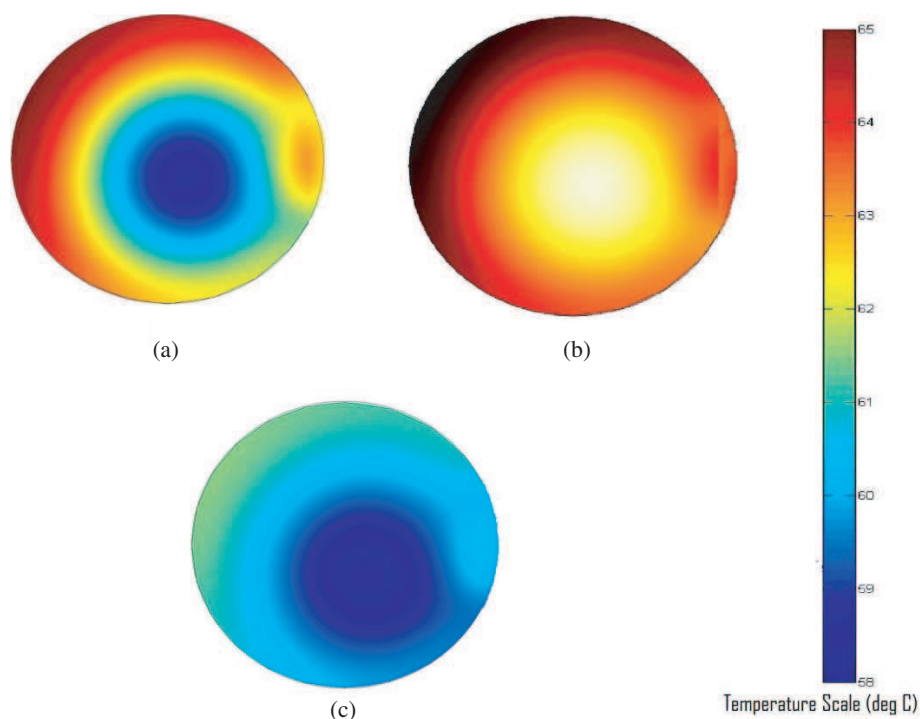


Figure 4: Temperature profile of a grape berry in 2450 MHz cavity at (a) 50 W/g for 5 secs, (b) 5 W/g for 15 secs and (c) 0.5 W/g for 60 secs.

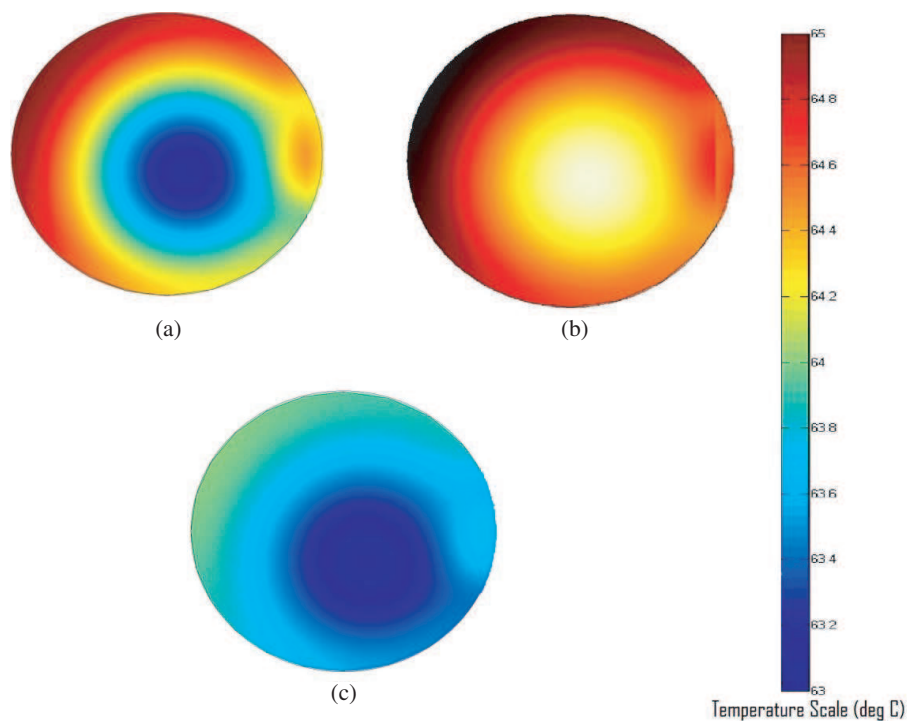


Figure 5: Temperature profile of a grape berry in 915 MHz cavity at (a) 50 W/g for 8 secs, (b) 5 W/g for 25 secs and (c) 0.5 W/g for 60 secs.

heating only. The heating rate was very high while using the power density of 50 W/g. Therefore the heating times for the first cycle were only 5 seconds and 3 seconds for 2450 MHz and 915 MHz respectively. Whereas, the maximum time limit of 60 seconds for the first was reached even before any part of the berry could reach 65°C. The heating pattern corroborates very well with the theoretical explanation given by Yen and Clary [10] for the puffy nature of the microwave dried grapes and their scanning electron microscopic images of the microwave dried grapes. The energy

distribution pattern appears to be the same for both 2450 MHz and 915 MHz. But the heating rates were higher for 2450 MHz than 915 MHz, which is explained by the dielectric properties at the corresponding frequencies. Though the heating time was slightly longer, the uniformity was better in 915 MHz than 2450 MHz which is indicated by the temperature scale in the Figures 4 and 5 (only 2°C difference between the hottest and the coldest spots for 915 MHz as against 7°C difference for 2450 MHz).

4. CONCLUSIONS

The dielectric properties of the grapes varied linearly with respect to temperature (5–80°C) and frequency (0.2–10 GHz). The linear models developed can be used for further simulation studies and for designing microwave processing equipments for grapes. The FEM simulations give a detailed insight into the temperature profile inside a grape berry subjected to microwave treatment. This also provides a more detailed visualization of the possible reasons for the puffy nature of the microwave dried raisins. Grapes can be effectively pretreated at 915 MHz in the industrial scale before convective drying, as 915 MHz has its own advantages in industrial applications than 2450 MHz.

ACKNOWLEDGMENT

The financial support by the Natural Sciences and Engineering Research council and Le Fonds Québécois de la Recherche sur la Nature et les Technologies is gratefully acknowledged.

REFERENCES

1. Dai, J., “Microwave-assisted extraction and synthesis studies and the scale-up study with the aid of FDTD simulation,” Ph.D. dissertation, Department of Bioresource Engg., McGill University, Canada, 2006.
2. Delisle, G. Y., K. L. Wu, and J. Litva, “Couples finite element and boundary element method in electromagnetics,” *Computer Physics Communications*, Vol. 68, 255–278, 1991.
3. Dev, S. R. S., T. Padmini, A. Adedeji, Y. Gariépy, and G. S. V. A. Raghavan, “Comparative study on the effect of chemical, microwave, and pulsed electric pretreatments on convective drying and quality of raisins,” *Drying Technology*, Vol. 26, No. 10, 1238–1243. 2008.
4. Dev, S. R. S., G. S. V. Raghavan, and Y. Gariépy, “Dielectric properties of egg components and microwave heating for in-shell pasteurization of eggs,” *Journal of Food Engineering*, Vol. 86, 207–214, 2008.
5. Dev, S. R. S., V. Orsat, Y. Gariépy, and G. S. V. Raghavan, “Optimization of microwave heating of in-shell eggs through modeling and experimental trials,” *ASABE AIM*, Providence, USA, June 29–July 2, 2008.
6. Tulasidas, T. N., “Combined convective and microwave drying of grapes,” Ph.D. thesis dissertation, Dept. of Bioresource Engineering, McGill University, Canada, 1994.
7. Tulasidas, T. N., G. S. V. Raghavan, F. van de Voort, and R. Girard, “Dielectric properties of grapes and sugar solutions at 2.45 GHz,” *Journal of Microwave Power and Electromagnetic Energy*, Vol. 30, No. 2, 117–123. 1995.
8. Fu, W. and A. Metaxas, “Numerical prediction of three-dimensional power density distribution in a multimode cavity,” *Journal of Microwave Power and Electromagnetic Energy*, Vol. 29, No. 2, 67–75, 1994.
9. Zhou, L., V. M. Puri, R. C. Anantheswaran, and G. Yeh, “Finite element modeling of heat and mass transfer in food materials during microwave heating — Model development and validation,” *Journal of Food Engineering*, Vol. 25, 509–529, 1995.
10. Yen, M. and C. D. Clary, “Why is the grape puff puffy? An analysis of MIVAC temperature curves,” Research note, VERC, Cati Publication, 1994.

Regularities of Semiconductor Powders Dynamics in Chladni Effect

V. I. Kuzmin¹ and D. L. Tytik²

¹Moscow State Institute of Radio Engineering, Electronics, and Automation
pr. Vernadskogo 78, Moscow 119454, Russia

²Frumkin Institute of Physical Chemistry and Electrochemistry
Leninskii pr. 31, Moscow 119991, Russia

Abstract— This article is a presentation of powder pattern dynamics (Chladni figures) on the plates in a variety of shapes and critical dimensions under acoustic and magnetic fields applied in the vicinity of bifurcation points. The study involved the use of powders with critical size of particles of diverse composition — semiconductor material B_4C and dielectric material SiO_2 . The study detected the acoustic field frequencies at which powder figures (B_4C) rearrange themselves on the plane by escaping into the third dimension (forming a vortex above the plane at the point of bifurcation). Dielectric powders (SiO_2) at certain frequencies form stationary vortex above the plane due to the natural lumpiness effect, which is the cause of existence of dominant sizes of material structures in the nature, regardless of their phase state. They are consistent with dominant values of time intervals (frequencies) forming the rhythm quantization system. The natural lumpiness effect serves as technological basis for the transfer of electromagnetic signals in various media at specific frequencies (transparency windows).

Combined effect of the acoustic and magnetic fields defines the specifics of powder figures (B_4C) on the plane and brings forth the problem of electromagnetic impact on powder materials with various physical and chemical properties. These experiments demonstrate that the phase state of a substance can be controlled through application of alternating fields of diverse origin along with critical values of wavelengths (frequencies).

1. INTRODUCTION

The Chladni effect consists in formation of stationary powder figures on the surface of plates under the influence of acoustic vibrations of different frequency. Despite applied importance of the effect, there are few experimental operations in this field, and the theory is developed for mostly simple flat systems [1, 2].

The results of modeling experiments on plates of different shape with semiconductor and dielectric powders of different dispersion are given in the article. When small fractions of powder ($< 60 \mu m$) and consistent frequencies of the acoustic field, stationary vortexes over the plate surface are recognized. The effect of magnetic field influence on figures formation from semiconductor powder (B_4C) is detected. The interconnection of formation of powder figures at certain frequencies of acoustic field with the effect of natural lumpiness [3] that fixes presence of sequence of dominating linear dimensions of the natural bodies presented by a geometrical progression is determined.

2. EXPERIMENT

Experiments were made with square and hexagon glass plates (sides of 42 cm and 21 cm accordingly) with the thickness of 2 mm. The sound dynamic loudspeaker with the power of 5 W is used as a source of acoustic field. A plate was rigidly fastened to dynamic loudspeaker diffuser in centre of mass. The metering circuit consisted of the audio-frequency generator (GZ-48) and a frequency meter when performing the experiments. The acoustic field varied over the range of $20 \div 10000$ Hz. At the beginning of the experiment, the powder was evenly put on the surface of the plate and was added in case of spillage due to the strong vibration during the experiment.

3. EXPERIMENTAL RESULTS

It is determined, that basic types of powder figures are reproduced for plates of various shape and are defined by a set of the consistent critical frequencies matching to the effect of natural lumpiness [3]. In addition, the contrast range of the structures gained extends when using powders with dispersion matching the same sequence of dominating sizes of solid bodies. In case of a hexagon plate and the semiconductor powder B_4C ($\sim 192 \mu m$) the influence of magnetic field on the dynamics of forming of powder figures is revealed. The effect is performed as a resonance one in narrow frequency band of the acoustic field ($80 \div 83$ Hz) and consists in their counter-clockwise

gyration on the plate surface (Fig. 1). Moreover, at the resonance frequency (82 Hz) the powder goes to a third dimension, forming a vortex over the plate surface. Gyration of a powder figure can be repeated many times by continuously changing frequency of acoustic field from 80 to 83 Hz.

The scale of critical frequencies of acoustic vibrations (see Table 1) which are consistent with the effect of natural lumpiness and with the values of frequencies gained in modeling experiments with powder figures (Chladni figures) on plates at certain frequencies of an acoustic field is known from the theory of critical levels in development of natural systems [4].

Figure 2 gives critical frequencies of acoustic field at which transformation of figures (powder with the dispersion $< 200 \mu\text{m}$) occurs.



Figure 1. Consecutive stages of transformation of powder figures at various frequencies (Hz).

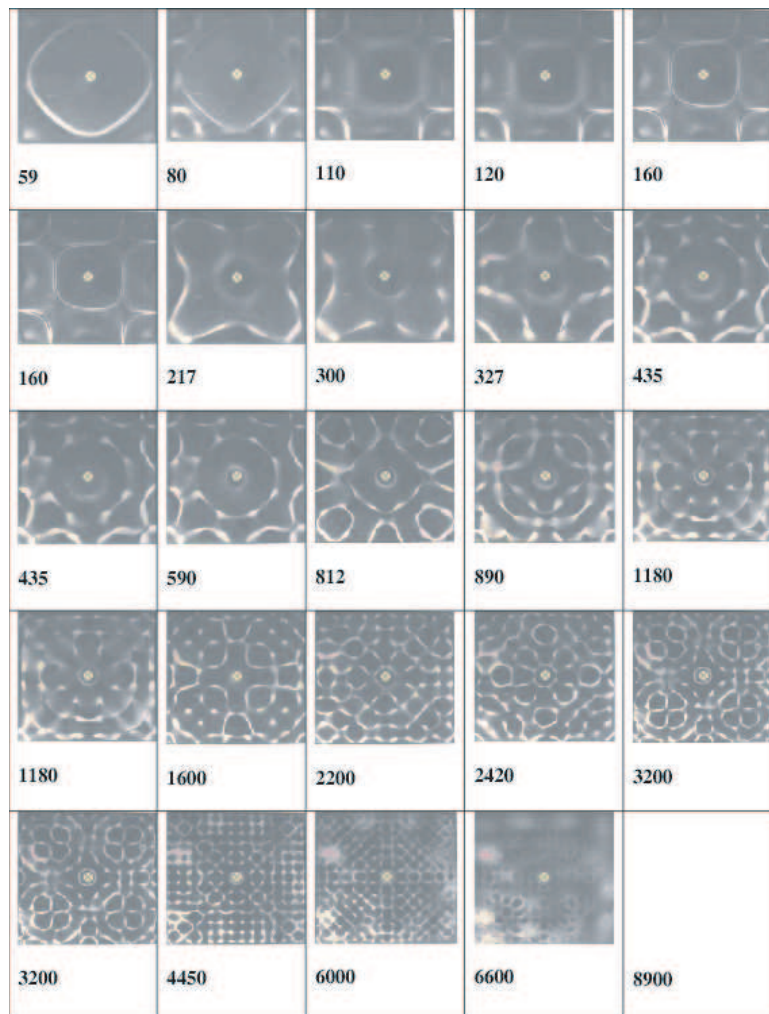


Figure 2. Critical frequencies (Hz) of acoustic field at which the change in structure of powder figures occurs.

Table 1.

Frequency, Hz	Boundary characteristics
8	Vibrato from infra-acoustic spectrum; makes music sense-feeling
21,6	Beginning of acoustic spectrum, 17–22 Hz
59	Extremity of spectrum of the most unpleasant dissonances
160	Background activity of the ear in the absence of external signal
435	A, the first octave — The basic tonometer for master tuning of musical instruments; sharp rise of sensitization to perception of frequency mismatch
1180	Maximum resonance peak of a middle ear; a local minimum of a threshold of perception
3210	Ability limit of the acoustical nerve to follow signals: An absolute minimum of the threshold of perception; the resonance frequency of external acoustic meatus; a maximum of the semantic information per frequency band
8730	Local maximum of the amount of aesthetic information per frequency band
23700	Extremity of acoustic spectrum

4. CONCLUSION

Forming of stationary powder figures at certain frequencies (Fig. 2) is intimately bound to the effect of natural lumpiness of M. A. Sadovsky [3] which is defined by the presence of preferential sizes of the individualities presented by the structures of natural systems [5]. Meanwhile, the physical-mechanical and physicochemical properties of natural systems do not essentially influence dominating linear dimensions, and preferential sizes of pieces within one hierarchical system vary no more than in two- or three times. The analysis of the effect of natural lumpiness shows, that it is based on intermittency of physical values at different levels of hierarchy of a substance.

The Chladni effect is detected at different levels of the substance structure as occurrence of equal structural patterns on consistent frequencies of external influence on the system. The effect is based on wave process of interacting of a coherent variation field with a medium which results in the modification of its phase state and occurrence of a sequence of sample patterns at certain frequencies. Correspondence of bifurcation points of Chladni figures to frequencies known from the scale of dominating linear dimensions of natural bodies shows, that for deriving of resonance effects in the system it is necessary to choose critical values of physical properties (powder dispersion, radiation power, magnetic field characteristics) in experiments. Consideration of coherent influence on the system allows viewing the dynamic models of forming of the complicated hierarchical systems of natural and artificial origins.

REFERENCES

1. Gough, C., "The violin: Chladni patterns, plates, shells and sounds," *Eur. Phys. J. Special Topics*, Vol. 145, 77–101, 2007.
2. Jenkins, C. H. M. and U. A. Korde, "Membrane vibration experiments: An historical review and recent results," *Journal of Sound and Vibration*, Vol. 295, No. 3–5, 602–613, 2006.
3. Sadovsky, M. A., *Geophysics and Physics of Explosion*, 335, Some Selected Works, Nauka Press, Moscow, 1999.
4. Zhirmunsky, A. V. and V. I. Kuzmin, *Critical Levels in the Development of Natural Systems*, Springer-Verlag, Berlin, 1988.
5. Kuzmin, V. I. and N. A. Galusha, *Methodological Problems*, Systems Research, Yearbook 2000, Editorial URSS, Moscow, 2002.

Double-folded Monopole Antenna with Coaxial Cable

Takehiko Tsukiji, Masaaki Yamasaki, and Yasunori Kumon

Department of Electronics and Computer Science, Faculty of Engineering, Fukuoka University
8-19-1, Nanakuma, Jounan-ku, Fukuoka 814-0180, Japan

Abstract— Previously, we proposed a small high-active-gain antenna called the double-folded monopole antenna using the coaxial cable [5]. This antenna has a relatively high resistance near $50\ \Omega$ even though antenna size is small with 0.15 wave length. The present paper is the first report of the coaxial cable loaded monopole antenna with reduced size. Using this antenna, we developed a different type of the double-folded monopole antenna with coaxial cable by a simple modification. Finally, we discuss about difference of new double-folded monopole antenna with coaxial cable from previously developed double-folded monopole antenna using coaxial cable.

1. COAXIAL CABLE LOADED MONOPOLE ANTENNA

We have worked for a long time to develop small antennas suitable for the recent small portable telephone, and reported several papers concerning to the Modified Transmission Line Antenna (MTLA) [1]. But there are some problems that the shape of the MTLA is a little bit complicated and design of the MTLA is not so easy.

It is considered that the simple antenna like a monopole antenna is desirable for mobile communication. It is known that loading a certain reactance component at feeding point can reduce size of a monopole antenna. When a short-circuited parallel transmission line of which length is less than a quarter wavelength is used for the loading element, we have a small monopole antenna called the parallel transmission line loaded monopole antenna as shown in Fig. 1(a) [2]. Fig. 1(b) shows the equivalent antenna for the parallel transmission line loaded monopole antenna of Fig. 1(a). Since the impedance of the parallel transmission line with short-circuited end increases with respect to its length, the resonant frequency of the parallel line loaded monopole antenna with length H decreases compared to the simple monopole antenna with same length.

So, our proposal is to use coaxial cable instead of the parallel transmission line loading as indicated in Fig. 2. This is the coaxial cable loaded monopole antenna. When relative dielectric constant of the coaxial cable is ϵ_r , specific wavelength of coaxial cable becomes $1/\sqrt{\epsilon_r}$ of the free space wavelength λ_0 , ($= c/f_0$). When the length of the coaxial cable of this antenna is $1/4$ of the specific wave length, impedance of the coaxial cable with short-circuited end can take very high value and this antenna resonates near the frequency f_0 which satisfy the antenna length $H = \lambda_0/4\sqrt{\epsilon_r}$, where $\lambda_0 = c/f_0$. Then we can realize a small antenna with length $H = \lambda_0/4\sqrt{\epsilon_r}$.

Figure 3 shows measured impedance characteristics of the coaxial cable loaded monopole antenna with length $H = 9.5$ cm. The type of coaxial cable is 5D2V, and $\epsilon_r = 2.5$, the resonant frequency is 400 MHz. While natural resonant frequency of monopole antenna with height $H = 9.5$ cm is 790 MHz, the coaxial cable loaded monopole antenna with same length can resonate at 400 MHz.

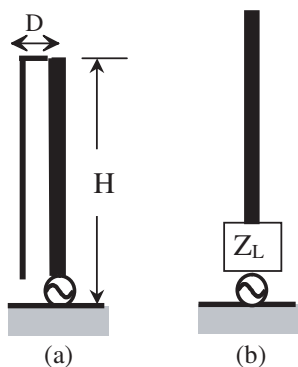


Figure 1: (a) A parallel line loaded monopole antenna. (b) Equivalent antenna for parallel line loaded monopole antenna.

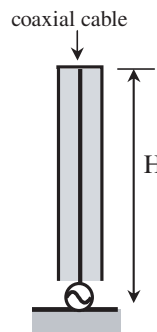


Figure 2: The coaxial cable loaded monopole antenna.

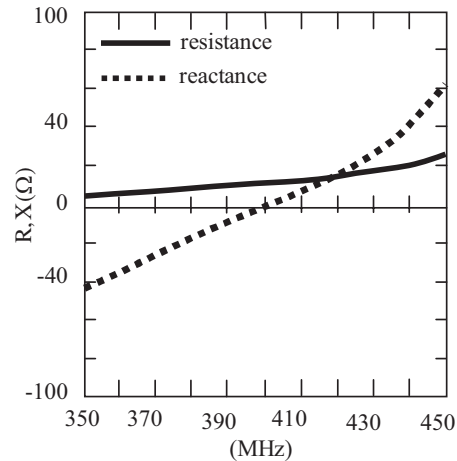


Figure 3: Impedance characteristics of coaxial cable loaded monopole antenna. $H = 9.5$ cm and coaxial cable is 5D2V.

It is said that about 50% antenna size reduction is realized by the coaxial cable loaded monopole antenna.

It should be noted that the resistance of this antenna at the resonant frequency becomes very low even though the antenna size is reduced. There arises another problem that the actual gain of this small monopole antenna will be reduced when the antenna size is reduced.

2. DOUBLE FOLDED MONOPOLE ANTENNA WITH COAXIAL CABLE

It is known that the typical folded monopole antenna shown in Fig. 4(a) has a relatively high resistance, since this antenna can operate in two modes, one is the dipole mode as shown in Fig. 4(b) and the other is the transmission line mode as shown in Fig. 4(c). In the dipole mode, the folded monopole antenna works as two parallel monopole antennas as shown in Fig. 4(b).

The impedance of the folded monopole antenna becomes 4 times that of a monopole antenna at its resonant frequency, where impedance of transmission line mode is infinity [3].

Our proposal is to construct the folded monopole antenna by using coaxial cable loaded monopole antennas in order to increase impedance of small monopole antenna. Thus developed the Double Folded Monopole Antenna with Coaxial Cable (DFMACC) is shown in Fig. 5, where both top ends of coaxial cable loaded monopole antennas are connected by a bridge conducting wire.

It is considered that this antenna should be called folded monopole antenna using coaxial cable loaded monopole antennas. But it not difficult to understand that the coaxial cable loaded monopole antenna is a kind of a folded antenna with open end. Then we dare say that new developed antenna shown in Fig. 5 should be called the DFMACC.

As it is explained in previous section, the coaxial cable loaded monopole antenna being used for the element antenna of the DFMACC can resonate when antenna height is a quarter of the specific wave length of the coaxial cable. Under this condition, impedance of the transmission line mode of DFMACC becomes infinity and high value of impedance of the DFMACC due to the folded

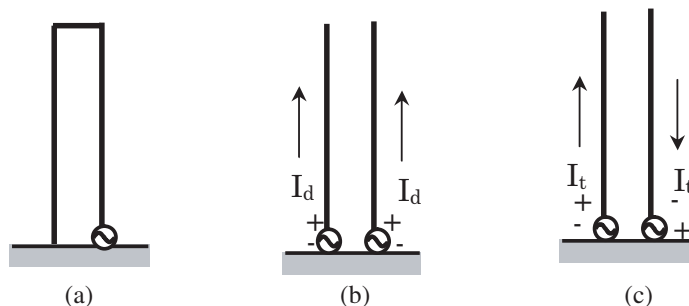


Figure 4: Folded monopole antenna and its principle of operation. (a) Folded monopole antenna. (b) Dipole mode operation of folded antenna. (c) Transmission line mode operation.

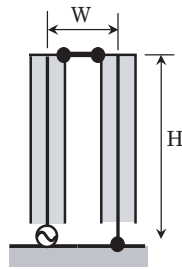


Figure 5: The Double Folded Monopole Antenna with Coaxial Cable (DFMACC).

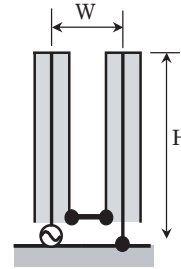


Figure 6: Previously reported DFMACC.

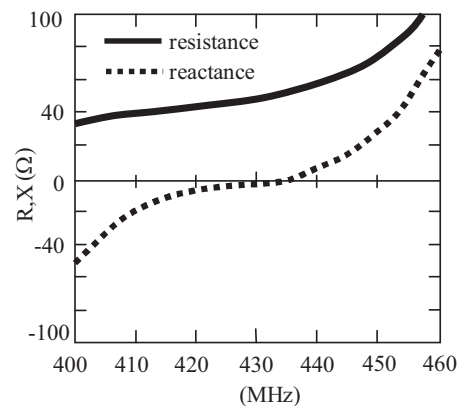


Figure 7: Impedance characteristics of DFMACC. $H = 9.5$ cm, $W = 1.45$ cm, and coaxial cable is 5D2V.

monopole antenna theory can be expected [4, 5].

When the DFMACC is operating near resonant frequency, this antenna works as parallel monopole antenna. Then potential distribution of each coaxial cable along its surface is identical. As the result, position of the bridge conductor of the DFMACC may not affect on characteristics of dipole mode operation, because there is no current flow on the bridge conductor.

Configuration of DFMACC introduced in the previous paper [5] is shown in Fig. 6. Difference of antenna configuration between Fig. 5 and Fig. 6 is the position of the bridge wire. Previously, we placed the bridge wire at lowest end of outer conductor of the coaxial cable as shown in Fig. 6. But in this paper, the bridge conductor is placed at the top of the coaxial cable as shown in Fig. 5.

We have examined impedance characteristics of both DFMACCs and have found no difference between impedance characteristics of these DFMACCs.

Measured impedance characteristic of the DFMACC of new type is shown in Fig. 7, where antenna height $H = 9.5$ cm, distance between center conductor of the coaxial cable is 1.45 cm and the type of coaxial cable is 5D2V.

It should be noted that this DFMACC shows relatively high resistance value like 50Ω at the resonant frequency 430 MHz and the antenna height of DFMACC measures only about 0.14 wave length.

In order to design a DFMACC with center frequency f , where its wavelength is c/f , we first calculate the specific wave length of the given coaxial cable with relative dielectric constant ϵ_r by equation,

$$\lambda_0 = \lambda / \sqrt{\epsilon_r}.$$

Then antenna length is determined by $H = \lambda_0/4$. Though the size of separation of coaxial cables W does not give significant effect on impedance characteristics of the DFMACC, $W = 0.1 H \sim 0.2 H$ is considered appropriate.

3. CONCLUSIONS

At the first, instead of the parallel transmission line for parallel line loaded monopole antenna, we examined the coaxial cable and developed the coaxial cable loaded monopole antenna. We can

realize about 50% reduction of the antenna size, but results in low impedance for the coaxial cable loaded monopole antenna.

In the next, applying the coaxial cable loaded monopole antenna to the folded antenna, we have developed the Double Folded Monopole Antenna with Coaxial Cable (DFMACC). Except for difference of the position of bridge conductor, newly developed DFMACC and previously developed DFMACC have the same configuration and almost same impedance characteristics.

Principle of the DFMACC is explained and design parameters for DFMACC are also presented.

It should be noted that DFMACC has relatively high impedance like 50 ohm even though height of the antenna has only 0.14 wavelength for resonant frequency.

Because of the small size and simple structure of this antenna, it is expected to be used widely for mobile communication or portable telephone.

REFERENCES

1. Tsukiji, T. and Y. Kumon, "Modified transmission line antenna for personal handy phone," *Conference Proceedings of ICCS'94*, 696, 1994.
2. Uchida, H., "Fundamentals of coupled lines and multiwire antennas," The Research Institute of Electrical Communication, Tohoku University, 291, 1967.
3. Stutzman, W. L. and G. A. Thiele, *Antenna Theory and Design*, 175, John Wiley & Sons, Inc., 1998.
4. Tsukiji, T. and Y. Kumon, "Analysis of the double folded monopole antenna," *Millennium Conference on Antennas & Propagation*, Dovor, Switzerland, 2000.
5. Tsukiji, T., Y. Kumon, and M. Yamasaki, "Double-folded monopole antenna using parallel line or coaxial cable," *IEE Pros.-Microw. Antennas Propag.*, Vol. 149, No. 1, 17, February 2002.

All-planar Penta-band Strip-loaded Slit Antenna for Laptop Applications

Ching-Wei Ling, Sy-Been Wang, and Shyh-Jong Chung

Department of Communication Engineering, National Chiao Tung University, Taiwan, R.O.C.

Abstract— In this study, an all-planar penta-band antenna for laptop applications is presented. This antenna is placed parallel to the upper edge of the laptop panel ($300 \times 200 \text{ mm}^2$) with a restricted available space ($120 \times 10 \times 0.4 \text{ mm}^3$). The antenna is mainly composed of two back-to-back strip-loaded slit antennas with different sizes and a T-shaped feeding network. Each strip-loaded slit antenna has two resonances, respectively provided by the metal strip and the slit. The measured 6-dB return loss bandwidth covers the GSM850/900/DCS/PCS/UMTS. Over the GSM850/900 and the DCS/PCS/UMTS bands, the average gains in the H -plane are about 2.06 dBi and 0.02 dBi, respectively. Good antenna features and the planar configuration make the proposed antenna attractive for ultra-thin laptop applications.

1. INTRODUCTION

Owing to the rapid growth in wireless communications, the antenna design for laptop computer is generally required to be capable of multiband operation. For the Wireless Wide Area Network (WWAN) penta-band application, the frequency bands cover the GSM850 (824–894 MHz), GSM900 (880–960 MHz), DCS (1710–1880 MHz), PCS (1850–1990 MHz), and UMTS (1920–2170 MHz). Besides, with the thin laptops getting readily available nowadays, the available antenna volume is reduced. Hence, the antenna design is a challenge for fitting the limited space inside the laptop computer and covering a wider bandwidth operation.

Some antennas for laptop computer applications have been published in the open literatures. Among these antenna designs, the achieved bandwidths are not wide enough for WWAN penta-band operation [1–3]. In [4], although it is designed for penta-band operation, a three-dimensional structure is needed. Thus, it is not promising for the ultra-thin laptop computer applications.

In this study, a penta-band strip-loaded slit antenna is proposed. The antenna covers the required bandwidths of GSM850, GSM900, DCS, PCS, and UMTS bands. By using a strip-loaded feed arrangement of the slit antenna, two resonances are provided by the metal strip and the slit, respectively. A wide bandwidth can be easily archived. The antenna is compact with dimensions of $120 \text{ mm} \times 10 \text{ mm}$. Besides, cause of its all-planar structure, the proposed antenna is suitable for ultra-thin laptop computer communications.

2. ANTENNA CONFIGURATION AND DESIGN

Figure 1 shows the geometry of the all-planar strip-loaded slit antenna for WWAN operation. The antenna is printed on both sides of a 0.4 mm thick FR4 substrate. This antenna is placed parallel to the upper edge of the laptop panel ($L_g \times W_g = 300 \text{ mm} \times 200 \text{ mm}$) with a restricted available space ($L_s \times W_s = 120 \text{ mm} \times 10 \text{ mm}$). The antenna is mainly composed of two back-to-back slit antennas (i.e., slit 1 and slit 2) with different sizes and a T-shaped feeding network. The larger strip-loaded slit antenna has a size of $L_{s2} \times W_s$ and the smaller antenna size of $L_{s4} \times W_s$. Each slit antenna is loaded with a metal strip extended from the T-shaped feeding network. The metal strips are placed within the slit with the length of L_{f2} and L_{f4} , respectively. The proposed antenna structure is simulated by the Ansoft High Frequency Structure Simulator (HFSS) [5], which is a commercial 3-D full-wave electromagnetic simulation software.

The feeding structure of the conventional slit antenna is shown in Fig. 2(a). A tuning-stub is printed at the back of the system circuit board for impedance matching. In this design, the slit antenna is loaded with a metal strip as shown in Fig. 2(b). The simulated return losses of antennas with two different feed structures are shown in Fig. 2(c). From the simulated results the strip-loaded feeding structure has a wider bandwidth than that of the straight feeding one. In addition, the strip-loaded feed (i.e., L-shaped feed) structure provides two resonances, which is contributed by the metal strip and the slit, respectively. Hence, a wider impedance bandwidth is achieved.

Base on the simulated result with the specific feed arrangement as described above, a pair of back-to-back slit antennas are designed for different operating frequencies. Here, the larger strip-loaded slit antenna (slit 1) is designed for lower operating band (GSM850/900) operation, and

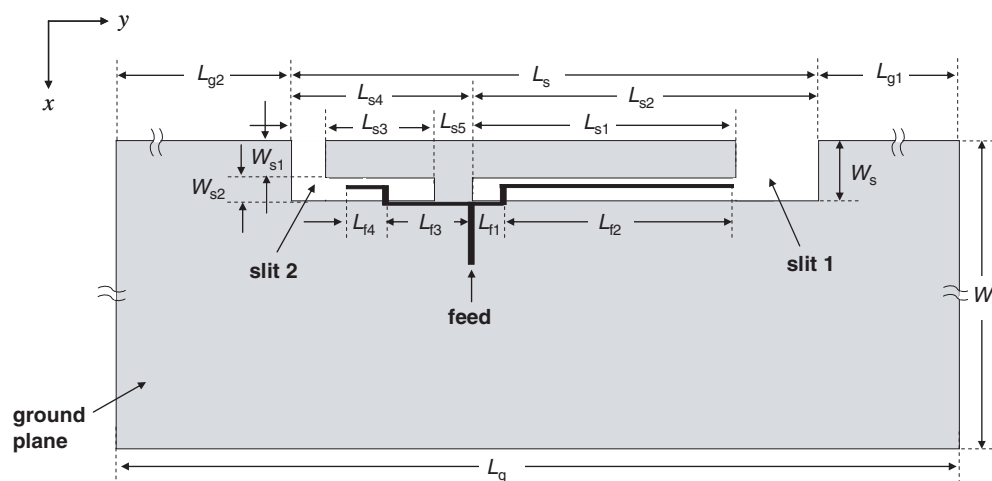


Figure 1: Geometry of the all-planar strip-loaded slit antenna for GSM850/900/DCS/PCS/UMTS operation in the laptop computer with $L_g \times W_g = 300 \text{ mm} \times 200 \text{ mm}$, $L_s \times W_s = 120 \text{ mm} \times 10 \text{ mm}$, $L_{g1} = 70 \text{ mm}$, $L_{g2} = 110 \text{ mm}$, $L_{s1} = 65 \text{ mm}$, $L_{s2} = 80 \text{ mm}$, $L_{s3} = 30 \text{ mm}$, $L_{s4} = 37 \text{ mm}$, $L_{s5} = 10 \text{ mm}$, $W_{s1} = 4 \text{ mm}$, $W_{s2} = 5 \text{ mm}$, $L_{f1} = 5 \text{ mm}$, $L_{f2} = 60 \text{ mm}$, $L_{f3} = 17 \text{ mm}$, and $L_{f4} = 22 \text{ mm}$.

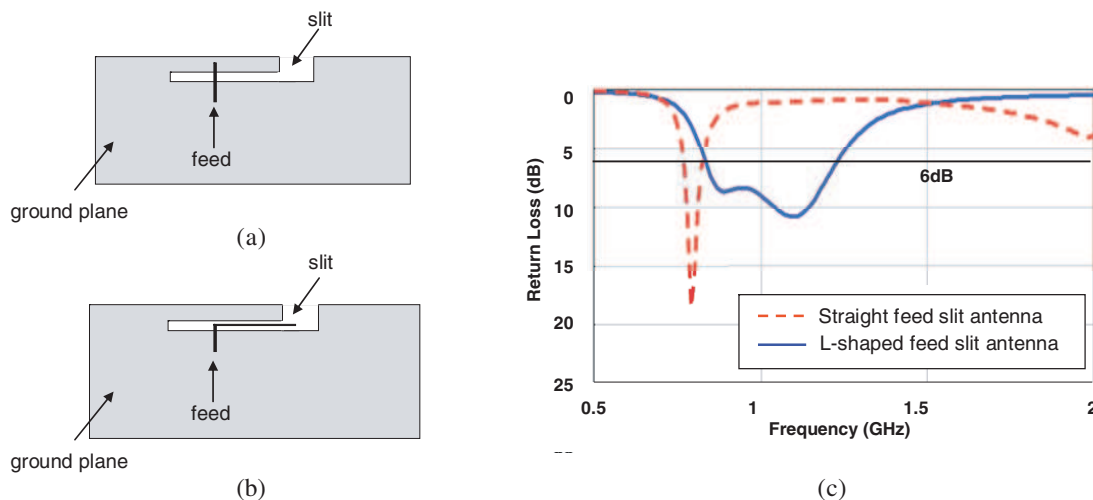


Figure 2: Geometry of the straight feed slit antenna, (b) geometry of the L-shaped feed slit antenna, and (c) simulated return losses of two antennas.

the smaller (slit 2) one is for the higher band (DCS/PCS/UMTS) operation. A T-shaped feeding network is using for the signal feed. Good impedance matching can be obtained by varying the position of the metal strip.

3. MEASUREMENT RESULTS

Figure 3 shows the measured return loss of the proposed antenna. The simulated return loss is plotted for comparison. A good agreement between the measurement and the simulation results is obtained. With the definition of 3:1 VSWR (6-dB return loss), a 140 MHz bandwidth at the lower band is achieved by two resonant modes. The higher band also has two resonances, and the bandwidth is about 460 MHz. For frequencies over two operating bands, the impedance matching is better than 3:1 VSWR. The wide bandwidth covers GSM850/GSM900/DCS/PCS/UMTS pentaband operation.

Figure 4 shows the measured radiation patterns at 860, 925, 1780, 1920, and 2080 MHz of the strip-loaded slit antenna. The radiation pattern is omnidirectional in the H -plane and quite stable over the whole frequency band. The measured peak and average gains for the frequencies of 860, 925, 1780, 1920, and 2080 MHz are listed in Table 1. Over the GSM850/900 and the GSM/1800/1900/UMTS bands, the average gains in this plane are about 2.06 dBi and 0.02 dBi, respectively. The antenna gain variations are less than 1 dB which shows the stable radiation

characteristics across the WWAN band. Good antenna features and the planar configuration make the proposed antenna attractive for wireless communications applications.

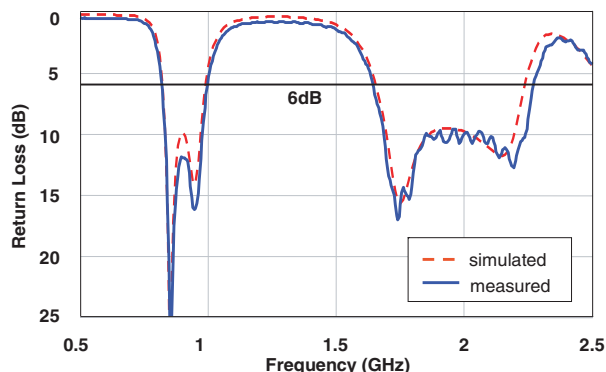


Figure 3: Measured and simulated return loss of the proposed antenna.

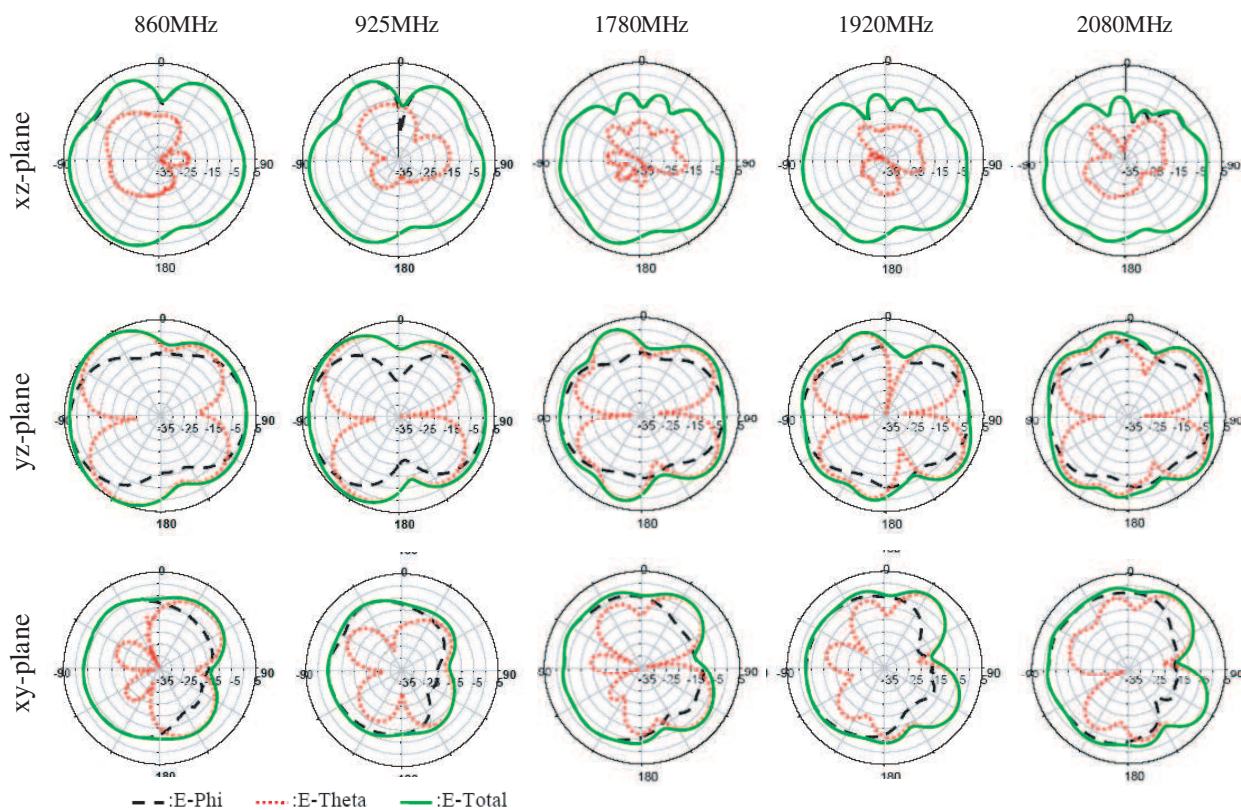


Figure 4: Measured radiation patterns at different operation frequencies.

Table 1: The measured peak and average gains at different operation frequencies.

Frequency (MHz)	Average Gain (dBi)			Peak Gain (dBi)		
	<i>xy</i> -plane	<i>yz</i> -plane	<i>xz</i> -plane	<i>xy</i> -plane	<i>yz</i> -plane	<i>xz</i> -plane
860	0.21	2.06	-4.61	3.14	5.08	-3.03
960	-0.70	1.54	-6.51	2.24	4.19	-3.63
1780	-2.28	-0.83	-3.23	1.57	2.08	-1.27
1920	-2.35	-0.40	-3.18	1.81	2.64	0.10
2080	-2.13	0.02	-1.72	19.1	2.75	1.30

4. CONCLUSIONS

An all-planar antenna of penta-band operation covering GSM850/900/1800/1900/UMTS operation for laptop applications is presented. The penta-band operation is achieved by introducing two back-to-back strip-loaded slit antennas with different sizes together with a T-shaped feeding network. Each strip-loaded slit antenna has two resonances, respectively provided by the strip metal and the slit. A wide operating band is achieved by changing the slit and the metal strip length to cover GSM850/900 operation, and a bandwidth of 460 MHz is obtained for GSM1800/1900/UMTS operation. Good radiation characteristic of the antenna across the operating bands is obtained. The proposed all-planar antenna is printed on a thin FR4 substrate so that it is especially suitable for embedding inside the ultra-thin laptop for WWAN communication.

ACKNOWLEDGMENT

This work was partly supported by the National Science Council, R.O.C., under Contract NSC97-2221-E-009-041-MY3 and MoE ATU plan.

REFERENCES

1. Wong, K. L. and L. C. Chou, "Internal cellular/WLAN combo antenna for laptop-computer applications," *Microw. Opt. Technol. Lett.*, Vol. 47, No. 4, 402–406, Nov. 2005.
2. Kuo, C. H., K. L. Wong, and F. S. Chang, "Internal GSM/DCS dual-band open-loop antenna for laptop application," *Microw. Opt. Technol. Lett.*, Vol. 49, No. 3, 680–684, Mar. 2007.
3. Duixian, L. and B. Gaucher, "A quadband antenna for laptop applications," *IWAT International Workshop on Antenna Technol.: Small and Smart Antennas Metamaterials and Applications*, 128–131, Mar. 2007.
4. Wang, X., W. Chen, and Z. Feng, "Multiband antenna with parasitic branches for laptop applications," *Electron. Lett.*, Vol. 43, No. 19, 1012–1013, Sep. 2007.
5. HFSS. Pittsburgh, PA, Ansoft Corporation.

Investigation of Radiation Efficiency and Bandwidth of Electrically Small MNG ZOR Metamaterial Antenna

Seung-Wook Lee, Jae-Hyun Park, and Jeong-Hae Lee

Department of Electronic Information and Communication Engineering, Hongik University
Seoul 121-791, Korea

Abstract— In this paper, the radiation efficiency and fractional bandwidth of an electrically small zeroth order resonance (ZOR) antenna based on mu-negative (MNG) metamaterials were theoretically investigated. To investigate the radiation efficiency and bandwidth of the electrically small antenna, various types of MNG ZOR antennas such as a meander line inductor and a spiral inductor with different current path have been designed. The equivalent circuits of MNG ZOR antennas are derived for theoretical analysis of an antenna. The parameters of antenna such as radiation resistance and dissipated loss have been obtained by the equivalent circuit of the MNG ZOR antennas. The dissipated loss and radiation resistance were affected by the current distribution of meander line and the direction of current path of the antenna. It is confirmed that both the radiation efficiency and bandwidth of the MNG ZOR antenna can be improved when the cancellation of current on the antenna is minimized if the losses are assumed to be the same.

1. INTRODUCTION

Metamaterial as an artificial material represents unconventional properties such as backward wave propagation, negative index refraction, and infinite wavelength propagation [1]. The metamaterial transmission line has been proven to be very attractive for the design of compact RF devices [2]. As it is known well, the composite right/left-handed (CRLH) transmission line (TL) has unique property of an infinite-wavelength wave at specific non-zero frequency because of zero permittivity and permeability [3, 4]. Thus, various size-independent RF devices using the infinite wavelength property of the CRLH TL, such as the zeroth-order resonator (ZOR) [5] and the ZOR antenna [6], have been reported. Recently, the ZOR antenna using artificial mu-negative (MNG) TL was also presented [7]. The mu-zero frequency of the MNG TL does not depend on its electrical length since an infinite wave length occurs at the zero permeability of the metamaterial TL.

In this paper, the radiation efficiency and the bandwidth of electrically small ZOR antennas using artificial MNG TL [7] are investigated based on an equivalent circuit with optimized parameters, full-wave simulation, and measurement. Since the mu-zero frequency determined by a series capacitance and series inductance, the antennas can be designed by a gap capacitor, meander line inductor, and spiral inductor. Thus, various types of MNG ZOR antennas such as a meander line inductor and a spiral inductor with a gap capacitor are presented. To analyze these antennas, the parameters of antenna such as radiation resistance and dissipated loss have been calculated by the equivalent circuit of the MNG ZOR antennas. In addition, the radiation efficiency and bandwidth of electrically small antenna with respect to the distribution of current on the antenna are investigated.

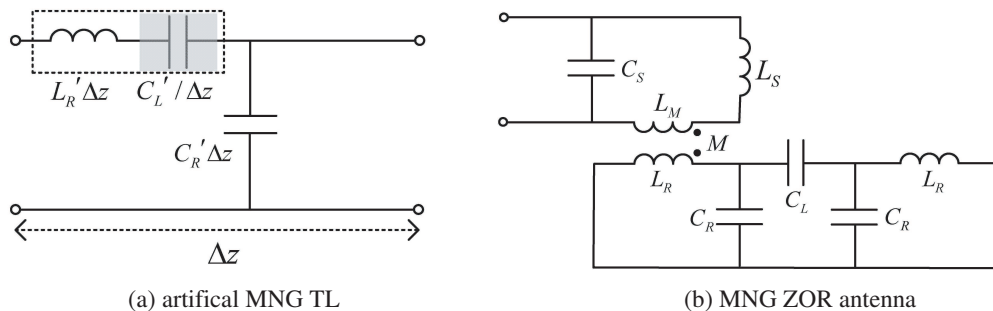


Figure 1: Equivalent circuit.

2. EQUIVALENT CIRCUIT MODEL OF ARTIFICIAL MNG TL AND MNG ZOR ANTENNA

The equivalent circuit of lossless ($R = 0$ and $G = 0$) artificial mu-negative (MNG) TL is realized by adding a series capacitance (C_L) to a host TL as shown in Fig. 1(a). The artificial MNG TL provides the MNG rejection band at the low frequency region and the right-handed (RH) propagation band at the high frequency region due to an artificially added series capacitance [7]. The mu-zero frequency of the resonator using the MNG TL can be controlled by varying a series capacitance and series inductance. To design the MNG ZOR antenna, a short-ended boundary condition must be applied to the antenna because the series resonance of MNG TL determines the ZOR frequency which supports the infinite wavelength. The ZOR frequencies are given as [7]

$$\omega_{ZOR(MNG)} = 1/\sqrt{L_R C_L} \quad (1)$$

The zeroth order resonant frequency is determined only by the $L_R C_L$ values loaded in the unit cell and, therefore, it is independent of the physical length of resonators.

Figure 1(b) shows the equivalent circuits of MNG ZOR antenna. The antenna uses an short-ended boundary and the feed line is designed to obtain magnetic coupling to MNG ZOR antenna [7]. L_R and C_L express series inductance of line (or meander line inductor) and capacitance of gap (or inter-digital capacitor), respectively. They determine the ZOR frequency of antenna. The impedance matching of MNG ZOR antenna can be achieved by adjusting the gap between the feed line and the antenna. M is the coefficient of a magnetic coupling between the feed line and the antenna.

3. INVESTIGATION OF RADIATION EFFICIENCY AND BANDWIDTH OF ELECTRICALLY SMALL MNG ANTENNA

To investigate the radiation efficiency and bandwidth of electrically small antenna with respect to the distribution of current on the antenna, various types of MNG ZOR antennas have been designed. The bandwidth of the antennas can be compared against the fundamental limits for small antennas using equations by (2). The theoretical bandwidth limit of (2) derived in [8] is used where $k = 2\pi/\lambda$ is a wave number and r is a radius of antenna volume. The radiation efficiency is calculated by (3) [9].

$$BW_{(-3\text{dB})} \approx 2/Q \text{ where } Q = 1/(kr) + 1/(kr)^3 \quad (2)$$

$$\text{Radiation efficiency} = R_{\text{radiation}}/(R_{\text{radiation}} + R_{\text{loss}}) \quad (3)$$

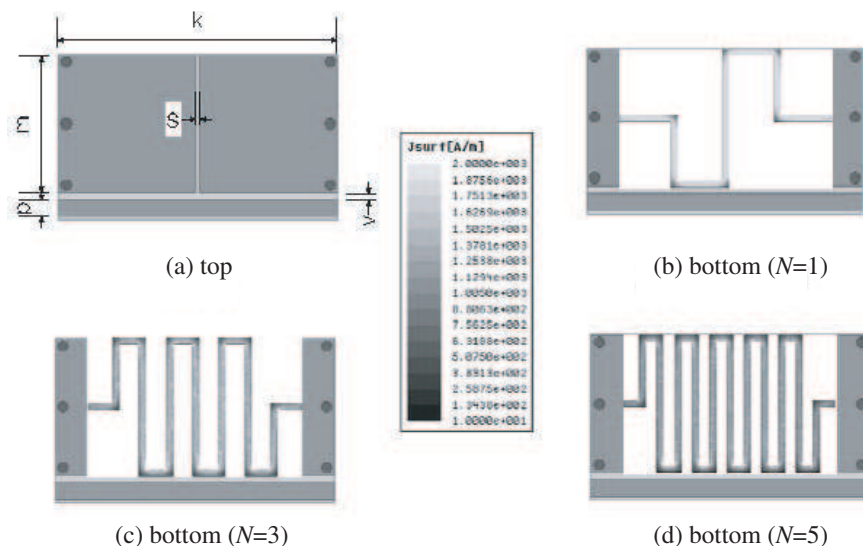


Figure 2: Geometry and Magnitude of surface current of meander line of MNG ZOR antennas. ($m = 4$ mm, $k = 8$ mm, $p = 0.5$ mm, $s = 0.1$ mm, $v = 0.2$ mm, N is the number of turns of meander line. (b) $kr = 0.267$ (c) $kr = 0.219$ (d) $kr = 0.202$).

3.1. Current Cancellation of MNG ZOR Antenna

Figure 2 shows the geometries of MNG ZOR antennas with different number of turns of meander lines. The characteristics of antennas were simulated using a duroid 5880 substrate with relative dielectric constant of 2.2 and height of 3.175 mm. Figs. 2(b), (c), and (d) show that the magnitude of surface current decreases as the number of turns of meander line increases. The characteristics of the MNG ZOR antennas with number of turns of meander line are presented in Table 1. As the number of turns increases, the radiation resistance decreases and the dissipated power loss increases due to current cancellation on adjacent meandered sections. This causes the radiation efficiency decrease rapidly while the bandwidth of the antennas increase, as compared with theoretical bandwidth limit, since the total resistance ($R_{rad} + R_{loss}$) increases.

Table 1: Antenna parameters of the MNG ZOR antennas with different number of turns of meander lines.

Number of turns	f_{MZR} (GHz)	L_R (nH)	C_L (pF)	R_{rad} (Ω)	R_{loss} (Ω)	-3 dB Fractional BW(%)	Radiation efficiency (%)	-3 dB Fractional BW (%) from (2)
1	2.592	24.11	0.16	0.513	1.844	1.505	21.7	3.553
3	2.132	36.61	0.15	0.332	3.359	1.689	9.2	2.004
5	1.962	40.50	0.16	0.268	4.541	1.784	5.6	1.583

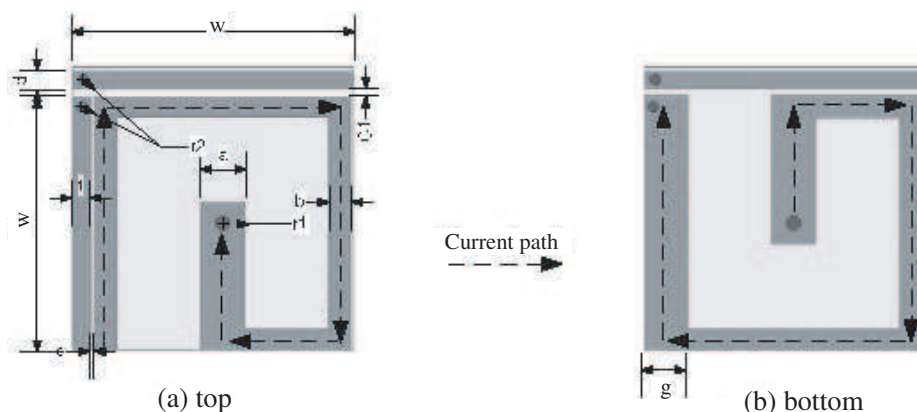


Figure 3: Geometry and surface current path for MNG ZOR antennas with the same current path. ($a = 1.2$ mm, $b = 0.6$ mm, $C1 = 0.2$ mm, $d = 0.5$ mm, $e = 0.1$ mm, $f = 0.5$ mm, $g = 1.2$ mm, $w = 7$ mm, $r1 = 0.15$ mm, $r2 = 0.2$ mm).

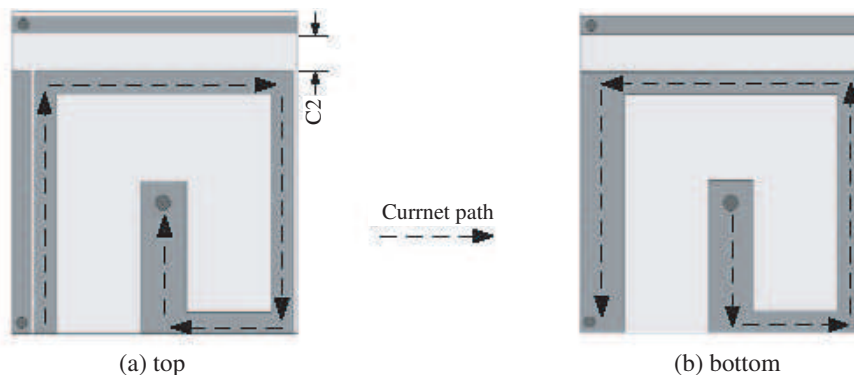


Figure 4: Geometry and surface current path for MNG ZOR antennas with the opposite current path. ($C2 = 1$ mm).

3.2. Effect of Current Direction

To investigate the effect of current path (or direction) on the characteristics of electrically small antenna, the MNG ZOR antennas with different current path have been designed. Fig. 3 shows the antenna which has the same current direction on top and bottom plate. In Fig. 4, the antenna has the opposite current direction on top and bottom plate. These antennas have the same geometry except for C_1 and C_2 (C_1 and C_2 are the distance between feed line and the antenna for impedance matching.) and size of $kr = 0.17$ and 0.204 , respectively. Table 2 gives a comparison of the characteristics of antennas with respect to the current direction. In case of the same current direction as shown in Fig. 3, the radiation resistance is higher than that of Fig. 4 since the cancellation of current is smaller and, thus, the amount of radiated power is larger. Because the antenna geometry is not changed except for distance between feed line and antenna, the variation of dissipated power is not observed. Therefore, the radiation efficiency of the antenna with the same current direction increases. It is confirmed that the cancellation of current by current direction of adjacent structure gives rise to the degradation of radiation efficiency. It is noted that these antennas were simulated using a duroid 5880 substrate with relative dielectric constant of 2.2 and height of 3.175 mm.

Table 2: Antenna parameters of the MNG ZOR antennas with different current direction.

Current path	f_{MZR} (GHz)	L_R (nH)	C_L (pF)	R_{rad} (Ω)	R_{loss} (Ω)	-3 dB Fractional BW(%)	Radiation efficiency (%)	-3 dB Fractional BW (%) from (2)
Fig. 3	1.446	45.253	0.267	0.136	1.355	0.740	9.12	0.955
Fig. 4	1.629	36.126	0.267	0.053	1.270	0.875	4.01	1.630

4. SIMULATED AND EXPERIMENTAL RESULTS OF MNG ZOR ANTENNA WITH THE SAME CURRENT DIRECTION

The MNG ZOR antenna with the same current direction has been fabricated using a duroid 5880 substrate ($\epsilon_r = 2.2$, height = 3.175 mm). The total size of an antenna is 7.7 mm \times 7.6 mm \times 3.175 mm without additional ground plane. Fig. 5(a) shows the simulated and measured return loss of the MNG ZOR antenna. In Fig. 5(a), the differences of experimental and simulated ZOR frequencies are due to interference between SMA connector and antenna and dimension tolerance of the fabrication. Fig. 5(b) shows the photograph of the MNG ZOR antenna.

Figure 6 shows the simulated and measured radiation patterns of the MNG ZOR antenna. In this structure, the surface current has the characteristics of in-phase loop current, which makes the omni-directional pattern. The radiation mechanism of the MNG ZOR antenna is similar to that of electrically small loop antenna. The measured radiation efficiency, -3 dB bandwidth and ZOR frequency of the MNG ZOR antenna are 8.6%, 0.727% and 1.496 GHz, respectively. It is noted that the -3 dB bandwidth is close to the theoretical bandwidth limit of [8]. The simulated and measured maximum gains are -8.5 dBi and -7.14 dBi, respectively.

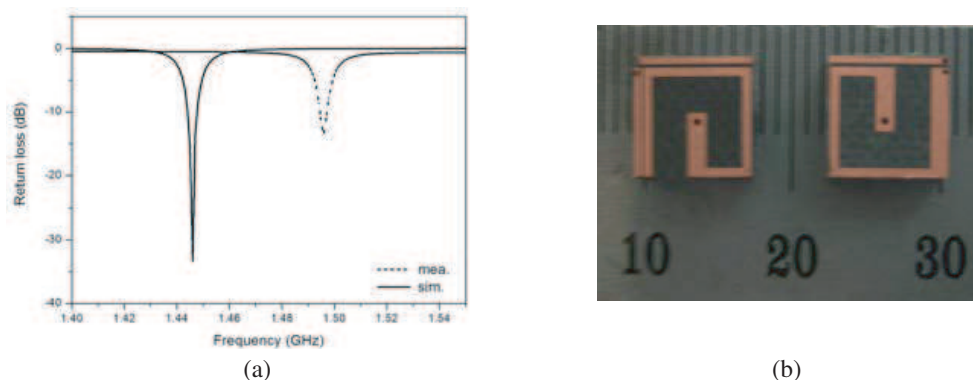


Figure 5: (a) Simulated and Measured return loss (b) photograph of the MNG ZOR antenna with the same current direction.

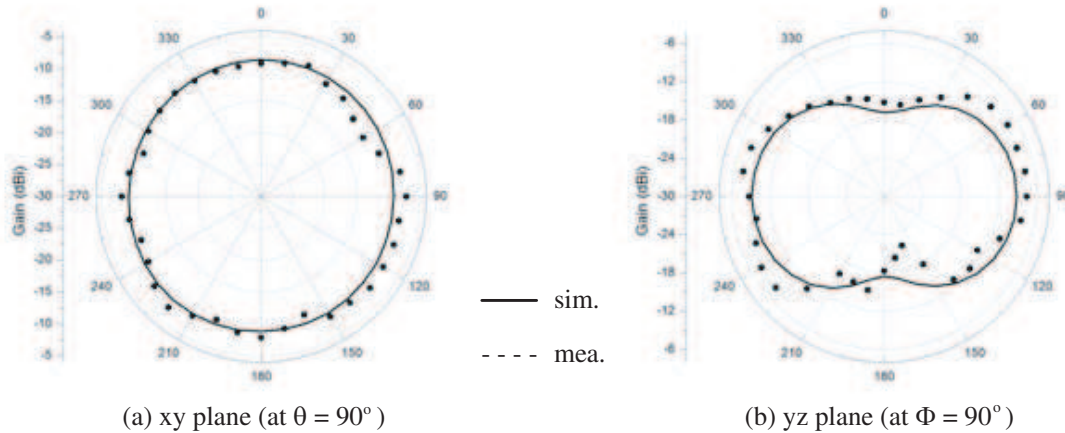


Figure 6: Simulated and Measured radiation patterns of the MNG ZOR antenna with the same current path

5. CONCLUSION

In this paper, the mu-zero resonance electrically small antennas using artificial mu-negative (MNG) TLs which have an infinite wavelength were theoretically investigated such as radiation efficiency and bandwidth. To investigate the radiation efficiency and bandwidth of electrically small antenna, various types of MNG ZOR antennas have been designed. The equivalent circuits of MNG ZOR antennas are derived for theoretical analysis of an antenna. Both the radiation efficiency and bandwidth of the MNG ZOR antenna can be improved when the cancellation of current on the antenna is minimized if the losses are assumed to be the same.

ACKNOWLEDGMENT

This work was supported by Korea Science and Engineering Foundation(KOSEF) grant funded by the Korea government (MOST) (No. R01-2007-000-20495-0(2008)).

REFERENCES

1. Veselago, V. G., "The electrodynamics of substances with simultaneously negative values of ϵ and μ ," *Soviet Physics Uspekhi*, Vol. 10, No. 4, 509–514, Jan. 1968.
2. Lai, A., K. M. K. H. Leong, and T. Itoh, "Infinite wavelength resonant antennas with monopolar radiation pattern based on periodic structure," *IEEE Microw. Antenna Propag.*, Vol. 55, No. 3, 868–876, Mar. 2007.
3. Engheta, N. and R. W. Ziolkowski, *Metamaterials: Physics and Engineering Explorations*, John Wiley & Sons, Press, 2006.
4. Caloz, C. and T. Itoh, *Electromagnetic Metamaterials: Transmission Line Theory and Microwave Applications*, John Wiley & Sons, Press, 2006.
5. Sanada, A., C. Caloz, and T. Itoh, "Novel zeroth-order resonance in composite right/left-handed transmission line resonators," *Asia-Pacific Microwave Conference*, Vol. 3, 1588–1591, 2003.
6. Lee, J.-G. and J.-H. Lee, "Zeroth order resonance loop antenna," *IEEE Transaction on Antennas and Propagation*, Vol. 55, No. 3, 994–997, 2007.
7. Park, J.-H., Y.-H. Ryu, S.-W. Lee, J.-H. Lee, E.-S. Park, and Y. -E. Kim, "Dual band antennas using metamaterial transmission lines," *IEEE AP-S*, San Diego, USA, July 2008.
8. Chu, L. J., "Physical limitations of small antennas," *J. Appl. Phys.*, Vol. 19, 1163–1175, Dec. 1948.
9. Pozar, D. M., *Microwave Engineering*, 3rd Edition, Wiley, Press, 2003.

Circularly Polarized Slotted Conductor-backed Coplanar Waveguide (CBCPW) Antenna Array with Sequentially Rotated Feeding Structure

Yow-Shyan Lin¹, Lieh-Chuan Lin¹, Toshihide Kitazawa², and Yu-De Lin¹

¹Department of Communication Engineering, National Chiao Tung University, Hsinchu, Taiwan

²Department of Electrical and Electronic Engineering, Ritsumeikan University, Kusatsu, Japan

Abstract— In this paper, circularly polarized slotted antenna arrays on conductor-backed coplanar waveguide (CBCPW) operating at Ku band are proposed. Radiating slots along the propagation direction of the parallel-plate mode in the CBCPW structure are etched to radiate into the air. By appropriately arranging the position and tilt angle for each slot, we can implement a kite-shaped linearly polarized antenna array with high gain and narrow beamwidth. Combining four linearly polarized arrays with a sequentially rotated feeding structure can produce a circularly polarized slotted CBCPW antenna arrays. Two arrangements of the sequential rotation method with the feeding phases in a $0^\circ, 90^\circ, 0^\circ, 90^\circ$ fashion and a $0^\circ, 90^\circ, 180^\circ, 270^\circ$ fashion are used. The measured gains are 24.889 dBiC for the $0^\circ, 90^\circ, 0^\circ, 90^\circ$ arrangement and 24.691 dBiC for the $0^\circ, 90^\circ, 180^\circ, 270^\circ$ arrangement, respectively. The bandwidths of the axial ratio (AR) below 3 dB are 330 MHz and 370 MHz,

1. INTRODUCTION

Conductor-backed coplanar waveguide (CBCPW) [1–4] is a commonly used waveguide structure in planar printed circuits. It has two dominant modes, the CBCPW mode and the parallel-plate mode. The CBCPW mode always leaks power into the background waveguide mode, the parallel-plate mode, as the wave propagates down the waveguide. Employing the design principles of slotted waveguide arrays in Elliott's book [5], we etch radiating slots along the propagation direction of the parallel-plate mode. By appropriately arranging the positions and the tilt angles of the radiating slots, we have designed a kite-shaped linearly polarized antenna in [6].

Modern satellite communication systems use circular polarization (CP) to maximize the polarization efficiency. Sequential rotation method [7, 8] is a way to generate circular polarization antennas with linearly polarized elements. To obtain circular polarization, we can put linearly polarized elements with element angular orientation and feed phases in a $0^\circ, 90^\circ, 0^\circ, 90^\circ$ or a $0^\circ, 90^\circ, 180^\circ, 270^\circ$ fashion. In this paper, we have implemented a slotted CBCPW antenna array with a right hand circular polarization (RHCP). The antenna is designed in the Ku band for the direct broadcast satellite (DBS) systems.

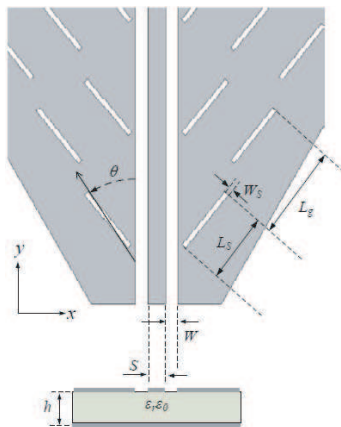


Figure 1: The top view and the cross-sectional view of the slotted conductor-backed coplanar waveguides.

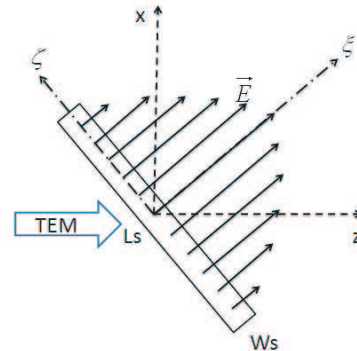


Figure 2: The electric field distribution in the slot.

2. DESIGN

Figure 1 shows the top view and the cross-sectional view of the slotted CBCPW antenna. Using the spectral domain approach [9], we can obtain the propagation constant ($k_y = \beta - j\alpha$) of the CBCPW mode. The propagation direction (in the angle of θ from the CPW waveguide direction) of the parallel plate-mode is determined by the equation $\theta = \cos^{-1}(\beta/k)$, where β is the phase constant of the CBCPW mode and k is the phase constant of the parallel-plate mode. We etch radiating slots along the propagation direction to radiate power into the air. Fig. 2 shows the electric field distribution in the slot as the wave passes through the slot. The tilt angle ϕ of each slot determines the normalized radiation resistance, as shown in Fig. 3. The tilt angle of each slot is arranged for impedance matching. Following the design procedure in [10], we can implement a kite-shaped linearly polarized antenna array as shown in Fig. 4.

Next, we use the sequential rotation method to achieve a circularly polarized antenna. An example that uses microstrip patches is illustrated in Fig. 5. To achieve a circularly polarized array, each element is rotated 90 degrees with respect to the neighboring one, and the feeding phases should be arranged in a $0^\circ, 90^\circ, 0^\circ, 90^\circ$ or a $0^\circ, 90^\circ, 180^\circ, 270^\circ$ fashion. A power divider with different arm lengths is used to achieve the phase difference. We use a 1-to-4 power divider with a $50\ \Omega$ coaxial cable as the input, connecting to four quarter-wave transformer $141\ \Omega$ CBCPW lines to match the $100\ \Omega$ input impedance of the load antenna. The phase difference is created by the line-length change. The top view of the power divider is shown in Fig. 6. Connecting the divider to four kite-shaped linearly polarized antennas, we can implement a circularly polarized slotted CBCPW antenna array. Fig. 7 shows the electric field direction of each element. By appropriately arranging the slots and feeding phases, we can make the antenna produce a RHCP wave.

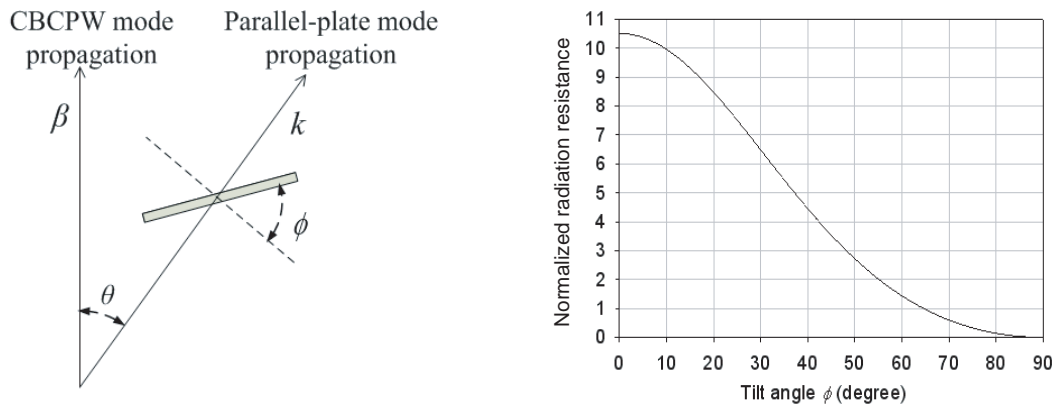


Figure 3: The propagation direction of CBCPW mode and parallel-plate mode and the normalized radiation resistance versus the tilt angle ϕ .

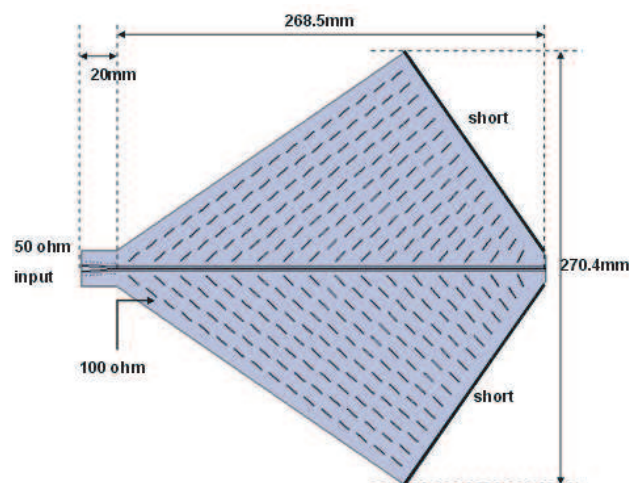


Figure 4: The kite-shaped linearly polarized antenna array.

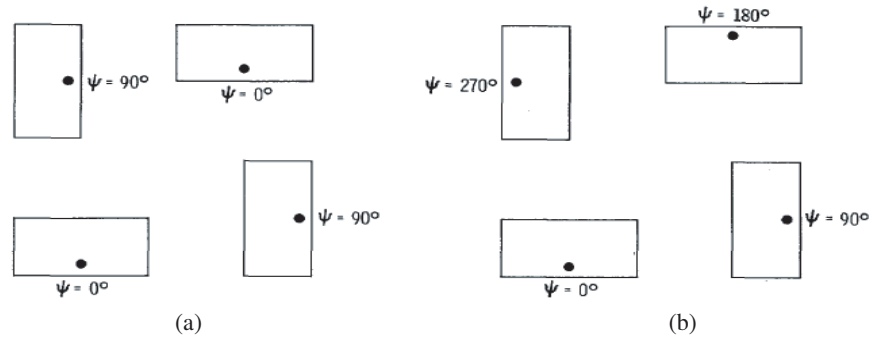


Figure 5: 2×2 microstrip arrays that generate CP with LP elements. (a) The $0^\circ, 90^\circ, 0^\circ, 90^\circ$ arrangement. (b) The $0^\circ, 90^\circ, 180^\circ, 270^\circ$ arrangement.

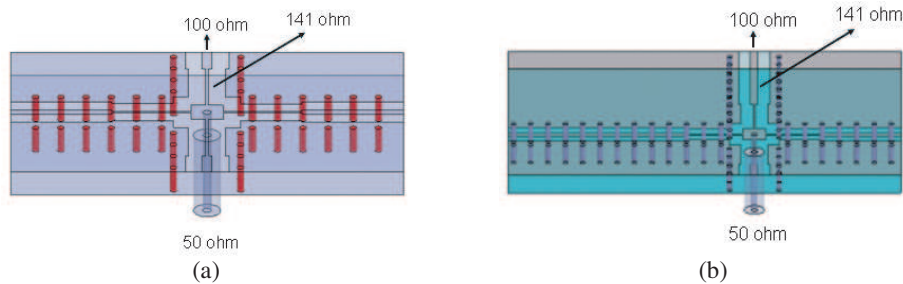


Figure 6: The 1-to-4 power divider. (a) The $0^\circ, 90^\circ, 0^\circ, 90^\circ$ arrangement. (b) The $0^\circ, 90^\circ, 180^\circ, 270^\circ$ arrangement.

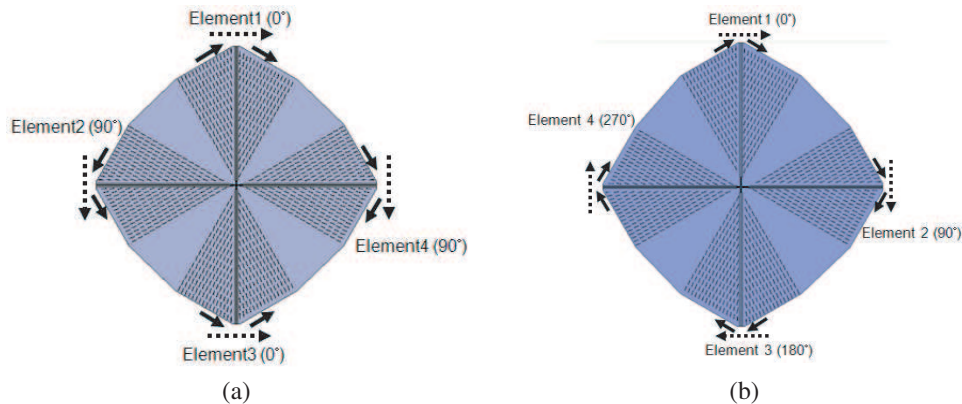


Figure 7: Circularly polarized slotted CBCPW antenna array with sequential rotation method. (a) The $0^\circ, 90^\circ, 0^\circ, 90^\circ$ arrangement. (b) The $0^\circ, 90^\circ, 180^\circ, 270^\circ$ arrangement.

3. MEASUREMENT RESULTS

The antenna is designed on the Rogers 4003 substrate, with the dielectric constant $\epsilon_r = 3.55$, the loss tangent $\tan \delta = 0.0027$, and the substrate thickness $h = 1.524$ mm. The structural parameters of the CBCPW are as follows: the center feed-line width $S = 0.6$ mm, and the gap width $W = 1$ mm. The characteristic impedance of the CBCPW is 100Ω . The impedance of the coaxial cable is 50Ω . The geometrical parameters of the slots are: the slot width $W_s = 0.5$ mm, the slot length $L_s = 9.6$ mm, and the distance between slots on the same radial line $L_g = 13.27$ mm. The total sizes of the antenna array are 535.02 mm \times 528.96 mm for the $0^\circ, 90^\circ, 0^\circ, 90^\circ$ arrangement, and 543.32 mm \times 536.64 mm for the $0^\circ, 90^\circ, 180^\circ, 270^\circ$ arrangement, respectively.

For the $0^\circ, 90^\circ, 0^\circ, 90^\circ$ arrangement, the return loss below -10 dB is from 10 GHz to 13.70 GHz. The measured RHCP gain at 12 GHz in the yz -plane is 24.889 dBiC. The axial ratio below 3 dB bandwidth is from 11.95 GHz to 12.28 GHz. For the $0^\circ, 90^\circ, 180^\circ, 270^\circ$ arrangement, the return loss below -10 dB is from 10 GHz to 13.88 GHz. The measured RHCP gain at 12 GHz in the yz -plane is 24.691 dBiC. The axial ratio below 3 dB bandwidth is from 11.9 GHz to 12.27 GHz, as shown in Figs. 8, 9, and 10, respectively.

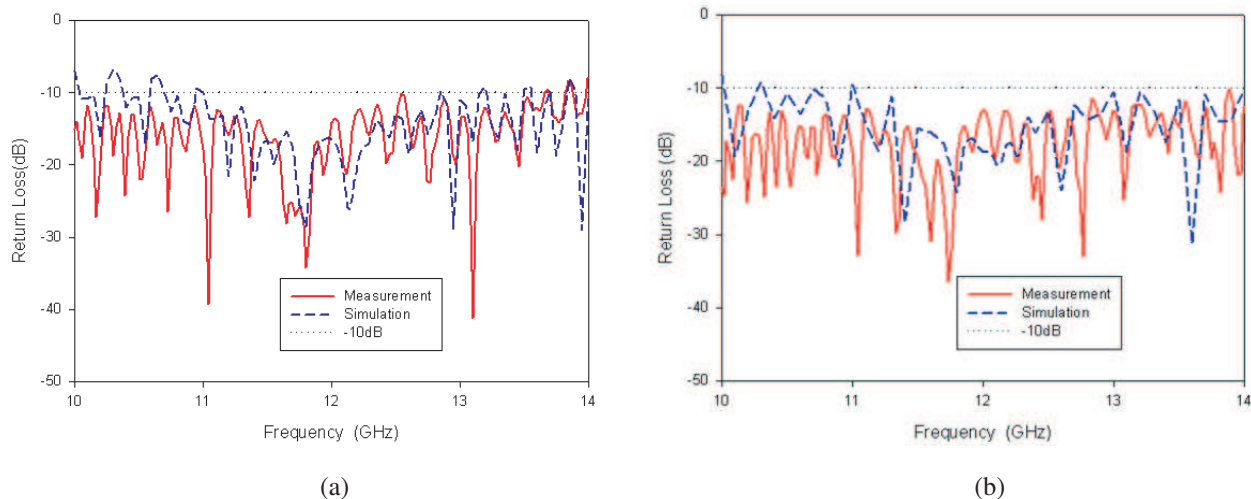


Figure 8: The measured and simulation return losses of the circularly polarized slotted CBCPW antenna. (a) The 0°, 90°, 0°, 90° arrangement. (b) The 0°, 90°, 180°, 270° arrangement.

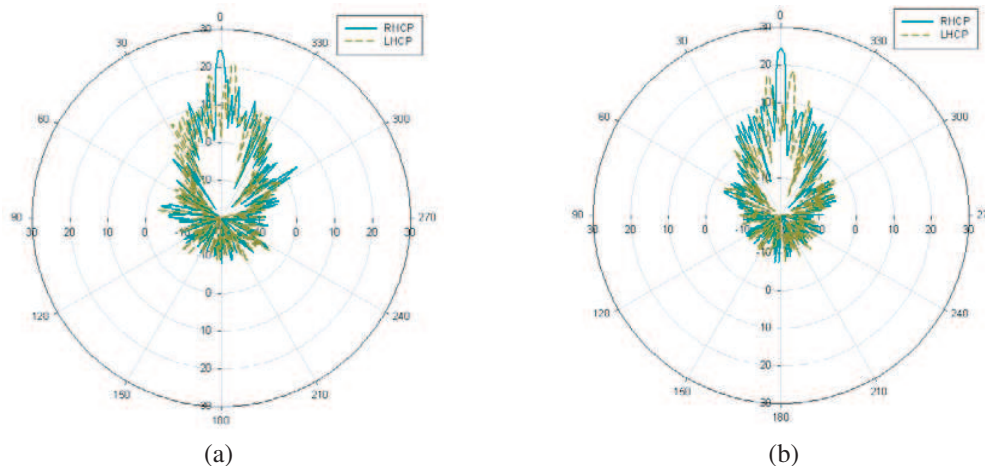


Figure 9: The measured RHCP and LHCP radiation patterns of the circularly polarized slotted CBCPW antenna. (a) The 0°, 90°, 0°, 90° arrangement. (b) The 0°, 90°, 180°, 270° arrangement.

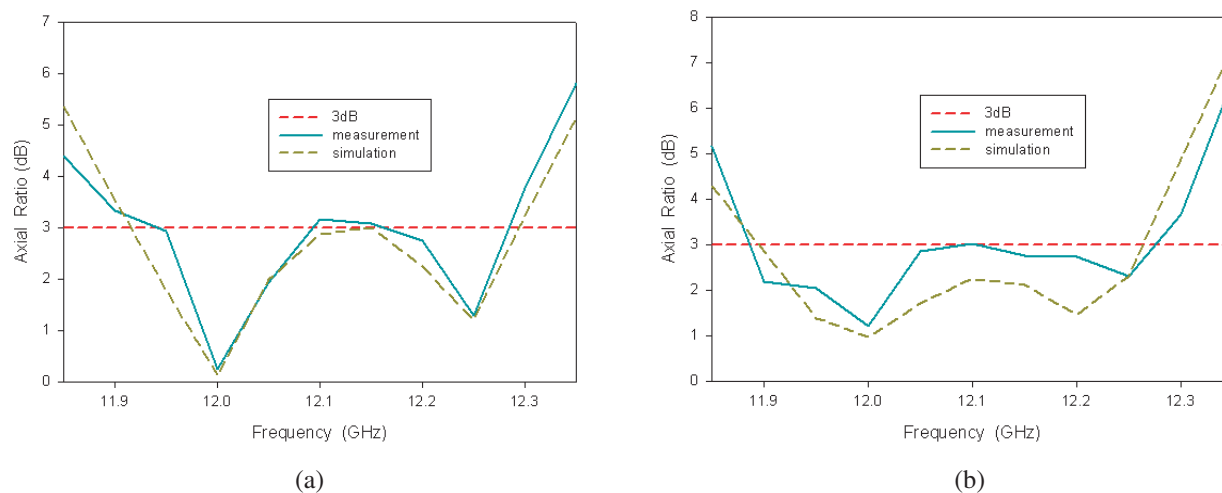


Figure 10: The measured and simulation axial ratios of the circularly polarized slotted CBCPW antenna. (a) The 0°, 90°, 0°, 90° arrangement. (b) The 0°, 90°, 180°, 270° arrangement.

4. CONCLUSION

A circularly polarized slotted CBCPW antenna array is proposed and implemented. By appropriately arranging the tilt angles and the positions of the radiating slots along the propagation direction of the leaky parallel-plate mode in the CBCPW structure, we can design a kite-shaped linearly polarized antenna arrays with high gain. Feeding four linearly polarized arrays with sequential rotation method can produce a circularly polarized antenna array. The circularly polarized antenna with high gain and sharp mainbeam is useful for applications such as the direct broadcast satellite systems.

ACKNOWLEDGMENT

The work was supported in part by the National Science Council under Grants NSC 95-2218-E-009-041.

REFERENCES

1. Shih, Y. C. and T. Itoh, "Analysis of conductor-backed coplanar waveguide," *Electronics Letters*, Vol. 18, No. 12, 538–440, Jun. 1982.
2. Jackson, R. W., "Mode conversion at discontinuities in finite-width conductor-backed coplanar waveguide," *IEEE Trans. Microwave Theory and Techniques*, Vol. 37, No. 10, 1582–1589, Oct. 1989.
3. Cheng, K. K. M. and J. K. A. Everard, "A new technique for the quasi-TEM analysis of conductor-backed coplanar waveguide structures," *IEEE Trans. Microwave Theory and Techniques*, Vol. 41, No. 9, 1589–1592, Sept. 1993.
4. Fang, S.-J. and B.-S. Wang, "Analysis of asymmetric coplanar waveguide with conductor backing," *IEEE Trans. Microwave Theory and Techniques*, Vol. 47, No. 2, 238–240, Feb. 1999.
5. Elliott, R. S., *Antenna Theory and Design*, Prentice Hall, Englewood Cliffs, NJ, 1981.
6. Lin, L.-C., Y.-S. Cheng, R. B. Hwang, T. Kitazawa, and Y.-D. Lin, "Slotted conductor-backed coplanar waveguide antennas," *International Symposium on Antennas and Propagation (ISAP2008)*, Oct. 2008.
7. Huang, J., "A technique for an array to generate circular polarization with linearly polarized elements," *IEEE Trans. Antennas Propag.*, Vol. 34, No. 9, 1113–1123, 1986.
8. Hall, P. S., J. S. Dahele, and J. R. James, "Design principles of sequentially fed, wide bandwidth, circularly polarized microstrip antenna," *IEE Proc.*, Vol. 136, No. 5, 381–389, Part H, 1989.
9. Itoh, T. and R. Mittra, "Spectral-domain approach for calculating the dispersion characteristics of microstrip lines," *IEEE Trans. Microwave Theory and Techniques*, Vol. 21, 496–499, Jul. 1973.
10. Ando, M., T. Numata, J.-I. Takada, and N. Goto, "A linearly polarized radial line slot antenna," *IEEE Trans. Antennas Propag.*, Vol. 36, No. 12, 1675–1680, Dec. 1988.

Fractal Electrodynamics: Analysis and Synthesis of Fractal Antenna Radiation Pattern

Aleksandr Nikolaevich Bogolyubov, Artem Aleksandrovich Koblikov,
and Natalia Evgenievna Shapkina

Faculty of Physics, Lomonosov Moscow State University, Russia

Abstract— The problem of fractal antenna radiation pattern synthesis is considered. The theory of the electromagnetic wave interaction with a fractal structure was developed recently and it is progressing rapidly. The term “fractal electrodynamics” is now embedded in literature.

1. INTRODUCTION

Unlike traditional methods, when smooth antenna radiation patterns are synthesized, the theory of fractal synthesis is based on the principle of scale invariance i.e., radiation characteristics with the replicated structure are scale-independent. Therefore, it makes possible to realize new modes in fractal electrodynamics and to find new fundamental properties. For example, the fractal elements disposition on the object body may essentially change the indication. Fractal antennas may be used in telecommunication, nonlinear radiolocation, search systems, radar detection etc.

Fractal radiation patterns are synthesized with the help of the Weierstrass function

$$f(x) = \sum_{n=1}^{\infty} \eta^{(D-2)n} g(\eta^n x) \quad (1)$$

where $1 < D < 2$; $\eta > 1$; g is a bounded periodic function.

Here D is a modified fractal dimension

$$D = -\log(N)/\log(r), \quad (2)$$

where N is a number of elements in one subarray; $r = r_1/r_2$; r_1 is an average distance between subarray (generator) elements; r_2 is an average distance between elements of a random exciter.

Technique of the synthesis of some types of radiation fractal characteristics for special symmetric antenna arrays are presented in [1]. Investigations were continued in [2] with analysis of Cantor concentric arrays with number of elements up to 754.

The theory of the electromagnetic wave interaction was created recently and now it is developing rapidly. Fractal structures are self-similar in different scales and do not have a characteristic size. That is why fractal structures are wide-range in electromagnetic sense. First time these antennas were studied in 1996. The wide-range property permits us to use fractal antennas with one base station in moving media under the control of several telecommunication systems [4].

As mentioned above, the fractal radiation pattern is synthesized with the help of the Weierstrass function (1). The functions are continuous and non-differential everywhere and fractal in all scales. With antenna array engineering, space distribution of radiators is the third variable when the current amplitude and phase are the first two variables. Then it is possible to control the antenna radiation pattern with the help of these three variables.

Let us consider the following symmetric antenna array as an example [7] (See Fig. 1).

Here $k = 2\pi/\lambda$ is a wave number, I_n , α_n are excitation current amplitude and phase; d_n is a distance between two neighbor feeds.

A normalized factor of the array is

$$g_N(u) = \left[\frac{1 - \eta^{(D-2)}}{1 - \eta^{(D-2)N}} \right] \sum_{n=1}^N i_n \cos(a\eta^n u + \alpha_n), \quad (3)$$

where the normalized amplitude of the current of excitation is

$$i_n = \eta^{(D-2)(n-1)}. \quad (4)$$

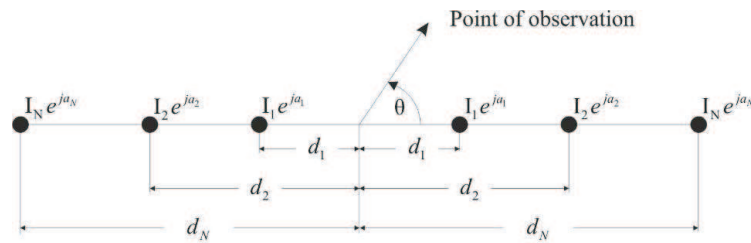


Figure 1: Symmetric antenna array of $2N$ elements with presented distribution of the excitation current distribution.

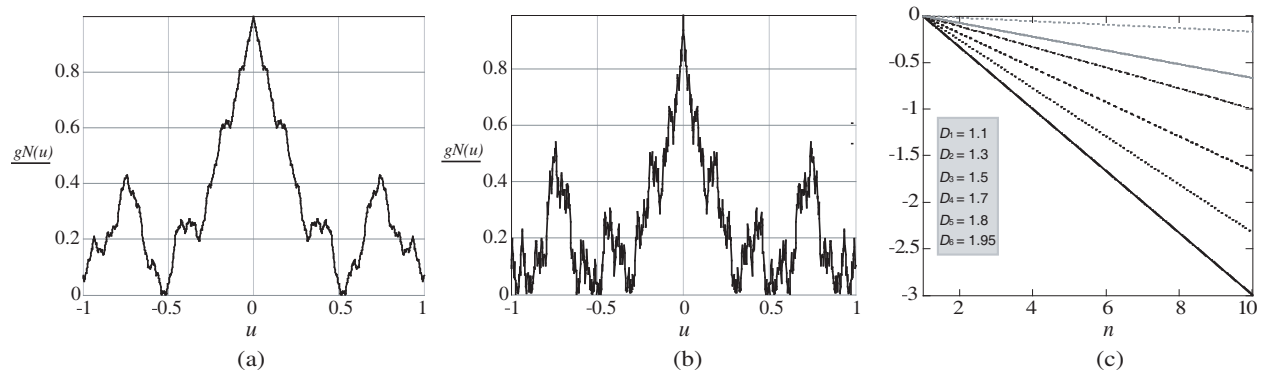


Figure 2: Normalized factor for Weierstrass array for different fractal dimensions D . ((a) $D = 1$; (b) $D = 1, 5$). In (c) normalized current distributions i_N for radiation patterns with different fractal dimensions D are presented in dependence of N .

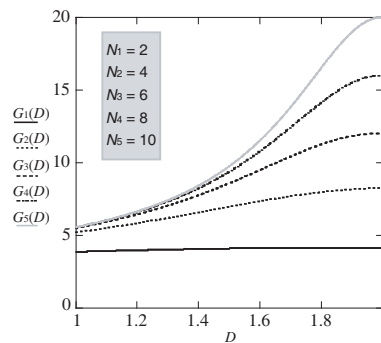


Figure 3: Antenna gain $G(u_0)$ in dependence of D for different N .

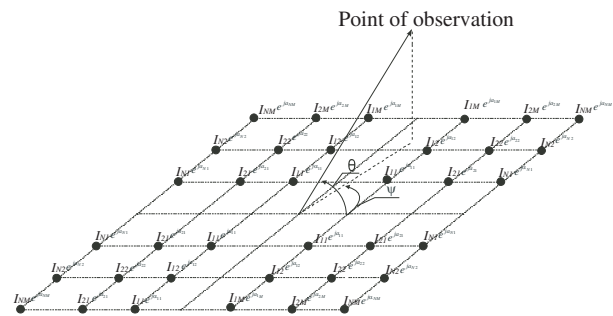


Figure 4: Symmetric antenna array of $2N \times 2N$ elements with presented distribution of the excitation current distribution.

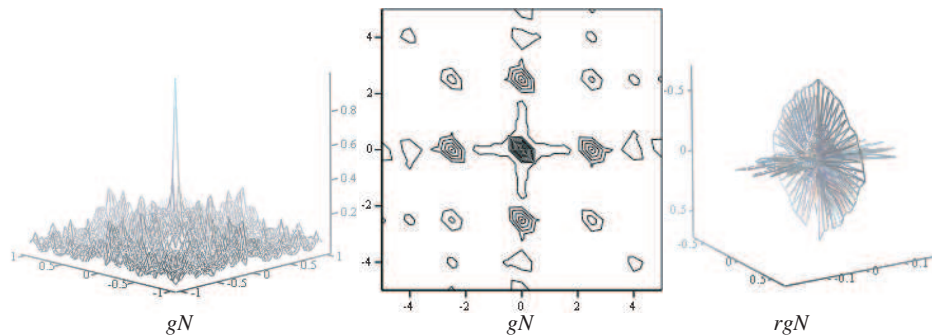


Figure 5: Normalized factor for Weierstrass array of $2N \times 2N$ elements for different fractal dimensions $D = 1, 5$.

Then the fractal dimension of the radiation pattern may be controlled by the array current distribution (See Fig. 2).

Antenna gain of this array is

$$G(u_0) = \frac{2f_N^2(u_0)}{\int_{-1}^1 f_N^2(u) du}, \quad \text{where } f_N^2(u) = 4 \sum_{m=1}^N \sum_{n=1}^N \eta^{(D-2)(m+n)} \cos(a\eta^m u + \alpha_m) \cos(a\eta^n u + \alpha_n). \quad (5)$$

It is evident that when \mathbf{D} decreases, the radiation pattern main lobe widens and the corresponding values $G(u)$ become less.

Using a similar method, we received the following results for the two-dimensional symmetric antenna array of $2N \times 2N$ elements (Fig. 4) that are presented in Fig. 5.

Now let us analyze a long radiating system L with continuous current distribution $I(z)$ (Fig. 6).

Let us consider the procedure of the radiation linear source synthesis for the generator general function $g(\theta) = 1 - |1 - \cos \theta|$, $0 \leq \theta \leq \pi$, that is transformed into the triangle function.

Let us analyze the following generator function: $g(\theta) = \sin^2 \theta$, $0 \leq \theta \leq \pi$. The first 6 steps of fractal radiation pattern synthesis are obtained basing on Fourier-Weierstrass transform.

The investigation shows that fractal antennas application permits us to develop new modes and find new properties improving operating characteristics of the objects thus making such antennas to be widely used. At present time, the mathematical modeling is one of the main methods for these structures' investigation as it allows to find optimal parameters a priori.

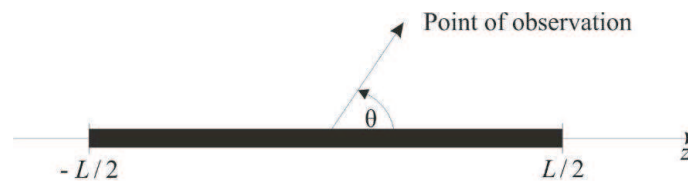


Figure 6: Geometry of continuous linear radiation system of L length disposed along z axis.

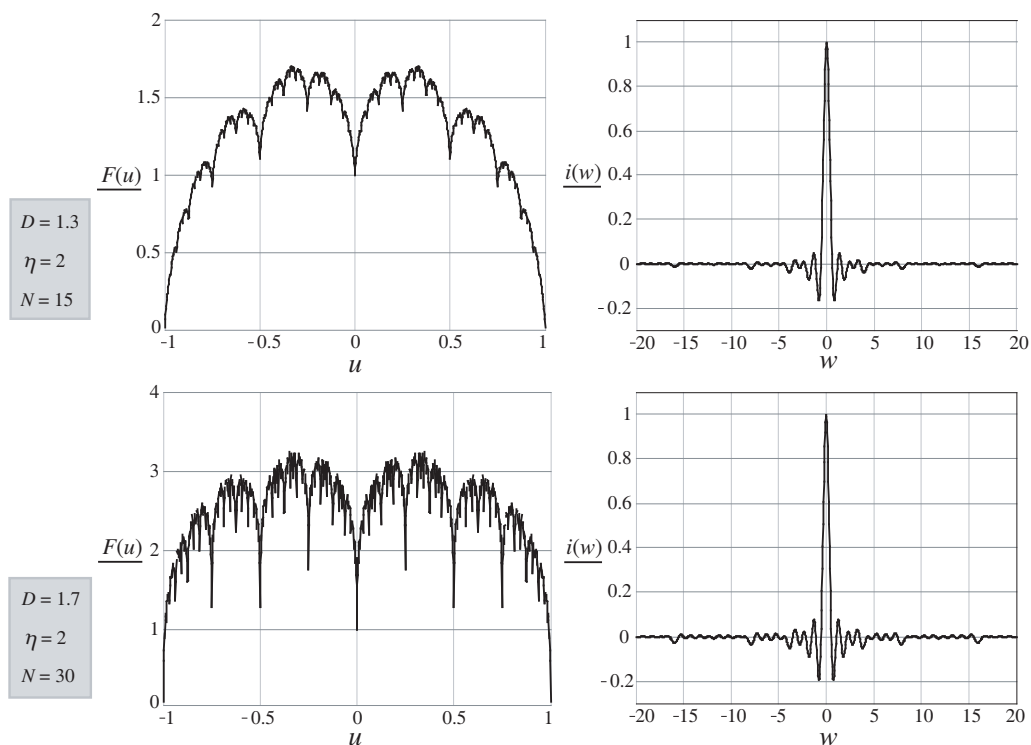


Figure 7: Synthesized radiation patterns for specified D values and normalized current distributions $i(s)$.

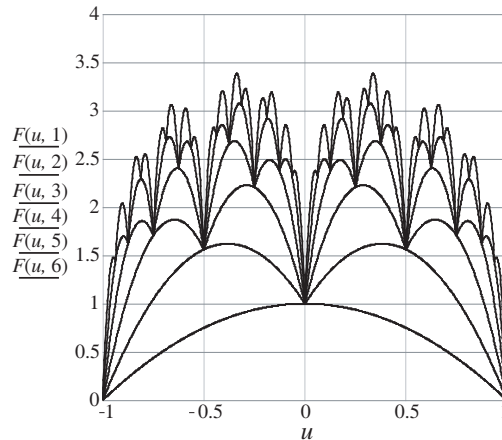


Figure 8: The first 6 steps of fractal radiation pattern synthesis ($N = 1-6$) for $D = 1, 7$ and $\eta = 2$.

ACKNOWLEDGMENT

This work was supported by the Russian Foundation for Basic Research, Project Nos. 06-01-00146.

REFERENCES

1. Liang, X., W. Zhensen, and W. Wenbung, "Synthesis of fractal pattern from concentric-ring arrays," *Electron. Lett.*, Vol. 32, No. 21, 1940–1941, 1996.
2. Jagard, D. L., "Fractal electrodynamics: Wave interaction with discretely self-similar structures," *Symmetry in Electrodynamics*, C. Baum and H. N. Kritikos. (Eds.), Taylor & Francis, London, 1995.
3. Werner, D. H. and P. L. Werner, "On the synthesis of fractal radiation patterns," *Radio Sci.*, Vol. 30, No. 1, 29–45, 1995.
4. Fractus, S. A., "New fractal antennas for compact and versatile telecommunication services," *Microwave Journal*, Vol. 43, No. 1, 196, 198, 200, 202, 204, Jan. 2000.
5. Bogolyubov, A. H., A. A. Koblikov, A. A. Petuhov, and N. E. Shapkina, "Fractals: Modeling and applications," *16th International Conference, "Radar-location and a radio communication,"* and *16th International Conference on Backs-electronics and Giro-magnetism*, (Section of 18th International Conference, "Electromagnetic field and materials,"), 91–95, Moscow, Firsanovka, Nov. 11–16, 2008.
6. Ilinsky, A. S., V. V. Kravtsov, and A. G. Sveshnikov, *Matematicheskie Modeli Elektrodinamiki*, Vyshaya Shkola, Moscow, 1991.

A 30 GHz Bow-tie Slot Antenna Fed by a Microstrip to CPW Transition

Angel Colin

Instituto de Física de Cantabria (CSIC-UC)
Av. Los Castros s/n, Santander 39005, Spain

Abstract— A modified bow-tie slot antenna fed by a microstrip to coplanar waveguide (CPW) transition, is designed for wide band operation. The design is suitable to be included in arrays for applications in radar and wireless communications, providing a possibility to be utilized in experiments based on studies of the cosmic microwave background (CMB). Simulation results in this study show around 43% bandwidth with VSWR < 2 in the frequency range from 25 to 40 GHz.

1. INTRODUCTION

With the advent of the new communications technologies, it turns to be possible and desirable to design a single antenna that operates in several bands as large as possible for a same set up system. Planar antennas are required firstly because they can be easily fabricated in small sizes, with low profile, light weight, high efficiency, and low cost. Moreover, they are easily adaptable to operate at radio and microwave frequencies by means uniplanar transmission lines connected to active or passive elements. Bow-tie slot antennas provide good impedance match, bidirectional radiation patterns, wide bandwidth, and low radiation loss; hence, they are widely investigated for many applications [1–3]. Commonly these antennas are designed to be integrated in array systems, in which they could operate at a single or at different bands simultaneously.

In this study, we present the computed radiation characteristics for a single element of this type antenna, taking into account both the unidirectional and bidirectional cases. To achieve the first one, we introduced a representative and movable metallic reflector plane placed below the substrate. The coupling between two-element aligned in the x - y directions is also presented. All simulations were made under the environment of the HFSS-Ansoft software, which is based on the finite element method.

2. ANTENNA STRUCTURE

A single element antenna is designed to work on a thin alumina substrate of 0.254 mm thickness, with 3 μm electroplated gold, relative permittivity of 10, and loss tangent of 0.001. The geometry and parameters of the antenna are shown in Fig. 1(a), where $a = 0.05$, $b = 0.25$, $c = 8$, $d = 5$, $e = 2.38$, $f = 0.12$, $g = 5.525$, $h = 0.05$, $i = 0.125$, $j = 0.05$, and $k = 7.6$. All dimensions are in mm. Bottom ground plane only covers the microstrip line section (c dimension). The width of the microstrip line and gaps of the CPW were calculated and optimized to be approximately 50 Ohm. Fig. 1(b) shows the experimental set up. The antenna could be attached to the metal mount with silver conductive epoxy (Epo-Tek H20E). The mount represents a metallic structure made of brass material in which a 50 Ohm hermetic seals with a coaxial jack/plug connector (Southwest Microwave, Inc.) could be integrated on its backside. A removable reflector plane is placed below the substrate in order to vary vertically its height. The centred pin-hole permits the connection between the pin-connector and the microstrip. The mount is designed to be used in direct contact with metal surfaces, as well as with the cold plate of cryostats when a low temperature experiment is required.

3. SIMULATED RESULTS

For this study, the numerical analysis was computed at the frequency $f_0 = 30$ GHz and the reflector plane placed below the substrate at three different distances, $\lambda_0/4$, $\lambda_0/2$, and λ_0 respectively. In all cases, we used an excitation wave port of 50 Ohm. The computed return losses and VSWR for a single element antenna are shown in Fig. 2. According to these plots, the results show good agreement to each other and present two prominent resonant frequencies around 28 and 39 GHz respectively. The antenna provides $\sim 43\%$ bandwidth in the operation range from 25 to 40 GHz. We observed that a third resonant frequency appears at 34 GHz when we introduced the reflector plane at λ_0 , and then is shifted up to 31 GHz by varying the height to $\lambda_0/4$.

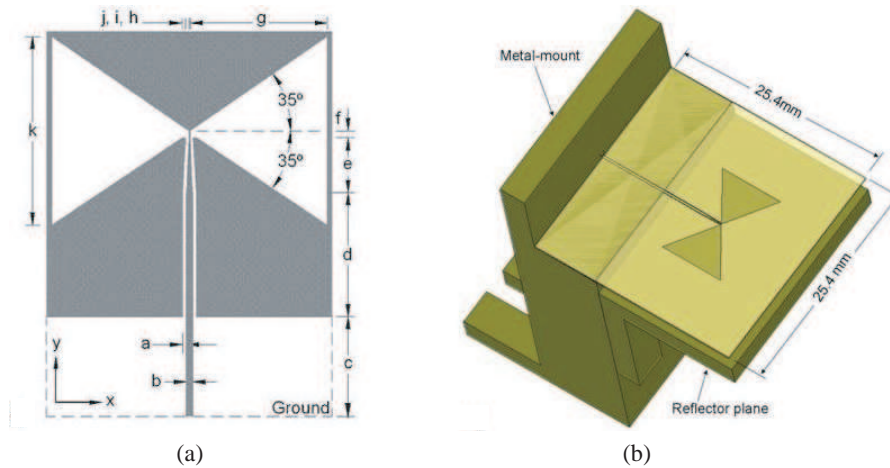


Figure 1: (a) Antenna geometry (not to scale) and parameters, (b) experimental set up (not to scale) with a removable reflector plane.

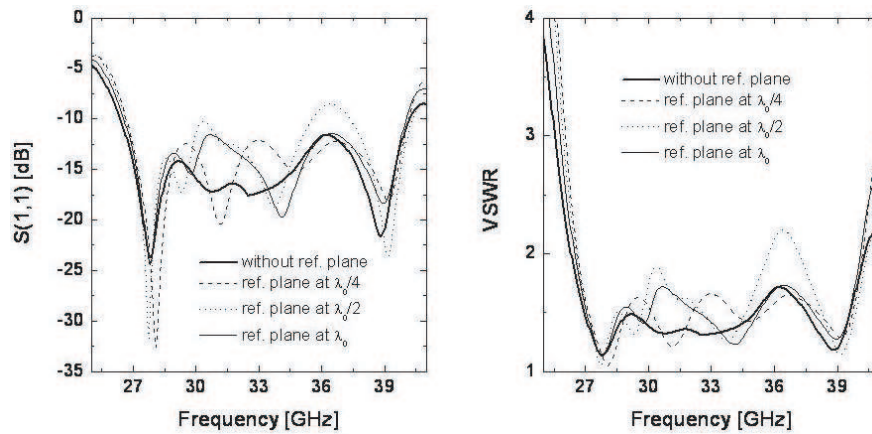


Figure 2: Simulated return losses and VSWR against frequency.

The gain radiation pattern in the x - z (H -Plane) and the y - z (E -Plane) is computed at 30 GHz and is shown in Fig. 3. The patterns are normalized to a maximum and minimum of 0 and -60 dB respectively, with 10 dB/div. The antenna presents an average of -10 dB of cross polarization level, and wide beamwidth of approximately 120° for the E - H planes. In wireless communications, one antenna can receive the signal from any direction with any polarization; hence this antenna could be utilized for this application. On the other hand, for the direct detection of specific electromagnetic signals, the antennas must be unidirectional and highly directive; to achieve this, the use of arrays can further improve the radiation patterns increasing the directivity and reducing the cross polarization levels as is shown in Fig. 3 (right), in which we simulated a configuration of 12 elements aligned in the x -direction separated to a distance of 16 mm since it is the optimal free-space distance due to the antenna's geometry. For this case, the side lobes decrease down to less than -20 dB in the main beamwidth of 60° , appearing two prominent side lobes around the main lobe. In most cases, the undesired side lobes can be eliminated using low-pass optical filters for the required frequency and hemispherical lenses to converge the entire signal to the receiving antenna, which in turn is connected and coupled to a detector, thus providing a possibility to be used in experiments based in the CMB detection.

The coupling between two elements was computed separately in two configurations of two-elements aligned in the x - y directions as are indicated in the insets of Fig. 4. In the first one, the elements are separated 16 mm. While in the second one, the antennas are separated vertically 10 mm and one element is flipped 180° around the x -axis in order to cancel the effects of the cross polarized fields [4]. In both cases, each element operates independently and is excited by means a wave port of 50 Ohm. The average coupling between the elements over the entire band is around -15 dB and -30 dB respectively. The lower coupling reveals a possibility for designs of large arrays

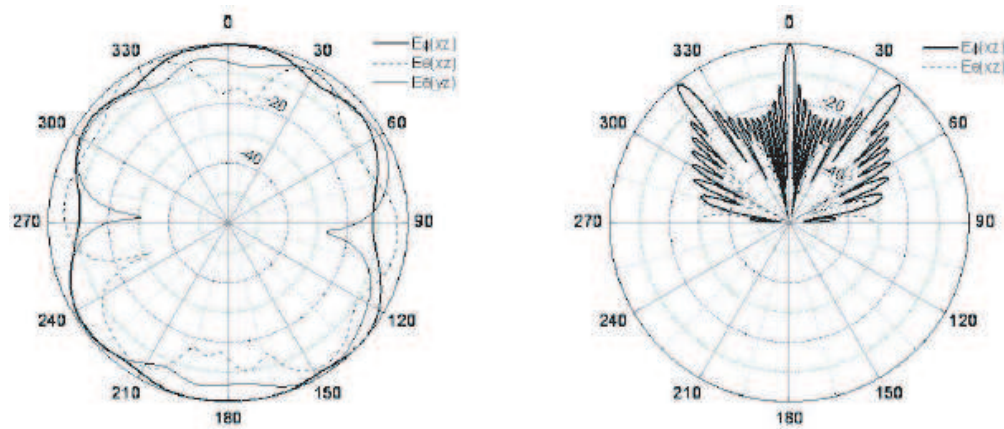


Figure 3: Simulated gain radiation patterns at 30 GHz for a single element (left), and for a 12 elements array aligned in the x -direction (right).

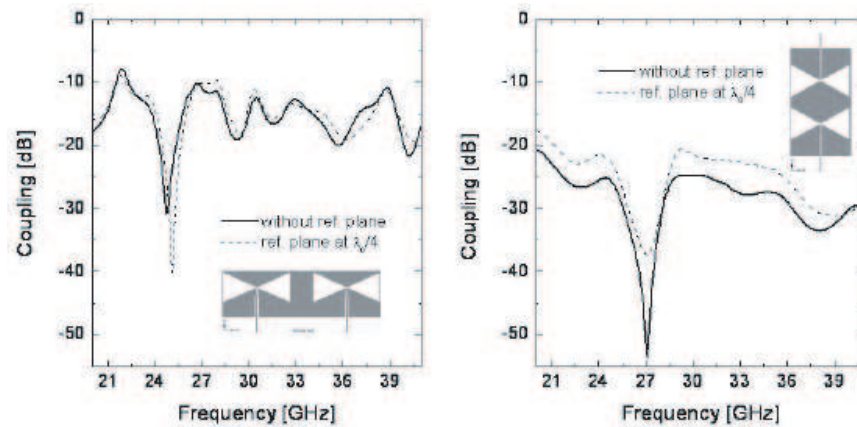


Figure 4: Computed coupling for two aligned elements.

to be applied in radar or phased-array systems.

4. CONCLUSION

Simulated results for a of bow-tie slot antenna have provided reliability and good expectation to be confirmed with the measurements of our prototypes.

REFERENCES

1. Angelopoulos, E. S., A. Z. Anastopoulos, and D. I. Kaklamani, "Ultra wide-band bow-tie slot antenna fed by a CPW-to-CPW transition loaded with inductively coupled slots," *Microwave Optical Technology Letter*, Vol. 48, No. 9, 1816–1820, 2006.
2. Marantis, L. and P. Brennan. "A CPW-fed bow-tie slot antenna with tuning stub," *IEEE Loughborough Antennas and Propagation Conference*, Loughborough, UK, March 2008.
3. Eldek, A., Z. Elsherbeni, and C. Smith, "Wideband slot bow-tie antennas for radar application," *IEEE Topical Conference on Wireless Communication Technology*, 0-7803-8197-1/03, 2003.
4. Eldek, A. A., A. Z. Elsherbeni, and C. E. Smith, "Rectangular slot antenna with patch stub for ultra wideband applications and phased array systems," *Progress In Electromagnetics Research*, PIER 53, 227–237, 2005.

Design of Gathered Elements for Reconfigurable-beam Reflectarrays Based on Patches Aperture-coupled to Delay Lines

E. Carrasco, M. Barba, and J. A. Encinar

Universidad Politécnica de Madrid

ETSI-Telecomunicación (B-403), Ciudad Universitaria S/N, Madrid 28040, Spain

Abstract— Reflectarrays based on patches aperture-coupled to delay lines are an attractive technological solution to achieve reconfigurable-beam antennas through the implementation of switches based on Micro-Electro-Mechanical Systems (MEMS). However, the high number of electronic devices and biasing lines required to control the phase-shift on large reflectarrays complicates the implementation of the control network and increases the manufacturing cost. The combination of two or more elements turning into a sub-array can reduce considerably the number of switches required to control the beam. In this contribution, a two-element sub-array is proposed allowing a very linear phase response with True-Time Delay (TTD).

1. INTRODUCTION

A printed reflectarray is defined by an array of metallizations printed on a surface which is illuminated by a feed, combining the main features of conventional reflectors and microstrip array antennas [1]. The elements of the reflectarray introduce certain phase change into the reflected field which produces a collimated or a shaped beam.

Reflectarray elements based on a patch coupled through an aperture to a delay line as that shown in Fig. 1(a) have demonstrated an important improvement in the bandwidth of large reflectarrays, by the introduction of TTD compensating the effects of the differential spatial phase delay [2]. This kind of elements have also been used for producing shaped-beams, as those required by Local Multipoint Distribution System (LMDS) base stations [3].

The use of aperture-coupled patches offers additional advantages over other configurations, specially for reconfigurable-beam applications. First, by printing the delay lines on a different layer than the radiating element, there is more room for the inclusion of control switches such as PIN diodes [4] or MEMS switches [5] attached to the delay line. An important advantage of this kind of element is the physical separation between the radiating section (patch and slotted ground plane) and the phase-shifter which includes the delay line, the MEMS and the biasing circuits, because the electronic devices are not directly exposed to the impinging RF.

However, for a large reflectarray with a reconfigurable beam, the cost and manufacturing complexity increases considerably because hundreds of control elements are required.

Combining two or more elements turning into a sub-array can reduce significantly the number of switches required to achieve the beam configuration. This gathering can be performed combining several radiating elements by a common delay line, in a similar way to the microstrip beam forming networks used to feed classical arrays. This gathering also increases the available area for obtaining TTD. Depending on the required phase distribution, gathering can produce a small distortion in the

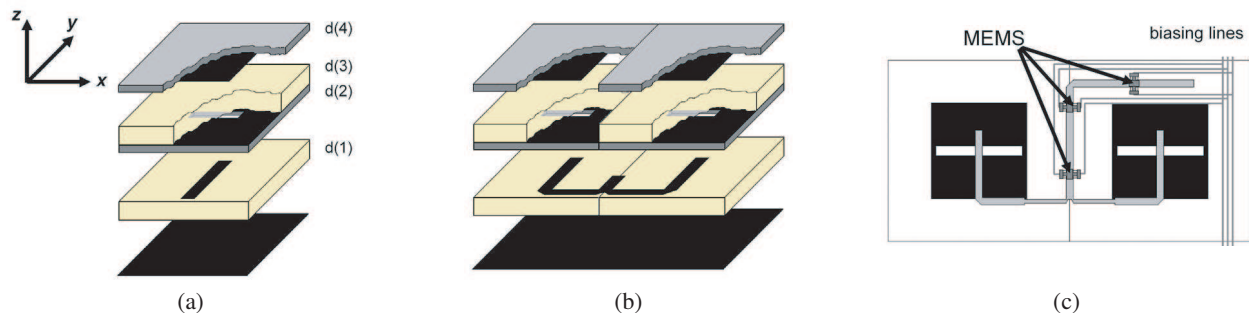


Figure 1: Gathered reflectarray element based on patches aperture-coupled to delay lines. (a) Expanded view of the individual element. (b) Expanded view of two element sub-array. (c) Top view of the two element sub-array showing the MEMS and biasing lines implementation in a series configuration.

radiation pattern when the phase of one element is replicated in the pair, but simplifies significantly the manufacturing and reduces the cost. The sub-array implementation in a reflectarray requires the careful definition of the required phase-shift in the reflectarray elements to obtain the desired beam without distortion or reduction in gain.

2. GATHERED ELEMENTS DESIGN

The proposed design consists of two reflectarray elements with vertical polarization whose delay lines are combined using a T-junction, similar to the microstrip beam forming networks used in classical arrays, with the aim of using a common delay line as is shown in Fig. 1(b). With this configuration, the control devices are shared by the two elements as is shown in Fig. 1(c). As the characteristic impedance of the delay line is $50\ \Omega$ ($w = 0.7\ \text{mm}$) and the common variable length line presents the same impedance, two $\lambda/4$ segments of $70\ \Omega$ ($w = 0.39\ \text{mm}$) have been used to match the lines (one for each element of the sub-array) taking into account the $100\ \Omega$ viewed in the junctions. By adjusting adequately the geometric parameters, a very linear phase curve, with low losses can be obtained. The period has been fixed to $18\ \text{mm}$, the patches are square with $9.5\ \text{mm}$ by side and the aperture dimensions are $8.6\ \text{mm} \times 1.0\ \text{mm}$. The dielectric features of the element are shown in Table 1.

Table 1: Dielectric substrates.

Layer	ϵ_r	$\tan\delta$	thickness (mm)
$d(4)$	3.380	0.0035	0.508
$d(3)$	1.067	0.0002	2.000
$d(2)$	3.380	0.0035	0.305
$d(1)$	1.000	0.0000	7.200

For the analysis of this sub-array two approaches have been considered and verified. The first approach consists of a full-wave simulation of the whole sub-array using CST Microwave Studio® [6]. By defining the boundary conditions, an infinite array has been analyzed for a normal incidence of the impinging wave. In this case, the two elements are analyzed together loading the sub-array with two ports as is shown in Fig. 2(a). The first port corresponds to a planar wave which impinges on the top of the sub-array (although an air box is necessary on the top of the sub-array, the phase reference is the top surface of the dielectric d_4 , defined in the Fig. 1(a)). The second port is set at the microstrip delay line, at $1.63\ \text{mm}$ from the T-junction. With this full-wave computation, the S matrix which characterizes the whole sub-array is obtained. The reflection coefficient of the gathered reflectarray element is computed by loading the port 1 with the intrinsic impedance of the vacuum and the port 2 with an open-ended microstrip line taking into account losses. The length of this line is varied to obtain a phase-delay. In a reconfigurable-beam reflectarray, this variation can be implemented by the introduction of MEMS along the line for a series configuration. This approach called full-wave is summarized in Fig. 2(b).

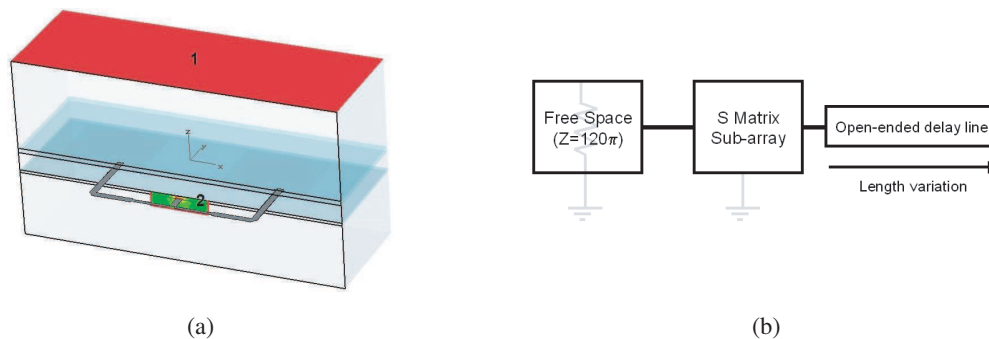


Figure 2: Full-wave approach of the complete sub-array (a) Geometry and ports definition with CST for the whole two-element sub-array. (b) Schematic of the approach.

The second approach to analyse this sub-array consists of computing, by the same full-wave tool, the S matrix which characterizes the individual element according with the ports defined in

Fig. 3(a). For the sub-array, both individual elements are equally oriented and have the same dimensions. Therefore, the S matrix can be duplicated and linked through each port 2 by a circuitual approach which characterizes the line network (T junction, bents and line segments). The port 1 of each individual S matrix is loaded in parallel with the intrinsic impedance of vacuum. The schematic of this connection is shown in Fig. 3(b), where the circuitual approach is performed using ADS software [7].

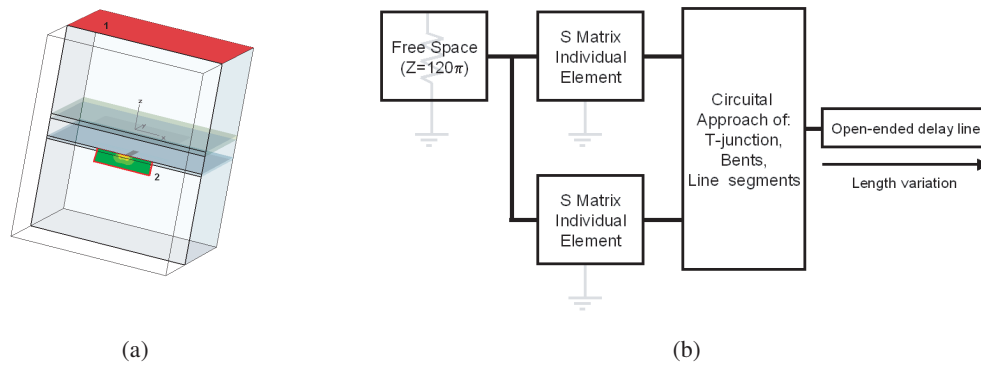


Figure 3: Combined technique dividing the sub-array in two elements joined with a circuitual approach. (a) Geometry and ports definition with CST for the individual element. (b) Schematic of the combined technique.

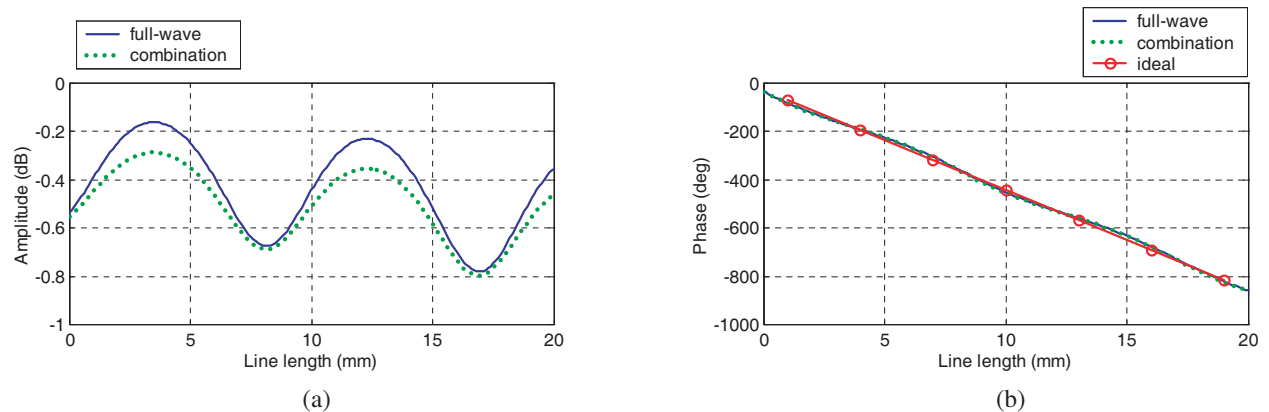


Figure 4: Reflection coefficient for the two-element sub-array obtained by the two described techniques. (a) Amplitude. (b) Phase compared with the ideal phase-shifter.

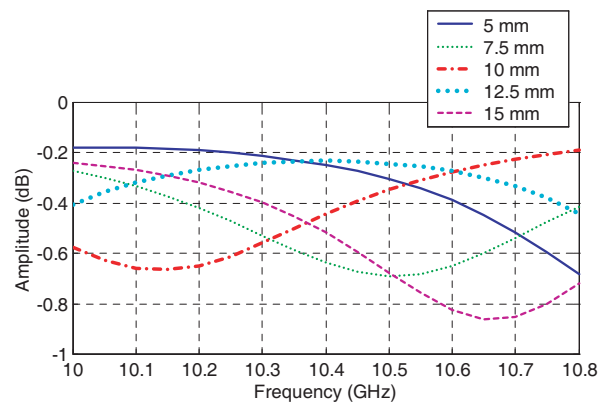


Figure 5: Reflection losses as a function of the frequency for different lengths of the delay line.

3. RESULTS

The reflection coefficient for the two-element sub-array has been computed at 10.40 GHz varying the length of the line and using the two previously described approaches. The amplitude and phase are shown in Fig. 4. The amplitude differences between each approach are better than 0.1 dB. The phase curves are practically the same for both methods and are compared with the ideal phase-shifter, where the phase is equal to $-2\beta L$, β is the propagation constant of the microstrip line, at the corresponding frequency, and L is the length of the delay line.

Finally, Fig. 5 shows the losses of the gathered reflectarray element as a function of the frequency for different states or lengths of the delay line.

4. CONCLUSIONS

The grouping of reflectarray elements based on patches aperture-coupled to delay lines has been presented as an interesting solution to reduce both: the number of electronic devices and the number of biasing lines in a large reflectarray with reconfigurable-beam. From the two-element sub-array it is clear that the required MEMS to control the phase states are reduced to a half. The design technique can be applied easily to more complex configurations, with more elements.

ACKNOWLEDGMENT

This work has been partially supported by the Spanish Ministry of Science and Innovation under project CICYT TEC 2007-63650 and by the Seventh Framework Program of the European Union under the ARASCOM Project.

REFERENCES

1. Huang, J. and J. A. Encinar, *Reflectarray Antennas*, Wiley-Interscience, New Jersey, 2008.
2. Carrasco, E., J. A. Encinar, and M. Barba, "Bandwidth improvement in large reflectarrays by using true-time delay," *IEEE Trans. on Antennas and Propagat.*, Vol. 56, No. 8, 2496–2503, 2008.
3. Carrasco, E., M. Arrebola, J. A. Encinar, and M. Barba, "Demonstration of a shaped beam reflectarray using aperture-coupled delay lines for LMDS central station antenna," *IEEE Trans. on Antennas and Propagat.*, Vol. 56, No. 10, 3103–3111, 2008.
4. Barba, M., E. Carrasco, J. E. Page, and J. A. Encinar, "Electronic controllable reflectarray elements in X band," *Journal of RF-Engineering and Telecommunications*, No. 9–10, 203–206, Frequenz, September/October 2007.
5. Mencagli, B., R. Vincenti, L. Marcaccioli, and R. Sorrentino, "Design of large mm-wave beam-scanning reflectarrays," *35th Europ. Microwave Conf.*, Paris, France, October 2005.
6. CST Microwave Studio®, www.cst.com.
7. Advanced Design System, www.agilent.com.

A Novel Design of Ultrawide-band Antenna

D. Bouchouicha¹, M. Latrach², F. Dupont¹,
A. Bremond¹, and L. Ventura³

¹STMicroelectronics, Rue Pierre et Marie Curie, BP 7155, Tours 37071, France

²Groupe RF & Hyperfréquences, ESEO

4 Rue Merlet de la Boulaye, BP 30926, Angers 49009, France

³Laboratoire de Microélectronique de Puissance

16 Rue Pierre et Marie Curie, Tours 37071, France

Abstract— A new design of Ultra Wide-Band circular slots antenna fed by Co-Planar Waveguide (CPW) is presented in this paper.

Antenna impedance and bandwidth are studied as function of the radius and the centers positions of two circular slots. Consequently, the broadband operation is achieved by adjusting, a shape of the ended CPW-fed. The obtained impedance bandwidth, assuming a limit of -10 dB return loss, is from 2.3 GHz to 20 GHz (about 159% fractional bandwidth). The peak gain increases from 4 dBi to 8 dBi according to the use frequency.

The proposed antenna is characterized by the simplicity in design and feeding, a very low cost and by a relatively stable radiation pattern over larger part of the bandwidth.

1. INTRODUCTION

In recent years, the demands for UWB technology has rapidly progressed in the wireless communication domains. The need for a very high speed and a multipurpose system of wireless communication imposes inevitably the use of antennas covering a wideband frequency.

Currently on mobile phone, for example, people may call; connect to the Internet, send video, watching television (TV)... Also with the development of digital terrestrial TV, new services are offered to subscribers. They include in particular an opportunity to view a broadcast TV on mobile multimedia receiver. This type of application can be effective in urban areas unless one is able to receive signals from the same issuer whose characteristics of polarization, amplitude and phase consecutively with different thoughts on sustained multiple trips. The reception of these signals allows digital processing to optimize the signal to noise ratio and hence the overall quality of the reception. To access to this reception quality, it is therefore necessary to determine broadband antenna sizes (integration in a laptop system). Several structures antennas have been designed to meet this demand, and different techniques of miniaturization and expanding bandwidth have been developed [2, 3].

In this paper, a new UWB CPW-fed slot antenna is proposed and a 159% fractional impedance bandwidth is achieved. Both numerical and experimental results show that the new design allows an improved antenna performance and offers a potential benefits in various UWB applications.

2. ANTENNA DESIGNING

The proposed antenna is composed of two non-concentric circular slots and feeding by a Co-Planar Waveguide (CPW) line as shown in Figure 1. Slots and CPW-fed are etched on the same layer on a surface of $70 \times 75 \text{ mm}^2$ by 1.6 mm thick on FR4 substrate with relative permittivity 4.4. r_1 and r_3 represent respectively the radius of the slots and d_1 represent the distance between the centers of the slots. The CPW-fed is a 50Ω line where the width $W = 1.88 \text{ mm}$ and the gap $s = 0.21$.

Simulations were made with HFSS simulator by varying the parameters of the antenna (r_1 , r_2 , r_3 , d_1) (see Figure 2). After optimization of theses parameters, we get a good matching between the antenna and CPW, for the following values: $r_1 = 23 \text{ mm}$, $r_2 = 10 \text{ mm}$, $r_3 = 6 \text{ mm}$, and $d_1 = 12.77 \text{ mm}$. These values give a very wide frequency bandwidth.

3. ANTENNA PERFORMANCES

The production of prototypes (Figure 3) was made both by chemical and mechanical etching. The measurements of the return loss up to 20 GHz have shown good agreement with the simulation results (Figure 4).

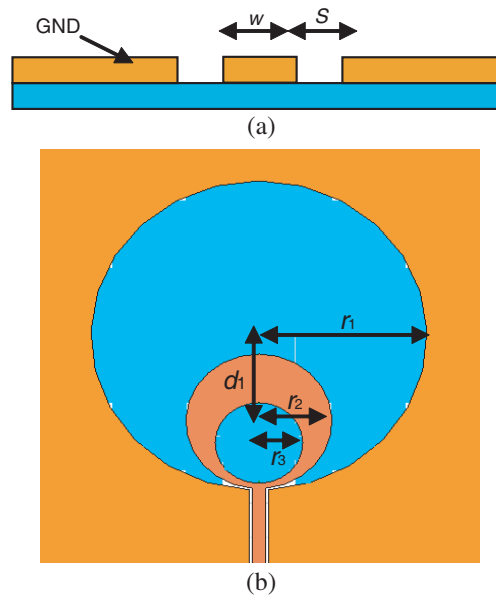


Figure 1: (a) Feed line (CPW), (b) antenna geometry.

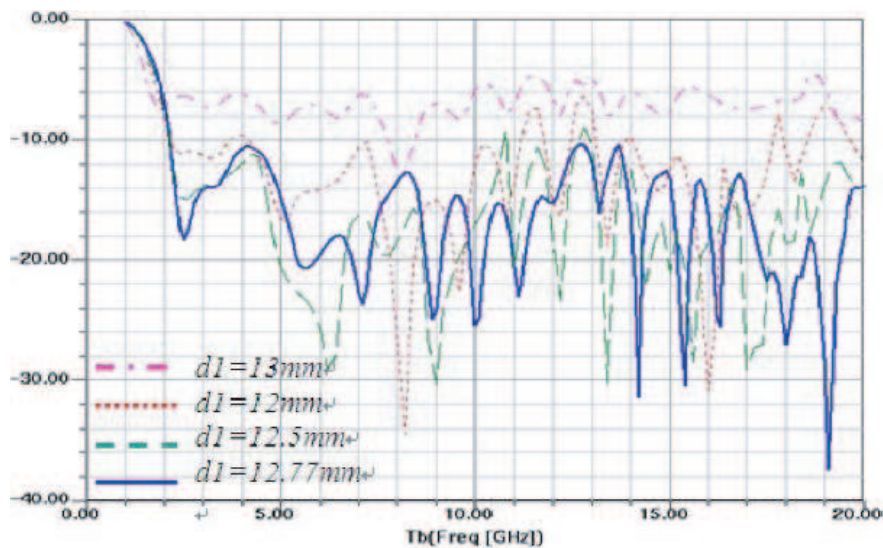


Figure 2: Antenna return loss.

In Figure 4, measured and simulated return losses are presented. We have simulated the antenna up to 25 GHz with HFSS and ADS simulators. We note that for high frequency, greater than 22 GHz, the results of HFSS and ADS are slightly different. This difference is due to the method of calculation used in the two softwares: MOM for ADS and MFE FOR HFSS.

As calculation method determines the mesh frequency and the number of cells per wavelength, difference between simulators results can be explain by this way. We have currently made S parameters measurement up to 20 GHz with our lab equipment. We plan to make additional measurement higher in frequency, in order to compare with the simulation done between 20 & 25 GHz.

This structure allows to have a design more compact than [2–4] and with larger bandwidth than [5, 6].

The results of antenna simulations with the optimum dimensions show that the peak gain of the antenna increases as a function of frequency from 1 GHz to 7.5 GHz. For high frequency (> 7.5 GHz) the gain have a fluctuation around 8 dBi. The gain is more than 4 dBi in the frequency range [2.3 GHz, 25 GHz] (Figure 5).

In Figure 6, we represent the distribution of the energy radiated in the space. This distri-



Figure 3: The photograph of the prototype antenna.

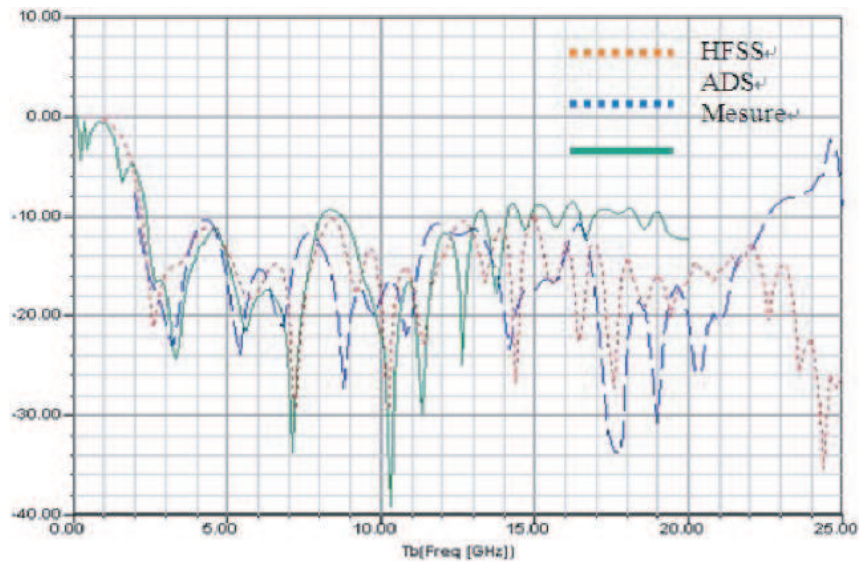


Figure 4: Antenna return loss.

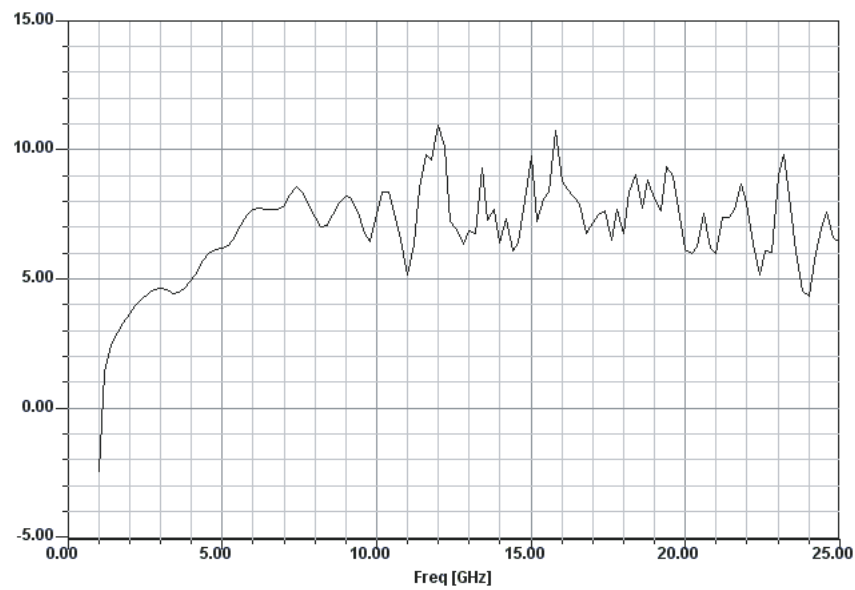


Figure 5: Maximum gain.

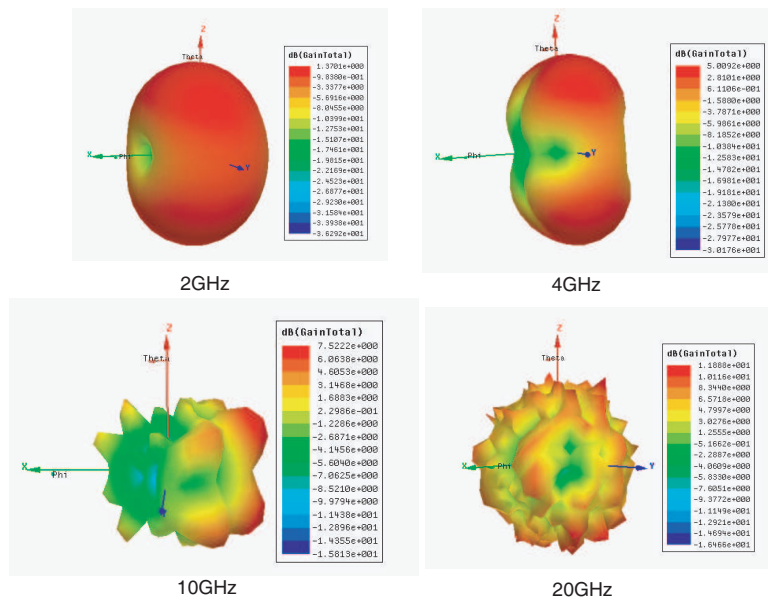


Figure 6: Antenna radiation.

tribution varies with a frequency. We have a quasi-unidirectional radiation for the low frequency [2 GHz, 4 GHz].

In the band [10 GHz–20 GHz], we have a radiation pattern with several lobes. We note that the number of lobes increases as a function of frequency.

This increased number of lobes is due to the stationary wave phenomenon. The stationary wave is produced in the slots. The number of the maximum and the minimum increase when the frequency increase. Because the wavelength is inversely proportional to the frequency and it becomes very small relatively to the slots dimensions in higher frequencies (Figure 7). The distribution of surface current represented in Figure 8 shows that the number of maximum increases.

In Figure 9, the radiation patterns of the E-field were presented at 2, 4, 10, and 20 GHz in the E -plane ($x-z$ plane) and H -plane ($y-z$ plane).

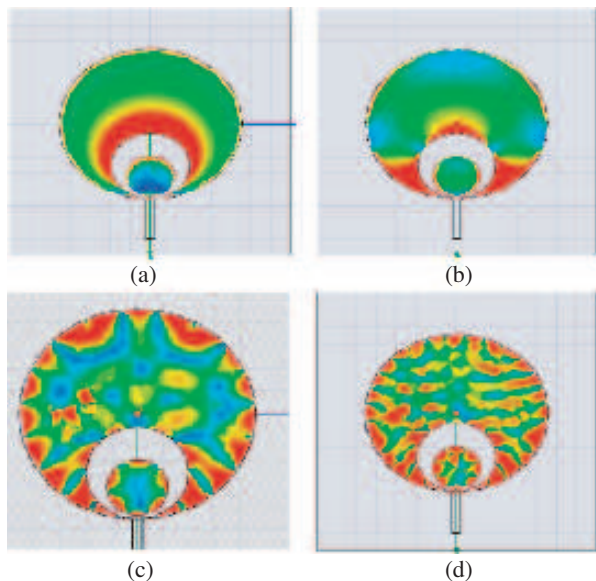


Figure 7: Intensity of the E field in the slots at (a) 2 GHz, (b) 4 GHz, (c) 10 GHz, and (d) 20 GHz.

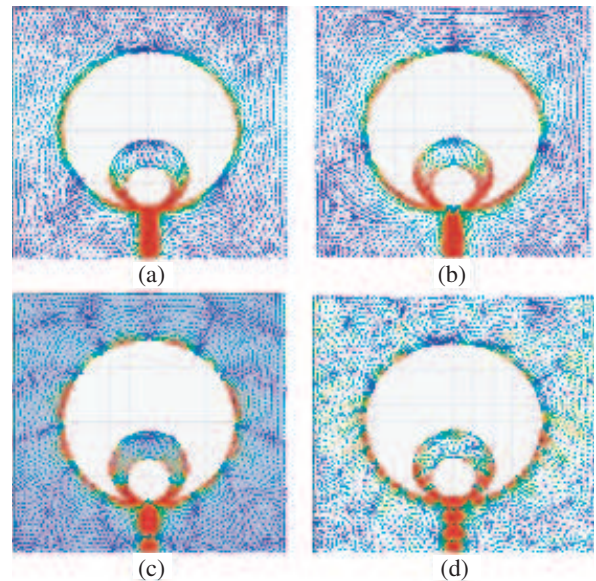


Figure 8: Surface current distribution: (a) 2 GHz, (b) 4 GHz, (c) 10 GHz, (d) 20 GHz.

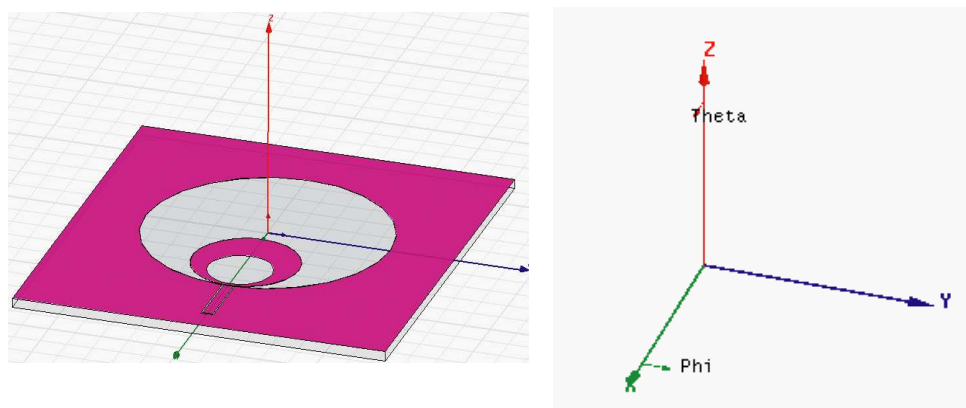
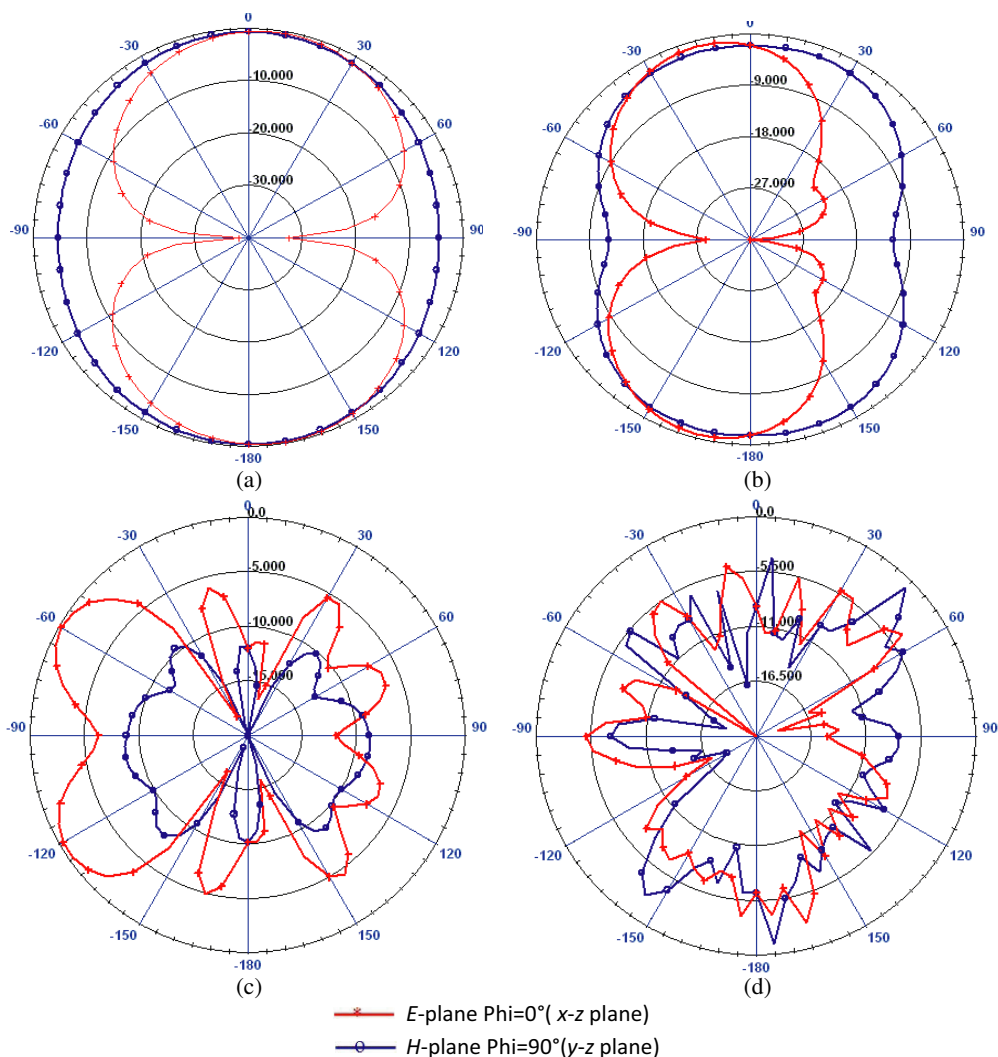


Figure 9: Radiation pattern: (a) 2 GHz, (b) 4 GHz, (c) 10 GHz, (d) 20 GHz.

4. CONCLUSION AND FUTURE WORK

New printed CPW-fed antenna for ultra wideband applications is proposed. The return losses measurement has been made up to 20 GHz and show a good correlation with the simulation

Higher frequencies characterization has been planned, because according to the simulations with HFSS simulator we have a return loss lower than -10 dB in the 20 to 25 GHz band.

We can explain the slight difference observed between the simulations results and measurements by the uses of SMA connectors and FR4 substrate which reach its frequency limits.

The results of the radiation pattern obtained with HFSS simulator shows the existence of many forms for different frequencies with a peak gain is more than 4 dBi.

REFERENCES

1. Le Bolzer, F. and A. Louzir, “Une nouvelle topologie d’antenne large bande pour WLAN a base de fentes annulaires,” *12èmes Journées Nationales Microondes*, 16-17-18 Mai, Poitiers, 2001.
2. Liu, Y. F., K. L. Lau, Q. Xue, and C. H. Chan, “Experimental studies of printed wide-slot antenna for wide-band applications,” *IEEE Antennas and Wireless Propagation Letters*, Vol. 3, 2004.
3. Chair, R., A. A. Kishk, and K. F. Lee, “Ultra wide-band coplanar waveguide-fed rectangular slot antenna,” *IEEE Antennas and Wireless Propagation Letters*, Vol. 3, 2004.
4. Sadat, S., M. Fardis, F. Geran, G. Dadashzadeh, N. Hojjat, and M. Roshandel, “A compact microstrip square-ring slot antenna for UWB applications,” *IEEE Antennas and Propagation Society International Symposium*, 4629–4632, 2006.
5. Li, P., J. Liang, and X. Chen, “Ultra-wideband printed elliptical slot antenna,” *IEEE Antennas and Propagation Society International Symposium*, Vol. 3A, 508–511, Jul. 3–8, 2005.
6. Li, P., J. Liang, and X. Chen, “CPW-fed printed elliptical slot antenna with fork-like tuning stub,” *European Microwave Conference*, Vol. 1, 4, Oct. 4–6, 2005.

Influence of Field Potential on the Speed of Light

Zi-Hua Weng

School of Physics and Mechanical & Electrical Engineering, Xiamen University
Xiamen 361005, China

Abstract— The paper discusses the affection of the scalar potential on the speed of light in the electromagnetic field, by means of the characteristics of octonion. In the octonion space, the radius vector is combined with the integral of field potentials to become one new radius vector. When the field potentials can not be neglected, the new radius vector will cause the prediction to departure slightly from the theoretical value of the speed of light. The results explain why the speed of light varies in diversiform optical waveguide. And there exist negative refractive indexes due to different scalar potentials in the gravitational field and electromagnetic field.

1. INTRODUCTION

The invariable speed of light is being doubted all the time. And this question remains as puzzling as ever. But the existing theories do not clarify why the speed of light has to keep unchanged, and then do not offer reasonable explain for this empirical fact. The paper attempts to reason out why the speed of light keeps the same in most cases, even in the electromagnetic field.

The invariable speed of light has not been validated in strong electromagnetic field, although the speed of light is variable in optical waveguide materials. Some experiments for the variable speed of light have been performed by L. V. Hau [1], M. L. Povinelli [2], and J. W. Moffat [3], etc. But all of these verifications are not dealt with the electromagnetic field potential, and have been validated in neither strong electromagnetic field nor gravitational field. So this puzzle of invariable speed of light remains unclear and has not satisfied results.

The algebra of quaternions [4] was first used by J. C. Maxwell to describe the electromagnetic field. The octonions [5] can be used to demonstrate the electromagnetic field and gravitational field simultaneously [6]. In the octonion space, the speed of light will be varied with the electromagnetic field potential as well as gravitational field potential. And there exist negative refractive indexes in optical waveguide materials, when the electromagnetic field potential is switched from positive to negative. This inference is coincided with that in the negative index materials [7].

2. OCTONION TRANSFORMATION

In the octonion space, the basis vector \mathbb{E} consists of the quaternion basis vectors \mathbb{E}_g and \mathbb{E}_e . The basis vector $\mathbb{E}_g = (1, \mathbf{i}_1, \mathbf{i}_2, \mathbf{i}_3)$ is the basis vector of the quaternion space for the gravitational field, and $\mathbb{E}_e = (\mathbf{I}_0, \mathbf{I}_1, \mathbf{I}_2, \mathbf{I}_3)$ for the electromagnetic field. And that the basis vector \mathbb{E}_e is independent of the \mathbb{E}_g , with $\mathbb{E}_e = \mathbb{E}_g \circ \mathbf{I}_0$.

$$\mathbb{E} = (1, \mathbf{i}_1, \mathbf{i}_2, \mathbf{i}_3, \mathbf{I}_0, \mathbf{I}_1, \mathbf{I}_2, \mathbf{I}_3)$$

The octonion physical quantity $\mathbb{D}(d_0, d_1, d_2, d_3, D_0, D_1, D_2, D_3)$ is defined as follows.

$$\mathbb{D} = d_0 + \Sigma(d_j \mathbf{i}_j) + \Sigma(D_i \mathbf{I}_i) \quad (1)$$

where, d_i and D_i are all real; $i = 0, 1, 2, 3$; $j, k = 1, 2, 3$.

When the octonion coordinate system is transformed into the other, the physical quantity \mathbb{D} will be transformed into the octonion $\mathbb{D}'(d'_0, d'_1, d'_2, d'_3, D'_0, D'_1, D'_2, D'_3)$.

$$\mathbb{D}' = \mathbb{K}^* \circ \mathbb{D} \circ \mathbb{K} \quad (2)$$

where, \mathbb{K} is the octonion, and $\mathbb{K}^* \circ \mathbb{K} = 1$; $*$ denotes the conjugate of octonion; \circ is the octonion multiplication.

When the spatial coordinates $d_1, d_2, d_3, D_0, D_1, D_2, D_3$ take part in the rotation, the octonion \mathbb{D} satisfies the following relation.

$$d_0 = d'_0 \quad (3)$$

In the above equation, the scalar part d_0 is preserved during the octonion spatial coordinates are transforming. Some invariants of electromagnetic field will be obtained from the characteristics of the octonion physical quantity.

Table 1: The octonion multiplication table.

	1	$\dot{\mathbf{i}}_1$	$\dot{\mathbf{i}}_2$	$\dot{\mathbf{i}}_3$	\mathbf{I}_0	\mathbf{I}_1	\mathbf{I}_2	\mathbf{I}_3
1	1	$\dot{\mathbf{i}}_1$	$\dot{\mathbf{i}}_2$	$\dot{\mathbf{i}}_3$	\mathbf{I}_0	\mathbf{I}_1	\mathbf{I}_2	\mathbf{I}_3
$\dot{\mathbf{i}}_1$	$\dot{\mathbf{i}}_1$	-1	$\dot{\mathbf{i}}_3$	$-\dot{\mathbf{i}}_2$	\mathbf{I}_1	$-\mathbf{I}_0$	$-\mathbf{I}_3$	\mathbf{I}_2
$\dot{\mathbf{i}}_2$	$\dot{\mathbf{i}}_2$	$-\dot{\mathbf{i}}_3$	-1	$\dot{\mathbf{i}}_1$	\mathbf{I}_2	\mathbf{I}_3	$-\mathbf{I}_0$	$-\mathbf{I}_1$
$\dot{\mathbf{i}}_3$	$\dot{\mathbf{i}}_3$	$\dot{\mathbf{i}}_2$	$-\dot{\mathbf{i}}_1$	-1	\mathbf{I}_3	$-\mathbf{I}_2$	\mathbf{I}_1	$-\mathbf{I}_0$
\mathbf{I}_0	\mathbf{I}_0	$-\mathbf{I}_1$	$-\mathbf{I}_2$	$-\mathbf{I}_3$	-1	$\dot{\mathbf{i}}_1$	$\dot{\mathbf{i}}_2$	$\dot{\mathbf{i}}_3$
\mathbf{I}_1	\mathbf{I}_1	\mathbf{I}_0	$-\mathbf{I}_3$	\mathbf{I}_2	$-\dot{\mathbf{i}}_1$	-1	$-\dot{\mathbf{i}}_3$	$\dot{\mathbf{i}}_2$
\mathbf{I}_2	\mathbf{I}_2	\mathbf{I}_3	\mathbf{I}_0	$-\mathbf{I}_1$	$-\dot{\mathbf{i}}_2$	$\dot{\mathbf{i}}_3$	-1	$-\dot{\mathbf{i}}_1$
\mathbf{I}_3	\mathbf{I}_3	$-\mathbf{I}_2$	\mathbf{I}_1	\mathbf{I}_0	$-\dot{\mathbf{i}}_3$	$-\dot{\mathbf{i}}_2$	$\dot{\mathbf{i}}_1$	-1

3. SPEED OF GRAVITATIONAL INTERMEDIATE BOSON

In the case for coexistence of the electromagnetic field and the gravitational field, the algebra of octonions can be used to describe the property of electromagnetic field and gravitational field.

According to the viewpoint of field theories, each fundamental interaction is mediated by the exchange of its intermediate bosons between particles. The gravitational interaction is mediated by the exchange of gravitational intermediate bosons between masses. Meanwhile the electromagnetic interaction is mediated by the exchange of electromagnetic intermediate bosons between charges. And that the gravitational intermediate boson and the electromagnetic intermediate boson can be combined together to become the photon. The latter can be interacted with either gravitational field or electromagnetic field.

With the feature of octonions, we find that the gravitational field potential has an influence on the speed of gravitational intermediate boson in the gravitational field. It means that the speed of gravitational intermediate boson is variable in the case for coexistence of the electromagnetic field and gravitational field, under the octonion coordinate transformation.

3.1. Radius Vector

In the octonion space for gravitational field and electromagnetic field, the octonion radius vector $\mathbb{R} = \Sigma(r_i \dot{\mathbf{i}}_i) + \Sigma(R_i \mathbf{I}_i)$. And that it can be combined with the octonion $\mathbb{X} = \Sigma(x_i \dot{\mathbf{i}}_i) + \Sigma(X_i \mathbf{I}_i)$ to become one new radius vector $\bar{\mathbb{R}} = \Sigma(\bar{r}_i \dot{\mathbf{i}}_i) + \Sigma(\bar{R}_i \mathbf{I}_i)$. The \mathbb{X} is the integral of field potentials.

$$\bar{\mathbb{R}} = \mathbb{R} + k_{rx} \mathbb{X} \quad (4)$$

where, $\dot{\mathbf{i}}_0 = 1$; $\bar{r}_i = r_i + k_{rx} x_i$; $\bar{R}_i = R_i + k_{eg} k_{rx} X_i$; $r_0 = v_0 t$; $R_0 = V_0 T$; $k_{rx} = 1$. t denotes the time, T is a time-like quantity. v_0 is the speed of gravitational intermediate boson; V_0 is the speed of electromagnetic intermediate boson. μ_e and μ_g are the coefficients for the electromagnetic field and gravitational field respectively. k_{eg} is a coefficient, and $k_{eg}^2 = \mu_e / \mu_g$.

In other words, the $\bar{\mathbb{R}}$ can be considered as the radius vector in the octonion space, with the basis vector $(1, \dot{\mathbf{i}}_1, \dot{\mathbf{i}}_2, \dot{\mathbf{i}}_3, \mathbf{I}_0, \mathbf{I}_1, \mathbf{I}_2, \mathbf{I}_3)$. When the octonion coordinate system is rotated, we obtain the radius vector $\bar{\mathbb{R}}'(\bar{r}'_0, \bar{r}'_1, \bar{r}'_2, \bar{r}'_3, \bar{R}'_0, \bar{R}'_1, \bar{R}'_2, \bar{R}'_3)$. From Eqs. (3) and (4), we have

$$\bar{r}_0 = \bar{r}'_0. \quad (5)$$

The above states that the scalar \bar{r}_0 remains unchanged when the coordinate system rotates in the octonion space. And that there may exist the special case of the $x_i \neq 0$ when $r_i = R_i = 0$.

3.2. Velocity

The velocity $\mathbb{V} = \Sigma(v_i \dot{\mathbf{i}}_i) + \Sigma(V_i \mathbf{I}_i)$ and the field potential $\mathbb{A} = \Sigma(a_i \dot{\mathbf{i}}_i) + k_{eg} \Sigma(A_i \mathbf{I}_i)$ can be combined together to become one new velocity $\bar{\mathbb{V}} = \Sigma(\bar{v}_i \dot{\mathbf{i}}_i) + \Sigma(\bar{V}_i \mathbf{I}_i)$ in the octonion space.

$$\bar{\mathbb{V}} = \mathbb{V} + k_{rx} \mathbb{A} \quad (6)$$

where, $\bar{v}_i = v_i + k_{rx} a_i$; $\bar{V}_i = V_i + k_{eg} k_{rx} A_i$; a_0 and A_0 are the gravitational scalar potential and electromagnetic scalar potential respectively.

In the above, the field potential \mathbb{A} consists of the gravitational field potential $\mathbb{A}_g = \Sigma(a_i \dot{\mathbf{i}}_i)$, and the electromagnetic field potential $\mathbb{A}_e = \Sigma(A_i \mathbf{I}_i)$.

$$\mathbb{A} = \mathbb{A}_g + k_{eg} \mathbb{A}_e \quad (7)$$

When the coordinate system is rotated, we have one velocity $\bar{\nabla}'(\bar{v}'_0, \bar{v}'_1, \bar{v}'_2, \bar{v}'_3, \bar{V}'_0, \bar{V}'_1, \bar{V}'_2, \bar{V}'_3)$. From Eqs. (3) and (6), we have the invariant about the speed of gravitational intermediate boson in the octonion space.

$$\bar{v}_0 = \bar{v}'_0 \quad (8)$$

The above means that the speed of gravitational intermediate boson, v_0 , will be variable, due to the existence of the scalar potential, a_0 , of the gravitational field. Obviously, it is not associated with the field potential of electromagnetic field.

4. SPEED OF ELECTROMAGNETIC INTERMEDIATE BOSON

In the octonion space for the electromagnetic field and gravitational field, with the property of the algebra of octonions, we find that the electromagnetic field potential has an effect on the speed of electromagnetic intermediate boson in the electromagnetic field. It states that the speed of electromagnetic intermediate boson is variable in the case for coexistence of the electromagnetic field and gravitational field, under the octonion coordinate transformation.

4.1. Radius Vector

In the octonion space, one new octonion quantity $\bar{\mathbb{R}}_q = \bar{\mathbb{R}} \circ \mathbf{I}_0^*$ can be defined from Eq. (4).

$$\bar{\mathbb{R}}_q = \Sigma(\bar{R}_i \mathbf{i}_i) - \Sigma(\bar{r}_i \mathbf{I}_i) \quad (9)$$

When the coordinate system is rotated, we have the radius vector $\bar{\mathbb{R}}'_q(\bar{R}'_0, \bar{R}'_1, \bar{R}'_2, \bar{R}'_3, \bar{r}'_0, \bar{r}'_1, \bar{r}'_2, \bar{r}'_3)$. From Eqs. (3) and (9), we have

$$\bar{R}_0 = \bar{R}'_0 \quad (10)$$

The above states that the scalar \bar{R}_0 remains unchanged when the coordinate system rotates in the octonion space. And it is easy to find Eq. (5) and Eq. (10) can not be established simultaneously.

4.2. Velocity

In the octonion space, one new octonion quantity $\bar{\nabla}_q = \bar{\nabla} \circ \mathbf{I}_0^*$ can be defined from Eq. (6).

$$\bar{\nabla}_q = \Sigma(\bar{V}_i \mathbf{i}_i) - \Sigma(\bar{v}_i \mathbf{I}_i) \quad (11)$$

When the coordinate system is rotated, we have the velocity $\bar{\nabla}'(\bar{V}'_0, \bar{V}'_1, \bar{V}'_2, \bar{V}'_3, \bar{v}'_0, \bar{v}'_1, \bar{v}'_2, \bar{v}'_3)$. From Eqs. (3) and (11), we have the invariant about the speed of electromagnetic intermediate boson in the octonion space.

$$\bar{V}_0 = \bar{V}'_0 \quad (12)$$

The above means that the speed of electromagnetic intermediate boson, V_0 , will be variable, due to the existence of the scalar potential, A_0 , of the electromagnetic field. Correspondingly, it is not dealt with the field potential of gravitational field. And Eq. (8) and Eq. (12) can not be established simultaneously also.

5. SPEED OF LIGHT

In some cases, the electric charge is combined with the mass to become the electron or proton etc., therefore we have the condition $\bar{R}_i \mathbf{I}_i = \bar{r}_i \mathbf{i}_i \circ \mathbf{I}_0$ and $\bar{V}_i \mathbf{I}_i = \bar{v}_i \mathbf{i}_i \circ \mathbf{I}_0$. It means that the gravitational field as well as the electromagnetic field has an influence on the movement of the electric charge with the mass. In other words, those electric charges with the masses take part in either gravitational interaction or electromagnetic interaction.

Similarly, the gravitational intermediate boson and the electromagnetic intermediate boson can be combined together to become the photon. While, these photons participate not only gravitational interaction but also electromagnetic interaction. As a result, the gravitational field potential and electromagnetic field potential both can impact the speed of light from Eqs. (8) and (12).

In the gravitational theory, the gravitational field potential has an effect on the speed of light. The inference is similar to the shift of spectral-line in Einstein's general relativity. In Maxwell's electromagnetic theory, the electromagnetic field potential has an influence on the speed of light in the glass etc. Therefore the concept of refractivity has to be introduced into the optics theory.

According to the viewpoint about the affection of field potentials on the speed of light, there may exist the negative refractive index due to different field potential. The conclusion may explain why there exist negative index materials or left-handed materials in a different way.

6. CONCLUSION

In the octonion space, the inferences about speed of light depend on the combinations of physical definitions. By means of definition combination of radius vector and velocity, the gravitational field potential as well as electromagnetic field potential are found to have the influence on the speed of light, in the case for coexistence of the gravitational field and electromagnetic field.

The speed of light changes with the gravitational field potential as well as electromagnetic field potential, and has a deviation from its theoretical value. The light speed variation has a limited effect on the movement of light, because the variation is quite small. Therefore the invariable speed of light is believed to be correct in most cases. However, when there is a very high potential of electromagnetic field, the light speed variation will become huge enough to impact the refractive index of materials obviously. There exist negative refractive indexes in optical waveguide materials, when the electromagnetic field potential is switched from positive to negative, or otherwise. This result is coincided with that in the negative index materials.

It should be noted that the study for influence of field potentials on the speed of light examined only one simple case with very weak field potentials in the gravitational field and electromagnetic field. Despite its preliminary characteristics, this study can clearly indicate that the field potentials in the gravitational field and electromagnetic field have an influence on the scalar invariants. For the future studies, the related investigation will concentrate on only the predictions of light speed variation due to the huge field potentials in the gravitational field and electromagnetic field.

ACKNOWLEDGMENT

This project was supported partially by the National Natural Science Foundation of China under grant number 60677039.

REFERENCES

1. Hau, L. V., S. E. Harris, Z. Dutton, and C. H. Behroozi, "Light speed reduction to 17 metres per second in an ultracold atomic gas," *Nature*, Vol. 397, No. 6720, 594–598, 1999.
2. Povinelli, M. L., "Slow light: Variable speed limit," *Nature Physics*, Vol. 2, No. 11, 735–736, 2006.
3. Moffat, J. W., "Variable speed of light theories," *Astrophysics and Space Science*, Vol. 283, No. 4, 505–509, 2003.
4. Adler, S. L., *Quaternionic Quantum Mechanics and Quantum Fields*, Oxford University Press, New York, 1995.
5. Cayley, A., *The Collected Mathematical Papers*, Johnson Reprint Co., New York, 1963.
6. Weng, Z.-H. and Y. Weng, "Variation of gravitational mass in electromagnetic field," *PIERS Proceedings*, 105–107, Beijing, China, March 23–27, 2009.
7. Soukoulis, C. M., S. Linden, and M. Wegener, "Negative refractive index at optical wavelengths," *Science*, Vol. 315, No. 5808, 47–49, 2007.

Mass Continuity Equation in the Electromagnetic Field

Ying Weng¹ and Zi-Hua Weng²

¹College of Chemistry & Chemical Engineering
Xiamen University, Xiamen 361005, China

²School of Physics and Mechanical & Electrical Engineering
Xiamen University, Xiamen 361005, China

Abstract— A theoretical method with the quaternion algebra was presented to derive the mass continuity equation from the linear momentum. It predicts that the strength of electromagnetic field and the velocity have the impact on the mass continuity equation. In the gravitational field and electromagnetic field, the mass continuity equation will change with the electromagnetic field strength, gravitational field strength, linear momentum, electric current, and the speed of light. The deduction can explain why the field strength has an influence on the anomalous transport about the mass continuity equation in the plasma and electrolytes etc.

1. INTRODUCTION

The conservation laws are important invariants for the electromagnetic field. In the electromagnetic field theory described by the vectorial quantity, the mass continuity equation is solely dealt with the mass rate and the divergence of linear momentum. However, this opinion can not explain why the field strength has an impact on the anomalous transport about the mass continuity equation in the plasma and electrolytes [1, 2].

The algebra of quaternion [3] was first used by J. C. Maxwell [4] to describe the property of electromagnetic field. Similarly, the quaternion can also be used to demonstrate the feature of gravitational field, although these two fields are quite different [5]. By means of the scalar invariant of quaternions, we find that the mass continuity equation is an invariant in the gravitational field and electromagnetic field. In the quaternion spaces, the definition of mass continuity equation can be extended to the case for coexistence of electromagnetic field and gravitational field.

Presently, the mass continuity equation [6] was limited to the case of weak gravitational strength. It is found out that all of related verifications are solely constrained to be in the range of weak field strengths, and have not been validated in the strong fields up to now. With the characteristics of octonions [7], we find some impact factors of the mass continuity equation. In the electromagnetic field and gravitational field, the velocity and the strengths of electromagnetic field and gravitational field have a few influences on the mass continuity equation.

The results state that the gravitational field strength and electromagnetic field strength have an influence on the mass continuity equation, although the impact of the field strengths are usually very tiny when the electromagnetic field and gravitational field both are weak. And then, the mass continuity equation is conserved in most cases. However, when the electromagnetic field and gravitational field are strong enough, their field strengths will affect the mass continuity equation obviously, and cause the anomalous transport in the plasma.

2. COORDINATES TRANSFORMATION

In the quaternion space, the basis vector for the gravitational field is $\mathbb{E}_g = (1, \mathbf{i}_1, \mathbf{i}_2, \mathbf{i}_3)$, and that for the electromagnetic field is $\mathbb{E}_e = (\mathbf{I}_0, \mathbf{I}_1, \mathbf{I}_2, \mathbf{I}_3)$. The \mathbb{E}_e is independent of the \mathbb{E}_g , with $\mathbb{E}_e = \mathbb{E}_g \circ \mathbf{I}_0$. The basis vectors \mathbb{E}_g and \mathbb{E}_e can be combined together to become the basis vector \mathbb{E} of the octonion space.

$$\mathbb{E} = (1, \mathbf{i}_1, \mathbf{i}_2, \mathbf{i}_3, \mathbf{I}_0, \mathbf{I}_1, \mathbf{I}_2, \mathbf{I}_3) \quad (1)$$

The octonion quantity $\mathbb{D}(d_0, d_1, d_2, d_3, D_0, D_1, D_2, D_3)$ is defined as follows.

$$\mathbb{D} = d_0 + \Sigma(d_j \mathbf{i}_j) + \Sigma(D_i \mathbf{I}_i) \quad (2)$$

where, d_i and D_i are all real; $i = 0, 1, 2, 3$; $j = 1, 2, 3$.

When the coordinate system is transformed into the other one, the physical quantity \mathbb{D} will become the octonion physical quantity $\mathbb{D}'(d'_0, d'_1, d'_2, d'_3, D'_0, D'_1, D'_2, D'_3)$.

$$\mathbb{D}' = \mathbb{K}^* \circ \mathbb{D} \circ \mathbb{K} \quad (3)$$

where, \mathbb{K} is the octonion, and $\mathbb{K}^* \circ \mathbb{K} = 1$; $*$ denotes the conjugate of octonion; \circ is the octonion multiplication.

In case of the d_0 does not take part in the coordinates transformation in the above, we have,

$$d_0 = d'_0, \mathbb{D}^* \circ \mathbb{D} = (\mathbb{D}')^* \circ \mathbb{D}'. \quad (4)$$

In the above equation, the scalar part is one and the same during the octonion coordinates are transformed. Some invariants including the mass continuity equation about the electromagnetic field will be obtained from this characteristics of octonions.

Table 1: The octonion multiplication table.

	1	$\dot{\mathbf{i}}_1$	$\dot{\mathbf{i}}_2$	$\dot{\mathbf{i}}_3$	\mathbf{I}_0	\mathbf{I}_1	\mathbf{I}_2	\mathbf{I}_3
1	1	$\dot{\mathbf{i}}_1$	$\dot{\mathbf{i}}_2$	$\dot{\mathbf{i}}_3$	\mathbf{I}_0	\mathbf{I}_1	\mathbf{I}_2	\mathbf{I}_3
$\dot{\mathbf{i}}_1$	$\dot{\mathbf{i}}_1$	-1	$\dot{\mathbf{i}}_3$	$-\dot{\mathbf{i}}_2$	\mathbf{I}_1	$-\mathbf{I}_0$	$-\mathbf{I}_3$	\mathbf{I}_2
$\dot{\mathbf{i}}_2$	$\dot{\mathbf{i}}_2$	$-\dot{\mathbf{i}}_3$	-1	$\dot{\mathbf{i}}_1$	\mathbf{I}_2	\mathbf{I}_3	$-\mathbf{I}_0$	$-\mathbf{I}_1$
$\dot{\mathbf{i}}_3$	$\dot{\mathbf{i}}_3$	$\dot{\mathbf{i}}_2$	$-\dot{\mathbf{i}}_1$	-1	\mathbf{I}_3	$-\mathbf{I}_2$	\mathbf{I}_1	$-\mathbf{I}_0$
\mathbf{I}_0	\mathbf{I}_0	$-\mathbf{I}_1$	$-\mathbf{I}_2$	$-\mathbf{I}_3$	-1	$\dot{\mathbf{i}}_1$	$\dot{\mathbf{i}}_2$	$\dot{\mathbf{i}}_3$
\mathbf{I}_1	\mathbf{I}_1	\mathbf{I}_0	$-\mathbf{I}_3$	\mathbf{I}_2	$-\dot{\mathbf{i}}_1$	-1	$-\dot{\mathbf{i}}_3$	$\dot{\mathbf{i}}_2$
\mathbf{I}_2	\mathbf{I}_2	\mathbf{I}_3	\mathbf{I}_0	$-\mathbf{I}_1$	$-\dot{\mathbf{i}}_2$	$\dot{\mathbf{i}}_3$	-1	$-\dot{\mathbf{i}}_1$
\mathbf{I}_3	\mathbf{I}_3	$-\mathbf{I}_2$	\mathbf{I}_1	\mathbf{I}_0	$-\dot{\mathbf{i}}_3$	$-\dot{\mathbf{i}}_2$	$\dot{\mathbf{i}}_1$	-1

3. VELOCITY

The radius vector is $\mathbb{R}_g = (r_0, r_1, r_2, r_3)$ in the quaternion space for gravitational field. For the electromagnetic field, the radius vector is $\mathbb{R}_e = (R_0, R_1, R_2, R_3)$. Their combination is the radius vector $\mathbb{R}(r_0, r_1, r_2, r_3, R_0, R_1, R_2, R_3)$ in the octonion space.

$$\mathbb{R} = r_0 + \Sigma(r_j \dot{\mathbf{i}}_j) + \Sigma(R_i \mathbf{I}_i) \quad (5)$$

where, $r_0 = v_0 t$. v_0 is the speed of light, t denotes the time.

In the quaternion space for the gravitational field, the velocity is $\mathbb{V}_g = (v_0, v_1, v_2, v_3)$. For the electromagnetic field, the velocity is $\mathbb{V}_e = (V_0, V_1, V_2, V_3)$. They can be combined together to become the octonion velocity $\mathbb{V}(v_0, v_1, v_2, v_3, V_0, V_1, V_2, V_3)$ in the octonion space.

$$\mathbb{V} = v_0 + \Sigma(v_j \dot{\mathbf{i}}_j) + \Sigma(V_i \mathbf{I}_i) \quad (6)$$

In some cases, the electric charge is combined with the mass to become the electron or proton etc., we have the relation $R_i \mathbf{I}_i = r_i \dot{\mathbf{i}}_i \circ \mathbf{I}_0$ and $V_i \mathbf{I}_i = v_i \dot{\mathbf{i}}_i \circ \mathbf{I}_0$, with $\dot{\mathbf{i}}_0 = 1$.

4. FIELD STRENGTH

From the Aharonov-Bohm effect, we find that the field potential is much more essential than the field strength. By means of the field potential and the quaternion operator, the field strength can be defined to cover the strengths of gravitational field and electromagnetic field.

The gravitational potential is $\mathbb{A}_g = (a_0, a_1, a_2, a_3)$, and the electromagnetic potential is $\mathbb{A}_e = (A_0, A_1, A_2, A_3)$. The gravitational potential and electromagnetic potential constitute the field potential $\mathbb{A}(a_0, a_1, a_2, a_3, A_0, A_1, A_2, A_3)$ in the octonion space.

$$\mathbb{A} = \mathbb{A}_g + k_{eg} \mathbb{A}_e \quad (7)$$

where, k_{eg} is the coefficient.

The octonion strength \mathbb{B} consists of gravitational strength \mathbb{B}_g and electromagnetic strength \mathbb{B}_e .

$$\mathbb{B} = \diamond \circ \mathbb{A} = \mathbb{B}_g + k_{eg} \mathbb{B}_e \quad (8)$$

where, the quaternion operator $\diamond = \Sigma(\dot{\mathbf{i}}_i \partial_i)$, with $\partial_i = \partial / \partial r_i$.

In the above equation, we choose two gauge conditions of field potential to simplify succeeding calculation. The gravitational potential gauge is $b_0 = \partial_0 a_0 + \nabla \cdot \mathbf{a} = 0$, and the electromagnetic potential gauge $B_0 = \partial_0 A_0 + \nabla \cdot \mathbf{A} = 0$. Where, $\mathbf{a} = \Sigma(a_j \dot{\mathbf{i}}_j)$; $\mathbf{A} = \Sigma(A_j \dot{\mathbf{i}}_j)$; $\nabla = \Sigma(\dot{\mathbf{i}}_j \partial_j)$.

The gravitational field strength $\mathbb{B}_g = \mathbf{g}/c + \mathbf{b}$ includes two components, $\mathbf{g}/c = \partial_0 \mathbf{a} + \nabla a_0$ and $\mathbf{b} = \nabla \times \mathbf{a}$. At the same time, the electromagnetic field strength $\mathbb{B}_e = \mathbf{E}/c + \mathbf{B}$ involves two parts, $\mathbf{E}/c = (\partial_0 \mathbf{A} + \nabla A_0) \circ \mathbf{I}_0$ and $\mathbf{B} = -(\nabla \times \mathbf{A}) \circ \mathbf{I}_0$.

In the Newtonian gravitational field theory, there are $\mathbf{a} = 0$ and $\mathbf{b} = 0$ specially.

5. LINEAR MOMENTUM

The linear momentum is one function of the field source, which is a combination of the gravitational field source and electromagnetic field source.

The linear momentum density $\mathbb{S}_g = m\nabla_g$ is the source of the gravitational field, and the electric current density $\mathbb{S}_e = q\nabla_g \circ \mathbf{I}_0$ is that of the electromagnetic field. They combine together to become the field source \mathbb{S} .

$$\mu\mathbb{S} = (\mathbb{B}/v_0 + \diamond)^* \circ \mathbb{B} = \mu_g\mathbb{S}_g + k_{eg}\mu_e\mathbb{S}_e + \mathbb{B}^* \circ \mathbb{B}/v_0 \quad (9)$$

where, $k_{eg}^2 = \mu_g/\mu_e$; q is the electric charge density; m is the inertial mass density; μ , μ_g , and μ_e are the constants.

The $\mathbb{B}^* \circ \mathbb{B}/(2\mu_g)$ is the energy density, and includes that of the electromagnetic field.

$$\mathbb{B}^* \circ \mathbb{B}/\mu_g = \mathbb{B}_g^* \circ \mathbb{B}_g/\mu_g + \mathbb{B}_e^* \circ \mathbb{B}_e/\mu_e \quad (10)$$

The octonion linear momentum density is

$$\mathbb{P} = \mu\mathbb{S}/\mu_g = \hat{m}v_0 + \Sigma(mv_j\mathbf{i}_j) + \Sigma(MV_i\mathbf{i}_i \circ \mathbf{I}_0) \quad (11)$$

where, $\hat{m} = m + \Delta m$; $M = k_{eg}\mu_e q/\mu_g$; $\Delta m = (\mathbb{B} \circ \mathbb{B}/\mu_g)/v_0^2$.

The above means that the gravitational mass density \hat{m} is changed with the strength of either electromagnetic field or gravitational field.

6. MASS CONTINUITY EQUATION

The applied force can not be covered by Maxwell's equations, which are derived from the definition of field source. Whereas, the applied force can be derived from the linear momentum. And that the applied force covers the mass continuity equation in the gravitational and electromagnetic fields.

In the octonion space, the applied force density \mathbb{F} is defined from the linear momentum density \mathbb{P} in the gravitational field and electromagnetic field.

$$\mathbb{F} = v_0(\mathbb{B}/v_0 + \diamond)^* \circ \mathbb{P} \quad (12)$$

where, the applied force includes the gravity, the inertial force, the Lorentz force, and the interacting force between the magnetic strength with magnetic moment, etc.

The applied force density \mathbb{F} is rewritten as follows.

$$\mathbb{F} = f_0 + \Sigma(f_j\mathbf{i}_j) + \Sigma(F_i\mathbf{I}_i) \quad (13)$$

where, $f_0 = \partial p_0/\partial t + v_0\Sigma(\partial p_j/\partial r_j) + \Sigma(b_j p_j + B_j P_j)$; $p_0 = \hat{m}v_0$, $p_j = mv_j$; $P_i = MV_i$.

We have the octonion applied force density $\mathbb{F}'(f'_0, f'_1, f'_2, f'_3, F'_0, F'_1, F'_2, F'_3)$, when the coordinate system rotates. And then, we have the following result by Eq.(4).

$$f_0 = f'_0 \quad (14)$$

When the right side is zero in the above, we have the mass continuity equation in the case for coexistence of the gravitational field and electromagnetic field.

$$\partial \hat{m}/\partial t + \Sigma(\partial p_j/\partial r_j) + \Sigma(b_j p_j + B_j P_j)/v_0 = 0 \quad (15)$$

Further, if the strength is zero, $b_j = B_j = 0$, the above will be reduced as follows.

$$\partial m/\partial t + \Sigma(\partial p_j/\partial r_j) = 0 \quad (16)$$

The above states that the gravitational strength and electromagnetic strength have the influence on the mass continuity equation, although the $\Sigma(b_j p_j + B_j P_j)/v_0$ and the Δm both are usually very tiny when the fields are weak. When we emphasize the definitions of applied force and velocity in gravitational and electromagnetic fields, the mass continuity equation will be the invariant equation under the octonion transformation.

7. CONCLUSION

The mass continuity equation will vary in the strong electromagnetic field or gravitational field, and has a deviation from the mass continuity equation described with the vectorial quantity. In the gravitational and electromagnetic fields, this states that the mass continuity equation will change with the electromagnetic field strength, gravitational field strength, linear momentum, electric current, and the speed of light. The deduction can explain why the field strength has an impact on the anomalous transport about the mass continuity equation in the plasma.

In the octonion space, the deductive results about the conservation laws and the invariants depend on the definition combinations in the case for coexistence of gravitational field and electromagnetic field. By means of the definition combination of the linear momentum, the quaternion operator, and the velocity, we have the conclusions about the mass continuity equation in the gravitational field and electromagnetic field.

It should be noted that the study for the mass continuity equation examined only one simple case of weak field strength. Despite its preliminary characteristics, this study can clearly indicate the mass continuity equation is an invariant and is only one simple inference due to the low velocity and the weak strengths of electromagnetic field and gravitational field. For the future studies, the investigation will concentrate on only some predictions about the mass continuity equation under the high speed and strong strength of electromagnetic field.

ACKNOWLEDGMENT

This project was supported partially by the National Natural Science Foundation of China under grant number 60677039.

REFERENCES

1. Escande, D. F. and F. Sattin, "When can the Fokker-Planck Equation describe anomalous or chaotic transport," *Physical Review Letters*, Vol. 99, No. 18, 185005, 2007.
2. Ciraolo, G., F. Briolle, C. Chandre, E. Floriani, R. Lima, M. Vittot, M. Pettini, C. Figarella, and P. Ghendrih, "Control of Hamiltonian chaos as a possible tool to control anomalous transport in fusion plasmas," *Physical Review E*, Vol. 69, No. 5, 056213, 2004.
3. Schwartz, C., "Calculus with a quaternionic variable," *Journal of Mathematical Physics*, Vol. 50, No. 1, 013523, 2009.
4. Maxwell, J. C., *A Treatise on Electricity and Magnetism*, Dover Publications Inc., New York, 1954.
5. Weng, Z.-H. and Y. Weng, "Variation of gravitational mass in electromagnetic field," *PIERS Proceedings*, 105–107, Beijing, China, March 23–27, 2009.
6. Lavoisier, A., *Elements of Chemistry*, trans. R. Kerr, Dover Publications Inc., New York, 1965.
7. Cayley, A., *The Collected Mathematical Papers*, Johnson Reprint Co., New York, 1963.

Adjoint Charge in Electromagnetic Field

Zi-Hua Weng

School of Physics and Mechanical & Electrical Engineering, Xiamen University
Xiamen 361005, China

Abstract— Making use of the octonion operator, the electromagnetic field generates an adjoint field theoretically. The source of adjoint field includes the adjoint charge and the adjoint current. The adjoint charge has an impact on the gravitational mass and the mass distribution in the electromagnetic field with its adjoint field, and causes further the predictions to departure slightly from the conservation of mass. The inferences can explain why the adjoint charge will influence the mass distribution in the gravitational field and electromagnetic field of celestial bodies. And then the adjoint charge can be considered as one kind of candidate for the dark matter.

1. INTRODUCTION

The mass and the ‘missing mass’ both are crucial physical conceptions for various field theories. There is only the conception of mass in the existing electromagnetic field and gravitational field, which are described with the vectorial quantity. But this perspective can not explain why there is the ‘missing mass’ [1, 2] in the universe up to now.

The algebra of quaternions [3] was first used by J. C. Maxwell to describe the electromagnetic field. While the octonions [4] can be used to demonstrate the characteristics of gravitational field and electromagnetic field, including the conservation of mass etc. The related theoretical inferences are only dealt with the quaternion operator but the octonion operator [5]. In the octonion space, the operator should be extended from the quaternion operator to the octonion operator.

Making use of the octonion operator, the electromagnetic field demonstrated by the octonions will generate an adjoint field. The source of adjoint field includes the adjoint charge and adjoint current. The adjoint charge and its movement can not be observed by usual experiments. However, when the adjoint charge is combined with the ordinary charge to become the charged particles, their movements will be accompanied by some mechanical or electric effects.

The electromagnetic field and its adjoint field both can be demonstrated by the quaternions, although they are quite different from each other indeed. With the property of octonions, we find that the adjoint charge has an influence on the conservation of mass in the electromagnetic field. The adjoint charge takes part in the gravitational interaction and impacts the mass distribution, and then can be considered as one kind of candidate for dark matter [6, 7].

2. OCTONION TRANSFORMATION

The quaternion spaces can be used to describe the electromagnetic field or the gravitational field. Meanwhile, two quaternion spaces can combine together to become an octonion space. The latter can be used to demonstrate the electromagnetic field and gravitational field simultaneously.

The quaternion space can be considered as the two-dimensional complex space, and the octonion space as the two-dimensional quaternion space. In the quaternion space for the gravitational field, the basis vector is $\mathbb{E}_g = (1, \mathbf{i}_1, \mathbf{i}_2, \mathbf{i}_3)$, and the radius vector is $\mathbb{R}_g = (r_0, r_1, r_2, r_3)$, with the velocity $\mathbb{V}_g = (v_0, v_1, v_2, v_3)$. For the electromagnetic field, the basis vector is $\mathbb{E}_e = (\mathbf{I}_0, \mathbf{I}_1, \mathbf{I}_2, \mathbf{I}_3)$, the radius vector is $\mathbb{R}_e = (R_0, R_1, R_2, R_3)$, with the velocity $\mathbb{V}_e = (V_0, V_1, V_2, V_3)$.

The \mathbb{E}_e is independent of the \mathbb{E}_g , with $\mathbb{E}_e = \mathbb{E}_g \circ \mathbf{I}_0$. The \circ denotes the octonion multiplication. The \mathbb{E}_g and \mathbb{E}_e can be combined together to become the basis vector \mathbb{E} of the octonion space.

$$\mathbb{E} = \mathbb{E}_g + \mathbb{E}_e = (1, \mathbf{i}_1, \mathbf{i}_2, \mathbf{i}_3, \mathbf{I}_0, \mathbf{I}_1, \mathbf{I}_2, \mathbf{I}_3) \quad (1)$$

In the octonion space, the radius vector \mathbb{R} is

$$\mathbb{R} = \Sigma(r_i \mathbf{i}_i) + \Sigma(R_i \mathbf{I}_i), \quad (2)$$

and the velocity \mathbb{V} is

$$\mathbb{V} = \Sigma(v_i \mathbf{i}_i) + \Sigma(V_i \mathbf{I}_i). \quad (3)$$

where, $r_0 = v_0 t$; v_0 is the speed of light, t is the time; the \circ denotes the octonion multiplication. $i = 0, 1, 2, 3, j = 1, 2, 3, \dot{\mathbf{i}}_0 = 1$.

In some special cases, one ordinary mass m can be combined with one ordinary charge q to become an ordinary particle, such as the proton and electron etc. And then, we can measure their various characteristics, and have following relation.

$$R_i \mathbf{I}_i = r_i \dot{\mathbf{i}}_i \circ \mathbf{I}_0; \quad V_i \mathbf{I}_i = v_i \dot{\mathbf{i}}_i \circ \mathbf{I}_0. \quad (4)$$

The octonion quantity $\mathbb{D}(d_0, d_1, d_2, d_3, D_0, D_1, D_2, D_3)$ is defined as follows.

$$\mathbb{D} = d_0 + \Sigma(d_j \dot{\mathbf{i}}_j) + \Sigma(D_i \mathbf{I}_i) \quad (5)$$

where, d_i and D_i are all real.

When the coordinate system is transformed into the other, the physical quantity \mathbb{D} will be transformed into one new octonion $\mathbb{D}'(d'_0, d'_1, d'_2, d'_3, D'_0, D'_1, D'_2, D'_3)$.

$$\mathbb{D}' = \mathbb{K}^* \circ \mathbb{D} \circ \mathbb{K} \quad (6)$$

where, \mathbb{K} is one octonion, and $\mathbb{K}^* \circ \mathbb{K} = 1$; $*$ denotes the conjugate of octonion.

If the d_0 does not take part in the above transformation, it satisfies the following relation.

$$d_0 = d'_0 \quad (7)$$

In the above equation, the scalar part d_0 is preserved during the octonion coordinates are transforming. Some scalar invariants of electromagnetic field will be obtained from this characteristics of the octonion.

Table 1: The octonion multiplication table.

	1	$\dot{\mathbf{i}}_1$	$\dot{\mathbf{i}}_2$	$\dot{\mathbf{i}}_3$	\mathbf{I}_0	\mathbf{I}_1	\mathbf{I}_2	\mathbf{I}_3
1	1	$\dot{\mathbf{i}}_1$	$\dot{\mathbf{i}}_2$	$\dot{\mathbf{i}}_3$	\mathbf{I}_0	\mathbf{I}_1	\mathbf{I}_2	\mathbf{I}_3
$\dot{\mathbf{i}}_1$	$\dot{\mathbf{i}}_1$	-1	$\dot{\mathbf{i}}_3$	$-\dot{\mathbf{i}}_2$	\mathbf{I}_1	$-\mathbf{I}_0$	$-\mathbf{I}_3$	\mathbf{I}_2
$\dot{\mathbf{i}}_2$	$\dot{\mathbf{i}}_2$	$-\dot{\mathbf{i}}_3$	-1	$\dot{\mathbf{i}}_1$	\mathbf{I}_2	\mathbf{I}_3	$-\mathbf{I}_0$	$-\mathbf{I}_1$
$\dot{\mathbf{i}}_3$	$\dot{\mathbf{i}}_3$	$\dot{\mathbf{i}}_2$	$-\dot{\mathbf{i}}_1$	-1	\mathbf{I}_3	$-\mathbf{I}_2$	\mathbf{I}_1	$-\mathbf{I}_0$
\mathbf{I}_0	\mathbf{I}_0	$-\mathbf{I}_1$	$-\mathbf{I}_2$	$-\mathbf{I}_3$	-1	$\dot{\mathbf{i}}_1$	$\dot{\mathbf{i}}_2$	$\dot{\mathbf{i}}_3$
\mathbf{I}_1	\mathbf{I}_1	\mathbf{I}_0	$-\mathbf{I}_3$	\mathbf{I}_2	$-\dot{\mathbf{i}}_1$	-1	$-\dot{\mathbf{i}}_3$	$\dot{\mathbf{i}}_2$
\mathbf{I}_2	\mathbf{I}_2	\mathbf{I}_3	\mathbf{I}_0	$-\mathbf{I}_1$	$-\dot{\mathbf{i}}_2$	$\dot{\mathbf{i}}_3$	-1	$-\dot{\mathbf{i}}_1$
\mathbf{I}_3	\mathbf{I}_3	$-\mathbf{I}_2$	\mathbf{I}_1	\mathbf{I}_0	$-\dot{\mathbf{i}}_3$	$-\dot{\mathbf{i}}_2$	$\dot{\mathbf{i}}_1$	-1

3. ELECTROMAGNETIC FIELD

By means of the octonion operator, the electromagnetic field will generate an adjoint field in the octonion space. The adjoint field is derived from the electromagnetic field potential. The source of adjoint field includes the adjoint charge and adjoint electric current. In case of the electromagnetic field is accompanied by the adjoint field, the adjoint charge has an influence on the gravitational mass, and then causes some mechanical or electric effects. As a result, the adjoint charge may be considered as one kind of candidate for the dark matter.

The electromagnetic field potential is

$$\mathbb{A}_e = \Sigma(A_i \mathbf{I}_i). \quad (8)$$

In the electromagnetic field, the field strength $\mathbb{B}_e = \Sigma(b_{ei} \dot{\mathbf{i}}_i) + \Sigma(B_{ei} \mathbf{I}_i)$ consists of the electromagnetic strength \mathbb{B}_{eg} and adjoint strength \mathbb{B}_{ee} .

$$\mathbb{B}_e = \diamond \circ \mathbb{A}_e = \mathbb{B}_{eg} + \mathbb{B}_{ee} \quad (9)$$

where, $\mathbb{B}_{ee} = \Sigma(b_{ei} \dot{\mathbf{i}}_i)$, $\mathbb{B}_{eg} = \Sigma(B_{ei} \mathbf{I}_i)$; $\diamond = \Sigma \dot{\mathbf{i}}_i (\partial / \partial r_i) + \Sigma \mathbf{I}_i (\partial / \partial R_i)$; $\partial_i = \partial / \partial r_i$.

In the above, we choose the following gauge conditions to simplify succeeding calculation.

$$\partial A_0 / \partial r_0 - \Sigma(\partial A_j / \partial r_j) = 0, \quad \partial A_0 / \partial R_0 + \Sigma(\partial A_j / \partial R_j) = 0. \quad (10)$$

The adjoint field strength \mathbb{B}_{ee} in Eq. (9) includes two components, $\mathbf{g}_e = (g_{e01}, g_{e02}, g_{e03})$ and $\mathbf{b}_e = (g_{e23}, g_{e31}, g_{e12})$.

$$\mathbf{g}_e/v_0 = \mathbf{i}_1(\partial_0 A_1 - \partial_1 A_0) + \mathbf{i}_2(\partial_0 A_2 - \partial_2 A_0) + \mathbf{i}_3(\partial_0 A_3 - \partial_3 A_0) \quad (11)$$

$$\mathbf{b}_e = \mathbf{i}_1(\partial_3 A_2 - \partial_2 A_3) + \mathbf{i}_2(\partial_1 A_3 - \partial_3 A_1) + \mathbf{i}_3(\partial_2 A_1 - \partial_1 A_2) \quad (12)$$

Meanwhile, the electromagnetic field strength \mathbb{B}_{eg} involves two parts, $\mathbf{E}_e = (B_{e01}, B_{e02}, B_{e03})$ and $\mathbf{B}_e = (B_{e23}, B_{e31}, B_{e12})$.

$$\mathbf{E}_e/v_0 = \mathbf{I}_1(\partial_0 A_1 + \partial_1 A_0) + \mathbf{I}_2(\partial_0 A_2 + \partial_2 A_0) + \mathbf{I}_3(\partial_0 A_3 + \partial_3 A_0) \quad (13)$$

$$\mathbf{B}_e = \mathbf{I}_1(\partial_3 A_2 - \partial_2 A_3) + \mathbf{I}_2(\partial_1 A_3 - \partial_3 A_1) + \mathbf{I}_3(\partial_2 A_1 - \partial_1 A_2) \quad (14)$$

The electric current density $\mathbb{S}_{eg} = q\bar{\nabla}_g \circ \mathbf{I}_0$ is the source of electromagnetic field, and its adjoint current density $\mathbb{S}_{ee} = \bar{q}\bar{\nabla}_g$ is that of adjoint field. And they can be combined together to become the field source \mathbb{S}_e . In the octonion space, the electromagnetic source \mathbb{S}_e can be defined from the electromagnetic field strength $\mathbb{B} = k_b \mathbb{B}_e$.

$$\mu\mathbb{S} = (\mathbb{B}/v_0 + \diamond)^* \circ \mathbb{B} = k_b(\mu_{ee}\mathbb{S}_{ee} + \mu_{eg}\mathbb{S}_{eg}) + \mathbb{B}^* \circ \mathbb{B}/v_0 \quad (15)$$

where, $k_b^2 = \mu_{gg}/\mu_{eg}$; μ_{gg} , μ_{ee} , and μ_{eg} are the coefficients.

The $\mathbb{B}^* \circ \mathbb{B}/(2\mu_{gg})$ is the field energy density.

$$\mathbb{B}^* \circ \mathbb{B}/\mu_{gg} = \mathbb{B}_e^* \circ \mathbb{B}_e/\mu_{eg}$$

The above means that the electromagnetic field and its adjoint field both make a contribution to the gravitational mass in the octonion space.

4. CONSERVATION OF MASS

In the electromagnetic field and its adjoint field, for one charged particle with inertial massless, the linear momentum density $\mathbb{P} = \mu\mathbb{S}/\mu_{gg}$ is written as

$$\mathbb{P} = \hat{m}v_0 + \Sigma(M_q V_i \mathbf{i}_i \circ \mathbf{I}_0) + \Sigma(M_e v_i \mathbf{i}_i). \quad (16)$$

where, $\hat{m} = (\mathbb{B}^* \circ \mathbb{B}/\mu_{gg})/v_0^2$; $M_q = qk_b\mu_{eg}/\mu_{gg}$; $M_e = \bar{q}k_b\mu_{ee}/\mu_{gg}$.

The above means that the gravitational mass density ($\hat{m} + M_e$) is changed with all kinds of field strengthes in the electromagnetic field and its adjoint field. From Eq. (6), we have one linear momentum density, $\mathbb{P}'(p'_0, p'_1, p'_2, p'_3, P'_0, P'_1, P'_2, P'_3)$, when the octonion coordinate system is rotated. And we obtain the invariant equation from Eqs. (7) and (16).

$$(\hat{m} + M_e)v_0 = (\hat{m}' + M_e')v'_0 \quad (17)$$

Under Eqs. (3), (7), and (17), we find the gravitational mass density ($\hat{m} + M_e$) remains unchanged.

$$\hat{m} + M_e = \hat{m}' + M_e' \quad (18)$$

The above means that the gravitational mass density ($\hat{m} + M_e$) will keep unchanged, under the octonion coordinate transformation in Eq. (6) in the electromagnetic field and its adjoint field.

5. CONCLUSION

In the octonion space, the electromagnetic field described by the octonion operator will generate an adjoint field. In some cases, the electromagnetic field will be accompanied by its adjoint field. And that the source of adjoint field will impact the mass distribution and the conservation of mass in the electromagnetic field and gravitational field, especially in the universe.

In the electromagnetic field with its adjoint field, the adjoint field exerts an influence on the gravity in two aspects. On the one hand, the adjoint charge presents to the quaternion space for the gravitational field, and is one part of the gravitational mass. The adjoint charge is similar to the mass, and possesses the characteristics of gravity. On the other hand, the gravitational mass density is changed with the electromagnetic strength and adjoint field strength. The gravitational mass takes part in the gravitational interaction, so that the adjoint field strength will effect the

gravity. It states that the conservation of mass will be changed with the adjoint field strength and adjoint charge. Therefore the adjoint charge can be considered as one kind of dark matter in the astronomy related to the electromagnetic field.

It should be noted that the study of adjoint charge in the electromagnetic field and its adjoint field examined only one simple case with very weak field strength in the electromagnetic field with its adjoint field. Despite its preliminary character, this study can clearly indicate the field strength of electromagnetic field and its adjoint field have an influence on the gravity and the conservation of mass. For the future studies, the related investigation will concentrate on only the predictions of the gravity fluctuation and the mass distribution, in the strong adjoint field strength of electromagnetic field with its adjoint field.

ACKNOWLEDGMENT

This project was supported partially by the National Natural Science Foundation of China under grant number 60677039.

REFERENCES

1. Zwicky, F., "On the masses of nebulae and of clusters of nebulae," *Astrophysical Journal*, Vol. 86, No. 3, 217–246, 1937.
2. Bournaud, F., P.-A. Duc, E. Brinks, M. Boquien, P. Amram, U. Lisenfeld, B. S. Koribalski, F. Walter, and V. Charmandaris, "Missing mass in collisional debris from galaxies," *Science*, Vol. 316, No. 5828, 1166–1169, 2007.
3. Adler, S. L., *Quaternionic Quantum Mechanics and Quantum Fields*, Oxford University Press, New York, 1995.
4. Cayley, A., *The Collected Mathematical Papers*, Johnson Reprint Co., New York, 1963.
5. Weng, Z.-H. and Y. Weng, "Variation of gravitational mass in electromagnetic field," *PIERS Proceedings*, 105–107, Beijing, China, March 23–27, 2009.
6. Krasnov, K. and Y. Shtanov, "Non-metric gravity: II. Spherically symmetric solution, missing mass and redshifts of quasars," *Classical and Quantum Gravity*, Vol. 25, No. 2, 025002, 2008.
7. Diemand, J., M. Kuhlen, P. Madau, M. Zemp, B. Moore, D. Potter, and J. Stadel, "Clumps and streams in the local dark matter distribution," *Nature*, Vol. 454, No. 7205, 735–738, 2008.

The Number of Energy Levels of a Quantum Particle in a Piecewise Constant Potential Field

M. D. Kovalev
BMSTU, Russia

Abstract— A formula for the number of energy levels of a quantum particle in an arbitrary one-dimensional piecewise constant potential field is derived. The only restriction is a finite number of segments of constant potential. The method used can be applied for the deduction of the similar formula for the number of TE- and TM-optical modes in a planar dielectric waveguide in a general case.

1. INTRODUCTION

We consider stationary states of a quantum particle in an arbitrary one-dimensional piecewise constant potential field. This is a classical problem of quantum mechanics. We establish a formula for the number of energy levels of a quantum particle in an arbitrary such field. The only restriction is a finite number of segments of constant potential. We call such segments — the layers. The formula obtained is effective. There are no obstacles to calculate quickly with the help of personal computer the number of energy levels for structures including large number of layers, using this formula. The deduction of the formula is based on the analysis of the recently obtained multilayer equation [1, 2], allowing to calculate eigenvalues of energy E of a quantum particle in a piecewise constant potential field. The result is obtained by the development of a method earlier used by the author for solving the same problem in a case of a field, with potential accepting only two various values [3, 4].

2. THE MATHEMATICAL FORMULATION OF THE PROBLEM

Let us consider a structure consisting of $n + 1 \geq 3$ layers, let U_1 , and U_{n+1} be the potentials in external layers of infinite width, and U_k — the minimal potential of the layers. The obvious condition of the existence of at least one stationary state (consequently, an energy level) of the particle in such a structure is the validity of the inequality $U_k < \min\{U_1, U_{n+1}\}$.

In a layer with potential U_j a stationary state of the quantum particle is described by the one-dimensional Schroedinger equation [5]

$$-\frac{\hbar^2}{2m} \frac{d^2\Psi}{dx^2} + U_j\Psi = E\Psi, \quad (1)$$

where $\Psi(x)$ is a wave function, m — the mass of the particle, E — the energy of the particle, \hbar — Plank constant. In the physical assumption of converging to zero on infinity wave function we have a boundary problem for an ordinary differential equation with discontinuous coefficient U_j . To obtain eigenfunctions of the problem well known solutions of these linear with constant coefficients differential equations in layers are sewed together on conditions of continuity of them and their first derivatives on borders of layers. Let $U_1 \leq U_{n+1}$. Then all energy levels of a particle are contained in the interval (U_k, U_1) .

Further for the sake of convenience let's assume $U_k = 0$. Passing to a new unit of lengths: $x' = \sqrt{\frac{2mU_1}{\hbar^2}}x$, and entering designations: $\frac{U_j}{U_1} = u_j \geq 0$ — the reduced potential of a layer, and $\frac{E}{U_1} = e$ — the reduced energy of a particle, from the Equation (1) we receive the equation:

$$-\frac{d^2\Psi}{dx'^2} + u_j\Psi = e\Psi.$$

Let's note, that each stationary state of the particle corresponds to an eigenvalue of reduced energy from an interval $(0, 1)$. Everywhere further we shall use these reduced values of length and energy, omitting, however, the accent in designation of reduced length.

3. THE MULTILAYER EQUATION

The basic in our approach is a new form of dispersion equation for our phenomenon, — the equation, called by the author a multilayer. For the first time it has appeared in [1, 6]. To write out the multilayer equation, we shall enter the characteristic q_j , $1 \leq j \leq n + 1$, of the layer depending on reduced energy e of the particle: $q_j = \sqrt{u_j - e}$. This characteristic is real if $e \leq u_j$, and imaginary $q_j = i\sqrt{e - u_j}$ if $e > u_j$. Let t_2, t_3, \dots, t_n be reduced widths of the layers, and $\gamma_j = q_j t_j$, $2 \leq j \leq n$. Let us compose two finite sequences Q_j , $2 \leq j \leq n + 1$ and P_j , $1 \leq j \leq n$, depending of the characteristics q_j . Namely, let $Q_2 = q_1$, and for $2 < j \leq n + 1$

$$Q_{j+1} = q_j \operatorname{th} \left(\gamma_j + \operatorname{arth} \left(\frac{Q_j}{q_j} \right) \right).$$

The values P_j are determined as : $P_n = q_{n+1}$, and for $1 \leq j < n$

$$P_{j-1} = q_j \operatorname{th} \left(\gamma_j + \operatorname{arth} \left(\frac{P_j}{q_j} \right) \right).$$

For each $2 \leq j \leq n$ we can write out the multilayer equation

$$\operatorname{th} \left(\gamma_j + \operatorname{arth} \left(\frac{Q_j}{q_j} \right) + \operatorname{arth} \left(\frac{P_j}{q_j} \right) \right) = 0.$$

The function $F_j(e)$ in the left-hand side of this equation is called a multilayer too. The multilayer function depends on the numbers j of the finite layer.

If we select the number k layer with the least (zero) potential, the multilayer equation looks like

$$\operatorname{itg} \left(t_k \sqrt{e} - \operatorname{arctg} \left(\frac{Q_k}{\sqrt{e}} \right) - \operatorname{arctg} \left(\frac{P_k}{\sqrt{e}} \right) \right) = 0. \quad (2)$$

Let's designate the imaginary part of the left-hand side function as $F_k^*(e)$. Then the following statement is valid.

Theorem. *The set of the roots of equation $F_k^*(e) = 0$ in interval $(0, 1)$ coincides with the set of eigenvalues of the reduced energy of the particle in our potential field. Besides the problem treated here, the multilayer equation is extremely important in the theory of optical waveguides [2]. It permits to calculate the eigenvalues of effective index of refraction for the planar multilayer dielectric waveguide. Using the method discussed here one can deduce formulas for the number of optical TE and TM-modes in an arbitrary planar dielectric waveguide.*

4. THE FORMULA FOR THE NUMBER OF THE ENERGY LEVELS

Below we shall write out the formula for the number of energy levels. We shall do with the following functions: $Q_j^*(e) = \frac{Q_j^*(e)}{\sqrt{e}}$ and $P_j^*(e) = \frac{P_j^*(e)}{\sqrt{e}}$. Let's consider two finite sequences: $Q_j^*(1 - 0) = A_j^Q$, $2 \leq j \leq n + 1$ and $P_j^*(1 - 0) = A_j^P$, $1 \leq j \leq n$. Obviously, $A_2^Q = Q_2^*(1 - 0) = 0$ and $A_n^P = P_n^*(1 - 0) = \sqrt{u_{n+1} - 1}$. The members of these sequences are real numbers or are equal to $-\infty$. The following lemma is proved by calculating of these limits.

Lemma. *If the members of a sequence A_j^Q are finite, the following formulas are valid: if $u_j > 1$, then*

$$A_{j+1}^Q = \frac{\sqrt{u_j - 1}, \operatorname{th}(t_j \sqrt{u_j - 1}) + A_j^Q}{1 + \frac{A_j^Q \operatorname{th}(t_j \sqrt{u_j - 1})}{\sqrt{u_j - 1}}},$$

If $u_j = 1$, then

$$A_{j+1}^Q = \frac{A_j^Q}{1 + A_j^Q t_j},$$

and if $0 \leq u_j < 1$, then

$$A_{j+1}^Q = \frac{A_j^Q - \sqrt{1 - u_j} \operatorname{tg}(t_j \sqrt{1 - u_j})}{1 + \frac{A_j^Q \operatorname{tg}(t_j \sqrt{1 - u_j})}{\sqrt{1 - u_j}}}.$$

In the case of infinite limits the similar formulas may also be written.

Let B_j , $2 \leq j \leq n$ be the sequence with elements real numbers, or symbol $+\infty$, determined as follows:

if $0 \leq u_j < 1$, then $B_j = -\sqrt{1-u_j} \lim_{e \rightarrow 1-0} \operatorname{ctg}(t_j \sqrt{e-u_j})$,

if $u_j > 1$, then $B_j = -\sqrt{u_j-1} \operatorname{cth}(t_j \sqrt{u_j-1})$,

and if $u_j = 1$, then $B_j = -\frac{1}{t_j}$.

Let's enter a function — the unit step:

$$\eta_-(x) = \begin{cases} 1, & \text{if } x > 0 \\ 0, & \text{if } x \leq 0. \end{cases}$$

Taking into account an opportunity of an infinite limit of argument, we shall consider also $\eta_-(+\infty) = 1$.

We are to introduce ones more function — the integer part of number x with the lack: $[x]_-$. We understand under this function the greatest integer strictly smaller then x if $x > 0$, and 0 if $x \leq 0$. For example: $[1]_- = [-1]_- = [0]_- = 0$.

And at last, let $\mu_j = \min(1, u_j)$. Then the formula for the number K of the energy levels looks like:

$$K = \sum_{j=2}^{k-1} \left[\frac{t_j \sqrt{1-\mu_j}}{\pi} \right]_- + \eta_-(B_j - A_j^Q) + \sum_{j=k+1}^n \left[\frac{t_j \sqrt{1-\mu_j}}{\pi} \right]_- + \eta_-(B_j - A_j^P) + \left[1 + \frac{t_k - \operatorname{arctg} A_k^Q - \operatorname{arctg} A_k^P}{\pi} \right]_- . \quad (3)$$

5. CONCLUSION

The calculation with the formula obtained is easily programmed and quickly performed on a personal computer for potential fields including a lot of layers.

ACKNOWLEDGMENT

The work was supported by RFBR grant 08-01-90102-Mol.

REFERENCES

1. Maer, A. A. and M. D. Kovalev, "Dispersion equation for eigenvalues of the effective refractive index in a multilayered waveguide structure," *Doklady Physics*, Vol. 407, No. 6, 766–769, Doklady Akademii Nauk, 2006.
2. Kovalev, M. D., "The multilayer equation," *Chebyshev Collection*, Vol. 7, No. 2(18), 99–105, Tula, 2006.
3. Kovalev, M. D., "The number of energy levels of a particle in a MWQ structure," *Computational Mathematics and Mathematical Physics*, Vol. 47, No. 9, 1496–1513, 2007.
4. Kovalev, M. D., "On energy levels of a particle in a comb like structure," *Doklady Physics*, Vol. 419, No. 6, 201–205, 2008.
5. Davydov, A. S., *Quantum Mechanics*, Science, Moscow, 1973.
6. Mayer, A. A., "The equation for energy eigenvalues in MQW structures with an arbitrary number of quantum wells", *Doklady Physics*, Vol. 407, No. 5, 175–180, 2006.

Effect of Exciter Shape on Magnetic Field and Its Impedance in the Vicinity of a Multilayer Slab Conductor

Mohammad Fatehi Marji¹ and Hossein Fatehi Marj²

¹Mine Exploitation Engineering Department, Faculty of Mining and Metallurgy
Yazd University, Yazd, Iran

²Electrical Engineering Department
Shahrbabak Islamic Azad University, Shahrbabak, Kerman, Iran

Abstract— If a coil is located in the vicinity of a slab conductor the distribution of magnetic field and the coil impedance will be changed due to conductor's electromagnetic induction. One of the main applications of changing in the electromagnetic field and coil impedance is in the non-destructive evaluation of conductors. In this study, effect of various coil shapes (i.e., elliptic and rhombic with different axes ratios) on the distribution of magnetic field was analyzed based on electromagnetic field distribution method which solves the Helmholtz equation in three dimensions semi-analytically. For solving an n -layer problem with several coil exciters, the boundary condition equations in between the two neighboring layers (and also the first and last layers opening to air) were arranged in a sparse matrix form. To solve this matrix, a suitable computer program was provided in MATLAB. Several example problems were solved showing the effects of elliptic and rhombic coil shapes on the magnetic field. The computed results were obtained considering several coil axes ratios. The effect of source frequency variations on the coil impedance was also analyzed and discussed. These computed results were given in suitable figures.

1. INTRODUCTION

Computation of electromagnetic field distribution (or other electromagnetic variables) caused by different shapes of exciters, near different shapes of conductors, have been an important interesting subject for many researches (for example in nondestructive testing methods) [1–9]. Some efforts have been done to find magnetic field and eddy current, above the surface of slab conductors and also within the slab [1–6]. Some other studies have evaluated the effect of slab conductors on impedance of the exciter [7, 8]. Many analytical and numerical methods have been used for the analysis of these conductor problems [10, 11].

In this study, the effect of different shapes of elliptic and rhombic coils on the magnetic field distribution near a multilayer slab conductor is evaluated. Changing in exciter shape causes some variations in the magnetic field. The variations assumed in the elliptic and rhombic coil shape exciters are: (i) Coil diameter, (ii) coil length, and (iii) angle of rotation around one of the coil axes. To produce a higher variation of magnetic field within the conductor layers, low frequencies should be used. The effect of multi-layer conductor on variation of coil impedance (with respect to frequency variations) is also considered. Finally, the effect of having a ferromagnetic conductor layer within the multi-layer slab conductor is considered too.

A powerful method of calculation is used to solve the problem [9]. This method has the capability of solving multi-layer conductor problems without any limitation for the number of layers and shape of exciters. The problem is evaluating the electromagnetic field distribution in three dimensions semi-analytically based on the solution of Helmholtz equation. A two dimensional Fast Fourier Transform (FFT) is used on the surface of the layers, and exponential functions are considered in vertical axis analytically. Some example problems are solved by the proposed method.

2. PROBLEM DEFINITION

Figure 1 demonstrates the general configuration of the problem. An elliptic or rhombic coil of an AC current $I = I_M \cos \omega t$ is located above a multilayer slab conductor, where $\omega = 2\pi f$, and f is the frequency. One of coils axes is located on x -axis with the inner diameter of a_1 , and the outer diameter of a_2 . The other axis is located on y -axis with the inner diameter of b_1 , and the outer diameter of b_2 . The coil can also rotate around x axis. The rotation angle is α , and the length of coil is L . The center of lower surface of coil is located at $x = y = o$, and $z = h$. The n layers of multi-layer conductor are located in $z < 0$ so that the surface of upper layer is at $z = 0$, and all of other layers surface are parallel to it. The conductivity and permeability of layer m are σ_m

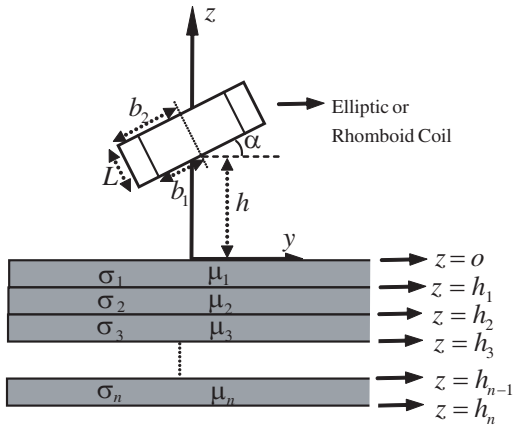


Figure 1: Geometrical configuration of elliptic or rhombic coil above n -layer slab conductor.

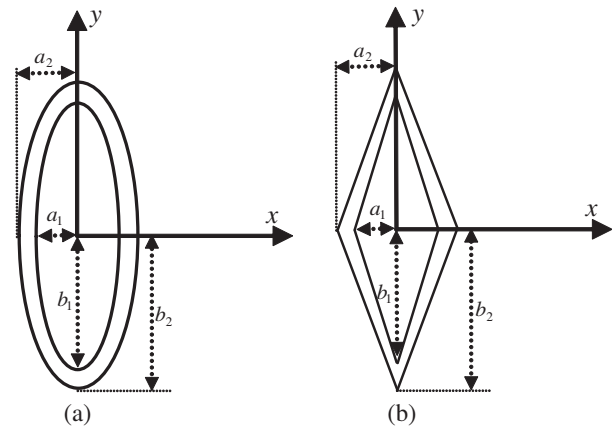


Figure 2: (a) Elliptic, and (b) rhombic coil, which act as exciter ($\alpha = 0^\circ$).

and μ_m , respectively, where m changes from 1 to n . The lower surface of m th layer is located at $z = h_m$.

Figure 2 shows an elliptic and rhombic coil in x - y plane, while $\alpha = 0^\circ$. The inner and outer diameters of coil on x -axis are $2a_1$ and $2a_2$; and on y -axis are $2b_1$ and $2b_2$, respectively. To solve the multi-layer problem we can use the method of reference [9]. This method is based on considering the separation of variables method to solve Helmholtz equations. The electromagnetic fields have exponential functions in z direction. The necessary equations can be obtained applying boundary conditions in common surface of all of two adjacent layers. In this method, the effect of exciter can be replaced by calculation of incident components of magnetic field in $z = 0$ in the absence of slab conductor. Using two dimensional FFT in x - y plane, this method solves the problem semi analytically. Using FFT overcomes the difficulties of: 1) Finding an equation for incident magnetic field due to an arbitrary shape exciter and 2) applying the Fourier transform and its inverse analytically.

3. EXAMPLE PROBLEM AND DATA EVALUATION

To evaluate the effects of coil shape on field distribution, a four layer conductor, has been solved for several shapes of exciters. Table 1 shows the electromagnetic parameters of the multilayer slab conductor.

In this example, a base problem is solved for both elliptic and rhombic coils. Then the effect of changing in coil diameter, length, and also rotation around its diameter, with respect to the base problem is considered. The data of the base problem are: $a_1 = b_1 = 4$ mm, $a_2 = b_2 = 5$ mm, $L = 1$ mm, $h = 4$ mm, $f = 15$ Hz, $I = 1$ A, $\alpha = 0^\circ$, and the number of coil turns is 50. Changing in coil diameter is considered for the following three cases: (i) $a_1 = 3$ mm, $a_2 = 4$ mm, (ii) $a_1 = 2$ mm, $a_2 = 3$ mm, and (iii) $a_1 = 1$ mm, $a_2 = 2$ mm. Changing in coil length is considered for (i) $L = 3$ mm, and (ii) $L = 5$ mm. Changing in coil angle is considered for four cases of (i) $\alpha = 10^\circ$, (ii) $\alpha = 20^\circ$, (iii) $\alpha = 30^\circ$, and (iv) $\alpha = 40^\circ$.

Figures 3 to 8 show the magnitude of magnetic field in $z = 0.5$ mm, $z = -1.5$ mm and $z = -3.5$ mm. Figure 3 and Figure 4 show the magnitude of magnetic field on x -axis with respect to the variation of diameter and length of elliptic and rhombic coil respectively. It should be noted that, for the base problem of Figures 5 to 8, the coil length is taken as $L = 3$ mm. Figure 5 and Figure 6 show the magnitude of magnetic field on x -axis with respect to the variation of coil angle,

Table 1: Electromagnetic parameters of conductor layers.

Layer	Location (mm)	σ (S/m)	μ_r
1	$z = 0 \rightarrow -1$	$\sigma_1 = 3.54 \times 10^7$	$\mu_{r1} = 1$
2	$z = -1 \rightarrow -2$	$\sigma_2 = 0.2 \times 10^7$	$\mu_{r2} = 100$
3	$z = -2 \rightarrow -3$	$\sigma_3 = 5.8 \times 10^7$	$\mu_{r3} = 1$
4	$z = -3 \rightarrow -4$	$\sigma_4 = 3.54 \times 10^7$	$\mu_{r4} = 1$

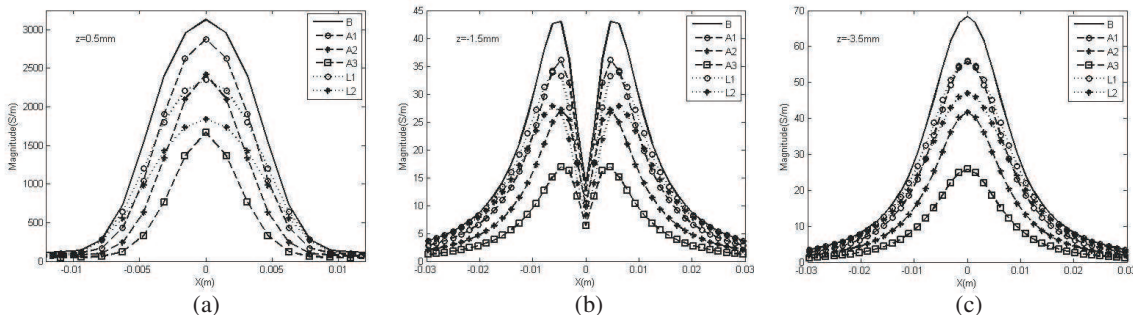


Figure 3: Magnitude of magnetic field on x -axis for elliptic coil with variation of diameter and length in (a) $z = 0.5$ mm, (b) $z = -1.5$ mm, (c) $z = -3.5$ mm. (B: Base Problem), (A1: $a_1 = 3$ mm, $a_2 = 4$ mm), (A2: $a_1 = 2$ mm, $a_2 = 3$ mm), (A3: $a_1 = 1$ mm, $a_2 = 2$ mm), (L1: $L = 3$ mm), (L2: $L = 5$ mm).

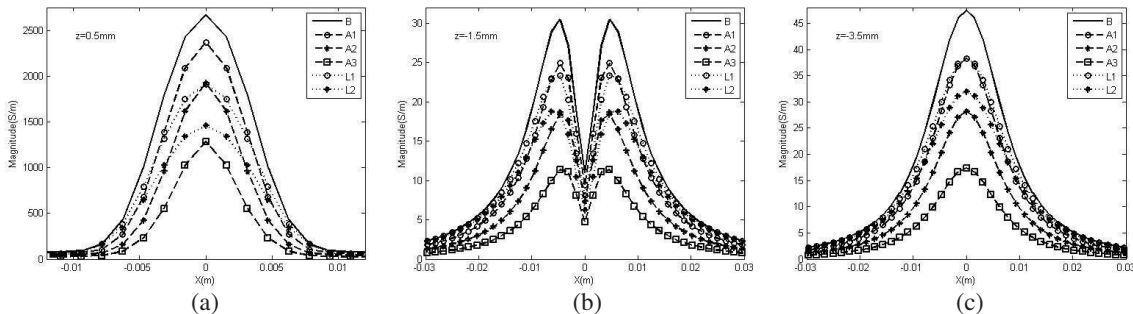


Figure 4: Magnitude of magnetic field on x -axis for rhombic coil with variation of diameter and length in (a) $z = 0.5$ mm, (b) $z = -1.5$ mm, (c) $z = -3.5$ mm. (B: Base Problem), (A1: $a_1 = 3$ mm, $a_2 = 4$ mm), (A2: $a_1 = 2$ mm, $a_2 = 3$ mm), (A3: $a_1 = 1$ mm, $a_2 = 2$ mm), (L1: $L = 3$ mm), (L2: $L = 5$ mm).

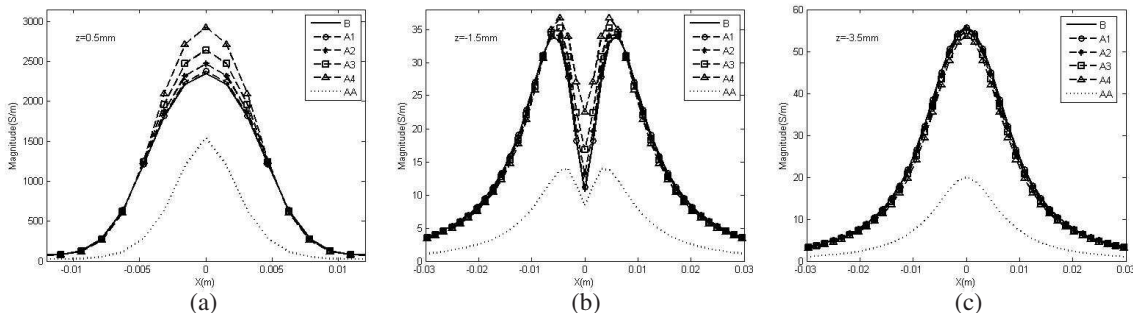


Figure 5: Magnitude of magnetic field on x -axis for elliptic coil with variation of coil angle, and both coil angle and coil diameter in (a) $z = 0.5$ mm, (b) $z = -1.5$ mm, (c) $z = -3.5$ mm. (B: Base Problem), (A1: $\alpha = 10^\circ$), (A2: $\alpha = 20^\circ$), (A3: $\alpha = 30^\circ$), (A4: $\alpha = 40^\circ$), (AA: $a_1 = 1$ mm, $a_2 = 2$ mm, $\alpha = 40^\circ$).

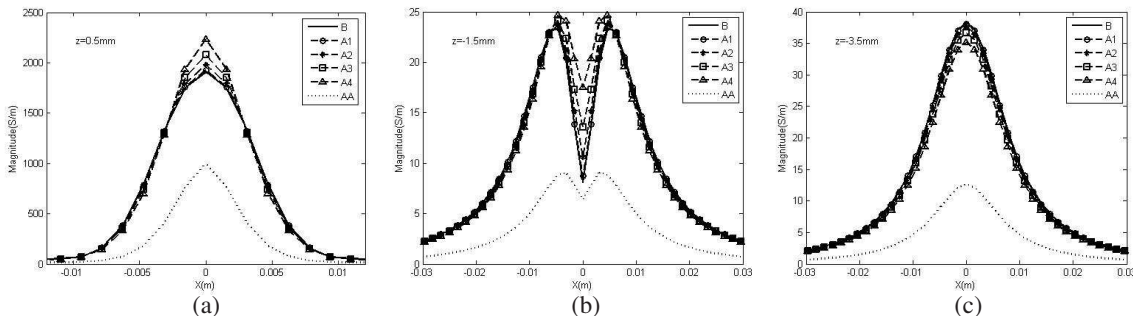


Figure 6: Magnitude of magnetic field, on x -axis for rhombic coil with variation of coil angle, and both coil angle and coil diameter in (a) $z = 0.5$ mm, (b) $z = -1.5$ mm, (iii) $z = -3.5$ mm. (B: Base Problem), (A1: $\alpha = 10^\circ$), (A2: $\alpha = 20^\circ$), (A3: $\alpha = 30^\circ$), (A4: $\alpha = 40^\circ$), (AA: $a_1 = 1$ mm, $a_2 = 2$ mm, $\alpha = 40^\circ$).

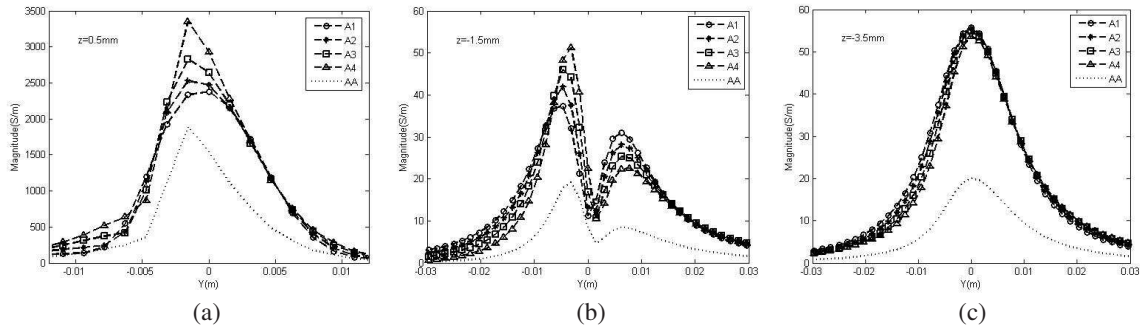


Figure 7: Magnitude of magnetic field, on y -axis for elliptic coil with variation of coil angle, and both coil angle and coil diameter in (a) $z = 0.5$ mm, (b) $z = -1.5$ mm, (iii) $z = -3.5$ mm. (B: Base Problem), (A1: $\alpha = 10^\circ$), (A2: $\alpha = 20^\circ$), (A3: $\alpha = 30^\circ$), (A4: $\alpha = 40^\circ$), (AA: $a_1 = 1$ mm, $a_2 = 2$ mm, $\alpha = 40^\circ$).

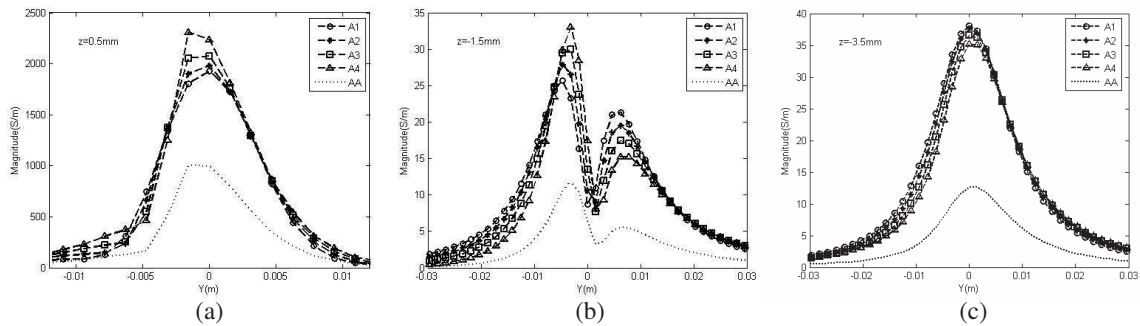


Figure 8: Magnitude of magnetic field, on y -axis for rhombic coil with variation of coil angle, and both coil angle and coil diameter in (a) $z = 0.5$ mm, (b) $z = -1.5$ mm, (iii) $z = -3.5$ mm. (B: Base Problem), (A1: $\alpha = 10^\circ$), (A2: $\alpha = 20^\circ$), (A3: $\alpha = 30^\circ$), (A4: $\alpha = 40^\circ$), (AA: $a_1 = 1$ mm, $a_2 = 2$ mm, $\alpha = 40^\circ$).

and both coil angle and diameter of elliptic and rhombic coils respectively. Figure 7 and Figure 8 give the same results as given in Figure 5 and Figure 6 but on y -axis.

Looking at these figures confirms that all effects of decreasing in diameter, increasing of length, and rotation around diameter, cause some decreasing in magnetic field. The decreasing in coil diameter, causes the ratio of magnetic field magnitudes with respect to their corresponding base values, slightly decreasing from $z = 0.5$ mm to $z = -3.5$ mm, but for the case of increasing in the coil length, this trend is reversed. For the case of increasing in the coil angle, the magnetic field magnitudes are higher than their corresponding base values, but this trend decreases from $z = 0.5$ mm to $z = -3.5$ mm, so that at $z = -3.5$ mm all of the results are nearly overlapped. As shown in these figures, the graphs related to changing in length are wider than other graphs. The rotation of coil around x -axis can disturbed the symmetrical shape of magnetic field distribution on y -axis, so that in some parts on the surface which coil is nearer to the conductor, the magnetic field magnitude is more than that value in other parts. The difference between the results compared to the corresponding values in other parts is also higher. By the way, coil angle has a little effect on magnitude and symmetrical shape of magnetic field in the lower layers. As a result, the variation of coil shape can be distinguished by the above mentioned rules.

To evaluate the effect of conductor layers on coil impedance at different frequencies, the base problem ($L = 3$ mm) is considered (case 2). To compare the effect of non-ferromagnetic conductor layers, the same problem is solved but for $\mu_{r2} = 1$ (case 1). The magnitude and phase of impedance changing are shown in Figure 9 and Figure 10 respectively. For a better showing, two ranges of frequency (i) $0 < f < 3$ kHz, and (ii) $0 < f < 20$ MHz, are considered in horizontal axis. As shown in these figures, the effect on magnitude of impedance changing will be increased with frequency increasing. This effect is pretty higher for the case of having a ferromagnetic layer (case 2) especially at low frequencies. The phase of coil impedance changing, starts from near zero for non-ferromagnetic (case 1), and from near 90° for the case 2, at low frequencies. As frequency increases the difference between the phases of the two cases decreases until frequencies raises to more than 10 kHz, where both of them will be overlapped and tends to -90° . These variations

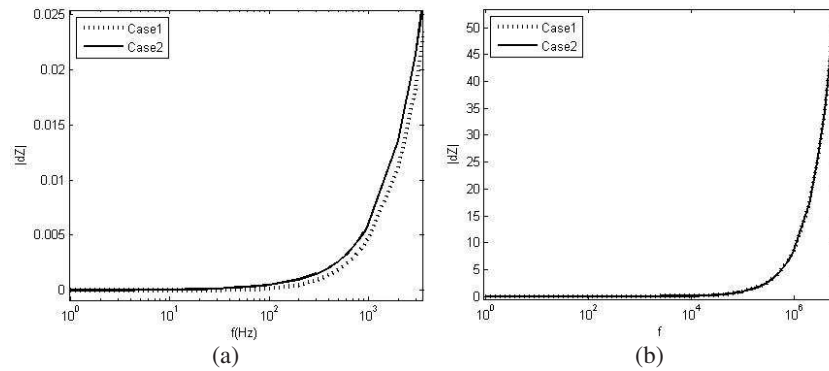


Figure 9: Magnitude of impedance changing of the coil due to multi-layer slab conductor with respect to frequency variations for (a) $0 < f < 3$ kHz, and (b) $0 < f < 20$ MHz. (Case 1: $\mu_{r2} = 1$), (Case 2: $\mu_{r2} = 100$).

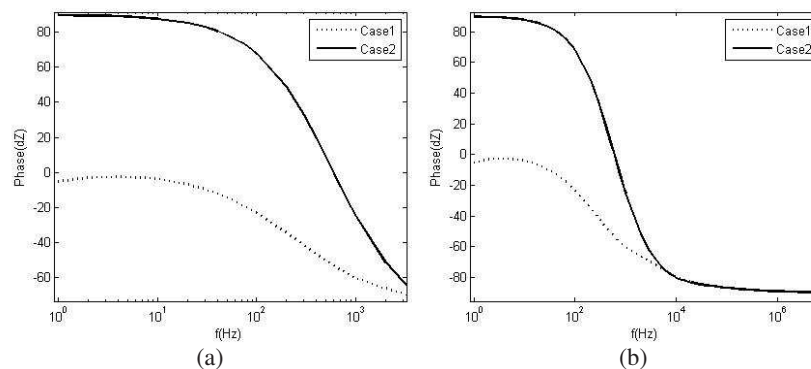


Figure 10: Phase of impedance changing of the coil due to multi-layer slab conductor with respect to frequency variations for (a) $0 < f < 3$ kHz, and (b) $0 < f < 20$ MHz. (Case 1: $\mu_{r2} = 1$), (Case 2: $\mu_{r2} = 100$).

are due to increasing in the normal component of magnetic field in the air for the case of having a ferromagnetic layer in between the layers (case 2) at low frequencies. As it is evident, at very high frequencies only the upper layer can affect the coil impedance.

4. CONCLUSION

In this study, the effects of variation of exciter shape in the vicinity of a multi layer slab conductor on the distribution of magnetic field have been calculated. Two kinds of coil shapes, elliptic and rhombic, with changing in their diameters, length, and angle of rotation around the diameter have been considered (different shapes of exciters). Alternatively, the effect of multi-layer slab conductor on exciter impedance for the case of having non-ferromagnetic conductors and conductors with a ferromagnetic layer is considered with respect to frequency variation. A semi-analytical method used for the analysis of the electromagnetic field distribution and the changing in coil impedance. This method employs the exponential functions in vertical direction (z) and the Fast Fourier Transform (FFT) in two dimensions (x and y) to solve multi-layer problems effectively. Using a MATLAB computer program, some example problems are solved. The computed results are shown in different figures and analyzed. These results provide some ideas to compare the field distribution of different shapes of exciters and to predict the effects of multi-layer conductors on the coil impedance.

REFERENCES

1. Tsaknakis, H. J. and E. E. Kriezis, "Field distribution due to a circular current loop placed in an arbitrary position above a conducting plate," *IEEE Trans. Geosci. R. Sensing J.*, Vol. 23, 834–840 1985.
2. Mirshekar-Syahkal, D. and R. F. Mostafavi, "Analysis technique for interaction of high-frequency rhombic inducer field with cracks in metals," *IEEE Trans. Magn.*, Vol. 33, No. 3, May 1997.

3. Sadeghi, S. H. H. and D. Mirshekar-Syahkal, "Accuracy of the image technique for calculating electromagnetic field induced at surface of ferromagnetic metal," *Rev. Prog. Nondest. Eval.*, Vol. 12, 2142–2150, Plenum Press, USA, 1993.
4. Panas, S. M. and A. G. Papayiannakis, "Eddy current in an infinite slab due to an elliptic current excitation," *IEEE Trans. Magn.*, Vol. 27, 4328–4337, 1991.
5. Pichenot, G. and T. Sollier, "Eddy current modeling for nondestructive testing," *8th ECNDT 2002*, CEA, SISC Bât 611 91191 Gif-sur-Yvette Cedex, France, 2002.
6. Dodd, C. V. and W. E. Deeds, "Analytical solution to eddy-current probe-coil problems," *J. Apply. Phys.*, Vol. 39, 2829–2838, 1963.
7. Uzal, E., I. Ozkol, and M. O. Kaya, "Impedance of a coil surrounding an infinite cylinder with an arbitrary radial conductivity profile," *IEEE Trans. Magn.*, Vol. 34, No. 1, January 1998.
8. Uzal, E., J. C. Moulder, S. Mitra, and J. H. Rose, "Impedance of coils over layered metals with continuously variable conductivity and permeability: Theory and experiment," *J. Apply. Phys.*, Vol. 74, No. 3, 1993.
9. Fatehi, H., S. H. H. Sadeghi, M. Fatehi, and R. Moini, "Computing electromagnetic field distribution due to an arbitrary shape exciter near multilayer slab conductors," *IEEE Trans. Magn.*, Vol. 41, No. 3, March 2005.
10. Sadidka, M. N. O., "A Simple introduction to finite element analysis of electromagnetic problems," *IEEE Trans. Edu.*, Vol. 32, No. 2, May 1989.
11. Murphy, R. K., H. A. Sabbagh, J. C. Treece, and L. W. Woo, "A volume-integral code for electromagnetic nondestructive evaluation," *11th Annual Review of Progress in Applied Computational Electromagnetics*, March 1995.

Effect of Variation of Slab Conductor Electromagnetic Parameters on the Electromagnetic Field Distribution

Hossein Fatehi Marji¹ and Mohammad Fatehi Marji²

¹Electrical Engineering Department

Shahrbabak Islamic Azad University, Shahrbabak, Kerman, Iran

²Mine Exploitation Engineering Department, Faculty of Mining and Metallurgy
Yazd University, Yazd, Iran

Abstract— If a slab conductor is located near an arbitrary shape exciter, the electromagnetic field distribution near its surface will be changed. These changes are due to the electromagnetic parameters (permeability and conductivity) of the conductor. The conductor's permeability and conductivity may be changed due to corrosion, heat, impact, etc. In this study, the effect of changes in the electromagnetic parameters of slab conductor on the electromagnetic field distribution near the surface of that conductor was analyzed. A semi-analytical potential scalar method was used for the analysis of the electromagnetic field distribution using the Fast Fourier Transform (FFT). It is a three dimensional method which solves the problem analytically in the vertical direction and numerically in the horizontal surfaces of the conductor. In this method, a slab conductor with variable electromagnetic parameters is divided into n layers of constant electromagnetic parameters (n should be sufficiently large depending on the range of variations). A suitable computer program was provided in MATLAB and several example problems were solved. The computed results showed the effect of conductivity changes under a constant permeability and also the effect of both conductivity and permeability changes on the electromagnetic field distribution. Various problems were solved and the results were compared with each other and given in suitable figures.

1. INTRODUCTION

The computation of electromagnetic field distribution around and within conductors is a main interesting subject of many researchers in different engineering fields such as power and mechanical engineering [1–7]. In the case of nonlinear problems many analytical and numerical methods have been used to solve the electromagnetic equations [2, 7, 9]. Various works have been done on the application of half space, slab and multilayer conductors using different shape of exciters [4, 5, 7, 9]. In many of these applications the magnetic field distribution, eddy currents and variation of exciter impedance have been calculated [4, 5, 8, 9].

The effect of variation of electromagnetic parameters (the conductivity σ and the permeability μ) in the vicinity of conductor surfaces is considered in this research. The variation of these parameters may be due to different effects such as heat, impact and corrosion which mainly occur on the surface of conductor. Uzal et al. [10] used various functions (i.e., hyperbolic, exponential, Gaussian functions) to model the variation of conductivity σ . In this study, the effect of variation of both σ and μ on the electromagnetic field distribution is analyzed in different regions of a slab conductor problem. The parameters variations are assumed to obey the exponential functions.

To solve the problem, a powerful method of calculation is necessary. In a recent work, a three dimensional semi-analytical method has been proposed using the potential scalar method for the calculation of multilayer slab conductor problems with arbitrary shape exciters [11]. In this paper, an elliptic loop is used as an exciter and the problem of parameters variation is changed to a multilayer problem and then is solved by the potential scalar method. The distribution of electromagnetic field near the surface of the exciter and within the parameters variation region is computed and the results are compared with the constant parameters case.

2. PROBLEM DEFINITION

Figure 1 demonstrates the general configuration of the problem. An elliptic current carrying loop of an AC current $I = I_M \cos \omega t$ is located above a slab conductor and parallel to it, where $\omega = 2\pi f$, and f is the frequency. The variations of conductivity σ and permeability μ can be occurring in upper surface of the slab and they can be modeling as exponential functions in z direction, which increase from $\sigma(0^-)$ and $\mu(0^-)$ in $z = 0^-$ to σ' and μ' in $z = (-d1)^+$. The electromagnetic

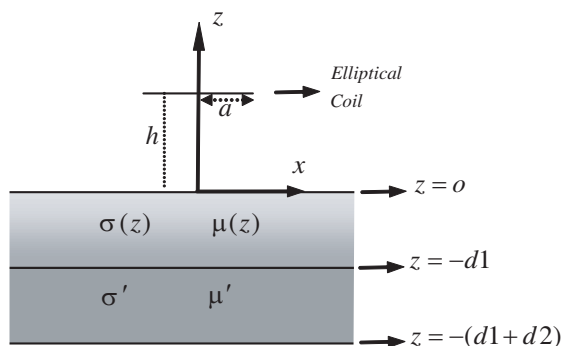


Figure 1: Geometrical configuration of conductivity and permeability variations near the surface of a slab.

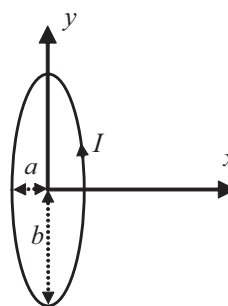


Figure 2: An elliptic current carrying loop, which act as an exciter above the slab.

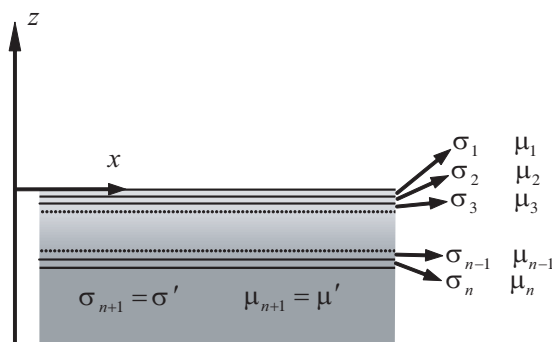


Figure 3: Modeling of the conductor as a multi layer problem.

parameters are constant within $-(d1 + d2) < z < -d1$. Figure 2 shows the elliptic exciter in $x-y$ plane. The small and big diameters of elliptic coil are $2a$ in x -axis and $2b$ in y -axis respectively.

Figure 3 shows how the problem indicated in Figure 1, can be changed into a multi layer problem. The region $-d1 < z < 0$ can be divided to n distinctive layers which conductivity and permeability of each layer are kept constant. They are equal to the amount of the exponential functions in the center of their corresponding layers. To achieve a reasonable accuracy, n has to be large enough. Considering the region $-d2 < z < -d1$ as a layer, the total number of layers will be $n + 1$.

To solve the multi layer problem the potential scalar method is used [11]. This method is based on considering the separation of variables method to solve Helmholtz equations. The electromagnetic fields have exponential functions in z direction. The necessary equations can be obtained by applying boundary conditions in the common surface of all two adjacent layers. In this method the effect of exciter can be replaced by calculation of the incident components of scalar potential in $z = 0$ in the absence of slab conductor. Using two dimensional FFT in $x-y$ plane, this method solves the problem semi-analytically. Using FFT overcomes the difficulties of: 1) finding an equation for incident magnetic field due to an arbitrary shape exciter and 2) applying the Fourier transform and its inverse analytically.

3. EXAMPLE PROBLEM AND DATA EVALUATION

To evaluate the effects of electromagnetic parameters on the field distribution, an example problem has been solved. In this example $d1 = d2 = 1.5$ mm, $a = 2$ mm, $b = 4$ mm, $n = 40$, $I = 1$ A, $h = 3$ mm, $\sigma' = 0.2 \times 10^7$ S/m, and $\mu' = \mu'_r \mu_0$, where $\mu_0 = 4\pi \times 10^{-7}$ is permeability of vacuum and $\mu'_r = 1000$. In the region of $-d1 < z < 0^-$, for the constant parameters the parameters are: $\sigma(z) = \sigma'$ and $\mu(z) = \mu'$. In this region two cases of parameters variations are considered: 1) conductivity variation and constant permeability case, where $\mu_1 = \mu'$, and 2) conductivity and permeability variation case. Each parameter variation has two forms of exponential changes: (i) Moderate changes, where the parameters variations start from $\sigma(0^-) = 0.125 \times 10^7$ S/m, $\mu(0^-) = 500\mu_0$ to

$\sigma(-d1) = 0.2 \times 10^7 \text{ S/m}$, $\mu(-d1) = 1000\mu_0$ and (ii) Rapid changes where the parameters variations start from $\sigma(0^-) = 0.05 \times 10^7 \text{ S/m}$, $\mu(0^-) = 100\mu_0$ to $\sigma(-d1) = 0.2 \times 10^7 \text{ S/m}$, $\mu(-d1) = 1000\mu_0$. The physical shape of slab in all of situations is the same. Figures 4 through 7 show the magnitude of magnetic field in $z = 0^-$, $z = 0^+$, $z = -1 \text{ mm}$ for frequencies $f = 2 \text{ Hz}$, 200 Hz , 20 kHz , and 2 MHz respectively.

Looking at these figures confirms that the effect of parameters variation on magnetic field is negligible in $z = 0^+$ (on the surface of the slab), especially in low frequencies. The tangential components of magnetic field are weak in this surface. As it is shown in Figure 7, at frequency of $f = 2 \text{ MHz}$, if the conductivity of slab conductor decreases, the tangential and normal components of magnetic field will decrease and increase respectively. On the other hand if the permeability of slab conductor decreases, the tangential and normal components of magnetic field will increase and decrease respectively. It should be noted that at very high frequencies the normal components decrease and the tangential components increase so that at infinite frequencies, the normal components of magnetic field will tends to zero, and its tangential components will tends to a constant value.

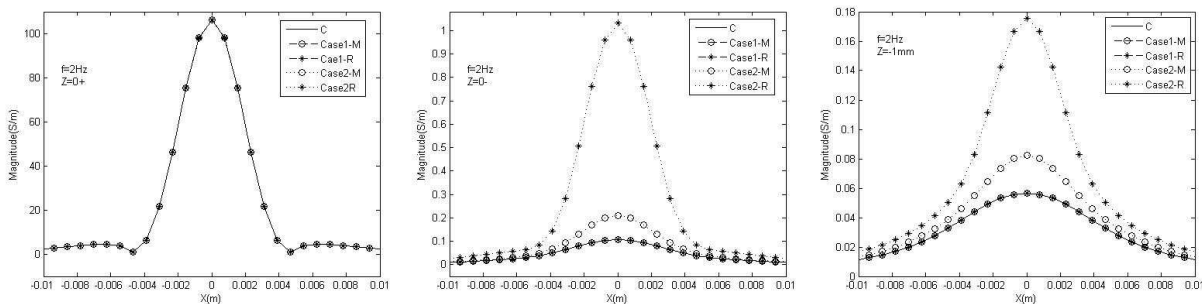


Figure 4: Magnitude of magnetic field $f = 2 \text{ Hz}$ in (i) $z = 0^+$, (ii) $z = 0^-$, and (iii) $z = -1 \text{ mm}$ (C: Constant Parameters), (M: Moderate Variation), (R: Rapid Variation).

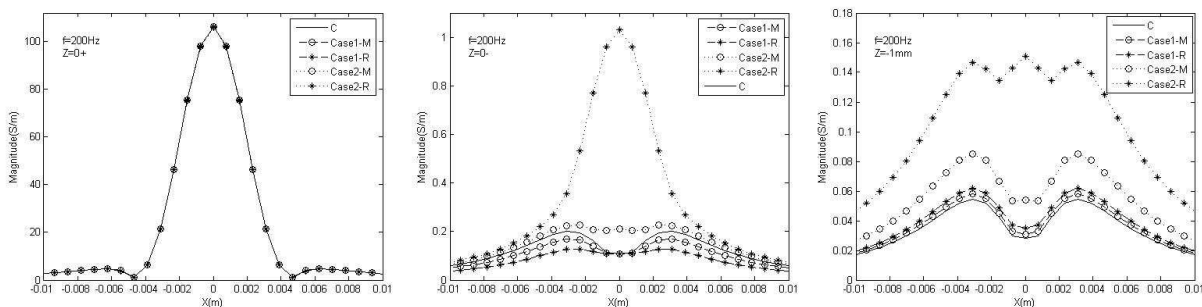


Figure 5: Magnitude of magnetic field $f = 200 \text{ Hz}$ in (i) $z = 0^+$, (ii) $z = 0^-$, and (iii) $z = -1 \text{ mm}$ (C: Constant Parameters), (M: Moderate Variation), (R: Rapid Variation).

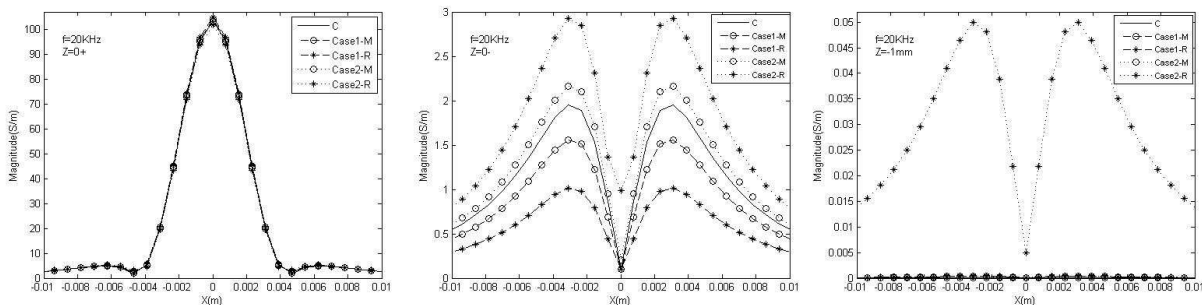


Figure 6: Magnitude of magnetic field $f = 20 \text{ kHz}$ in (i) $z = 0^+$, (ii) $z = 0^-$, and (iii) $z = -1 \text{ mm}$ (C: Constant Parameters), (M: Moderate Variation), (R: Rapid Variation).

In $z = 0^-$, The normal components of magnetic field are weak compare to $z = 0^+$. In this surface, if the conductivity of slab conductor decreases, the tangential components of magnetic field will decrease and its normal components will increase slightly (at high frequencies). On the other hand if the permeability of slab conductor decreases, both tangential and normal components of magnetic field will increase. Increasing in frequency leads to decreasing in normal components and increasing in tangential components.

In $z = -1$ mm, increasing in all parameters and frequency leads to decreasing of tangential components and normal components so that at high frequencies the magnitude of field is very close to zero. The only exception is the increasing of tangential component due to increasing frequency from $f = 2$ Hz to $f = 200$ Hz.

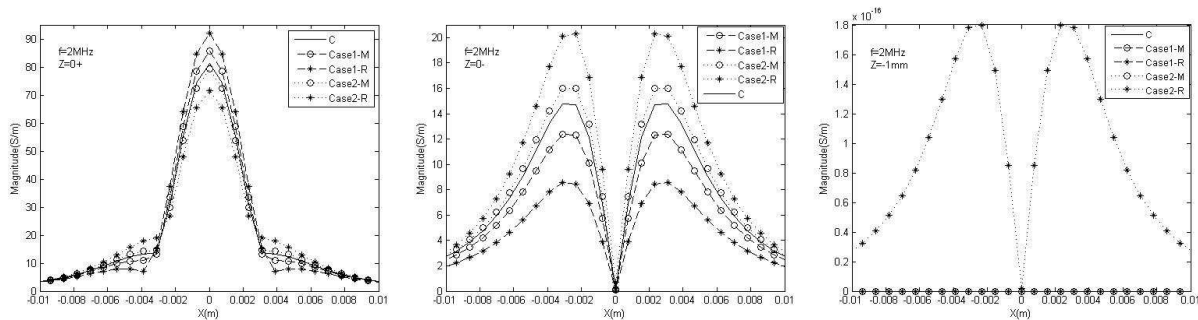


Figure 7: Magnitude of magnetic field $f = 2$ MHz in (i) $z = 0^+$, (ii) $z = 0^-$, and (iii) $z = -1$ mm (C: Constant Parameters), (M: Moderate Variation), (R: Rapid Variation).

4. CONCLUSION

In this study, the effects of variation of electromagnetic parameters of a slab conductor on the distribution of magnetic field caused by an elliptic exciter have been calculated. Some evidences such as corrosion, heat, and impact may decrease these parameters. A slab conductor with variable parameters is replaced by multi layer conductors with constant parameters. A semi-analytical potential scalar method is used for the analysis of the electromagnetic field distribution. This method employs the exponential functions in vertical direction (z) and Fast Fourier Transform (FFT) in two dimensions (x - y plane) to solve multilayer problems effectively. Using a computer program which provided in MATLAB, some example problems are solved in different cases of conductivity and permeability variations. The computed results are shown and analyzed. These results show the effects of parameters variations in several frequencies. These results can also provide some directions for measuring the amount of electromagnetic parameter variations in an inverse approach.

REFERENCES

1. Hammond, P., "The calculation of the magnetic field of rotating machines part 3," *Proc. IEE*, Vol. 5145, 508–515, 1962.
2. Baruch, G., G. Fibich, and S. Tsynkov, "Numerical solution of the nonlinear Helmholtz equation with axial symmetry," *J. Comput. Appl. Math.*, Vol. 204, No. 2, 477–492, 2007.
3. Sadeghi, S. H. H. and D. Mirshekar-Syahkal, "Accuracy of the image technique for calculating electromagnetic field induced at surface of ferromagnetic metal," *Rev. Prog. Nondest. Eval.*, Vol. 12, 2142–2150, Plenum Press, USA, 1993.
4. Panas, S. M. and A. G. Papayiannakis, "Eddy current in an infinite slab due to an elliptic current excitation," *IEEE Trans. Magn. J.*, Vol. 27, 4328–4337, 1991.
5. Tsaknakis, H. J. and E. E. Kriezis, "Field distribution due to a circular current loop placed in an arbitrary position above a conducting plate," *IEEE Trans. Geosci. R. Sensing J.*, Vol. 23, 834–840, 1985.
6. Uzal, E., I. Ozkol, and M. O. Kaya, "Impedance of a coil surrounding an infinite cylinder with an arbitrary radial conductivity profile," *IEEE Trans. Magn.*, Vol. 34, No. 1, January 1998.
7. Mirshekar-Syahkal, D. and R. F. Mostafavi, "Analysis technique for interaction of high-frequency rhombic inducer field with cracks in metals," *IEEE Trans. Magn.*, Vol. 33, No. 3, May 1997.

8. Dodd, C. V. and W. E. Deeds, “Analytical solution to eddy-current probe-coil problems,” *J. Appl. Phys.*, Vol. 39, 2829–2838, 1963.
9. Kolyshkin, A. A. and Remi Vailancourt, “Analytical solution to eddy-current testing problems for a layered medium with varying properties,” *IEEE Trans. Magn.*, Vol. 33, No. 4, July 1997.
10. Uzal, E., J. C. Moulder, S. Mitra, and J. H. Rose, “Impedance of coils over layered metals with continuously variable conductivity and permeability: Theory and experiment,” *J. Appl. Phys.*, Vol. 74, No. 3, 1993.
11. Fatehi, H. and M. Fatehi, “New scalar potential method for computation of electromagnetic variables in multilayer slab conductors,” *IEEE Trans. Magn.*, Vol. 41, No. 3, March 2005.

Developments in Noise Temperature of Cryogenically Cooled InP HEMT Amplifiers Versus Physical Temperature

R. J. Davis and A. Wilkinson

Jodrell Bank Centre for Astrophysics, Alan Turing Building, University of Manchester, M13 9PL, UK

Abstract— Radiometer design is largely driven by the need to suppress $1/f$ -type noise induced by gain and noise temperature fluctuations in the amplifiers which would be unacceptably high for a simple total power system. A differential pseudo-correlation radiometer is a scheme in which signals from the sky and from a black-body reference load are combined by a hybrid coupler, amplified in two independent amplifier chains, and separated out by a second hybrid.

Most HEMT amplifiers we have used seem to have a noise temperature that flattens out around 20 K physical temperature. In the case of the InP HEMT amplifiers used in Planck this is not the case and both noise temperature and gain vary with the physical temperature of the Front End Module (FEM), because the properties of the HEMT devices are still dependent on physical temperature at 20 K. In this paper measurements are shown which demonstrate this effect and an empirical behaviour is found which agrees with a theoretical model of M. Pospieszalski. If the temperatures are extrapolated to 4 K physical temperature, the noise temperature could be considerably improved.

1. INTRODUCTION

The advances made in cooler technology have now made it feasible to cool to temperatures around 4 K and below. Most work with transistor amplifiers have only cooled to 20 K. This is due both to the solid state physics of the devices used so far and to the cooler technology. In this paper, we show results of noise temperatures made on radiometers at 300 K down to 20 K physical temperatures.

2. RADIOMETER MEASUREMENTS

The LFI instrument on the ESA Planck spacecraft, with its arrays of cooled pseudo-correlation radiometers, represents an advance in the state of the art over the sensitivity of COBE and WMAP Bersanelli & Mandolesi 2000 [1]. It is particularly designed to have maximum freedom from systematic errors both in total power and polarization. The LFI radiometer design is largely driven by the need to suppress $1/f$ -type noise induced by gain and noise temperature fluctuations in the amplifiers which would be unacceptably high for a simple total power system. A differential pseudo-correlation scheme is adopted, in which signals from the sky and from a black-body reference load are combined by a hybrid coupler, amplified in two independent amplifier chains, and separated out by a second hybrid.

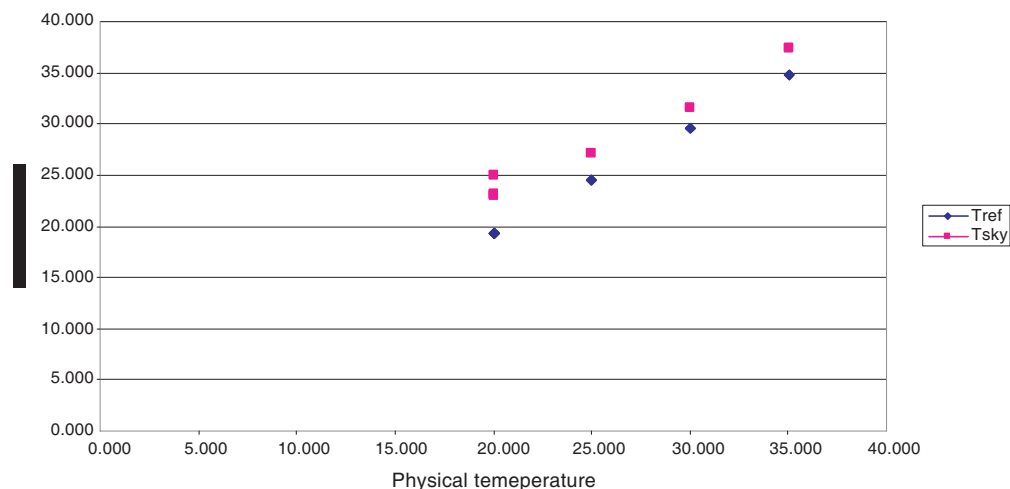


Figure 1: First 30 GHz amplifiers sensitivity to physical temperature.

The work that was done in the design and development of these radiometers involved testing them over a range of conditions both as part of the space qualification but also in determining their susceptibility to various physical conditions.

These results concerning temperature susceptibility have turned out to be interesting in their own right giving us an insight into the behaviour of InP HEMT devices as amplifiers.

Figures 1–5 show noise temperature versus physical temperature for one 30 GHz set and three 44 GHz sets of amplifiers over various temperature ranges.

These measurements do not represent the state of the art results especially when considering systematic errors but were conducted to examine the susceptibility to physical temperature. The measurements were made using waveguide loads controlled by a Lakeshore temperature controller to give Y-factors in the standard way. The cryogenic system was cooled by a standard closed cycle He refrigerator.

Figure 1 shows the example of a set of 30 GHz amplifiers over a range of 20 to 35 K. The linear behaviour seen does not go through 0 and if extrapolated gives a noise temperature of 6 K at the lowest physical temperatures. Fig. 2 shows the second set of 44 GHz amplifiers. The noise temperature drops linearly from a physical temperature of 300 K to 60 K and then flattens off below this temperature down to 20 K. Fig. 3 shows the third set of 44 GHz amplifiers and again is linear from 300 K to 60 K. It then appears to flatten off down to 35 K and then starts to steepen down to 20 K. Fig. 4 shows the first set of 44 GHz amplifiers which again are linear from 300 K to 60 K and then flatten down to 35 K and then steepen up in the final part from 35 K to 20 K. Fig. 5 shows the lower temperature range for this first set of amplifiers and linear fit down to a lowest noise temperature of 6 K at the lowest temperatures.

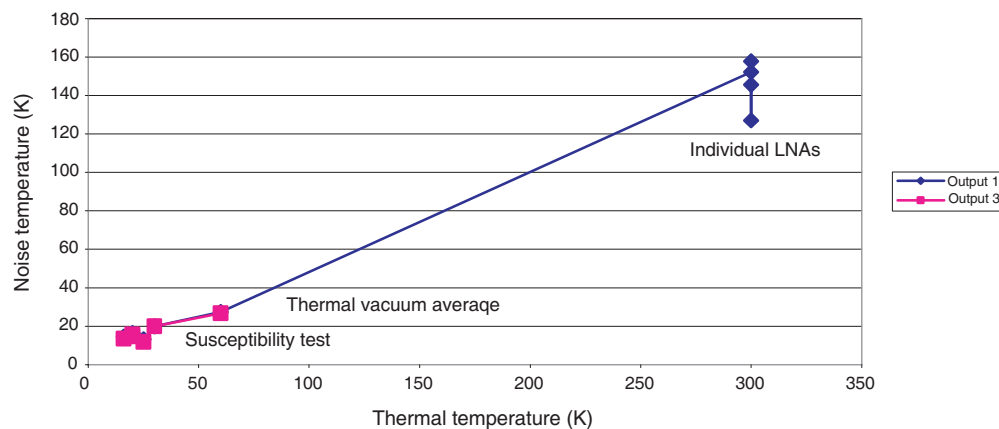


Figure 2: Second 44 GHz amplifiers sensitivity to physical temperature.

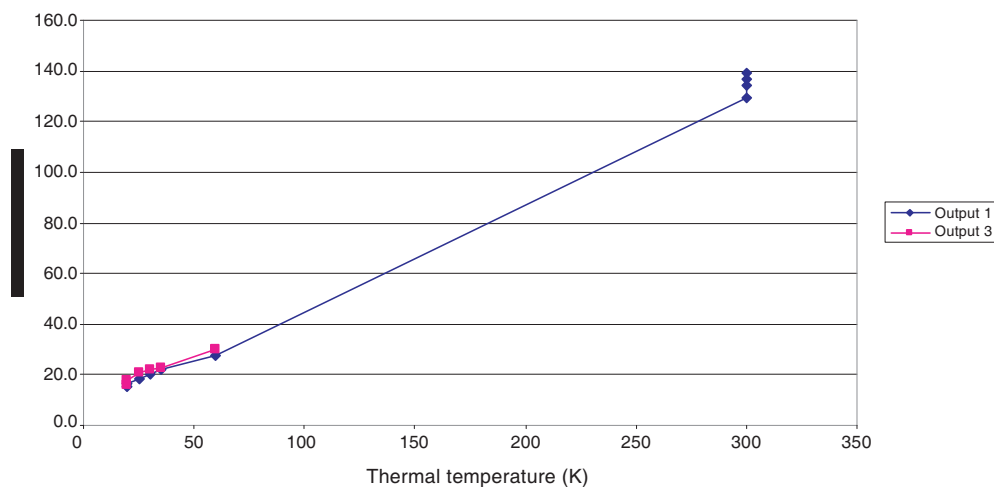


Figure 3: Third 44 GHz amplifiers sensitivity to physical temperature.

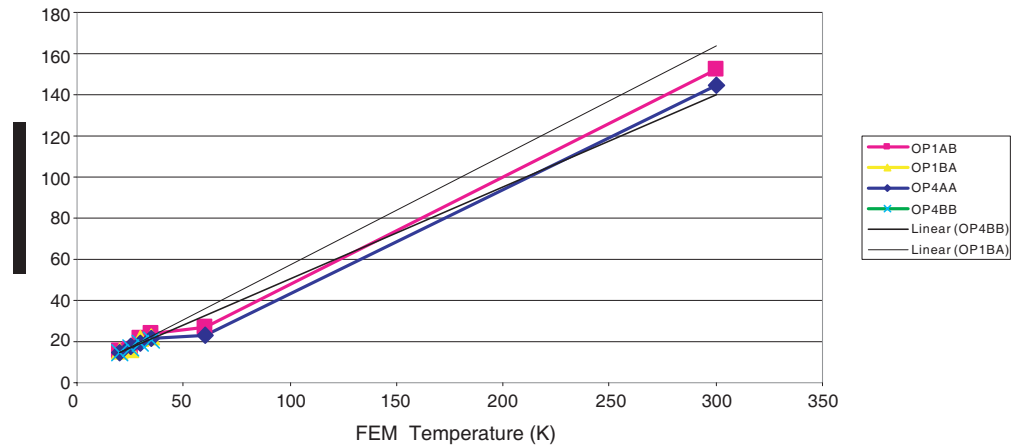


Figure 4: First 44 GHz amplifiers sensitivity to physical temperature.

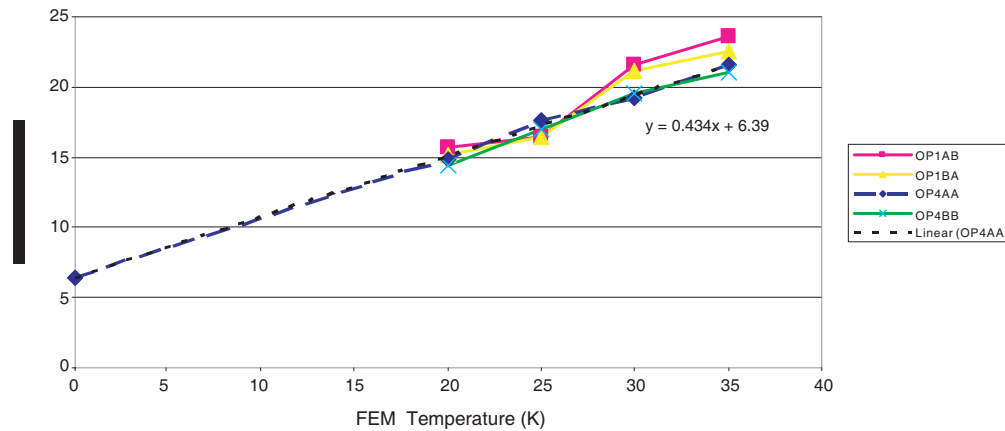


Figure 5: First 44 GHz amplifiers sensitivity to physical temperature with straight line fit to the lower temperature range from 35 to 25 K which shows that if this behaviour continues to 0 K a 6 K noise temperature would ensue.

The common result from all these measurements is a linear fit for the upper temperature range from 300 to 60 K. The experimentally observed dependence of noise temperature T_n of InP HEMTS vs ambient temperature T_a approximately decreases linearly with T_a between 300 and 80 K while below 80 K approximately decreases with $\sqrt{T_a}$ (Pospieszalski [2, 3]). In fact the data in Fig. 5 show the dependence of noise temperature approximately proportional to $\sqrt{T_a}$. The cryostat could not be taken much below 20 K, but for these amplifiers if the behaviour to 4 K physical temperature continues, extrapolation would have taken the noise temperature from ~ 15 K to ~ 6 K.

REFERENCES

1. Bersanelli, M. and N. Mandolesi, "Design concept of the planck-LFI instrument," *Astrophysical Letters Communications*, Vol. 37, No. 171, 2000.
2. Pospieszalski, M. W., L. D. Nguyen, M. Lui, T. Liu, M. A. Thompson, and M. J. Delaney, "Very low noise and low power operation of cryogenic AlInAs/GaInAs/InP HFET'S," *Proc. 1994 IEEE MTT-S Int. Microwave Symp.*, 1345–1346, San Diego, CA, May 1994.
3. Pospieszalski, M. W., "Extremely low-noise amplification with cryogenic FET's and HFET's: 1970–2004," *Microwave Magazine*, Vol. 6, No. 3, 62–75, Sep. 2005.

Design and Development of Low Cost and Light Weight Cavity and Microstrip Band Pass Filters for Communication Systems

Jagdish Shivhare¹ and S. B. Jain²

¹Department of Electronics and Communication, Institute of Technology and Management
Sector-23 A, Gurgaon, Haryana, India

²Department of Electronics and Communication
Indira Gandhi Institute of Technology, Indraprasth University Campus, Delhi, India

Abstract— The main objective to introduce the ABS plastic in place of metal and other substrates for cavity and planar structure communication filters is to reduce the weight and cost. The specific gravity of ABS plastic is 1.05 gm/cm^3 against 2.7, 8.5, 8.9 gm/cm^3 for commercial Aluminum, Brass and Copper respectively. The cost of ABS plastic substrate may be substantially less than compared to the cost of RT-Duroid laminates. Some Cavity Band Pass Filters at centre-frequencies of $(53.5 \pm 1.5) \text{ MHz}$, $(86.5 \pm 4) \text{ MHz}$, $(324 \pm 4) \text{ MHz}$, $(600 \pm 9) \text{ MHz}$, $(1200 \pm 150) \text{ MHz}$, $(1537.5 \pm 7.5) \text{ MHz}$, $(1636 \pm 10) \text{ MHz}$, $(4190 \pm 20) \text{ MHz}$, $(4590 \pm 20) \text{ MHz}$, $(5.850\text{--}5930) \text{ GHz}$ have been developed and tested. Two-hairpin line filters at $1537.5 \pm 10 \text{ MHz}$ and $1575.5 \pm 10 \text{ MHz}$, also have been developed and tested [1].

1. INTRODUCTION

Presently metal is invariably used to make electrical filters. Therefore their cost is high. The electrical characteristic of ABS plastic show minor changes at normal operating temperature, humidity and frequency. The dielectric properties are sufficiently good. ABS plastic exhibit a flat module curve over a wide temperature range. Dimensional tolerance can be maintained with 0.003 mm/mm . Machining characteristics are similar to those of non-ferrous metals. The plastic may be drilled, punched, die-cut, routed, sawn and turned. Favorable electrical, mechanical physical and environmental properties may increase its applicability as an alternative to metal, to fabricate precise filters such as helical, combline, interdigital and coaxial cavity band pass filter in different frequency ranges. The ABS plastic may be used in place of PTFE substrate for planar structures [2].

The performance of two hairpin line (micro strip) band pass filters at 1537.5 MHz and 1575.5 MHz have been verified with the help of standard filters. The achieved insertion loss is high, due to higher dissipation factor. The insertion loss comes down closer to the loss of soft PTFE substrate (RT-Duroid # 5870) of 1.58 mm thick with dielectric constant of 2.32 by doubling the thickness of ABS Plastic sheet. However the 3 dB bandwidth is also doubled. So, if insertion loss/band width is not criteria, the very low cost hair pin line filters may be developed by using the ABS plastic in place of any other PTFE substrate [3].

2. DESIGN THEORY

The existing design theory for any type of cavity band pass filter is applicable. No Correction, in design is required while using ABS plastic in place of metal. However, a few graphs have to be generated to use the ABS plastic as a substrate for hairpin line Structure. Here, the design theory available for RT-Duroid #5870, of dielectric constant 2.32 and thickness 1.58 mm has been used to calculate the dimensions of hair pin line band pass filter [4].

3. DESIGN PROCEDURE

The existing design procedure and tables for any type of cavity, helical, combline, inter digital, coaxial cavity filters may be utilized. Similarly, design procedures available for planar structures such as parallel coupled, hairpin line band pass filters may be used [1–3].

4. IMPORTANT PROPERTIES OF ABS PLASTIC

The electrical characteristic of ABS plastic show minor changes with temperature, humidity and frequency. The dielectric properties are sufficiently good to be considered for a number of electrical applications. It exhibits a flat modulus curve which varies only slightly over a wide temperature range. ABS exhibits high impact values. Good impact figures are maintained even at temperature

as low as -40 deg C. Unlike other thermoplastics, it is not significantly affected by variation in strain rate.

The ABS is resistant to weak acids and inorganic bases. Concentrated nitric and sulphuric acid produce disintegration. It is swelled, softened or dissolve by the most of low order aromatics, Ketones, esters etc. The ABS plastic can be metallised. Therefore an enclosure made of metallised ABS plastic behaves electrically in a similar manner as the metallic enclosure.

5. SILVER PLATING ON ABS PLASTIC

ABS with 10% Butadine is more suitable for electroplating than ABS with 16 to 27% Butadine. Several trials were conducted for electroplating on ABS plastic. The articles are immersed in mixture of chromic and sulphuric acid to improve mechanical adhesion. Poor etching leads to skip plating or poor adhesion of the plate and possible blistering. Thus etched articles are to be treated with sensitizer and activators Stannous chloride & Palladium chloride solutions are used for this purpose. The deposited palladium nuclei on the plastic surface, initiates electroless plating of copper or nickel or gold or other metals.

We had carried out electroless copper deposition for our work. The purpose of plating on ABS is to get highly conductive coating. For this, it is finally deposited with electro plated copper and silver.

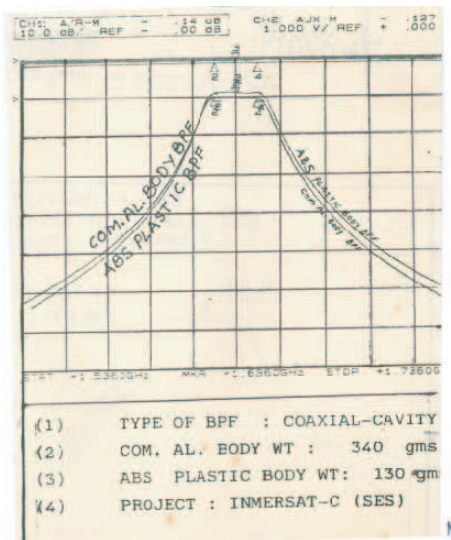


Figure 1: Coaxial cavity band pass filter.

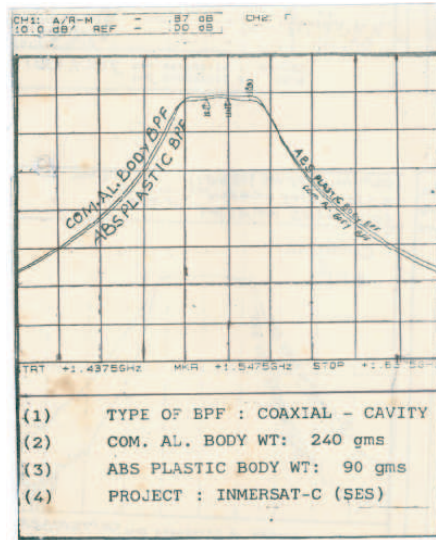


Figure 2: Coaxial cavity band pass filter.

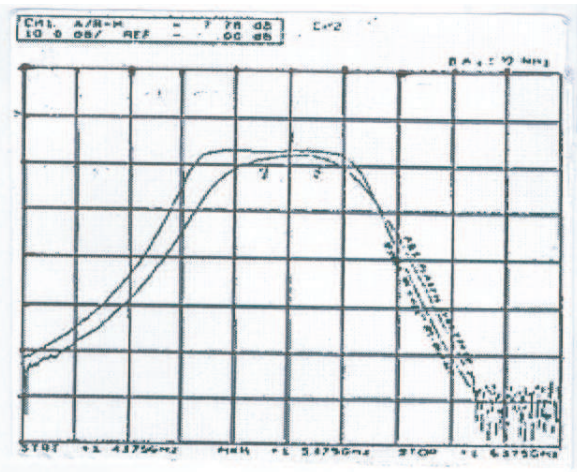


Figure 3: Hair pin line Microstrip band pass filter.

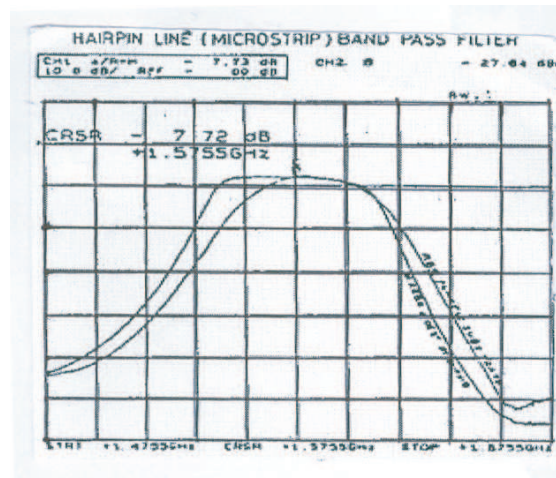


Figure 4: Hair pin line Microstrip band pass filter.

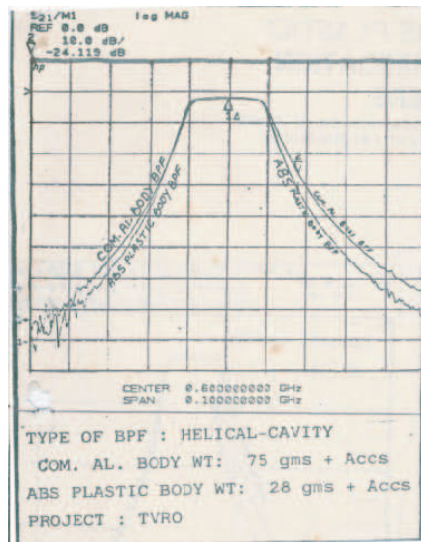


Figure 5: Helical band pass filter.

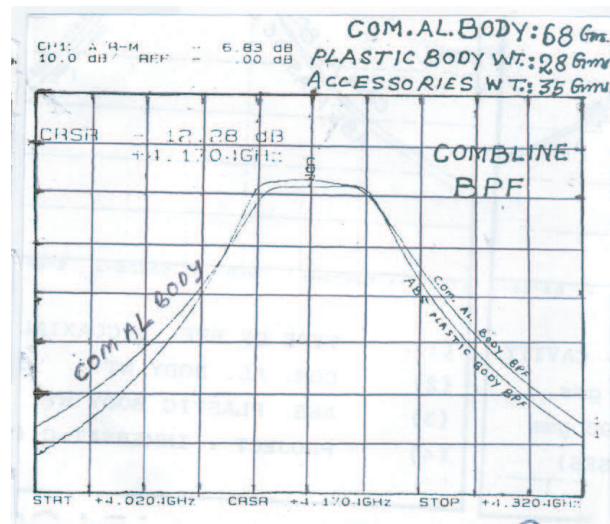


Figure 6: Compline band pass filter.

6. CONCLUSION

A number of cavity and microstrip band pass filters have been tried upto 6 GHz.

The performance of the cavity as well as microstrip filters have been tested in temperature range of -20 deg C to $+60$ deg C. There is minor shift in the centre frequency without affecting band width and stop band attenuation. It has been noticed that the shift in the frequency depends upon the size and structures of the filters. Particularly, at the higher frequencies, the size of the fingers in compline filter is very small and becomes a cause of shift in centre frequency. But it is less than the commercial aluminum body filter. The observed frequency shift in hair pin line filter is less than that in the compline cavity filters. Electronic performance is fully satisfactory, but mechanical performance is yet to be improved.

ACKNOWLEDGMENT

The author wishes to acknowledge the assistance and support of the technical staff of Institute of Technology and Management, Gurgaon.

REFERENCES

1. Zerev, A. I., *Handbook of Filter Synthesis*, John Wiley and Sons, New York, 1967.
2. Atia, A. I. and A. E. Willand, "Inter-cavity coupling," *IEEE Trans. MTT*, Vol. 23, No. 6, 519–521, June 1975.
3. Arneseri, R. F., "Coupling loops/tapping positions for cavity band pass filters," *Microwave and RF*, November 1986.
4. Matthaie, G. L., et al., *Microwave Filter, Impedance Matching and Coupling Structures*, Dedham, MA, Architect, House, 1998.
5. Levy, R., R. V. Synder, and G. L. Metthaei, "Design of helical band pass filters" *IEEE Trans. MTT*, March 2002.
6. Broomfield, C. and J. Everard, "High Q helical filters," *IEEE Explorer*, May 4–8, 2003.
7. "Helical bandpass filter design," *IEEE Explorer*, October 2007.
8. <http://www.helicalfilters.com>.
9. <http://microwaveproducts.com>.

Temperature Dependable Microwave Dielectric Model for Frozen Soils

V. L. Mironov and Yu. I. Lukin

The Kirensky Institute of Physics of SB, RAS, Russia

Abstract— In this paper, the results of measurement of complex dielectric permittivity of loam soil in the range of temperatures from 25°C to –20°C and frequencies from 0.5 GHz to 15 GHz are given and the temperature dependable dielectric model for this soil has been developed. The measurements were carried out in the course of both of freezing and thawing process with the phase transition effects being considered.

1. INTRODUCTION

Data processing in the radar and radiothermal remote sensing of the land requires the knowledge about influence of the geophysical parameters such as, temperature, soil moisture, and mineralogy on the soil complex permittivity (CP) frequency spectra. Therefore, it is significant to develop adequate dielectric model which takes into account these geophysical parameters. There is the generalized refractive mixing dielectric model (GRMDM) for moist soils suggested in [1], and [2] for thawed and frozen soils, respectively. This model allows to predict the CP frequency spectra for an individual moist soil as a function of spectroscopic parameters dependable on soil texture and temperature. In the case of thawed soils, the GRMDM has been advanced to establish a parameterized physical dependence of spectroscopic parameters on the temperature [3, 4] giving rise to the temperature dependable generalized refractive mixing dielectric model (TD GRMDM). Meanwhile, the TD GRMDM in the case of frozen soils has not been developed yet.

To solve this problem we conducted measurement of the CP frequency spectra for a loam soil in the range of temperatures from 25°C to –20°C and frequencies from 0.5 GHz to 15 GHz. On the basis of this dielectric data the TD GRMDM was developed for this soil. The measurements were conducted and the respective TD GRMDM worked out in the case of both freezing and thawing processes. While processing the dielectric data measured, we dealt with such types of soil water as liquid and icy unbound water, as well as bound water, having different dielectric properties. The relevant GRMDM spectroscopic parameters were separately determined for all the types of soil water as a function of the temperature. Finally, an assemblage of physical parameters consisting of volumetric expansion coefficients, starting low frequency dielectric constants, activation energies, entropies of activation, starting conductivities, and conductivity incriminations were derived to turn the GRMDM into a TD GRMDM pertaining to a given soil texture, with main emphasis on being made on frozen soil condition. These physical parameters, in conjunction with dry soil CP and maximum bound water fraction value, were shown to be an all-sufficient set of parameters to make possible predictions of the moist soil CP as a function of frequency, volumetric moisture, and temperature.

2. CONCEPT OF TD GRMDM

According to the GRMDM version established in [3], the dielectric constant (DC) ϵ' and loss factor (LF) ϵ'' can be calculated using the following formulas:

$$\epsilon' = n^2 - \kappa^2, \quad \epsilon'' = 2n\kappa; \quad n^* = \sqrt{\epsilon} = n + i\kappa, \quad \epsilon = \epsilon' + i\epsilon'', \quad (1)$$

where ϵ , and n^* are complex dielectric constant and complex index of refraction, while n and κ are the real and imaginary parts of the complex index of refraction.

The complex index of refraction of soil-water mixture including description in case both of free soil water (FSW) and bound soil water (BSW) can be expressed in the following form:

$$\frac{n_s^*(m_g, f, t) - 1}{\rho_d(m_g)} = \begin{cases} \frac{n_m^* - 1}{\rho_m} + \frac{n_b^*(f, t) - 1}{\rho_b} \cdot m_g, & 0 \leq m_g \leq m_{gt}; \\ \frac{n_m^* - 1}{\rho_m} + \frac{n_b^*(f, t) - 1}{\rho_b} \cdot m_{gt} + \frac{n_q^*(f, t) - 1}{\rho_q} \cdot (m_g - m_{gt}), & m_{gt} \leq m_g, \end{cases} \quad (2)$$

for the temperatures $t \geq t_f$ in case of freezing cycle.

$$\frac{n_s^*(m_g, f, t) - 1}{\rho_d(m_g)} = \begin{cases} \frac{n_m^* - 1}{\rho_m} + \frac{n_b^*(f, t) - 1}{\rho_b} \cdot m_g, & 0 \leq m_g \leq m_{gt}; \\ \frac{n_m^* - 1}{\rho_m} + \frac{n_b^*(f, t) - 1}{\rho_b} \cdot m_{gt} + \frac{n_c^*(f, t) - 1}{\rho_c} \cdot (m_g - m_{gt}), & m_{gt} \leq m_g, \end{cases} \quad (3)$$

for the temperatures $t < t_f$ in case of freezing. Here, t_f is the soil freezing points. A set of parameters in (2) and (3) consists of: 1) bulk soil density soil ρ_d , soil mineralogy composite parameters $\frac{n_m - 1}{\rho_m}$ and $\frac{k_m}{\rho_m}$; 2) gravimetric soil moisture m_g , which is the mass ratio of water to dry material in a sample; 3) maximum bound soil water fraction m_{gt} ; 4) real indexes of refraction (RIR) n_m , n_q , n_b , and n_c , imaginary indexes of refraction (IIR) κ_m , κ_q , κ_b , and κ_c , specific densities ρ_d , ρ_m , ρ_b , ρ_q , and ρ_c , regarding bulk soil, mineral content of soil, bound soil water (BSW), liquid soil water (LSW), and icy soil water (ISW), respectively. RIR and IIR are the following functions of DC and LF:

$$n_p = \frac{1}{\sqrt{2}} \sqrt{\sqrt{\epsilon_p'^2 + \epsilon_p''^2} + \epsilon_p'}, \quad (4)$$

$$\kappa_p = \frac{1}{\sqrt{2}} \sqrt{\sqrt{\epsilon_p'^2 + \epsilon_p''^2} - \epsilon_p'}. \quad (5)$$

Here the value p represent all the substances and should be substituted by b , q , and c to account for an appropriate type of soil water. The DC and LF as a function of frequency for all the types of soil water are supposed to follow the Debye formulas:

$$\epsilon_p' = \epsilon_{\infty p} + \frac{\epsilon_{0p} - \epsilon_{\infty p}}{(1 + 2\pi f \tau_p)}, \quad (6a)$$

$$\epsilon_p'' = \frac{\epsilon_{0p} - \epsilon_{\infty p}}{(1 + 2\pi f \tau_p)} 2\pi f \tau_p + \frac{\sigma_p}{2\pi \epsilon_r f}. \quad (6b)$$

Here ϵ_{0p} and $\epsilon_{\infty p}$ are the DCs in the low-frequency and high-frequency limit, respectively, f is the wave frequency in Hertz, τ_p is the relaxation time in second, σ_p is the ohmic conductivity in S/m, and ϵ_r is the DC for free space, which is equal to $8.854 \cdot 10^{-12}$ F/m.

Similar to the approach used for the thawed soils [4], the value of ϵ_{0p} as a function of temperature is expressed in the form of Clausius-Massotii formula:

$$\epsilon_{0p}(T) = \frac{1 + 2 \exp(F_p(t_s) - \beta_p(t - t_s))}{1 - 2 \exp(F_p(t_s) - \beta_p(t - t_s))}, \quad (7)$$

where β_p is the volumetric expansion coefficient, t and t_s are current and starting temperatures by centigrade. The function $F_p(t)$ can be written in the form

$$F_p(T) = \ln \left(\frac{\epsilon_{0p}(t) - 1}{\epsilon_{0p}(t) + 2} \right). \quad (8)$$

For the dependence of relaxation time the Debye formula is used:

$$\tau_p(T) = \frac{48 \cdot 10^{-12}}{T} \exp \left(\frac{\psi_p}{T} - \theta_p \right), \quad (9)$$

where the value τ_p is given in picosecond, the parameters, $\psi_p = \Delta H_p/R$ and $\theta_p = \Delta S_p/R$, are proportional to the activation energy, ΔH_p , and entropy of activation, ΔS_p , respectively, T is absolute temperature, and R is the universal gas constant. Finally, the conductivity, σ_p , has a linear dependence on the temperature, like that of the ionic solutions:

$$\sigma_p(t) = \sigma_p(t_s) + \beta_{\sigma p}(t - t_s). \quad (10)$$

Here, $\beta_{\sigma p}$ is the temperature incrementation coefficient, while $\sigma_p(t_s)$ is the value of conductivity at a starting temperature t_s . The temperature in (10) is to be assigned in degrees by centigrade.

As a result, to make dielectric predictions, the temperature dependable GRMDM needs the input parameters shown in Table 1.

Table 1: Temperature dependable GRMDM parameters.

n_d	Dry soil RI
κ_d	Dry soil NAC
m_{gt}	Maximum BW fraction
$\epsilon_{0b}(ts)$	Starting low frequency limit DC for BSW
$\beta_b(K^{-1})$	Volumetric expansion coefficient for BSW
$\psi_b(K)$	Activation energy coefficient for BSW
θ_b	Entropy of activation coefficient for BSW
$\sigma_b(ts)(S/m)$	Starting conductivity for BSW
$\beta_{\sigma b}(S/mK)$	Temperature incrementation coefficient for conductivity for BSW
$\epsilon_{0u}(ts)$	Starting low frequency limit DC for FSW
$\beta_u(K^{-1})$	Volumetric expansion coefficient for FSW
$\psi_u(K)$	Activation energy coefficient for FSW
θ_u	Entropy of activation coefficient for FSW
$\sigma_u(ts)(S/m)$	Starting conductivity for FSW
$\beta_{\sigma u}(S/mK)$	Temperature incrementation coefficient for conductivity for FSW

3. TEMPERATURE DEPENDABLE DIELECTRIC MODEL FOR LOAM SOIL

The measurements of spectrum of CDP of the loam soil of different moisture in the range of temperatures 25°C to –20°C and frequencies from 0.5 GHz to 15 GHz has been made. The measurements have been made in the process of both freezing and thawing. While processing the dielectric data measured, we dealt with such types of soil water as liquid and icy unbound water, as well as bound water, having different dielectric properties. According to [1] the parameters of temperature dependable GRMDM are derived from GRMDM with considering a set of temperatures. Hereby at the first step the parameters of GRMDM of soil considered for every temperature have been found with the same fitting procedure as used in [1, 2]. These parameters are given in Table 2. Since icy water in the soil depends on temperature weakly and can be accepted as constant we were not able to calculate τ_u and σ_u with the fitting routine and these parameters are accepted to be equal to those corresponding to the ice.

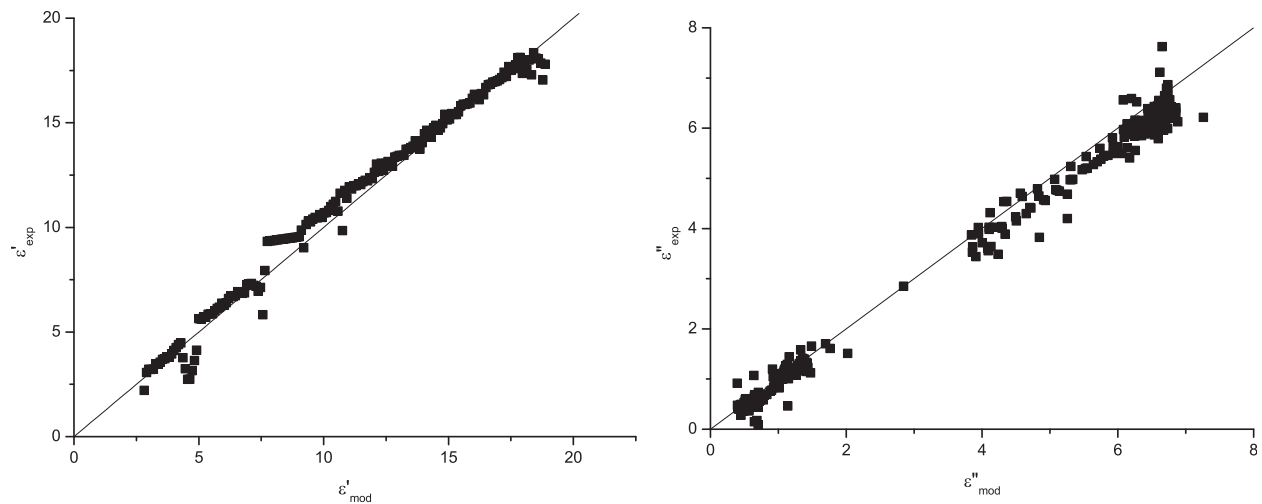
At the next step the parameters of temperature dependable GRMDM of the loam soil has been found with fitting by (7)–(10). The parameters derived are given in Table 3 and do not dependent on the temperature, nevertheless ensuring dependence of the complex dielectric permittivity on the temperature.

Table 2: GRMDM spectroscopic parameters at different temperatures.

Temperature, °C	Spectroscopic parameters								
	$\frac{n_m-1}{\rho_m}$	$\frac{\kappa_m}{\rho_m}$	$m_{gt}(g/g)$	ϵ_{0b}	$\tau_b(ps)$	$\sigma_b(S/m)$	ϵ_{0u}	$\tau_u(ps)$	$\sigma_u(S/m)$
25	0.39	0	0.09	48.8	14.41	1.48	92.1	9.13	1.16
20				48.6	14.38	1.38	93.1	10.23	1.07
10				49.6	18.09	1.22	102.1	13.22	0.98
5				48.1	18.84	1.21	104.2	16.93	0.68
0				48.1	22.87	1.08	101.1	17.84	0.82
–3				44.8	23.43	1.11	102.9	19.36	0.83
–6				45.9	26.50	0.98	7.3	∞	0
–8				48.4	24.88	0.89	6.9	∞	0
–10				33.5	29.63	0.74	6.6	∞	0
–15				25.6	39.99	0.70	6.5	∞	0
–20				20.8	48.94	0.60	6.2	∞	0

Table 3: Temperature dependable GRMDM parameters for the loam soil.

Water type	$\epsilon_{0p}(t_{sp})/t_{sp}$	$\epsilon_{\infty p}(t)$	$\beta_p(K^{-1})$	$\psi_p(K^{-1})$	θ_p	$\sigma_p(t_{sp})(S/m)/t_{sp}$	$\beta_{\sigma p}(S/m \cdot K^{-1})$	ρ_p
Liquid $p = q, t > t_f$	92/25°C	4.9	0.00012	2032	2.831	$1.16 \cdot 2\pi\epsilon_r f / 25^\circ\text{C}$	0.01414	1
Icy water $p = q, t < t_f$	6.2/-20°C	6.2	0	∞	0	0	0	0.915
Bound $p = b,$ $t > t_f$	48.8/25°C	14.8	-0.00014	1455	0.472	$1.46 \cdot 2\pi\epsilon_r f / 25^\circ\text{C}$	0.01907	1
Bound $p = b,$ $t < t_f$	46.1/-6°C	8.78	-0.00585	2625	4.831	$1.46 \cdot 2\pi\epsilon_r f / 25^\circ\text{C}$	0.01907	1

Figure 1: Comparison of measured values of ϵ' and ϵ'' with calculated values based on the temperature dependable GRMDM.

Since we considered water in soil to be in different phase states, the parameters in Table 3 are given for each type of different phase states: liquid water and ice water. The bound water was not found to be in frozen state. Nevertheless, the transition phase process in bound water has been observed at the negative temperature and two different states of bound water were considered separately.

To estimate the correlation between the predictions obtained with the temperature dependable GRMDM and the measured Dcs and LFs, the latter were plotted in Fig. 1 versus predicted values were calculated with the use of the formulas (1)–(10) and parameters shown in Table 3. It can be seen that the measured and calculated values of Dcs and LFs exhibit a high degree correlation with coefficient of standard deviation to be $SD = 0.55$ for dielectric constant and $SD = 0.27$ for loss factor.

4. CONCLUSIONS

In this paper, the results of measurement of CDP of loam soil in the range of temperatures from 25°C to -20°C and frequencies from 0.5 GHz to 15 GHz are given and the temperature dependable dielectric model for this soil has been developed. The measurements were carried out in case both of the freezing process and the thawing process in order to identify phase transition effect. A challenging aspect in terms of data processing technique is the presence of bound water (as high as 9% mass). Because of that, we dealt with two type of water (bound and unbound) in the sample of soil which have different dielectric properties. In this paper both types of water were processed separately.

As a result, an assemblage of parameters consisting of volumetric expansion coefficients, starting low frequency dielectric constants, activation energies, entropies of activation, starting conductivi-

ties, and conductivity incrementations were derived for both of positive and negative temperature range. These, in conjunction with dry soil complex dielectric constant and maximum bound water fraction, were shown in [4] to be an all-sufficient set of parameters to make possible predictions of complex dielectric constants of moist soil as a function of frequency, volumetric moisture, and temperature. The analyses proved the temperature dependable GRMDM to provide for the CDP prediction with the absolute errors $SD = 0.55$ and $SD = 0.27$ for DC and LF respectively in terms of standard deviation with including frozen soils.

The results obtained can be extended to apply to any type of soil, since it includes the physical parameters, unlike empirical fitting.

ACKNOWLEDGMENT

The work was supported by the RFBR-CNRS grant No. 09-05-91061.

REFERENCES

1. Mironov, V. L., M. C. Dobson, V. H. Kaupp, S. A. Komarov, and V. N. Kleshchenko, "Generalized refractive mixing dielectric model for moist soils," *IEEE Trans. Geosci. Remote Sensing*, Vol. 42, No. 4, 773–785, 2004.
2. Mironov, V. L., V. H. Kaupp, S. A. Komarov, and V. N. Kleshchenko, "Frozen soil dielectric model using unfrozen water spectroscopic parameters," *Proc. IGARSS'03*, Vol. 7, 4172–4174, 2003.
3. Mironov, V. L., S. V. Savin and R. D. Roo, "Dielectric spectroscopic model for tussock and shrub tundra soils," *Proc. IGARSS'07*, 726–731, 2007.
4. Mironov, V. L. and S. V. Fomin, "Dependable microwave dielectric model for moist soils," *PIERS Online*, to be published, Beijing, 2009.

Mobile Location Method of Radio Wave Emission Sources

P. Gajewski, C. Ziólkowski, and J. M. Kelner

Military University of Technology, Poland

Abstract— This paper deals with the new location method of radio wave sources, based on the Doppler effect. In this method, position of the radio signal source is calculated on the basis of momentary frequency measurements taken by mobile receiver. Theoretical and simulating analysis of the presented methodology was made before empirical verification process was introduced. General outline of the method on the basis of the Doppler effect and preliminary empirical verification results are presented.

1. INTRODUCTION

Over that last decade, the emerging location service of electromagnetic waves sources has found numerous applications in the commercial as well as the military radio systems. In this paper, we concentrate on location service of a subscriber in radio communication networks.

Several methods for subscriber location in radio communication nets have been already presented like [1] ÷ [5]: access station identification — so-called Cell ID or Cell of Origin (CoO), Angle of Arrival (AoA), Time of Arrival (ToA), Time Difference of Arrival (TDoA), Received Signal Strength (RSS), Global Positioning System (GPS).

Each of foregoing methods have some advantages and some disadvantages too. Disadvantages of foregoing methods make difficult for practical utilization. These factors have motivated the development of new location methods based on analytic description of the Doppler effect. The analytic description of this problem [6] makes it possible to calculate exactly the value of the received signal parameters especially frequency offset. In this paper, the theoretical basis as well as empirical verification of frequency offset measurement is described.

2. ANALYTIC DESCRIPTION OF THE DOPPLER EFFECT

The analytic description of the Doppler effect results from solution of Maxwell equations. In the case of free space, the Faraday and the Ampere equations as well as the property of vector field double rotation are the basis for the following wave equation describing the vector of the electric field strength:

$$\frac{1}{c^2} \frac{\partial^2}{\partial t^2} \mathbf{E}(\mathbf{x}, t) + \Delta \mathbf{E}(\mathbf{x}, t) = -\mu_0 \frac{\partial}{\partial t} \mathbf{i}_0(\mathbf{x}, t) \quad (1)$$

where $\mathbf{x} = (x, y, z)$ is the space co-ordinate, $\mathbf{i}_0(\mathbf{x}, t) = (i_x(\mathbf{x}, t), i_y(\mathbf{x}, t), i_z(\mathbf{x}, t))$ is the vector of density of current density, $\Delta = \frac{\partial^2}{\partial x^2} + \frac{\partial^2}{\partial y^2} + \frac{\partial^2}{\partial z^2}$ — Laplacian.

In [8] we have concentrated on two considerations:

- the linear antenna system i.e., we assume that the current density vector has the form

$$\mathbf{i}_0(\mathbf{x}, t) = (0, 0, i_z(\mathbf{x}, t)) = i_0(t) \cdot I(z) \cdot \delta(x) \cdot \delta(y) \quad (2)$$

- the motion of signal source model in x co-ordinate direction with v velocity.

Thus the problem has been reduced to solve the following second orders partial differential equation.

$$\frac{1}{c^2} \frac{\partial^2}{\partial t^2} E(\mathbf{x}, t) + \Delta E(\mathbf{x}, t) = -\mu_0 \frac{\partial}{\partial t} [i_0(t) \cdot I(z) \cdot \delta(x - vt) \cdot \delta(y)] \quad (3)$$

The analytic form of the of electric field phase generated by moving transmitter is ([6]):

$$\Phi(\mathbf{x}, t) = \omega_1 t - \beta_1 k x - \beta_1 R_0(\mathbf{x}, t) - \frac{\pi}{2} \quad (4)$$

where $R_0(\mathbf{x}, t) = \sqrt{(x - vt)^2 + (1 - k^2) \cdot (y^2 + z^2)}$, $\beta_1 = \omega_1/c = \beta/(1 - k^2)$, $\omega_1 = \omega_0/(1 - k^2) = 2\pi f_0/(1 - k^2)$, $k = v/c$.

Hence, the Doppler frequency expresses the following dependence ([7])

$$f_D(\mathbf{x}, t) = f(\mathbf{x}, t) - f_0 = \frac{k}{1 - k^2} \left[k + \frac{x - vt}{R_0(\mathbf{x}, t)} \right] f_0 \quad (5)$$

The $f_D(\mathbf{x}, t)$ is linear dependent on the frequency carrier, whereas the dependence on velocity and space co-ordinates has a more complex character. Location calculation are made on the basis of the above formula and the described value of Doppler frequency shifts as a function of movement and coordinates of signal source parameters. The temporal frequency value $f(\mathbf{x}, t) = f_0 + f_D(\mathbf{x}, t)$ measurement over mobile station is the basis of the new method of the subscriber location.

3. NEW LOCATION METHOD OF RADIO SIGNALS SOURCES

The illustration of the subscriber location methodology is shown in Figure 1. Measurement of the Doppler frequency offset is base of this method. The Doppler curves for five different locations of subscriber (station) are presented in Figure 2. The diverse courses of the Doppler curves (Figure 2) are characteristic for every subscriber location. It determinates methodology of the frequency offset value using to three-dimensional location.

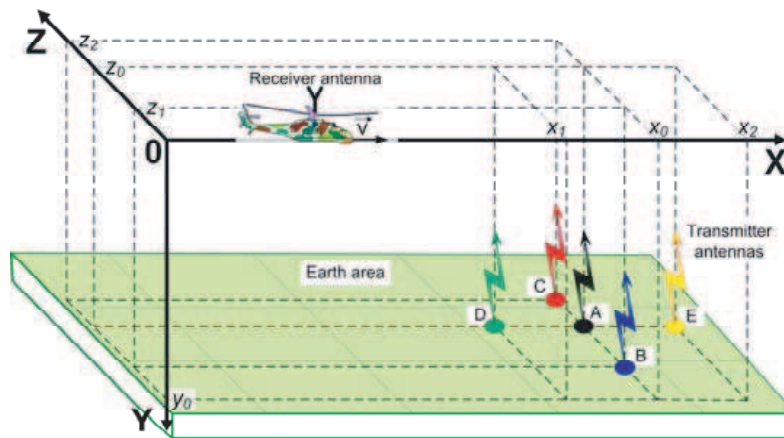


Figure 1: Space structure of the mutually mobile station and five station locations [6].

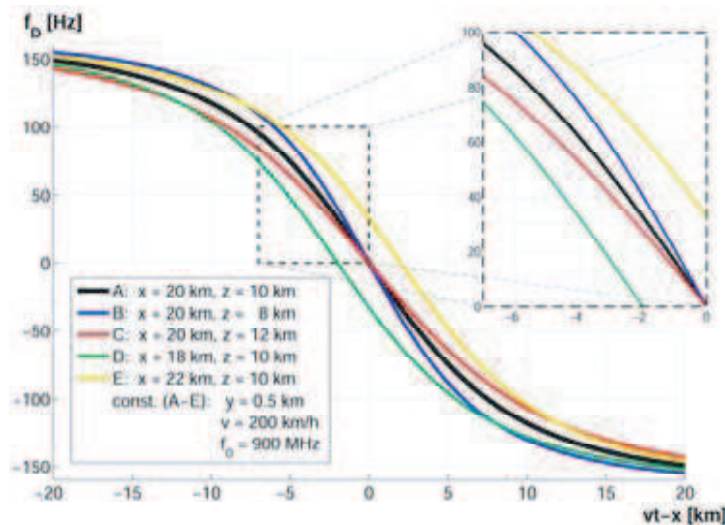


Figure 2: Doppler curves vs. the mobile station to subscriber $vt - x$ distance.

After elementary transformation of the expression (5) for two moments t_1 and t_2 the formulas

described x and z co-ordinates are following ([8] ÷ [9]):

$$\begin{cases} x = v \frac{t_2 A(t_1) - t_1 A(t_2)}{A(t_1) - A(t_2)}, \\ z = \pm \sqrt{\frac{\left[\frac{v(t_1 - t_2) A(t_1) A(t_2)}{A(t_1) - A(t_2)} \right]^2}{1 - k^2} - y^2}, \end{cases} \quad (6)$$

where

$$A(t) = \frac{\sqrt{1 - F^2(t)}}{F(t)}, \quad F(t) = \frac{f_D(t)}{f_0} \frac{1 - k^2}{k} - k \quad (7)$$

This methodology and also method of bearing and three-dimensional location has been described in patent application [8].

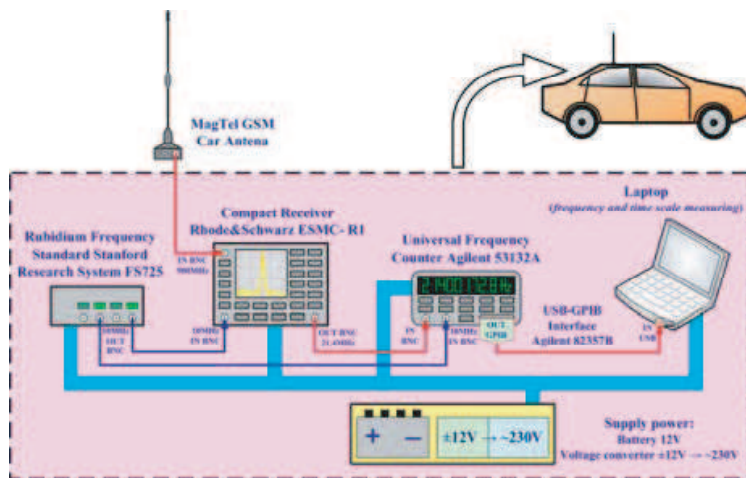


Figure 3: Structure of mobile test stand used in empirical verification.

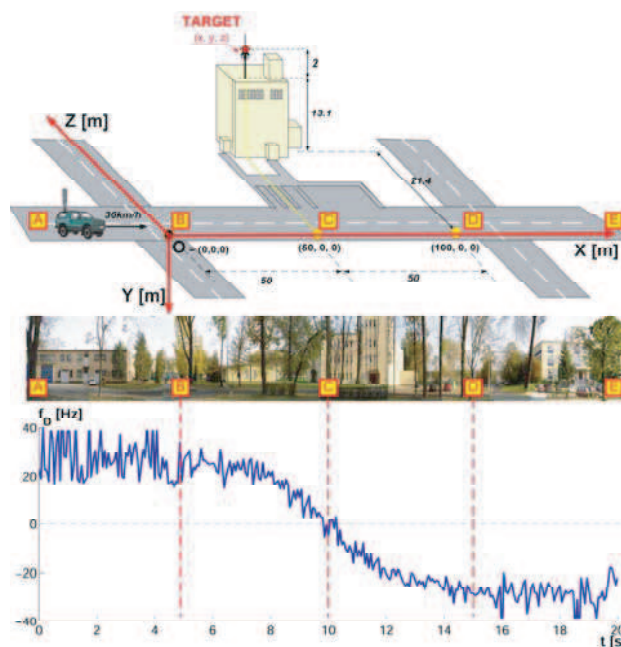


Figure 4: Measuring route with characteristic points A ÷ E and example course of Doppler frequency.

4. EMPIRICAL RESULTS AND DISCUSSION

Measurement station (Figure 3) consisted of: MagTel GSM Car Antena, Compact Receiver Rhode-Schwarz ESMC R1, Universal Frequency Counter Agilent (HP) 53132A, a notebook with implemented Frequencer software. Data from the frequency meter were sent to computer by USB-GPIB Interface Agilent 82357A. Receiver and frequency meter were additionally stabilized with Rubidium Frequency Standard Stanford Research System FS725. All the elements of the test stand were situated in a car vehicle. Battery and voltage converter were used to supply power to these elements.

In experiment, source (target) was situated in position relative the begin of the right-handed cartesian co-ordinate system in point B. On rout section A ÷ B vehicle with receiver was speeded up to 36 km/h, on section B ÷ D vehicle moves with constant velocity 36 km/h (in this interval were made momentary frequency measurements) and on section D ÷ E vehicle stopped. The vehicle average velocity on rout section B ÷ D was calculated on the basis of the riding time measurements.

In order to precision valuation of this location methodology following new quality measure Δr , further called location error, was determined [7] ÷ [9].

Average values of the source co-ordinates (Table 1) were calculated on the basis of Doppler frequency courses.

The obtained results shows that the Doppler frequency offset value could be used for radio signal sources location.

Table 1: Results of measuring and calculation.

$(x_0, y_0, z_0) = (50,0; 13,4; 21,4) \text{ m}$									
$y_0 = 13,4 \text{ [m]}$									
number of measuring	average velocity of vehicle $v \text{ [km/h]}$	co-ordinates of located radio emission sources			co-ordinates errors			location error	
		$r_0 = 25,25 \text{ m}$ $r = \sqrt{(z^2 + y^2)}$ [m]	$x_0 = 50,0 \text{ m}$ x [m]	$z_0 = 21,4 \text{ m}$ z [m]	$\Delta r = r - r_0 $ Δr [m]	$\Delta x = x - x_0 $ Δx [m]	$\Delta z = z - z_0 $ Δz [m]	$\Delta R = \sqrt{(\Delta x^2 + \Delta z^2)}$ ΔR [m]	
1	36,00	25,654	49,511	21,876	0,404			0,682	
2	36,00	25,054	49,347	21,170	0,196			0,692	
3	36,99	25,302	50,040	21,462	0,052			0,074	
4	36,00	24,800	49,337	20,869	0,450			0,850	
5	36,00	25,753	50,792	21,992	0,503			0,989	
6	35,06	25,493	50,385	21,687	0,243			0,480	
7	36,00	25,265	49,658	21,419	0,015			0,343	
8	35,53	24,950	49,642	21,047	0,300			0,503	
9	36,00	24,867	49,824	20,948	0,383			0,485	
10	36,00	25,617	49,977	21,833	0,367			0,434	
		25,753	50,792	21,992	0,503	0,792	0,592	0,989	MAX
		25,276	49,851	21,430	0,291	0,392	0,344	0,553	AV
		24,800	49,337	20,869	0,015	0,023	0,019	0,074	MIN

5. CONCLUSION

The experiment results give possibility to do initial opinion of location method precision. Possibility of these results comparison with different location methods is basis of this opinion. This comparison permits to infer about large effectiveness of the new method. Errors estimation of individual co-ordinates Δx , Δz and location errors Δr in presented method were below 1 m (Table 1).

It is needed to emphasize, that this method is dedicated first of all to location in open area, where it occurs so-called: down-to-earth space propagation or free space propagation. The measuring rout in this experiment could be classified as suburban terrain. On this stage of empirical verification, the test rout was choice by possibilities of test realization. The measuring rout in section B ÷ D was chosen to conditions which were reminding down-to-earth space propagation (direct visibility of antennas on whole measuring rout section). There are buildings beside the section B ÷ D, which cause the signals reflections. It is visible in disturbance of the Doppler frequency course on sections A ÷ B and D ÷ E (Figure 4).

This empirical test is initial usefulness verification of this new location method. Many tests in different space conditions should be conducted, to get the full information of method effectiveness.

ACKNOWLEDGMENT

This work was supported in part by the Polish Ministry of Science and Higher Education under Grant N N517 394334 and by the Department of Electronics, Military University of Technology under Grant PBW 506.

REFERENCES

1. Küpper, A., *Location-based Services*, John Wiley & Sons Ltd., Chichester, UK, Aug. 2005.
2. *An Introduction to Mobile Positioning*, Mobile Lifestreams Limited, 1999.
3. Gupta, I. J., “Stray signal source location in far-field antenna/RCS ranges,” *IEEE Antennas and Propagation Magazine*, Vol. 46, No. 3, 20–29, Jun. 2004.
4. Zhao, Y., “Standardization of mobile phone positioning for 3G systems,” *IEEE Communications Magazine*, Vol. 40, No. 7, 108–116, Jul. 2002.
5. Vossiek, M., L. Wiebking, P. Gulden, J. Weighardt, C. Hoffmann, and P. Heide, “Wireless local positioning,” *IEEE Microwave Magazine*, Vol. 4, No. 4, 77–86, Dec. 2003.
6. Gajewski, P., J. M. Kelner, and C. Ziółkowski, “Subscriber location in radio communication nets,” *Journal of Telecommunications and Information Technology*, No. 2/2008, 88–92, Apr.–Jun. 2008.
7. Rafa, J. and C. Ziółkowski, “Influence of transmitter motion on received signal parameters — Analysis of the Doppler effect,” *Wave Motion*, Vol. 45, No. 3, 178–190, Jan. 2008.
8. Ziółkowski, C., J. Rafa, and J. M. Kelner, “Sposób namiaru i lokalizacji źródeł przestrzennych fal radiowych z wykorzystaniem efektu Dopplera (Method of direction finding and location of the space radio wave sources using Doppler effect),” Polish patent application No. P381154, Warsaw, Poland, Nov. 27, 2006; “Biuletyn Urzedu Patentowego (Polish Patent Office Newsletter), Vol. XXXVI, No. 12(899)/2008, 24, Jun. 9, 2008 (in Polish).
9. Kelner, J. M., C. Ziółkowski, and L. Kachel, “The empirical verification of the location method based on the Doppler effect,” *Proceedings 17th International Conference on Microwaves, Radar and Wireless Communications MIKON’2008*, Vol. 3, 755–758, Wrocław, Poland, May 19–21, 2008.

Temperature and Mineralogy Dependable Model for Microwave Dielectric Spectra of Moist Soils

V. L. Mironov and S. V. Fomin

Kirensky Institute of Physics, SB RAS, Krasnoyarsk, Russia

Abstract— In this paper, a physically based dielectric model in microwave band for moist soils is developed to account for both the temperature and granulometric mineralogy of the soil. The generalized refractive mixing dielectric model (GRMDM) previously developed by V. L. Mironov et al. was used as a mean to determine the spectroscopic parameters for 5 soils which complex dielectric constant spectra were measured and presented in Technical Report EL-95-34, December 1995 by J. O. Curtis et al. The measurement results used covered the temperatures of 10, 20, 30, and 40°C, gravimetric clay contents from 0 to 0.76 g/g, and frequencies from 0.3 to 26.5 GHz. Relating to each individual soil, such GRMDM spectroscopic parameters as dielectric constants in low frequency limit, relaxation times, and ohmic conductivities, pertaining to both bound and unbound soil water, were fitted as functions of temperature with the Clausius-Mossotti, Debye and linear equations, respectively. As a result, a set of physical parameters for a temperature dependable generalized refractive mixing dielectric model (TD GRMDM), consisting of the volumetric expansion coefficients, activation energies, entropies of activation and others, were obtained. Finally, the parameters of the TD GRMDM as functions of gravimetric clay content were fitted to yield the closing set of polynomial formulas, which, in conjunction with the TD GRMDM, represent a temperature and mineralogy dependable soil dielectric model (TMD SDM). Thus developed, the TMD SDM provides for predictions of the complex dielectric constant of moist soils as a function of moisture, wave frequency, temperature and gravimetric clay content. Further the TMD SDM prediction error was estimated with the use of the independent dielectric data.

1. INTRODUCTION

Dielectric models of the soil are an essential part in the algorithms used for data processing with regard to the problems of radar and radiothermal remote sensing [1]. Recently, a mineralogy based spectroscopic dielectric model (MBSDM) [2, 3] has been developed and validated over a large dielectric data set [4] to ensure microwave dielectric spectra predictions as a function of moisture and soil texture at the fixed temperature of 20°C. This model is based on the generalized refractive mixing dielectric model (GRMDM) introduced in [5]. The MBSDM physically based provided for a substantially less error of predictions as compared with the ones delivered by the semiempirical dielectric model (SDM) of [1], though the latter is at present considered as a routine tool for predicting complex dielectric constant (CDC) spectra of moist soils in the microwave band. At the same time, there was developed a dielectric model [6] accounting for temperature variations, provided an individual type of the soil in terms of mineral content and texture be considered. Meanwhile, a joint impact of soil texture and temperature on the dielectric spectra of moist soils has not been analyzed yet. In this paper, such a task was formulated and accomplished. Using the methodology of the temperature dependable refractive mixing dielectric model (TD GRMDM) of [6] and the dielectric data set of [4], for each of 5 individual soils of [4], there were derived the assemblages of the TD GRMDM physical parameters. The latter consist of volumetric expansion coefficients, starting dielectric constants in low frequency limit, activation energies, entropies of activation, starting conductivities, and conductivity incrimination coefficients, pertaining to the bound and unbound types of soil water. Further, the TD GRMDM parameters obtained were fitted as a function of clay percentage with polynomial functions. Derived by this way, coefficients of the polynomial fits, in conjunction with dry soil CDC and maximum bound water fraction value, are considered as input parameters for a new temperature and mineralogy dependable soil dielectric model (TMD SDM) presented in this paper. To make assessments of the error of the TMD SDM predictions, the latter were calculated in the multidimensional domain, which included wave frequency, soil moisture, soil texture, and temperature, to be further correlated with the respective values measured in [4] for 11 soils. The error of the predictions obtained with the TMD SDM proved to be on the same order as that of the MBSDM predictions estimated in [2, 3].

2. THE TMD SDM CONCEPT

From a physical viewpoint, the complex dielectric constant (CDC) of a thawed moist soil, $\varepsilon_s(\mu, m_v, f, t)$, must depend on a vector variable, characterizing soil mineralogy and texture, μ , volumetric percentage of water in soil, m_v , wave frequency, f , and temperature, t . As a function of volumetric moisture, m_v , the complex index of refraction (CIR) of moist soil,

$$n_s^*(\mu, m_v, f, t) = \sqrt{\varepsilon_s(\mu, m_v, f, t)}, \quad (1)$$

can be expressed [5] in the form of the refractive mixing dielectric model (RMDM):

$$\begin{aligned} \sqrt{\varepsilon_s(\mu, t, f, m_v, t)} &= \sqrt{\varepsilon_d(\mu, t)} + \left(\sqrt{\varepsilon_b(\mu, t, f)} - 1 \right) [m_v + (m_{vt} - m_v) H(m_v - m_{vt})] \\ &+ \left(\sqrt{\varepsilon_u(\mu, t, f)} - 1 \right) (m_v - m_{vt}) H(m_v - m_{vt}) \end{aligned} \quad (2)$$

where, $\varepsilon_d(\mu, t)$, is the CDC of dry soil, $\varepsilon_b(\mu, f, t)$ and $\varepsilon_u(\mu, f, t)$ are the CDCs of the bound and unbound (free) soil water, respectively, m_{vt} is the maximum bound water fraction (MBWF), and $H(x)$ denotes the Heaviside step function: $u(x) = 1$ if $x > 0$, and $u(x) = 0$ if $x \leq 0$. The bound water is adsorbed on the surface of soil solids, while the unbound soil water exists in liquid droplet phase. The MBWF is such an amount of water in soil that any additional water added to the soil in excess of this amount behaves as unbound water. As seen from (1), the CIR is a piecewise linear function of soil moisture, with the MBWF being a transition point in terms of slope angle between the two linear legs relating to the bound, $m_v \leq m_{vt}$, and unbound, $m_v > m_{vt}$, moisture ranges. The application of the RMDM is limited to a given type of soil at the fixed values of wave frequency, and temperature. The CIR for dry soil, $n_d^*(\mu, t)$, as well as the ones for the bound, $n_b^*(\mu, f, t)$, and unbound, $n_u^*(\mu, f, t)$, types of soil water, alongside with the MBWF, are considered as the RMDM parameters. The CIR can be expressed through the index of refraction (IR), n , and normalized attenuation coefficient (NAC), κ :

$$n = \text{Re}n^* \text{ and } \kappa = \text{Im}n^* \quad (3)$$

which determine a moist soil medium in terms of wave phase velocity and wave attenuation, respectively. The RI and NAC are understood here as a proportion of the propagation constant and standard attenuation coefficient in a medium, to the free space propagation constant, respectively.

If the RI and NAC are known, the respective dielectric constant (DC), $\varepsilon' = \text{Re}\varepsilon$, and loss factor (LF), $\varepsilon'' = \text{Im}\varepsilon$, can be easily calculated using the following formulas:

$$\varepsilon' = n^2 - \kappa^2, \quad \varepsilon'' = 2n\kappa. \quad (4)$$

The inverse transformation is available through the following equations:

$$n\sqrt{2} = \sqrt{\sqrt{(\varepsilon')^2 + (\varepsilon'')^2} + \varepsilon'}, \quad \kappa\sqrt{2} = \sqrt{\sqrt{(\varepsilon')^2 + (\varepsilon'')^2} - \varepsilon'}. \quad (5)$$

The IR and NAC relating to the bound and unbound soil water can be determined as a function of frequency through fitting formula (2) to the moisture dependences measured at varying frequencies. From that fitting, the values of IR and NAC relating to the dry soil are derived as well. The respective DCs and LFs follow from (4).

With this approach [5], the DC and LF spectra relating to both the bound and unbound types of soil water were shown to follow the Debye formula:

$$\varepsilon_p(\mu, f, t) = \varepsilon'_p(\mu, f, t) + i\varepsilon''_p(\mu, f, t) = \varepsilon_{p\infty} + \frac{\varepsilon_{p0}(\mu, t) - \varepsilon_{p\infty}}{1 - i2\pi f\tau_p(\mu, t)} + \frac{i\sigma_p(\mu, t)}{2\pi f\varepsilon_0} \quad (6)$$

where p is any one of b, u ; $\varepsilon_{p0}(\mu, t)$ and $\varepsilon_{p\infty}(\mu, t) = 4.9$ are the low- and dielectric constants in low and high frequency limit, $\tau_p(\mu, t)$ is the relaxation time, and $\sigma_p(\mu, t)$ is the ohmic conductivity, each specific to the bound, $p = b$, and unbound, $p = u$, forms of soil water. Finally, $\varepsilon_0 = 8.854 \text{ pF/m}$ is the permittivity of vacuum. As a result, the values of $n_d(\mu, t)$, $\kappa_d(\mu, t)$, $m_{vt}(\mu, t)$, $\varepsilon_{0b}(\mu, t)$, $\varepsilon_{0u}(\mu, t)$, $\tau_b(\mu, t)$, $\tau_u(\mu, t)$, $\sigma_b(\mu, t)$, and $\sigma_u(\mu, t)$ are considered as spectroscopic parameters in the frame of the GRMDM developed in [5]. With the fitting procedures like in [3] or [5], these can be determined

from routine dielectric spectra measurements conducted for an individual type of moist soil at a given temperature.

In order to make the GRMDM expressed with formulas (1)–(6) a temperature dependable generalized refractive mixing dielectric model (TD GRMDM), some of the GRMDM spectroscopic parameters were represented as a function of temperature [6]. The dependence of the dielectric constant in low frequency limit on the temperature was taken in a form of the Clausius-Mossotti equation [7]:

$$\varepsilon_{0p}(\mu, t) = \frac{1 + 2 \exp(F_p(\mu, t_s) - \beta_p(\mu)(t - t_s))}{1 - \exp(F_p(\mu, t_s) - \beta_p(\mu)(t - t_s))} \quad (7)$$

where β_p is the volumetric expansion coefficient, t and t_s are the current and starting temperatures by degrees centigrade. The function $F_p(t)$ is given with the equation

$$F_p(\mu, t) = \ln[(\varepsilon_{p0}(\mu, t) - 1)/(\varepsilon_{p0}(\mu, t) + 2)]. \quad (8)$$

The relaxation time was expressed with the Debye relaxation formula [7] accounting for the temperature dependence:

$$\tau_p(\mu, t) = \frac{48 \times 10^{-12}}{t + 273.15} \exp\left(\frac{\Delta H_p(\mu)}{(t + 273.15)R} - \frac{\Delta S_p(\mu)}{R}\right) \text{ (ps)} \quad (9)$$

where ΔH_p and ΔS_p are the activation energy and entropy of activation, respectively, and R is the universal gas constant. Finally, the conductivity, σ_p , was suggested to have a linear dependence on the temperature, which is characteristic for the ionic solutions:

$$\sigma_p(\mu, t) = \sigma_p(\mu, t_s) + \beta_{\sigma p}(\mu)(t - t_s). \quad (10)$$

here, $\beta_{\sigma p}$ is the temperature incrementation coefficient for conductivity. While $\sigma_p(\mu, t_s)$ is the value of conductivity at a starting temperature, t_s .

As a result, to make the CDC predictions for an individual type of soil, $\varepsilon(\mu, m_v, f, t)$, with the use of the Equations (1)–(10), an assemblage of which represents the TD GRMDM [6], the following input parameters must be known; $n_d(\mu, t_s)$, $\kappa_d(\mu, t_s)$, $m_{vt}(\mu, t_s)$, $\varepsilon_{0b}(\mu, t_s)$, $\beta_b(\mu)$, $\varepsilon_{0u}(\mu, t_s)$, $\beta_u(\mu)$, $\Delta H_b(\mu)/R$, $\Delta S_b(\mu)/R$, $\Delta H_u(\mu)/R$, $\Delta S_u(\mu)/R$, $\sigma_b(\mu, t_s)$, $\beta_{\sigma b}(\mu)$, $\sigma_u(\mu, t_s)$, and $\beta_{\sigma u}(\mu)$.

In the following section, a technique will be outlined to derive the TD GRMDM parameters for individual soils.

3. TD GRMDM PARAMETERS FOR INDIVIDUAL SOILS

In [4], the dielectric data were measured over the frequency ranges from 45 MHz to 26.5 GHz, with the moistures spanning from nearly dry samples to the ones saturated up to field moisture capacity. The clay content in the soils varied from close to 0% to 76% by weigh. At the temperatures of 10, 20, 30, and 40°C, the values of GRMDM spectroscopic parameters, $\varepsilon'_d(\mu, t)$, $\varepsilon''_d(\mu, t)$, $m_{vt}(\mu, t)$, $\varepsilon_{0b}(\mu, t)$, $\varepsilon_{0u}(\mu, t)$, $\tau_b(\mu, t)$, $\tau_u(\mu, t)$, $\sigma_b(\mu, t)$, and $\sigma_u(\mu, t)$, were derived by fitting simultaneously the CDCs calculated with the formulas (1)–(6) to the DC and LF spectra measured for each individual soil within the frequency range from 0.3 to 26.5 GHz, at the moistures available. Earlier, this methodology was applied in [2, 3]. In this analysis only 5 soils of [4] were involved, with their clay proportion by weigh being of 0, 14, 34, 54, and 76%. Further, similar to [6], the GRMDM parameters obtained were fitted with the Equations (7)–(10) to derive the TD GRMDM parameters for each individual soil, complimenting the GRMDM ones, pertaining to a starting temperature of 20°C, that is, $\beta_b(\mu)$, $\beta_u(\mu)$, $\Delta H_b(\mu)/R$, $\Delta S_b(\mu)/R$, $\Delta H_u(\mu)/R$, $\Delta S_u(\mu)/R$, $\beta_{\sigma b}(\mu)$, and $\beta_{\sigma u}(\mu)$. As the next step, the TD GRMDM parameter were fitted as functions of clay content, C , to yield the equations describing the TMD SDM. The latter are given in the following section. Similar to [2, 3], the clay content, C , was used as the only variable to account for the soil mineralogy and texture parameter μ .

4. TDM SDM EQUATIONS

The following sequence of equations was derived as a result of fitting the TD GRMDM parameters with the expressions (7)–(10):

$$n_d(C, t_s) = 1.634 - 0.539 \cdot 10^{-2}C + 0.2748 \cdot 10^{-4}C^2 \quad (11)$$

$$\kappa_d(C, t_s) = 0.03952 - 0.04038 \cdot 10^{-2}C \quad (12)$$

$$m_{vt}(C, t_s) = 0.02863 + 0.30673 \cdot 10^{-2}C \quad (13)$$

$$\varepsilon_{0b}(C, t_s) = 79.8 - 85.4 \cdot 10^{-2}C + 32.7 \cdot 10^{-4}C^2 \quad (14)$$

$$\beta_b(C) = 8.67 \cdot 10^{-19} - 0.00126 \cdot 10^{-2} \cdot C + 0.00184 \cdot 10^{-4} \cdot C^2 - 9.77 \cdot 10^{-10} \cdot C^3 - 1.39 \cdot 10^{-15} \cdot C^4 \quad (15)$$

$$\varepsilon_{0u}(C, t_s) = 100 \quad (16)$$

$$\beta_u(C) = 1.11 \cdot 10^{-4} - 1.603 \cdot 10^{-7} \cdot C + 1.239 \cdot 10^{-9} \cdot C^2 + 8.33 \cdot 10^{-13} \cdot C^3 - 1.007 \cdot 10^{-14} \cdot C^4 \quad (17)$$

$$\Delta H_b(C)/R = 1467 + 2697 \cdot 10^{-2} \cdot C - 980 \cdot 10^{-4} \cdot C^2 + 1.368 \cdot 10^{-10} \cdot C^3 - 8.61 \cdot 10^{-13} \cdot C^4 \quad (18)$$

$$\Delta S_b(C)/R = 0.888 + 9.7 \cdot 10^{-2} \cdot C - 4.262 \cdot 10^{-4} \cdot C^2 + 6.79 \cdot 10^{-21} \cdot C^3 + 4.263 \cdot 10^{-22} \cdot C^4 \quad (19)$$

$$\Delta H_u(C)/R = 2231 - 143.1 \cdot 10^{-2} \cdot C + 223.2 \cdot 10^{-4} \cdot C^2 - 142.1 \cdot 10^{-6} \cdot C^3 + 27.14 \cdot 10^{-8} \cdot C^4 \quad (20)$$

$$\Delta S_u(C)/R = 3.649 - 0.4894 \cdot 10^{-2} \cdot C + 0.763 \cdot 10^{-4} \cdot C^2 - 0.4859 \cdot 10^{-6} \cdot C^3 + 0.0928 \cdot 10^{-8} \cdot C^4 \quad (21)$$

$$\sigma_b(C, t_s) = 0.3112 + 0.467 \cdot 10^{-2}C \quad (22)$$

$$\beta_{\sigma b}(C) = 0.0028 + 0.02094 \cdot 10^{-2} \cdot C - 0.01229 \cdot 10^{-4} \cdot C^2 - 5.03 \cdot 10^{-22} \cdot C^3 + 4.163 \cdot 10^{-24} \cdot C^4 \quad (23)$$

$$\sigma_u(C, t_s) = 0.05 + 1.4 \cdot (1 - (1 - C \cdot 10^{-2})^{4.664}) \quad (24)$$

$$\beta_{\sigma u}(C) = 0.00108 + 0.1413 \cdot 10^{-2} \cdot C - 0.2555 \cdot 10^{-4} \cdot C^2 + 0.2147 \cdot 10^{-6} \cdot C^3 - 0.0711 \cdot 10^{-8} \cdot C^4 \quad (25)$$

where C must be assigned in percent.

The assemblage of formulas (1)–(25) constitutes the temperature and mineralogy dependable soil dielectric model (TMD SDM), which provides for CDC predictions of moist soils as a function of frequency, soil moisture, clay content, and temperature. In the following sections a correlation analysis between the TMD SDM predictions and measured values of CDCs will be conducted to estimate the error of that predictions.

5. VALIDATION OF THE TMD SDM PREDICTIONS

To perform such a validation of the TMD SDM, the correlation analysis was carried out on the basis of all dielectric data available in [4], including the data related to the remaining 6 soils of [4], which were not used for obtaining the Equations (11)–(25). The results of validation are presented in Fig. 1. As seen from Fig. 1, the TMD SDM provided predictions for both the CDs and LFs with the reasonable correlation coefficients, $R_{DC} = 0.99$ and $R_{LF} = 0.98$. The respective standard deviations, $SD_{DC} = 1.91$ and $SD_{LF} = 1.284$, are also reasonable, considering the whole set of

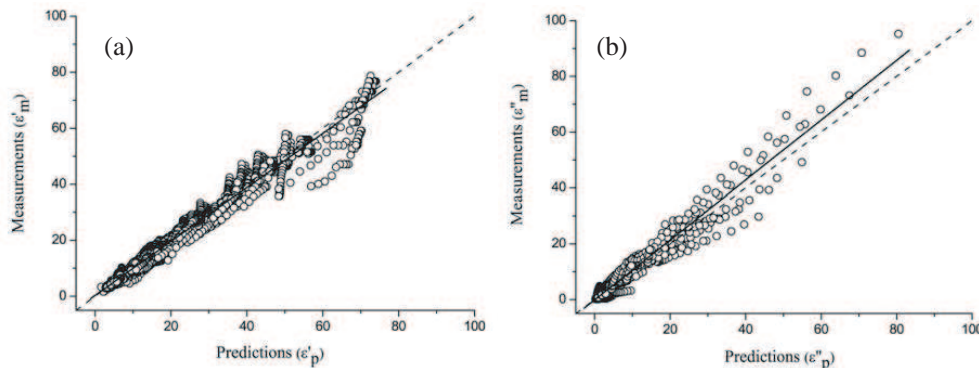


Figure 1: Correlation of the TMD SDM predictions, $\varepsilon'_p, \varepsilon''_p$, for DCs (a) and LFs (b) with the measured ones, $\varepsilon'_m, \varepsilon''_m$, with the data for all soil types and temperatures available in [4] being included. Solid and dotted lines represent linear fits and bisectors, respectively. Correlation coefficients, R_{DC} and R_{LF} , and standard deviations, SD_{DC} and SD_{LF} , are equal to: $R_{DC} = 0.991, R_{LF} = 0.978, SD_{DC} = 1.91, SD_{LF} = 1.283$. The linear fits are expressed as follows: $\varepsilon'_m = 0.3167 + 0.963\varepsilon'_p, \varepsilon''_m = 0.1104 + 1.073\varepsilon''_p$.

measured dielectric data employed. These values are close to the ones achieved with the use of the MBSDM [3], which can be applied only at the starting temperature of 20°C.

6. CONCLUSIONS

Summing up the results, the following has to be stated as primary findings of this research. The proposed and substantiated TMD SDM is the first physically based model taking into account the temperature and mineralogy impact on CDC microwave dielectric spectra of most soils using the dependence of soil water CDC, for both bound and unbound, on the frequency and temperature with the use of the well known Debye and Clausius-Massotii laws, as well as the linear dependence of soil water ionic conductivity on the temperature. The error of the predictions obtained with the TMD SDM proved to be on the same order as that of the MBSDM predictions, which has never been previously achieved for a broad variety of soils with existing empirical models, simultaneously in a domain of frequency, moisture, temperature, and soil texture variables.

ACKNOWLEDGMENT

This research was supported by the Siberian Branch of the Russian Academy of Sciences, Interdisciplinary Project # 6, and Russian Foundation for Basic Research, project 09-05-91061.

REFERENCES

1. Dobson, M. C., F. T. Ulaby, M. T. Hallikainen, and M. A. El-Rayes, "Microwave dielectric behavior of wet soil — Part II: Dielectric mixing models," *IEEE Trans. Geosci. Remote Sensing*, Vol. 23, No. 1, 35–46, 1985.
2. Mironov, V. L., L. G. Kosolapova, and S. V. Fomin, "Soil dielectric model accounting for contribution of bound water spectra through clay content," *PIERS Online*, Vol. 4, No. 1, 31–35, 2008.
3. Mironov, V. L., L. G. Kosolapova, and S. V. Fomin, "Physically and mineralogically based spectroscopic dielectric model for moist soils," *IEEE Trans. Geosci. Remote Sensing*, Vol. 47, No. 7, 2009 (to be published).
4. Curtis, J. O., C. A. Weiss, Jr., and J. B. Everett, "Effect of soil composition on dielectric properties," *Technical Report EL-95-34*, December 1995.
5. Mironov, V. L., M. C. Dobson, V. H. Kaupp, S. A. Komarov, and V. N. Kleshchenko, "Generalized refractive mixing dielectric model for moist soils," *IEEE Trans. Geosci. Remote Sensing*, Vol. 42, No. 4, 773–785, 2004.
6. Mironov, V. L. and S. V. Fomin, "Temperature dependable microwave dielectric model for moist soils," *PIERS Proceedings*, 831–835, Beijing, China, March 23–27, 2009.
7. Dorf, R. C., *The Electrical Engineering Handbook*, 2nd Edition, Boca Raton, CRC Press LLC, FL, 1997.

Cable Transmission Lines Magnetic Field Compensation

M. Sh. Misrikhanov¹, N. B. Rubtsova², and A. Yu. Tokarskij¹

¹JSC Federal Network Company Branch “Main Power Networks of the Center”, Russian Federation

²RAMS Institute of Occupational Health, Moscow, Russian Federation

Abstract— The typical dual transforming station (TS) 10/0.4 kV built in residential building with an arrangement of 0.4 kV cable transmission lines (CL) under ceiling in asbestos-cement pipes is examined. Under typical arrangement of each phase cable and zero wire bundle in separate pipe on floor surface, located above TS on 965 mm distance from CL, CL currents ($I_{CL} = 1800$ A) at maximal symmetric load induce magnetic field (MF) value up to $H = 100$ A/m, that in 25 times exceeds general public hygienic norms in the Russian Federation (maximum permissible level it is equal 4 A/m). The method of phases and zero wire virtual cables axes rapprochement is developed. The arrangement of cables of phases and zero wire in cable bundle can be chosen for minimization of distance between axes of their virtual cables. Such CL design allows decreasing of MF intensity of MT on surface of living room up to 5×10^{-3} A/m.

1. INTRODUCTION

Transforming stations (TS), built in inhabited or office buildings are source of occupational and environmental magnetic field exposure and can be human health risk factor. It causes of magnetic fields levels in residential buildings decrease.

2. POWER FREQUENCY MAGNETIC FIELDS CREATED BY CABLE TRANSMISSION LINES AND WAYS OF ITS DECREASE

For example, we shall examine dual TS 10.0/0.4 kV located on ground floor of apartment house (Figure 1). Cable transmission lines (CL) 0.4 kV from transformers (T) 10.0/0.4 kV to cable distributive substation 0.4 kV (CDS) are placed in asbestos-cement pipes. On the second floor on distance of 965 mm from CL the floor of premises is located. Power frequency (PF) magnetic field (MF) general public exposure permissible limit value (PLV) is equal to 4 A/m ($5 \mu\text{T}$). This value is obligatory in premises of any house.

The arrangement of CL bundles inside of asbestos-cement pipes is shown in Figure 2. At scheduled switching-off of one of the transformer all power supply is carried out through the second transformer; in this TS operating mode CL phase current module value at symmetric loading will be 1800 A.

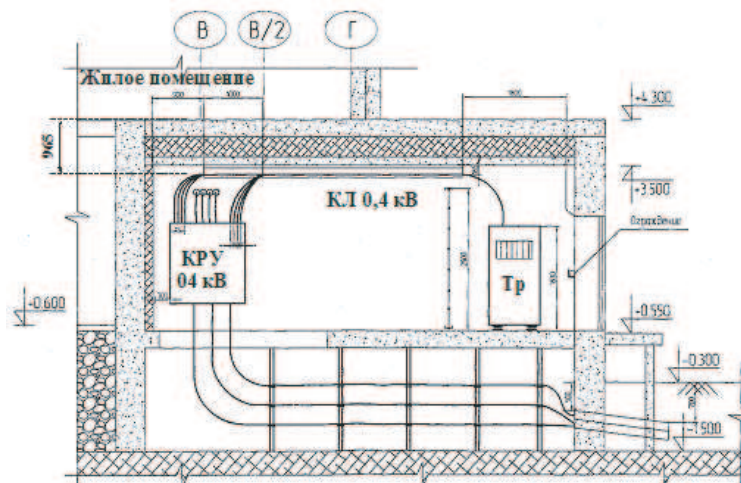


Figure 1: Section of TS 10.0/0.4 kV, located in ground floor of apartment house.

Created by CL currents MF strength distribution at apartment house floor surface, that situated above TS, is shown in Figures 3 and 4. Figure 3: configuration A — curve 1, configuration B — curve 2 under symmetrical loading. ($I_{phase} = 1800$ A. Figure 4: under asymmetrical loading

($\dot{I}_A = 1800 \text{ A}$, $\dot{I}_B = 900e^{j120^\circ} \text{ A}$, $\dot{I}_C = 900e^{j120^\circ} \text{ A}$, $\dot{I}_0 = 900e^{j180^\circ} \text{ A}$): configuration A — curve 1' and configuration B — curve 2'.

PLV 4.0 A/m of general public exposure in premises of any house is exceeded from 16 to 25 times under symmetrical loading regime and from 5.5 to 17 times under asymmetrical loading.

Maximal rapprochement of cable heteronymic phases and zero wire axis in cable bundles with the purpose to decrease MF received as a result and also increasing of CL distance from the surface of premises floor downwards on 10 cm allow to lower MF level up to value (Figure 5) $H_{\max} \leq 4 \text{ A/m}$ [1]. However “residual” CL MF value $1 \div 2 \text{ A/m}$ in aggregate with MF emitted by electrical household appliances (kitchen electric stoves, electrical teapots, heaters, etc.), can lead to excess of PF MF MPV for premises.

The further restriction of levels of MF intensity by method of rapprochement of axes of cables of heteronymic phases and zero wire is impossible, because of geometrical sizes of cables itself. Therefore the method of rapprochement of virtual cables axes application is expedient [2, 3].

Let's examine two parallel cables A1 and A2 under current \dot{I} with current in everyone, located from each other in $2R$ distance. From the middle of distance between cables we shall lead a circle in radius R . In the center of circle we shall place XOY coordinates axes so that the axis OX will be under α corner to straight line connecting axes of cables (Figure 6). In point D located on distance

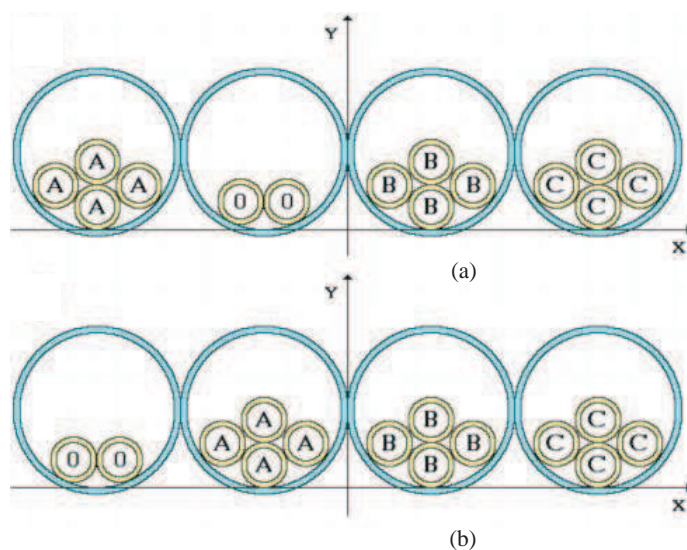


Figure 2: The arrangement of CL cable bundles in asbestos-cement pipes.

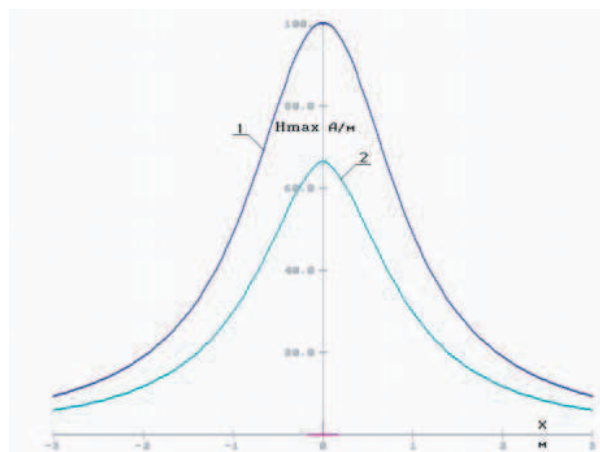


Figure 3: Created by CL MF value H_{\max} distribution at apartment house floor surface under symmetrical loading, configuration A — curve 1, and configuration B — curve 2.

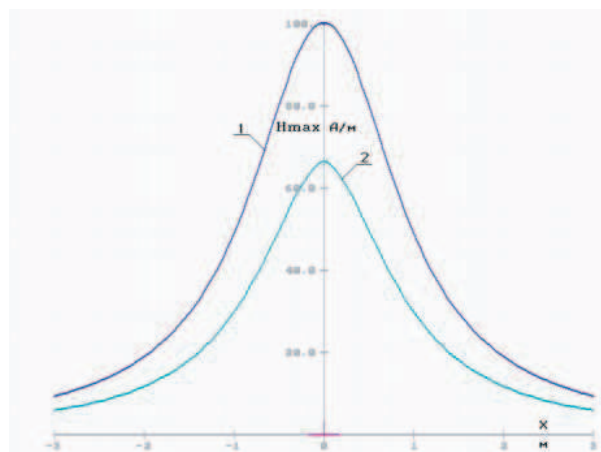


Figure 4: Created by CL MF value H_{\max} distribution at apartment house floor surface under asymmetrical loading: configuration A — curve 1', and configuration B — curve 2'.

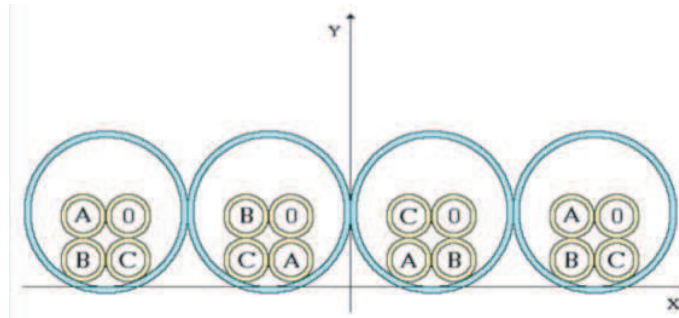


Figure 5: Maximal rapprochement of cable heteronymic phases and zero wire in cable bundles.

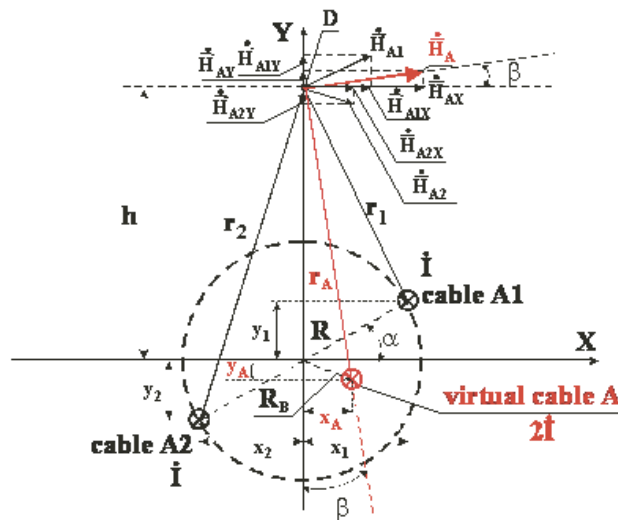


Figure 6: To determination of virtual cable A under current $2\dot{I}$ axis coordinates created in point D MF level equal to MF value created by two real parallel cables A1 and A2 under current \dot{I} .

h from the center of a circle on axis OY , currents of cables create MF; its intensity is the result of summation on axes OX and OY . On its basis resulting MF intensity \vec{H}_A is defined Angle β of \vec{H}_A vector inclination to OX axis determines by equation:

$$\beta = \text{arctg} \frac{H_{AY}}{H_{AX}}. \quad (1)$$

From point D let's lead a line, perpendicular \vec{H}_A to vector in the direction to XOY coordinates center (Figure 6). Then on distance $r_A = \frac{2I}{2\pi H_A}$ from point D on this line the axis of cable A that is virtual analogue of A1 and A2 cables is possible to arrange. This cable A creates by its current $2\dot{I}$, in point D MF with strength vector identical to vector \vec{H}_A .

Cable A axis coordinates determine by equations:

$$x_A = r_A \sin \beta, \quad y_A = h - r_A \cos \beta. \quad (2)$$

Virtual cable axis is located inside of circle on distance $R_B < R$ from the center. At increase up to N_k numbers of cables in bundle and constant $N_k I_k$ value MF mutual compensation lead to decrease of \vec{H}_{kY} component module, and increase of \vec{H}_{kX} component module. It, according to Formulas (1) and (2), lead to decrease as β angle, and x_A, y_A coordinates, i.e., the virtual cable center becomes closer to the center of circle.

In regular intervals arrangement of phase cables and zero wire on perimeter of the circles with united center, allow to receive CL with axis of virtual cables of phases and zero wire will be on distances considerably smaller than diameters of real cables.

Applying the principle of the maximal rapprochement of virtual cables axes it is possible to receive various CL designs; some of cables are shown in Figure 7.

Let's examine design of CLs shown in Figures 7(a) and 7(b). CL presented in Figure 7(a) consists of one bundle containing on $N_A = N_B = N_0 = 4$, A, B phase cables and zero wire (0) with each section 240 mm^2 , cables diameter $Dm_A = Dm_B = Dm_0 = 3 \text{ cm}$. This CL contains also $N_c = 8$ phase cables with 120 mm^2 section and $Dm_c = 2 \text{ cm}$ diameter each. Zero wire axes are on perimeter of circle with radius $R_0 = 2.12 \text{ cm}$ with angle $\alpha_0 = 45^\circ$ of inclination to OX axis. Characteristics

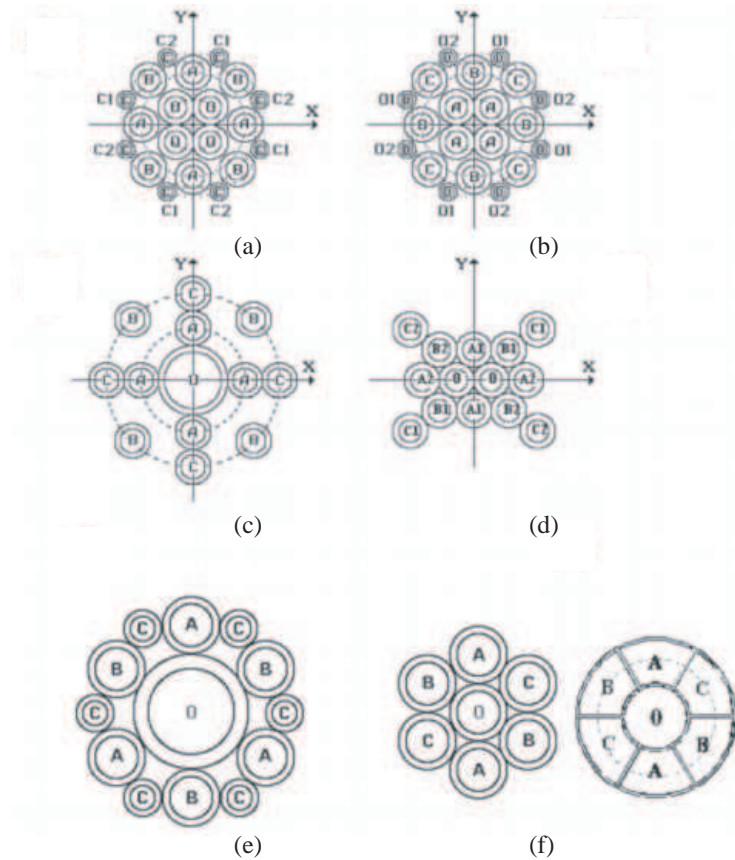


Figure 7: CL some design, constructed by method minimization of distance between axes of virtual cables.

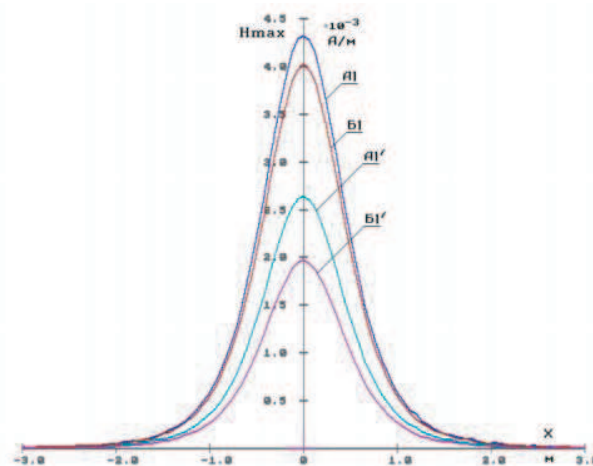


Figure 8: Distribution of MF strength, created at the surface of living room floor above TS by CL arrangement according 7(a) and 7(b) schemes: curve A1 and B1 — symmetrical regime of loading, curve A1' and B1' — asymmetrical regime of loading.

A phase: $R_A = 4.1$ cm, $\alpha_A = 0^\circ$; B phase: $R_B = 5.1$ cm, $\alpha_B = 45^\circ$; four C1 semi-phase cables: $R_{C1} = 5,75$ cm, $\alpha_{C1} = 20^\circ$; C2 semi-phase cables $R_{C2} = 5,75$ cm, $\alpha_{C2} = -20^\circ$.

Cable line bundle configuration shown in Figure 7(b) differs from 7(a) by change the places of cable phases included in bundle: 0 to A, A to B, B to C, and C to 0.

Comparison of MF H_{max} levels at apartment house floor surface examined above 10.0/0.4 kV TS (Figure 1) created by traditional design CL (see Figures 3 and 4), with cable lines designed by schemes given in 7(a) and 7(b) shows that CL of nontraditional design create MF levels many times less (Figure 8), accordingly, in 23000 and 25000 times H_{max} less under symmetrical load, and in 26000 and 35000 times less under asymmetrical load. Thus maximal MF level H_{max} at the floor surface of living room under symmetrical regime of loading is less 4.5 mA/m.

Use of CL, grouped by method of the virtual cables axes maximal rapprochement, allows lowering considerably very much environmental MF levels.

REFERENCES

1. Misrikhanov, M. Sh., N. B. Rubtsova, and A. Yu. Tokarskij, "Cable line magnetic field levels decrease by method of minimization of distance between axes of phase cables and zero wire," *Reports of 9th Russian Scientific-technical EMC Conference*, 608–612, St-Petersburg, VITU, 2006 (in Russian).
2. Misrikhanov, M. Sh., N. B. Rubtsova, and A. Yu. Tokarskij, "Cable line magnetic field levels decrease by method of minimization of distance between axes of virtual cables and zero wire," *Reports of 9th Russian Scientific-technical EMC Conference*, 613–618, St-Petersburg, VITU, 2006 (in Russian).
3. Misrikhanov, M. Sh., N. B. Rubtsova, and A. Yu. Tokarskij, Cable transmission line, Patent RF No. 2273934, Published 10.04.2006, Bul. No. 10, 2006 (in Russian).

The Calibration Technique for Moist Soils Complex Permittivity Measurements in the Microwave Band

V. L. Mironov and Yu. I. Lukin

The Kirensky Institute of Physics of SB, RAS, Russia

Abstract— In the present work, the calibration method of waveguide in measurement of complex dielectric permittivity spectrum of wet soils with coaxial sample holder in microwave frequency range is proposed. This method is convenient for soil measurement. With the view of effect of transition units connecting waveguide to sample holder, the approach includes calibration procedure by the use of measurement of S -scattering matrix for two empty sample holders of different lengths. As an example, the results of measurement of complex dielectric permittivity spectrum of loam soil at positive and negative temperature are given.

1. INTRODUCTION

Dielectric models of the soil and vegetation are an essential part in the algorithms used for data processing with regard to the problems of radar and radio thermal remote sensing. From this viewpoint, measurement methods of complex dielectric permittivity (CDP) of soils at temperatures and in frequency range are developing. It is significant to account effect of joint units on measurement process.

The coaxial-waveguide method is widely used for measuring spectrum of complex dielectric permittivity. This method allows measuring CDP of samples of as high so low CDP value in wide frequency range. However, the effect of waveguide elements can result in significant errors in measuring. There are some calibration methods to take into account features of a waveguide circuit installation containing a measuring cell [1–5]. The following calibration method can be defined. The theoretically account of waveguide elements as it was suggested in [1]. And the second way is to carry out calibration measurement with calibration samples of known dielectric permittivity over the all considered frequency range. The first method is not universal because of it is suitable for simple constructions of measurement waveguide only. In case of composite construction, the solving of waveguides elements is getting difficult. The second method usually requires to use liquids as calibration sample and in case of soil measurements, we have to construct universal measurement sample holder, which can be filled with as liquids so and soils.

In the present work, a calibration method of waveguide in measurement of complex permittivity spectrum of wet soils in microwave frequency range is proposed, with coaxial sample holder being applied as a measuring cell. The calibration procedure proposed is based on measurements of S -scattering matrix for two empty sample holders of different lengths. This approach allows to use the same sample holders for both the calibration and soil dielectric measurements.

2. EXPERIMENTAL SETUP

The experimental setup for carrying out measurement of spectrum of CDP measurements is shown in Fig. 1. The sample holder with soil attached to vector network analyzer ZVK with transition units. The vector network analyzer allows for the measurement of frequency spectrum of the S -scattering matrix of the attached device in frequency range from 10 MHz to 40 GHz. The temperature chamber was used to supply required temperature regime. The temperature in temperature chamber automatical controlled by personal computer.

3. THE CDP RETRIEVING

The coaxial sample holder can be divided into the following parts: The section containing the sample soil under study and adapter units matching with the connectors of the vector network analyzer and them located on the ends of sample section. The transmission matrix of the entire waveguide in terms of transmission matrices of the waveguide parts can be expressed as [1, 6]:

$$\mathbf{T} = \mathbf{T}_1 \mathbf{T}_x \mathbf{T}_2, \quad (1)$$

where \mathbf{T}_1 , \mathbf{T}_2 are transmission matrices of adapter units located on the left and right of sample section respectively. \mathbf{T}_x — Transmission matrix of sample section. The elements of matrices (1)

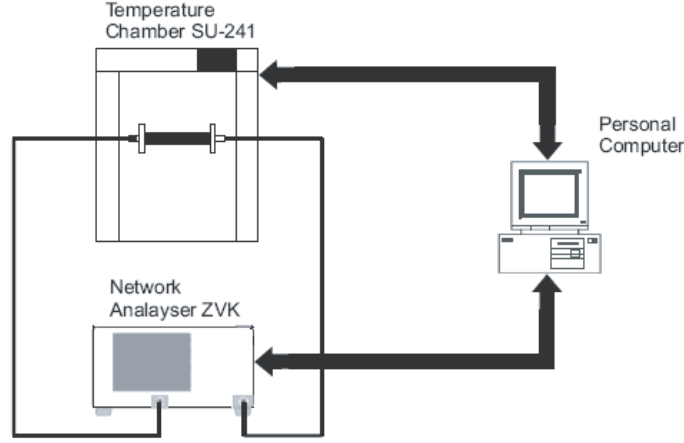


Figure 1: The scheme of the experimental setup.

are determined from the elements of scattering matrix by [6]:

$$\mathbf{T}_i = \begin{pmatrix} t_{11}^i & t_{12}^i \\ t_{21}^i & t_{22}^i \end{pmatrix} = \begin{pmatrix} \frac{1}{S_{21}^i} & -\frac{S_{22}^i}{S_{21}^i} \\ \frac{S_{11}^i}{S_{21}^i} & \frac{S_{21}^i S_{12}^i - S_{11}^i S_{22}^i}{S_{21}^i} \end{pmatrix}, \quad i = 1, x, 2. \quad (2)$$

In case of single mode regime in coaxial waveguide and homogeneous sample: $S_{11}^x = S_{22}^x$, $S_{12}^x = S_{21}^x$ which are result in

$$t_{12}^x = -t_{21}^x. \quad (3)$$

Taking into account (3), the Equation (1) can be expressed in terms of t_{11} , t_{12} , t_{21} , t_{22} :

$$\begin{cases} t_{11} = t_{11}^1 t_{11}^2 t_{11}^x + (-t_{12}^1 t_{11}^2 + t_{11}^1 t_{12}^2) t_{12}^x + t_{12}^1 t_{21}^2 t_{22}^x, \\ t_{12} = t_{11}^1 t_{12}^2 t_{11}^x + (-t_{12}^1 t_{12}^2 + t_{11}^1 t_{22}^2) t_{12}^x + t_{12}^1 t_{22}^2 t_{22}^x, \\ t_{21} = t_{21}^1 t_{11}^2 t_{11}^x + (-t_{22}^1 t_{11}^2 + t_{21}^1 t_{21}^2) t_{12}^x + t_{22}^1 t_{21}^2 t_{22}^x, \\ t_{22} = t_{21}^1 t_{12}^2 t_{11}^x + (-t_{22}^1 t_{12}^2 + t_{21}^1 t_{22}^2) t_{12}^x + t_{22}^1 t_{22}^2 t_{22}^x. \end{cases} \quad (4)$$

If the sample holder is empty: $S_{22}^x = 0$, $S_{21}^x = \exp(ik_0d)$, i.e., $t_{11}^x = \exp(-ik_0d)$, $t_{12}^x = 0$, $t_{22}^x = \exp(ik_0d)$. Here $k_0 = \frac{2\pi}{c}f$ is propagation constant in air, d is the sample length. With specifying $t_{ij} = t_{ij}^e$, Equation (4) reduce to

$$\begin{cases} t_{11}^e = t_{11}^1 t_{11}^2 \exp(-ik_0d) + t_{12}^1 t_{21}^2 \exp(ik_0d), \\ t_{12}^e = t_{11}^1 t_{12}^2 \exp(-ik_0d) + t_{12}^1 t_{22}^2 \exp(ik_0d), \\ t_{21}^e = t_{21}^1 t_{11}^2 \exp(-ik_0d) + t_{22}^1 t_{21}^2 \exp(ik_0d), \\ t_{22}^e = t_{21}^1 t_{12}^2 \exp(-ik_0d) + t_{22}^1 t_{22}^2 \exp(ik_0d). \end{cases} \quad (5)$$

The system of Equation (5) can be considered as the system of the linear algebraic equations with respect to eight unknown variables: $t_{11}^1 t_{11}^2$, $t_{12}^1 t_{21}^2$, $t_{11}^1 t_{12}^2$, $t_{12}^1 t_{22}^2$, $t_{21}^1 t_{11}^2$, $t_{22}^1 t_{21}^2$, $t_{21}^1 t_{12}^2$, $t_{22}^1 t_{22}^2$, which are characteristics of adapter units. For its single-valued determination it is necessary to supplement (5) with additional four equations. Thus the elements of transition matrix T t_{11}^e , t_{12}^e , t_{21}^e , t_{22}^e of one empty holder is add with that of second empty holder of the different length. After solving the system of the eight independent equations we determine that

$$\begin{cases} t_{11}^1 t_{11}^2 = \frac{t_{ij}^{e1} \exp(ik_0d_2) - t_{ij}^{e2} \exp(ik_0d_1)}{\exp(ik_0(d_2 - d_1)) - \exp(-ik_0(d_2 - d_1))}, \\ t_{12}^1 t_{22}^2 = \frac{t_{ij}^{e2} \exp(-ik_0d_2) - t_{ij}^{e1} \exp(-ik_0d_1)}{\exp(ik_0(d_2 - d_1)) - \exp(-ik_0(d_2 - d_1))}, \end{cases} \quad (6)$$

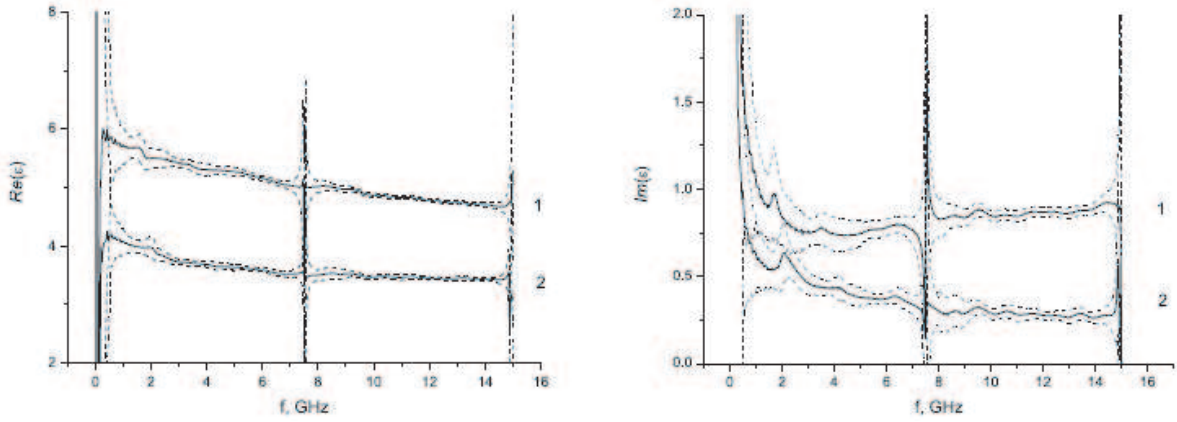


Figure 2: The spectrum of $\text{Re}(\epsilon)$ and $\text{Im}(\epsilon)$ of loam soil at temperatures 1: $T = 25^\circ\text{C}$ and 2: $T = -30^\circ\text{C}$. The dashed curve determines confidence interval of CDP.

where $i, j = 1, 2$ indicate the first and the second empty sample holder. After the measurement of soil sample have been made the elements of transition matrix of sample section can be expressed by means of the parameters of adapter units (6) and those of whole waveguide T $t_{11}^e, t_{12}^e, t_{21}^e, t_{22}^e$ as follows

$$t_{11}^x = \frac{t_{22}^1 t_{22}^2 t_{11} - t_{12}^1 t_{22}^2 t_{21} - t_{22}^1 t_{21}^2 t_{12} + t_{12}^1 t_{21}^2 t_{22}}{(t_{21}^1 t_{12}^2) (t_{12}^1 t_{21}^2) - (t_{11}^1 t_{12}^2) (t_{22}^1 t_{21}^2) - (t_{12}^1 t_{22}^2) (t_{21}^1 t_{11}^2) + (t_{11}^1 t_{11}^2) (t_{22}^1 t_{22}^2)}, \quad (7a)$$

$$t_{22}^x = \frac{t_{21}^1 t_{12}^2 t_{11} - t_{11}^1 t_{12}^2 t_{21} - t_{21}^1 t_{11}^2 t_{12} + t_{11}^1 t_{11}^2 t_{22}}{(t_{21}^1 t_{12}^2) (t_{12}^1 t_{21}^2) - (t_{11}^1 t_{12}^2) (t_{22}^1 t_{21}^2) - (t_{12}^1 t_{22}^2) (t_{21}^1 t_{11}^2) + (t_{11}^1 t_{11}^2) (t_{22}^1 t_{22}^2)}. \quad (7b)$$

In case of full matching of impedances of the elements of waveguide, the denominator of (8) can be shown to be equal to unit. Assuming the permeability of soil to be close to the unit, the complex dielectric permittivity of sample can be found by

$$\sqrt{\epsilon} = \frac{c}{2\pi df} \arccos\left(\frac{t_{11}^x + t_{22}^x}{2}\right). \quad (8)$$

4. EXPERIMENTAL RESULTS

The results of measurement of loam soil at mass moisture $M = 9\%$ and temperatures of $t = 25^\circ\text{C}$ and $t = -30^\circ\text{C}$ are shown in Fig. 2. The dashed curve determines confidence interval of CDP which is associated with retrieving method precision. The confidence interval has been calculated in according with the classical approach to error of indirect measurement.

It is seen high error areas at some frequencies. Analyses of (6) has shown that such areas are related to the wavelengths $\lambda_m = 2 \frac{d_2 - d_1}{m}$, where m is integer i.e., at every multiply of half-wavelength of difference of the calibration sample holder lengths. From (8), it follows high error areas at the wavelengths $\lambda_m = 2 \frac{d_s \text{Re}(\sqrt{\epsilon})}{m}$ i.e., at every multiply of half-wavelength of relative the measuring sample holder length. Beyond these ranges, the proposed method provided quiet reasonable error of the CP measurements relating to both the thawed and frozen soils, with the relative error estimates not exceeding the values of ($\frac{\Delta \text{Re}(\epsilon)}{\text{Re}(\epsilon)} = 4\%$, $\frac{\Delta \text{Im}(\epsilon)}{\text{Im}(\epsilon)} = 20\%$) and ($\frac{\Delta \text{Re}(\epsilon)}{\text{Re}(\epsilon)} = 3\%$, $\frac{\Delta \text{Im}(\epsilon)}{\text{Im}(\epsilon)} = 10\%$) respectively.

5. CONCLUSION

The calibration method of waveguide in measurement of complex dielectric permittivity spectrum of wet soils with coaxial sample holder in microwave frequency range at both of positive and negative temperature is proposed. This method includes calibration technique with using two empty sample holders. The proposed calibration technique is convenient in measurement of soil because of implementation the same sample holders as in measurement in the calibration procedure. As an example, the results for the measurement errors are analyzed in the case of CPs spectra pertaining to a loam soil measured in both thawed and frozen conditions. There was found a

serious of frequencies ranges in which the measurement error increased to a large extend due to a resonance effects existing in a measuring cell. Beyond these ranges the proposed method provided quiet reasonable error of the CP measurements relating to both the thawed and frozen soils, with the relative error estimates not exceeding the values of ($\frac{\Delta \text{Re}(\epsilon)}{\text{Re}(\epsilon)} = 4\%$, $\frac{\Delta \text{Im}(\epsilon)}{\text{Im}(\epsilon)} = 20\%$) and ($\frac{\Delta \text{Re}(\epsilon)}{\text{Re}(\epsilon)} = 3\%$, $\frac{\Delta \text{Im}(\epsilon)}{\text{Im}(\epsilon)} = 10\%$) respectively. In the method proposed, the resonance frequency ranges can be avoided with the use of sample holders of varying lengths.

ACKNOWLEDGMENT

The work was supported by the Siberian Branch of the Russian Academy of Sciences, Integration Project 6.

REFERENCES

1. Bois, K. J., F. Handjojo, A. D. Benally, K. Mubarak, and R. Zoughi, "Dielectric plug-loaded two-port transmission line measurement technique for dielectric property characterization of granular and liquid materials," *IEEE Trans. Instrum. Meas.*, Vol. 48, No. 6, 1141–1148, Dec. 1999.
2. Zheng, H. and C. E. Smith, "Permittivity measurements using a short open-ended coaxial line probe," *IEEE Microwave and Guided Wave Letter*, Vol. 1, No. 11, 337–339, Nov. 1991.
3. Folgero, K., "A broad-band and high-sensitivity dielectric spectroscopy measurement system for quality determination of low-permittivity fluids," *Meas. Sci. Technol.*, Vol. 6, 995–1008, 1995.
4. Folgero, K., "Bilinear calibration of coaxial transmission/reflection cells for permittivity measurement of low-loss liquids," *Meas. Sci. Technol.*, Vol. 7, 1260–1269, 1996.
5. Baker-Jarvis, J., E. J. Vanzura, and W. A. Kissick "Improved technique for determining complex permittivity with the transmission/reflection method," *IEEE Trans. Microwave Theory Tech.*, Vol. 38, No. 8, 1096–1103, 1990.
6. Helszajn, J., *Passive and Active Microwave Circuits*, Wiley, 1978.

Estimating the Ore Volume in AC Smelting Furnaces Using Finite-Element Analysis of Surface Current Density

A. Jeremic and A. Atalla

McMaster University, Hamilton, Canada

Abstract— One of the primary reasons for large power fluctuations in smelting furnaces is loss of contact between the electrode and ore. Therefore one of important aspects of controlling power fluctuations is a predictive algorithm for the positioning of the electrode. Most of the existing solutions are non-model based algorithms that focus on blind prediction of load resistance. In this paper we propose a model-based approach that estimates the volume ratio of solid and liquid phases of the ore. The resulting estimates can then be used in predictive algorithms for vertical positioning of the electrode since the height of the ore is directly related to the volumes of solid and liquid phases.

1. INTRODUCTION

The effective utilization of furnaces through the increase of furnace capacity and productivity are heavily dependent on efficient algorithms for the control of the furnaces. Namely, incorrectly positioned Sodeberg electrode can create large power fluctuations thus increasing the final cost and furthermore consuming more power than needed. Predictive algorithms for the control of the electrode positioning have been a subject of considerable interest in metallurgic industry in recent years. One of the main problems that needs to be addressed is accurate estimation of the electrode position with the respect to the ore. To this purpose it would be extremely beneficial to accurately estimate the ore volume, its shape and position in the furnace.

In order to achieve this goal we first need to develop an adequate mathematical model of the current distribution in a submerged arc furnace as a function of ore volume, size and position. The distribution of current in submerged furnaces has been addressed in previous work.

In [1] the authors modeled a horizontal slice taken through the three Persson-type electrode of a round furnace. A quasi-static state was assumed. Dhinaut computed the current path from the electrodes through the furnace contents of a round furnace using the CFD package FLUENT. The AC current was analyzed at a single time point. In [2] the authors calculated electric current distribution, temperature and flow patterns in a segment of six-in line rectangular nickel furnace. In addition they measured the voltage drop in the slag. They found that there was substantial voltage drop between the electrode and the slag which they attributed to the presence of an arc which gives rise to a plasma layer around the electrode. More recently, in [3, 4] the results for mathematical modeling of nickel furnaces have been presented.

In the present work, we propose to develop an inverse model that can be used to estimate ore volume, position and shape. Inverse models are complementary to commonly used forward models in which the parameters in the system are assumed to be known and the behavior of the system is simulated. Opposite to this inverse model assume that the physical parameters are not know and attempt to estimate them using physical measurements and reasonably accurate mathematical models. Obviously, due to the computational complexity of the inverse approach certain approximations are needed.

In Section 2, we develop a mathematical model for the current distribution in the submerged AC furnace assuming a two-phase system consisting of liquid phase (melted) and solid phase (ore). The two phases obviously have different conductivities which consequently creates different spatial distributions of the corresponding current density. In Section 3, we derive the parametric model and propose an estimation algorithm for estimating the ore parameters using the ground current flowing out of the furnace through the shielding. In Section 4, we demonstrate the applicability of the proposed technique using numerical simulations.

2. MATHEMATICAL MODEL

Since the frequency of the current is low (50–60 Hz) the quasi-static formulation of Maxwell laws is adequate mathematical model for the current distribution

$$\begin{aligned}\nabla \times E &= -\frac{\partial B}{\partial t} \\ \nabla \times H &= J \\ \nabla \cdot D &= \rho \\ \nabla \cdot B &= 0\end{aligned}\tag{1}$$

where E denotes the electric field intensity, H is the magnetic field, D is the electric flux density, B is the magnetic field, J is the electric current density and ρ is the electric charge density.

In a harmonic analysis it is assumed that the system is driven by a single frequency i.e., the current entering the furnace through the electrode is modeled as a sinusoidal wave. As a consequence all the variables of interest will have a single sinusoidal response i.e., assuming that the current entering the furnace is

$$I_i = I_0 \sin \omega t\tag{2}$$

than the variables of interest are given by

$$\begin{aligned}B(r, t) &= B_0 \sin(\omega t + \phi_B) \\ H(r, t) &= H_0 \sin(\omega t + \phi_H) \\ E(r, t) &= E_0 \sin(\omega t + \phi_E) \\ D(r, t) &= D_0 \sin(\omega t + \phi_D)\end{aligned}$$

where we use subscript 0 to denote amplitudes and variable ϕ to denote corresponding phase shifts. Note that in the case of linear and frequency independent permittivity/permeability the number of phase shift variables is reduced to two.

The solution to the above equations is well known for simple and regular geometries. In realistic problems however the structure usually consists of various subregions with different electro-magnetic properties (electric permittivity and/or magnetic permeability). Therefore, we model the furnace as a volume G of $M = 3$ homogeneous subregions separated by closed surfaces $S_i, i = 1, \dots, M$. Note that similar problem is often encountered in bioelectromagnetism and the corresponding solution is given through the Geselowitz equations in the integral form

$$\begin{aligned}\mathbf{B}(\mathbf{r}, t) &= \mathbf{B}_0(\mathbf{r}, t) + \frac{\mu_0}{4\pi} \sum_{i=1}^M (\sigma_i^- - \sigma_i^+) \cdot \int_{S_i} \phi(\mathbf{r}', t) \frac{(\mathbf{r} - \mathbf{r}')}{\|\mathbf{r} - \mathbf{r}'\|^3} \times dS(\mathbf{r}') \\ \mathbf{B}_0(\mathbf{r}, t) &= \frac{\mu_0}{4\pi} \int_G \frac{\mathbf{J}(\mathbf{r}', t) \times (\mathbf{r} - \mathbf{r}')}{\|\mathbf{r} - \mathbf{r}'\|^3} d^3r',\end{aligned}\tag{3}$$

where μ_0 is the magnetic permeability of the vacuum and σ_i^- and σ_i^+ be the conductivities of the layers inside and outside S_i respectively.

Similarly, the potential $\phi(\mathbf{r}, t)$ is given by (Geselowitz)

$$\begin{aligned}\frac{\sigma_k^- + \sigma_k^+}{2} \phi(\mathbf{r}, t) &= \phi_0(\mathbf{r})(\sigma_i^- - \sigma_i^+) + \frac{1}{4\pi} \sum_{i=1}^M (\sigma_i^- - \sigma_i^+) \int_{S_i} \phi(\mathbf{r}', t) \frac{(\mathbf{r} - \mathbf{r}')}{\|\mathbf{r} - \mathbf{r}'\|^3} \cdot dS(\mathbf{r}'), \\ \phi_0(\mathbf{r}, t) &= \frac{1}{4\pi} \int_G \frac{\mathbf{J}(\mathbf{r}', t) \cdot (\mathbf{r} - \mathbf{r}')}{\|\mathbf{r} - \mathbf{r}'\|^3} d^3r',\end{aligned}\tag{4}$$

where we k is chosen so that $\mathbf{r} \in G_k$.

However the implementation of the above solutions for the furnace problem requires two important modifications. First, the magnetic permeability of different sub-regions can be different and not equal to permeability of the vacuum. More importantly, the last subregion (layer) represents electromagnetic shield around the furnace which is grounded. Enforcing these conditions in the Geselowitz equations yields non-analytical solution i.e., one of discretization techniques either

boundary elements or finite elements is required. In order to deal with this problem we propose to use the finite-element formulation of the problem. We implement the Maxwell equations using commercial finite-element solver COMSOL and build the geometry using the structure illustrated in Figure 1. The details of the furnace structure were kindly provided to us by James Wikson, Hatch.

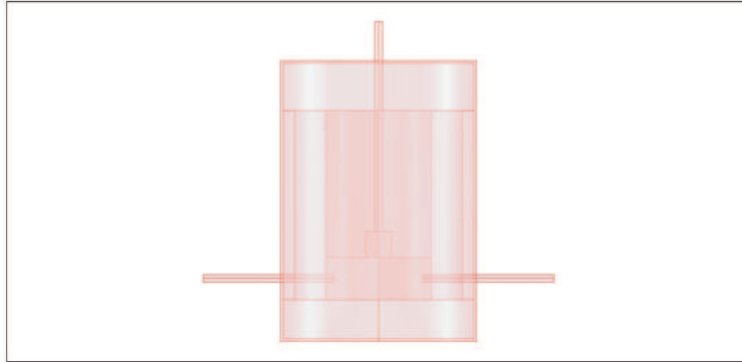


Figure 1: COMSOL geometry of the furnace.

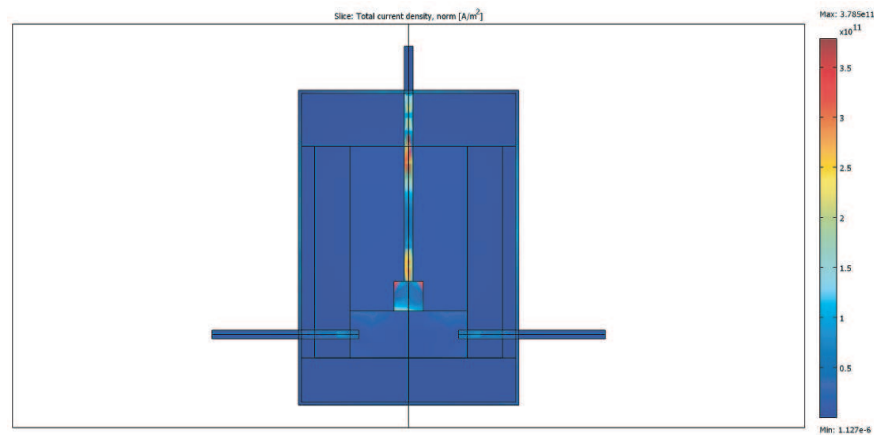


Figure 2: Long-axis map of current density — rms value.

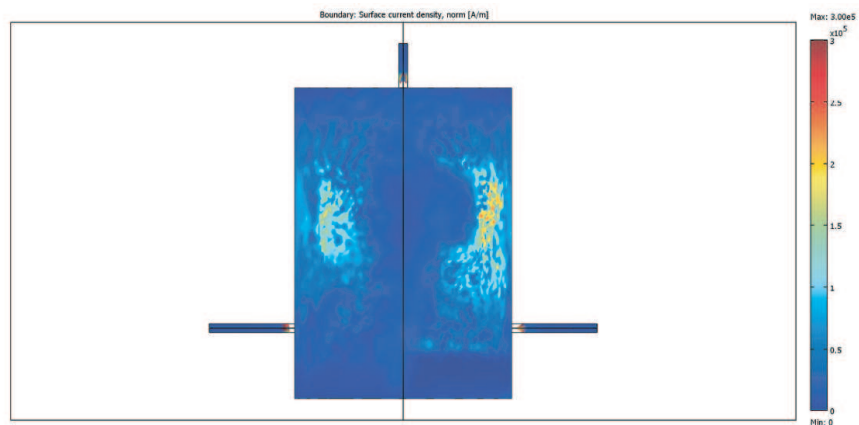


Figure 3: Shielding map of current density — rms value.

3. PARAMETRIC MODEL

In this section we introduce our parametric description of our mathematical model. First let us assume there are q points at which the outer layer of the furnace is shielded. Next let $J_i(t_j)$ denote the current density flowing through the i -th ground $i = 1, \dots, q$. Then the current density can be written as

$$J_i(t_j) = f_i(t_j) + e_i(t_j) \quad (5)$$

where $f_i(t_j)$ denotes COMSOL finite-element solution for point r_i and time t_j and e_i denotes the modeling error and measurement noise. Obviously the FE solution depends on variety of parameters: furnace geometry, electromagnetic properties of materials used for furnace bath and conductive bottom, nickel ore location, shape and size, the current flowing into the furnace through the electrode.

Note that in the process of melting the ore volume will be splitting into larger and larger number of smaller parts. Therefore we assume that the ore volume consists of p parts. In order to simplify problem we assume that all of these pieces can be modeled as prolate spheroids with center of masses \mathbf{r}_l^o , radiuses R_l and the axes of anomaly $\boldsymbol{\theta}_l = [a_l, b_l, c_l]$. Therefore we assume that the l th ore segment is modeled as

$$\mathcal{R}_{\uparrow} = \{\mathbf{r} : (\mathbf{r} - \mathbf{r}_l^o)^T F(a_l, b_l, c_l, \psi, \phi)^{-1} (\mathbf{r} - \mathbf{r}_l^o) \leq 1\}$$

where

$$F = T(\phi, \psi) \begin{bmatrix} a_l^2 & 0 & 0 \\ 0 & b_l^2 & 0 \\ 0 & 0 & c_l^2 \end{bmatrix} T^T(\phi_l, \psi_l)$$

ψ_l and ϕ_l are the orientation parameters (in 3D). The matrix $T(\phi_l, \psi_l)$ is the rotation matrix given by

$$T(\phi_l, \psi_l) = \begin{bmatrix} \cos\phi_l & \sin\phi_l & 0 \\ -\sin\phi_l & \cos\phi_l & 0 \\ 0 & 0 & 1 \end{bmatrix} \cdot \begin{bmatrix} \cos\psi_l & 0 & \sin\psi_l \\ 0 & 1 & 0 \\ -\sin\psi_l & 0 & \cos\psi_l \end{bmatrix} \quad (6)$$

We will further assume that the conductivities of nickel ore are unknown both in a solid and liquid phase σ_s and σ_l , respectively. Let us define the conductivity parameter vector $\boldsymbol{\sigma} = [\sigma_l, \sigma_s]^T$. We will further assume that all of the furnace parameters are known as well. Therefore the COMSOL solution can be written in the parametric form

$$f_i(t_j) \sim f_i(\boldsymbol{\alpha}, p, t_j) + e_i(t_j) \quad \boldsymbol{\alpha} = [\mathbf{r}_1^{oT}, \boldsymbol{\theta}_1^T, R_1, \dots, \mathbf{r}_p^{oT}, \boldsymbol{\theta}_p^T, R_p]^T \quad (7)$$

Note that the number of ore segments is not known.

Next, we assume that the current density is measured at grounding points and that time samples are taken at uniformly spaced time points $t_j, j = 1, \dots, n$. In addition, we assume that data acquisition is repeated during several periods in order to improve the signal-to-noise (SNR) ratio. Then, the q -dimensional measurement vector of this array obtained at time t_j in the k th cycle is

$$\mathbf{y}_j = \mathbf{f}_j(\boldsymbol{\alpha}, p) + \mathbf{e}_j, \quad (8)$$

where $\mathbf{y}_j = [J_1(t_j), \dots, J_q(t_j)]^T$, $\mathbf{f}_j(\boldsymbol{\alpha}, p, t_j) = [f_1(\boldsymbol{\alpha}, p, t_j), \dots, f_q(\boldsymbol{\alpha}, p, t_j)]^T$ is the vector solution computed using finite elements, and $\mathbf{e}_j = [e_1(t_j), \dots, e_q(t_j)]^T$ is additive noise.

4. PARAMETER ESTIMATION

First we define the estimation algorithm assuming that estimates for the number of segments \hat{p} is known. To compute estimates $\boldsymbol{\alpha}$ and $\boldsymbol{\sigma}$ as a preliminary approach we propose to use least-squares estimator which minimizes the following cost functions iteratively

$$c_{\alpha}(\boldsymbol{\alpha}, p) = \sum_{j=1}^n \|\mathbf{y}_j - \mathbf{f}_j(\boldsymbol{\alpha}, p, \hat{\boldsymbol{\sigma}})\|^2 \quad c_{\sigma}(\boldsymbol{\sigma}, p) = \sum_{j=1}^n \|\mathbf{y}_j - \mathbf{f}_j(\hat{\boldsymbol{\alpha}}, p, \boldsymbol{\sigma})\|^2 \quad (9)$$

and thus

$$\hat{\boldsymbol{\alpha}}^p = \operatorname{argmin} c_{\alpha}(\boldsymbol{\alpha}, p) \quad \hat{\boldsymbol{\sigma}}^p = \operatorname{argmin} c_{\sigma}(\boldsymbol{\sigma}, p) \quad (10)$$

In order to find the unknown number of parameters we propose the model order selection using forward error propagation

- Step 1: Set $p = 1$
- Step 2: Calculate corresponding $\hat{\alpha}^p$ and $\hat{\sigma}^p$ using the above cost functions and calculate corresponding errors c_1^p and c_2^p .
- Step 3: Set $p = p + 1$
- Step 4: Repeat steps 2–4 for relatively small number of segments i.e., for $p \leq 10$
- Step 5: Pick $\hat{p} = \operatorname{argmin} c_\alpha^p + c_\sigma^p$

5. NUMERICAL EXAMPLES

We now present numerical results that demonstrates the applicability of the proposed algorithms. The furnace model was created using input current of 1 kA, operating temperature 3000 K. In forward simulation we used nickel conductivity set to 13.8×10^6 s/m at 25°C and 0.815×10^6 s/m at 3000 K. The conductivity of the shielding was set to 1.12×10^7 s/m. The relative permeability of nickel liquid, nickel ore, and shield were set to 1, 600 and 4000 respectively. The volumetric mesh was created using 15902 elements with 20830 degrees of freedom for the torso (electromagnetic) model and 1856 elements and 6190 degrees of freedom for the heart (diffusion) model.

In Figures 2 and 3 we illustrate the current density map in the long-axis resection as well as on the shielding surface. In both cases the ore volume is assumed to be spherical with radius 1 and axes (0.04, 0.02, 0.03) with location (0.1, 0.5, 0.5) respectively. Note all the dimensions are relative with respect to furnace bath dimensions. As it can be seen the surface map is asymmetric due to the asymmetric geometry of the ore.

In Figures 4 and 5, we illustrate the estimation results. In Figure 4, for reference purposes, we illustrate the estimation error when the shape i.e., location, size and axes is known. In Figure 5, we illustrate the estimation error when the ore parameters are not known. In both cases we assumed that the nickel phase conductivities are not known. The presented results represent average results for 100 runs in which the conductivity search point was set using nickel conductivity at 25°C. As expected when the number of parameters is larger (Figure 5) the performance deteriorates however the level of estimation error is still acceptable when compared to results that are obtained by simply calculating the portion of the liquid mass using the total power consumed by the furnace.

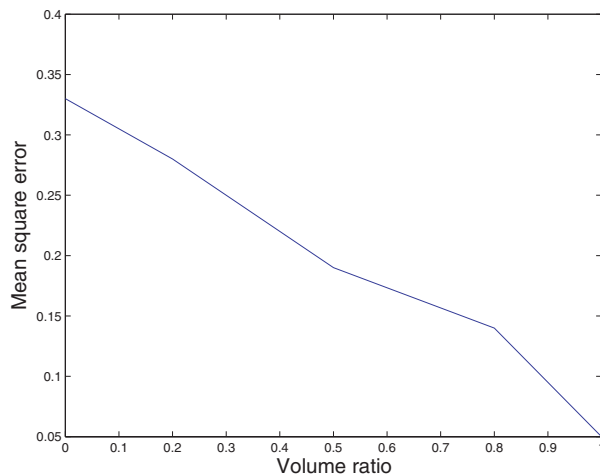


Figure 4: Mean square error — known shape.

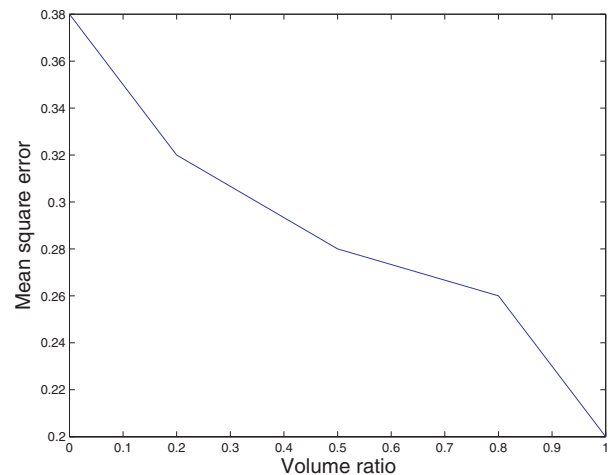


Figure 5: Mean square error — unknown shape.

6. CONCLUSIONS

We addressed the problem of estimating the ore volume using finite-element method and shielding currents. To model the nickel ore we used parametric model assuming elliptic shape of the ore segments. This model can be extended to model an arbitrary region using a three-dimensional spatial Fourier transform but that would significantly increase computational complexity. To the best of our knowledge this is a first attempt to estimate the ore volume using the shielding currents and our preliminary results indicate that the problem is invertible i.e., the unknown parameters can be estimated.

REFERENCES

1. Bermudez, A., M. C. Muniz, and J. Bullon, “Numerical computation of the aeromagnetic field in the electrodes of a three-phase arc furnace,” *Int. Jnl. for Numerical Methods in Engineering*, Vol. 46, 649–658, 1999.
2. Dhainaut, M., “Simulation of the electric field in a submerged arc furnace,” *Prof. INFACON X*, 605–613, 2004.
3. Sheng, Y. Y., G. A. Irons, and D. G. Tisdale, “Transport phenomena in electric smelting of nickel matte: Part 1. Electric potential distribution,” *Metallurgical and Materials Transactions B*, Vol. 29B, 77–83, Feb. 1998.
4. Sheng, Y. Y., G. A. Irons, and D. G. Tisdale, “Transport phenomena in electric smelting of nickel matte: Part 2. Mathematical modelling,” *Metallurgical and Materials Transactions B*, Vol. 29B, 77–83, Feb. 1998.
5. Vonesh, E. F. and V. M. Chinchilli, *Linear and Nonlinear Models for the Analysis of Repeated Measurements*, Marcel Dekke, New York, 1997.

3D AGILD Mechanical Modeling for Simulations of New Materials

Jianhua Li^{1,2}, Feng Xie², Ganquan Xie², Chien-Chang Lin¹, and Michael Oristagi³

¹Department of Mechanical and Automation Engineering, Da-Yeh University, Taiwan

²Department of Modeling and Inversion, GL Geophysical Laboratory, USA

³Schlumberger-Doll Research Center, Cambridge, MA, USA

Abstract— The Advanced Global Integral and Local Differential (AGILD) modeling is a development of GILD modeling. AGILD preserves the all merits of GILD method and is simpler than GILD. In this paper, a new 3D mechanical differential integral strip equation is derived. The new mechanical equation on strip boundary and LAME differential equation in the internal domain are coupled to construct AGILD mechanical (AGILDME) modeling. AGILDME can be applied in developing of new materials such as nanometer materials and left hand materials; it can be used in the areas of stirring, geophysics, GPR, nondestructive testing etc. sciences and engineering.

1. INTRODUCTION

The Global Integral and Local Differential (GILD) Modeling and Inversion, GILD-SOR Modeling and Inversion for E-O-A Strategic Simulation have been developed by Xie and Li in 1999 [1, 2]. Xie et al. developed 3-D electromagnetic modeling and nonlinear inversion in 2000 [3]. In 2001, Feng Xie et al. developed a fast GILD mechanical and flow modeling for micro scale visualization and digit movie realization [4]. In 2002 and 2003, Xie, Lin and Li developed GILD mechanical modeling for nanometer materials simulations [5, 6]. The AGILD electromagnetic modeling and inversion was proposed by Xie and Li in 2004 [7]. F. Xie et al. developed AGILD mechanical modeling [8] and AGILD flow modeling. Li et al. developed 3D and 2D stochastic AGILD electromagnetic and mechanical modeling in 2006 [9]. In 2007, Li, Lin and Xie developed AGILD wavelength match tomography ray mechanical modeling [10], Lin, Li, and Xie developed improved isoparameter FEM [11]. In this paper, according proposed AGILD mechanical modeling in [8], we develop 3D AGILD mechanical modeling for simulations of new materials.

The description plan of this paper is as follows. The introduction is described in Section 1. In Section 2, we present 2.5D strip mechanical differential integral equation on the boundary strip zone. AGILD mechanical modeling is developed in Section 3. We describe the advantages and applications of the AGILDME modeling in Section 4. The simulations of the AGILDME modeling is presented in Section 5. The Sections 6 will conclude this paper.

2. 3D STRIP MECHANICAL DIFFERENTIAL INTEGRAL EQUATION

In this section, we present the 3D strip mechanical differential integral equation on the boundary strip zone Ω_s [8],

$$u(r) = u_b(r) - \int_{\Omega_s} \varepsilon(G_b(r', r)) D(E, \nu, E_b, \nu_b) \varepsilon(u(r')) dr' + \int_{\partial\Omega_i} [\sigma(G_b)u - \sigma(u)G_b] d\vec{s} \quad (1)$$

where $u(r)$ is displacement, $u_b(r)$ is initial incident displacement in the background medium, $G_b(r', r)$ is the displacement Green's tensor in background medium, $\varepsilon(G_b(r', r))$ is the strain Green's tensor in background medium, $D(E, \nu, E_b, \nu_b)$ is the variation of the mechanical materials, $\varepsilon(u(r'))$ is the strain. Ω_s is a strip domain located between the double boundary layers $\partial\Omega_0 \cup \partial\Omega_i$, and with $E - E_b \neq 0$ and $\nu - \nu_b \neq 0$, $\partial\Omega_0$ is the external boundary of the strip domain Ω_s . $\partial\Omega_i$ is the internal boundary of the strip domain Ω_s , E is the Young's modulus, ν is Poisson's ratio, E_b is the background Young's modulus, ν_b is the background Poisson's ratio, ρ is the density, ρ_b is the background density, ω is the angle frequency, ε is the strain, and σ is the stress.

3. ADVANCED GILD MECHANICAL MODELING

In this section, we describe Advanced AGILD mechanical modeling [8].

3.1. Finite Element Equation of the Boundary Strip Equation

The strip domain Ω_s is inside the double-layered boundary. Ω_s is divided into a strip set Ω_s^h of the cubic elements with 8 nodes. The point r is located in external layer, r' is located in the internal layer $\partial\Omega_i$ and Ω_s^h . $\partial\Omega_i$ is divided into a set $\partial\Omega_i^h$ of the rectangle elements which is the internal layer of Ω_s^h . The differential integral Equation (1) is discretized as

$$u^h(r_i) = u_b^h(r_i) - \int_{\Omega_s^h} \varepsilon(G_b(r', r_i)) D(E, \nu, E_b, \nu_b) \varepsilon(u^h(r')) dr' - \int_{\Omega_s^h} \omega^2(\rho - \rho_b) G_b(r', r_i) u^h(r') dr' + \int_{\partial\Omega_i} [\sigma(G_b) u^h - \sigma(u^h) G_b] d\vec{s} \quad (2)$$

where $u^h(r_i)$ is the finite element approximation of $u(r_i)$, Equation (2) is collocation finite element equation of the (1). The Equation (2) is the matrix equation

$$K_{bb}u_b^h + K_{bd}u_d^h = Q_b^s \quad (3)$$

3.2. Finite Element Equation in the Internal Domain

In the internal domain D which is inside $\partial\Omega_i$, we use Galerkin FEM method and the cubic element to discretize the Lamé displace field differential equation

$$L(E, \nu)\sigma(u) + \rho\omega^2u = f \quad (4)$$

The Galerkin finite element equation is as follows

$$\int_{\partial\Omega_i^h} \sigma(u^h)_n \phi d\vec{s} - \int_{\Omega_d^h} \varepsilon^T(\phi) D(E, \nu) \varepsilon(u^h(r')) dr' + \rho\omega^2 \int_{\Omega_d^h} u^h \phi dr' = \int_{\Omega_d^h} f^h \phi dr' \quad (5)$$

where Ω_d^h is the finite element domain of the internal domain D , $\partial\Omega_i^h$ is the finite element set of $\partial\Omega_i$, ϕ is the finite element base tensor function, Equation (5) is the matrix equation.

$$K_{db}u_b^h + K_{dd}u_d^h = Q_d^s \quad (6)$$

where u_b^h is the displace field on the finite element external boundary $\partial\Omega_0^h$, u_d^h is the magnetic field inside the finite element internal domain Ω_D^h , K_{db} is the finite element matrix in internal domain Ω_D^h and relative to $\partial\Omega_0^h$, K_{dd} is the finite element matrix in internal domain Ω_D^h and relative to Ω_D^h , K_{db} and K_{dd} are sparse matrices.

3.3. The Advanced GILD Mechanical (AGILDME) Modeling

The collocation finite element matrix Equation (3) and the Galerkin finite element matrix Equation (6) are coupled to construct the advanced GILD mechanical modeling. The GILD mechanical modeling matrix inversion is assembled element by element from the internal domain to the boundary in parallel [8].

4. ADVANTAGES

The Finite Element Method (FEM) is an effective method for mechanical modeling, However, FEM method meets difficulties in solving massive matrix for simulation of the large scale and micro scale and dynamic mechanical problem, in particular, nanometer materials and various dispersive materials. AGILDME modeling provides a fast layer to layer algorithm to solve big matrix.

Other difficulty of FEM is the artificial boundary for truncating infinite domain of dynamic mechanical problem. The inaccurate radiation boundary condition in FEM will degrade its accurate. 3D AGILDME modeling uses the strip mechanical differential integral equation on the boundary strip zone that is exact boundary condition to truncate infinite domain. 3D AGILDME is perfect and high performance parallel algorithm with over 90% parallel rate.

5. APPLICATIONS

The AGILDME has wide applications in developing of new materials such as nanometer materials and left hand materials; the modeling can be used in the areas of stirring, geophysics, GPR, nondestructive testing etc. sciences and engineering. Several applications show that AGILDME modeling method is fast and accurate.

6. THE SIMULATION OF AGILDME MODELING FOR NANOMETER CRYSTAL

Authors use the AGILD mechanical modeling to develop a flow animal visualization imaging. Then an AGILD periodic mechanical modeling for nanometer crystal deformation is developed. The very reasonable 3D nanometer crystal deformation under 0.001 dyn point force is shown in Figures 1 and 2. The crystal deformation imaging is made by Lee Xie's AGILDME software in GLGEO.

Figure 1 shows the Deformation in Section $y = 0$ nm, while Figure 2 the Deformation in Section $y = 20$ nm.

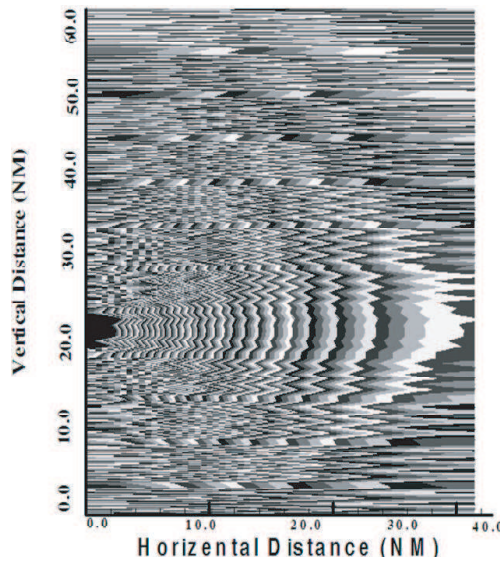


Figure 1: Deformation in Section $y = 0$ nm.

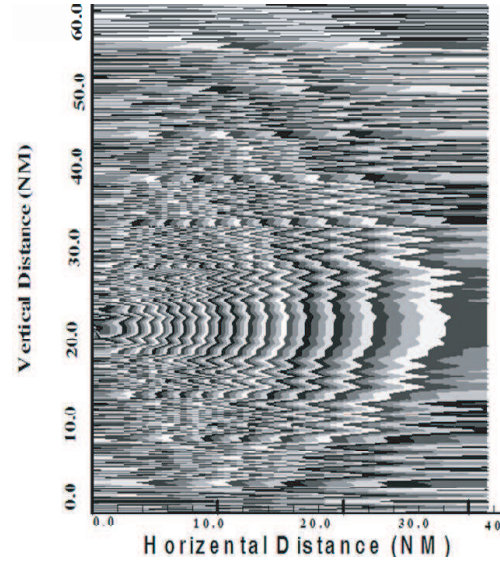


Figure 2: Deformation in Section $y = 20$ nm.

7. CONCLUSION

The 3D AGILDME modeling has wide applications. It can be applied in developing of new materials such as nanometer materials and left hand materials; it can be used in the areas of stirring, geophysics, GPR, nondestructive testing etc. sciences and engineering. The modeling is suitable for parallelizing. The simulation tests show that AGILDME modeling method is fast and accurate for large scale data analysis.

ACKNOWLEDGMENT

This research was partially supported by the National Science Council through Grant NSC 97-2811-E-212-002 and NSC-097-2221-E-212-013.

REFERENCES

1. Xie, G. and J. Li, "New parallel stochastic global integral and local differential equation modeling and inversion," *Physica D*, Vol. 133, 477–487, 1999.
2. Xie, G. and J. Li, "GILD-SOR modeling and inversion for E-O-A strategic simulation," *Institute for Mathematics and Computer Science (IMACS) Series Book in Computational and Applied Math.*, Vol. 5, 123–138, 1999.
3. Xie, G., J. Li, E. L. Majer, D. Zuo, and M. L. Oristaglio, "3-D electromagnetic modeling and nonlinear inversion," *Geophysics*, Vol. 65, No. 3, 804–822, 2000.
4. Xie, F., J. Li, L. Xie, and G. Xie, "Advanced GILD mechanical and flow modeling for digital movie visualization," *GL Geophysical Laboratory Technology Report GLAGILDME*, 2005.
5. Xie, G., C.-C. Lin, and J. Li, "New 3D GILD mechanical modeling and inversion," *Mathematica Applicata*, Vol. 16, No. 2, 149–156, 2003.
6. Lin, C.-C., G. Xie, J. Li, and B. Lin, "Deformation analysis for materials using GILD mechanical modeling," *The Chinese Journal of Mechanics-Series A*, (A Special Issue Dedicated to the Seventieth Birthday of Professor Thomas Chi Tsai), Vol. 19, No. 1, 73–81, 2003.
7. Xie, G., J. Li, and F. Xie, "Advanced GILD EM modeling and inversion," *PIERS Online*, Vol. 1, No. 1, 105–109, 2005.

8. Xie, F., L. Xie, J. Li, and G. Xie, "GILD mechanical field modeling," SM05 Elasticity, *XXII ICTAM*, Adelaide, Australia, August 25–29, 2008.
9. Li, J., G. Xie, and F. Xie, "New stochastic AGLID EM modeling and inversion," *PIERS Online*, Vol. 2, No. 5, 490–494, 2006.
10. Li, J., C.-C. Lin, and G. Xie, "AGILD WMT ray-tracing interactive tomography," FSM01 Acoustics, *XXII ICTAM*, Adelaide, Australia, August 25–29, 2008.
11. Lin, C.-C., J. Li, G. Xie, and M. Oristaglio, "Improved isoparameter FEM for plastic and EM modeling," *PIERS Online*, Vol. 4, No. 2, 231–237, 2008.

Error and Domain of Applicability Studies for the Schmutge's Dielectric Model of Moist Soils

V. L. Mironov¹, J.-P. Wigneron², F. Demontoux³, S. V. Fomin¹, and L. G. Kosolapova¹

¹Kirensky Institute of Physics SB RAS, Krasnoyarsk, Russia

²EPHYSE INRA Centre Bordeaux Aquitaine, France

³Bordeaux University, IMS Laboratory, France

Abstract— In this paper, there was studied correlation of dielectric predictions for moist soils with the measured values, regarding the well known empirical dielectric model proposed by J. R. Wang and T. J. Schmutge. The analysis is based on the measured dielectric data borrowed from the Technical Report EL-95-34, by J. O. Curtis et al., in which the assemblage of soils measured included all of grain-size distributions that are observed in nature, with measurements being performed over the frequency range from 45 MHz to 26.5 GHz at the moistures spanning from the nearly dry samples to the ones saturated close to the field capacity values. As far as it concerns the dielectric constant, the Schmutge model was shown to be applicable in the frequency range from 0.3 to 14 GHz to the soils beyond the ensemble of soils with dielectric data of which it was developed. In the case of loss factor, this model was found to provide for accurate dielectric predictions only over the frequency range from 5.0 GHz to 14 GHz, concerning the ensemble of dielectric data independently measured.

1. INTRODUCTION

An adequate dielectric model is an essential element of all the data processing algorithms used in the radar and radio thermal remote sensing of the land. The well known Schmutge dielectric model for moist soils [1] is used in the algorithms of radio brightness data processing [2]. This model is based on the dielectric data measured only at three frequencies 1.4, 1.412 and 5.0 GHz, moistures varying from 0 to the field capacity values, and soil clay contents from 0 to 62 percent. Regarding the soil mineralogy properties, the Schmutge dielectric model uses the clay and sand gravimetric percentages as the only input parameters. The dielectric predictions by this model are accurate with regard to all the dielectric data used for its development in [1]. The main cause for good accuracy achieved is that it takes into account the property of the initially adsorbed molecules of the bound water in soil. At the same time, a domain of applicability and error of the Schmutge model have not been studied yet, regarding other frequencies and soils. This problem is analyzed by the authors on the bases of the comprehensive dielectric data set available in [3]. The data base taken from [3] covers the frequency range from 0.045 to 26.5 GHz, clay contents from 0 to 76 percent and the moistures up to field capacity values.

2. THE EMPIRICAL MODEL CONCEPT

The empirical approach of the Schmutge model [1] deals with the direct mixing of the dielectric constants of moist soil constituents. It bases on the straightforward combination of the dielectric constants of ice, bound and free water, air, and rock. The expressions for the complex dielectric constant, ε , of a soil-water mixture are given by

$$\varepsilon = W\varepsilon_b + (P - W)\varepsilon_a + (1 - P)\varepsilon_r, \quad W \leq W_t \quad (1)$$

$$\text{with } \varepsilon_b = \varepsilon_i + (\varepsilon_w - \varepsilon_i) \frac{W}{W_t} \gamma \quad (2)$$

$$\text{and } \varepsilon = W_t\varepsilon_b + (W - W_t)\varepsilon_w + (P - W)\varepsilon_a + (1 - P)\varepsilon_r, \quad W > W_t \quad (3)$$

$$\text{with } \varepsilon_b = \varepsilon_i + (\varepsilon_w - \varepsilon_i) \gamma. \quad (4)$$

Here P is the porosity of the dry soil. ε_a , ε_w , ε_r , and ε_i , are the dielectric constants of air, water, rock, and ice, respectively. ε_b stands for the dielectric constant of the initially absorbed water (bound water). With W is designated the volumetric water content in the soil, W_t is the transition moisture. γ is a parameter which can be chosen to best fit (1)–(4) to the experimental data. The complex dielectric constant has the real and imaginary parts further referred to as the dielectric constant (DC), ε' , and the loss factor (LF), ε'' .

For the LF at low frequencies it is necessary to add ohmic conductivity losses. Therefore, the total LF, ε_t'' , has to be written in the form

$$\varepsilon_t'' = \varepsilon'' + \alpha W^2 \quad (5)$$

where ε'' is given by (1)–(4) and α is the parameter chosen to best fit Formula (5) to the measured ε_t'' at low frequencies. Applying regression analysis, over the dielectric data set available in [1] at frequencies 1.4 and 5.0 GHz the authors of [1] determined the parameters γ , W_t , as a function of wilting point WP as follows:

$$\gamma = -0.57WP + 0.481, \quad W_t = 0.49WP + 0.165, \quad (6)$$

with correlation coefficients being of 0.79 and 0.91 for γ and W_t , respectively. The wilting point (WP) of soils in percent of dry weight was previously obtained by Schmutge et al. [4] from a multiple regression analysis of over 100 data sets of soil moistures characteristics. The expression for WP in terms of volumetric water content (cm^3/cm^3) was redetermined by the same procedure and the result is expressed in the form

$$WP = 0.06774 - 0.00064S + 0.00478C \quad (7)$$

where C and S are the clay and sand contents of dry soil, in percent by weight. The values of parameter $\alpha(C)$ derived from linear fitting with the use of data given in [1] at the frequencies of 1.4 and 5.0 GHz can be expressed with the formulas

$$\alpha = 0.532C \text{ at } 1.4 \text{ GHz}; \quad \alpha = 0 \text{ at } 5.0 \text{ GHz}. \quad (8)$$

while fitting in [1] the complex dielectric constants calculated with the use of (1)–(5) to the measured ones, the liquid water complex dielectric constant, ε_w at the frequency of 1.4 GHz was assigned with the following values of DC, $\varepsilon_w' = 79.5$, and LF, $\varepsilon_w'' = 6.63$. At the frequency of 5.0 GHz, the authors of [1] suggested to calculate the water complex dielectric constant with the use of the Debye formula, which are shown below

$$\varepsilon_w' = \varepsilon_\infty + \frac{\varepsilon_0 - \varepsilon_\infty}{1 + (2\pi f\tau_w)^2}, \quad \varepsilon_w'' = \frac{\varepsilon_0 - \varepsilon_\infty}{1 + (2\pi f\tau_w)^2} 2\pi f\tau_w + \frac{\sigma_w}{2\pi\varepsilon_r f}. \quad (9)$$

In Formulas (9), the value f designates wave frequency, while the values ε_0 , and $\varepsilon_\infty = 4.9$, τ_w , and σ_w , are the low and high frequency limits DC, relaxation time, and ohmic conductivity, respectively. While ε_r is the DC of the vacuum. In order to use Formula (9) the respective spectroscopic parameters have to be known. To derive the spectroscopic parameters, ε_0 , τ_w , and σ_w , we fitted Formula (9) at the frequency of 1.4 GHz to the values of $\varepsilon_w'(1.4 \text{ GHz}) = 79.5$ and $\varepsilon_w''(1.4 \text{ GHz}) = 6.63$ given by Schmutge et al. in [1] thus obtaining the following spectroscopic parameters:

$$\varepsilon_0 = 80, \quad \tau_w = 9.28 \cdot 10^{-12}, \text{ s and } \sigma_w = 0.04232, \text{ Sm/m}. \quad (10)$$

As a result, the values of $\varepsilon_w' = \varepsilon_w'(f)$ $\varepsilon_w'' = \varepsilon_w''(f)$ can be calculated with the use of (9) and (10) at any frequency assigned. At the frequency of 5.0 GHz, we obtained the numerical values for DC, $\varepsilon_w' = 74.1$ and LF, $\varepsilon_w'' = 20.4$, of the water dielectric constant, which should be used in Formulas (1)–(4). With the Equations (9) and (10) being available, the set of Formulas (1)–(8) are sufficient to make predictions of the DCs and LFs as a function of volumetric moisture, and clay content not only at the frequencies of 1.4 and 5.0 GHz, but at any frequency assigned, thus allowing to validate the Schmutge model dielectric predictions for the values measured in [3] in a large frequency range from 0.045 to 26.5 GHz. In the following section, the error and frequency domain of the Schmutge model applicability is analyzed.

3. ERROR AND FREQUENCY DOMAIN OF APPLICATION

To consider the frequency domain of application and error for the Schmutge model, the DCs and LFs predictions provided with this model were correlated with the measured ones available in [3]. The DCs and LFs measured in [3] belong to a broad variety of 11 soils, clay gravimetric contents varying from 0 to 76%. The values of DC and LF were measured in an extended frequency range from 0.045 to 26.5 GHz at the moistures spanning from air dry soils to those saturated at field

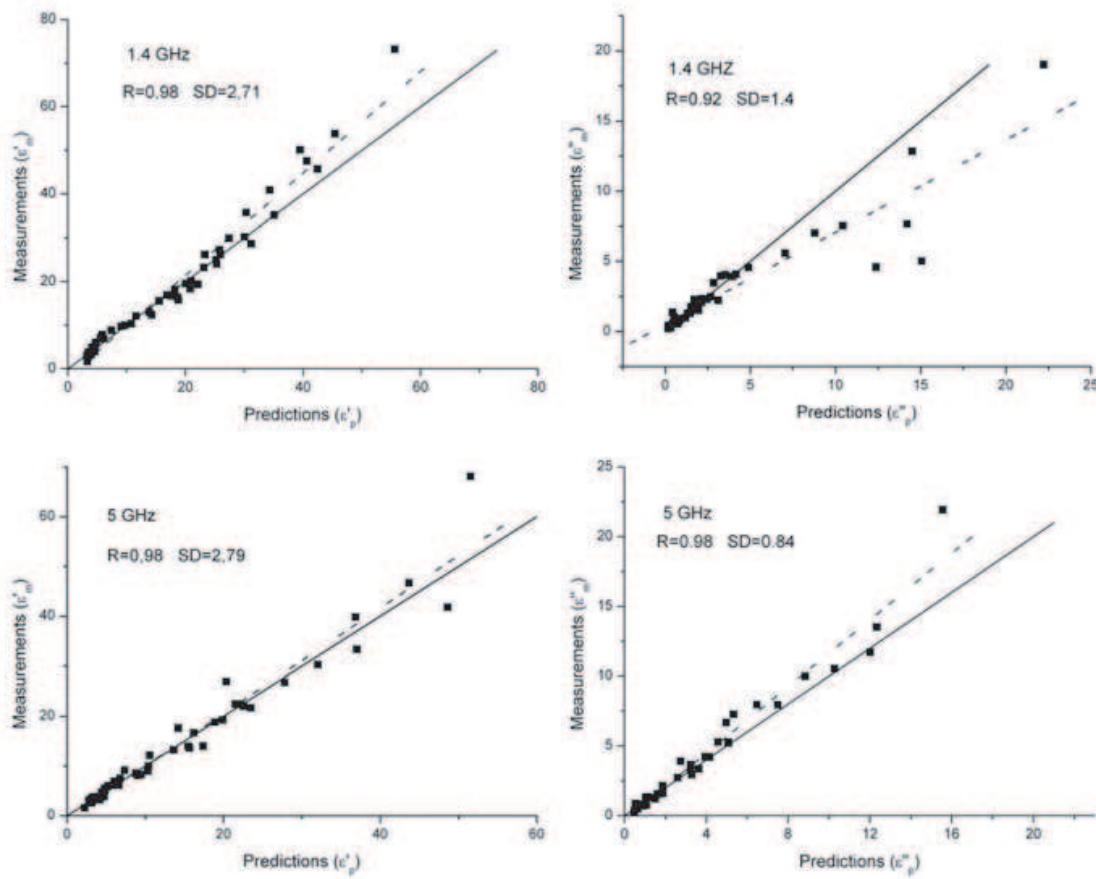


Figure 1: Correlation of the Schmugge model predictions, ε'_p , ε''_p , for DC and LF with the measured ones, ε'_m , ε''_m , available in [3]. Solid and dotted lines represent bisectors and linear fits, respectively. The frequencies, correlation coefficients, R , and standard deviations, SD , are shown in the respective graphs. The linear fits are expressed as follows: $\varepsilon'_m = -1.89 + 1.17\varepsilon'_p$, $\varepsilon''_m = 0.49 + 0.66\varepsilon''_p$ for 1.4 GHz and $\varepsilon'_m = -0.55 + 1.05\varepsilon'_p$, $\varepsilon''_m = -0.31 + 1.20\varepsilon''_p$ for 5 GHz.

capacity. First of all, we validated the predictions obtained with the Schmugge model at 1.4 and 5.0 GHz. In this case, all the input parameters in Formulas (1)–(8) are directly available from [3].

Figure 1 shows the DC, ε' , and LF, ε'' , measured as a function of the DC and LF predictions calculated with the Formulas (1)–(10).

As seen from Fig. 1, in the case of DC there is a good correlation between the measured and predicted values, with the correlation coefficients and standard deviations being on the same order at both frequencies. While the predicted LFs at the lower frequency of 1.4 GHz appeared to be noticeably less correlated with the measured ones. For this frequency, not only the values of correlation coefficient and standard deviation are found to be lower and greater, respectively, than the ones relating to the frequency of 5.0 GHz, but also a substantial squint of the linear fits relative to the bisectors are clearly observed. At the same time, the Schmugge model predictions for the LFs calculated at the frequency of 1.4 GHz showed a lot better correlation to the ones measured for the variety of soils used for its developing [1].

With this in mind, we correlated the DCs and LFs calculated with the Formulas (1)–(10) to the ones measured for two groups of frequencies: $f = 0.3; 0.5; 1.4; 5; 14$ GHz and $f = 5; 10; 14$ GHz. The result of that analysis presented in Fig. 2 proves the Schmugge model to give good DC predictions the soil types and frequencies other than those used for its development. On the other hand, in the case of the LF, the Schmugge model was found to provide for predictions with acceptable error only at the frequency of 5.0 GHz (see Fig. 1). We extended this frequency range to the higher frequencies, with the value of parameter α in (2) being equal to zero as calculated in [1], and found good correlation between the predicted values with the LFs measured in [3] for other soils in the extended frequency range, from 5.0 to 14 GHz, as seen from Fig. 2.

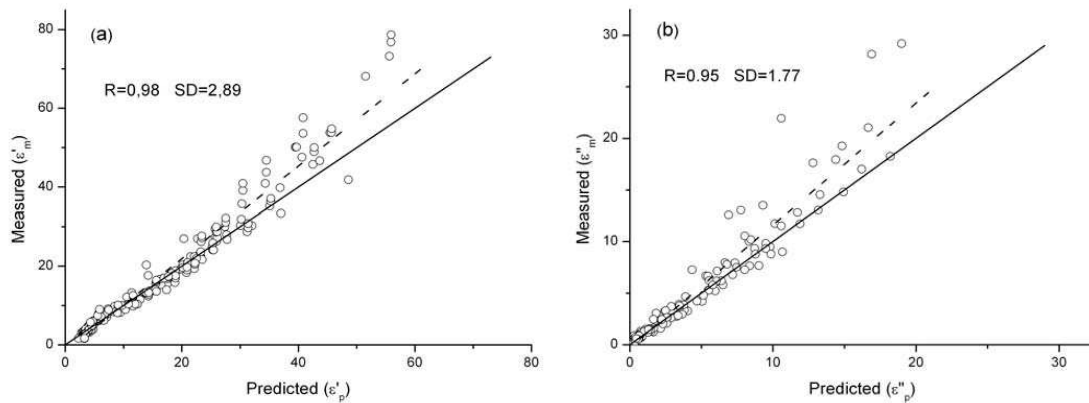


Figure 2: Correlation of the Schmugge model predictions, ε'_p , ε''_p , for DC (at the frequencies of 0.3, 0.5, 1.4, 5.0 and 14 GHz) and LF (at the frequencies of 5.0, 10 and 14 GHz) with the measured ones, ε'_m , ε''_m , available in [3]. Solid and dotted lines represent bisectors and linear fits, respectively. The frequencies, correlation coefficients, R, and standard deviations, SD, are shown in the respective graphs. The linear fits are expressed as follows: $\varepsilon'_m = -1.54 + 1.17\varepsilon'_p$, $\varepsilon''_m = -0.23 + 1.18\varepsilon''_p$.

4. CONCLUSION

As far as it concerns the DC, the Schmugge model provides for the predictions on the same order of error with regard to all frequencies, soils and moistures independently measured in [3] as it does for the soils, frequencies and moistures measured in [1], to develop this model. As a result the Schmugge model was shown to be applicable to the soils beyond the ensemble of soils with dielectric data of which it was developed and not only for the frequencies of 1.4, 1.412 and 5.0 GHz, but in the whole range from 0.3 to 14 GHz. At the same time in the case of LF, the Schmugge model was found to provide for accurate dielectric predictions only over the frequency range from 5 to 14 GHz, concerning the ensemble of soils independently measured in [3].

ACKNOWLEDGMENT

This research was supported by the RFBR-CNRS grant No. 09-05-91061.

REFERENCES

1. Wang, J. R. and T. J. Schmugge, "An empirical model for the complex dielectric permittivity of soils as a function of water content," *IEEE Trans. Geosci. Remote Sens.*, Vol. GE-18, No. 4, 288–295, 1980.
2. Wigneron, J.-P., et al., "L-band microwave emission of the biosphere (L-MEB) model: Description and calibration against experimental data sets over crop fields," *Remote Sens. Env.*, Vol. 107, 639–655, 2007.
3. Curtis, J. O., C. A. Weiss, Jr., and J. B. Everett, "Effect of soil composition on dielectric properties," Technical Report EL-95-34, Dec. 1995.
4. Schmugge, T., T. Whilheit, W. Webster, Jr., and P. Gloersen, "Remote sensing of soil moisture with microwave radiometers-II," NASA TN D-8321, National Aeronautics and Space Administration, Sep. 1976.

Effect of Antireflective Surface at the Radiobrightness Observations for the Topsoil Covered with Coniferous Litter

V. L. Mironov¹, P. P. Bobrov^{1,2}, A. S. Yashchenko^{1,2},
I. V. Savin¹, and A. V. Repin^{1,2}

¹Kirensky Institute of Physics, SB RAS, Krasnoyarsk, Russia

²Omsk State Pedagogical University, Omsk, Russia

Abstract— In radio thermal remote sensing of the land, a spot on the earth surface emitting the signal received by the microwave radiometer antenna may be partially or completely covered by forest. We developed a theoretical model to calculate radiobrightness of the layered topsoil. Using this model we derived the dielectric constants pertaining to the separate layers of topsoil. For this purpose, we applied the least squares method for fitting the calculated diurnal radiobrightness dependences to those measured. The forest soil covered with coniferous litter was modeled by a three steps dielectric profile, the interfaces between the separate layers being smooth. The theoretical modeling conducted confirmed that, at the moments of maximal radiobrightness, an antireflective layer was formed on the topsoil surface, most probably due to nonisothermal upward moving of soil moisture. At that, the theoretically calculated dielectric constant of the litter antireflecting layer was found to be on the same order as the value measured in laboratory conditions.

1. INTRODUCTION

One of the goals of the SMOS program (Soil Moisture and Ocean Salinity) of the European Space Agency is regional monitoring of soil surface moisture with the use of the space born radiometer at the frequency of 1.4 GHz [1]. As forest areas approximately cover the third of the land, a spot on the land surface radiating towards the radiometer antenna may be partly or completely covered with forest. Once the forest canopy is semi-transparent at the frequency of 1.4 GHz, the studies of radiating properties pertaining to the forest soil covered with litter are of significant interest [2]. Nevertheless, only a few papers are available in the literature regarding the problem of radio thermal radiation of the forest soil covered with the organic matter. For instance, moisture estimations through radiobrightness measurements were carried out in [3] in the case of grassy litter. While the authors of [4] founded that the litter in deciduous forest noticeably affects the radiobrightness observed. In this paper, we studied the influence of coniferous forest litter on the radiobrightness diurnal cycles.

2. MEASUREMENT DESCRIPTION

The measurements were carried out at the test site “Pogorelsky Bor” of the Institute of Forest SB RAS located near the city of Krasnoyarsk (Russia). The soil radiation was measured at the look angle of 45° relative to nadir. The bandwidths of the radiometer at 1.4 and 6.9 GHz were equal to 60 MHz and 200 MHz, respectively. The fluctuation sensitivity of radiometers was about 0.3 K. The directional patterns of receiving antennas at the –3 dB level were about 22°. The metal sheet reflecting the sky radiation and the smooth water surface were used as standards to calibrate the radiometers. The radiobrightnesses of metal sheets were taken of 3 K and 5 K at the frequencies of 1.4 and 6.9 GHz, respectively. The radiobrightness of the smooth water surface was estimated according to the Fresnel reflection coefficient and Debye model for the water permittivity. An absolute error of calibration was estimated to be of about 3–5 K. The measurements of radiobrightness, T_b , were carried out with intervals from 20 to 40 minutes. While the meteorological data of the atmosphere and the temperature in the topsoil were acquired with the frequency once per minute, using the Campbell Scientific Inc weather station. In addition, the moisture of topsoil was determined by the thermostat-weight method twice a day.

Since measurement of soil radiobrightness inside a forest environment isn't possible due to absence of strong contrast between radio thermal radiations pertaining to the soil and sky, the second being shaded by the forest canopy, the test site was set up outside the forest. In the process of preparing a test site out of forest, the 20 cm topsoil layer was removed from the plot of 25 square meters, located in the forest glade. Intact soil clods of adequate thickness were taken from the adjoining coniferous forest and placed instead of the removed topsoil, to develop an artificial forest topsoil covered with litter.

3. RESULTS OF MEASUREMENT

According to our observations of radiobrightness diurnal cycles for the bare soil, the topsoil radiobrightness and emissivity maxima relating to the bare soils were found to take place from 03:00 to 06:00 pm and from 06:00 to 08:00 pm, respectively. Taking into account the relationship, $T_b = \chi T$, between the radiobrightness, T_b , and absolute thermodynamic temperature, T , where χ is emissivity, the time shift of about from 2 to 3 hours between the two maximums can be explained by continuing topsoil drying, which increases emissivity after its thermodynamic temperature reached maximum and started to decrease. Finally, in spite of thermodynamic temperature decrease, the radiobrightness remains increasing due to increase in emissivity.

The radiobrightness diurnal cycles measured for the topsoil covered with coniferous litter are shown in Fig. 1. In contrast to a bare soil radiobrightness diurnal cycle, the radiobrightness maxima observed in Fig. 1 are seen in the early morning hours from about 03:00 to 06:00 am. This interval of time is, first, shifted to about 12 hours earlier, relative to the one pertaining to a bare soil, and, second, it corresponds to minimal topsoil temperatures. Taking into account the formula $T_b = \chi T$, the maximum radiobrightness in the early morning hours for the topsoil covered with litter must occur only due to increase in its emissivity.

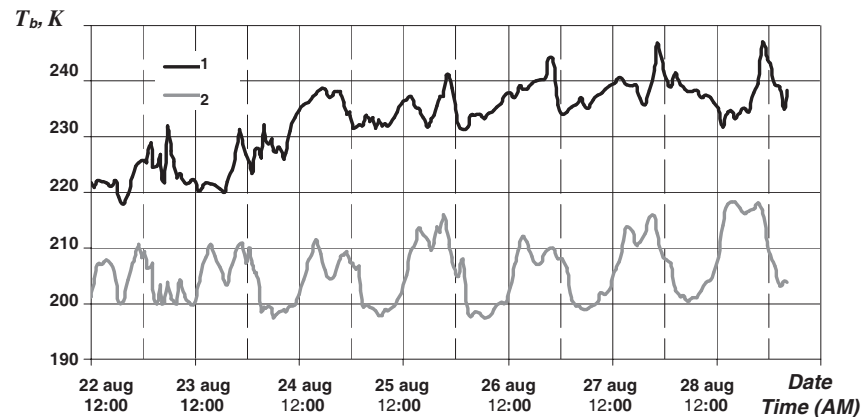


Figure 1: Diurnal cycles of T_b of the litter-covered soil at the horizontal polarization and frequencies of 6.9 GHz (1) and 1.4 GHz (2).

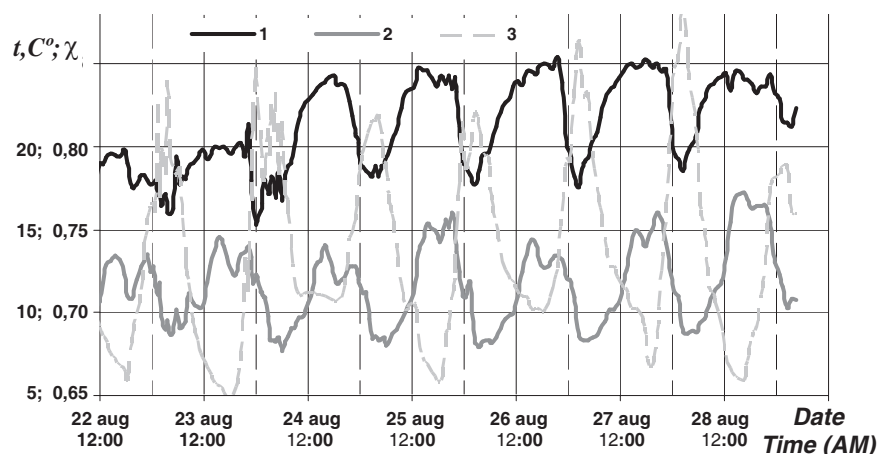


Figure 2: The time dependence of the litter-covered soils emissivity on the horizontal polarization of at frequencies 6.9 GHz (1) and 1.4 GHz (2); the time dependence of the thermodynamic temperature of the forest litter at the depth of 0.5 cm (3).

The respective diurnal cycles of emissivity are shown in Fig. 2 alongside with the thermodynamic temperature cycle. As seen from Fig. 2, the maximums of emissivity coincide with the minimums of thermodynamic temperature, and vice versa, which proves the origin of this maximum due to increasing in emissivity. As follows from Figs. 1 and 2, the emissivity minimum at the frequency

of 6.9 GHz are seen more distinctly, as compared to the radiobrightness ones. This fact suggests that only the most upper thin surface layer, which lies within the sensing depth of the radiometer at 6.9 GHz, must mainly affect a total emissivity of the topsoil covered with litter. The nature of radiobrightness diurnal cycle pertaining to the topsoil covered with litter is analyzed in the following section.

4. SIMULATION OF THE TOPSOIL EMISSIVITY

We carried out numerical simulation for the radiobrightness diurnal cycle. In the process of simulation, there were used data from [6] on the complex permittivity (CDP) of coniferous litter, as well as the results of CDP measurements conducted by us for the samples of litter collected from the measurement plot. When modeling the emission of soil covered with coniferous litter, the topsoil matter was assumed to be isothermic. This assumption caused the error of 5–7 K in the modeled radiobrightness, which exceeds an absolute calibration error of both radiometers. Despite that, the results of simulations allowed to bring to understanding the nature for the maximum radiobrightness of a topsoil covered with litter to occur in the morning hours. Since the relative frequency bandwidth of both radiometers did not exceed 4%, the radiobrightness temperature simulation was carried out only at the medium frequencies. As showed the analysis carried out, the antenna pattern impact on the simulated radiobrightness at the horizontal polarization did not exceed 3 K, which appeared to be less than the radiometers calibration error. Therefore, the simulation was conducted for the case of plane wave, with the incident angle being of 45 degrees.

The radiobrightness temperature of the soil covered with forest litter was calculated by the formula

$$T_b = (1 - R)T \quad (1)$$

where $R = |r|^2$ is the reflection coefficient by power, r is the reflection coefficient by amplitude, T is the absolute temperature of the topsoil at the depth of 1 cm. Comparison of T_b measured and that calculated with either isothermal or nonisothermal topsoil proved the thermodynamic temperature in topsoil at the depth of 1 cm be very close to the effective temperature used in the isothermal model. Therefore, the further modeling was performed with the use of the thermodynamic temperature at the depth of 1 cm.

The reflection coefficient of multilayer medium was determined by using the following expression [5]:

$$r = \frac{r_0 + r'_1 \exp(-2ik_1\Delta X)}{1 + r_0 r'_1 \exp(-2ik_1\Delta X)}, \quad (2)$$

where r is a complex reflection coefficient of the topsoil at the air-soil boundary, r_0 — complex Fresnel's coefficient at the same boundary, r'_1 is the reflection coefficient at boundary between the air-soil layer and the one situated under it, $k_{z1} = k_0 \sqrt{\varepsilon_1 - \sin^2 \theta}$ is a normal to the boundary projection of the wave number vector pertaining to the first layer, $k_0 = 2\pi/\lambda_0$ is a wave number in the vacuum, ε_1 , ΔX are the complex permittivity and thickness of the first upper layer, respectively, $i = \sqrt{-1}$.

The topsoil soil CDP dependence on depth, x , is determined by the percentage of organic matter present in the soil. In reality, the real part of the CDP $\varepsilon'(x)$ changed from 1.2 in the most top layer to 11 at the depth of 4–5 cm. For the permittivity profile, the expression proposed in [4] was applied:

$$\varepsilon'(x) = \varepsilon_l + (\varepsilon_l - \varepsilon_p) \cdot \left(1 - \left(\frac{1}{1 + \exp\left(-\frac{x-x_p}{Q_p}\right)} \right) \right) + (\varepsilon_p - \varepsilon_s) \cdot \left(1 - \left(\frac{1}{1 + \exp\left(-\frac{x-x_s}{Q_s}\right)} \right) \right) \quad (3)$$

where ε_l , ε_p , and ε_s are the permittivities (real parts of the CDP) of the non overrotten litter, partly overrotten litter, and mineral soil, respectively; x is the depth coordinate, x_p is the average depth at which the non overrotten litter borders the partly overrotten litter, x_s — the average depth at which the partially overrotten litter borders the mineral soil; Q_p , Q_s are the parameters to determine the thickness of transitional layers between the basic layers named above. A transition layer has the thickness equal to about $10Q$. The typical permittivity profile of topsoil covered with coniferous litter, is shown in Fig. 3.

To find the relationship between the real and the imaginary parts of litter CDP we used the CDPs of coniferous litter from [6], as well as the CDP values for the topsoil samples picked up at the measurement site and obtained by us in the laboratory conditions.

Figure 4 shows the results of simulation for one of the emissivity diurnal cycles measured. For the data in Fig. 4, the difference between emissivities modeled and measured did not exceed 0.01, or 2–3 K in the respective radiobrightnesses. The maximum difference of the overall data did not exceed 0.03 or 7 K. To ensure, when fitting, good agreement between the modeled and measured radiobrightnesses, with the data measured increasing, we had to increase the litter permittivity, as well as its thickness. In the case of wave frequency of 1.4 GHz, at the moments of emissivity maxima observed at 03:30 and 10:00 am (see Fig. 2), the CDPs derived through fitting were found to be of 1.2–i0.05 and 4.0–i0.4 for the non overrotten and partly overrotten litter layers, respectively. These values were found to be close to the ones measured in the laboratory conditions for the samples collected. At the same time, the thickness of the overrotten litter layer was found to be close to a quarter wavelength, as estimated for the overrotten medium. These facts make feasible to suggest that the partly overrotten layer may act as an antireflective one, thus increasing the emissivity of the forest soil in the morning hours. Apparently, the variations of permittivity in the partly overrotten layer could occur because of dew fallout or as a result of nonisothermal transport of soil moisture from underlying space.

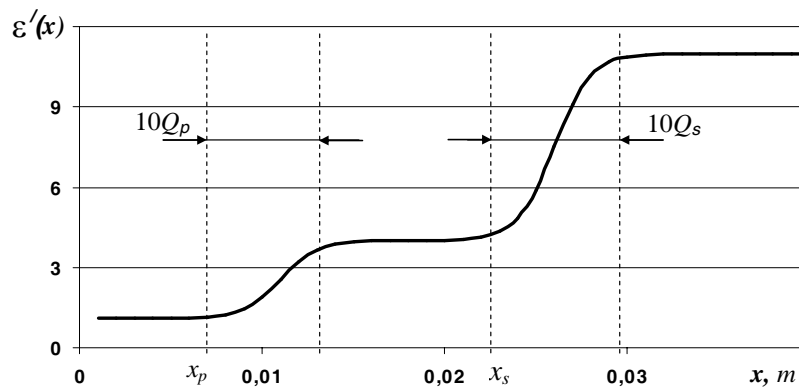


Figure 3: The depth dependence of the real part of the dielectric permittivity of soil, covered with forest litter. The boundaries of transitional layers ($10Q_p$, $10Q_s$) are designated with pointers.

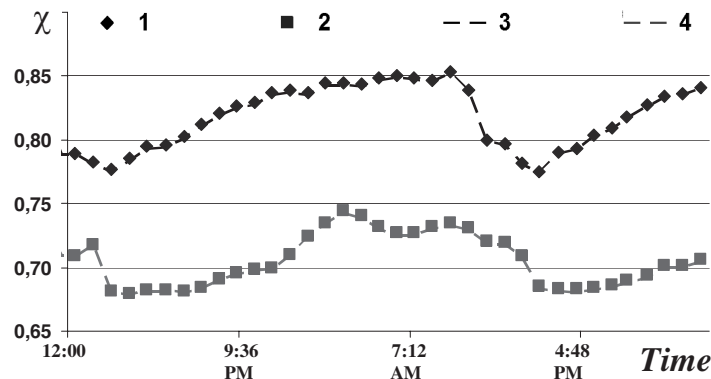


Figure 4: A diurnal emissivity cycle for horizontal polarization. The emissivities measured and modeled are given by symbols 1, 2 and 3, 4, respectively, with 1, 3, and 2, 4 pertaining to the frequencies of 1.4 and 6.9 GHz, respectively.

5. CONCLUSIONS

The carried out studies showed that the diurnal radiobrightness cycles of the forest soil covered with litter is substantially different from that of bared soils, with the radiobrightness maxima occurring when the soil temperature is minimal. It was found that the layer of partially overrotten litter induces an antireflective effect, making both the radiobrightness and emissivity to rise in the early morning hours. This effect should be taken into account in the data processing algorithms relating to radio thermal remote sensing of soil moisture over the forest territories. There was also proved that the permittivity of the topsoil layered due to presence of forest litter can be retrieved from emissivities measured at two frequencies, using both polarizations.

ACKNOWLEDGMENT

The work was supported by the RFBR-CNRS grant No. 09-05-91061.

REFERENCES

1. Kerr, Y., P. Waldteufel, J.-P. Wigneron, et al., “Soil moisture retrieval from space: The Soil Moisture and Ocean Salinity (SMOS) mission,” *IEEE Transactions on Geoscience and Remote Sensing*, Vol. 39, No 8, 1729–1735, 2001.
2. Grant, J. P., J.-P. Wigneron, A. A. Van de Griend, et al., “A field experiment on microwave forest radiometry: L-band signal behaviour for varying conditions of surface wetness,” *Remote Sens. Environ.*, Vol. 109, No. 1, 10–19, 2007.
3. Schwank, M., C. Mätzler, M. Guglielmetti, and H. Flüher, “L-band radiometer measurements of soil water under growing clover grass,” *IEEE Transactions on Geoscience and Remote Sensing*, Vol. 43, No. 10, 2225–2237, 2005.
4. Schwank, M., M. Guglielmetti, C. Mätzler, and H. Flüher, “Testing a new model for the l-band radiation of moist leaf litter,” *IEEE Transactions on Geoscience and Remote Sensing*, Vol. 46, No. 7, 1982–1992, 2008.
5. Brehovskih, L. M., *Waves in Layered Media*, Nauka, Moscow 1973 (in Russian).
6. Kleshchenko, V. N., S. A. Komarov, and V. L. Mironov, “Dielectric properties of needle litter,” *Journal of Communications Technology and Electronics*, Vol. 47, No. 11, 1202–1205, 2002.

Monitoring of Satellite Thermal Pattern of an Ocean Front as a Hydrodynamic Convergence

Shigehisa Nakamura
Kyoto University, Kyoto, Japan

Abstract— This is an over view of an ocean front as a hydrodynamic convergence. The water motion on the earth surface may have a conversion process and a diversion process. In this work a case of ocean process as a conversion process is the author's interest. On the bases of the knowledge obtained by monitoring of satellite thermal pattern of an ocean front, a notice on a hydrodynamic convergence is given for more advanced understanding of the ocean front as found on the sea surface.

1. INTRODUCTION

An over view of an ocean front is introduced as a problem of convergence in the field of “hydrodynamics”. Hydrodynamic includes problem of convergence and divergence though the ocean scientist has recently shown on a global problem of convergence in the ocean [1]. As for the ocean front, the author introduces some overview with consideration of the factor “convergence” in this work.

This work concerns an over view of an ocean front as a hydrodynamic convergence. The author has noted the ocean front formed by two waters, i.e., a coastal and ocean waters to be found as a line on the sea surface. This ocean front can be well monitored by using a satellite. This technique has helped the author's finding of the specific properties of an ocean front on the sea surface. By this time, it was discussed mainly about several specific patterns of an ocean front, for example, in the northwestern Pacific. Similar pattern can be found in the Atlantic (around the Gulf Stream) or in the South Pacific (as the western boundary flow off the eastern boundary of Australia). After the author's monitoring of satellite thermal pattern of the ocean front in the northwestern Pacific, it is clarified that the front has a close relation to the western boundary current named as “Kuroshio”. The front pattern is significantly governed by the costal configuration and varies its spacial pattern with the time elapse. The author has first introduced several cases that including some specific pattern of the ocean front at a shot reduced from the signals directly received by a system of an antenna and a software for the data processing. Successively, several case of timely change process of the ocean surface front has been obtained during a continuous satellite monitoring of the sea surface in the foot print covering the interested ocean front. This monitoring has given a key to the author for helping to develop a model of ocean front evolution on the sea surface referring to his understanding of hydrodynamics. Adding to the above, it was found that a satellite thermal plateau and a satellite thermal pinnacle can be understood as the specific cases a physical processes after an application of Stefan-Boltzmann's radiation theory. A satellite thermal pinnacle could be a set of concave facets as a part of the sea surface waves concentrating at the related pixels in the monitoring. A satellite thermal plateau could be formed by an ensemble of the set considered above for the pinnacle. The author has to take it necessary to relate these processes to the meteorological processes on the sea surface. Several cases of the interested processes were well related to an effect of a set of wind induced waves radiated out of a distant storm (more than one thousand kilometer far from the interested area) even in the satellite's foot print covering. Following the author's satellite monitoring of the ocean front evolution, it is clarified that the front is an example of a line where the waters converge to maintain the ocean front.

The author introduces an overview of the ocean front as a problem on convergent.

2. A KEY TO CONVERGENCE IN OCEAN

First, the author has to note a key to convergence in the ocean [1]. Now, the knowledge of hydrodynamics leads us to see where the convergent and divergent areas are existing in the ocean, and to help our dynamical understanding of the motion of the global ocean. An understanding of an ocean front might be a way to get a trigger for seeing the convergent line as the ocean front on the sea surface. One of the ideas to this problem might be to consider a global circulation of the ocean waters.

That is to say, one of the most recent reviews on the global ocean circulation is noted a pattern of surface ocean circulation combined to a deep ocean circulation. It is now understood as that

a significant convergent is seen in the area between Green Land and New Found Land on the sea surface at the north arctic zone in the Atlantic. This convergence might be governed by the transport of the tropical water by Gulf Stream and by the effect of latitudinal cooling of the water at meeting the Arctic water. This could be understood as that of a specific example of the ocean front formed by two waters of the Arctic water and of the tropical waters. This convergence is connected to an area of water sinking down to form a deep water circulation. An estimated age of the ocean water tells us that the oldest deep water is at the mid of the North Pacific. This suggests us the ocean surface in the North Pacific must be the area of divergence. The author now is facing to solve a local problem in relation to a global process of the ocean circulation referring to the distribution of the ocean fronts as the convergent zones in the ocean.

3. OCEAN CURRENT

Pioneer work on the ocean current must be developed by Ekman [2]. In order to see the ocean current off the northwestern Pacific, Suda [3] had his energetics of the ocean current. Sverdrup et al. [4] noted his overview on “dynamics of ocean currents” in 1942. As for “the Gulf Stream”, Stomme [5] had given an overview. Following these works, the ocean current could be taken as a geostrophic current. There has no attention had been no concept of “ocean front” which is formed by a contact of the coastal and ocean waters.

in fact, the ocean front is just neighbor the ocean current. The ocean current is between the coastal water and the ocean water. The author dare write that the ocean front has well found after launching a satellite for monitoring the ocean surface.

4. SATELLITE MONITORING OF OCEAN FRONT

As for the ocean front, satellite monitoring is an effective to see a thermal pattern time to time. The recent advance of electronic techniques have been helpful for finding the ocean front evolution as a physical process.

By this time, it had been discussed mainly about the variation of the ocean flow pattern for a quick report in a purpose in hydrographic practice.

On the other hand, Grimsaw and Yi [6] developed their mathematical theory on evolution of a potential vorticity front over a topographic slope. Adding to the above, Viera and Grimshaw [7] discussed on topographic forcing of mesoscale phenomena in the ocean, for example, filamentations, vortex formations and detachment.

Under the above noted satge, Kyoto University had developed a research project to use satellite for monitoring ocean processes. The author had take part of this project to start in 1980s. A simple system of an antenna and data processing function for a personal computer, is introduced for monitoring the ocean front evolution referring to the signals directly received at a station settled on the coast facing the northwestern pacific.

5. OCEAN FRONT EVOLUTION

The author has found that the ocean front is approximately same location to the axis of the ocean current. This makes us it easy to see the ocean current variations referring to the real time ocean front evolutions which are reduced after processing the directly received satellite signals as the satellite passing time just above the station settled on the coast.

Since the research project started, several interesting processes on the sea surface have been found. One of the contributive results must be satellite thermal monitoring of storm flood spreading around Kuroshio flow as the ocean current [8].

Successively, Nakamura [9, 10] has presented his notice on shear flow effect to Kuroshio meandering in the northwestern pacific.

6. SATELLITE THERMAL PLATEAU AND PINNACLE

Monitoring of the satellite thermal ocean front, the author found satellite thermal plateau and pinnacle in mid of the Pacific [for example, 11]. This pinnacle was found under the normal operation of the monitoring so that it could be realized as one of the physical processes.

It was realized that the satellite thermal plateau was an effect of the wind induced wave group which was radiated out of the distant storm zone. In this case, the location of the storm (a storm growing to Typhoon in the Pacific) was more than 1000 km far from the monitoring station. The meteorological factors support that the satellite thermal plateau was coincides well to the swell propagating area between the storm and the station facing the ocean.

In the cold season of the Asian monsoon area, the satellite thermal plateau has been seen at the northwesterly when the atmospheric cold front is passing just neighbor the station. That time, wind stress is a cause to induce a wind induced wave group off the coast of the down wind area on the sea.

7. APPLICATION OF STEFAN-BOLTZMANN'S RADIATION THEORY

A physical background of the above noted process of the satellite thermal plateau and pinnacle requires a set of concave wave facets with a focus just neighbor the sensor mounted on the satellite. This is a necessary condition. So that it is necessary in order to identify the process relating to the ocean surface waves.

Nevertheless, the other factor must be introduced to satisfy a required sufficient condition. For this, an application of Stefan-Boltzmann radiation theory with an assumption of the ocean surface as a black body. When the radiation theory is applied to the concave wave facets noted above, the satellite thermal plateau and pinnacle can be understood in the scope of physics. Although, the author has to note that no reference data of waves is found for the satellite thermal pinnacle yet.

8. GLIMPSE OF OCEAN CIRCULATION

As stated above, ocean front is a line formed at meeting the coastal water and ocean water. The line on the sea surface as an ocean front is in a process of evolution, though the process is not well understood in a scope of geophysical dynamics.

Before the ocean front evolution is discussed, the scientists had have leaned that an ocean current is exist in a belt zone between the coastal water and ocean water.

A history of the ocean expeditions undertaken by the research ship "Meteor" was the first project covering the most area of the ocean in the world. The modern ocean surveys and the systematic ocean observation by the ships and boats under the international co-operative project have been undertaken to compile bathymetric pattern of the ocean waters. Nevertheless, the specific ocean front has started in these years after the satellite operation for some monitoring of the ocean front evolution.

The scientists know well that the ocean has a three dimensional structure. The understanding of the updated ocean pattern might be seen, for example, what is described by Kuhlbrodt et al. [1]. Then, the sink of the ocean in the world is in the arctic area near the Atlantic. The tropical warm water is transported in the western part of the northern Atlantic, and the Atlantic surface water is going down to form a deep sea current. This deep sea current be a current to pass along the western part of the Atlantic. In the deep layer of the Indian Ocean, this current is nearly parallel to the south circum polar current in the surface layer. The Atlantic deep water get to the south of the Pacific dissipating its dissolved oxygen, and flow across the equator to enter the deep basin of the northwestern Pacific. The deep water in the basin of this area in the Pacific is understood the oldest at present. When the transportation of the Atlantic surface layer is continued for a long time, the deep water mass in the Pacific basin must increase, and this increase of the deep water could be a trigger of a large scale upwelling of the upper warm water in the Pacific subtropical water. This upwelling let to spread the warm water to the coastal zone. Then, the coastal water meeting to the Pacific warm water may form a line of fluid convergent, i.e., the Kuroshio front found in the northwestern Pacific, for example.

The minor Kuroshio flow variations might be governed by a condition of the tropical waters as the source of Kuroshio to affect a climatologic effect. Another trigger effective to climate might be the upwelling off the Peru, that is, named as "El Nino".

What the author noted above, it can be seen that there has been no interest for divergence of the ocean water, even though this divergence is important as much as the convergence in the ocean in a global scale. Now, the ocean front evolution is a glimpse of the ocean circulation even when the pattern is occasionally distorted by the meteorological effect on the ocean surface area.

9. GLOBAL UNDERSTANDING OF OCEAN FRONT EVOLUTION

With what the author has noted above, it can be seen that the ocean front evolution is a simple convergent line, and only a glimpse of the ocean front evolution should be closely related to the global process of the ocean circulation.

10. CONCLUSION

An overview of the research on ocean front evolution is briefly introduced. This is a simple ocean front evolution though the author takes it to be a glimpse of the ocean circulation of a three dimensional process in a global scale. In the related history, the initial stage of the related research had looked to be trivial for the human activity. Research on the ocean current has had helped our understanding about what is the ocean just around the area of human activity. Monitoring of satellite thermal pattern of the ocean front evolution has effective to see what process is actually appearing on the sea surface. The compiled survey data and the satellite monitoring are more effective to realize a three dimensional process of the ocean circulation. Increase of our experience, knowledge, and systematic survey of the ocean surly lead to give us a key for the important information about the global ocean circulation which is effective even to a glimpse of the variation of the circulation.

REFERENCES

1. Kuhlbrodt, T., A. Griesel, M. Montoya, A. Levermann, M. Hofmann, and S. Rahmstorf, "On the driving processes of the Atlantic meridional overturning circulation," *Reviews of Geophysics*, Vol. 45, No. 2004RG000166, 1–32, 2007.
2. Ekman, V. W., "On the influence of the earth's rotation on ocean currents," *Arkiv fur Matematik Astronomik och Fysik*, Vol. 2, No. 11, 1905–06, Kungskansliet, Svenska Vettern, Akademy, Stockholm, 1905.
3. Suda, K., "On the dissipation of energy in the ocean current (2nd paper)," *Geophysical Magazine*, Vol. 10, 131–243, Tokyo, 1936.
4. Svedrup, H. U., M. W. Johnson, and R. H. Fleming, *The Oceans*, 1087, Prentice-Hall, Inc., Englewood, New Jersey, 1942.
5. Stommel, H., *The Gulf Stream*, 202, University of California Press, 1958.
6. Grimshaw, R. and Z. Yi, "Evolution of a potential vorticity over a topographic slope," *Journal of Physical Oceanography*, Vol. 21, 1240–1255, 1991.
7. Viera, F. and R. Grimshaw, "Topographic forcing of mesoscale phenomena: filamentations, vortex formations and detachment," *Journal of Physical Oceanography*, Vol. 24, 1433–1448, 1994.
8. Nakamura, S., "Satellite thermal monitoring of storm flood spreading around Kuroshio flow," *Bulletin of the Disaster Prevention Research Institute*, Vol. 43, 31–39, Kyoto University, 1993.
9. Nakamura, S., "Shear flow effect to Kuroshio meandering in the northwestern Pacific," *Hydrodynamics*, 939–944, edited by A. T. Chwang, J. H. W. Lee, and D. Y. C. Leung, Hong Kong, 1996.
10. Nakamura, S., "A dynamical understanding of Kuroshio front," *Hydrodynamics*, 449–453, edited by H. Kim, S. H. Lee, and S. J. Lee, Seoul, 1998.
11. Nakamura, S., "An example of observed thermal structure of sea surface at an offshore tower," *La mer — Bulletin*, Vol. 35, 125–126, Societe franco-japonaise d'oceanographie, 1997.

Monitoring of Satellite Thermal Pattern of Ocean Front in Relation to a Double Diffusion Process

S. Nakamura
Kyoto University, Japan

Abstract— After monitoring of satellite thermal pattern of an ocean front evolution, the author has had a step to see a double diffusion process on an interface related to an ocean front evolution. This double diffusion process is significant in the ocean, though it is enough to consider a simple diffusion process in the coastal water or in the riverine water. Some note is given to have a key to understand the process under the sea surface even referring to a satellite thermal pattern of an ocean front evolution.

1. INTRODUCTION

This work concerns a problem on monitoring of satellite thermal pattern of an ocean front evolution in relation to a double diffusion process found just around an interested front. As is well understood, this ocean front is formed by a contact of the two waters in the coast and in the offshore zone of the ocean.

Double diffusion process seems to be a specific process though there are many cases just like to the case in the ocean. Exactly, a diffusion process of a mixture of many elements in the natural processes as a multiple diffuse process. For simplicity of the problem here, the author would introduce a simplified case of a specific double diffusion found in the ocean. That is, a double diffusion found just around an ocean front in evolution.

This case could be helpful for the other similar cases found in nature or in some artificial cases. What is introduced here in this work could be a key to solve “double diffusion” in a scope of generalized physical process which could be expressed to realize by application of a mathematical technique.

2. SPECIFIC PROPERTY OF OCEAN WATER

As has been well understood by this time, the ocean water contents in the ocean controls the density of the water. Several ions, of the inorganic elements, the dissolved materials and the suspended materials are the contents of the ocean water. The ocean scientists have had taken conveniently that any ocean water sample could be specified by the two main factors, the salinity and the water temperature. These two factors determine density of the water in the ocean surface layer. As for a case of deep sea, compressibility of the ocean water is important. This means that the motion of the ocean water could be a densimetric motion in the gravity field of the Earth. With the ocean survey for a long time of many years, it has been introduced a double diffusion process as a fluid mechanics during a period of 1990s in a scope of hydrodynamics.

3. DIFFUSION PROCESSES

Each of the salinity and the water temperature has a diffusive property respectively. It is understood that the diffusivities of the two factors, i.e., of salinity and of water temperature.

A formulation for each interested diffusion process is simple. Usually an equation expressed as follow is taken to be a starting to analyze and solve a diffusion process, that is,

$$d(S, T)/dt = \partial(S, T)/\partial t + u\nabla(S, T) = -\nabla(\kappa\nabla(S, T)) \quad (1)$$

where, salinity and temperature are denoted as “ S ” and “ T ” in a vector velocity field of ocean water. Timely derivative and spacial derivative are expressed as “ d/dt ” or “ $\partial/\partial t$ ” and “ ∇ ”, respectively. A coefficient of diffusion is denoted as “ κ ”.

Mathematical form of the equation is essentially same for each case of S and T . Though there is some difference of the value of κ for S and for T . It should be aware of that salinity is an index of material contents (solvents and suspended). So that, “diffusion” of S is a process of some material translation processes. As for the temperature, the “diffusion” of T is for a thermal energy transfer. With this, it should be introduced κ for S and κ for T , respectively.

Nevertheless, actual process in the ocean is not so simple so that it is difficult to see the processes of S and T at the same time at an instant.

Adding to the above, the two diffusion processes interact each other. That is, one of a typical double diffusion process.

At present stage, the scientists in the fields of oceanography have never had any idea for applying several contributions on double diffusion in the fields of fluid mechanics.

4. PHENOMENOLOGICAL NOTICES

Essentially, this difference of the two factors raises some problem of double diffusion in a scope of fluid mechanics. Dynamics of ocean front evolution has been studied as a simple process of the water density. In ocean, density of the water in the ocean is easily defined by the two factors at formulating water motion in the ocean under the earth's gravity field.

An ocean front is evolving at any time and at any location. The author has had introduced a model for an ocean front evolution for a purpose of his realizing what thermal pattern found on the sea surface after monitoring by using his simple system for directly receiving a satellite signal at a time just passing above his station settled on the coast facing ocean.

In the author's experience, it is easy to monitor thermal pattern on the sea surface when a satellite monitoring technique is applied and it is hard to find salinity distribution even on the ocean surface after any available sensor mounted on a satellite. Salinity observation is possible if a sensor has a much higher resolution. Then, the author has to consider another available technique to see the ocean front evolution.

The author considers fortunate or unfortunate when the most effective factor for monitoring the ocean surface thermal pattern is to apply a satellite monitoring of a real time signal.

5. SATELLITE THERMAL MONITORING

Boldly, a thermal factor is the most effective for finding the ocean front evolution which is found between the coastal water and ocean water. A case of the monitored thermal patterns monitored in an area of the NW Pacific in practice, could be seen by a simple model with an understanding of classic hydrodynamics, though to the details it must be referred to an advanced contributions in geophysical hydrodynamics. Another specific example is an eddy and a front monitored in the area of the NE Atlantic. Formulation of the water motion may be simple in form when one factor may be enough to consideration. In some specific cases, information of salinity is important for analyzing salt finger or salt lens in relation to the Mediterranean outflow. Nevertheless, the author has to note here no existing satellites is for the author's purpose of detecting any structure of the water motion under the ocean surface even around an interface as the extension of the ocean front on the ocean surface. What is noted above is left to be discussed in future in relation to any process found in the global ocean circulation in order to obtain a key to global warming control system.

6. OCEAN FRONT EVOLUTION

As stated above, we have to work to contribute for our dynamical understanding of ocean. For our present understanding of this problem, it is strongly expected to have an advanced technique for monitoring the ocean surface.

At present, a combined system is available for the author's purpose and our promotion for the much more advanced understanding of the ocean.

Now, the author feels it necessary to introduce you an outline of oceanography which might help us to find a key to promote our research work in the world.

In Figure 1, a simplified illustration is introduced. At the top (A), a specific example of the ocean front evolution is shown. Warm and cold ocean waters forms an ocean front which is evolving.

Thermal pattern along a transect ("P to Q" and "S to R") of a survey ship is shown in a simplified form. In case of A in Figure 1, the evolution process might be as shown as an adiabatic process (see B in Figure 1). Nevertheless, actual pattern obtained by observation is affected by conduction and double diffusion processes to find a pattern (see C in Figure 1). What noted above is for the ocean surface pattern. This pattern could be realized when a satellite thermal pattern.

In the case as shown in Figure 1, the locations, P, Q, R, and S, might be plotted on a ST-diagram. In D of Figure 1, the ST-diagram tells us that conduction and diffusion might be important at understanding the ocean to the details. In Figure 1 (see D), a parameter σ_t (sigma-t) shows isopycnal line. When $\sigma_t=0$ for cold water and $\sigma_t=1$ for warm water, a water particle at P have various paths to get to R in the area even in the square formed by PQRS. In order to see

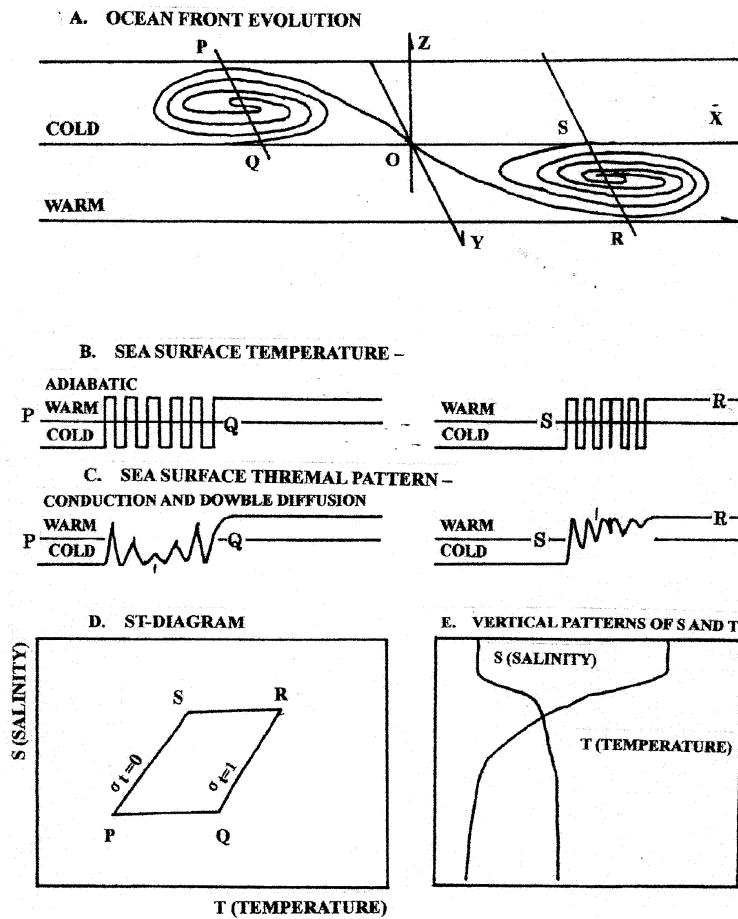


Figure 1: Double diffusion process during an ocean front evolution.

what path is actually found, a dynamical model should be developed in order to predict what path is for the minimum energy loss of a interested water particle moving, for example, from P to R. In order to get a proper dynamical model, an advanced formulation should be found for in practical applications.

However, the ocean has a three dimensional structure. The structure is not so simple. In the surface layer of the ocean (for example, a case of mid-latitude zone), vertical structure of salinity and temperature could be demonstrated as shown in E of Figure 1. This shows a simplified example of some specific observation.

7. CONCLUSIONS

In this work, the author has introduced a double diffusion problem as a key to obtain an advanced understanding of the ocean. For this purpose, it is effective to utilize the satellite thermal pattern of real time which is reduced by a personal computer system which helps to receive directly the interested satellite signal in need.

Monitoring of Satellite Thermal Pattern of a Drifting Ocean Front

S. Nakamura

Kyoto University, Japan

Abstract— This is a note to a drifting ocean front which had been observed during a monitoring of an interested satellite thermal pattern. The pattern is obtained after processing a satellite signal directly received at a station. The author notes a typical case of the ocean front estimated out of the line found as a spacial maximum of thermal gradient on the sea surface. Spacial thermal pattern of the sea surface temperature found in the satellite is usually in drifting. It is now necessary what had been taken as an ocean front found by satellite monitoring. The pattern of the ocean front reduced from the direct measurement of the ocean surface in-situ should be considered in relation to the satellite thermal pattern of a drifting ocean front for effective data utilization. What is noted above is in need for the next step of the research of global ocean circulation in relation to the global warming effect.

1. INTRODUCTION

This work concerns about a problem of drifting ocean front. The author has been studied on satellite thermal pattern of a ocean front evolution as a part of the research project of Kyoto University. After his works on the satellite thermal pattern as an approximate ocean front, it is necessary to see what drifting pattern of the ocean front could be possible in a scope of hydrodynamics. The author has thought it necessary to note now about a problem of the ocean front which is taken as a maximum thermal gradient on the sea surface in the foot print of the satellite monitoring sensor. For this purpose, the author refers to the data which has had obtained by receiving directly the interested satellite signal at the satellite passing time above his station. The author feels it also necessary to note about the ocean front pattern obtained referring to the data in-situ obtained by the survey ships.

This work is the first note to problem on drifting ocean front. What are noted in this text must be in consideration at evaluating the global ocean circulation governed by the climate change interaction.

2. OCEAN CURRENT AROUND OCEAN FRONT

It has been well understood that the ocean current on the sea surface is only a part of the global ocean circulation. This circulation should be understood as a three dimensional (3D) process now. Nevertheless, the fact shows that the upper layer of the ocean has been seen after the air-sea interaction on the sea surface under the earth's gravity field.

The ocean current in the surface layer is a densimetric property and strongly controlled by the earth's rotation, and it has been taken as that the ocean current is geostrophic. Several mathematical models had developed in order to demonstrate the intensified western boundary current. The pattern of this current has been found ever by the ships' survey, for example, as the "Gulf Stream" in the Atlantic or as the "Kuroshio" in the NW Pacific. In the area off the eastern Australia, a similar intensified western boundary current has been found.

The ocean geostrophic current noted above is governed by the sea water density which is a function of salinity and water temperature. The other minor factors is considered to be not so effective for current pattern, though compressibility is effective for the sea water in the deeper part under the surface layer.

3. OCEAN THERMAL FRONT

The ocean thermal front is formed by meeting of the waters in the coastal zone and in the ocean. This means that the geostrophic current in the NW Pacific is an intensified western boundary current. This current forms a part of "wind-induced circulation" in the upper layer. In this work, a little consideration is pay for the water in the deeper part of the ocean.

As is known well for the ocean thermal pattern, the axis of the ocean current in the NW Pacific is located just neighbor of the border of the two waters. The border is called as the "ocean thermal front" for convenience. The ocean thermal front can be easily monitored by an interested satellite. The ocean thermal front is defined as the line formed by the thermal maximum gradient on the ocean surface. This front can be monitored by the satellite.

Pattern of an ocean thermal front can be generally undulated. This front changes its spacial and timely form as seen in the satellite monitored pattern. For example, this pattern could be described boldly by a sinusoidal pattern on the ocean surface as seen A in Figure 1. In some drifting of this front might be looked as if it were distorted a pattern shown in the right side of A in Figure 1. There might be an unidentified forcing to the front.

4. PATTERN OF DRIFTING OCEAN THERMAL FRONT

A distorted pattern of the front is assumed to be shown as seen in B of Figure 1, for the author's convenience. The cold and warm water masses, for example, is assumed to form a front on the ocean surface. Then, thermal patterns along the transect M, N, P, Q, and R, can be shown as C in Figure 1. As far as we concern the data in-situ observed by a ship, the thermal pattern in C should be distorted if a drifting affecting the thermal pattern in B of Figure 1. In fact, it takes a certain time for ship's observation along the line of M, for example. The pattern for M is a step pattern demonstrating thermal gap at the location of the ocean thermal front. The pattern for R looks to be same to the pattern for M. Though, the pattern N, P, or, Q is a little difference in pattern along the corresponding line (cf. D in Figure 1).

The author has understanding that a limited data only for the lines as the transects suggests hardly to find a thermal pattern as assumed in B of Figure 1.

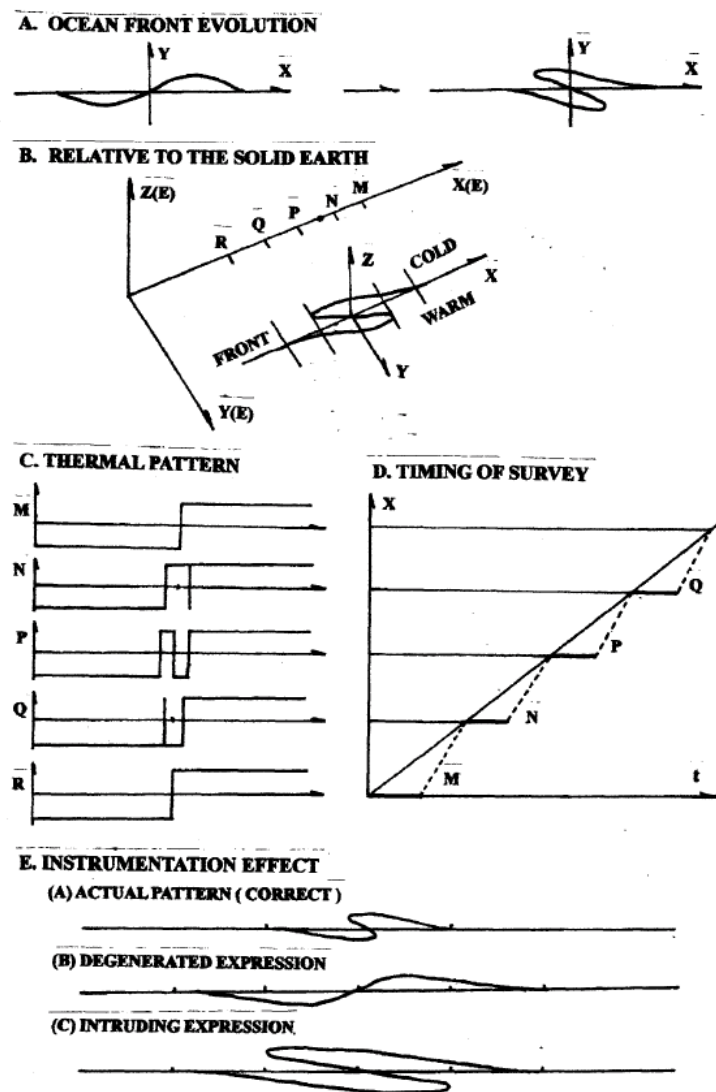


Figure 1: Evolution of a drifting ocean front.

5. OBSERVATION BY FLOATING SURVEY SHIPS

In a case of the observation in-situ by survey ships, it takes a certain time to obtain the data, for example, along the line M starting at a time on a day to get to the other end of the line M at several hours or more. On the other hand, a satellite monitoring might have the necessary data of the sea surface thermal pattern in the area covering the zone from the line M to the line R in several minutes, for example.

In a several minutes monitoring, any drifting effect of the ocean thermal front might be not so significant. Nevertheless, a time interval of several hours for completing an operation of observation by ship in-situ has an inevitable drifting effect in the operation. Now, it must be aware of that any one of the survey ships are floating and drifting. So that, positioning of any survey ship does not mean the positioning of the actual observation at the time.

The author, here, has to notice that the operation ambiguity might be in the data so that it is necessary for us to be careful at reading the several data sets in the interested area of the ocean covering the drifting ocean front.

6. INSTRUMENTATION ON BOARD FOR OPERATION

The author has to remark to positioning and timing for an operation of instrumentation. In fact, a survey ship can get a data from the sea surface to the sea floor. Even though, it is hard to identify the exact positioning of the location for operation under the sea surface referring to the precise positioning of the survey ship.

For example, assume that an actual ocean thermal pattern is (A) of E in Figure 1. Drifting effect might give us a data for another solution. One of the possible cases might be as is (B) of E in Figure 1. The other one might be as is the case (C) of E in Figure 1.

7. CONCLUSIONS

A problem of drifting ocean front is studied referring to the result of monitoring of satellite thermal pattern of an ocean thermal front. A note on ocean current is given in relation to the ocean thermal pattern. This makes us to refer to the satellite data for his monitoring of satellite thermal pattern of a drifting ocean front. An ocean front distorts after an shearing effect to the ocean front formed between the two water masses. The ocean front has been taken as one of the related indices for understanding the ocean currents around the front.

The ocean current is taken to be geostrophic. Geostrophic ocean current in the gravity field is governed by the gradient of water density. This is mainly determined by the two factors of salinity and water temperature. The interested ocean current should be understood in a scope of geophysical hydrodynamics. Generally, the ocean front is evolving time to time so that its pattern is not simple as the author's model. Though, it is important for us to realize ocean current after a model.

Some specific thermal pattern along a section crossing the front might be well demonstrated by a model. Even though, the author uses to trust a satellite thermal pattern on the ocean surface to be true if the data in-situ at or in any part or point is well identified.

The author raised a problem of ocean surface thermal pattern in-situ obtained by the survey ships. Ambiguity of positioning in the ocean along a survey line might be caused by drift effect of the ocean thermal front.

Essentially the satellite thermal pattern should be compared to the data on the sea surface. Nevertheless, the author has to notice about an "instrumentation effect". This effect controls the accuracy of the data obtained on the sea surface.

An actual pattern might be obtained under a certain survey condition for a correct pattern. Drifting effect of the ocean thermal pattern causes to get a degenerated or intruding pattern. It is conditional what pattern is correctly founded in the survey data on the ocean surface. Adding to the above, the author has to notice that the ocean structure under the sea surface could give a key to monitoring the drifting ocean thermal front by electromagnetic waves application. The key must be effective to see the global warming control system.

Application of Microwave Radiometry for Urban Heat Island Study

E. N. Kadygrov¹, E. A. Vorobeva¹, I. N. Kuznetsova²,
V. V. Folomeev¹, and E. A. Miller¹

¹ Central Aerological Observatory, Russian Federation

² Hydrometeorological Centre of Russia, Russian Federation

Abstract— Last decade or so for temperature profiling in atmospheric boundary layer were used passive microwave radiometers with the frequencies in molecular oxygen absorption band. One of the widely used instrument was MTP-5H — A single channel an angular-scanning microwave temperature profiler. MTP-5 was developed in 1990–1992 by the scientists from several leading institutions of Russia. For studying urban heat island in Moscow region, three passive microwave radiometers (MTP-5H) were used. These devices worked simultaneously for continuous measurements of atmospheric boundary layer temperature profile up to 600 m. In this report, quantitative parameters of Moscow urban heat island (UHI) will be presented.

1. INTRODUCTION

The numbers of researches dedicated to the UHI study considerably increased in recent years. This investigations show that anthropogenic stress in the form of powerful sources of gas and aerosol pollutants as well as water vapor and supplemental heat sources can greatly influence the intensity and the form of the environment response in the large industrial cities and megalopolises. These factors lead to special climate formation in megalopolis. For study of UHI ordinary were used near-surface data from meteorological stations at the city and in suburb. As a result, the fundamental factors of the UHI formation were formulated (Oke, 1977).

Nevertheless, it is clear that UHI is one of the atmospheric phenomena, which requires further study. For this study it is necessary to have a representative data on the vertical thermal structure over the cities. Usually for this purpose balloon-borne instrumentation (such as free and tethered sounding balloons or constant volume free balloons), aircraft techniques and facilities, tower sensors were used. But these devices are costly and cannot provide continuous measurements. So during last two decades or so, atmospheric boundary layer (ABL) observations have been enhanced by remote sensing techniques.

Our technology was based on using passive microwave remote sensing or radiometric method. These passive techniques involve measurements of radiation emitted from the atmosphere, instead of detection of scattered energy due to natural or artificial atmospheric targets. One of the advantages of microwave radiometric device includes the possibility to provide measurements in practically all weather conditions in urban area. It also allows continuous unattended measurements, which provide long time series and time-height cross sections.

For the investigation of UHI in Moscow were used three passive microwave radiometers simultaneously. This simultaneous measurement had two objectives. The first was to determine a Megacity impact to the ABL parameters which led to creation of UHI. The second objective was to investigate the ABL stability and its influence a radiation balance near the ground surface.

2. MEASUREMENTS AND INSTRUMENT DESCRIPTION

During 2000–2009, three microwave temperature profiles (MTP-5H) were used simultaneously in Moscow region for continuous measurements of the atmospheric boundary layer (ABL) temperature profile. One MTP-5H was installed in the center of Moscow city. The second in the north part of Moscow (Dolgoprudny), and the third about 50 km west ward from the Moscow city center (Zvenigorod). The relative position of the devices is shown on Figure 1.

Zvenigorod town has little industry, low traffic intensity and due to topography good air ventilation. So it can be considered as an undisturbed rural site. In Dolgoprudny, radiosond data is also obtained.

The temperature profiles were obtained “round-the-clock” every 5 minutes up to altitude of 600 m with a 50 meters grid. MTP-5H microwave radiometer is single channel solid state Dicke-type super heterodyne receiver (radiometer). The working frequency is ~ 60 GHz. The radiometer has sensitivity of 0.04 K for integration time of 1 second. The antenna is a scalar horn with beamwidth of about 6° and has low response outside the main lobe. The MTP5 is self calibrating angular scanning single-channel microwave radiometer. The specifications of MTP-5H is shown on Figure 2.

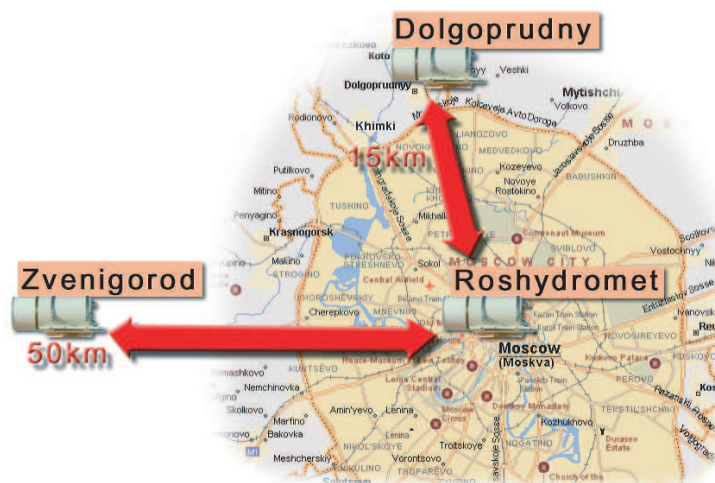


Figure 1: The relative position of three microwave temperature profiles (MTP-5H).

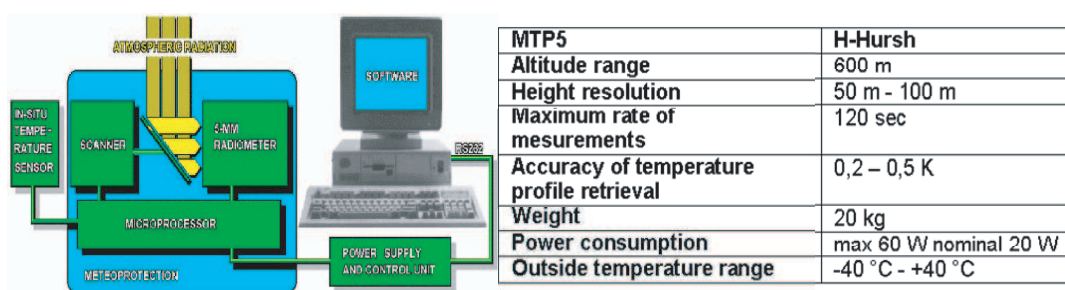


Figure 2: Specifications of MTP-5H instruments.

Calibration of the receiver is achieved by 0.1°C temperature control and a switched internal noise generator. A one point absolute calibration is achieved either by viewing an external target or by knowing the emission temperature in the horizontal direction.

3. RESULTS

The examples of data obtained by radiometers is shown on Figure 3.

The results show that the strongest response of the temperature on the urban influence was observed in the near surface layer of the atmosphere. As were shown by the measurements, the whole 600 m layer was convective unstable at that time. The stability of ABL leads to an increase of pollution and moisture in Moscow and blocks cooling in the evening. The heat absorbed by the buildings and asphalt roads also acts to retain warmth. As a result of these factors, the cooling in the suburbs happens faster.

It is evident that at nights and in the mornings even under the relatively clean conditions, the large city affects the thermal field. But the level of the urban heat dome is not high. The upper boundary of the dome goes approximately up to 300 m. The largest temperature gradients were fixed between the city and its suburb ($1.5\text{--}3.5^{\circ}\text{C}$) inside the lowest atmospheric layer (0–100 m). In the afternoon (from 12:00 up to 18:00) the concentrations of pollutants and water vapor in the urban air decreased to the levels with week influence on the thermal processes in ABL and UHI decreased. The temperature difference between Moscow and Zvenigorod in the layer 0–100 m did not exceed 1°C . An intensification of UHI near the ground was observed after 18:00. An increase of city-suburb difference was observed after 21:00 in the layer 0–100 m. Diurnal spread of the temperature difference in the layer 300 m did not exceed 1.0°C ($0.1\text{--}1.0^{\circ}\text{C}$). It was equaled 0.7°C in the layer 600 m ($-0.5\text{--}+0.2^{\circ}\text{C}$). Under the high polluted conditions (July 20, 2002) nocturnal and morning (0:00 to 9:00) city-suburb difference inside the layer 0–100 m was from 2.6 to 8.2°C . The UHI was conserved and its top reached 600 m in the afternoon, but its intensity even in the lowest layer of the atmosphere rarely exceeds $1\text{--}2^{\circ}\text{C}$. Our studies confirmed that UHI is observed generally at night.

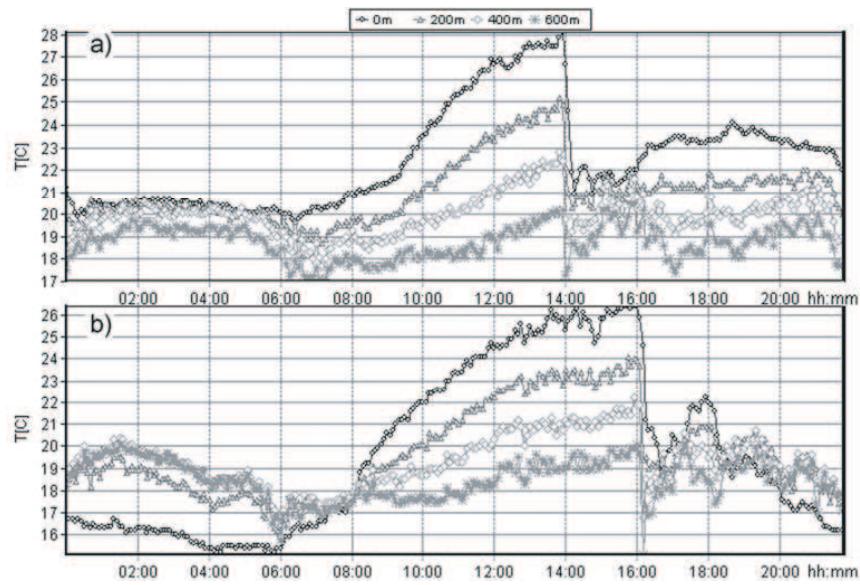


Figure 3: Temperature variations at different heights during the atmospheric front passage. (a) Moscow, (b) Zvenigorod. June 20, 2001.

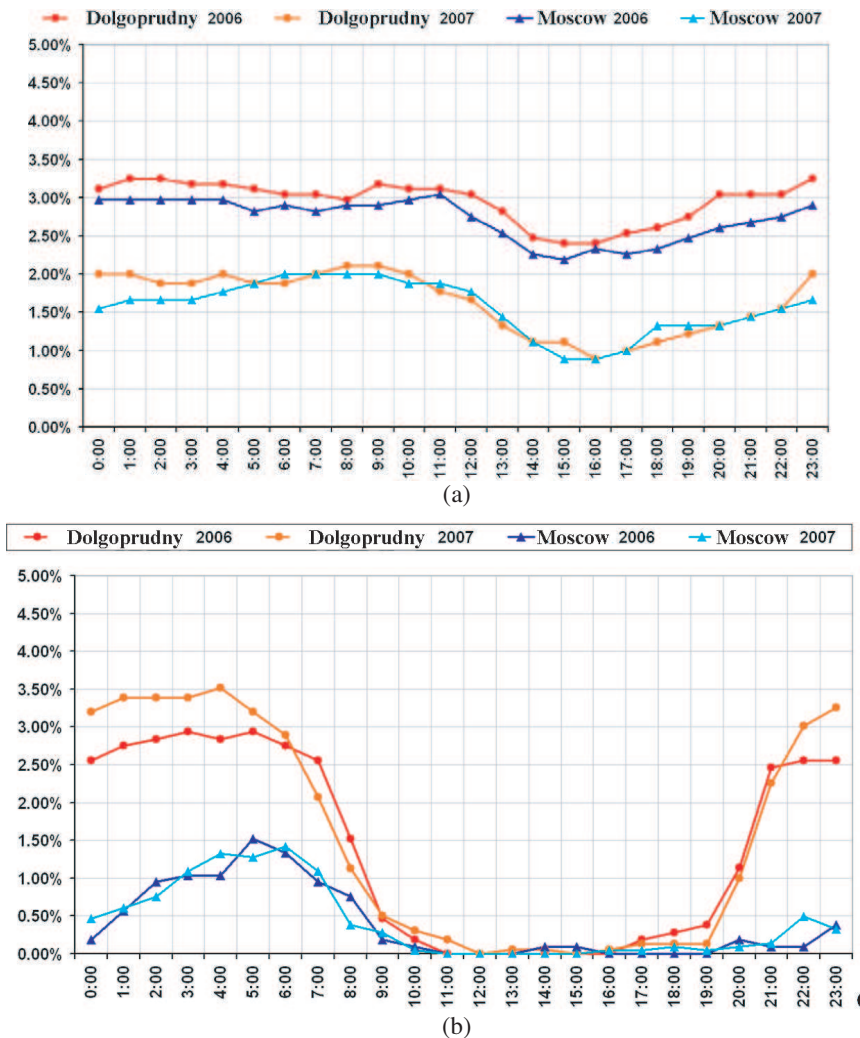


Figure 4: The diurnal distribution of inversions. For Dolgoprudny & Moscow. (a) Winter period, (b) summer period 2006–2007.

It was also calculated features of vertical temperature gradient for each 100 meters above the city and above suburb at two seasons (summer, winter). It was also calculated parameters of temperature inversions in city center and in suburb and its seasonal variations (Figure 4).

The Figure 4 shows that amount of inversions in winter in Moscow and Dolgoprudny is very close. The abrupt difference in the quantity of inversions for two winters 2007 and 2006 is explained by very warm winter months in 2007. But for summer season in 2007 and 2006, it can be seen appreciable distinction in frequency of cases and in time, when inversion was formed. At nights, a quantity of inversions in Dolgoprudny in winter and in summer is very close. While in the center of Moscow in summer, this quantity is two times smaller than in winter months. In summer, inversions is very rare in both places. The similar results were obtained by the authors for 2001. The maximum difference between the city and its suburb is in summer. It is probably connected with the differences in underlying surface characteristics.

4. CONCLUSIONS

Continuous temperature profiles observations in atmospheric boundary layer on the basis of stationary and mobile microwave profilers allow to obtain unique data and to investigate the UHI over the big cities. And its clear that remote sensing in studying UHI is very efficient.

Two types of UHI were identified on the basis of the temperature profile measurements: The warmer dome of the urban heat at all levels, and low warmer dome in combination with the lens of the cold air above it. The lens of cold, placed under the dome is a result of both radiation balance deformation in more humid and polluted urban air and more active mixing processes in more unstable urban air.

UHI exists not only under the conditions accompanied by the elevated pollution levels, but also under that one when relatively clear air does not accumulate urban polluting outbreaks.

The most pronounced UHI is observed in the morning and at night. The accumulation of the pollutants and water vapor in the urban air occurs this time and UHI reaches its maximal intensity. During the day, the UHI is broken down or remains only in the low 300 meters.

REFERENCES

1. Kadygrov, E. N., G. S. Golitsin, and I. N. Kuznetsova, "Study of urban heat island on the basis of microwave remote sensing data," Reports of Russian Academy of Science, Vol. 385, No. 4, 541–548, 2002.
2. Khaikine, M. N., I. N. Kuznetsova, E. N. Kadygrov, and E. A. Miller, "Investigation of thermal-spatial parameters of an urban heat island on basis of passive microwave remote sensing," *Theoretical Applied Climatology*, Vol. 84, No. 1–3, 161–169, 2006.
3. Oke, T. R., *Boundary Layer Climates*, Methen & Co., Ltd, London, 1977.
4. Kadygrov, E. N. and D. R. Pick, "The potential for temperature retrieval from an angular-scanning single-channel microwave radiometer and some comparison with in situ observations," *Meteorol. Appl.*, Vol. 5, 393–404, 1998.
5. Cadeddu, M. P., G. E. Peckham, and C. Gaffard, "The vertical resolution of ground-based microwave radiometers analyzed through a multiresolution wavelet technique," *IEEE Trans. on Geosc. and Remote Sensing*, Vol. 40, 531–540, 2002.
6. Viazankin, S. A., E. N. Kadygrov, N. F. Mazurin, A. V. Troitsky, and G. N. Shur, "Comparison of data on the temperature profile and its inhomogeneity structure obtained by microwave radiometer and tall meteorological mast," *Russian Meteorology and Hydrology*, Vol. 3, 34–44, 2001.

Radiative Transfer and the Eigenfunction Approach in Different Geometries

Juris Freimanis^{1,2}

¹Ventspils International Radio Astronomy Center, Ventspils University College, Latvia

²Institute of Astronomy, University of Latvia, Latvia

Abstract— The relations between eigenfunctions of homogeneous radiative transfer equation and Green's function for inhomogeneous transfer equation in infinite medium and different geometries (plane-parallel, spherical, cylindrical) are discussed. Expressions for cylindrical eigenfunctions of polarized radiative transfer equation are obtained. It is shown that in nonplanar geometries Green's function usually is not a linear superposition of eigenfunctions.

1. INTRODUCTION

Currently most of radiative transfer calculations are numerical solutions of the matrix transfer equation for Stokes vector, within framework of realistic, complicated three-dimensional geometric models, with inhomogeneous, anisotropic and probably gyrotropic scattering medium, with redistribution of radiation over frequencies etc. Nevertheless analytic results for the simplest models are benchmarks for numerical calculations at least because they provide the general behaviour and singularities of the solution. Correct reproduction of the singularities is essential for the numerical solution to be stable and to converge to exact solution.

Generalized eigenfunctions of stationary monochromatic plane-parallel radiative transfer equation in homogeneous isotropic infinite medium [1–5] have proved to be a powerful tool which allows to obtain analytic results in classical radiative transfer theory for both unpolarized and polarized radiation (see, for example, [6–9]). By the way, analytic Green's functions with account for polarization and quite general scattering laws for both infinite [3, 5] and semi-infinite medium [7, 9] were written down.

Up to now, some explicit expressions for eigenfunctions, without account for polarization, in the simplest nonplanar geometries — spherical [10] and cylindrical [11, 12] — have been obtained as well. Green's function in infinite medium was also obtained for different scattering laws, and on different basis: i) spherical symmetry, isotropic scattering without account for polarization, implicit invocation of spherical eigenfunctions by means of Fourier transformation [13], ii) spherical symmetry, anisotropic scattering without account for polarization, direct invocation of spherical eigenfunctions [10], iii) general anisotropic scattering of polarized radiation, spherical symmetry, construction and subsequent decomposition of auxiliary plane-parallel transfer problem without use of spherical eigenfunctions [14], iv) the same for cylindrical symmetry [15, 16].

In this paper some review of these results is made. Covariant differentiation of Stokes vector is introduced, and formal expressions for cylindrical eigenfunctions with account for polarization are obtained, but it is shown that their suitability for use in applications, and the construction of Green's function in particular, is doubtful.

In Section 2, the basic physical conditions assumed to be valid are defined. In Section 3, the expressions for plane-parallel eigenfunctions are recalled, and they are written down in case of spherical and cylindrical symmetry as well. Some summary is made in Section 4.

2. THE PHYSICAL CONDITIONS

Let us describe polarized radiation as in [3, 14] by Stokes vector in circular polarization (CP) representation. Further in this paper all the vectors, matrices and so on are designated just as in [14], and the reader is urged to seek for definitions in that paper.

Let us assume that the problem obeys the following physical conditions:

1. The medium is homogeneous, isotropic and infinite, and it possesses no circular dichroism nor circular birefringence.
2. The scattering (and the extinction) process is monochromatic.
3. The radiation field is stationary.

4. The scattering matrix is physically valid accordingly to Konovalov [17] almost everywhere on the interval $z \equiv \cos \theta \in [-1, 1]$, where θ is the scattering angle, and quasidiagonal in Stokes-Poincaré representation:

$$\mathbf{\Gamma}(z) = \begin{pmatrix} a_1(z) & b(z) & 0 & 0 \\ b(z) & a_2(z) & 0 & 0 \\ 0 & 0 & a_3(z) & c(z) \\ 0 & 0 & -c(z) & a_4(z) \end{pmatrix}. \quad (1)$$

5. In CP representation, all the functions

$$u_{mn}(z) = [\mathbf{\Gamma}(z)]_{mn} (1-z)^{-\frac{|m-n|}{2}} (1+z)^{-\frac{|m+n|}{2}}, \quad (2)$$

where $m, n = 2, 0, -0, -2$, are entire functions.

6. Single scattering albedo λ satisfies the inequalities

$$0 < \lambda \equiv \frac{1}{2} \int_{-1}^1 a_1(z) dz \equiv p_{00}^0 + p_{0,-0}^0 < 1, \quad (3)$$

where p_{mn}^l is the expansion coefficient for the element (m, n) of the scattering matrix in CP representation, $\Gamma_{mn}(\cos \theta)$, in generalized spherical functions [14].

7. For all azimuthal harmonics $s = 0, \pm 1, \pm 2, \dots$, the dispersion matrix $\mathbf{\Lambda}_s(z)$ (see [3, 14]) is nonsingular on the sides of the cut $z \in [-1, 1]$:

$$\det \mathbf{\Lambda}_s^\pm(\mu) = \det \lim_{\varepsilon \rightarrow +0} \mathbf{\Lambda}_s(\mu \pm i\varepsilon) \neq 0 \quad \text{for } \mu \in [-1, 1]. \quad (4)$$

3. EIGENFUNCTIONS OF THE HOMOGENEOUS TRANSFER EQUATION IN DIFFERENT GEOMETRIES

3.1. Plane-parallel Symmetry

The homogeneous transfer equation is [3, 5]:

$$\mu \frac{\partial \mathbf{I}(\tau, \mu, \varphi)}{\partial \tau} = -\mathbf{I}(\tau, \mu, \varphi) + \frac{1}{4\pi} \int_0^{2\pi} \sum_{s=-\infty}^{+\infty} e^{-is(\varphi-\varphi')} d\varphi' \int_{-1}^1 \mathbf{P}_s(\mu, \mu') \mathbf{I}(\tau, \mu', \varphi') d\mu', \quad (5)$$

where τ is the optical depth, and $\vartheta = \cos^{-1} \mu \in [0, \pi]$, $\varphi \in [0, 2\pi)$ are the polar and azimuthal angles characterizing the direction of propagation of radiation. As was shown in [3, 4, 5, 18], the eigenvalue spectrum for mutually independent azimuthal Fourier components of Stokes vector consists of the continuous spectrum $\eta \in [-1, 1]$ and the set of discrete eigenvalues $\eta_i \notin [-1, 1]$; these last are specific for each azimuthal component of index s , and their number is finite for each s . The corresponding eigenfunctions of Eq. (5) in case of continuous spectrum $\eta \in [-1, 1]$ are

$$\mathbf{I}_s(\tau, \mu, \varphi; \eta) = e^{-\frac{\tau}{\eta} - is\varphi} \boldsymbol{\varphi}_s(\mu, \eta), \quad (6)$$

where the “reduced eigenfunction” is

$$\boldsymbol{\varphi}_s(\mu, \eta) = \frac{\eta \boldsymbol{\psi}_s(\mu, \eta)}{2} \frac{1}{\eta - \mu} + \boldsymbol{\chi}_s(\eta) \delta(\mu - \eta) = (-1)^s \sum_{l=|s|}^{\infty} \frac{2l+1}{2} \mathbf{P}_s^l(\mu) \mathbf{R}_s^l(\eta). \quad (7)$$

In case of discrete spectrum $\eta_i \notin [-1, 1]$ the adjoint functions can be present [4]. If they are not, Eqs. (6) and (7) remain valid with η_i instead of η , and without the term containing delta function but with multiplier $\mathbf{M}_s(\eta_i)$ in Eq. (7). If the adjoint functions do exist, the reduced eigenfunction $\boldsymbol{\varphi}_s(\mu, \eta_i)$ is replaced by the expression [5, 9, 14]

$$\boldsymbol{\chi}_s(\mu, \eta_i) = \frac{\eta_i}{2} \frac{\boldsymbol{\psi}_s(\mu, \eta) \boldsymbol{\pi}_s^{-1}(\eta) \mathbf{M}_s^{0i}(\eta)}{\eta - \mu} \widehat{\mathbf{D}}_i(\eta) \Big|_{\eta=\eta_i} = (-1)^s \sum_{l=|s|}^{\infty} \frac{2l+1}{2} \mathbf{P}_s^l(\mu) \mathbf{C}_s^l(\eta_i), \quad (8)$$

and two additional matrices, one of them polynomial in τ and the other polynomial in η_i , appear as multipliers in the eigenfunction of Eq. (5).

In Eqs. (7) and (8), functions $\psi_s(\mu, \eta)$, $\lambda_s(\eta)$, $\pi_s^{-1}(\eta)$ and $\mathbf{M}_s^{0i}(\eta)$ are smooth enough functions leading to well-defined singular integral equations with Cauchy type kernels in different applications of this mathematical apparatus. It was proved [5] that for each s the set of functions $\{\varphi_s(\mu, \eta), \chi_s(\mu, \eta_i)\}$ constitute orthogonal basis allowing to expand all integrable functions of $\mu \in [-1, 1]$ belonging to certain Banach spaces. The Green's function for infinite medium [5, 14] expresses by eigenfunctions of type Eq. (6) for different eigenvalues η as their linear superposition, as it usually is in many problems of mathematical physics.

3.2. Spherical Symmetry

If the radiation field is spherically symmetric then it has no azimuthal dependence, and one deals only with zeroth azimuthal Fourier components of Stokes vector and phase matrix. The homogeneous transfer equation is

$$\mu \frac{\partial \mathbf{I}(\tau, \mu)}{\partial \tau} + \frac{1 - \mu^2}{\tau} \frac{\partial \mathbf{I}(\tau, \mu)}{\partial \mu} = -\mathbf{I}(\tau, \mu) + \frac{1}{2} \int_{-1}^1 \mathbf{P}_0(\mu, \mu') \mathbf{I}(\tau, \mu') d\mu'. \quad (9)$$

Eigenfunctions can be formally constructed multiplying Eq. (9) from the left by matrix $\mathbf{P}_0^l(\mu)$, integrating over $\mu \in [-1, 1]$ and using differentiation and recurrent formulae for cylindrical functions (see [19]). It appears that the spherical eigenfunctions of transfer equation contain just the same matrices $\mathbf{R}_0^l(\eta)$ which are present in Eqs. (7) and (implicitly) (8) in case $s = 0$, and consequently all spherical eigenvalues η must be simultaneously plane-parallel eigenvalues of the zeroth Fourier component; one obtains formal series containing spherical modified Bessel functions $(\eta/\tau)^{1/2} I_{l+1/2}(\tau/\eta)$ and spherical McDonald's functions $(\eta/\tau)^{1/2} K_{l+1/2}(\tau/\eta)$. All such linearly independent solutions of Eq. (9) are exhausted if we take only nonnegative eigenvalues $\eta \in (0, 1]$ and $\eta_i \notin (-1, 1]$, $\text{Re } \eta_i > 0$, with the following corresponding eigenfunctions (see [20]):

$$\mathbf{I}_{(1)}(\tau, \mu; \eta) = \frac{1}{4\pi\eta^2} \sqrt{\frac{\pi\eta}{2\tau}} \sum_{l=0}^{\infty} (-1)^l (2l+1) I_{l+\frac{1}{2}} \left(\frac{\tau}{\eta} \right) \mathbf{P}_0^l(\mu) \mathbf{R}_0^l(\eta), \quad (10)$$

$$\mathbf{I}_{(2)}(\tau, \mu; \eta) = \frac{1}{4\pi\eta^2} \sqrt{\frac{2\eta}{\pi\tau}} \sum_{l=0}^{\infty} (2l+1) K_{l+\frac{1}{2}} \left(\frac{\tau}{\eta} \right) \mathbf{P}_0^l(\mu) \mathbf{R}_0^l(\eta). \quad (11)$$

The expression (11) with just such normalization can be obtained in an alternative way: each plane-parallel eigenfunction given by Eq. (6) in the domain $\tau > 0$ can be regarded as a linear superposition of spherical eigenfunctions, and this superposition can be decomposed for $\text{Re } \eta > 0$ similarly as it was done while deriving spherically symmetric Green's function in [14]. Similar transformation can be done with the expression containing the generalized eigenfunctions $\chi_s(\mu, \eta_i)$ as well. The result is: due to properties of cylindrical functions for large index, Eq. (10) is an absolutely convergent series without singularities in the domain $\tau \in [0, \infty)$, $\mu \in [-1, 1]$, and Eq. (11) is a very strongly divergent series. In fact, the eigenfunction Eq. (11) does not exist (it is called Sobolev-Schwartz type generalized function in [10, 11] but the respective authors have not shown how to project any function not infinitely differentiable using similar projection operator). Due to this, in spherically symmetric case it is not seen how to use some mathematical technique offering possibilities comparable with those of singular integral equations. Until now, nobody has proved theorems about the completeness of spherically symmetric eigenfunctions (at least as generalized functions) in some functional spaces. As a result, the Green's function for infinite medium is not a superposition of spherical eigenfunctions for different eigenvalues η ; the corresponding lengthy expressions (they can be found in [14]) have some resemblance with Eqs. (10) and (11) but the order of different operations, namely, summation of series and integration over different variables, must be strictly observed in them.

3.3. Cylindrical Symmetry

Cylindrically symmetric radiation field means that Stokes vector is dependent only on radial spatial coordinate r , or (equivalently) optical distance from symmetry axis τ . The dependence of Stokes vector on the direction of propagation can be arbitrary if directional angles are defined in a cylindrically symmetric manner. It is appropriate to characterize the direction of propagation by polar

and azimuthal angles of spherical coordinate system, (ϑ, φ) . Polar axis can be defined as parallel or perpendicular to the axis of cylindrical symmetry [1, 11, 12, 15].

Here we shall use the same definitions as are used in [15, 16]: polar axis is perpendicular to the axis of cylindrical symmetry, azimuth is counted from the positive direction of cylindrical symmetry axis, and the reference plane for Stokes parameters goes through polar axis in the point of observation and the direction of propagation of radiation. This choice means that the reference plane for Stokes parameters generally rotates if the point of observation moves along some path of propagation. The homogeneous transfer equation is

$$\begin{aligned} & \mu \frac{\partial \mathbf{I}(\tau, \mu, \varphi)}{\partial \tau} + \frac{(1 - \mu^2) \sin^2 \varphi}{\tau} \frac{\partial \mathbf{I}(\tau, \mu, \varphi)}{\partial \mu} - \frac{\mu \sin 2\varphi}{2\tau} \frac{\partial \mathbf{I}(\tau, \mu, \varphi)}{\partial \varphi} + \frac{\sin 2\varphi}{2\tau} \mathbf{r} \mathbf{I}(\tau, \mu, \varphi) \\ & = -\mathbf{I}(\tau, \mu, \varphi) + \frac{1}{4\pi} \int_0^{2\pi} \sum_{s=-\infty}^{+\infty} e^{-is(\varphi-\varphi')} d\varphi' \int_{-1}^1 \mathbf{p}_s(\mu, \mu') \mathbf{I}(\tau, \mu', \varphi') d\mu', \end{aligned} \quad (12)$$

where $\mu = \cos \vartheta$, and the last term in the left-hand side accounts for the rotation of polarization reference plane along the path of propagation; it is somewhat similar to covariant differentiation with use of Christoffel symbols in general relativity [21]. Such term should be added to the left-hand sides of Eq. (4) in [15] and Eqs. (5) and (8) in [16] but its omission (it happened due to overlooking) has no impact on the results of those papers because the transfer equation was solved indirectly there. The 4×4 rotation matrix \mathbf{r} in CP representation is defined by its elements as

$$[\mathbf{r}]_{mn} = -in \delta_{mn}, \quad m, n = 2, 0, -0, -2, \quad (13)$$

or $\mathbf{r} = \text{diag}(-2i, 0, 0, 2i)$, where i is the imaginary unit.

Laletin [11] obtained cylindrically symmetric eigenfunctions of transfer equation in case of isotropic scattering neglecting polarization. Kolesov [12] tried to do the same for anisotropic scattering without polarization but his set of cylindrical eigenfunctions is not complete. Probably the simplest way how to obtain eigenfunctions of Eq. (12) is to formally decompose the plane-parallel eigenfunction of some fixed azimuthal index $s = \sigma$ given by Eq. (6) in the domain $\tau > 0$ for the part of the continuous spectrum $\eta \in (0, 1]$, as well as their counterparts for the discrete spectrum $\text{Re } \eta_i > 0$, into cylindrically symmetric constituents – similarly as the cylindrically symmetric Green's function was derived [15, 16]. The result is as follows:

$$\begin{aligned} \mathbf{I}_\sigma(\tau, \mu, \varphi; \eta) &= \frac{(-1)^\sigma}{\pi \eta} \sum_{l=|\sigma|}^{\infty} (2l+1) \sum_{k=-[\frac{l+\sigma}{2}]}^{[\frac{l-\sigma}{2}]} (-1)^k e^{-i(\sigma+2k)\varphi} \mathbf{P}_{\sigma+2k}^l(\mu) \mathbf{R}_\sigma^l(\eta) \\ &\times \left[\sum_{j=1}^l d_{\sigma+2k, j}^l \left(\frac{\pi}{2}\right) d_{\sigma j}^l \left(\frac{\pi}{2}\right) K_j \left(\frac{\tau}{\eta}\right) + \frac{1}{2} \delta_{l-\sigma, 2[\frac{l-\sigma}{2}]} d_{\sigma+2k, 0}^l \left(\frac{\pi}{2}\right) d_{\sigma 0}^l \left(\frac{\pi}{2}\right) K_0 \left(\frac{\tau}{\eta}\right) \right], \end{aligned} \quad (14)$$

where $d_{mn}^l(\beta)$ are Wigner d-functions [22], and $\eta \in (0, 1]$. Similar but still more complicated strongly divergent series can be obtained for the discrete spectrum.

McDonald's functions persistent in Eq. (14) are unbounded for $\tau \rightarrow 0$; probably a linear combination of formal expressions (14) can be used in order to obtain modified Bessel functions $I_j(\tau/\eta)$ providing convergent series bounded for $\tau \rightarrow 0$ but unbounded at infinity. Again, similarly as in spherical case, no completeness theorems for cylindrical eigenfunctions are known, and Green's function for infinite medium [15, 16] is not a linear superposition of eigenfunctions for different η .

4. CONCLUSION

The eigenfunction technique being so fruitful in case of plane-parallel symmetry has limited value in case of spherical or cylindrical geometry of radiative transfer problems. The outer Green's function for these curvilinear geometries, $\mathbf{G}(\tau, \mu, \varphi; \tau', \mu', \varphi')$ in case $\tau > \tau'$, looks similar to linear combination of eigenfunctions, but in fact it is not such a combination. The inner Green's function ($\tau < \tau'$) is markedly different for both geometries.

From the computational viewpoint, it can be preferable to substitute the analytic expressions of Green's function for these curvilinear geometries into the integral terms of Eqs. (9) and (12), respectively, in order to calculate directly the source function.

ACKNOWLEDGMENT

This investigation was funded from the basic financing of Ventspils International Radio Astronomy Center.

REFERENCES

1. Case, K. M. and P. F. Zweifel, *Linear Transport Theory*, Addison-Wesley Publishing Company, Reading, Massachusetts, 1967.
2. Schnatz, T. W. and C. E. Siewert, “Radiative transfer in a Rayleigh-scattering atmosphere with true absorption,” *J. Math. Phys.*, Vol. 11, No. 9, 2733–2739, 1970.
3. Domke, H., “Transfer of polarized light in an isotropic medium. Singular eigensolutions of the transfer equation,” *JQSRT*, Vol. 15, No. 7/8, 669–679, 1975.
4. Konovalov, N. V., “Asymptotic properties of the solutions of transfer equation in plane-parallel slabs,” PhD Thesis, Institute of Applied Mathematics of the USSR Academy of Sciences, Moscow, 1982.
5. Freimanis, J., “On the completeness of system of eigenfunctions and adjoint functions of transfer equation of polarized radiation,” *Investigations of the Sun and Red Stars*, Vol. 32, 20–116, 1990.
6. Mika, J., “Fundamental eigenvalues of the linear transport equation,” *JQSRT*, Vol. 11, No. 6, 879–891, 1971.
7. Domke, H., “Transfer of polarized light in an isotropic medium. Biorthogonality and the solution of transfer problems in semi infinite media,” *JQSRT*, Vol. 15, No. 7/8, 681–694, 1975.
8. Domke, H., “Biorthogonality and radiative transfer in finite slab atmospheres,” *JQSRT*, Vol. 30, No. 2, 119–129, 1983.
9. Freimanis, J., “Transfer of polarized light in homogeneous isotropic semi infinite medium if the generalized eigenfunctions of transfer equation exist,” *Investigations of the Sun and Red Stars*, Vol. 36, 18–84, 1993.
10. Kolesov, A. K., “Green’s functions for the equation of radiative transfer in an infinite homogeneous medium with spherically symmetric distribution of the sources,” *Astrophysics*, Vol. 20, No. 1, 86–95, 1984.
11. Laletin, N. I., “Elementary solutions for neutron transport equations in problems with cylindrical and spherical symmetry,” *Atomic Energy*, Vol. 20, No. 6, 585–586, 1966.
12. Kolesov, A. K., “Radiative transfer in media with cylindrical symmetry,” *Doklady AN SSSR*, Vol. 287, No. 1, 115–118, 1986.
13. Case, K. M., R. Zelazny and M. Kanal, “Spherically symmetric boundary-value problems in one-speed transport theory,” *J. Math. Phys.*, Vol. 11, No. 1, 223–239, 1970.
14. Freimanis, J., “On Green’s function for spherically symmetric problems of transfer of polarized radiation,” *JQSRT*, Vol. 96, No. 3–4, 451–472, 2005.
15. Freimanis, J., “On Green’s function for cylindrically symmetric fields of polarized radiation,” *11th Electromagnetic & Light Scattering Conference. Extended Abstracts*, 21–24, University of Hertfordshire, Hatfield, Hertfordshire, U.K., September 2008.
16. Freimanis, J., “On Green’s function for cylindrically symmetric fields of polarized radiation,” *JQSRT*, 2009, in press.
17. Konovalov, N. V., “Polarization matrices corresponding to transformations within Stokes cone,” Preprint No. 171, Institute of Applied Mathematics of the USSR Academy of Sciences, Moscow, 1985.
18. Germogenova, T. A. and N. V. Konovalov, “Spectrum of the characteristic equation of transfer theory with accounting for polarization,” Preprint No. 62, Institute of Applied Mathematics of the USSR Academy of Sciences, Moscow, 1978.
19. Abramowitz, M. and I. A. Stegun, editors, *Handbook of Mathematical Functions with Formulas, Graphs and Mathematical Tables*, Dover Book, New York, 1965.
20. Freimanis, J., “On the eigenfunction approach for radiative transfer problems with spherical symmetry,” *Physica Scripta*, Vol. T77, 148–149, 1998.
21. Landau, L. D. and E. M. Lifshitz, *Theory of Field*, “Nauka” Publishing Company, Moscow, 1988.
22. Brink, D. M. and G. R. Satchler, *Angular Momentum*, Clarendon, Oxford, 1975.

Widely Wavelength-tunable Soliton Generation and Few-cycle Pulse Compression with the Use of Dispersion-decreasing Fiber

Alexey Andrianov¹, Sergey Muraviev¹, Arkady Kim¹, and Aleksei Sysoliatin²

¹Institute of Applied Physics, Russian Academy of Sciences
46 Ulyanov st., Nizhny Novgorod 603950, Russia

²Fiber Optics Research Center, Russian Academy of Sciences
53 Vavilov st., Moscow 119333, Russia

Abstract— We have developed an all-fiber source of both, widely wavelength tunable femtosecond solitons and few-cycle optical pulses. It is based on Raman self-frequency shift of soliton pulse in dispersion-decreasing fibers (DDF) and subsequent spectrum broadening due to supercontinuum generation in a short highly nonlinear fiber and its further compression in a fiber compressor. High-quality sech-shaped 50 fs solitons with the wavelength tunable in the range of 1.6–2.1 μm were obtained at the output of dispersion-decreasing fiber. The solitons were used as a pump for the generation of smooth and tunable supercontinuum, which was then compressed down to 24 fs duration corresponding to 4 optical cycles at the central wavelength of 1.8–1.9 μm .

1. INTRODUCTION

Creation of laser systems for generating few-cycle optical pulses comprising a small number of field oscillations at different wavelengths has been widely discussed in the recent years. The interest in such few-cycle pulses is explained by both, basic problems of the actively developed extreme nonlinear optics [1, 2] and their practical applications, including high harmonic generation and advance to the attosecond durations [2]. Many research groups use for generation of few-cycle pulses a master oscillator generating femtosecond pulses at a fixed wavelength that are further converted in nonlinear optical media so as to enrich the signal spectrum and then to compress the pulse to few-cycle duration. In this respect, fiber systems are of particular interest for both, nonlinear conversion and construction of femtosecond master oscillator. Initial pulses may be additionally smoothly wavelength-tuned due to Raman self-frequency shift in a special highly nonlinear fibers [3–5] and then spectrally broadened, if necessary, also in the nonlinear waveguides during supercontinuum generation [6, 7]. These ultrabroadband optical pulses may further be compressed in a linear compressor down to few-cycle durations [8–10]. It is worthy of notice that the fiber laser systems have already generated quite short pulses both, using external compressor [9, 10] and in the all-fiber setup with the use of strongly nonlinear fibers [11, 12]. In the present work we propose to use dispersion-decreasing silica fibers for smooth tuning of initial pulses in a broad wavelength interval. One of the advantages of this technique is more efficient frequency tuning of a soliton-type optical pulse due to its location in the frequency domain close to the zero dispersion point [13, 14] and, as a consequence, shorter output pulse duration due to adiabatic compression of the soliton pulse in dispersion-decreasing fiber [15]. Additionally, supercontinuum is actually generated in a section of a similar fiber of smaller diameter, with the zero dispersion point shifted to the longer wavelength region. Thus, this combination is capable of providing an all-fiber source of few-cycle pulses based on dispersion-decreasing fiber. The proposed technique allows one to generate few-cycle pulses in the mid-infrared range that has been poorly developed in terms of extreme nonlinear optics.

2. TUNABLE SOLITON GENERATION IN DDF

Here we propose the following scheme of an all-fiber laser system for the generation of tunable few-cycle pulses using dispersion-decreasing fibers. These fibers can provide efficient usage of Raman self-frequency shift of a soliton pulse propagating in DDF, as well as adiabatic compression of such a pulse as it approaches the zero dispersion point [15]. This allows one to implement broadband central wavelength tuning of optical pulse in the range wider than 400 nm using an erbium-doped fiber system and to obtain rather short output femtosecond pulses. Further, making use of spectral broadening by supercontinuum generation in a rather short strongly nonlinear fiber and subsequent compression in the appropriate linear fiber one can obtain few-cycle optical pulses. The schematic of the experimental setup is shown in Fig. 1. The source of optical pulses is a femtosecond fiber laser passively modelocked at 21-st harmonic of the ring cavity [16] generating 230 fs pulses with the

repetition rate of 600 MHz at the wavelength of 1.57 μm . The signal is amplified up to an average power of 150 mW in erbium-doped amplifier and is fed to a 39 m-long tapered silica DDF. The group velocity dispersion of this single-mode silica fiber is anomalous and increases in magnitude for wavelengths larger than the zero dispersion wavelength that may be shifted towards longer wavelengths by controlling the waveguide contribution to the dispersion when the fiber diameter is changed. In the experiments we used the fiber where the zero dispersion wavelength was shifted from 1.45 μm at the input to 1.7 μm at the output.

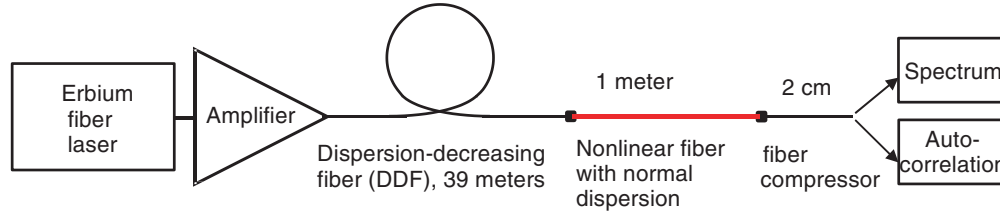


Figure 1: Schematic of the experimental setup.

Such a choice of fiber dispersion properties ensures central wavelength tuning of the signal in the 1.6–2 μm range and high-quality output pulse compressed down to 50–60 fs. As was shown in our previous work [13, 14], the pulse should be launched in DDF in the neighborhood of zero dispersion in its anomalous part, when nonlinear effects lead to formation of a soliton pulse. For sufficient input power, when a considerable part of the pulse power is accumulated in one soliton, during its further propagation in the fiber this pulse experiences strong Raman frequency shifting [4, 17]. Energy losses accompanying soliton propagation leading to a decrease in pulse intensity and slowing down the Raman self-frequency shift may be compensated by adiabatic pulse compression by means of smooth reduction of anomalous dispersion coefficient along the fiber [15]. Thus, by specifying an appropriate law of anomalous dispersion decrease in DDF it is possible to maintain high conversion efficiency throughout the fiber. Besides, by reducing the absolute magnitude of dispersion along the fiber one can compress the pulse, thus providing a smooth sech-shape at the output by virtue of the soliton effects. The central wavelength of the output pulse is determined by fiber length and Raman shift rate which, in turn, depends on soliton energy. Numerical simulation based on the generalized nonlinear Schrödinger equation [18] shows that, in a fiber with the above mentioned dependence of group velocity dispersion on wavelength and coordinate z along the fiber, given sufficient energy, the input pulse evolves to one or several fundamental solitons whose central frequency Ω decreases continuously so that the soliton moves almost along the constant dispersion line $\beta_2(\Omega, z) \approx \text{const}$ nearly at the same distance from the zero dispersion point in frequency domain [13, 14, 19]. The local second-order frequency-dependent dispersion coefficient $\beta_2(\omega, z) = \partial^2 \beta / \partial \omega^2$, where β is propagation constant, fully determines the dispersion properties of the fiber in the corresponding section z , given slow variation of fiber parameters along its length. Results of numerical calculations of changes in the spectra of pulses of different power propagating in DDF are presented in Fig. 2. The picture of spectrum evolution clearly shows the initial stage of pulse compression and spectrum broadening as the pulse approaches the zero dispersion point, as well as subsequent formation of a stable quasi-soliton at a constant distance from the dispersion zero line, that is accompanied only by slight radiation of dispersive waves.

The main features of the resulting quasi-soliton pulse may be investigated using a rather simple mathematical model. The rate of Raman self-frequency shift for a soliton in a fiber with nonlinearity γ (in our fibers it was $5 \text{ W}^{-1} \text{ km}^{-1}$) and characteristic Raman response time T_R (typically 5 fs)

$$\frac{d\Omega}{dz} = -\frac{8}{15} \frac{|\beta_2| \gamma T_R}{T^4} \quad (1)$$

strongly depends on soliton duration $T = 2|\beta_2|/(\gamma W) \approx 0.567 T_{FWHM}$, which in turn is determined by the local value of second-order dispersion β_2 and soliton energy W [17, 18]. Adiabatic decrease of dispersion as a result of changes in fiber diameter leads to soliton compression, so that the Raman self-frequency shift stabilizes the local value of second-order dispersion, $\beta_2(\Omega, z) = \text{const}$, due to dispersion growing with decreasing frequency. The latter equality gives us the soliton frequency dependence $\Omega(z)$ along the fiber. Thus, the condition of the equality of Raman shift rate of fundamental soliton to soliton frequency rate following from the stationary propagation model and

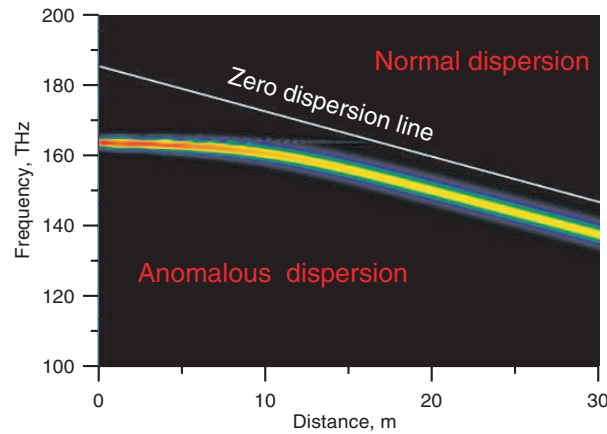


Figure 2: Pulse spectrum evolution during propagation in DDF.

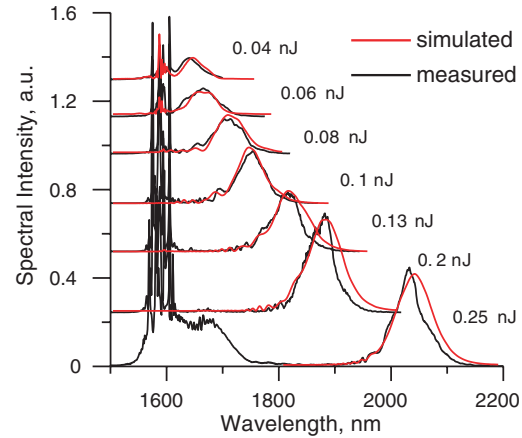


Figure 3: Soliton spectra at DDF output for different values of power.

supported by numerical modeling, provides the following relations for soliton energy W , its central frequency Ω , and duration T :

$$\beta_2(\Omega, z) = \left(\frac{T_R \gamma^4 W^4}{30s} \right)^{1/3}, \quad T = \frac{30^{2/3}}{15} \left(\frac{T_R \gamma W}{s} \right)^{1/3}. \quad (2)$$

Here, $s = d\omega_c/dz$ (where $\beta_2(\omega_c, z) = \text{const}$) is the rate of constant dispersion points in frequency space. The first relation in Eq. (2) defines implicitly soliton central frequency in the course of propagation along the fiber. Thus, for a given dispersive dependence, there exists a one-parametric family of frequency-tunable quasi-solitons whose duration and constant dispersion line along which the soliton is moving are determined by its energy W only. Smaller energy solitons move along the line of smaller local dispersion and have longer duration, so that the Raman shift rate sharply increasing with decreasing duration [17] allows the pulse to be detuned from the zero dispersion point. It should be noted that the minimum soliton duration is also limited by linear and nonlinear higher-order effects.

Limitation of the minimum pulse duration caused by closeness to zero dispersion point (actually, the impact of third-order dispersion $\beta_3 = \partial^3 \beta / \partial \omega^3$) that is the first to manifest itself in our experiment may be obtained from the following simple consideration. In order the soliton to be realized, the main part of its spectrum must lie in the region of anomalous dispersion, which imposes a condition on the duration of the transform-limited pulse, $T \gtrsim \beta_3 / \beta_2$, where the dispersion factors are taken at central frequency. Making use of this restriction and the relationship between parameters of the frequency-tunable soliton and local value of second-order dispersion (2) one can find minimum energy W_{\min} and the corresponding minimum duration T_{\min} at which such a pulse may exist:

$$W_{\min} \propto \frac{\beta_3^{3/5} s^{2/5}}{T_R^{2/5} \gamma}, \quad T_{\min} \propto \frac{\beta_3^{1/5} T_R^{1/5}}{s^{1/5}}. \quad (3)$$

For the pulse energy approaching a minimum one, energy losses due to linear wave radiation under the action of third-order dispersion increase, which eventually leads to fast soliton breakdown.

In our experiments with DDF we investigated spectrum shape and autocorrelation trace at the fiber output for different values of output pulse energy. The soliton spectra at DDF output given in Fig. 3 and corresponding autocorrelation traces demonstrate a well-pronounced sech-shape of a transform limited pulse. About 70% of the input pulse energy is converted into a long-wave soliton; the remainder of energy is in the spectral peak around 1.6 μm and may be filtered, if necessary, by a bandpass filter. Minimum pulse duration of 50 fs is attained at relatively small input pulse energy of about 0.06 nJ, which agrees with the estimates (3); at still smaller energies, the pulse ceases to be transform limited. Therefore, on the one hand, minimum pulse duration in DDF is limited and is attained at relatively small pulse energy; on the other hand, pulse duration grows slowly with increasing energy and significant wavelength tuning, which allows using DDF as a tunable source of high-quality pulses for further compression. Thus, DDFs can provide efficient conversion of the

input pulse regardless of its shape into widely wavelength tunable high quality solitonic pulses, which can be further compressed down to few-cycle durations by using spectral broadening via self-phase modulation in the highly-nonlinear fiber and subsequent recompression in the standard telecom fiber.

3. SUPERCONTINUUM GENERATION AND PULSE COMPRESSION

For further pulse shortening we employed strong spectral broadening of the signal by means of self-phase modulation that may occur in the fiber with small normal dispersion maintaining a rather high pulse quality [20], even for the characteristic values of peak intensity and nonlinearity typical for DDF solitons. We made use of a fiber with low normal dispersion in a wide wavelength range up to $2.2\ \mu\text{m}$. Such a constant-diameter fiber was made of the preform same as that used for DDF; the only difference was a smaller core diameter, thanks to which the zero dispersion wavelength is shifted to the long wavelength region. A strongly chirped pulse was obtained at the output of the fiber. The spectrum of this chirped pulse for three different values of energy at the DDF input is shown in Fig. 4 together with the spectrum of the soliton used for pumping. It is clear from the figure that, in conformity with the theory [20], a nearly symmetric spectrum broadening occurs in a nonlinear waveguide with normal dispersion, with the supercontinuum central wavelength varying together with the soliton central wavelength. The measured spectra agree qualitatively well with the numerical computations.

The pulse chirp and duration at the output of a normal-dispersion fiber assessed by the autocorrelation function for maximum power predicted possible compression down to 20–25 fs during propagation in a section of a standard anomalous-dispersion fiber about 2 cm long. Indeed, after adjusting compressor length we obtained a pulse whose autocorrelation function is presented in Fig. 5 and spectrum coincides with the supercontinuum spectrum taken before pulse compression. We used these data and the appropriate algorithm [21] to reconstruct the pulse phase and intensity. Half-width maximum-intensity pulse duration was 24.5 fs, which corresponds to four optical cycles at the wavelength of $1.9\ \mu\text{m}$.

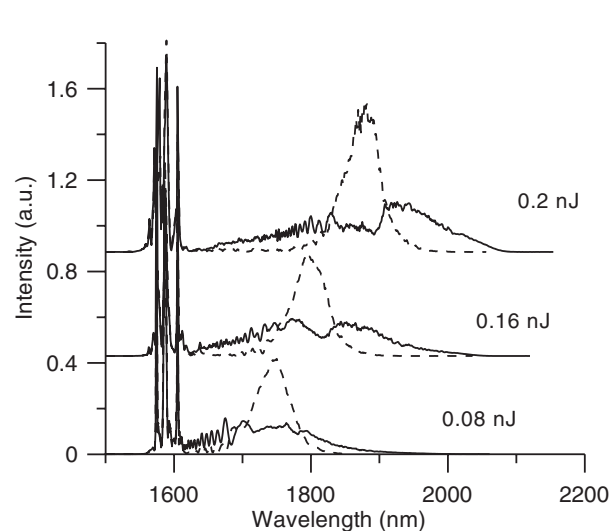


Figure 4: Spectra of supercontinuum (solid curves) and of the soliton (dashed curves) used for its generation for different input power of the signal.

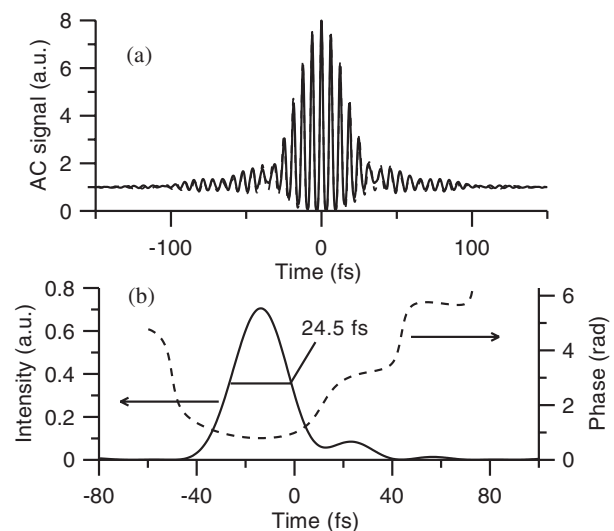


Figure 5: Autocorrelation function of 24 fs compressed pulse (a); pulse intensity and phase reconstructed from autocorrelation and spectral measurements (b).

4. CONCLUSION

We proposed an all-fiber scheme of constructing a laser system for generation of few-optical-cycle pulses, using the Raman self-frequency shift of optical soliton pulse in dispersion-decreasing fibers and supercontinuum generation, with the central wavelength smoothly tunable in a wide ($> 400\ \text{nm}$) range. This design, which we believe to be the first of its kind, can produce widely tunable few-cycle pulses in the range of $1.6\text{--}2.1\ \mu\text{m}$ and in near infrared with the use of second harmonic generation. The proposed all-fiber laser system is based only on telecommunication components which make it

easy-to-use, reliable in operation and rather low-cost. We believe that the proposed scheme has a number of merits interesting for solution of diverse scientific problems.

ACKNOWLEDGMENT

The work was supported in part by the Russian Foundation for Basic Research, grant No. 07-02-00596.

REFERENCES

1. Wegener, M., *Extreme Nonlinear Optics*, Springer-Verlag, Berlin, 2005.
2. Brabec, T. and F. Krausz, "Intense few-cycle laser fields: Frontiers of nonlinear optics," *Rev. Mod. Phys.*, Vol. 72, No. 2, 545, 2000.
3. Dianov, E. M., A. Y. Karasik, P. V. Mamyshev, et al., "Stimulated-Raman conversion of multisoliton pulses in quartz optical fibers," *JETP Lett.*, Vol. 41, No. 6, 242, 1985.
4. Mitschke, F. M. and L. F. Mollenauer, "Discovery of the soliton self-frequency shift," *Optics Letters*, Vol. 11, No. 10, 659, 1986.
5. Nishizawa, N. and T. Goto, "Widely wavelength-tunable ultrashort pulse generation using polarization maintaining optical fibers," *IEEE J. Select. Topics Quantum Electron.*, Vol. 7, No. 4, 518, 2001.
6. Dudley, J. M., G. Genty, and S. Coen, "Supercontinuum generation in photonic crystal fiber," *Rev. Mod. Phys.*, Vol. 78, No. 4, 1135, 2006.
7. Nishizawa, N. and T. Goto, "Widely broadened super continuum generation using highly nonlinear dispersion shifted fibers and femtosecond fiber laser," *Japanese J. of Appl. Phys.*, Vol. 40, No. 4B, L365, 2001.
8. Husakou, A. V. and J. Herrmann, "Supercontinuum generation of higher-order solitons by fission in photonics crystal fibers," *Phys. Rev. Lett.*, Vol. 87, 203901, 2001.
9. Tauser, F., F. Adler, and A. Leitenstorfer, "Widely tunable sub-30-fs pulses from a compact erbium-doped fiber source," *Opt. Lett.*, Vol. 29, No. 5, 516, 2004.
10. Adler, F., A. Sell, R. Huber, and A. Leitenstorfer, "Attosecond relative timing jitter and 13 fs tunable pulses from a two-branch Er: fiber laser," *Opt. Lett.*, Vol. 32, No. 24, 3504–3506, 2007.
11. Matsui, Y., M. D. Pelusi, and A. Suzuki, "Generation of 20-fs optical pulses from a gain-switched laser diode by a four-stage soliton compression technique," *IEEE Photonics Technology Letters*, Vol. 18, No. 17, 1831–1833, 2006.
12. Hori, T., N. Nishizawa, and T. Goto, "Generation of 14 fs ultrashort pulse in all fiber scheme by use of highly nonlinear hybrid fiber," *Ultrafast Phenomena XIV*, 31, Springer-Verlag, Berlin, 2005.
13. Andrianov, A. V., S. V. Muraviov, A. V. Kim, et al., "Generation of optical soliton pulses smoothly tunable in a wide frequency range in silica fibers with variable dispersion," *JETP Lett.*, Vol. 85, No. 8, 364–368, 2007.
14. Andrianov, A. V., S. V. Muraviov, A. V. Kim, et al., "DDF-based all-fiber optical source of femtosecond pulses smoothly tuned in the telecommunication range," Vol. 17, No. 11, 1296, 2007.
15. Chernikov, S. V., D. J. Richardson, E. M. Dianov, et al., "Picosecond soliton pulse compressor based on dispersion decreasing fibre," *Electronics Letters*, Vol. 28, No. 19, 1842, 1992.
16. Tamura, K., H. A. Haus, and E. P. Ippen, "Self-starting additive pulse mode-locked erbium fibre ring laser," *Electronics Letters*, Vol. 28, No. 24, 2226, 1992.
17. Gordon, J. P., "Theory of the soliton self-frequency shift," *Optics Letters*, Vol. 11, No. 10, 662, 1986.
18. Agrawal, G. P., *Nonlinear Fiber Optics*, Academic, San Diego, 2001.
19. Chernikov, S. V. and P. V. Mamyshev, "Femtosecond soliton propagation in fibers with slowly decreasing dispersion," *J. Opt. Soc. Am. B*, Vol. 8, No. 8, 1633, 1991.
20. Tomlinson, W. J., R. H. Stolen, and C. V. Shank, "Compression of optical pulses chirped by self-phase modulation in fibers," *J. Opt. Soc. Am. B*, Vol. 1, No. 2, 139–149, 1984.
21. Naganuma, K., K. Mogi, and H. Yamada, "General method for ultrashort light pulse chirp measurement," *IEEE Journal of Quantum Electronics*, Vol. 25, No. 6, 1225–1233, 1989.

Soliton Resonances in Dispersion Oscillating Optical Fibers

Andrey Konyukhov¹, Leonid Melnikov¹, Vladimir Khopin²,
Vladimir Stasuyk³, and Alexej Sysoliatin⁴

¹Saratov State University, Saratov, Russia

²Institute of High Purity Substances, N. Novgorod, Russia

³Pritel, Naperville IL, USA

⁴Fiber Optics Research Center, Moscow, Russia

Abstract— A novel method to increase the pulse repetition rate by means of fission of second-order solitons in the fiber with periodically modulated dispersion is studied. The experiments confirm the results of numerical simulations. The efficient doubling of the pulse repetition rate takes place in dispersion oscillating fiber (DOF). Good agreement between theory and experiment was obtained.

1. INTRODUCTION

The possibility to generate high quality femtosecond pulses around the 1550 nm wavelength at high repetition rates is important for exploring the potential of ultra-high speed optical time division multiplexed (OTDM) communications. In addition a pulse source with high repetition rate is very essential for optical computing systems, laser spectroscopy and other scientific applications. In this Letter a technique for increasing the repetition rate of a given periodic pulse sequence by splitting of high-order solitons is studied. It is known that the soliton splitting can be stimulated by self-steepening [1, 2], Raman scattering [3, 4] and cubic dispersion [5]. However, it is difficult to control the soliton splitting by these effects. For soliton management, fibers with variable dispersion or nonlinearity were proposed [7–14].

The multisoliton dynamics have their own periodicity [6]. At a distance less than the first half of the soliton period $0.5z_0$, the pulse splits into pulses which have different carrier frequencies. In the second half of the period the process reverses itself. An abrupt change of the dispersion or the nonlinear coefficient interrupts the periodic soliton recovery, and the soliton remains splitted into many daughter solitons. In segmented fiber, the multiple breakups of each soliton generate Cantor set fractals [7]. A step change in dispersion, a localized loss element or filter will generate pairs of pulses with wavelengths that are upshifted and downshifted from the input wavelength [8]. The maximum spectral separation occurs at locations that correspond to $0.5z_0$ for second-order soliton and to $0.225z_0$ for third-order soliton.

There are many contributions to nonlinear pulse propagation in periodic transmission lines with multisegmented fibers. The dispersion-managed soliton [9], split-step soliton [10, 11] and stationary rescaled pulse [12] have been discovered, and they have been analyzed with a focus on the pulse stability. It was shown [13] that periodic perturbation in nonlinear Schrödinger equation induce the generation of dispersive waves and/or the splitting of soliton. Splicing losses and transient processes that arise due to stepwise change of the dispersion restrict the application of multisegmented fibers for soliton splitting.

2. SIMULATION

A longitudinal sine-wave modulation of the fiber core diameter leads to the smooth oscillation of the fiber dispersion [14]. When the period of the modulation of the fiber diameter approaches the soliton period z_0 , the soliton splits into pulses propagating with different group velocities. In this work we report experimental realization of the soliton splitting by highly nonlinear dispersion oscillating fiber (DOF).

For analysis of the soliton splitting, the generalized nonlinear Schrödinger equation was solved.

$$\frac{\partial A}{\partial z} + \alpha A(z, t) = -i \frac{\beta_2(z)}{2} \frac{\partial^2 A}{\partial t^2} + \frac{\beta_3(z)}{6} \frac{\partial^3 A}{\partial t^3} + i \left(P_{NL} + i \frac{2}{\omega_0} \frac{\partial P_{NL}}{\partial t} \right), \quad (1)$$

where $A(z, t)$ is the complex pulse envelope in a comoving frame, $\alpha = 0.0795 \text{ km}^{-1}$ is the loss coefficient, and ω_0 is the carrier frequency of the pulse. Functions $\beta_2(z)$ and $\beta_3(z)$ take into account dispersion varying along the fiber length. Nonlinear polarization P_{NL} includes effects of

Kerr nonlinearity and delayed Raman scattering [6]. The modulation of the fiber core diameter leads to a variation of both the dispersion and the effective nonlinearity. The variation of the effective nonlinearity is much less than the variation of the dispersion [14] and can be neglected.

3. EXPERIMENT

The highly nonlinear DOF with sine-wave diameter modulation was fabricated in the Fiber Optics Research Center. The corresponding variation of the fiber dispersion is approximated by

$$\beta_{2,3}(z) = \bar{\beta}_{2,3} (1 + 0.2 \sin(2\pi z/z_m + \varphi_m)), \quad (2)$$

where $\bar{\beta}_2 = -12.76 \text{ ps}^2 \text{ km}^{-1}$, $\bar{\beta}_3 = 1.4 \text{ ps}^3 \text{ km}^{-1}$, $z_m = 0.16 \text{ km}$ is the modulation period, φ_m is the modulation phase. Using a 0.8 km length (z) of DOF in these experiments, then $\varphi_m = 0$ at one fiber-end and $\varphi_m = \pi$ at the other fiber-end, according to Eq. (2). Thus, the modulation phase will be different for pulses launched into opposite fiber-ends. Therefore, the nature of the soliton splitting will depend on direction of the light propagation.

Pulse dynamics is calculated in the temporal frame equal to the period $T = 100 \text{ ps}$ of the pulse train used in experiments. The input pulse is

$$A(0, t) = 1.76 \frac{N}{T_0} \sqrt{\frac{|\bar{\beta}_2|}{\gamma}} \text{sech} \left(1.76 \frac{t}{T_0} \right), \quad (3)$$

where N is the soliton order [6], T_0 is the temporal full width half maximum of $|A(0, t)|^2$, $\gamma = 8.2 (\text{W km})^{-1}$ is nonlinear coefficient.

Figure 1 illustrates the experimental setup. Pritel UOC provides 2-picosecond transform-limited pulses centered at 1550 nm at a 10 GHz repetition rate. The picosecond pulses are amplified by an erbium-doped fiber amplifier. The pulses have typical energies of 2 pJ–20 pJ. Output pulses were characterized using an optical spectrum analyzer (OSA), autocorrelator “Femtochrome” and wide-bandwidth oscilloscope “Agilent Infinium DCA 86100A”. The spectral resolution of OSA was set to 0.002 nm. To detect the doubling of the pulse repetition rate, autocorrelator had a scan range that exceeded the period of input pulse train. To obtain the maximum separation between pulses, the nearly resonant regime $z_m \simeq z_0$ was realized. For initial pulse width $T_0 = 2.1 \text{ ps}$ the soliton period is $z_0 = 0.506 T_0 (\bar{\beta}_2)^{-1} = 0.175 \text{ km}$.

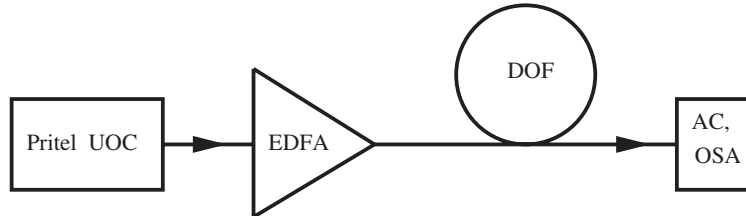


Figure 1: Experimental setup: Pritel UOC, picosecond pulse source; EDFA, Er-doped fiber amplifier; DOF, dispersion oscillating fiber.

At the initial stage the pulse repeat the typical evolution of the breather then splits into separate pulses moving with different velocities (Fig. 2). To initiate the splitting process, two modulation periods of DOF are sufficient (Fig. 2(a)). The normalized intensities of output pulses are 0.36 and 1.0 in Fig. 2(a). Such asymmetry arises due to the strong effect of the Raman scattering. Without this effect the dispersion oscillation would initiate splitting of second-order soliton into two pulses with equal amplitudes [14]. By means of numerical simulations we have found that effect of the Raman scattering on the splitting of second-order solitons can be controlled by the phase of periodical modulation of the fiber dispersion (2). For $\varphi_m = \pi$ (2) the soliton splits into two pulses with identical amplitudes.

The splitting of the soliton was detected both by the autocorrelation curves (Fig. 2(b)) and by change of the spectrum of the output pulse (Fig. 2(c)). The bandwidth of the oscilloscope is not sufficient to detect the output as separate pulses (Fig. 2(d)). The envelope of the spectrum of initial pulses has sech^2 shape. After the splitting the spectrum envelope become broken down (Fig. 2(c)). Such structure of output spectrum appears due to interference between two pulses with

shifted carrier frequencies. In the frequency domain the first pulse with the peak intensity equal 0.36 (Fig. 2(a)) is blue-shifted ($\omega_0 - \bar{\omega} = -0.043$ THz), while the second is red-shifted ($\omega_0 - \bar{\omega} = 0.084$ THz). Here $\bar{\omega}$ is the mean-weighted frequency of the pulse.

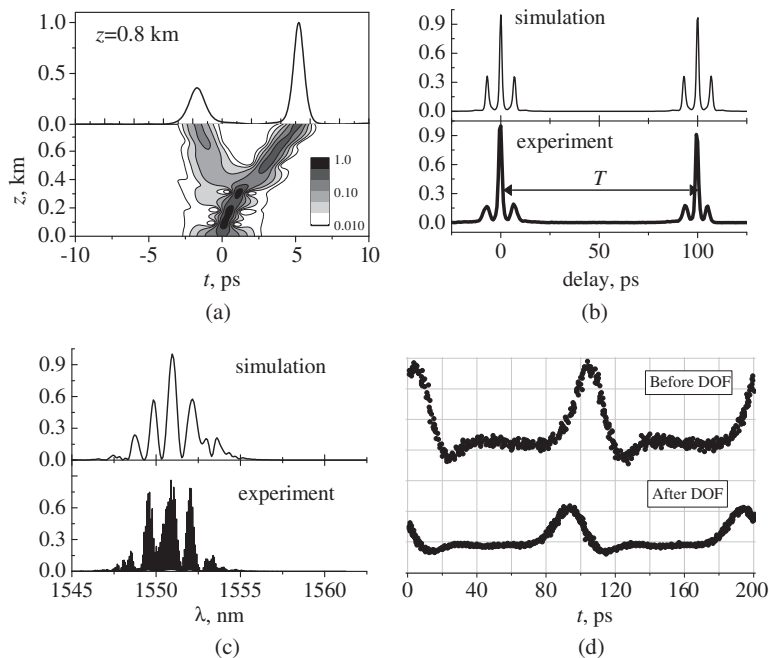


Figure 2: Pulse splitting in dispersion oscillating fiber. (a) Contour plot of pulse trajectory (bottom) and intensity pulse shape at $z = 0.8$ km (top); (b) autocorrelation traces for output pulses; (c) output spectrum; (d) oscilloscope record. $\varphi_m = 0$, $T_0 = 2.1$ ps, input power is 167 mW, for simulation $N = 1.85$ was used.

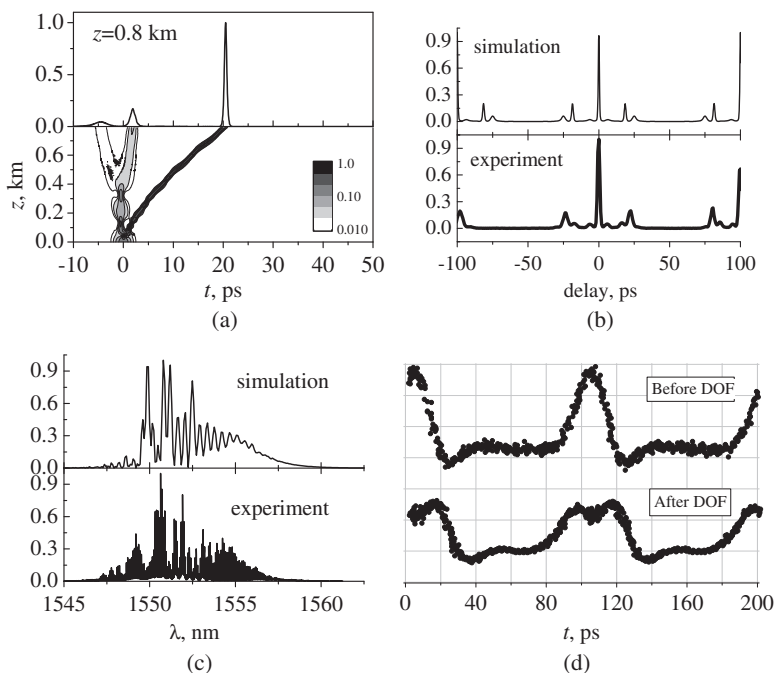


Figure 3: Splitting of soliton under the effect of Raman scattering. (a) Contour plot of pulse trajectory (bottom) and intensity pulse shape at $z = 0.8$ km (top); (b) autocorrelation traces for output pulses; (c) output spectrum; (d) oscilloscope record. Input power is 279 mW, $N = 2.66$. Other parameters are the same as in Fig. 2.

The splitting of the soliton into three pulses is shown in the Fig. 3. Maximum temporal sep-

aration between output pulses detected by autocorrelation curve (Fig. 3(b)) and wide-bandwidth oscilloscope (Fig. 3(d)) is 25 ps. Due to the Raman scattering a high-intensity pulse appears after the propagation through only 0.1 km of the fiber (Fig. 3(a)). The central frequency of this pulse is red-shifted ($\omega_0 - \bar{\omega}$) = 0.36 THz. Two other pulses that appears after propagation 0.4 km in DOF have frequency shifts -0.08 THz and 0.04 THz correspondingly. As result the output spectrum become broadened (Fig. 3(c)). Fine structure of the spectrum envelope arises due to interference between frequency shifted pulses.

The temporal separation between output pulses increases with the increasing of the peak intensity of input pulse (Figs. 4(a) and (b)). The pulse splitting process begins after one half of the modulation period of DOF (Fig. 4(a)). In this regime the maximum temporal separation equal to the half of the period of initial pulse sequence $T/2 = 50$ ps was achieved.

Due to the stimulated Raman scattering the spectrum mainly broadens into the range of long wavelengths. The spectrum of the pulse with the highest peak intensity (Fig. 4(c), $1555 \text{ nm} < \lambda < 1560 \text{ nm}$) separates from the spectra of other two pulses.

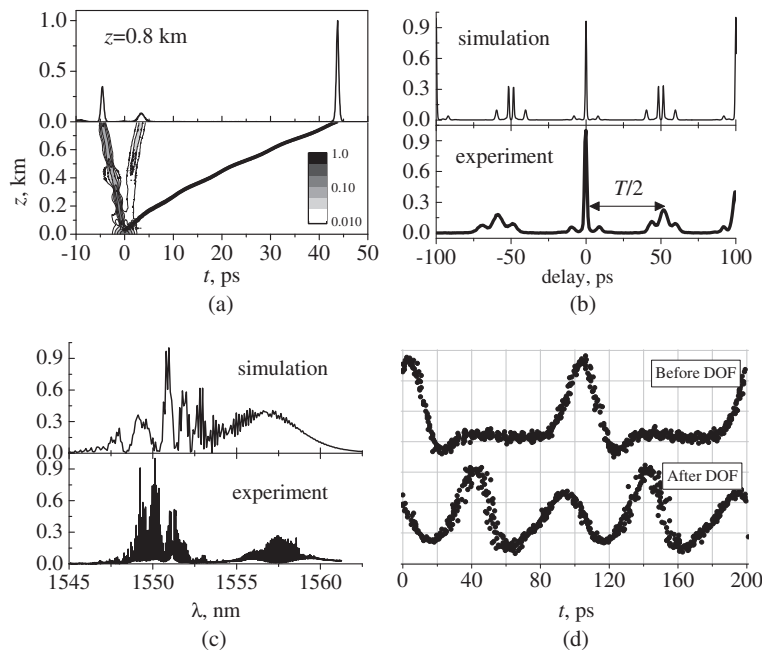


Figure 4: Doubling of the pulse repetition rate. (a) Contour plot of pulse trajectory (bottom) and intensity pulse shape at $z = 0.8$ km (top); (b) autocorrelation traces for output pulses; (c) output spectrum; (d) oscilloscope record. Input power is 325.5 mW, $N = 3.1$. Other parameters are the same as in Fig. 2.

4. CONCLUSION

In conclusion, we have proposed the novel method to multiply the pulse repetition rate of high frequency pulse train in passive fiber. The soliton splitting initiated by DOF was demonstrated. Good qualitative agreement between theory and experiment takes place. Optimization of DOF parameters will allow construction of the all-fiber high-repetition rate source which will produce transform-limited, sech-shaped pulses. Due to the periodical modulation of the fiber dispersion carrier frequencies of resulting pulses are located symmetrically with respect to the initial pulse frequency while the intrapulse Raman scattering contributes to the long-wavelength portion of the spectrum. The initial phase of dispersion modulation function of DOF plays an important role in soliton fission. The splitting process is mainly dependent on the soliton order N which is determined by the pulse peak intensity. Modulation of the pulse peak intensity allows to control both the temporal separation between output pulses and width of output spectrum. The technique described here is simple and efficient.

ACKNOWLEDGMENT

This study was supported in part by BRHE REC-006 and RFBR 08-02-12091of grants. Authors wish to thank Dr. K. V. Reddy for his contribution to this work. A. Sysoliatin's e-mail address is

alexs@fo.gpi.ru.

REFERENCES

1. Ohkuma, K., Y. H. Ichikawa, and Y. Abe, "Soliton propagation along optical fibers," *Opt. Lett.*, Vol. 12, No. 2, 516–518, 1987.
2. Golovchenko, E. A., E. M. Dianov, A. M. Prokhorov, and V. N. Serkin, "Decay of optical solitons," *JETP Lett.*, Vol. 42, 87–91, 1985.
3. Tai, K. and A. Hasegawa, "Fission of optical solitons induced by stimulated Raman effect," *Opt. Lett.*, Vol. 13, 392–394, 1988.
4. Dianov, E. M., A. Y. Karasik, P. V. Mamishev, A. M. Prokhorov, V. N. Serkin, M. F. Stelmah, and A. A. Fomichev, *JETP Lett.*, Vol. 41, No. 6, 294–297, 1985.
5. Wai, P. K., C. R. Menyuk, Y. C. Lee, and H. H. Chen, "Nonlinear pulse propagation in the neighborhood of the zero dispersion wavelength of monomode optical fibers," *Opt. Lett.*, Vol. 11, 464–466, 1986.
6. Agrawal, G., *Nonlinear Fiber Optics*, Academic Press, 1989.
7. Sears, S., M. Soljacic, M. Segev, D. Krylov, and K. Bergman, "Cantor set fractals from solitons," *Phys. Rev. Lett.*, Vol. 84, 1902–1905, 2000.
8. Lee, K. and J. Buck, "Wavelength conversion through higher-order soliton splitting initiated by localized channel perturbations," *J. Opt. Soc. Am. B*, Vol. 20, 514–519, 2003.
9. Smith, N. J., F. M. Knox, N. J. Doran, K. J. Blow, and I. Bennion, *Electron. Lett.*, Vol. 32, 54, 1996.
10. Driben, R. and B. A. Malomed, "Split-step solitons in long fiber links," *Opt. Commun.*, Vol. 185, 439–456, 2000.
11. Driben, R., B. A. Malomed, and P. L. Chu, "Solitons in regular and random split-step systems," *J. Opt. Soc. Am. B*, Vol. 20, No. 11, 2338–2348, 2003.
12. Inoue, T., H. Tobioka, and S. Namiki, "Stationary rescaled pulse in alternately concatenated fibers with $O(1)$ -accumulated nonlinear perturbations," *Phys. Rev. E*, Vol. 72, 025601(R), 2005.
13. Hasegawa, A. and Y. Kodama, "Guiding center solitons," *Phys. Rev. Lett.*, Vol. 66, 161–164, 1991.
14. Bauer, R. G. and L. A. Melnikov, "Multi-soliton fission and quasi-periodicity in a fiber with a periodically modulated core diameter," *Opt. Commun.*, Vol. 115, 190–195, 1995.

Application of Bioradiolocation for Estimation of the Laboratory Animals' Movement Activity

L. N. Anishchenko¹, A. S. Bugaev², S. I. Ivashov¹, and I. A. Vasiliev¹

¹Remote Sensing Laboratory, Bauman Moscow State Technical University, Russia

²Moscow Institute of Physics and Technology, Russia

Abstract— A method for estimation of the laboratory animals' movement activity by means of bioradar is proposed. The method could be used in time of zoo-psychological and pharmacological experiments. The experimental results for different states for the animal are presented. Specific features of frequency spectrums for these states are analyzed.

1. INTRODUCTION

Radiolocation of biological objects named as bioradiolocation is an intensively developing area of bio-medical engineering. There are some important medical tasks which could be applications fields of radiolocation, among them are disaster medicine (searching of survivals under debris and rubbles of buildings), monitoring of breath and heart beating parameters for burned patients (it would cut down the number of used contact sensors and thus decrease the risk of infection inoculation into burning wounds), sleep apnea diagnostics, monitoring of breath and heart beating parameters for sick persons, which are the carriers of extra-hazardous infections (it would decrease the risk of medical staff infection), and etc [1, 2].

Besides the over listed fields of application there is an interest in usage of bioradiolocation for remote diagnostics of rats and other laboratory animals by estimation of their moving activity in time of zoo-psychological and pharmacological experiments.

At present, invasive methods of physiological parameters determination are used during testing of some medicine and poisonous substances on laboratory animals. Their moving activity used to be estimated visually by researcher. It could be pointed another method that is currently in use for animals' behavior reaction analysis. Specially designed video tracking system such as Ethovision [3] can be applied to decrease a workload of the researcher and create automatic approach to estimation of moving activity. The main disadvantage of this type of systems is necessity to use sophisticated software and some restriction on long time recording with duration more than several hours because of data storage capacity limitations. So, that is why in most cases estimation of rats' moving activity is carried out by researcher visually [4], which might cause in the quality of obtained information.

Doppler radar has advantage of direct measurements of animal's moving parameters. It can be used for creation of a fully automatic moving activity integral estimation procedure. In this case the size of data is so small comparing to the video file that it would allow to record data continuously during several days or more. Moreover in condition of creation special recognition algorithms of radar signals that were reflected from animal, it would be possible to discriminate different types of its movements (horizontal and vertical activities, grooming, steady state). In that case bioradiolocation can be also applied to data analysis of the open field experiments.

Several experiments were carried out to investigate possibilities of laboratory animals' movement estimation by means of radar. These experiments and their results are given below.

2. EXPERIMENTAL INSTALLATION

Multi-frequency radar with quadrature receiver designed at the Remote Sensing Laboratory was used in experiments with laboratory rats. The radar had following technical characteristics:

Number of frequencies	16
Sampling frequency	62.5 Hz
Operating frequency band	3.6–4.0 GHz
Distance space resolution	0.5 m
Recording signals band	0.03–5 Hz
Dynamic range of the recording signals	60 dB
Dimensions of antennas block	150 × 370 × 370 mm

This radar was created for distant monitoring of movement activity, breathing and pulse of human. But it could be also used for tracking movement of small laboratory animals. The main

problem is that the rat is just a little bit bigger than space resolution ability of the device. And since the bioradar was created for human's observation, the heartbeat frequency band of rats (6–7.5 Hz [5]) is higher than recording signal band.

Sketch of the experimental set up for estimation of animal's movement activity by means of radar is given on Figure 1. During experiment the animal was placed into a box with dielectric walls. Transmitting and receiving antennas of the radar were pointed to the box.

The signal reflected from the animal was recorded for further processing. Distance between antennas' block and carton was approximately 1 m. Such short distance was caused by relatively small scattering cross section of an animal. Video signal was recorded also by means of a simple web-camera placed over the box. Information about behavior and movement activity of the animal during the experiment recorded by the camera was used for comparison with and identification of radar signals. This gives possibility to recognize different type of animals' movement and its behavior.

Two albino female rats 4 months old were used as experimental animals.

Several short term experiments were carried out, during which all types of animal's behavior were present. Data base of such signal is used for creation of a signal processing algorithm, which should be able to recognize vertical and horizontal movements of a rat automatically.

3. RESULTS OF THE EXPERIMENTS

Below the results of the experiments are presented. In Figure 2 record of radar signals reflected from the animal is shown. Periods of steady state and movement activity can be well recognized even without any additional processing.

For further processing special algorithm for space focusing were created. This algorithm is used for estimation the distance to the object of investigation. The result of the signal processing in

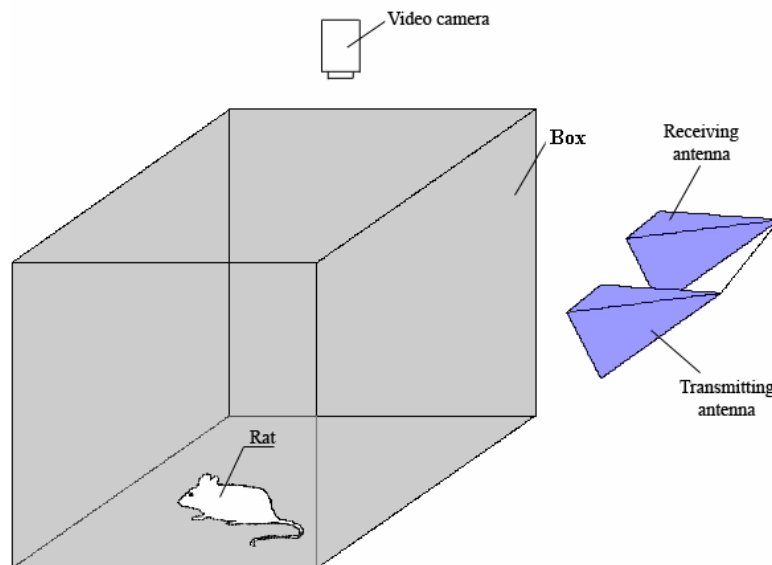


Figure 1: Sketch of the experimental installation.

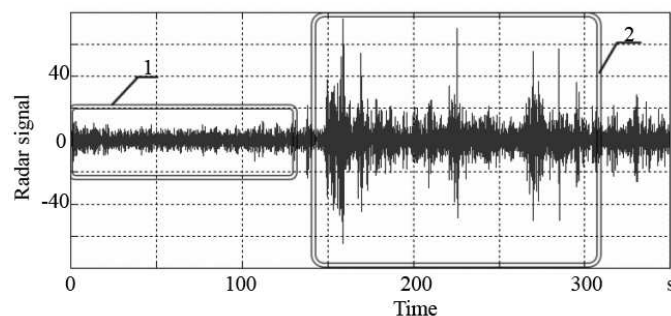


Figure 2: Radar signal reflected from an animal (1 — steady state, 2 — physical activity).

this case is “range-frequency” matrix. The cells of the “range-frequency” matrix where object is located contain information about frequency spectrum of the received signal.

Specific frequency spectrums for different animal condition were obtained. They are given in Figure 3. The spectrums differ one from another greatly by magnitude and form. That is why it is possible to distinguish grooming from steady state, sleeping or active movement of the animal. To make it easier to compare the frequency spectrums for different states of the animal, amplitude of the frequency spectrum is represented by using of nonlinear scale for vertical axis that is proportional to square root of amplitude.

In Figure 3(a) the spectrum for active movements of animal is presented. During the experiment the rat was exploring internal space of the box floor. It was moving along walls of the box and sometimes took vertical positions. The main feature of the received frequency spectrum in this case is its maximum amplitude. It is much higher than for any other state of the rat. In Figure 3(b) the spectrum for a steady state is given. It is clearly seen that the maximum amplitude in this case is more than 3 times lower than for the active movements. During the experiment the rat was calmly sitting in the corner of the carton and rarely moved its head or turned.

Figure 3(c) presents the spectrum while the rat was sleeping. Power of the received signal in this case is extremely low. But because of fact that the animal was not moving at all the breathing harmonic of the rat can be seen on the spectrum. The breathing frequency of the rat during sleeping was 1.5 Hz. This is in good agreement with available data [5].

Spectrum for grooming movements of the rat is given in Figure 3(d). The specific feature of the spectrum is a local maximum near 4 Hz. There is no any published information about typical frequencies for grooming. But radar measurements give experimental results that grooming frequency band spans from 2 to 4 Hz and greatly depend on time of day. During daytime the grooming frequency was lower at for night. The main problem of this type of movement is that the animal can turn during grooming very intensively and these movement artifacts may mask the valid signal.

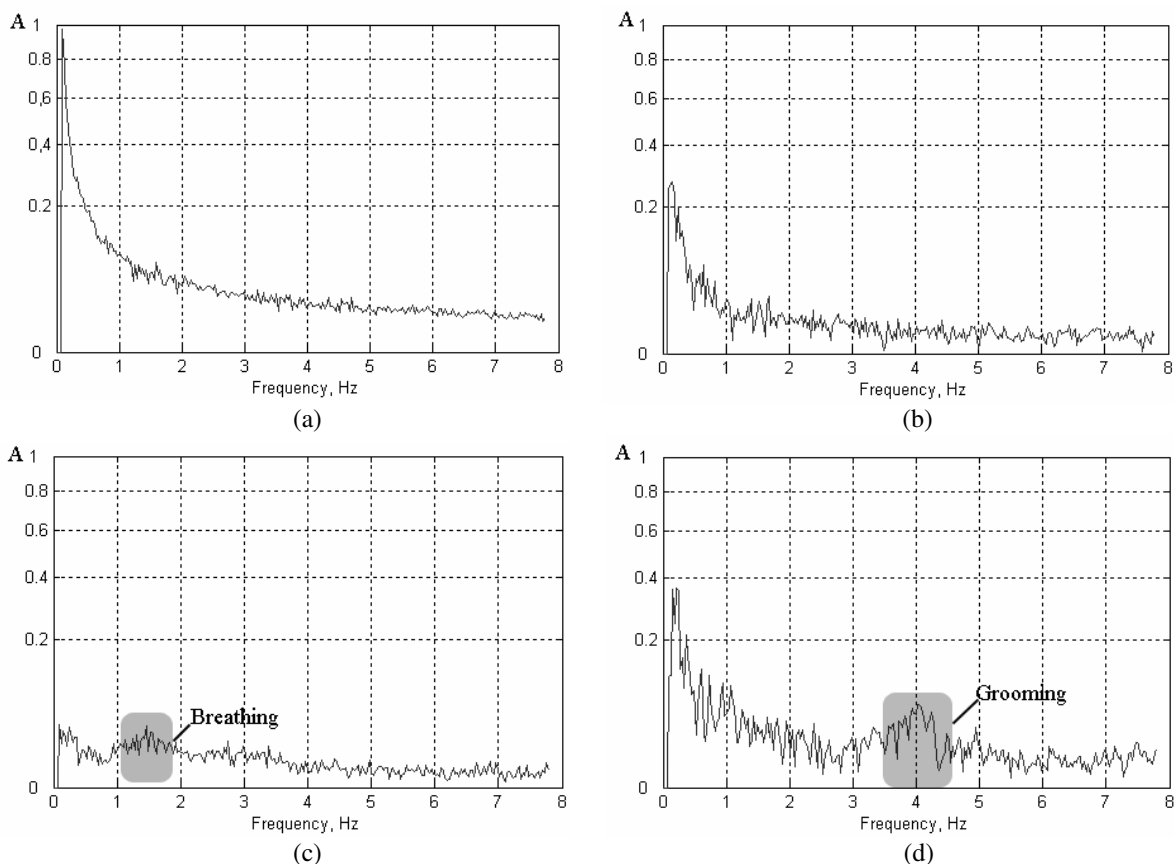


Figure 3: The frequency spectrums amplitudes A of the radar signals for animal’s different conditions ((a) — active movements, (b) — steady state, (c) — sleeping, (d) — grooming).

4. CONCLUSIONS

Bioradiolocation can be used for estimation of movement activity of small laboratory animals. It is possible to distinguish different states of animal. It was shown that while sleeping breathing frequency of the animal can be estimated without any additional procedures. This could be enough for control of animal state in pharmacology.

At present algorithms for vertical and horizontal rats' movement activity is under construction. After creating such algorithm it will be possible to use bioradiolocation not only in pharmacology, but also in zoo-psychology for observation of animal movement in the open-field.

A new bioradar is supposed to be created. It will operate at higher frequency band of 14–15 GHz. This would increase resolution capability of the radar at experiments with small laboratory animals and thus improve the quality of received information.

ACKNOWLEDGMENT

Support for the research was provided by the grants of the Russian Foundation for Basic Research # 09-07-00038-a and the Russian Science and Education Ministry # 2.1.2/700.

REFERENCES

1. Staderini, E. M., "UWB radars in medicine," *IEEE Aerospace and Electronic Systems Magazine*, 13–18, January 2002.
2. Ivashov, S. I., V. V. Razevig, A. P. Sheyko, and I. A. Vasilyev, "Detection of human breathing and heartbeat by remote radar," *Progress In Electromagnetics Research Symposium*, 663–666, Pisa, Italy, March 28–31, 2004.
3. Site of the firm Noldus, Ethovision 3.1, <http://www.noldus.com/animal-behavior-research/products/ethovision-31>.
4. Ciešlar, G., J. Fiolka, J. Mrowiec, et al., "Influence of long-term exposure to static, high voltage electric field antioxidant activity in rats," *XXVIIIth General Assembly of the International Union of Radio Science 2005*, New Delhi, India, [http://rp.iszf.irk.ru/hawk/URSI2005/pdf/K06.1\(0462\)](http://rp.iszf.irk.ru/hawk/URSI2005/pdf/K06.1(0462)), Vol. 34, No. 10, 1064–1076, 1986.
5. <http://www.labanimal.ru/?catid=10#3>.